Defects in Semiconductors
ICDS-19
Part 2

Editors:

Gordon Davies and
Maria Helena Nazaré

ttp TRANS TECH PUBLICATIONS

Materials Science Forum

ISSN 0255-5476

As of January 1992 combined with Crystal Properties and Preparation

See back inside cover for scope and subscription information

REPORT DOCUMENTATION PAGE

Form Approved OMB No. 0704-0188

1. AGENCY USE ONLY (Leave blank)	2. REPORT DATE	3. REPORT TYPE AND DATES COVERED
	23 January 1998	Conference Proceedings

4. TITLE AND SUBTITLE

Nineteenth International Conference of Defects in Semiconductors

5. FUNDING NUMBERS

F6170897W0091

6. AUTHOR(S)

Conference Committee

7. PERFORMING ORGANIZATION NAME(S) AND ADDRESS(ES)

Aviero University
3810 Aveiro
Aveiro
Portugal

8. PERFORMING ORGANIZATION REPORT NUMBER

N/A

9. SPONSORING/MONITORING AGENCY NAME(S) AND ADDRESS(ES)

EOARD
PSC 802 BOX 14
FPO 09499-0200

10. SPONSORING/MONITORING AGENCY REPORT NUMBER

CSP 97-1035

11. SUPPLEMENTARY NOTES

Three volumes.

12a. DISTRIBUTION/AVAILABILITY STATEMENT

Approved for public release; distribution is unlimited.

12b. DISTRIBUTION CODE

A

13. ABSTRACT (Maximum 200 words)

The Final Proceedings for International Conference of Defects in Semiconductors, 21 July 1997 - 25 July 1997

Emphasis will be given on the properties of wide-bandgap materials, including quantum enhancement of effective band-gaps, semiconductors (silicon and III-V materials), plus radiation effects on detector materials. Topics will also include: GaN, Nanostructures, Large bandgap materials, defects in Epitaxial growth, self-organizing rare earth, metastable defects, pairs and complexes, defect reactions, radiation effects on detector material.

14. SUBJECT TERMS

Semiconductors, Electronic Devices

15. NUMBER OF PAGES

1864

16. PRICE CODE

N/A

17. SECURITY CLASSIFICATION OF REPORT	18. SECURITY CLASSIFICATION OF THIS PAGE	19. SECURITY CLASSIFICATION OF ABSTRACT	20. LIMITATION OF ABSTRACT
UNCLASSIFIED	UNCLASSIFIED	UNCLASSIFIED	UL

Defects in Semiconductors
ICDS-19
Part 2

Defects in Semiconductors
ICDS-19

Part 2

Proceedings of the 19th International Conference on Defects in Semiconductors, Aveiro, Portugal, July 1997

Editors:

Gordon Davies and Maria Helena Nazaré

TRANS TECH PUBLICATIONS LTD
Switzerland • Germany • UK • USA

ISBN 0-87849-786-2 (3-Vol. Set)
0-87849-787-0 (Part 1)
0-87849-788-9 (Part 2)
0-87849-789-7 (Part 3)

Volumes 258-263 of
Materials Science Forum
ISSN 0255-5476

***Distributed** in the Americas by*

Trans Tech Publications Ltd
PO Box 699, May Street
Enfield, New Hampshire 03748
USA
Phone: (603) 632-7377
Fax: (603) 632-5611
e-mail: ttp@ttp.net
Web: http://www.ttp.net

and worldwide by

Trans Tech Publications Ltd
Brandrain 6
CH-8707 Uetikon-Zuerich
Switzerland
Fax: +41 (1) 922 10 33
e-mail: ttp@ttp.ch
Web: http://www.ttp.ch

Printed in the United Kingdom
by Hobbs the Printers Ltd,
Totton, Hampshire SO40 3WX

Table of Contents

PART 2

Section 8. Silicon carbide

Section 9. Diamond

Section 10. Indium phosphide

Section 11. Gallium arsenide: Impurities

Section 12. Antisite defects and EL2

Section 13. Gallium arsenide: radiation damage

Section 14. Gallium phosphide

Section 15. Gallium nitride

Section 16. Other III-V compounds

Materials Science Forum Vols. 258-263 (1997) pp. 677-684

THEORY OF 3d TRANSITION METAL DEFECTS IN 3C-SiC

H. Overhof

AG Theoretische Physik, Fachbereich Physik, Universität - GH Paderborn, D – 33098 Paderborn, FRG

Keywords: SiC, transition metal defects, hyperfine interactions

Abstract. Results of ab-initio electronic structure calculations for isolated 3d transition metal defects in 3C-SiC are presented. We discuss isolated point defects located on the Si and on the C lattice sites and also on the two interstitial sites with tetrahedral symmetry. We compare our results with the experimental data (most of which are available to date for the 4H- and 6H-polytypes only). We conclude that some of the states observed by electron paramagnetic resonance and identified to be related to Cr and Mo cannot be isolated substitutional defects.

Introduction.

Transition metal (TM) defects which can be introduced either by doping or which can be present as contaminants usually have several charge states and are electrically active. In silicon the pioneering electron paramagnetic resonance (EPR) studies by Ludwig and Woodbury [1] have provided most of the experimental information about the electronic properties of 3d TM isolated point defects. In the following years also pairs and aggregates of TMs with other point defects in silicon have been studied. Combining both experimental and theoretical studies [2, 3] a nearly complete picture of 3d TM defects in silicon has emerged.

In contrast, our knowledge of the 3d TM point defects in SiC is still rather preliminary (for a recent review of the experimental EPR work, see [4]): For most of the TM defects for which paramagnetic states have been detected by EPR not even the lattice position could be determined experimentally.

Although both constituents of the SiC lattice are group IV elements, several properties of the SiC crystal are more common to ionic compounds than to a covalent semiconductor. Compared to other semiconductors SiC presents the additional difficulty for the theoretical analysis that it has several polytypes with different inequivalent lattice sites and rather large unit cells with low symmetry. To reduce the computational effort we have started our investigation with the simplest polytype, the cubic 3C-SiC lattice which has one type of lattice sites for Si and C only. This appears to be a promising approach because most of the properties of *deep* defects in SiC do not depend much on the polytype and the symmetry of the site: For deep TM levels (see e.g. Baur et al. [4]) and also for the silicon vacancy Vac_{Si} [5] the hyperfine interaction (hfi) constants e.g. are remarkably insensitive to the polytype and the site (quasicubic or hexagonal) of a given sublattice.

However the electronic properties of a given TM defect change immediately if built in on a C site as compared to a TM defect on a Si site. The same is true for TMs as interstitial point defects on the highly symmetrical sites where the TMs are tetrahedrally surrounded by four C ligands (TM_{TC} in the notation of Wang *et al.* [6]) or by four Si (TM_{TSi}) ligands.

Computational.

In our calculations we use the standard Local Spin-Density Approximation of the Density Functional Theory (LSDA-DFT) for the implementation of exchange and correlation effects. The resulting Kohn-Sham equations are solved self-consistently using the Linear Muffin-Tin-Orbital (LMTO) method in the Atomic-Spheres approximation (ASA) [7]. This method has been successfully applied to calculate the electronic structure of TM point defects in Si [3, 8] and also in II-VI semiconductors [9]. We thus have some confidence that the method will work in SiC as well.

Basically in the LMTO-ASA method the crystal is represented by overlapping spheres centered around the atomic sites ("atomic spheres"). In order to fill the space without too much overlap

defect	TM_{Si}		TM_C		TM_{TC}		TM_{TSi}	
	$E^{+/0}$	$E^{0/-}$	$E^{+/0}$	$E^{0/-}$	$E^{+/0}$	$E^{0/-}$	$E^{+/0}$	$E^{0/-}$
Vac	0.54	1.06	2.3	–				
Sc	–	0.35	2.0	2.1	–	–	1.9	–
Ti	–	–	2.25	–	–	–	1.7	2.5
V	1.95	–	2.1	–	–	–	1.1	1.8
Cr	1.45	–	1.8	–	2.05	2.6	0.45	–
Mn	1.8	–	1.7	2.5	1.5	2.0	–	–
Fe	1.55	–	1.6	–	1.2	1.9	2.1	–
Co	2.15	–	–	–	1.35	2.8	–	–
Ni	1.1	1.85	–	–	0.5	–	–	–
Mo	1.1	1.85	–	–	0.5	–	–	–

Table 1:
Calculated charge transfer energy levels (in eV above E_v) for the vacancies and isolated TM point defects at the high-symmetry positions for 3C-SiC. Only single donor and single acceptor levels are given, – indicates that the level does not exist in 3C-SiC.

one introduces additional spheres centered around the tetrahedral interstitial TC and TSi ("empty") sites. In our calculations we use a Green's function approach. The Green's function G of the crystal with a point defect is obtained from the Green's function G_0 of the unperturbed crystal by solving a Dyson equation in the rather small volume surrounding the point defect where the impurity potential ΔV is strong. Thus most of the symmetry information of the underlying crystal is contained in G_0 while the chemical information is supplied by ΔV. This method offers the advantage that real isolated point defects are treated in an otherwise perfect lattice and that charge states and spin states can be chosen at will. The main disadvantage is that the use of the ASA prevents us from treating lattice relaxations.

When this method is applied to cubic SiC one major change with respect to the Si case stems from the fact that the lattice is made up from two different atoms, C and Si, with quite different covalent radii and ionicities. If we use the same radius (the Wigner-Seitz radius) for all atomic and empty sites we end up with Si atomic spheres that contain two valence electrons only, while the C atomic sphere contains 4.3 electrons. Fixing the ASA sphere radii in such a way that the number of valence electrons contained in the Si and C spheres are nearly equal we would end up with a C atomic sphere volume that is only 1/3 of that of the Si atomic sphere. Such a small atomic sphere presents nasty problems for $3d$ TM defects substituting for C: we have to divide the electron states into core states of the inner s and p shells and into valence states in our approach. This cannot be done properly unless the core states fit into the ASA spheres. For the lighter $3d$ TM elements with rather extended $3p$ states this condition cannot be satisfied when located in the small C (and TSi) spheres .

We, therefore, have taken the ASA sphere radii as 2.14 r_B and 1.885 r_B, respectively, which results in 2.37 (3.88) valence electrons in the Si (C) atomic sphere. The rest of the valence charge is found in the larger TC (1.14 unit charges) and the smaller TSi atomic spheres (0.60 unit charges). For the early $3d$ TMs on the carbon sites we find even with this rather moderate choice of the ASA sphere radii that the $3p$ states do not fit well into the ASA spheres. We, therefore, had to treat the $3p$ states for Sc to Cr (and also the $4p$ states for Mo) as valence states. We have further made use of the scissors operator technique by Baraff and Schlüter [10] in order to adjust the LDA fundamental band gap for cubic SiC (1.3 eV) to the experimental value of 2.3 eV.

In the following we discuss the electronic structure of TM point defects in terms of energies for the single particle states (which are the eigenvalues determined self-consistently from the Kohn-Sham equations see e.g. [3]) and also in terms of charge transfer energies. The latter are determined

by a comparison of the total energies obtained for a given point defect in the two charge states in question.

Results.
For $3d$ TM defects in silicon, Zunger [2] and Beeler et al [3] have shown how the single particle states change if one passes along the TM series. In a previous paper [11] we have shown the differences of electronic structure for TM point defects in SiC with respect to Si. In particular we have emphasized that the electronic structure is quite different for point defects on the Si and the C sites, respectively. In a similar way TM defects on TM_{TC} and TM_{TSi} interstitial sites have been shown to be different. In Table 1 we give a list of the single donor and single acceptor charge transfer energy levels $E^{+/0}$ and $E^{0/-}$ for all substitutional $3d$ TM defects.

We can summarize these results by stating that for all TM point defects on Si and on C sites we find low-spin ground states for all charge states. For Mn_{Si}, Fe_{Si}, Co_{Si}, and Ni_{Si} high-spin states are also possible, however these turn out to be excited states with an excitation energy in the 0.2 to 0.8 eV range. In all other cases of substitutional $3d$ TM point defects we do not even find a gap state configuration that could give rise to a possible high-spin.

It is interesting to compare the electronic structures of $3d$ TM_{Si} in crystalline silicon with that of the same TM_{Si} on an analogous site in 3C-SiC. In Fig. 1 we display the magnetization densities and induced particle densities for Fe_{Si} in the high-spin state (S=4/2) in Si [8] and in 3C-SiC. Although for the 3C-SiC lattice the nearest neighbor distances are considerably smaller we see immediately that the magnetization density for Fe_{Si} in Si is much more localized as compared to Fe_{Si} in 3C-SiC. In particular the magnetization densities at the nearest and next nearest neighbors are significantly

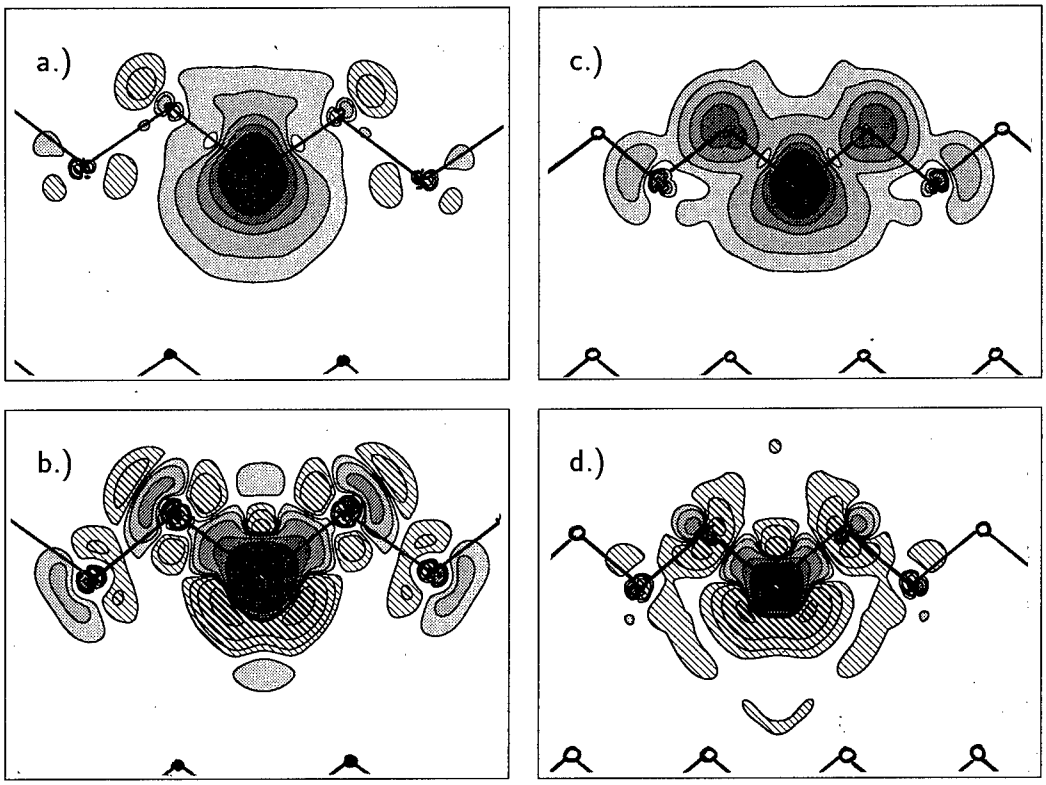

Figure 1: Contour plot in the 110 plane of the magnetization density (a.) and of the total induced particle density (b) of substitutional iron in silicon in the high-spin (S=4/2) state compared to Fe_{Si} in 3C-SiC (c.,d.) Hatched areas indicate negative densities.

different for both lattices. In contrast, the induced particle density (that is the difference between the particle densities of the crystal with a TM_{Si} and that of an undisturbed crystal) is much more localized for Fe_{Si} in SiC when compared with Fe_{Si} in Si. This is rather unexpected: in Si and in more ionic compound semiconductors (see e.g. [9] for 3d TMs in CdTe) the magnetization densities are considerably more localized than the induced particle densities. Of course the induced particle densities cannot be observed experimentally. The magnetization densities, however, can be compared with experimental ligand hfi data. The comparison [8, 9] convincingly shows that the theoretical magnetization densities are realistic.

An interstitial TM in the TC position has relatively much space because it is surrounded tetrahedrally by the four small carbon atoms. This TM is further surrounded by six relatively large silicon atoms which, although somewhat farther apart, nearly balance the crystal field of the nearest neighbors. The crystal field splitting in this case is very small and we have a high-spin ground state for all 3d TM_{TC} defects in all charge states.

For the TSi position of the TM interstitials the nearest neighbors are the rather large Si atoms which give rise to a large crystal field splitting which cannot be significantly reduced by the smaller and more distant carbon next nearest neighbors. Consequently the interstitials at the TSi positions again have a low-spin ground state and their single particle state energy eigenvalues are generally lower than those of the TC interstitials.

In principle one can determine the likely positions for point defects in thermal equilibrium calculating the total energies for the different lattice sites. In this study we are limited to total energy calculations without lattice relaxations. Wang et al [6] have shown for simple point defects in cubic SiC that relaxation energies can be as large as a few eV. Therefore a comparison of unrelaxed total energies for TM point defects does not seem meaningful.

Since the SiC lattice is so compact the exchange energy splitting of the single particle states (and in particular of those states that transform according to the e irreducible representation of T_d) is at least as large as in the case of the TM impurities in Si. Because screening in the more ionic SiC compound is less effective than in Si, the charge transfer energies for the different charge states differ more strongly than in the case of Si.

The general trends have already been reported in [11]. We therefore shall concentrate in the main part of this paper on results for the relatively few TM species for which experimental data have been reported so far. Since relatively little work has been done for 3C-SiC we shall rely on the fact that experimentally the paramagnetic properties of TM defects do not differ much in the different polytypes.

Scandium.

In Fig. 2 we sketch the energetic positions of the single particle energies calculated for an isolated Sc atom, the Vac_C and Vac_{Si} vacancies, and for the Sc_C and Sc_{Si} TM point defects in the neutral charge state (we shall always give the charge state of a defect rather than the formal oxidation state throughout this paper).

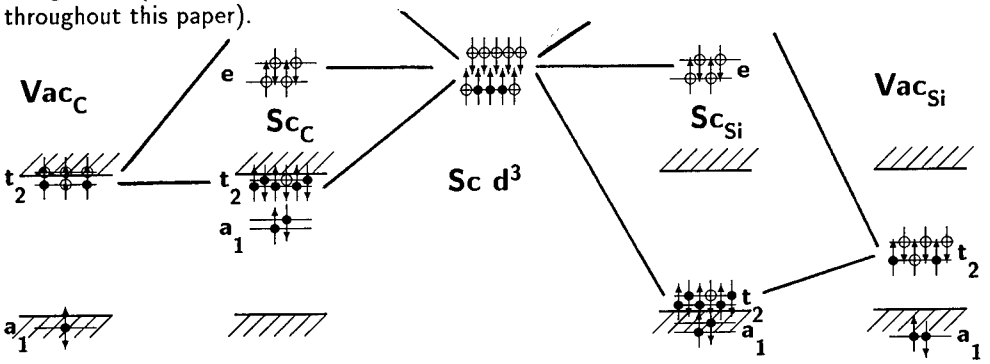

Figure 2: Single particle energies for a Sc atom (center), the two vacancies, and the two Sc substitutional point defects.

defect	TM_{Si}	TM_C	TM_{TC}	TM_{TSi}	exp.[a]
^{45}Sc	20.7	30.2	–	58.2	54.
^{51}V	-89.5	-6.6	-45.0	-52.0	180.
^{53}Cr	3.5	4.3	14.5	0.7	$\sim$ 27.
^{95}Mo	38.0	7.0	20.2	–	90.

[a]Baur et al. 1997

Table 2:
Mean isotropic part (in MHz) of the hyperfine interaction with the TM nucleus calculated for various tetrahedral lattice positions are compared with averaged experimental data.

The atomic $3d$ states are split by the crystal field into states that transform according to the e and the t_2 irreducible representations, respectively. For the e-like states there are no vacancy orbitals to interact with. For Sc being an "early" $3d$ atom the d-states are only loosely bound and, therefore, the e-like states are resonances located some 5 eV above the conduction band edge and hardly resolved at all. For $3d$ TMs that are heavier than vanadium the e-like states form localized states in the gap. The d-states that transform according to t_2 interact with the dangling-bond states and form bonding and anti-bonding states. The dangling bond states that transform according to the t_2 irreducible representation are located in the lower half of the fundamental band gap for the silicon vacancy Vac_{Si} (the state that transforms according to a_1 gives rise to a resonance just below the valence band edge). For Sc the resulting bonding t_2 state has a significantly larger energetic distance to the atomic Sc- d states as compared to the distance to the Vac_{Si}-derived t_2 states. This ensures that the bonding gap state thus formed is essentially dangling-bond like with ($\sim$ 12 %) Sc d-admixture. This can be seen in Fig. 3 a where the magnetization density for Sc_{Si} is displayed in a (110) plane. Since the p-like magnetization density is with $\sim$ 4% only a factor of three smaller than the d-like magnetization density, the dipolar hyperfine coupling for Sc_{Si} stems predominantly from the p-like dangling bonds and is similar to the dipolar coupling of the Vac_{Si} vacancy states. The anti-bonding states that transform according to t_2 are resonances that are situated high up in the conduction band, but still d-like in character.

For the $3d$ TMs on the carbon lattice site the electronic structure of the C vacancy leads to remarkable differences: The dangling bond states of the carbon vacancy Vac_C (see Fig. 2) give rise to localized gap states that transform according to the a_1 (fully occupied) and the t_2 irreducible representations and both states are located in the upper half of the fundamental band gap. As in the case of Vac_{Si} the t_2 states are only partially occupied. Since the energetic position of the t_2 states of Vac_C is close to the conduction band edge, for most TMs these dangling bond states will be higher in energy than the TM-derived d-states.

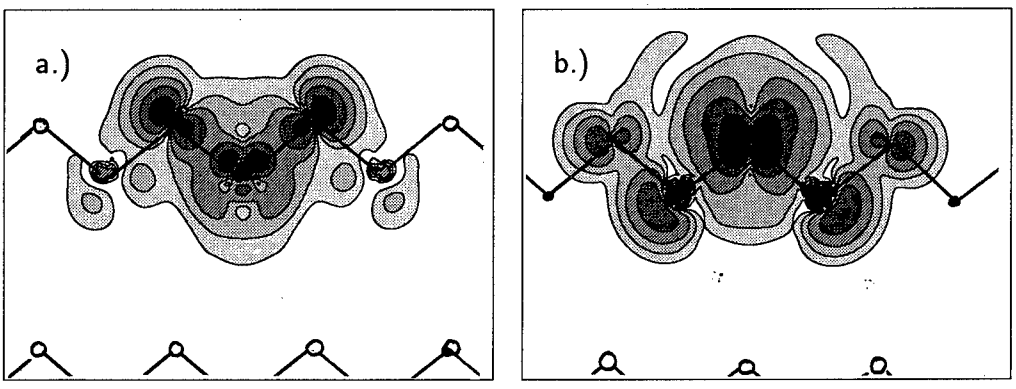

Figure 3: Contour plot of the magnetization density in the (110) plane for Sc in 3C-SiC a.) on a Si site and b.) on a C site.

This has the consequence that the bonding t_2 states of the substitutional TM on a carbon site will be predominantly d-like with little resemblance to dangling bonds. For Sc_C (see Fig. 3 b) the t_2-like bonding gap state shows a 40 % d-admixture.

orbital	$a(Sc_C)$
1s	–26.4
2s	–99.1
3s	+ 29.6
valence band	+ 114.1
total	+ 30.2

Table 3:
Contributions from the core shells (in MHz) to the isotropic part of the hyperfine interaction with the Sc_C nucleus.

Hence the dipolar hyperfine interaction of Sc_C is due to the d-like spin density. Comparing the dipolar hfi of the Sc_{Si} and Sc_C point defects we find that both dipolar interactions with the Sc nucleus are comparable.

No Sc-related defects have been reported to date in 3C-SiC. Instead, EPR results for 6H and 4H SiC have been reported [12, 13] which have been analyzed as S=1/2 centers with an anisotropic hfi. While in [13] it is assumed that the paramagnetic state observed in 6H-SiC is due to a Sc_{Si} point defect the Paderborn group provides evidence that it must be a neutral Sc_C point defect instead. There are essentially two arguments that substantiate the Sc_C interpretation: the ligand hfi with four Si ligands has been resolved by [12] which strongly suggests that there are four nearest Si neighbors. For a Sc_{Si} point defect our calculations show that the hfi with the four ^{13}C nearest neighbor ligands could not have been overlooked. Another strong argument for the Sc_C utilizes the fact that the EPR spectra are observed in thermal equilibrium simultaneously with nitrogen. Since nitrogen is a shallow donor and diamagnetic when ionized the samples must have been n-type (see Table 1). According to our calculations a Sc_{Si} point defect cannot be paramagnetic except in p-type material. For Sc a deep acceptor level has been observed in photocapacitance measurements [14] at E_v + 0.55 eV. This level could be due to a Sc_{Si} point defect.

If we compare the calculated isotropic hfi with the ^{45}Sc nucleus with the value observed experimentally we find a large discrepancy for the Sc_C point defect whereas the agreement for the Sc_{TSi} point defect would be nearly perfect. From our previous calculations of the isotropic hfi of $3d$ TM point defects in Si [8] and in CdTe [9] we conclude that this must not be considered as an argument that Sc is located on a Si lattice site: In all cases the calculated isotropic hfi values for $3d$ TM point defects values have been found to be smaller in modulus than the experimental values and the discrepancy usually was as large as a factor of two. This should be contrasted with the much closer (~10 %)agreement of the calculated values for the contact interaction when compared with experimental data.

The explanation is not quite clear: For the s-like a_1 states the contact hfi arizes from the magnetization density at the nucleus. For d-electrons the magnetization density at the nuclear site is zero. The observed isotropic hfi arises from a polarization of the s-electrons in the inner "core" shells and in the valence band due to the exchange interaction: the exchange interaction is more attractive for the majority spin and tends to expand the majority spin component of the very localized $1s$ and $2s$ shells while the $3s$ and valence band majority spin states are less localized than the $3d$ states and therefore contracted. The resulting contributions displayed in Table 3 show that the resulting value is the rather small difference of rather large contributions. This alone would account for some scatter of the theoretical data. The fact that our calculated data are systematically smaller than the experimental data must be attributed to a deficit of the LDA.

Titanium.

Titanium, omnipresent in SiC as a contaminant emerging from graphite components in the growth apparatus, does not produce a gap state in 3C-SiC. It is, however, known that the Ti_{Si} isoelectronic neutral point defect binds excitons [17]. For Ti_{Si} in 3C-SiC we do not find a gap state since the bonding states transforming according to t_2 form a resonance 0.5 eV just below the valence band edge. The lowest unoccupied single particle state transforms according to the e irreducible representation and is calculated to be 1.2 eV *above* the conduction band edge in 3C-SiC in general agreement with location of the acceptor level observed in 4H-SiC [15, 4, 16]. The anti-bonding t_2 single particle state is a week resonance very high in the conduction band.

According to our calculations there is no alternative to the Ti_{Si} lattice site: Ti_C would have a

gap state with $E^{+/0} = E_v + 1.9$ eV and would be paramagnetic with S = 1/2 for p-type samples. Both the TC and the TSi interstitials would also give rise to gap states, in the positive charge state the $^4A_2$ orbital singlet ground state certainly would not have been missed by EPR experiments, if this defect was present.

Vanadium.

Vanadium is another deep TM contaminant originating from the graphite. For the V_{Si} point defect we find a donor level at $E^{+/0} = E_v + 1.95$ eV which compares well with the level at $E_v + 1.7$ eV found experimentally [18] for 3C-SiC. Neutral V_{Si} is found to be paramagnetic with a ^2E ground state in 3C-Sic. According to our calculation the excited $^2T_2$ state is found to be higher in energy by 1.0 eV, a value that compares well with the 0.83 eV found experimentally [18]. From the extensive EPR work the hfi with the ^{51}V nucleus is found to be subject to a (dynamical) Jahn-Teller effect. The isotropic hfi $a_{exp} = 180$ MHz found experimentally [18] is again a factor of two larger than our calculated value of $a_{theor} = 87$ MHz (see Table 1) as is common for LSDA calculations of the hfi with $3d$ TM ions in semiconductors [8, 9].

Negatively charged V_{Si}^- has been observed by EPR [4] in 6H-SiC and in 4H-SiC, but not in 3C-SiC. According to our calculations the negative charge state is not stable in 3C-SiC because the e single particle state moves just above the conduction band edge if doubly occupied.

The identification of the experimentally observed vanadium-related defects with V_{Si} is corroborated by our calculations as most properties found experimentally are compatible with our results. The V_C defect, which has a donor level at $E^{+/0} = E_v + 2.2$ eV and an excited level at $E_c + 1.6$ eV, would give rise to a hfi with the ^{51}V nucleus that amounts to $a_{theor} = -6.6$ MHz only and this discrepancy to the experimental value cannot be accounted for. The TC and TSI interstitial positions for vanadium defects can be ruled out: V_{TC} would have four different spin states in 3C-SiC which could not have passed unobserved. The V_{TSi} point defect would have both a Spin 1/2 and a Spin 2/2 paramagnetic state as is observed experimentally for the V defect. The charge transfer energy level would be $E^{+/0} = E_v + 1.1$ eV and in contrast to the experimental observation the lower V_{TSi}^+ state would have the Spin = 2/2.

Chromium.

Our calculations give two charge transfer energy levels for Cr_{Si}, with $E^{++/+}(Cr_{Si}) = E_v + 0.65$ eV and $E^{+/0}(Cr_{Si}) = E_v + 1.45$ eV. Strangely enough, neither the Cr_{Si}^+ state (^2E with S = 1/2) nor the Cr_{Si}^0 state ($^3A_2$ with S = 1, i. e. an orbital singlet) have been detected by EPR. In contrast, two states of Chromium with $3d^3$ and S = 3/2 and one $3d^4$ state with S = 4/2 have been detected in 6H-SiC [19, 20]. From the results of our calculations for chromium in 3C-SiC we must conclude that the states in question cannot be identified with the Cr_{Si}^- or Cr_{Si}^{--} acceptor states of Cr: both the ground states of Cr_{Si}^- and Cr_{Si}^{--} would be low-spin (spinless) states and the same would hold for Cr substituting for C. Of course, our calculations treat 3C-SiC instead of 6C-SiC, but for the latter material the additional trigonal field certainly would not weaken the cubic field (which is dominated by the nearest neighbors) and, therefore, the ground state spin should not be different.

Instead we propose that the S = 4/2 state is a neutral Cr_{TC}^0 interstitial while the S = 3/2 state could either be the Cr_{TC}^- interstitial acceptor state or a Cr_{TC}^+ interstitial donor state. Our calculations for 3C-SiC predict that for Cr_{TC}^+ the ground state should be a S=5/2 high spin state but this should not be taken as a firm prediction because

i the trigonal field is not present in our calculations and

ii any lattice relaxation will strongly influence the relative contributions to the crystal field originating from the Si and C neighboring shells.

Hence for the S = 3/2 state a distinction between donor and acceptor state is not really possible.

Molybdenum.

Molybdenum is isoelectronic to chromium and also has two charge transfer energy levels if built in as Mo_{Si}, with $E^{++/+}(Mo_{Si}) = E_v + 1.65$ eV and $E^{+/0}(Mo_{Si}) \approx E_v + 2.3$ eV. This is in line with the observation that in slightly n-type 6H SiC the Mo^+ state is observed which disappears after

p-type doping [21]. In contrast to the case of chromium, the Mo^{+} state (^2E with S = 1/2) and also the Mo^{0} state ($^3A_2$ with S = 1) have been detected by EPR. These findings would be fully compatible with our theoretical results, which also exhibit a $^3T_2 - {}^3A_2$ -splitting of 1.3 eV, in general agreement with the 1.1 eV splitting observed by MCDA [4]. However, as in the case of chromium a molybdenum-related $3d^3$, S = 3/2 state has been found in 6H-SiC and in 15R-SiC which, according to our calculations for 3C-SiC, can also not be identified with the Mo^{-}_{Si} or Mo^{-}_{C} acceptor states of Mo: again both the ground states of Mo^{-}_{Si} and Mo^{-}_{C} are calculated to be low-spin states and there is no possibility to construct high-spin states because of the 1.3 eV $t_2 - e$-splitting for the single particle states.

We tentatively propose that the S = 3/2 state could either be the Mo^{-}_{TC} interstitial acceptor state or a Mo^{+}_{TC} interstitial donor state. Again calculations for 3C-SiC predict that for Mo^{+}_{TC} the ground state should be a S = 5/2 high spin. As in the case of Cr we conclude that for the S = 3/2 of Mo no clearcut distinction between donor and acceptor state can be made on the basis of the present results. This does of course imply that we have Mo on two distinctly different lattice sites in SiC, Mo_{Si} and Mo_{TC}.

Acknowledgements. The author has benefitted from valuable suggestions and open discussions with Prof. J.-M. Spaeth and Dr. S. Greulich-Weber.

References.

[1] G.W. Ludwig and H.H. Woodbury, in Solid State Physics, ed. by H. Ehrenreich, F. Seitz, and D. Turnbull (Academic Press, New York, 1962), Vol. 13, p. 223.
[2] A. Zunger, in Solid State Physics, ed. by H. Ehrenreich, F. Seitz, and D. Turnbull (Academic Press, New York, 1986), Vol. 39, p. 275.
[3] F. Beeler, O.K. Andersen, and M. Scheffler, Phys. Rev. B **41**, 1603, (1990).
[4] J. Baur, M. Kunzer, and J. Schneider, phys. stat. sol. (b) (in press).
[5] T. Wimbauer, D. Volm, B. K. Meyer, A. Hofstaetter, and A. Scharmann, Proc. 23^{rd} Int. Conf. Phys. Semic., ed. by M. Scheffler and R. Zimmermann (World Scientific, Singapore, 1996), p. 2645).
[6] C. Wang, J. Bernholc, and R.F Davis, Phys. Rev. B **38**, 12 752, (1988).
[7] O. Gunnarsson, O. Jepsen, and O.K. Andersen, Phys. Rev. B **27**, 7144, (1983).
[8] H. Weihrich and H. Overhof, Phys. Rev. B **54**, 4680, (1996).
[9] M. Illgner and H. Overhof, Semic. Science and Technol. **11**, 977, (1996).
[10] G. A. Baraff and M. Schlüter, Phys. Rev. B **30**, 3460, (1984).
[11] H. Overhof, MRS Conf. Proc. **442**, 637 (1997).
[12] M. März, J. Reinke, S. Greulich-Weber, J.-M. Spaeth, H. Overhof, E.N. Mokhov, A.D. Roenkov, and E.N. Kalabukhova, Semic. Science and Technol. **98**, 439, (1996).
[13] P.G. Baranov, I.V.Il'in, E.N.Mokhof, A.D.Roenkov, and V. A. Kramtsov, Phys. Solid State **39**, 44, (1991).
[14] V. S. Ballandovich, Sov. Phys. Semicond. **25**, 174, (1991).
[15] K. Maier, H. D. Müller, and J. Schneider, Mat. Sci. Forum **83-87**, 1883, (1992).
[16] T. Dalibor, G. Pensl, H. Matsunami, T. Kimoto, W. I. Choyke, A. Schöner, and N. Nordell, phys. stat. sol. (b) **202**, (1997)(in press).
[17] L. Patrik and W. J. Choyke, Phys. Rev. B **10**, 5091, (1974).
[18] K. F. Dombrowski, U. Kaufmann, M. Kunzer, K. Maier, J. Schneider, V. B. Shields, and M. G. Spencer, Appl. Phys. Lett. **65**, 18 034, (1994).
[19] P. G. Baranov, V. A. Khramtsow, and E. N. Mokhov, Semic. Sci. Technol. **9**, 1340, (1994).
[20] K. F. Dombrowski, Diploma thesis, Freiburg, 1995 (unpublished).
[21] J. Baur, M. Kunzer, K. F. Dombrowski, U. Kaufmann, J. Schneider, P. G. Baranov, and E. N. Mokhov, Proc ISCS-23, St Petersburg, (1996).

Materials Science Forum Vols. 258-263 (1997) pp. 685-690

A DEEP PHOTOLUMINESCENCE BAND IN 4H SiC RELATED TO THE SILICON VACANCY

E. Sörman, N. T. Son, W. M. Chen, C. Hallin, J. L. Lindström and E. Janzén

Department of Physics and Measurement Technology, Linköping University, S-581 83 Linköping, Sweden

Keywords: SiC, vacancy, ODMR, electron irradiation

Abstract. We report on an irradiation induced **p**hotoluminescence (PL) band in 4H SiC and the corresponding **o**ptically **d**etected **m**agnetic **r**esonance (ODMR) signals from this band. The deep PL band has, as expected for the 4H polytype with its two inequivalent defect sites, two no-phonon lines. These are at 1352 and 1438 meV. The intensity of the PL lines is reduced after a short anneal at 750° C. ODMR measurements with above band gap excitation show that four spin triplet (S=1) states with a weak axial character are detected via this PL band. Two of these triplet states can be selectively excited with the excitation-energy of the two PL lines. They can therefore be detected separately and only then can the well documented and characteristic hyperfine interaction of the silicon vacancy in SiC be resolved. Because of the correlation between the irradiation dose and the signal strength, the well established annealing temperature and the characteristic hyperfine pattern, we suggest that this PL band is related to the isolated silicon vacancy in 4H SiC. The spin state (S=1) implies a charge state of the vacancy with an even number of electrons. We therefore suggest that the observed signals are from either the neutral or the doubly negative silicon vacancy.

Introduction.

SiC has for decades been considered to be a very promising semiconductor but several problems, related to the material quality, did earlier prevent a technological exploitation. Now most of this problems have been overcome, high quality material can be grown and research around this material is going through an intense phase of development.

SiC is the classical example of polytypism i. e. it appears in many different but closely related crystal structures. In the unit cell of the 4H SiC crystal there are two possible configurations of the next nearest neighbours around an atom. These two inequivalent atomic sites are referred to as the hexagonal and the cubic site.

The properties that stand out when 4H SiC is compared to the other polytypes are the wide band gap and the high, nearly isotropic electron mobility. Since the polytype is also relatively easy to grow and wafers are sold commercially, it is often the most interesting one for semiconductor device applications.

Ion implantation seems to be the most suitable method to dope SiC. When the material is bombarded with ions (or electrons) with high energy, the atoms in the lattice can actually be pushed out of their places. The primary defects created in this way are the vacancies and interstitials. In a binary compound like SiC, the anti-sites are also regarded as primary defects. In contrast to silicon do the primary defects in SiC seem to be stable at room temperature [1-4]. They are then not only of a great scientific interest but also of great technological, since the primary rather than the secondary defects will have the largest influence on the properties of irradiation damaged material.

The primary defects are also fundamentally interesting. At quite an early stage in semiconductor science (late sixties and early seventies) could **e**lectron **s**pin **r**esonance (ESR) measurements reveal a lot about the microscopic properties of the vacancies in silicon. Less is still known about the vacancy in diamond, but the properties of the negative charge state has been thoroughly analysed by ESR [5]. The different charge states of the vacancy in silicon seem to have a much stronger lattice relaxation than in diamond. The extreme relaxation in silicon results in a reversing of the expected ordering of the different charge states in the band-gap. It is therefore not strange that these two fundamental point defects have served as interesting model cases in the development of defect theories [6]. Since SiC in a way is a mixture of the two, it is now interesting if some of the properties of its vacancies can be investigated.

In optically detected magnetic resonance (ODMR) one measures the fractional change in the luminescence, that a magnetic resonance in a local defect induces. The technique is in a sense complementary to the ESR technique, since the short lived excited states of defects are investigated, rather than the more permanently populated ground states. If the radiation induced defects in 4H SiC form recombination centres, ODMR is the appropriate method to investigate these.

Samples and Equipment.

The samples used were all high quality epitaxial layers, grown by chemical vapour deposition. The nitrogen concentration in these samples is in the 10^{14} cm^{-3} range [7]. In order to produce the primary defects, the samples were irradiated with 2.5 MeV electrons in doses ranging from 10^{16} to 10^{18} cm^{-2}.

For the X-band (≈ 9.22 GHz) ODMR experiments we used a modified Bruker ER-200D electron spin resonance spectrometer equipped with a cylindrical TE_{011} microwave cavity with optical access. UV-light from an argon-ion laser was used for above band gap excitation, while a tuneable Ti:sapphire laser was used for resonant excitation of the studied defects. In the ODMR experiments the luminescence passed appropriate optical filters before detection with a liquid nitrogen cooled germanium photo-diode (North Coast). The PL experiments were carried out using a 0.46 m grating monochromator (Jobin-Yvon) equipped with a silicon CCD detector. The sample temperature could be varied from room temperature down to liquid helium temperature in both the ODMR and the PL experiments.

Photoluminescence.

The irradiation induces radiative defects that gives several PL bands in 4H SiC. The band we will concentrate on here has, as expected for the 4H polytype with its two inequivalent defect sites, two sharp no-phonon lines. As seen in Fig. 1a, these are at 1354 and 1440 meV and we will refer to these lines as the V1 and V2 line (the line positions are slightly shifted in this sample). The line width is only 0.3 meV in the best samples. The lines are accompanied by phonon replicas, among which the LA at 77 meV and the LO at 104 meV can be recognised.

The intensity of this band increases with irradiation dose up to 10^{17} cm^{-2}, but not further. Isochronal annealing experiments show that the intensity of the band stays approximately constant up to 700°C and then drops at 750° C. This temperature is identical to the annealing temperature of the silicon vacancy in irradiated 3C and 6H SiC [1, 3]. The annealing temperature was established via the ESR signal from the negative silicon vacancy.

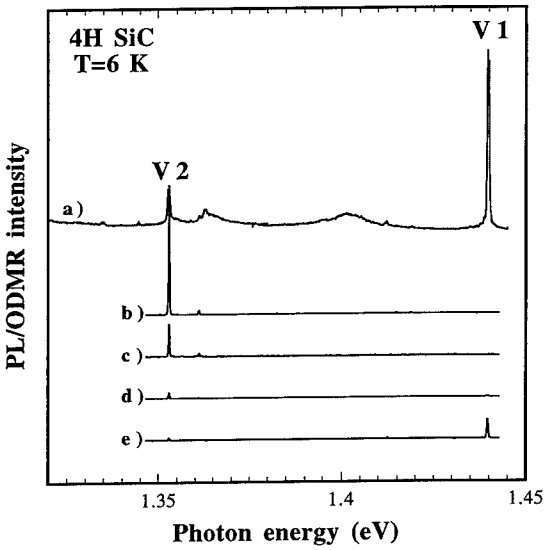

Figure 1: The deep PL band (a) and the excitation spectrum of the ODMR signal when the field is locked at the T_{V2a} (b), T_{V1b} (c), T_{V2b} (d) and T_{V1a} (e).

The intensity of the PL lines stays approximately constant up to 30 K and is reduced to one quarter of the low temperature strength at 60 K.

ODMR.

The ODMR spectrum shown in Fig. 2a can be detected via the PL band discussed above. The spectrum consists of the four different signals that are marked and labelled in the illustration. They all consists of two lines whose splitting vary in the relatively simple fashion indicated in Fig. 3, when the crystal is rotated in the magnetic field. The splitting is only governed by the angle between the magnetic field and the c-axis of the crystal. This angular dependence of the ODMR signals is characteristic for a spin triplet state (S=1) with axial symmetry. In a simple case like this, the angular dependence can be fitted by the following expression [8]:

$$B = \frac{1}{g\mu_B}\left(h\nu \pm \frac{D}{2}\left(3(\cos\theta)^2 - 1\right) + AM_I\right)$$

Here; g is the gyromagnetic ratio, μ_B is the Bohr magneton, D is the zero-field splitting of the magnetic sub-levels, A describes isotropic hyperfine interaction and θ is the angle between the c-axis of the crystal and the magnetic field. The parameters of such a function can be fitted to the four different ODMR signals. The resultant fitting and the corresponding parameters are shown in Fig. 3 and Table I respectively. Since no hyperfine structure could be resolved in this experiment, the last term was not included in the fit. It will however come in use later.

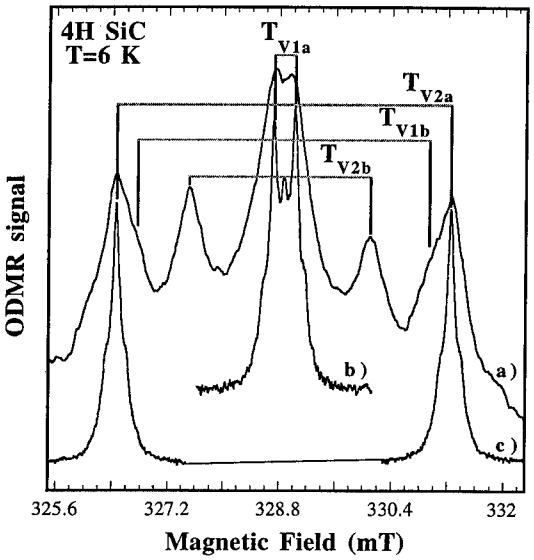

Figure 2: ODMR spectrum with above band gap excitation (a) and with selective excitation with the V1 (b) and V2 (c) line energy. The magnetic field direction is 10° off the c-axis of the crystal. The naming of the four ODMR signals is introduced.

A. Spectral Dependence.

To sort out the correspondence between the four different ODMR signals and the two PL lines, ODMR was measured when only one of the PL lines was detected at a time. The conclusions from such an experiment are that the T_{V1a} and T_{V1b} signals are detected from the V1 line and the T_{V2a} and T_{V2b} are detected from the V2 line.

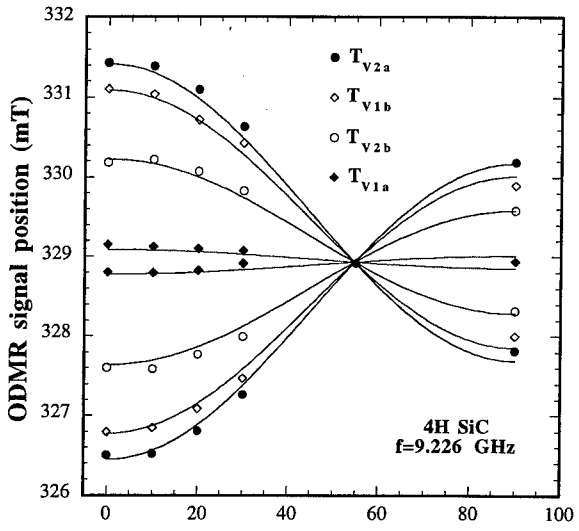

Figure 3: Angular dependence of the four ODMR signals detectable with above band gap excitation. The lines indicate the fits that are obtained with the parameters in Table I.

B. Resonant Excitation.

If the magnetic field is locked at the position of one of the ODMR signals and the excitation energy is scanned through the energy region of the PL band, as in Fig. 1b-d, it becomes apparent that two of these triplet-states can be excited resonantly. The resonance energies are in fact identical to the energies of the no-phonon lines in the PL spectra. The concluded correlation between the PL lines and the ODMR signals from this experiment agrees with the results from the spectral dependence experiment described in the previous section. This experiment gives in addition a direct one-to-one correspondence between the triplet-states and the PL lines. It should

now be understandable why the ODMR signals are named in the way they are. Apart from the T which stands for triplet, the V1 or V2 indicates the correspondence to the PL lines and the a or b marks if the triplet state is resonantly excitable (a) or if it is only detected with above band-gap excitation (b).

The T_{V1a} and T_{V2a} ODMR signals can, as indicated in Fig. 2b-c, be detected separately if resonant excitation is used. It then becomes possible to resolve the hyperfine structure of these two ODMR signals. Each resonance line has a symmetric pair of inner and outer satellites that are split by 0.30 and 0.60 mT respectively. If the hyperfine structure of the T_{V2a} signal is fit with Lorenzian functions with identical line-widths (Fig. 5), the intensity of the inner and outer satellites are found to be 27% and 4% of the central line. The analysis of the T_{V1a} is more difficult, since the two hyperfine structures interfere even at the angle where the splitting of the two resonances is the largest (Fig. 2b). Apart from the problem that it is very hard to extract a relative intensity for the outer satellites the other parameters (splitting and intensity of the inner satellites) are within the accuracy identical to those of the T_{V2a} state. The hyperfine structure is isotropic and can therefore be represented by the A value in the spin Hamiltonian.

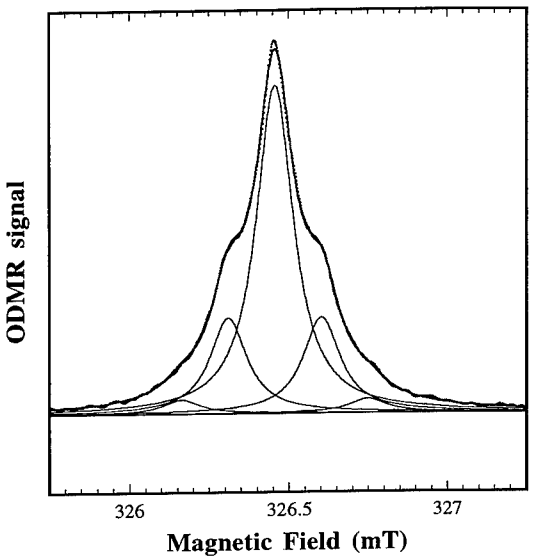

Figure 5: A blow-up of the hyperfine structure of the T_{V2a} signal (dots) fitted with five pair-wise coupled and equidistant Lorenzians (lines).

No resonant excitation is possible for the T_{V1b} and T_{V2b} signals in this excitation interval (below 1460 meV).

The weak line at 1.36 eV in the two first excitation spectra (Fig. 1b-c) corresponds to another near lying triplet signal. This signal does however not have the same characteristic hyperfine splitting as the T_{V1a} and T_{V2a} signals. It should therefore originate from another defect system.

Table I: The spin Hamiltonian parameters of the four triplet states detectable with above band gap excitation and the correspondence to the PL lines.

Triplet-states	g paralell ± 0.002	g perp. ± 0.002	D (10^{-8} eV) ± 0.2	A (10^{-8} eV)	PL line label and energy (eV)
T_{V1a}	2.004 *	2.004 *	1.8 *	3.5	V1 (1.438)
T_{V1b}	2.004	2.004	25		V1 (1.438)
T_{V2a}	2.004 *	2.004 *	28.8 *	3.5	V2 (1.352)
T_{V2b}	2.004	2.004	15		V2 (1.352)

*) Higher accuracy since the T_{V1a} and T_{V2a} signals can be studied separately.

Discussion.

As described earlier, the PL signal strength is strongly correlated to the irradiation dose. The high energy electrons, used in the irradiation, are expected to produce single defects [6] and these primary irradiation induced defects do not seem to be mobile at room temperatures [3]. It therefore seems probable that the origin of theses signals is an isolated primary defect and not an impurity. The observed annealing temperature of 750°C has earlier been associated with the silicon vacancy in irradiated SiC [1, 3].

The ESR signal from the negative charge state of the silicon vacancy (V_{Si}^-) has been detected in 3C, 4H and 6H SiC [1, 3, 9]. The signal is isotropic and has an effective spin S=1/2. The true spin state of this defect has recently been shown to be S=3/2, as expected for a non-distorted V_{Si}^- state [9]. The V_{Si}^- state in SiC is thereby more similar to the V^- in diamond than V^- in silicon. The hyperfine structure of this V_{Si}^- signal is very similar in the three polytypes. It consists of an inner isotropic part with symmetric pairs of satellites with falling intensities and a weak outer anisotropic structure. This hyperfine structure is the expected for an un-relaxed silicon vacancy in SiC. The inner structure then results from the interaction with twelve equivalent silicon atoms (the next-nearest neighbours). The inner pair of satellites are from those defect sites where one of the twelve silicon atoms is nuclear-spin active (4.7% of them has nuclear spin I=1/2) and the outer from those with two. Theoretically such satellites should be equidistant and should have an intensity of 28% and 3.7% for the inner and outer ones, respectively. The weak outer structure is then from interaction with the four tetrahedrally oriented carbon neighbours (among which only 1.1% has nuclear spin I=1/2). Non of the common impurities in SiC (H, Ti, V, B, Al, N) would cause such a hyperfine pattern.

The hyperfine structure that we observe for the T_{V1a} and T_{V2a} seems to be exactly the same as for the V_{Si}^- in 4H SiC. Following from the discussion above, the inner satellites are then from interaction with I=1/2 and the outer from Σ I=1. The A value in Table I is calculated assuming this model. Most probably because of noise problems we cannot observe the very weak satellites from the carbon neighbours but both the relative intensities and the splittings of the inner structure is the same as for the V_{Si}^-.

The triplet states that we observe can not be formed by the five electrons of the V_{Si}^-. In order to explain the similarity in the hyperfine structure, the particles forming the triplet states that we observe must have a similar localisation as the spin-active electrons of the V_{Si}^-. The most probable candidates are then the neutral or the doubly negative charge state of the silicon vacancy, which both with their even number of electrons can form triplet states. Some kind of exciton like state, with a coulombically attracted delocalised hole, is less probable since it, because of the weaker localisation, would have an averaged hyperfine interaction that is weaker than for the V_{Si}^-.

The sharpness of the PL lines is typical for bound exciton or internal recombinations, but the bound exciton alternative is ruled out by the strength of the hyperfine interaction (see above). The sharp PL lines would then be from internal transitions of this vacancy state at the two inequivalent sites in 4H SiC. Since the excited state from which the radiative transition starts must be in the band-gap, the ground state has to be at least 1.44 eV below the conduction band. In an earlier work on the analogue defect system in 6H SiC [10] we were, via complementary ESR measurements, able to assign the signal to the neutral silicon vacancy. We have not been able to do this final assignment in the 4H polytype. In view of the very strong similarities between the defect systems in the two polytypes, it seems reasonable to assume that the signals described here also originates from the neutral charge state.

References:

1. H. Itoh, M. Yoshikawa, I. Nashiyama, S. Misawa, H. Okumura, S. Yoshida, IEEE Transactions on Nuclear Science **37** (6), 1732 (1990)
2. H. Itoh, M. Yoshikawa, I. Nashiyama, S. Misawa, H. Okomura and S. Yoshida, Journal of Electronic Materials, Vol. **21** (7), 707 (1992)
3. Jürgen Schneider and Karin Maier, Physica B **185**, 199-206 (1993)
4. Balona and Loubster J. Phys. C: Solid St. Phys. **3**, 2344 (1970), The F spectrum is undoubtly the ESR signal from the V_{Si}^-.
5. J. Isoya, H. Kanda, Y. Ushida, S. C. Lawson, S. Yamasaki, H. Itoh, Y. Morita, Phys. Rev. B **45** (3), 1436 (1992)
6. See for example: Point Defects in Semiconductors II, J. Bourgoin and M. Lanoo, Springer-Verlag, Berlin (1983)
7. O. Kordina, A. Henry, J. P. Bergman, N. T. Son, W. M. Chen, C. Hallin, E. Janzén, Appl. Phys. Lett. **66** (11), 1373 (1995)
8. For example: Paramagnetic Resonance, J. E. Pake, W. A. Benjamin, New York, (1962)
9. T. Wimbauer, D. Volm, B. K. Meyer, A. Hofstätter, A. Scharman, Proceedings of ICPS 23, World Scientific, Singapore, 2645 (1996)
10. "An irradiation induced defect in 6H SiC related to the silicon vacancy", E. Sörman et al., accepted for publication in Phys. Rev. B (Sep. 15 1997)

Materials Science Forum Vols. 258-263 (1997) pp. 691-696

THERMAL ACTIVATION ENERGIES FOR THE THREE INEQUIVALENT LATTICE SITES FOR THE B_{Si} ACCEPTOR IN 6H-SiC

A. O. Evwaraye[1], S. R. Smith, W. C. Mitchel[1], H. McD. Hobgood[2]*, G. Augustine[2] and V. Balakrishna[2]
[1]Air Force Research Laboratory, Wright-Patterson AFB, OH 45433 USA
[2]Northrop Grumman Corp., Science and Technology Center, Pittsburgh, PA 15235 USA
***Present address: Cree Research, Inc. Durham, NC 27713, USA)**

Keywords: Silicon Carbide, boron, admittance spectroscopy

Abstract. Boron is known to substitute for silicon in the SiC lattice. The 6H polytype of SiC has three inequivalent lattice sites in the Si sublattice and the B_{Si} acceptor is expected to display three separate energy levels, one for each inequivalent lattice site. We have used both thermal admittance spectroscopy (TAS) and high temperature Hall effect to study the shallow boron acceptor levels in bulk 6H-SiC. Fitting of temperature dependent Hall effect data gave only a single acceptor level per sample for B_{Si} with values that varied from 0.29 to 0.39 eV. With TAS we were able to identify, for the first time, three separate energy levels and have assigned them to the h, k_1 and k_2 sites of B_{Si}. The energies are: $E_h = E_V + 0.27$ eV, $E_{k1} = E_V + 0.31$ eV and $E_{k2} = E_V + 0.38$ eV. We attribute variations in the Hall effect activation energy to the affects of compensation of one or more of these levels.

Introduction.

Silicon carbide is receiving considerable interest due to its potential to provide improved performance in high temperature and high power applications over silicon and gallium arsenide. One of the distinguishing features of silicon carbide is its propensity to form in a variety of different crystal structures referred to as polytypes. The difference between the polytypes is the stacking sequence of the closed packed Si-C bilayers along the c-axis. Over 175 different polytypes have been discovered but only three are important for electronic applications, the lone zincblende polytype, 3C, and two wurtzite polytypes, 4H and 6H. This variation in stacking sequence results in inequivalent lattice sites associated with hexagonal or cubic stacking. It is well established that nitrogen, the most common donor in SiC, exhibits different donor levels depending on the lattice site it occupies, three different levels in 6H-SiC, at 0.081, 0.137 and 0.142 eV for the h, k_1 and k_2 lattice sites [1,2], and two levels in 4H-SiC, near 0.05 and 0.10 eV for the h and k sites [3-5]. The situation is not as clear for the acceptors however. Boron is believed to be responsible for two types of defects in SiC, a relatively shallow acceptor level around 0.3 - 0.4 eV above the valence band and a deeper center, known as the D-center, which is presently believed to be a complex of boron and some other defect. Electron spin resonance [6-8] studies of the boron acceptor in 6H-SiC show that boron, in this configuration, like nitrogen, substitutes for silicon and occupies one of the three inequivalent lattice sites. The photoluminescence study of Ikeda et al. [9] suggests inequivalent lattice sites for boron as well. However, to date, electrical measurements such as Hall effect, admittance spectroscopy and DLTS have observed only one level associated with the shallow acceptor. There is, however a large variation in the reported energy for the acceptor, with values ranging from $E_V + 0.32$ [10] to

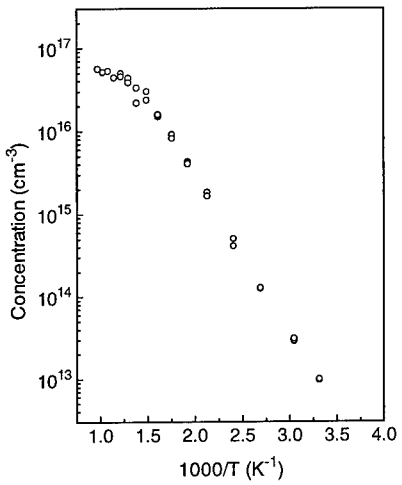

Fig. 1: Carrier concentration versus inverse temperature for 6H-SiC:B sample A.

E_V + 0.39 eV [11]. Temperature dependent Hall effect experiments in our laboratory give a range of values from 0.28 to 0.39 eV [12].

In this paper we report the results of thermal admittance spectroscopy and high temperature Hall effect studies of p-type bulk 6H-SiC samples. We report three energy levels due to the B_{Si} acceptor and associate them with the three inequivalent lattice sites in 6H-SiC. This is believed to be the first report of the energy levels associated with boron on the inequivalent lattice sites.

Experiment

The samples were cut from wafers of 6H-SiC grown by physical vapor transport [13]. These samples were undoped but dominated by boron in various concentrations. The room temperature resistivity of the samples varied from $3X10^2$ to $1X10^6$ Ωcm. Circular Schottky diodes were fabricated on these samples as has been described elsewhere [14]. Capacitance-voltage (C-V) measurements were made with a 1 MHz-capacitance meter. Because of the high resistivity at room temperature it was not possible to take C-V measurements at that temperature so these measurements were taken at temperatures from 370 to 500 K. Free carrier concentrations for the individual samples were determined from the C-V experiments. The thermal admittance spectroscopy experiment is described in reference 15. In this experiment the conductance and capacitance of a Schottky diode are measured as functions for frequency and temperature and defect energies are determined from this data. A benefit of this technique is that shallow levels can be studied.

Additional samples van der Pauw samples were cut from adjacent portions of the wafers for temperature dependent Hall effect measurements. Contacts were either bare Al or Al/Ta covered with gold. Contacts were annealed for two minutes a 925°C in forming gas. Hall effect and resistivity measurements were made with a special

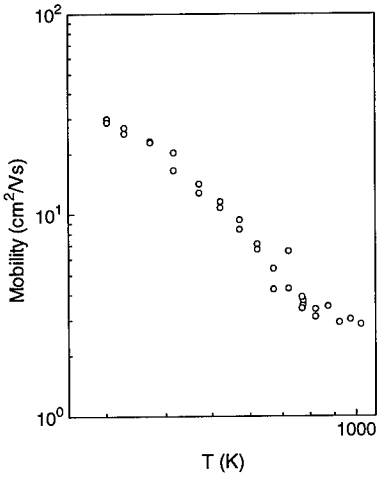

Fig. 2: Mobility versus temperature for 6H-SiC sample from fig. 1.

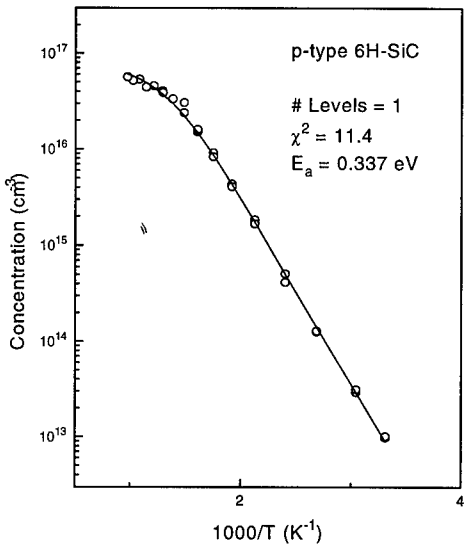

Fig. 3: Least squares fit to hole concentration versus 1/T for data from figure 1.

high temperature sample mount to temperatures up to 1000 K.

Results and Discussion.

Typical temperature dependent Hall effect results are shown in figs. 1 and 2 for a relatively lightly doped sample. The carrier concentration clearly shows saturation at the highest temperatures and the mobility shows the decrease with increasing temperature typical of phonon scattering. This degradation in the mobility is the ultimate limiting factor on how high a temperature measurements can be made at. Figure 3 is a fit of the carrier concentration data to the charge balance equation [1,3]. We used 1.68 for the hole effective mass [16] and 4 for the acceptor degeneracy factor, g. In no case were we able to force even two levels into the fit. The activation energies for the SiC:B samples in this study varied from 0.294 to 0.338 eV. The boron concentrations obtained from the fits varied from a low of about $1X10^{17}$ cm^{-3}, as seen in fig. 3, to near 10^{19} cm^{-3}.

Thermal admittance spectroscopy measurements were made on all samples up to 350 K. The normalized conductance spectra (G/ω) for two samples, A and B, taken at 1kHz, are compared in fig. 4 to show the typical results. One major peak was detected in all samples but, as can be seen in the figure, the peak temperature varied some what from sample to sample, suggesting different activation energies. No other peaks were observed in these samples over the temperature range of measurement. In particular, the D-center was not detected. Besides the apparent energy, the symmetry of the peaks varied as well and this is also apparent in the figure. The peak for sample B appears symmetric while that for sample A is clearly asymmetric, an indication of the presence of multiple levels in the

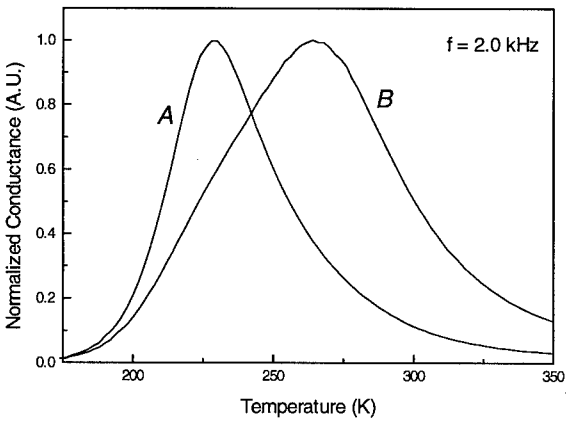

Fig. 4: Boron related TAS response for samples A and B showing shift in peak positions and asymmetry.

peak. Most samples showed signs of multiple levels within the TAS spectrum. In order to examine the structure of the spectra better a commercially available curve fitting program was used to examine them. Figure 5 shows the spectrum for sample B with the results of the curve fit. The circles are the data and the solid line is the fit. Also shown are the three peaks that were necessary to fit the data. An attempt to use two peaks gave a significantly worse fit, while more than three peaks did not significantly improve the fit. The spectrum for each sample was fitted independently for each measuring frequency and the peak temperatures were used in an Arrhenius plot of $\ln(e_n/T^2)$ versus 1/kT to determine the activation energies of the levels. The energies for the three peaks in fig. 5 were determined in this manner to be 0.27, 0.31 and 0.38 eV. Comparing these results to the case of the nitrogen donor levels we have assigned the lowest energy to the hexagonal site and the higher two to the cubic sites but we have no evidence to directly support this assignment at present. We found the same energies for all samples but not all samples had all three levels. The sample to sample variation in energy for each level was less than 10%.

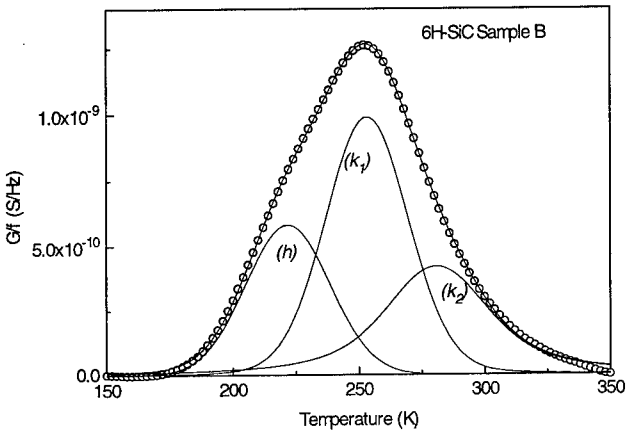

Fig. 5: Fit of TAS data for sample C. Circles are the data, The solid line is the fit. Dashed lines are the three peaks comprising the fit.

We have also observed these same levels in n-type material using Optical Admittance Spectroscopy. Here we scanned the incident wavelength rather than the temperature and measured the change in conductance versus incident wavelenght. Fitting of the near band edge region showed three peaks that we have attributed to excitation of ionized acceptors, that is to an optically induced transition of an electron from a charged boron center to the conduction band. The defect energy was found by subtracting the optical peak energy from the band gap. This procedure gave 0.27, 0.31 and 0.38 eV for the boron energy levels in n-type material, where the acceptors are normally completely compensated, in agreement with the TAS results on the neutral acceptors in p-type material.

Table I lists all of the samples studied and the energy levels observed, as well as the activation energy from Hall effect. It will be immediately noticed that the Hall effect energies do not precisely correspond to the TAS energies. We also note that the relative magnitudes of the various peaks in the TAS fits varied from sample to sample. The latter variations cannot be explained by compensation effects alone because, as can be seen in the table, at least two samples

show only the shallow level and not the deeper ones. At present we do not have an explanation for this but note that we have seen similar effects for the two levels of nitrogen in 4H-SiC where the individual peaks are separated and clearly discernible. We also note that in a recent study Matusmoto et al. [17] suggest that the B_{Si} defect is not a simple substitutional defect and that there are differences between the lattice relaxation between the hexagonal and cubic sites. Such differences might lead to differences in the capture cross section which could affect the apparent concentration and even the energy of the defects. None the less, the reported values for the activation energy of the boron acceptor in 6H-SiC all fall within the energies we have determined from our fits [9-11,16]. With regards to the variation in Hall effect energies, we believe that compensation effects are responsible for this as well as for the wide variation in Hall effect activation energies reported in the literature for this defect. In highly compensated samples the hexagonal level will be compensated and the measured activation energy will be in between the two cubic levels. In lightly compensated material the hexagonal site level will dominate, particularly if high temperature data is not taken.

TABLE I: Energy levels of boron acceptor observed in 6H-SiC samples

Sample	E_h(0.27eV)	E_{k1}(0.31eV)	E_{k2}(0.37eV)	E_{hall}(eV)
A	Yes	No	No	0.338
B	Yes	Yes	Yes	0.302
C	Yes	Yes	Yes	0.320
D	Yes	No	No	0.320
E	No	Yes	Yes	0.331
F	Yes	No	No	0.329
H	No	Yes	Yes	0.294

Conclusions.

We have measured three energies associated with the boron shallow acceptor in 6H-SiC with thermal admittance spectroscopy and have identified them with boron atoms on the three inequivalent silicon lattice sites. The energies 0.27, 0.31 and 0.37 eV have been associated with the h, k_1 and k_2 sites respectively. Temperature dependent Hall effect measurements up to 1000 K have found similar levels but could not identify more than one level per sample. We attribute the variations in the reported values of the B_{Si} acceptor to variations in compensation that change the dominant level from sample to sample.

Acknowledgments:

The authors would like to acknowledge the assistance of Mr. G. Landis, Mr. R. Lesse and Mr. C. Culp, as well as the support and encouragement of Dr. P. M. Hemenger.

References:

1. W. Suttrop, G. Pensl, W. J. Choyke, R. Stein, and S. Leibenzeder, J. Appl. Phys. **72**, 3708 (1992).
2. C. Raynaud, F. Ducroquet, G. Guillot, L. M. Porter, and R. F. Davis, J. Appl. Phys. **76**, 1956 (1994).

3. W. Götz, A. Schöner, W. Suttrop, W. J. Choyke, R. Stein, and S. Leibenzeder, J. Appl. Phys. **73**, 3332 (1993).
4. T. Kimoto, A. Itoh, H. Matsunami, S. Sridhara, L. L. Clemen, R. P. Devaty, W. J. Choyke, T. Dalibor, C. Peppermuller, and G. Pensl, Appl. Phys. Lett. **67**, 2833 (1995).
5. A. O. Evwaraye, S. R. Smith, and W. C. Mitchel, J. Appl. Phys. **79**, 7726 (1996).
6. H. H. Woodbury and G. W. Ludwig, Phys. Rev. **124**, 1083 (1962).
7. G. E. G. Handeman and G. B. Gerritsen, Phys. Lett. **20**, 623 (1966).
8. A. G. Zubatov, I. M. Zaristikii, S. N. Lukin, E. N. Mokhov, and V. G. Stepanor, Sov. Phys. Solid State **27**, 197 (1985).
9. M. Ikeda, H. Matsunami, and T. Tanaka, Phys. Rev. B **22**, 2842 (1980).
10. W. Suttrop, G. Pensl, and P. Lanig, Appl. Phys. A **51**, 231 (1990).
11. G. A. Lomikina, Sov. Phys. Solid State **7**, 475 (1965).
12. W. C. Mitchel, M. Roth, A. O. Evwaraye, P. W. Yu, and S. R. Smith, J. Electron. Mat. **25**, 863 (1996).
13. H. M. Hobgood, D. L. Barrett, J. P. McHugh, R. C. Clarke, S. Sriaram, A. A. Burk, J. Greggi, C. D. Brandt, R. H. Hopkins, and W. J. Choyke, J. Cryst. Growth **109**, 17 (1991).
14. A. O. Evwaraye, S. R. Smith, and W. C. Mitchel, J. Appl. Phys. **75**, 3472 (1994).
15. A. I. Veinger, Yu. A. Vodokov, Yu. I. Kozlov, G. A. Lomakina, E. I. Mokhov, V. G. Oding, and V. I. Sokolov, Sov. Tech. Phys. Lett. **6**, 566 (1980).
16. W. R. L. Lambrecht, S. Limijumnong, S. Rashkeev, and B. Segall, physica status solidi, to be published.
17. T. Matsumoto, O. G. Poluektov, J. Schmidt, E. N. Mokhov, and P. G. Baranov, Phys. Rev. B **55**, 2219 (1997).

Materials Science Forum Vols. 258-263 (1997) pp. 697-702

OPTICAL ABSORPTION AND ZEEMAN STUDY OF 6H-SiC:Cr

A. Dörnen[1], B. Kaufmann[1], J. Baur[2], M. Kunzer[2], J. Schneider[2], and P. Baranov[3]

[1] **4. Physikalisches Institut, Universität Stuttgart, Box 80 11 40, D–70550 Stuttgart, Germany**

[2] **Fraunhofer-Institut für Angewandte Festkörperphysik, D-79108 Freiburg, Tullastr. 72, Germany**

[3] **A.F. Ioffe Physico-Technical Insitute, 194021 St.Petersburg, Russia**

Keywords: SiC:Cr, PL, Zeeman effect, EPR

Abstract. We report a Zeeman photoluminescence (PL) study of the three zero-phonon lines I_1 (9587.3 cm^{-1}), I_2 (9515.6 cm^{-1}), and I_3 (9321.5 cm^{-1}) in $6H$-SiC. These lines are found as the dominant PL system in chromium-doped material. The Zeeman effect reveals optical transitions which involve a triplet state and at least one Kramers doublet. The results favor to identify the lines with charge-transfer transitions involving the charge states $Cr^{4+}(3d^2)$ and $Cr^{5+}(3d^1)$. From absorption spectroscopy we find the double acceptor level $Cr^{2+/3+}$ 1.85 eV above the valence band.

Introduction

Silicon carbide gives rise to several charge states of a transition-metal impurity, due to its large electronic band gap. In the $6H$ polytype vanadium has been found to be amphoteric, since a donor and an acceptor level is introduced by the charge states $V^{5+}(3d^0)[D^+]$, $V^{4+}(3d^1)[A^0, D^0]$, and $V^{3+}(3d^2)[A^-]$, see Ref. [1–5]. The strong optical transitions $^2T_2 \longleftrightarrow {}^2E$ of the V^{4+} ion have been observed in absorption and photoluminescence (PL) [1] as well as in the magneto-circular dichroism in the optical absorption (MCDA) [6]. The V-related acceptor level also has been found in deep level transient spectroscopy [7].

Titanium on the other hand exists only in the neutral charge state $Ti^{4+}(3d^0)$ in $6H$-SiC. Only for the $4H$ polytype the donor level enters the band gap and Ti^{3+} is found to be thermodynamically stable in n-type material [3]. In $6H$-SiC and in cubic SiC ($15R$) an excitonic luminescence transition occurs [8, 9]. The electron is localized in the d shell of titanium and binds the hole coulombically (Ti^{3+},h_b). Optically detected magnetic resonance (ODMR) studies of the PL have confirmed that electron-phonon coupling stabilizes the $3d^1$ configuration in the excitonic complex [10].

Recent studies of the electron-paramagnetic resonance (EPR) on chromium-doped $6H$-SiC have identified two charge states of chromium: $Cr^{3+}(3d^3)$ and $Cr^{2+}(3d^4)$ by spin states of $S = 3/2$ and $S = 2$ and corresponding hyperfine interaction, respectively [11, 12]. In PL spectra of the identical samples we find a set of three zero-phonon lines at around 1.15 eV. These lines were previously observed by Gorban and Slobodyanyuk [13]. By comparing spectra from $4H$, $6H$, and $15R$ material it was shown that the three lines I_1, I_2, and I_3 found in the $6H$ polytype are due to the three inequivalent lattice sites h, k_1, and k_2 of the crystal structure. In this study we investigate the Zeeman effect of these lines and tentatively assign them to charge-transfer transitions of chromium ions between the charge state $Cr^{4+}(3d^2)$ and $Cr^{5+}(3d^1)$. The samples used in this study were grown by liquid-phase epitaxy and doped with chromium in the melt. The substrate was removed to study the epitaxial layer (thickness 500 μm) by MCDA and PL. Luminescence and absorption measurements as well as Zeeman spectroscopy were performed with a Fourier-transform-infrared spectrometer which is described in Ref. [5].

Photoluminescence and Absorption spectra.

Photoluminescence spectra of chromium-doped n-type $6H$-SiC samples recorded between 1.4 and 0.7 eV show the three lines I_1, I_2, and I_3 as the dominant optical transitions as depicted in Fig. 1. Weak satellites of I_1 and I_3 are due to inclusions of $4H$ polytype crystallites. The PL lines do not show up in the n- and p-type substrate, respectively. In the identical sample three MCDA signals are found (marked by arrows in Fig. 1) spectroscopically close to the PL lines but do not coincide with the positions of I_1, I_2, and I_3.

The transitions I_1, I_2, and I_3 are not observed in absorption, instead a broad band is found which has the characteristic shape of a photoionization band with an onset at around 1.17 eV. This band is not found in usual n-type samples. Therefore, we assign the absorption band to the photoionization process $Cr^{2+} \rightarrow Cr^{3+} + e_{CB}$. The corresponding double acceptor level $A^{2-/-}$ is then located at E_{VB} + 1.85 eV (bandgap energy E_g = 3.02 eV).

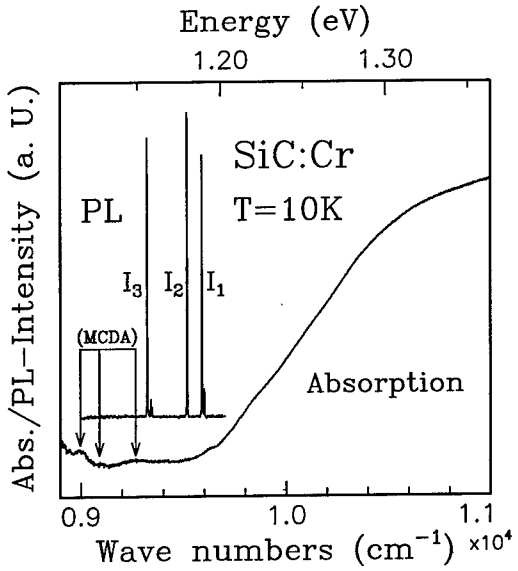

Figure 1: *PL and absorption spectrum of SiC:Cr. In absorption a photoionization band shows up with an onset at 1.17 eV. The luminescence lines I_1, I_2, and I_3 are those reported by Gorban et al.* [13]. *The lines do not show up in the absorption spectrum. Arrows mark the positions were MCDA transitions have been observed* [12].

Zeeman spectra.

The Zeeman splittings of the lines I_1, I_2, and I_3 are shown in Fig. 2. Each line shows a triplet splitting. Additionally, each Zeeman-triplet line of I_1 and I_3 splits into a further doublet if the field is not aligned perpendicular to the hexagonal c axis. No further splitting occurs in I_2.

To analyze the Zeeman effect for each of the three inequivalent lattice sites in terms of a triplet and a doublet in trigonal environment (C_{3v} symmetry) we use the general Hamiltonian

$$\mathcal{H}_{\mathrm{Zee}} = g'\mu_{\mathrm{B}} S'_z B_z + g_{||}\mu_{\mathrm{B}} (S_z B_z) + g_{\perp}\mu_{\mathrm{B}} (S_x B_x + S_y B_y) + D\left[S_z^2 - \tfrac{1}{3}S(S+1)\right] . \quad (1)$$

The operator S'_z is the z component of the Pauli spin matrix of spin $S = 1/2$ to describe the Zeeman splitting of the doublet in terms of a fictitious angular momentum (terms including S'_y and S'_z are omitted since no splitting is being observed perpendicular to the c axis). The triplet is described by the spin matrices **S** of a system with spin $S = 1$. The zero-field splitting D of the triplet, which is possible in C_{3v} symmetry, is described by the last term in Eq. (1).

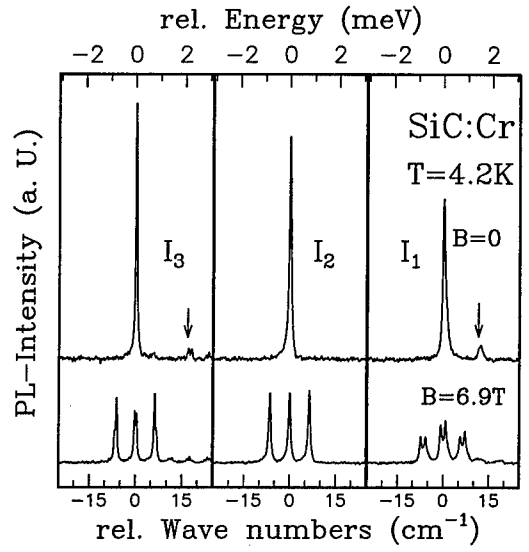

Figure 2: *Zeeman splitting with field* **B** *aligned parallel to the c axis. Arrows in the zero-field spectrum indicate the transitions of the 4H inclusions*

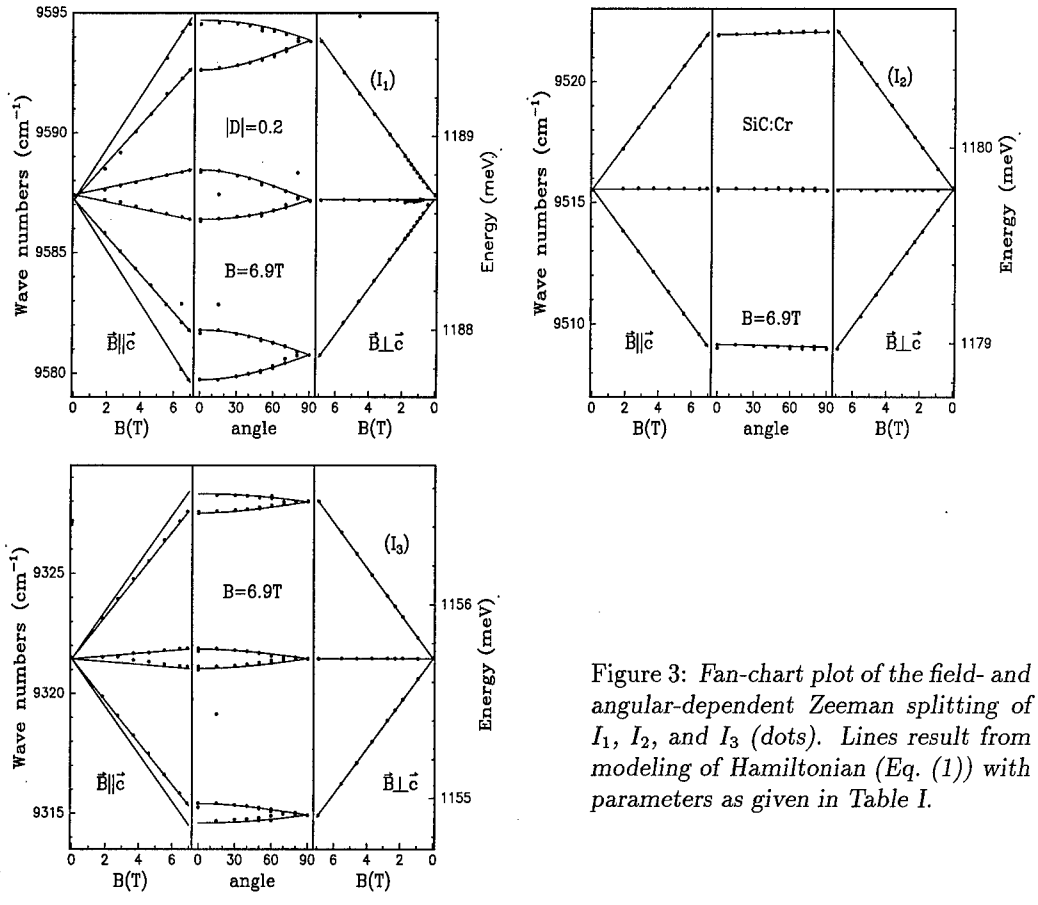

Figure 3: *Fan-chart plot of the field- and angular-dependent Zeeman splitting of I_1, I_2, and I_3 (dots). Lines result from modeling of Hamiltonian (Eq. (1)) with parameters as given in Table I.*

With this Hamiltonian, the Zeeman splitting can be described completely well. In Fig. 3 the experimental data of the fan-chart plot (points) and the eigenvalues of the Hamiltonian in Eq. (1) is plotted. The parameters found from the fit are given in Table I.

Table I: Result of the Zeeman fit.

	$S=1$			$S=1/2$	
	$g_{\|\|}$	$g_\perp$	$\|D\|(\mathrm{cm}^{-1})$	g'	site
I_1	2.00(2)	2.03(2)	0.2 cm^{-1}	0.65(3)	h
I_2	1.98(2)	2.01(2)	-	0.00	k_2
I_3	2.00(2)	2.02(2)	-	0.25	k_1

Discussion.

In SiC of the $6H$ polytype three inequivalent lattice sites exist, the hexagonal-like site h and the cubic-like sites k_1 and k_2. Up to the second-neighbor shell the atoms are coordinated as in the wurzite and cubic zincblende structure for site h and k, respectively. Higher neighbor shells differentiate site k_1 from site k_2. An ion placed on the hexagonal-like site h is affected by a stronger axial field than an ion on a cubic-like site, as has been shown for the Ti-bound exciton [8, 10] and for $V^{4+}(3d^1)$ [6, 5].

From the work of Gorban and Slobodyanyuk [13] it is clear that the three lines I_1, I_2, and I_3 belong to one specific center with each line representing one inequivalent lattice site. In the Zeeman spectra presented here significant influence of the trigonal crystal field shows up in two ways: (i) A zero-field splitting is observed in the triplet of I_1, and (ii) a pronounced anisotropy is found in the Zeeman splitting of the doublet of I_1 and I_3 with $g_\perp$ being completely quenched.

It is suggested that site h among the three crystallographic sites also yields strongest trigonal impact on the electronic level scheme of the optical center. The zero-field splitting found for I_1 is therefore strong evidence that the corresponding center is located on the hexagonal site h. This corresponds to the fact that also the doublet shows the strongest anisotropy in the line I_1. Similarly, the line I_3 belongs to the cubic-like site k_1 with the stronger trigonal CF component. Consequently, the line I_2, which shows no doublet splitting, is assigned to the center at the cubic-like site k_2 with the weakest trigonal CF component.

An important question arises with the doublet splitting of I_1 and I_3 and its absence in I_2. By symmetry properties a trigonal CF may quench $g_\perp$ but not $g_{||}$. Especially, the missing of the doublet splitting in I_2, the line which is due to the most isotropic site k_2, strongly motivates not only one but two Kramers doublets with g_I and g_II, respectively, to be involved in the two-fold splitting. In total four Zeeman transitions are possible between two Kramers doublets. The two Zeeman lines found here are thus assigned to the allowed transitions, where no spin flip is necessary ($\Delta m_S = 0$). The other two forbidden transitions, where the spin state has to change ($\Delta m_S = \pm 1$) are not observable. Assuming two Kramers doublets has two important consequences:

(i) A consistent number of particles is involved in the final and in the initial state of the optical transition.

(ii) g' corresponds to the difference in the g factors of the two Kramers doublets: $g' = g_\mathrm{I} - g_\mathrm{II}$ (Whereas the forbidden transitions would be described by the sum of the g factors $g_\mathrm{I} + g_\mathrm{II}$)

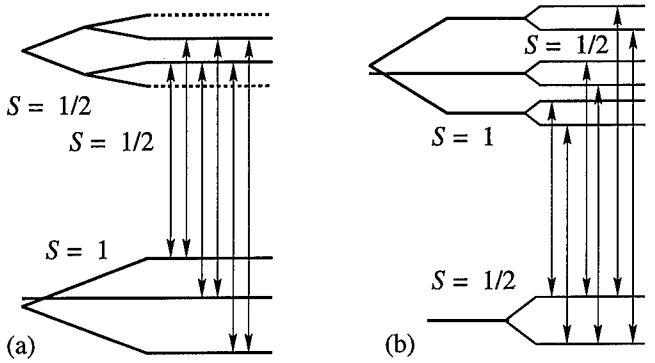

Figure 4: *Two alternative level schemes to explain the Zeeman effect. The schemes apply to each of the PL lines I_1, I_2, and I_3. (a) Both doublets belong to the initial state. (b) Triplet and one doublet belong to the initial state*

For the most isotropic cubic-like site it is expected that g_{II} and g_{I} are equal within experimental uncertainty and thus $g' = 0$ results. On the other hand as the centers I_3 and I_1 are affect by a stronger trigonal CF g_{I} becomes different from g_{II}, as will be discussed below.

Thermalization effects within the Zeeman lines have not been found between 4.2 and 2.0 K. Therefore, it is not possible to decide whether triplet and doublet(s) belong to the initial or final state of the transition. Two different level schemes (Fig. 4) are consistent with the optical transitions.

(a) In the optical transition two electrons participate. The excited state is made up of two uncoupled Kramers doublets. In the ground state both particles couple to the triplet.

(b) The excited state consists of the triplet and a bound hole as a third particle. After recombination one electron remains which results in an Kramers doublet in the ground state.

Both models are based on a core system and a secondary particle with the exchange too small to be resolved in the optical spectra. This is only conceivable if no Coulomb interaction occurs between core and secondary particle. Otherwise a spectrum typical of donor-acceptor recombination would be expected.

Origin of the transitions

The experimental results clearly show that the PL spectrum cannot be due to simple crystal-field transitions within Cr^{2+} or Cr^{3+}. EPR has shown that the corresponding ground states are due to $S = 2$ and $S = 3/2$ with $D = 1.285$ and $1.53\ \mathrm{cm}^{-1}$, respectively [12]. The characteristics of the Zeeman pattern studied here are distinctly different from the EPR results.

A triplet like that observed here is expected for the $^3A_2$ ground state of $Cr^{4+}(3d^2)$. For the isoelectronic configuration of $V^{3+}(3d^2)$ on the h site a similar D term splitting of the triplet has been found with $D = 0.36\ \mathrm{cm}^{-1}$ [1]. Also the g factors of V^{3+} of $g_{||} = 1.976$ and $g_{\perp} = 1.961$ are close to what is found in the present study.

Anisotropic Kramers doublets with $g_{\perp} = 0$ result from holes bound at shallow acceptor aluminum [14]. However, in this case $g_{||}$ is only slightly site-dependent and quenching of $g_{\perp}$ results from the valence band (VB) structure, since the top of the VB transforms like the $\Gamma_{5,6}$ (point symmetry C_{3v}). The origin of the secondary particle inferred by the model could be due to such a shallow state of a particle bound nearby the optical center. But at least for the other Kramers doublet the anisotropy is site-dependent and resembles the spin-orbit states of a ^2E level. For the ^2E level of $V^{4+}(3d^1)$ $g_{||} = 1.751$ and $g_{\perp} = 0$ was found for the ground state at the h site, whereas for the cubic-like sites the effective $g_{||}$ factors are close to 2 [6]. The

variation of $g_{||}$ among the three inequivalent sites is about 0.25, which is about 2 times smaller than the site-dependent variation of g'. Therefore the variation of g' between the three sites could hint to one Kramers doublet of a ^2E state, namely of $Cr^{5+}(3d^1)$. Since the many-particle spin-orbit coupling parameter for Cr^{5+} is expected to be larger than for V^{4+} changes in $g_{||}$ of 0.65 between site h to k_2 seem conceivable. However it remains puzzling that by optical excitation two ionization processes occur from stable Cr^{3+} to Cr^{5+}.

It is suggested that the luminescence transition is due to the recombination of the secondary particle with the d-shell. With this background the transitions (a) and (b) of the level scheme in Fig. 4 are of the type

$$\text{(a) } [Cr^{5+}, e_b] \longrightarrow Cr^{4+}, \qquad \text{(b) } [Cr^{4+}, h_b] \longrightarrow Cr^{5+},$$

where e_b and h_b denote an electron and a hole bound at a site nearby, respectively. As discussed above, in the composite excited state no Coulomb interaction should occur. Therefore, the scheme (b) with neutral Cr^{4+} in the excited state seems preferable. Nevertheless, the center needs more investigation for a complete understanding.

Conclusion. In summary, we present a Zeeman study of the PL lines I_1, I_2, and I_3 which are found to be the dominant optical transitions in chromium-doped $6H$-SiC. The transitions show properties of the crystallographic sites. A model is presented which is based on a charge-transfer luminescence process in which Cr^{4+} is involved. Most probably Cr^{4+} captures a hole which yields Cr^{5+}. The experiments not only imply an ordinary acceptor level in the gap, also there should be a donor state. It is suggested that chromium like vanadium is amphoteric. From absorption spectroscopy we find evidence that the double acceptor level $A^{2-/-}$ ($Cr^{2+/3+}$) is 1.85 eV above the valence band.

References

[1] J. Schneider, H. Müller, W. Wilkening, F. Fuchs, A. Dörnen, S. Leibenzeder, and R. Stein, Appl. Phys. Lett. **56**, 1184 (1990).

[2] A. Dörnen, Y. Latushko, W. Suttrop, G. Pensl, S. Leibenzeder, and R. Stein, Mat. Sci. Forum **83-87**, 1213 (1992).

[3] K. Maier, H. D. Müller, and J. Schneider, Mat. Sci. Forum **83-87**, 1183 (1992).

[4] M. Kunzer, U. Kaufmann, K. Maier, and J. Schneider, Mater. Sci. Eng. **29**, 118 (1995).

[5] B. Kaufmann, A. Dörnen, and F. S. Ham, Phys. Rev. B **55**, 13009 (1997).

[6] M. Kunzer, H. D. Müller, and U. Kaufmann, Phys. Rev. B **48**, 10846 (1993).

[7] J. R. Jenny, J. Skowronski, W. C. Mitchel, H. M. Hobgood, R. C. Glass, G. Augustine, and R. H. Hopkins, Appl. Phys. Lett. **68**, 1963 (1996).

[8] P. J. Dean and R. L. Hartmann, Phys. Rev. B **5**, 4911 (1972).

[9] L. Patrick and W. J. Choyke, Phys. Rev. B **10**, 5091 (1974).

[10] K. M. Lee, L. S. Dang, G. D. Watkins, and W. J. Choyke, Phys. Rev. B **32**, 2273 (1985).

[11] P. G. Baranov, V. A. Khramtsov, and E. N. Mokhov, Semicond. Sci. Technol. **9**, 1340 (1994).

[12] J. Bauer and M. Kunzer and J. Schneider, to be published in Phys. Stat. Sol.(a) **162** (1997).

[13] I. S. Gorban and A. V. Slobodyanyuk, Fiz. Tverd. Tela (Leningrad) **16**, 263 (1974), – [Sov. Phys. – Solid State **16**, 173 (1974)].

[14] L. S. Dang, K. M. Lee, G. D. Watkins, and W. J. Choyke, Phys. Rev. B **45**, 391 (1980).

Materials Science Forum Vols. 258-263 (1997) pp. 703-708

HIGH-FREQUENCY EPR STUDIES OF SHALLOW AND DEEP BORON ACCEPTORS IN 6H-SiC

J. Schmidt[1], T. Matsumoto[1], O.G. Poluektov[1], A. Arnold[1], T. Ikoma[1], P.G. Baranov[2] and E.N. Mokhov[2]

[1]Huygens Laboratory, University of Leiden, P.O. Box 9504, 2300 RA Leiden, The Netherlands

[2]A.F. Ioffe Physico-Technical Institute, Politechnicheskaya 26, 194021 St. Petersburg, Russia

Keywords: EPR, acceptors, SiC

Abstract. A high-frequency pulsed EPR/ENDOR study at 95 GHz on ^{13}C-enriched single crystals of boron-doped 6H-SiC is reported. This type of spectroscopy, owing to its superior spectral resolution, allows the elucidation of the electronic and atomic structure of the shallow and deep boron acceptors in SiC.

Introduction

The group-III elements B, Al and Ga are the most important acceptor impurities in SiC. They have been studied using Hall effect, DLTS and optical spectroscopy [1]. It was discovered that B creates a shallow as well as a deep acceptor level. The shallow B center (sB) with an activation energy of 0.30-0.39 eV was observed in Hall effect studies and admittance spectroscopy measurements. The deep B center (dB) was first detected by photoluminescence measurements [2,3]. It was suggested that the characteristic high-temperature bright-yellow luminescence in B-doped 6H-SiC is due to recombination involving the N donor and the dB center. Based on this suggestion the ionization energy of the dB center was estimated to be more than 0.65 eV. DLTS investigations [4,5] and capacitane methods [6] also point to the presence of a shallow and of a deep acceptor level. The activation energies were estimated to be between 0.22 eV and 0.35 eV for sB and between 0.55 eV and 0.75 eV for dB.

The shallow acceptors introduced in SiC by the group III impurities have been studied using EPR [9-16], ODMR [16-20] and ENDOR at conventional frequencies [21,22]. It appears that the behaviour of the sB acceptor is strikingly different from that of the shallow Al (sAl) and shallow Ga (sGa) acceptors. The resonance conditions of the unpaired spin related to the sAl and sGa acceptors reflect the properties of the uppermost Γ_9 valence-band hole and indicate an effective-mass-like character of these acceptors but with reduced orbital-momentum contribution resulting from the localization. In contrast, the EPR spectrum of the sB acceptor did not show effective-mass-like behaviour. The contribution of the orbital angular momentum appears to be almost negligible ($g \approx 2$) and, for instance, EPR signals of sB could be observed in 3C-SiC without any unaxial stress applied to the crystal in contrast to sAl and sGa in the same material.

The difference in behaviour of sB on the one hand and sAl and sGa on the other hand was explained by considering the difference in the atomic radii [15,16]. It was proposed that B, which substitutes for Si but which has an atomic radius smaller than Si, occupies an off-centre position owing to chemical rebonding, i.e., it relaxes away from the neighbouring C along the B-C bond. In contrast to the behaviour of the sB acceptor, Al and Ga atoms substituting for

Si occupy on-centre positions and as a consequence an effective-mass-like behaviour is observed for the sAl and sGa acceptors.

The theoretical description of the sB acceptor has been reinterpreted several times. In the model proposed by Zubatov et al. [10] the main spin density was located on the dangling bond of a carbon atom neighbouring the boron along the B-C connection line. In more recent publications [22,23,24] a new description was given on the basis of ENDOR and ODMR investigations. In this model the valence electron is donated to boron by a neighbouring carbon atom thus forming B^- - C^+ bond. The unpaired electron of C^+ is uniformly distributed among the three remaining bonding orbitals. The authors call this model the boron-induced carbon acceptor.

The first magnetic-resonance observation of dB acceptors in SiC was made using ODMR techniques [19,20,25,26]. The ODMR spectra were recorded by monitoring the intensity of the yellow luminescence band in 6H-SiC. The most intense ODMR lines showed nearly axial symmetry around the hexagonal c-axis with $g_{\parallel}$=2.02-2.03 and $g_{\perp}$=2.0. The low resolution did not allow the observation of B hf structures to connect the spectra unambigously with a B impurity. Subsequent EPR studies at 9.5 GHz on the dB acceptor in 6H-SiC confirmed the ODMR results and were also successful for dAl and dGa [13-16]. Preliminary ENDOR measurements of dB revealed ^{11}B signals [27]. Later EPR spectra of dB were also observed in 4H-SiC and 3C-SiC [28].

The features of the EPR spectra of dAl and dGa are almost identical to those observed for dB. Importantly no effective-mass-like behaviour was observed for these three deep acceptors. The orientational dependencies of the EPR spectra indicate that the deep centers of B, Al and Ga have the same, nearly axial symmetry around the hexagonal c-axis in the hexagonal polytypes of SiC and around the <111> axis in 3C-SiC.

It was proposed [13-16] that the dB, dAl and dGa acceptors consist of a group-III element on a Si position accompanied by a neighbouring carbon vacancy (A_{Si}-V_C). It was argued that this center has near axial symmetry around the c-axis and that the hyperfine interaction with B, Al and Ga nuclei is of the same order of magnitude as for sB, sAl and sGa which were established to be B_{Si}, Al_{Si} and Ga_{Si} centers. Interestingly the deep acceptors of these group-III elements show almost the same behaviour.

Here we present the results of a high-frequency (95 GHz) EPR and ENDOR study of the sB and dB acceptor in 6H-SiC. The high-spectral resolution of this technique allows us to measure very accurately the g-tensors of the various shallow boron and deep boron sites. Moreover the hyperfine tensors of the ^{11}B (I=3/2) nuclear spin was determined together with those of ^{13}C (I=½) and ^{29}Si (I=½) nuclear spins of neighbouring atoms. The results allow us to propose a consistent model for the electronic structure of the shallow and deep boron acceptor in 6H-SiC.

Experimental

The samples used in the experiment were free-standing epitaxial layers with ^{11}B compensated during diffusion. The epitaxial layers were grown by the sublimation sandwich method [29] in vacuum at temperatures between 1700-1750 ^{0}C. As grown the epitaxial layers were *n*-type owing to the presence of nitrogen donors. Boron was diffused at a temperature of about 2000

^{0}C. Two types of samples were studied: ^{13}C-enriched crystals of 6H-SiC and crystals with natural isotopic abundance of carbon. The experiments were performed on a home-built, high-frequency, pulsed EPR/ENDOR spectrometer operating at 95 GHz. A detailed description of the set-up has been given elsewhere [30,31]. The measurements were performed at 1.5 K using a liquid-helium bath cryostat.

Results and discussion

Shallow boron-acceptor

In agreement with previous reports three types of centers were observed in the EPR spectra. One hexagonal (hex) and two quasi-cubic sites (k_1 and k_2). The hex site has its g_z-axis along the crystal c-axis the other two are found with their g_z axes directed along the 6 equivalent orientations within the hexagonal lattice which are 110^0 (or 70^0) away from the c-axis. The directions of the g_y axes of k_1 and k_2 are in a plane spanned by the c-axis and the g_z-axis whereas the g_x-axes are perpendicular to this plane. The finding that the deviation of g_z from g_e is zero is a strong indication that the unpaired electron is located in the p_z-orbital pointing from the neighbouring carbon to the boron atom because the expectation value of the orbital angular momentum along this direction is zero. This conclusion is further supported by measurements of the ^{13}C hf interactions. In the ^{13}C-enriched sample hyperfine lines are observed in the EPR spectrum which are assigned to a carbon nearest to boron. This is the largest hf interaction found for boron centers and it was regarded as the evidence that boron substitutes for a silicon atom. The ^{13}C hf tensor shows axial symmetry with its principal axis parallel to the g_z-axis for all sites. The isotropic hf constant $a = +(40.8 \pm 0.5) \times 10^{-4}$ T and the anisotropic hf constant $b = +(14.8 \pm 1) \times 10^{-4}$ T. This result shows that there is direct spin density on the p_z-orbital of the carbon nearest to boron (see Fig. 1). If for instance the unpaired spin would be located on the three C-Si "back-bonds" as suggested in the "boron-induced carbon-acceptor" model [22-24], the sign of b would be negative, in contrast to our finding. An estimate of the spin density on the carbon atom from a and b yields 3% s-character and 27% p-character. This suggests that the four orbitals of carbon are shifted from sp^3 hybrid orbitals to three sp^2 hybrid orbitals and one pure p orbital in which the unpaired spin is mainly localized. This means that the carbon atom is relaxed away from boron. We believe that the same shift happens for boron as the covalent radius of boron is smaller than for silicon and since there is no bond between carbon and boron.

ENDOR spectra of ^{11}B (I=3/2) have also been obtained for the three centers k_1, k_2 and hex. The parameters are almost the same as those obtained in [22]. Again the hf tensor of ^{11}B is axially symmetric. The values and signs of a and b can be explained very nicely by the dipole-dipole interaction of the ^{11}B nuclear spin with the unpaired spin in the p_z-orbital of the nearest carbon. The spin density on the central carbon is estimated to be about 38% whereas it is negligible on boron. The total spin density on the three Si neighbours of the central carbon is 2.4%. From ENDOR experiments on the remote ^{29}Si and ^{13}C nuclei an estimate can be made of the distribution of the remaining ≈60% spin density in the crystal. We find that it is rather smoothly distributed with a Bohr radius r_0 = 2.2 Å. This value is in reasonable agreement with estimates from Effective Mass Theory.

Deep boron-acceptor

In analogy to the sB center an EPR and ENDOR study at 95 GHz was carried out on the dB acceptor. The main results can be summarized as follows. First it was established that the spin multiplicity of this center S=½. Second, in contrast to the sB acceptor the g-tensors are almost axial with g_z parallel to the c-axis for the hexagonal as well as for the quasi-cubic sites. The

values of g_z, g_y and g_x are such that $(g_z\text{-}g_e) >> (g_x\text{-}g_e)$, $(g_y\text{-}g_e)$ and that $g_x \neq g_y$, i.e., there is a small non-axiality. Third the EPR spectrum of the ^{13}C-enriched sample does not exhibit hyperfine satellite lines in contrast to the sB acceptor. The maximum ^{13}C hf interaction in the ENDOR spectrum is 7.8 MHz (3×10^{-4} T). Fourth a hyperfine line in the EPR spectrum with a hf splitting of about 40×10^{-4} T is tentatively assigned to ^{29}Si. Fifth the hf and quadrupole interaction with ^{11}B is again small and given by $a_B^{hex} = 2.6 \pm 0.8$ MHz, $a_B^{qc} = 3 \pm 1.5$ MHz, $b_B^{hex} = 1.7 \mp 0.3$ MHz, $b_B^{qc} = 3.1 \mp 0.9$ MHz and $q = 63$ kHz for all sites.

Following Baranov et al. [13,27] it is proposed that the dB acceptor consists of a boron on a silicon position with an adjacent carbon vacancy along the hexagonal axis (see Fig. 2). Apparently for energetic reasons, this carbon vacancy combines always with an adjacent boron along the c-axis. The observed directions of the principal axes and principal values of the g-tensor are in agreement with this model. The g_z-axis is found parallel to the vacancy-boron axis and the g_x axis is found in the $[11\bar{2}0]$ plane because a small Jahn-Teller distortion is expected to make one silicon atom inequivalent with respect to the other two. Moreover it is predicted that g_z deviates most strongly from g_e because there is a non-zero value related to ℓ_z, the z-component of the orbital angular momentum. The proposed model for the dB acceptor could predict a large hf interaction of the ^{29}Si. Assuming that the line at 40×10^{-4} T from the main line of the dB acceptor is related to ^{29}Si, we estimate the spin density at the silicon positions surrounding the carbon vacancy of the order of 25-30%. The largest ^{13}C hf interaction of 7.8 MHz observed in the ^{13}C ENDOR spectrum is assigned to the nine carbon atoms adjacent to the three Si atoms surrounding the vacancy and would correspond to a total spin density on these nine C atoms of 7.2%. It is interesting to note that apart from the two ^{13}C ENDOR lines separated by 7.8 MHz, the other ^{13}C lines are grouped closely around the ^{13}C Zeeman frequency. This indicates that the spin density is for almost 100% localized on the three silicons surrounding the vacancy and on the nine adjacent carbon atoms. In contrast the ^{13}C ENDOR spectrum of the sB acceptor exhibits a much more gradual distribution of the ENDOR lines typical for a more shallow center where the spin density is distributed over a larger volume.

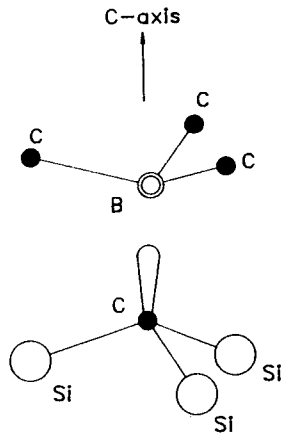

Fig. 1 The atomic structure of the hexagonal site of the shallow boron acceptor in 6H-SiC at low temperature.

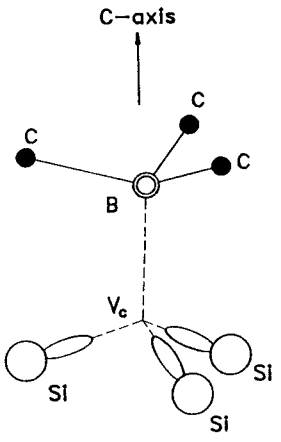

Fig. 2 The atomic structure of the deep boron acceptor in 6H-SiC at low temperature.

From the ^{11}B hf interaction data it is clear that there is a negligible spin density on boron. According to our model the anisotropic part of the hf interaction b_B is thus determined by the dipole-dipole interaction between the unpaired spin in the three dangling bonds of the silicon atoms and the nuclear spin of ^{11}B. To estimate the value of b_B we used a point-dipole approximation assuming sp^3 orbitals on the three Si atoms. We placed 75% of the fractional charge f at 0.77 Å from the Si atoms on their connection lines with the vacancy and assumed 25% of the fractional electron spin to be located on the silicon nucleus. For a value f = 30% on one of the Si hybrid orbitals this leads to b_B = + 1.1 MHz in good agreement with the experimentally observed value.

The discussion of the EPR and ENDOR results leading to the proposed models for the shallow- and deep-boron acceptor has been rather sketchy because of the limited space available in this report. For a detailed description the reader is referred to two publications [32,33].

Conclusions

The high-frequency EPR/ENDOR study at 95 GHz enables us to present a consistent model of the electronic structure of the shallow and deep boron acceptor at low temperature. With regard to the shallow-boron acceptor it is concluded that about 40% of the spin density is located on the p_z-orbital of a carbon which is nearest to boron. The p_z-orbital is along the C-B connection line and the C-B bond is a dangling bond. Boron is neutral and carries no direct spin density. There is a relaxation of the carbon atom, carrying the spin density, and the boron atom away from each other. It is further concluded that about 60% of the spin density is distributed in the crystal with a Bohr radius of 2.2 Å. With regard to the deep-boron acceptor it is concluded that here a boron also occupies a silicon position but now accompanied by a neighbouring carbon vacancy along the hexagonal c-axis. The spin density is distributed over a smaller volume than in the case of the shallow-boron acceptor.

The results of these two studies demonstrate the high spectral resolution and the high sensitivity of EPR spectroscopy at 95 GHz. It is possible to disentangle the EPR spectrum of the various shallow and deep boron acceptor sites in the 6H-SiC crystal. Moreover a high resolution is obtained in the ENDOR spectra which allows the separation of the ^{13}C, ^{29}Si and ^{11}B nuclear transitions.

Acknowledgement

This work forms part of the research program of the "Stichting voor Fundamenteel Onderzoek der Materie" (FOM) with financial support from the "Nederlandse Organisatie voor Wetenschappelijk Onderzoek" (NWO). Further support was obtained from the HCM program of the Commission of the European Community under contract no. ERBCHRXCT93028 and ERBCIPDCT940612, P.G.B. thanks the financial support given by NWO under grant 047.005.12.96. T.I. thanks the financial support from "JSPS Fellowship for Research at Centers of Excellence Abroad". T.M. thanks for the financial support by a "Grant-in-Aid for Encouragement of Young Scientists.

References

1. G. Pensl, R. Helbig, Festkörperprobleme, Advances in Solid State Physics **30**, 133 (1990).

2. H. Kuwabara, S. Yamada, Phys. Status Solidi **A30**, 739 (1975).
3. M. Ikeda, H. Matsunami, T. Tanaka, Phys. Rev. **B22**, 2842 (1980).
4. M.M. Arikin, A.A. Lebedev, A.L. Syrkin, A.V. Suvorov, Sov. Phys. Semicond. **19**, 69 (1985).
5. W. Suttrop, G. Pensl, P. Laning, Appl. Phys. **A51**, 231 (1990).
6. V.S. Ballandovich, E.N. Mokhov, Semiconductors **29**, 187 (1995).
7. M. Ikeda, H. Matsunami, T. Tanaka, J. Luminescence **20**, 111 (1979).
8. G.C. Rybicki, J. Appl. Phys., **78**, 2996 (1995) and references therein.
9. H.H. Woodbury, G.W. Ludwig, Phys. Rev. **124**, 1083 (1961).
10. A.G. Zubatov, I.M. Zaritskii, S.N. Lukin, E.N. Mokhov, V.G. Stepanov, Sov. Phys. Solid State **27**, 197 (1985).
11. K. Maier, J. Schneider, W. Wilkening, S. Leibenzeder, R. Stein, Materials Science and Engineering **B11**, 27 (1992).
12. N.P. Baran, V.Ya. Bratus, A.A. Bugai, V.S. Vikhnin, A.A. Klimov, V.N. Maksimenko, T.L. Petrenko, V.V. Romanenko, Phys. Solid State **35**, 1544 (1993) and references therein.
13. P.G. Baranov, E.N. Mokhov, Semicond. Sci. Technol. **11**, 489 (1996).
14. P.G. Baranov, E.N. Mokhov, Sov, Phys. Solid. State **38**, 5 (1996).
15. P.G. Baranov, I.V. Ilyin, E.N. Mokhov, Solid State Comm. **100**, 371 (1996).
16. P.G. Baranov, Defect and Diffusion Forum **148-149**, 129 (1997).
17. K.M. Lee, Le Si Dang, G.D. Watkins, W.J. Choyke, Phys. Rev. Letters **45**, 390 (1980).
18. P.G. Baranov, V.A. Vetrov, N.G. Romanov, V.I. Sokolov, Sov. Phys. Solid State **27**, 2085 (1985).
19. P.G. Baranov, N.G. Romanov, Appl. Magn. Res. **2**, 361 (1991).
20. P.G. Baranov, N.G. Romanov, Mater. Science Forum **83-87**, 1207 (1992).
21. T.L. Petrenko, V.V. Teslenko, E.N. Mokhov, Sov. Phys. Semicond. **26**, 874 (1992).
22. R. Müller, N. Feege, S. Greulich-Weber, J.-M. Spaeth, Semicond. Science Technol. **8**, 1377 (1993).
23. J. Reinke, R. Müller, M. Feege, S. Greulich-Weber, J.-M. Spaeth, Mat. Science Forum **143-147**, 63 (1994).
24. E.J. Adrian, S. Greulich-Weber, J.-M. Spaeth, Solid State Comm. **94**, 41 (1995).
25. N.G. Romanov, V.A. Petrov, P.G. Baranov, E.N. Mokhov, V.G. Oding, Sov. Tech. Phys. Lett. **11**, 483 (1985).
26. P.G. Baranov, N.G. Romanov, V.A. Vetrov, V.G. Oding, Proc. of the 20th International Conference on the Physics of Semiconductors, World Scientific, Singapore, 1855 (1990).
27. P.G. Baranov, E.N. Mokhov, A. Hofstätter, A. Scharmann, JETP Lett. **63**, 848 (1996).
28. P.G. Baranov, I.V. Ilyin, E.N. Mokhov, Phys. Solid State, to be published.
29. Y.A. Vodakov, E.N. Mokhov, N.G. Ramm, A.D. Roenkov, Krist. und Techn. **5**, 729 (1979).
30. R.T. Weber, J.A.J.M. Disselhorst, L.J. Prevo, J. Schmidt, W.Th. Wenckebach, J. Magn. Res. **81**, 129 (1989).
31. J.A.J.M. Disselhorst, H. van der Meer, O.G. Poluektov, J. Schmidt, J. Magn. Res. **115**, 183 (1995).
32. T. Matsumoto, O.G. Poluektov, J. Schmidt, P.G. Baranov, E.N. Mokhov, Phys. Rev. **B55**, 2219 (1997).
33. A. Arnold, T. Ikoma, O.G. Poluektov, P.G. Baranov, E.N. Mokhov, J. Schmidt, Phys. Rev., submitted for publication.

Materials Science Forum Vols. 258-263 (1997) pp. 709-714

GAS AND HEAT TREATMENT EFFECTS ON THE DEFECT STRUCTURE OF *a*-SiC:H FILMS

T. Friessnegg[1], M. Boudreau[2], P. Mascher[2], P.J. Simpson[3] and W. Puff[1]
[1] Institut für Technische Physik, Technische Universität Graz, A-8010 Graz, Austria
[2]Department of Engineering Physics, McMaster University, Hamilton, Ontario, Canada
[3]The Positron Beam Laboratory, Department of Physics and Astronomy, The University of Western Ontario, London, Ontario, Canada

Keywords: *a*-SiC:H, positron annihilation, positronium, defects, gas desorption

Abstract. Open volumes formed during the film growth of *a*-SiC:H are interconnected throughout the amorphous network via channels and can trap gases at the large internal surfaces. The gases can be desorbed from the internal surfaces by heat treatments and leave behind an increased areal density of defects in the sample. A nano-crystalline structure grows upon annealing and irreversible structural changes take place, when breaking of Si-H and C-H bonds and formation of additional Si-C and C-C bonds lead to film densification.

Introduction

Many applications of *a*-SiC:H films arise from the fact that the optical properties such as the optical energy gap or the refractive index of the film can be varied by changing the composition, Si/C in the film. However, the increase in the defect density associated with carbon incorporation limits its potential use as a wide band gap electronic material [1].
In the growth of *a*-SiC:H using the organic source DTBS (ditertiary butyl silane) the film composition can be controlled by the flow rate of the gas source [2]. High C-concentrations in the films are obtained at high gas flow rates. Then CH_3 groups from the source are not sufficiently broken by the plasma and are directly incorporated into the film. These groups terminate the matrix around this configuration [3] and create microvoids which are filled with hydrogen and CH_n groups. With increasing temperatures these trapped species are successively released increasing the void size. There are some indication from thermal desorption and positron beam measurements [4] that these internal surfaces are interconnected and allow gases to diffuse out of the sample.
In this contribution this topic is further investigated by positron lifetime measurements and gas and heat treatments. The effect of annealing on the bond structure and on the amorphous network is studied by Fourier transform infrared spectroscopy (FTIR) and atomic force microscopy (AFM) respectively.

Experimental Details

The samples were deposited in the electron cyclotron resonance chemical vapor deposition (ECR-CVD) system at McMaster University [5]. Films were deposited on various substrates to allow for different techniques in the post deposition characterization. The film density was measured by depositing the film on a 2 μm Al foil and weighing the foil before and after the deposition. Table 1 summarizes the deposition parameters and some film characteristics for the sample sets A and B.
Isochronal annealing in vacuum was carried out in steps of 50 °C from 200-650 °C for 30 min at each temperature. After each annealing step FTIR spectra were recorded at room temperature relative to an uncoated FZ-Si substrate and the Si-C, Si-H and C-H absorption bands were analyzed.
The positron lifetime measurements were carried out on film B deposited on a tantalum substrate. This substrate was chosen to maximize the positrons backscattering at the *a*-SiC:H/Ta interface, leading to enhanced fraction of positrons annihilating in the film. In order to obtain reliable values of the lifetimes and intensities in the film, it is important to define and correct for the fraction *f* of

positrons transmitted through the film as precisely as possible. This fraction was determined by measuring the Doppler-broadening S parameter for positrons from a conventional ^{22}Na source (as used in the lifetime measurement) and for slow positrons from a variable energy positron beam. Because of their higher energies positrons from the conventional source probe in both film and substrate resulting in a S parameter

$$S_{total} = (1-f)S_{film} + fS_{substrate} \quad (1)$$

with the contributions S_{film} and $S_{substrate}$ from the film and the substrate respectively. The S_{film} parameter was calculated by averaging the S parameter profiling data in the energy range 5-30 keV. The fraction f of positrons transmitted through the film, when using the conventional source, is given by

$$f = \frac{S_{total} - S_{film}}{S_{substrate} - S_{film}}. \quad (2)$$

In the analysis of the lifetime spectra for sample B the lifetimes and intensities for the bare Ta substrate were subtracted with fraction f=.79 from the measured spectrum. The remaining spectrum was then decomposed into three components with well separable lifetimes of typically 0.13, 0.4, and 4 ns which can be attributed to the *a*-SiC:H film only.

Table 1: Deposition and film characteristics of the investigated *a*-SiC:H films.

	Sample A	Sample B
Substrates	FZ-Si (hi res)	Tantalum
Deposition rate [Å/min]	180	250
Deposition temperature [°C]	250	200
Power [W]	1000	1000
Thickness [μm]	2.1	15.5
Si/C ratio	0.36	0.30
Density [g/cm^3]	2.21	1.90

Results and discussion

The IR absorption measurements were performed in order to investigate the effect of the vacuum annealing on the Si-C, Si-H, and C-H absorption bands. Then the Si-C, Si-H and C-H absorption bands located at 780 cm^{-1}, 2100 cm^{-1} and 2900 cm^{-1} respectively, were analyzed by plotting the absorption coefficient as a function of radiation using the Beer-Lambert law without any corrections for multiple reflections (this simplification induces an error less than 6% [6]). With increasing annealing temperature the absorption peaks for SiH_n and CH_n become significantly smaller reflecting desorption of bonded hydrogen. A noticeable increase of the mode at ~1500 cm^{-1} after annealing at 600 °C is observed, which indicates that the films become more interconnected due to the formation of C-C bonds. The Si-H, C-H, Si-C and Si-O bond concentrations have been estimated from the SiH_n, CH_n, and SiC stretching mode bands using the formula

$$N = A_s \int \frac{\alpha(\nu)}{\nu} d\nu \cong \frac{A_s}{\nu_0} \int \alpha(\nu) d\nu \qquad (3)$$

where A_s is the reciprocal cross section of a given vibration mode, ν_0 is the center band wave number, and $\alpha(\nu)$ is the absorption coefficient. The A_s values have been taken from literature

$A_{s\,(\text{Si-H})} = 1.4\ 10^{20}\ \text{cm}^{-2}$ Ref. [7-9]

$A_{s\,(\text{C-H})} = 1.35\ 10^{21}\ \text{cm}^{-2}$ Ref. [6,7,9]

$A_{s\,(\text{Si-C})} = 2.13\ 10^{19}\ \text{cm}^{-2}$ Ref. [7]

$A_{s\,(\text{Si-O})} = 1.5\ 10^{19}\ \text{cm}^{-2}$ Ref. [7]

The bond concentration for CH_n is an order of magnitude higher than for SiH_n (Fig. 1), indicating that a high concentration of hydrocarbons are incorporated into the film. Bonded hydrogen starts to dissociate after 400 °C and is observed for both the SiH_n and CH_n modes. After annealing at 450 °C the film becomes partly oxidized, as can be seen from the increase of the SiO_2 mode in agreement with Auger measurements on this sample. We believe that residual oxygen in the vacuum tube diffuses through the low density region into the film, then saturates some of the dangling bonds, which were created by the escape of bonded hydrogen. The slight decrease in the $SiC/SiCH_n$ mode could be the result of film thinning. It is interesting to note that after 550 °C annealing the maximum absorption frequency for the SiH_n modes shifts from 2100 to 2125 cm^{-1}. This upward shift in frequency can be due to two possible effects: First, the so-called induction effect can occur when the nearest neighbor silicon atoms are progressively replaced by carbon [10]. On the other hand, it has been suggested that the shift in the absorption band for SiH_n to higher wavenumbers is due to Si-H bonds located on the interior surfaces of microvoids [11]. However, the observed desorption of C from the film makes the induction effect rather unlikely.

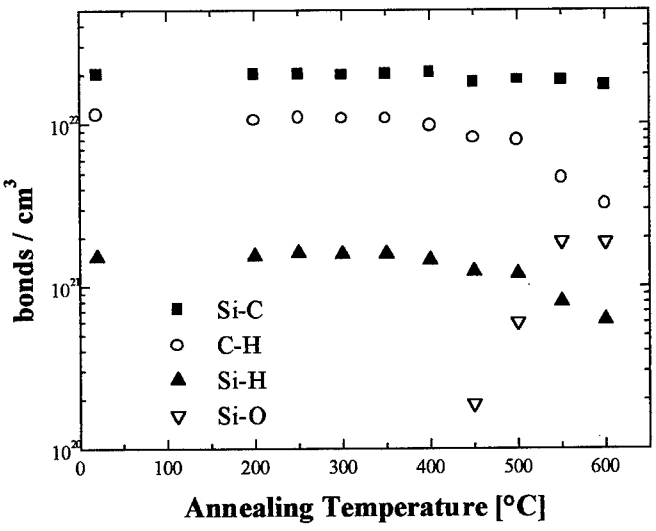

Fig. 1: Variation of the Si-C, Si-H, C-H and Si-O bond densities with the annealing temperature for sample A

A dominating intermediate-lived component ($\tau_2 \sim 0.4$-0.5 ns) was present in all samples. The values of τ_2 observed in *a*-Si:H are in the range of 400-600 ps [12-14] and have been attributed to the

presence of quadri- and pentavacancies and/or vacancy clusters. In this light our lifetime can be interpreted as due to annihilation of positrons trapped by vacancy clusters. The shortest lived component (τ_1) and the long lived component (τ_3) are attributed to annihilation of para-Ps and ortho-Ps respectively. The formation of Ps depends on several factors, an important one being the availability of sufficient space for the Ps. Because the wave function of the positron in the Ps atom overlaps other electrons in the medium (leading to the so-called pick-off annihilation), the ortho-Ps lifetime (τ_3) is significantly shorter than its vacuum value of 140 ns. The lifetime and the intensity of the long-lived component indicate that Ps is already formed in the "as deposited" state of the sample (Table 2).

Table 2: Ortho-Ps lifetime and intensity measured in vacuum at RT and 400 °C for sample B. The Ps fraction is calculated by ($4/3 \times I_{ortho}/100$)

Temperature	τ_{ortho} [ns]	I_{ortho} [%]	Ps-fraction
RT	4.27	8.0	.11
400°C	4.80	17.0	.23

Upon annealing at 400 °C we observe a substantial increase in the ortho-Ps characteristics. The lifetime changes to a higher value indicating a lower pick-off annihilation rate at high temperatures and the intensity increases significantly by 9%. Assuming no ortho-para conversion and therefore using the ratio for the annihilation probabilities from the para and ortho state of 1:3, the total fraction of positrons that form Positronium can be calculated. This fraction changes from 0.11 for the "as deposited" sample to 0.23 at 400 °C indicating that additional open volumes are created by the heating of the sample.

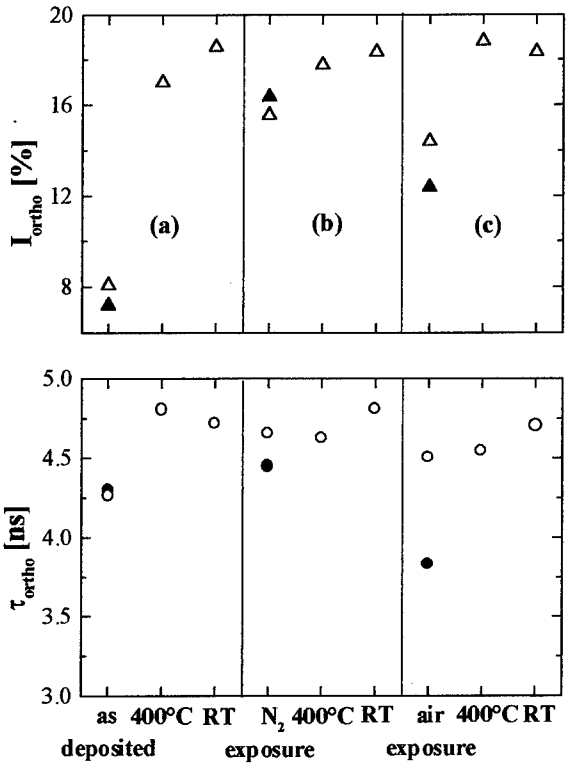

Fig. 2: Series of gas and heat treatments of sample B. All measurements are in chronological order. The solid symbols indicate measurements at 1 atm in the corresponding ambient. Measurements in vacuum ($p<5\times10^{-7}$ Torr) are all marked by open symbols. Measurements were taken at RT, 400 °C and after cooling down to RT for (a) the "as deposited" film (b) after 1 hr nitrogen exposure at 1 atm and (c) after 1 hr air exposure.

In order to relate the observed increase of the ortho–Ps component to desorption of gases, we studied the influence of gases on the positron characteristics in our film. For this purpose we heat-treated an "as deposited" film in vacuum and exposed this film afterwards to nitrogen and air (Fig. 2). The film was first annealed in vacuum at 400 °C, then cooled to room temperature. As discussed above the temperature increase causes an increase mainly in the ortho-Ps intensity. Cooling down to room temperature causes a slight additional increase of this intensity. Exposure to nitrogen at atmospheric pressure decreases the ortho-Ps intensity, indicating that the Ps formation probability has decreased. It is interesting to note that an increase in the ortho-Ps lifetime is observed after evacuating the chamber, which commensurate with a decrease in the pick-off annihilation rate. Heating up to 400 °C increases the ortho-Ps intensity again and the positron annihilation characteristics after cooling to room temperature indicate that the sample essentially returned to the state after the first heating. Air exposure causes a more pronounced decrease in the ortho-Ps lifetime and its intensity as one expects from the quenching of Ps by oxygen, which is reflected in particular in the increase of the ortho-Ps lifetime after evacuating the sample chamber. Heat-treatment of the sample up to 400 °C and subsequent cooling to room temperature recycles the sample indicating that the adsorbed gases were desorbed from the film by the heat treatment. These experiments indicate clearly that gases can be ad- and desorbed from internal surfaces of open volumes in the sample. These open volumes are interconnected through channels allowing for the gases to penetrate into the sample.

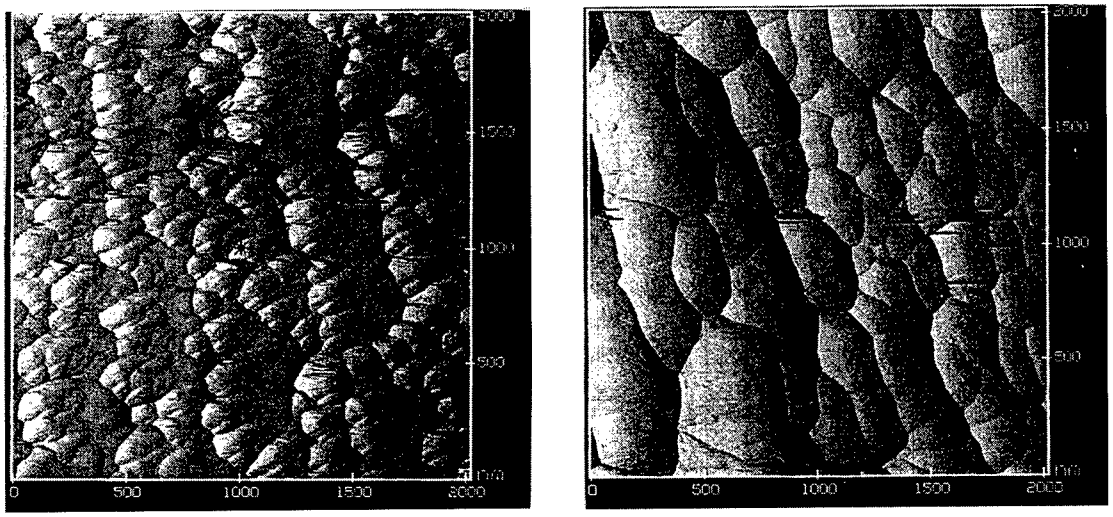

(a) (b)

Fig. 3: Atomic force microscopy images for sample B a) "as deposited" and b) after 24 hrs annealing at 450 °C. The scaling in the x and y directions is in units [nm]

Figure 3 shows two atomic force microscopy images recorded for the "as deposited" film and after vacuum annealing for 24 hours at 450 °C. Nano-grains with diameter of approximately 1000 Å are already present in the "as deposited" sample. These grains are separated by non-granular regions. The structural changes observed after 450 °C point clearly toward a crystallization process in the film. First an increase in the number of these grains is observed, then at higher temperatures grain growth takes places essentially removing all non-granular regions. The diameter of the grains at this point of annealing is a few 100 nm. From considering the relatively small size of these grains it is evident that a large number of grain boundaries are present in the material. This implies a large internal surface area which can act as traps for gases.

Conclusion

We have found that effects of heat treatment and gas exposure of *a*-SiC:H films on the positron characteristics may be interpreted generally in terms of activation/deactivation of positron or positronium traps as a result of removal/adsorption of gases on the internal surfaces. These open volumes can effectively trap gases during film growth or after deposition from the ambient. With increasing temperature the gases are desorbed from the interconnected internal surfaces of these open volumes and are released from the sample. This increases the areal density of the defects and is observable by enhancement in positronium formation. To our knowledge the capability of ad- and desorbing gases from internal surfaces has not been reported yet for *a*-SiC:H films and can possibly expand the wide range of applications of this material. Additional experiments are necessary in this context to clarify if *a*-SiC:H could be used as a molecular filter. In particular the mechanisms of gas adsorption and release from the internal surfaces could be subject to forthcoming experiments. The growth of a nano-crystalline structure is observable upon annealing. At sufficiently high temperatures thermal breaking of Si-H bonds and C-H bonds takes place and results in irreversible structural changes and film densification due to new bond formation in the film.

Acknowledgements

We wish to thank Dr. S. Dannefaer at University of Winnipeg for many useful discussions and for providing the *insitu*-annealing lifetime equipment.

References

1. D. Kruangani et al., Mater. Res. Soc. Symp. Proc. **95**, 609 (1987)
2. M. Boumerzoug, M. Boudreau, P. Mascher and P. E. Jessop, Mat. Res. Soc. Symp. Proc. **339**, 381 (1994)
3. D.L. Williamson, A.H. Mahan, B.P. Nelson, R.S. Crandall, Appl. Phys Lett. **55**, 783 (1989)
4. T. Friessnegg, M. Boudreau, P. Mascher, P.J. Simpson, and W. Puff, Mat. Res. Symp. Proc. Vol. **442**, 667 (1997)
5. M.G. Boudrau, M. Boumerzoug, P. Mascher and P.E. Jessop, Appl. Phys. Lett. **63**, 3014, (1993)
6. A. Guivrac'h, J. Richard, M. Le Contellec, E. Ligeon and J. Fontenille, J. Appl. Phys. **51**, 2167, (1980)
7. D.K. Basa and F.W. Smith, Thin Solid Films, **192**, 121 (1990)
8. W.A. Lanford and M.J. Rand, J. Appl. Phys. **49**, 2474, (1978)
9. K. Mui, D.K. Basa, and F.W. Smith, Phys. Rev. B **25**, 8089, (1987)
10. H. Wiedner, M. Cardona and C.R. Guarnieri, phys. stat. sol. B **92**, 99 (1979)
11. A.H. Mahan, P. Raboisson, D.H Williamson and R. Tsu, Solar Cells **21**, 117 (1987)
12. H. E. Schäfer, R. Würshum, R. Schwarz, D. Slobodin, and S. Wagner, Appl. Phys. A **43**, 295 (1987)
13. R. Suzuki, Y. Kobayashi, T. Mikado, A. Matsuda, P.J. McElheny, S. Mashima, H. Ohgaki, M. Chiwaki, T. Tomimasu, Jpn. J. Appl. Phys. **30**, 2438 (1991)
14. S. Dannefaer, D. Kerr, and B.G. Hogg, J. Appl. Phys. **54**, 155 (1983)

Materials Science Forum Vols. 258-263 (1997) pp. 715-720

CAPACITANCE SPECTROSCOPY OF DEEP CENTRES IN SIC

A.A. Lebedev and N.A. Sobolev
A.F. Ioffe Physico-Technical Institute,194021 St. Petersburg, RUSSIA

Keywords: Deep centres, DLTS, Silicon carbide, luminescence, structural defects.

Abstract. In the present work the parameters and distribution of deep centres in 6H and 4H SiC epitaxial layers and pn junctions grown by sublimation in an open system and by CVD were investigated. The deep level ionization energies and hole and electron capture cross - sections were determined by the DLTS and i-DLTS techniques. The possible structure of the observed centres and its influence on polytype transformation is discussed.

Introduction.

Silicon carbide is a wide band gap material (Eg = 3,2 eV for 4H SiC and Eg = 3,0 eV for 6H SiC) which can be used for producing high temperature and high power devices. It is well known that deep levels in semiconductors can influence different parameters of devices: carrier lifetime, breakdown voltage, electroluminescence intensity, etc. So, investigation of deep levels is a very important direction of SiC physics. In this paper we try to describe our present understanding of properties of deep levels in SiC and their relation to the structural defects in this material.

Samples.

The p-n structures studied in this work were grown on the (0001) Si face of single-crystal silicon carbide substrates of polytypes 6H and 4H. We investigated p-n structures fabricated by the sublimation sandwich method (SE p-n structures) [1], CVD p-n junctions prepared by CREE (CVD p-n structures) [2] and CVD epilayers grown on Lely SiC [3] substrates in our laboratory [4] and those prepared by sublimation growth of a p^+ emitter on CREE CVD n-type epilayers [5].

In all cases the dopants were Al (p-type) and N (n-type). The thickness of epilayers was 1-2 μm for p-type and 5-10 μm for n-type. In the case of Lely-SE structures, the p^+ emitter was grown directly on a Lely substrate without any intermediate weakly doped n-type layers. Ohmic contacts were produced by deposition of metal films (Ni for n-type and [Al + Mo + Au] system for p-type) with the subsequent annealing at ~1900^0C.

It was found that the experimental value of uncompensated donor impurity concentration (N_d-N_a) was equal to the N_d-N_a value obtained by measuring the capacitance of Schottky barriers formed on the n-layer surface prior to p^+- emitter growth (or to the N_d-N_a value taken from the specification), and C-U characteristics plotted in C^{-2}-U coordinates were linear in the voltage range studied.

Deep level parameters.

It was found that the same deep levels which had been observed in SE grown samples are present in CVD p-n structures [L-centre (Ev + 0,24 eV),"shallow boron" (Ev+0.35 eV), i-centre (Ev+0.52 eV), D-centre (Ev + 0.58 eV), S-centre (Ec - 0.35 eV), R - centre (Ec - 1.27

eV)]. The concentration of D-centres in the initial SE epitaxial layers was found to increase upon additional diffusion of boron, and that of i-centres to become higher after fabricating a p-n structure by ion-beam doping with Al.

Table. Parameters of the main detected Deep Centers.

Polytype	Type of centre	Energy position, eV	Electron cross-section, cm^2 (σ_n)	Hole cross-section, cm^2 (σ_p)	Participation in recombination processes
6H SiC	S	Ec - 0.35	10^{-15}	1-3 10^{-13}	radiation-free
	R	Ec - 1.27	10^{-14}	1-2 10^{-15}	radiation-free
	L	Ev + 0.24	10^{-18}	2-4 10^{-15}	?
	i	Ev + 0.52	2-6 10^{-21}	1-3 10^{-17}	DEL
	D	Ev + 0.58	1-3 10^{-20}	1-3 10^{-16}	"boron"
4H SiC	analoge L	Ev + 0.27	< 10^{-17}	5-6 10^{-15}	?
	analoge i	Ev + 0.5	< 10^{-21}	5 10^{-17}	DEL
	analoge D	Ev + 0.54	1-3 10^{-21}	1-3 10^{-16}	"boron"

It has been found that i- and D-centres in 6H are associated with yellow and green ("boron" and "defect") electroluminescence bands, respectively [6, 7] Also, it has been found that the R and S centres may govern the recombination processes in 6H SiC p-n structures [8]. In 4H SiC, acceptor centres were found, having approximately the same ionization energies and a similar ratio of hole and electron capture cross-sections σp and σn (σp/σn>>1); these centres initiated analogous electroluminescence processes [9, 10] (see the table).

In the CVD structures studied the highest concentrations were observed for i-centres and for D-centres closely related to them in parameters and properties. Previously, the i-centre was found in 6H-SiC crystals irradiated with aluminum ions and in intentionally undoped SE epitaxial silicon carbide layers [11]. The introduction of scandium also led to the formation of the given centre in 6H SiC and to the appearance of "defect" electroluminescence (DEL) ($h\nu_{max 6H\ SiC}$ ~ 2.35 эВ) [12]. It was shown that all DEL characteristics can be described in terms of the donor-acceptor recombination model: nitrogen level - i-centre [7]. Also known is that DEL can be brought into existence by irradiation of SiC with electrons, neutrons and some types of ions [13]. Thus the formation of i-centre is not related to any single type of impurity, but may occur for a variety of reasons, including irradiation. This points to a purely defect origin of the centre.

Self compensation of the SiC epilayers.

Previously, the net concentration of deep acceptor centres (E_{na}) in SE p-n structures has been found to be invariably higher by an order of magnitude than the net concentration of donor-like deep centres [6]. The E_{na} values in SE structures with Nd - Na = 10^{17} cm^{-3} amounted to 10-50% of Nd-Na . The E_{na} value was little affected by variation of the concentration of shallow donor levels. So, at Nd-Na = 10^{18} cm^{-3} the degree of compensation was as low as 3%, and at Nd-Na = 10^{16} cm^{-3} overcompensation of epitaxial layers occurred. We observed in CVD p-n structures the same dependence of E_{na} on Nd-Na (figure 1), but with net concentration of deep acceptor centres in CVD p-n structures being invariably smaller by 2-3 orders of magnitude than in SE p-

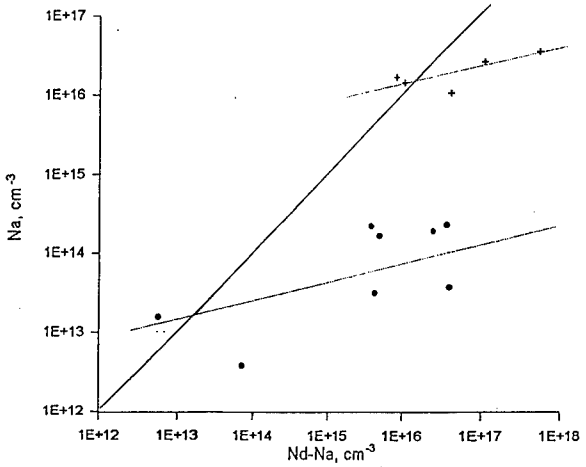

Figure 1. Dependence of the net concentration of deep acceptor centers on Nd-Na concentration in SE (+) and CVD (•) p-n structures. Straight line corresponds to E_{na} equal to 0.5 (Nd-Na).

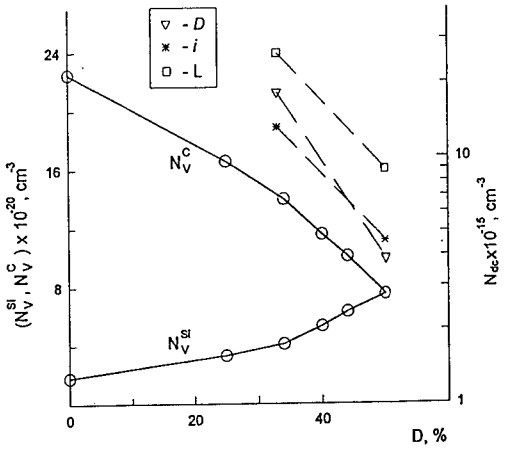

Figure 3.Dependences of carbon (N_V^C) and silicon (N_V^Si) vacancy concentration from [17] and concentration of detected deep acceptors (D, i and L centers) on SiC polytype degree of hexagonality

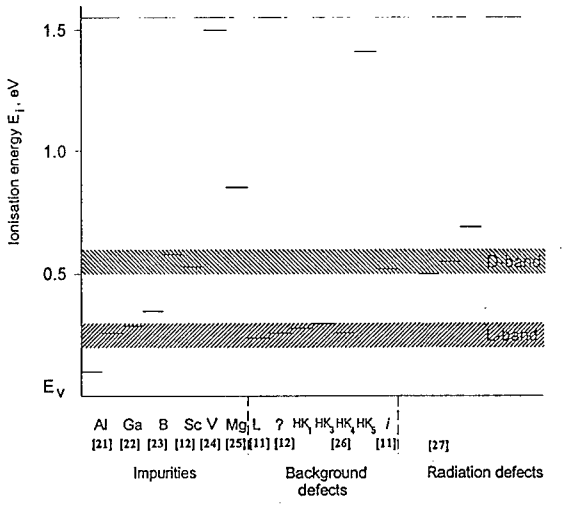

Figure 2. Distribution of the observed deep centers in lower half of 6H SiC forbidden gap.

n structures with the same value of Nd - Na. So, no overcompensation of CVD epilayers occurred down to Nd-Na ~ 10^{14} cm^{-3}.

During our experiments on CVD growth on Lely 6H SiC substrates we observed inversion of the conductivity type of growing epilayers, depending on the C/Si ratio in the gas phase. Increasing this ratio from 1 to 5-8 reduced the concentration of uncompensated donor levels in the films grown from 1-3 10^{18} cm^{-3} to 2-4 10^{16} cm^{-3}. At higher C/Si ratios the resulting layers were of p-type with the Na - Nd concentrations varying from 1 10^{16} (C/Si ~ 8) to 6-8 10^{17} cm^{-3} (C/Si =10-15). An investigation of the p-type layers grown in this work has shown that for all Na-Nd values their conductivity is governed by the presence of deep acceptor centres lying in the energy interval Ev + (0.15 - 0.25) eV, with parameters close to those of structural defects (L-centre, Ev + 0,24 eV) always present in sublimation-grown 6H SiC.

X-ray investigation.

An X-ray study [14] of SiC p-n structures prepared by various technological methods on the basis of SE epilayers showed that the minimum half-widths of X-ray diffraction peaks are mainly observed for structures with the maximum DEL intensity (high concentration of i-centres) or with 3C SiC inclusions present. In the same work an assumption was made that centres activating DEL are formed during stress relaxation in an epitaxial layer, e.g., in the course of its growth or during irradiation with subsequent annealing. It has also been shown previously that CVD epilayers have, as a rule, high dislocation density (~ 10^3 - 10^5 cm^{-2}), which exceeds by 1-2 orders of magnitude the value for epitaxial layers prepared by sublimation epitaxy (SE) [15].

In additional experiments we made an attempt to grow n-type epilayers by SE on a 6H SiC substrate with high density of dislocation (~ 10^5 cm^{-2}), usual for CREE substrates. In this experiments we obtained 3C-SiC films under the same growth conditions as those commonly used for growth of 6H SiC SE films. It is known that CVD SiC layers are grown at much lower temperatures than in the case of SE layers, ~1500 and 2000 ^{0}C respectively. Thus it may be assumed that in gas phase epitaxy the temperature is not high enough to enable stress relaxation through formation of i-centres or inclusions of other polytypes. In the given case such a relaxation may occur via formation of a large number of dislocations.

Discussion.

An analysis of the results obtained and published data has shown that the ionization energies of the majority of acceptor centres known for SiC fall within two narrow bands in the lower half of the forbidden gap: "L-band": Ev + 0.2 ÷0.3 eV (L-centre, Al, Ga) and "D-band": Ev + 0.5 ÷0.6 eV (D-centre, i-centre, Sc) (Figure 2). Thus, it may be assumed that the "L-band" and "D-band" are related to defect complexes which are characteristic of SiC and whose ionization energies change only slightly upon addition of extra impurity atoms.

It has been shown [16,17] that the concentration of carbon vacancies, which are intrinsic lattice defects characteristic of SiC, depends on the polytype and decreases with increasing polytype hexagonality. In Fig.3 we show simultaneously the vacancy concentrations from [17] for different SiC polytypes and the average deep acceptor concentration in 6H and 4H SiC SE pn structures. It can be seen that there is good correlation between the decrease in the vacancy concentration and that in the concentration of deep acceptor levels with increasing degree of polytype hexagonality.

In [18,19] it was shown that by varying the C/Si ratio in the zone where sublimation SiC layers are grown or by introducing some impurities one can perform heteroepitaxy of 3C and 4H films on 6N SiC substrates. For example, growth in a medium containing admixtures of Sc, Al and B produced 4H SiC epitaxial films. (Note that above impurities form in 6H SiC deep centres with energies falling within the "L-band" and "D-band.") To account for the observed dependence, the author of Ref. 18 offered an explanation that as the stress in the lattice increases with increasing concentration of carbon vacancies, the bonds between atoms at cubic sites become more energetically favourable. This leads to a restructuring of the crystal and to polytypic transformation. Based on the aforesaid, it may be concluded that both 3C SiC and DEL activator centres are formed by the same mechanisms, which should be accompanied by stress relaxation in the epitaxial layer.

Conclusion.

1. It was found that in 6H and 4H SiC there are no less than three types of deep acceptors which are present in materials produced by different technological methods and which take part in main recombination processes. These centres are related to carbon vacancies always present in SiC crystals.

2. It may be assumed that each SiC polytype has its own equilibrium concentration of defects (carbon vacancies). When this concentration is changed by any technological means (introducing impurities or changing C/Si ratio during growth, using for growth substrates with high density of dislocation, irradiation or implantation) generating excess defects, the crystal will try to return again to the equilibrium vacancy concentration. This may be achieved as follows: (a) formation of inclusions of other polytypes having lower degree of hexagonality as compared with the substrate, (b) increase in the concentration of deep acceptors belonging to "L-band" or "D-band", (c) increase in the dislocation density (low temperature case).

This, in our opinion, means that if introduction of some impurities may lead to transformation of the polytype of a growing SiC film and formation of deep acceptors from "L-band" or "D-band", then implantation or irradiation of an already grown SiC layer can not only produce the above-noted deep acceptors, but also cause transformation of the layer polytype. So, this means that it is possible, under certain conditions of irradiation and subsequent annealing (or some other type of treatment), to achieve a polytype transformation of an already grown SiC layer and to fabricate in this way SiC-based heterostructures.

This supposition of the present work agrees with the results of Ref. [20], where the stability of 6H SiC blue light-emitting diodes (LED) fabricated by liquid-phase epitaxy was investigated. In Ref. [20] it was found that passage of forward current through some of the structures caused degradation of their parameters, which manifested itself in both a decrease in the quantum yield of a LED and in a shift of the emission peak to the green region of the spectrum, where the maximum of the "defect" EL in 6H SiC is situated. Investigation of degraded structures revealed the presence of 3C SiC in the strained layer.

Acknowledgments.

The author is grateful to V.V. Zelenin and N.S. Savkina for epitaxial growth and A.S. Tregubova and M.P. Scheglov for x-ray investigation. This work was supported in part by Arizona University (USA) and Schneider Group Research centre (France).

References

1. M.M.Anikin, A.A.Lebedev, S.N.Pyatko, A.M.Strel'chuk and A.L.Syrkin, *Mater.Sci.Eng,* **B11**, 113, (1992).
2. J.W.Palmor, J.A.Edmond, H.S.Kong and C.H.Carter Jr. *Physica B* ***185*** p. 461, (1993).
3. J.A Lely *Ber.Dt.Keram.Ges.* **55** .. 229-231, (1955):
4. V.V.Zelenin, A.A.Lebedev, S.M.Starobinets, V.E.Chelnokov to be published in *Material Science and Engineering*, 1997.
5. N.S.Savkina, A.A.Lebedev, A.A.Mal'tsev, N.K.Poletaev, M.G.Rastegaeva, A.M.Strel'chuk and V.E.Chelnokov, *Inst. Phys. Conf.* Ser. No. 142 Chapter 3 501 (1996).
6. A.A.Lebedev and V.E.Chelnokov. *Diamond films and Related Materials* V **3**, p 1393, (1994).
7. A.N.Andreev, M.M.Anikin, A.A.Lebedev, N.K.Poletaev, A.M.Strel'chuk, A.L..Syrkin, V.E.Chelnokov. *Semiconductors* 28, 430 (1994).
8. M.M.Anikin, A.S.Zubrilov, A.A.Lebedev, A.M. Strel'chuk, and A.E.Cherenkov, Sov.Phys.Semicond. V25, N3, p 289-293 (1991).
9. M.M.Anikin, A.A.Lebedev, N.K.Poletaev, A.M.Strel'chuk, A.L..Syrkin, V.E.Chelnokov. *Semiconductors* 28, 288 (1994).
10. A.A.Lebedev, N.K.Poletaev,. *Semiconductors* 30, 238 (1996).
11. M.M.Anikin, A.A. Lebedev, A.L.Syrkin, A.V. Suvorov. *Sov. Phys. Semicond.*, 19, 69 (1985).
12. V.S.Balandovich. *Fiz.Techn. Poluprov.*, **25**, 287 (1992).
13. V.V.Makarov, N.N.Petrov. *Fiz. Tv. Tela*, **8**, 1272 (1966).
14. A.A.Lebedev, M.P.Scheglov, T.V.Sokolova. *Tech. Phys. Lett.* 21, 654 (1995).
15 A.A.Lebedev, A.S. Tregubova, A.A. Glagovskii, M.P.Scheglov, V.E Chelnokov *Abstr E- MRS Conf*, June 4-7, , Strasbourg,France, p A-15 (1996).
16. Yu.A. Vodakov and E.N. Mokhov *Inst. Phys. Conf. Ser No 137* 197, (1994).
17. N.D. Sorokin, Yu.M. Tairov, V.F. Tsvetkov , M.A. Chernov *Sov. Phys. Crystallogr*, **28**, 780, (1983).
18. Yu.A. Vodakov, G.A. Lomakina and E.N. Mokhov *Sov. Phys. Solid. State* **24**, 1377 (1982).
19. Yu. Vakhner and Yu.M. Tairov, *Sov. Phys. Solid State* **12**, 1543 (1970).
20. G.Zienther and D. Theis, *IEEE Trans. Electron devices* ED-28,425 (1981).
21.G.A.Lomakina et al., *Sov.Phys.Solid State*, **12**, 2356 (1970).
22. Yu.A.Vodakov, et.al., *Phys.Stat.sol(a)* **35**, 37 (1976).
23. A.I.Veigner.,et.al., *Sov.Techn.Phys.Lett*, **5**, 566 (1980).
24. W.C.Mitchel, et.al, *Inst. Phys. Conf.* Ser. No. 142 Chapter 2, 313 (1996).
25. E.N.Kolabukova, et.al., *Inst. Phys. Conf.* Ser. No. 142 Chapter 2 333 (1996).
26. N.I.Kuznetsov, et.al., to be published in *Semiconductors* (1997).
27. G.C.Rybick, *J.Appl. Phys*, **78**, 2996, (1995).

Materials Science Forum Vols. 258-263 (1997) pp. 721-726

NATIVE AND ELECTRON IRRADIATION INDUCED DEFECTS IN 6H-SiC

T. Friessnegg and S. Dannefaer
Department of Physics, University of Winnipeg, Winnipeg, MB R3B 2E9, Canada

Keywords: SiC, vacancies, electron irradiation, positron annihilation

Abstract. Differences in the concentration of native defects were found in variously doped samples. The concentration of these grown in clusters is at least in the range of 10^{16} cm^{-3}. An order of magnitude larger concentration of grown in defects is found in the heavily n-type material. Monovacancies are observed after electron irradiation at 100 K in bulk n-type 6H-SiC. These vacancies are in the neutral charge state and do not represent shallow positron traps. At about 375 K a large fraction of these vacancies anneal by Frenkel pair recombination.

Introduction

Recent advances in the crystal growth of 6H-SiC allow the production of high quality 2 inch wafers by a commercialized process. Nevertheless, the behavior of impurities and especially native and irradiation induced point defects have been studied insufficiently. Just in the recent years a certain progress has been made in this field, resulting in a few comprehensive reviews [1, 2].
The responses from fundamental vacancy type defects identified by electron paramagnetic resonance (EPR) and positron annihilation spectroscopy can be summarized: In 2 MeV proton irradiated p-type 3C-SiC films an EPR line (T5) was found [3] which was ascribed to a singly-positive carbon vacancy (V_C^+); this resonance was not observed in n-type material. Itoh *et al.* [4] also found an EPR line (T1) after 1 MeV electron irradiation of n-type 3C-SiC, which was interpreted as arising from negatively charged silicon vacancies (V_{Si}^-). Itoh *et al.* [3] did also report the presence of the T1 line in p-type 3C-SiC epilayers irradiated with protons. They discussed the origin of a dominant 1.913 eV photoluminescence line [5] observed in 2 MeV electron irradiated (2×10^{17} e^-/cm^2) epi-layers in conjunction with EPR measurements and concluded that this line results from radiative transitions between the bottom of the conduction band and the electronic level of V_{Si} located 0.50 eV above the valence band. Positron lifetime experiments have shown [6] that electron irradiation of n-type bulk 6H-SiC at room temperature formed two neutral defects and that no such defects could be detected in p-type 6H-SiC. The introduction rates for these neutral defects are ~100 times higher than those observed by EPR, which suggests that EPR only detects a small fraction of vacancies being positively charged while positrons observe the dominant and neutral vacancies [7].
Both neutral defects exhibit an annealing stage very close to room temperature and similar annealing steps where observed for V_C^+ and V_{Si}^- by EPR in 3C SiC [4]. This suggests that annealing could occur during the irradiation as well as during storage at room temperature over an extended period of time. In the present work we present positron annihilation results after low temperature electron irradiation to investigate if long-range migration of vacancies takes place at room temperature.

Experimental Details

The samples were bulk n- and p-type wafers with various doping concentrations (Table 1) and were obtained from Cree research. For the low temperature irradiation a vacuum chamber was designed where sample set 3 was cooled down to liquid nitrogen temperature in order to prevent annealing during irradiation. The samples were irradiated with 2.2 MeV to a dose of 6×10^{16} e^-/cm^2. During the irradiation the sample temperature increased to 100 K due to heating of the sample and sample-holder by the incident electron beam. After the irradiation the source sample-sandwich arrangement

was assembled at liquid nitrogen temperature and the assembly was transferred to the cryostat without increasing the temperature beyond 100 K.
Isochronous annealing for 1 hr at each temperature step was carried out in the cryostat up to 70 °C. Heat treatments at higher temperatures samples were performed in a separate furnace for 30 min at each step.

Results and discussion

We conducted a survey of 5 wafers in the "as received" state. The lifetime spectra containing 7×10^6 counts were decomposed into two components and χ^2 values of 1.0 to 1.1 were typically obtained. In Table 1 the average and bulk lifetimes calculated from these fits are presented together with the corresponding defect lifetimes and intensities. The trapping rates were calculated from the simple trapping model [8].

Table 1: Positron lifetime parameters for "as grown" p- and n-type 6H-SiC wafers. The bulk lifetimes and trapping rate κ were calculated using the two state trapping. Doping concentrations correspond to N_D-N_A for n-type and N_A-N_D for p-type samples. The error values quoted for sample 1 are also representative for the other samples.

Sample	Doping type	Doping conc. [cm^{-3}]	τ_1 [ps]	τ_D [ps]	I_D [%]	τ_{Avg} [ps]	τ_{Bulk} [ps]	κ [ns^{-1}]
1	p	1.1×10^{17}	138±1	271±20	8±1	150±1	144±2	0.3
2	p	7.3×10^{18}	141	343	4	148	144	0.1
3	n	5.2×10^{17}	138	292	5	145	141	0.2
4	n	6.0×10^{17}	140	300	6	150	144	0.2
5	n	3.8×10^{18}	132	256	26	165	151	1.0

The lifetime parameters for the highly N-doped sample 5 are significantly different from the rest of the samples indicating a substantially higher defect concentration in this sample. The lifetime spectra of all other samples are characterized by a dominant τ_1 lifetime. The much longer lifetime τ_D=302±30 ps (averaged value) with intensities varying between 5-10% arises from annihilations in vacancy clusters [6]. From the trapping rate their concentration can be estimated [9, 10, 11] in the range of 10^{16} cm^{-3} for the p- and the lightly n-type samples. These defects are formed independent of the doping type. The bulk lifetime, calculated from the two state trapping model is constant at 143±2 ps for wafers 1 to 4. The higher τ_{Bulk} for wafer 5 indicates that the assumed two state trapping model cannot be applied in this case. This discrepancy can be explained by the presence of an additional defect component in this sample. The 302 ps defect lifetime was also assumed to be present in this sample and was therefore fixed in the analysis. Table 2 shows the lifetime parameters obtained from these fits for the "as grown" and annealed wafer 5. The bulk lifetime calculated from this agrees very well with the value observed for the other samples and confirms the applicability of the assumed model. For the additional defect component in this sample we find a lifetime of 160 ps with a remarkable high trapping rate (2.9 ns^{-1}) reflecting a high defect concentration (~3×10^{17} cm^{-3}) of these positron traps. It is worth noting that also the trapping rate for the 302 ps of the vacancy

clusters is considerable higher in this sample than in all other wafers suggesting an about 5 times higher concentration for the vacancy cluster. Since a 160 ps lifetime is only observed in the highly nitrogen doped sample the dopant could have an influence on the formation of this defect. For high doping concentrations the Fermi level is close to the band edges and changes only very little with temperature. Therefore the position of the Fermi level could have an influence on the formation of these defects during growth of the sample. However, these defects seem not to be electrical active since no carrier saturation with nitrogen concentration occurs in this doping range as was reported by Tsvetkov *et al.* [12]. According to their Fig. 4, the nitrogen doping concentration is about a factor 20 higher than the actual carrier concentration reflecting that only a small fraction of donors is ionized at room temperature.

Table 2: Lifetime parameters fitted for the "as grown" and 1400 °C annealed sample 5 with a fixed defect lifetime of τ_{D2} = 302 ps lifetime. The bulk lifetimes and trapping rates κ_1,κ_2 were calculated by using the three state trapping model.

Sample 5	τ_1 [ps]	τ_{D1} [ps]	I_{D1} [%]	I_{D2} [%]	τ_{Bulk} [ps]	κ_1 [ns^{-1}]	κ_2 [ns^{-1}]
as grown	93±5	161±2	63±3	13±0.3	144±2	2.9±0.4	1.0±0.1
annealed	93	158	66	12	144	2.9	0.9

Kawasuso *et al.* [13] observe a defect giving a lifetime of 183 ps with a concentration of 2×10^{17} cm^{-3} in "as grown" N doped samples with nitrogen concentration comparable to wafers 3 and 4. They report a sharp annealing step for these defects at 1400 °C. However, annealing of our sample 5 at 1400 °C does not change the trapping into the τ_{D1} and τ_{D2} defects indicating a high binding energy for both types of defects (Table 2).

In Table 3 the positron lifetime results for the "as grown" sample 3 and after 100 K irradiation are presented together with the Doppler broadening S and W parameters.

Table 3: Positron lifetimes and Doppler-broadening S and W (normalized to FZ-silicon and to the bulk value) parameters for the "as grown" and the "as irradiated" sample 3. The measuring temperature for the "as irradiated" sample was 80 K.

Sample 3 treatment	τ_1 [ps]	τ_2 [ps]	I_1 [%]	τ_{Avg} [ps]	τ_{Bulk} [ps]	S/S_{Bulk}	W/W_{Bulk}
as grown	138 ±1	292 ±15	95 ±2	145 ±1	141 ±2	1.000	1.000
as irradiated	150	286	92	161	156	1.009	1.027

Irradiation has introduced additional vacancies as observable by the increase in the average lifetime. The bulk lifetime, calculated for the "as irradiated" sample has a value of 156 ps which clearly indicates that trapping rates are not calculable from the two state trapping model.
The lifetime spectrum for the irradiated sample is dominated by the lifetime τ_1 with 92% intensity in this component. This lifetime is due to vacancies because $\tau_1>\tau_{Bulk}$=144 ps. A longer lifetime component (τ_2) with only 8% intensity is also observed in this sample.

The increase in S parameter for the irradiated sample is very small suggesting that the defect specific S parameter for the vacancies created by the irradiation is very close to the bulk value. This is understandable in view of the lifetime τ_1 for these defects, which is also in close proximity to the bulk value. An interesting feature is shown by the W parameter. After irradiation its value increases by about ~3% compared to the "as grown" sample indicating the annihilation of positrons with core electron with high momentum in the irradiation-induced defects.

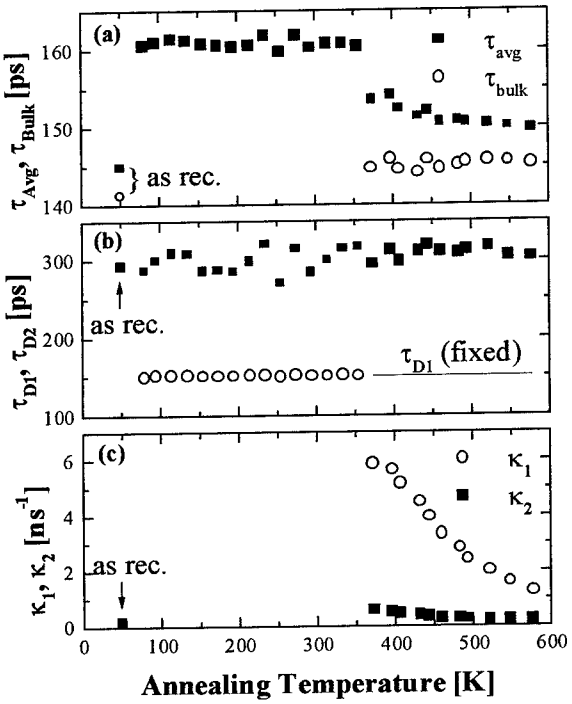

Fig. 1: Positron lifetime parameters for the irradiated at 100 K sample as a function of annealing temperature. The sample was measured at 80 K after annealing between 95 and 275 K, at 250 K after annealing between 275 and 375K and at room temperature after annealing between 375 and 575 K. Results for annealing temperatures up to 375 K are from free two-term fits. For higher annealing temperatures the defect lifetime τ_{D1}=150 ps was fixed and trapping rates were calculated from the three state trapping model.

To examine the thermal stability of these defects isochronal annealing was performed. In Fig. 1 are shown the lifetime results for the irradiated sample as a function of annealing temperature. The lifetime parameters show no change for annealing up to 375 K. We note that one cannot exclude annealing of defects in this temperature range, because the saturation trapping into the defects makes the modified bulk lifetime irresolvable in this sample. First at 375 K annealing of defects becomes observable in the lifetime data and is reflected by the decrease of the average lifetime after this annealing step. Three term fits were employed in the analysis of the spectra between 375 and 575 K annealing temperatures and the defect lifetime, constant in the annealing range up to 375 K, was fixed to its average value of 150 ps. In this manner the modified bulk lifetime could be resolved and the trapping rates could be calculated from the three state trapping model. The trapping rate decreases by more than 80% indicating a major reduction of the defects created by the irradiation in the temperature range between 375 and 575 K. The trapping rate into the defect with a lifetime τ_{D1} is at least 6 ns^{-1} at 350 K (Fig. 1) and the decrease in the trapping rate is commensurate with that

observed earlier [7] for room temperature irradiated sample up to 300 °C. This lifetime can be attributed to monovacancies. The monovacancy in diamond yields a value close to 150 ps [9]. Theoretical calculations suggest that the carbon vacancy should yield a lifetime of 153 ps [14]. However, it is expected that also silicon vacancies (V_{Si}) are formed by the irradiation. The absence of a corresponding defect lifetime could be explained if silicon vacancies exhibit a lifetime that differs from the V_C by less than ~50 ps. In this case the two defects would not be resolved as separate lifetimes and τ_{D1} would be a mixture of τ_{V_C} and $\tau_{V_{Si}}$. Theoretical calculations suggest that the silicon vacancy should yield a lifetime of 192 ps [14]. After room temperature irradiation under the same irradiation conditions we observed a slightly higher defect lifetime (160-170 ps) [6, 7].

Our annealing data show that the vacancies anneal to a large extend in the temperature range between 350 and 600 K so if V_{Si} contributes to the observed lifetime τ_{D1}, both V_C and V_{Si} anneal in this temperature range. However, there is evidence from EPR measurements [4] that both V_C^+ and V_{Si}^- exhibit an annealing stage at around 430 K, in view of this we cannot exclude that the observed τ_{D1} lifetime indeed arises from both V_C and V_{Si}. We note that a second lifetime (τ_{D2}) is also observed in this sample, but due to the smallness of the trapping rate for this lifetime no physical interpretations are possible at this point.

For the "as irradiated" sample and after annealing at 175, 275 and 355 K respectively, temperature scans were conducted. Since no temperature dependencies were observed in the lifetime parameters we can conclude, that the irradiation induced defects are in the neutral charge state *and* do not represent shallow positron traps.

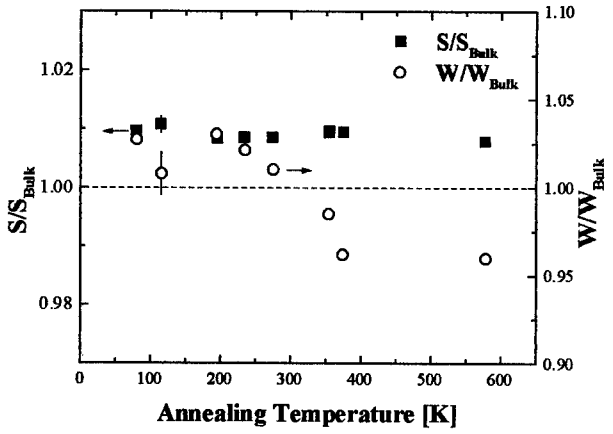

Fig. 2: Normalized (to the bulk value) S and W parameters as a function of annealing temperature for sample 3 irradiated with 2.2 MeV electrons to a dose of 6×10^{16} e^-/cm^2 at 100 K. For measuring temperatures see caption of Fig. 1. The dashed line indicates the bulk level for S and W.

In Fig. 2 are shown the Doppler parameters S and W as a function of annealing. In order to facilitate a comparison the measured S and W values are normalized to their bulk values. There is no measurable change in the S parameter, but this is not surprising, since S is very close to the bulk value anyway. However, an important observation can be made for the W parameter. W is *larger* than 1 after irradiation and then decreases to a value below 1 after annealing at 355 K. However the lifetime data do not show any changes yet in this temperature range.

The S parameter only increases by 1% even for a trapping rate 6 ns^{-1}. Thus the defect specific S parameter is very close to the bulk value, which is in agreement with the lifetime data. The only definite "annealing" response arises from the W parameter. The decrease in W between ~300 and 400 K indicates a significant reduction in high momentum contribution relative to W_{Bulk}. The bulk W parameter contains contributions from both Si-core and C-core electrons with Si-core giving

contribution to W less than that for C-core (*i.e.* diamond exhibits a wider electron momentum distribution than silicon). Trapping by either type of vacancies would decrease core contributions from each sublattice, so that W/W_{Bulk} would be less than 1. The larger-than-one W/W_{Bulk} value therefore suggests that an interstitial is situated close to the vacancy providing "additional" core contribution. Between 300 and 375 K most of these interstitals are removed by recombination and migration away from the vacancy. The few remaining vacancies then result in the (expected) lower than 1 value for W/W_{Bulk}. Thus at ~375 K the main inventory of Frenkel pairs has been removed and a slower removal of the remaining vacancies occurs up to 500 K. During this annealing W does not change which indicates that vacancies do not migrate to form complexes with *e.g.* impurities up to 600 K.

Conclusion

A survey of several 6H SiC bulk wafers with different doping type and concentration shows that small vacancy clusters are present in all samples. The concentration of these grown in clusters is in the range of 10^{16} cm^{-3}. An order of magnitude larger concentration of grown in defects is found in heavily doped n-type material. The defects in this sample are most likely monovacancies and larger vacancy clusters being stable even after heat treatments at 1400 °C.
Neutral monovacancies are created by electron irradiation in 6H SiC. We cannot exclude the possibility that both V_C and V_{Si} contribute to the observed defect lifetime of 150 ps. The S parameter for these defects is close to the value of bulk SiC. The vacancies are present in form of Frenkel pairs and anneal to a large extend in the temperature interval between 300 and 400 K.

Acknowledgements

We wish to thank Dr. W. Puff at Technische Universität Graz for the high temperature annealing of the as grown samples. This work was supported by the Natural Science and Engineering Research Council of Canada.

References

1. G. Pensl and W.J. Choyke, Physica B **185**, 264 (1993).
2. J. Schneider and K. Maier, Physica B **185**, 199 (1993).
3. H. Itoh, M. Yoshikawa, I. Nashiyama, S. Misawa, H. Okumura and S. Yoshida, J. of Electronic Materials **21**, 707 (1992).
4. H. Itoh, M. Yoshikawa, L. Wei, S. Tanigawa, I. Nashiyama, S. Misawa, H. Okumura, and S. Yoshida, Mat. Res. Soc. Symp. Proc. **262**, 331 (1992).
5. H. Itoh, M. Yoshikawa, I. Nashiyama, H. Okumura, S. Misawa, and S. Yoshida, J. Appl Phys. 77, 837 (1995).
6. S. Dannefaer, D. Craigen, and D. Kerr, Phys. Rev. B **51**, 1928 (1995).
7. T. Friessnegg and S. Dannefaer, Mat. Res. Symp. Proc. Vol. **442**, 625 (1997).
8. R.N. West, Adv. Phys. **22**, 263 (1973).
9. S. Dannefaer, J. Phys. C.: Solid State Phys. **1**, 599 (1982).
10. P. Mascher, S. Dannefaer, and D. Kerr, Phys. Rev. B **40**, 11764 (1989).
11. S. Dannefaer, N. Fruensgaard, S. Kupca, B. Hogg, and D. Kerr, Can. J. Phys. **61**, 451 (1983).
12. V.F. Tsvetkov, S.T. Allen, H.S. Kong and C.H. Carter Jr, in Proc. of International Conference on SiC and Related Materials, September 18-21, Kyoto, Japan (1995).
13. A. Kawasuso, H. Itho, S. Okada, and H. Okumura, J. Appl. Phys. **80**, 5639 (1996).
14. G. Brauer, W. Anwand, E.-M. Nicht, J. Kuriplach, M. Sob, N. Wagner, P.G. Coleman, M.J. Puska, and T. Korhonen, Phys. Rev. B **54**, 2512 (1996).

Materials Science Forum Vols. 258-263 (1997) pp. 727-732

RAMAN SCATTERING ANALYSIS OF DEFECTS IN 6H-SiC INDUCED BY ION IMPLANTATION

A. Pérez-Rodríguez[1], O. González-Varona[1], L. Calvo-Barrio[1,2], J.R. Morante[1], H. Wirth[3], D. Panknin[3], W. Skorupa[3]

[1]EME, Dept. Física Aplicada i Electrònica, Universitat de Barcelona, Avda. Diagonal 645-647, 08028-Barcelona, Spain
[2]Serveis Científico-Tècnics, Universitat de Barcelona, C/Lluís Solé Sabarís, 08028-Barcelona, Spain
[3]Forschungszentrum Rossendorf e.V., Institut für Ionenstrahlphysik und Materialforschung, Postfach 510119, D-01314 Dresden, Germany

Keywords: 6H-SiC, Raman scattering, ion implantation, damage, defect annealing

Abstract. The Raman scattering analysis of 6H-SiC wafers implanted with Al^+ ions has been performed as a function of the implantation temperature (from room temperature to 1300°C) and annealing procedure. The analysis of the intensity of the main Raman modes from the as-implanted samples has allowed to observe a significant reduction of residual damage when the temperature increases up to about 1050°C, where a minimum damage is obtained. For higher temperatures, there is a further increase of damage. This contrast with the behaviour from the annealed samples, for which low damage levels are measured except for the sample implanted at room temperature. This is related to the fact that for this sample the implanted layer is fully amorphized during implantation, and correlates with the high stability of amorphous SiC. Finally, the spectra from the as-implanted samples also show the presence of disorder induced bands in the 70-600 cm^{-1} region.

Introduction

SiC is a wide bandgap semiconductor with a strong potential for the development of electronic devices and circuits which have to operate under hard environment conditions, as high temperature and chemically aggressive mediums [1]. Among the different polytypes, 6H-SiC is interesting for electronic applications due to the availability of single crystal wafers already in a commercial stage, being envisaged in the next future a strong enhancement of crystalline quality and wafer size. The development of electronic devices and integrated circuits has to take into account the low diffusion coefficients of impurities in SiC. This forces to use ion implantation for selective doping of the active areas in the devices. In this context, one of the main drawbacks of this material is the very high stability of the defects induced by ion implantation, which are important to be investigated.

In principle, there are two main candidates for p-type doping in SiC, B and Al. Although the lower mass of B implies a lower level of damage in the implanted layer in relation to Al, Al is much more interesting for p-type doping due to its lower ionization energy. In this framework, the Raman scattering analysis of Al^+ ion implantation processes in 6H-SiC has been performed as a function of the implant temperature and anneal procedure. Raman scattering constitutes a powerful non destructive technique for the structural analysis of SiC, being very sensitive to the presence of residual damage and process related defects in the material [2].

Experimental Details

n-type 6H-SiC layers (thickness 5 μm, $7x10^{15}$ cm^{-3}) epitaxially grown on 6H-SiC (001) wafers were implanted with Al^+ ions at different temperatures (T_{imp}) in the range from Room Temperature (RT) to 1300°C. In all the wafers four implantations have been performed at different energies and doses in order to obtain a 400 nm thick implanted layer buried at a depth of 200 nm with a constant Al concentration of $5x10^{19}$ cm^{-3}. The parameters of the implants were: (i) E=500 keV, dose=$1.1x10^{15}$ cm^{-2}; (ii) E=360 keV, dose=$6.5x10^{14}$ cm^{-2}; (iii) E=260 keV, dose=$4.8x10^{14}$ cm^{-2} and (iv) E=180 keV, dose=$4.4x10^{14}$ cm^{-2}. Pieces from these wafers were furnace annealed in vacuum at 1550°C during 10 minutes.

Raman scattering measurements were performed in backscattering configuration, using a Jobin-Yvon T64000 spectrometer coupled with an Olympus metallographic microscope. The samples were excited with an Ar^+ laser working at a wavelength of 488 nm. For this excitation wavelength, 6H-SiC has a very low absorption. According to this, the depth of the region investigated is determined by the axial focal tolerance of the microscope, which for the used measurement conditions is estimated to be of 0.5-0.6 μm. According to this, the buried implanted layer is included in the collection volume of the microscope.

The excitation power density on the samples has been in the range 0.65 to 0.80 Mw/cm^2. For these values, no thermal effects have been observed in the spectra. Measurements have been made in the broad spectral range between 50 cm^{-1} and 1900 cm^{-1}, to determine the contribution of the different modes in the spectra. Finally, the peaks have been fitted with Lorentzian and Gaussian functions, to determine their spectral features. All the measured spectra have been compared with those obtained at the same conditions on a virgin (not processed) SiC epi layer.

Results and Discussion

The Raman spectra measured on the different samples show a strong dependence of the intensity of the main Raman modes on the processing parameters. This is related to the implantation induced damage, which determines a decrease in the intensity of the modes [2]. The level of damage in the different samples has been quantified by the normalized relative intensity of the Raman line, I_n, which is defined as the ratio $I_n = (I_o-I)/I_o$, being I_o and I the intensities of the peak measured in the reference and processed samples, respectively. For very low damage, the intensity of the peak is very similar to that from the reference spectrum and $I_n \approx 0$. An increase of damage leads to a decrease of I in relation to I_o and I_n increases. If the material in the scattering volume is amorphized, crystalline peaks vanish from the spectra and $I_n=1$. According to this, I_n has a value between 0 (absence of damage) and 1 (amorphization), and the value of this parameter allows to quantify the level of damage between both extreme cases.

Figure 1 shows the relative intensity of the TO peak (789 cm^{-1}) versus T_{imp} for the samples as-implanted. We have to remark that all the peaks in the spectra show the same behaviour. For the sample implanted at room temperature, the spectra do not show any detectable contribution from the crystalline peaks ($I_n=1$). As will be shown later, broad bands related to amorphous material arise in the spectra. This indicates the amorphization of the implanted layer. At higher temperatures (200°C or higher), full amorphization of the implanted layer is avoided. For T_{imp} in the range 200°C to 1050°C, I_n decreases down to a minimum value of about 20%. This is observed for the sample implanted at about 1050°C. The low value of I_n obtained for this sample indicates the high structural quality of the implanted layer, with a low level of damage. This has been corroborated with Rutherford Backscattering (channelling) measurements of surface-near damage. For temperatures

higher than 1050°C, I_n increases up to about 40%, which indicates an increase in the concentration of defects. The higher stability of these defects in relation to those induced at lower temperatures - which are significantly reduced by implanting at 1050°C- suggests their different nature. Further experiments in the T_{imp} range from 950°C to 1150°C are required to clarify this.

This behaviour contrasts with the data from the annealed samples, which are also shown in Fig. 1. In this case, almost all the samples show very similar values of I_n, corresponding to low damage levels, and only the sample implanted at RT shows a higher value of I_n. This points out the presence in this sample of a high concentration of residual defects.

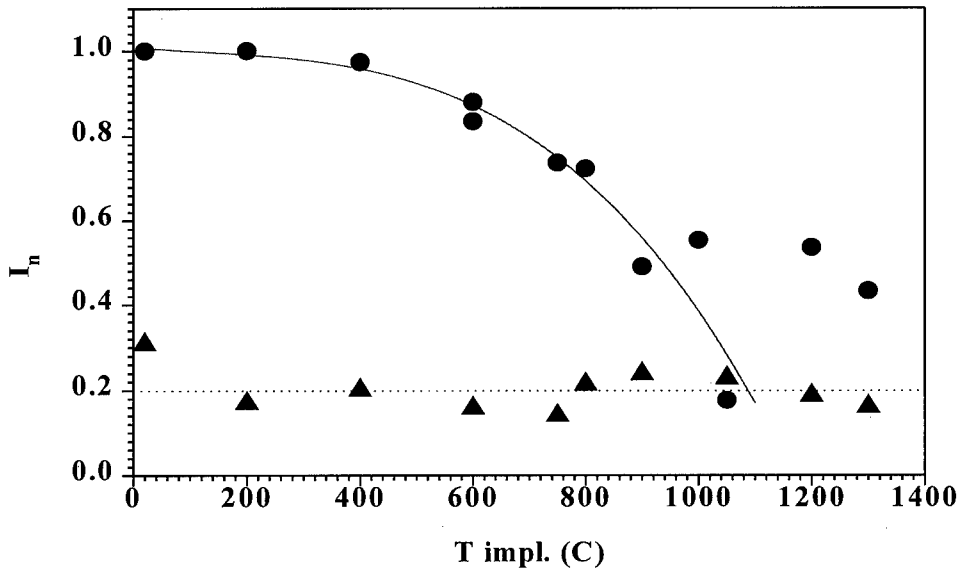

Fig. 1. Normalized relative intensity of the TO Raman line versus implantation temperature for the as-implanted (circle) and annealing (triangle) samples.

The similar values of I_n for the samples obtained with T_{imp} > RT and annealed suggest a similar content of defects in these layers. The low value of I_n indicates that annealing at 1550°C allows to obtain an efficient damage recovery, in spite of the complex behaviour from the as-implanted samples. The lower defect recovery observed in the sample implanted at RT is likely related to the amorphization of the sample during implantation, which determines a loss of the chemical order in addition to long range order [3], with the partial destruction of Si-C bonds and formation of Si-Si and C-C bonds. The high stability of these bonds has been claimed for the difficulty to achieve recrystallization of SiC [4]. Heera et al [5] have observed that thermal and ion beam induced annealing of amorphized SiC leads to a high density of structural defects, with columnar structure, and even inclusions of 3C polytype. The formation of 3C-SiC in the recrystallized layer has also been reported by Kawase et al [6], which have observed a high density of stacking faults related to the growth of 3C polytype inclusions for samples thermally annealed at 1500°C. These authors have also measured a higher leakage current from diodes obtained in these layers in relation to those from samples implanted at 1000°C, where amorphization is clearly avoided. This has been interpreted as related to trapping defects induced by recrystallization of the highly stable amorphous layer.

Figure 2 shows the Raman spectra measured in the broad spectral region from 50 cm^{-1} to 1900 cm^{-1} from different as-implanted samples. As already indicated, the spectrum from the sample implanted at RT shows the presence of three broad amorphous bands, centred at about 240 cm^{-1}, 516 cm^{-1} and 1414 cm^{-1}, and with values of Full Width at Half Maximum (FWHM) in the range of 200-250 cm^{-1}. These bands are very similar to those measured from SiC layers implanted with Ge at doses above the threshold for amorphization [4], and were interpreted as related to Si-Si (240 cm^{-1}, 516 cm^{-1}) and C-C (1414 cm^{-1}) related vibrational modes. This points out the absence of a complete chemical order in the amorphous layer. The presence of these bands corroborates the formation of a continuous amorphous layer in this sample.

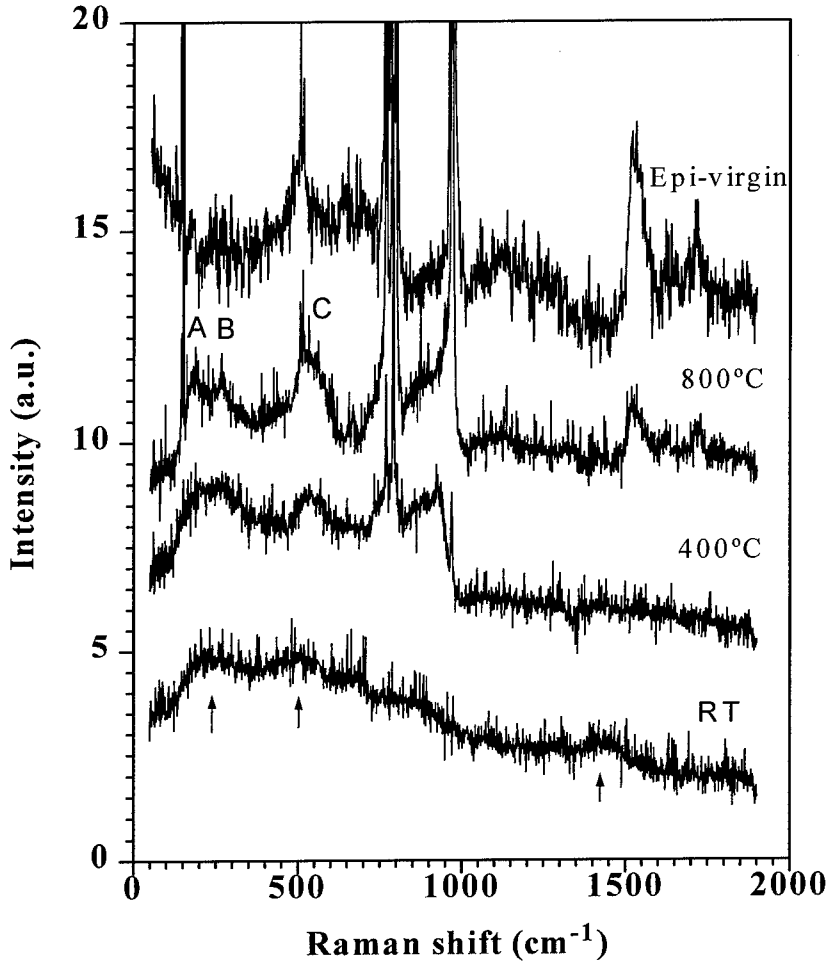

Fig. 2. Raman spectra from the as-implanted samples, showing the presence of the amorphous and disorder induced bands. The spectra are arbitrarily shifted.

The spectra from the samples implanted at higher temperatures show the presence of three additional bands in the 50-600 cm^{-1}. These bands have been labelled as A, B and C in Fig. 2. They are centred at about 185 cm^{-1} (band A), 260 cm^{-1} (band B) and 540 cm^{-1} (band C), and have values of FWHM of the order of 70-100 cm^{-1}. According to this, these bands appear in the same spectral region than those related to the Si-Si vibrational modes from amorphous SiC. After annealing, no detectable contribution from these bands is observed in the spectra.

Similar bands have been observed from samples implanted with other ions as Ge^+ and B^+ at doses above the threshold for amorphization [4]. From the similar spectral position of the bands in relation to the amorphous Si-Si modes, these bands were suggested as related to the presence of highly disordered domains in the implanted samples. Hu et al have also observed a broad band centred at around 200 cm^{-1} in Al doped 4H-SiC epilayers [7]. This band appears in the same region than those labelled A and B in this work, and has been interpreted as related to disorder in the layer caused by the Al atoms.

This interpretation is also supported by Nakashima et al [8], which have reported the assymetric broadening and distortion of the bands from disordered SiC crystals. The Raman spectra from these crystals show broad band contributions at about 150 cm^{-1} -close to the folding TA mode from 6H-SiC- and a complex band structure around 255 cm^{-1}. These spectra have been interpreted in terms of the relaxation of the wavevector conservation rule in the disordered crystals, which are modelled as crystalline domains with different stacking structure.

All these results strongly suggest the A, B and C bands to be determined by disorder in the implanted layer. The evolution with the implantation temperature is not clear, although some trend from gaussian-like shaped bands towards more structured peaks is observed as T_{imp} increases. The absence of these bands from the annealed structures points out the efficient structural recovery of the samples with the annealing procedure.

Conclusions

The analysis of the relative intensity I_n of the main line in the Raman spectra has allowed to quantify the level of residual damage induced by the Al implantation process, as a function of the implantation temperature and annealing procedure. For the as-implanted samples, the damage decreases when T_{imp} increases up to about 1050°C, where it has a minimum. However, a further increase of T_{imp} -up to 1300°C- leads again to an increase of damage to about 40%.

After annealing, the spectra from the samples implanted at temperatures of 200°C or higher are very similar, and only for the sample where the implanted layer was fully amorphized a higher level of damage is observed. According to these data, for the annealing conditions used in this work (1550°C, 10 minutes) the temperature of implantation is not a critical parameter for the final defect density provided that fully amorphization of the implanted layer is avoided. Finally, the spectra from the as-implanted samples also show the presence of three bands in the 70-600 cm^{-1} spectral region likely induced by disorder effects. These bands disappear with the annealing, which points out the efficient damage recovery of the implanted layers with the used annealing conditions.

Acknowledgements

One of the authors (H.Wirth) would like to acknowledge the financial support provided by Daimler Benz AG.

References

1. H. Morkoç, S. Strite, G.B. Bao, M.E. Lin, B. Sverdlov, M. Burns, J. Appl. Phys. **76**, 1363 (1994).
2. S. Nakashima, M. Hangyo, IEEE J. Quantum Elect. **25**, 965 (1989).
3. C. Serre, L. Calvo-Barrio, A. Pérez-Rodríguez, A. Romano-Rodríguez, J.R. Morante, R. Kögler, V. Heera, W. Skorupa, J. Appl. Phys. **79**, 6907 (1996).
4. A. Pérez-Rodríguez, Y. Pacaud, L. Calvo-Barrio, C. Serre, W. Skorupa, J.R. Morante, J. Electron. Mater. **25**, 541 (1996).
5. V. Heera, R. Kögler, W. Skorupa, J. Stoemenos, Appl. Phys. Lett. **67**, 1999 (1995).
6. D. Kawase, T. Ohno, T. Iwasaki, T. Yatsuo, Inst. Phys. Conf. Ser. **142**, 513 (1996).
7. R. Hu, C.C. Tin, Z.C. Feng, J. Liu, Y. Vohra, Inst. Phys. Conf. Ser. **142**, 354 (1996).
8. S. Nakashima, H. Ohta, M. Hangyo, B. Palosz, Philos. Mag. B **70**, 971 (1994).

Materials Science Forum Vols. 258-263 (1997) pp. 733-738

VACANCY-TYPE DEFECTS IN PROTON-IRRADIATED SiC

W. Puff[1], P. Mascher[2], A.G. Balogh[3] and H. Baumann[4]
[1] Institut für Technische Physik, Technische Universität Graz, Petersgasse 16, 8010 Graz, Austria
[2] Department of Engineering Physics, McMaster University, Hamilton, Ontario, Canada
[3]Department of Material Science, Technical University Darmstadt, Darmstadt, Germany
[4] Institut für Kernphysik, J.W.Goethe Universität Frankfurt, Frankfurt/Main, Germany

Keywords: SiC, irradiation, defects, positron annihilation

Abstract Annealing of defects introduced by proton irradiation of bulk n- and p-type 6H-SiC has been investigated by positron lifetime spectroscopy and Doppler-broadening measurements. It is shown that in both materials positrons are sensitive to radiation induced defects. There are three main annealing stages, one in the 100 °C to 300 °C region, the second one from 700 °C to 800 °C and the third one above 1000 °C. After annealing at 1300 °C all radiation induced defects have annealed out. During annealing, the formation of larger defect complexes can be observed.

Introduction

Silicone carbide is, because of its unique thermal and electronic properties the semiconductor of choice for specific high-temperature, high-power, or high-frequency applications that are not suitable for Si- or GaAs-based devices. For the development of such advanced devicés, however, a much better understanding of the basic microstructural properties, in particular the existence and stability of defect structures is important. In the recent years some progress has been made in this field, resulting in a few comprehensive reviews [1-5].
Investigations of structural and particularly radiation induced defects in semiconductor materials are of fundamental importance for the physics of semiconductors. Nevertheless, the nature of many radiation induced centres has not yet been identified. Additional information can be obtained by applying not only conventional techniques, as e.g. photo-luminescence spectroscopy (PL), electron spin resonance (ESR), or optically detected magnetic resonance (ODMR), but also new methods that allow selective investigation of different types of structural defects. Recent years have seen extensive utilisation of the positron annihilation method, which is very sensitive and can be applied selectively to vacancy-type defects [6-8]. The data obtained by this method and their correlation with the results of other investigations have demonstrated the great promise of the positron annihilation technique in the diagnostics of structural defects in semiconductor materials.
Several studies concerning defects in 3C-SiC as well as 6H-SiC and 4H-SiC have been carried out, including a few positron investigations [9-20], but the microscopic identification of defects and the understanding of their electronic properties are far from complete. ESR data on 3C- and 6H-SiC suggest the formation of silicon (V_{Si}) and carbon (V_C) vacancies [21, 22] upon electron irradiation and V_C [23] upon proton irradiation. It is suggested that after proton irradiation, V_C^0 exists in n-type material and V_C^+ in p-type material [23], while after electron irradiation, V_C^+ was found in n-type samples [14]. Theoretical considerations suggest, at least for native carbon vacancies, a double donor nature [24]. On the other hand, positron annihilation experiments on electron irradiated 6H-SiC show in n-type material both carbon and silicon vacancies, whereas in p-type material no vacancies were detected [16, 25], while other lifetime experiments could not identify carbon vacancies [9-11]. After proton irradiation very recently, however, vacancies were detected by Doppler-broadening experiments also in p-type 6H-SiC [20].
First experimental results of the annealing of non-equilibrium defects show that the stability of the defects depends on a number of factors such as the mode of introduction, radiation dose, growth

condition, and type of impurity [9-13]. Because of the high activation energy for interstitial and vacancy diffusion in this binary compound, primary radiation defects, in particular isolated vacancies, are thermally stable at room temperature and far above. It has been recently established, that the annealing of the silicon vacancy in 3C-SiC takes place in two main stages, one at 150 °C and one around 750 °C [21]. Comparable data for the carbon vacancy are not known.
At temperatures above 750 °C, when the silicon vacancy in SiC becomes mobile, complexing of V_{Si} with other intrinsic point defects is likely to occur. As in the case of secondary radiation defect centres in silicon [26], complexes of the type V_{Si}-oxygen, V_{Si}-donor, V_{Si}-acceptor, as well as divacancy centres, may be formed. Similar complexes with V_C are likely to occur. However, a microscopic understanding of such defect complexes in SiC so far practically does not exist.
In the present work we continue our former investigation [20] by studying the annealing behaviour of point defects in n- and p-type proton irradiated 6H-SiC in the temperature range between room temperature and 1600 °C using both positron lifetime spectroscopy and Doppler-broadening measurements.

Experimental details

The samples were three sets of research grade 6H-SiC single crystalline wafers obtained from Cree Res. Inc., two n-type with carrier concentrations of 1.7×10^{18} cm^{-3} and 3.2×10^{18} cm^{-3}, respectively, the third one p-type (6.2×10^{18} cm^{-3}). The n-type samples were irradiated with 5 MeV protons to a fluence of 1×10^{16} cm^{-2} or 1×10^{15} cm^{-2}, the p-type sample to a fluence of 1×10^{16} cm^{-2}. The temperature of the specimens was kept below 220 K during irradiation. The 20 min isochronal annealing was done in air from room temperature to 1000 °C and from there to the highest temperatures in an Ar atmosphere.
The positron lifetime and Doppler-broadening measurements were performed at room temperature. For the lifetime measurements, a conventional fast-fast coincidence system having a time resolution of 136 ps full width at half maximum (FWHM) was used. A ^{22}NaCl positron source of about 30 μCi deposited onto a 1.35 mg/cm^2 Al foil was sandwiched by two samples. Each lifetime spectrum contained at least 5×10^6 counts, and up to three spectra were collected per data point. Numerical analyses of the spectra were performed using the computer program PFPOSFIT [27] taking into account a source correction due to the contribution of positrons annihilating in the Al foil supporting the positron source. Details of the analysis procedure and the physical background can be found in [28]. The Doppler-broadening of the annihilation line was measured using an intrinsic Ge detector with a resolution (FWHM) of 1.18 keV at 497 keV (close to the 511 keV annihilation γ energy). Digital stabilisation on the annihilation peak and on a reference peak (^{207}Bi) was employed. Each measurement lasted 2000 seconds and was repeated at least 10 times. A total of about 4×10^7 counts were recorded for each spectrum. The numerical analysis of the Doppler spectra was performed by determining the shape parameters S and W. The S parameter (representing the fraction of positrons annihilating mainly with the valence electrons) is defined as the ratio of the counts in a central region of the spectrum and the total amount of counts, whereas the W parameter (representing the fraction of annihilations with the core electrons with larger momentum) is defined as the ratio of counts in the wing region of the spectrum to the total counts in the peak [8].

Results and discussion

Before irradiation the lifetime spectrum is dominated by one component, τ_1, with an intensity in the 90 % range (see Table 1). This component arises from annihilations in the bulk whereas the longer component, τ_2, is due to vacancy clusters. The presence of these defects for both types of dopant suggests that these clusters are formed independent of the doping type. These cluster were still observable after annealing at 1600 °C indicating a high thermal stability of these grown in defects.

From the measured spectra one can calculate the mean lifetime according to, $\tau_{mean}=(I_1\tau_1+I_2\tau_2)$, and from the simple two-state trapping model [8] the bulk lifetime, $\tau_b = (I_1/\tau_1+I_2/\tau_2)^{-1}$, and the trapping rate $\kappa=I_2/I_1(1/\tau_b-1/\tau_2)$ due to the defects. The bulk lifetime is of particular importance since it refers to the annihilations from the perfect "crystalline" regions of the crystal and hence is a material constant. For samples E356 and E103 the bulk lifetime has a value of 143±2 ps in good agreement with experimental [16, 17, 29] as well as calculated [30] values. With this bulk lifetime the trapping rate due to these clusters can be estimated. We get a value for κ in the range 0.2 (E103) to 0.4 (E356) ns^{-1}, which, according to Ref. 16 indicates a concentration of the vacancy complexes of about $2x10^{16}$ cm^{-3} to $4x10^{16}$ cm^{-3}. For sample H007 the value for the bulk lifetime is much higher, τ_b=155 ps. This could be caused by an additional defect component in the sample. We were not successful in separating such a component during the analysis. The reason might be, that the defect lifetime component is very close to the bulk lifetime.

Table 1: Lifetime and Doppler-broadening results for the three samples investigated: The values for the as-grown, as-received after irradiation and the annealed samples are shown. Typical errors for the short lifetimes are ± 2 ps, for the second lifetime ± 10 ps, and for the intensities ± 1 %.

Sample	Treatment	Doping type and carrier concentration [cm^{-3}]	τ_1 [ps]	τ_2 [ps]	I_1 [%]	I_2 [%]	τ_{bulk} [ps]	τ_{mean} [ps]	S/S_{bulk}	W/W_{bulk}
H007	as-grown	n $1.7x10^{18}$	141	333	84.8	15.2	155	170	1	1
	10^{16} p/cm^2		160	283	57,5	42,5	-	212	1.034	0.938
	annealed		137	333	83,4	16,6	152	170	0.999	1.001
E356	as-grown	n $3.2x10^{18}$	136	290	90.2	9.8	143	151	1	1
	10^{15} p/cm^2		153	247	54.2	45.8	-	196	1.039	0.933
	annealed		136	296	94,5	5.5	140	145	0.999	0.996
E103	as-grown	p $6.2x10^{18}$	139	289	95.0	5.0	143	147	1	1
	10^{16} p/cm^2		137	253	69.0	31.0	-	173	1.025	0.965
	annealed		138	328	93,7	6.3	143	150	1.001	0.999

After irradiation the values of the long-lived component changes because the newly created defects overwhelm the weak response from the vacancy clusters. Moreover, for the two n-type samples the short lifetime component becomes larger too. The S parameter increases as one might expect due to the introduction of vacancies; for the same reason the W parameter decreases. The fact that we can not extract the bulk lifetime after irradiation indicates that all positrons get trapped in defects (saturation trapping) and, therefore, the trapping model can't be applied.

After proton irradiation the presence of both V_C and V_{Si} have been reported in 3C-SiC [23, 31] by ESR. However, there is no doubt that 5 MeV protons might also induce divacancies, V_C–V_{Si}. The observed short lifetime component after irradiation has to be attributed to monovacancies. Theoretical calculations [30] gives for V_C a lifetime of 153 ps, for V_{Si} 192-194 ps, and for V_C–V_{Si} 214 ps. Since the two monovacancy lifetimes are very close together we were not successful in separating the two lifetimes. We, therefore, come to the conclusion that both V_C and V_{Si} contribute to the defect lifetime. From the positron point of view the carbon vacancy can not be in the positive charge state as proposed by ESR measurements [23]. Positrons observe the neutral and dominating carbon vacancy [25], whereas ESR only observes a small fraction of V_C being positively charged. The longer lifetime component has to be attributed to divacancies. In Fig. 1 the annealing behaviour of the mean lifetime, τ_{mean}, is shown. We observe for both n-type samples an annealing stage at about 150 °C. For the p-type sample this annealing stage can not be seen since the scatter of the

mean lifetime values is too large. On the other hand the normalised S and W parameter values (Fig. 2) show pronounced annealing stages for all samples in the temperature range 100 to 300 °C. Especially the normalised W parameters increase conspicuously in this temperature range. There is evidence from ESR measurements [32] that both vacancies, V_C as well as V_{Si}, exhibit an annealing stage at around 150 °C.

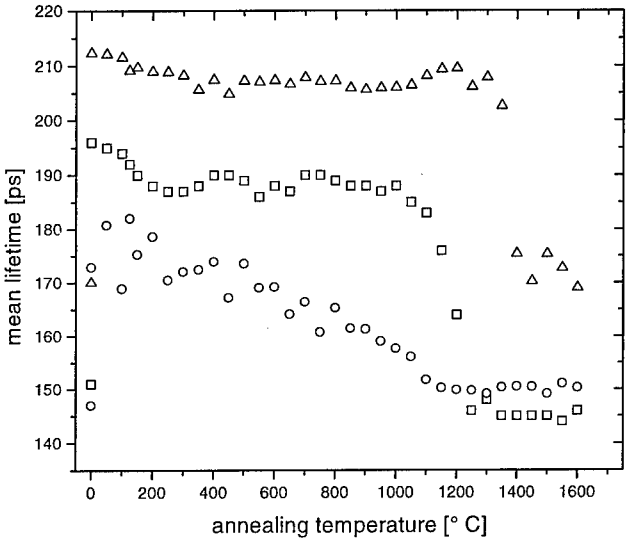

Fig. 1: Mean lifetime, τ_{mean}, as a function of annealing temperature together with the as-received values before irradiation: Δ (H007), □ (E356), ○ (E103). The uncertainties are within the size of the symbols.

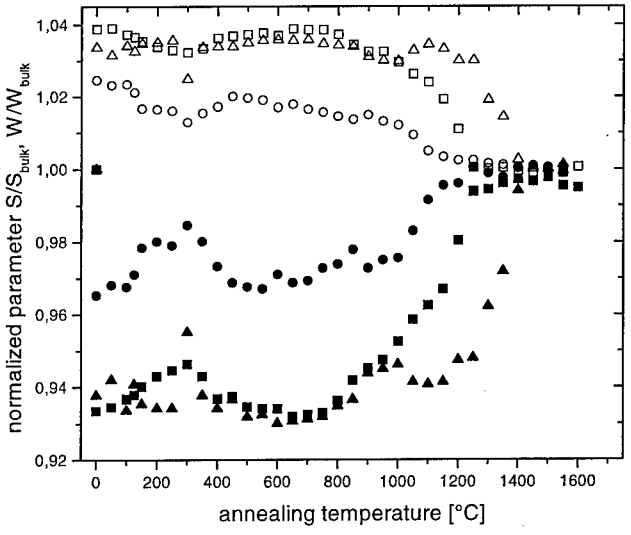

Fig. 2: Doppler-broadening S/S_{bulk} and W/W_{bulk} parameters as a function of annealing temperature.
Δ (H007), □ (E356), ○ (E103). The uncertainties of the parameters are within the size of the symbols.

The annealing behaviour of the two n-type samples agree very well up to around 1000 °C. At 750 °C the Doppler-parameter start to change, indicating that the vacancies become mobile and start to anneal. It is interesting to note, that the mean lifetime does not show this pronounced onset; for sample E356 the annealing start at 1000 °C with a dramatic decrease of the intensity of the second

lifetime component, indicating that the divacancies anneal out. At about 1250 °C the as-received values for the lifetime and the Doppler parameters are obtained. Sample H007 on the other hand show a clustering of defects in the range 1000 °C to 1200 °C, reaching the as-irradiated values at around 1450 °C. This different behaviour may arise from slight differences in the environment of the radiation induced defects. We do not know at the moment if there is any correlation between this annealing behaviour and the observed long mean lifetime in this sample.
Contrary to earlier positron studies on electron irradiated SiC [16] we observe also in p-type samples a substantial effect on the positron parameters after proton irradiation. It is worth to be noted that the increase in the mean lifetime and the change in the Doppler-parameter is smaller in comparison to the n-doped samples. We again observe the distinct annealing stage at about 150 °C (Fig. 2). The change especially in the W parameter shows the onset of the vacancy migration at about 700 °C and after some clustering in the range 800 °C to 1000 °C the main annealing stage. In this sample, all the defects are annealed out at 1300 °C.

Conclusions

Positron lifetime and Doppler-broadening measurements in proton irradiated n- and p-type 6H-SiC have shown that in both samples the irradiation induced defects anneal out in three main stages. In the range 100°C to 300 °C (recombination of vacancies and interstitials), 700 °C to 800 °C (the vacancies become mobile), higher than 1000 °C (the divacancies anneal out). Thereafter the as-received values of the positron parameters are obtained. Detailed analyses show that the most sensitive parameter for studying the annealing behaviour is the Doppler W parameter.

Acknowledgements

In Canada this work has been supported by the Natural Sciences and Engineering Research Council of Canada.

References

[1] G. Pensl and R. Helbig, Festkörperprobleme **30**, 133 (1990).
[2] J. Schneider and K. Maier, Physica B **185**, 199 (1993).
[3] G. Pensl and W.J. Choyke, Physica B **185**, 264 (1993).
[4] H. Morkoç, S. Strite, G.B. Gao, M.E. Lin, B. Sverdlov, and M. Burns, J. Appl. Phys. **76**, 1363 (1994).
[5] MRS Bulletin Vol. **22** No. 3 (1997).
[6] W. Brandt and A. Dupasquier, Positron Solid State Physiscs (Amsterdam: North Holland) (1983).
[7] Y.-J. He, B.-S. Cao, and Y.C. Jean, Positron Annihilation (Zürich: Trans. Tech. Publications) (1995).
[8] A. Dupasquier and A.P. Mills jr, Positron Spectroscopy of Solids (Amsterdam: IOS Press) (1995).
[9] A.I. Girka, V.A. Kuleshin, A.D. Mokrushin, E.N. Mokhov, S.V. Svirida, and A.V. Shishkin, Sov. Phys. Semicond. **23**, 790 (1989).
[10] A.I. Girka, V.A. Kuleshin, A.D. Mokrushin, E.N. Mokhov, S.V. Svirida, and A.V. Shishkin, Sov. Phys. Semicond. **23**, 1337 (1989).
[11] A.I. Girka, A.D. Mokrushin, E.N. Mokhov, V.M. Osadchiev, S.V. Svirida, and A.V. Shishkin, Sov. Phys. JETP **70**, 322 (1990).
[12] A.D. Mokrushin, A.I. Girka, and A.V. Shishkin, phys. stat. sol. (a) **128**, 31 (1991).
[13] A.I. Girka, A.D. Mokrushin, E.N. Mokhov, S.V. Svirida, and A.V. Shishkin, Mater. Sci

Forum **105-110**, 1021 (1992).
[14] H. Itoh, M. Yoshikawa, I. Nashiyama, L. Wei, S. Tanigawa, S. Misawa, H. Okumura, and S. Yoshida, Hyperfine Inter. **79**, 725 (1993).
[15] A.A. Rempel and H.-E. Schaefer, Appl. Phys. A **61**, 51 (1995).
[16] S. Dannefaer, D. Craigen, and D. Kerr, Phys. Rev. B **51**, 1928 (1995).
[17] W. Puff, M. Boumerzoug, J. Brown, P. Mascher, D. Macdonald, P.J. Simpson, A.G. Balogh, H. Hahn, W. Chang, and M. Rose, Appl. Phys. A **61**, 55 (1995).
[18] N. Hayashi, H. Watanabe, K. Sakai, K. Kuriyama, Y. Ikeda, H. Maekawa, and T. Miura, Mater. Sci. Forum **196-201**, 1243 (1995).
[19] A. Kawasuso, H. Itoh, S. Okada, and H. Okumura, J. Appl. Phys. **80**, 5639 (1996)
[20] W. Puff, A.G. Balogh, P. Mascher, and H. Baumann, Proc. Internat. Symposium on Materials Science Applications of Ion Beam Techniques (Zürich: Trans Tech Publications) (in print)
[21] H. Itoh, N. Hayakawa, I. Nashiyama, and E. Sakuma, J. Appl. Phys. **66**, 4529 (1989).
[22] O. Chauvet, L. Zuppiroli, J. Ardonceau, I. Solomon, Y.C. Wang, and R.F. Davis, Mater. Sci. Forum **83-87**, 1201 (1992).
[23] H. Itoh, M. Yoshikawa, I. Nashiyama, S. Misawa, H. Okumura, and S. Yoshida, J. Electron. Mater. **21**, 707 (1992).
[24] J. Bernholc, S.A. Kajihara, C. Wang, A. Antonelli, and R.F. Davis, Mater. Sci. Eng. B **11**, 265 (1992).
[25] T. Friessnegg and S. Dannefaer in Defects in Electronic Materials II edited by J. Michel, T. Kennedy, K. Wada and K. Thonke (Pittsburgh: Mater. Res. Soc.) p.625 (1997).
[26] G.D. Watkins, in Deep Levels in Semiconductors, ed. S.T. Pantelides (Yverdon: Gordon and Breach) p. 177 (1992).
[27] W. Puff, Comput. Phys. Commun. **30**, 359 (1983).
[28] W. Puff and X.-T. Meng, J. Appl. Phys. **73**, 648 (1993).
[29] M. Forster, W. Claudy, H. Hermes, M. Koch, K. Maier, J. Major, H. Stoll, and H.-E. Schaefer, Mater. Sci. Forum **105-110**, 1005 (1992).
[30] G. Brauer, W. Anwand, E.-M. Nicht, J. Kuriplach, M. Sob, N. Wagber, P.G. Coleman, M.J. Puska, and T. Korhonen, Phys. Rev. B **54**, 2512 (1996).
[31] H. Itoh, M. Yoshikawa, I. Nashiyama, H. Okumura, and S. Yoshida, IEEE Trans. Nucl. Sci. **37** (1990) 1732.
[32] H. Itoh, M. Yoshikawa, L. Wie, S. Tanigawa, I. Nashiyama, S. Misawa, H. Okumura, and S. Yoshida, in Defect Engineering in Semiconductor Growth, Provcessing and Device Technology, edited by S. Ashok, J. Chevalier, K. Sumino and E. Weber (Pittsburgh: Mater. Res. Soc.) p.331 (1992).

Materials Science Forum Vols. 258-263 (1997) pp. 739-744

THEORETICAL STUDIES ON DEFECTS IN SiC

P. Deák*, A. Gali*, J. Miró* and R. Guiterrez, A. Sieck**, Th. Frauenheim****

***Physical Institute, TU Budapest, Budafoki út 8, H-1111 Budapest, HUNGARY**
****Institute of Physics, TU Chemnitz, Reichenhainer Str. 70, D-09107 Chemnitz, GERMANY**

Keywords: silicon carbide, oxygen, nitrogen, theory

Abstract

Preliminary results of an attempt to acquire general knowledge about the behavior of defects in various polytypes of SiC, by means of theoretical methods, are presented. Ab initio LCGTO-LDA calculations in a molecular cluster model of the cubic crystal have been carried out on oxygen and nitrogen defects. Results of these, as well as those of plane wave LDA supercell calculations on structural defects in the literature are used to calibrate and reparametrize a quantum molecular dynamics method with density functional based tight binding Hamiltonian and a quasi-static semi-empirical quantum chemical method, respectively.

Introduction

Unlike in the case of silicon or GaAs, a general database on the behavior of impurities in SiC is still in construction. Experience with other semiconductors has shown that comparison of experimental findings with theoretical model calculations helps their interpretation immensely. Self-consistent semi-empirical quantum chemical electronic structure calculation methods applied to a cyclic cluster model of the defective solid have contributed fruitfully to this process in the past for light impurities (H, N, O) in silicon (e.g. refs. [1-3]) and are still useful as fore-runners to more accurate ab initio LDA studies [4-5].

Silicon carbide represents a lot more difficult case for theory than silicon. First, one of the host atoms, carbon, is a light atom with an incompletely screened core. This requires a full potential treatment or very special pseudoptentials, causing considerable increase in computational time either way. For that reason the number of attempts to calculate defect properties is scarce and are mostly restricted to single point defects in tetrahedral (T_d) environment (e.g. refs [6-11]). Second, the SiC polytypes of practical importance, 4H and 6H, require extremely large molecular clusters or supercells in defect calculations. For that reason, calculation have been carried out almost solely in SiC(3C). Our intention is to use the results of ab initio LDA defect calculations in 3C material to calibrate - or if necessary reparametrize - semi-empirical methods for use in 4H and 6H. This paper presents preliminary results of that effort.

Calculational methods

Three methods have been used in this work. Ab initio LDA calculations with a Gaussian basis set were carried out on $X_{34}Y_{37}H_{60}$ molecular cluster models (MCM) of SiC(3C) using a version of the AIMPRO Code [12]. Four Gaussians were used for the expansion of each valence s and p orbitals of Si, C, and O. Three Gaussians were used for hydrogen and five for nitrogen. Also three Gaussians were placed at each bond center except those involving a hydrogen on the perimeter. The geometry of the perfect MCM was optimized subject to C_{2v} symmetry with respect to all atomic coordinates. In defect calculations, the hydrogen atoms and their immediate neighbors were kept fixed.

The most advanced semi-empirical quantum chemical electronic structure method is MNDO [13]. It is a Hartree-Fock based method with neglection of diatomic differential overlaps and an intuitive realization of the effective valence Hamiltonian theory of manybody systems, through application of empirical atomic data for one-center, and parametrized functions in remaining two-center integrals [14]. In such a way MNDO accounts for most of the dynamic correlation in the ground state. The parameters are adjusted to fit observed properties of small molecules. We have tried both well established parametrizations: AM1 [15] and PM3 [16]. Calculations for the solid have been carried

out by using 32 atom and 128 atom cyclic cluster models (CCM) [3]. Total energy was minimized in the perfect CCM with respect to all atomic coordinates. Afterwards, only second neighbors were allowed to relax around defects .

The typical range of HF based semi-empirical methods is about a 100 atoms (not counting hydrogen). For larger systems, or for quantum molecular studies, a tight binding scheme is more appropriate. With this in mind, we have tested a non orthogonal DF-TB formalism [17]. The Slater-type basis functions are solutions of the ab initio LDA equations of the isolated atoms, and the potential in the crystalline case is a sum of the atomic potentials. Matrix elements are calculated between any pair of atoms (no first or second neighbor restriction). The total energy is calculated as the sum of the band structure energy and a parametrized repulsion term, which is fitted to self-consistent LDA results on molecules. Crystalline calculations are carried out in 64 and 216 atom supercell models (SCM) using the $\mathbf{K} = 0$ approximation. The formalism is built in into a molecular dynamics code. The geometry of the perfect SCM was fully optimized, while second neighbor relaxation was allowed around defects.

LDA Results

Calculations have been carried out on substitutional defects N_C, N_{si}, O_C, O_{Si}, and on the interstitial O_i.

Earlier, the electronic structure of substitutional nitrogen in SiC(3C) was calculated using LDA-SCM [11] and the vibration bands by phenomenological Green function theory [18], however, both with restriction to T_d symmetry. In our calculation N_C remains, indeed, on-center (T_d), with 3 % outward relaxation of the first neighbors. N_{Si}, on the other hand, goes off-center in the $[\bar{1}\,\bar{1}\,\bar{1}]$ direction by 0.36 Å (C_{3v} reconstruction). The length of the three N-C bonds are 1.63 Å, while the distance to the fourth carbon atom is 2.42 Å. These values are to be compared to the bond length of 1.47 Å in trimethilamine. Due to the type of its relaxation, N_{si} is a shallow effective mass single donor with a gap level close to the "CB-edge" of the MCM. N_C, with its C_{3v} reconstruction however, is a deep single donor with a level around midgap. (No donor state was predicted for N_C in ref. [11].) The different symmetry of the cluster and of the defect environment prevents at present an accurate determination of the vibration frequencies. The nitrogen related stretching frequency for N_C is around 672 cm^{-1}, compared to 625 cm^{-1} obtained in ref. [18], while those of N_{Si} are around 668 and 797 cm^{-1}, in comparison to 620 and 1080 cm^{-1} in ref. [18]. We find N_C energetically favored over N_{Si} by 0.35 eV. Due to the significant relaxation and reconstruction, this value is much less than the 3.84 eV, found in ref. [11]. It also means that under suitable conditions, a small amount of nitrogen can be found at Si sites. This would mean a lower doping efficiency, because of the deep donor nature of N_{si}. Beside formation of complexes with interstitials or divacancies, this may be another reason for the observed low activation rate of nitrogen dopants.

Oxygen has only been investigated in the interstitial position in SiC(3C) by using the HF-based non-empirical PRDDO method on big, and ab initio HF with correlation corrections on smaller MCM-s [19]. Our calculations reproduces that geometry within 0.05 Å. The oxygen is trivalent in an asymmetric YLID structure with two Si and one C neighbors. One of the Si-O distances is 1.90 Å. This is more of an electrostatic interaction than a real covalent bond. Therefore no gap level is associated with this defect The characteristic vibration frequencies are 960, 650, 641, and 612 cm^{-1}.

We are not aware of calculations on substitutional oxygen in the literature. Our results show that O_C moves off center by 0.79 Å in the [001] direction (C_{2v} symmetry). The length of the O-Si bond are 1.62 Å, the SiOSi bond angle is 146°. O_{Si} behaves similarly, with an 0.68 Å displacement, O-C bond length of 1.78 and COC bond angle of 120°. This is in accordance with the fact that the difference in the frequencies of the asymmetric and symmetric stretching modes in dimethilether is small (182 cm^{-1}). Therefore, achieving the ideal bond angle in O_C competes with the aspiration for the ideal bond length. In case of O_{Si} the two trends are easily reconciled because of the bigger ideal angle. Both oxygen substitutionals are hyper deep double donors with a level below midgap. The characteristic vibration frequencies for O_{Si} are 722, 693 and 150 cm^{-1}. In comparison in dimethilether the corresponding values are 1122, 940 and 413 cm^{-1}. The decrease is due to the longer bonds. At present we do not have the vibration frequencies of O_C yet. Preliminary calculations indicate however, that this latter is energetically favored.

Semi-empirical Results

Although both the AM1 and PM3 parametrizations of the MNDO methods give very good results for a number of molecules containing Si, C, and H (see Table 1), they are less successful in describing crystalline Si or SiC, and defects in them. AM1 reproduces the bond length, binding energy and bulk modulus of both solids quite accurately, but gives a disastrous electronic structure for Si and unreasonable charge distribution for defects in SiC. PM3 is somewhat less accurate in the first three properties but a lot better as far as the electronic structure is concerned. However, the charge transfer in SiC is too low, and the bending force constants are disastrously low both in Si and SiC. This leads too serious errors in calculating formation energies for structural defects in both solids. The calculations for the oxygen substitutional led to incorrect reconstruction of the environment in all cases. The reason for these failures is that these parametrizations were based on a large number of molecules with a carbon skeleton, and hardly any with a silicon one. Tests on diamond and its structural defects gave satisfactory results with both methods.

Therefore we decided to establish new parameters for silicon within the PM3 scheme [20], extending the set of Si-C-H systems used by Stewart [16] with crystalline Si and SiC. (The PM3 parameters of C and H were kept). For calculations on the crystals, a 32 atom cyclic cluster model was used (see, e.g., ref. [3]). The mean square error of the results on molecules, shown in Table 1, are not substantially different from those of the established sets. This is important to preserve the main advantage of such methods: the possibility of testing the accuracy of defect results on molecules with similar bonding structure.

Table 1: Mean square errors of semi-empirical methods for molecules Si_2, Si_3, SiH, SiH_2 (S=1,3), SiH_3 (q=+,0,-), SiH_4, Si_2H_6, Si_3H_8, cyclo-$(SiH_2)_6$, H_3SiCH_3, $H_2Si(CH_3)_2$, $HSi(CH_3)_3$, $Si(CH_3)_4$.

Si-C-H systems	sample	AM1	PM3	Present
ΔH [kcal/mol]	15	21.677	7.390	28.619
d_{Si-Si}, d_{Si-C} [Å]	6	0.244	0.263	0.039
ν_{Si-Si}, ν_{Si-C} [cm^{-1}]	17	29.160	40.653	14.507
μ [D]	3	.279	.260	.275
IP [eV]	5	.242	.471	.389

The results for the perfect solids are given on the right hand side in Tables 2-3, compared with experimental data [21-25]. Only the binding energies, interatomic distances, and ionization thresholds were involved in the parametrization. (In case of molecules, also skeletal vibration frequencies and dipole moments were fitted.) Apparently, in both cases the stretching force constants are a bit too high (see the Raman frequency and the bulk modulus). The bending force constants are right, for the lower part of the phonon spectrum (not shown here) is well reproduced. The error in the stretching force constant is aggravated when switching to a 128 atom CCM in SiC, because of the increasing ionicity. This is the reason for the increase in the formation energy of the vacancy. In case of silicon that is still acceptable, for the extended range of relaxation (not used here) will compensate this effect. In case of SiC, however, the value is much too high, so the parametrization has

Table 2: Comparison of calculated and observed properties of c-Si

	DF-TB	**Exptl.**	**PM3 reparametrized**	
Property	Si_{64}	Si_∞	Si_{32}	Si_{128}
E_b [eV]	-4.31	-4.70	-4.60	-4.71
d_{Si-C} [Å]	2.344	2.351	2.339	2.324
IP [eV]	4.26	5.35	5.58	5.37
ν_{Raman} [cm^{-1}]	550	518	555	-
$E_f(V)$ [eV]	-	3.6	3.84	5.3

to be repeated using a Madelung term for the 32 atom CCM. (The 128 atom CCM is much to big for use in parametrization). A lower bulk modulus has to be achieved for both solids anyway.

Table 3: Comparison of calculated and observed properties of SiC(3C)

	DF-TB		Exptl.	PM3 reparametrized	
Property	$Si_{108}C_{108}$	$Si_{32}C_{32}$	SiC_∞	$Si_{16}C_{16}$	$Si_{64}C_{64}$
E_b [eV]	-6.93	-6.22	-6.34	-6.51	-6.67
d_{Si-C} [Å]	1.887	1.898	1.888	1.858	1.852
Ionicity	0.19	0.19	(0.44)*	0.38	0.40
IP [eV]	5.27	5.33	6.51	7.30	6.76
B [Mbar]	1.95	2.02	2.24	2.94	3.05
$E_f(V_C)$ [eV]	-	5.6	(5.9)*	4.47	8.36

* Values from high quality ab initio calculations. Ionicity from ref. [26], formation energy from ref. [7].

Using the present parameters, the substitutional and anti-site defects of SiC have been calculated in a 32 atom CCM, allowing for D_{2d} symmetry in the case of vacancies. The results are presented in Table 4 in comparison to ab initio LDA supercell calculations [7] (where the symmetry was restricted to T_d). The formation energies of Si_C and C_{Si} are overestimated by about 1.5 eV due to the higher force constants. In case of V_C this is compensated by a considerable symmetry lowering relaxation relative to the results of ref. [7]. The very high value for V_{Si} can be understood looking at the relative changes in atomic charges (Δq). The 4th neighbor shell in the 32 atom CCM is the only one where the atoms are in direct interaction with repeated defects in neighbor cells. This shows up in the pile up of Δq. V_{Si} is the only case where this effect spreads inside the CCM. Investigations in the bigger CCM are under way.

Table 4: Calculated formation energies, relaxation of first neighbors (D_{2d}), gap states, as well as the change in charge relative to the ideal case on the n-th neighbor shell for substitutional structural defects.

	V_C		Si_C		V_{Si}		C_{Si}	
	ref. [7]	PM3*	ref. [7]	PM3*	ref. [7]	PM3*	ref. [7]	PM3*
E_f [eV]	5.9	4.5	7.3	8.9	6.8	11.4	1.1	2.41
Δr [%]	< 1	- 5	+12	+ 7	no data	+ 6	- 8	-7
$\Delta\vartheta$ [°]	0	- 2	0	< 1	0	< 1	0	< 1
$\Delta q(1)$		-0.36		-0.29		+0.33		+0.43
$\Delta q(2)$		0.00		-0.11		-0.03		-0.01
$\Delta q(3)$		-0.03		-0.01		+0.06		+0.00
$\Delta q(4)$		+0.23		+0.36		-0.25		-0.04

The calculations on the anti-site defect did not result in gap levels. In the case of V_C and V_{Si}, however, a localized a_1 state is occupied at -5.1 and -6.3 eV, respectively, relative to the vacuum level. In comparison to the experimental ionization threshold, these values correspond to 1.4 and 0.2 eV above the VB edge, respectively. The 1.4 eV for V_C is to be compared to the values 1.66 [8], 1.67 [9] 1.69 [6], while the 0.2 eV for V_{Si} to 0.54 [8,9] and 0.35 [6], keeping in mind that in those calculations the values refer to a Jahn Teller unstable state (t_2), because of the lack of electronic and/or atomic relaxation. In addition to the occupied levels, we find unoccupied localized states (e) in the gap. The electronic transition energy from the occupied defect levels were calculated in the frozen orbital approximation to be 0.9 and 1.1 eV in case of V_C and V_{Si}, respectively. To obtain the occupancy levels, the formation energy of the singly and doubly positive charge states have been calculated. Figure 1 shows the formation energies as function of the position of the Fermi level relative to vacuum. V_C turns out to be a negative U system. This is different from the prediction of ref. [7], and is due to the energy lowering D_{2d} relaxation. The charge state changes at -4.2 eV, i.e., E(0/++) is almost 2.4 eV above the VB edge. V_{Si} is, on the contrary, a positive U system, with E(++/+) at0.3 eV and E(+/0) at 0.9 eV above the VB edge. It should be noted however, that the calculation of occupation levels can have a relatively large error, due to the ~ 0.1 eV error in the formation energies.

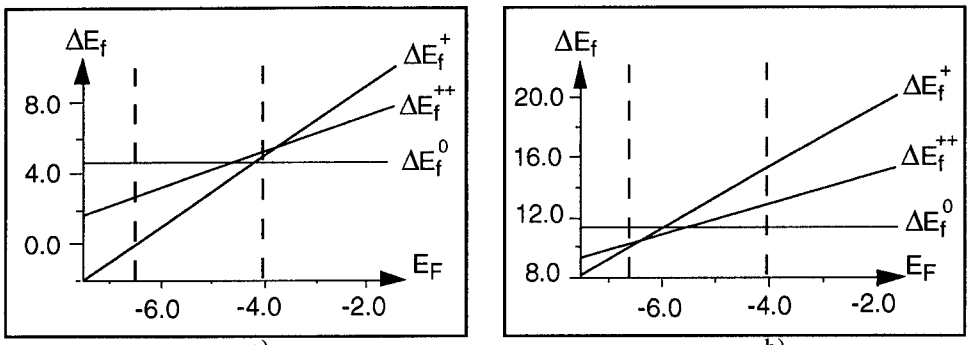

Figure 1.: The formation energies of V_C (a) and V_{Si} (b) in the 0, +, and ++ charge states, as functions of the Fermi level position relative to the vacuum level. The dashed lines indicate the experimentally determined position of the band edges (using the electronaffinity of SiC(6H) ref. [24] and the gap of SiC(3C)).

The results above show that these methods are, in principle, capable of describing defect processes in SiC rather accurately, but further studies are needed before turning to the parametrization of oxygen and nitrogen.

DF-TB Results

Tests have been run using the DF-TB method on the cubic 64 and 216 atom SCM-s as well. The results (shown on the left hand side of Tables 2-3) have the same characteristics as those of the semi-empirical quantum chemical method, except of the ionization threshold which is to low. A significant difference is in the ionicity in SiC which is much lower. This is an obvious consequence of the lack of self-consistency and must be the reason for the low bulk modulus in SiC, too. On the other hand, the vacancy formation energy is very well reproduced. Work to include oxygen is in progress. Also, an attempt will be made to include a charge dependent term in the Hamiltonian to make the method self-consistent.

Conclusions

Using ab initio LCGTO-LDA molecular cluster calculations, we have shown that N on Si sites in SiC(3C) is a $[\bar{1}\,\bar{1}\,\bar{1}]$ off-center substitutional of C_{2v} symmetry, with a deep donor level around midgap. We have given approximate vibration frequencies for this defect. Since the energy difference relative to the shallow donor N_C is less than 0.4 eV, this defect should influence the activation efficiency of nitrogen dopants. At sufficiently high doping levels it should be seen in infrared. We have also shown that oxygen is a [001] off-center substitutional with hyper deep donor levels below midgap at both sites. Preliminary calculations on these and structural defects using a semi-empirical quantum chemical (PM3) and a density functional based non-orthogonal tight binding (DF-TB) method have shown that these methods are suitable for defect studies on big systems (like the 4H and 6H polytypes), but they need further work for inclusion of charge self-consistency (DF-TB) and readjustment of parameters (PM3).

Acknowledgment

The Hungarian authors acknowledge the support of the grants OTKA- T22139, FKFP-0289/97 and the grant JF-667/96 of the Hungarian-US Joint Fund for Science and Technology. The German authors thank the Deutsche Forschungsgemeinschaft for its support.

References

[1] P. Deák, L.C. Snyder, and J. W. Corbett, Phys. Rev. B **37**, 6887 (1988).
[2] P. Deák, L. C. Snyder, M. Heinrich, C. R. Ortiz and J. W. Corbett: Physica B **170**, 253 (1991).
[3] P. Deák, L. C. Snyder and J. W. Corbett, Phys. Rev. B **45**, 11612 (1992).
[4] A. Gali, J. Miró, P. Deák, C. P. Ewels and R. Jones, J. Phys: Condens. Matter. **8**, 7713 (1996).
[5] C. P. Ewels, R. Jones, S. Öberg, J. Miró and P. Deák, Phys. Rev. Lett. **77**, 865 (1996).
[6] Y. Li and P. J. Lin-Chung, Phys. Rev. B **36**, 1130 (1987).
[7] C. Wang, J. Bernholc, and R. F. Davis, Phys. Rev. B **38**, 12752 (1988).
[8] D. N. Talwar and Z. C. Feng, Phys. Rev. B **44**, 3191 (1991).
[9] L. Wenchang, Zh. Kaiming, and X. Xide, J. Phys.: Condens. Matter. **5**, 891 (1993).
[10] A. Fukumoto, Phys. Rev. B **53**, 4458 (1996).
[11] T. Miyajima, N. Tokura, A. Fukumoto, H. Hayashi and K. Hara, Jpn. J. Appl. Phys. **35**, 1231 (1996).
[12] AIMPRO is described at **http://newton.ex.ac.uk/people/resende/aimpro_notes.html** , while the underlying theory is outlined in the paper R. Jones, Philos. Trans. R. Soc. London, Ser. A **341**, 351 (1992).
[13] M. J. S. Dewar and W. Thiel, J. Am. Chem. Soc. **99**, 4899 (1977).
[14] W. Thiel, Tetrahedron **44**, 7393 (1988).
[15] M. J. S. Dewar and C. Jie, Organometallics **6**, 1486 (1987).
[16] J. J. P. Stewart, J. Comp. Chem. **10**, 221 (1989).
[17] D. Porezag, Th. Frauenheim, Th. Köhler, G. Seifert and R. Kaschner, Phys. Rev. B **51**, 12947 (1995).
[18] D. N. Talwar and Z. C. Feng, Inst. Phys. Conf. Ser. Vol. **137** [IOP Publishing, Bristol 1994].
[19] M. A. Roberson, S. K. Estreicher, and C. H. Chu, J. Phys. Condens. Matter. **5**, 8955 (1993).
[20] P. Deák, to be published
[21] D. D. Wagman, W. H. Evans, V. B. Parker, I. Halow, S. M. Baily and R. H. Schumm, "Selected Values of Chemical Thermodynamic Properties", NBS Techn. Notes No. **270-3** [US GPO, Washington DC, 1968]
[22] "Physics of Group IV Elements and II-V Compounds", Vol. **17a** of Landolt Börnstein Tables, ed. O. Madelung, M. Schulz, and H. Weiss [Springer, Berlin 1982]
[23] C. Sebenne, D. Bolmont, G. Guichar and M. Balkanski, Phys. Rev. B **12**, 3280 (1970).
[24] G. Brauer, W. Anwand, E.-M. Nicht, J. Kuriplach, M. Sob, N. Wagner, P. G. Coleman, M. J. Puska and T. Korhonen, Phys. Rev. B **54**, 2512 (1996).
[25] S. Dannefaer, P. Mascher, and D. Kerr, Phys. Rev. Lett, **56**, 2195 (1986).
[26] W. R. L. Lambrecht, Chapter XI. in "III-Nitrides", ed. J. I. Pankove and T. D. Moustakas in the series "Semiconductors and Semimetals" ser. ed. E. Weber and B. Willardson [Academic Press, New York 1996], in press.

Materials Science Forum Vols. 258-263 (1997) pp. 745-750

FORMATION AND RELAXATION OF HYDROGEN-RELATED DEFECTS IN THE SUBSURFACE REGION OF DIAMOND FILMS

Kazushi Hayashi *, Takashi Sekiguchi [1], and Hideyo Okushi
Electrotechnical Laboratory, 1-1-4, Umezono, Tsukuba, Ibaraki 305, Japan
[1]Institute for Materials Research, Tohoku University, Sendai 980-77, Japan

Keywords : hydrogen, diamond films, metastability, cathodoluminescence

Abstract We report the metastability of hydrogen-related defects in hydrogen-plasma-treated diamond films. In the cathodoluminescence spectra, a specific broad peak at around 2.3 eV is observed in the subsurface region of the diamond films treated at 800 ℃. The peak is not observed in those treated below 500 ℃; however, it suddenly appears after low-energy (~ 10 kV) electron beam irradiation. Corresponding to this phenomenon, the irradiation also leads to a decrease in the sheet resistance of the films. These results indicate the existence of a metastable configuration of hydrogen-related defects, which relaxes by the low-energy electron beam irradiation.

Introduction

It is widely recognized that hydrogen exhibits very complex behavior in many semiconductors [1]. Hydrogen terminates dangling bonds, passivates shallow and deep levels, and introduces extended defects in the semiconductors. The hydrogen atoms easily incorporate in the crystals during growth and processing, and tend to form complexes with other defects and impurities. Hence, understanding of the role of hydrogen is of particular importance from both scientific and practical view points.

Due to its hydrogen-rich growth environments, diamond films prepared by chemical vapor deposition (CVD) have a layer in which hydrogen is incorporated in the region near the surface [2-6]. The conductivity of this layer is high and can be removed by oxidation using acid solutions or oxygen-ambient annealing [2-8]. Recently, we have found the hydrogen-related luminescence from the subsurface region [9,10]. The correlation between the origin of this luminescence and that of the high conductivity is not well understood at the present stage.

In this study, we have investigated the cathodoluminescence (CL) spectra and the sheet resistance (whose inverse corresponds to the conductivity) of the subsurface region of diamond films treated with hydrogen/deuterium plasma in various conditions. We have found the metastability of hydrogen-related defects; the low-energy (as low as 10 kV) electron beam irradiation leads to a relaxation of hydrogen-related defects into a stable configuration.

Experimental procedure

Diamond films were deposited on synthetic Ib diamond (001) substrates (4.0 x 4.0 x 0.3 mm^3) with 0.5 % CH_4 diluted by H_2 gas [11] using a microwave plasma-enhanced CVD reactor. The gas pressure, the total gas flow rate, and the microwave power were 25 Torr, 400 sccm, and 750 W, respectively. The growth duration was 6 h and the resultant film thickness was approximately 2 μm. The substrate temperature measured by a thermocouple attached to the backside of the susceptor was maintained at 800 ℃. After deposition, the films were oxidized by acid solution of H_2SO_4 and HNO_3 at 200 ℃ for 15 min, followed by a thermal annealing at 400 ℃ for 30 min in N_2 atmosphere. After oxidation, they were again exposed to hydrogen or deuterium plasma for 15 min using the same system for the deposition. The substrate temperatures during plasma treatment were 300, 500, and 800 ℃ under similar conditions for the deposition.

The CL from the surface region was observed at room temperature using a quantitative electron-beam tester [12] with a CCD array detection system. The typical acquisition time and scanning area for measurements were 30 sec and 400 μm x 400 μm, respectively. The accelerating voltage of the electron beam was fixed at 1.5 kV and the beam current was approximately 1 nA (the depth of the probe from the surface is approximately 30 nm).

For the sheet resistance measurements, Ohmic contacts, 800 μm in diameter, were deposited at the corners of the samples by vacuum evaporation of a Au/Ti (200 nm/50 nm) bilayer. The *I-V* measurements between two Ohmic contacts were conducted in vacuum at various temperatures.

Depth profiles of deuterium in the films were obtained by SIMS analysis using Cs^+ ions with an accelerating voltage of 14.5 kV. The sputtering rate of diamond due to the bombardment of 14.5 keV Cs^+ is estimated to be 2.1 Å/sec.

Results

Cathodoluminescence

Figure 1 shows the CL spectra obtained from the hydrogenated and the oxidized diamond films. The hydrogenation temperature and duration were 800 ℃ and 15 min, respectively. A broad peak at around 2.3 eV is observed in the spectrum of the hydrogenated films. On the other hand, the peak is not observed in conventional oxidized films, while the other features remain.

Contrary to the above results, the features observed in the films hydrogenated below 500 ℃ are quite different from those observed at 800 ℃. As shown in Fig. 2, the peak was not observed in the films hydrogenated at 500 ℃ at first (as labeled "Before"). However, the peak suddenly appears after low-energy (~ 10 kV) electron beam irradiation (as labeled "After"). The same phenomena were also observed in diamond films hydrogenated at 300 °C. In the figure, it is found that the peak produced by the electron-beam irradiation can be reproduced by the mixture of two Gaussian peaks at 2.3 eV with the half-width of 0.4 eV and at 1.8 eV with the half-width of 1 eV, respectively.

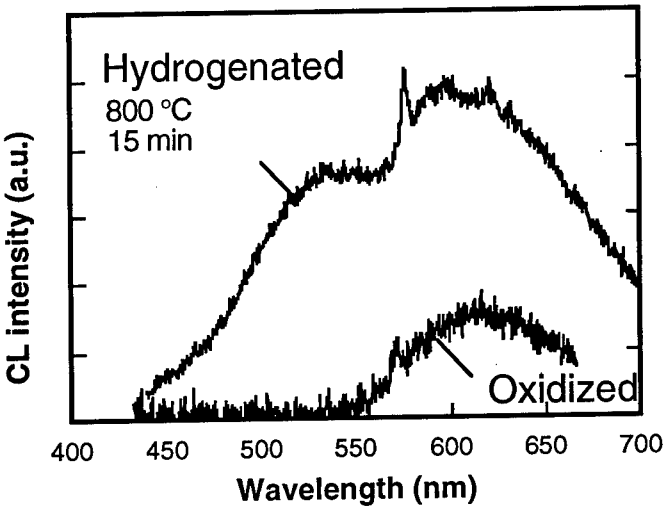

Fig. 1 CL spectra obtained from the hydrogenated and the oxidized diamond films. The hydrogenation temperature and duration were 800 °C and 15 min, respectively.

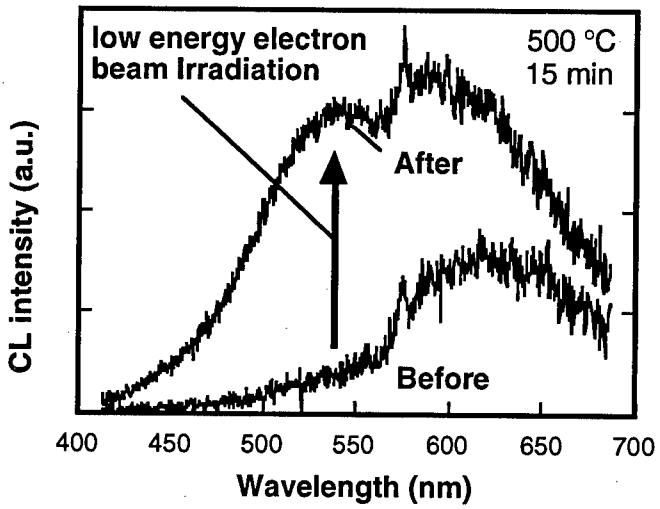

Fig. 2 CL spectra obtained from the hydrogen-plasma treated diamond films before and after low-energy electron irradiation. The hydrogenation temperature and duration were 500 °C and 15 min, respectively.

Sheet resistance

Figure 3 shows the sheet resistance of the diamond films hydrogenated at (a) 300, (b) 500, and (c) 800 ℃ as a function of reciprocal temperature. The sheet resistance was estimated from the linear part of the *I-V* measurements between two of four Ohmic contacts on the samples. The sheet resistance in the diamond film hydrogenated at 800 ℃ is around 1 x 10^5 Ω at room temperature and nearly constant in the temperature range between 93 and 400 K. The observed properties corresponds to those in the as-deposited diamond films obtained in our previous study [6,10]. On the other hand, the sheet resistance at room temperature in the films hydrogenated below 500 ℃ are one order of

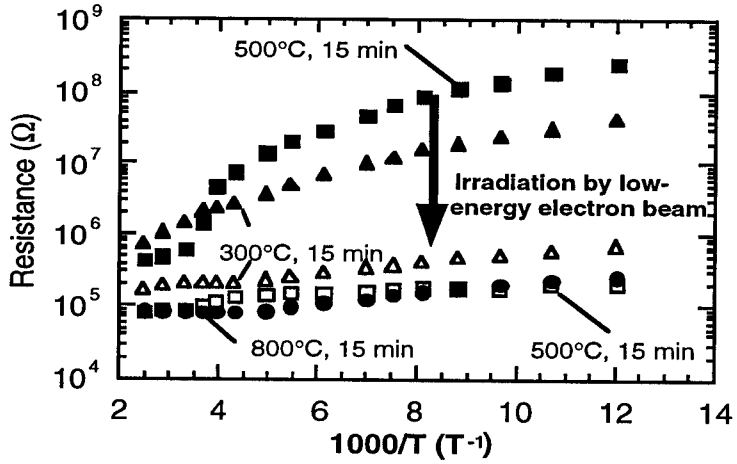

Fig. 3 Sheet resistances of the diamond films hydrogenated at (a) 300, (b) 500, and (c) 800 °C as a function of reciprocal temperature.

magnitude higher than that at 800 ℃ and they exhibit temperature dependence between 93 and 400 K.
After the low energy electron beam irradiation, however, the sheet resistance of the films hydrogenated at both 300 and 500 ℃ decreases. The temperature dependence observed before the electron beam irradiation has also disappeared. It means that the conductivity of the films treated below 500 ℃ becomes the same as that at 800 ℃ after the electron beam irradiation.

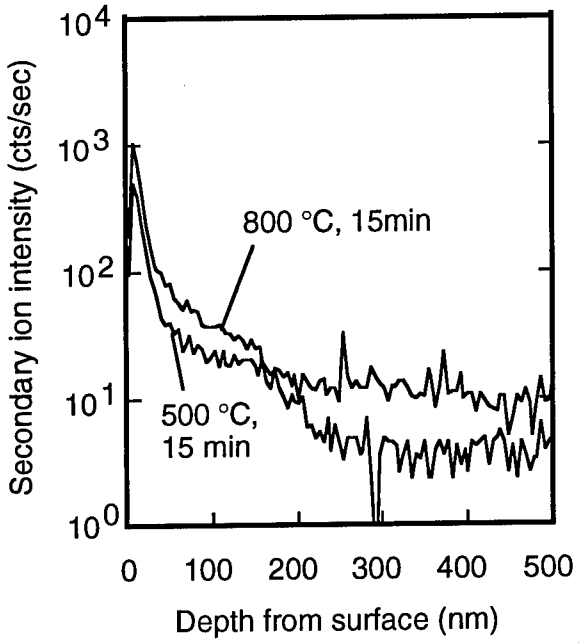

Fig. 4 Typical depth profiles of deuterium in the diamond films treated with deuterium plasma at 500 and 800 °C under the similar condition as that for the hydrogen.

SIMS
In order to clarify whether the hydrogen incorporates at low temperature or not, the depth profiles of deuterium were examined by SIMS analysis. Figure 4 shows the typical depth profiles of deuterium in the diamond films treated with deuterium plasma at 500 and 800 ℃ under the similar condition as that for the hydrogen. The profiles exhibit a high concentration of deuterium in the subsurface region (down to 50 nm from the surface) of both films and, then, a plateau region with a lower concentration for the deeper region. The result confirms that the hydrogen incorporates in the subsurface region of the diamond even by the low temperature hydrogenation.

Discussion

Origin of the CL peak at 2.3 eV
As mentioned above, we have observed a broad CL peak at around 2.3 eV in the hydrogenated films but not in the oxidized films. The energy level of this peak is close to that of the peak for which Gippius *et al.*, have reported a luminescence line at 2.272 eV in a proton-implanted diamond [13]. However, the half-width of the present CL peak is two orders of magnitude broader than that observed by Gippius *et al*,. The appearance

and disappearance of the CL peak is reversible with the successive hydrogenation and oxidation treatment. It should be noted that the depth profile of deuterium shown in Fig. 4 corresponds to the depth distribution of the CL peak at 2.3 eV, which was obtained by the accelerating voltage dependence of the CL spectra in our previous study [9,10]. This suggests that the luminescent states of the CL peak at 2.3 eV exist only in the subsurface region where high concentration hydrogen incorporates. The above arguments lead to the conclusion that the broad peak at around 2.3 eV originates from the hydrogen-related defects of the diamond films.

Relaxation of hydrogen-related defects by electron beam irradiation

On the other hand, as is shown in Fig. 2, the CL peak at around 2.3 eV is not observed at first for the low-temperature hydrogenation below 500℃. However, the peak appears after the low-energy electron beam irradiation. Corresponding to this phenomenon, the electron beam irradiation leads to a change of the sheet resistance of the films. Judging from SIMS data shown in Fig. 4, the change of the sheet resistance has been attributed to the change in configuration of hydrogen-related defects rather than whether the hydrogen incorporates or not. Therefore, it is concluded that the low-temperature hydrogenation leads to a different configuration of hydrogen-related defects from those achieved at 800 ℃, and that they are transfered by the electron-beam irradiation of as low as 10 kV into the configuration which causes the CL peak at 2.3 eV or the high conductivity. In other words, the low-energy (as low as 10 kV) electron beam irradiation leads to a relaxation of metasatble hydrogen-related defects created by the low-temperature hydrogenation into a stable configuration achieved by the hydrogenation at 800 ℃.

In general, electron beam irradiation (typically on the order of MeV) produces a large number of vacancies and interstitial atoms in the crystal, resulting in the formation of many kinds of defect configurations. In the present case, however, the possibility of the formation of vacancies or interstitial atoms and the decomposition of the hydrogen complexes can be neglected because of the low-energy electron irradiation (as low as 10 kV). Important points of the present case are as follows; the properties observed after the irradiation are exactly the same as those observed in the films treated at higher temperatures, which generally gives a more stable configuration. Hence, the low-energy electron irradiation is expected to enhance the annealing effect of the films rather than the introduction of new defects in the films or the removal of the hydrogen atoms from its complexes. In this case, the recombination process of hole-electron pairs excited by the electron irradiation may play an important role, as is discussed in terms of "recombination-enhanced defect reaction" in the problem of the formation and relaxation of defects in semiconductors [14].

Configuration of hydrogen-related defects

Concerning the configuration of the hydrogen-related defects, we have no direct evidence at present. However, according to muon-spin-rotation experiments [15], tetrahedrally localized muonium is stable at low temperatures and converts to the bond-centered (BC) site between 350 and 800 K. Above 800 K, only the BC muonium centers have been observed. The motion of muonium (or hydrogen) from the tetrahedral site to the BC site has been considered to be an activated process and, from theory, a barrier for the relaxation of hydrogen from the tetrahedral site to BC site is estimated to be around 2 eV [16-18]. Therefore, it is speculated that such a configuration is involved in the hydrogen-related defects and the motion of hydrogen from the tetrahedral site to the BC site occurs due to the low-energy electron beam irradiation.

The result of one-to-one correspondence between the appearance of the CL peak at 2.3 eV and the decrease of the sheet resistance is also an interesting problem. It is noted that the energy state which give rize to the CL peak at 2.3 eV is not be compatible with the origin of the high conductivity, since the conductivity is associated with shallow acceptors in the diamond [9,10]. In order to explain the result, we must consider at least two kinds of

energy states associated with the stable hydrogen-related defects. Further detailed study will be needed to clarify the mechanism of the present phenomena.

Conclusions

We report, for the first time, the metastability of the hydrogen-related defects in the subsurface region of diamond films. The low-energy electron beam irradiation leads to a change in both the CL spectra and the conductivity of the films. The SIMS depth profile obtained from the films treated with deuterium plasma confirms that a high concentration of deuterium exists in both subsurface of the films. The results indicate that a metastable configuration of hydrogen-related defects exists and relaxation into a stable state occurs by the low-energy (~ 10 kV) electron beam irradiation.

Acknowledgments

The authors are grateful to S. Hara, S. Yamanaka, H. Watanabe and, K. Kajimura for their useful discussion. Useful advise from T. Shimizu, Y. Toyoshima, K. Arai, and P. L. Hacke is also gratefully acknowledged.

References

*On leave from Kobe Steel Ltd., Electronics and Information Technology Laboratory, 1-5-5, Takatsukadai, Nishi-ku, Kobe 651-22, Japan.

1. S. J. Pearton, J. W. Corbett, and M. Stavola. Hydrogen in Crystalline Semiconductors (Springer, Berlin, 1992).
2. M. I. Landstrass and K. V. Ravi. Appl. Phys. Lett. **55**, 1391 (1989).
3. T. Maki, S. Shikama, M. Komori, Y. Sakaguchi, K. Sakuta, and T. Kobayashi, Jpn. J. Appl. Phys. **31**, L1446 (1992).
4. Y. Mori, A. Hatta, T. Ito, and A. Hiraki, Jpn. J. Appl. Phys. **31**, L1718 (1992).
5. H. Kiyota, E. Matsushima, K. Sato, H. Okushi, T. Ando, M. Kamo, Y. Sato, M. Iida, Appl. Phys. Lett. **67**, 3596 (1995).
6. K. Hayashi, S. Yamanaka, H. Okushi, and K. Kajimura, Appl. Phys. Lett. **68**, 376 (1996).
7. J. Shirafuji and T. Sugino, Diamond and Related Materials **5**, 706 (1996).
8. H. Kawarada, H. Sasaki and A. Sato, Phys. Rev. B **52**, 11351 (1995).
9. K. Hayashi, H. Watanabe, S. Yamanaka, H. Okushi, K. Kajimura, and T. Sekiguchi, Appl. Phys. Lett. **69**, 1122 (1996).
10. K. Hayashi, S. Yamanaka, H. Watanabe, T. Sekiguchi, H. Okushi, and K. Kajimura, J. Appl. Phys. **81**, 744 (1997).
11. K. Hayashi, S. Yamanaka, H. Okushi, and K. Kajimura, Appl. Phys. Lett. **68**, 1220 (1996).
12. T. Sekiguchi and K. Sumino, Rev. Sci. Instrum. **66**, 4277 (1995).
13 A. A. Gippius, V. S. Vavilov, A. M. Zaitsev, and B. S. Zhakupbekov, Physica **116B**, 187 (1983).
14. J. D. Weeks, J. C. Tully and L. C. Kimering, Phys. Rev. **B12**, 3286 (1976).
15. E. Holzschuh, W. Kündig, P. F. Meier, B. D. Patterson, J. P. F. Sellschop, M. C. Stemmet, and H. Appel, Phys. Rev. A**25**, 1272 (1982).
16. T. L. Estle, S. Estreicher, and D. S. Marynick, Phys. Rev. Lett. **58**, 1547 (1987).
17. P. Briddon, R. Jones, and G. M. S. Lister, J. Phys. C **21** L1027 (1988).
18. S. P.Mehandru, A. B. Anderson, and J. C. Angus, J. Mater. Res. **7**, 689 (1992).

Materials Science Forum Vols. 258-263 (1997) pp. 751-756

HYDROGEN AND HYDROGEN-LIKE DEFECTS IN DIAMOND

S.H. Connell[1], J.P.F. Sellschop[1], R.D. Maclear[1], B.P. Doyle[1], I.Z. Machi[1], R.W.N. Nilen[1], J.E. Butler[2] and K. Bharuth-Ram[3].

[1] Schonland Research Centre, University of the Witwatersrand, P.O. Wits, 2050, South Africa
[2] Chemistry Division, Naval Research Laboratory, Washington DC, USA
[3] Physics Department, University of Durban-Westville, Durban 4000, South Africa

Keywords: diamond, hydrogen, defects

Hydrogen is known to passivate active dopants in the diamond lattice, catalyse the growth of CVD diamond and to affect many of the physical and electrical properties of diamond. Positrons, muons, protons, and atoms formed from these positive particles have been used to study the behaviour of hydrogen in diamond. This paper reviews the results of these complementary studies.

1. Introduction

Hydrogen is one of the most important defects within the diamond lattice. Its presence is known to affect both the physical and electrical properties, including passivation of dopants [1,2]. Hydrogen also catalyses the metastable growth of CVD diamond [3,4]. Various configurations for hydrogen trapping in the bulk have been proposed - these include trapping at vacancies, dislocations, internal C-H related configurations, or at defects like A and B centres [5,6] and auto-trapped systems like the bond-centred (H_{BC}), the bonding-anti-bonding (H_2^*) and the tetrahedral molecular (H_{2T}) configurations [7-9].

Much information on hydrogen in diamond has been inferred from the behaviour of its chemical analogue atom, muonium. The large magnetic moment of the muon and the correlation of the emission direction of its decay positron with its polarisation enable it to sensitively interrogate and reveal information concerning its chemical and dynamical behaviour. In this regard, the bound states with electrons of the positron (positronium, Ps), the muon (muonium, Mu) and the proton (hydrogen, H) form an interesting set of hydrogenic impurities in diamond. The results of experiments with these systems are reviewed in this paper. The chemistry of at least the Mu and the H systems in diamond are assumed to be very similar, due to the near equality of their reduced masses. It is interesting to compare what has been learned from each of these "atoms" in diamond, as the degree of classical behaviour varies.

2. Positron Annihilation Spectroscopy

Positrons injected into crystalline molecular insulators rapidly thermalise, diffusing and interacting with the lattice either as a (dressed) positron or even as positronium. The electron density and momentum distribution sampled by the positron in the configuration from which it annihilates are obtained from the life-time of the implanted positrons and the 2-γ

annihilation radiation (line-broadening), respectively [10]. In diamond hydrogen and muonium are found or formed. The question was whether positronium also formed in diamond.

Fig. 1 shows an age-momentum curve typical of pure diamond. Also shown for comparison is a curve for quartz which typifies positronium formation as seen in some crystalline molecular insulators. The vertical axis plots a parameter characterising the broadness of the momentum distribution of the positron-electron system (1-S of [11]) against the positron age. In quartz 25% of the positrons are found in a state with a narrow momentum distribution which annihilates rapidly, as expected for para-positronium. What remains is pick-off annihilation from the ortho-positronium state, showing the broader momentum distribution of the crystal electrons. In the case of diamond, on the other hand, almost all (>95%) of the positrons annihilate from a configuration with a large momentum distribution ($\Delta p \approx 3.5$ keV/c) and a lifetime shorter than that of vacuum para-positronium ($\tau \approx 114$ ps [10]). Evidently, positronium does not form in pure bulk diamond. A second positron configuration is also observed in diamond. It has a longer lifetime and smaller momentum spread (both sample dependent). It is linked to positron trapping and annihilation at lattice defects. The transition from the first to the second state occurs at a rate of approximately 10^9 s^{-1} at room temperature, and is well described by a two-state trapping model [11].

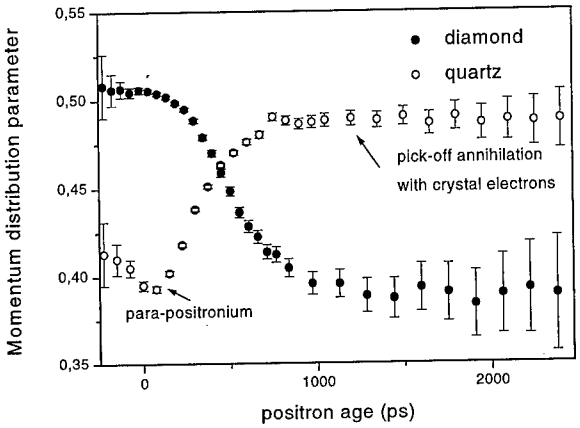

Fig. 1. Age-momentum correlation measurements on quartz and diamond.

The most probable positron configuration in diamond is considered to be the formation of a band-like state. The positron wavefunction is delocalised, and can be found to first order by considering it to be in the combined potential of the carbon cores and (self-consistent) valence electron distributions. In diamond, two related features distinguish this distribution from other similar systems. There is the highest degree of electron localisation in the covalent bonds, and the *s* and *p* character of these bonds leads to a double humped structure [12]. Although the positron distribution is strongly repelled by the cores to the interstitial

regions, the dominant contribution to the quantity $|\psi(r_e)\psi^*(r_p)|$ representing the integrated positron-electron overlap comes from the intra-bond regions [13]. This results in the short lifetime (large electron density) and broad momentum distribution of this configuration.

Strong evidence confirming the model of the bulk positron state in pure diamond as a delocalised but inhomogenously distributed band-like state may be seen in Fig. 2 below. This schematic figure shows a polar plot of the measurement of the anisotropy of a parameter characterising the broadness of the longitudinal projection of the electron-positron momentum distribution with a calculation for the above model using density functional theory (DFT). The inset is a cross section from the DFT calculation of the overlap $|\psi(r_e)\psi^*(r_p)|$ in the (110) plane[11].

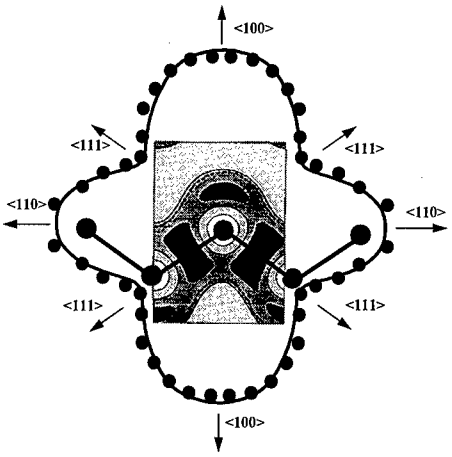

Fig. 2. Polar plot of experimental (•) and DFT calculated (solid line) anisotropy of electron-positron momentum distribution in diamond.

3. Muon Spin Rotation

Muonium may be regarded as a chemical analogue of hydrogen with respect to static properties. In diamond, as in other elemental semiconductors, three different type of muonium (Mu) signals have been observed, two of which come from paramagnetic states and one from a diamagnetic environment. One of the paramagnetic signals (Mu_T) is attributed to Mu located in the tetrahedral interstices [14]. The second paramagnetic signal (Mu_{BC}) is established to be due to Mu located at a strongly relaxed bond-centred site [15,16]. The configuration responsible for the diamagnetic component, μ^+_D, is so far not well understood.

Mu_T is highly mobile with a diffusion constant D_{Mu} of $10^{-3}cm^2/s$ and interacts with defects (for example, trapping at vacancies, and possibly the passivation of boron acceptors, as well as interaction with nitrogen containing defect complexes)[17]. The Mu_T state is not the most stable configuration for Mu in diamond. There is a thermally activated first order transition

from Mu_T to Mu_{BC} with an activation energy of approximately 1.3 eV [18]. The Mu_{BC} state , on the other hand, is found to be stable. In analogy, bond-centred hydrogen is believed to be a stable configuration for hydrogen in diamond.

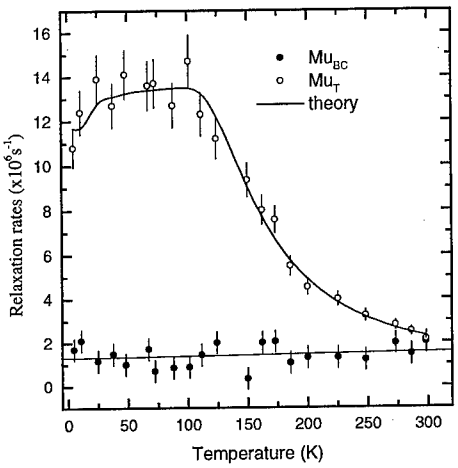

Fig. 3: The relaxation rate of the muon spin ensemble for isotropic muonium (Mu_T), and anisotropic muonium (Mu_{BC}) in natural p-type diamond.

4. Elastic Recoil Detection Analysis (ERDA) of Hydrogen

We have applied ERDA to study the behaviour of implanted and as-grown hydrogen in many types of natural and synthetic high pressure high temperature and CVD diamonds [19-20]. Hydrogen was implanted with an energy of 50 keV, at a dose of $3x10^{16}cm^{-2}$ into the samples which corresponds to an concentration ≈ 5% in the implanted region. Two vacancies should be produced for each hydrogen ion implanted, but the damage profile is distributed differently to the range profile. Some of the samples were also pre-damaged with 80 keV carbon ions, producing a damage layer between the implanted hydrogen layer and the surface with 80 vacancies per implanted carbon ion. Fig. 3 shows a typical implanted hydrogen profile (as-implanted and after a 1473 K 30 min. anneal) together with a TRIM calculated profile of the carbon pre-damage layer and the damage created by the implanted hydrogen.

In all diamond samples the implanted hydrogen were found to be deeply trapped within its own implanted range distribution even after the anneal. The implanted hydrogen concentration is at least three orders of magnitude higher than any intrinsic defect or impurity concentration in the region of its initial implant distribution. Thus, although some hydrogen may trap at existing vacancies or at nitrogen containing defect complexes, this cannot account for the bulk of the trapping sites. There is also no evidence of hydrogen migration towards the vacancy-rich implant damage distribution or the pre-damage distribution.

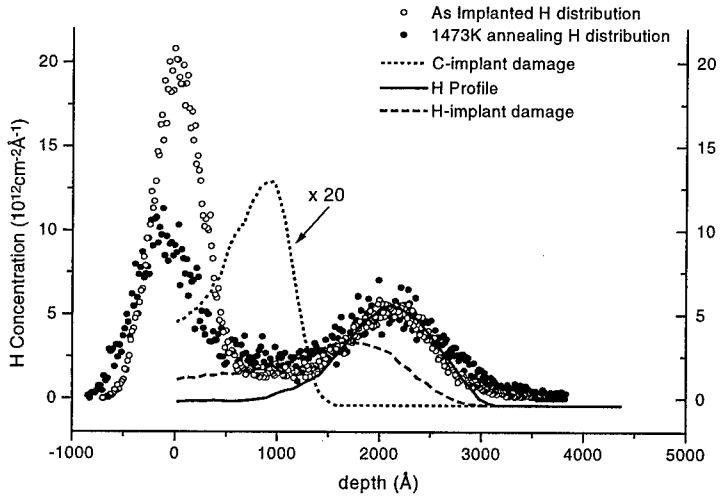

Fig. 4. Depth profile of implanted hydrogen as-implanted and after a 1473 K 30 min. anneal. The calculated damage distribution profiles are also shown.

Auto-trapping mechanisms are therefore considered to be strong candidates explaining the deep trapping of implanted hydrogen. The possible auto-trapping mechanisms include tetrahedral hydrogen (H_T), bond-centred hydrogen (H_{BC}), the H_2^* configuration (neighbouring occupancy of the bond-centred and anti-bonding sites (H_{BC}-H_{AB})), as well as the H_2 molecule in the T-site (H_{2T}). Comparing stabilities of double H configurations, one finds that the sequence H_{2T} : twice H_{BC} : H_2^* are separated by calculated potential energy differences of 1.3 eV and 2.0 eV with H_2^* being the most stable [9]. H_{BC} is calculated to be 2.4-1.9 eV more stable than H_T[8,9]. A path for H diffusion via tetrahedral and hexagonal interstitial sites (T-sites and H-sites) has been calculated to give a barrier of 1.21 eV [7,8]. A path for H_{BC} diffusion via neighbouring bond-centred configurations in (110) planes yields activation energies of 0.1, 1.9 and 2.4 eV for H^+, H^0 and H^- respectively [7]. Our experimental results would rule out H_T and H^+_{BC} as diffusion pathways. The MSR results also imply that the bond-centred configuration is more stable than the tetrahedral configuration.

5. Conclusions

Experimental results for the interaction with diamond of positrons, muons, protons, and atoms formed from these positive particles have been presented. The ERDA measurements on implanted hydrogen distributions show that the hydrogen is self-trapped in its implantation range. MSR results support the existence of three muonium states, and show that Mu_T is highly mobile, but that Mu_{BC} is stable. Recent measurements show evidence for Mu-defect/impurity interactions [21]. The MSR results also imply that the bond-centred

configuration is more stable than the tetrahedral configuration. Thus the auto-trapped configurations, H_{BC}, H_2^*, H_{2T} may account for the deep trapping of hydrogen in diamond.

In positron life-time and momentum-distribution measurements the annihilation radiation characteristics are also dominated by momentum- and space-distributions of the intra-bond rather than the interstitial electron distributions.

References

[1] K.M. McNamara, B.E. Williams, K.K. Gleason, B.E. Scruggs, J. Appl. Phys. 76 (1994) 2466

[2] A.G. Ulyashin, R.B. Gelfand, N.V. Shlopak, A.M. Zaitiv, A.V. Denisenko, A.A. Melnikov, Diamond Relat. Mater. 2 (1993) 1516

[3] DG Goodwin and JE Butler in *Handbook of Industrial Diamonds and Diamond Films* Ed. MA Prelas, G Popovici and K Bigelow. (Marcel Dekker, Inc. 1996), (in press).

[4] JE Butler and RL Woodin, Phil. Trans. R. Soc. Lond., A342 (1993) 209

[5] D.D. Koleske, S.M. Gates, B.D. Thoms, J.N. Russell, Jr., and J.E. Butler, J. Chem. Phys. 102(2) (1995) 992

[6] B.D. Thoms and J.E. Butler, Surface Science, 328, (1995) 291

[7] S.P. Mehandru, A.B. Anderson and J.C. Angus, J. Mater. Res. 7 (1992) 689

[8] T.L. Estle, S.K. Estreicher and D.S. Marynick, Phys. Rev. Lett. 58 (1987) 1547

[9] P Briddon, R Jones and GM Lister, J. Phys. C 21 (1988) L1027

[10] R.N. West, Adv. Phys. 22 (1973) 263

[11] R.W.N. Nilen, U. Lauff, S.H. Connell, H. Stoll, A Siegle, H. Schneider, Castellaz, J. Kraft, K. Bharuth-Ram, J.P.F.Sellschop and A.Seeger, Appl. Surf. Sc 116 (1997) 198

[12] W.G. Schmidt and W.S. Verwoerd, Phys. Lett. A 222 (1996) 275

[13] R.W.N. Nilen, S.H. Connell, D.T. Britton, C.G. Fischer, E.J. Sendezera, P. Schaaff, W.G. Schmidt, J.P.F. Sellschop, W.S. Verwoerd, J. Phys: Condens. Matt.(1997) (in press)

[14] A. Mainwood and A.M. Stoneham, J. Phys. C 17 (1980) 2513

[15] S.F.J. Cox and M.C.R. Symons, Chem. Phys. Lett. 126 (1986) 516

[16] J.W. Schneider, R.F. Kiefl, K.H. Chow, S. Johnston, J. Sonier,T.L. Estle, B. Hitti, R.L. Lichti, S.H. Connell, J.P.F. Sellschop, C.G. Smallman, T.R. Anthony, and W.F. Banholzer, Phys. Rev. Lett. 71 (1993) 557

[17] C.G. Smallman, S.H. Connell, K. Bharuth-Ram, J.P.F.Sellschop, R.W.N. Nilen, M. Hampele, J. Major, R.Scheuermann, A.Seeger , T. Stammler, Hyp. Int. C1, (1996)440

[18] W. Odermatt, Hp. Baumeler, H. Keller, W. Kündig, B.D. Patterson, J.W. Schneider, J.P.F. Sellschop, M.C. Stemmet, S.H. Connell and D.P. Spencer, Phys. Rev. B 38 (1988) 4388

[19] S.H.Connell, E.Sideras-Haddad, C.G.Smallman, J.P.F.Sellschop, I.Z. Machi, K.Bharuth-Ram, Nucl. Instr. Meth. B118 (1996) 332

[20] IZ Machi, SH Connell, P Schaaff, BP Doyle, RD Maclear, K Bharuth-Ram, P Formenti and JPF Sellschop, Nucl. Instr. Meth., B127/128 (1997) 212.

[21] SH Connell, *et al*, to be published.

Materials Science Forum Vols. 258-263 (1997) pp. 757-762

FINE STRUCTURE OF THE BORON BOUND EXCITON IN DIAMOND

H. Sternschulte, S. Wahl, K. Thonke, R. Sauer, T. Ruf [1], M. Cardona [1], T.R. Anthony [2]
Abteilung Halbleiterphysik, Universität Ulm, D-89069 Ulm, Germany
[1] MPI für Festkörperforschung, Heisenbergstraße 1, D-70569 Stuttgart, Germany
[2] GE Corporate Research and Development, Schenectady, New York 12309, USA

Keywords: diamond, cathodoluminescence, boron bound exciton, fine structure

Abstract. Low temperature cathodoluminescence has been measured on boron doped natural and synthetic diamond crystals that show very narrow linewidths due to low internal strain. This allows us to resolve a novel fourfold fine structure in both components of the bound exciton doublet which is known from previous work. Temperature-controlled measurements lead to a level scheme with a 2 meV ground state splitting of the neutral boron acceptor and a 3.3 meV splitting in either of the two initial doublet exciton states. The ground state splitting is in excellent agreement with data from former excitation spectroscopy on boron acceptors in the infrared and from recent Raman spectroscopy on boron doped diamonds. The initial state splitting which we measured to be 11.4 meV is discussed in terms of spin-orbit interaction of the holes. The 3.3 meV exciton splitting remains unidentified.

Introduction

High quality crystalline diamonds, either natural or synthetic, exhibit two fundamental optical signatures at low temperatures near the band-edge. One is the emission (or absorption) of free excitons (FE) defining the excitonic gap at E_{gx} = 5.418 eV [1,2,3] with due account of wavevector conserving lattice phonons accompanying the recombination in the indirect band structure. Preferential coupling of TA- and TO-phonons is observed in the optical spectra, with $\hbar\Omega$(TA) = 87 meV and $\hbar\Omega$(TO) = 141 meV [3]. The other signature is luminescence from localized or bound excitons (BE) when boron is present in the diamonds. Boron is an acceptor and the only shallow impurity known in diamond [4]. It has an ionization energy E_i = 370 meV [5,6] and binds an exciton with a localization energy E_{loc} = 51 meV, giving rise to emission at ≈ 5.355 eV. Since boron doping perturbs the translational symmetry of the lattice, optical emission of the BE is allowed as no-phonon (NP) transitions in addition to phonon-assisted transitions. These near-band-edge optical features have been studied intensely in previous years despite the experimental difficulties in the ultra-violet photon energy region. It was found in particular [3] that the FE and BE luminescence spectra have both a specific narrow substructure in their emission lines present in all phonon replicas. For the FE, there is a thermally activated higher-energy component with a ≈ 7 meV peak-to-peak spacing from the lower-energy component. This doublet was ascribed [3] to electron recombination with fourfold Γ_8^+ and twofold Γ_7^+ holes, respectively, split apart by spin-orbit interaction Δ_0. At the time of this interpretation, the only value of the spin-orbit interaction available in the literature was Δ_0 = 6 meV as experimentally determined from cyclotron resonance measurements under tunable light excitation [7]. The BE lines also show a narrow substructure in sufficiently strain-free specimens, seen in the NP-, TA-, and TO-phonon replicas. It consists of a doublet split by ≈ 12 meV whose higher energy component is thermally activated [3]. The original notation of the doublet was D_0 and D_0' for the BE^{NP} transition, and D_1 and D_1' for the BE^{TO} transition [3]. This doublet was ascribed to electron recombination with Γ_8 or Γ_7 bound holes, respectively, in the radiative BE decay thus assigning the 12 meV to spin-orbit interaction in the BE having twice the value found for free holes [3].

In this paper, we re-investigate, with much higher resolution than previously, the BE luminescence spectra in low-strain natural type IIa diamonds and synthetic high-pressure-high temperature (HPHT) single crystalline diamonds. The latter have controlled $^{12}C/^{13}C$ isotope compositions from 1 % ^{13}C to 98 % ^{13}C. In all these specimens we find a novel fourfold fine structure in either of the two known doublet components of the BE^{NP} transition. This novel fine structure is not observed in the phonon replicas since coupling to the phonons strongly broadens the transitions.

Experimental

The preparation of the isotopically controlled HPHT crystals has been described in a previous paper [8]. The boron concentration in these samples as well as in the nearly strain free natural diamonds is low and allows for the simultaneous detection of FE and BE exciton spectra. We employ cathodoluminescence (CL) with a continous-flow cryostat keeping the samples at low temperature by using liquid nitrogen or liquid helium as coolant. Excitation was performed with a 6 keV electron beam of ≈ 1 mm diameter and a typical current of 1 μA from a RHEED electron gun. The emitted light was dispersed by a 1 m monochromator and detected by a UV-optimized, LN_2 cooled CCD camera. All spectra were recorded with the optimal resolution of our system corresponding to $\Delta\lambda \approx 0.03$ nm or $\Delta(h\nu) \approx 0.5$ meV.

Results and Discussion

Fig. 1 displays the near-band-edge CL spectra recorded from HPHT samples with isotopic compositions of 1 % ^{13}C and 98 % ^{13}C. The sample temperature of 36 K was determined by fitting Boltzmann tails to the high-energy portions of the FE spectra. In the 98 % ^{13}C specimen, all transitions appear up-shifted in energy as compared to the 1 % ^{13}C specimen of

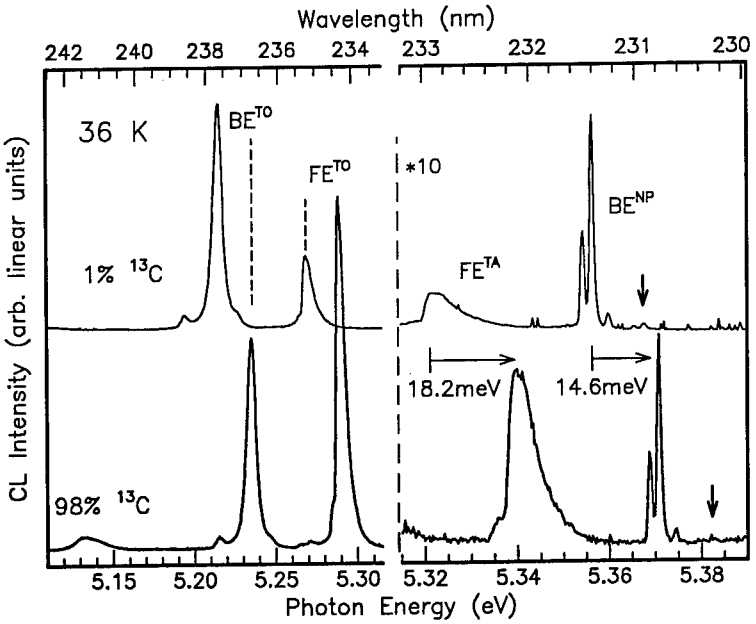

Fig. 1: CL spectra at 36 K sample temperature of two diamonds with 1 % and 98 % ^{13}C. The energy scale at the right hand has been expanded. The intensity scale has been expanded by a factor of 10. Horizontal arrows indicate the isotope-mass-induced energy shifts of the FE^{TA} and the BE^{NP} lines. The BE^{NP} lines show the novel fine splitting. The vertical arrows indicate the positions where at higher temperature the excited components of the BE^{NP}, spaced by 11.4 meV, appear, showing the same novel fine splitting (cf. Fig. 2).

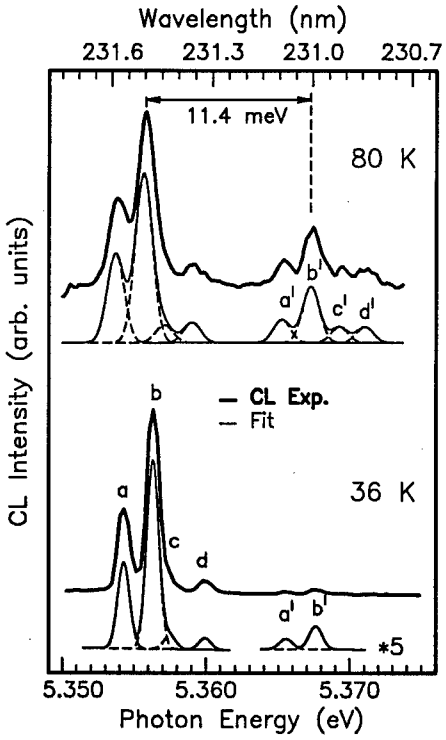

Fig. 2: Doublet structure of the BE^{NP} transition (spacing 11.4 meV) and novel identical fine structure found in both doublet componentes. For transition energies, see Table 1. Upper spectra: experimental curves, lower spectra: computer-simulated spectra using Gaussian broadened lines with FWHM of 1 meV (at 36 K) and 1.4 meV (at 80 K) corresponding to the experimental linewidths.

natural carbon abundance, in accord with former findings in crystals of similar isotopic compositions [9]. Indicated in Fig. 1 are the values of 14.6 meV for the shift of the BE^{NP} transition and 18.2 meV for the FE^{TA} transition, the difference being related to the isotope effect implicit in the TA-phonon frequencies. The novel fine structure is visible on the BE^{NP} lines. At first sight, this seems to be a triplet splitting, however closer inspection and computer fits demonstrate a fourfold splitting. As mentioned in the introduction, the structure of the BE transition known heretofore is a doublet with a spacing of $\approx$ 12 meV [3]. In Fig. 1, the position of the higher-energy doublet component is indicated by an arrow for both samples. At higher temperatures this component is activated, as expected, and exhibits the same novel fine structure as the lower-energy doublet component seen in Fig. 1. This is depicted in detail in Fig. 2. Here, the split transitions are labeled (a ... d) and (a' ... d') in the two doublet components. To better identify the fine structure, computer fits to the spectra were made using Gaussian broadened lines with linewidths (FWHM) corresponding to the experimental linewidths. These are 1.0 meV at 36 K and 1.4 meV at 80 K. The fits firmly establish that each doublet component contains four lines resulting in the same luminescence pattern. The line positions are listed in Table 1. When the temperature is raised, lines c and d are thermally activated together leaving lines a and b in a constant intensity ratio. From this temperature behavior, we deduce the level scheme shown in Fig. 3. The exciton complex has a lower state labeled A°X and an excited state labeled (A°X)' with 11.4 meV excess energy. Either of these states is split by 3.3 meV. The final state is the neutral acceptor, A°, which is split by 2.0 meV.

This 2.0 meV splitting lends itself to a straightforward interpretation. Previous absorption measurements on the electronic excitation spectrum of the boron acceptor (at that time erroneously considered to be aluminum, see [4]) had shown that boron has a ground state split by 2 meV [5]. Later, photothermal ionization spectroscopy on boron acceptors yielded the same result [6]. Application of

Line	hν (eV)	Line	hν (eV)
a	5.3538	a'	5.3652
b	5.3558	b'	5.3672
c	5.3572	c'	5.3692
d	5.3591	d'	5.3711

Table 1: Photon energies of BE^{NP} components at 80 K.

uniaxial stress [5] and electric fields [10] demonstrated that these two levels are bound hole states of Γ_8 (lower energy) and Γ_7 (higher energy) symmetry deriving from the Γ_8^+ and Γ_7^+ valence bands, respectively. This would mean that the spin-orbit interaction of free holes, Δ_0 = 6 meV [7], is reduced to Δ_B = 2 meV when the hole is bound at the acceptor boron. Very recent Raman measurements confirm the existence of the split boron ground state and its Γ_8/Γ_7 assignment as well, with Δ_B = 2.07 meV for natural diamonds and Δ_B = 2.01 meV for ^{13}C diamond [11]. Our present value of 2.0 meV for the A° ground state splitting is in excellent agreement with all these data.

The splittings in the exciton state, 11.4 meV and 3.3 meV, are more difficult to explain. The previous interpretation [3] ascribed the 11.4 meV to the spin-orbit splitting of the holes in the A^0X complex while the experimental value which had been reported for the free hole was Δ_0 = 6 meV. This is not consistent with the strong reduction of Δ_0 for the tightly bound hole in the neutral acceptor as discussed above. However, recent theoretical work using the relativistic LMTO (linear muffin-tin-orbital) method determined Δ_0 to be 13 meV [12].This value is considered to be rather accurate (it is not affected by the so-called "gap problem" inherent in the local density approximation (LDA) used in the LMTO calculations). Assuming that 13 meV is the best value for Δ_0 available at present, it is tempting to associate the experimental 11.4 meV splitting energy to the spin-orbit interaction of the holes in the A^0X state thus remaining with the previous interpretation but with the new value of Δ_0. In this picture, the free-hole value of Δ_0 = 13 meV would be reduced to Δ_B = 2 meV for the localized hole in the neutral acceptor the exciton case being in between. A reduction of Δ_0 = 13 meV to 11.4 meV for the bound exciton seems reasonable while the strong reduction to Δ_B = 2 meV for the single hole at the acceptor appears very large. We note, however, that all literature data [5,10,11] agree that the ground state splitting of the bound hole by 2 meV derives from the Γ_8^+ and Γ_7^+ valence bands, respectively.

The smaller splitting value in the exciton, 3.3 meV, also remains to be identified. There are several interactions in the bound exciton that can lead to splittings, such as jj-coupling of the two holes, crystal-field effects, and valley-orbit interactions of the bound electron due to the many-valley nature of the diamond band structure. None of these effects is quantitatively known in diamond. In contrast, such effects have intensely been studied in silicon. For the acceptor Al (E_i=68.7 meV), isochoric to Si, like boron in diamond, the splitting of the J = 0 (Γ_1) and J = 2 ($\Gamma_3+\Gamma_5$) two-hole states amounts to ≈ 1.2 meV, the crystal-field splitting of the J = 2 state is ≈ 0.3 meV [13], and the valley-orbit splitting of the electron in the (lower energy) J = 0 two-hole state into Γ_1, Γ_3, and Γ_5 substates amounts to ≈0.12 meV [14]. The magnitude of such effects is expected to be larger in diamond owing to the significantly larger binding potential of the acceptor boron in diamond.

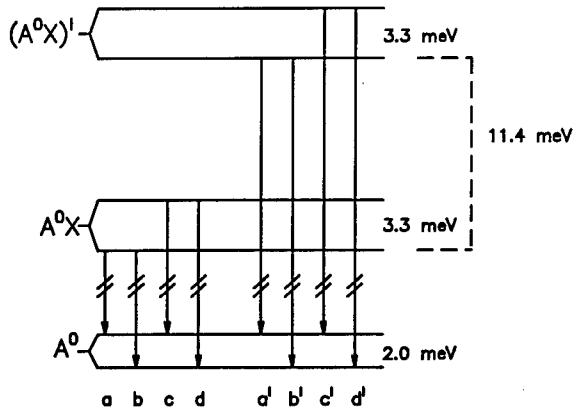

Fig. 3: Recombination level scheme: Fine structure transitions from the initial states of the acceptor bound excitons A°X and (A°X)' to the final neutral acceptor state, A°.

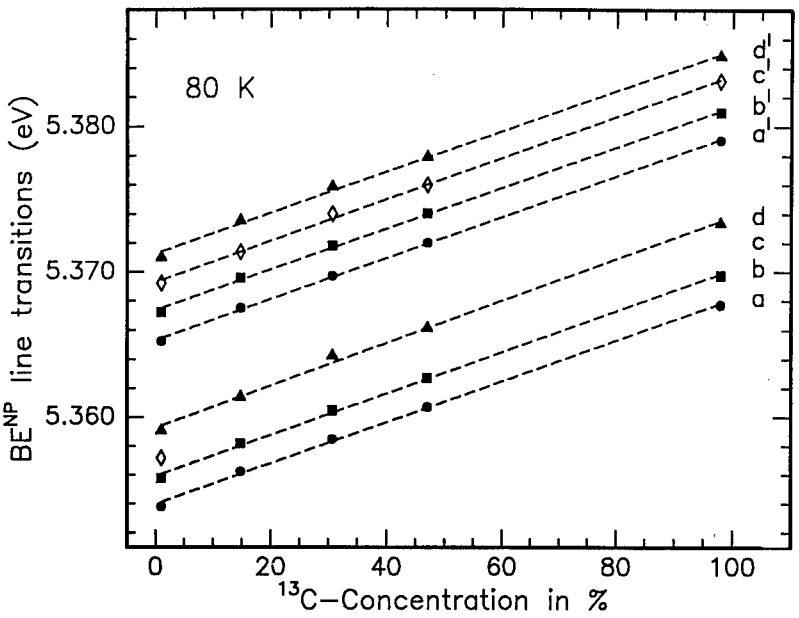

Fig. 4: Energy shifts of the BE^{NP} fine structure components (a ... d) and (a' ... d') versus ^{13}C isotope content. The data refer to 80 K sample temperature.

However, any specific interpretation of the 3.3 meV exciton splitting energy would have to be speculative at present.

We consider again the influence of the isotope composition on the BE^{NP} transition energies which was mentioned earlier (cf. Fig. 1). Values for ^{12}C and ^{13}C diamonds were reported previously [9], with a difference for the BE^{NP} lines of (14 ± 0.7) meV. In our experiments shown in Fig. 4 we employed specimens with a ^{13}C content of 1 %, 15 %, 31 %, 47 %, and 98 %. The energy difference between the isotopically "pure" diamonds amounts to (14.6 ± 0.3) meV in agreement with the value in Ref. [9]. In addition, we find that the line positions depend linearly on the isotope composition. This applies to all spectral components of the BE^{NP} including the four individual fine structure transitions in both main doublet lines. The evaluation of the corresponding phonon-assisted transitions BE^{TA} and BE^{TO} which we have also recorded delivers the dependence of the phonon energies on the carbon mass which has not been reported before. Such data will be published separately [15].

We conclude by mentioning that the near-band-edge photon energies that we measure in natural type IIa diamonds are ≈ 4 meV larger than in the synthetic HPHT diamond specimen of equivalent 1 % ^{13}C composition. According to Fig. 4 all line positions of the synthetic, isotopically controlled diamonds follow almost exactly straight lines. Therefore, we infer that the comparatively large 4 meV energy difference applies to all synthetic specimens. (All energy values cited in the text refer to the synthetic diamonds.) This difference may be related to a different lattice constant found for natural IIa diamonds (a_0 = 3.56706 Å) and HPHT diamonds (a_0 = 3.56714 Å) [16]. The model outlined in Ref. [9] explains only a small fraction of the observed energy difference when these lattice constants are employed in the calculation. Work is in progress to determine the lattice constants of the present specimens.

Conclusion

We have observed a fourfold fine structure in both doublet components of the bound exciton radiation in diamond. This structure is independent of the ^{13}C content and was observed in natural and synthetic HPHT crystals. A level scheme for the BE radiation was derived, with an acceptor ground state splitting of 2.0 meV in excellent agreement with data from excitation spectroscopy and Raman scattering on boron acceptors. The splittings in the bound exciton, 11.4 meV and 3.3 meV, cannot unambiguously be explained at present. A recent theoretical value for the spin-orbit interaction, Δ_0 = 13 meV, would explain the main splitting of 11.4 meV, with a reasonable reduction of the value Δ_0 for free holes to that for the holes localized in the bound exciton. However, this leaves us with a very large reduction of Δ_0 to the value 2.0 meV found for the single hole in the neutral acceptor. This discrepancy needs further investigations.

The authors gratefully acknowledge the financial support by the Deutsche Forschungsgemeinschaft (DFG contract No. Sa 520) under the auspices of the trinational "D-A-CH" cooperation of Germany, Austria, and Switzerland on the "Synthesis of Superhard Materials".

References

[1] C.D. Clark, P.J. Dean, and P.V. Harris, Proc. Roy. Soc. A **227**, 312 (1964)
[2] P.J. Dean and J.C. Male, Proc. Roy. Soc. A **227**, 330 (1964)
[3] P.J. Dean, E.C. Lightowlers, and D.R. Wight, Phys. Rev. **140**, A352 (1965)
[4] E.C. Lightowlers and A.T. Collins, J. Phys. D: Appl. Phys. **9**, 951 (1976)
[5] P.A. Crowther, P.J. Dean, and W.F. Sherman, Phys. Rev. **154**, 772 (1967)
[6] A.T. Collins and E.C. Lightowlers, Phys. Rev. **171**, 843 (1968)
[7] C.J. Rauch, Proc. Internat. Conf. Semicond. Physics, Exeter 1962 (Institute of Physics and the Physical Society, London 1963, p. 276)
[8] W.F. Banholzer and T.R. Anthony, Thin Solid Films **212**, 1 (1992)
[9] A.T. Collins, S.C. Lawson, G. Davies, and H. Kanda, Phys. Rev. Lett. **65**, 891 (1990)
[10] E. Anastassakis, Phys. Rev. **186**, 760 (1969)
[11] H. Kim, R. Vogelsang, A.K. Ramdas, S. Rodriguez, M. Grimsditch, and T.R. Anthony, to be published in Phys. Rev. Lett.
[12] M. Willatzen, M. Cardona, and N.E. Christensen; Phys. Rev. B**50**, 18054 (1994)
[13] K.R. Elliott, G.-C. Osbourn, D.L. Smith, and T.C. McGill, Phys. Rev. B**17**, 1808 (1978) and further references herein
[14] V.A. Karasyuk, M.L.W. Thewalt, S. An, E.C. Lightowlers, and A.S. Kaminskii, Phys. Rev. B**54**, 10543 (1996)
[15] T. Ruf, M. Cardona, H. Sternschulte, S. Wahl, K. Thonke, R. Sauer, P. Pavone, and T.R. Anthony; submitted to Solid State Commun.
[16] H. Holloway, K.C. Hass, M.A. Tamor, T.R. Anthony, and W.F. Banholzer, Phys. Rev. B**44**, 7123 (1991)

Materials Science Forum Vols. 258-263 (1997) pp. 763-768

INVESTIGATION OF ION-IMPLANTED BORON IN DIAMOND

K. Bharuth-Ram[1,3], B. Ittermann[2], H. Metzner[3], M. Füllgrabe[2], M.Heemeier[2], F. Kroll[2], F. Mai[2], K. Marbach[2], P. Meier[2], D. Peters[2], H. Thiess[2], H. Ackermann[2], J.P.F. Sellschop[4], H.-J. Stockmann[2], K.P.Lieb[3], and M. Uhrmacher[3]

[1] Physics Department, University of Durban-Westville, Durban 4000, South Africa
[2] Fachbereich Physik, Universität Marburg, 35032 Marburg, Germany
[3] II. Physik Institut and SFB 345, Universität Göttingen, 37073 Göttingen, Germany
[4] University of the Witwatersrand, WITS 2050, Johannesburg, South Africa.

Keywords: boron, diamond, ion implantation, β-NMR

Abstract :

The fraction of boron atoms that take up defect-free sites on ion implantation in diamond has been investigated in β-NMR measurements. Polarized ^{12}B nuclei were produced in the reaction $^{11}B(d,p)^{12}B$ with 1.5 MeV deuterons and recoil implanted into a diamond Ib sample. Depolarization resonance spectra were measured in an external magnetic field of 1.0 kG at sample temperatures ranging from 300 K to 800 K, showing that the polarised ^{12}B atoms retain their polarisation on implantation in diamond. The polarization asymmetry at the Larmor frequency yielded a fraction of boron atoms at defect-free tetrahedrally symmetric sites of 12(1)% at 300 K, increasing to 17(2) % at 800 K. The resonance spectra also showed evidence that some of the implanted boron atoms were at low symmetry sites.

Measurements after pre-implantation of the diamond sample with 50 - 220 keV Li^+ ions showed no significant change of the fraction of boron atoms that are implanted at defect-free symmetric sites in the diamond lattice.

1. Introduction

Amongst the naturally occurring diamonds, the rare type IIb diamonds are *p*-type semiconducting, due to low levels of boron which forms an acceptor level at 0.37 eV [1-2]. This fact, coupled with some of the intrinsic properties of diamond such as its wide band gap (5.4 eV), high thermal conductivity, high carrier mobility and extreme hardness, have prompted considerable activity in attempts at producing doped *p*- and *n*-type semiconducting diamond layers.

For a dopant atom to be electrically active it must reside on a regular lattice site, usually substitutional. Ion implantation, with its control of dopant species, implantation dose and distribution, offers an attractive means of incorporating dopants atoms in the diamond lattice. The process, however, is invariably accompanied by lattice damage, which produces compensating defects or lattice strain in the neighbourhood of the dopant atom. These must be annealed out if diamond based semiconducting devices are to be realised. Several attempts at producing *p*-type diamond layers by ion implantation of boron atoms have been made, employing a variety of implantation conditions and annealing procedures.

Braunstein *et al.* [3] implanted B atoms at doses of 3 x 10^{14} cm^{-2} and 1 x 10^{16} cm^{-2} into types Ia and IIa diamonds. The low dose implantations produced no observable change in the electrical characteristics of the samples. The high dose implantations, on annealing, resulted in a graphitised layer on the sample surface, which, when removed, left behind a thin B-doped layer with an electrical conductivity of about 10 $\Omega^{-1}cm^{-1}$. The conductivity was characterised by an activation energy of 0.063 eV at temperatures T< 500 K, and 0.32 eV at T> 500K in the diamond Ia sample, and 0.024 eV in the type IIa diamond. Sandhu *et al.* [4] investigated optical absorption spectra and electrical characteristics of B implanted natural diamonds that had been pre-damaged with ^{12}C bombardment. The implantations at liquid nitrogen (LN) temperature were followed by rapid anneal at 1373 K. The optical absorption spectra showed a sharp absorption band at 2962 cm^{-1}, which corresponds to the activation energy of boron in semiconducting IIb diamond. A series of studies on diamond IIa samples implanted with different ratios of B and C was carried out by Prins [5]. The implantations were done at LN temperature, and were followed by a two stage annealing process, first a rapid anneal at 500 °C and then a further anneal at 1200 °C in an argon atmosphere. Samples with B:C ratios of 7:3 and 8:2 showed electrical conductivities with activation energy $\varepsilon_A \approx$ 0.37 eV in the temperature interval 350-500 K and 450-600 K, respectively. Vavilov *et al.* [6] have reported the production of diamond *p-n* junctions by implantation with B and P ions.

In the present measurements we investigate the implantation sites of boron atoms recoil implanted into diamond at extremely low concentration, and focus, in particular, on the fraction of B atoms that take up defect-free sites. To achieve this we exploit some of the unique features of the β-NMR technique as applied to spin-polarised nuclear probes [7]. The NMR measurements detect directly the depolarisation of the implanted B nuclei and hence are sensitive to the lattice structure in the immediate neighbourhood of the implanted probes.

2. **Experimental**

Details of the β-NMR technique is given in ref. [7] and references contained therein. Aspects relevant to the present measurements are presented below. In essence the method consists of implanting polarized β-unstable nuclei in a host, and using a radio-frequency (rf) field to depolarise the probes. The resonance frequency for depolarization identifies the implantation sites of the probes and the β asymmetry parameters (amplitude and resonance width) yield the fraction of probes at a particular site.

The diamond sample was made up of 'tiles' of synthetic type Ib diamonds, each of 5mm x 5mm surface x 3 mm thickness. The diamonds were cut and polished parallel to (100) planes, aligned with the aid of Laue x-ray photographs, and brazed onto a copper backing. The effective sample area presented to the collimated ^{12}B recoils was 10 x 10 mm^2. The diamond sample was mounted between the pole pieces of the magnet on the axis of a coil that provided a high frequency depolarization field, B_{rf}.

^{12}B β-emitting probe nuclei ($I^{\pi} = 1^+$, $t_{1/2}$= 20.3 ms) were produced in the $^{11}B(d,p)^{12}B$ reaction by bombarding a thin ^{11}B target (of thickness 120μg/cm^2 B evaporated on 100μg/cm^2 of Al) with 1.5 MeV deuterons from the Tandetron Accelerator at the Strahlenzentrum, University of Giessen. The ^{12}B ejected at a recoil angle of 45(6)° from

the primary target were implanted into a diamond sample. This choice of recoil angle is known to yield the maximum polarization (of 10%) in the ^{11}B(d,p) reaction [8]. Because of reaction kinematics the polarized probes were implanted in the diamond sample with energies broadly distributed between 0 and 450 keV, giving a homogeneous distribution up to a depth of 600 nm in the sample. The typical implantation flux was approximately 10^5 cm^{-2} s^{-1}, giving a ^{12}B concentration in the implantation volume of $\leq 10^8$ cm^{-3}. At this dilute concentration each probe can be considered as isolated, and there is no overlap of implantation induced damage cascades.

3. Results and Discussion

The nuclear polarization P of the implanted ^{12}B probes was detected via the asymmetry a of the angular distribution of the β radiation emitted in the ^{12}B decay. The β distribution is given by

$$W(\alpha) = 1 + v/c \; A \; P \cos\alpha$$

where v/c is the average β velocity relative to the velociy of light, A is the asymmetry coefficient of the particular β decay, and α the angle between $\boldsymbol{v}$ and $\boldsymbol{P}$.
The β asymmetry is defined as the relative difference between parallel (0°) and anti-parallel (180°) emission relative to the polarization direction. The asymmetry is thus given by

$$a = [W(0^o) - W(180^o)] / [W(0^o) + W(180^o)] = v/c \;\; A \; P \, .$$

Measurement of the asymmetry therefore gives directly the polarization P.

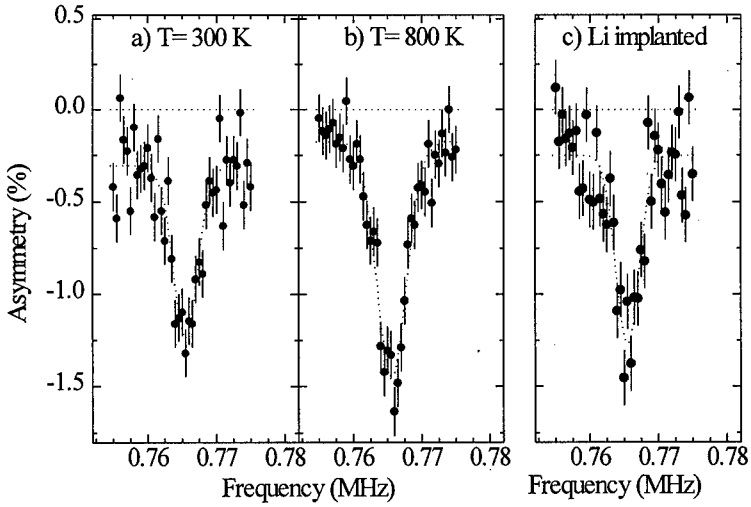

Fig. 1 : Resonance depolarisation spectra observed at sample temperatures a) 300 K and b) 800 K, and c) in the Li pre-damaged sample at 800 K. The dotted lines represent the zero reference lines and Gaussian fits to the data.

Figures 1 (a) and (b) show depolarization spectra at the Larmor resonance frequency observed at sample temperatures of 300 K and 800 K, respectively. These spectra show that the implanted ^{12}B atoms maintain at least part of their polarisation in diamond, although the detected effect is relatively low. This is in contrast to the earlier observation of Kuno *et al.* [9], who, while observing the polarisation of implanted boron atoms in hexagonally oriented graphite (grafoil) found that in their diamond sample the polarisation was destroyed. A possible reason for the failure to observe the boron polarisation in the earlier measurements, may be that the diamond sample used was very much smaller than that used in our measurements (effective surface area 10 mm x 10 mm), and that the low polarisation (1.2 % at 300 K) was not discernable above background events.

Resonance signals at the Larmor frequency ν_L (= 0.7655 MHz for ^{12}B in a field of B_0= 1.001 kG) corresponds to depolarization of probes in a diamagnetic charge state at sites with zero electric field gradient (EFG), i.e. sites of cubic (or tetrahedral) symmetry. The integrated area of such a resonance measures the fraction f_s of diamagnetic probes at defect free sites of cubic symmetry, when normalized to the maximum depolarization effect observed under comparable experimental conditions (10%) [7]. Normalization of our observed spectra gives f_s = 12(1) % at 300 K, increasing to f_s = 17(2) % at 800 K. We cannot decide from our data whether the so far 'missing' probe fractions have different resonance frequencies but are still polarised, or if they have lost their polarisation due to some fast process with a relaxation rate $\lambda > 1/\tau_\beta$ (τ_β is the beta-decay lifetime of the ^{12}B probe).

There exist two sites of tetrahedral symmetry in the diamond lattice, the substitutional and the tetrahedral interstititial. In the absence of defects, polarised ^{12}B probe atoms at both sites will give resonance at the Larmor frequency. From comparison of our data with Monte-Carlo simulations [10] of the implantation process and from the observation of immobile probes up to a sample temperature of 800 K, we assign the defect free fraction seen in our measurements to boron at substitutional sites.

The resonance spectra at 300 K and 800 K were measured together with zero reference measurements at 1.0 MHz above the Larmor frequency. In both cases free fits to the data found a non-zero baseline, confirming that an additional fraction of boron exists on perturbed sites. At 800 K the asymmetry signal of these perturbed fractions were very much reduced, indicating that annealing of radiation damage contributes to the oberved increase of f_s with temperature. This is consistent with earlier observations [11,12] of an annealing stage at 650 K, and attributed to interstitial migration and recombination with vacancies.

Motivated by the strong difference in the fraction of substitutional boron observed in silicon samples containing different levels of *p*- and *n*-type dopants [13], a check on the effect of a pre-implanted Li layer in the diamond overlapping the boron implantation profile was made. $^7Li^+$ ions, from the Göttingen ion implanter IONAS, were implanted in the diamond sample, to a total dose of 1.0 x 10^{16} cm^{-2}. Several implantation energies in the range 50 - 220 keV were used to give a uniform implantation profile and a dopant concentration $\approx$ 2 x 10^{20} cm^{-3}. The subsequent depolarisation resonance spectrum obtained at 800 K is shown in Fig. 1(c). No enhancement of the fraction of implanted B atoms at defect free sites is evident above that observed in the undamaged sample. The Li ions

produce, on average, 75 vacancies per implanted ion. It is worth noting that despite the presence of this high level of lattice damage the β-NMR technique is still sensitive to those probes which are implanted at undamaged symmetric sites.

4. Conclusions

Our results show that the recoil implanted ^{12}B nuclei maintain their polarisation in diamond although the polarisation is relatively low. With the low dose implantation used in the present measurements a significant fraction (12-17%) of boron atoms at defect-free substitutional sites can be achieved. The depolarisation spectra also show evidence of an additional fraction of boron at perturbed sites. These perturbations may arise when the boron has nearest neighbour point defects such as vacancies, di-vacancies or self interstitials, created when the recoiling B atoms dissipate their kinetic energy. Some of these defects may be healed on annealing. Indeed our results at 800 K show evidence of annealing of some of these defects. Further restoration of the lattice around the implanted atoms presumably may be achieved by annealing above 1200 K, as observed by Quintel *et al.* [12], to yield a higher fraction of implanted atoms at substitutional sites.

Finally, pre-implantation of the diamond with Li^+ ions in the boron implantation range, to a dopant concentration of 2×10^{20} cm^{-3}, produced no observable change in the fraction of substitutionally implanted boron ions.

Acknowledgements:

We thank De Beers Industrial Diamonds (Pty) Ltd. who supplied the diamonds, M. Rebak for the expert construction of the target, F. Harbsmeier for assistance with the Li implantation, and Profs. E Salzborn and G. Clausnitzer and the technical staff of the Strahlenzentrum Giessen for their assistance. This work was partially supported by the BMBF, contract no. AC4-MAR, and the SFB-383 of the SFB.

References

1. A.T. Collins and E.C. Lightowlers, in "The Properties of Diamonds" ed. J.E. Field (Academic Press, New York, 1979), pp 79-81, 1986.
2. R. M. Chrenko, Phys. Rev. **B7**, 4560 (1973).
3. G. Braunstein and R. Kalish, J. Appl. Phys. **54**, 2106 (1983).
4. G.S. Sandhu, M.L. Swanson and W.K. Chu, Appl. Phys. Lett. **55**,1397 (1989).
5. J.F. Prins, Phys. Rev. **B38**, 5576 (1988).
6. V.S. Vavilov, M.S. Gukasyan, M.I. Guseva, E.A. Konorova, F. Sergienko, Sov. Phys. Doklady **16**, 856 (1972)
7. B. Ittermann, H. Ackermann, E. Diehl, B. Fischer, H.-P. Frank and H.-J. Stöckmann, Hyp. Int. **79**, 591 (1993).
8. M. Tanaka, S. Ochi, T. Minamisono, A Mizobuchi, K. Sugimoto, Nucl. Phys. **A263**, 1 (1976)

9. Y. Kuno, J. Imazato, K. Nishiyama, K. Nagamine, T. Yamazaki, K. Matsuta, S. Ise, Y. Nojiri, T. Minamisono, Hyp. Int. **39**, 253 (1988).
10. J.F. Ziegler, J.P. Biersack, U. Littmark, "The Stopping and Range of Ions in Solids", (Pergamon, New York) 1985.
11. C.D. Clark, R.W. Ditchburn and H.B. Dyer, Proc. Roy. Soc. (London) **A235**, 305 (1956).
12. H. Quintel, K. Bharuth-Ram, H. Hofsäss, M. Restle and C. Ronning, Nucl. Instr. Meth. **B118**, 72 (1996).
13. H. Metzner, G. Sulzer, W. Seelinger, B. Ittermann, H.-P. Frank, B. Fischer, K.-H. Ergezinger, R. Dippel, E. Diehl, H.-J. Stöckmann, H. Ackermann, Phys. Rev. **B42**, 11419 (1990).

Materials Science Forum Vols. 258-263 (1997) pp. 769-774

ISOTOPIC SHIFTS OF THE N3 OPTICAL TRANSITION IN DIAMOND

Gordon Davies[1], I. Kiflawi[2], G. Sittas[2] and H. Kanda[3]

[1] Department of Physics, King's College London, Strand, London WC2R 2LS, UK.
[2] J.J. Thomson Physical Laboratory, University of Reading, Reading RG6 6AF, UK.
[3] NIRIM, 1-1 Namiki, Tsukuba, Ibaraki 305, Japan.

Keywords : Isotope effects, diamond.

Abstract We show the N3 zero-phonon line, at 2.985 eV in natural diamond, is shifted by $+4.5 \pm 0.2$ meV in ^{13}C diamond and that the energies of all the phonons seen in the vibronic band are smaller in the ratio $\sqrt{12/13}$ compared to ^{12}C diamond. The zero-phonon shift can be understood in terms of contributions from the lattice expansion, from the different vibrational frequencies in the ground and excited electronic states, and from the Jahn-Teller effect in the excited state. In ^{12}C diamond doped with ^{15}N the zero-phonon line is shifted by $+0.23 \pm 0.12$ meV, with no detectable change in the vibronic bandshape.

1. Introduction

Nitrogen can exist in diamonds as isolated substitutional atoms, and as pairs of substitutional nitrogen atoms ("A" centres) and clusters of four N atoms and a vacancy ("B" centres) : see Woods [1] for a review. Other small but significant concentrations of centres of nitrogen can also exist. Of particular interest here is the well-known "N3" optical centre, which is observable also in EPR as the "P2" resonance [2]. It consists of three nitrogen atoms arranged on substitutional sites as nearest neighbours to one common atomic site, with a vacancy at that site [3, 4]. The centre produces a characteristic optical band with its zero-phonon line at 2.985 eV in natural diamond. N3 centres can be produced by heating diamonds which contain A centres and isolated N [5], by heating diamonds rich in B centres [6], or by heating diamonds which contain only isolated N atoms [7, 8].

In this paper we examine the effects of isotope doping on the N3 centre. In Section 2 we describe the experimental methods used in this work and the effects on the vibronic band of isotopic substitution of the host lattice and of the nitrogen impurity. In Section 3 we show that the effect of ^{13}C doping can be understood in terms of other known properties of the centre if Jahn-Teller effects are included.

2. Experimental details.

Diamonds with concentrations of between 4.5 and 6×10^{19} cm^{-3} dispersed nitrogen atoms were made by the high temperature, high pressure method. Synthetic diamonds with different isotope compositions have been used : standard ^{12}C+^{14}N diamond, ^{13}C+^{14}N diamond, and ^{12}C + ^{14}N+^{15}N diamond. The ^{15}N samples were made by doping the synthesis capsule with ^{15}N-labelled aniline, but these samples were always contaminated with ^{14}N. The ratio of ^{15}N to ^{14}N was measured for samples from each batch using the relative intensities of the isotopically shifted lines in the spectrum of the H1a centre [9]. In contrast, the ^{13}C samples were essentially pure isotope samples. All the natural diamonds contained both A and B centres.

The infrared absorption spectra were measured at room temperature using a Perkin-Elmer 580B spectrometer to establish the concentrations of single nitrogen atoms and of the A and B nitrogen aggregates. Spectra in the visible and ultra-violet regions were measured at 77 K, using either a Perkin-Elmer model 330 spectrometer or a Hilger Monospek grating monochromator.

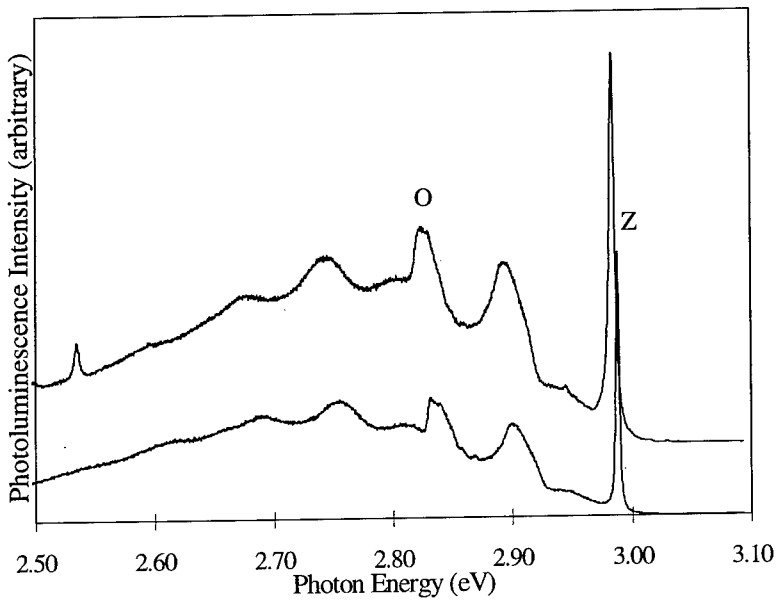

Figure 1. The photoluminescence measured at 77 K of the N3 centre in a natural diamond (upper curve) and a $^{13}C+^{14}N$ diamond (lower curve). Z labels the zero-phonon line and the sharp cut-off at O marks the maximum energy of the optic mode phonons.

The synthetic and natural diamonds were annealed at temperatures between 2200 and 2700 °C under a stabilising pressure using the equipment described in [10]. Heating synthetic diamonds between 2500 and 2700 °C caused the aggregation of the single N atoms to form A and B aggregates, as monitored by the infra-red absorption spectra [11], and also created N3 centres. In samples with 4.5 to 6×10^{19} cm^3 dispersed N atoms we observed an integrated absorption in the zero-phonon line at 77 K of about 0.6 nm cm^{-1} (or 40 cm^{-2}) after heating at 2650 °C for 4 to 5 hours.

Figure 1 shows the photoluminescence of the N3 centre in a natural diamond and in a $^{13}C+^{14}N$ diamond. The shift in the zero-phonon energy is :

$$h\nu_{13} - h\nu_{12} = 4.5 \pm 0.2 \quad \text{meV}. \tag{1}$$

Within experimental uncertainties, the energies (measured from the zero-phonon line) of all the features in the vibronic sideband of the ^{13}C diamond are reduced by a factor $\sqrt{12/13}$ relative to those in the ^{12}C diamond. Consequently, at this level of measurement it appears that all the modes of vibration of the centre are dominated by the motion of C atoms, and that we may ignore the N atoms.

In contrast, a nominally $^{12}C+^{15}N$ diamond and a $^{12}C+^{14}N$ diamond have spectra with extremely similar shapes. The only detectable difference in the N3 spectra is that the zero-phonon line is shifted to higher energy in the ^{15}N sample by 0.14 ± 0.07 meV. From the H1a absorption line the ^{15}N diamond contained the isotopes in the ratio $^{15}N : {}^{14}N = 0.6 : 0.4$. The N3 centre contains three N atoms, so that with this isotope ratio we would expect a mean of 1.8 ^{15}N atoms in the centres. Consequently, the shift for complete replacement is expected to be 3/1.8 times larger than observed, giving

$$h\nu_{15} - h\nu_{14} = 0.23 \pm 0.12 \quad \text{meV}. \tag{2}$$

3. Discussion of the ^{13}C isotope effects.

We identify 3 contributions to the isotope shift of the N3 zero-phonon line.

a) Diamonds made from ^{13}C have a lattice spacing which is smaller than those made from ^{12}C by the fractional change [12 - 14] $\Delta a/a = 1.5 \times 10^{-4}$. The resulting shift of the zero-phonon line is $\Delta h\nu_s = 3L\,(c_{11} + 2c_{12})\,\Delta a/a$, where the elastic constants $(c_{11} + 2c_{12}) = 1326$ GPa [15, 16], and $3L = 1.8 \pm 0.4$ meV/GPa [17, 18] is the response of the N3 zero-phonon line to a hydrostatic compressive stress. Evaluation gives the N3 line at 0.36 ± 0.08 meV higher energy in ^{13}C than ^{12}C.

b) The zero-phonon line is a transition between the zero-point energy states of all the vibrational modes of the N3 centre. A detailed account of the isotope effects on the modes has been given by Hughes [19] for the situation where there is no Jahn-Teller effect. We give here a simplified single-mode version of this case, so that we can later contrast the different behaviour of a Jahn-Teller system. The adiabatic potential in the electronic ground state is written, for a single-mode, as $V_g = \frac{1}{2}m\omega^2Q^2$ where m is the effective mass of the mode, ω its frequency and Q is the displacement coordinate. The zero-point energy level, from which the zero-phonon line originates at low temperature, has an energy $E_g^o = \frac{1}{2}\hbar\omega$. In the excited state the potential becomes $V_e = E_o + \frac{1}{2}m\omega^2Q^2 + aQ$ where E_o is the increase in electronic energy at $Q = 0$ and the term aQ represents the electron-lattice interaction which is linear in the displacement Q. Consequently $V_e = E_o + \frac{1}{2}m\omega^2\left(Q + a/m\omega^2\right)^2 - a^2/2m\omega^2$, producing harmonic vibrations with the zero- point energy level at $E_e^o = E_o - a^2/2m\omega^2 + \frac{1}{2}\hbar\omega$. The zero-phonon transition occurs at the difference in energy of E_o^e and E_o^g, which is simply $E = E_o - a^2/2m\omega^2$, and E is independent of the mass m. With coupling to many modes E is still independent of the mass of the modes as long as the electronic state couples only linearly to the displacement modes [19]. Higher order coupling changes the zero-point energies in the ground and excited states and the energy of the zero-phonon line is then, in the limit of zero temperature,

$$h\nu = E + \tfrac{1}{2}\sum_i \left(\hbar\omega_i^e - \hbar\omega_i^g\right), \tag{3}$$

where ω_i^e is the (angular) frequency of the i^{th} mode of vibration in the electronic excited state of the N3 centre, and ω_i^g is the frequency of the mode in the ground electronic state. It is expected that $\omega^g \approx \omega^e$ for lattice modes. We have noted that the effect on the vibronic bandshape of changing the isotopes is that all the modes of vibration are affected as though they only involve carbon atoms. In the harmonic approximation, which is adequate here, the sum in equation 3 will therefore change by the ratio $\sqrt{12/13}$ when the lattice is changed from ^{12}C to ^{13}C, and the zero-phonon energy will depend on the isotope : $h\nu_{13} - h\nu_{12} = \frac{1}{2}\left(\sqrt{12/13} - 1\right)\sum\left(\hbar\omega_i^e - \hbar\omega_i^g\right)$. Here, $\hbar\omega_i^e$ and $\hbar\omega_i^g$ are for ^{12}C. Following Hughes [19] we estimate the summation from the temperature dependence of the energy of the zero-phonon line, which is determined by two types of contribution. One is the effect of lattice expansion, which produces a shift in the zero-phonon line analogous to the

isotope-induced expansion discussed above, with the fractional change in lattice parameter replaced by the linear expansion of the crystal at the temperature of measurement. This contribution can be evaluated explicitly using the known expansion of diamond [20]. The second contribution to the shift comes from the fact that in the ground and excited electronic states the vibrational quanta of each mode may be slightly different as a result of the changed chemical bonding. At temperature T a mode of energy $\hbar\omega$ has a mean occupation number of $n(\omega) = 1/(\exp(\hbar\omega/kT) - 1)$. The zero-phonon transition involving that mode occurs at an energy $n(\omega^g)(\hbar\omega^e - \hbar\omega^g)$ different from the transition at zero K. Consequently the contribution from all the modes to the temperature dependence of the energy of the line is $\Delta h\nu(T) = \sum n(\omega)(\hbar\omega^e - \hbar\omega^g)$. At low temperature this expression emphasises the lowest energy phonons and the energy of the N3 zero-phonon line has only been measured over the limited temperature range 0 to 400 K [21]. We proceed empirically here by noting that over this range the shift of the N3 line, after allowing for the effects of lattice expansion, is proportional to the temperature dependence of the lowest indirect energy gap of diamond, which is known over a significantly larger range of temperature, 0 to 700 K [22]. Allowing for expansion, between 0 and 400 K the N3 line shifts by 5.0 meV [23] while the lowest energy gap shifts by 24.7 meV [24]. The isotope shift of the energy gap 13.5 ± 2 meV [24] therefore scales to 2.7 ± 0.4 meV for the N3 line. This argument, calculating the isotope shift from the temperature dependence, would fail if there were high energy local vibrational modes at the centre, since they would not be populated at useable temperatures. However, no such modes are observed at the N3 centre (figure 1).

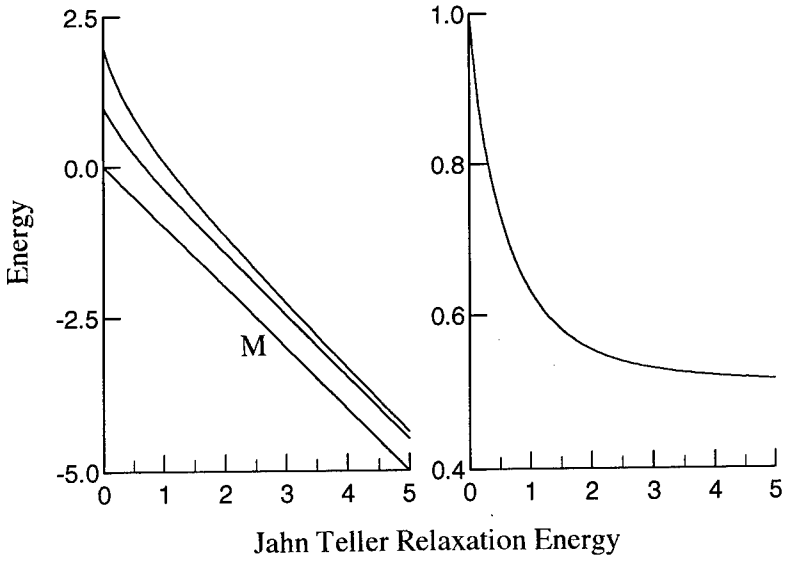

Figure 2. At left, the two curved lines show the energies of the lowest levels in the E × e Jahn-Teller system, as a function of the Jahn-Teller relaxation energy. The zero-point energy is the energy difference between the lowest energy level and the straight line "M", which shows the energy of the minimum of the vibrational potential surface. The zero-point energy is shown explicitly at the right; it approaches the value of 0.5 in the limit of large Jahn-Teller relaxation energy. The energy unit is the mode quantum $\hbar\omega$.

c) The final term comes from a re-examination of the zero-point energy in the ground and excited states. It has been suggested that the excited state undergoes a Jahn-Teller relaxation

of energy $E_{JT} \approx 0.7\hbar\omega$ [25, 26] where $\hbar\omega$ is the effective quantum of the E modes. The Jahn-Teller relaxation energy is $E_{JT} = k^2/2m\omega^2$ where k is a linear electron-phonon coupling term analogous to a in the non-degenerate electronic case, and E_{JT} is also independent of the mass m. The vibronic energy levels are shown in figure 2, calculated using the standard Hamiltonian for this problem (equations 2.2.1, 2.2.6 of [27]). We note that in contrast to the non-degenerate case, the zero-point energy is a function of the relaxation energy, and reduces as E_{JT} increases. Qualitatively, the optical centre moves in the "Mexican hat" potential (figure 6 of [28]). In the limit of large k there is complete rotational freedom in the trough of this hat, and the zero-point motion is reduced to a contribution of only $\frac{1}{2}\hbar\omega$ from the constrained radial motion in that space. For $E_{JT} = 0.7\hbar\omega$ the zero-point energy is $E_0^e = 0.68\hbar\omega$. In the electronic ground state, the two components of the E modes each contribute a zero-point energy of $\frac{1}{2}\hbar\omega$, giving a total zero-point energy of $E_0^g = \hbar\omega$. Consequently the zero-phonon line, which occurs between the zero-point levels, is lowered in energy by $|E_0^e - E_0^g| = 0.32\hbar\omega$ as a result of the reduced zero-point energy in the excited state. This energy shift is linear in the vibrational quantum, and so when the mass of the mode is changed from 12 to 13 units, this reduction in the zero-phonon energy is further decreased by a factor $\sqrt{12/13}$. Assigning again, from figure 1, the value of 90 meV to $\hbar\omega_{12}$, this effect increases the zero-phonon energy in ^{13}C relative to ^{12}C by $0.3(1 - \sqrt{12/13})\hbar\omega_{12} \sim 1.1$ meV.

The sum of the three isotope effects gives a total expected shift of $h\nu_{13} - h\nu_{12} \sim 4.2$ meV which is similar to the measured value of equation 1.

It is striking that the isotope effects of nitrogen, at the core of the optical centre, are negligible. For the electronic ground state this is qualitatively consistent with the analysis of ENDOR data which place the active electron on the C atom next to the vacancy [4]. Recent theoretical work [29] also places the ground electronic state distant from the N atoms, but locates the excited state close to the N atoms.

4. Summary

The production of N3 centres in specially synthesised diamonds has allowed the effects of isotope substitution to be investigated. There is little effect on the N3 bandshape when ^{15}N is substituted for ^{14}N, and the zero-phonon energy is perturbed by only 0.23 ± 0.12 meV; this value coincides with the only other report we are aware of for a shift of a zero- phonon line in diamond with nitrogen isotope substitution (the 389 nm line, [30, 31]. The N3 optical spectrum shows a significant shift of 4.5 meV on substituting ^{13}C for ^{12}C, and this effect can be closely reproduced when the linear Jahn-Teller coupling is included. This term, which we are not aware has had to be used in the interpretation of any other data for point defects in crystals, is very significant at this centre.

We acknowledge helpful discussions with FS Ham, A Mainwood and AT Collins, and experimental assistance from JR Hird.

References

1. G.S. Woods in *Properties and Growth of Diamond*, edited by Gordon Davies, published by INSPEC for the Institution of Electrical Engineers, pp. 98 – 100 (1994).
2. G. Davies, C.M. Welbourn and J.H.N. Loubser in *Diamond Research 1978*, published by De Beers Industrial Diamond, Ascot, UK, pp. 23 – 30 (1978).
3. J.A. van Wyk, J. Phys. **C15**, L981 (1982).
4. J.A. van Wyk and J.H.N. Loubser, J. Phys. **C5**, 3019 (1993).
5. R.M. Chrenko, R.E. Tuft and H.M. Strong, Nature **270**, 141 (1977).
6. M.R. Brozel, T. Evans, and R.F. Stephenson, Proc. R. Soc. London **A361**, 109 (1978).
7. A.T. Collins and M. Stanley J Phys. **D18**, 2537 (1985).
8. S. Satoh and H. Sumiya in *High Pressure Research in Physics*, editors : M. Senoo,

K. Suito, T. Kabayashi and H. Kabota, published by Elsevier B.V. and The Society of Material Science, Japan, p. 183 (1995).
9. G.S. Woods and A.T. Collins, J. Phys. **C15**, L949 (1982).
10. T. Evans and Z. Qi Proc. R. Soc. London **A381**, 159 (1982).
11. G.S. Woods Proc. R. Soc. London **A407**, 219 (1986).
12. H. Holloway, K.L. Hass, M.A. Timor, T.R. Anthony, and W.F. Banholzer Phys. Rev. **B44**, 7123 (1991).
13. H. Holloway, K.L. Hass, M.A. Timor, T.R. Anthony, and W.F. Banholzer Phys. Rev. **B45**, 6353 (1992).
14. T. Yamanaka, S. Morimoto and H. Kanda Phys. Rev. **B49**, 9341 (1994).
15. M.H. Grimsditch and A.K. Ramdas Phys. Rev. **B11**, 3139 (1975).
16. A.K. Ramdas, S. Rodriguez, M. Grimsditch, T.R. Anthony and W.F. Banholzer Phys. Rev. Lett. **71**, 189 (1993).
17. P.A. Crowther and P.J. Dean J. Phys. Chem. Solids **28**, 1115 (1967).
18. R.J. Wedlake, PhD thesis, University of Reading, UK, unpublished (1970).
19. A.E. Hughes, Proc. Phys. Soc. **88**, 449 (1966).
20. G.A. Slack and S.F. Bartram J. Appl. Phys. **46**, 89 (1975).
21. A. Halperin and O. Nawi, J. Phys. Chem. Solids **28**, 2175 (1967).
22. C.D. Clark, P.J. Dean and P.V. Harris, Proc. Roy. Soc. London **A277**, 312 (1965).
23. G. Davies, J. Phys. **C7**, 3797 (1974).
24. A.T. Collins, S.C. Lawson, G. Davies, H. Kanda, Phys. Rev. Lett. **65**, 891 (1990).
25. G. Davies and M.F. Thomaz, Proc. Roy. Soc. **A362**, 405 (1978).
26. G. Davies, Portugal. Phys. **12**, 241 (1981).
27. F.S. Ham in *Electron Paramagnetic Resonance* edited by S Geshwind, New York : Plenum Press, 1 (1972).
28. M.D. Sturge, Sol. St. Phys. **20** 91 (1967).
29. J. Goss and R. Jones, private communication (1997).
30. A.A. Gippius, A.M. Zaitsev and V.S. Vavilov Sov. Phys. Semicond. **16** 256 (1982).
31. A.A. Gippius, private communication (1997).

Materials Science Forum Vols. 258-263 (1997) pp. 775-780

BREAKDOWN OF THE VACANCY MODEL FOR IMPURITY-VACANCY DEFECTS IN DIAMOND

R. Jones, J. P. Goss, P. R. Briddon[1], and S. Öberg[2]
Department of Physics, University of Exeter, Exeter, EX4 4QL, United Kingdom
[1]Department Of Physics, University of Newcastle upon Tyne, Newcastle, NE1 7RU, United Kingdom
[2]Department of Mathematics, University of Luleå, Luleå, S97 187, Sweden

Keywords : diamond, vacancy model, *ab initio* calculations, vacancy-impurity complexes.

Abstract. The vacancy model for impurity vacancy defects in semiconductors assumes that the ground and low energy excited states are derivable from the four sp^3-hybrid orbitals on the atoms bordering the vacancy. There are many cases where this model works but we describe here a counter-example concerning the lowest excited state of the [V-N_3] defect in diamond. It is shown that a shallow electron trap, localised *outside* the vacancy, is involved in the first excited state and responsible for the N2 and N4 optical bands associated with this defect.

Introduction.

The ground state and lowest excited states of vacancy and vacancy-impurity complexes in semiconductors have, since the pioneering work of Coulson and Kearsley [1], been considered to arise from the four sp^3 orbitals of the radicals bordering the vacancy. Indeed, this principle has been remarkably successful in leading to an understanding of the magnetic and optical properties of many defects [2, 3, 4, 5, 6, 7]. It has even been extended to the case when the vacant lattice site is occupied by a transition metal impurity like Pt or Au [8].

The vacancy in diamond.

To give a single example in detail, consider the isolated vacancy. The four sp^3-hybrids lead to an a_1 gap level lying below a t_2 level which, in the case of V^-, contains three electrons. The strong exchange splitting in diamond leads to a large separation of the $t_2^{\uparrow}$- and $t_2^{\downarrow}$-levels and hence to a filling of the spin-up orbitals. The resulting one-electron configuration is $a_1^2 t_2^{\uparrow\uparrow\uparrow}$ – maximising the effective spin in agreement with Hund's rule – which corresponds to a $^4A_2$ ground-state. The lowest optical excitation then involves the promotion of the $a_1^{\downarrow}$ electron to the unoccupied $t_2^{\downarrow}$ orbital. The energy of this $^4T_1$ excited state formed from the hybrids is then calculated to be 3.3 eV using density-functional-theory [9]. This is in excellent agreement with the zero-phonon-line (ZPL) of the ND1 band, attributed to this defect, which lies at 3.149 eV [10].

Vacancy-impurity complexes.

Similar calculations of the optical transition energies for vacancy-impurity complexes based on the energy differences between multiplets primarily constructed from the sp^3 orbitals are in reasonable agreement with experimental data when available [4, 5, 6]. [V-N] is optically active in both the neutral and negative charge states, giving rise to the ZPLs at 2.156 ($^2E \rightarrow {}^2A$) and 1.945 eV ($^3A_2 \rightarrow {}^3E$) respectively. These transitions can be understood from the gap states arising from the dangling-bond hybrids: the trigonal symmetry splits the t_2 one-electron level into a (filled) a_1 below an e-level containing one (two) electrons in the neutral (negative) case (illustrated in Fig. 1).

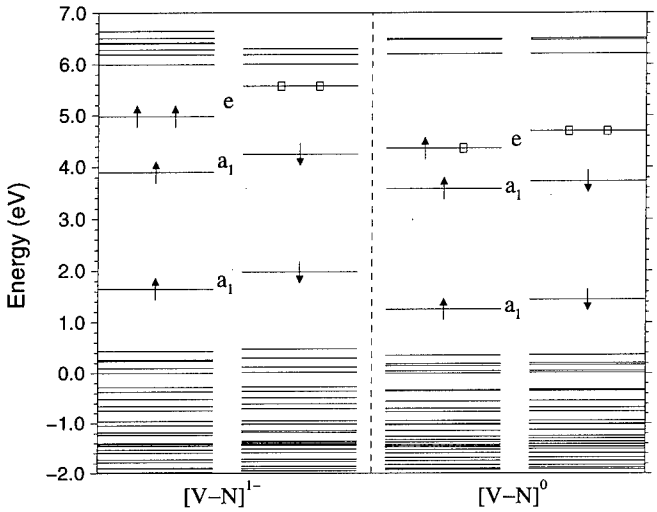

Figure 1: Spin-polarised Kohn-Sham levels in the vicinity of the band gap for the [V-N] defect in diamond. The occupied levels arising from the sp^3 hybrids (a_1 and e) are indicated by arrows. Unoccupied gap levels are indicated by boxes. Also indicated are the symmetries of the gap-levels.

The optical transitions are then simply the promotion of an electron from the a_1- to e-level. Si is also known to form a complex with a vacancy. However, in this centre the impurity does not lie at a lattice site, but moves to a site equidistant from six C-neighbors (D_{3d} symmetry). The resultant one-electron structure is akin to that of a di-vacancy: two doublets lie deep in the band-gap, and in the negative charge state contain 7 electrons. This gives rise to an optical transition between the doublets estimated at 1.86 eV (*c.f.* experimental value of 1.68 eV), but more importantly this is a transition between two orbitally degenerate multiplets $^2E' \rightarrow {}^2E''$ which provides a ready explanation for the complex, 12-line ZPL structure [5].

All this suggests that the vacancy model provides an excellent description of these defects. However, we show here that the [V-N_3] defect is a counter example to the rule that only the sp^3-hybrids are important to describe the low energy optical excitations and an additional orbital — not derived from these hybrids — is involved in the lowest excited state and plays apart in the interpretation of the N2 and N4 optical lines associated with the defect.

The [V-N_3] centre.
The trigonal symmetry of [V-N_3] (shown schematically in Fig. 2) splits the t_2-levels into an e-level (derived mainly from the N lone pairs) lying below an a_1-level (predominantly localised on the C radical) [5].

In the neutral charge state, the resulting $a_1^2 e^4 a_1^{\uparrow}$ one-electron configuration leads to a $^2A_1$ ground state and the centre is identified with the well-known P2 S=1/2 paramagnetic defect [11]. Electron nuclear double resonance (ENDOR) studies [12] indeed show that the spin density of this trigonal defect arises from the C-radical which weakly overlaps the three equivalent nitrogen nuclei: the fraction of the spin-density on each N-atom is just 2.8% [13]. The defect is also associated with *three* optical transitions [14, 15, 16]. The most intense is between the $^2A_1$ ground state and a ^2E excited state at 2.985 eV labelled N3. This is due to the one-electron transition: $e^{\downarrow} \rightarrow a^{\downarrow}$, and a recent study [17] revealed shifts in the ZPL with ^{15}N and ^{13}C of 0.2±0.1 and 4.5 meV respectively. Our previous calculation gave the transition energy to be

2.8 eV [5].

Now, the lowest a_1 level arising from the four sp^3-orbitals is close to the valence band edge and plays no part in any optical effects. According to the vacancy model, there are then no other gap states present and consequently no other internal spin-conserving transitions are possible. However, there are two weak optical bands at 2.596 eV (N2) and $\sim$ 3.7 eV (N4) which are believed to arise from the same centre. The N2 system is unusual in that there is no evidence of a ZPL which implies that it involves an excited state having a small dipole matrix element with the ground state. Thomaz and Davies suggested [15] that the symmetry of the excited state is A_2 which is consistent with a forbidden optical transition with the ground A_1 state. This A_2 state must then be the lowest excited state of the defect. However, an A_2 state in a trigonal defect can only be generated by occupying an e orbital with two electrons. It is clearly not possible within the vacancy model to produce this configuration since in the ground state there are four electrons in the e-level and only one available hole in the upper a_1 level.

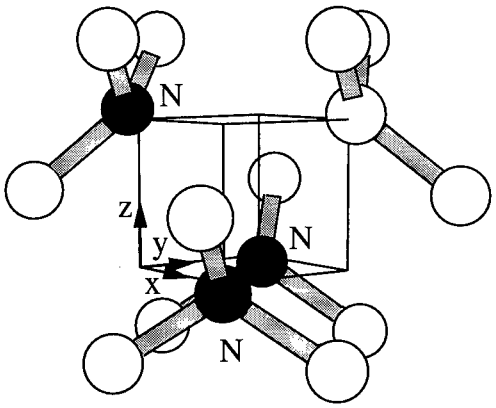

Figure 2: A schematic representation of the [V-N_3] centre showing the nearest and next-nearest neighbours of the vacated site. The N atoms are shown in black.

We shall show here that the lowest excited state is an A_1 state and involves an additional level not accounted for in terms of the vacancy model.

Method.

To discuss the origin of this level we have repeated the spin-polarised local density functional cluster calculation of the levels of [V-N_3] (as published in Ref. [5]) using two larger clusters composed of 85 ($N_3C_{40}H_{42}$) and 130 ($N_3C_{67}H_{60}$) atoms respectively. Both clusters gave similar results and we present the results for the larger cluster. Details of the method have been given previously and will not be repeated here [5, 18].

Results.

Fig. 3 shows the spin-up and -down Kohn-Sham levels of the neutral defect for the relaxed 130-atom cluster. The arrows show the gap levels arising from the sp^3-hybrids. The conduction-band minimum (E_c) is taken to be represented by the Kohn-Sham level at around +0.5 eV. The fully-occupied e-level lies around E_c-3.5 eV separating two a_1 levels. The lower a_1-level around E_c-5.0 eV arises from a symmetrical combination of the sp^3-hybrids. The upper $a_1^{\uparrow}$-level around E_c-1.9 eV is occupied whilst the $a_1^{\downarrow}$-level near E_c-0.93 eV is empty. Hence the calculations lead to the $^2A_1$ ground-state configuration, as described above.

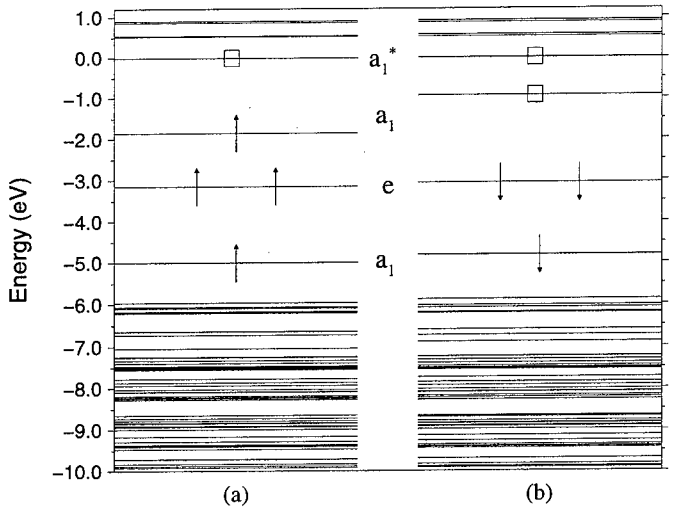

Figure 3: Spin-polarised Kohn-Sham levels in the vicinity of the band gap for the neutral [V-N_3] defect in diamond. (a) spin-up levels, (b) spin-down levels. The occupied levels arising from the sp^3 hybrids (a_1 and e) are indicated by arrows. Unoccupied gap levels are indicated by boxes. Also indicated are the symmetries of the gap-levels.

High in the gap there is an other level — which we shall denote by a_1^* — close to the conduction band. Previously, we took this level to indicate the beginning of the conduction band but are now inclined to the view that it is a shallow electron trap. The associated wave-function has very little amplitude on N or the unique C atoms. Instead, it seems to arise from bonds outside the defect core. The transition energy calculated from the difference in total energies when a electron is promoted between $a_1^{\uparrow}$ and $a_1^{\uparrow *}$ is 2.43 eV. Similarly, the transition energies calculated for the promotion of an $e^{\downarrow}$ electron to the $a_1^{\downarrow}$ and $a_1^{\downarrow *}$ levels are 2.9 and 3.6 eV. These transition energies agree very well with the N2, N3 and N4 optical bands associated with the defect at 2.596, 2.985 and ~3.7 eV.

The largest electric dipole matrix element is for the N3 transition and leads to a lifetime of 30 ns – compared with 10 ns found previously in a 70 atom cluster. The N2 and N4 matrix elements are considerably smaller than those for N3 because the a_1^* wavefunction is localised outside the cage containing the vacancy. These elements are smaller by factors of 0.03 and 0.20 respectively. Recalling that the optical absorption intensity varies as the square of these, we realise that the ZPLs of the N2 and N4 bands will hardly be visible – consistent with the experimental observations. Thus the absence of a ZPL for the N2 band is due to the different localisation regions of the ground- and excited-states rather than indicating the presence of an A_2 excited state. However, since the N2 band is vibronic in nature, the distortion accompanying the vibrations of the atoms must increase the overlap between the a_1 and a_1^* orbitals if the vibronic side-bands are to become visible.

Finally, we note that although the assumption that the lowest excited state has A_2 symmetry would explain the lack of a ZPL in the N2 band, a different explanation has to be invoked to account for the low intensity of the N4 band. The explanation given here in terms of a shallow a_1^* trap localised outside of the vacancy automatically explains the existence of the N2 and N4 bands and their low intensities.

The presence of the $^2A_1^*$ state lying between the ground $^2A_1$- and ^2E-states reduces the intensity

of the N3 luminescence. Time resolved luminescence experiments [15] show that this non-radiative $^2E \rightarrow {}^2A_1^*$ transition is thermally activated with a barrier of about 0.55 eV. Thus the lifetime of the ^2E-state is 8 ns at 800K and increases as the temperature is lowered. Other non-radiative transitions to different defects, notably A-centres, then become important and the lifetime depends on the concentration of these. It reaches 41 ns in samples with the smallest population of A-centres. Finally, direct tunnelling between the ^2E and $^2A_1^*$ states may also be important. The radiative lifetime has been variously estimated from 41 ns to about 150 ns depending on the model used to describe tunnelling. It is clear that the latter value is incompatible with the 30 ns calculated here.

In conclusion, the N2 and N4 optical transitions in [V-N_3] arise from promotion of electron from the a_1-orbital localised on the C-radical, and the e-orbitals localised on the N-atoms, to an a_1^*-orbital localised outside the vacancy. The dipole strengths of the transitions are very small because of the different localisation regions of the orbitals. These transitions *cannot* be understood as arising between the four sp^3-hybrid orbitals of the vacancy.

The lowest optical excitation of the neutral vacancy, which gives rise to the 1.673 eV GR1, band is believed to involve multiplets derived from the four sp^3-hybrids. However Stoneham and Mainwood [19] have recently argued that the GR2-8 optical bands around 2.88 eV, also associated with the neutral vacancy, involve an orbital not derived from these hybrids. This orbital, labelled v, appears to be either drawn out of the conduction band or arises from the result of a strong electron-electron interaction, and is present in the excited state of the transition. It is located about 0.3 eV above the valence band top. The actual transition is then from the ground $a_1^2t_2^2$, ^1E-state of the neutral vacancy to the excited $v^1a_1^1t_2^2$, $^1T_1$-state.

It is clear that the vacancy model must break down for highly energetic transitions, but what is surprising for the [V-N_3] defect is that it breaks down in the first excited state.

Finally we note that shallow traps localised outside the vacancy core may also be present in other defect systems, e.g. transition metal impurities in silicon, and would be expected to have an effect on electron trapping rates.

We thank the HPCI for an allocation of computer time on the Cray T3D at Edinburgh and the SP2 at Daresbury. S.Ö. thanks NFR and TFR in Sweden for financial support, and also PDC at KTH for computer time on the SP2. We also thank Marshall Stoneham and Alison Mainwood for communicating their results before publication.

References.

1. C. A. Coulson, and M. J. Kearsley, Proc. Roy. Soc., Lond., A, **241**, 433 (1957).
2. A. M. Stoneham, *Defects in Solids*, (Oxford University Press, London), 1975.
3. M. Lannoo, and J. Bourgoin, *Point defects in semiconductors*, Vols. I and II, Springer series in Solid-State
4. J. E. Lowther, J. Phys. Chem. Solids **45**, 127 (1984).
5. J. Goss, R. Jones, S. J. Breuer, P. R. Briddon, and S. Öberg, Phys. Rev. Lett. **77**, 3041 (1996).
6. R. Jones, J. E. Lowther, and J. Goss, Appl. Phys. Lett. **69**, 2489 (1996).
7. A. Mainwood, and A. M. Stoneham, J. Phys. Condens. Matter **9**, 2453 (1997).
8. G. D. Watkins, Physica, **117-118B**, 9 (1983).
9. S. J. Breuer, and P. R. Briddon, Phys. Rev. **51**, 6984 (1995).
10. G. Davies, S. C. Lawson, A. T. Collins, A. Mainwood, and S. J. Sharp, Phys. Rev. B **46**, 13157 (1992).
11. W. V. Smith, I. L. Gelles, and P. P. Sorokin, Phys. Rev. Lett. **2**, 39 (1959).

12. J. H. N. Loubser, and A. C. J. Wright, Diamond Research 1973, published by de Beers Industrial Diamond Division, Ascot, UK, p 16.
13. J. A. van Wyk, and J. H. N. Loubser, J. Phys.: Condens. Matter **5**, 3019 (1993).
14. C. D. Clark, R. W. Ditchburn, and H. B. Dyer, Proc. Roy. Soc., Lond., A **237**, 75 (1956).
15. M. F. Thomaz, and G. Davies, Proc. R. Soc., Lond., A **362**, 405 (1978).
16. G. Davies, C. M. Welbourn, and J. H. N. Loubser, Diamond Research 1978, published by de Beers Industrial Diamond Division, Ascot, UK, p 23.
17. G. Davies, I. Kiflawi, G. Sittas, and H. Kanda, J. Phys.: CondensMatter **9**, 3871 (1997).
18. R. Jones, and P. R. Briddon, *Identification of Defects in Semiconductors*, ed. M. Stavola, *Semiconductors and Semimetals*, treatise editors, R. K. Willardson, A. C. Beer, and E. R. Weber, Academic Press, in press.
19. A. M. Stoneham, and A. Mainwood, in *Shallow Levels in Semiconductors*, ed. C. A. J. Ammerlaan and B. Pajot, World Scientific, Singapore, 1997, in press.

Materials Science Forum Vols. 258-263 (1997) pp. 781-786

A FIRST PRINCIPLES STUDY OF INTERSTITIAL Si IN DIAMOND

J. P. Goss, R. Jones[1], S. J. Breuer[2], P. R. Briddon[3], S. Öberg[4]
School of Physical Sciences, Dublin City University, Dublin 9, Ireland.
[1]Department of Physics, Stocker Road, University of Exeter, Exeter, Devon, EX4 4QL, United Kingdom.
[2]Edinburgh Parallel Computer Centre, The University of Edinburgh, Edinburgh, EH9 3JZ, United Kingdom.
[3]Department of Physics, University of Newcastle upon Tyne, Newcastle, NE1 7RU, United Kingdom.
[4]Department of mathematics, University of Luleå, Luleå, S95187, Sweden.

Keywords : diamond, *ab initio* calculations, silicon, interstitial.

Abstract. The results of first principles calculations using AIMPRO (a local-density-functional code) are presented to describe the stability of interstitial Si in diamond. It is found that the ⟨100⟩ and ⟨110⟩ split-interstitial configurations are only local minima in the total energy surface. T_d interstitial Si reconstructs to form a substitutional Si site close to a self-interstitial. The difference in total energy between the split configuration and the substitutional-Si-self-interstitial complex is more than 6 eV. It is concluded that Si would not adopt an interstitial location in diamond as has been previously suggested from experimental evidence. Interestingly the self-interstitial remains bound to the substitutional Si with a binding energy around 1 eV.

Introduction.

Impurities and lattice disorder can have a profound effects on the electronic, optical and mechanical properties in any material. The most common dispersed impurities in both natural and synthetic diamonds are nitrogen and boron. Although both hydrogen and oxygen are believed to be present in large quantities, it is not clear whether these impurities form dispersed defects or are present in inter-granular regions or inclusions. Synthetic diamond samples often contain impurity species dictated by the particular growth method: for example Ni centres arise from the solvent-catalyst in high-temperature high-pressure growth, and material sputtered from the substrate, chamber walls and/or filaments can be included during chemical vapour deposition (CVD). This has led to Si contamination of CVD wafers.

It is now unambiguously established that the 1.682 eV zero-phonon-line (ZPL) in diamond is due to a centre involving Si; the integrated intensity of the fine structure correlates with the natural abundances of the three Si isotopes [1]. The 1.682 eV ZPL is made up of twelve resolved lines, four for each Si isotope. This complex structure is believed to arise from the optical transition between doubly degenerate ground and excited states. Early speculation assigned this peak to interstitial Si (Si_i), or even an interstitial complex made up from two Si atoms sharing a single lattice site [5]. However, recent first principles calculations [2] show that a complex made up from a substitutional Si impurity at the centre of a di-vacancy gives a good account of the optical data.

However, it has recently been suggested [3] that there are *two distinct* Si-related centres that *coincidentally* produce optical activity at close to the same energy. One is responsible for the 12-line structure, and the second gives a very broad peak, centred around 1.682 eV. It is speculated that the latter arises from an interstitial Si impurity.

There is very little theoretical work published on the equilibrium structure and specifically the

stability of interstitial Si in diamond. The only study to the knowledge of the authors is that of Bicai and Shangda [4], who examined the approximately ⟨100⟩-oriented Si-C and Si-Si split-interstitials (previously suggested by Vavilov *et al.* [5]), as well as the substitutional Si centre. In their study atomic clusters containing only the central defect atoms (Si-C in the case of the split-interstitial), their four carbon neighbours and twelve H terminators were used. They were relaxed according to a semi-empirical (MNDO) method and formation energies were estimated using discrete-variation density-functional-theory calculations on larger (but still modest at only 53 atoms) clusters. The relatively large covalent radius of Si and the size of the clusters used must put the results of Ref. [4] in some doubt.

If the Si interstitial forms preferentially in a ⟨100⟩ split configuration, it would be instructive to make a comparison with the structure of the ⟨100⟩ self-interstitial (C_i). This has previously been examined using the same techniques as employed in this present study [6], and the ⟨100⟩ configuration was found to be the lowest energy structure. In the 1+, neutral and 1- charge states, the highest occupied Kohn-Sham level is two-fold degenerate but partially filled. This leads to a Jahn-Teller distortion, lowering of the symmetry of the C_i centre to D_2, and the degenerate level splits. The gap-levels arise from p-like orbitals centred on each of the C atoms at the centre of the defect. The geometry was found to be relatively insensitive to charge state, with a central C-C length of 1.26 Å and back-bonds of 1.40 Å. If one of the C atoms in the self-interstitial is then replaced by a Si atom, the highest symmetry the centre could adopt would be C_{2v}. Then one might expect a similar electronic structure to that of the self-interstitial. This is discussed further below.

It is interesting to note that the speculation in the literature is exclusively for a ⟨100⟩ split-interstitial configuration. However, to the knowledge of the authors no systematic study into the stability of interstitial Si has yet been performed. We present here the results of density functional calculations on a number of likely configurations.

Method.

We report here the results of local-density-functional and local-spin-density-functional calculations performed on large, hydrogen terminated atomic clusters using AIMPRO (*ab initio* modelling program). The method has been described in detail elsewhere [10]. Electron-ion interactions are treated using the norm-conserving pseudopotentials from Ref.[11], except in the case of hydrogen, for which the bare Coulomb potential is used. The electron wavefunctions are expanded in sets of atom centred s-, p_x-, p_y- and p_z-Gaussian orbitals and the charge density fitted by s-Gaussian functions. The basis for the C and Si atoms at the core of the defects and those C atoms surrounding them consists of 4 sets of independent atom-sited s- and p-Gaussian orbitals with different exponents for the expansion of the electronic wavefunction, and a linear combination of 4 (C) and 5 (Si) s-Gaussian functions for the fit to the charge density. The basis used at each of the remaining atomic sites consisted of fixed linear combinations of s- and p-Gaussian orbitals with four or two different exponents for the wavefunction expansions for C and the surface H atoms respectively. The charge density fit for the H atoms consisted of 3 s-Gaussians. The clusters used in this present study consist of 71, 132 and 266 atoms: $SiC_{30}H_{40}$, $Si_nC_{72-n}H_{60}$ ($n = 0$ or $n = 1$) and $SiC_{165}H_{100}$.

Results.

With no experimental evidence for the geometry of an interstitial silicon one should examine all likely configurations. The primary candidates are the tetrahedral interstitial site, and the ⟨100⟩- and ⟨110⟩-oriented split interstitials. A Si atom has a covalent radius of 1.17 Å compared to a C single bond at 0.77 Å [7]. Therefore it is unlikely that Si would sit in a bond centre, as is the case with interstitial N [8] and O [9] which have much smaller covalent radii (0.70 and

0.66 Å respectively [7]). (Both interstitial N and interstitial O actually sit out of the bond, i.e. the C-N-C and C-O-C bond angles are somewhat less than 180°.)

The ⟨100⟩-split-interstitial.
All but the surface H atoms were relaxed in the 132 atom cluster, subject to a C_{2v} symmetry constraint. The final structure possessed Si-C bonds of 1.62, 1.62, and 1.49 Å and the central C atom possessed two C-C bonds of 1.37 Å. In order to establish whether this was the lowest energy symmetry of the centre, a small perturbation was made to the relaxed geometry so that the C_{2v} symmetry was broken, and the cluster relaxed again. The final structure was very close to the C_{2v} structure and the total energy had not been lowered. It is concluded that a ⟨100⟩ Si split-interstitial would have C_{2v} symmetry. The Kohn-Sham levels show that the ⟨100⟩-centre gives rise to two deep gap states, as can be seen in Fig. 1. Unlike the self-interstitial these levels are filled and associated with orbitals located on the central Si-C (~ -3.5 eV) and a p-orbital on the Si atom (~ -0.5 eV). The two empty levels marked with boxes are associated with strained back bonds (the lower level) and the p-orbital on the central carbon atom. The centre may also give rise to shallow levels close to the valence bands (see Fig. 1): since the Kohn-Sham levels are discrete, it is not clear exactly where the band-edges lie. These shallow levels arise from the strained C-bonds close to the Si atom.

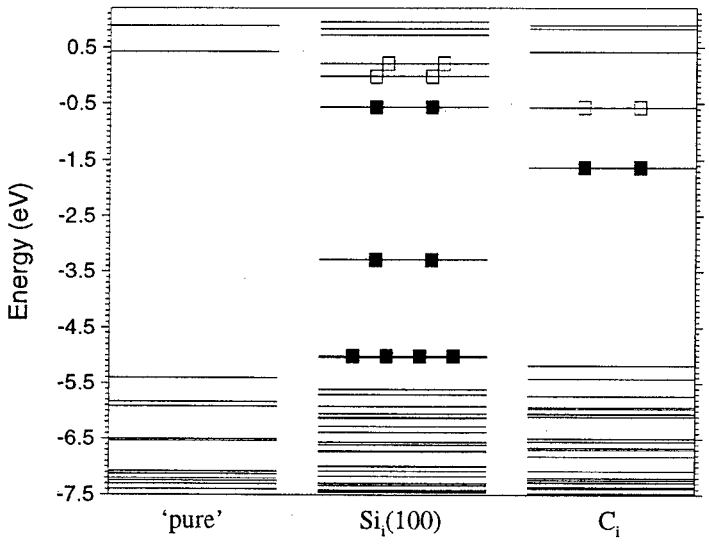

Figure 1: The Kohn-Sham eigenvalues for the ⟨100⟩ Si split-interstitial. The filled boxes indicate a filled, spin-averaged level, and the empty boxes represent empty levels. The 'pure' Kohn-Sham levels are those calculated for the 131-atom cluster containing no defect atoms. The eigenvalues of the D_2 symmetry relaxed self-interstitial are plotted for comparison.

The ⟨110⟩-split-interstitial.
The ⟨110⟩ oriented split-interstitial structure was also relaxed in the 132 atom cluster, again keeping the surface H atoms fixed. The final structure retained some of the ⟨110⟩ split-interstitial character, but the central C atom was pushed into a site resembling a bond-centre between the Si atom and one of its C neighbours. After displacing the central C atom in the ⟨110⟩-direction (away from the Si atom) by 0.2 Å and relaxing again, the system was found to have reconstructed to form a substitutional Si atom neighboured by an approximately ⟨100⟩-

oriented self-interstitial. The accompanying drop in total energy from the ⟨110⟩ local minimum was in excess of 6 eV.

The tetrahedral interstitial.
Preliminary simulations for Si at the tetrahedral interstitial site were performed using the relatively small 71-atom cluster centred on the tetrahedral interstitial site. However, since this cluster possesses overall tetrahedral symmetry, it allowed an initial determination of the stability of Si in various high-symmetry configurations. If interstitial Si prefers the tetrahedral site, when displaced along (say) ⟨111⟩, the relaxation should return the Si atom to the centre or result in a higher energy structure. However, the Si atom did not return to the centre, but instead moved to one of its neighbouring lattice sites, ejecting a C atom from the cluster. This shows that there is a strong propensity for the Si to move off site, but the cluster is clearly too small to accommodate the interstitial Si centre. Therefore we relaxed the cluster containing Si starting at the T_d site in the 132-atom cluster. Again, the Si atom moved off the T_d site. It formed bonds with three of its neighbours but found a minimum in energy with Si-C bond-lengths of 1.7 Å. After a small perturbation (the central C atom was moved off the trigonal axis by 0.075 Å) the Si atom moved to form four strong Si-C bonds (1.72-1.75 Å) and a ⟨100⟩ oriented C_i was ejected. This confirms that the T_d interstitial is unstable and generates an interstitial carbon atom as suggested by the calculations in the smaller cluster.

Summary.
The results of our calculations provide strong evidence that Si would not remain at an interstitial location in diamond (at least in the neutral charge state), but instead would eject a self-interstitial into the nearby lattice. A question remains however: does the interstitial C centre ejected by the Si atom migrate away, or is it bound to the substitutional Si atom? This is addressed below.

Substitutional Si – self-interstitial complexes.

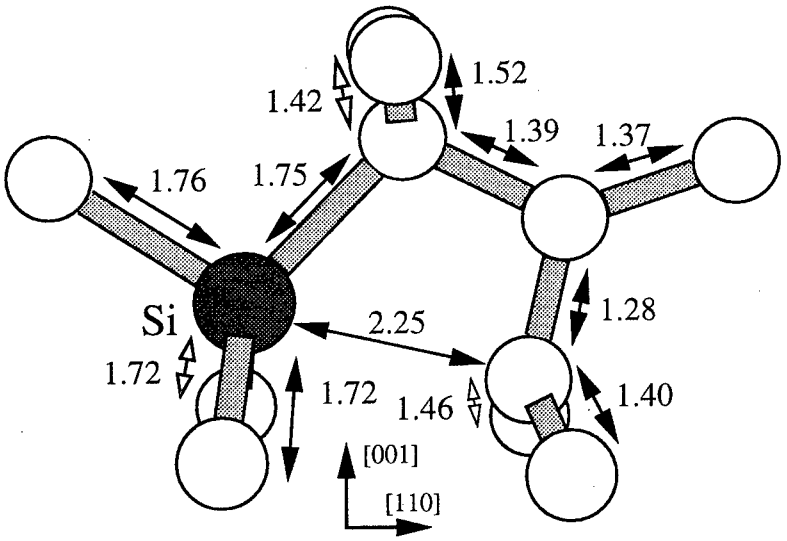

Figure 2: A schematic representation of the lowest energy geometry of a Si_s-C_i complex. The distances marked are in Å. Where bonds are out of the plane of the page, those marked with hollow arrow-heads are into the page, and those with solid arrow-heads, out of the page.

In order to accommodate complexes of Si at a substitutional site with a self-interstitial at various separations, it is necessary to use a relatively large cluster. Therefore clusters of 266 atoms were relaxed. Of those configurations studied, the lowest in energy was approximately planar with the Si_s and C_i separated by a single lattice site (shown schematically in Fig. 2). Separating the Si atom and the self-interstitial by another lattice site increased the total energy by around 1 eV, and placing the Si atom at a site neighbouring the self-interstitial resulted in a total energy around 1.8 eV higher than that of the geometry shown in Fig. 2.

The electronic structure (Kohn-Sham eigenvalues) of the relaxed Si_s-C_i system is plotted in Fig. 3, alongside those of the neutral, D_2 symmetry $\langle 100 \rangle$ carbon split-interstitial and the isolated substitutional Si centres, relaxed in 132 and 131 atom clusters respectively. The wavefunctions of the two deep gap levels are made up from p-orbitals on the two C atoms in the self-interstitial, and there is no significant amplitude on the Si atom. From Fig. 3 one can see that an optical transition mechanism exists between the two gap states. However, since these orbitals arise from the nearly orthogonal p-lobes on the two C-interstitial atoms, the dipole matrix element associated with this transition is very small. In fact, using the pseudo-wavefunctions to calculate the dipole matrix element, the estimated lifetime of such a transition is around 1 μs. It is unlikely that such an inefficient transition mechanism would be observed experimentally. Even if it was, since neither the ground nor excited states have any appreciable amplitude on the Si atom, identifying the transition with Si might prove difficult.

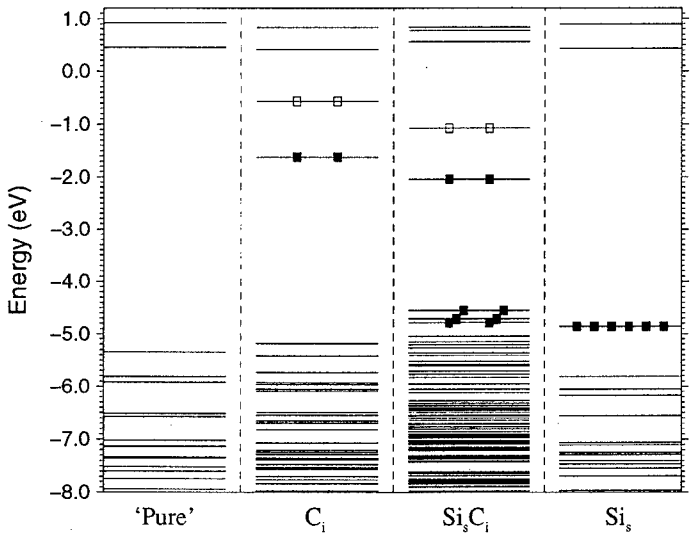

Figure 3: The Kohn-Sham eigenvalues for the D_2 symmetry self-interstitial, the complex of substitutional Si with the self-interstitial, and the tetrahedral substitutional Si centres. The filled boxes indicate a filled, spin-averaged level, and the empty boxes represent empty levels. The 'pure' cluster is the same as in Fig. 1.

Substitutional Si.

Also indicated in the plot for the Si_s-C_i complex in Fig. 3 are a number of shallow levels a few tenths of an eV above the valence band. These eigenvalues are associated with the substitutional Si atom, but arise from the surrounding compressed C-C bonds, and also have only a small amplitude on the Si impurity. We have relaxed Si under a number of symmetry constraints

in the 131 atom cluster. According to our calculations isolated substitutional Si possesses tetrahedral symmetry, and gives rise to a shallow level of t_2 symmetry at about E_v+1 eV. Note, the exact position of the level is uncertain due to the uncertainty in the position of the top of the valence band. For example, taking the top of the valence band to be the highest occupied orbital in the 'pure' cluster, the Si_s level would be at ~0.5 eV above the valence band.

It is interesting to note that although the Si atom forms bonds with its four neighbours that are around 11% longer than the bulk C-C bond-lengths, the surrounding lattice absorbs the expansion very close to the Si atom, so that the C-C back-bonds are compressed by less than 0.5%. Any vibrational modes are likely to be resonant with bulk modes, and have not been calculated as of this time.

Si-Si ⟨100⟩-split-interstitials.
Finally, preliminary calculations in a 72-atom cluster centred at a lattice site show that the ⟨100⟩ split-interstitial made up from two Si atoms is around 4 eV higher in energy than a ⟨100⟩ Si-C split-interstitial and a substitutional Si atom. This is unsurprising in light of the results presented above.

Conclusions.
The difference in total energy between the neutral Si_s–C_i system and the neutral ⟨100⟩ split-interstitial Si_i model was more than 6 eV. We conclude that a neutral interstitial Si would be unstable in diamond. However, there is a ~1 eV binding energy of the C_i centre to the substitutional Si atom. This centre possesses deep gap levels between which there is a low transition probability. The fact that the gap levels are not localised on the Si atom would mean that there would be no Si-related fine structure in the ZPL, although there may be in any phonon-side-bands. These results give no support for the assignment of the broad peak around 1.682 eV to an interstitial Si centre.

We thank the HPCI for an allocation of computer time on the Cray T3D at Edinburgh and the SP2 at Daresbury.

References.

1. C. D. Clark, H. Kanda, I. Kiflawi, and G. Sittas, Phys. Rev. B **51**, 16681 (1995).
2. J. P. Goss, R. Jones, S. J. Breuer, P. R. Briddon, and S. Öberg, Phys. Rev. Lett. **77**, 3041 (1996).
3. M. R. Correia, T. Monterio, E. Pereira, and L. C. Costa, De Beers Diamond Conference, Cambridge, 1996, pp. 4.1.
4. Pan Bicai, and Xia Shangda, Phys. Rev. B **49**, 11444 (1994).
5. V. A. Vavilov, A. A. Gippius, A. M. Zaitsev, B. V. Deryagin, B. V. Spitsyn, and A. E. Alenksenko, Sov. Phys. Semicond. **14**, 1078 (1980).
6. S. J. Breuer, and P. R. Briddon, Phys. Rev. B **51**, 6984 (1995).
7. WebElements resource:
   URL http://www.chemie.uni-regensburg.de/pub/web-elements/web-elements-home.html.
   See J. Chem. Soc., Chem. Commun., 1907-1910 (1994) for further details.
8. I. Kiflawi, A. Mainwood, H. Kanda, and D. Fisher, Phys. Rev. B **54**, 16719 (1996).
9. J. P. Goss, C. D. Latham, R. Jones, P. R. Briddon, and S. Öberg, unpublished.
10. R. Jones, Phil. Trans. Roy. Soc. London Ser. A **341**, 351 (1992); *Identification of Defects in Semiconductors*, ed. M. Stavola, *Semiconductors and Semimetals*, treatise editors, R. K. Willardson, A. C. Beer, and E. R. Weber, Academic Press.
11. G. B. Bachelet, D. R. Hamann and M. Schlüter, Phys. Rev. B **26**, 4199 (1982).

Materials Science Forum Vols. 258-263 (1997) pp. 787-792

RADIATION DAMAGE OF SILICON AND DIAMOND BY HIGH ENERGY NEUTRONS, PROTONS AND α PARTICLES

Alison Mainwood, J. Cunningham[1] and D. Usher

Physics Department, King's College London, Strand, London WC2R 2LS, U. K.
[1]Physics Department, Blackett Laboratory, Imperial College, London SW7 2AZ, U. K.

Keywords: silicon, diamond, radiation damage, modelling, annealing.

Abstract

In the new generation of particle accelerators, such as the Large Hadron Collider, the detectors and electronics will have to operate under very high doses of radiation. Silicon is known to suffer considerable degradation under radiation and new materials, such as diamond, are being investigated to replace it. This paper uses two of the sophisticated simulations of the interaction of particles with matter to investigate the damage caused by a range of particles at energies near those which are expected. However, much of the damage caused to the solid by the displacement of atoms into interstitial positions anneals out as the irradiation proceeds, when the interstitials migrate back to recombine with the vacancies. We can record the energy of the displaced interstitial and assume that those with low energies are most likely to recombine. Then, comparison with experimental damage data allows us to extrapolate to find the surviving radiation damage due to the complete range of particles and energies.

The primary damage due to 1 MeV neutrons in diamond and silicon is 68±7 and 112±2 vacancies per neutron cm^{-1}, respectively. However, many of these vacancies recombine with the displaced interstitials while the irradiation takes place, so the observed damage is only 35±7 and 67±5 cm^{-1}. These vacancies are distributed throughout the thickness of a thin wafer, except for the first 200nm, but the damage from protons and alpha particles is concentrated a few microns below the surface.

1. Introduction

Low energy particles incident on a solid interact with it in two ways. If they are charged, they ionise the material by scattering the electrons into higher energy states, and they may also knock atoms off their lattice sites[1]. The displaced (knock-on) atoms may have considerable energy and may collide with other atoms causing a cascade of further damage. At higher energies, where the particle may be moving at relativistic velocities, further processes such as Cherenkov emission and pair (electron-positron) production, may become significant, or the particle may interact with the nucleus of the lattice atom in a non-elastic way.

All these processes have been simulated in the program GEANT[2] which was written to allow particle physicists to design particle detectors and the infrastructure around particle accelerators. However, they were not concerned with the damage caused to the solid materials, and although it is possible to infer the energy of knock-on atoms produced, the damage cascades are ignored.

TRIM[3] was written to simulate ion implantation, so it follows the knock-on atoms and traces the damage they cause, but cannot deal with particles other than ions, or high energy processes.

We have combined the two simulations so that we can study the initial interaction of the particles with diamond and silicon, and then trace the further damage caused by the knock-on

atoms, in Section 2. In each case, the damage caused by a 1 MeV particle to a wafer of diamond or silicon 300μm thick is discussed, so that the results can be easily compared in Table I, where some other energies are included.
However, the interstitial atoms in silicon and diamond can migrate at room temperature, and in silicon, the vacancy is mobile too. Most of the interstitials, unless they are projected far from their original site, are likely to migrate back and recombine with the vacancy. These annealing effects are considered in Section 3. The consequences in terms of electronic properties are briefly discussed in Section 4.

2. Primary damage

2.1 Neutrons

Because neutrons have no charge, the main interaction they have with the solid is a ballistic one, where they collide with atoms[1]. The cross-section of this interaction is small at low energies, but extremely energy-dependent and complex at higher energies where nuclear interactions become important[4]. GEANT uses code from two further simulations, MICAP[5] and FLUKA[6], to simulate low and high energy neutrons respectively. In practice, at energies less than about 10 MeV, the GEANT results are very close to those assuming that a simple conservation of momentum interaction was taking place[7].

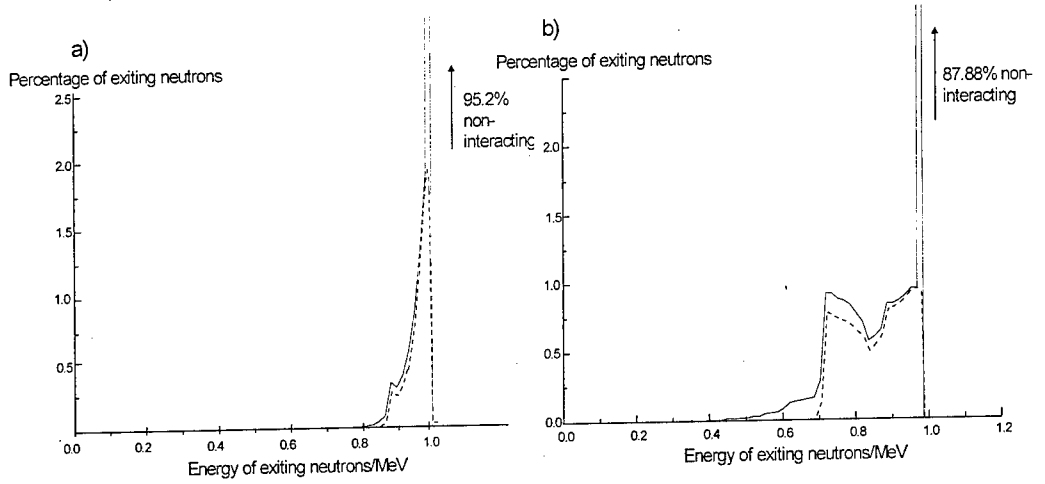

Fig 1: A histogram of the percentage of neutrons which penetrate 300 μm of a) silicon, b) diamond. The width of the energy interval is 20 keV. The broken line shows those which interact with just a single lattice atom.

Most of the neutrons do not interact with the material at all, as can be seen in Fig. 1, but when they do, the energy transferred to knock-on atoms is high enough for them to cause substantial further damage. Therefore, the vacancy production per 1 MeV neutron is approximately constant throughout the wafer at 68±7 and 112±2 cm^{-1} in diamond and silicon respectively, after the first 200 nm of the thickness. The damage is likely to be in the form of clusters of vacancies, which may form disordered or amorphous regions after a very high dose.

2.2 Electrons

Most of the energy lost by the electrons is due to electronic excitation of the semiconductor, with Bremsstralung a minor factor at the low energies considered here. The electrons may also displace atoms by the recoil from Rutherford scattering as they pass close to the nucleus, but the mass difference means that the knock-on atoms have low energies[8] and are unlikely to cause further damage. The cross-section[8] is such that most of the electrons pass right through the 300 μm wafer, so the damage is in the form of isolated vacancies distributed evenly through the diamond and silicon wafers at a rate of 1.5±3 and 1.72±.02 cm^{-1}, respectively.

2.3 Protons

Protons are slowed down by ionisation, but at the same time when they are scattered by the nuclei, enough energy is transferred for the knock-on atoms to cause a cascade of damage[1]. Because a proton is itself an ion, TRIM can model its interactions with the solids adequately at non-relativistic energies (less than about 5 MeV). The cross-section for Rutherford scattering increases as the ion slows down, so most of the damage is caused at the end of the path of the proton, which is stopped within the wafer. This effect is well-known by those who use ion-implantation to induce radiation damage to dope semiconductors - they use a range of implantation energies to achieve an even doping profile. Figure 2 shows the distribution of vacancies produced by 1 MeV protons in diamond and silicon.

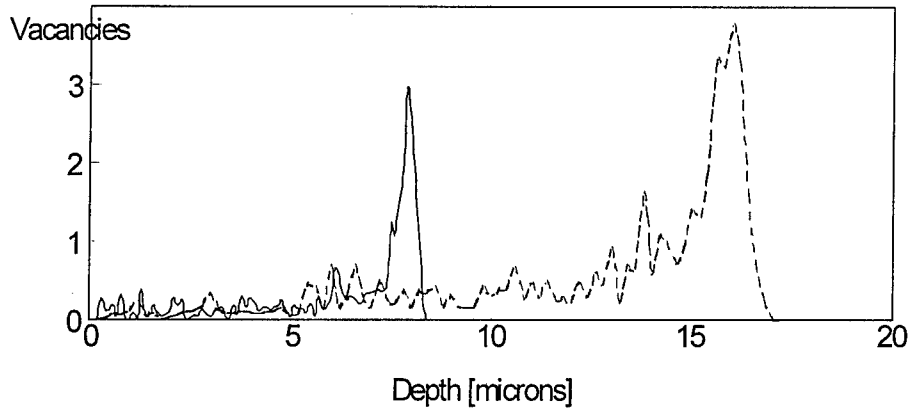

Figure 2: The distribution of vacancies created by 1 MeV protons in diamond (solid line) and silicon (broken line), before annealing.

2.4 α particles

The interactions are very similar for protons and α particles, except for the α's greater charge and mass. The α particle's damage is therefore greater and shallower as is shown in Fig. 3.

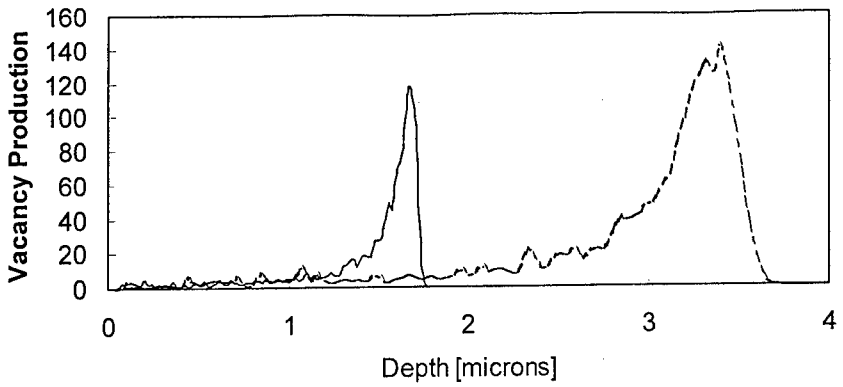

Figure 3: The distribution of vacancies created by 1 MeV α particles in diamond (solid line) and silicon (broken line), before annealing.

3. Annealing processes

Estimates of the migration energy of self interstitials in silicon[9] and diamond[10] vary, but most agree that they are mobile at room temperature. Vacancies in silicon are also mobile, so if the irradiation takes place at room temperature, we would expect the radiation damage to anneal out as the irradiation proceeds by the recombination of vacancies and interstitials. If multiple vacancies are being formed, or amorphous regions, the normal migration processes may not apply. If the materials reach high temperatures during the irradiation, then the damage products become even more mobile. However, for low doses of irradiation, we suggest that the knock-on atoms which are projected with a lower energy than some threshold value are likely to recombine, while those projected further away at a higher energy, persist in the crystal. This would apply to all the knock-on atoms, whether displaced by the particle or by other knock-on atoms.

Experimental radiation damage rates differ widely, and this variation gives rise to the large errors quoted in the rest of this paper. Palmer[11] reviewed the damage due to electrons in diamond, and concluded that 0.1 to 0.25 vacancies cm^{-1} were produced per 1 MeV electron by room temperature annealing, and ten times that number at 15 K, when the annealing effects would not occur. This value agrees well with our primary damage rate. Looking at the energy distribution of knock-on atoms produced by 1 MeV electrons[8], and assuming that only 10% survive the annealing process, gives us a threshold energy of 173±30 eV for the knock-on atoms in diamond whose associated vacancies survive. The same calculation on silicon, using Van Lint's estimate[12] of only 2% of primary vacancies surviving after irradiation, gives us a threshold energy of 190 eV.

The vacancies which survive after irradiation are those whose atoms were displaced with an energy greater than these threshold values, whatever the particle or ion displacing them. Table I summarises all the damage rates, before and after annealing.

Because the neutron or electron damage is spread throughout the thickness of the wafer, the distribution is still constant after annealing. However, the knock-on atoms at the end of the proton and α particle tracks will have been displaced when the particle has lost most of its energy, so will have low energies themselves, and the annealed damage will have a flatter distribution than that shown in Figs. 2 and 3. This is illustrated for protons in Fig. 4.

Table I: The concentration of vacancies produced per incident particle in a 300 μm wafer of diamond or silicon. Experimental values are given where available.

	Diamond		Silicon	
	created	after annealing	created	after annealing
1 MeV neutron cm^{-1}	68±7	35±7	112±2	67±8
2 MeV neutron cm^{-1}		42±7		112±7
1 MeV electron cm^{-1} Experimental	1.5±.3 1.0-2.5[11]	0.15±.0 5 0.1-0.25[11]	1.72 ±.02	0.03±.01 0.03[12]
2 MeV electron cm^{-1} Experimental	1.7±.3	0.34±.15 0.1 - 0.2 [11] 0.7[14]	2 .07±.02	0.04±.02
1 MeV proton	7.9±.2	1.1±.5	18.5±.5	1.3±.3
2 MeV proton		1.3±.5		1.9±.5
1 MeV α particle	51±2	9±4	134±7	12±4
2 MeV α particle		10±4		13±4

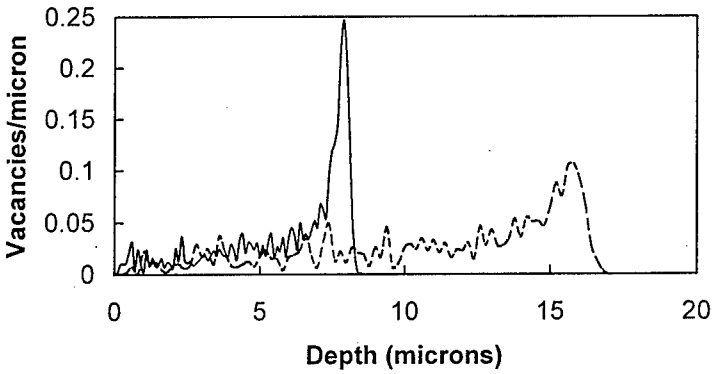

Figure 4: Vacancies surviving the annealing processes produced by 1 MeV protons in diamond (solid line) and silicon (broken line)

4. Consequences of radiation damage

What those who are designing particle detectors or radiation-hard electronics actually want to know, is not the rate of primary damage caused by a particle, or even the vacancy distribution after annealing, but how the radiation damage affects the electronic properties of the material. In diamond, very little is known about the effects of radiation damage except that for doses up to the equivalent of about 10^{15} neutrons cm^{-2}, the electrical resistance and the efficiency of a

diamond detector actually increases as the new defects produced compensate in-grown defects[13]. Above that dose the properties start to degrade. Silicon does not appear to have this "priming" mechanism. Mobile radiation damage products are trapped at donors and cause type inversion - where n-type silicon becomes p-type after a dose of 10^{13} neutrons cm^{-2}. Following through the rates of production of damage could allow us to put limits on the dose of particles which will have these effects. However, the original experimental data is so uncertain that gross extrapolation of it is not justified at present. For example, there is some work being completed at the moment which suggests that the surviving vacancy concentration produced by 1.9 MeV electrons in diamond is near to 0.7 cm^{-1}[14], rather than the 0.1 to 0.2 cm^{-1} deduced by Palmer[11]. If this proves to be the true rate, then the vacancy concentrations in diamond given in Table 1 due to other particles, is a substantial underestimate.

5. Conclusions

Using a combination of simulations of the interactions of particles with matters, we can calculate the effect that neutrons, electrons, alpha particles and protons have on diamond or silicon wafers. The primary damage caused by the particle itself and the atoms it displaces is consistently higher in silicon than in diamond. Once the annealing effects are taken into account, where the mobile interstitials migrate back to recombine with the vacancies, the surviving damage is very similar in the diamond to that in the silicon wafers. However, the defects created in diamond do not cause the same degree of degradation of electronic properties that those created in silicon do, so in terms of the performance of a detector or electronic material, diamond is considerably more radiation-hard than silicon.

Acknowledgments: This work was supported by the EPSRC.

References

[1] E. W. J. Mitchell, in "The Physical Properties of diamond" ed. R. Berman (Clarendon: Oxford) 1965, p364.
[2] R. Brun and A. McPherson, GEANT user guide, Data Handling Division, CERN (1992).
[3] J. F. Zeigler, "The stopping and range of ions in solids" (A. Wheaton & Co.: Exeter) 1985; J. P. Biersack and L. G. Hassmark, Nucl. Instr. Meth. **B174**, 274 (1980)
[4] S. Beever, Los Alamos Nuclear Data Viewer, http://t2.lanl.gov/
[5] J. O. Johnson and T. A. Gabriel, Technical Report ORNL/TM-10196, (ORNL), 1987; TM-10340 (ORNL), 1988.
[6] P. A. Arnio, Nucl. Instr. Meth. **A336**, 98 (1993).
[7] J. Cunningham, MSc thesis, Imperial College London, 1996; J Cunningham, A. Mainwood, J.F. Hassard and D. Colling, to be published.
[8] G. H. Kinchin and R. S. Pease, Rep. Prog. Phys. **18**, 1 (1955)
[9] G. D. Watkins in "Radiation damage in semiconductors" ed. P. Baruch (Dunod, Paris) 1965 p97; G. D. Watkins and K. L. Brower, Phys. Rev. Lett. **36**, 1329 (1976)
[10] G. Davies, in "Properties and Growth of Diamond" ed. G. Davies, (INSPEC, IEE: London) 1994, p185.
[11] D. W. Palmer, in "Properties and Growth of Diamond" ed. G. Davies, (INSPEC, IEE: London) 1994, p143.
[12] V. A. J. Van Lint, Nucl. Instr. Meth. **A253**, 453 (1987)
[13] L. Allers, A. S. Howard, J. F. Hassard and A. Mainwood, Diamond Rel. Mater. **6**, 353 (1997); A. Mainwood *et al*, J. Phys. D **28**, 1279 (1995).
[14] S. C. Lawson, private communication (1997).

Materials Science Forum Vols. 258-263 (1997) pp. 793-798

STUDY OF DEFECTS IN DIAMOND FILMS BY ELECTRICAL MEASUREMENTS

L.Pereira [1], E.Pereira [1] and H.Gomes [2]
[1] Departamento de Física, Universidade de Aveiro, 3810 Aveiro, Portugal
[2] Sector de Electrotecnia e Computação, Universidade do Algarve, 8000 Faro, Portugal

Keywords: Diamond films, Electrical properties, Microstructure defects, Raman

Abstract. Applications of polycrystalline diamond films are clearly influenced by the structural defects that arising in growth process of the material. In this work, as-grown free-standing diamond films (ca 3μm thick) are analysed by dc measurement and Raman spectroscopy. The temperature effect on the electrical behaviour shown by devices made using Au and Al or only Au electrodes is studied showing that in temperature range 360 – 410 K structural changes take place, modifying the electrical behaviour of the devices. This structural changes, that are irreversible, are predominantly originated in non-diamond phases, as shown by Raman spectra.

Introduction

The usual microstructure of diamond thin films grown by microwave plasma assisted chemical vapour deposition (MPCVD) presents many defects, most of them arising from structural deformations that appears in grain boundaries in the growth process. The known structural defects also appears from the different surface orientation of microcrystals as well from states originating at dangling bounds.

Many of these defects are electrically active, in particular when localised at the grain boundaries [1] that have predominantly non-diamond phases. As the importance of diamond optoelectrical applications increases, the study of carrier generation and transport in this grain boundaries, becomes more important. In order to understand the importance of these defects in the properties of the material, the study of the electrical properties and their correlation with the structural morphology as well the structure features shown by Raman spectroscopy is necessary.

The electrical properties of polycrystalline diamond thin films show significant variations due to thermal annealing at high temperatures (ca 600 K) in vacuum, oxygen or hydrogen [2 - 4]. These alterations have been attributed to the hydrogen passivation of defect states or to the presence of disordered graphitic regions between the grains.

In this work we describe the effects of heating at low temperatures (400 K) on the current-voltage (I-V) characteristics of gold / diamond / gold junctions and Al / diamond / Au diodes. Also, the current behaviour in a temperature range between 10 K and 400 K is studied and the correlation with the Raman spectra before and after annealing shows that even at 360 K irreversible changes in the film characteristic occurs. An attempt to correlate the defect in non-diamond phases with the electrical behaviour is made.

Experimental

Diamond films were prepared by microwave plasma assisted CVD in a RFA system at a pressure of 40 Torr and 800 ± 80 °C, in <111> p-type silicon substrate. The gas concentration was of 99 % of H_2 and 1 % of CH_4 and the microwave power was of 4 KW (2 KW in one minute initially). The total time of the deposition was 14 hours. The substrate has been previously polished with diamond powder of 0.25 μm grain size and cleaned before the deposition.

After deposition, the silicon substrate was completely removed by acid attack, leaving free-standing diamond films with a thickness of 2.9 ± 0.4 μm as shown by infrared measurements.

A morphological study has been performed on a Nanoscope Atomic Force Microscope at room temperature, on both surfaces of the samples (we call back surface the surface that was previously in contact with the silicon substrate).
Micro-Raman spectra was been taken at room temperature, in a Renishaw 2000 micro-Raman System attached to an optical microscope giving a spatial resolution of the order of one micron.
To prepare the devices from the free-standing diamond films, metal contacts has been deposited in both sample surfaces, by evaporation in a turbomolecular pump system in a clean room.
For temperature measurements between 20 and 300 K a closed He cryostat cycle has been used. For higher temperatures, a temperature controlled steel chamber was used. All the systems are conveniently earthed to avoid undesired noise measurements. The DC characteristics were obtained using a Keithey model 487 picoammeter / voltage source, with a resolution of 1 pA and 1 mV. The small-signal admittance measurements were carried out with a Fulke PM model 6306 RLC meter system.

Results
Figure 1 shows an atomic force microscopy (AFM) image of the front surface of the diamond films.

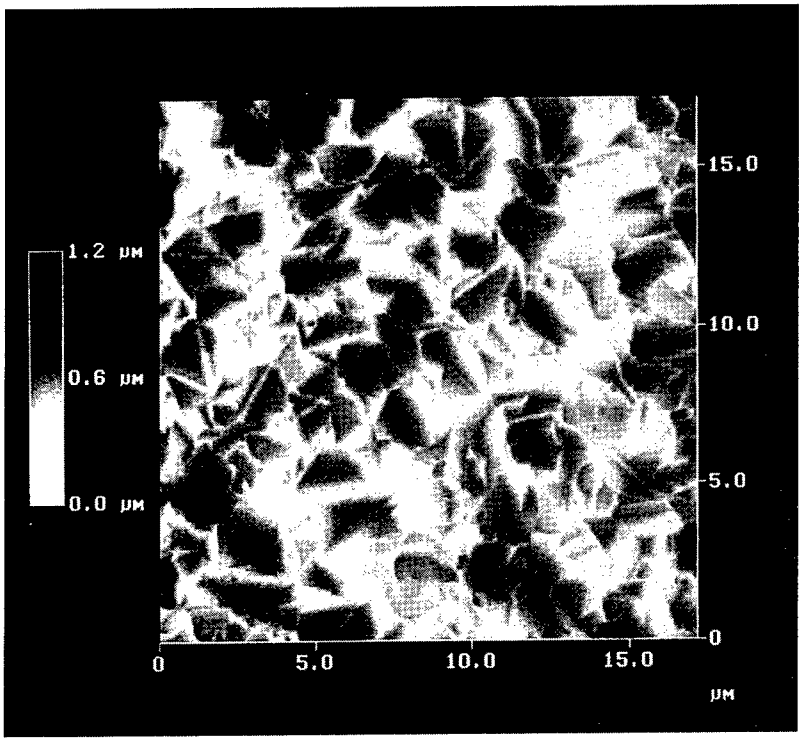

Figure 1. Atomic Force Microscopy image of front surface of diamond film. All samples shows similar morphology.

The current density is higher in the symmetrical junction.

The back side presents a much smother surface than the front surface, as expected from the contact with the substrate during growth. Typical crystal size is ca 1 μm and with <111> preferential orientation. The roughness is less than 1 μm. All the samples have similar surface morphology.
In Fig. 2 the device characteristics for the two kind of junctions (Au / diamond / Au and Al / diamond / Au) are shown, at room temperature. The Au / diamond / Au has a symmetrical junction, as expected from the both gold / diamond interfaces.

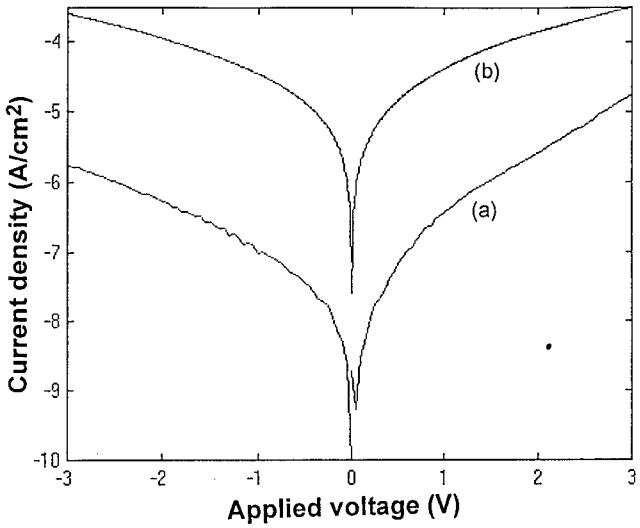

Figure 2. Current – voltage characteristics obtained at room temperature for a (a) rectifying contact (Al / diamond / Au) structure and (b) for a symmetrical junction (Au / diamond / Au).

From the I-V characteristics for the diode (Al / diamond / Au) under forward bias, (positive voltages applied to the gold electrode), we conclude that the Al / diamond / Au device shows a rectifying behaviour. For 3 V applied voltage we get a current about ten times larger in forward bias. Capacitance / voltage measurements at 100 Hz give an acceptor density of 1×10^{17} carrier / cm^3.

Current dependence on temperature was studied in the Au / diamond / Au device, from 10 to 420 K. The heating rate was about 0.2 °C s^{-1}. The results are shown in figure 3, where current is plotted against reciprocal temperature.

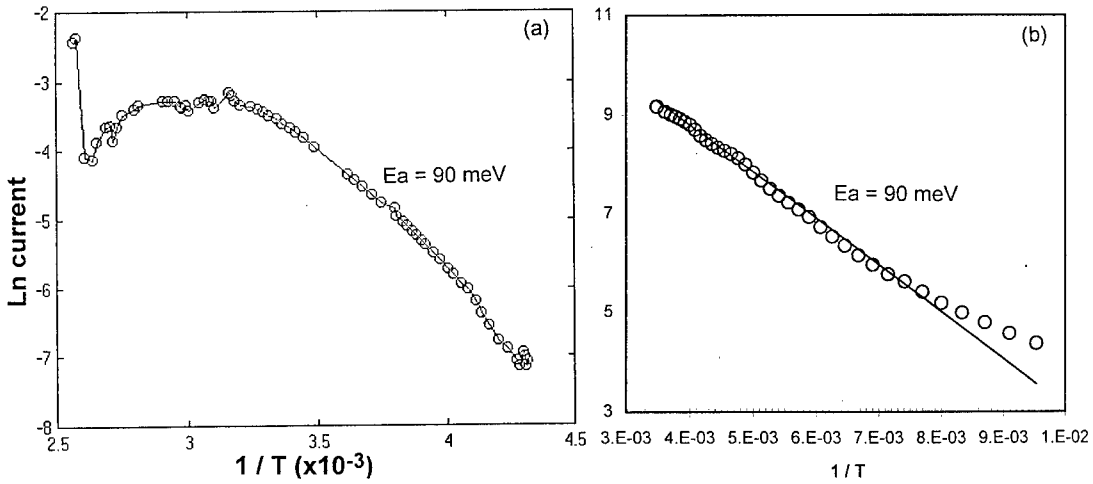

Figure 3. The effect of temperature on the magnitude of the device current for a symmetrical junction (a) high temperature range and (b) low temperature range. The activation energy is about 90 meV.

Below 40 K we get a very slow temperature dependence of current intensity, indicating a tunnelling process (Fowler-Nordheim injection). Above this temperature the dependence becomes exponential up to ca 320 K, with an activation energy of ca 90 meV. However, above this temperature a departure from the exponential behaviour of the current intensity is observed. The current actually decreases reaching a minimum at 390 K. Above this temperature the conductivity increases again. Curves such as those present in figure 3 have been previously reported at high temperatures (ca 600

K) [2] and tentatively explained in terms of a structural change and / or evolution of weakly bounded hydrogen in the non-diamond region between grains. Upon cooling the device to room temperature we get a decrease in current intensity as compared with the value before the heating process. I-V curves at room temperature after the sample has been heated to 360 and 410 K are shown in figure 4. When the current dependence with temperature was studied after the sample has been treated at 410 K, we found that now the activation energy was 190 meV, as shown in figure 5 without any drop in intensity in the region of 350 – 410 K.

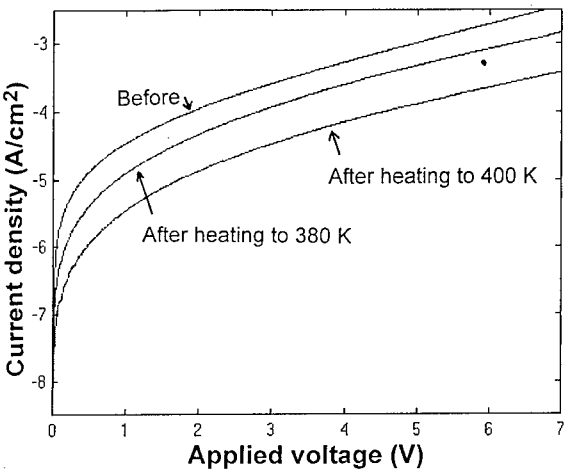

Figure 4. The effect of two successive thermal cycles in vacuo on the magnitude of the device current

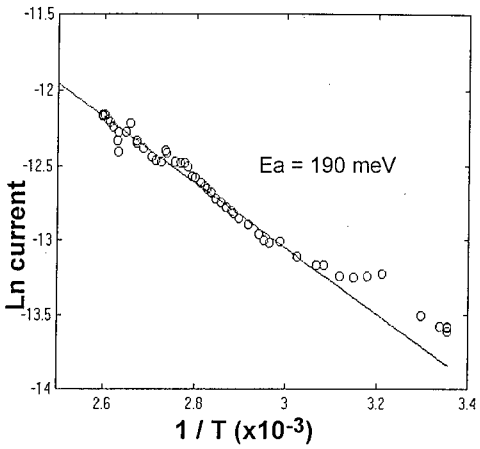

Figure 5. Arrhenius plot of the device current after heating process.

The changes are therefore irreversible. The I-V behaviour of a rectifier device (Au / diamond / Al) was also studied in the temperature range 300 – 410 K as shown in figure 6.

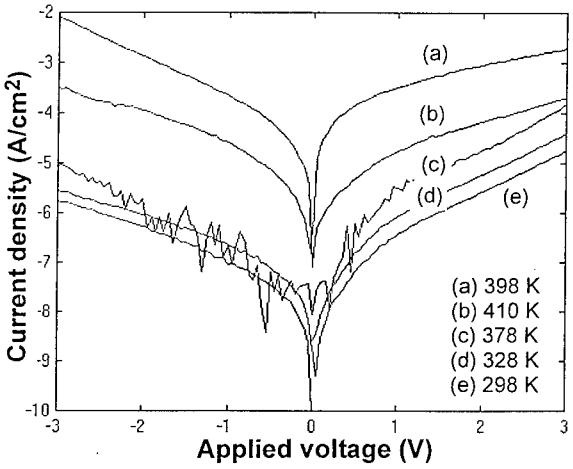

Figure 6. Temperature dependence in the rectifying device current-voltage characteristics

It is observed that in range of 360 to 390 K the signal is noisy, suggesting that in this temperature range structural changes take place. It is the same temperature region where the symmetrical device presented an anomalous behaviour. This hypothesis is also reinforced by the fact that above 390 K a reversal of the rectification at low applied fields takes placeand the current decreases with the temperature.

This result is interpreted as due to the fact that the structural changes of the defects that occur with the heating process modifies the density and nature of the carriers originated at different structural defects. But, in contrast with the

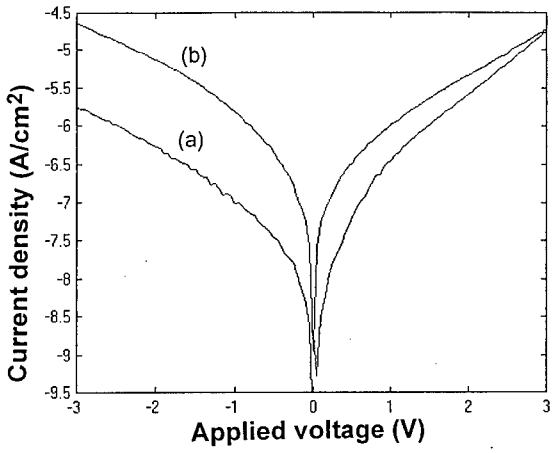

Figure 7. Room temperatute I-V characteristics of the rectifyier device (a) before and (b) after heat treatment.

symmetrical device, the current at room temperature in the rectifier device presents an increase after the heating (figure 7). This can be due to the different main conduction process in both kind of devices accompanied by a lowering of the Al / diamond Schottky barrier.

Raman spectra were recorded before and after the sample has been heated to 410 K, as shown in figure 8. Apart from the diamond Raman peak at 1332 cm^{-1}, that do not present any appreciable change, it can be seen that some changes occurred in the non diamond phases. It is to be noted that for the Raman spectrum an He-Ne laser was used in order to enhance the non-diamond contributions. The spectrum does not change with time. Thus irreversible changes occurs in the non-diamond phases in the temperature range of 320 – 410 K.

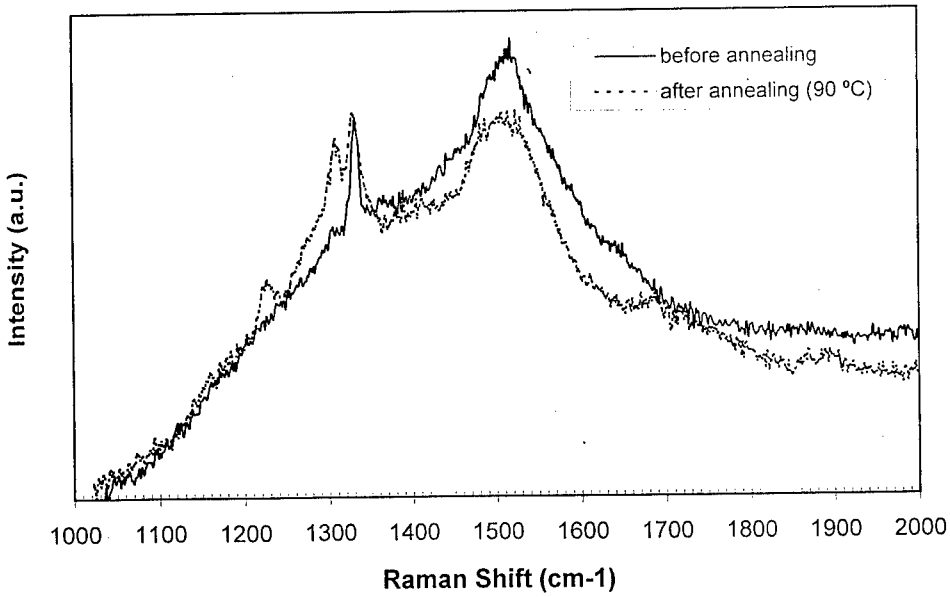

Figure 8. Raman spectrum of diamond film before and after heating treatment. After heating, there is a change in the non-diamond region of the spectrum.

Conclusions

Polycrystalline diamond thin films present many structural defects that influences the electrical conduction of the material. The structure of this defects are temperature dependent. Even at temperatures as low as 320 – 400 K irreversible changes occur in the electrical behaviour of the

films accompanied by changes in the Raman spectrum of non-diamond phases. In a symmetrical device a decrease of room temperature conductivity occurs. Also a higher thermal activation energy is found (190 vs 90 meV). The rectifying device becomes more symmetrical, but with a reversal in the rectification. In this case the room temperature conductivity is higher than before the heating process approaching the values found for the symmetrical situation. Thus, the Schottky barrier between the diamond film and Al has been modified showing the importance of structural non-diamond defects in the optoelectrical applications of diamond films.

References

1. B.Fiegi, R.Kuhnert, M. Ben-Chorin and F.Koch, *Appl. Phys. Lett.*, **65** (1994) 371
2. Y.Muto, T.Sugino, J. Shirafuji and K. Kobashi, *Appl. Phys. Lett.*, **59** (1991) 843
3. D.M. Malta, J.A. von Windheim, H.A.Wynands and B.A. Fox, *J.Appl. Phys.*, **77** (1995) 1536
4. W. Ebert, A. Vescan, P.Gluche, T.Borst and E.Kohn, *Diamond Relat. Mater.*, **6** (1997) 329

Materials Science Forum Vols. 258-263 (1997) pp. 799-804

VALENCE CONTROLS AND CODOPING FOR LOW-RESISTIVITY *n*-TYPE DIAMOND BY *ab initio* MOLECULAR-DYNAMICS SIMULATION

[1]Takeshi Nishimatsu, [1,2]Hiroshi Katayama-Yoshida and [3]Nozomi Orita
[1]Department of Condensed Matter Physics, The Institute of Scientific and Industrial Research (ISIR), Osaka University, Osaka 567, Japan
[2]PRESTO, Japan Science and Technology Corporation (JST), Saitama 332, Japan
[3]Electrotechnical Laboratory, Tsukuba 305, Japan
E-mail address of Nishimatsu is `nisimatu@cmp.sanken.osaka-u.ac.jp`

Keywords : ab initio calculation, n-type diamond, codoping, low-resistivity diamond

Abstract.
Based upon *ab initio* molecular dynamics simulation, we have proposed a new valence control method, "a codoping method" (doping *n*- and *p*-type dopants at the same time), in order to fabricate a low-resistivity *n*-type diamond. We calculated the stable atomic configuration and electronic structure of the codoping of *n*- (nitrogen or phosphorus) and *p*-type (boron) dopants. We found that the codoping of nitrogen and boron is the best candidate to make the low-resistivity *n*-type diamond. We discuss the universality of codoping method for valence control in wide band gap semiconductors.

Introduction.
Diamond is the most promising materials for the application of the high-speed, high-temperature, and high-power electronic-devices. It is well known that *p*-type semiconducting diamonds which have an accepter level right upper the valence band ($E_v + 0.35$eV) can be made by doping of boron (**B**) as acceptors. But that of *n*-type diamonds is very difficult because of the self-compensation (uni-polarity) in the super-wide band gap ($E_g = 5.6$eV) semiconductor. In order to make materials design for the fabrication of the low-resistivity *n*-type diamond, we study the nature of the donor states of phosphorus (**P**) and nitrogen (**N**) and propose a valence control method by "a codoping method" (doping *n*- and *p*-type dopants at the same time) in diamond using *ab initio* molecular-dynamics simulations including 64 atoms in a super-cell. Our results of isolated **P** and **N** impurities were same as earlier works[1, 2]. We find that codoping of **P** and **B** cannot prevent the large breathing mode lattice relaxation around **P** which is due to the **P**'s larger covalent radius and is the origin of **P**'s small solubility in diamond. But we find that codoping of **N** and **B** prevent the bond breaking and that this codoping is a good candidate to fabricate the low-resistivity *n*-type semiconducting diamond.
Contrast to the *p*-type doping, the fabrication of the low-resistivity *n*-type diamond is very difficult. Possible candidates for the dopants to make shallow donor levels in diamond are **P** and **N**. The difficulty in doping **P** into diamond is explained by the large breathing relaxation of stiff lattice of diamond around **P** which is due to the **P**'s larger covalent radius and is the origin of **P**'s small solubility in diamond (see Table 1). If **P** was doped in diamond with codopant **B** and the **B** acted a role of a absorber of the lattice relaxation, the large formation energy (10.4eV) of substitutional **P** impurity[2] would be reduced.
Electron Spin Resonance (ESR) study[3] and first principle calculations[1, 2] show that the substitutional **N** impurity breaks one of four bonds to nearest neighbor carbons (**C**) and distort itself and one opposite **C** to the direction of **[111]** and $[\bar{1}\bar{1}\bar{1}]$, respectively. The reason of this large lattice-relaxation is that the large electronegativity of **N** gathers one donor electron around itself, then strong Coulomb repulsion breaks one **C**–**N** bond and makes a lone pair on **N** and

Table 1: Isolated substitutional donor impurity in diamond. Arrows indicate the atomic displacement of each atoms in the unit of normal **C**–**C** length.

	diamond:N	diamond:P
irreducible representation of wave function of donor state (unrelaxed)	A_1	T_2
degree of degeneracy (unrelaxed)	1	3
total energy gain of lattice relaxation	−0.38eV	−3.7eV
lattice relaxation	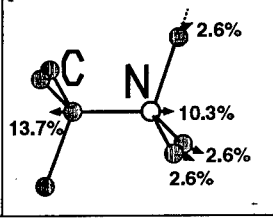	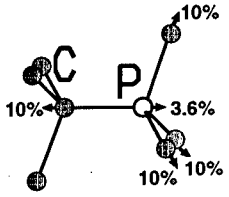

a dangling bond on opposite **C** (see Table 1 and Fig. 1a and b). In order to avoid this bond breaking, we propose a new codoping method using donor **N** and acceptor **B** for making the **N**–**B**–**N** complex in diamond, which divides one donor electron into half and half on two **N** atoms through the mediating **B** atom and prevents the bond breaking.

Calculation Method.

To confirm our expectation, we carried out *ab initio* molecular dynamics simulation[4, 5] with the periodic boundary conditions of super-cells containing 64 atoms of **C**, **P**, **N** and **B**. Electron wavefunctions and charge density are expanded into plane waves with cut off energy 59 and 118 Ry, respectively, by using norm conserving pseudopotential[6]. Bloch functions at the Γ-point are used in the calculations. Calculated lattice constant of diamond is 3.51×10^{-10}m and in good agreement with the experimental data 3.57×10^{-10}m. Our *ab initio* molecular dynamics simulation to seek the most stable atomic structure of isolated substitutional **N** impurity in diamond (Fig. 1a and b) results same as Kajihara *et al.*'s[2]. Our calculation indicates that the donor level due to **N** impurity is 1.70eV below the conduction bands ($E_c - 1.70$eV) and in good agreement with the experimental data of $E_c - 1.7$eV[7].

Codoping P and B.

As stated above, if **P** was doped in diamond with codopant **B** and the **B** acted a role of a absorber of the lattice relaxation around **P**, the large formation energy (10.4eV) of substitutional **P** impurity[2] would be reduced and one would get the higher solubility.

To evaluate the lattice relaxation under codoping, we seek most stable atomic configuration of **P**–**B**–**P** complex, **P**–**B**–**C**–**P** complex and a **P**–**B** pair with far located **P** (**P**–**B**–...–**P**). The calculation results indicate that codopant **B** does not absorb the lattice relaxation around **P**.

Codoping N and B.

Most stable atomic configuration of fully relaxed codoped **N**–**B**–**N** complex in diamond (say diamond:N_2B) are also determined by *ab intio* molecular dynamics simulation (Fig. 1c and d). It shows that the codoping of **N** donors and **B** acceptor prevents bond breaking and restrict the atomic distortions from the normal substitutional position less than 6.2% of normal **C**–**C** bond length. In Fig. 1, we draw iso-charge-density surface which includes 30% of donor electron. We

Table 2: Total energy comparison. Calculated total energies par super cell in different two nitrogens and one boron configurations relative to the **N–B–N** configuration. The **N–B–N** configuration is the most stable one in the calculation. In table, "**N–B–...–N**" means "a **N–B** pair and far located **N** in diamond".

configuration	total energy (eV)
N–B–N	0.0
N–B–...–N	0.668
N–B–C–N	1.23

obtain the delocalized shallower donor state in **N–B–N** complex (Fig. 1d) compared with the single **N** impurity (Fig. 1b).

We compare the total energy of **N–B–N**, **N–B–C–N** and **N–B–...–N** (a **N–B** pair and far located **N**) in diamond and find that **N–B–N** is the most stable configuration (see Table 2). In diamond, one **N** and one **B** may attract each other with reducing the Coulomb energy because of their opposite charge. So, the question may be rephrased whether the **N–B** pair attracts another **N**. If the total energy gain of bond breaking of the isolated substitutional **N** impurity was enough large, it would be more stable than **N–B–N** complex in diamond to put one **N** far from the **N–B** pair. But it does not happen in our *ab initio* electronic structure calculation.

Conclusion and Remarks.

Isolated substitutional **P** impurity in diamond acts as shallow donor, however, it solubility is extremely low because of the higher formation energy (10.4eV) relative to **N** (−3.4eV) due to **P**'s larger atomic radius[2]. Since **N** and **B** can be easily doped with large solubility to diamond, our codoping method is the best candidate of shallow donors which has large solubility i.e. realizing the low-resistivity n-type diamond.

We have previously proposed the materials design for the fabrication of low-resistivity p-type GaN (E_g = 3.3eV) using a codoping at the same time by **Si** (or **O**) donors and **Mg** (or **Be**) acceptors[8]. Our predictions are confirmed by **GaN** molecular beam epitaxy (MBE) crystal growth by Brandt *et al.* using **Be** as the acceptor and **O** as the codopnat[9]. Brandt *et al.* obtained highly conductive p-type **GaN** films as high as 50 /Ω·cm by codoping. We have also observed carrier concentration enhancement of p-type **ZnSe** (E_g = 2.7eV), up to 7×10^{18}cm^{-3}, and **ZnS** (E_g = 3.3eV) by codoping with active **N** and **Te** by using a δ-doping technique[10]. It seems that the codoping concept is the universal valence control method in order to overcome the self-compensation (uni-polarity) in the wide-gap and super-wide-gap semiconductors (such as **GaN** and diamond), because of the following three reasons. (1) Codoping p- and n-type dopants at the same time reduces the lattice-relaxation energy (chemical pressure) of the crystal upon doping because p-type dopant has smaller atomic radius and n-type one does larger atomic radius. (2) Codoping allows us to achieve higher mobilities to render isolated Coulomb scatters into dipole scatters by the codopants. (3) Codoping p- and n-type dopants at the same time reduces the Coulomb (Madelung) energy of the dopants and stabilizes the doped crystals using Coulombic pressure.

Acknowledgments.

Super computational time was provided by Institute for Solid State Physics, University of Tokyo and Computer Center Osaka University.

This work was supported by a Grant-In-Aid for Scientific Research from the Ministry of Education, Science, and Culture, Japan.

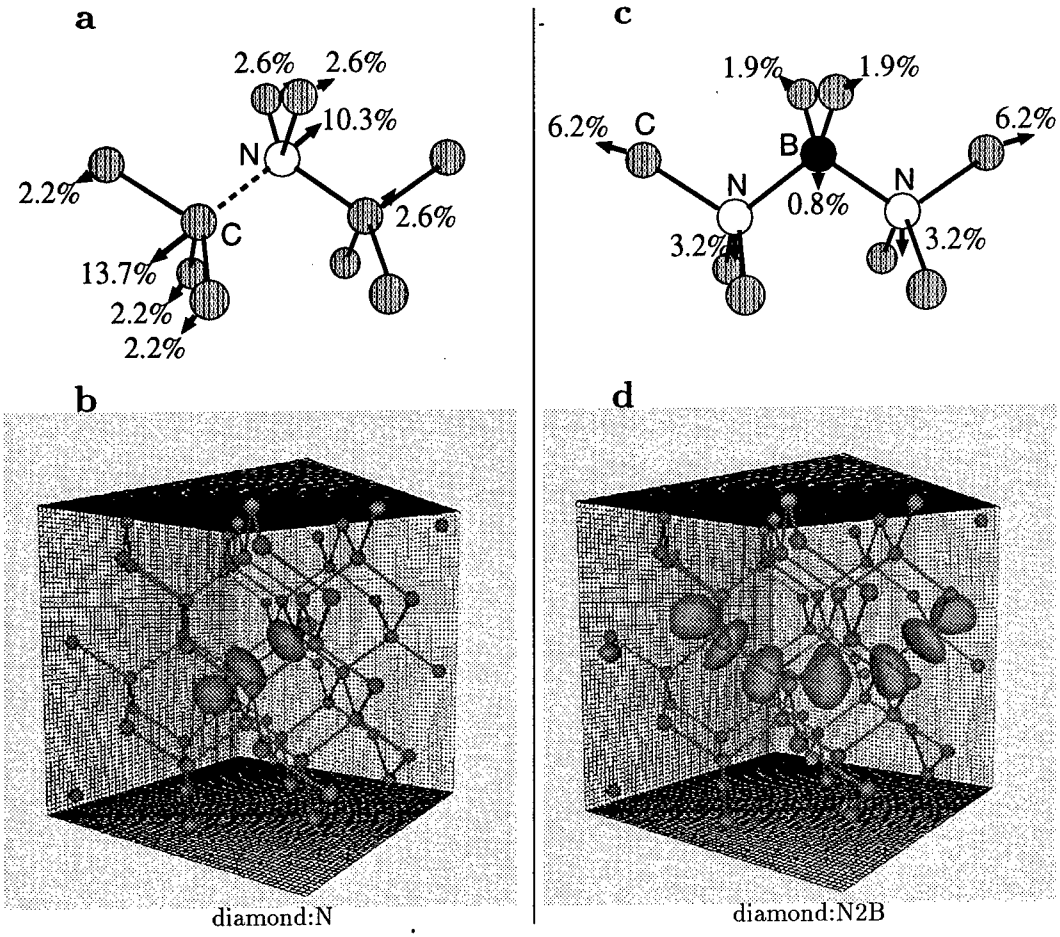

Figure 1: **a**, Atomic displacement of diamond:N. The breaking bond is indicated with dashed line. **b**, Relaxed diamond:N. **c**, Atomic displacement diamond:N_2B. **d**, Relaxed diamond:N_2B. In figure **b** and **d**, arrows indicate the atomic displacement of each atoms in the unit of normal **C–C** length. In figure **b** and **d**, iso charge density surfaces which include 30% of the donor electron are plotted. Mesh of these figures is boundaries of super-cell. The donor electron is divided into half and half on two **N** atoms through the mediating **B** atom (**d**) and prevents the bond breaking (**c**). The wider spreading donor electron of diamond:N_2B than diamond:N foretells the low resistivity.

References.

1. G. B. Bachelet, G. A. Baraff, and M. Schlüter, Phys. Rev. B **24**, 4736 (1981).
2. S. A. Kajihara, A. Antonelli, J. Bernholc, and R. Car, Phys. Rev. Lett. **66**, 2010 (1991).
3. W. V. Smith, P. P. Sorokin, I. L. Gelles, and G. J. Lasher, Phys. Rev. **115**, 1546 (1959).
4. R. Car and M. Parrinello, Phys. Rev. Lett. **55**, 2471 (1985).
5. M. C. Payne, M. P. Teter, D. C. Allan, T. A. Arias, and J. D. Joannopoulos, Rev. Mod. Phys. **64**, 1045 (1992).
6. N. Troullier and J. L. Martins, Phys. Rev. B **43**, 1993 (1991).
7. R. G. Farrer, Solid State Commun. **7**, 685 (1969).
8. T. Yamamoto and H. Katayama-Yoshida, Jpn. J. Appl. Phys. Lett. **36**, L180 (1997).
9. O. Brandt, H. Hui Yang, Kostial, and K. H. Ploog, Appl. Phys. Lett. **69**, 2707 (1996).
10. H. D. Jung, C. D. Song, S. Q. Wang, K. Arai, Y. H. Wu, Z. Zhu, T. Yao, and H. Katayama-Yoshida, Appl. Phys. Lett. **70**, 1143 (1997).

Materials Science Forum Vols. 258-263 (1997) pp. 805-812

INTRINSIC MODULATION DOPING IN InP-BASED HETEROSTRUCTURES

W.M. Chen, I.A. Buyanova, W.G. Bi[1] and C.W. Tu[1]
Department of Physics and Measurement Technology
Linköping University, S-581 83 Linköping, SWEDEN
[1]Department of Electrical and Computer Engineering
University of California, La Jolla, CA 92093-0407, USA

Keywords : intrinsic, doping, antisite, InP, InGaAs, off-stoichiometric, MBE, HEMTs

Abstract
We review our recent results from a new approach for n-type modulation doping in InP-based heterostructures, where grown-in intrinsic defects are utilized to provide charge carriers without requiring an external shallow impurity doping source. The success of such an intrinsic modulation doping concept is clearly demonstrated by the example cases of InGaAs/InP heterostructures, designed to resemble high electron mobility transistor (HEMT) structures or modulation-doped quantum wells. Unambiguous experimental evidence on the formation of a dense two-dimensional electron gas (2DEG) ($> 1\times10^{12}$ cm^{-2}) in the InGaAs active layer near the InGaAs/InP heterointerface is provided from magneto-transport and magneto-optical studies. The formation of the 2DEG is shown to be a direct consequence of electron transfer from the InP barrier intrinsically doped by P_{In} antisites, preferably introduced during off-stoichiometric growth of InP. Experimental results from undoped and extrinsically doped reference samples with identical structures are presented for comparison. Important issues such as doping efficiency, electron mobility, thermal stability, etc., are addressed. Advantages and disadvantages of the intrinsic modulation doping approach are discussed as compared to the extrinsically doping method by shallow dopants.

Introduction
The ability in drastically tailoring electronic properties by doping of impurities has made semiconductors the backbone for modern electronics. Ever since the semiconductor technology revolutionized the electronics industry, there have been long-standing and continuing efforts in finding the best-suited dopants and in optimizing doping processes and mechanisms. Rapid developments in innovative growth techniques and new device structures in recent years have urged a better and deeper understanding of dopants and doping processes.

Selective or modulation doping represents one of the essential steps in fabrication of modern quantum structures and devices based on InP-based heterostructures, which are now well recognized as being among the most promising electronic material systems for applications in optoelectronics and high frequency electronics. Such doping has traditionally been done by extrinsic doping, i.e. by incorporating shallow impurity donor or acceptor dopants in the structures via diffusion or ion implantation or in situ incorporation during growth of the host crystal. There are, however, still many problems remaining, such as [1]

- contamination due to impure doping source;
- memory effects;
- thermal instability of dopants;
- inter-diffusion and out-diffusion;
- damage of materials due to implantation and high temperature diffusion processes of dopants;
- configurational metastability, etc.

There will most likely be more problems emerging during the course of future development in growth and processing technology. These problems are and will be found to be unacceptable for certain devices, in particular those modern devices of lower dimensionality and of submicron or nanometer size, where a high precision of doping and interface profiles is crucial. A large international effort has therefore been devoted to seek for both a better control of the existing doping processes and a better doping mechanism. A vast majority of the research work reported so far on this issue have been largely limited to the extrinsic doping concept, i.e. doping by foreign impurities.

We have recently proposed [2] a new and different approach for n-type modulation doping in InP-based heterostructures, namely intrinsic doping, where intrinsic defects are utilized to provide the required doping without an external doping source. The success of such an intrinsic doping concept

is clearly evident from our results obtained from InGaAs/InP HEMT structures, where the n-type modulation doping is provided by P_{In} antisites, preferably introduced during off-stoichiometric growth of InP.

In this paper we shall provide an overview of the intrinsic doping approach. We shall first give a brief summary of physical properties of the P_{In} antisite, showing that it fulfils the basic requirements for a dopant. In the main body of the paper we shall review the experimental evidence for the success of the intrinsic doping approach. Detailed physical properties of the intrinsic modulation doping which are important for a useful dopant will be discussed, including doping efficiency, mobility and thermal stability. Advantages and disadvantages of the intrinsic doping approach will also be discussed as compared to the conventional extrinsic doping method.

Experimental

The lattice-matched $In_{0.53}Ga_{0.47}As$/InP heterostructures studied in this work were grown by gas source molecular beam epitaxy (GS-MBE), on semi-insulating Fe-doped InP substrate. Three types of structures were grown and studied: 1) intrinsically doped InGaAs/InP structures grown at low temperature (LT) of 265 °C (denoted as InGaAs/LT-InP); 2) extrinsically doped InGaAs/InP structures by shallow Si donors grown at normal temperature of 480 °C; 3) undoped InGaAs/InP structures grown at normal high temperatures (HT) of 480 °C (referred to as InGaAs/HT-InP or the reference sample). The design of these structures is identical except the top InP layer and is shown in Fig.1 and Table I. For the intrinsically doped InGaAs/InP, the entire structures were intentionally undoped and were grown at a normal temperature of 480 °C except the top InP layer which was grown at 265 °C. The reference sample was also grown with an identical structure except that the top InP layer was in this case grown at 480°C. In the extrinsically doped InGaAs/InP structures, the top InP was grown at normal temperature (480 °C) but was intentionally doped by shallow Si donors.

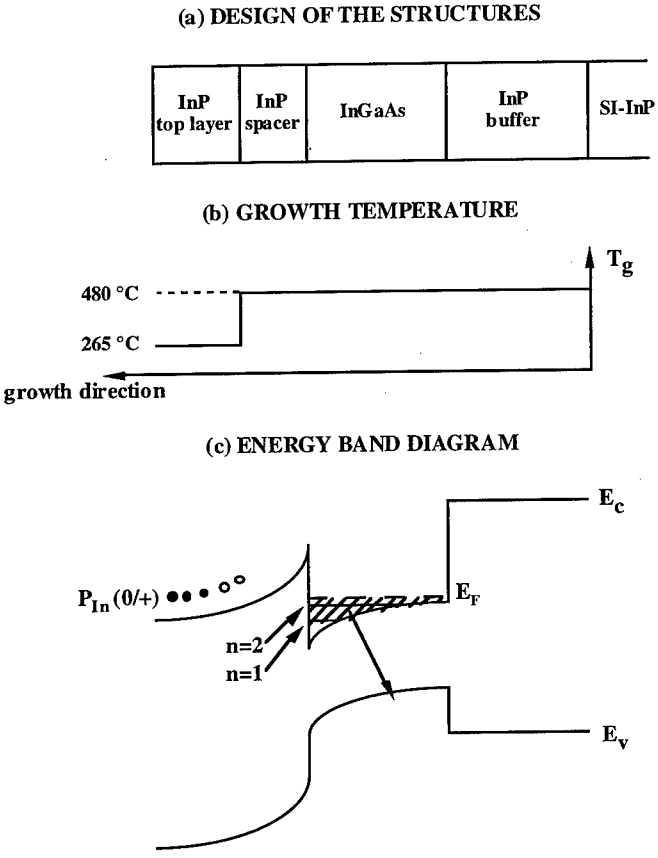

Fig.1 (a) The design of the InGaAs/InP heterostructures studied in this work. (b) A chart of the growth temperatures of the InGaAs/LT-InP structure (the solid curve) and of the reference sample (the dashed curve). (c) A schematic picture of the energy band diagram for the InGaAs/LT-InP structure. For simplicity only two subbands of the 2DEG are drawn in the figure. The filling of the 2DEG is depicted by the shaded region. The arrow across the InGaAs bandgap indicates the PL transition between the 2DEG and photo-excited holes upon optical excitation, shown in Fig. 5.

Table I A list of the selected samples studied in this work. "Ex-doping" refers to extrinsic doping by impurities.

SAMPLE STRUCTURES	PARA-METERS	INTRINSICALLY DOPED InP/InGaAs STRUCTURE	EXTRINSICALLY DOPED InP/InGaAs STRUCTURE	UNDOPED InP/InGaAs STRUCTURE
InP top layer	T_g Thickness Ex-doping	265 °C 500 Å none	480 °C 500 Å Si-doped	480 °C 500 Å none
InP spacer	T_g Thickness Ex-doping	480 °C 100 Å none	480 °C 100 Å none	480 °C 100 Å none
InGaAs active layer	T_g Thickness Ex-doping	480 °C 400 Å none	480 °C 400 Å none	480 °C 400 Å none
InP buffer	T_g Thickness Ex-doping	480 °C 5000 Å none	480 °C 5000 Å none	480 °C 5000 Å none
InP substrate		semi-insulating	semi-insulating	semi-insulating

These structures were experimentally investigated by transport and optical techniques, mainly Shubnikov-de Haas (SdH) oscillations, Hall measurements, photoluminescence (PL), PL excitation (PLE) and magneto-optical spectroscopy. All of these experiments were performed with the aid of an Oxford Instruments special SM4000 optical cryostat with a built-in split-coil 5T superconducting magnet. Lithographically defined Hall bars with six In ohmic contacts were fabricated on the samples for electrical SdH measurements. Hall effect measurements were done at 0.2 T, with the Van-der-Pauw geometry. All transport data were taken by a low-amplitude dc-current (1-5 mA) technique. PL, excited at 2 mW by the 6328 Å line of a He-Ne laser, was spectrally dispersed by a grating monochromator and was collected by a cooled Ge-detector. A tungsten-halogen lamp in combination with a grating monochromator was used as the excitation source in the PLE experiments.

P_{In} antisite in InP - a defect meets basic requirements for a dopant

The development of the intrinsic doping concept stems from our earlier experimental observation [3-6] that the intrinsic P_{In} antisite can be preferably introduced during off-stoichiometric growth of InP at low temperatures (~ 260 - 350 °C) by GS-MBE. In those earlier studies, the free electron concentration of the LT-InP films was found to monotonically increase with decreasing growth temperatures [3, 4] (Fig. 2a). At 265 °C a saturation electron concentration of ~ $3x10^{18}$ cm^{-3} is

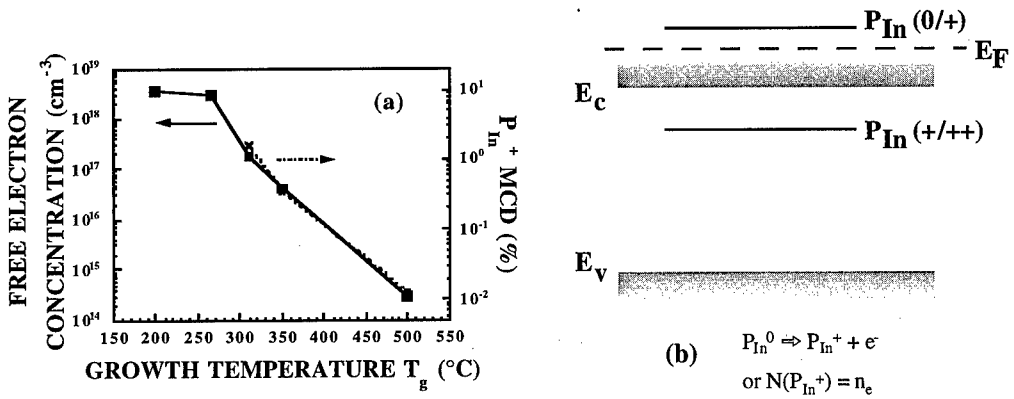

Fig. 2 (a) Correlation between the free-electron concentration and the MCDA intensity (scaling with the concentration) of the P_{In}^+ antisite in LT-InP as a function of the growth temperature T_g. (b) Energy levels of the P_{In} antisite in LT-InP.

reached when the LT-InP exhibits a metallic n-type conduction. The reason for this high n-type conductivity was shown to be due to the abundant presence of the P_{In} antisite, which is a deep double donor [4,5]. The high electron concentration is provided by the auto-ionization of the P_{In} antisite via its first ionization stage, i.e. the (0/+) level, which is located at E_c + 0.12 eV resonant with the conduction band [5] (Fig. 2b). The (+/++) level of the P_{In} antisite was shown to lie within the forbidden bandgap at E_c - 0.23 eV [6]. The observation was first considered to be rather disappointing at the time as the original motivation for LT-InP was to obtain undoped, semi-insulating InP, inspired by the success in off-stoichiometric, As-rich LT-GaAs. The P_{In} antisite, on the other hand, provides properties which are regarded as basic requirements for a dopant, i.e.

- known chemical identification (P_{In})
- established electronic properties
  P_{In} (0/+): E_c + 0.12 eV
  P_{In} (+/++): E_c - 0.23 eV
- control of doping concentration (by varying T_g).

The P_{In} antisite can therefore be employed as an intrinsic n-type dopant in LT-InP.

Intrinsic modulation doping by P_{In} antisite

When the intrinsically doped LT-InP epilayers (by the P_{In} antisite) are used as doped regions in InP-based heterostructures, modulation doping can readily be achieved without invoking an external doping source. In Fig.1 we first show schematic pictures of the InGaAs/LT-InP structures together with a growth temperature ramp and a corresponding energy band diagram. Due to electron transfer from the LT-InP barrier to the InGaAs active layer, a notch potential is formed near the heterointerface where the 2DEG is confined (Fig. 1). A chart of growth temperature for the reference sample is also shown in Fig. 1 as the dashed curve for easy reference.

Below we shall first provide experimental evidence, from optical and transport studies, on the formation of a 2DEG in the InGaAs channel due to the intrinsic modulation doping.

Transport properties of the InGaAs/InP structures

To establish the formation of a 2DEG, quantum transport measurements by SdH oscillations were carried out. In Fig. 3, a SdH oscillation spectrum taken at 1.5 K from the InGaAs/LT-InP structure is shown by the upper curve, with the external magnetic field normal to the heterointerface plane [2]. There are clearly more than one period of the magneto-resistance oscillations vs. reciprocal magnetic field, indicating the presence of a dense carrier gas. Assuming a 2D nature of the carrier gas (to be shown below) two subbands of the 2D gas are shown to be readily occupied, from a detailed analysis of the SdH oscillations. The sheet concentrations of the first and second subbands of the 2D gas are determined to be n_1=6.75×10^{11} cm^{-2} and n_2=4.75×10^{11} cm^{-2}, respectively, yielding a total sheet concentration of 1.15×10^{12} cm^{-2}. This is deduced from an analysis of the period of the SdH oscillations in reciprocal magnetic field $\Delta(1/B)=2e/hn_i$, with the aid of Fourier transformation of the SdH data. Here n_i denotes the sheet concentration of free carriers for the ith subband, e is the electron charge and h is the Planck's constant.

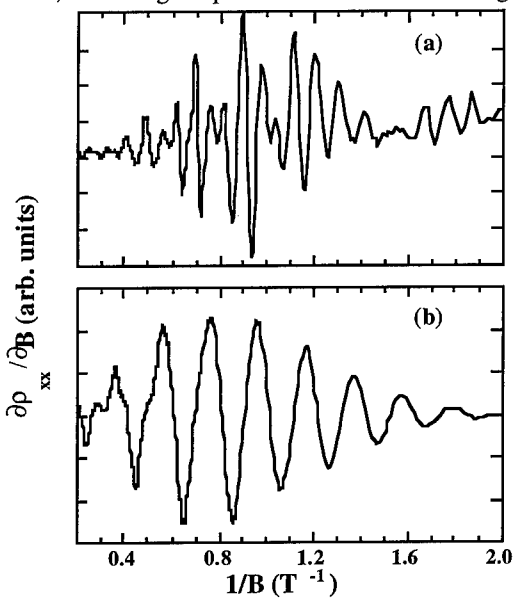

Fig. 3 SdH oscillation spectra taken at 1.5 K in dark from the InGaAs/LT-InP structure (the upper curve) and the reference sample (the lower curve), with the external magnetic field normal to the heterointerface plane. The additional structure at low reciprocal magnetic fields is due to spin splittings. From reference 2.

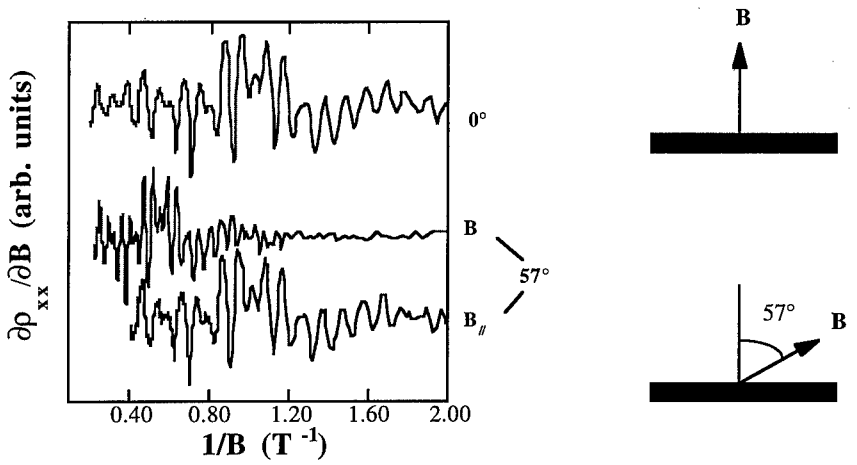

Fig. 4 SdH oscillation spectra taken at 1.5 K in dark from the InGaAs/LT-InP structure, when the external magnetic field is along and at 57 degrees off the growth direction (the upper and middle curve, respectively). The lowest curve is a replot of the middle one, but when only the component of the magnetic field along the growth direction is taken into account. It is clear that it is identical to the upper curve, proving the 2D character of the 2DEG.

The concentration of the corresponding 2D gas in the undoped reference sample, taken under the same experimental conditions, is shown to be much lower. This can be clearly seen by the lower curve in Fig. 3, where only a single and much larger period of the magneto-resistance oscillations is observed [2]. A detailed analysis of the SdH data reveals the concentration in the reference sample to be 2.37×10^{11} cm^{-2}, where only one subband is partially occupied. This value is about an order of magnitude lower as compared to the 2DEG density in the InGaAs/LT-InP structures discussed above, and is mainly induced by electron transfer from residual donors in the undoped InP buffer layer [7].

The 2D character of the carrier gas is revealed from an angular dependence study of the SdH oscillations, shown in Fig. 4. The period of the SdH oscillations obeys a cosine relation of the relative angle between the magnetic field and the growth direction.

From the Hall measurements the 2D carrier gas is determined to be a 2D electron gas with a mobility $\mu_e \approx 1.3\times10^4$ cm^2/Vs. It should be noted that this value is much higher than $\mu_e \approx 5\times10^2$ cm^2/Vs determined independently for a single LT-InP layer grown at the same temperature (i.e. 265 °C) [4].

Optical properties of the InGaAs/InP structures

Parallel optical studies have been carried out on the same InGaAs/InP structures, to further support the formation of the 2DEG and to provide additional information on optical properties of the structures. In Fig. 5 we show PL spectra obtained from the intrinsically doped InGaAs/LT-InP structure [2]. The photon energy of the PL emission at around 0.8 eV (Fig. 5) is consistent with the bandgap of $In_{0.53}Ga_{0.47}As$. The PL spectrum resembles that observed in similar InGaAs/InP and InGaAs/AlInAs HEMT structures [8], where the conventional shallow donors were employed to achieve n-type modulation doping, and was attributed to the recombination between the 2DEG and the photo-excited holes in the InGaAs layer. The splitting of the PL emission in the magnetic field (Fig. 5) is therefore dominated by the Landau level splitting of the monitored 2DEG. The 2D nature can again be shown by an angular dependence study of the Landau level splitting. The electron mass value $m_e^* \approx 0.05m_0$, can be determined from the Landau level splitting observed in the PL experiments (Fig. 5).

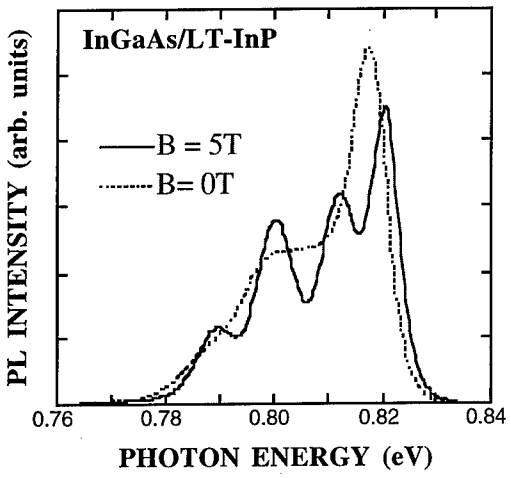

Fig. 5 PL spectra at 1.5 K obtained from the InGaAs/LT-InP structure, due to recombination of the 2DEG and photo-excited holes shown by the arrow in Fig.1, at zero magnetic field (the dashed curve) and 5 T (the solid curve). From reference 2.

Optically detected quantum oscillations (ODQO) [9] identical to the SdH oscillations were observed by detecting this PL emission at the highest photon energy, proving that the PL emission originates from the same 2DEG which gives rise to the electrical SdH oscillations. The ODQO studies also reveal the same sheet concentration of the 2DEG as that deduced from the SdH oscillations.

The key experimental results from the above transport and optical studies of the intrinsically doped InGaAs/LT-InP structures can be summarized as follows:

- 2DEG (from SdH, PL and ODQO)
- $m_e^* \approx 0.05m_0$, (from PL)
- PL photon energy at ~ 0.8 eV (from PL)
- $\mu_e \approx 1.3\times10^4$ cm^2/Vs (from Hall).

As to where the 2DEG is located, there are in principle three possibilities in the structures, i.e. the LT-InP top layer, the InGaAs channel and the undoped InP buffer layer. The buffer layer can be easily ruled out since it is expected to be bulk-like and thus 3D rather than 2D as observed. LT-InP can also be excluded based on the following arguments. The effective mass value $m_e^* \approx 0.05m_0$ differs from the electron mass value $m_e^* = 0.07m_0$ in InP but lies well within the range $m_e^* \approx (0.04\text{-}0.06)m_0$ of the electron effective mass determined for $In_{0.53}Ga_{0.47}As$ [10]. The electron mobility $\mu_e \approx 1.3\times10^4$ cm^2/Vs is much higher than $\mu_e \approx 5\times10^2$ cm^2/Vs determined independently for a single LT-InP layer grown at the same temperature (i.e. 265 °C) [4]. Also, the photon energy of the PL emission is consistent with the bandgap of $In_{0.53}Ga_{0.47}As$ but not InP.

All the experimental facts given above lead to the conclusion that a dense 2DEG is formed in the InGaAs active layer, as a result of electron transfer from the LT-InP barrier. This demonstrates the success of the intrinsic modulation doping in the InGaAs/InP structures.

Other important properties, advantages and disadvantages

Below we shall discuss other important properties of the intrinsic modulation doping which determine the value of a dopant in practical applications. They include doping efficiency, mobility and thermal stability.

The (0/+) level of the P_{In} antisite lies well above the bottom of the conduction band, in contrast to the usual case when the shallow donor level is slightly below the bottom of the conduction band. This may lead to a higher efficiency in the electron transfer from the doped region to the active 2D channel. Our self-consistent theoretical calculations on such HEMT structures by the coupled Poisson-Schrödinger model have shown that the 2DEG concentration can be increased by

approximately a factor of two when the donor level raises from the typical value (~ E_c - 0.007 eV) of shallow dopants to the (0/+) level of the P_{In} antisites at ~E_c + 0.12 eV [2].

The quantum mobility for each occupied subband of the 2DEG in the intrinsically doped structure is about a factor of 1.5-2 higher than that in the extrinsically doped structure, as shown in Table II, from an analysis of fast Fourier transformation of the SdH oscillations [11]. Since both alloy and interface scattering should be nearly identical for both structures, an enhanced quantum mobility can only be due to a reduced scattering of the 2DEG by remote dopants in the intrinsically doped structure. The Hall mobility of the intrinsically doped structure seems, on the other hand, lower than that in the extrinsically doped structure (Table II). Such a lowering in the Hall mobility measured through the entire structure may not necessarily mean a lower Hall mobility of the 2DEG, but reflects the presence of a strong parallel conduction by the LT-InP layer. In fact a significant contribution from such a parallel conduction is evident from the facts that the total Hall concentration is much higher than the 2DEG concentration determined by SdH in the intrinsically doped structure (Table II). This is in contrast to the situation in the extrinsically doped structure, where the total Hall concentration is found to be almost the same as the 2DEG concentration indicating a negligible contribution from the parallel conduction. A detailed investigation of the transport properties is now undertaken to exclude the contribution from the parallel conduction and to extract reliable information on the mobility of the 2DEG.

Thermal stability is a very important factor determining whether a dopant is of practical use, i.e. whether it can survive during over-growth and processing of device structures at an elevated temperature. Our preliminary results from post-growth annealing of the intrinsically doped structure at 500 °C, without gas protection, show a reduction of the 2DEG concentration. This may be due to either the instability of the dopant or the instability of the InP surface. The latter is known to be unstable at above 400 °C. A more detailed study is now in progress.

The unique features of the intrinsic doping approach proposed in this work provide many advantages over the conventional doping by shallow impurity dopants. Above all, no external doping source and procedure are required, which implies not only a reduced risk of side effects such as contamination and memory effects but also avoiding damage by implantation or high temperature diffusion processes of extrinsic dopants. One of obvious disadvantages is, however, a rather limited choice of dopants.

Further investigations are now in progress to understand detailed physical properties connected to the intrinsic doping in InP-based heterostructures and to explore a full potential in device applications as an alternative doping mechanism.

Table II Concentrations (n) and mobilities (μ) of the 2DEG from the intrinsically and the extrinsically doped InGaAs/InP structures studied in this work. Both the quantum mobilities μ_1 and μ_2 deduced from SdH and the Hall mobilities are given. The subscripts 1 and 2 denote the 1st and the 2nd subband of the 2DEG, respectively.

PARAMETERS	INTRINSICALLY DOPED InP/InGaAs STRUCTURE	EXTRINSICALLY DOPED InP/InGaAs STRUCTURE
n_1 (From SdH)	6.75×10^{11} cm^{-2}	6.2×10^{11} cm^{-2}
μ_1 (From SdH)	15500 cm^2/Vs	7000 cm^2/Vs
n_2 (From SdH)	4.75×10^{11} cm^{-2}	2.2×10^{11} cm^{-2}
μ_2 (From SdH)	30500 cm^2/Vs	19500 cm^2/Vs
n_{total} (From SdH)	1.15×10^{12} cm^{-2}	8.4×10^{11} cm^{-2}
n_H (From Hall)	5.7×10^{12} cm^{-2}	8×10^{11} cm^{-2}
μ_H (From Hall)	13000 cm^2/Vs	24000 cm^2/Vs

Summary
A review is given on a novel modulation doping approach in InP-based heterostructures by employing intrinsic defects such as the P_{In} antisites, without invoking an external doping source. The success of this approach is clearly demonstrated by our results from the InGaAs/LT-InP heterostructures, where the required n-type doping in the InP barriers is efficiently provided by the P_{In} antisites preferably introduced during off-stoichiometric growth of LT-InP by GS-MBE. The formation of the resulting 2DEG near the InGaAs/InP heterointerface, due to electron transfer from the intrinsically doped InP barrier, is evident from transport and optical studies. Important physical properties of the intrinsic modulation doping have been discussed, together with their advantages and disadvantages as compared to the extrinsically doped structures. Though it has only been demonstrated for InGaAs/InP heterostructures, the principle of the intrinsic doping concept is in fact rather general and can be extended to applications in other electronic material systems.

Acknowledgements
We are grateful to A.V. Buyanov, T. Lundström, P. Dreszer, E.R. Weber, W. Walukiewicz, B.W. Liang, B. Monemar, E. Sörman, J.A. Wolk, D. Wasik, H.J. Sun and G.D. Watkins for valuable contributions in connection to this work. This work has been supported by the Swedish Council for Engineering Sciences (TFR), the Swedish Natural Science Research Council (NFR) and an AASERT grant from the U.S. Air Force Office of Scientific Research (AFOSR, F49620-93-1-0367TU).

References
1. P. Müller, T. Bachmann, E. Wendler and W. Wesch, J. Appl. Phys. **75**, 3814 (1994); S.L. Jackson, M.T. Fresina, J.E. Baker and G.E. Stillman, Appl. Phys. Lett. **64**, 2867 (1994); J.A. Wolk, W. Walukiewicz, M.L.W. Thewalt and E.E. Haller, Phys. Rev. Lett. **68**, 3619 (1992).
2. W.M. Chen, I.A. Buyanova, A.V. Buyanov, T. Lundström, W.G. Bi and C.W. Tu, Phys. Rev. Lett. **77**, 2734 (1996).
3. B.W. Liang, P.Z. Lee, D.W. Shih and C.W. Tu, Appl. Phys. Lett. **60**, 2014 (1992).
4. P. Dreszer, W.M. Chen, K. Seendripu, J.A. Wolk, W. Walukiewicz, B.W. Liang, C.W. Tu and E.R. Weber, Phys. Rev. **B47**, 4111 (1993)
5. W.M. Chen, P. Dreszer, A. Prasad, A. Kurpiewski, W. Walukiewicz, E.R. Weber, E. Sörman, B.Monemar, B.W. Liang and C.W. Tu, J. Appl. Phys. **76**, 600 (1994).
6. W.M. Chen, P. Dreszer, E.R. Weber, E. Sörman, B. Monemar, B.W. Liang and C.W. Tu, J. Electron. Mater. **22**, 1491 (1993); P. Dreszer, W.M. Chen, D. Wasik, R. Leon, W. Wulukiewicz, B.W. Liang, C.W. Tu and E.R. Weber, J. Electron. Mater. **22**, 1487 (1993).
7. I.A. Buyanova, T. Lundström, A.V. Buyanov, W.M. Chen, W.G. Bi and C.W. Tu, Phys. Rev. **B55**, 7052 (1997).
8. D.G. Hayes, M.S. Skolnick, D.M. Whittaker, P.E. Simmonds, L.L. Taylor, S.J. Bass and L. Eaves, Phys. Rev. **B44**, 3436 (1991); Yong-Hang Zhang, De-Sheng Jiang, R. Cingolani and K. Ploog, Appl. Phys. Lett. **56**, 2195 (1990).
9. I.A. Buyanova, W.M. Chen, A. Buyanov, W.G. Bi and C.W. Tu, Appl. Phys. Lett. **69**, 809 (1996).
10. C.K. Sarkar, R.J. Nicholas, J.C. Portal, M. Razeghi, J. Chevrier and J. Massies, J. Phys. **C18**, 2667 (1985).
11. E. Skuras, R. Kumar, R.L. Williams, R.A. Stradling, J.E. Dmochowski, E.A. Johnson, A. Mackinnon, J.J. Harris, R.B. Beall, C. Skierbeszewski, J. Singleton, P.J. van der Wel and P. Wisniewski, Semicond. Sci. Technol. **6**, 535 (1991).

Materials Science Forum Vols. 258-263 (1997) pp. 813-818

PRESSURE DEPENDENT TWO-DIMENSIONAL ELECTRON TRANSPORT IN DEFECT DOPED InGaAs/InP HETEROSTRUCTURES

D. Wasik[1], L. Dmowski[2], J. Mikucki[1], J. Lusakowski[1], L. Hsu[3,4], W. Walukiewicz[4], W. G. Bi[5] and C. W. Tu[5]

[1] Inst. of Experimental Physics, Warsaw Univ., Hoza 69, 00-681 Warsaw, POLAND
[2] High Pressure Res. Ctr. "Unipress" PAS Sokolowska 29/37, 01-142 Warsaw, POLAND
[3] Physics Department, Univ. of California at Berkeley, Berkeley, CA 94720 USA
[4] Materials Sciences Division, Lawrence Berkeley National Laboratory, Berkeley, CA 94720 USA
[5] Dept. of Elec. and Comp. Eng., Univ. of California at San Diego, La Jolla, CA 92093 USA

Keywords: pressure, heterostructure, InGaAs, InP

Abstract. We have measured the transport properties of InGaAs/InP heterostructures where donor-like native defects incorporated in a low temperature grown InP barrier are used as a source of electrons. Conductance of such structures shows comparable contributions from low mobility electrons in the InP barrier and from the two-dimensional electron gas (2DEG) at the heterostructure interface. We used high hydrostatic pressure to eliminate the low mobility conductance and were able to determine the parameters of two-dimensional electron gas. We find that the highest two-dimensional electron mobility of 3×10^4 cm^2/Vs is determined by the scattering from the background ionized impurities located in the InGaAs quantum well.

Introduction.

Transport properties of two-dimensional electron or hole gases have been extensively studied in a variety of semiconductor systems. Introduction of the concept of modulation doping in which charge carriers are spatially separated from the parent dopants has produced structures with extremely high mobilities. Low temperature electron mobilities exceeding 10^7 cm^2/Vs have been observed in AlGaAs/GaAs modulation doped heterostructures (MDH) [1-3]. In lattice matched InGaAs/InP MDHs, alloy disorder scattering limits the electron mobility to about 1.3×10^5 cm^2/Vs [4].

Typically MDHs are doped with shallow hydrogenic impurities. It has been found recently that undoped InP layers are highly conducting when grown at sufficiently low temperature [5-7]. The electrons responsible for the conductivity originate from native defects tentatively identified as P_{In} with energy levels located at about 120 meV above the conduction band edge [7]. Since the incorporation of the defects can be controlled by the growth temperature, they can be used to dope InP based heterostructures. The feasibility of using defect doping to produce an InGaAs/InP MDH has been recently demonstrated and heterostructures with electron mobilities in excess of 10^4 cm^2/Vs have been fabricated [8].

Hydrostatic pressure is frequently used to change occupation of highly localized defects [9]. Previous studies have shown that in low temperature grown InP the location of the defect energy level relative to the conduction band can be changed with hydrostatic pressure. Application of hydrostatic pressure results in a downward shift of the defect energy with a pressure derivative of $d(E_d)/dP$ = 100 meV/GPa [7]. Therefore, hydrostatic pressure can be used to change the concentration of the conduction band electrons. This is in contrast to shallow hydrogenic impurities whose energy levels follow the conduction band edge under pressure. We show in this work that hydrostatic pressure can be used to control transport properties of defect doped InGaAs/InP MDHs. Specifically, it can be used to eliminate parallel transport in the InP barrier and to make easier the determination of characteristics of the 2D electron gas confined at the InGaAs/InP interface.

Experimental.

InGaAs/InP heterostructures were grown using gas-source molecular beam epitaxy [5]. The sequence of the layers in the structures studied in this work is shown in Fig. 1. Two types of layers with a nominally undoped InP spacer of 5 and 10 nm were grown. Also a control structure

with both the spacer and the top InP layer grown at the normal temperature of 480 °C was investigated. The parameters of the structures measured at about 70 K are listed in Table 1.

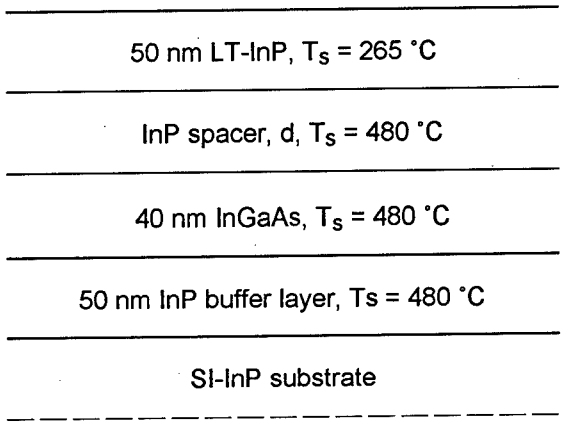

Figure 1. Schematic representation of the InGaAs/InP heterostructure.

Table 1

Structure	Spacer width (nm)	Hall density (cm^{-2})	Hall mobility (cm^2/Vs)
1699	N/A	7×10^{11}	1.2×10^4
1700	10	2.7×10^{12}	2.3×10^4
1908	5	4.8×10^{12}	6.6×10^3

Pressure dependent Hall concentrations and mobilities measured at about 70 K are shown in Figs. 2 and 3. Sample 1699 grown at 480 °C shows n-type conductivity with Hall concentration and mobility practically independent of pressure. This indicates that the conductivity originates from shallow residual impurities with pressure independent binding energies. On the other hand, as shown in Figs. 2 and 3, we observe a significant decrease in Hall concentrations and an increase in Hall mobilities in structures 1700 and 1908 which contain LT InP layers. This means that in these LT MDHs the electron mobility increases with decreasing electron density, a surprising result since for scattering by ionized impurities, the 2D electron mobility is expected to increase with increasing electron density [4].

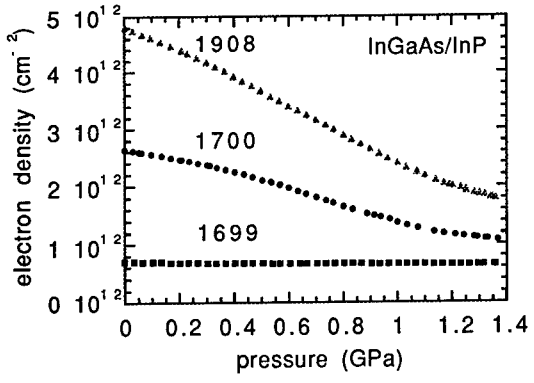

Figure 2. Hall electron densities as functions of pressure in three different structures.

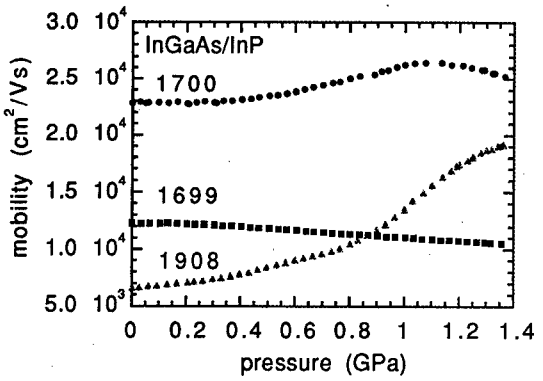

Figure 3. Hall mobility versus pressure in different structures.

To better understand the transport in those structures, we have performed Shubnikov-de Haas (SdH) measurements at atmospheric pressure. As shown in Fig. 4, single period oscillations were observed in the control structure indicating that only the ground subband is occupied in the quantum well. However, the 2D density deduced from the period of the oscillations as function of inverse magnetic field amounts to only 2.9×10^{11} cm^{-2}, which is considerably less than the total Hall concentration of 7×10^{11} cm^{-2} measured in this sample. Also, a strong non-oscillatory magnetoresistance has been observed in this sample indicating a contribution to the conduction from low mobility electrons.

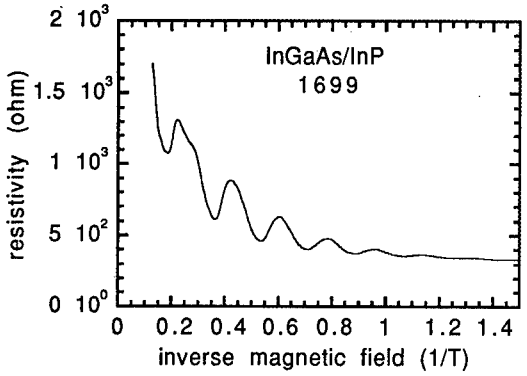

Figure 4. Magnetoresistance versus inverse magnetic field in the control structure

As can be seen in Fig. 5, much more complex SdH oscillations are observed in structure 1908. An analysis of the oscillations demonstrates that two subbands are occupied with 7.38×10^{11} cm^{-2} and 4.72×10^{11} cm^{-2} electrons located in the ground and first excited subband, respectively. Again the deduced total concentration of 2D electrons of 1.21×10^{12} cm^{-2} is lower than the measured Hall concentration of 4.8×10^{12} cm^{-2} and a large non-oscillatory background magnetoresistance is also observed in this structure.

The results in both structures attest to the presence of low mobility carriers. In sample 1699 these carriers are most likely located in the 500 nm thick buffer layer. On the other hand, in the LT-grown structures, the contribution of the highly conducting top LT InP layer is an additional and most likely the dominant channel for low mobility conduction.

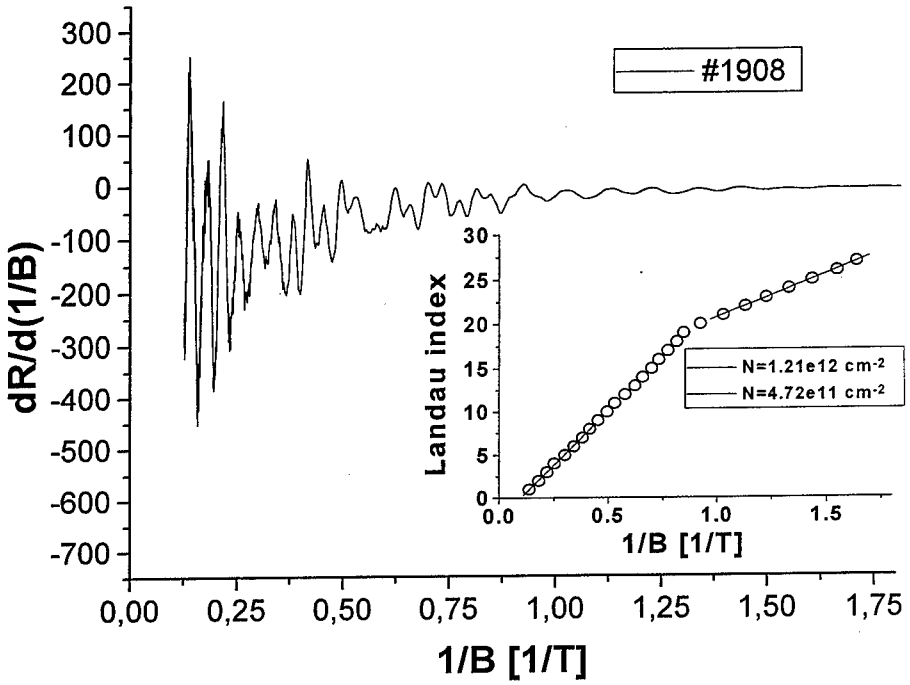

Figure 5. First derivative of magnetoresistance versus inverse magnetic field in structure 1908. The inset shows indexes of the Landau levels corresponding to two distinctly different periods of oscillations indicating that at least two subbands are occupied.

Data analysis and discussion.
In order to separate the contributions from 2D electron gas and the additional low mobility conductance, we use standard expressions for parallel transport [10].

$$n_H\mu_H = \Sigma_i\, n_i\mu_i \qquad (1)$$

and

$$n_H\mu_H^2 = \Sigma_i\, n_i\mu_i^2 \qquad (2)$$

where n_H and μ_H are the concentration and the mobility determined from Hall effect measurements and n_i and μ_i are concentrations and mobilities of parallel conducting layers. There are four possible conducting channels in the structure shown in Fig. 1.: 1) the undoped InP buffer layer; 2) the 2D electron gas confined at the bottom InP/InGaAs interface; 3) the 2D electron gas at the top InGaAs/InP interface and 4) the 3D electrons in the top InP layer. In the control structure 1699 the bottom and the top InP layers were grown at the same temperature therefore they should have similar concentrations of residual donors. However, since the bottom layer is one order of magnitude thicker than the top layer, we can assume that the conductivity originates from layers (1) and (2) only.

In structure 1699 a 2D electron gas density of $n_2 = 2.9 \times 10^{12}\,cm^{-2}$ was deduced from SdH oscillations. The 2D electrons originate from residual donors in the buffer layer and are confined at the bottom InP/InGaAs interface. We have calculated that in order to transfer these electrons to the interface it is required that the buffer layer contains $N_b = 2.5 \times 10^{16}\,cm^{-3}$ of residual donors. This concentration is close to the electron concentration range of 1 to $2 \times 10^{16}\,cm^{-3}$ typically

found in InP or InGaAs layers grown in our system. The sheet density of electrons in the buffer layer $n_1 = LN_{b1} - n_2 = 9.6 \times 10^{11}$ cm^{-2}, where $L = 5 \times 10^{-5}$ is the layer thickness.

Using the known values of n_H, μ_H, n_1 and n_2, we solve Eqs. (1) and (2) to determine the mobilities $\mu_1 = 3.5 \times 10^3$ cm^2/Vs and $\mu_2 = 1.8 \times 10^4$ cm^2/V. The 3D mobility μ_1 appears to be in a lower range of mobilities expected in bulk InP for the donor concentration $N_{b1} = 2.5 \times 10^{16}$ cm^{-3} and corresponds to the total ionized impurity concentration of about 1.7×10^{17} cm^{-3} [11]. Assuming this value as a background impurity concentration, we have calculated the 2D electron mobility using the methods of ref. [4]. We find that at low temperatures, background impurity scattering is the dominant mechanism limiting 2D electron mobility at 1.45×10^4 cm^2/Vs. The calculated mobility is close to the experimentally measured mobility of $\mu_2 = 1.8 \times 10^4$ cm^2/Vs.

As is seen in Fig. 3 incorporation of LT top layers significantly affects the transport properties of the structures. Previous studies have shown that about 5×10^{18} cm^{-3} of native donor-like defects are incorporated into InP grown at 265 °C [7]. This leads to an electron concentration of 4×10^{18} cm^{-3} and a mobility of about 600 cm^2/Vs at 77 K. Thus it is expected that the conductivity in structures with LT grown top layers will be dominated by 2D electron transport at the top InGaAs/InP interface with a possible contribution from 3D electrons in the LT grown layer. Only a small contribution would be found from the electron transport in the buffer layer and at the bottom InP/InGaAs interface. Since the InP buffer layer was grown at the same conditions as the control sample, we can assume that the concentration and mobility of electrons in the buffer layer and at the bottom interface are the same in both types of structures.

Analysis of SdH oscillations in structure 1908 yields a value of $n_3 = 1.21 \times 10^{12}$ cm^{-2} for the concentration of 2D electrons at the top interface. Using Eqs (1) and (2) and the known parameters for the parallel conduction in the buffer and LT layers, we find $\mu_3 = 9 \times 10^3$ cm^2/Vs and $\mu_4 = 650$ cm^2/Vs for the 2D mobility at the top interface and 3D mobility in the LT layer, respectively. It should be noted that the present determination of μ_4 is very close to the 580 cm^2/Vs measured previously in a single LT InP layer [7].

The above analysis shows that at the ambient pressure, up to four parallel channels can contribute to the conductivity, making an analysis of the charge transport very complicated in the LT structures. Thus in sample 1908 only 34% of the total conductivity can be attributed to 2D transport at the top InGaAs/InP interface. It has been shown previously that hydrostatic pressure causes a downward shift of the energy level of the localized donor defect leading to a freeze-out of electrons in LT InP layer [6,7]. Application of the pressure of 1.4 GPa to an InP layer grown at 265 °C reduces the electron concentration by a factor of 300 and the electron mobility by the factor of 2 [6]. This large reduction of electron concentration leads to elimination of the parallel conduction of the low mobility electrons in LT layer .

As is seen in Figs. (3) and (4) the pressure induced freeze-out results in a decrease of the measured effective Hall concentration and an increase of the effective electron mobility in LT MDHs. We find from ref. 7 that at pressures exceeding 1.1 GPa the electron concentration and thus also the parallel conduction in the LT InP layer are reduced by more than one order of magnitude. Under such conditions, the parallel conduction becomes negligible compared to the 2D conduction at the top InGaAs/InP interface. Subtracting a small contribution from the conduction in the buffer layer and at the lower InP/InGaAs interface, we find $n_3 = 1.2 \times 10^{12}$ cm^{-2}, $\mu_3 = 2.1 \times 10^4$ cm^2/Vs and $n_3 = 5.7 \times 10^{11}$ cm^{-2}, $\mu_3 = 3.1 \times 10^4$ cm^2/Vs for the 2D electron gas concentrations and mobilities in structures 1908 and 1700, respectively. Since in sample 1700 only one subband is occupied, we can estimate the 2D electron mobility from a scaling argument. We have calculated that in the control sample with an electron concentration of 2.9×10^{11} cm^{-2} the background ionized impurity mobility is equal to 1.4×10^4 cm^2/Vs. Since, as it has been shown before, [4] the background ionized impurity mobility depends on the electron density as $n^{1.2}$, we expect a mobility of 3.26×10^4 cm^2/Vs for the electron density of 5.7×10^{11} cm^{-2} in structure 1700. The estimated mobility is in good agreement with the experimental value of 3.1×10^4 cm^2/Vs. This results provides additional support for our previous finding that background ionized impurity scattering is the dominant mechanism limiting the low temperature mobilities in LT MDHs.

The above results show that in LT InGaAs/InP MDH at atmospheric pressure there is a large contribution from parallel conduction in the LT InP layer and in the buffer layer. This additional

conduction channel could be eliminated by reducing the buffer layer thickness from 500 nm to 100 nm and the thickness of the top LT InP layer from 50 nm to 10 nm. In the case of LT layers, a similar effect could be achieved by slightly increasing the growth temperature from 265 °C to 300 °C. According to ref. 6 this would result in a more than one order of magnitude lower defect concentration.

In our calculations we have assumed that the defect incorporation mechanism is the same for a single LT InP layer as for a LT InP layer grown on an InGaAs film in a MDH. This is not necessarily true as the formation energy of charged donor defects depends on the Fermi energy, which in turn depends on the location of the conduction band relative to the donor level [12]. In a single LT InP layer, the conduction band is located 120 meV below the defect level. However, in a LT MDH, electrons are transferred to the InGaAs well which has its conduction band about 370 meV below the defect level in InP. Although, in principle, this effect should lead to higher concentration of defects in MDHs, it should be stressed that the effect will be very small if the defect incorporation is controlled by growth induced non-stoichiometry of LT InP films.

Conclusions.

We have shown that standard LT InGaAs/InP MDHs exhibit significant 3D conduction parallel to that of the 2DEG. This undesirable conduction can be significantly reduced by the application of hydrostatic pressures higher than about 1.1 GPa. We find that in all MDHs the 2D mobility is limited by scattering from the background ionized impurities. The highest 2D mobility of 3.1×10^4 was observed in a MDH with a spacer width of 10 nm. This mobility is about 4 times smaller than the intrinsic mobility limit predicted for InGaAs based MDHs[4].

Acknowledgments.

The authors would like to thank Prof. M. Baj for useful discussions. This work was supported in part by the Director, Office of Energy Research, Office of Basic Energy Sciences, Materials Sciences Division of the U.S. Department of Energy under Contract No. DE-AC03-76SF00098 (LBNL) and in part by an AASERT grant from U.S. Air Force Office of Scientific Research (AFOSR, F49620-93-1-0367TU) (UCSD).

References.

1. L. Pfeiffer, K.W. West, H. L. Stormer and K.W. Baldwin, Appl. Phys. Lett. 55, 1888 (1989).
2. T. Saku, Y. Kirayama and Y. Horikoshi, Japn. J. Appl. Phys. **30**, 902 (1991).
3. W. Walukiewicz, in "Semiconductor Interfaces and Microstructures" ed. Z.C. Feng (Singapore: World Scientific) pp. 1-30 (1992).
4. W. Walukiewicz, H.E. Ruda, J. Lagowski and H.C. Gatos, Phys. Rev. B **30**, 4571 (1984).
5. B.W. Liang, P.Z. Lee, D. Shih and C.W. Tu, Appl. Phys. Lett., **60**, 2104 (1992).
6. P. Dreszer, W.M. Chen, K. Seendripu, J.A. Wolk, W. Walukiewicz, B.W. Liang, C.W. Tu, Phys. Rev. **47**, 4111 (1993).
7. P. Dreszer, W.M. Chen, D. Wasik, W. Walukiewicz, B.W. Liang, C.W. Tu and E.R. Weber, Proceedings ICDS-17, eds. H. Heinrich and W. Jantsch, Mat. Sci. Forum, Vols. **143-147**, pp. 1081-1085 (1994).
8. W.M. Chen, I.A. Buyanova, A.V. Buyanov, T. Lundstrom, W.G. Bi and C.W. Tu, Phys. Rev. Lett. **77**, 2734 (1996).
9. M. Baj, L. H. Dmowski and T. Slupinski, Phys. Rev. Lett. **71**, 3529 (1993).
10. R.L. Pertritz, Phys. Rev. **110**, 1254 (1958).
11. W. Walukiewicz, J. Lagowski, L. Jastrzebski, P. Rava, M. Lichtensteiger, C.H. Gatos and H.C. Gatos, J. Appl. Phys. **51**, 2659 (1980).
12. L. Hsu, W Walukiewicz and E.E. Haller, These conference proceedings.

Materials Science Forum Vols. 258-263 (1997) pp. 819-824

STUDY OF IRON-RELATED DEFECTS IN SI-InP BY POSITRON ANNIHILATION SPECTROSCOPY

B. Marí, F.J. Navarro, M.A. Hernández and J.L. Ferrero[1]

Dpt. de Física Aplicada, Universitat Politécnica de València, 46071 València, Spain
[1] Inst. de Ciència de Materials, Universitat de València, 46100 Burjassot, Spain

Keywords: Indium Phosphide, iron, positron annihilation, radiation damage

ABSTRACT

Positron lifetime technique has been used to obtain information about the interaction between Fe and In-vacancy (V_{In}) type defects created after irradiation with thermal neutrons in SI-InP. It has been observed that In-vacancies induced by irradiation are able to trap positrons (τ=300ps). From the results in the as-irradiated SI-InP samples it is inferred that iron originates V_{In}-Fe complexes (τ=340ps). The temperature dependence of the lifetime parameters in the range 15-297 K can be interpreted as evidence for a neutral charge state associated to these complexes.

INTRODUCTION

Iron is normally employed to obtain InP with high resistivities. Fe atoms act as deep acceptors and compensate the residual shallow donors. Nevertheless, this method also introduces many problems in regard to understand the charge compensation mechanism of iron: The total concentration of Fe atoms necessary to get an effective compensation and render the material semi-insulating has to be much higher than the concentration of the residual shallow donors. From some recent studies of the absorption coefficient of InP:Fe single crystals [1], it was concluded that high concentrations of iron tend to form Fe aggregates due to the low value of the solubility limit, which would explain the excess of iron in the InP matrix.

The main purpose of this work was to check on the validity of the model proposed above for the explanation of compensation mechanism of iron in InP. To provide an experimental basis for discussing this question, we have measured the neutron dose dependence of the lifetime parameters (lifetimes τ, intensities I) of positrons in InP and InP:Fe and also the temperature dependence of the lifetime spectra in InP:Fe samples.

Irradiation with thermal neutrons, besides being a very useful method for doping purposes of semiconductors when a precise amount of impurities is required [2], it can be alternatively used to produce indium vacancy related defects [3], and induce changes in the electronic structure of the iron clusters capables of being detected by positron annihilation spectroscopy. This technique has demonstrated its capability in the characterization of defects in semiconductors [4].

EXPERIMENTAL

For comparison purposes two types of InP single crystal samples have been studied: one of them without iron and the other containing an iron concentration of about 10^{17} cm^{-3}. In both of them, neutron irradiation were performed in air at fluences from $1.06x10^{15}$ to $2.6x10^{17}$ $n°cm^{-2}$ in order to obtain transmuted tin concentrations ranging from $2x10^{15}$ to $2x10^{18}$ cm^{-3}.

In the irradiated samples, the positron lifetime measurements were conducted using the spectrometer described in ref. 3 having a time resolution of 260 ps (full width at half-maximum). The source material ($^{22}NaCl$) was enclosed between two kapton foils (10 μCi). Each lifetime spectrum contained about $3x10^6$ counts, accumulated during a time period of 10-15 hours. The lifetime spectra were fitted using the Positronfit program [5] to a sum of exponential decays subtracting two source corrections due to the contribution of positrons annihilating in the positron source (τ^{1c} = 382ps; I^{1c} = 8%) and in air(τ^{2c} =1ns; I^{2c} = 1%). In order to achieve a statistically good fit the spectra had to be decomposed into two components.

After irradiation, a second set of measurements were performed on the Fe-doped sample. It was transferred at 14K to a closed cycle He cryostat and the temperature dependence of the lifetime parameters were obtained by measuring at 15 K, from 15 to 300 K in 50 K intervals. In this case, the temperature was raised to the required value and maintained for 15-20 h. For this set of measurements the time resolution was 310 ps.

RESULTS AND DISCUSSION

The time spectrum of unirradiated samples has been fitted with one exponential decay component; the values obtained (246 ± 2 ps for InP and 247 ± 2 ps for InP:Fe) agree with those reported for these materials by Dlubek *et al* [6]. A two-terms fit, as suggested by other authors [7] yields a very low value for I_2 (less than 1-2%) and does not substantially improve the variance of the fit. The lifetime value found in InP:Fe means that the nature and concentration of dopant does not affect the positron annihilation in the bulk, in agreement with the results reported by Bretagnon *et al* [7] for InP.

In the figures 1 and 2 the evolution of the lifetime parameters as a function of the transmuted tin concentration is shown for both InP and InP:Fe samples. In InP, a second lifetime with a value τ_2 = 300 ± 9 ps is clearly obtained with an increasing intensity, I_2, up to values of 80 %; τ_1 decreases with the tin concentration from 245 to 170 ps. In InP:Fe, the shortest lifetime is constant near to a mean value of 210 ± 6 ps; the long lifetime, τ_2, increases from 309 ± 5 ps to 340 ± 7 ps with an intensity that reachs a maximum value of 35%.

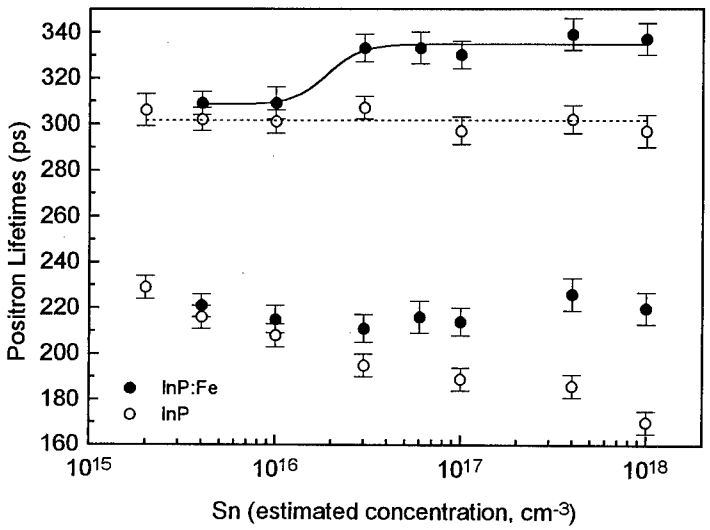

Fig.1. Positron lifetimes (τ_1, τ_2), obtained from two-component analyses, as a function of the expected tin concentration in Fe-undoped InP and semi-insulating InP.

According to previous works, the second lifetime of 300ps obtained in InP can be assigned to positrons trapped at In monovacancy type defects forming during irradiation [8]; the decrease of τ_1, in the framework of the one-state trapping model, indicates that the positron trapping rate to the In vacancies is on the increase with the neutron dose.

It has to be noted that quite differences are found in the lifetime parameters between the Fe-doped and the undoped InP samples. In InP:Fe, the increase of τ_2 means that the positron trapping in the 300 ps-configuration tends to disappear which can be explained accepting that a new positron trap is formed during irradiation with mainly two characteristics: a) A lower electronic density than that associated to the V_{In} (that explained the lifetime higher, τ_2^{Fe}-τ_2 = 40 ps; and the I_2^{Fe} lower than I_2 for the highest fluences used in this work) ; b) it would be related to the presence of iron in the InP matrix, which is, in principle, the only difference between the two kinds of starting materials.

The lack of positron trapping by the 300-ps configuration in the InP:Fe samples could be due to the dissociation of iron precipitates/clusters caused by the energetic particles (γ, β^-) involved in the doping process. Iron precipitates are created during the growth due to the high concentration of Fe atoms in the melt, which exceed the solubility limit [1]. Fragments of these clusters or isolated Fe atoms tend to associate with the products of the irradiation, V_{In} and tin atoms, forming complexes of the type //V_{In}-Fe//Sn-Fe//V_{In}-Sn-Fe//.

In regard to the charge state of the positron traps induced by irradiation in InP:Fe, the temperature dependence of the mean lifetime, $\tau = I_1\tau_1+I_2\tau_2$, shown in figure 3 can be interpreted as evidence for a neutral charge state. According to Puska *et al* [9], the positron trapping rate at low temperatures for negatively charged defects tends to increase with decreasing temperatures, while for neutral traps it is expected not to be temperature dependent. In our case, if the induced defects were negatively charged an increase in τ at low temperatures would be observed instead of the evolution shown.

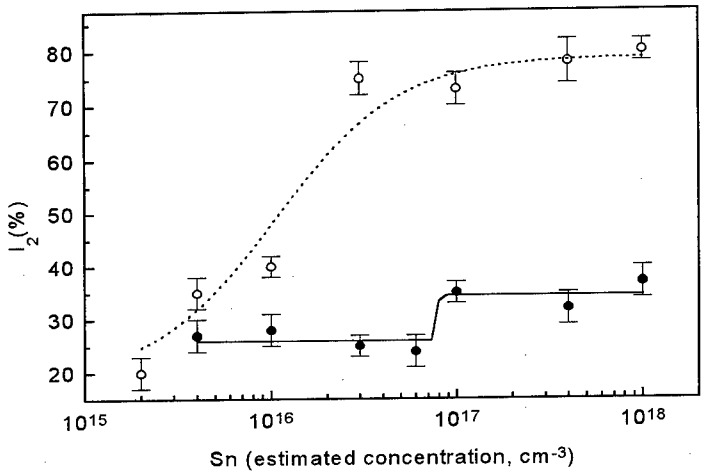

Fig.2. I_2 versus tin concentration in Fe-undoped InP (empty circles) and semi-insulating InP (full circles).

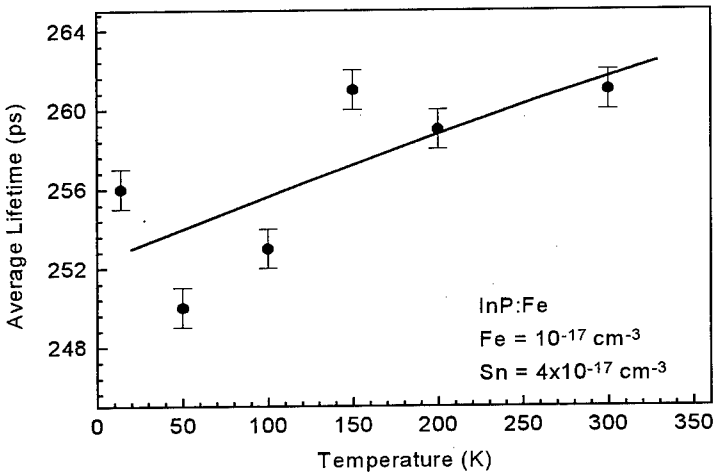

Fig. 3. The evolution of the average lifetime, $\tau=\tau_1I_1+\tau_2I_2$, in neutron irradiated InP:Fe as a function of the measuring temperature.

CONCLUSIONS

Clear evidence of positron trapping has been observed in neutron irradiated InP. The lifetime associated to In-vacancies is $\tau = 300$ ps. The lifetime of 340 ps found in the Fe-doped InP is mainly associated with //V_{In}-Fe//Sn-Fe//V_{In}-Sn-Fe// complexes formed during irradiation. At temperatures in the interval $15 \leq T \leq 297$ K, these complexes exhibit annihilation characteristics attributed to neutral charge states.

ACKNOWLEDGEMENTS

This work was supported in part by the Generalitat Valenciana under grant GV-3235/95, and by the Ministerio de Educación y Ciencia grant no. PB95-0741.

REFERENCES

1. R. Fornari, E. Gilioli, M. Moriglioni, M. Thirumavalavan and A. Zappettini, J. Crystal Growth **166**, 576(1996).
2. M.A. Vesaghi, Phys. Rev. B **25**, 5436(1982).
3. F.J. Navarro, L.C. Damonte, B. Marí and J.L. Ferrero, J. Appl. Phys. **79** (12), 9043(1996).
4. C. Corbel, M. Stucky, P. Hautojärvi, K. Saarinen and P. Moser, Phys. Rev. B **38**, 8192 (1988).
5. P. Kirkegaard and M. Eldrup, Comp. Phys. Commun. **7** 401(1974).
6. G. Dlubek, O. Brümmer, F. Plazaola, P. Hautojärvi and K. Naukarinen, Appl. Phys. Lett. **46**, 1136(1985).
7. T. Bretagnon, S. Dannefaer and D. Kerr, J. Appl. Phys. **73** (9), 4697(1993).
8. B. Marí, F.J. Navarro, M.A. Hernández and J. Riera, Nucl. Inst. Method B **120** 240(1996).
9. M.J. Puska and R.M. Nieminen, Rev. Mod. Phys. **66** (3), 841(1994).

Materials Science Forum Vols. 258-263 (1997) pp. 825-830

HOMOGENEITY OF Fe-DOPED InP WAFERS USING OPTICAL MICROPROBES

L.F.SANZ[1], M.A.GONZALEZ[1], M.AVELLA[1], A.ALVAREZ[1], J.JIMENEZ[1], R.FORNARI[2]
[1] Física de la Materia Condensada, ETS Ingenieros Industriales, 47011 Valladolid Spain
[2] MASPEC-CNR Institute, via Chiavari 18/A, 43100 Parma, Italy

Keywords:InP, Fe-doping, photocurrent, photoluminescence, homogeneity

Abstract.

The homogeneity of semiinsulating Fe-doped InP is studied by means of photoetching and two spatially resolved techniques: Scanning Photocurrent (SPC) and Scanning Photoluminescence (SPL). These techniques provide complementary information about the local compensation and the iron distribution. As an example the homogeneity of wafers cut from an annealed LEC crystal is studied. The comparison with previous investigation on wafer-annealed Fe doped InP showed that ingot annealing does not produce comparable uniformity improvements.

Introduction

Semiisulating InP is an important material for optoelectronics and high frequency microelectronic applications. Electric compensation is obtained by adding iron to the charge before growing the crystal by LEC (Liquid Encapsulated Czochralski) method. However, big amounts of iron in the melt are required to get high resistivity due to the low segregation of iron in InP (distribution coefficient k~0.0001) [1]. This low segregation coefficient results in non-uniform distribution, together with excess of iron, which can produce contamination of the layers grown on these substrates by iron outdifussion [2,3]. Substitutional iron Fe_{In}, is electrically active; it introduces a mid-gap acceptor, that compensates residual shallow donors; it can be either neutral, Fe^{3+}, or ionised, Fe^{2+} ($[Fe^{2+}]=N_D-N_A$). Several crucial issues have to be considered in order to obtain good substrates: i) to minimise the iron content necessary to get semiinsulating material, ii) to obtain substrates with good electrical properties (high mobility and high resistivity) and iii) to produce homogeneous material.

The improvement of the material in the terms above described has been attempted by thermal treatments [4,5,6]. However, in order to check the benefits of these treatments, experimental techniques providing information about the homogeneity of these substrates at both long (mm's) and short (μm's) ranges are required. Fe-doped InP has been seen to be very sensitive to optical beams, in particular high contrast maps can be obtained by SPC (Scanning Photocurrent) [7,8] and SPL (Scanning Photoluminescence) [9]. We present herein

results concerning the photoluminescence and photocurrent mapping of InP:Fe wafers cut from the central part of annealed Fe-doped InP crystals grown by the LEC (Liquid Encapsulated Czochralski) method.

Samples and experimental set-up

Samples were sliced from a thick (2 cm) block cut from an Fe-doped InP ingot. Prior to being cut in wafers this block was annealed at 900 °C for 60 hours in phosphorous vapour (~1bar). The resistivity and the Hall mobility of the samples generally increased by the thermal treatment; however the variation was dependent on the distance of the corresponding wafer from the extremes of the annealed block. In particular, the resistivity was found to increase by a factor 3-5 in the wafers close to the external surfacebut only 1-2 in the center of the block (see ref. 5 for details). Wafers were etched by a selective DSL (Dilute Sirtl applied with light) solution [10].

SPC measurements were carried out at liquid nitrogen temperature. The optical excitation is done with the 1320 nm line of a cw YAG laser focused onto the sample through a high magnification long distance work microscope objective. The cryostat with the sample was mounted on a motorised x-y stage allowing to scan along both x and y axes. Details of the experimental set-up are given elsewhere [7,8].

SPL measurements were carried out at room temperature. Optical excitation was done with the 514.5 nm line of an Ar^+ laser through the microscope objective. The diameter of the laser beam onto the sample is about 1 μm. The sample was mounted on a motorised xy stage. Band to band photoluminescence emission was analysed with a monochromator and detected by a cooled photomultiplier.The monochromator was set at wavelength, λ_{max}, such that the maximum PL intensity was recorded for each point of the map. of the maximum luminescence emissionwas selected. Photoluminescence intensity maps at λ_{max} are obtained by the displacement of the sample under the focused laser beam.

Results and discussion

SPC measurements were done under 1320 nm excitation; this light excites holes from neutral iron levels Fe^{3+}, and electrons from the ground state, ^5E, of ionised Fe^{2+}. For this wavelength the optical cross section for holes is one order of magnitude larger than the optical cross section for electrons [11]. Besides, $[Fe^{3+}]>>[Fe^{2+}]$ for high resistive material, which should mean that the extrinsic photocurrent is mainly driven by holes. The photocurrent intensity is proportional to the compensation ratio $[Fe^{3+}]/[Fe^{2+}]$ [7]; the higher this ratio, the higher the photocurrent. Thus, the photocurrent contrast reveals changes in this ratio.

SPC maps of as-grown and ingot annealed samples are shown in fig 1. Photocurrent fluctuations are in the same range for both as-grown and ingot annealed samples. From these results, it can be argued that ingot

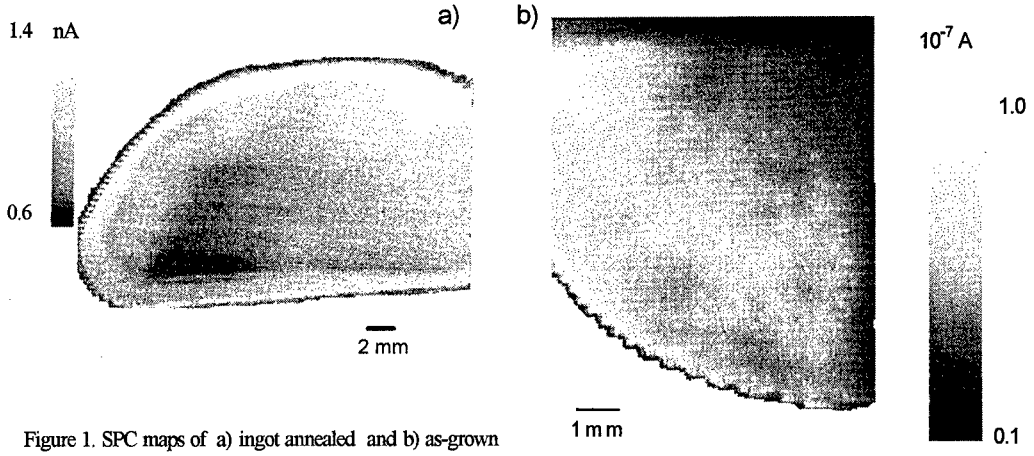

Figure 1. SPC maps of a) ingot annealed and b) as-grown InP:Fe wafers

annealing does not result in a substantial improvement of the homogeneity in terms of $[Fe^{3+}]/[Fe^{2+}]$ ratio. It should be noted that non uniformity is mainly related to local fluctuations of [Fe3+], while net donor concentration is rather homogeneous in as-grown material [8, 12]. In addition to this, some areas characterised by high photocurrent are observed in the annealed sample.

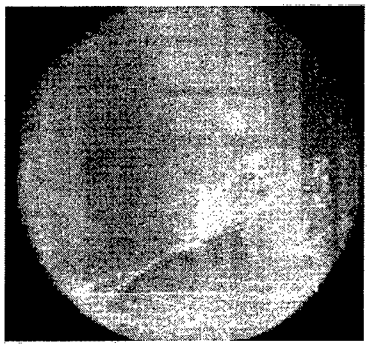

Figure 2.- Photoluminescence map after 60h ingot annealing at 900ºC and cooling rate of 1ºC/min. (size= 42x36.75 mm)

DSL etching evidences the presence of different inhomogeneities. In particular, before annealing, doping growth striations and dislocations decorated by microdefects are revealed. After ingot annealing, the dislocation atmospheres spread out, though decorating microdefects are not solved. Doping growth striations are almost completely removed.

A photoluminescence map of a wafer cut from the annealed block is shown in fig 2. Features with the typical shape of doping growth striations can be seen. This evidences the high sensitivity of PL mapping, since SPC and photoetching were unable to reveal these features after annealing. Since a complete redistribution of iron is not achieved for ingot annealing, it can be concluded that ingot annealing is not the adequate way to optimize InP homogeneity [8]. This crystal has some twins, as can be observed on the whole wafer PL map. The higher PL intensity around the twin suggests that this region is depleted of iron, probably gettered by the dislocations present at the grain boundary [13].

Recent studies have demonstrated that shallow donor losses and iron diffusion are the main mechanisms accounting for the changes in the electric properties of annealed InP [5]. It is interesting to note that the spatial correlation between SPL and SPC maps is not one to one. In fact, some regions present correlation, while other are anticorrelated. It should be noted that a good correlation, high PL and high PC, is observed around some defects revealed by DSL, as dislocations, twins Fig.3. It should be noted that the high PL is associated with Fe-denuded areas, while high PC means high $[Fe^{3+}]/[Fe^{2+}]$ ratios. In order to reconcile these two experimental evidences, it must be assumed that the dislocations are acting as gettering centers for both Fe and residual donors. The region around this defect is therefore denuded of both species.This further proves that crystallographic defects play an important role (as "sinks") during the thermal treatments. Recently, we demonstrated that wafer annealing gives improved electrical properties and good homogeneity [8], in that case it was argued that the proximity of the wafer surface (also playing as a "sink") was responsible for the improved homogeneity.

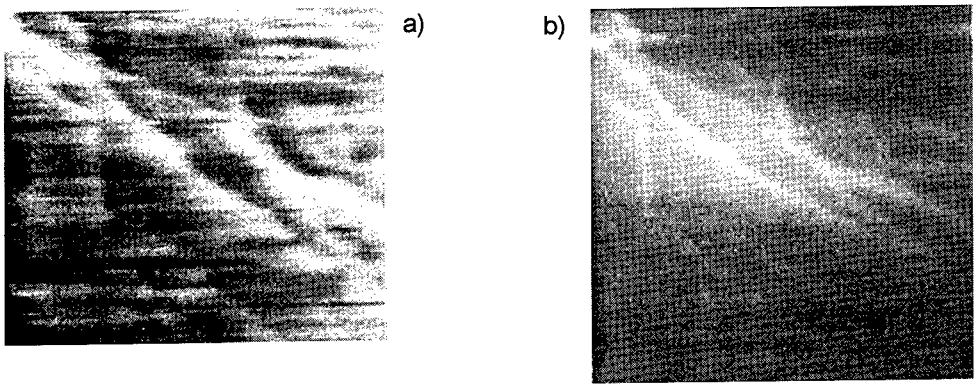

Figure 3.- a) SPL map (1x0.9 mm^2) and b) SPC map (1x1 mm^2) of a microdefect in the ingot annealed sample.

In summary combined SPC and SPL studies of Fe-doped InP are of high interest, since they provide complementary information about very important features of these substrates. In particular, they are able to assess the homogeneity of the wafers at both long and short range in terms of local compensation and total iron content. Ingot annealed InP was studied and the consequences in terms of uniformity were discussed, showing that ingot annealing does not produce significant improvements in terms of homogeneity.

Acknowledgements This work was funded by CICYT (project Mat 94-0042). Financial support from the Spanish-Italian International Cooperation Program is acknowledged.

References

1. G.Müller; Phys. Scripta **35**, 201 (1991)

2. J. Chevrier, M.Armand, A.M. Huber and N.T.Linh; J.Electron. Mater. **9**, 75 (1980)

3. H.Kamada, S.Shinoyama and A.Katsui; J.Appl.Phys. **55**, 315 (1984).

4. M. Uchida, K.Kainosho, M.Ohta and O.Oda; Proc. 8th Int. Conf. on InP and Related Materials (1996) IEEE Catalog #96CH35930, p.43

5.A.Zappettini, R.Fornari and R.Capelletti; Mater. Sci.Eng. B **45**, 147 (1997)

6. R. Fornari, A.Zappettini, E.Gombia, R. Mosca, K.Cherkaoui and G.Marrakchi; J.Appl. Phys. **81**, 7604 (1997)

7.M. Avella, J. Jimenez, A. Alvarez, M.A. Gonzalez and L.F. Sanz, Mater. Sci. Eng. B**28**, 111 (1994)

8.M.Avella, J.Jimenez, A.Alvarez, R.Fornari, E.Gilioli and A.Sentiri; J.Appl. Phys. (to be published)

9. J.Y.Longere, K. Schohe, S. Krawczyk, R. Coquille, H. L'Haridon and P.N. Favennec, J. Appl. Phys. **68**, 755 (1990)

10.T. Takanohashi and K. Nakajima, J. Appl. Phys. **65**, 3933 (1989)

11.A. Alvarez, M. Avella, J.Jimenez, M.A. Gonzalez and R. Fornari, Semicond. Sci. Technol. **11**, 941 (1996)

12.W. Meier, H. Ch. Alt, Th. Vetter, J. Völkl and A. Winnacker; Semicon. Sci. Technol. **6**, 297 (1991)

13. D.B.Holt, G.Salviati; J.Cryst. Growth **100**, 497 (1990)

Materials Science Forum Vols. 258-263 (1997) pp. 831-836

OSMIUM RELATED DEEP LEVELS IN p-InP AND THEIR INTERACTION WITH ALPHA RADIATION

Shazia Parveen, Aurangzeb Khan, Umar S. Qurashi, N. Zafar, M. Zafar Iqbal, L. Köhne*, A. Dadgar* and D. Bimberg*

Semiconductor Physics Laboratory, Department of Physics, Quaid-i-Azam University, Islamabad, Pakistan.

*Institut für Festkörperphysik, Technische Universität Berlin, Hardenbergstr. 36, 10623 Berlin, Germany.

Keywords: Transition-metal impurities, InP, Defect complexes, Radiation effects.

Abstract. We report results of a combined electrical and optical DLTS study of Os-doped p-type InP grown by low pressure metalorganic chemical vapour deposition (LP-MOCVD). Two prominent deep levels in the lower half band-gap, labelled OsA and OsB, and one in the upper half (Os1) have been attributed to osmium. Detailed comparison of reduced-reverse bias, electrical injection and optical DLTS spectra yields important information on their relative capture cross-sections for the majority and minority carriers, necessary to ascertain their role in determining the electrical properties of the material.

Preliminary results of the investigations of the response of the Os-related deep-levels in p-InP to irradiation with alpha particles, are also reported. The minority carrier (electron) level Os1 is found to show a strong enhancement while the majority carrier levels OsA and OsB show only a slight increase with irradiation. The strong enhancement of Os1 indicates that this defect is either a complex of Os with the radiation-induced primary defects such as the two types of vacancies and interstitials or is electrically activated by the introduction of these defects.

Introduction

Semi-insulating substrates are the primary need of the emerging InP-based fast electronic and optoelectronic device technology. The semi-insulating character is achieved by compensating the residual donors and acceptors. Doping with transition metals (TM), known to introduce near-mid gap deep levels in most semiconductors, is commonly used for obtaining semi-insulating behaviour in semiconductors. Although the deep acceptor iron is currently used to compensate n-type InP but it suffers from the severe limitation of a low thermal stability owing to its large diffusion coefficient [1]. There is, consequently, a high level of research activity, directed at exploring alternative dopants in InP to produce thermally stable semi-insulating InP.

Heavier transition metals are expected to be thermally more stable candidates as compared to 3d-TMs due to their smaller diffusion coefficients. A systematic research effort to this end has recently been initiated by us. As part of this program, doping by 5d-TM osmium has been tried for this

purpose. Two prominent deep levels in the lower half band-gap and one in the upper half have been detected [2, 3]. The aim of this report is to provide results of a deep level characterization study of this impurity in p-type InP using both electrical and optical deep level transient spectroscopy focussed, in particular, on the investigation of the relative carrier capture cross-sections for electrons and holes. Preliminary results of an irradiation study to investigate the nature of these defect states are also reported here.

Experimental Details

The samples were grown by low pressure metalorganic chemical vapour deposition (LP-MOCVD) at a typical temperature of 640°C, using trimethyl-indium, phosphine, dimethyl-zinc for p-type doping and silane for n-type doping, with hydrogen as the carrier gas. For osmium doping osmocene [$Os(C_2H_5)_2$] precursor was used. The epitaxial structures consisted of 2-3 μm thick p-layers on top of which n^+ layers, 0.7-1 μm in thickness, were grown. Mesa type junction diodes with diameters 200-800 μm were fabricated by photolithography and wet chemical etching. Ohmic contacts in the form of circular dots were provided to the top n^+ layer and uniformly on the back surface by vacuum evaporation/alloying of appropriate metallic films. The devices were then mounted on ceramic chip-carriers and/or TO-5 headers with bonded leads for electrical and optical measurements.

Deep level investigations were conducted by using the electrical deep level transient spectroscopy (DLTS) and optical deep level transient spectroscopy (ODLTS) techniques. DLTS and ODLTS measurements were carried out with a computer controlled system made by SPC Electronics, Japan. Optical excitation was provided by a light emitting diode with a peak emission wavelength of 780 nm. For some of the DLTS measurements, a manual, high sensitivity DLTS system based on the lock-in principle was also employed. The samples were irradiated at room temperature with 5.48 MeV alpha particles from a 9 μCi ^{241}Am radioactive source.

Results and Discussion

Deep Level Spectra

The typical DLTS spectra for the majority and minority carrier emission are shown in Fig. 1 (a) and (b), respectively. Two prominent hole emitting deep levels labeled OsA and OsB are clearly seen in the majority carrier spectrum while an electron emitting level Os1 is observed in the minority carrier injection spectrum. Apart from these dominant deep levels, a small peak labeled OsC can also be seen on the low temperature shoulder of the OsB peak.

The emission rate signatures of these levels are shown on the Arrhenius plots given in Fig. 2. The thermal activation energies and $\sigma(\infty)\, e^{\Delta S/k}$ values for the different deep levels obtained from the slopes and intercepts of the respective Arrhenius plots are given in Table I - here $\sigma(\infty)$ is the carrier capture cross-section at $1/T = 0$ and ΔS is the entropy change accompanying thermal emission of the carrier, k being the Boltzmann constant. It may be added here that all the three prominent peaks are

observed to exhibit a pronounced shift with the change in applied bias during DLTS scans indicating a strong enhancement of the emission rates by the junction electric field. The detailed quantitative analysis of this field dependence will be the subject of a separate study.

Optical DLTS

It is well recognized that some important minority carrier deep levels may remain undetected in electrical injection DLTS in case their capture cross-section for majority carriers is greater than their minority carrier capture cross-section, since both kinds of carriers are present during the capture process. In order to investigate the presence of any such levels in our samples and also to obtain detailed information on the relative capture cross-sections for the two types of carriers, we carried out optical DLTS (ODLTS) experiments using light pulses with above band-gap photon energy for deep level filling.

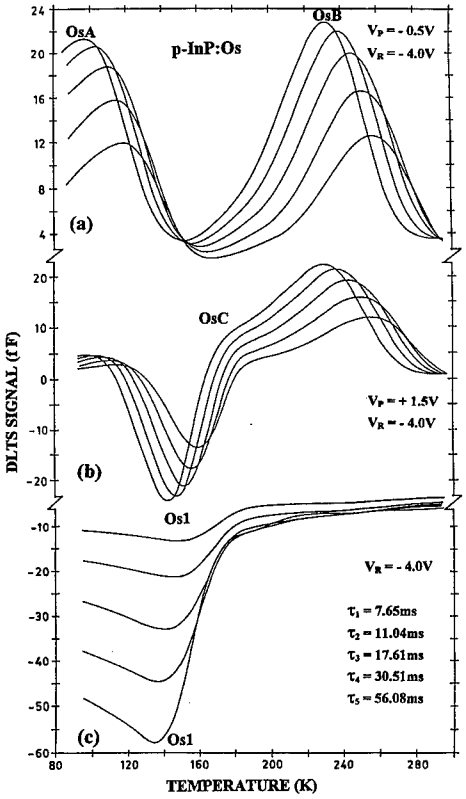

Fig.1. DLTS spectra of p-type InP:Os for five different emission time constants τ_1-τ_5: (a) majority carrier emission spectra, (b) minority carrier electrical injection spectra and (c) minority carrier optical (ODLTS) injection spectra.

The ODLTS spectra are also displayed in Fig. 1(c) for better comparison with the electrical DLTS spectra. The majority carrier peaks show a dramatic disappearance in the ODLTS spectra - while the minority carrier peak due to the level Os1 is seen to undergo a pronounced increase under optical excitation, by a factor of ~ 2.4, as compared to the electrical injection scan. To further verify these observations we carried out ODLTS experiments with different light intensities. The peaks corresponding to the levels OsA and OsB

TABLE I. Parameters of hole and electron levels in Os-doped MOCVD grown p-InP.

Label	Position		$\sigma(\infty)\, e^{\Delta S/k}$ ($x10^{-17}$ cm^2)	N_T($x10^{13}$ cm^{-3})
	peak (@230 s^{-1}) (K)	deep level (eV)		
OsA	148	E_V+0.21	9.7	3.9
OsB	264	E_V+0.39	6.0	5.1
Os1	179	E_C-0.32	3.9 x 10^3	>20.2

remain unobservable even with the smallest light intensity, whereas Os1 shows a systematic variation of the peak height with the excitation intensity. In contrast, the response of these peaks to electrical injection of minority carriers (Fig.1(b)), shows a very different behavior. The OsA peak undergoes a strong reduction with respect to the majority carrier emission spectrum but OsB shows no or very slight reduction in the electrical injection spectrum.

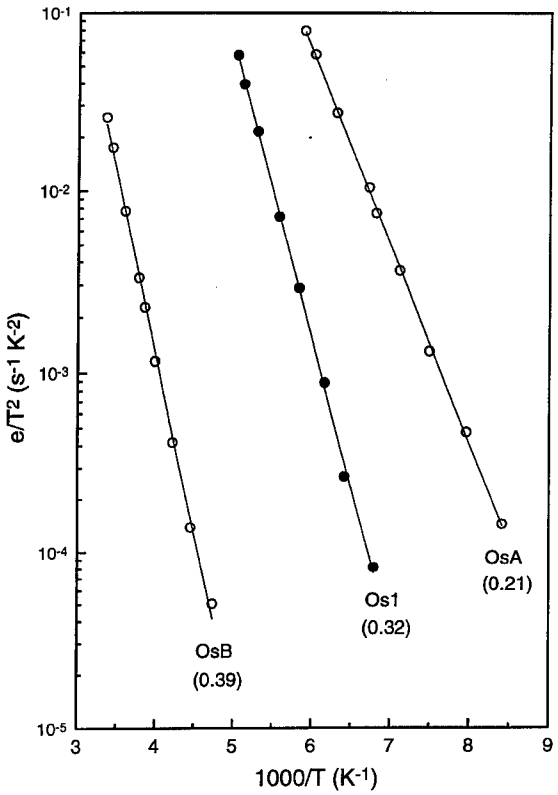

Fig. 2. Arrhenius plots of thermal emission rates of the prominent levels observed in the spectra of Fig. 1. Symbols represent the experimental data while the lines are the least squares fits to the data.

These results can be interpreted in terms of the competing capture rates c_n and c_p for electron and hole capture at the respective deep levels. Considering the fact that $c_n = \sigma_n n$ and $c_p = \sigma_p p$, where σ's represent the capture cross-sections and n and p, the electron and hole densities, respectively, it is clear that the observed peak height for a given deep level will be determined by the relative concentrations of minority and majority carriers, (n/p) for our n^+p diodes, and the ratio of the two capture cross-sections. Whereas n<p in our electrical injection measurements, $n \cong p$ for optical injection since light is incident directly on the junction in our mesa diodes. Comparison of the DLTS data from our electrical and optical experiments, therefore, allows us to draw important conclusions about the relative capture cross-sections (σ_n/σ_p) of electrons and holes for a particular deep level. Further, the relative magnitudes of the capture cross-section of a particular type of carrier for the different deep levels can be inferred. From a detailed comparison of our spectra described above we draw the following conclusions in order to achieve a consistent interpretation of all the observations:

i) $\sigma_n \geq \sigma_p$ for both OsA and OsB since they are not observed in ODLTS,

ii) electrical injection experiments imply that consistency with (i) requires $\sigma_n > \sigma_p$ for OsA while $\sigma_n \cong \sigma_p$ for OsB,

iii) observation of Os1 in electrical injection DLTS and increase in ODLTS implies that $\sigma_n >> \sigma_p$ for Os1,

iv) different responses of OsA and OsB to electrical injection imply that $\sigma_{nB} << \sigma_{nA}$.

Effects of Alpha Irradiation

High energy irradiation can act as a useful probe for the microscopic structure of the defects. In order to investigate the nature of the Os-related defects described above we studied the response of our samples to 5.48 MeV alpha radiation. The electrical DLTS spectra of our samples before and after irradiation with an α-particle dose of ~$1.33 \times 10^{10} cm^{-2}$ at room temperature are shown in Fig.3. Whereas the peaks due to the levels OsA and OsB show a slight increase, the peak corresponding to Os1 shows a significant increase after irradiation - the peak height increases by a factor of ~1.4 at +1.5 V excitation pulse. Two small majority carrier peaks between OsA and OsB are due to the well known levels H3 and H4 produced by irradiation of p-type InP [4]. These significant peaks appear small here because of much higher concentrations of the osmium related levels in our samples. Further irradiation of the samples does not cause any appreciable further increase in the concentration of Os1, while OsA and OsB show slight increase.

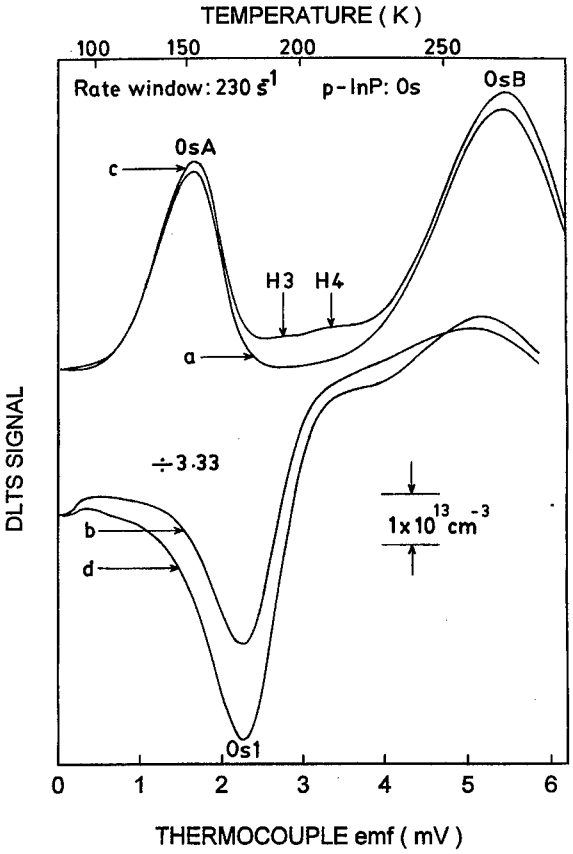

Fig. 3. DLTS spectra of p-InP:Os showing the effects of irradiation by alpha-particles: (a) and (b) are the majority and minority carrier emission scans, respectively, before irradiation, while (c) and (d) are the corresponding spectra after irradiation.

It was carefully established that the increase in Os1 was not caused by any spurious effects such as an increase in injection efficiency of our diodes by irradiation. No measurable change in the current-voltage or capacitance-voltage characteristics of our samples was observed following irradiation. The increase in the peak Os1, therefore, reflects a real enhancement of the concentration of the associated defect by radiation. This increase can be interpreted in the following possible ways:

a) Activation of the electrically inactive osmium atoms by radiation e.g. by transformation from the interstitial to the substitutional sites as a result of vacancy generation by high energy radiation. This would imply that Os1 is either a substitutional Os atom itself or a complex involving a substitutional Os atom.

(b) Os1 is a complex defect involving an interstitial or a substitutional Os atom in combination with some other defect, whose concentration is enhanced by irradiation. For instance, any of the

primary radiation induced defects, P_i, In_i interstitials or the corresponding antisite defects, may be the complexing partner of Os in Os1.

Detailed further investigations using techniques sensitive to the defect microstructure, such as magnetic resonance spectroscopy, would clearly be needed to resolve the above mentioned models. Meanwhile, it may be pointed out that our investigations [3] based on secondary ion mass spectroscopy (SIMS) already indicate the existence of a significant concentration of electrically unactivated transition metal atoms in our TM doped MOCVD InP, in general, making the first of the above two proposals an attractive possibility. The small increase in OsA and OsB with irradiation also suggests a contribution of the radiation-induced primary defects, indicating their complex character. A detailed analysis of these effects and the effects of osmium impurity on the radiation-induced deep levels in InP is in progress and will be reported elsewhere.

Conclusions

Electrical and optical DLTS investigations on Os-doped, p-typed InP crystals grown by MOCVD have been presented. Two prominent hole levels and one electron level associated with Os have been observed and characterized. Comparison of the electrical and optical injection spectra provide interesting information on the properties of the deep levels observed. In particular, definite conclusions regarding the relative electron and hole capture cross-sections have been drawn for the various levels, indicating that OsB can be expected to be an efficient recombination center with $\sigma_n \cong \sigma_p$. Preliminary results of a study of the effects of alpha-irradiation on Os related deep levels have also been presented. These show a clear enhancement of the level Os1 by irradiation, providing useful insights into the possible models for its microstructure.

The collaboration between Quaid-i-Azam University, Islamabad and Technische Universität, Berlin, is supported by a Commission of European Communities project (contract No. CI1-CT93-0076).

References

1. H. Kamada, S. Shinoyama and A. Katsui, J. Appl. Phys., **55**, 2881 (1984).
2. A. Dadgar, L. Köhne, M. Zafar Iqbal and D. Bimberg, Proceedings of 23rd International Conference on Physics of Semiconductors, editors, M. Scheffler and R. Zimmermann, World Scientific, Singapore, p. 2837 (1996).
3. A. Dadgar, L. Köhne, J.Y. Hyeon, T. Grundemann, O. Stenzel, M. Straβburg, M. Kuttler, R. Heitz, D. Bimberg and H. Schumann, J. Crystal Growth, **170**, 173 (1997).
4. Aurangzeb Khan, Umar S. Qurashi, N. Zafar, M. Zafar Iqbal, A. Dadgar and D. Bimberg, Proc. ICDS 19, 1997 and references therein.

Materials Science Forum Vols. 258-263 (1997) pp. 837-842

A SHARP DEFECT–ANNEALING STAGE BELOW ROOM TEMPERATURE IN IRRADIATED N-TYPE INDIUM PHOSPHIDE

A. Canimoglu and D W Palmer

Physics and Astronomy Subject Group, University of Sussex, Brighton BN1-9QJ, UK

Keywords : InP, irradiation, DLTS, low temperature annealing, Frenkel pairs.

Abstract : We have irradiated n-type InP Schottky diodes at 85K using 1.0 MeV protons and have investigated the irradiation-induced defects by in-situ DLTS measurements between 85K and 350K. It is expected that in such irradiation most of the radiation-damage collisions produce rather simple lattice defects. We find that the DLTS spectrum shows strong lattice-defect peaks centred near 115K, 205K and 315K, of which the 115K peak is removed during the first DLTS measurement to room temperature. In isochronal heatings performed at steady zero applied bias the latter defect disappears in a sharp annealing stage centred near 197K for 30-minute heatings, and isothermal heatings in the same bias condition indicate defect annealing by first-order reaction kinetics. The isochronal data are consistent with an annealing activation energy and a pre-factor of approximately 0.65eV and $1x10^{13}$ s^{-1} respectively. This pre-factor value indicates that the annealing involves a small number of defect jumps, and therefore strongly suggests that the annealing stage near 197K is due to interstitial-vacancy combination within a close Frenkel-pair structure of indium or phosphorus; it seems likely to be the former. By standard DLTS procedures we find the thermal ionisation energy and electron-capture cross-section of the defect to be 0.20eV and 2×10^{-15} cm^2.

1. Introduction

Indium phosphide is of increasing interest for electronic and opto-electronic devices, and information is therefore needed on the properties and natures of lattice defects that may be produced in this semiconductor during crystal growth, ion-implantation processing etc. The defects present in the device material result from all the defect reactions that take place during the growth and processing, including those that can occur at room temperature itself. The use of InP as a material for space-satellite solar cells is also of considerable interest since such cells are found [1, 2] to be more radiation resistant than those made from Si or GaAs; that observation suggests that irradiation-induced defects may easily anneal in InP. Irradiation of InP at low temperature, as in the present work, is a controllable means of introducing and studying defects that are unstable or mobile at room temperature in this semiconductor.

Early studies by Deep Level Transient Spectroscopy (DLTS) on n-InP electron irradiated at room temperature [3,4] showed the presence of at least seven electron-trapping irradiation-induced defects having thermal ionisation energies to the conduction band of between 0.09eV and 0.66eV, and that significant defect annealing occured at room temperature. Further studies [5-7] on n-InP showed the production, by room temperature electron irradiation, of a metastable defect whose electronic level depended on whether the diode sample was cooled at zero or reverse bias. Investigations of the properties of irradiation-induced defects in p-InP have also been made [8-9] and have shown that electron-hole recombination can enhance the annealing of defects introduced by electron irradiation at low temperature. Irradiation of p-InP by 2.0 MeV protons near 293K has been shown [9] to produce many of the defects that can be created by electron irradiation.

Concerning low temperature irradiation of n-type InP, studies [11] by the positron-annihilation technique have shown a broad defect-annealing stage at 150-200K after irradiation by 2.0 MeV electrons at 20K followed by storage at 77K; the data indicated that the annealing involved the

disappearance of vacancies. Diffuse X-ray scattering data from semi-insulating InP without warming above 8K after irradiation by 3 MeV electrons near 5K have been interpreted in terms of the presence of irradiation-induced Frenkel pairs [12, 13]. Associated studies [14, 15] on s.i. InP, using the magnetic circular dichroism of optical absorption (MCDA) at 1.17 and 1.27 eV after similar low temperature irradiation, have shown removal of those absorptions in stages centred near 150K, the removal being attributed to the annealing of two kinds of Frenkel pair defect.

Here we present results of DLTS studies on n-InP that show a sharp defect annealing stage near 200K after irradiation by 1.0 MeV protons at 85K and provide the values of the ionisation energy E_n and the electron-capture cross-section σ_n of the defect concerned.

2. Experimental Procedures

The samples used in this work were cut from LEC-grown n-type indium phosphide of carrier concentration approximately $4x10^{15}$ cm^{-3} at 293K, supplied by Wafer Technology Ltd (UK). Following chemical etching in methanol / 10%-bromine and cleaning, an ohmic contact was made, by tin alloying in a flowing HCl/nitrogen gas mixture, to the non-polished side of the sample, and silver was evaporated in high vacuum to form one or two Schottky diodes of diameter 1.0 mm on the polished surface. The diodes used in these studies showed satisfactory current-voltage characteristics with reverse-breakdown potentials of at least 5 Volts.

For the measurement and irradiation, the sample, on a TO5 transistor header, was mounted in a continuous-flow Oxford-Instruments-Ltd cryostat, held in a vacuum chamber in a beam-line of the University of Sussex 3 MV Van de Graaff Ion Accelerator. The experimental arrangement allowed irradiation of the sample (through the Schottky layer) at temperatures below 300K and in-situ studies on the diode sample, before and after irradiation, by capacitance-voltage-temperature measurements and by majority-carrier Deep Level Transient Spectroscopy (DLTS). The irradiations were made (at zero applied bias and without bias pulsing on the diode sample) using 1.0 MeV protons to doses of about 5×10^{11} cm^{-2}. Since the silver Schottky layer was thin (about or less than 0.1 μm) it produced very little reduction in the energy of the irradiating protons, and in consequence the concentration of the irradiation-induced defects was essentially uniform in the near surface region of the n-InP, of thickness about 2 μm, investigated in the C(V,T) and DLTS measurements. The elecronic measurement system used a Boonton Model 72B capacitance meter, in conjuction with a IEEE488-interfaced two-time box-car analyser and a similarly interfaced multi-time digital recorder for computer acquisition of C(T) and DLTS data.

3. Results and Discussion

Figure 1(a) shows an DLTS spectrum obtained between 85K and 350K before irradiation and immediately after 1.0 MeV proton irradiation at 85K of an n-InP diode sample. The spectrum after the irradiation shows additional strong peaks centred near 115K, 205K and 315K, together with a small peak near 95K. We find those peaks to be consistent features of the first DLTS spectra from our samples after irradiations near 85K, and it is clear that they are due to irradiation-induced defects. Since the momentum-transferring collisions of 1.0 MeV protons with the indium and phosphorus atoms of the sample are very dominantly by inter-nuclear coulomb interactions, collisions that impart only low energies to the atoms of the sample have the largest probabilities; in consquence, the mean number of atomic displacements per atom-displacing collision is small and the lattice defects created in InP by 1.0 MeV protons are very likely to include signficant fractions of rather simple defects such as close Frenkel pairs of indium and of phosphorus, interstitials and vacancies that are somewhat more separated and also divacancies.

Figure 1(b) shows the DLTS spectrum obtained immediately after the measurement of Fig. 1(a), ie after the sample, irradiated at 85K, had been heated to 350K in the condition of pulsed reverse bias for that first 85K-350K DLTS measurement. It is seen that the spectrum of Fig. 1(b) does not

contain the peak near 115K that was present in the post-irradiation spectrum of Fig. 1(a), that the peak near 205K had become sharper, and that the small peak near 95K and the large peak near 315K were almost unchanged.

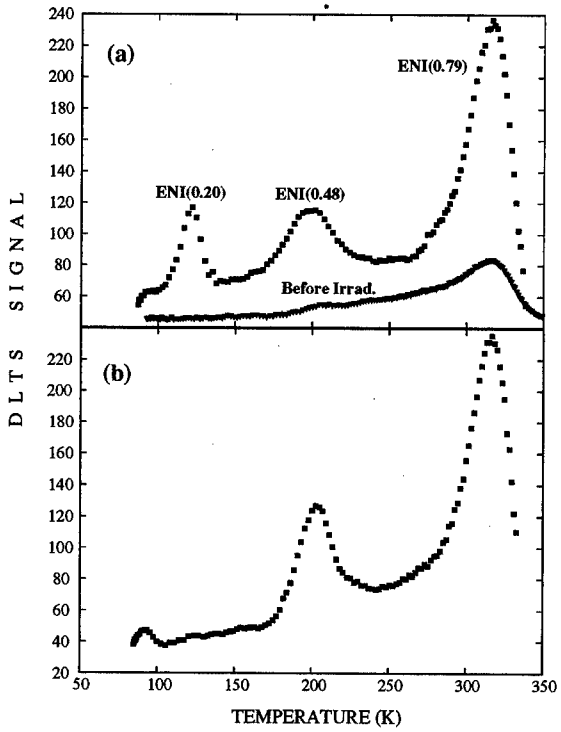

Fig. 1 : Majority-Carrier DLTS spectra of n-InP (V_R=3.0V, V_{PH}=2.0V, e_n=46s^{-1}) :

(a) DLTS spectrum before irradiation (lower curve), and first spectrum after irradiation at 85K by 1.0 MeV protons, without heating above 85K before making that DLTS measurement.

(b) DLTS spectrum obtained after cooling the sample to 85K immediately after the post-irradiation DLTS measurement of (a) above.

We deduce that during the first 85-350K DLTS post-irradiation measurement, total annealing occurred of the irradiation-induced defect responsible for the 115K DLTS peak and that other defect processes took place relating to the defect or defects that give rise to the 205K peak.

In Fig. 2 we show the results, in the form of Arrhenius plots, of our measurements on the thermally induced electronic excitations to the conduction band from the defect states that produce the 115K, 205K and 315K DLTS peaks. These data were obtained, in the standard way, by determining the temperature of each peak maximum as a function of the DLTS emission rate-window. We

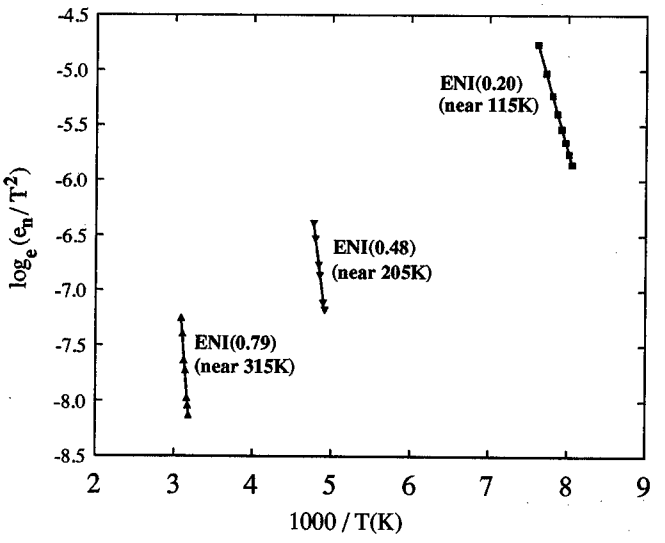

Fig. 2 : Electron-emission Arrhenius plots for the DLTS peaks centred near 115K, 205K and 315K, that are shown in Fig. 1(a).

have found no change in the height of the 115K peak during DLTS measurements upto 150K, and so we have confined our Arrhenius-data measurements on that peak to temperatures below 150K after sample irradiation at 85K.

The values of the thermal ionisation energies E_n and electron-capture cross-sections σ_n for the three main DLTS peaks, as found from the data of Fig. 2, are presented in Table 1.

Table 1 :

DLTS Peak	E_n (eV)	σ_n (cm^2)	Name
115K	0.20 ±0.01	2×10^{-15}	ENI (0.20)
205K	0.48 ±0.01	7×10^{-12}	ENI (0.48)
315K	0.79 ±0.03	2×10^{-11}	ENI (0.79.)

In our nomenclature for the defects, the notation "ENI" means "Electron trap in N-type material after Irradiation", and the number in the associated parentheses is the measured E_n value in eV for the particular defect.

The defect ENI(0.48) may be the same as that of E_n equal to 0.44 eV reported for LEC n-InP after 1 MeV electron irradiation at room temperature [4]. But it is possible that, because of the strong changes of defect stabilities and mobilities with temperature, the defects resulting from irradiation at low temperature, as in the present work, are different from those produced by room temperature irradiations. Defect-impurity complexes may also not be the same in different n-InP materials.

In this paper we concentrate on the properties of the defect ENI(0.20) that produces the 115K DLTS peak. We find that the temperature at which it anneals depends on the voltage biasing conditions during the heat treatments. During the reverse-bias and voltage-pulsing of a DLTS measurement the defect disappears in a rather sharp annealing stage centred near 170K. However, in the absence of applied bias and pulsing, it anneals in the vicinity of 200K.

Figure 3(a) shows the height of the 115K DLTS peak (corresponding to the ENI(0.20) defect) as a function of isothermal heatings at 205±1K. After each DLTS measurement upto 150K the diode sample was heated to, heated at and cooled from the 205K annealing temperature in the condition of zero applied bias and zero pulsing (diode disconnected from external circuitry). In terms of spectra such as the post-irradiation spectrum of Fig. 1(a), we define the ENI(0.20) peak height, proportional to the concentration of the ENI(0.20) defect, as the absolute DLTS signal at the peak maximum minus an assumed linearly increasing background drawn across the bottom of the DLTS peak. It is seen in Fig. 3(a) that the ENI(0.20) defect concentration decreased progressively towards zero during heating at 205K.

The isothermal annealing data of Fig. 3(a) plotted in the form of the logarithm of the ENI(0.20) peak height as a function of heating time are shown in Fig. 3(b). The near-linearity of the function indicates that the annealing occurs with first-order reaction kinetics.

In further experiments we have studied the isochronal annealing of the ENI(0.20) defect in the temperature range 175K to 220K. The procedure was the same as in the isothermal annealing measurements described above, except that each heating was at a temperature 5^o above that of the previous heating. Figure 4 shows the experimental data points (solid squares) for isochronal heatings of thirty minutes each, together with theoretical isochronal annealing data (unfilled circles) calculated assuming first-order annealing kinetics, a reaction pre-factor of 1.0×10^{13} s^{-1} and a reaction activation energy of 0.65 eV. The combination of pre-factor and energy values was chosen so that the calculated data produced 50% annealing at the temperature of 197K at which that occured experimentally, and so that, also, the steepness of the calculated annealing near 197K was similar to that of the experimental data. It is seen that these theoretical points fit reasonably to the experimental data.

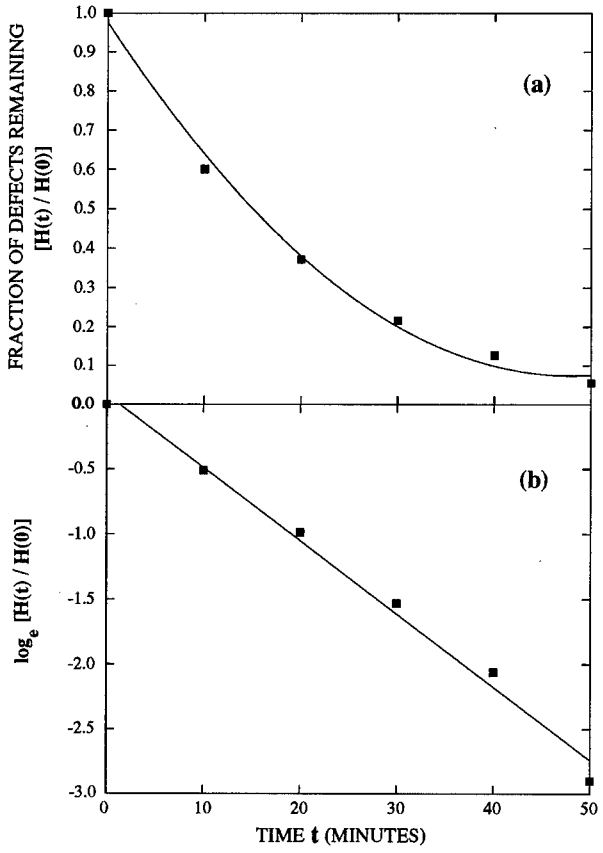

Fig. 3 : Isothermal annealing at 205±1K, in the condition of zero bias and zero pulsing, of the defect ENI(0.20) that produced the peak centred near 115K seen in the DLTS spectrum of Fig. 1(a):

In (a), the ordinate is the ratio [H(t)/H(0)] of the height of the DLTS peak after heating for a total time t at 205K compared to the height immediately after irradiation at 85K.

The ordinate in (b) is the natural logarithm of that in (a).

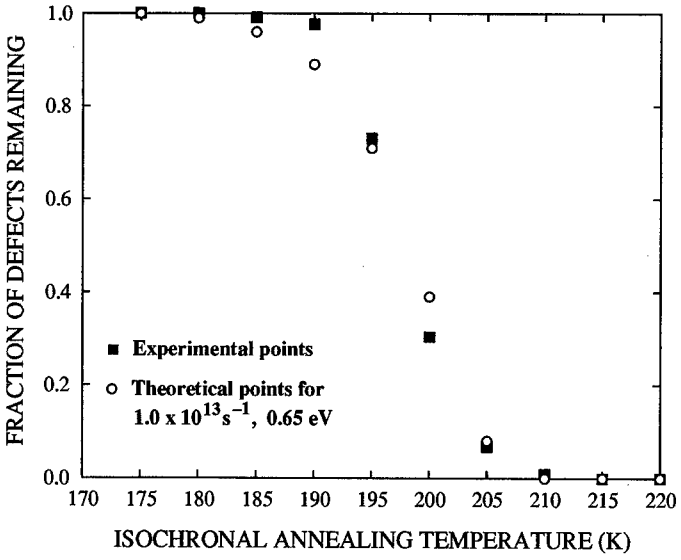

Fig. 4 : Experimental data (shown by solid squares) for isochronal (thirty minute) annealing, in the condition of zero bias and zero pulsing, of the defect ENI(0.20) that produced the peak centred near 115K seen in the DLTS spectrum of Fig. 1(a), compared to theoretical data (unfilled circles) calculated for a first -order annealing reaction of pre-factor value 1.0×10^{13} s^{-1} and activation energy of 0.65 eV.

Since for a first-order annealing reaction of a lattice defect the pre-factor value is expected to be equal approximately to $[\nu_0 / n_j]$, where ν_0 is the maximum vibration frequency of the atoms asociated with the defect, and n_j is the number of atom jumps required for the annealing of each defect, the deduced value of about 1×10^{13} s^{-1} for the pre-factor indicates that n_j is the order of

unity. We deduce that the ENI(0.20) defect is a composite defect for which the thermal annealing reaction is a process of combination of its component defects or of their separation, in which, in either case, the number of atomic jumps is small. Either process would be a first-order annealing reaction in accordance with the measured data of Fig. 3(b).

Noting those deductions from our experimental data and also, as stated previously, that the majority of the defects created by 1.0 MeV proton irradiation are very likely to be rather simple defects, we propose that the ENI(0.20) defect is a form of Frenkel-pair structure. In such case the annealing process that occurs at about 200K is the recombination or the separation of the component intersitial and vacancy. It seems likely that the annealing of the ENI(0.20) defect is responsible for or involved in the decrease in positron trapping at 150-200K in strongly n-type InP after high-dose irradiation by 2.0 MeV electrons at 20K [11] and also for the removal at 100-200K of the MCD optical absorption in s.i. InP electron-irradiated at low temperature [14, 15]. In each of those irradiated InP materials, interactions among defects at high concentrations may have caused the defect annealing to take place over a wider temperature range than in the present DLTS studies of irradiation-induced defects at low concentrations. Considering information on III-V semiconductors generally, we suggest that the ENI(0.20) defect in irradiated n-InP involves an indium Frenkel pair, but point out that, in analogy with irradiation-induced electron-trapping defects that anneal below 300K in n-GaAs [16, 17], it may arise from a double atomic displacement.

4. Summary

This DLTS investigation has shown that irradiation of n-type InP at 85K creates a lattice defect that has an electron ionisation energy to the conduction band of 0.20±0.01eV, and, under the condition of zero applied bias, is removed completely in a sharp annealing stage centred near 200K with an annealing activation energy of about 0.65eV. We suggest that the defect is or includes an indium Frenkel-pair. We find also that the thermal stability of the defect depends on the biasing conditions applied to the diode sample.

We are pleased to acknowledge financial support from the UK Engineering and Physical Sciences Research Council for this work and express our thanks also to the University of Nigde, Turkey, for a research studentship bursary to one of us (A.C).

References

[1] M. Yamaguchi, C. Uemura and A. Yamamoto, J. Appl. Phys. **55**, 1429 (1984)
[2] M. Yamaguchi, T. Okuda and S. J. Taylor, Appl. Phys. Lett. **70**, 2180 (1997)
[3] M. Levinson, J. L Benton, H. Temkin and L C Kimerling, Appl. Phys. Lett. **40**, 990 (1982)
[4] P.R. Tapster, J. of Crystal Growth **64**, 200 (1983)
[5] M. Levinson, J. L Benton and L C Kimerling, Phys. Rev. B 27, 6216 (1983)
[6] M. Levinson, M. Stavola, J. L Benton and L C Kimerling, Phys. Rev. B **28**, 5848 (1983)
[7] M. Stavola, M. Levinson, J. L Benton and L C Kimerling, Phys. Rev. B **30**, 832 (1984)
[8] A. Sibille and E. V. K. Rao, J. of Crystal Growth **64**, 194 (1983)
[9] A. Sibille. Phys. Rev. B **35**, 3929 (1987)
[10] G. C. Rybicki and W. S. Williams, Mat. Res. Soc. Symp. Proc. **325**, 311 (1994)
[11] M. Törnqvist, J. Nissilä, F. Kiessling, C. Corbel, K. Saarinen, A.P. Seitsonen and P. Hautojärvi, Materials Science Forum **143-147**, 347 (1994) [ICDS-17]
[12] K. Karsten and P. Erhart, Materials Science Forum **143-147**, 365 (1994) [ICDS-17]
[13] A. Pillukat, K Karsten and P Ehrhart, Phys. Rev. B **53**, 7823 (1996)
[14] K. Karsten and P. Erhart, Phys. Rev. B **51**, 10508 (1995)
[15] H. Hausmann and P. Erhart, Materials Science Forum **196-201**, 1261 (1995) [ICDS-18]
[16] K. Thommen, Radiation Effects **2**, 201 (1970)
[17] A. C. Irvine and D.W. Palmer, Phys. Rev. B **49**, 5695 (1994) .

Materials Science Forum Vols. 258-263 (1997) pp. 843-848

ALPHA RADIATION–INDUCED DEEP LEVELS IN p-InP

Aurangzeb Khan, Umar S. Qurashi, N. Zafar, M. Zafar Iqbal, A. Dadgar* and D. Bimberg*

Semiconductor Physics Laboratory, Department of Physics, Quaid-i-Azam University, Islamabad, Pakistan.

*Institut für Festkörperphysik, Technische Universität Berlin, Hardenbergstr. 36, 10623 Berlin, Germany.

Keywords: Radiation-induced defects, InP, DLTS, Defect reactions.

Abstract. Deep level defects induced by alpha radiation in p-type InP crystals, grown by low pressure metalorganic chemical vapour deposition (LP-MOCVD) have been studied by deep-level transient spectroscopy (DLTS). Two prominent hole-emitting levels with thermal activation energies 0.34 eV and 0.39 eV to the valence band and two electron-emitting levels with activation energies 0.22 eV and 0.29 eV in the upper half-gap have been detected immediately after irradiation by 5.48 MeV alpha particles. These have been identified with the H3, H4 and E_C and E_A defects, respectively, hitherto observed as a result of electron, proton and/or gamma irradiation. Interesting transformations of the majority carrier deep levels are observed both with minority carrier injection and room temperature annealing. In particular, an additional hole level H5 at E_V+0.58 eV is produced in the majority carrier spectrum as a result of ~40 hours of room temperature (~20°C) storage or more rapidly as a result of minority carrier injection. Similarly a third minority carrier level E_D at E_C-0.37 eV appears after several days of room temperature storage following irradiation. No additional electron level is observed in optical DLTS. On the other hand the hole levels are found to completely disappear on optical injection. The hole capture cross-sections of H4 and H5 are found to be temperature dependent but the capture barrier energy for H5 is found to be significantly different from a recently reported value. The observed changes in the DLTS spectra do not necessarily require the hitherto proposed transformation of H4 into H5. The observed properties can be interpreted in terms of no or partial transformation. Similarly, the recently suggested transformation of H5 into E_A is not supported by our data.

Introduction

InP is one of the most important compound semiconductors currently being developed for the next generation of fast electronic devices and optoelectronic applications. Radiation-induced defects form an important subject of current research on this material not only because of its direct relevance to the attractive potential of InP for solar cell technology but also due to the highly interesting fundamental insights into defect physics recently brought to light by such studies [1-8]. High energy electrons [1], protons [2] and gamma rays [3] have, hitherto, been used for such studies

on InP. We report preliminary results on the investigations of defects induced by alpha radiation in p-type InP grown by metal-organic chemical vapour deposition (MOCVD) technique. MOCVD grown InP solar cells have been recently demonstrated to show superior photovoltaic properties as compared to the diffused junction liquid phase epitaxial devices [4]. It is, therefore, of added importance to investigate the radiation induced defects in MOCVD InP, leading up to a detailed understanding of the radiation response/recovery of the devices based on this material.

Experimental Details

Our samples consist of n^+p junctions grown by low-pressure MOCVD on p^+ InP substrates at a typical temperature of 640°C using hydrogen as the carrier gas. The devices are mesa diodes, 800 μm in diameter, photolithographically defined and etched into epitaxial structures consisting of 0.7-1 μm thick n^+ layers deposited on top of 2-3 μm thick p-type layers with a typical net acceptor background doping $3x10^{16}$ cm^{-3}. Ohmic contacts in the form of circular dots on the top n^+ layer and uniformly on the back surface, were provided by vacuum evaporation/alloying of appropriate metallic films. The finished devices were mounted on TO-5 headers with bonded leads for electrical measurements.

Deep level transient spectroscopy (DLTS) has been used to investigate the deep level defects employing a sensitive DLTS setup based on lock-in detection principle. A computer controlled DLTS system with optical excitation source emitting at 780 nm wavelength was used for carrying out optical DLTS (ODLTS) measurements. 5.48 MeV alpha particles from a 9 μCi ^{241}Am radioactive source have been used for irradiation of samples at room temperature. Detailed current-voltage (I-V) and capacitance-voltage characteristics (C-V) of the samples were measured before and after each irradiation to monitor the quality of the diodes.

Results and Discussion

a. Deep-level Spectra

Fig. 1 shows the typical deep level spectra for majority carrier and minority carrier emission on a sample before and after irradiation. Traces (a) and (c) clearly show the absence of any measurable hole and electron deep levels in the as-prepared samples which makes these samples ideal for our study. Irradiation introduces two prominent majority carrier levels, named H3 and H4, and two minority carrier levels E_A and E_C, as seen in the spectra (b) and (d), respectively, taken a few minutes after irradiation. The labels for these deep levels have been adopted from earlier irradiation work [5] on InP using other types of radiation, after comparing the measured emission rate signatures given in Fig. 2. The majority carrier spectrum also shows some unresolved deep level signal at the low temperature end presumably corresponding to the hitherto observed low

concentration levels H1 [5] and H2 [6], while the high temperature end of our spectrum shows an additional level H7 with a small concentration. The emission rate data for this level, also included in Fig.2, yield an energy position E_v+ 0.79 eV for this level, which is different from the earlier reported energy position of H7 [2] with a similar peak position. This difference in the energy value may arise from the uncertainty of measurements on the peak positions of the small and broad peak corresponding to this level and possible interference of the peak H5 discussed in the following section.

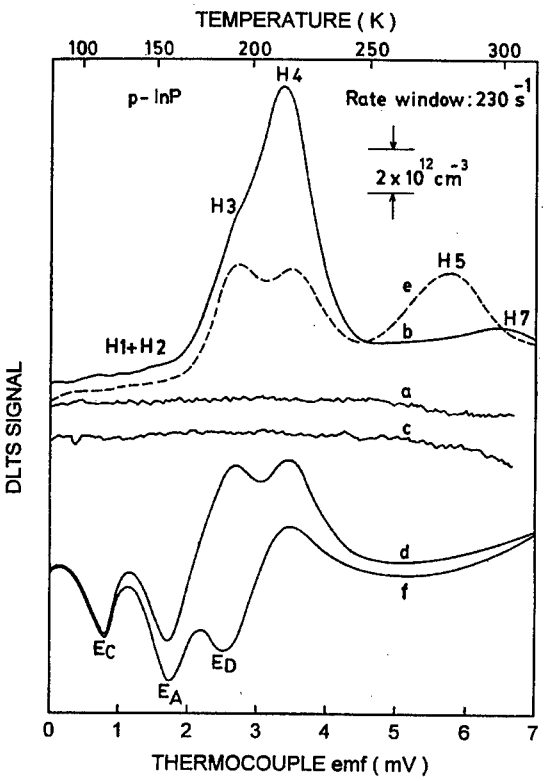

Fig.1. DLTS spectra of p-type InP before and after α-irradiation: Majority carrier emission scans (a) before irradiation, (b) immediately after irradiation and (e) immediately after first injection scan. Minority carrier spectra (c) before irradiation, (d) after irradiation (after scan b) and (f) after 12 days of storage (at ~32°C) following irradiation.

b. Room temperature storage and injection-induced effects

Interestingly, the majority carrier emission spectrum obtained after the minority carrier injection scan, shown by the trace (e) in Fig 1, exhibits marked transformation with respect to the corresponding spectrum before injection, trace (b). In particular, the peaks H3 and H4 have reduced significantly while a new peak H5 has been generated. This effect has been observed before [3, 9, 10] and interpreted [3, 9] as the transformation of the deep-level defect H4 into H5. It is to be noted, however, that the change in the concentrations (peak heights) of these two levels are far from equal. This would suggest that these changes are not necessarily the result of a direct mutual transformation between these two levels. These changes may occur independently in H4 and H5 as a result of room temperature annealing. The propsed transformation between the two is thus, either not required at all or, at best, partial. We have observed two additional properties of these levels which tend to reinforce this new interpretation. These are: (i) the generation of the peak H5 to almost 80% of the injection-induced value during ~40 h of room temperature storage (~20°C), without any simultaneous reduction in H3 or H4 (ii) stability of H5 after injection while H3 and H4 decay significantly during storage after injection. Fig. 3 presents the experimental evidence for both these effects. Fig. 3(a) shows majority carrier spectra taken at different times after irradiation but before any injection of minority carriers has been done. The peak H5 is almost absent in our spectra taken immediately after irradiation. As the storage time is increased, H5 shows substantial increase

in its concentration while H3 and H4 remain constant. Fig 3(b) shows successive majority carrier spectra taken after injection of minority carriers has been carried out. These scans have been taken over a period of 46 days - the samples being stored at a constant temperature of ~20°C in between the scans. H3 and H4 are seen to decrease by 50 and 57% respectively, while H5 stays more or less constant in peak height.

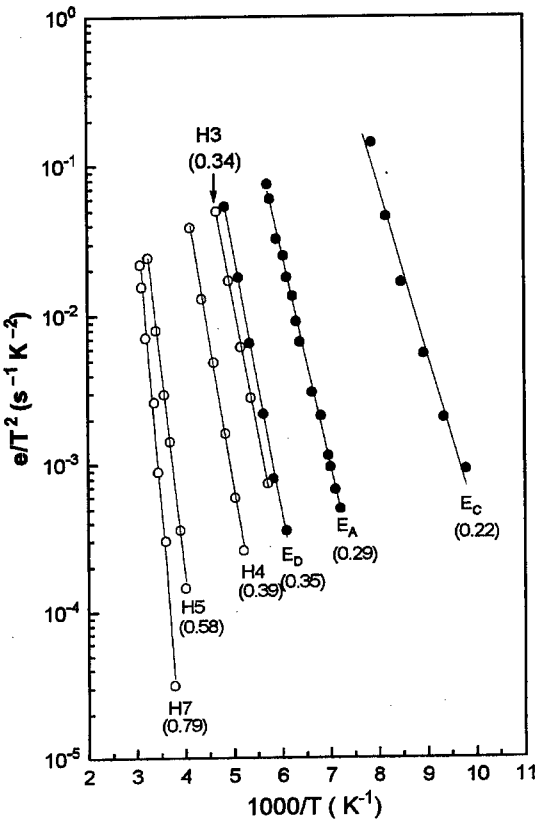

Fig. 2. Emission rate signatures of the alpha-irradiation induced deep levels. Solid lines are the least squares fits to the data. H denotes hole-emitting levels while E denotes electron-emitting levels. The numbers within brackets are the thermal activation energies of the carriers from the respective deep levels to the nearest band edge.

c. Minority Carrier levels

The minority carrier spectra show only two levels E_A and E_C after irradiation as depicted in Fig. 1, trace (d). However, the minority carrier spectrum (trace f) shows a pronounced additional peak E_D after storage of the sample at room temperature (~32°C) for at least 12 days. This new peak seems to be characteristic of the MOCVD grown InP as inferred from a comparison of the published data [7] on Czochralski and liquid phase material with recent reports and our own work on MOCVD crystals. However, the slow room temperature anneal-in of this level observed by us has not been reported before.

Another recent work [8] on gamma-radiation induced defects in MOCVD InP suggests a correlation between the minority carrier level E_A and the hole level H5 i.e. that H5 is transformed into E_A at a certain level of minority carrier injection. Our experiments on the systematic study of the variation of majority and minority carrier DLTS spectra with injection current, to be reported in detail later, do not support this suggestion. Our measurements clearly suggest that H5 is diminished as a result of efficient minority carrier (electron) capture with increase of injection current and the level E_A is observed to rise, as normally expected, with injection. These two effects do not necessarily happen at the same injection level and, therefore, the two levels, H5 and E_A, do not have to be related.

In order to search for any hitherto undiscovered minority carrier levels, we have also carried out optical DLTS (ODLTS) experiments using above band-gap (hν = 1.61 eV) light excitation. No new levels, in addition to E_A, E_C and E_D, have been observed. However, the majority carrier peaks are completely overshadowed by the minority carrier peaks even though the former deep levels have higher concentrations, which implies that the electron capture cross-sections for H3, H4 and H5 are larger than their hole capture cross-sections.

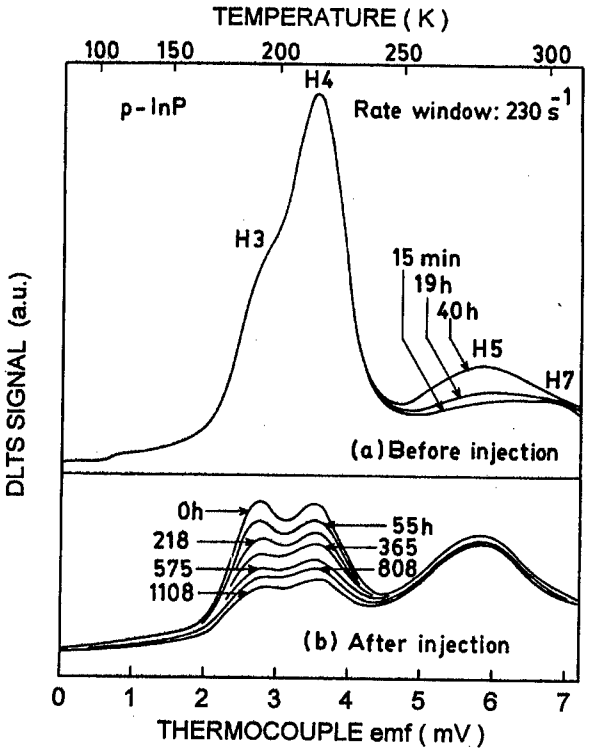

Fig. 3. Room temperature storage effects on DLTS spectra (a) before and (b) after minority carrier injection. The times shown are in (a) after irradiation prior to injection and in (b) after an injection scan.

d. Capture cross-sections

The hole capture cross-sections of the deep levels H4 and H5 have been directly measured by variation of the excitation pulse-width method. They have been found to be temperature dependent for both the levels, although the temperature dependence is seen to be weaker for H4. Both these sets of data fit well with an Arrhenius law showing that capture is mediated by multiphonon emission with a capture barrier energy of ~0.042 eV and 0.18 eV for H4 and H5, respectively. Our capture barrier height for H4 is not too different from the value reported by Ando et al [3]. The two reported values for H5 show widely different capture barrier energy - Walters et al [2] report it to be ~ 0.13 eV while McKeever et al [8] report a much higher value of 0.35 eV, although same or similar material has been used in these studies. The reason for this discrepancy has not been given in these publications. Our measurements clearly cast doubt on the reported higher value of McKeever et al [8].

(e) Electric Field Dependence

The thermal emission from the levels H4 and H5 has been found to be enhanced by the junction electric field in agreement with the observation of Messenger et al [11]. The detailed quantitative determination and analysis of this field dependence is in progress and will be reported later.

Conclusions

Preliminary results on alpha-radiation induced deep levels in p-InP grown by MOCVD have been reported. The model suggesting the transformation of the level H4 into H5 is shown to be questionable in the light of our experimental investigations. It seems to be more probable that the pronounced reduction in H3 and H4 accompanied by the generation of H5 by minority carrier injection are unrelated recombination-enhanced defect reaction phenomena. The recently proposed inter-conversion of H5 and E_A are also not supported by our results. The observed apparent transformation can be understood by the usual minority carrier capture effects. Data on the temperature dependence of hole capture cross-sections of H4 and H5 show that the capture process is mediated by multiphonon emission with 0.042 eV and 0.18 eV as the respective capture barrier energies.

The collaboration between Quaid-i-Azam University, Islamabad and Technische Universität, Berlin, is supported by the Commission of European Communities project (contract No. CI1-CT93-0076).

References

1. A. Sibille, J. Suski and M. Gilleron, J. Appl. Phys., **60**, 595 (1986).
2. R. J. Walters and G. P. Summers, J. Appl. Phys., **69**, 6488 (1991).
3. K. Ando, M. Yamaguchi and C. Uemura, Phys. Rev. B **34**, 3041 (1986).
4. R. J. Walters, S. R. Messenger, H. L. Cotal and G. P. Summers, J. Appl. Phys., **80**, 4315 (1996).
5. A. Sibille and J. C. Bourgoin, Appl. Phys. Lett., **41**, 956 (1982).
6. A. Sibille, Phys. Rev. B **35**, 3929 (1987).
7. T. Bretagnon, G. Bastide and M. Rouzeyri, Phys. Rev. B **41**, 1028 (1990).
8. S. W. S. McKeever, R. J. Walters, S. R. Messenger and G. P. Summers, J. Appl. Phys., **69**, 1435 (1991).
9. M. Yamaguchi, K. Ando, A. Yamamata and C. Uemura, J. Appl. Phys., **58**, 568 (1985).
10. C. J. Keavney, R. J. Walters and P. J. Drevinsky, J. Appl. Phys., **73**, 60 (1993).
11. S. R. Messenger, R. J. Walters and G. P. Summers, J. Appl. Phys., **71**, 4201 (1992).

Materials Science Forum Vols. 258-263 (1997) pp. 849-854

SITE STABILITY, DIFFUSION, AND CHARGE DYNAMICS FOR MUONIUM IN GaAs

T.L. Estle[1], K.H. Chow[2] S.F.J. Cox[3], E.A. Davis[4], B. Hitti[5], R.F. Kiefl[6], R.L. Lichti[7], and C. Schwab[8]

[1]Physics Department, Rice University, Houston, TX 77251, USA
[2] Sherman Fairchild Labs, Lehigh University, Bethlehem, PA 18015, USA
[3]ISIS, Rutherford-Appleton Laboratory, Chilton OX11 0QX, UK
[4]Department of Physics, University of Leicester, Leicester LEI 7RH, UK
[5]TRIUMF, Vancouver, BC V6T 2A3, Canada
[6]University of British Columbia, Vancouver, BC V6T 1Z1, Canada
[7]Physics Department, Texas Tech University, Lubbock, TX 79409, USA
[8]Centre National de la Recherche Scientifique, PHASE, 67037 Strasbourg, France

Keywords : Muonium, Hydrogen, Dynamics, Diffusion, GaAs

Abstract. The motion and charge dynamics of muonium states in GaAs have been investigated. In heavily-doped n-type GaAs, Mu^- is stable to high temperatures. It resides in a T_{Ga} interstice where it is immobile to 500K. At high ϵ^- concentrations Mu_T acts as a recombination center and a rapid $-/0$ charge cycle occurs above 750K. In semi-insulating and lightly-doped n-type GaAs a different set of charge-state transitions yield $0/+$ cycles above 550K. These samples show some evidence of a BC to T site change for Mu^0 near 200K. Due to its high mobility, the charge cycles allow Mu^0_T to dominate diffusion even when it is not the equilibrium state. Mu^+ occupies two locations in p-type GaAs. The low-temperature state, presumably Mu^+_{BC}, becomes mobile near 200K and traps at a second site above 400K.

Introduction

Investigations over nearly two decades have provided a great deal of information on neutral muonium (Mu^0) centers in semiconductors, identifying their locations within the crystal and their electronic structure, mobility and thermal stability.[1] This richness is based on the hyperfine characteristics of these paramagnetic centers. Hyperfine spectra identified two neutral centers in several diamond and zincblende structured semiconductors including GaAs. These centers are known as Mu^0_T and Mu^0_{BC}. The former is located within the tetrahedral (T) interstices of these structures and is highly mobile, hopping rapidly among T-sites at all temperatures, by tunnelling at low temperatures and by thermally activated hops at higher temperatures. GaAs was among the first materials in which these motions were fully characterized.[2] The bond-centered (BC) neutral is stationary at low temperatures, residing near the center of a stretched host bond and is the ground state configuration for Mu^0 in silicon. Muonium hyperfine level-crossing spectra in GaAs gave the first detailed experimental information on the Mu^0_{BC} structure.[3] Most of what is known about isolated neutral interstitial hydrogen in semiconductors has been inferred from muonium studies along with theoretical calculations.[4,5]

In contrast, similar experimental information regarding the charged muonium centers is recent and much more limited. Both Mu^+ and Mu^- are diamagnetic, yielding essentially identical transverse field (TF) muon-spin rotation (μSR) spin-precession spectra consisting of a single line due to the μ^+ magnetic moment (S=1/2, $\gamma_\mu = 2\pi \times 135.5$MHz/T). The same would also be true for the analog of hydrogen passivation complexes, *ie.* a bound Mu-Dopant pair. The III-V compounds, of which GaAs can be considered the prototype, provide excellent hosts for studying the diamagnetic centers because essentially all of the host nuclei have dipole moments and many have spins greater than 1/2, thus quadrupole moments as well. Interactions of III-V nuclear and muon moments lead to different linewidths for the diamagnetic μSR signal depending on details of the Mu site and motional properties, and offer the possiblity of quadrupolar features from which greater structural detail can be gleaned.

Recent studies [6-9] of n– and p–type GaAs have provided information about Mu^+ and Mu^- with the simplest results coming from heavily doped crystals where these states dominate. In p–type GaAs(Zn) at a concentration of $3 \times 10^{19} cm^{-3}$ only a diamagnetic signal is seen in low temperature TF-μSR and accounts for all the muon polarization. This signal is attributed to Mu^+. Theory says this state is stable in the BC-site, but we do not yet have the experimental evidence to determine the structural details.

In n–type GaAs(Si) doped to a concentration of $4 \times 10^{18} cm^{-3}$, the low–temperature mix of states is more complex, but above 200K a 100% diamagnetic signal is seen. We are continuing to work on the lower temperature features, but existing evidence implies that both neutrals are present and suggests more than one diamagnetic state. For a static center, the nuclear dipolar interactions lead to damping of the TF precession signals described by a Gaussian envelope. The TF-μSR Gaussian rate constant for the diamagnetic signal in this n–type sample is constant indicating a stationary center up to nearly 500K, above which dynamic features are observed. The field dependence of these rates at 5K decreases near 0.2T with $\mathbf{B} \parallel \langle 100 \rangle$ for n–type GaAs(Si) but is essentially field independent for p–type GaAs(Zn) up to 3T, demonstrating non-identical Mu centers.[6] The n–type curve gives quadrupolar decoupling information and implies that the nearest neighbor atoms are along $\langle 111 \rangle$ directions from the muon for which the dipolar width vanishes in the Van Vleck limit. Observation of quadrupolar level–crossing resonance (QLCR) spectra for metallic n–type GaAs has made the structure of Mu_T^- more definite.[7] Equivalent results for GaAs(Si) and GaAs(Te) indicate that the observed state is an isolated Mu^- rather than a Mu-Donor complex since these donors occupy sites in opposite sublattices. The QLCR spectrum is dominated by four lines from gallium nuclei and has a lower field line with a hint of structure which is assigned to more distant As neighbors. The combination of QLCR spectra and the $\langle 100 \rangle$ quadrupolar decoupling curve led to the conclusion that Mu_T^- is located within a tetrahedral interstice with Ga nearest neighbors, generally consistent with theoretical expectations. The dependence of the TF-μSR Gaussian linewidth as a function of field for the other main crystallographic directions support this conclusion. The best fit to this structural model implies a significant inward relaxation of the four Ga atoms and a slight outward relaxation for second neighbor As atoms.[7]

Mu^0 Stabilities

As mentioned in the Introduction, the motional dynamics of Mu_T^0 were throughly investigated some time ago.[2] These studies showed a minimum hop rate between adjacent T-sites near 80K with faster rates at lower temperatures, a signature of quantum diffusion (tunnelling), and at higher temperatures from thermally activated, or more likely thermally assisted, motion. The relevant point here is that the *minimum* rate is above 10^8 hops per second and remains orders of magnitude faster than any other muonium center at all temperatures. The Mu_T^0 TF-μSR precession signals show increasing relaxation rates from 200 to 300K, while so-called repolarization curves of the visible polarization *vs* longitudinal field show that this state is still present at 350K.[1] These early data give about a 60% Mu_T^0 fraction at low temperatures. The Mu_{BC}^0 state represents about 35% of the implanted muons at low temperatures and its relaxation rate increases rapidly near 150K implying a transition out of that state, usually interpreted as ionization. The diamagnetic signal increases by a somewhat smaller amount begining at about that temperature in a different sample. At intermediate n–type doping levels of $\sim 10^{15} cm^{-3}$ to $10^{17} cm^{-3}$ we observe a peak in the field–dependent longitudinal depolarization rates due to spin-flip scattering between conduction electrons and Mu^0 centers which identifies the anisotropic Mu_{BC}^0 center under conditions where the TF-μSR signal is not observable. In the more lightly doped material this signature of Mu_{BC}^0 loses intensity between about 180 and 240K, while the overall relaxing amplitude and the rate outside that peak increase.[10]

Figure 1 shows the low–field longitudinal depolarization rate in weakly–doped n–type GaAs as a function of temperature. These data were analyzed with two components, one relaxing and a second non-relaxing; however, the relaxing signal below 200K most likely consists of two parts, one from each neutral site. The changes near 200K indicate a transition into the stronger relaxing state, expected to be the T-site if both neutrals are involved, as well as an increase

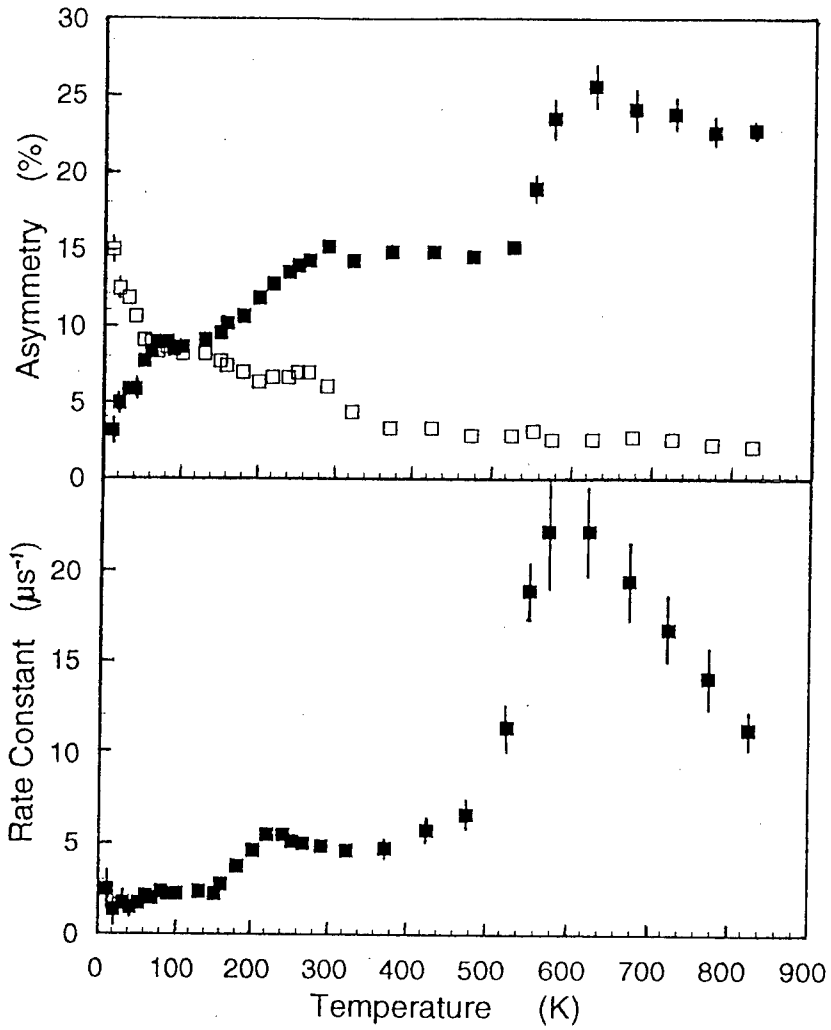

Figure 1. Low-field longitudinal depolarization data as a function of temperature for $3\times10^{15}cm^{-3}$ n-type GaAs(Si). (a) The relaxing (filled) and non-relaxing asymmetries and (b) the depolarization rates for the relaxing component.

in the measured depolarization rate in that region. We interpret these data as evidence of a Mu^0 site transition from BC to T suggesting that the T-site is the more stable of the two. Some relevant additional information comes from the diamagnetic amplitude in recent data on semi-insulating GaAs where there is an increase in amplitude between 150 and 200K followed by a slower decrease from 200 to 400K before the increase associated with ionization of Mu^0_T is observed. One explanation of this behaviour would be competing ionization and site changes as exit routes from Mu^0_{BC}. We note that transitions between fast and slow relaxing fractions in longitudinal depolarization data have also been cited by others as evidence for BC to T site changes, although at temperatures varying with doping concentration.[11] It is clear that Mu^0_T remains present to higher temperatures than does Mu^0_{BC} but there remains some uncertainty regarding transition identifications. Therefore, the question of which Mu^0 center is the ground state in GaAs should probably remain open for now since these data are not conclusive.

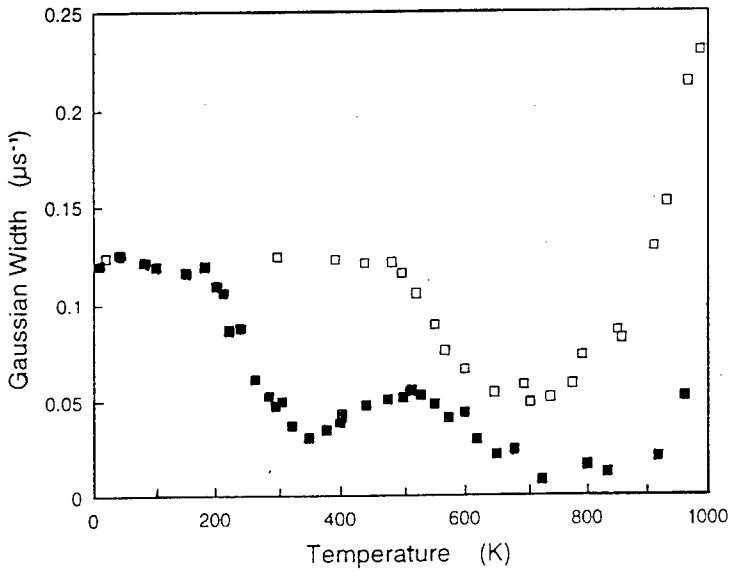

Figure 2. (a) Comparison of the temperature dependence for TF-μSR Gaussian relaxation rates for Mu^+ in GaAs(Zn) [filled squares] and Mu^- in GaAs(Si) [open squares].

Mu^+ and Mu^- Motional Dynamics

The low transverse–field relaxation rate for metallic n–type GaAs(Si) was measured from room temperature to approximately 1000K,[8] as shown in Fig. 2. A second sample was recently examined below room temperature, and the rate was constant. These data indicate that Mu_T^- is stationary below 500K. The decrease above 500K suggests the onset of diffusion, a conclusion confirmed by zero–field (ZF) relaxation measurements from 500K to 640K.[8] The ZF data were fit with a dynamic Kubo–Toyabe function with the dipolar parameter fixed to that obtained for the stationary state. The resulting hop rate has an activated form over nearly two decades yielding an activation energy of 0.73(1) eV and a prefactor of $5.6(5) \times 10^6$MHz. Comparison to the diffusion of Mu_T^0 discussed earlier shows how dramatic the changes are with charge state. Even though these are both T-site species, at room temperature Mu^- is moving more slowly by a factor of $\approx 10^{10}$. The major difference may be that the T_{As} regions are raised in energy for Mu^- while T_{Ga} is stabilized compared to Mu^0 by the partial ionicity of the Ga-As bond Even with the questions of zero-point energy and other quantum effects, the implication for hydrogen in GaAs is that the H^- ion is far less mobile than a neutral T-site atom.

As also shown in Fig. 2, the diamagnetic state in heavily–doped p–type GaAs:Zn behaves quite differently from Mu^-. The TF Gaussian rate shows a decrease starting near 200K, indicating the onset of motion. Above a minimum near 300K these data show a flat maximum from about 450 to 600K typically assigned to trapping. ZF measurements verify this picture: the hop rate increases from 200 to 300K and then decreases to again become quasi-static between 450 and 600K. Quadrupolar decoupling curves, similar to those used prior to Mu^- QLCR, with the transverse field applied along a ⟨100⟩ direction show vastly different behaviour in the two static regions. In addition to the different low–field relaxation rates in Fig. 2, below 200K the decoupling curve is flat up to near 3T while near 500K the rate drops to near zero with a characteristic field of about 0.1T.[9] These data clearly imply two quite different Mu^+ locations in p–type GaAs, one at low temperatures and a second at higher temperatures after detrapping from the first. One possibility for two sites are the BC and the T_{As} cage region which becomes attractive for Mu^+ in this slightly ionic compound. However, a likely alternative at high temperatures is Mu trapped at the Zn acceptor forming the analog of an H-Zn passivation complex. We plan QLCR measurements to identify the Mu^+ states and sites in p-type GaAs.

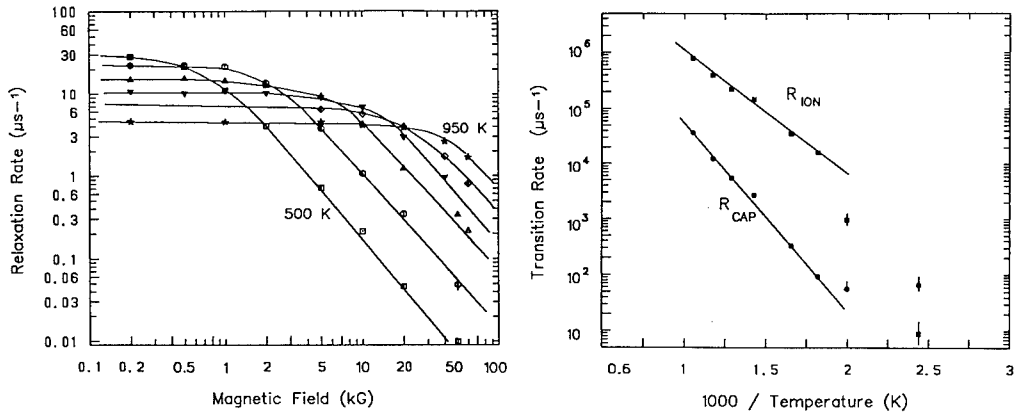

Figure 3. (a) Measured longitudinal depolarization rates for GaAs(Si) doped at $3 \times 10^{15} cm^{-3}$, and (b) the transition rates extracted for a $0/+$ electron capture/ionization charge cycle involving Mu_T^0.

Cyclic Charge–State Transitions

At the highest temperatures shown in Fig. 2 both the Mu^+ and Mu^- relaxation rates show a sharp upturn. Similarly the longitudinal rates show a rapid rise around 550K and a peak at high temperatures in Fig. 1 involving all of the implanted muons. These are characteristic features associated with the rapid cyclic charge–state transitions seen at high temperatures in many semiconductors. We have examined this region more thoroughly for several GaAs samples. In heavily–doped n–type GaAs(Si) we measured longitudinal depolarization rates in two widely separated fields, 48mT and 2.9T, at identical temperatures from roughly 850K to 1000K.[7] This data set allows extraction of the two transition rates in a two–state charge cycle if the hyperfine constant of the neutral center is known. A more complete field dependence measured at 900 and 1000K allowed the relevant neutral state to be identified as Mu_T^0. Transition rates from fits with the hypefine constant fixed determined the transition processes to be electron and hole capture with the muon remaining at the T-site, *ie.* a cycle between Mu_T^- and Mu_T^0. The capture cross sections of $16.0 \pm 0.6 Å^2$ for e^- capture by Mu^0 and $2600 \pm 200 Å^2$ for h^+ capture by Mu^- are fully consistent with the expected geometric and Coulomb capture processes. This result establishes Mu_T as a recombination center which is typical of deep–level defects in semiconductors, and implies that the $T(-/0)$ level for Mu does not lie close to either band edge. Since the mass difference should not alter carrier trapping cross sections or electronic energies by very much, we argue that the hydrogen will also be a recombination center in GaAs and that the corresponding level is also deep within the gap. Furthermore, this result implies that hydrogen diffusion when H^- should be the equilibrium state most likely procedes by this charge cycle with the diffusive motion dominated by a short–lived highly mobile H_T^0.

Figure 3 presents the field–dependent longitudinal data and fit results for a lightly–doped n–type GaAs(Si) sample. Similar data were obtained for semi–insulating GaAs and for an n–type sample at a concentration near $10^{17} cm^{-3}$. Preliminary low–field rates were previously published for weakly n–type and semi–insulating GaAs showing the onset of a charge cycle at about 550K.[10,12] Fits to each constant–temperature field dependence (as in Fig. 3a) to a two–state cycle identified a $0/+$ cycle for the two lower concentrations while the higher concentration sample behaved much like the very heavily doped one just discussed. The resulting transition rates, shown in Fig. 3b, are consistent with electron ionization and capture. The hyperfine constants, which were allowed to vary for each temperature, are completely consistent with the temperature dependence expected for Mu_T^0 as extrapolated from low–temperature TF–μSR spectra. The capture step of the cycle is activated by about half the average band gap over this temperature range and yielded a reasonable cross section. We thus conclude that this

cycle is properly identified as involving $Mu_T^0 \rightleftharpoons Mu^+ + e^-$ in a combined electron ionization and capture cycle. The lack of any additional energy barrier associated with a site change during the capture transition suggests a possible $Mu_T^{\ddagger}$ state as suggested for the trap site in p–type GaAs. The ionization step yields an energy parameter of about 0.450eV. Fits for the semi-insulating sample gave an essentially identical ionization energy. This appears to be very good confirmation that these two samples have similar muonium charge cycles above 550K. Each sample also shows a second cycle for a small fraction of the muons which continues to lower temperatures. Thus far we have not identified this additional cycle in either sample with certainty. Both appear consistent with $0/+$ at the BC site, although we cannot rule out other options.

Conclusions

A consistent picture for the Mu^- center in n–type GaAs has been achieved, including its location at a T_{Ga} region, its diffusive characteristics, and stability against dynamic charge exchange. Observation of a $-/0$ charge cycle due to electron–hole recombination at Mu_T implies a deep $0/-$ level for H in GaAs. Although both reside at T-sites, Mu^- is less mobile than Mu_T^0 by a huge factor, remaining static to near 500K. By implication H^- should be immobile to at least that temperature. On the microsecond timescale of the μSR experiments, we find no evidence for Mu-Donor complexes. Results on Mu^+ in p–type GaAs are more tantalizing and additional experiments are needed to discriminate between possible explanations. Identification of $0/+$ cycles involving Mu_T^0 in lightly–doped n-type GaAs yields an ionization energy of 0.45eV and suggests a possible T_{As} site for the Mu^+ center. The switchover from $0/+$ to $-/0$ charge dynamics in n–type GaAs occurs below a donor concentration of $10^{17} cm^{-3}$. Overall, significant progress has been achieved in understanding the muonium states and dynamics in GaAs; however, a number of major problems remain to be solved before the full picture can emerge.

Acknowledgements

This work was partially supported by the United States National Science Foundation, the Robert A. Welch Foundation, the National Sciences and Engineering Research Council of Canada, the Engineering and Physical Sciences Research Council of the United Kingdom, and a NATO Collaborative Research Grant.

References

[1] For reviews of muonium in semiconductors see B.D. Patterson, Rev. Mod. Phys. **60**, 69 (1988): R.F. Kiefl and T.L. Estle in *Hydrogen in Semiconductors*, ed. by J. Pankove and N.M. Johnson (Academic Press, New York, 1990) p547.
[2] R. Kadono, et al., Hyperfine Int. **64**, 635 (1990); J.W. Schneider, et al., Mater. Sci. Forum **83-87**, 569 (1992).
[3] R.F. Kiefl, et al., Phys. Rev. Lett. **58**, 1780 (1987).
[4] For recent summary see T.L. Estle and R.L. Lichti, Hyperfine Int. **97/98**, 171 (1996).
[5] See eg. S.K. Estreicher, Mater. Sci. Engr. Reports **14**, 1 (1995).
[6] K.H. Chow, et al., Hyperfine Int. **86**, 645 (1994).
[7] K.H. Chow, et al., Phys. Rev. B **51**, 14762 (1995).
[8] K.H. Chow, et al., Phys. Rev. Lett. **76**, 3790 (1996).
[9] K.H. Chow, et al., Hyperfine Int. **105**, 309 (1997).
[10] R.L. Lichti, Phil. Trans. **A350**, 323 (1995).
[11] R. Kadono, et al., Phys. Rev. B **50**, 1999 (1994).
[12] R.L. Lichti, et al. Hyperfine Int. **86**, 711 (1994).

Materials Science Forum Vols. 258-263 (1997) pp. 855-860

STRUCTURE AND REORIENTATION OF THE Si_{As}-H AND Zn_{Ga}-H COMPLEXES IN GALLIUM ARSENIDE

Aldo Amore Bonapasta*, Paolo Giannozzi°, and Mario Capizzi‡
***Consiglio Nazionale delle Ricerche - Istituto di Chimica dei Materiali (ICMAT), Via Salaria Km 29.500, CP-10 I-00016 Monterotondo Scalo, ITALY**
°Scuola Normale Superiore, Piazza dei Cavalieri 7, I-56126 Pisa, ITALY
‡INFM-Dip. di Fisica, Univ. La Sapienza, P.le A. Moro 2, I-00185 Roma, ITALY

Keywords: dopants, hydrogen, gallium arsenide.

Abstract
The structure and the reorientation kinetics of the Si_{As}-H-Ga and of the Zn_{Ga}-H-As complexes in GaAs have been investigated by first-principle local-density-functional calculations. In both complexes, the H atom is located next a bond-centered site. However, the H atom is bonded to the Si acceptor, in the former complex, and to one of the As atoms nearest neighbor of the acceptor, in the latter complex. Despite this different chemical bonding, the two complexes have similar vibrational properties and reorientation kinetics. These results are in good agreement with experiments, except for unusually high reorientation rates of the H complex as measured by anelastic relaxation in *p*-type GaAs:Zn. The energy barrier opposing the reorientation of the Zn_{Ga}-H-As complex, as well as two different tunneling models cannot account for those high reorientation rates, which are most likely related to reorientation processes involving H, Zn, and other defects or impurities.

Introduction.
Infrared-absorption (IR) spectroscopy provides an important tool for the investigation of the microscopic structure of the complexes which are formed in semiconducting materials by H and impurity atoms.[1] The study of the localized vibrational modes (LVM) of hydrogen has allowed to identify the H-*X* bonds involved in the complex, where *X* is the dopant or one of its nearest neighbors. Moreover, a uniaxial stress may induce frequency shifts and lifts of degeneracy in the IR spectra which suggest the complex symmetry and the location of the H atom.[1,2] When a H atom is located next a bond-centered site (BC), see Fig. 1,

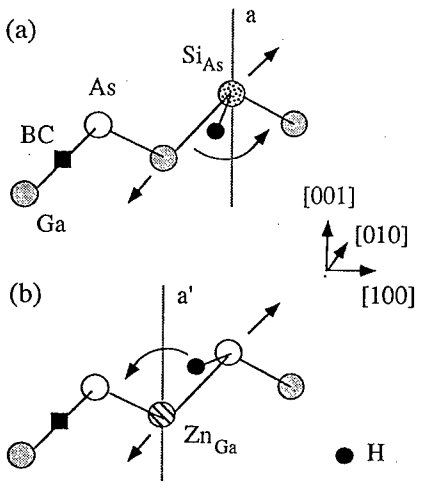

Figure 1. (a) The off-axis bond-centered (BC) configuration of the Si_{As}-H_{BC}-Ga complex (see the text). A BC site on the Ga-As bond is represented by a solid square. The arrows show the directions of the atomic displacements with respect to the unrelaxed geometry. A circular path is also shown, describing a possible H motion around the Si acceptor; (b) same as (a), in the case of the Zn_{Ga}-H_{BC}-As complex.

a stress-induced-alignement technique allows to investigate the H motion around the dopant atom.[1, 3-6] As an example, Fig. 1(a) shows the *off-axis* BC configuration of the complex formed in GaAs by a H atom and a Si acceptor located at an As site (Si_{As}). In this configuration, the H atom is next the BC site of the Si_{As}-Ga bond, *off* the bond axis. Figure 1(a) shows also a circular path relative to the H motion from an off-axis BC site to the BC site of a neighboring Si_{As}-Ga bond. A H complex with a BC configuration has a trigonal symmetry with four threefold axis along the four, equivalent

[111] directions. A uniaxial stress applied along a [110] direction lowers the symmetry of the system and induces a H motion toward the most favorable configuration. If the stress is applied at low temperature, the H_{BC}-X complex - where H_{BC} stands for a H atom next the BC site - may not reorient among its new non-equivalent configurations. The H-stretching band splits, therefore, into several components, which allows to determine the symmetry of the center.[3,4,6] Moreover, the distribution of the H atoms among the non-equivalent BC sites causes an optical dichroism.

Complex	Bond	ν	E_a	Ref.
Si:B-H	Si-H	1903	0.22	3
GaAs:Zn_{Ga}-H	As-H	2146.9	0.037	2,10
GaAs:Be_{Ga}-H	As-H	2036.9	0.37	5
GaAs:Si_{As}-H	Si-H	2094.7	0.26	6
GaAs:C_{As}-H	C-H	2635.1	0.50	2

Table I. Experimental values of the H stretching frequencies ν and activation energies E_a for the reorientation of different H-acceptor complexes in c-Si and c-GaAs. The values of ν and E_a are given in cm^{-1} and eV, respectively.

When the stress is removed in a properly prepared sample, the H complexes reorient among the equivalent complex configurations and measurements of the dichroism decay time at different T's may be performed. This allows to estimate both the activation energy (E_a) and the rates of the complex reorientation.[1, 3-6] The activation energies given by IR spectroscopy have generally been estimated by assuming that the reorientation mechanism is a thermally activated process which involves single jumps over a barrier and can be described by an Arrhenius formula. However, in the case of B-H complexes in crystalline silicon (c-Si), a deviation from the Arrhenius behavior has been observed and a satisfactory agreement with the experiment has been found by using the Flynn-Stoneham thermally-assisted-tunneling model.[7,8] In this model, the lattice distortion caused by a light interstitial - which is relevant in the case of H_{BC} - inhibits a simple tunneling of H from site to site and only when thermal fluctations give rise to a coincidence geometry, tunneling may occur. Other models account for a non-Arrhenius behavior. As an example, the reorientation of nitrogen in diamond was explained at high temperature by a model involving a thermally assisted jump and at low temperature by a tunneling process from one orientation to another which occurs in thermally-populated vibrational states.[9]

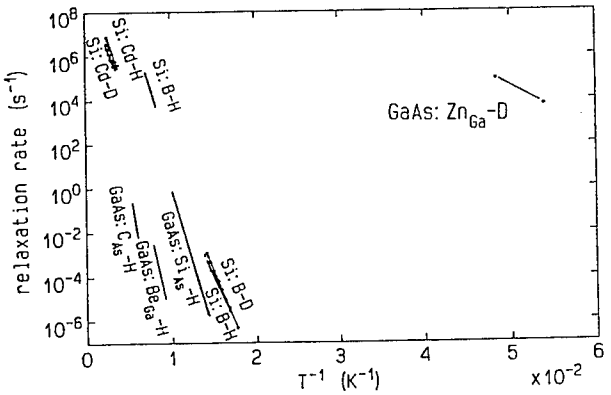

Figure 2. Experimental reorientation rates of different H- and D-acceptor complexes in c-Si and c-GaAs. The figure is taken from Ref. 10, with permission.

The values of the H stretching frequencies ν and of the activation energies E_a for the reorientation process of several H complexes are reported in Table I. The corresponding reorientation rates for different H- as well as D-acceptor complexes are given in Fig. 2. In the case of GaAs:Zn, activation energies for the complex reorientation and corresponding reorientation rates have been measured by anelastic relaxation (AR).[10] For the complexes reported in Table I, but for the Zn complex, IR

measurements give quite similar values for both the activation energies and the parameters describing the effects of the stress on the H frequencies (not reported in the Table).[6] The same complexes are also characterized by similar reorientation rates for temperatures ranging from 70 K to 120 K, see Fig. 2. These similarities are surprising, especially in the case of the Be_{Ga}-H and Si_{As}-H complexes where both experimental[6] and theoretical results[11,12] suggest quite different H local bondings. In fact, the H atom is bonded to the acceptor, in the case of As-site acceptors, to one of the As nearest neighbors of the acceptor, in the case of Ga-site acceptors.
Recent AR investigations in deuterated GaAs:Zn[10] have reported quite high reorientation rates at low temperature (~20 K) for the D complexes. In terms of an Arrhenius scheme, these measurements would lead to a low activation energy, 37 meV. However, an Arrhenius expression does not fit the experimental data, while a fair agreement has been found with the Flynn-Stoneham thermally-assisted-tunneling formula.[8] The same AR investigations have not observed a reorientation of the Zn_{Ga}-H complex at temperatures higher than 20 K. This is quite surprising because the H local bonding in the Zn_{Ga}-H complex should be similar to that of the Be_{Ga}-H complex which reorients, instead, at 120 K with an activation energy of 0.37 eV.
In the present paper, first-principle calculations have been performed to investigate the structure and the reorientation mechanisms of the Si_{As}-H and Zn_{Ga}-H complexes. Moreover, the properties of the H complexes formed by As-site acceptors have been compared with those of H complexes formed by Ga-site acceptors in order to explain the very low reorientation energy of the Zn_{Ga}-H complex. Two tunneling models have been also investigated in the case of the Zn_{Ga}-H complex.

Methods

The equilibrium geometries of the Si_{As}-H and of the Zn_{Ga}-H complexes have beeen investigated by performing *ab initio* total energy and atomic force calculations in a local-density-functional framework and in a supercell approach. The geometry of supercells containing the H and the acceptor atoms has been fully relaxed by minimizing the Hellmann-Feynman forces on the atoms. The exchange-correlation functional of Ceperley-Alder has been used together with norm-conserving pseudo-potentials and planewave basis sets; **k**-space integration has been performed with the use of the special-points technique. Separable ab-initio pseudopotentials have been used in the case of Ga, As and Si atoms.[13] Details on the theoretical methods are given in Ref. 14. The hydrogen vibrational frequencies have been evaluated in the harmonic approximation. The dissociation energy of the bonds formed by the hydrogen atom has been estimated as in Ref. 14. Convergence tests have been performed on the atomic pseudopotentials and on the structural and electronic properties of the H complexes. A reasonable convergence of the calculated values has been obtained by using 32-atom supercells, the (4,4,4) **k**-point mesh, and cutoffs of 18 or 22 Ry.

Results and discussion

In the case of the Si_{As}-H complex, three different configurations with trigonal symmetry (not shown here) have been considered. The BC configuration is the stable one, with the H atom *off* the Si_{As}-Ga bond-axis, in slight disagreement with a previous theoretical study[11] (details of the equilibrium geometry are given in Table II).

X	Y	X-Y	ΔX	ΔY	H-X	H-Y	ß	E_a	E_d	ν
Ga	Si_{As}	3.04	0.34	0.29	1.69	1.56	21.7	0.22	2.0	2002
Zn_{Ga}	As	3.21	0.49	0.32	1.74	1.54	12.3	0.24	1.6	2156

Table II. Theoretical results for the geometrical parameters and the H stretching frequencies ν relative to the Si_{As}-H_{BC}-Ga and Si_{As}-H_{BC}-Ga complexes in their stable configurations (see the text). The atomic displacements ΔX and ΔY are measured with respect to the positions of the unrelaxed lattice, as shown in Fig.1. ß is the angle formed by H with respect to the X-Y bond, see Fig. 1. E_a is the activation energy for the complex reorientation. E_d is the dissociation energy of the H-Si bond in the Si_{As}-H_{BC}-Ga complex and of the H-As bond in the Si_{As}-H_{BC}-Ga complex. Atomic displacements and bond lenghts are given in Å, energy in eV, angles in degree.

A strong H-Si bond is slightly perturbed by the presence of the neighboring Ga atom, as shown by the H-Si and H-Ga bond lengths and confirmed by the plot of the valence charge density given in

Fig. 3(a). The dissociation energy of the H-Si bond, 2.0 eV, and the calculated H stretching frequency, 2002 cm^{-1}, are in good agreement with the experimental values, 2.10 eV and 2095 cm^{-1}, [2] respectively. Configurations with trigonal symmetry have been investigated also in the case of the ZnGa-H complex. Once more, the *off-axis* BC configuration is the stable one, see Fig. 1(b) and Table II, where the geometrical parameters of the stable configuration are given. The H atom is mainly bonded to the As atom of the ZnGa-As bond involved in the complex formation. The H-As bond is slightly perturbed by the Zn acceptor, as shown by the distribution of the valence charge density given in Fig. 3(b) and by the values of the H-As and H-Zn bond lengths. The dissociation energy and the H stretching frequency evaluated for the H-As bond in the complex agree very well with the experimental counterparts, 1.6 eV and 2147 cm^{-1},[2] respectively. Thus, present results support the suggestion based on IR studies that the configuration of the ZnGa-H complex is BC, similar to that of the BeGa-H complex, and that the measured H stretching frequency is related to a H-As bond.[2] Present results also indicate that H has a quite similar local bonding in SiAs-HBC-Ga and ZnGa-HBC-As complexes, as shown by the distributions of the electronic charge densities given in Figs. 3(a) and 3(b). Moreover, the two complexes have comparable dissociation energies for the H bonds and close H-stretching frequencies.

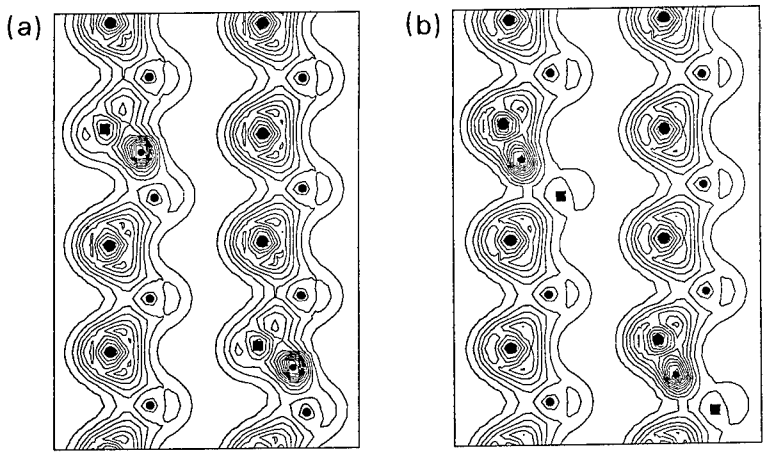

Figure 3. Contour plots in the (110) plane of the electronic charge density for the stable BC configuration of the H-acceptor complexes (see the text): (a) Si_{As}-H_{BC}-Ga complex; (b) Zn_{Ga}-H_{BC}-As complex. Solid squares indicate the acceptors; solid circles of different size, from the largest to the smallest, indicate the As, Ga and H atoms, in the order.

In order to investigate the reorientation kinetics of the H complexes, the most favourable path for the H motion has been found by moving the H atom along different, selected paths and by relaxing the supercell structure for each position of the H atom. In c-Si:B, a similar procedure has given an estimate of the energy barrier for the reorientation of the H-B complex in good agreement with experimental results.[3,15] In the case of the ZnGa-HBC-As complex, different circular paths have been considered, which go from the BC equilibrium site of the H atom toward an equivalent BC site of a neighboring ZnGa-As bond on a (110) plane, see Fig. 1(b) (hydrogen locations off the (110) plane have higher energies). These calculations show that the total energy increases when the H atom moves from its equilibrium position up to a location midway the BC sites at the beginning and at the end of the chosen path. This location is, for symmetry reasons, on a [001] axis passing through the location of the Zn atom in the unrelaxed lattice, see the axis labeled a' in Fig. 1(b). In order to establish the minimum energy for the complex reorientation, a radial path has been considered where the H atom is located along the a' axis. The H atom has been located at different distances from the position of the Zn atom in the unrelaxed lattice and the structure of the supercell has been relaxed. This procedure has found a minimum barrier energy of 0.24 eV. In this configuration, there is a weak Zn-H bonding interaction and a negligible interaction of H with its As nearest neighbors. Similar calculations have been performed in the case of the SiAs-HBC-Ga complex. The investigated circular

path for the H motion is shown in Fig. 1(a). The minim barrier energy, 0.22 eV, has been found along the [001] axis passing through the location of the Si atom in the unrelaxed lattice, see the axis labeled *a* in Fig. 1(a). The calculated barrier energy is in good agreement with the experimental reorientation energy of 0.26 eV.[6] In the minimum barrier configuration, the H local bonding is quite similar to that found in the case of Zn.

The present results, which indicate that the reorientation kinetics of the ZnGa-HBC-As complex is quite similar to that of the SiAs-HBC-Ga complex, imply reorientation rates for the former complex close to those given in Fig. 2 for the latter complex. Although present results do not exclude that a deviation from an Arrhenius behavior could be observed at low temperature, they cannot account for the high reorientation rates observed by AR measurements in the case of the Zn acceptor.[10] A possible role of tunneling processes has been then considered by investigating, at a qualitative level, a model involving H tunneling between excited vibrational states as well as the Flynn-Stoneham thermally-assisted-tunneling model. In the first case, the tunneling model gives a reorientation frequency almost costant in the range of temperature from 20 K to 150 K, at variance with the experimental findings. In the case of the Flynn-Stoneham model, only a very simple test has been performed. In this model, the jump rate depends on three parameters, the thermal energy to access the coincidence geometry *Ec*, a tunneling matrix element, and the Debye temperature. In the case of the ZnGa-HBC-As and SiAs-HBC-Ga complexes, a "natural" choice for the coincidence geometry is represented by a geometry symmetric with respect to the *a* (or *a'*) axis shown in Fig. 1. In this symmetric configuration, the potential created by the crystal may be represented by two symmetric wells separated by a potential barrier, which allows tunneling between two BC sites as required by the Flynn-Stoneham model. The thermal energy *Ec* relative to this coincidence geometry is about 0.4-0.5 eV, which is comparable with the energy barrier of 0.24 eV found for the complex reorientation in absence of tunneling and too high with respect to the value used to fit the results of the AR measurements (0.037 eV).[10]

Conclusions.

Present results agree well with experiments but for the high reorientation rates measured by AR in the case of the Zn acceptor in GaAs. The ZnGa-H-As complex has static and dynamic properties similar to those of the BeGa-H-As complex, as expected. The former complex has vibrational properties and reorientation kinetics similar to those of the SiAs-H-Ga complex. This last result seems quite reasonable at the light of the similarities experimentally observed in the case of the BeGa-H-As and the SiAs-H-Ga complexes. On the other hand, neither the value estimated for the energy barrier opposing the complex reorientation, nor the analysis of two different tunneling models have allowed to account for the high, unusual reorientation rate measured in deuterated GaAs:Zn. Therefore, those reorientation rates do not involve a simple H- Zn complex, but more likely involve a complex formed by H (D), Zn, and other defects or impurities.

References

1. M. Stavola and S. J. Pearton, in "Hydrogen in semiconductors", ed. by J.I. Pankove and N.M. Johnson, Semiconductors and Semimetals Vol. 34 (Academic, San Diego, 1991), p. 139.
2. J. Chevallier, B. Clerjaud, and B. Pajot, in Ref. 1, p. 447.
3. K. Bergman *et al.*, Phys. Rev. **B38**, 9463 (1988).
4. M. Stavola *et al.*, Phys. Rev. Lett. **61**, 2786 (1988).
5. M. Stavola *et al.*, Phys. Rev. **B39**, 8051 (1989).
6. D. M. Kozuch *et al.*, Phys. Rev. **B48**, 8751 (1993).
7. Y. M. Cheng and M. Stavola, Phys. Rev. Lett. **73**, 3419 (1994).
8. A. M. Stoneham, J. Chem. Soc. Faraday Trans. **86**, 1215 (1990).
9. C. A. J. Ammerlaan and E. A. Burgemeister, Phys. Rev. Lett. **47**, 954 (1981).
10. G. Cannelli *et al.*, Solid State Comm. **98**, 873 (1996).
11. L. Pavesi and P. Giannozzi, Phys. Rev. **B43**, 2446 (1991).
12. P. Briddon and R. Jones, in "Shallow Impurities in Semiconductors", ed. by G. Davies (Trans. Tech, Zurich, 1991), p. 169.
13. R. Stumpf, X. Gonze, and M. Scheffler, Res. Report of the Fritz-Haber-Institut, Berlin (FRG), April 1990.
14. A. Amore Bonapasta, Phys. Rev. **B48**, 8771 (1993).
15. C.G. Van de Walle *et al.*, Phys. Rev. **B39**, 10791 (1989).

Materials Science Forum Vols. 258-263 (1997) pp. 861-866

AB INITIO STUDY OF THE C_{As} LOCAL OSCILLATOR IN GALLIUM ARSENIDE

K. Petzke, C. Göbel, C. Schrepel and U. Scherz

Inst. für Theoretische Physik, Technische Universität Berlin, Hardenbergstr. 36, D-10623 Berlin

Key Words: GaAs:C, anharmonicity, local vibrational mode, density-functional theory

Abstract

We present an ab initio study of the anion-site substitutional impurity C_{AS} in GaAs. The local vibrational mode (LVM) at this defect shows a distinct fine structure due to a ligand induced isotope effect. Furthermore, precise experiments and model calculations have shown, that the LVM can not be completely understood without anharmonic forces [7] [8]. We use ab initio density-functional theory to calculate both the energy and the fine structure of the LVM. We first perform calculations within the harmonic approximation, which show good agreement with experimental results on some properties, but significant deviations at others. Therefore, we take the third and fourth order anharmonic elastic potential into account by using a Green's function technique.

Introduction

The C_{AS} impurity in GaAs plays an important role in semiconductor technology. Infrared absorption at the LVM at this impurity is a standard method to measure the dopant concentration. Consequently, this centre has been subject to detailed experimental studies. In Ref. [3] W. M. Theis et al. were able to conclude from their precise measurements of the fine-structure of the LVM, that the Carbon impurities are located at the As positions of the lattice and therefore act as shallow acceptors. In Ref. [4] B. V. Shanabrook et al. show, that the line shift of the LVM of 0.02 meV is small, when it is transformed from the neutral to the charged state. They attribute this to the weak binding of the hole to the shallow acceptor.

In the recent work [7], Leigh and Newman present new high-resolution measurements of the LVM. They demonstrate, that their data can only be approximated but not be fully understand within a harmonic model. This is strong evidence that anharmonic effects are not negligible. H. Ch. Alt discovered a thermally activated line, whose energy is shifted down by 0.4 meV [8]. It was attributed to a transition from the first excited oscillator state to the second. According to his model, the line shift is the result of an anharmonic disturbance to the harmonic oscillator.

In the first step of our calculations we obtain the harmonic elastic potential of a perfect GaAs crystal in order to take hybridization effects of the LVM with the host modes into account. In the second step we include the impurity centre. The atoms in the vicinity of the defect are moved away from their positions of the perfect crystal in order to minimise the energy of the disturbed crystal. In the third step we calculate the harmonic elastic potential in the vicinity of the defect. These results enable us to calculate a cluster of up to 489 virating atoms and to obtain the energy of the LVM in the harmonic approximation. In the fourth step, we include the anharmonic effects at the impurity by using a Green's functions technique.

Parameters of the ab initio calculations

All ab initio calculations are performed using density-functional theory. We use a modified program originating from the Fritz-Haber-Institute, Berlin, Germany [6]. In particular, the program has been ported by us to the Cray T3D massive parallel computer at the Konrad–Zuse–Zentrum für Informationstechnik, Berlin. The calculations of the first step (perfect crystal) are described in detail in Ref. [9].

We use a plane wave basis set, pseudopotentials and LDA. The Ga potential is calculated with the standard Bachelet, Haman and Schlüter scheme [2]. It includes a model core for non–linear core correction (nlcc). The As and C potentials were generated using the Troullier and Martins scheme [5].

We carefully tested our numerical procedure by varying the supercell size, the number of k points and the plane wave cut off energy. For the force constants, we take the difference between the Hellman–Feynman forces on a given atom in two slightly different configurations. Therefore, we use these force differences as our convergence criteria. Full convergence is reached with a cut off energy around 60 Rydberg. Our calculations are done at 33 Rydberg. This causes the forces to be calculated about 1,5% too strong.

Another source of error is the restricted description of the relaxation. In particular, a low cut off energy results in a force pushing the atoms too far away from the impurity centre. Because of the anharmonicity described below, this results in a weaker harmonic potential. A numerical analysis shows, that this decrease of the force constants compensates about 50% of the direct error due to the low cut off energy.

We also test the k–point sampling on a cubic supercell with eight atoms, see Fig. 1. If the impurity centre is negatively charged, the k–point sampling is uncritical. Even with the 2x2x2 mesh, the error is less than 3%. This is consistent with the general observation, that a small set of k–points is sufficient for semiconductors. If one electron is removed, a hole is produced in the system, which is only weakly bound to the shallow acceptor. From the effective mass model, one can estimate the radius of the hole's wave functions - it is over twice as big, as the length of the eight atom test cell. Such delocalized wave functions are very sensitive to k–point sampling. As can be seen from Fig. 1, not even the 6x6x6 mesh can be considered converged in this case.

Fortunately, the situation is much better, as Fig. 1 suggests. A similiar self-compensation effects, which we observed for the convergency with respect to the cut off energy, also acts with the k–point sampling. We have used just one k–point in the 64 atom supercell, which corresponds to the 2x2x2 mapping in the eight atom test cell. We estimate an error of at most 3% for the charged acceptor, but over 10% in the neutral case. As will be shown below, the actual difference between the neutral and charged acceptor is less than 2%.

Relaxation at the impurity centre

The first tests are done with a small cubic supercell containing eight atoms. After one As has been replaced with Carbon, we calculate forces of 2.4 $eV\AA^{-1}$ on the four Gallium neighbors pointing towards the impurity. This fits well with the empirical chemical model, that the Carbon atom is smaller than the substituted Arsenic.

For all further calculations of the disturbed crystal, we use a fixed cubic supercell containing 64 atoms. To compensate the strong forces, we allow the nearest neighbor Gallium atoms of the impurity to move inwards. A plot of the total energy over the displacement shows a minimum at 0.344 Åwith the acceptor in its neutral state.

We use this relaxed configuration to calculate new force constants in the vicinity of the defect, using the same procedure, as for the perfect crystal: one atom is displaced, and the change of

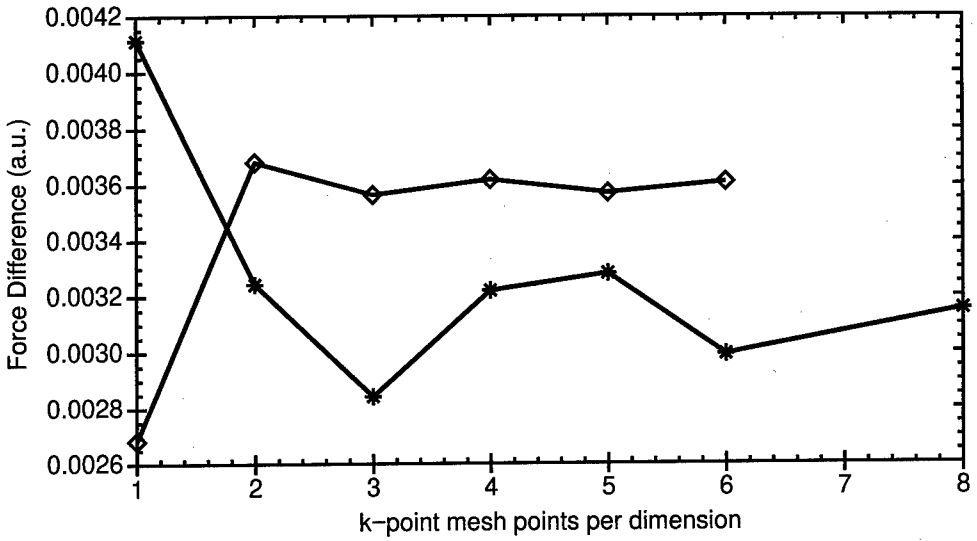

Figure 1: Convergency of a typical result property, which is the difference between the Hellman-Feynman forces on a given atom, after some atoms of the cell have changed their position slightly. The calculation was performed on an 8 atom cell with the acceptor in its neutral (stars) or negatively charged (diamonds) state.

the Hellman-Feynman forces between that atom and the other atoms is analyzed. We then set up a cluster of 489 atoms including the impurity centre and calculate the vibrational modes of this system. We find, that a threefold degenerate LVM, which has 95% of its vibration energy located on the central C atom, shows up at 60.9 meV. However, the experimental result is 72.15 meV [7].

This discrepancy can be attributed to the incomplete relaxation in our calculation. By moving the Gallium ligands towards the impurity centre, we bend the back-bonds of each of the Gallium ligands to Arsenic atoms. This bending results in a force pulling away the ligands from the impurity centre. By letting those twelve Arsenic atoms of the second shell relax, we can reduce those bending forces and thus increase the relaxation of the first shell, resulting in shorter and thus stronger C–Ga bonds. To increase the precision even further, we also include relaxation of those 24 Gallium atoms of the third and fifth shell around the impurity centre, that are bound to any of the atoms of the second shell. More is not possible, because we already reach the borders of the 64 atom cluster.

We only include symmetry–conserving relaxations of the atoms. This results in 7 degrees of freedom: one for the innermost shells and two for each other shell. Instead of calculating a seven-dimensional energy surface, we use the Hellman–Feynman forces to calculate the relaxation. This is no problem, as the additional displacements are small, no atom is moved by more than 0.07 Å from the position, that it had before. The first shell of atoms is moved inwards by an additional 0.045 Å. This change may look rather insignificant, but it causes the force constant for the vibration of the central impurity atom to increase from $1.63 \cdot 10^{-4}$ Nm^{-1} to $2.07 \cdot 10^{-4}$ Nm^{-1}.

We investigate the impurity both in its neutral and its negatively charged state. Experiments show, that the line shift between those two is only 0.02 meV [4]. The authors attribute this to the weak binding of the additional electron at the impurity. Our relaxation calculations directly verify that conclusion: the maximum displacement of an atom due to the change of

the charge state is 0.01 Å.

Results using the harmonic approximation

We calculate new force constants for the defect atoms and its first neighbors in the relaxed position and set up a model cluster with 489 atoms. Solving the dynamical matrix yields the data for 1467 vibrational modes. To obtain the density of states in the cluster, the sharp eigenenergies of the vibrational modes are replaced with Gaussians. In Fig. 2, we compare the cluster's density of states to the results of calculations for the perfect crystal. Because of the high difference between the frequency of the LVM and the perfect crystal's host modes, the visible differences in the DOS are completely insignificant to the results. If the cluster's size is reduced to 191 atoms, the eigenvalue of the LVM changes by less than 1 μeV.

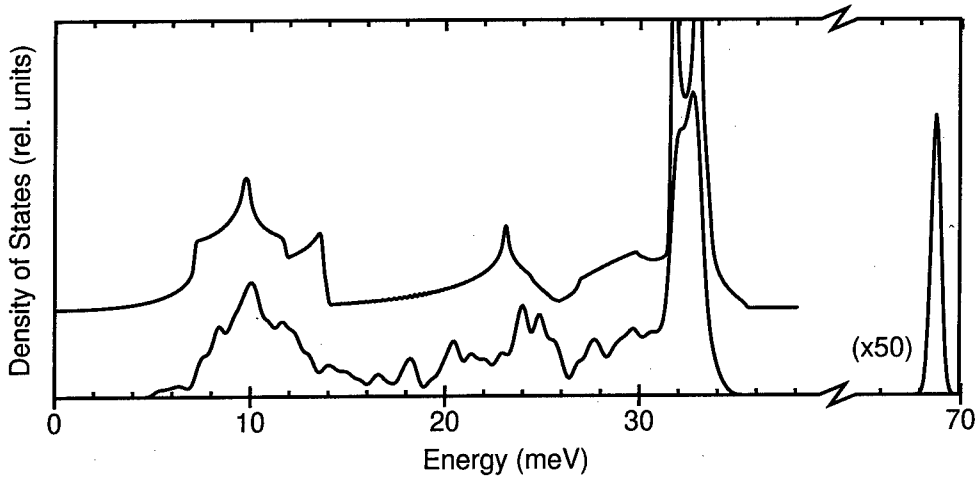

Figure 2: Density of phonon states in Gallium Arsenide. The upper curve has been calculated for the perfect crystal, the lower for a cluster of 489 vibrating atoms. The cluster calculations include the Carbon impurity centre, resulting in a split off mode at 68.9 meV.

There are two stable C isotopes: most common is ^{12}C, but ^{13}C can also be observed in experiments. The centre can be in the charge states 0 and -1. For those four configurations, we obtain the energy of the LVM as follows: ^{12}C: 68.9 meV, ^{12}C^{-}: 68.3 meV, ^{13}C: 66.2 meV and ^{13}C^{-}: 65.7 meV. The isotope shift ^{12}C $\rightarrow^{13}$ C is calculated as 2.56 meV (neutral) or 2.53 meV (negatively charged). This is in good agreement with the experimental value of 2.60 meV [7].

The line shift between the neutral and the charged state of the acceptor is calculated as -0.6 meV compared to the experimental value of $+0.02$ meV [4]. As stated above, the configuration with the neutral acceptor is very sensitive to the k–point sampling, so our result of -0.6 meV can be fully attributed to numerical errors.

The energy of the mode varies slightly, if the mass of the Gallium ligands is changed. There are two stable Gallium isotopes: ^{69}Ga and ^{71}Ga. Unless the sample has been specifically prepared, those isotopes will appear with their natural quantities of 60.4% ^{69}Ga and 39.6% ^{71}Ga. We repeat the cluster calculations for all possible configurations of ^{69}Ga and ^{71}Ga ligands. The sharp eigenvalues of the LVM's in each case are broadened with a Gaussian shape and weighed with the natural probability of the isotopes. The result is the theoretical fine-structure, shown in Fig. 3. The calculations also verify the model presented by Leigh and Newman [7]. In particular, the left and right main peaks are a combination of three independant modes.

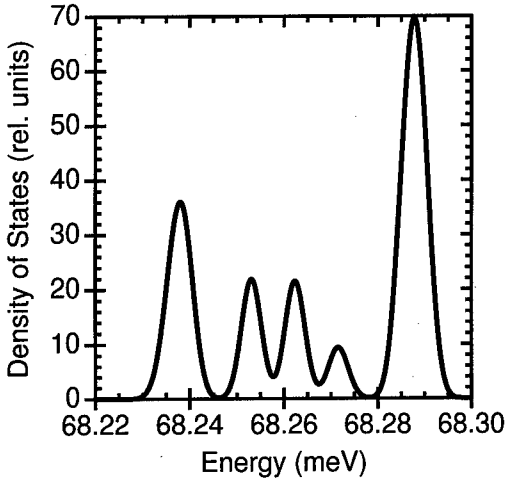

Figure 3: Calculated fine structure of the LVM at $^{12}C_{As}$ in GaAs.

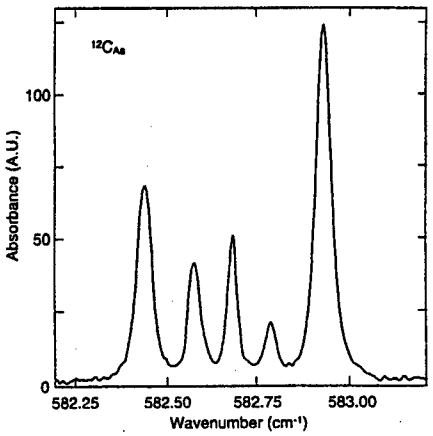

Figure 4: Meassured fine structure of the LVM at $^{12}C_{As}$ in GaAs, according to [7].

The location and intensity of the maxima of the theoretical fine-structure (Fig. 3) fits well to the experiment (Fig. 4). However, the splitting between the two main peaks is calculated as 0.049 meV for both ^{12}C and $^{12}C^{-}$, which is in discrepancy to the experimental value of 0.060 meV. Next, we perform a fit by hand, where we change the force constants to reproduce the experimental value of the ligand induced isotope shift. This fitting requires to change some force constants by over 20%. This value is much larger than the uncertainity of the ab initio results estimated above, at least for the negatively charged acceptor. We conclude from this, that we cannot neglect the anharmonic contributions of the potential.

Corrections due to third and forth order potential

Most discussions about anharmonicity in the literature study the effects of a 3rd respective 4th order potential. They are calculated by performing a standard multi-dimensional Taylor expansion of the elastic potential $U(\mathbf{r}_1, \mathbf{r}_2, \ldots)$. For simplicity, we first consider the potential of the central C impurity only:

$$V_3 = \frac{1}{6} \sum_{i,j,k=1}^{3} \phi^{(3)}_{ijk} \Delta r_i \Delta r_j \Delta r_k \qquad \text{with} \qquad \phi^{(3)}_{ijk} = \frac{\partial^3 V}{\partial r_i \partial r_j \partial r_k}$$

$$V_3 = \frac{1}{24} \sum_{i,j,k,l=1}^{3} \phi^{(4)}_{ijkl} \Delta r_i \Delta r_j \Delta r_k \Delta r_l \qquad \text{with} \qquad \phi^{(4)}_{ijkl} = \frac{\partial^4 V}{\partial r_i \partial r_j \partial r_k \partial r_l}$$

Due to the symmetries of the tetrahedral group, many of the matrix elements of $\phi^{(3)}$ and $\phi^{(4)}$ are zero or equal to each other. In our coordinate system, the impurity is at the origin and the Ga ligands are located in the directions $\begin{pmatrix}-1\\-1\\-1\end{pmatrix}$, $\begin{pmatrix}-1\\1\\1\end{pmatrix}$, $\begin{pmatrix}1\\-1\\1\end{pmatrix}$ and $\begin{pmatrix}1\\1\\-1\end{pmatrix}$. Then only $\phi^{(3)}_{123}$, $\phi^{(4)}_{1111}$ and $\phi^{(4)}_{1122}$ are independant elements. Using density functional theory, we calculate their values as 47 eVÅ^{-3}, 618 eVÅ^{-4} and -32 eVÅ^{-4}, respectively. We also calculate force constants for the anharmonic interaction of the impurity centre with its neighbors in third and fourth order.

A good test for the potential is Newton's law, that all forces in a closed system add to zero. The forces are determined by building the potential's derivative with respect to the atomic position. If the central impurity and its four neighbors are considered, Newton's law is only

fullfilled for the third order potential. In case of the fourth order potential, even the forces on the first and second nearest neighbors combined compensate only three quarters of the forces, that act on the central atom due to $\phi^{(4)}_{1111}$.

The third order potential leads to a correction, that is second order in perturbation theory: an eigenstate (or mode) of the second order potential splits into two different eigenstates and then combines again to the same or another eigenstate. We use a Green's function technique [1] [10] to numerically calculate that effect. The result is -1.32 meV for neutral ^{12}C at T = 0K.

The fourth order potential leads to a correction, that is first order in perturbation theory: an eigenstate couples directly to another eigenstate. With the Green's function technique, we calculate a correction of +3.29 meV. As we have only included the most important force constants so far, that result has to be considered prelimary.

With both corrections, the mode is shifted from 68.9 meV to 70.8 meV. The deviation from the experimental value of 72.15 meV is therefore largely reduced.

Conclusions

We have shown, that it is possible to calculate several properties of a local vibrational mode from first principles. However, wrong results are obtained, if the relaxation of the atoms around the impurity is not treated exactly. The relaxation also compensates several numerical errors, that orginate from a poor k–point sampling and a low cut off energy. Further improvement of the results can be achieved, if anharmonicity is taken into account.

Acknowledgements

We thank the Fritz–Haber–Institut, Berlin, for providing their computer program fhi93cp and fhi94md. We thank the Konrad–Zuse–Zentrum für Informationstechnik, Berlin for providing CPU time on a Cray T3D massive parallel system and for their support.

References

[1] R. A. Cowley 1963, *Adv. Phys.* **12**, 421.

[2] G. B. Bachelet, D. R. Hamann, M. Schl"uter 1982, *Phys. Rev. B.* **26**, 4199.

[3] W. M. Theis, K. K. Bajaj, C. W. Litton and W. G. Spitzer 1982, *Appl. Phys. Lett.* **41**, 70-72.

[4] B. V. Shanabrook, W. J. Moore, T. A. Kennedy and P. P. Ruden 1984, *Phys. Rev. B.* **30**, 3563-3565.

[5] N. Troullier, José Luís Martins 1991 *Phys. Rev. B.* **43**, 1993.

[6] R. Stumpf und M. Scheffler 1994, *Computer Physics Communications* **79**, 447.

[7] R. S. Leigh, R. C. Newman et al 1994, *Semicond. Sci. technol.* **9**, 1054-1061.

[8] H. Alt 1995, *Mater. Sci. Forum* **196-201**, 1577-1582.

[9] K. Petzke, C. Schrepel and U. Scherz 1997, *Z. Physik. Chemie* **201**, 317-322.

[10] 'The Physics of Phonons', G. P. Srivastava, pages 167–172.

Materials Science Forum Vols. 258-263 (1997) pp. 867-872

SPECTROSCOPY OF NITROGEN-RELATED CENTERS IN GALLIUM ARSENIDE

H. Ch. Alt[1], B. Wiedemann[2] and K. Bethge[2]

[1]FB 06 - Physikalische Technik, Fachhochschule München, Postf. 20 01 13, D-80001 München
[2]Institut für Kernphysik, Univ. Frankfurt, August-Euler-Str. 6, D-60486 Frankfurt
GERMANY

Keywords: GaAs, N impurity, local modes (LVM), FTIR, spark source mass spectrometry (SSMS)

Abstract. Nitrogen-rich poly- and monocrystalline GaAs has been investigated by Fourier transform infrared absorption spectroscopy and radiofrequency spark source mass spectrometry. N concentrations in the 10^{16}-cm^{-3} range are found in poly samples. A linear relationship exists between the total chemical nitrogen contamination and the intensity of the 470-cm^{-1} local vibrational mode. An estimate for the calibration factor is given. The line shape parameters of this line, being significantly different from local modes of other anion site light impurities, are discussed.

Introduction

The investigation of light impurities in GaAs is of great interest for the development and optimization of crystal growth technology as well as for the physical understanding of these defects itself. Whereas there is now a considerable amount of experimental and theoretical work available concerning the common impurities/dopants H, B, C, O and Si, the behavior of N in this material is widely unknown.

Particularly suitable for the investigation of light impurities in GaAs is the local vibrational mode (LVM) spectroscopy, as LVMs can often be detected as sharp bands in low-temperature infrared (IR) absorption spectra. From LVM spectroscopy it is known that B, C and Si usually form simple substitutional defects, with B_{Ga}, C_{As} and Si_{Ga}, respectively, being the most common species [1-4]. Hydrogen, like in other semiconductors, is incorporated in complexes, preferably in H-acceptor and H-donor centers [5]. O occurs interstitially, as in Si, however also in an off-center position, close to the As lattice site [6,7]. The knowledge concerning the behavior of N in GaAs is only scarce. Nitrogen is present during crystal growth as N_2, used as an ambient gas in the liquid encapsulated Czochralski (LEC) or vertical gradient freeze (VGF) process, or as pyrolitic boron nitride (pBN) used for the crucible. From radiofrequency spark source mass spectrometry (SSMS) [8] it is known that commercial semi-insulating (SI) LEC GaAs grown under nitrogen atmosphere contains nitrogen in the 10^{15}-cm^{-3} range. In the polycrystalline starting material the concentration can be higher by an order of magnitude. It has been suggested that isovalent nitrogen (N_{As}) doping could lead to lattice hardening effects similar to In [9], however, experimental results are not available.

Optically detected evidence for N in GaAs was first reported by Kachare et al. [10]. After implantation of high-energy $^{14}N^+$ ions into SI GaAs, a broad band at 480 cm^{-1} was observed in IR absorption. The band was attributed to substitutional N_{As}. Further work was done on epitaxially grown GaAs:N. Using vapor phase epitaxy with NH_3 added to the carrier gas, nitrogen-doped epitaxial layers of GaAs can be grown [11,12]. These layers also show N-correlated absorption at about 470 cm^{-1} and, at low temperatures, excitonic emission resembling to GaP:N. Photoluminescence investigations under pressure [13,14] proved that isolated N and N-N pairs in GaAs have electronic levels resonant with the conduction band, which are driven into the gap under pressure. In bulk crystals, also N-H complexes have been found, identified by the high-frequency H vibrations between 2000 and 3000 cm^{-1} [15].

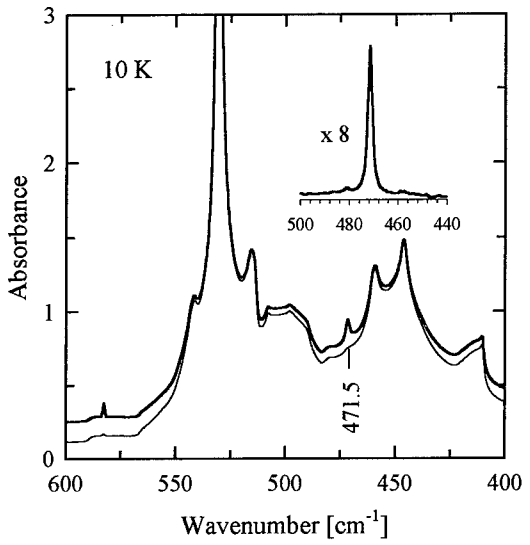

Fig. 1. Low-temperature FTIR absorption spectra of nitrogen-rich (bold line) and nitrogen-lean (small line) GaAs. The inset shows the N-related LVM obtained from the difference spectrum.

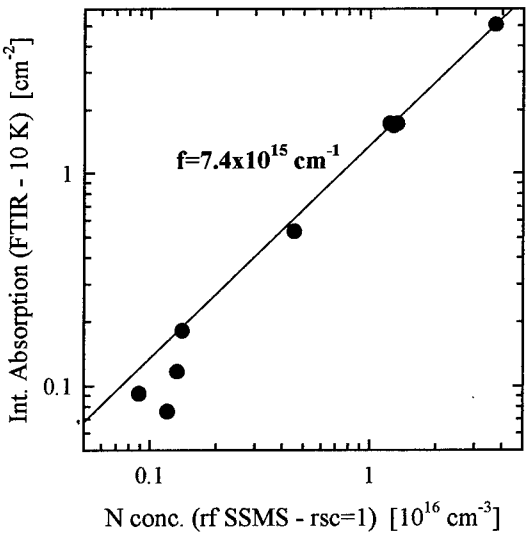

Fig. 2. Correlation between the integrated absorption of the 471-cm^{-1} line and the total N concentration.

This study is focused on nitrogen-rich poly- and monocrystalline bulk GaAs. The correlation of Fourier transform infrared (FTIR) absorption data with SSMS results allows for the first time the quantitative assessment of nitrogen in this material.

Experimental details

GaAs samples were selected with respect to the N concentration as measured by SSMS under ultrahigh vacuum conditions. The equipment is an upgraded high-resolution 21-110 type Mattauch-Herzog mass spectrometer with simultaneously detecting ion sensitive Q plate and a computerized Syncotec microdensitometer. The determination of the nitrogen concentration [N] depends on the relative sensitivity coefficient (RSC) for N. This coefficient, defined as the ratio $RSC=[N]_{SSMS}/[N]_{true}$, is expected to be between 0.3 and 3. For the present study RSC=1 is assumed [16]. The FTIR measurements have been carried out on a high-resolution vacuum instrument (Bruker IFS 113v) in the temperature range between 10 and 300 K. A Si bolometer (4 K) was used as a detector.

Results and discussion

GaAs samples with a chemical N concentration above 10^{15} cm^{-3} (as determined by SSMS) always show a band at about 471 cm^{-1} in the infrared absorption spectrum (Fig. 1). The line is superimposed to the multiphonon spectrum of GaAs, between the TO+LA structure at ~450 cm^{-1} and the strong 2 TO structure at ~525 cm^{-1} [17]. For the quantitative evaluation of the line, the absorption spectrum of a nitrogen-lean (below the SSMS detection limit of 1×10^{14} cm^{-3}) LEC GaAs sample was subtracted. In accordance with previous work [10,11], from the line frequency and temperature dependence (see below) it is deduced that the LVM of a light impurity is causing this line.

The integrated absorption of the line is

proportional to the defect concentration. From Fig. 2 it is obvious that there is a strictly linear relationship between the integrated absorption and the total N concentration. This linear relationship extents over nearly 2 orders of magnitude and the fit goes through zero. Therefore we conclude that the dominant fraction of the N contamination of the crystal is incorporated in the defect giving rise to the 471-cm^{-1} line. The calibration factor f=[N]/(Int. Absorption) derived from this relation is 7.4×10^{15} cm^{-1}. This value is close to the calibration factor of 7×10^{15} cm^{-1} for the LVM of substitutional carbon C_{As} [18]. The LVM of the nitrogen-hydrogen complex at 2947 cm^{-1} [15] is also observed in some N-rich polycrystalline samples. However, the intensity is low and the relation above shows that only a minor fraction of N is bound in this complex.

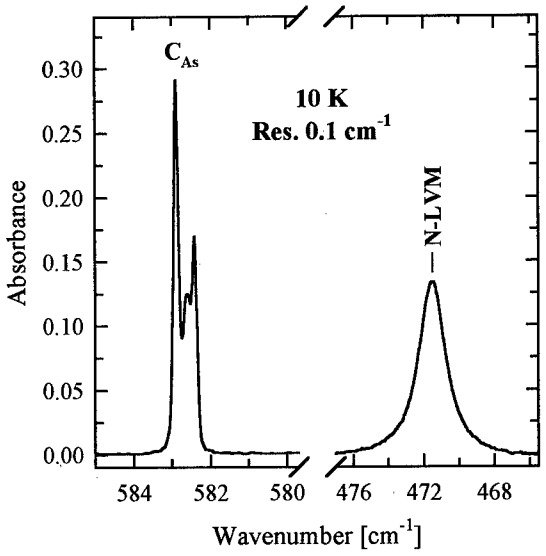

Fig. 3. High-resolution FTIR spectrum of a poly-crystalline GaAs sample showing both the C_{As} and the N LVM.

From its first observation in N-implanted

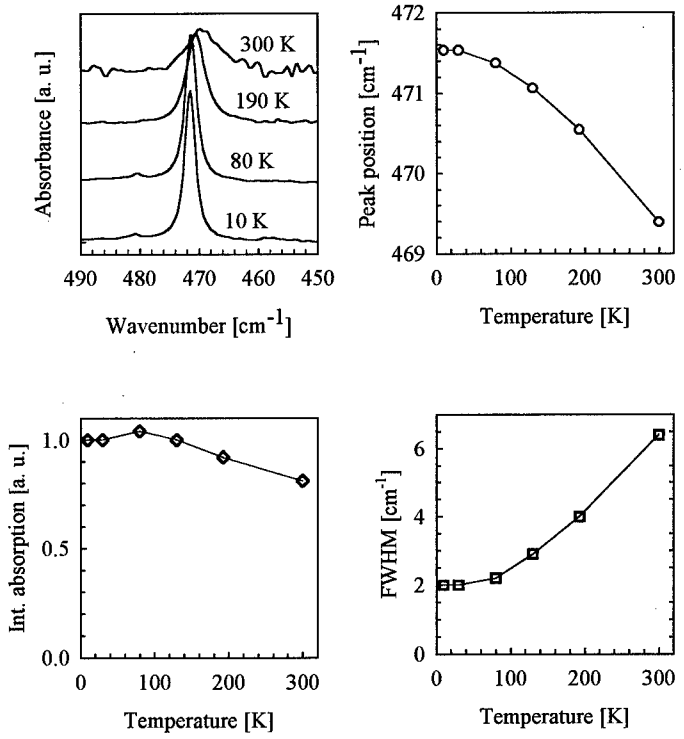

Fig. 4. Line shape and line shape parameters of the N-related 471-cm^{-1} line as a function of temperature.

samples, it has been suggested that the 471-cm^{-1} line is due to N_{As} [10]. This assignment is mainly driven by the plausible argument that a group V impurity will substitute the anion in a III-V semiconductor and by the similarity to N in GaP. Nitrogen doping in GaP has been studied extensively because of the importance for the light-emitting process in GaP based diodes [19].

In this case nearest neighbor atoms are Ga atoms and a fine-structure splitting of the line caused by the 2 host isotopes ^{69}Ga and ^{71}Ga is expected. However, this is not observed as can be seen from the high-resolution spectra in Fig. 3 which are taken at 10 K. Whereas the sample shows the well-known fine structure of the C_{As} LVM (not fully resolved because of the limited resolution of 0.1 cm^{-1}), the N-related LVM is a comparatively broad band (FWHM $\approx$ 2.0 cm^{-1}) and has no structure. Details of the temperature dependence of the nitrogen LVM are shown in Fig. 4. The peak position of the line shifts from 471.54 cm^{-1} at 10 K to 469.39 cm^{-1} at 300 K. The FWHM increases from 2.0 to 6.4 cm^{-1}. It should also be mentioned that a very small side band exists at 480.9 cm^{-1}. This line can be detected up to temperatures of 100 K. At higher temperatures it merges with the main band. No thermal activation could be detected in this limited temperature range.

In Fig. 5 the behavior of the N-related LVM is compared with the other anion site light impurities in GaAs: ^{28}Si (384 cm^{-1}), ^{12}C (583 cm^{-1}), and ^{11}B (602 cm^{-1}). All these LVMs show the host isotope fine structure. Furthermore, the frequencies of these modes follow closely a $1/\sqrt{m}$ dependence whereas the N mode has a considerably lower frequency. This could mean that the force constant between the N atom and its neighbors is lower than in the other cases. This, however, is unlikely because the Ga-N bond should be strong. The FWHMs of the other modes are below 1 cm^{-1} (with the exception of the relatively heavy Si atom) and, therefore, by a factor of two lower. Line broadening can be caused by a reduced lifetime of the vibrational state. In the case of the 471-cm^{-1} vibration, it can be assumed that elastic scattering of band phonons is the dominant process [20]. No quantitative theory is available at present concerning the influence on the linewidth of a LVM. However, the absorption due to band phonons in the region the N band is only by a factor of two higher than in the region of the Si_{As} line. Keeping in mind that this line still shows a fully resolved host isotope fine structure, it is questionable that the same fine structure is completely smeared out for the N band. In summary, all these differences cast some doubt on the assignment of the 471-cm^{-1} LVM as isolated N_{As}.

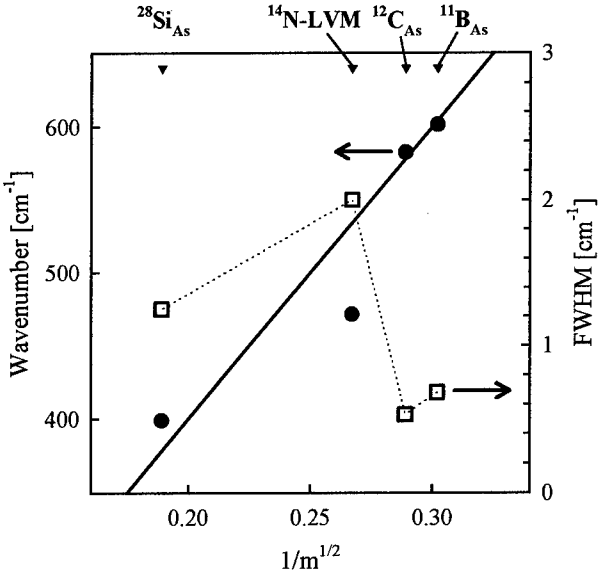

Fig. 5. Comparison of the N mode with other anion site light impurities. The bold line shows a fit of the mode frequency versus $1/m^{1/2}$. The dotted line is only a guide for the eye.

Conclusion

N concentrations in the 10^{16}-cm^{-3} range have been detected by SSMS in polycrystalline GaAs samples. In GaAs single crystals, grown by the LEC or VGF technique under nitrogen atmosphere, concentrations in the 10^{15}-cm^{-3} range have been verified. Using FTIR absorption spectroscopy, it is found that most of the incorporated nitrogen is bound in the defect giving rise to the 471-cm^{-1} LVM. A tentative calibration factor f for this line of

f=7.4×10^{15} cm^{-1} is derived. The line does not show any fine-structure splitting due to neighboring host Ga atoms. The low-temperature FWHM is larger than expected for an isolated anion site impurity. Further theoretical and experimental work is necessary for the understanding of these striking differences of the N-related LVM in GaAs.

References

1. F. Thompson, S. R. Morrison, and R. C. Newman in "Radiation Damage and Defects in Semiconductors" (Inst. Phys. Conf. Ser. 16), pp. 371-376 (1973).
2. R. C. Newman, F. Thompson, M. Hyliands, and R. F. Peast, Solid State Commun. **10**, 505 (1972).
3. W. M. Theis, K. K. Bajaj, C. W. Litton, and W. G. Spitzer, Appl. Phys. Lett. **41**, 70 (1982).
4. R. C. Newman, Semicond. Sci. Technol. **9**, 1749 (1994).
5. S. J. Pearton, J. W. Corbett, and M. Stavola in "Hydrogen in Crystalline Semiconductors" (Berlin: Springer), chapters 5 and 6 (1992).
6. J. Schneider, B. Dischler, H. Seelewind, P. M. Mooney, J. Lagowski, M. Matsui, D. R. Beard, and R. C. Newman, Appl. Phys. Lett. **54**, 1442 (1989).
7. H. Ch. Alt, Semicond. Sci. Technol. **6**, B121 (1991).
8. B. Wiedemann, unpublished results.
9. F. Moravec, B. Stepanek, and P. Doubrava, Cryst. Res. Technol. **26**, 579 (1991).
10. A. H. Kachare, W. G. Spitzer, A. Kahan, F. K. Euler, and T. A. Whatley, J. Appl. Phys. **44**, 4393 (1973).
11. R. Schwabe, W. Seifert, F. Bugge, R. Bindemann, V. F. Agekyan, and S. V. Pogarev, Solid State Commun. **55**, 167 (1985).
12. V. Riede, H. Neumann, H. Sobotta, R. Schwabe, W. Seifert, and S. Schwetlick, phys. stat. sol. (a) **93**, K 151 (1986).
13. D. J. Wolford, J. A. Bradley, K. Fry, and J. Thompson in "Proc. of the 17th Int. Conf. on the Physics of Semiconductors" (New York: Springer), pp. 627-630 (1984).
14. X. Liu, M. E. Pistol, L. Samuelson, S. Schwetlick, and W. Seifert, Appl. Phys. Lett. **56**, 1451 (1990).
15. W. S. Hahn, B. Clerjaud, D. Cote, F. Gendron, C. Porte, W. Ulrici, D. Wasik, and W. Wilkening, in "Materials Science Forum", vols. **143-147** (Zurich: Trans Tech), pp. 277-282 (1994).
16. In the case of boron it has been verified that the RSC is close to 1.
17. W. Cochran, S. J. Fray, F. A. Johnson, J. E. Quarrington, and N. Williams, J. Appl. Phys. **32**, 2102 (1961).
18. H. Ch. Alt and B. Dischler, Appl. Phys. Lett. **66**, 61 (1995).
19. D. G. Thomas and J. J. Hopfield, Phys. Rev. **150**, 680 (1966).
20. R. J. Elliot, W. Hayes, G. D. Jones, H. F. MacDonald, and C. T. Sennett, Proc. R. Soc. A **289**, 1 (1965).

Materials Science Forum Vols. 258-263 (1997) pp. 873-878

ATOMIC CONFIGURATION OF OXYGEN NEGATIVE-U CENTER IN GaAs

A. Taguchi and H. Kageshima
NTT Basic Research Labs., Atsugi-shi, Kanagawa, 243-01, Japan

Keywords: GaAs, oxygen, atomic configuration, charge state, formation energy, negative-U

Abstract. We investigated the atomic configuration of an oxygen negative-U center in GaAs, which has a Ga-O-Ga structure, by using an *ab-initio* pseudopotential method. We calculated stable atomic configurations and formation energies for two possible Ga-O-Ga structures: Ga-{O-V_{As}}-Ga and Ga-O_i-Ga. The three charge states 0, 1−, and 2− were considered. For both O-V_{Ga} and Ga-O_i-Ga structures, the stable atomic configuration depends on the charge state. For the Ga-O_i-Ga structure, the configuration change due to the change in the charge state shows the same tendency as that observed in infrared local-vibrational-mode absorption measurements. On the other hand, the configuration change in the O-V_{As} structure does not show the same tendency. The calculated formation energy shows that the O-V_{As} structure does not have the negative-U nature, but the Ga-O_i-Ga structure does. These results show that the Ga-O_i-Ga structure is that of the oxygen negative-U center in GaAs, although the O-V_{As} structure has been thought to be the structure.

I. Introduction

Oxygen is one of the most common contaminants in semiconductors. Studies relating to the electrical properties of oxygen in GaAs started in the early 1960's, and it was found that by oxygen doping GaAs becomes semi-insulating [1]. Below-band-gap near-infrared absorption studies showed that GaAs:O samples contains deep impurity states [2]. A midgap level was found in GaAs, grown in oxygen enriched ambient, by deep level transient spectroscopy measurements [3]. At that time, however, an atomic structure of the oxygen center was unclear. To investigate the atomic structure, infrared local-vibrational-mode (LVM) absorption measurement is a powerful method. For the dominant oxygen center in GaAs, a set of three lines has been observed [4]. The three lines have been explained by assuming a Ga-O-Ga structure (one oxygen atom couples with two Ga atoms) and by taking account of the natural abundance of Ga isotopes. From detailed experiments of a short-time illumination and thermal treatments, it was shown that this Ga-O-Ga structure takes three charge states 0, 1−, and 2−.[6]. For a neutral charge state, the LVM absorption frequencies are around 731 cm^{-1}. For 1− and 2− charge states, the absorption frequencies of the three lines are quite similar and they are around 714 cm^{-1}. The similarity of the LVM frequencies for the 1− and 2− charge states indicates that the atomic configurations are very similar between these two negatively charged states. On the other hand, the atomic configuration for the neutral charge state must be different from those for the negatively charged states, since the LVM frequencies are different. The larger absorption frequency for the neutral charge state than that for the negatively charged states indicates that the Ga-O bonds are stronger for the neutral charge state than for the negatively charged states. Experiments on the thermal stability of the charge states show that the 1− charge state is meta-stable, and hence the Ga-O-Ga center has the negative-U nature [6].

The atomic configuration of this oxygen negative-U center has been thought to be similar to that of the A-center in silicon [5]: an oxygen atom occupies the As substitutional site, but it moves along the <001> direction and couples with two Ga atoms. The center is termed O-V_{As}. This atomic structure seems to be well accepted. Theoretical investigations of this structure have been carried out by Jones and Öberg by using a 71-atom H-terminated cluster, $OGa_{16}As_{18}H_{36}$, with the local-density-functional approximation [7]. The wave functions were

expanded by Gaussian basis. It was reported that the O-V_{As} structure may take five charge states from 1+ to 3−. The calculated results show that the oxygen atom couples with two Ga atoms for the negatively charged states, while the As substitutional site is the most stable site for the 1+ and neutral charge states. Since the surrounding four Ga atoms are equivalent at the As substitutional site, this site does not have the Ga-O-Ga structure. Jones and Öberg claimed the charge state assignment to the atomic configuration estimated from the experimental results [6]. Their discussion of the negative-U nature was limited, although it is the most remarkable feature of this center. Therefore, re-examination of the Ga-O-Ga structure is necessary.

To clarify the atomic configuration of the oxygen negative-U center in GaAs, we investigated two structures: the previously proposed O-V_{As} structure and the interstitial oxygen structure (a Ga-O_i-Ga structure), which is another structure that may show three LVM absorption lines due to an oxygen atom coupled with two Ga atoms. We considered the experimentally observed three charge states 0, 1−, and 2−, and calculated the stable atomic configurations for each charge state. To investigate the negative-U nature, the formation energy was calculated as a function of the Fermi level. In the next section, the calculation method is briefly explained. The obtained stable atomic configurations and the formation energies are shown and discussed in Sec. III.

II. Calculation method

The calculations were carried out within the local-density-functional approximation. For the exchange-correlation interaction, a form of the Ceperley-Alder type was adopted [8]. For Ga and As, soft-pseudopotentials with a form proposed by Troullier and Martin were used [9, 10]. The ultra-soft-pseudopotential developed by Vanderbilt was used for the pseudopotential of oxygen [11, 12]. This oxygen pseudopotential has already been applied to the Si system [13]. The pseudo-wave-function was expanded by a plane-wave basis set. The kinetic-energy cutoff was taken to be 20.25 Ry. A 32-atom supercell was used and the lattice around the oxygen atom was relaxed by minimizing the total energy. The conjugate-gradient technique was used for optimizing both the electronic structure and the atomic configuration [14].

III. Results and discussion

For the O-V_{As} structure, the presently obtained stable atomic configurations are shown in Fig. 1. The figure is drawn on a (110) plane. Open circles denote the ideal GaAs lattice sites. For the neutral charge state, the As substitutional site is the most stable site. The oxygen atom occupies the As substitutional site, and the four surrounding Ga atoms move inward to the oxygen atom. The Ga-O bond length is 2.17 Å. When the oxygen becomes negatively charged, the As substitutional site is no longer the most stable site. The oxygen atom moves toward the Ga plane along the <001> direction, and becomes stable by coupling with two Ga atoms. The Ga-O bond lengths are 1.99 Å for the 1− charge state and 1.88 Å for the 2− charge state. The bond angles of Ga-O-Ga are 118° and 136° for the 1− and 2− charge states, respectively. The presently obtained tendency of the atomic configuration for the three charge state is similar to that previously reported by Jones and Öberg [7]. They reported that the As substitutional site is the most stable site for the neutral charge state, and the Ga-O-Ga structure is stable for the negatively charged states. However, we can not compare the present calculated results with their results in detail, since they did not report the atomic configurations for the 0 and 1− charge states.

As already mentioned, the LVM experiments suggest similar atomic configurations for the 1− and 2− charge states. However, the presently calculated stable configurations for these negatively charged states are different as can be clearly seen in Fig. 1. The Ga-O bond seems to be stronger for the 2− charge state than for the 1− charge state, since the Ga-O bond length is shorter and the Ga-O-Ga bond angle is closer to 180° in the 2− charge state than those in the 1− charge state. If the experimentally assigned charge states are correct, the calculated atomic configurations for the charge states can not explain the LVM absorption frequencies.

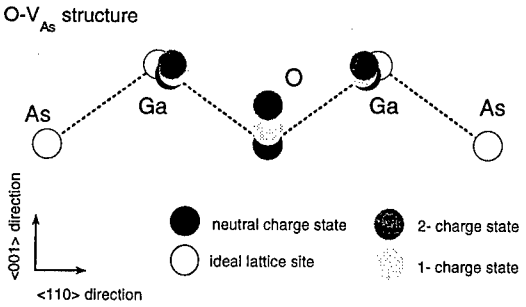

FIG. 1 Atomic configuration of the O-V_{As} structure for the neutral, 1−, and 2− charge states. The (110) plane was drawn. Open circles denote the ideal GaAs lattice sites. Shadow circles are the calculated stable atom positions for the neutral, 1−, and 2− charged states.

Another pronounced nature of the oxygen center in GaAs is the negative-U nature. To investigate the negative-U nature, we calculated the formation energy of the O-V_{As} structure as a function of the Fermi level [15]. The results are shown in Fig. 2. The total energy of the neutral charge state was taken as the energy reference, and the Fermi level is measured by the calculated bandgap. When the Fermi level was at the top of the valence band, the formation energies for the negatively charged states are larger than that of the neutral charge state. Therefore, the neutral charge state is most stable. As the Fermi level rises, the formation energies for the negatively charged states decrease. At around the midgap, the 1− charge state is most stable. When the Fermi level becomes close to the bottom of the conduction band, the 2− charge state is most stable. Therefore, three charged states 0, 1−, and 2− can be observed as a stable state depending on the Fermi level. The present calculated results show that the O-V_{As} structure does not have a negative-U nature. This does not agree with the experimental results.

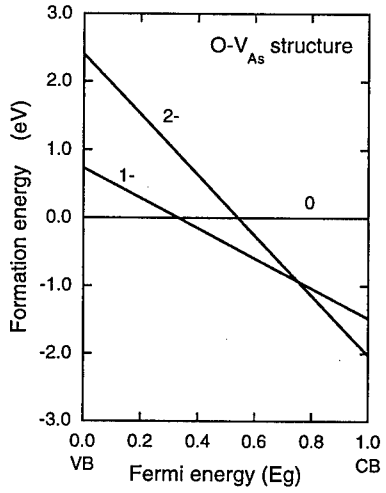

FIG. 2 Formation energy for O-V_{As} structure as a function of the Fermi level. The Fermi energy was measured by the bandgap. The neutral state was taken as the reference. Here, "0", "1−", and "2−" denote the charge states.

Although the O-V_{As} structure has been widely accepted, the presently calculated results for both the stable atomic configurations and the formation energies indicate that the experimentally observed LVM absorption signals are not due to the O-V_{As} structure.

The interstitial oxygen, Ga-O_i-Ga, is another candidate for the experimentally observed Ga-O-Ga structure. If a site shifted from the Td interstitial site to a Ga plane along the <001> direction is more stable than the Td interstitial site, the Ga-O_i-Ga structure will appear. For the neutral charge state, the calculated stable atomic configuration is shown in Fig. 3. The figure is drawn on a (110) plane. For this charge state, the oxygen atom locates at the middle of two Ga atoms. This site is more stable by 0.9 eV than the Td interstitial site surrounded by four Ga atoms. A strong coupling seems to be formed between the oxygen atom and the two neighboring Ga atoms. The Ga-O bond length is 1.94 Å. The bond angle of Ga-O-Ga is 165°.

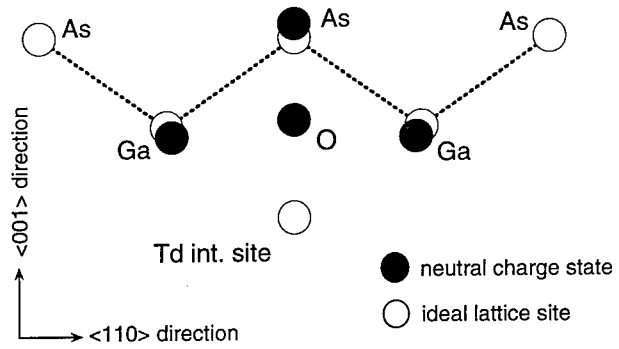

FIG. 3 Atomic configuration of Ga-O_i-Ga structure for the neutral charge state. Open circles indicate the ideal GaAs lattice sites and the Td interstitial site. Filled circles are the calculated stable atom positions.

For the 1− and 2− charge states, the stable atomic configurations change dramatically from that for the neutral charge state, as shown in Fig. 4. The oxygen atom moves toward the Td interstitial site. For these two negatively charged states, the atom positions are quite similar. This is consistent with the experimentally observed LVM absorption frequencies, which are nearly equal for the 1− and 2− charge states. The Ga-O bond lengths are 1.89 and 1.92 Å for the 1− and 2− charge states, respectively. Although the Ga-O bond lengths for the negatively charged states are close to those for the neutral charge states, the angle of the Ga-O-Ga bond changes dramatically form 165° for the neutral charge state to 114° and 113° for the 1− and 2− charge states. Hence, the Ga-O bonds for the negatively charged states may be weaker than those for the neutral charge state. This tendency is the same as that observed in the LVM absorption measurements for different charge states.

We also calculated the formation energy for the Ga-O_i-Ga structure as shown in Fig. 5. The total energy of the Td interstitial oxygen in the neutral charge state was taken to be the energy reference. When the Fermi level is close to the top of the valence band, the neutral charge state is the most stable state. As the Fermi level rises and approaches the bottom of the conduction band, the 2− charge state becomes the most stable state. The 1− charge state is not stable at any Fermi level. This clearly shows that the 1− charge state is meta-stable and that the Ga-O_i-Ga structure has a negative-U nature. This agrees with the experimentally estimated charge state assignment, that the 1− charge state is meta-stable [6]. Therefore, if we regard the Ga-O_i-Ga structure as the dominant oxygen center in GaAs observed in the LVM

measurements, the experimentally observed main features, which are the negative-U nature and the LVM frequencies depending on the charge state, are well explained.

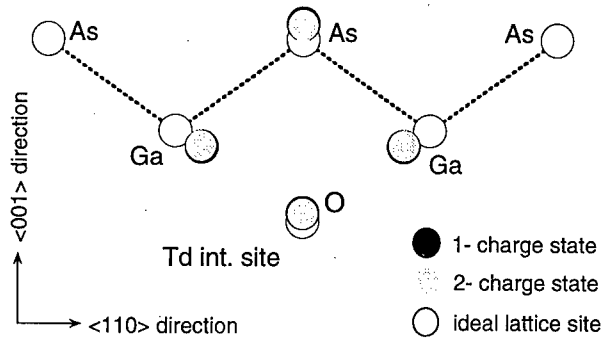

FIG. 4 Atomic configurations of the Ga-O_i-Ga structure for the 1− and 2− charge states. Filled circles shows the atom positions for the 1− charge state and shadow circles for the 2− charge states. The atom positions for the negatively charged states are quite similar.

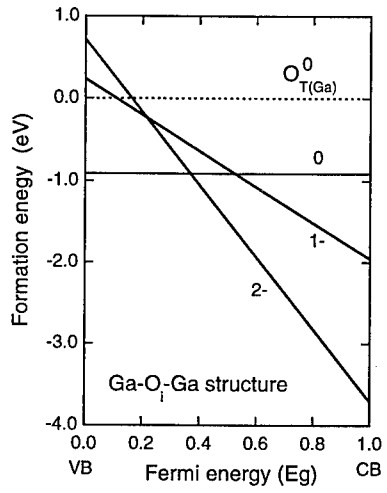

FIG. 5 Formation energy for the Ga-O_i-Ga structure as a function of the Fermi level. The Fermi energy was measured by using the calculated bandgap. A total energy for oxygen at the T_d interstitial site surrounded by four Ga atoms was taken as the reference. It is clearly seen that the 1− charge state is not stable at any Fermi level.

IV. Conclusion

We calculated the stable atomic configuration and the formation energies for the O-V_{As} and Ga-O_i-Ga structures for the 0, 1−, and 2− charge states. The calculated atomic configurations of the O-V_{As} structure can not explain the LVM frequencies for different charge states, while those of the Ga-O_i-Ga structure explain them. Moreover, the calculated results show that the O-V_{As} structure does not have the negative-U nature, but the Ga-O_i-Ga structure has the nature. Therefore, we can conclude that the experimentally observed LVM signals from the

oxygen negative-U center are not due to the O-V_{As} structure but are due to the Ga-O_i-Ga structure, although the O-V_{As} structure has been thought to be the structure.

Acknowledgments
The authors would like to thank Dr. K. Shiraishi and Dr. K. Wada for their continuous discussions. They also thank Dr. K. Takahei and Dr. Y. Hirayama for their fruitful suggestions, and Dr. N. Uesugi and Dr. M. Makino for their interest in this work.

References
[1] C. H. Gooch, C. Hilsum, and B. R. Holeman, J. Appl. Phys. Suppl. **32**, 2069 (1961).
[2] M. D. Sturge, Phys. Rev. **127**, 768 (1962); A. L. Lin, E. Omelianovski, and R. H. Bube, J. Appl. Phys. **47**, 1852 (1976).
[3] J. Lagowski, D. G. Lin, T. Aoyama, and H. C. Gatos, Appl. Phys. Lett. **44**, 336 (1984).
[4] C. Song, W. Ge, D. Jiang, and C. Hsu, Appl. Phys. Lett. **50**, 1666 (1987); X. Zong, D. Jang, W. Ge, and C. Song, Appl. Phys. Lett. **52**, 628 (1988); J. Schneider, B. Dischler, H. Seelewind, P. M. Mooney, J. Lagowski, M. Matsui, D. R. Beard, and R. C. Newman, Appl. Phys. Lett. **54**, 1442 (1989).
[5] Y. Lee and J. W. Corbett, Phys. Rev. B **13**, 2653 (1976).
[6] H. Ch. Alt, Phys. Rev. Lett. **31**, 3421 (1990).
[7] R. Jones and S. Öberg, Phys. Rev. Lett. **69**, 136 (1992).
[8] J. P. Perdew and A. Zunger, Phys. Rev. B **23**, 5048 (1981).
[9] N. Troullier and J. Martins, Phys. Rev. B **43**, 1993 (1991).
[10] H. Kageshima and K. Shiraishi, *submitted to Phys. Rev. B*
[11] D. Vanderbilt, Phys. Rev. B **41**, 7892 (1991).
[12] J. Yamauchi, M, Tsukada, S. Watanabe, and O. Sugino, Surf. Sci. **341**, L1037 (1995).
[13] H. Kageshima, Surf. Sci. **357/358**, 312 (1996); H. Kageshima and K. Shiraishi, Surf. Sci. **380**, 61 (1997).
[14] M. P. Teter, M. C. Payne, and D. C. Allen, Phys. Rev. B **40**, 12255 (1989); O. Sugino and A. Oshiyama, Phys. Rev. Lett. **68**, 1858 (1992).
[15] L. Pabesi and P. Giannozze, Phys. Rev. B **46**, 4621 (1992).

Materials Science Forum Vols. 258-263 (1997) pp. 879-884

Ga VACANCIES AS COMPENSATING CENTERS IN HOMOGENEOUSLY OR δ-DOPED GaAs(Si) LAYERS

T.Laine[1], K.Saarinen[1], P.Hautojärvi[1], C.Corbel[1],
L.N.Pfeiffer[2], P.H.Citrin[2], M.J.Ashwin[3], and R.C.Newman[3]
[1]Laboratory of Physics, Helsinki University of Technology, P. O. Box 1100, 02015 HUT, Finland
[2]Bell Laboratories, Lucent Technologies, Murray Hill, New Jersey 07974
[3] IRC for Semiconductor Materials, Imperial College of Science, Technology and Medicine, London, SW7 2BZ, UK

Keywords: superlattice, compensation, positron spectroscopy

Abstract. The positron annihilation method was used to investigate the type and concentration of compensating centers in homogeneously or δ-doped GaAs(Si) layers grown by molecular beam epitaxy (MBE). The results show the presence of Ga vacancies and negative ions in both type of layers. The negative ion is attributed to the Si_{As} in homogeneously doped GaAs(Si) and to the Ga_{As} in δ-doped GaAs(Si). The concentrations of Ga vacancies and negative ions increase strongly when the Si concentration exceeds 5 x 10^{18} cm^{-3} in homogeneously doped GaAs(Si) and 1 x 10^{13} cm^{-2} in δ-doped GaAs(Si). Furthermore, the results in the superlattice indicate that the defects observed by the positron are located in undoped material between the delta planes.

1. Introduction

The *n*-type doping of GaAs by Si atoms is a straightforward procedure until above 10^{19} cm^{-3} a strong deactivation of free carriers occurs [1]. The Si-doping of GaAs in delta planes (δ-doping) has been proposed as a method to overcome the problems [1]. Recently we have studied the compensating defects both in homogeneously doped GaAs(Si) [2] and in δ-doped GaAs(Si) [3].

Positron annihilation spectroscopy can be used to study point defects in semiconductors, and in particular, vacancies [4]. Positrons are trapped at vacancy defects, which is experimentally observed as an increase in the positron lifetime and a narrowing of the momentum distribution of the annihilating electron-positrons pairs. In addition to vacancies, positron measurements are sensitive to ion-type acceptors, since positrons are localized at the Rydberg state around the negative ions at low temperatures.

In this paper we report on the observations of Ga vacancies and negative ions in homogeneously doped and δ-doped GaAs(Si). The strong electrical deactivation observed in homogeneously GaAs(Si) can be largely explained by these two types of defects. The Ga vacancies and negative ions found in δ-doped GaAs(Si) are shown to locate between the delta planes.

2. Experimental arrangements

Homogeneously doped GaAs(Si) samples were grown by molecular beam epitaxy (MBE) on (100)-oriented GaAs substrates at 900 K [5]. The thickness of the Si doped overlayer was 2 μm. The Si-doping concentration in the four samples studied were (in units of 10^{18} cm^{-3}) approximately 2, 3, 9, and 50. Here the samples are referred as "low" (L), "medium" (M), "high" (H), and "very high" (VH), respectively. The strong electrical deactivation was seen only in the H and VH samples. δ-doped GaAs(Si) samples were grown by MBE on (100) oriented GaAs wafers at temperature of 670 K [6]. The planar Si-doping concentration varied as follows: 0.01 ML (6.1 x 10^{12} cm^{-2}), 0.02 ML (14 x 10^{12} cm^{-2}), 0.09 ML (59 x 10^{12} cm^{-2}) and 0.26 ML (175 x 10^{12} cm^{-2}). The strong electrical deactivation was seen in two last samples which were well above the critical

planar Si-doping concentration 1 x 10^{13} cm^{-2}. As the reference sample we measured one *p*-type Be doped (4 x 10^{16} cm^{-3}) GaAs layer grown by MBE.

Positron annihilation in the epitaxially grown layers of Si were measured using the low-energy positron beam technique [4]. Doppler broadening of the 511-keV radiation gives information about the momentum distribution of annihilating electrons. The momentum distribution is usually described in terms of the valence and core annihilation parameters S and W. The S parameter, defined as the relative amount of annihilation events over the energy range (511 ± 0.95) keV around the peak centroid, represents the electron-positron pairs with longitudinal momentum component $p_L / m_0 c \leq 3.7 \times 10^{-3}$ that arise mainly from annihilations with valence electrons (m_0 is the electron mass and c is the speed of light). The core annihilation parameter W is the fraction of positron annihilations with the core electrons in the momentum range $p_L / m_0 c$ = (15-20)x10^{-3}. When vacancy defects are detected in the samples, S parameter increases and W parameter decreases. The two-detector coincidence technique [7] was also applied to study the momentum distribution $p_L / m_0 c$ = (10-40)x10^{-3} of annihilating core electrons and to thereby identify the sublattice of the vacancy defects.

3. Homogeneously doped GaAs(Si)

Fig. 1 shows the valence annihilation parameter S as a function of the incident positron energy for H and VH Si doped GaAs overlayers on top of a SI GaAs substrate. The reference curve in Fig. 1 shows the level of the S parameter in Be doped GaAs which is the defect-free bulk material. The S parameter for H and VH Si doped GaAs is clearly higher indicating that the Si doped layers contain a large concentration of open volume defects. At E > 25 keV the S parameter decreases towards the reference level which means that positrons annihilate in the substrate with a low defect concentration.

Coincidence measurements of core electron momentum distributions were performed on the

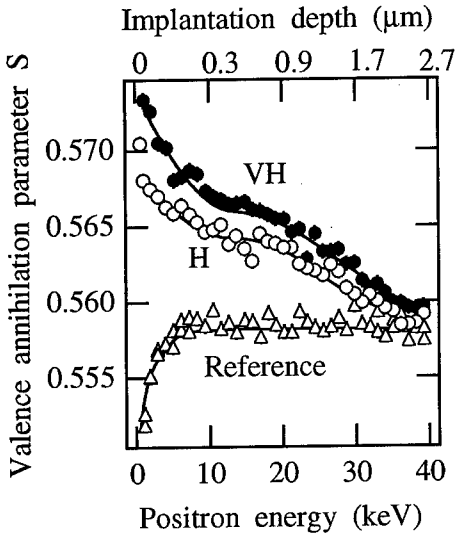

Fig. 1. The S parameter as a function of positron implantation energy in a defect-free reference GaAs and in two, 2 μm thick Si doped GaAs layers. The mean implantation depth corresponding to the positron energy scale is indicated on the top axis.

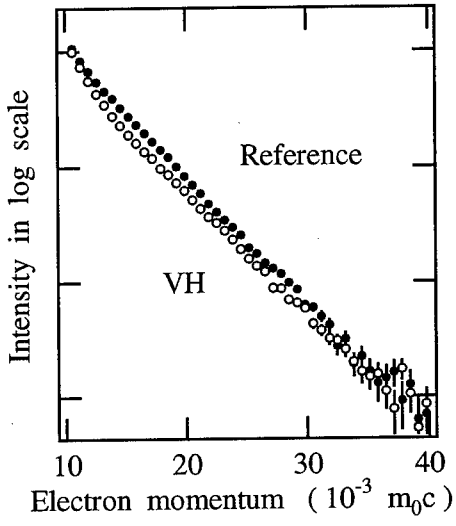

Fig. 2. The core electron momentum distribution in Be doped GaAs (●) and in GaAs([Si] =5x10^{19} cm^{-3}) (○). The momentum distribution $\rho(p)$ of the defect-free reference GaAs has a noticeably higher intensity than that in the VH sample [2].

Be doped and VH Si doped GaAs samples at room temperature [2]. The high-momentum parts of the area normalized Doppler curves are plotted as filled and open circles in Fig. 2. The momentum distribution $\rho(p)$ of Be doped GaAs is characteristic of free positrons in a GaAs lattice and has a noticeably higher intensity than that in the VH sample. This result clearly shows the effect of positrons trapped at vacancies in the VH sample: at open-volume defects, the overlap between positrons and core electrons of the surrounding atoms is reduced.

The shape of the distribution in the VH sample is also different from that in the GaAs lattice. Although the differences are small, the momentum distribution curve $\rho(p)$ in the VH sample is not so steep than in the Be doped reference sample. According to the theory [7], for free positrons in GaAs, the dominant contribution to the measured core electron momentum distribution comes from the 3d electrons of Ga atoms (Z=31). The 3d electrons of As atoms (Z=33) are more tightly bound, leading to a broader momentum distribution and a reduced overlap with the positrons. The broader distribution in the VH sample therefore indicates that the relative amount of positron annihilations with the As core electrons is larger at the vacancy than in the GaAs lattice. This implies that the vacancy in the VH sample is surrounded by As atoms and is thus associated with the Ga sublattice. Furthermore, the core electron momentum distribution (not shown in Fig. 2) associated with irradiation-induced V_{Ga} [8] has the same intensity and shape as the vacancy in the VH sample. This leads us to conclude that the vacancy observed in the VH sample is a Ga vacancy.

In Be doped GaAs the S parameter is seen to be nearly temperature independent in Fig. 3 [2], which is typical for free positron annihilation in the bulk. The temperature dependence of the S parameter is similar in all four Si doped samples. The S parameter is first constant at 10-100 K, then increases from 100 K to 200 K, and finally reaches a plateau around 300 K. The plateau levels were confirmed by experiments between 300-600 K (not shown). The temperature dependence of Fig. 3 indicates that another defect must be competing with the Ga vacancy for trapping positrons in Si doped GaAs at 20 K. These competing defects are attributed to negative ions, which have no open volume associated with them [8].

To quantify the concentration of vacancies and ions, the temperature dependence of the S parameter was analyzed using a positron trapping model [8]. The adjustable parameters in the fitting procedure were the concentration of vacancies c_v, the concentration of ions c_{ion}, the positron trapping coefficient μ_{ion} and the positron binding energy $E_{b,ion}$. The solid lines in Fig. 3 are the fits to the measured S parameters. As a result, the S parameter analysis gives $E_{b,ion} = (40\pm10)$ meV and $\mu_{ion} = (4.5\pm1.0)\times10^{16}\ T^{-1/2}\ s^{-1}$ (T is in degrees of Kelvin). Fixing these two parameters, $E_{b,ion}$ and μ_{ion}, the concentrations of vacancies c_v and negative ions c_{ion} can be accurately fitted.

The fitted concentrations of vacancies c_v and negative ions c_{ion} are illustrated in Fig. 4 [2]. Two results are immediately apparent. First, the concentrations of defects increase when [Si] increases, particularly going from the L and M samples to the H and the VH samples. Second, the magnitudes of both c_v and c_{ion} relative to [Si] in the respective samples change dramatically: in the L and M samples, the combined sum of these defect concentrations is < 25 % of the Si doping concentration, while in the H and VH samples this fraction is > 50 % [Si]. It is clear that the sharp decrease in activity when [Si] > 5×10^{18} cm^{-3} correlates strongly with the summed concentrations of negative ions and vacancies in the H and VH samples.

To identify the nature of these defects and determine the possible importance of other defects as well, the results of the present work have to be combined with those obtained in previous studies [5,9,10]. As a result in MBE-grown highly Si doped GaAs (i. e. [Si] > 5×10^{18} cm^{-3}), the most likely assignment of the negative ion species is Si_{As}^{-}, and of the Ga vacancy is $(Si_{Ga}\text{-}V_{Ga})^{2-}$. These two defects are dominant for their generic type. Together, they account for a large part of the observed compensation of heavily Si doped GaAs. Recently a scanning tunneling microscopy has also used together with positron spectroscopy to identify the vacancy and ion-type defects in highly Si doped GaAs bulk crystals [11].

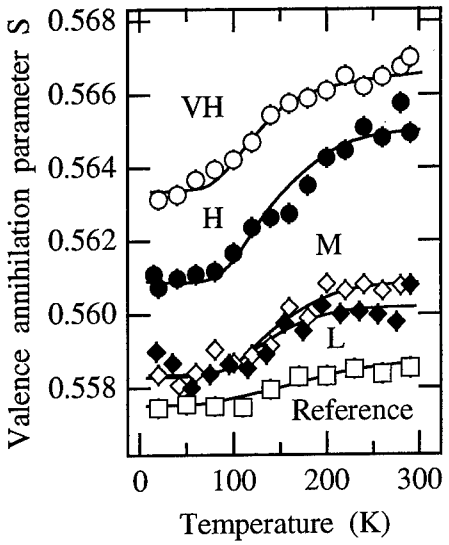

Fig. 3. The S parameter was measured in Be doped GaAs (❑), and in Si doped GaAs samples with [Si]≈1x10^{18} cm^{-3} (◆), 3x10^{18} cm^{-3} (◇), 9x10^{18} cm^{-3} (●), and 5x10^{19} cm^{-3} (○), all as a function of temperature between 20 K and 300 K [2].

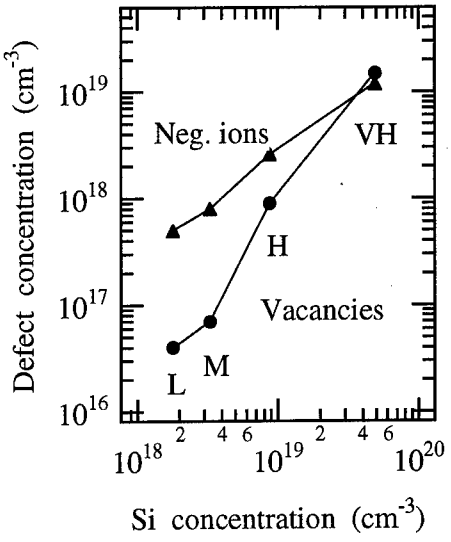

Fig. 4. The concentration of negative ions (▲) and the concentration of Ga vacancies (●) as a function of Si concentration in four Si doped GaAs samples. The dopant activation ([n] / [Si]) decreases strongly when the Si concentration changes from M to H [2].

4. δ-doped GaAs(Si)

The S parameters in the Be doped and in the Si δ-doped samples are plotted against the measurement temperature in Fig. 5 [3]. The S parameter in Be doped GaAs increases smoothly as a function of temperature, which is typical for a sample where only free positron annihilation in the lattice is observed. The S parameters in the $[Si]_A$ = 0.01 ML and $[Si]_A$ = 0.02 ML GaAs samples are slightly larger than in Be doped GaAs. In $[Si]_A$ = 0.09 ML and $[Si]_A$ = 0.26 ML GaAs the S parameter is even larger, indicating that the positron trapping at vacancies increases with the planar Si concentration. Altogether, the temperature behavior of the S parameter is similar to that observed in homogeneously doped GaAs(Si).

A coincidence measurement of core electron momentum distribution was also performed in the $[Si]_A$ = 0.26 ML GaAs sample at room temperature with an incident positron energy of 20 keV [3]. The shape and the intensity of the momentum distributions for VH homogeneously doped GaAs(Si) and for $[Si]_A$ = 0.26 ML GaAs are similar. This result leads to the conclusion that also in $[Si]_A$ = 0.26 ML GaAs, the observed vacancy is associated with the Ga sublattice .

The S parameter analysis of the temperature data was done in a similar way as in the case of homogeneously doped GaAs(Si). In the samples $[Si]_A$ = 0.01 ML and $[Si]_A$ = 0.02 ML the concentrations of vacancies and negative ions were estimated to be below 10^{18} cm^{-3} [3]. The solid lines in Fig. 5 represent the fits to the measured S parameters in the $[Si]_A$ = 0.09 ML and $[Si]_A$ = 0.26 ML samples. As a result the positron binding energy is $E_{b,ion}$ = (40±10) meV and the positron trapping coefficient is μ_{ion} = (4.5±1.0)x10^{16} $(T/K)^{-0.5}$ s^{-1}. The fitting gives the concentrations of c_v = 0.7(3)x10^{18} cm^{-3} and c_{ion} = 2.6(2)x10^{18} cm^{-3} in the $[Si]_A$ = 0.09 ML sample. The corresponding concentrations in the $[Si]_A$ = 0.26 ML sample are respectively $c_v \geq$ 2.1x10^{19} cm^{-3} and $c_{ion} \geq$ 1.8x10^{19} cm^{-3}.

The amount of positron annihilations at the δ-layers was estimated by solving the positron

diffusion-annihilation equation in the superlattice structure corresponding to the samples studied in this work [12]. We find (Fig. 6) that less than 1 % of positrons are annihilating at the delta planes. The positively charged δ-layers are thus totally repulsive to positrons and practically all annihilations take place in the material between them. A similar conclusion has been earlier reached in δ-doped Si [13]. Hence, the vacancies and the negative ions detected by positrons are located in the undoped regions between the δ-planes.

The type of the negative ion is an interesting question. The IR LVM experiments have shown that the concentrations of Si_{As}, Si_{Ga}-Si_{As} and Si-X increase when the planar doping $[Si]_A$ increases from 0.03 ML to 0.12 ML [6]. The formation of the Ga vacancies and negative ions is detected in the present work at these same doping concentrations. However, since the spreading the δ-layers is only 5.6 Å [6] and they are totally repulsive to positrons, the defects are not related to Si impurities but they are intrinsic defects between the δ-layers. The positron trapping parameters $E_{b,ion}$ and μ_{ion} of the negative ion are the same as those detected for Ga antisites in electron irradiated GaAs [14]. Moreover, the Ga antisite is the only negatively charged intrinsic defect in GaAs according to theoretical calculations [9]. We thus associate the negative ion with the Ga antisite defect.

Finally the formation mechanism of vacancies and negative ions in the GaAs layers between the delta planes can be discussed. *A priori*, the defects are either (i) created at the delta planes during the growing process whereafter they diffuse to the area between delta planes, or (ii) formed directly in the regions between the delta planes during the growth. The first mechanism seems to be more unlikely for two reasons. Since the spreading of Si-atoms is negligible, it can also be expected that the out-diffusion of negative ions like Ga_{As}^{2-} from the delta planes is probably also very small. Secondly, the charge states of these defects and the delta planes do not favor the diffusion mechanism, because the delta plane has a positive charge.

Some arguments seem to indicate that the formation of vacancies and negative ions is similar in the homogeneously doped and δ-doped GaAs(Si). The ratio of the vacancy and ion concentrations is c_v/c_{ion}=0.3(1) in $[Si]_A$=0.09 ML GaAs and c_v/c_{ion}=1.2 in $[Si]_A$=0.26 ML GaAs.

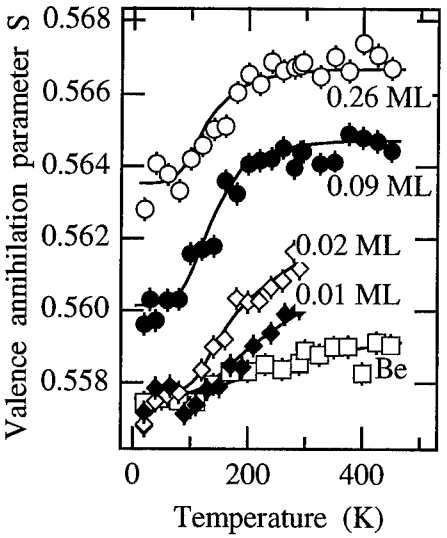

Fig. 5. The S parameter was measured in Be doped GaAs (❑), in Si δ-doped GaAs, 0.01 ML ($6.1x10^{12}$ cm^{-2}) (◆), 0.02 ML ($14x10^{12}$ cm^{-2}) (◇), 0.09 ML ($59x10^{12}$ cm^{-2}) (●) and 0.26 ML ($175x10^{12}$ cm^{-2}) (○), as a function of temperature 20-450 K [3].

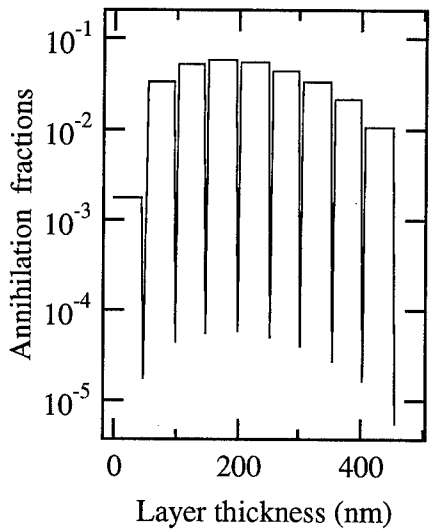

Fig. 6. Annihilation fractions of different layers were calculated for $[Si]_A$ = 0.01 ML GaAs with the electric field 7 kV / cm and with the positron energy 8 keV (the details are explained in Ref. 12). The total annihilation fraction is 0.03 % in the delta layers.

In homogeneously doped GaAs(Si) layers this ratio was determined as c_v/c_{ion}=0.3(1) in [Si] = 0.9 x 10^{19} cm^{-3} and c_v/c_{ion}=1.3 in [Si] = 5.0 x 10^{19} cm^{-3} doped GaAs [2]. The similarity of c_v/c_{ion} in homogeneously doped and δ-doped GaAs(Si) suggests that the formation process of these defects is the same in both cases. Consequently, either the diffusion of the defects formed in the δ-layer is very fast or the defects are formed between the layers already during the growth. The latter is possible if the Fermi level rises high between delta planes when the Si-doping concentration increases. As demonstrated by calculations [9], this decreases the formation energies of negative vacancy and ion-type defects. However, as discussed earlier [15], the grown-in defects may dissociate or transform to other species, thus complicating the comparison to theoretical calculations performed in equilibrium conditions.

5. Conclusions

We have studied the point defects in homogeneously doped and δ-doped GaAs(Si). The results show the presence of Ga vacancies and negative ions in both type of layers. The defects in homogeneously doped GaAs(Si) explain the strong electrical deactivation which is seen in high Si-doping concentrations. The defects found in δ-doped GaAs(Si) are located in the undoped material between the delta planes.

[1]E. F. Schubert, *Doping in III-V Semiconductors*. (Cambridge University Press, Cambridge, 1993); *Delta-Doping of Semiconductors*. (Cambridge University Press, Cambridge, 1995).
[2]T. Laine, K. Saarinen, J. Mäkinen, P.Hautojärvi, C. Corbel, L. N. Pfeiffer and P.H. Citrin, Phys. Rev. B **54**, 11050 (1996).
[3]T. Laine, K. Saarinen, J. Mäkinen, P. Hautojärvi, C. Corbel, M. J. Ashwin and R. C. Newman, Appl. Phys. Lett. (to be published).
[4]*Positron Spectroscopy of Solids*, edited by A. Dupasquier and A. P. Mills (IOS Press, Amsterdam, 1995).
[5]S. Schuppler, D. L. Adler, L. N. Pfeiffer, K. W. West, E. E. Chaban, and P. H. Citrin, Appl. Phys. Lett. **63**, 2357 (1993); Phys. Rev. B **51**, 10527 (1995).
[6]R. C. Newman, M. J. Ashwin, M. R. Fahy, L. Hart, S. N. Holmes, C. Roberts, X. Zhang, and J. Wagner, Phys. Rev. B **54**, 8769 (1996).
[7]M. Alatalo, H. Kauppinen, K. Saarinen, M.J. Puska, J. Mäkinen, P. Hautojärvi, and R.M. Nieminen, Phys. Rev. B **51**, 4176 (1995).
[8]C. Corbel, F. Pierre, K. Saarinen, P. Hautojärvi, and P. Moser, Phys. Rev. B **45**, 3386 (1992).
[9]J. E. Northrup, and S. B. Zhang, Phys. Rev. B **47**, 6791 (1993); S. B. Zhang, and J. E. Northrup, Phys. Rev. Lett. **67**, 2339 (1991).
[10]J. Maguire, R. Murray, R. C. Newman, R. B. Beall, and J. J. Harris, Appl. Phys. Lett. **50**, 516 (1987).
[11]J. Gebauer, R. Krause-Rehberg, C. Domke, Ph. Ebert, and K. Urban, Phys. Rev. Lett. **78**, 3334 (1997).
[12]T. Laine, K. Saarinen, P. Hautojärvi, C. Corbel, M. J. Ashwin, and R. C. Newman, *Proceedings of the 11th International Conference on Positron Annihilation*, (to be published).
[13]D. T. Britton, P. Willutzki, W. Triftshäuser, E. Hammerl, W. Hansch, and I. Eisele, Appl. Phys. A **58**, 389 (1994).
[14]K. Saarinen, S. Kuisma, J. Mäkinen, P. Hautojärvi, M. Törnqvist, and C. Corbel, Phys. Rev. B **51**, 14152 (1995).
[15]R. E. Pritchard, S. A. McQuaid, L. Hart, R. C. Newman, J. Mäkinen, H. J. Bardeleben, and M. Missous, J. Appl. Phys. **78**, 2411 (1995).

Materials Science Forum Vols. 258-263 (1997) pp. 885-892

Positron annihilation and scanning tunneling microscopy used to characterise defects in highly Si-doped GaAs

J. Gebauer[1], R. Krause-Rehberg[1], C. Domke[2], Ph. Ebert[2], and K. Urban[2]

[1]*Fachbereich Physik, Martin-Luther-Universität Halle-Wittenberg, D-06099 Halle, Germany*

[2]*Institut für Festkörperforschung, Forschungszentrum Jülich GmbH, D-52425 Jülich, Germany*

Keywords: GaAs, positron annihilation, scanning tunneling microscopy, V_{Ga}-Si_{Ga} complexes

ABSTRACT

Positron annihilation and scanning tunneling microscopy (STM) were combined to characterise defects in highly silicon doped GaAs. An increasing density of monovacancies was observed by positron lifetime spectroscopy with increasing Si-doping concentration. These vacancies were identified by STM as Si_{Ga}-V_{Ga} complexes. The concentration of shallow positron traps increased with the Si concentration too. The shallow traps are identified by STM as Si_{As} acceptors. The STM results suggest that positron trapping at shallow traps can also be related to small Si clusters. The defects are thermally stable at least up to 880°C. We demonstrate that the combination of positron annihilation and scanning tunneling microscopy is a powerful tool to obtain microscopic data on the concentration and nature of point defects.

1 INTRODUCTION

Compound semiconductor materials like GaAs offer a wide variety of important electronic applications. A wide use of such materials, however, was limited in the past with respect to the application of Silicon. This is mainly due to the presence of native defects which influence strongly the material properties. Defects are commonly observed in compound semiconductors, at concentrations much larger than in Si. A detailed knowledge on the native defects, e.g. their microscopic nature and macroscopic density, is thus crucial to understand the physical properties of compound semiconductors.

An important problem, for instance, is the compensation of free carriers in highly Si-doped GaAs. It has been proposed that this behavior is due to the amphoteric character of Si in GaAs, since Si can be incorporated both as donor (Si_{Ga}) and acceptor (Si_{As}) [1]. However, the upper limit of the concentration of Si_{As} acceptors as determined by NEXAFS was not sufficient to explain the observed compensation [2]. Spectroscopy of the local vibration modes (LVM) of infrared absorption provides information on the presence of additional defects. These are larger Si agglomerates like Si_{As}-Si_{Ga} dimers and defect complexes containing a Si_{Ga} donor and an unknown point defect X, where it was speculated that X could be a Ga vacancy V_{Ga} [3]. It was, however, difficult, to determine reliably the defect densities from LVM measurements.

The examples given above show that often detailed information on defects cannot be given using a particular technique alone. A combination of different techniques may solve this problem. In the present study we combine positron annihilation with scanning tunneling microscopy (STM) [4,5]. Positron annihilation is a powerful tool for the characterisation of vacancy-type defects in semiconductors [6]. Positron trapping in vacancies can be observed as an increase of the positron lifetime or as a narrowing of the Doppler-broadened 511 keV annihilation peak. In addition, positrons are sensitive to negative ions which can trap positrons in their shallow potential at low

temperatures [7]. However, it is mostly not possible to unambiguously identify a defect from the positron signals alone. This is also found in highly n-doped GaAs: It is not clear whether the observed monovacancies are As vacancies, V_{as}, only [8,9]; isolated Ga vacancies, V_{Ga} [10]; defect complexes like Te_{As}-V_{Ga} [11]; or any combination of the above mentioned defects. Moreover, the identity of the shallow positron traps commonly found in GaAs could never be cleared by positron annihilation. STM, on the other hand, provides atomically resolved images of bulk defects exposed by cleavage on the surface, thus giving a direct identification of the defects observed. However, the exact measurement of the concentration of bulk defects by STM may be difficult due to the formation of additional defects, i.e. vacancies after cleavage [5]. In this work, the compensating defects in highly Si-doped GaAs were studied by a combined use of positron annihilation and scanning tunneling microscopy. Positrons will be used to proof the concentration of bulk defects, particular vacancies, whereas STM will be used to identify the defects.

2 EXPERIMENTAL

We investigated highly Si-doped bulk-GaAs by positron lifetime spectroscopy in correlation to STM observations. The samples were cut from seed-grown GaAs crystals having four different Si-concentrations, measured by secondary ion mass spectroscopy (SIMS): 1×10^{18}, 2.7×10^{18}, 1.2×10^{19}, and $(2.5–6)\times10^{19}$ cm^{-3}. The carrier concentrations were determined by Hall effect measurements to be 7×10^{17}, 1×10^{18}, 4.5×10^{18}, and 1.8×10^{18} cm^{-3}. The low carrier concentrations indicate a strong compensation as it is commonly observed in highly Si-doped GaAs [1].

Positron annihilation was performed using a conventional fast-fast coincidence system with a time resolution of about 250 ps. The temperature could be varied between 20 to 500 K. A $^{22}NaCl$ positron source having an activity of 8×10^{5} Bq, covered with 1.5 µm Al foil was placed between a pair of identical samples [11,12]. The positron lifetime spectra were analyzed with the trapping model [13] after source and background corrections [12]. Basically 5×10^{6} events were measured in each lifetime spectrum.

A positron lifetime spectrum consists of a sum of exponential decay terms which are characterized by their respective intensities I and positron lifetimes τ. In a defect-free crystal positrons annihilate from the delocalized bulk state with a single lifetime τ_{bulk}. If positrons are trapped in a vacancy a second lifetime τ_{vac} is found which is always longer than τ_{bulk}. Thus, if positrons detect vacancies, the average positron lifetime τ_{av} increases distinctly. $\tau_{av}=\Sigma\ I_i\ \tau_i$ is the weighted sum over the different lifetime components present in the spectrum. A decomposition of the spectra yields additional information on the defect related lifetime τ_{vac} which is characteristic for the observed open volume, i. e. the size of the vacancy. As the result of the lifetime experiment, the positron trapping rate κ_{vac} related to the defect density c_{vac}, can be calculated by

$$\kappa_{vac} = \mu\ c_{vac} = \frac{1}{\tau_{bulk}} \frac{\left(\tau_{av} - \tau_{bulk}\right)}{\left(\tau_{vac} - \tau_{av}\right)}. \qquad (1.)$$

The constant μ is the so called trapping coefficient which must be determined using an independent reference method for each defect type [14].

In addition, measurements of the Doppler broadened 511 keV annihilation peak were performed at room temperature using a high purity Ge detector. The annihilation spectra were characterized by the line-shape parameters S and W. S is defined as the number of annihilation counts in the central (low momentum) region of the annihilation peak divided by the total number of counts. W is defined as the number of counts in the wing (high momentum) region of the peak divided by the total. Positron annihilation in vacancy defects yields an increase of S and a decrease of W compared to their values in defect-free material since annihilation in defects occurs mainly with low-momentum electrons (see, e.g., ref. [6]). Annealing was performed in a conventional furnace under vacuum

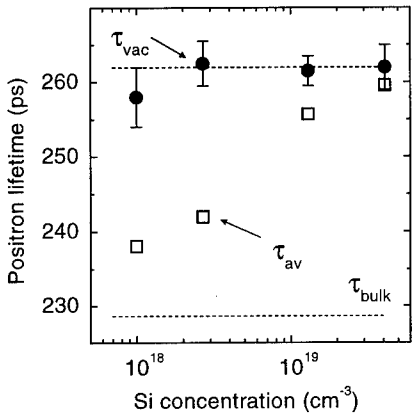

Fig. 1: Average positron lifetime τ_{av} and defect related lifetime τ_{vac} as a function of the Si concentration in GaAs at room temperature. The error for τ_{av} is in the order of the symbol height.

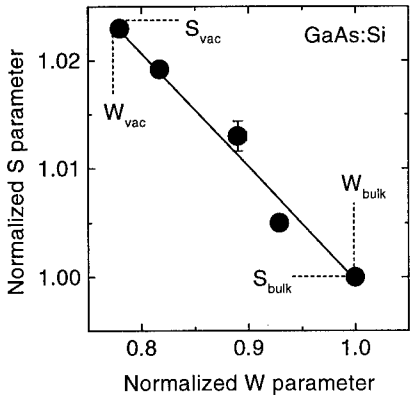

Fig. 2: *S* parameter as a function of the *W* parameter for highly Si-doped GaAs. *S* and *W* are normalized to the values found in a defect-free reference.

conditions (10^{-4} Torr) with the samples covered by large pieces of undoped GaAs to prevent a loss of As during heating.

Samples originating from the same wafers were also cleaved in ultra-high vacuum to form clean (110) surfaces and transferred to the STM without braking the vacuum (by using a dual chamber system). STM investigations were then performed at room temperature. The defects, exposed by the cleavage process on the surface, were identified and their concentration determined [5].

3 Positron Annihilation

3.1 Positron Annihilation Measurements at Room Temperature

The results of the positron lifetime measurements at room temperature are shown in Fig. 1. About 1×10^7 counts were collected for each spectrum and the measurements were repeated at least five times to obtain an improved accuracy. The average positron lifetime τ_{av} increases from 238 to 259 ps with increasing Si-doping concentration. These values are well above the bulk lifetime, τ_{bulk}, measured to be (228.5±1) p s in an undoped GaAs reference sample showing no positron trapping in defects. τ_{bulk} is in good agreement with previous results [9,11] and theoretical predictions [15]. An analysis in terms of a two-state (i.e. one defect) trapping model yields a defect related lifetime τ_{vac} of (262±2) ps independent of the particular sample (Fig. 1). An analysis with more than one defect type did not yield additional lifetime components. A lifetime of about 260 ps is typical for positron annihilation in monovacancies in GaAs [8-11,15]. Thus, an increasing density of monovacancies was observed with increasing Si concentration. The positron lifetime data alone, however, does not allow detailed conclusions on the nature of these vacancies.

The Doppler-broadening measurements can be used to provide additional information. The fraction η of positrons annihilating in defects is given by

$$\eta = \frac{S - S_{bulk}}{S_{vac} - S_{bulk}} = \frac{W_{bulk} - W}{W_{bulk} - W_{vac}} = \frac{\tau_{av} - \tau_{bulk}}{\tau_{vac} - \tau_{bulk}} \qquad (2)$$

where S and W are the measured Doppler broadening parameters. S_{vac} and W_{vac} correspond to complete annihilation in the defect; whereas S_{bulk} and W_{bulk} correspond to the defect-free bulk. η is directly related to the defect density. It can be seen, that S depend linearly on W as well as on τ_{av} if only the defect concentration changes, but not the defect type [16]. A deviation from the S-W linearity is expected if more than one defect type traps positrons, i.e. if we would detect different

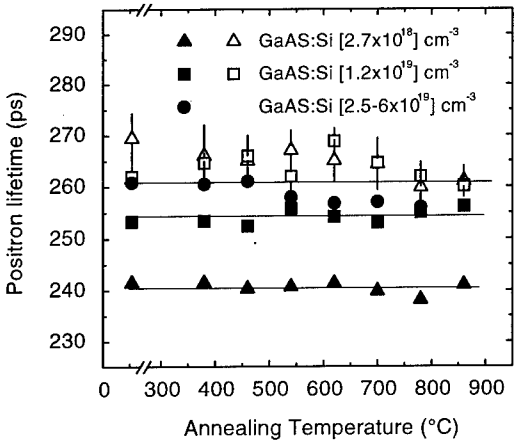

Fig. 3: Average positron lifetime τ_{av} (filled symbols) and defect related lifetime τ_{vac} (open symbols) in highly Si doped GaAs during isochronal annealing.

types simultaneously. As can be seen in Fig. 2, S depend always linearly on W in highly Si doped GaAs and we detect thus always one and the same type of vacancy in all samples.

3.2 Annealing Behavior

The thermal stability of the defects was proofed by isochronal annealing for 15 min. The results of the annealing studies are shown in Fig. 3. The average positron lifetime as well as the defect related lifetime remain unchanged for annealing temperatures up to 880°C. The mono-vacancies observed in highly Si-doped GaAs are thus stable up to 880°C. Corbel et al. [8] observed an annealing stage at about 500°C for the native As vacancies in low n-doped GaAs. The extraordinary high thermal stability of the vacancies in highly Si-doped GaAs is thus a strong hint that we do observe Ga-vacancy related defects. A similar thermal stability was already found for monovacancies in highly Te-doped GaAs [11], attributed to Te_{As}-V_{Ga} complexes. The simple isolated Ga vacancy, on the other hand, was found to be highly mobile after electron irradiation even at room temperature [17,18]. Thus, a very likely assignment of the vacancies detected in highly Si-doped GaAs is a defect complex containing a Ga-vacancy and another defect, most likely a Si dopant atom. However, the detailed structure of this complex cannot be deduced from the positron annihilation measurements.

3.3 Positron Annihilation Measurements as a Function of Temperature

The average positron lifetime is shown as a function of temperature in Fig. 4 for highly Si-doped GaAs and an unoped GaAs reference sample. For the reference sample only a small, but systematic variation of the average positron lifetime was observed with varying temperature. Such a behavior is typical for positron annihilation in the defect-free lattice: the positron lifetime decreases slightly at low temperatures due to the increase of the electron density caused by lattice expansion [9]. At high temperatures ($T > 300$ K) a constant positron lifetime was found in the Si doped samples which agrees with the room temperature values discussed above. With decreasing temperature, however, the average positron lifetime decreases strongly between 100 to 300 K. Nearly constant levels are reached at $T < 100$ K slightly above the positron lifetime found in undoped GaAs. This behavior can only be explained by the presence of additional defects which trap positrons only at low temperatures [7]. The lifetime of these defects must be close to the bulk lifetime, indicating that the additional defects do not have an open volume. These so-called shallow positron traps are commonly identified to be negatively charged ions which can trap positrons in their shallow potential only at low temperatures. At high temperatures ($T > 300$K) a strong thermal detrapping from the shallow potential occurs. Negative ions are commonly detected by positrons in as-grown GaAs [9,11]. Up to now, little is known on their microscopic nature from positron annihilation data. This is because the annihilation parameters (lifetime and Doppler broadening) equals that of the defect-free bulk [7]. Negative ions can thus be only detected if competitive trapping at vacancy defects and ions occurs, resulting in a temperature dependence of the positron lifetime (or the

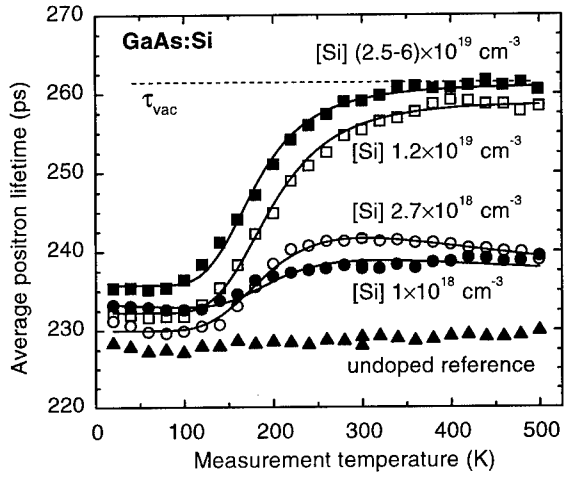

Fig. 4: Average positron lifetime τ_{av} as a function of the sample temperature for differently Si-doped GaAs and an undoped GaAs reference sample. Solid lines are fits to the temperature-dependent trapping model (see text).

Doppler broadening parameters) similar to our case. Nevertheless, we can extract important information from the temperature-dependent measurements.

Firstly, we will discuss the charge state of the vacancies. At low temperatures, the competitive positron trapping at vacancies and negative ions must have the same temperature dependence since the positron lifetime is constant between 20 to 80 K (Fig. 4). Detrapping from the ions can be neglected in this temperature range [7]. The trapping coefficient of negative ions and consequently also of the vacancies has a temperature dependence like $T^{-1/2}$ [19]. That means, the vacancies are also negatively charged. This agrees with theoretical expectations for mono-vacancies in highly n-doped GaAs [20].

Secondly, at very low temperatures ($T <$ 100 K), no detrapping from the negative ions occurs. Thus we determine the trapping rate κ_{ion} at negative ions from the data at 20 K using a two-defect trapping model assuming positron trapping at vacancies and negatively charged ions:

$$\kappa_{ion} = \mu_{ion}(20K)\, c_{ion} = \frac{\kappa_{vac}(20\,K)\left(\tau_{vac} - \tau_{av}\right) + \tau_{bulk}^{-1}\left(\tau_{bulk} - \tau_{av}\right)}{\left(\tau_{av} - \tau_{ion}\right)}. \qquad (3)$$

The lifetime at the ions, τ_{ion}, was assumed to be equal to τ_{bulk}. In order to calculate κ_{ion}, we have to know κ_{vac} at 20 K, which was calculated to be 1.5×10^{16} s^{-1} using the temperature dependence of positron trapping at negatively charged vacancies [17].

To check this results, we thirdly fitted the average positron lifetime as a function of temperature taking into account positron detrapping from the negatively charged ions (e.g. [17,21]). This can be described by the positron detrapping rate δ_{ion} which is given by

$$\delta_{ion} \propto \mu_{ion}\,(k_B T)^{3/2} \exp\left(-\frac{E_{b,ion}}{k_B\, T}\right) \qquad (4)$$

where $E_{b,ion}$ is the binding energy of positrons in the shallow potential around negative ions and c_{ion} is their density [22]. The density of vacancies and negative ions was calculated from their respective trapping rates (see below). We used these densities as fixed input parameter in the analysis leaving $E_{b,ion}$ be the only fitting parameter. A good agreement to the data was obtained as indicated by the solid lines in Fig. 4. The binding energy was consistently found to be $E_{b,ion}$=(70±15) meV in reasonable agreement to the value (50±10) meV found for Ga_{As} antisites in electron irradiated GaAs [21]. Temperature-dependent measurements performed after annealing at 880°C exhibit exactly the same behavior of the positron lifetime as a function of temperature as the measurements presented in Fig. 4 did (not shown). Thus, the negative ions are thermally stable at least up to 880°C like similar to the vacancies. An identification of the negative ions from positron annihilation measurements is, however, not possible as stated above.

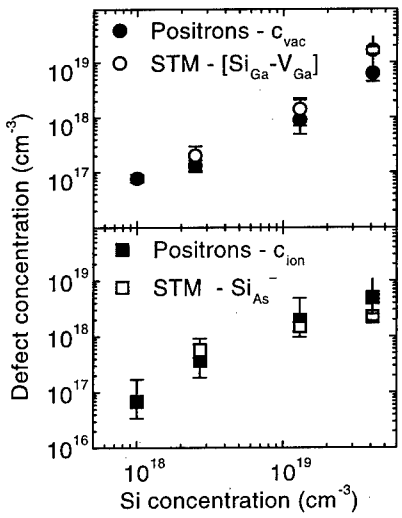

Fig. 5: (a) Concentration of monovacancies c_{vac} (positrons) and Si_{Ga}-V_{Ga} complexes (STM) versus the Si concentration. (b): The same for negatively charged ions (positrons) (c_{ion}) and Si_{As} acceptors (STM). c_{vac} and c_{ion} are lower-limit estimations for the highest Si density due to saturated positron trapping.

3.4 Defect densities from positron annihilation

Fig. 5. shows the density of vacancies (Eq. 1) and negatively charged ions (Eq. 3) as a function of the Si concentration. Trapping coefficients of μ_{vac}= $(1\pm0.5)\times10^{15}$ s^{-1} at room temperature [14] and μ_{ion}= $(5\pm2)\times10^{16}$ s^{-1} at 20 K [21] were used to calculate the defect densities from the respective trapping rates. Strong increases of the defect densities were found with increasing Si concentration. Note that the values for the highest doped sample are lower-limit estimations due to saturated positron trapping (τ_{av} is close to τ_{vac}). It must be further pointed out that the concentrations of negative ions are order of magnitude estimations only (note the large error bars in Fig. 5). This arise mostly due to uncertainties of the trapping coefficients and there temperature dependenceies, which cannot be directly measured. Moreover, the value estimated for c_{ion} depends on the vacancy density c_{vac} via κ_{vac} as can be seen from Eq. 3. The error for c_{ion} is thus much larger than the error for the vacancy density.

4 Identification of the Defects Using Scanning Tunneling Microscopy

By using positron annihilation alone, we were not be able to give an unambiguous identification of the observed defects. Due to this reason, scanning tunneling microscopy measurements were performed on the defects exposed by cleavage on the nonpolar (110) surface of highly Si-doped GaAs samples, cut from the same wafers as the samples investigated by positron annihilation. The GaAs (110) surface is well suited for the identification of defects [23,24] due their simple 1×1 reconstruction and the absence of surface states in the band gap . Five defects having significant concentrations were observed: Si_{Ga} donors, Si_{As} acceptors, Si cluster, isolated Ga vacancies, V_{Ga}, and complexes containing a Si_{Ga} donor and a Ga vacancy [5]. Any other defect, if present, has a concentration well below the sensitivity limit of about 2×10^{17} cm^{-3}. In particular, no As vacancies were observed by STM. Thus, As vacancies V_{As} or defect complexes related to V_{As} are not detected by positrons in highly Si-doped GaAs. This is consistent with the results from the annealing experiments (see above) but it clearly contradicts the previous interpretation that positrons detect always As vacancies in n-doped GaAs [8,9]. It appears that As vacancies are only detected by positrons in low n-doped material, where we cannot draw conclusions from the present work.

The vacancies observed by positrons in the bulk must reside in the Ga sublattice. However, it was observed that isolated Ga vacancies are formed after cleavage on the surface due to a low-temperature Langmuir desorption [5]. The driving force for this vacancy formation is assumed to be due to the Fermi-level effect: negatively charged cation vacancies can easily be formed on the surface to compensate the n-type dopant atoms. Similar observations were done on Zn-doped GaAs (p-type), where anion vacancies are formed to compensate the p-type Zn-dopant atoms [25]. Thus, the amount of Ga vacancies observed on the surface does not reflect the bulk density. In order to separate out the pure surface vacancies from those present in the bulk, an extrapolation back to the cleavage time was performed [5]. Within the frame of the errors, however, no isolated Ga vacancies should be present at cleavage time. The large concentration of V_{Ga} observed is thus mainly surface

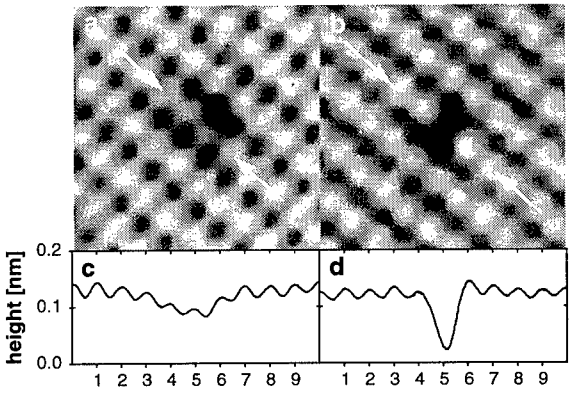

Fig. 6: Constant-current STM images of the occupied (a) and empty (b) states of Si_{Ga}-V_{Ga} complex. Lines along the atomic rows are marked with arrows [(c) and (d)].

related and cannot explain the concentration of monovacancies observed by positrons in the bulk.

High resolution STM images of the occupied and empty states of the second vacancy defect are shown in Fig. 6 (a,b). The defect consists of a missing empty dangling bond and a slightly raised neighboring empty dangling bond [Fig. 6 (d)]. This defect was identified to be a Si_{Ga}-V_{Ga} complex due to its structure which is analogous to that observed for Zn_{Ga}-anion-vacancy complexes on p-doped GaAs and InP (110) surfaces, where only charge state and sublattice are interchanged [25]. Here, the missing empty dangling bond is the sign for the Ga vacancy, whereas the raised empty dangling bond is the signature of the Si_{Ga} donor. The concentration of the defect complexes in the bulk was determined from the measured surface concentration. The results are shown in Fig. 5 (a) (open circles) together with the density of monovacancies estimated from positron annihilation. A good agreement was obtained. Thus, the monovacancies detected by positrons are identified to be Si_{Ga}-V_{Ga} complexes. This finding is in agreement with recent results obtained on highly Si-doped GaAs MBE-layers, where Ga-vacancy-related defects were found by positron annihilation [25].

Only one type of negatively charged ions, namely the Si_{As} acceptor, was detected by STM. The concentration of this defect can be obtained with a good accuracy from STM measurements since it can be observed up to six layers below the surface [24]. The concentration was measured for each subsurface layer and the bulk densities were calculated [Fig. 5(b)]. A surprisingly good agreement to the positron results for negative ions was obtained if one bears in mind the large errors for c_{ion} from the positron measurements. Note the quantitative disagreement for the highest Si doping density. This disagreement may be explained by the errors for c_{ion}. However, a large concentration of Si clusters was also observed in this sample. It appears likely that these Si clusters trap positrons, because a local band bending similar to that one of Si_{As} acceptors was observed around the clusters. The Si clusters are enclosed precipitates (no interface defects). Thus, no additional positron lifetime component is expected if positrons are trapped at Si clusters, since the positron lifetime in Si is close to the lifetime in bulk GaAs. Therefore, the quantitative discrepancies may also be explained by positron trapping at two different kind of shallow positron traps: Si_{As} acceptors and Si-clusters.

5 SUMMARY

Positron annihilation and scanning tunneling microscopy were successfully correlated. We demonstrated that a combination of this two different methods can be used as a powerful tool to study the microscopic nature and concentration of point defects. The vacancies, detected by positron lifetime spectroscopy, are identified by STM to be Si_{Ga}-V_{Ga} complexes. Their concentration increases with the Si-doping concentration. The shallow positron traps, detected at low temperatures, are mainly Si_{As} acceptors in good correlation to the STM measurements. Compensation of free carriers in highly Si-doped GaAs can thus only be understood if all the different kind of defects are considered. The simultaneous presence of several kinds of native defects is in

agreement with theoretical predictions [27] and may explain the differences recognized in earlier studies regarding the compensation in highly Si-doped GaAs.

REFERENCES

[1] E. F. Schubert, *Doping in III-V semiconductors* (University of Cambridge Press, Cambridge, 1993).
[2] S. Schuppler, D. L. Adler, L. N. Pfeiffer, K. W. West, E. E. Chaban, and P. H. Citrin; Phys. Rev. B **51**,10527 (1995).
[3] J. Maguire, M. Murray, R. C. Newman, R. B. Beall, J. J. Harris; Appl. Phys, Lett. **50**, 516 (1987); For a recent review, see: R. C. Newman; Semic. Sci. Technol. **9**, 1749 (1994).
[4] J. Gebauer, R. Krause-Rehberg, C. Domke, Ph. Ebert, and K. Urban, Phys. Rev. Lett. **78**, 3334 (1997).
[5] C. Domke, Ph. Ebert, M. Heinrich, and K. Urban, Phys. Rev. B **54**, 10288 (1996).
[6] *Positron spectroscopy of solids*, edited by A. Dupasquier and A. P. Mills (IOS Press, Amsterdam, 1995).
[7] K. Saarinen, P. Hautojärvi, A. Vehanen, R. Krause, and G. Dlubek; Phys. Rev. B **39**, 5287 (1989).
[8] C. Corbel, M. Stucky, P. Hautojärvi, K. Saarinen, and P. Moser; Phys. Rev. B **38**, 8192 (1988).
[9] K. Saarinen, P. Hautojärvi, P. Lanki, and C. Corbel; Phys. Rev. B **44**, 10585 (1991).
[10] S. Fujii, A. Uedono, and S. Tanigawa; Hyperfine Interactions **79**, 719 (1993).
[11] R. Krause-Rehberg, H. S. Leipner, A. Kupsch, A. Polity, and Th. Drost; Phys. Rev. B **49**, 2385 (1994).
[12] B. Somieski, T. E. M. Staab, and R. Krause-Rehberg; Nucl. Instr Meth. A **381**, 128 (1996).
[13] T. E. M. Staab, B. Somieski, and R. Krause-Rehberg; Nucl. Instr Meth. A **381**,141 (1996).
[14] R. Krause-Rehberg and H. S. Leipner, Appl. Phys. A **5**, 457 (1997).
[15] S. Pöykkö, M.J. Puska, M. Alatalo, and R.M. Nieminen; Phys. Rev. B **54**, 7909 (1996).
[16] L. Liszkay, C. Corbel, L. Baroux, P. Hautojärvi, M. Bayhan, A. W. Brinkmann, and S. Tatarenko, Appl. Phys. Lett. **64**, 1380 (1994).
[17] C. Corbel, F. Pierre, K. Saarinen, P. Hautojärvi, and P. Moser; Phys. Rev. B **45**, 3386 (1992).
[18] A. Polity, F. Rudolf, C. Nagel, S. Eichler, and R. Krause-Rehberg; Phys. Rev. B **55**, 10467 (1997).
[19] M. J. Puska and R.M. Nieminen; Rev. Mod. Phys. **66**, 841 (1994).
[20] M. J. Puska, J. Phys. Condens. Matter **1**, 7347, (1989); H. Seong and L. J. Lewis, Phys. Rev. B **52**, 5675 (1995).
[21] K. Saarinen, A. P. Seitsonen, P. Hautojärvi, and C. Corbel; Phys. Rev. B 52, 10932 (1995).
[22] M. Manninen and R. M. Nieminen; Appl. Phys. A, **26**, 93 (1981).
[22] G. Lengel, R. Wilkins, G. Brown, M. Weimer, J. Gryko, and R. E. Allen; Phys. Rev. Lett. **72**, 836 (1994); Ph. Ebert, K. Urban, and M. G. Lagally, ibid. **72**, 840 (1994).
[23] M. B. Johnson, P. M. Koenraad, W. C. van der Vleuten, H.W. M. Salemink, and J. H. Wolter; Appl. Phys. Lett. **63**, 3636 (1993); R.M. Feenstra, J.M. Woodall, and G. Pettit; Phys. Rev. Lett. **71**, 1176 (1993); J. F. Zheng, X. Liu, N. Newman, E. R. Weber, D. F. Ogletree, and M. S. Salmeron; ibid. **72**, 1490 (1994).
[24] Ph. Ebert, M. Heinrich, M. Simon, C. Domke, K. Urban, C. K. Shih, M. B. Webb, and M. G. Lagally.; Phys. Rev. B **53**, 4580 (1996).
[25] T. Laine, K. Saarinen, J. Mäkinen, P. Hautojärvi, C. Corbel, L. N. Pfeiffer, and P. H. Citrin; Phys. Rev. B **54**, 11050 (1996).
[26] J. E. Northrup and S. B. Zhang; Phys. Rev. B **47**, 6791 (1993).

Materials Science Forum Vols. 258-263 (1997) pp. 893-898

CHEMICAL TRENDS IN ELECTRONIC PROPERTIES OF ARSENIC VACANCY-3d TRANSITION METAL PAIRS IN GALLIUM ARSENIDE

Ecio J. França[1] and Lucy V. C. Assali[2]
[1]Escola Federal de Engenharia de Itajubá, CP 50, 37500-000, Itajubá,MG,Brazil
[2]Instituto de Física da Universidade de São Paulo, CP 66318, 05315-970,SP,Brazil

Keywords: arsenic vacancy, transition metal, GaAs

Abstract. In this work we report theoretical investigations of the chemical trends in the electronic properties of arsenic vacancy-3d transition metal pairs (TM_{Ga}-ϑ_{As}) in GaAs. The analysis of the one-electron energy spectra of the electronic structure of the complexes lead to the conclusion that the pairs in trigonal symmetry can be described by two different microscopic models. For TM = V, Cr, Mn, and Fe the gap energy levels are 3d-related orbitals. For TM = Co, Ni, and Cu the gap energy levels are divacancy-like states, having a dangling-bond character. Therefore the physical properties of the pairs are related to molecular orbitals which have distinct characteristics depending on the occupation of the 3d orbitals of the TM impurity.

Introduction

Isolated TM atoms have a $3d^m4s^n$ configuration and, when used as dopants, intentionally or not, in GaAs, they occupy preferencially the Gallium metal site (TM_{Ga}).They are observed in several charge states, acting as donors and acceptors, showing ionization and/or inter d transitions [1-10]. Several pair complexes related to TM ions have been, experimentally, observed. However, their physical modelling is not yet completed and their impact in material's properties is little understood. Among them, the most common are associated to a TM_{Ga} and a ϑ_{As} as nearest-neighbors in the lattice.

A complex related to a V_{Ga} and an intrinsic defect has been observed by different experimental techniques [11-16]. This center has a trigonal symmetry (C_{3v}) and a $^4T_1$ ground state ($^4A_2 + {}^4E$, S=3/2). It was tentatively assigned to the complex $(V_{Ga}^- - \vartheta_{As}^+)^0$, which could be interpreted as a d^3 defect orbital in the material band gap.

Complexes related to Cr in GaAs have been reported. From *Photoluminescence* (**PL**) experiments, an emission at 0.839 eV was observed [4,9,10,17,18] and was attributed to $(Cr_{Ga}^- - \vartheta_{As}^+)^0$, with ground state $^2T_5$ ($^5E + {}^5A_1$) pertubed by C_{3v} field due to the ϑ_{As} in the nearest-neighbor site. The transition responsable by the luminescence is $^5E \rightarrow {}^5T_2$, where ^5E is the first excited state. Another **PL** line group was attributed to a inner charge transfer transition from Cr_{Ga} to ϑ_{As} in the neutral complex $(Cr_{Ga}^- - \vartheta_{As}^+)^0$ $(d^4) \rightarrow (Cr_{Ga}^0 - \vartheta_{As}^0)^0$ (d^3), where the $(Cr_{Ga}^0 - \vartheta_{As}^0)^0(d^3)$ complex is metastable [10,17].

Several complexes related to Mn_{Ga} impurity in GaAs, in C_{3v} symmetry, have been identified by *Electron Paramagnetic Resonance* experiments [19-22]. However, due to the spectra complexity and similarity, it has been difficult to assign a microscopic model to them. The $Mn_{Ga} - \vartheta_{As}$ complex is one of the suggestions [19], with an $^6A_1$ ($S = 5/2$) ground state.

From **PL** experiments, two complexes related to Cu_{Ga} and ϑ_{As} have been observed [23,24]. Differently from other $TM_{Ga} - \vartheta_{As}$ complexes, the **PL** spectra related to $Cu_{Ga} - \vartheta_{As}$ are not well resolved and are like the ones related to shallow impurities.

In this work we investigate the microscopic structure of $GaAs : TM_{Ga} - \vartheta_{As}$ centers to study the chemical trends in the electronic properties along the 3d series. The calculations were performed by using the *spin-unrestricted* multiple-scattering Xα theory within the framework of the Watson-sphere-terminated molecular-cluster model [25]. This approach is well documented and has been used in previous calculations for pair complexes in semiconductors [26,27]. All

complexes analysed were considered in a configuration where one TM impurity replaces a Ga host atom (TM_{Ga}) and the As site at nearest-neighbor is vacant (ϑ_{As}). The divacancy ϑ_{Ga}-ϑ_{As} is simulated by removing the Ga and As nearest-neighbors. The defect pair is surrounded by 24 atoms (12 Ga and 12 As) such that the cluster has trigonal symmetry. Lattice relaxations and distortions were not taken into account.

Results and Discussions

Complexes Related to 3d-TM Orbitals

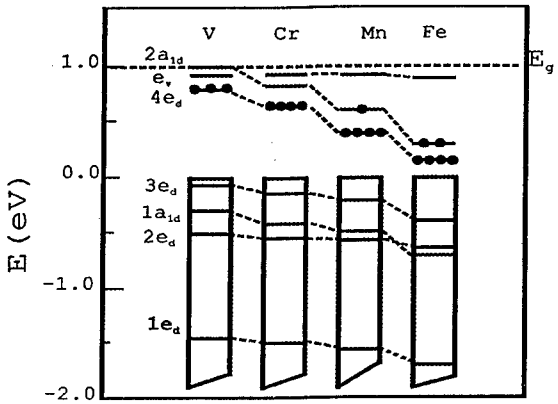

Figure 1: Self-consistent electronic structure spectra of $TM_{Ga} - \vartheta_{As}$ complexes in GaAs , with TM= V, Cr, Mn and Fe . The Gap levels occupancy is indicated by dots (•) and orbitals inside the valence band are assumed to be completely filled . The energy zero is set at the valence band maximum.

We first analyse the results obtained for the *spin-restricted* electronic structure of the GaAs: $TM_{Ga} - \vartheta_{As}$ pairs, where TM = V, Cr, Mn, and Fe. Figure 1 shows the self-consistent one-electron results for these complexes. The occupancy of the gap energy levels is indicated by dots (•) and orbitals inside the valence band are assumed to be completely filled. Figure 2 shows the charge distribution, in percentage, in the TM_{Ga} spheres for the 3*d*-related levels. The results depicted in these figures lead to the conclusion that the stable complex impurity energy levels can be described by interactions between the molecular orbitals of the isolated TM_{Ga} impurities and the arsenic vacancy.

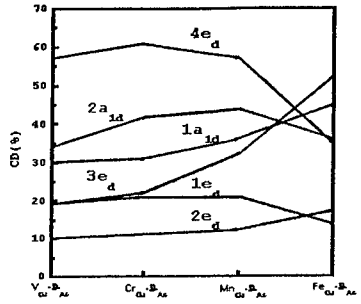

Figure 2: Distribution of charge, in percentage, for 3d-derived states, inside TM_{Ga} spheres . The orbitals are labeled as in fig.1 .

Arsenic vacancy in GaAs introduces a t_2 energy level in the gap, occupied with one electron.

When the symmetry is lowered from Td for ϑ_{As} to C_{3v} for $TM_{Ga} - \vartheta_{As}$ pairs, the dangling-bond like t_2 energy level splits into two orbitals with a_1 and e symmetries. On the other hand, an isolated TM_{Ga} impurity gives rise to $3d$-derived gap and resonances states with t_2 and e symmetries which split, in C_{3v} symmetry of the complexes, into a non degenerated a_1 energy level and a pair of degenerated e energy levels.

In the electronic structure of the pairs, showed in Fig. 1, the $3d$-derived energy levels in the valence band are described by the electronic configuration $3e_d$, $1a_{1d}$, $2e_d$ and $1e_d$, with significative charge distribuitions in $3d-TM_{Ga}$ sphere (Fig. 2). The $2a_{1d}$ and $4e_d$ energy levels, displayed in Fig.1, as well as another e_d orbital, located in the conduction band ($5e_d$) and not shown in figure, are originated from the e and t_2 orbitals of the isolated TM_{Ga} impurities, splitted by C_{3v} field. The e_v gap energy level, located between $2a_{1d}$ and $4e_d$ orbitals, has a dangling-bond character, being a ϑ_{As} orbital. As one proceeds from lighter to heavier impurities, the one-electron energy of the $3d$-derived orbitals move down into the band gap, becoming progressively less localized. In the opposite, the $3d$ character increases in the resonance states.

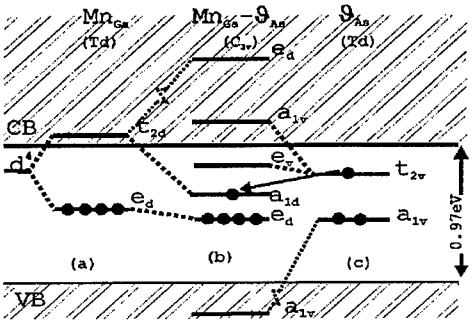

Figure 3: Schematic representation of the impurity levels of the $Mn_{Ga} - \vartheta_{As}$ complex in GaAs as originated from interaction betweeen molecular orbitals of the isolated impurities . (a), (b) and (c) indicate the one electron impurity levels for substitutional manganese (Mn_{Ga}) [3], for $Mn_{Ga} - \vartheta_{As}$ complex and for arsenic vacancy (ϑ_{As}) .

The complexes molecular orbitals formation can be schematically represented as in Fig. 3, for the particular case of the $Mn_{Ga} - \vartheta_{As}$ complex. The ϑ_{As} e_v orbital has a higher energy than the Mn_{Ga} a_{1d} energy level. Therefore, the complex one-electron ground state configuration is $e_d^4 a_{1d}^1 e_v^0$. This picture could lead to a misleading idea that the stable pair could be described by the notation $(Mn_{Ga}^- - \vartheta_{As}^+)^0$ and interpreted as a d^5 defect orbital in the GaAs band gap. However, for all complexes depicted in Fig.1, the total charge (electrons plus protons) inside the TM impurity spheres is almost null, showing clearly that there is no transfer of one electron from ϑ_{As} to TM_{Ga} impurity. This is a clear demonstration that covalent effects prevent charge transfer to the TM impurity sphere by compensating the increase in one unit of the gap-level occupancy. On the other hand, the Coulumb attraction could be the predominant driving force for pair formation, lowering the complexes orbital energies relative to the isolated impurities orbital energies in the same d^N configuration. Consequently, an isolated TM impurity in a d^N configuration will present a d^{N+1} configuration when paired to an arsenic vacancy nearest-neighbor. This picture can be understood thinking that in complexes the TM_{Ga} impurity has only three, instead of four, As nearest-neighbors. These conclusions show that the unified consistent scheme for the pseudoatomic properties of isolated TM_{Ga} impurities in GaAs can be applied to the complexes $TM_{Ga} - \vartheta_{As}$ as well, with TM = V, Cr, Mn, and Fe.

The self-consistent results using the *spin-unrestricted* scheme show that the $TM_{Ga}-\vartheta_{As}$ centers,

with TM = V, Cr, Mn, and Fe, have a high spin configuration. Therefore, they can be described by the entries in Table 1.

Table 1: Ground state electronic properties of neutral $TM_{Ga} - \vartheta_{As}$ complexes in GaAs. The multiplet configuration is obtained from the one-electron results.

Complex	one-electron configuration	Spin	Multiplet	atomic configuration	Multiplet (Expt.)
$V_{Ga} - \vartheta_{As}$	$4e^2_{d\uparrow}\, 2a^1_{1d\uparrow}\, 5e^0_{d\uparrow}\, 4e^0_{d\downarrow}\, 2a^0_{1d\downarrow}\, 5e^0_{d\downarrow}$	3/2	$^4A_2$	d^3	$^4A_2 + ^4E$
$Cr_{Ga} - \vartheta_{As}$	$4e^2_{d\uparrow}\, 2a^1_{1d\uparrow}\, 5e^1_{d\uparrow}\, 4e^0_{d\downarrow}\, 2a^0_{1d\downarrow}\, 5e^0_{d\downarrow}$	2	^5E	d^4	$^5E + ^5A_1$
$Mn_{Ga} - \vartheta_{As}$	$4e^2_{d\uparrow}\, 2a^1_{1d\uparrow}\, 5e^2_{d\uparrow}\, 4e^0_{d\downarrow}\, 2a^0_{1d\downarrow}\, 5e^0_{d\downarrow}$	5/2	$^6A_1$	d^5	$^6A_1$
$Fe_{Ga} - \vartheta_{As}$	$4e^2_{d\uparrow}\, 2a^1_{1d\uparrow}\, 5e^2_{d\uparrow}\, 4e^1_{d\downarrow}\, 2a^0_{1d\downarrow}\, 5e^0_{d\downarrow}$	2	^5E	d^6	—

The one-electron crystal field energy splitting, related to the $3d$ gap and conduction states, is $\approx 2\ eV$. Therefore the many-electron configuration energies will be located in this range, which is the range of $3d$ inter configuratin transition energies. The hibridization regulates the energy level splitting as well as maintains sufficiently orbital localization to permit $3d$ inter configuration transitions.

Complexes Related to Divacancy-Like Orbitals

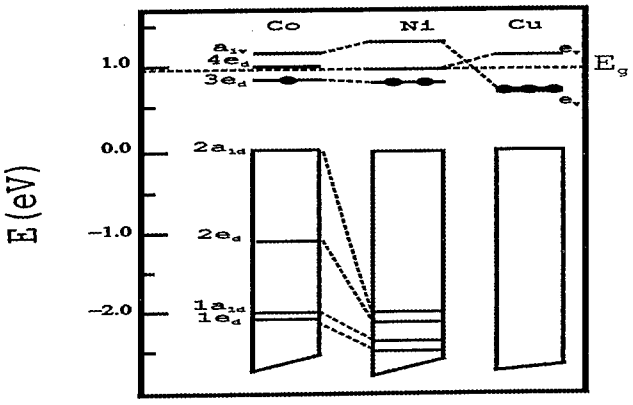

Figure 4: Self-consistent electronic struture spectra of $TM_{Ga} - \vartheta_{As}$ complexes in GaAs, with TM=Co,Ni and Cu . The gap levels occupancy is indicated by (•) and orbitals inside the valence and conduction bands are assumed to be completely filled or empty, respectively . The energy zero is set at the valence band maximum .

The results obtained for the *spin-restricted* electronic structure of the GaAs:TM_{Ga}-ϑ_{As} systems, where TM = Co, Ni, and Cu are shown in Fig. 4. The energy levels occupancy is indicated by dots (•) and orbitals in the valence and conduction bands are assumed to be completely filled or empty, respectively. Figure 5 shows the charge distribution, in percentage, in the TM_{Ga} spheres for the $3d$-related levels. The results depicted in these figures lead to the conclusion that the stable complex impurity energy levels can be described as divacancy-like states ($\vartheta_{Ga} - \vartheta_{As}$), having a dangling-bond character.

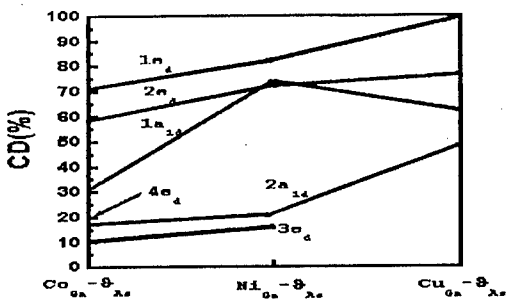

Figure 5: Distribution of charge, in percentage, for 3d-derived states, inside TM_{Ga} spheres . The orbitals are labeled as in Fig.4 .

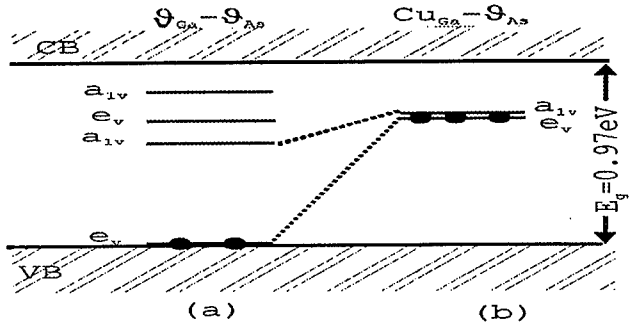

Figure 6: One-electron energy of the band gap impurity levels of : (a) the divacancy ($\vartheta_{Ga} - \vartheta_{As}$) and (b) the $Cu_{Ga} - \vartheta_{As}$ complex in GaAs .

The resonance $3d$-derived states, $1e_d$, $1a_{1d}$, $2e_d$, and $2a_{1d}$, move down into the valence band, becoming progressively more localized, when going from Co to Cu. On the other hand, the $3d$ character decreases in the $3e_d$ gap state when one moves to higher values of the TM impurity atomic number. Although this occupied gap level has a non negligible $3d$ character for $Co_{Ga} - \vartheta_{As}$ and $Ni_{Ga} - \vartheta_{As}$ complexes, the ground state properties of all three neutral complexes are dittated by a dangling-bond like orbital. The divacancy $\vartheta_{Ga} - \vartheta_{As}$ could be undestood as an association between a ϑ_{Ga} (acceptor - $a_{1v}^2 t_{2v}^3$; Td symmetry) and a ϑ_{As} (donor - $a_{1v}^2 t_{2v}^1$; Td symmetry). The presence of ϑ_{As} in the nearest-neighbor of the ϑ_{Ga} reduces the local symmetry to C_{3v}, splitting the molecular orbitals in $a_{1v}^2 a_{1v}^2 e_v^1$ (ϑ_{Ga}) and $a_{1v}^2 a_{1v}^1 e_v^0$ (ϑ_{As}). The ϑ_{As} transfers one electron to ϑ_{Ga} orbitals and the final configuration is $a_{1v}^2 a_{1v}^2 e_v^2 a_{1v}^0 e_v^0 a_{1v}^0$, as showing in Fig. 6(a). The molecular orbitals formation of these complexes can be described by the picture displayed in Fig. 6 for the $Cu_{Ga} - \vartheta_{As}$ complex.
The self-consistent results using the *spin-unrestricted* scheme show that the $TM_{Ga} - \vartheta_{As}$ centers, with TM = Co, Ni, and Cu, have a low spin configuration. Therefore, they can be described as delocalized impurity states, showing no inter d transitions.

Acknowledgements

The autors acknowledge support from Brasilian agency CNPq.

References

1. A. Zunger, Solid State Phys. **39**, 275 (1986).
2. M. J. Caldas, A. Fazzio, and A. Zunger, Phys. Rev. B **29**, 599 (1984).
3. A. Fazzio and J. R. Leite, Phys. Rev. B **21**, 4710 (1980).
4. A. M. Hennel, Acta. Phys. Pol **A79**, 15 (1991).
5. A. M. Hennel, Semiconductors and Semimetals **38**, 189 (1993).
6. B. Clerjaud, J. Phys. C: Solid State Phys. **18**, 3615 (1985).
7. A. G. Milnes, Adv. Electron. and Electron. Phys. **61**, 63 (1983).
8. U. Kaufamann and J. Schneider, Festkorperprobleme - Adv. Solid State Phys. **20** , 87(1980).
9. *Deep Centers In Semiconductors*, ed. S. T. Pantelides (Gordon and Breach Sci. Publ., New York, 2ed.,1992).
10. K. A. Kikoin and V. N. Fleurov, *Transition Metal Impurities in Semiconductors* (World Scientific, Singapore) (1994).
11. H. Terao, H. Sunakawa, K. Ohata, and H. Watanabe, *Semi- Insulating III-V Materials*, ed. S.Makram-Ebeid and B.Tuck (Shiva Publishing, Nantwich, UK, 1982), vol.**54**.
12. P. S. Gladkov and K. B. Ozanyan, Phys. Stat. Sol. **(a)108**, K125 (1988).
13. A. M. Vasson, A. Vasson, C. A. Bates, and A. F. Labadz, J. Phys. C: Solid State Phys. **17** , L837 (1984).
14. V. W. Rampton, M. K. Saker, and W. Ulrici, J. Phys. C: Solid State Phys. **19**, 1037 (1986).
15. A. Gőrger, B. K. Meyer, J-M. Spaeth and A. M. Hennel, Semicond. Sci. Technol. **3**, 832 (1988).
16. N. Butler, L. J. Chalils, M. Sahraoni-Tahar, B. Salce, and W. Ulrici, J. Phys.: Condens. Matter. **1**, 1191 (1989).
17. R. A. Vanen, K. A. Kikoin, M. A. Messerer, and L. Ya Pervova, Sov. Phys. Semicond. **22**, 155 (1988).
18. J. A. L. Simpson, C. A. Bates, J. Barrau, M. Brosseau, and V. Thomas, Semicond. Sci. Technol. **3**, 178 (1988).
19. K. H. Segsa and S. Spenke, Phys. Stat. Sol. **(a) 27**, 129 (1975).
20. V. F. Masterov, S. B. Mikhrin, B. E. Samorukov, and K. F. Shtel'Makh, Sov. Phys. Semicond.**17**, 796 (1983).
21. G. Kűhn and S. Waterwig, Phys. Stat. Sol. **41**, K13 (1977).
22. R. S. Title, J. Appl. Phys. **40**, 4902 (1962).
23. H. P. Gislason, B. Monemar, Z. G. Wang, Ch. Uihlein, and P. L. Liu, Phys. Rev. B **32**, 3723 (1985).
24. Z. G. Wang, H. P. Gislason, and B. Monemar, J. Appl. Phys. **58**, 230 (1985).
25. A. Fazzio, J. R. Leite, and M.L.de Siqueira, J. Phys. C **12**, 3469 (1979).
26. L. V. C. Assali and J. R. Leite, Mater. Sci. Forum **83-87**, 143 (1992).
27. W. M. Orellana and L. V. C. Assali, Mater. Sci. Forum **143-147**, 775 (1994).

Materials Science Forum Vols. 258-263 (1997) pp. 899-904

PERTURBED ANGULAR CORRELATION MEASUREMENTS AND LATTICE SITE LOCATION OF Br IN GaAs

M. Wehner, M. Risse, R. Vianden, M. Dalmer[1], H. Hofsäss[1], M.C. Ridgway[2], M. Petravic[2] and the ISOLDE - Collaboration[3]

Institut für Strahlen- und Kernphysik, Nußallee 14 - 16, D - 53115 Bonn, Germany

[1] Fakultät für Physik, Universitätsstraße 10, D - 78434 Konstanz, Germany

[2] Department of Electronic Materials Engineering, Research School of Physical Sciences and Engineering, Australian National University, Canberra ACT 0200, Australia

[3]CERN, CH - 1211 Geneva, Switzerland

Keywords: GaAs, Br, Vacancy-Interstitial model, PAC, Emission Channelling, SIMS

Abstract. Perturbed angular correlation (PAC) measurements with the probe ^{77}Br(^{77}Se) in semiinsulating GaAs gave evidence for a metastable behaviour of the Br_{As} double donor, similar to the well known EL2 and DX defects in GaAs. Since, according to theoretical calculations, this would imply a substitutional lattice position of Br in GaAs, we applied the emission channelling technique for a lattice site location measurement. After 30 keV implantation of the electron emitter ^{82}Br(^{82}Kr) and subsequent annealing at 1123 K, channelling of the emitted electrons was observed along the <100> and <110> crystal axis, which is expected for a substitutional lattice site occupation of the emitters. Since a quantitative analysis of the data requires the knowledge of the emitter depth profile, it was determined by secondary ion mass spectroscopy (SIMS). A broadening of the depth profile due to Br diffusion during the annealing process was observed for a sample implanted with $1 \cdot 10^{13}$ Br / cm^2 at 160 keV. However, SIMS spectra of a second sample implanted with a higher dose ($3 \cdot 10^{13}$ Br / cm^2, 160 keV) indicated some precipitation of Br. The theoretical channelling effect has been calculated in the many-beam formalism, taking into account the results of the SIMS measurements. The experimental channelling effect is consistent with the assumption that 38(10) % of the emitters occupy substitutional lattice sites. The remaining Br probes most probably are found in precipitates.

Introduction

Since halogens represent shallow donors in II-VI compound semiconductors, there are numerous studies of this subject. In contrast to this, information on the behaviour of group VII elements in III-V compounds is sparse. To our knowledge, there are no experimental results concerning lattice site location, diffusion data, and solid solubility of halogens in III-V semiconductors. Likewise, little is known about the position of gap levels introduced by group VII impurities or the formation of halogen-related defect complexes.

In previous experiments [1,2], we studied the incorporation of the halogen probe nucleus ^{77}Br(^{77}Se) and its interaction with defects by means of the perturbed angular correlation (PAC) technique in several III-V compound semiconductors. The PAC method detects the local charge distribution present at the site of a nuclear probe and thus is sensitive to the microscopic surrounding of the probe atom. In semiinsulating (si) GaAs doped with low Br concentrations, after annealing 100 % of the probes were found to be subjected to a uniform, axially symmetric electric field gradient (EFG),

whose principal component V_{ZZ} was determined to be oriented along the <111> axis. Based on the assumption that Br is incorporated on the As site in GaAs, the observed EFG had been interpreted in terms of the formation of a relaxed configuration of the isolated substitutional Br_{As} double donor. The existence of such a configuration is predicted by theoretical calculations [3], which were performed originally in order to explain the metastability of the DX and EL2 defect in GaAs. Further evidence for a metastable behaviour of halogens in III-V compounds was given by the observation of the persistent photoconductivity (PPC) effect for I in GaAs [4], which is a typical behaviour of DX defects.

Thus the study of halogen impurities in GaAs and other III-V compounds by means of a microscopic technique like PAC can be expected to yield new insights into the mechanisms of metastable defects in these materials. However, the verification of the validity of the model proposed in ref. [1] requires the application of complementary experimental techniques. In particular the experimental determination of the lattice site of the Br impurity in GaAs is required.

Experimental Details

The principles of the PAC technique are well known and discussed in ref. [5]. In defect studies, the EFG present at the site of a nuclear probe decaying via a suitable γ-γ cascade is measured. An EFG arises from any deviation of the charge distribution around the probe atom from cubic symmetry and can be caused by trapping a defect in the vicinity of the probe. The EFG is detected through its hyperfine interaction with the nuclear quadrupole moment Q of the intermediate state of the γ-γ cascade. This quadrupole interaction causes a perturbation of the angular correlation of the cascade. The perturbed angular correlation can be observed by coincident detection of both γ quanta and is apparent as a modulation of the lifetime curve of the intermediate state. The analysis of the perturbation pattern yields information on magnitude, symmetry and orientation of the EFG. In its principal axis system the traceless EFG tensor is commonly characterised by the largest component V_{ZZ} and the asymmetry parameter $\eta = (V_{XX} - V_{YY}) / V_{ZZ}$. Its magnitude is usually expressed by the quadrupole interaction frequency $\nu_Q = e \cdot Q \cdot V_{ZZ} / h$. Thus the information on the EFG derived from the PAC experiment reflects the microscopic structure of the probe atom–defect complex. Probe atoms in different local environments can be distinguished and their fractions can be derived from their individual contribution to the perturbation pattern.

The PAC measurements presented here were performed using the excited $5/2^-$ level in ^{77}Se, which is populated by the β^+ and EC decay of ^{77}Br ($t_{1/2}$ = 57 h). Time differential coincidence spectra of the 755 – 250 keV cascade were recorded with BaF_2 scintillation detectors arranged in a plane around the sample. The intermediate state has a half-life of $t_{1/2}$ = 9.68 ns and a quadrupole moment of Q = 1.1(5) b [6]. The γ–γ cascade has an exceptionally large anisotropy of $A_{22} = -0.454$ [7], which compensates to some extent its low population (< 2%).

Two different techniques were applied to introduce the ^{77}Br probe nuclei into the GaAs sample. Since GaAs contains 50 % ^{75}As, the probes can be produced directly in the sample by irradiation with 33 MeV α-particles via the nuclear reaction ^{75}As(α, 2n)^{77}Br. This recoil implantation method, which is discussed in detail in ref. [2], results in a relatively homogeneous probe distribution with low Br concentrations of $10^{14} - 10^{15}$ cm^{-3} up to a depth of about 200 µm in the sample. Furthermore, the ion implantation technique was applied. At the ISOLDE / CERN facility samples were implanted at room temperature with 60 keV ^{77}Rb and ^{77}Kr, both short-lived parent isotopes of ^{77}Br. In contrast to the situation after recoil implantation, the probe nuclei are now found in a narrow implantation profile at a depth of several hundret Å with a high peak concentration (typically $10^{17} - 10^{19}$ cm^{-3}).

The annealing of all samples investigated in this study was carried out for 120s at 1123 K in a rapid thermal annealing (RTA) set-up. Previously, the samples had been protected against As evaporation

by pyrolytic deposition of a ≈ 800 Å thick Si_3N_4 cap. Only one sample was annealed with a proximity cap.

The emission channelling technique has been proven to be successful in the determination of impurity lattice sites in ion implanted semiconductors. In emission channelling experiments, single crystal samples are doped with radioactive probe atoms acting as emitters of light charged particles like β^-, conversion electrons, β^+, or α-particles. From the channelling and blocking effects of the emitted particles along different atomic rows and planes, the lattice site of the emitter can be deduced [8]. A quantitive analysis of electron channelling effects requires the quantum mechanical treatment of channelling and dechannelling electrons. Based on the dynamical theory of electron diffraction, the many-beam formalism was developed for that purpose [9].
In the present study, the isotope ^{82}Br was applied as a probe nucleus for electron emission channelling experiments for the first time. It was produced by neutron activation of KBr and implanted at the Bonn isotope separator with a dose of $3 \cdot 10^{13}$ cm^{-2}. The implantation energy was chosen as low as 30 keV, since the corresponding low depth of the implant profile results in a reduction of the dechannelling of the emitted electrons. The ^{82}Br nuclei decay by β^- emission (E_{max} = 444 keV) with a half-life of 35.3 h to ^{82}Kr. After annealing of the sample and removal of the Si_3N_4 cap in HF, electron emission yields around the <100> and <110> crystal axis were measured with a Si surface barrier detector (angle resolution 0.3°) at the Konstanz three-axis goniometer. In order to reduce the background, only β^- particles with energies above 200 keV were accepted.

Secondary ion mass spectroscopy (SIMS) was applied to measure the depth distribution of 160 keV Br implants in GaAs before and after annealing. Negatively charged Br ions were detected by sputtering with a 10 keV Cs^+ ion-beam.

Results

In si-GaAs after recoil implantation and annealing at 1123 K the PAC-spectrum displayed in fig. 1 was measured. All probe nuclei are found in the same microscopic environment, characterised by a uniform quadrupole interaction (ν_Q = 299(2) MHz) with an axially symmetric EFG. Figure 1 clearly shows the <111> orientation of V_{zz}. For the interpretation of the PAC results, knowledge of the lattice site of the parent isotope Br is decisive. However, the few theoretical studies dealing with the lattice site of halogens in GaAs give contradictory results: while Ohno et al. propose an interstitial position near the bond center site for Cl in GaAs [10], Uliyashin et al. [11] come to the conclusion, that F is incorporated on the As site in GaAs. We found evidence for a substitutional lattice site of Br in III-V compounds in PAC experiments with ^{77}Br in n-type InAs, where, after annealing at 923 K, all probes were

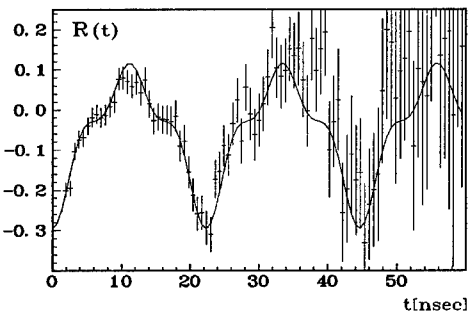

Fig. 1: PAC-spectrum of si-GaAs after 120 s 1123 K RTA, detectors oriented along <111> crystal axis.

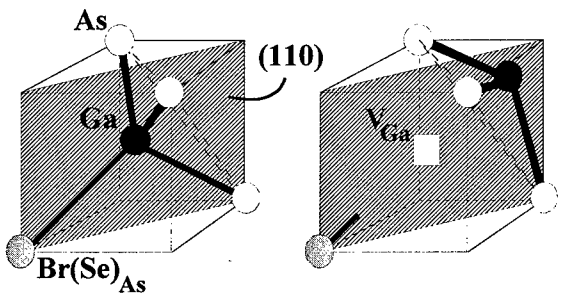

Fig. 2: Substitutional (left) and relaxed (right) configuration of the Br_{As} impurity according to the V-I model.

found in an undisturbed cubic environment [1]. The interpretation of the PAC data in GaAs is based on the assumption that Br is dissolved on the As site. Br_{As} could act as a double donor, for which theoretical calculations [3] predict metastable properties similar to well known defects in GaAs, namely the DX centre and the EL2 defect, which is identified with the As_{Ga} double donor. According to this so called vacancy-interstitial (V-I) model, besides the simple substitutional donor or double donor state (fig. 2, left), a configuration induced by a large lattice relaxation could be stable. For an anion site (double) donor like Br_{As}, a neighbouring Ga atom is expected to be displaced along the <111> crystal axis in this configuration (fig. 2, right). Such a relaxation would break the cubic symmetry around the Br probe and could account for the properties of the EFG observed in the PAC experiment.

A verification of the validity of this model requires – among others – the experimental proof that Br remains substitutional on the As site in the Br–defect complex observed in the PAC experiment. For that purpose the emission channelling technique was applied, which requires the introduction of probe nuclei by ion implantation. As discussed above, the resulting depth distribution of the probe nuclei differs very much from that after recoil implantation. In order to enable a comparison of the results of both techniques, PAC experiments with si-GaAs samples implanted with various doses of 60 keV ^{77}Br were performed. It was found that the fraction of Br probes subjected to the 299 MHz quadrupole interaction decreases as the implantation dose increases. The remaining probe nuclei are found in a heavily disturbed environment, characterised by a large, non-uniform EFG (typically $\nu_Q = 650$ MHz, $\delta = 20$ %). All PAC experiments had been performed without removal of the Si_3N_4 cap. However, a later experiment with ^{82}Br showed that after annealing 36 % of the Br probe nuclei were found either in the cap or, most probably, at the sample–cap interface. If the results of the PAC experiments are corrected for this effect, the fraction of probe nuclei experiencing the 299 MHz quadrupole interaction depends on the Br concentration as shown in fig. 3. This concentration represents the Br peak-concentration derived from simulations with the transport of ions in matter (TRIM) programme [12]. The error bars are due to a large uncertainty in the determination of the implantation dose of about 30 %.

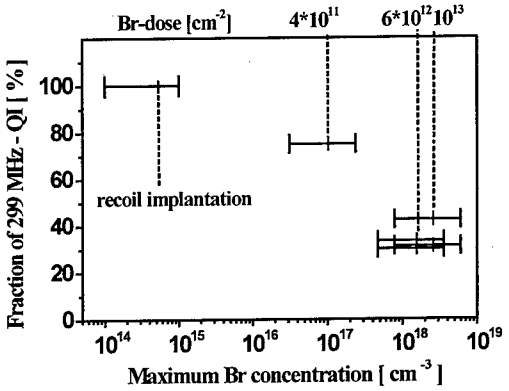

Fig. 3: Fraction of probes subjected to the 299 MHz quadrupole interaction in dependence of the maximum volume concentration of the Br probe.

SIMS measurements were performed with two si-GaAs samples: The first sample was implanted with 160 keV stable Br to a dose of $1 \cdot 10^{13}$ cm^{-2}. A comparison of the results before and after annealing (120s, 1123 K RTA, proximity cap) showed diffusion of the Br probes into the bulk during annealing, resulting in a 15 % broadening in the full width half maximum (FWHM) of the Br depth profile. Since the statistics of this measurement was poor and the depth of the sputtered crater had not been measured, a second experiment was performed with a sample implanted with 160 keV Br and a

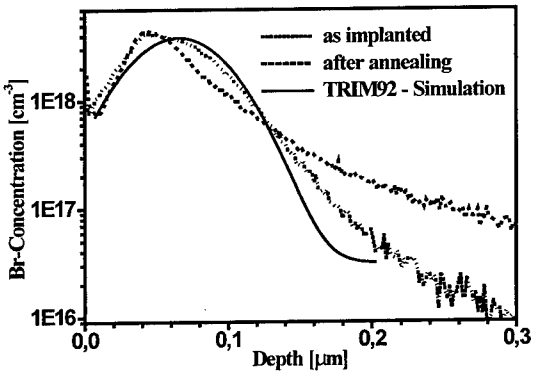

Fig. 4: TRIM simulation and SIMS profiles of si-GaAs implanted with 160 keV $3 \cdot 10^{13}$ Br / cm^2 pre- and post-annealing.

dose of $3 \cdot 10^{13}$ cm^{-2}. Figure 4 shows the SIMS results for this sample together with the TRIM simulation. It is apparent, that annealing causes a diffusion against the concentration gradient in the depth region between 60 and 115 nm. This behaviour is characteristic of precipitation of an implanted impurity [13]. However, for the sample implanted with the lower dose, no diffusion against the concentration gradient was observed. In the region of low Br concentration, annealing results in diffusion of the dopant into the bulk. From measurements of the crater depth (accuracy 5 %) the concentration maximum was observed at a depth 24 % less than that predicted from TRIM simulations.

The results of emission channelling measurements performed on a si-GaAs sample implanted with 30 keV ^{82}Br at a dose of $3 \cdot 10^{13}$ / cm^2 are shown in fig. 5. A channelling effect of the emitted β^- particles was observed for the <100> as well as the <110> axis. In the zincblende structure a flux peak in <110> crystal direction is expected only for a substitutional lattice site of the electron emitters. The quantitative analysis requires a comparison of the experimental results with calculated emission channelling spectra. For that purpose the emission yield as a function of the tilt angle around the <100> and <110> axis is calculated in the many-beam formalism under the assumption of a substitutional lattice site of all emitters. The calculations require the knowledge of the emitter depth profile. Since the SIMS results revealed a decisive influence of the annealing procedure, many-beam calculations were carried out for different depth distributions of the Br probes. It was found that variations in the width of the implant profile almost had almost no influence on the theoretical channelling effect. The 15 % broadening observed in the SIMS measurements on the sample implanted with the lower dose changes the theoretical calculations by less than 1 %. However, the calculations were found to depend significantly on the projected range. Assuming an emitter depth profile according to the TRIM simulation (range r = 17.1 nm, FWHM = 17.4 nm) gives rise to a maximum yield of $Z^{max} = 2.51$. If this theoretical emission profile is fitted to the experimental data as shown in fig. 5, it can be derived that 59(10) % of the probe nuclei occupy substitutional lattice sites. In this interpretation the remaining probes contribute to a "random" signal, i.e. the emitted electrons show no channelling effect. However, the SIMS measurements shown in fig. 4 indicate a shift of the 160 keV implantation profile towards the surface compared to the TRIM simulation. If the projected range of the 30 keV implant was also 24 % less than the TRIM prediction, the depth distribution can be expected to be described by r = 13 nm and FWHM = 14.6 nm. For this dopant profile the many-beam calculations result in an increase of Z^{max} by 30 – 40 %, which leads to a decrease of the substitutional fraction to 38(10) %.

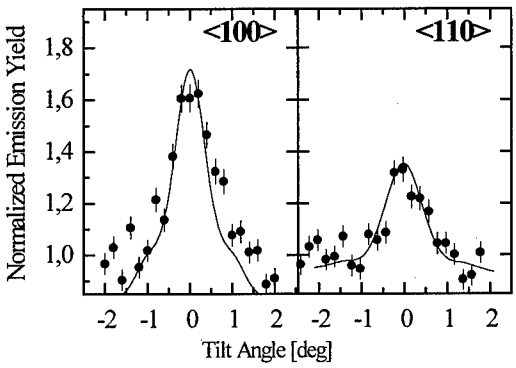

Fig. 5: <100>- and <110>- axial channelling effects of β^- particles emitted in the decay of ^{82}Br, implanted into si-GaAs (30 keV, $3 \cdot 10^{13}$ cm^{-2}) after 120 s annealing at 1123 K.

Discussion

Information on the atomic depth distribution and solubility of Br in GaAs was derived from SIMS. For ions implanted with 160 keV at a dose of $3 \cdot 10^{13}$ cm^{-2} and an annealing temperature of 1123 K, evidence of the formation of Br precipitates was found. Apparently the solid solubility of Br is limited to the order of several 10^{18} Br / cm^3. However, in the region of low Br concentrations diffusion of the dopant into the bulk was observed, as anticipated.

In emission channelling experiments it was found that a relatively high fraction of the implanted Br occupies substitutional lattice sites. However, a quantitative analysis of this fraction was found to depend significantly on the projected range of the emitters. It was assumed that the emitter depth profile after 30 keV implantation shows the same deviations from the TRIM simulation as observed in SIMS measurements for a sample implanted with the same dose, however at a higher energy of 160 keV. Then the emission channelling results are consistent with the assumption, that 38(10) % of the ^{82}Br probes are dissolved on substitutional lattice sites. Since the local Br concentration in case of the 30 keV implantation is increased by a factor of 3.5 as compared to the 160 keV implantation, according to the SIMS results Br precipitation is expected to an even higher degree for the sample studied by emission channelling. For precipitated Br, no channelling of the emitted electrons is expected, which is consistent with the experimental data.

In PAC experiments performed with si-GaAs samples implanted with 60 keV ^{77}Br at doses around $1 \cdot 10^{13}$ cm^{-2}, a fraction of 30 to 43 % of the probes was found in a well defined microscopic environment, characterised by a quadrupole interaction (ν_Q = 299(2) MHz) with a uniform, axially symmetric EFG. Within the experimental error this fraction agrees well with the amount of Br on substitutional lattice sites derived from the emission channelling experiment. However, it has to be noted that the maximum Br concentration in the channelling experiment was about $1.4 \cdot 10^{19}$ cm^{-3}. PAC experiments in this concentration range have not yet been performed and a further decrease of the 299 MHz–fraction cannot be excluded. Nevertheless, the fact that no undisturbed fraction was observed in the PAC experiment seems to justify the identification of the fraction of Br probes subjected to the 299 MHz interaction with substitutional Br. According to the PAC data, the remaining probes were found in a heavily disturbed environment, which could be associated with ^{77}Br in precipitates.

In conclusion, the present SIMS and emission channelling data indicate a substitutional lattice site location for that fraction of Br probes which were found to be subjected to the uniform 299 MHz quadrupole interaction in PAC experiments. Thus the experimental data are consistent with the V-I model, which predicts the formation of a relaxed configuration of the substitutional anion site (double) donor Br_{As}, where a neighbouring Ga atom is displaced into the lattice along the <111> axis, while the donor remains substitutional.

References

1. M. Wehner, P. Friedsam, R. Vianden, S.G. Jahn and D. Forkel-Wirth, Mat. Sci. For. **196-201** pp. 1419-1424 (1995)
2. M. Wehner, R. Vianden, D. Forkel-Wirth and S.G. Jahn, Hyp. Int. C1 pp.215-218 (1996)
3. J. Dabrowski and M. Scheffler, Mat. Sci. For. **83-87** pp. 735-750 (1992)
4. H. Bemelmans, G. Borghs and G. Langouche, Phys. Rev. Lett. **61** pp. 856-860 (1994)
5. H. Frauenfelder and R.M. Steffen in " α-, β- and γ-ray spectroscopy" ed. K. Siegbahn, (Amsterdam: NHPC), pp. 997-1198 (1965)
6. R.B. Firestone and V.S. Shirly in "Table of isotopes", 8th edition, **Vol. 1** (1996)
7. M. Mohsen and F. Pleiter, Hyp. Int. **39** pp. 123-128 (1988)
8. H. Hofsäss and G. Lindner, Phys. Rep. **201(3)** pp. 121-184 (1991)
9. H. Hofsäss, U. Wahl and S.G. Jahn, Hyp. Int. **84** p. 24 (1994)
10. I. Ohno and T. Sasaki, Mat. Sci. For. **196-201** pp. 543-548 (1995)
11. A.G. Uliyashin, Yu. A. Bumay, V.E. Malahovskaya and N.V. Shlopak, Mat. Sci. For. **83-87** pp. 1009-1014 (1992)
12. J. Biersack and L.G. Haggmark, Nucl. Instr. Meth. **174** p. 257 (1980)
13. M.C. Ridgway and P. Kringhøj, Appl. Phys **77** pp. 2375-2380 (1995)

Materials Science Forum Vols. 258-263 (1997) pp. 905-910

EQUILIBRIUM VACANCIES IN Te-DOPED GaAs STUDIED BY POSITRON ANNIHILATION

J. Gebauer[1], R. Krause-Rehberg[1], M. Lausmann[1], G. Lippold[2]

[1]*Fachbereich Physik, Martin-Luther-Universität Halle-Wittenberg, D-06099 Halle, Germany*

[2] *Fakultät für Physik- und Geowissenschaften, Universität Leipzig, Linnéstraße 5, D-04103 Leipzig, Germany*

Keywords: GaAs, equilibrium defects, post-growth annealing, positron annihilation, Ga vacancy

ABSTRACT

The formation of vacancies in thermal equilibrium in GaAs was studied by means of positron annihilation. Highly Te-doped (1.5×10^{18} cm^{-3}) GaAs samples were annealed at 1000°C in a two-zone furnace under controlled As vapor pressure (p_{As}) and fast quenched in water. Annealing at short times (up to 60 min) introduces monovacancies having a density of about 3×10^{17} cm^{-3} independent of p_{As}. At long annealing times (90 h), however, the vacancy density depends on p_{As}: At a high pressure (p_{As} about 5 bar) the density remains unchanged whereas at a low pressure (p_{As} about 0.2 bar) the density of monovacancies decreases to about 1×10^{17} cm^{-3}. The results can be explained by the formation of Ga–vacancy related defects in highly n-doped GaAs with varying stoichiometry. The vacancy densities are in good agreement with recent theoretical estimations.

1 INTRODUCTION

It is now well known that annealing of GaAs at high temperature and at appropriate As vapor pressure may induce a change of the electrical properties due to a change of the stoichiometry [1]. Annealing can be used to improve the homogeneity of GaAs material which is of great technological importance [1]. It is clear that native point defects should play a key role to explain the observed behavior. However, equilibrium defects in GaAs are not well understood and still a matter of discussion [2]. Especially, little is known on the formation of vacancies and their dependence on the crystal stoichiometry at high temperatures. This is mainly due to the lack of appropriate experimental tools. Positron annihilation, however, is a powerful method for the study of vacancy defects in semiconductors [3]. In the past, native vacancies in GaAs were studied by positron annihilation mainly in as–grown material, i.e. as obtained from the manufacturer [4-6]. It was found that in slightly n–doped GaAs ($n\approx10^{16}$ cm^{-3}) native As vacancies exist [4]. In highly n–doped material, however, evidence was found by positrons that complexes consisting of Ga vacancies and dopant atoms are present [5,6]. Up to now, no systematic work was done to investigate high temperature equilibrium defects in GaAs by positron annihilation. The purpose of this work is thus to present first results of our studies on equilibrium defects introduced by annealing in GaAs under defined As vapor pressure. We will show that annealing at high temperature introduces Ga–vacancy–related defects in highly n–doped GaAs due to their dependencies on the As vapor pressure. Moreover, the vacancy densities are in agreement with recent theoretical estimations.

2 EXPERIMENTAL

2.1 Sample material and annealing

The material used in this study was device–quality Te–doped GaAs, grown by the liquid encapsulated Czochralski (LEC) method. The carrier density was measured by the Hall effect to be (1.4-1.5)×10^{18} cm^{-3}. A Te density of about (1.5-2)×10^{18} cm^{-3} was detected by secondary ion mass spectroscopy (SIMS). Other impurities have densities below 3×10^{16} cm^{-3}. The two–inch wafers were divided into samples of the size 5×5 mm^2.

Annealing was performed in quartz–glass ampoules arranged in a two–zone furnace, allowing us to adjust sample temperature and As vapor pressure independently. Prior to the annealing, the GaAs samples were cleaned using HCl to remove the native oxide. The ampoules itself were etched using a $HCl:HNO_3$ (3:1) solution to remove residual impurities. After annealing, the samples were fast quenched into water in order to preserve the equilibrium defects. The quenching rate was estimated to be 40 K/s by using a specially prepared ampoule having a K–type thermocouple in it. Prior to the positron lifetime measurements a layer of about 100 μm was removed from the annealed GaAs samples by etching in a bromine (3%) methanol solution.

2.2 Positron lifetime spectroscopy

Positron lifetime spectroscopy was performed using a conventional fast-fast coincidence system having a time resolution of about 250 ps. The temperature could be varied between 20 to 600 K. A $^{22}NaCl$ positron source having an activity of 8×10^5 Bq, covered with 1.5 μm Al foil was placed between a pair of identical samples. The positron lifetime spectra were analyzed with the trapping model after source and background corrections [7]. Mostly 5×10^6 events were measured in each lifetime spectrum. It has been recently shown that such a high statistic is crucial for a proper decomposition of the positron lifetime spectra [8].

During diffusion through a crystal, positrons may be trapped in vacancies. This can be observed as an increase of the positron lifetime, since the electron density in the vacancy is reduced compared to the bulk. Hence, the average positron lifetime τ_{av}, which is the weighted sum over the individual lifetime components, depends on the vacancy density. τ_{av} may thus vary between the lifetime τ_{bulk} measured in a defect–free sample and the lifetime of positrons in the vacancy, τ_{vac}. The vacancy–related lifetime τ_{vac} can be obtained by a numerical decomposition of the positron lifetime spectra regardless of the defect density. As the experimental result, the trapping rate κ_{vac} of positrons into vacancies can be calculated by:

$$\kappa_{vac} = \frac{1}{\tau_{bulk}} \frac{\left(\tau_{av} - \tau_{bulk}\right)}{\left(\tau_{vac} - \tau_{av}\right)} = \mu_{vac}\, c_{vac} \qquad (1)$$

κ_{vac} is related to the defect density via μ_{vac}, which is the so–called trapping coefficient. μ_{vac} must be determined by an independent method for each defect type. μ_{vac} is known to be 1×10^{15} s^{-1} for negatively charged monovacancies in GaAs at room temperature [9]. μ_{vac} is expected to increase with decreasing temperature proportional to $T^{-1/2}$ for negatively charged vacancies, whereas μ_{vac} should be independent of temperature for neutral vacancies. At low temperatures, negatively charged non–open volume defects like Ga_{As}^{2-} antisites, are able to trap positrons in their shallow Coulomb potential [10]. The lifetime of such shallow positron traps is expected to be close to τ_{bulk}. The average lifetime will thus decrease with decreasing temperature, provided positron trapping occurs at both types of defects.

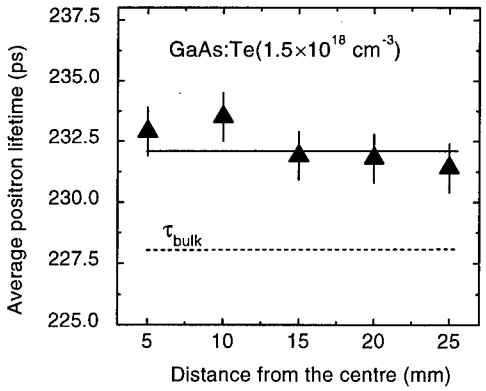

Fig. 1: Average positron lifetime versus the radial sample position across a 2–inch GaAs:Te wafer.

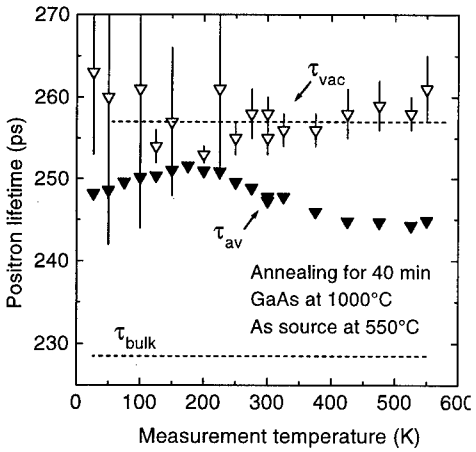

Fig. 2: Average positron lifetime τ_{av} and vacancy-related lifetime τ_{vac} as a function of the measurement temperature for annealed GaAs:Te.

3 RESULTS

3.1 Spatial distribution of vacancies in the substrate

The positron lifetime was measured as function of the distance from the wafer center along one radius prior to the annealing experiments. The results are shown in Fig. 1. Firstly, the average positron lifetime is slightly above the bulk level for all positions, indicating the presence of a low number (about 3×10^{16} cm^{-3}) of vacancies. Secondly, and more important, the average positron lifetime is independent of the exact position of the sample in the material. This is not a trivial finding, since it is known that the electrical properties in semi–insulating GaAs wafers exhibit differences in form of a W–shaped profile [1]. However, this was not observed in our Te–doped samples. We can thus neglect the influence of the exact sample position on the results in the further discussion.

3.2 Short–time annealing

The average positron lifetime τ_{av} and the vacancy-related lifetime τ_{vac} are shown in Fig. 2 as a function of the measurement temperature for a sample annealed 40 min at 1000°C with the As source at 550°C. The As vapor pressure over pure As is about 0.2 bar at 550°C [11]. The average positron lifetime is well above the bulk level, τ_{bulk}, indicating a large density of vacancies. A value of τ_{vac}=(257±3) ps was found for the defect–related lifetime by a decomposition of the lifetime spectra. This is a typical value for monovacancies in GaAs [4-6,12]. The average positron lifetime increases first and then decreases with decreasing temperature. The increase of τ_{av} is typical for positron trapping in a negatively charged vacancy, since it is known that the trapping coefficient μ_{vac} should vary like $T^{-1/2}$ [12]. Thus, the monovacancies introduced by the annealing process are negatively charged as one would expect for the native vacancies in highly n–doped GaAs [13]. The vacancy concentration was calculated by Eq. (1) to be about 3×10^{17} cm^{-3}. It was shown in an earlier work that the monovacancies in highly Te–doped GaAs can be identified as Te_{As}–V_{Ga} complexes [5]. Thus, the monovacancies observed after annealing may also be assigned to such complexes.

At low temperatures (T<200 K), spectra decomposition becomes more difficult and the average positron lifetime decreases. Thus, additional defects are found at low temperatures with a positron lifetime smaller than τ_{vac} , i.e. closer to τ_{bulk}. The presence of such additional defects hampers the decomposition of the lifetime spectra as it is indicated by the large errors for τ_{vac}. These additional defects are known to be negatively charged ions which can trap positrons in their shallow potential

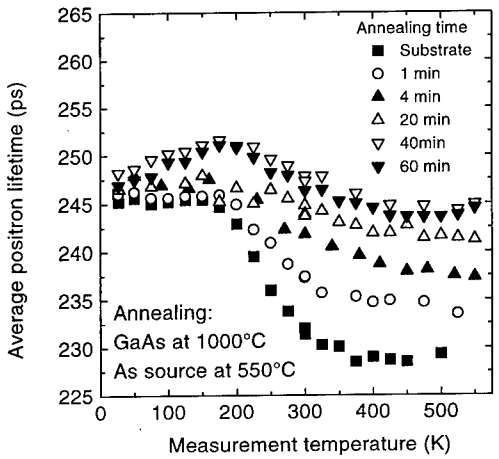

Fig. 3: Average positron lifetime versus the measurement temperature for GaAs:Te, different times annealed at 1000°C with an As source at 550°C (p_{As}≈0.2 bar).

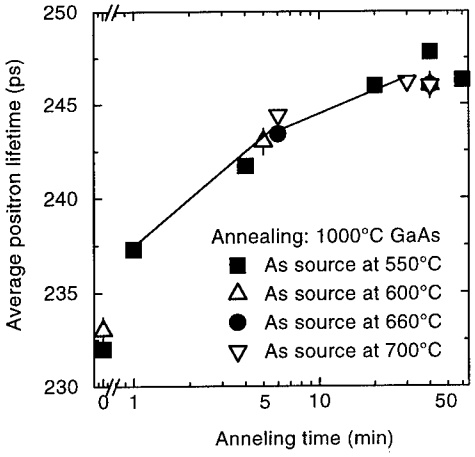

Fig. 4: Average positron lifetime at room temperature as a function of the annealing time for GaAs annealed at various As pressures.

only at low temperatures. Such ions are commonly found by positrons in GaAs and it was speculated that this could be Ga_{As}^{2-} antisites [10]. The density of the ions is relatively low (in the order of 10^{16} cm^{-3}) compared to the density of the vacancies (about 3×10^{17} cm^{-3}). This must be concluded since τ_{av} decreases only slightly below 200 K. Thus, it appears possible that shallow positron trapping in our samples is induced by a low level of extrinsic impurities.

Thereafter, we performed annealings for different short times (Fig. 3). The average positron lifetime exhibits always the same behavior as a function of the measurement temperature, as it was shown above. However, the absolute value of τ_{av}, i.e. the vacancy density, increases with increasing the annealing time up to 60 min. By decomposing the lifetime spectra we obtained consistently a defect related lifetime of about 257 ps. Thus, the same vacancy defect is present in all samples for which the concentration increases with the annealing time.

Annealings were then performed with the As vapor pressure increased by raising the As source temperature to 600, 660, and 700°C, corresponding to As vapor pressures of about 0.7, 2.5, and 5 bar [11], respectively. The average positron lifetime at room temperature is shown for all samples as a function of the annealing time in Fig. 5. No differences were found for the different As vapor pressures. Thus, at short times (about 60 min) no influence of the ambient As vapor pressure on defects can be detected. This is not surprising, since As diffusion is relatively slow, thus preventing an influence on the crystal stoichiometry by in- or out-diffusion of As within short times. The strong increase of the vacancy density must thus have its origin in intrinsic properties.

LEC GaAs is intentionally grown under As-rich conditions and contains thus a large As excess. By slowly cooling down the sample during growth process, this excess As is able to form precipitates as they are commonly found in As–rich GaAs [1,14]. Our post–growth annealings at 1000°C may then dissolve the excess As in the matrix leading to a strongly As–enriched crystal. Then, the Ga vacancies should be the most abundant native point defect due to their low energy of formation in highly n-doped, As-rich GaAs [15,16]. At least a part of this equilibrium vacancies is then frozen in by the fast quenching process. However, the isolated Ga monovacancy is known to be highly mobile after electron irradiation already at room temperature [17]. Thus, the formation of more stable defect complexes appears likely, most probably containing a Ga vacancy and a dopant atom [5,6].

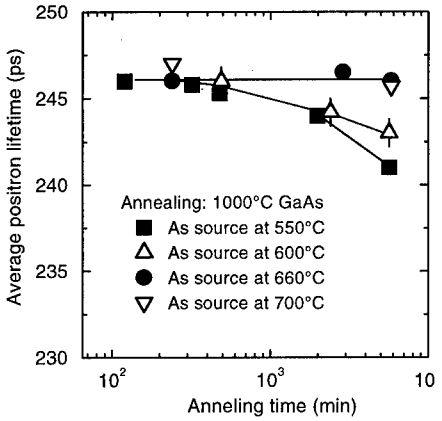

Fig. 5: Average positron lifetime τ_{av} at room temperature for GaAs annealed at various As pressures for long times.

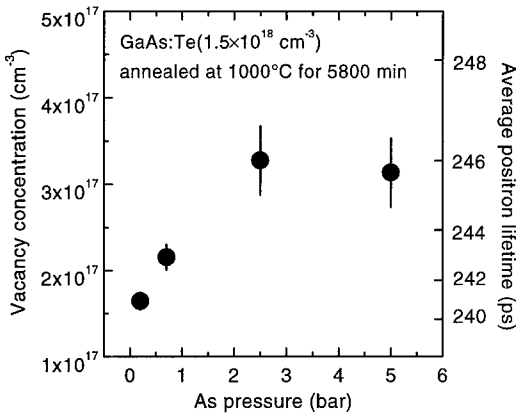

Fig. 6: Concentration of monovacancies in GaAs:Te as a function of the As vapor pressure after annealing at 1000°C for 90 h.

3.3 Long-time annealing

It seems that equilibrium between native defects and ambient As pressure was not reached at short annealing times due the limited As diffusion. For this reason we extended the annealing time up to 90 h for the different As vapor pressures. Positron lifetime measurements as a function of the temperature were performed for all these samples. Again, τ_{av} behaves similar to the results already shown in Figs. 2 and 3. The lifetime spectra could always be decomposed into two components. The defect–related lifetime τ_{vac} was always about 255–260 ps in agreement with the results for short annealing times. The average positron lifetime measured at room temperature is then shown in Fig. 5 for the samples annealed up to 90 h. τ_{av} remain nearly constant at about 246 ps for annealing times up to 500 min. This agrees with the maximum level already reached by applying a 40 min annealing. By increasing the annealing time up to 90 h the average lifetime decreases for samples annealed under low As pressures (0.2 and 0.7 bar), but remains constant at 246 ps for the samples annealed under high As pressure. Thus, the density of monovacancies decreases with decreasing As pressure. The correlation between As pressure and vacancy concentration is shown in Fig. 6. About $3x10^{17}$ cm^{-3} monovacancies exist after annealing under high As pressures (2 and 5 bar), whereas the concentration decreases by a factor of two for the lowest As pressure (0.2 bar). The positive correlation between As pressure and vacancy density indicate, that Ga vacancies are the dominant equilibrium vacancies in highly n–doped GaAs. If the As vacancy would be the dominant native monovacancy, one would expect that out–diffusion of As at low As vapor pressures increases the vacancy concentration.

SIMS measurements were performed on the samples annealed under an As pressure of 0.2 bar. The Te density remains unchanged compared to as–grown material. Moreover, no indication was found for an increased level of other impurities, i.e. their concentrations are at least one order of magnitude below those of the vacancies. Thus, we indeed observed intrinsic defects without uncertainties due to contamination. In addition, the carrier density was determined by Hall effect measurements for the samples annealed under an As pressure of 0.2 bar. The carrier density increases continuously by $2x10^{17}$ cm^{-3} with increasing annealing time, i.e. with decreasing the density of negatively charged monovacancies on a similar amount.

Beside the lack of direct experimental evidence on equilibrium vacancies in GaAs, there exist several theoretical studies on this topic [15,16,18]. There is a general agreement that in highly n–doped As–rich GaAs the Ga vacancy should be the defect with the lowest energy of formation, i.e. the energetically most favorable one. This is in agreement to our findings. In a recent first principles

study, Pöykkö et al. [16] estimated the density of Ga vacancies to be in the lower 10^{17} cm^{-3} range in As–rich GaAs, doped with 10^{18} cm^{-3} donors. The good quantitative agreement to our data appears to be notable. Tan et al. [19] derived the density of negatively charged Ga vacancies in highly n-doped GaAs from their Fermi-level-effect model. The equilibrium density of Ga vacancies at 1000°C in As-rich GaAs, donor doped to 10^{18} cm^{-3}, was calculated to be about 2×10^{17} cm^{-3}, which is also in good agreement to our data.

4 SUMMARY

Equilibrium vacancies in highly n-doped GaAs, introduced by annealing under controlled As vapor pressure, were studied by means of positron annihilation. The density of the vacancies increases with the As pressure during annealing. Thus, the equilibrium vacancies in highly n–doped GaAs belong to the Ga sublattice. Our findings are in agreement with theoretical estimations that the Ga vacancy should be the most abundant native defect under thermal equilibrium conditions in highly n-doped GaAs. However, due to our earlier results on as-grown GaAs [5,6] we believe that the Ga vacancies are part of a defect complex with a dopant atom.

ACKNOWLEDGEMENTS

We like to thank Dr. M. Jurisch (Freiberger Compund Materials GmbH) for providing us with the sample material and for his continuous, stimulating interest on this work. We also wish to thank Dr. H. S. Leipner (University Halle) for valuable discussions. This work was supported by the Deutsche Forschungsgemeinschaft.

References

[1] O. Oda, H. Yamamoto, M. Seiwa, G. Kano, T. Inoue, M. Mori, H. Shikamura, and M. Oyake, Semicond. Sci, Technol. **7**, A215 (1992).
[2] D. T. J. Hurle; Mater. Sci. For. **196**, 179 (1995) .
[3] *Positron spectroscopy of solids*, edited by A. Dupasquier and A. P. Mills (IOS Press, Amsterdam, 1995).
[4] C. Corbel, M. Stucky, P. Hautojärvi, K. Saarinen, and P. Moser; Phys. Rev. B **38**, 8192 (1988); K. Saarinen, P. Hautojärvi, P. Lanki, and C. Corbel; Phys. Rev. B **44**, 10585 (1991).
[5] R. Krause-Rehberg, H. S. Leipner, A. Kupsch, A. Polity, and Th. Drost; Phys. Rev. B **49**, 238 (1994).
[6] J. Gebauer, R. Krause-Rehberg, C. Domke, Ph. Ebert, and K. Urban, Phys. Rev. Lett. **78**, 3334 (1997).
[7] T. E. M. Staab, B. Somieski, and R. Krause-Rehberg; Nucl. Instr Meth. A **381**,141 (1996).
[8] B. Somieski, T. E. M. Staab, and R. Krause-Rehberg; Nucl. Instr Meth. A **381**, 128 (1996).
[9] R. Krause-Rehberg and H. S. Leipner, Appl. Phys. A **5**, 457 (1997).
[10] K. Saarinen, P. Hautojärvi, A. Vehanen, R. Krause, and G. Dlubek; Phys. Rev. B **39**, 5287 (1989).
[11] J. R. Arthur, J. Phys. Chem. Solids 28, 2257 (1967).
[12] M. J. Puska and R. M. Nieminen; Rev. Mod. Phys. **66**, 841 (1994).
[13] M. J. Puska, J. Phys. Condens. Matter **1**, 7347, (1989); H. Seong and L. J. Lewis, Phys. Rev. B **52**, 5675 (1995).
[14] M. Jurisch, T. Flade, B. Hoffmann, A. Köhler, J. Korb, U. Kretzer, T. Reinhold, B. Weinert, Mater. Sci. Eng. B **44**, 198 (1997).
[15] S. B. Zhang and J. E. Northtrup; Phys. Rev. Lett. **67**, 2339 (1991).
[16] S. Pöykkö, M. J. Puska, M. Alatalo, and R. M. Nieminen; Phys. Rev. B **54**, 7909 (1996).
[17] C. Corbel, F. Pierre, K. Saarinen, P. Hautojärvi, and P. Moser; Phys. Rev. B **45**, 3386 (1992); A. Polity, F. Rudolf, C. Nagel, S. Eichler, and R. Krause-Rehberg; Phys. Rev. B **55**, 10467 (1997).
[18] T. Y. Tan, H. M. You, and U. Gösele; Appl. Phys. A 56, 249 (1993).

Materials Science Forum Vols. 258-263 (1997) pp. 911-916

SPECTROSCOPIC INVESTIGATION OF NEUTRAL NIOBIUM IN GaAs

D. Ammerlahn[1], B. Clerjaud[2], D. Côte[2], L. Köhne[1], M. Krause[2], D. Bimberg[1]
[1] Institut für Festkörperphysik, Technische Universität Berlin, Hardenbergstrasse 36, D-10623 Berlin, Germany
[2] Laboratoire d'Optique des Solides, Université Pierre et Marie Curie, case 80, 4 Place Jussieu, F-75252 Paris cedex 05, France

Keywords : niobium, 4d impurities, GaAs

Abstract. Niobium doped GaAs has been investigated by photoluminescence, absorption and photoluminescence excitation spectroscopy. Photoluminescence and absorption experiments reveal only a sharp transition at 6416.4 cm^{-1} whereas photoluminescence excitation spectroscopy evidences a broad triple peak band around 9000 cm^{-1}. Experiments under uniaxial stress on the 6416.4 cm^{-1} transition are reported. All the results are discussed in the frame of neutral niobium energy levels diagram.

Introduction.

Although 3d transition metal impurities have been extensively studied in III-V materials [1, 2], the reports on the heavier 4d elements and in particular the spectroscopic results are rather scarce and concern mainly luminescence measurements obtained with ion implanted materials. The most documented system is probably niobium in GaAs. The first reports on this system concerned luminescence measurements in niobium implanted GaAs [3, 4]; a sharp luminescence slightly above 6400 cm^{-1} was observed and interpreted as being due to negatively charged niobium (Nb^{2+}). The same luminescence has been observed in niobium doped liquid encapsulated Czochralski (LEC) grown bulk material [5-7]; Zeeman experiments led to assign the luminescence transition to neutral niobium (Nb^{3+}). Further Zeeman experiments were performed with bulk materials grown by the horizontal gradient freeze method [8]; these results allowed to assign the emission line to the $^1A_1 \rightarrow {}^3A_2$ neutral niobium internal transition. The equivalent 3d system is vanadium; absorption experiments allowed to detect four excited states of neutral vanadium in GaAs [9]. Therefore, in order to get a better knowledge of the GaAs:Nb^{3+} system, we have investigated it by absorption and photoluminescence excitation spectroscopy. Experiments under uniaxial stress have also been performed.

Experiments.

The investigated samples have been supplied by Wacker Chemitronic. The ingot has been grown by the LEC technique in a quartz crucible. Niobium has been added into the melt.

Absorption experiments are performed by Fourier transform spectroscopy using Bomem DA3+ or DA8 interferometers equipped with CaF_2 or KBr beam splitters and cooled InSb or HgCdTe detectors. The samples are cooled in Oxford Instruments CF 1204 or CF 204 continuous flow cryostats allowing to work at variable temperature down to liquid helium temperatures. A home made uniaxial stress system is inserted inside the cryostat .

Two different set-ups are used for the photoluminescence experiments. In both cases, the luminescence is excited either with the visible or the 1.09 μm lines of an argon ion laser or a titanium-sapphire laser. The first set-up is the same Fourier transfom system as used for the absorption experiments; it is also used for emission experiments under uniaxial stress. In the second one, the luminescence is analyzed by a conventional grating monochromator and then detected with a cooled germanium detector; the exciting laser beam is amplitude modulated by a mechanical

chopper and the detector is connected to a lock-in amplifier. In this second set-up, the sample is cooled by an Air Liquide variable temperature cryostat.

For photoluminescence excitation (PLE) experiments, the light emitted by a quartz-tungsten lamp is modulated and "filtered" by the same monochromator as for the photoluminescence ones. The emitted light around 6400 cm^{-1} is detected by the same detection system as for luminescence experiments and the sample is cooled in the Air Liquide cryostat.

Photoluminescence and absorption results.
In photoluminescence experiments, a sharp line (linewidth 0.15 cm^{-1}) at 6416.4 cm^{-1} is observed at liquid helium temperature as it was the case in previous investigations [3-8]. Some phonon assisted transitions at lower energies are also observed as shown in Fig. 1.

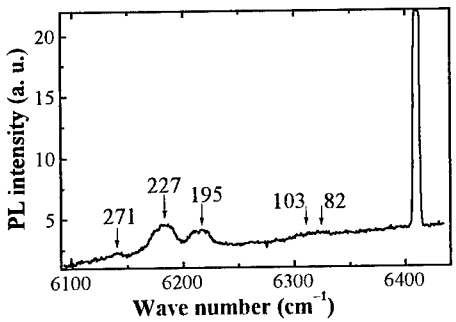

Fig. 1. GaAs:Nb photoluminescence. The low energy peaks correspond to phonon assisted transitions.

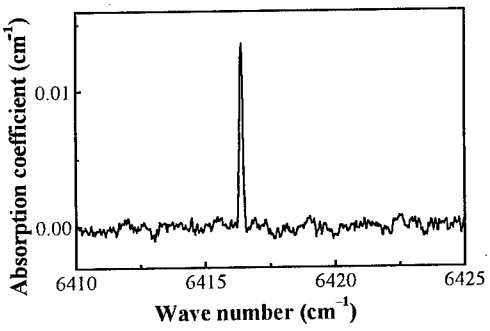

Fig. 2. GaAs:Nb absorption spectrum.

The same line at 6416.4 cm^{-1} is observed in absorption experiments as shown in Fig. 2. No other niobium related line in the spectral range 500-11000 cm^{-1} could be observed. This contrasts with the situation for neutral vanadium where three additional transitions are observed in absorption [9]. That is why, in order to get information on other electronic levels, we have performed photoluminescence excitation spectroscopy experiments, the results of which are described in the next section.

Experiments have been performed at higher temperatures up to 40 K. Up to 10 K there is no change. Above this temperature, the line shifts slightly towards low energies and broadens. No other line appears.

Photoluminescence excitation spectroscopy results.
The only sub-bandgap transition observed is a broad band in the range 8400-9500 cm^{-1}. This band is shown in Fig. 3; it has a triple peak band shape. No associated zero phonon transitions could be detected.

Discussion of the absorption, photoluminescence and PLE results.
We do not see any other possibility for explaining the Zeeman data on the emission sharp line at 6416.4 cm^{-1} than the interpretation given in [8] i.e. the $^1A_1 \rightarrow {}^3A_2$ internal transition of Nb^{3+} substituting a gallium atom. In particular the possibility for the excited state of the transition to be ^1E is ruled out by the selection rules in polarized light when the magnetic field is away from a fourfold axis. We shall take this result as the starting point of this discussion. This transition is spin forbidden in first order, but the $^3A_2$ state transforms according to the Γ_5 irreducible representation of the T_d

group and the $^1A_1$ one like the Γ_1 representation. Therefore an electric dipole transition (the electric dipole moment transforms as Γ_5) is not fully forbidden. In fact, the transition is partly allowed because of the admixture of $^3T_2$ into $^3A_2$ and of $^3T_1$ into $^1A_1$ by the spin-orbit coupling.

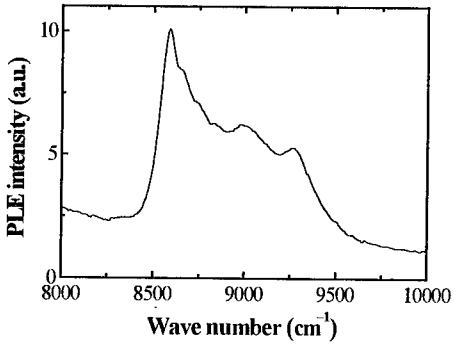

Fig. 3. Photoluminescence excitation spectrum of the $^1A_1 \rightarrow {}^3A_2$ emission.

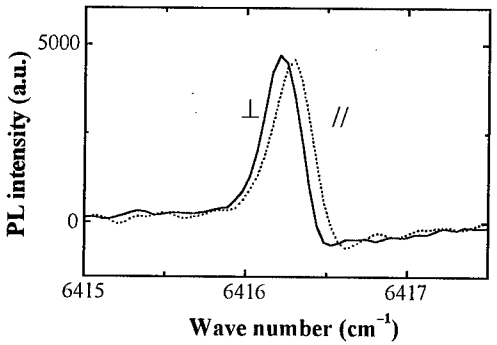

Fig. 4. Polarized light emission when a 200 MPa <001> stress is applied to the sample.

The broad transition seen in the PLE experiments has a triple peak shape; such a shape is characteristic of a transition towards an electronic triplet coupled to τ_2 modes of vibration. It has similarities with the broad absorption band observed in the GaAs:V^{3+} system due to the $^3A_2 \rightarrow {}^3T_1$ transition. This transition is dipole electric allowed in first order; it is expected to be quite intense and therefore detected by absorption; however, one has to keep in mind that the integrated intensities are the relevant quantities to be compared. As the band is very broad, it is quite possible that its integrated intensity is much larger than the $^3A_2 \rightarrow {}^1A_1$ sharp line one even though its maximum is lower. In the GaAs:V^{3+} case, the maximum of the $^3A_2 \rightarrow {}^3T_1$ absorption band is only seven times higher than the $^3A_2 \rightarrow {}^1A_1$ sharp line even though its integrated intensity is orders of magnitude larger. Therefore we think that the broad band around 9000 cm^{-1} can safely be assigned to the $^3A_2 \rightarrow {}^3T_1$ transition.

More surprising is the non observation of other transitions. In the GaAs:V^{3+} case, absorption towards the $^3T_2$ and ^1E excited states could also be detected [9]. In fact, the $^3T_2$ state is mainly evidenced as being the emitting level of the luminescence of V^{3+} and the corresponding absorption is the weakest of all and is hardly seen. The $^3A_2 \rightarrow {}^3T_2$ transition is electric dipole allowed only because of the admixture of $^3T_2$ into $^3A_2$ and of $^3T_1$ into $^3T_2$ by spin-orbit coupling, this last admixture being the most important because of the small energy gap between the two levels involved. It can be understood relatively easily why this transition is not observed in the Nb^{3+} case: on the one hand, the $^3T_2$ level is above the $^1A_1$ because of the stronger "field" for 4d than for 3d impurities and therefore is not the emitting level; on the other hand, the absorption might not be observed because of a smaller solubility limit for niobium than for vanadium.

The most striking problem is the location of ^1E. In the conventional "B, C, Dq" scheme it should be anyhow below $^1A_1$; in the strong field asymptotic behavior, it should even be midway between $^3A_2$ and $^1A_1$. In such a case, one could understand why it is not seen in absorption. The $^3A_2 \rightarrow {}^1E$ transition is only allowed because of the admixture of $^3T_2$ into $^3A_2$ and of $^3T_1$ and $^3T_2$ into ^1E by the spin-orbit coupling; these admixtures should be quite small because of the large energy gaps involved. This interpretation, leads to an original situation for d impurities: the emitting level is not the lowest excited state of the system.

Experiments under uniaxial stress.
Experiments under compressive uniaxial stress have been performed on the $^3A_2 \leftrightarrow {}^1A_1$ transition both in absorption and luminescence.

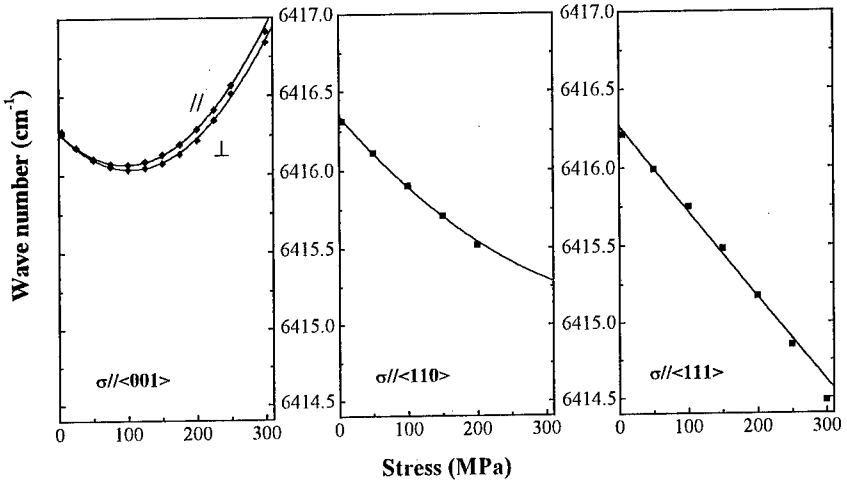

Fig. 5. Stress effects on the $^3A_2 \leftrightarrow {}^1A_1$ transition.

When the stress is applied along a fourfold axis, with natural light, one observes a broadening of the transition and a shift. Experiments with polarized light allow to see that the line splits in fact into two fully polarized components the high energy one being observed when the polarization of the light is parallel to the stress axis and the low energy one when it is perpendicular; this is shown in Fig. 4. The splitting between the two components increases linearly with the stress and amounts to $d = 0.3$ cm^{-1}/GPa. More surprising is the shift which is clearly non linear as shown in Fig. 5; in fact, it varies almost quadratically with the stress. It has to be noted that experiments under stress at temperatures up to 40 K did not evidence any new line neither in absorption nor in emission.

When the stress is applied along a threefold axis, no splitting is observed. A linear shift is observed with a slope -5 cm^{-1}/ GPa as shown in Fig. 5.

When the stress is applied along a twofold axis, we could not detect any splitting with natural light; only a nearly linear shift could be detected as shown in Fig. 5.

Discussion of the experiments under uniaxial stress.
In first order, the $^1A_1$ and $^3A_2$ states can be only coupled to totally symmetric strains as both of these states correspond to orbital singlets. This means that in first order, one should expect only a linear shift of the $^3A_2 \leftrightarrow {}^1A_1$ transition under uniaxial stress; moreover, it should be the same for all stress directions.

As mentioned earlier, the $^3A_2$ state is indeed a Γ_5 state which can be split by a uniaxial stress. This is a higher order effect which occurs only because of the admixture of $^3T_2$ into $^3A_2$ by the spin orbit coupling. This means that in fact the splitting of the $^3A_2$ state under uniaxial stress reflects the one of the $^3T_2$ state. Let us consider the effect of a tetragonal stress. Under such a stress, the Γ_5 state splits into two sublevels corresponding to the Γ_4 and Γ_5 representations of the D_{2d} group. The selection rules state that the $\Gamma_4(^3A_2) \leftrightarrow \Gamma_1(^1A_1)$ is allowed only for light polarized along the stress direction

whereas the $\Gamma_5(^3A_2)\leftrightarrow\Gamma_1(^1A_1)$ is allowed only for light perpendicular to the stress direction. Comparison with the experiment shows that $\Gamma_4(^3A_2)$ is the lowest and $\Gamma_5(^3A_2)$ the highest sublevels of $^3A_2$ under tetragonal compressive stress. It can easily be seen that the effect of a <001> stress within $^3A_2$ is equal to the one within $^3T_2$ multiplied by $4\lambda^2/\Delta^2$ where λ is the spin-orbit constant and Δ the $^3T_2$-$^3A_2$ splitting. If we note $b\sigma$ the splitting of the $^3T_2$ level, σ being the applied stress, the splitting of the $^3A_2$ level is $d\sigma = b\sigma.4\lambda^2/\Delta^2$. The λ/Δ ratio can be evaluated to be around 25.10^{-4} from the Zeeman measurements as $g = 2\text{-}8\lambda/\Delta = 1.98$ [8]. This leads to a splitting of the $^3T_2$ level given by $b = 12$ cm^{-1}/MPa. This is a very large value; for comparison the same value for the GaAs:V^{3+} case is 0.4 cm^{-1}/MPa [10]. As a matter of fact, in this last case, no stress splitting of the ground state could be observed [10]. No splitting is observed for a trigonal stress as their effect within $^3T_2$ is probably quenched by a Jahn-Teller effect due to the coupling of this state to ε modes of vibration as it is the case for the GaAs:V^{3+} system. A splitting of the $^3A_2$ state under <110> stress should be observed, but it should be half of the one under <001> stress and therefore too small to be observed experimentally.

The much larger sensitivity to strains for 4d than for 3d impurities is in fact expected as the overlaps of the 4d orbitals with the ligand orbitals are larger than those of 3d impurities. This is probably true for all levels and this provides a further argument for the non observation of other absorption transitions. In the GaAs:V^{3+} case, $^3T_2$, and ^1E were evidenced by their sharp zero-phonon absorption transitions arising from $^3A_2$. The linewidth of these transitions was an inhomogeneous one governed by the internal strains in the crystal. In the niobium case, these zero-phonon transitions should be much broader because of the larger sensitivity to strains and therefore too weak to be observed. This argument does not apply to the $^3A_2\leftrightarrow{}^1A_1$ transition which occurs between two orbital singlets which are insensitive to non symmetric strains. More over this transition is only weakly sensitive to totally symmetric strains as the $^1A_1$ and $^3A_2$ levels are nearly parallel in a Tanabe Sugano diagram.

Up to now, we have explained the linear splitting of the $^3A_2\leftrightarrow{}^1A_1$ transition under tetragonal stress, but not the quadratic behavior. The process considered for explaining the splitting extended further would give also a quadratic contribution of the form $b^2\sigma^2.\lambda^2/\Delta^3$. As Δ should be around 8000 cm^{-1}, this contribution is one order of magnitude smaller than the linear one at higher stress and therefore, it cannot be the reason for the behavior experimentally observed. As mentioned earlier, the ^1E level is most probably below $^1A_1$; these two states having the same spin, they can be coupled by a strain transforming as the Γ_3 representation of the T_d group. <001> and <110> stress induce such strains. Such a coupling will induce a quadratic shift of the $^1A_1$ level of the form $V^2\sigma^2/\Delta'$ where Δ' is the $^1A_1$-^1E splitting and V a coefficient measuring the stress inter level mixing strength. Comparison with the experiment gives $V = 0.25$ cm^{-1}/MPa for $\Delta' = 3000$ cm^{-1}; it has to be noted that this is not a large value. It is for instance 50 times smaller than the value of the coefficient b measuring the intra $^3T_2$ stress sensitivity.

Therefore in order to interpret all the stress results, we consider three effects: i) a splitting of $^3A_2$ due to a large intra state coupling of $^3T_2$ to Γ_3 strains, ii) a quadratic shift of $^1A_1$ due to the inter level mixing of ^1E and $^1A_1$ by Γ_3 strains and iii) a linear hydrostatic shift of $^1A_1$ with respect to $^3A_2$ which is the same for all stress directions.

Conclusion.

The $^1A_1$ and $^3T_1$ excited states of neutral niobium in GaAs are evidenced spectroscopically directly. It appears that the $^1A_1$ emitting level is not the lowest excited state. The splitting of the ground state by strains of Γ_3 symmetry reflects the splitting by these strains of the $^3T_2$ excited state. The quadratic shift of the $^3A_2\leftrightarrow{}^1A_1$ transition by Γ_3 strains is interpreted as being due to a repulsion of $^1A_1$ caused by the inter level coupling of ^1E and $^1A_1$ by Γ_3 strains. Neutral niobium is much more sensitive to

strains than neutral vanadium. We believe that this property is not restricted to niobium and that in general 4d impurities are more sensitive to strains than the corresponding 3d's.

References.

1. B. Clerjaud, J. Phys. C: Solid State Physics **18**, 3615 (1985).
2. B. Clerjaud, in "Current Issues in Semiconductor Physics" ed. A. M. Stoneham (Bristol: Adam Hilger) pp. 117-168 (1986).
3. V. V. Ushakov, A. A. Gippius, V. A. Dravin and S. F. Kanster, Fiz. Tekh. Poluprovn. **15**, 1535 (1981) (English transl. Sov. Phys. Semicond. **15**, 890 (1981)).
4. V. S. Vavilov, V. V. Ushakov and A. A. Gippius, Physica **B117/118**, 191 (1983).
5. G. Aszodi, H. Ennen, J. Weber, U. Kaufmann and A. Axmann, 4th Lund Int. Conf. on Deep Level Impurities in Semiconductors (Eger: Hungary 1983) unpublished.
6. H. Ennen, Thesis, Albert-Ludwigs-Universität, Freiburg (1983).
7. in Landolt-Börnstein New Series, Group III, Vol. **22**, Subvol. **b** (1989).
8. S. Gabilliet, V. Thomas, J. P. Peyrade, J. Barrau and C. A. Bates, Phys. Lett. **A119**, 197 (1986).
9. B. Clerjaud, C. Naud, B. Deveaud, B. Lambert, B. Plot, G. Bremond, G. Benjeddou, G. Guillot and A. Nouailhat, J. Appl. Phys. **58**, 4207 (1985).
10. D. Côte, Thesis, Université Pierre et Marie Curie, Paris (1988).

Materials Science Forum Vols. 258-263 (1997) pp. 917-922

Yb LUMINESCENCE CENTRES IN MBE-GROWN AND ION-IMPLANTED GaAs

A.A.Gippius, V.M.Konnov, N.N.Loyko, V.V.Ushakov, T.V.Larikova, I.P.Kazakov, V.A.Dravin, and N.A.Sobolev*
P.N.Lebedev Physical Institute of the Academy of Sciences of Russia,
Leninsky prospect 53, Moscow 117924, Russia
***A.F.Ioffe Physicotechnical Institute of the Academy of Sciences of Russia,**
Polytekhnicheskaya str. 29, St.Petersburg 194021, Russia

Keywords: gallium arsenide, rare earth elements, luminescent complexes

Abstract. Due to high chemical activity of rare earth (RE) elements their associations with other dopants are quite common. In the present work we demonstrate that Yb can be rendered optically active in GaAs if it is incorporated in some luminescence complexes which enhance the optical transition probabilities and/or efficiency of energy transfer from electrons and holes to Yb luminescence centres. The Yb doping was produced either in the process of MBE growth or by ion implantation. It has been found that co-doping (by ion implantation) with oxygen is a prerequisite of optical activity of Yb in GaAs. The characteristic f-f luminescence of Yb^{3+} is emitted by three-component complexes, for example (Yb+O+S/Se/Te). Formation and destruction of Yb related centres imply complicated reactions between their components, at least some of them being mobile at the post-implantation annealing temperatures (500-700°C).

1. Introduction

Rare-earth (RE) doped Si and III-V semiconductors have received increased attention for their possible use in optoelectronic devices which are expected to combine sharp, temperature stable, atomic-like emission due to internal electronic transitions within 4f-shell of RE impurities with the efficient electrical pumping of this emission by the energy transfer from the excited system of electrons and holes [1].

Intensity of f-f luminescence in RE doped semiconductors is determined by the following factors:

- total amount of RE luminescence centres, limited by rather low solubility of RE atoms in covalent semiconductors (which makes non-equilibrium doping techniques preferable) and by the fact that usually only a fraction of RE atoms incorporated in the crystal can be made optically active;
- general quality of RE doped crystals (in the case of ion implantation — the residual damage) which determines the efficiency of competing non-radiative processes;
- efficiency of energy transfer from electrons and holes to RE luminescence centres;
- probability of optical transitions within 4f shell of RE centres.

The latter two characteristics depend upon the structure of luminescence centres, that is on the lattice position of RE impurity and on its possible association with other impurities and/or defects. Due to high chemical activity of RE elements, their associations with other chemical dopants are quite common. It is known that co-doping of RE in II-VI compounds is a prerequisite for their optical activity [2] and photoluminescence efficiency of RE in ionic hosts is usually highest for RE complexes. For Er-doped silicon it has been reported that the addition of oxygen and fluorine enhances the Er^{3+} emissions [3]. In III-V compounds the intensity of luminescence of Er^{3+} in $Al_xGa_{1-x}As$ was found to be dramatically increased by oxygen co-doping. On the other hand, oxygen co-implantation into GaAs : Er generally resulted in weaker Er^{3+} emission than those for the samples implanted with Er alone[4]. An explanation was that (Er+Al+O) complexes, formed in the ternary compounds, might be more efficient emitters than other Er-related centres.

As far as ytterbium is concerned it was found that in InP the luminescent properties of Yb are independent of the growth and doping techniques and that Yb atoms occupy only one type of lattice site (the most probable — substitutional location Yb_{In}) which is made possible by size matching of the Yb^{3+} and In^{3+} ions and favoured also by the admixture of ligand (<111> directional) wave function (covalency effects) [5]. It was suggested that optical activity of Yb in III-V compounds must be related to its substitutional location largely due to covalency effects which relax the parity selection rule and make parity forbidden dipole transition in the 4f-shell possible [6]. It was found that optical activity of Yb implanted in III-V binary and ternary compounds correlated with the substitutional fraction of Yb as determined by Rutherford back scattering (RBS)/channeling technique. In GaAs the substitutional fraction of Yb was below the sensitivity of the method [5], it was thought to be the reason for very weak (if any) Yb luminescence generally reported for GaAs doped with Yb either by ion implantation or during epitaxial growth.

In the present work we demonstrate that Yb can be rendered optically active in GaAs if it is associated with other impurities (in our case oxygen and chalcogens S, Se, Te) which enhances the optical transitions probabilities and/or the efficiency of energy transfer from electrons and holes to Yb luminescence centres.

2. Experimental

Two techniques were used to produce Yb related luminescence centres in GaAs. One of them was ion implantation of both Yb and co-activators (O, S, Se, Te) into commercial GaAs of various origin. We used a set of energies and doses to produce a flat profile of dopants with concentration in the range $(10^{17} \div 10^{19})cm^{-3}$ up to the depth of 150 nm. Alternatively we introduced Yb in GaAs during MBE growth with subsequent implantation of oxygen coactivator. In all cases ion implantation was followed by annealing up to 800°C. The photoluminescence (mostly at 77K) was recorded by the standard lock-in technique using liquid-nitrogen-cooled photomultiplier.

3. Results

3.1. Bulk GaAs

The characteristic lines due to $(^2F_{5/2} — ^2F_{7/2})Yb^{3+}$ transitions in bulk GaAs are observed in the range (9800÷10200) Å, i.e. (1.264÷1.215) eV, where in some samples more than one hundred lines can be found, and in the range (10300÷11000) Å, i.e. (1.203÷1.126) eV, with much less intensity. Basing upon the analysis of the spectra for various samples and for various annealing conditions it was possible to separate and nominate for convenience several most important groups of lines referring to various centres (Fig. 1):

- X_1 and X_2 systems with emission lines at 10060 Å (1.2321 eV) and 10054 Å (1.2329 eV) respectively;
- Y_1 and Y_2 systems differing by the ratio of intensities of lines at 9886 Å (1.2533 eV), 9898 Å (1.2518 eV), 9905 Å (1.2509 eV) and 9908 Å (1.2505 eV). The lines of X_1/X_2 and Y_1/Y_2 systems were found to correlate with much weaker groups of lines in the range (10200÷11000) Å, shifted by 70.6, 69.5 and ~67 meV for X_1, X_2, and Y_1/Y_2 systems respectively. These weaker lines can be attributed to phonon assisted transitions.

3.1.2. The role of oxygen

We have performed systematic studies of oxygen co-doping of Yb-implanted GaAs basing upon our previous results on Yb-implanted InP and GaAs where it was found that of the three co-dopant used (O, F, Li) oxygen produced the largest enhancement of Yb luminescence [7,8]. Implantation of Yb or Yb in combination with oxygen was performed into GaAs samples with various concentration of background impurities controlled by secondary ions mass spectroscopy (SIMS) technique.

Implantation of Yb alone (up to the concentration of $10^{19}\,cm^{-3}$) into GaAs samples with background impurities concentration of about $10^{17}\,cm^{-3}$ produced no luminescence characteristic of f-f

Yb^{3+} transitions, in agreement with the data reported in the literature. Combined implantation (Yb+O) into the same samples produced a number of luminescence lines belonging to the X and Y systems. For the series of samples with background impurities (Se, O, Si, C etc.) concentration of about

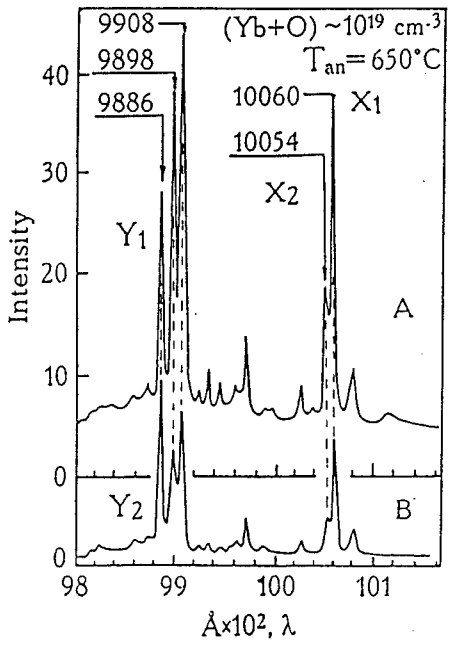

Fig. 1. Luminescence spectra of Yb-related X and Y centres for various (A and B) samples.

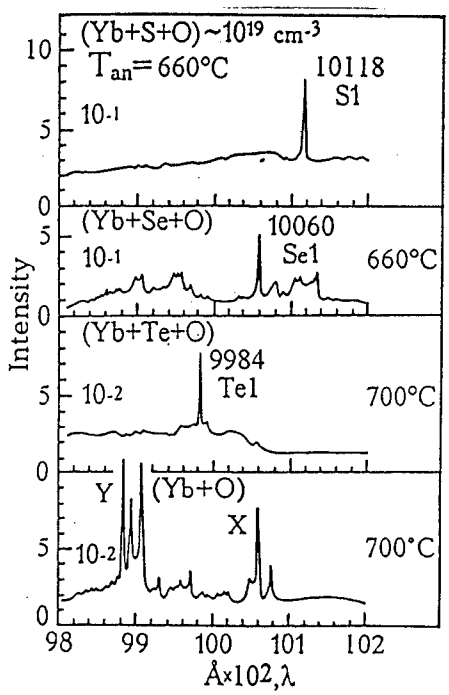

Fig. 2. Spectra of Yb-related centres for various combinations of co-dopants

10^{18} cm^{-3} the implantation of Yb alone produced appreciable Yb^{3+} luminescence. Its intensity varied by more than an order of magnitude within this series of identically implanted samples. Combined implantation (Yb+O) produced much more intense Yb^{3+} luminescence with much lower dispersion of the intensity within the series. In all cases the Yb^{3+} luminescence was observed within the range of annealing temperatures (550÷700)°C. It can be concluded from these results that oxygen (implanted or background) plays a crucial role in the optical activation of Yb atoms implanted in GaAs.

3.1.3. Chalcogen coactivators

Occurrence of various combinations of (Yb+O)-related lines in various samples subjected to identical implantation and annealing procedures suggested that the Yb luminescence centres might be complexes incorporating (besides oxygen) some other components. It was natural to look for unidentified components of Yb-related complexes among the background impurities detected in part of our samples by SIMS technique (Se, O, Si, C etc). To establish the role of at least some of these impurities we performed the co-doping of Yb-implanted GaAs samples (containing relatively low concentration of background impurities) with chalcogen impurities S, Se and Te. In the first experiment we implanted Yb in combination with either S or Se or Te. No Yb-related luminescence was found. In the second experiment three species were implanted in the same samples: Yb, O and either S or Se or Te. In this case the Yb-related luminescence was observed (which confirmed the important role played by oxygen in the optical activation of Yb in GaAs) with lines specific for each of the chalcogen impurities (Fig. 2). These lines could be seen starting from the concentration

of co-dopants 10^{18} cm^{-3} (which is comparable to or higher than the concentration of background impurities). At the concentration of about 10^{19} cm^{-3} they dominated in the spectra. The following are the data on these luminescence structures referring to (three-components) Yb-related centres.

Sulfur (S_1 centre): implantation of (Yb+O+S) produced a line at 10115 Å (1.2254 eV) which at sulfur concentration 10^{19} cm^{-3} dominated in the spectrum and was an order of magnitude more intense than X and Y systems at the reference (implanted by Yb+O) parts of the samples. Similar to X and Y systems we found a weak line at 10924 Å (1.1347 eV), supposedly phonon-assisted transition, shifted by 90.7 meV from the zero-phonon line.
Tellurium (Te_1 centre): in (Yb+O+Te) implanted samples we found a line at 9984 Å (1.2415 eV), accompanied by a weak line at 10462 Å (1.1848 eV), shifted by 56.7 meV. The Te_1 line, similar to the case of sulfur, dominated in the spectrum at tellurium concentration 10^{19} cm^{-3} being about an order of magnitude lower in intensity than the S_1 line.
Selenium (Se_1 centre): in the case of (Yb+O+Se) implantation it was difficult to separate the Se-related line at implants concentration (10^{17}÷10^{18}) cm^{-3}. It was only at Se concentration 10^{19} cm^{-3} that the line at 10060 Å (1.2321 eV), previously referred to as X_1, became dominant in the spectrum, so it was evident that X_1 centre was in fact (Yb+O+Se) complex.
Basing upon these results it can be suggested that considerable fraction of luminescence lines observed in (Yb+O) implanted samples might be due to other background impurities, still to be identified.

3.1.4. Radiation defects
The role of radiation defects in the formation of Yb-related centres is not clear. Certainly we can not exclude the participation of radiation defects under the conditions of strong radiation damage produced by ion implantation, but as far as luminescence centres mentioned in the previous section are concerned, there is no direct evidence that these centres incorporate radiation defects. On the other hand, we have found other Yb-related centres which seem to incorporate some components of radiation damage. The experimental conditions were the following.

GaAs samples implanted with (Yb+O) and annealed to optimize Yb-related luminescence (in particular, X and Y systems) were irradiated with 1 MeV protons with the fluence of 10^{14} cm^{-2}, which quenched completely both the edge emission and Yb-related luminescence. Annealing at relatively low temperatures (~400°C) produced new luminescence structures Z_1 (9964 Å, 1.2440 eV) and Z_2 (9972 Å, (1.2430 eV) which correlated with lines at 10512 Å (1.1791 eV) and 10536 Å (1.1765 eV) shifted from Z_1 and Z_2 by 64.9 and 66.5 meV respectively. Within the annealing temperature range (400÷500)°C Z-centres dominated in the spectra while X and Y systems were very weak. After annealing at ~550°C Z-system disappeared and at 600°C X and Y systems appeared again (Fig. 3).

Z-centres can be either the initial (prior to proton irradiation) X or Y centres modified by the capture of some component of proton induced radiation damage (released at higher temperatures) or some new (Yb+O)-based complexes incorporating radiation damage. The latter suggestion seems more probable since there is an annealing temperature interval (at ~500°C) when practically no Yb-related emissions (X, Y, Z etc) are observed in proton-irradiated samples. It should be noted that Z-centres must be rather efficient since their luminescence was observed in the conditions when radiation damage (monitored by quenching of the edge emission) was not completely annealed.

3.2. MBE grown GaAs
In MBE grown GaAs doped with 10^{18}cm^{-3} of Yb no Yb^{3+} related luminescence was found in as-grown material. The characteristic Yb^{3+} luminescence (Fig.4) could be observed only after additional implantation of oxygen and subsequent annealing. The implantation and annealing conditions necessary for "activation" of Yb^{3+} luminescence in MBE grown layers were found to be basically the same as those for the bulk material.

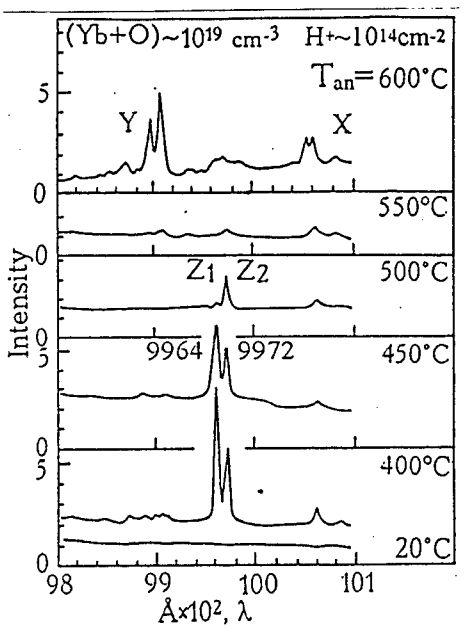

Fig. 3. Annealing behaviour of X, Y and Z luminescence systems in (Yb+O)-implanted and proton bombarded GaAs.

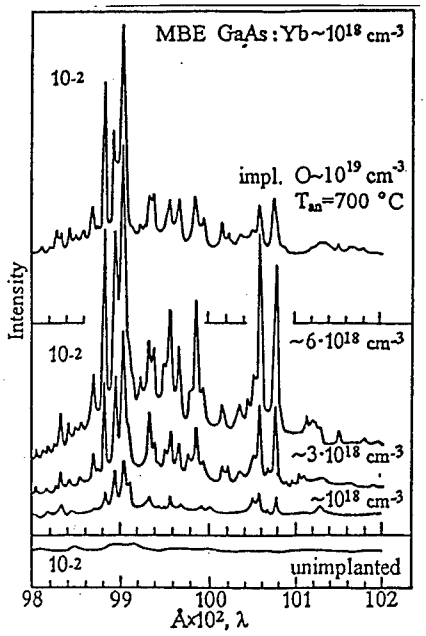

Fig. 4. Spectra of GaAs doped with Yb during MBE growth and implanted with oxygen coactivator

4. Discussion

Due to chemical activity of rare earth elements their association with other dopants are quite common. Among optically active Yb-related centres we have identified complexes comprising Yb, O and chalcogen impurities S, Se, Te. These complex luminescence centres are rather efficient, the intensity of luminescence of, say, (Yb+O+S) complex is comparable to the intensity of Yb related luminescence in GaP and even in InP, where high optical activity of Yb was attributed to isolated substitutional Yb^{3+} ions. It should be born in mind that the correlation between optical activity of Yb and Er and their lattice position is not definitely established. First of all, it is not evident that the substitutional RE atoms detected by RBS/channeling measurements are the same RE atoms that are seen in luminescence experiments. Moreover there are some data which show that Er atoms loose their optical activity when located substitutionally [9]. On the other hand, it is not excluded that Yb atoms can move from interstitial sites to substitutional sites when they form optically active complexes with O and S (or Se, Te), as it was observed for (Er+O) doping of GaAs [10]. It can be suggested that lattice position of RE atoms might not be the only (and even not the most important) factor of their optical activity if they are incorporated in some complex aggregated centres. Formation and destruction of Yb related complexes implies complicated reactions between their components, at least some of them being mobile at the corresponding annealing temperatures. It is worth

noting that our preliminary studies have demonstrated that even more complicated aggregates can be formed comprising, for instance, implanted Yb, O, S and background Se atoms.
Basing upon our data we can draw some preliminary conclusions concerning the correlation of the atomic structure of Yb-related complexes and their characteristics. First of all, one can see systematic change of the zero-phonon optical transition energy E_0 within a group of similar centres: Yb+O+S/Se/Te, that is the transition energy (1.1347/1.1615/1.1848 eV) increases and the value of $\delta=E_f-E_0$ (E_f - the energy of free Yb^{3+} ion transition) decreases (45.1/38.4/29.0 meV) with the increase of the coactivator size. If we accept the assignment of weak lines in the region (10200÷11000) Å to phonon-assisted transitions then another trend is seen: the phonon energy decreases (90.7/70.6/56.7 meV) with the increase of the S/Se/Te coactivator mass. The kinetics of reactions of formation of Yb related complexes should also depend upon the mass (size) of their components. We have found systematic increase of the annealing temperatures (580/620/650°C) at which Yb+O+S/Se/Te centres start to form. At present it is not possible to separate the roles of the two coactivators as far as the energy structure of the luminescence centres is concerned: the definite correlation between the transition energies and properties of one of the coactivators (S/Se/Te) does not exclude the contribution of another (oxygen). Oxygen seems to be an ever-present component of Yb-related luminescence centres in GaAs (though no centres with oxygen co-activator alone have so far been found), so it is possible that its main role is in the energy transfer process.

5. Conclusion

Yb related luminescence complexes described in this work represent the optical manifestation of the well known chemical (and gettering) activity of rare earth elements. The formation of luminescence complexes comprising rare earth elements and other impurities or defects must be quite common so a considerable fraction of Yb luminescence in GaP and InP might be due to such complexes rather than isolated Yb ions.

6. Acknowledgements

The authors appreciate the financial support provided by the Russian Foundation for Basic Research (RFBR project N 96-02-18206), the National Program "Physics of Solid State Nanostructures" (N 97-1046), INTAS-RFBR (N 95-0531) and CRDF (N 235)

References

1. Rare Earth Doped Semiconductors, ed. G.S.Pomrenke, P.B.Klein, D.W.Langer, Material Research Society Symposium Proceedings, v.301, 1993, Material Research Society, Pittsburgh, Pennsylvania.
2. R.Boyn, *phys. stat. sol. (b)*, **48**, pp.11-47, 1988.
3. J.Michel, J.L.Benton, R.F.Ferrante, D.C.Jacobson, D.J.Eaglesham, E.A.Fitzgerald, Y.-H.Xie, J.M.Poate and L.C.Kimerling, *J. Appl. Phys.*, **70**, No.5, pp.2672-2677, 1991.
4. J.E.Colon, D.W.Elsaesser, Y.K.Yeo, R.L.Hengehold and G.S.Pomrenke, in [1], pp.169-174.
5. A.Kozanecki and R.Graetzschel, *J. Appl. Phys.*, **68**, No.2, pp.517-522, 1990.
6. A.Kozanecki, in [1], pp.219-224.
7. V.M.Konnov and N.N.Loiko, *Bulletin of the Lebedev Physics Institute*, No.12, pp.20-23, 1993, Allerton Press, Inc./New York.
8. V.M.Konnov, N.N.Loiko and V.A.Dravin, *Bulletin of the Lebedev Physics Institute*, No.3, pp,20-23, 1994, Allerton Press, Inc./New York.
9. A.Kozanecki, M.Chan, C.Jeynes, B.Sealy and K.Homewood, *Sol. St. Comm.*, **78**, No.8, pp.763-766, 1991.
10. K.Takahei, A.Taguchi and Y.Horikoshi, *J. Appl. Phys.*, **76**, No.7, pp.4332-4339, 1994.

Materials Science Forum Vols. 258-263 (1997) pp. 923-928

ARSENIC INTERSTITIAL PAIRS IN GaAs*

P. Papoulias,[†] C. G. Morgan,[†] J. T. Schick,[‡] J. I. Landman,[†] and N. Rahhal-Orabi[†]
[†] Department of Physics and Astronomy, Wayne State University, Detroit, MI 48202, USA
[‡] Department of Physics, Villanova University, Villanova, PA 19085, USA

Keywords: interstitial, complex, gallium arsenide

Abstract. First-principles molecular dynamics calculations have been used to identify and study the properties of energetically favorable As interstitial pair complexes.

Introduction.

Lately there have been continuing investigations into the properties of GaAs grown at low temperatures (LT GaAs) as a result of its exceptionally high resistivity and short carrier lifetimes. The above properties make LT GaAs a good candidate for high-speed and high-voltage photoconductive switches and fast, high-sensitivity, wide bandwidth photodetectors [1]. LT GaAs is generally grown by molecular-beam epitaxy (MBE) with substrate temperatures around 200–400 °C, followed by annealing at a higher temperature [2, 3].

While it is known that LT GaAs contains an excess of As, particle induced X-ray emission (PIXE) indicates the presence of more As than can be accounted for from observed antisite concentrations [4]. The remaining excess As is often assumed to be in the form of As interstitials [4, 5], on the basis of ion channeling measurements and the rapid diffusion of some of the As-containing defects which is often observed in LT GaAs. However, As-antisite-related donor defects generally control the electrical behavior of LT GaAs, even when antisites contribute less than half of the reported deviation from stoichiometry.

There is also evidence for significant concentrations of As interstitials, electrically inactive and with an unknown microscopic structure, in GaAs grown at higher temperatures. A detailed analysis [6] of titration experiments [7] and measurements of the density and lattice parameter [8] of GaAs grown by either liquid-encapsulated Czochralski (LEC) or horizontal Bridgman (HB) techniques indicates that melt-grown GaAs is As-rich, due to the creation of the large number of As interstitials during growth, unless extra Ga is added to the melt. Despite the indication that interstitials are present in greater number than vacancies at growth, the Fermi level at growth appears to be controlled by vacancies, leading to the conclusion that the interstitials are electrically inactive.

Finding the most favorable defect configurations for the excess As in GaAs which has been attributed to As interstitials is the primary focus of this work. Theoretical investigations of the microscopic structure of these defect configurations is complicated by the fact that there are an enormous number of potential locations for excess As atoms within the lattice. Previous work by Chadi shows that there are both donor and acceptor defects among the lowest energy configurations for isolated As interstitials [9]. Furthermore, these calculations show that there are many configurations within 0.5 eV of the lowest energy configuration [9], indicating that diffusion barriers may be small, which is consistent with experimental results showing high mobility of As interstitials. This mobility leads to the hypothesis that these defects may move through the crystal until they form complexes with other point defects, or each other.

We address this problem numerically with the application of the first-principles total energy method due to Sankey and Niklewski [10], which is based on density functional theory using the local density approximation (LDA). The method employs a basis of pseudoatomic orbitals, with norm-conserving pseudopotentials [11] of the Ceperley-Alder form [12], as parameterized by

Perdew and Zunger [13]. We use the Harris-Foulkes energy functional [14, 15], which is shown to give similar results to self-consistent calculations for GaAs [16]. For this work we have used 130 atom rectangular and 218 atom cubic supercells with energies computed at a single special k point. Even though a smaller cell is sufficient for dynamics involving a single interstitial, these larger cells are necessary in order to accommodate the increased strain during the dynamics for two interstitials, so that large changes in configuration may occur, and the low energy defect structures may be found.

Discussion.

We have searched for the minimum energy complex involving a pair of As interstitials by using a large variety of starting configurations including tetrahedral, hexagonal, two-fold-bonded, and various split interstitials, and doing a quenched molecular dynamics calculation to find the lowest energy configurations. Combinations of these configurations and distorted versions of these were also used as starting points. The As split interstitial was previously found to be the lowest energy configuration for a single interstitial As in GaAs [9]. The binding energy of the lowest energy complex found here, formed from a pair of interstitials, is 2.56 eV relative to two isolated neutral As split interstitials. This strong binding energy ensures that at all temperatures up to the melting temperature there will be a significant number of these complexes present as compared to the number of isolated split interstitials, if the total number of interstitials is substantial.

The lowest energy complex is found to be a nearest-neighbor pair of split interstitials as shown in Fig. 1, with the positions of the four central atoms (atoms 1-4 in the figure) and their nearest neighbors given in Table 1. Two As atoms sharing an As site (atoms 1 and 2) form one of the split interstitials, and the remaining As-Ga pair (atoms 3 and 4) reside on a neighboring Ga site. The four central atoms of the defect form a quadrilateral lying roughly in a (110) plane. The lengths of the bonds that form the sides of this quadrilateral are all between $0.4112a$ and $0.4333a$, where a is the bulk lattice constant. The smaller bond lengths in the As interstitial pair defect are reminiscent of the separation between atoms of pure arsenic metal, which is 2.2% smaller than the separation between atoms in GaAs.

The Ga and the As opposite to it in the quadrilateral (atoms 4 and 2 in the figure) are four-fold coordinated, as are atoms in defect-free GaAs. The other two As atoms (atoms 1 and 3), which are at opposite vertices of the quadrilateral, are triply coordinated, as are As atoms in pure metallic As. In order to accommodate the amount of strain resulting from two extra atoms in such a small volume, the atoms in the defect region should relax away from each other. Since the split interstitial on the As site is slightly more tightly bound than the split interstitial on the Ga site, the latter is more likely to relax away. As can be seen in Fig. 1, the As atom which is sharing the Ga site (atom 3) has moved outward in the direction of its normal neighbor (atom 5), which is also displaced.

Table 1. Positions of defect atoms and the atoms to which they are bonded as measured from the center of the split interstitial located at the arsenic site in units of the bulk lattice constant.

Atom		x	y	z	Neighbor	x	y	z
1	As	0.0024	-0.1834	0.1072	Ga	0.3554	-0.3121	0.2616
2	As	-0.0024	0.1834	-0.1072	Ga	-0.2424	0.3244	0.2217
					Ga	0.3285	0.3093	-0.3412
3	As	-0.3544	-0.0246	-0.2507	As	-0.5277	0.0988	-0.6198
4	Ga	-0.1536	-0.3829	-0.2303	As	-0.4775	-0.5554	-0.0134
					As	0.0686	-0.5300	-0.5513

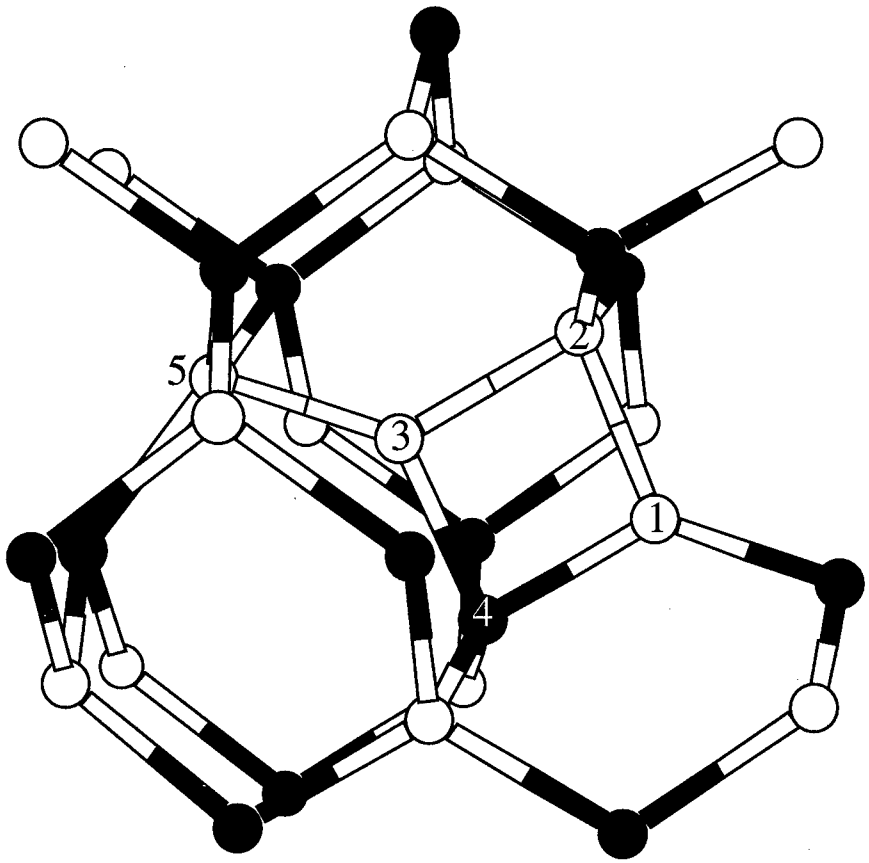

Fig. 1: The low energy configuration of two excess As atoms in GaAs in which the atoms labeled 1 and 2 are centered on an As site and atoms labeled 3 and 4 are centered on a Ga site. Black circles represent Ga and white represent As.

Bond angles between the four atoms of the complex are reduced compared to those of the bulk. Moving counterclockwise from atom number 1 in Fig. 1, the interior angles of the quadrilateral are 90°, 76°, 90°, and 79° for vertices 1, 2, 3, and 4, respectively. The other bond angles for the triply coordinated As atoms at the vertices are all between 118° and 120°. The remaining bond angles at the four-fold bonded sites range from 84° to 139°. The variation in angles is largely the result of relaxation to reduce the strain in the neighborhood of the defect. The range of values of bond angles is distributed differently from the case of the isolated split interstitial. Most notably, there are angles around 90° which is quite close to the bulk As metal value. However, the existence of the threefold coordinated As atoms in the As interstitial pair defect is similar to the existence of triply coordinated As atoms in the isolated split interstitial. These threefold coordinated atoms also occur for the reconstructed GaAs(110) surface, as well as in pure metallic As.

The strain contributed by the As interstitial pair complex can be measured in terms of the increase in distance between the point at the center of the complex and the normal nearest and next nearest neighbors of the lattice sites occupied by the two split interstitials. The center of the complex corresponds closely to the center of a nearest neighbor bond in the bulk lattice. The six nearest neighbor atoms are located at opposite ends of a line that coincides with the location of this bulk bond; this line connects the two split interstitials that make up the complex. The twelve atoms that make up the second neighbors are located in a band around this line. The six nearest neighbors are displaced away by an average of $0.079a$, and the next-nearest neighbors are displaced an average $0.030a$ away, where a is the lattice constant. We conclude that the larger expansion along the axis between the two lattice sites occupied by the defect is due to the fact that the nearest neighbors are directly bonded to the complex whereas the next nearest neighbors are not. If the diffuse "clouds" of As interstitials which have been observed in GaAs [17] are made up of As interstitial pairs, as we propose, this asymmetry in the strain due to each interstitial pair is likely to affect the relative orientations of the interstitial pairs in the "cloud".

There are no levels in the gap for the lowest energy As interstitial pair complex, indicating that this complex will be electrically inactive. The existence of this strongly bound complex, which will remain neutral for all Fermi levels within the gap, can explain how high concentrations of electrically inactive As interstitials can be present in GaAs during growth from the melt. Isolated interstitials cannot explain this, since the low energy isolated As interstitial configurations include both electrically active donors and acceptors, which should be capable of compensating added dopants. The pair complex has two localized energy levels near the valence band maximum. One corresponds to a charge distribution largely centered on the As and Ga split interstitial (atoms 3 and 4); the other is centered on the other two defect atoms. Furthermore,there is a localized state in the conduction band which appears to be localized on the Ga and As split interstitial pair. Comparison with other atomic configurations which have total energies within 0.5 eV above this configuration reveals similar electronic configuration and structural arrangements.

In conclusion, we have performed first principles molecular dynamics calculations to determine the lowest energy configuration of a defect involving a pair of extra As atoms in GaAs. We find that the structure is a pair of split interstitials centered on nearest neighbor sites in the cell. We have reported the local configuration and the effects of the defect on strain in the lattice. We propose that the existence of this strongly bound complex can explain the observations of large concentrations of electrically inactive As interstitials in LT GaAs and in GaAs during growth from the melt.

References.

* This work was supported in part by the Air Force Office of Scientific Research under Grants F49620-96-1-0167 and F49620-97-1-0479, and by grants of HPC time on the SGI Power Challenges at the DOD HPC Aberdeen and TACOM-TARDEC Centers and on the Cray C90 at the DOD HPC CEWES Center.

1. F. W. Smith, in *Low Temperature (LT) GaAs and Related Materials*, edited by G. L. Witt, R. Calawa, U. Mishra, and E. Weber, MRS Symposia Proceedings No. 241 (Materials Research Society, Pittsburgh, 1992), p. 3.
2. T. Muritani, T. Shimanoe, and T. Mitsui, J. Cryst. Growth **45**, 302 (1978).
3. F. W. Smith, A. R. Calawa, C.L. Chen, M. J. Manfra, and L. J. Mahoney, IEEE Electron Device Lett. **9**, 77 (1988).
4. K. M. Yu and Z. Liliental-Weber, Appl. Phys. Lett. **59**, 3267 (1991).
5. See, *e.g.* R. E. Pritchard *et al.*, J. Appl. Phys. **78**, 2411 (1995).
6. D. T. J. Hurle, Materials Science Forum **196-201**, 179 (1995); J. Phys. Chem. Solids **40**, 613, 627, 639, and 647 (1979); and other references cited by D. T. J. Hurle in these papers.
7. O. Oda *et al.*, Semiconductor Science and Technology **7**, A215 (1992).
8. V. T. Bublik *et al.*, Sov. Phys. Crystallog. **18**, 218 (1973).
9. D. J. Chadi, Phys. Rev. B **46**, 9400 (1992).
10. O. F. Sankey and D. J. Niklewski, Phys. Rev. B **40**, 3979 (1989).
11. D. R. Hamann, M. Schlüter, and C. Chiang, Phys. Rev. Lett. **43**, 1494 (1979).
12. D. M. Ceperley and G. J. Alder, Phys. Rev. Lett. **45**, 566 (1980).
13. J. Perdew and A. Zunger, Phys. Rev. B **23**, 5048 (1981).
14. J. Harris, Phys. Rev. B **31**, 1770 (1985).
15. W. M. C. Foulkes, Ph.D. thesis, University of Cambridge, 1987.
16. M.-H. Tsai, O. F. Sankey, and J. D. Dow, Phys. Rev. B **46**, 10464 (1992).
17. L. Charniy and V. Bublik, Journal of Crystal Growth **135,** 302 (1994).

Materials Science Forum Vols. 258-263 (1997) pp. 929-932

ELECTRICAL PROPERTIES OF LOW TEMPERATURE GROWN GaAs

M. Stellmacher[1], J. Nagle[1], K. Khirouni[2] and J.C. Bourgoin[3]

[1]Thomson, Laboratoire Central de Recherche, Domaine de Corbeville, B.P. n° 10, 91140 Orsay Cedex, France

[2]Laboratoire des Semiconducteurs, Faculté des Sciences de Monastir, Route de Kairouan, 5000 Monastir, Tunisia.

[3]Groupe de Physique des Solides, Université Paris 7, C.N.R.S., Tour 23, 2 place Jussieu, 75251 Paris Cedex 05, France

Keywords : *Admittance spectroscopy, TLG, GaAs, percolation, precipitates, EL2.*

ABSTRACT. We characterize low temperature grown GaAs layers by admittance spectroscopy. We demonstrate that the data are characteristic of a percolation regime around insulating regions. We evaluate the associated relaxation time, from which we deduce the average distance between these insulating regions. This distance being equal to the separation between As precipitates, we conclude that the insulating regions are induced by these precipitates, thus illustrating that As precipitates produce depleted regions in their vicinity.

I. INTRODUCTION

The electronic conduction in low temperature grown GaAs layers has been extensively studied because most of the applications for these layers are based on their semi-insulating character. The temperature dependence of the d.c. conductivity suggests that electron transport occurs *via* hopping in a defect band [1-8] located near the middle of the gap. These defects are said to be "EL2 like" because their energetical location in the gap is similar but not equal, to that of the EL2 defect [9]. However, it has also been suggested that this semi-insulating character is a result of the overlap of insulating regions originating from the presence of As precipitates [10-12]. Indeed, if these As precipitates are metallic, they induce the formation around them of space charge regions, i.e. depleted from electrons.

No direct evidence of the presence of depleted regions around As precipitates has yet been reported. The aim of this communication is to present one, based on the fact that, in the presence of insulating regions, electron conduction takes place *via* a percolation regime. We shall identify this regime by admittance spectroscopy.

II. CONDUCTION BY PERCOLATION

We consider an inhomogeneous medium composed of insulating regions (IR) which have a capacitance, C_e, embedded in a resistive material in which electrons move with a mobility μ. In order to examine the frequency response of such medium, we modelize it by a three dimensional lattice, each branch being occupied at random either by a capacitance Ce or a conductance σ_e, the average conductance between two adjacents IRs. The admittance of this lattice is then computed for different probabilities to find a capacitance or a conductance on a given branch. The result is illustrated in Figure 1 for three different structures, which remain of small dimensions owing to the available

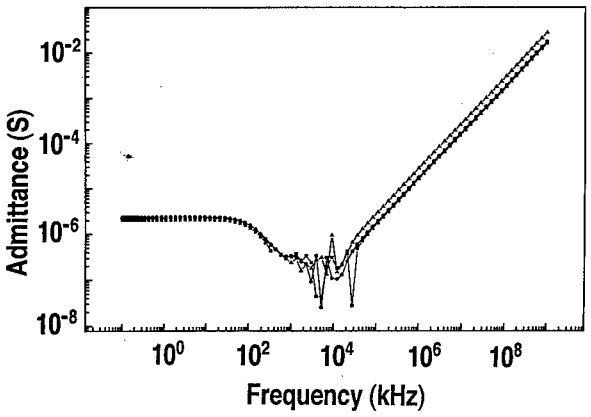

Fig. 1 – Admittance versus frequency computed for three different structures : 6 × 24 × 24 (▲), 5 × 20 × 20 (●) and 4 × 16 × 16 (■) using $C_p = 10^{-13}$ F and $\sigma_p = 3.8 \times 10^{-7}$ s with a probability 0.4 to find a capacitance on a given bound.

size of the computer. The admittance presents a minimum. The oscillations around the minimum are a consequence of the size of the structure through the way the capacitances and conductances are distributed on the branches for a given distribution probability. As expected, for a probability far from 0 or 1, the admittance becomes a constant conductance Σ at low frequency and a pure capacitance C at high frequency. As a consequence, one can write the admittance as:

$$Y(\omega) = \Sigma + jC\omega \qquad (1)$$

For this expression to exhibit a minimum i.e. to be characteristical of a percolation regime, it is necessary to introduce a relaxation time θ in the expression of Σ, i.e. write :

$$\Sigma = \frac{Y_0}{1 - j\omega\theta} \qquad (2)$$

This relaxation time corresponds physically to the scattering time between two adjacent IRs. For IRs separated by an average distance ℓ :

$$\theta = \ell \mu^{-1} E^{-1} \qquad (3)$$

where E is the electric field. The minimum of $Y(\omega)$ occurs for the frequency ω_m such that :

$$\left(\omega_m^2 \theta^2 + 1\right)^2 - \theta^2 z^2 - 2z\theta = 0 \qquad (4)$$

with

$$z = Y_0/C \qquad (5)$$

Evidence for a percolation regime is given by the existence of the minimum and by the fact that there is a direct relationship between ω_m, Y_0 and C. In the situation considered here, Y_0 is temperature dependent while C is not, and this relationship can therefore be checked by looking at the change of ω_m versus Y_0 when T varies.

III. EXPERIMENTAL RESULTS

A series of layers, grown by molecular beam epitaxy for various substrates temperatures ranging from 150 to 400 K, have been studied by admittance spectroscopy. Contacts on the layers separated by about 10 nm, are taken by AuGe alloying at 450° C for few minutes.The measurements have been performed, with an HP impedance analyzer in the range 10 to 10^7 Hz, at variable tempera-

tures, above 300 K. Typical data are given in Figure 2. From these data, one derives the temperature dependence of Y_0 (see Fig. 3), the relationship between ω_m and Y_0 (see Fig. 4) and an estimate of θ as discussed in the next section.

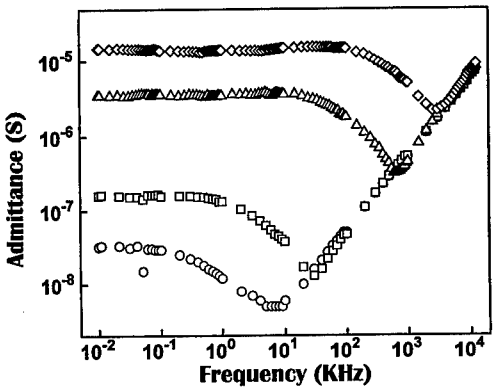

Fig. 2 – Admittance versus frequency measured at 316 (○), 352 (□), 414 (Δ) and 451 (◊) K on a layer grown at 450 K.

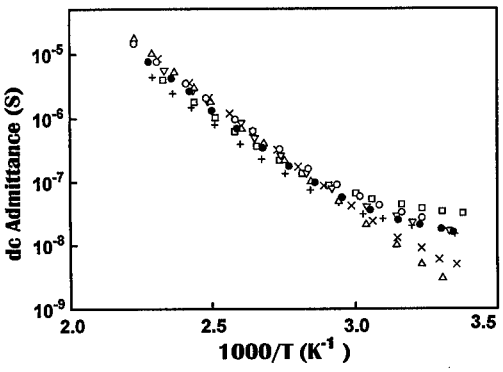

Fig. 3 – Temperature dependence of the d.c. admittance in layers grown at 423 (○), 436 (□), 473 (+), 498 (▽), 523 (×), 673 (Δ) K.

IV. DISCUSSION

At high frequencies, $Y(\omega)$ is a pure capacitance C which is typically of the order of 1 pF. The relationship between ω_m and Y_0 allows to deduce $\theta \simeq 10^{-5}$ s^{-1} from a couple of (ω_m, Y_0) values since C is known. In the experimental configuration, $E \simeq 10^{-2}$ Vcm^{-1}; moreover, Hall effect measurements performed on the studied layers indicate that free carriers are electrons with a mobility $\mu \sim 10^3$ cm^2 v^{-1} s^{-1}. Consequently, from the value of θ, one deduces using expression (3) the average distance between IRs : $\ell \sim 10^{-6}$ cm.

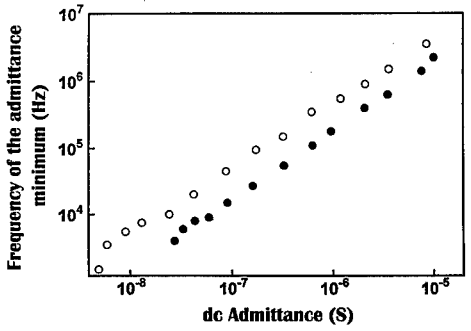

Fig. 4 – Relationship between the d.c. admittance and the frequency of the admittance minimum in layers grown at 448 (●) and 523 (○) K.

In order to demonstrate the validity of the analysis, this length must be compared with the distance between precipitates. Precipitates have been observed using electron microscopy in layers grown at similar temperature after annealing [13]. Here, an annealing at 450° C is performed while making the ohmic contacts. A concentration of precipitates grown around 350° C, i.e. for which we have presented the data, is 10^{16} cm^{-3} . This corresponds to a distance of 3×10^{-6} cm, i.e. the length we deduced from admittance spectroscopy data when analyzed in terms of percolation.

Finally, the fact that the conductivity data are in agreement with electron microscopy observation demonstrates that the As precipitates indeed induce insulating regions around which conduction electrons percolate.

V. REFERENCES

1. D.C. Look, D.C. Walters, G.D. Robinson, J.R. Sizelove, M.G. Mier and C.E. Stutz, J. Appl. Phys. **74**, 306 (1993).
2. K. Zhang and D.L. Miller, J. Electron. Mat. **22**, 1433 (1993).
3. B. Nabet, A. Youtz, F. Castro, P. Cooke and A. Paolella, Appl. Phys. Lett. **67**, 1748 (1995).
4. X. Liu, A. Prasad, W.M. Chen, A. Kurpiewski, A. Stoschek, Z. Liliental-Weber and E.R. Weber, Appl. Phys. Lett. **65**, 3002 (1994).
5. D.C. Look, J. Appl. Phys. **70**, 3148 (1991).
6. D.C. Look, D.C. Walters, L.O. Manasreh, J.R. Sizelove, C.E. Stutz and K.R. Evans, Phys. Rev. B **42**, 3578 (1990).
7. Z.Q. Fang and D.C. Look, J. Electron. Mat. **22**, 1429 (1993).
8. J.K. Luo, H. Thomas, D.V. Morgan, D. Westwood and R.H. Williams, Semicond. Sci. Technol. **9**, 2199 (1994).
9. D.C. Look, G.D. Robinson, J.R. Sizelove and C.E. Stutz, Appl. Phys. Lett. **62**, 3004 (1993).
10. A.C. Warren, J.M. Woodall, J.F. Freeouf, D. Grischkowsky, M.R. Melloch and N. Otsuka, Appl. Phys. Lett. **57**, 1331 (1990).
11. A.C. Warren, J.M. Woodall, P.D. Kirchner, X. Yiu, X. Guo, F.H. Pollack and M.R. Melloch, J. Vac. Sci. Technol. **B10**, 1904 (1992).
12. A.C. Warren, J.M. Woodall, P.D. Kirchner, X. Yiu, F. Pollak, M.R. Melloch, N. Otsuka and K. Mahalingam, Phys. Rev. B **46**, 4617 (1992).
13. M.R. Melloch, N. Otsuka, K. Mahalingam, A.C. Warren, J.M. Woodall and P.D. Kirchner, Mat. Res. Soc. Symp. Proc. **241** (1992 Material Research Society), p. 113.

Materials Science Forum Vols. 258-263 (1997) pp. 933-938

TRAPS FOUND IN GaAs MESFETS: PROPERTIES LOCATION AND DETECTION

B.K. Jones and M.A. Iqbal
School of Physics and Chemistry, Lancaster University
Lancaster, LA1 4YB, UK
b.jones@lancaster.ac.uk

Keywords : traps, GaAs MESFETs, DLTS, noise, dispersion, semi-insulating substrate

Abstract. The activation energy and capture cross section of the traps found in a selection of commercial GaAs Field Effect Transistors (GaAsFETs) have been measured with both ohmic channel and current saturation bias using a variety of transient, frequency dispersion and noise spectroscopy techniques. The nine defects which are commonly found, and their measured properties, are influenced by the device structure as well as the materials from which it is composed. The properties of the traps found will be described together with their location and origin.

Introduction.

Traps located within semiconductor devices degrade their performance. They result in excess noise and various transient and frequency dependent effects. These effects occur mainly at low frequencies but they also affect the performance of high frequency devices in mixer and oscillator applications. Some show an increase in their density during some degradation processes and can strongly affect the performance of the device before failure. In GaAs Field Effect Transistors (GaAsFETs) they are involved in various 'sidegating' or 'backgating' effects in which a voltage to the substrate, remote from the device, can alter the device properties and 'kink' effects in which kinks are found in the current in the saturation region. These are caused by changes in trap occupation in the substrate caused by the application of the substrate voltage or by filling by hot carriers from the channel to give a change in the pinch-off voltage. In order to improve devices it is important to know the properties and location of the defects.

In n-channel devices both electron-like and hole-like traps are found. The 'type' is defined by the sign of the DLTS transient. The electron traps are located in the neutral channel and produce small effects. These are the traps which would be expected from normal materials investigations using DLTS on surface barriers placed on the surface of the material. The hole-like traps are usually the most prominent and are found to be located in the free surface (H2) or the semi-insulating substrate. These traps also have the unusual properties that they are hole-like in an n-type channel and that their filling and emptying times are (nearly) equal. The location, formation and reason for the activity of these traps will be discussed.

Samples and Experiment.

A very systematic study has been made of the defects in GaAs MESFETs over a temperature range 77K-330K under Ohmic and current saturation bias, using a variety of techniques: conductance DLTS with gate or substrate excitation, a novel transient modelling method to determine the trap location, mutual conductance dispersion, output conductance dispersion, excess noise and substrate oscillations[1-12]. Details of the experimental methods can be found in the references

The specimens studied were commercial devices: Toshiba type S8831 with 0.8μm gate length, 13dB gain and 8 GHz cut-off frequency, and Avantek (now Hewlett-Packard) type ATF-10100 with 0.3μm gate length 13.0dB gain and 5GHz cut-off frequency. Other devices show similar effects. The devices were characterised at DC in the ohmic channel condition using the Fukui method[9]. In this method the ohmic channel resistance is measured as a function of gate bias and suitable fitting

procedures are used. This gives the pinch-off voltage, the fully open gated channel resistance and the total access region series resistance. The values found at room temperature were 1.01V, 1.38Ω and 4.88Ω for device TF10 and 0.93V, 1.70Ω and 4.57Ω for device TF4. Several samples of each type were investigated but detailed results from only these two are presented here.

Results.

A total of nine generally occurring traps have been detected. The values of activation energy and capture cross-section found by the different measurement techniques with the device under different biases were essentially the same. There were no systematic differences but the variation between devices and techniques was considerably larger than the experimental uncertainty of the technique. For this reason we quote the temperature at which the emission time constant is 0.2s rather than the cross-section so that there is no propagation of the error in the activation energy. Also very similar results have been reported in the literature for individual traps and in tabulations of GaAs trap data[13,14]. These properties are described in Table 1.

Table 1 Summary of the trap energy and cross-section parameters found in this investigation. The trap numbering (H1, H2 etc.) is our own. The trap cross-section is given by T(0.2s)K, which is the temperature at which the trap transient time constant is 0.2s. The time-dependence of the transient is also given. This is explained further in the text.

Trap label	ΔE(eV)	T(0.2s)(K)	Transient shape	Location	Device used
H0	0.935	360	Square-root	Substrate	Toshiba and Avantek
H1	0.716	307	Square-root	Substrate	Avantek
H2	0.622	270	Exponential	Surface	Toshiba
H3	0.448	199	Square-root	Substrate	Toshiba
H4	0.351	176	Square-root	Substrate	Toshiba
H5	0.137	106	Exponential	Surface(?)	Toshiba
H6		<=77	-	Substrate(?)	Toshiba
E1	0.256	168	Exponential	Channel	Toshiba
E2	0.85	338	Exponential	Channel(?)	Toshiba and Avantek

The knowledge of the locations of the traps within the device is of critical importance in order to improve the device performance. This has been investigated in detail using the bias dependence of the trap signatures[4-6,10,11] and also a modification of the conductance DLTS method to incorporate device modelling[1,8]. The basic effects can be seen by the DLTS spectra shown in Figure 1. These curves were taken under current saturation bias. The relative sensitivities of the different traps varies using different experimental methods and biases. The peaks do not have the classic shape, the electron traps show a weaker response than the hole traps and (not visible here) the hole traps have symmetrical filling and emptying times.

There are three groups of traps. Electron traps E1 and E2 are located within the device channel. The hole-like trap H2 is located at the surface of the device between the gate and drain or source. This region is long and there is a significant resistance in the channel beneath it so the occupation of these surface traps can affect the performance. Charge flows from the gate into the surface to produce a field-effect change in resistance[7]. This is the most significant trap since it usually gives

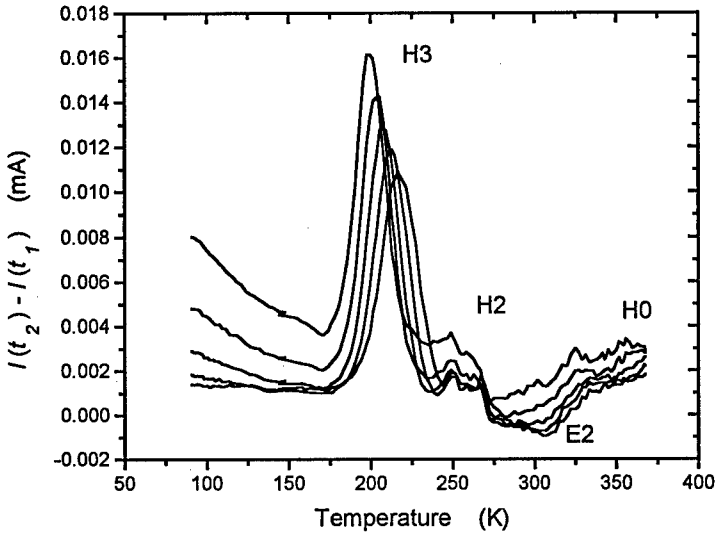

(a)

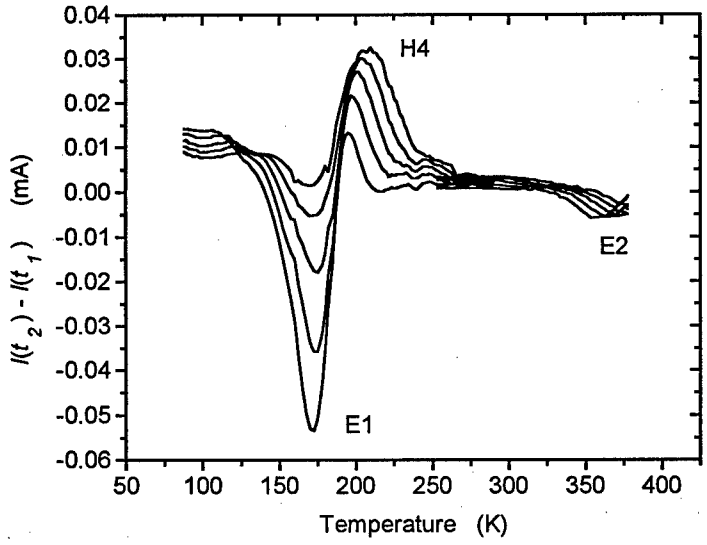

(b)

Figure 1. Typical experimental results with appropriate curve fits for sample TF10 in current saturation. The rate windows presented are between 12.5 ms and 200 ms in steps of a factor of two. The lines join the data points.
(a) Mutual conductance DLTS (TDLTS), with a gate excitation corresponding to a more open channel during the transient (V_{GS}= -0.8, -0.9, -0.8 (V)) (NTDLTS), at a constant drain bias of 1.8V.
(b) Output conductance DLTS (ODLTS), with gate excitation corresponding to a larger drain voltage during the transient(NODLTS), at constant gate bias of 0.8V. The output data are presented as $I_D = V_D/R_L$ where R_L = 147 Ω.

a strong signal in the audio frequency region. The remaining traps that have been clearly identified, H0, H1, H3 and H4, are located in the substrate and are all hole-like traps.. The channel-substrate interface acts approximately like an N-P$^-$ junction. Really the semi-insulating material is a relaxation semiconductor, which makes a full analysis difficult. At the far end of the depletion region the bands bend so that the Fermi level passes from mid-gap to the level for p-type material near the valence band. By charge neutrality a change in occupancy of traps here produces a corresponding change in occupancy for the donors at the edge of the conducting channel and hence a resistance change. Since the excitation only produces a marginal change in the depletion width we find a trap time constant which is a balance between concurrent filling and emptying. This mechanism produces the hole-like nature, symmetrical filling and emptying times and a transient which is not exponential [exp-t/τ] but the square root function [(1-exp-t/τ)$^{1/2}$] as observed[4-6,10].

The reason for the relative sensitivity of the different techniques and biases for the different traps is complex. Essentially the method which gives the strongest signal and reveals most traps is conductance DLTS on the Ohmic channel but several methods need to be used so that a trap signature is not always totally obscured by the strong signal from another trap which may not show up using a different method. The various DLTS methods involve very strong excitation with large departures from equilibrium. The other methods study the device in near equilibrium, with little excitation and hence detect traps at the Fermi level at a relevant part of the sample.

We observe very consistent results between devices, which suggests that the traps seen are very generally produced. This contrasts strongly with results on different semi-insulating substrate material which produces a variety of different results even from the same nominal source material[15]. One reason for this may be that some, or all of the substrate traps are located at the interface between the pure buffer layer, placed between the doped channel and the semi-insulating substrate, and the substrate itself. There is evidence that the trap density can be reduced by cleaning the substrate carefully before depositing the buffer layer.

Conclusions.

There is a good agreement between the trap parameters measured in different ways although the variation is considerably bigger than can be understood by the detail of the experiments themselves. It is essential to understand device operation in detail in order to interpret the results with confidence. Conductance DLTS in Ohmic bias is the best measurement method. Other methods can give good results. The large effects seen due to traps in the semi-insulating substrate are usually reduced by trying to improve the quality of the substrate or adding high purity, near-intrinsic, buffer layers between the substrate and channel. Further study of the traps in the semi-insulating material is needed but probably most of those observed are inherent in the compensation process undertaken in the semi-insulating conversion. More study is needed on the relaxation semiconductor properties of the substrate in order to reduce the effects of substrate traps efficiently.

Acknowledgements.

This report has relied on the considerable work of former members of the group.

References.

1. G Jin and B.K. Jones, "Characterisation of the Time-dependent Properties of GaAsFETs", *Semicond. Sci. Technol.*, **5**, 395-403, (1990).
2. M.A. Abdala and B.K. Jones, "Correlation between Trap Characterisation by Low Frequency Noise, Mutual Conductance Dispersion, Oscillations and DLTS in GaAs MESFETs", *Solid-State Electron.*, **35**, 1713-19, (1992).
3. M.A. Abdala and B.K. Jones, "Low Frequency Oscillations in GaAs MESFETs", *Solid-State Electron.*, **36**, 237-45, (1993).
4. N. Sengouga and B.K. Jones, "Modelling the Transient Response of Channel-Substrate Interface Traps to Gate Voltage Steps in GaAs FETs", *Solid-State Electron.*, **36**, 229-36, (1993).
5. N. Sengouga and B.K. Jones, "Modelling of the Transient Response of Substrate Traps to the Substrate Voltage in GaAsFETs", *IEEE Trans.*, **ED 40**, 471-9, (1993).
6. N. Sengouga and B.K. Jones, "Backgating Effects in GaAs FETs with a Channel-Semi-insulating Substrate Boundary", *Solid-State Electron.*, **38** 413-21, (1995).
7. G. Jin and B.K. Jones, "The effect of traps at the free surface of GaAs field effect transistors", *J. Appl. Phys.*, **80**, 6340-8, (1996).
8. G. Jin and B.K. Jones, "A Conductance DLTS System to Analyse Multiple Exponential Decays", *Semicon. Sci. Technol.*, **3**, 1083-93, (1988).
9. H. Fukui, "Determination of the basic device parameters of a GaAs MESFET", *Bell Syst. Tech. J.*, **58**, 771-97, (1979).
10. N. Sengouga, "Hole traps in GaAs FETs: characterisation and backgating effects", *PhD Thesis, Lancaster University,* (1991).
11. M.A. Abdala, "Characterisation of traps in GaAs MESFETs by low frequency noise, g_M dispersion and oscillations methods", *PhD Thesis, Lancaster University,* (1991).
12. B.K. Jones, "Low-Frequency Noise Spectroscopy", *IEEE Trans.*, **ED41**, 2188-2204, (1994).
13. A. Mitonneau, G.M. Martin and A. Mircea, "Hole traps in bulk and epitaxial GaAs crystals", *Electron. Lett.*, **13**, 666-7, (1977).
14. G.M. Martin, A. Mitonneau and A. Mircea, "Electron traps in bulk and epitaxial GaAs crystals", *Electron. Lett.*, **13**, 191-3, (1977).
15. B.K. Jones, J. Santana and T. Sloan, "Defects in Neutron Irradiated LEC SI-GaAs", This conference.

Materials Science Forum Vols. 258-263 (1997) pp. 939-944

INFLUENCE OF DOPANT SPECIES ON ELECTRON MOBILITY IN HEAVILY DOPED SEMICONDUCTORS

G. Kaiblinger-Grujin, H. Kosina, Ch. Köpf, and S. Selberherr

Institute for Microelectronics, TU Vienna
Gusshausstrasse 27-29
A-1040 Vienna, Austria

Keywords : electron mobility, ionized impurity scattering, Thomas-Fermi atomic model

Abstract

We present a new theoretical approach to study the influence of the dopant species on the electron drift mobility in doped semiconductors under low electric fields. The charge distribution of the impurities is described by the Thomas-Fermi theory in the energy functional formulation. We have included many-particle effects, such as dispersive screening and multiple scattering, which become important in heavily doped semiconductors. Analytical expressions for the scattering cross section for various species of dopants using the Born approximation up to second order are derived. Monte Carlo simulations including all important scattering mechanism have been performed for Si, GaAs, and InP in the doping concentration range of 10^{15} to 10^{21} cm^{-3}. The dependence on donor species is significant for concentrations beyond 10^{18} cm^{-3}, whereas the minority electron mobility is not affected by different dopants. Not only confirm the results the experimental data of the mobility enhancement of minority electrons compared to majority electrons in degenerated semiconductors but also the lower electron mobility in As-doped Si in comparison to P-doped Si.

Introduction

As semiconductor device dimensions decreasingly approach 0.1 μm, it becomes necessary to have accurate values of the majority and minority electron mobilities in advanced semiconductor device simulation. Despite the importance of these quantities for device applications, such as bipolar transistors which are controlled by minority carrier flow in heavily doped regions, theoretical treatments are quite limited. There still remains a tendency in numerical simulation to assume that majority and minority mobilities are equal, although experiments have shown that majority and minority mobilities may differ by a factor of 3 in heavily doped Si[1][2][3][4].

Moreover, there is no theoretical model to date which explains the different mobility data for As- and P-doped Si for impurity concentrations higher than $10^{18}\,cm^{-3}$. The difference between the electron mobility in As- and P-doped samples is up to 32 % at $N_I = 4 \cdot 10^{21}\,cm^{-3}$ [5]. Ignoring these phenomena can lead to incorrect interpretation of device data which strongly depend on doping concentration.

There were several attempts in the past to explain these different mobilities. Ralph et al. [6] introduced a central-cell scattering potential determined empirically using bound state energies of donors. Later, El-Ghanem and Ridley [7] employed a square-well impurity core potential. Bennett and Lowney investigated the majority and minority electron mobility in Si [8][9][10] and GaAs [11]. They introduced different scale factors in the interaction potential for majority and minority electrons.

The basis of our theoretical approach is the Thomas-Fermi (TF) theory [12][13]. This semi-classical treatment of the atom in the energy functional formulation yields the impurity charge density as a function of the atomic and electron numbers as well as a variational parameter which defines the size of the valence electron charge cloud. Knowing the charge density we obtain analytical expressions for the differential scattering cross section using the Born formalism up to second order to account for the charge sign of the impurity center.

Charge Density of Ionized Impurities

The total valence charge density (in units of the electron charge e) of an unscreened impurity atom with atomic number Z and electron number N in a solid is given by

$$\rho_{ion}(r) = Z\delta(r) - \rho_e(r) \tag{1}$$

$$N = \int \rho_e(\vec{r}) d^3r \tag{2}$$

The first term at the right hand side of Eq. (1) describes the nuclear charge density distribution concentrated in the origin. The second term, $\rho_e(r)$ is the electron charge density of the impurity ion. There are numerous methods to calculate the electron charge density distribution. As we are interested in analytical solutions, we use the semi-classical TF model. Its basic idea is to treat the valence electrons as a degenerate Fermi gas of nonuniform, spherically symmetric electron density in a positively charged background at zero temperature. Under this assumption we get a local relation between the electron charge density and the Fermi energy. The total energy consists of the classical Coloumb potential energy of electron-electron E_{e-e} and electron-nucleus interactions E_{e-n}, and the kinetic energy E_k. Hence we define the total energy functional ($\hbar = m = 1$)

$$E_0 = E_k + E_{e-n} + \lambda E_{e-e} \tag{3}$$

$$E_k = c_k \int \rho_e(r)^{5/3} d^3r \tag{4}$$

$$E_{e-n} = -\frac{Z}{\epsilon_{Sc}} \int \frac{\rho_e(r)}{r} d^3r \tag{5}$$

$$E_{e-e} = \frac{1}{2\,\epsilon_{Sc}} \int\int \frac{\rho_e(r)\rho_e(\vec{r'})}{\mid \vec{r} - \vec{r'} \mid} d^3r\, d^3\vec{r'} \tag{6}$$

with $c_k = \frac{3}{10}(3\pi^2)^{2/3}$ and a correlation parameter λ. We assume the electron charge density distribution to be of the form

$$\rho_e(r) = \frac{N\,\alpha^2}{4\pi} \frac{\mathrm{e}^{-\alpha r}}{r} \tag{7}$$

Its Fourier transform

$$F(q) = \frac{N\alpha^2}{q^2 + \alpha^2} \tag{8}$$

is called the atomic form factor of the charge distribution. The variational parameter α has to be determined by minimizing E_0. Calculating the first derivative of the total energy with

respect to the variational parameter α and the electron number N we get two equations for α and λ:

$$0 = \frac{\partial E}{\partial \alpha} \tag{9}$$

$$0 = \left.\frac{\partial E}{\partial N}\right|_{N=Z} \tag{10}$$

Condition Eq. (10) makes the chemical potential vanish for a neutral atom. Solving Eq. (9) and Eq. (10) with respect to λ and α we obtain finally

$$\alpha = \frac{Z^{1/3}}{c_k^*} \frac{1 - 2\left(\frac{Z}{N}\right)}{\frac{5}{3} - 4\left(\frac{Z}{N}\right)^{1/3}} \tag{11}$$

with $c_k^* = \frac{\Gamma(4/3)}{2}\left(\frac{3\pi}{4}\right)^{2/3}\left(\frac{3}{5}\right)^{7/3}$.

Scattering potential

We assume randomly located impurities of concentration N_I. With increasing N_I the average distance R between two impurities decreases such that scattering processes become important in which two or even more ions are involved simultaneously. To include multi-potential scattering to first order, we let pairs of impurities act as scattering centers. Since the impurity ion in a solid is screened by free carriers, the effective potential in momentum space for a pair of impurities can be written as

$$\mathcal{U}(q) = V_0 \frac{Z - F(q)}{q^2 + \beta^2 G(\xi,\eta)} \left(1 + \exp(-i\,\vec{q}\cdot\vec{R})\right) \tag{12}$$

with $V_0 = \frac{2m^*}{\hbar^2}\frac{e^2}{\epsilon_{Sc}}$. In Eq. (12) linear screening is assumed. ϵ_{Sc} is the dielectric constant of the semiconductor, and β the inverse Thomas-Fermi screening length which for an un-compensated semiconductor is given by

$$\beta^2 = \frac{4\pi n e^2}{\epsilon_{Sc}\, k_B T} \frac{\mathcal{F}_{-1/2}(\eta)}{\mathcal{F}_{1/2}(\eta)}. \tag{13}$$

Here, $k_B T$ is the thermal energy, q the momentum transfer, and n the free carrier concentration (no compensation is assumed). The screening function [14]

$$G(\xi,\eta) = \frac{1}{\mathcal{F}_{-1/2}(\eta)} \frac{1}{\xi\sqrt{\pi}} \int_0^\infty \frac{x}{1 + \exp(x^2 - \eta)} \ln\left|\frac{x+\xi}{x-\xi}\right| \mathrm{dx}$$

$$\xi^2 = \frac{\hbar^2 q^2}{8 m^* k_B T} \qquad \eta = \frac{E_F - E_C}{k_B T} \tag{14}$$

represents the dielectric response of the conduction electrons to an external charge. $\mathcal{F}_j$ denotes the Fermi integral of order j and η is the reduced Fermi energy. To avoid numerical integration in the Monte Carlo procedure we use a rational approximation for G of the form

$$G(\xi,\eta) \approx \frac{1 + a\xi^2 + b\xi^4}{1 + c\xi^2 + d\xi^4 + e\xi^6}. \tag{15}$$

The unknown coefficients a, b, c, d, e which have to be chosen such as to match the screening function at zero and for infinity[15].

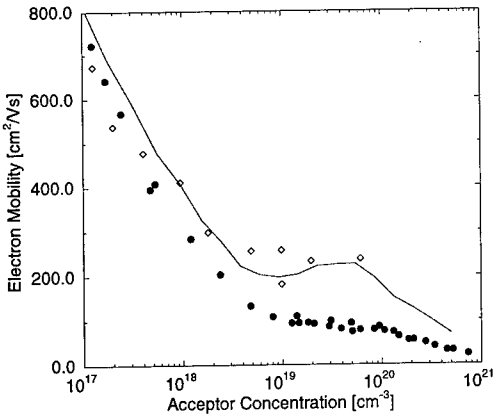

Figure 1: Minority electron mobility in B-doped Si. Simulation: solid line; experimental data from [4]: open diamonds; majority mobility data: filled circles [5]

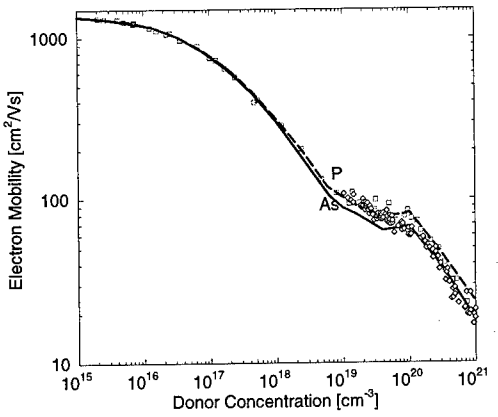

Figure 2: Majority electron mobility in P- and As-doped Si. Simulation: solid (As) and dashed lines (P); experimental data from [5]: open diamonds (As); open squares (P)

Scattering Rate

With a given scattering amplitude $f(q)$ the differential scattering cross section σ is defined as

$$\sigma(q) = \frac{(2\pi\hbar)^3}{m^{*2}v_g(k)}|f(q)|^2\rho(E) \tag{16}$$

This expression is valid for arbitrary density of states ρ and group velocity v_g. Using the total cross section

$$\sigma_{tot}(k) = \frac{2\pi}{k^2}\int_0^{2k}\sigma(q)q\mathrm{dq}, \tag{17}$$

the total scattering rate is given by

$$\lambda(k) = N_p v_g \sigma_{tot}(k) \tag{18}$$

where $N_p = N_I/2$ is the density of impurity pairs.

Results and Discussion

We present calculated mobilities for Si, GaAs, and InP at 300 K. The transport problem is solved by a Monte Carlo method. To avoid numerical integration for scattering rates in the Born approximation by calculating Eq. (17) and Eq. (18), we make use of an acceptance/rejection scheme[16].

All impurities were assumed to be ionized. In addition to ionized impurity scattering which is the main scattering process in heavily doped semiconductors, we took also into account acoustic intra-valley scattering, phonon inter-valley scattering, and electron-plasmon scattering. The latter effect lowers the mobility in p-type material significantly and is responsible for the dip in the minority mobility at about $N_I = 10^{19}$ cm^{-3}, which corresponds to the maximum strength of the electron-plasmon interaction[17]. The Pauli exclusion principle was included by means of a rejection technique assuming equilibrium Fermi-Dirac statistics for the final states.

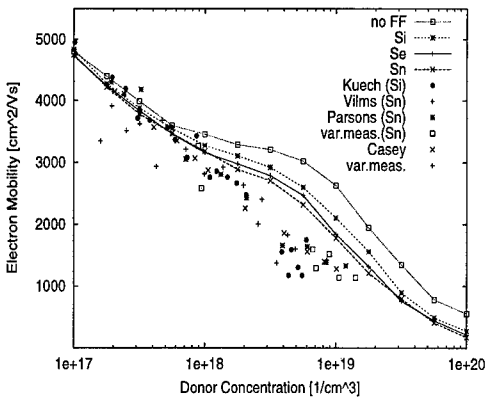

Figure 3: Majority electron mobility in GaAs for different donors

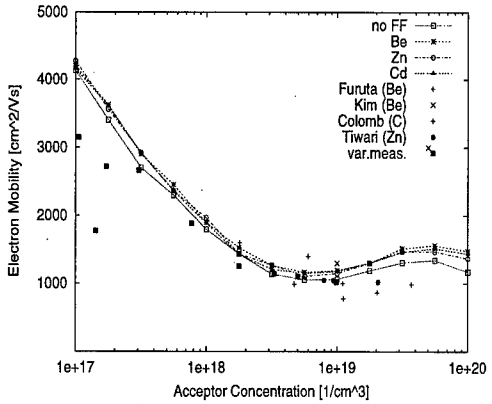

Figure 4: Minority electron mobility in GaAs for different acceptors

We have found that the momentum-dependent form factor strongly influences the scattering cross section with icreasing doping concentrations, especially for minority electrons. Then larger scattering angles are becoming more probable such that the q-dependence of the atomic form factor cannot be neglected. The vanishing electron-plasmon interaction and the stronger repulsion are responsible for the increase of the minority electron mobility up to $4 \cdot 10^{19}\, cm^{-3}$ and the generally higher mobility in p-type Si (Fig. 1). The squared difference between Z and $F(q)$ is higher compared to P-doped Si for the same energy because the effective charge of As-ions is larger than that in P-ions. Hence, the electron mobility is always lower in As-doped samples than in P-doped samples (Figs. 2). For n-GaAs our results confirm the lower mobility for donors with increasing atomic number Z above 10^{18} cm^{-3}. The mobility values may differ up to 20% at 10^{19} cm^{-3} for Si and Sn-doping, respectively (Fig. 3). In case of p-GaAs the influence of $F(q)$ leads to an small increase of the mobility for acceptors. No significant dependence on the dopant species is observed over the whole concentration range (Fig. 4). In Fig. 5 and Fig. 6 the electron mobility in InP for different dopants is shown. These results are in agreement with the experiments of Anderson [18] who found no significant difference for various species. Unfortunately, the uncertainty and scattering of the available experimental data is of the same order of magnitude as the difference of the mobilities for various dopants. Hence, it is in general very difficult to evaluate the simulation results quantitatively.

Conclusion

We have shown that consideration of the spatial charge distribution of the impurities is essential to explain the dopant-dependent electron mobility in heavily doped semiconductors. Hence, the failure of explaining different minority and majority electron mobilities for various dopant species in the past was due to neglecting the q-dependence of the atomic form factor which leads to different effective charges of the ionized dopants. Furthermore, in Si the two-ion correction is important over the whole doping range, whereas dispersive screening and the second Born correction are becoming important at $N_I = 10^{18}$ cm^{-3}. Due to the lack and inconsistency of experimental data for the minority electron mobility of all investigated semiconductors, it is difficult to compare our simulation results quantitatively for this particular case. It is hoped that the results outlined here will stimulate more experimental work to establish the different electron mobilities observed for various species of donors in n- and p-type semiconductors.

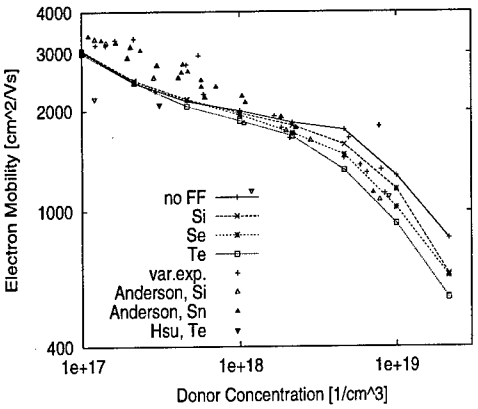

Figure 5: Majority electron mobility in InP for different donors

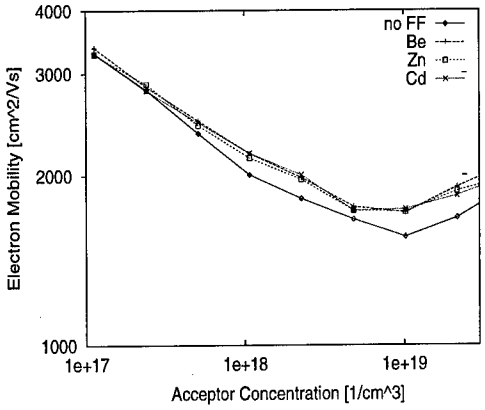

Figure 6: Minority electron mobility in InP for different acceptors

References

[1] J. Dziewior, Appl.Phys.Lett. **35**, 170 (1979).

[2] I. Leu and A. Neugroschel, IEEE Trans.Electron Devices **40**, 1872 (1993).

[3] A. Neugroschel, IEEE Electron Device Lett. **EDL-6**, 425 (1985).

[4] S. Swirhun, D. Kane, and R. Swanson, in *Int.Electron Devices Meeting* (San Francisco, 1986), pp. 24–27.

[5] G. Masetti, M. Severi, and S. Solmi, IEEE Trans.Electron Devices **ED-30**, 764 (1983).

[6] H. Ralph, G. Simpson, and R. Elliot, Physical Review **11**, 2948 (1975).

[7] H. El-Ghanem and B. Ridley, J.Phys.C:Solid State Phys. **13**, 2041 (1980).

[8] H. Bennett, Solid-State Electron. **26**, 1157 (1983).

[9] H. Bennett and J. Lowney, J.Appl.Phys. **71**, 2285 (1992).

[10] H. Bennett and J. Lowney, in *Workshop on Numerical Modeling of Processes and Devices for Integrated Circuits NUPAD IV* (Seattle, 1992), pp. 123–128.

[11] J. Lowney and H. Bennett, J.Appl.Phys. **69**, 7102 (1991).

[12] E. Fermi, Rend.Accad.Naz.Lincei **6**, 602 (1927).

[13] L. Thomas, Proc.Camb.Philos.Soc. **23**, 542 (1927).

[14] D. Ferry, *Semiconductors* (Macmillan, New York, 1991).

[15] H. Kosina and G. Kaiblinger-Grujin, Solid-State Electron. (1997), accepted for publication.

[16] C. Jacoboni and P. Lugli, *The Monte Carlo Method for Semiconductor Device Simulation* (Springer, Wien-New York, 1989).

[17] M. Fischetti, Physical Review B **44**, 5527 (1991).

[18] D. Anderson, N. Apsley, P. Davies, and P. Giles, J.Appl.Phys. **58**, 3059 (1985).

Materials Science Forum Vols. 258-263 (1997) pp. 945-950

CREATION OF Ga_{As} ANTISITES IN GaAs BY TRANSMUTATION OF RADIOACTIVE $^{71}As_{As}$ TO STABLE $^{71}Ga_{As}$

R. Magerle [1], A. Burchard [1], D. Forkel-Wirth [2], M. Deicher [1] and the ISOLDE-Collaboration [2]

[1] Fakultät für Physik, Universität Konstanz, D-78457 Konstanz, Germany
[2] CERN / PPE, CH-1211 Geneva 23, Switzerland

Keywords: GaAs, Ga_{As} antisite, transmutation doping

Abstract. Radioactive ^{71}As ions implanted into GaAs can be used to create isolated Ga_{As} antisites in a quantitative way through their decay via ^{71}Ge to ^{71}Ga. Photoluminescence spectroscopy is used to identify the defect levels associated with $^{71}Ga_{As}$ via their production rate defined by the nuclear life-time of ^{71}Ge. Experiments are presented which prove that implanting radioactive ^{71}As into GaAs and choosing the right timing for annealing the implantation induced defects leads to the formation of isolated $^{71}Ga_{As}$ involving most of the originally implanted ions. Despite this fact, no photoluminescence line between 0.9 eV and 1.515 eV related to Ga_{As} sites has been observed.

Introduction

Photoluminescence (PL) spectroscopy is a standard technique to detect defect levels in semiconductors. However, the assignment to a particular defect is often a puzzle. In general, an unambiguous chemical identification of a defect level is provided only by the observation of an element specific property, like the isotope mass, the nuclear spin, or the isotope abundance. One element specific property that can be used to identify defect levels is the nuclear life-time of a radioactive isotope undergoing a chemical transmutation. If the questioned level is due to a defect in which the parent or daughter isotope is involved the concentration of that defect will change with the characteristic time constant of the radioactive decay. This has been demonstrated [1] for GaAs doped with radioactive ^{111}In decaying to ^{111}Cd where ion implantation has been used for doping with the radioactive isotopes and a quantitative link between PL intensity and defect concentration was obtained.
An important class of intrinsic defects in compound semiconductors of type *AB* are antisites where an *A* atom is placed on a *B* site or vice versa. It is still an open question what the levels of the Ga_{As} antisite in GaAs are. From valence arguments Ga_{As} should act as a double acceptor. In agreement with this GaAs grown from a Ga rich melt is often *p*-type with an acceptor state at 78 meV and exhibits a photoluminescence (PL) emission at 1.441 eV [2]. Therefore this level and this emission is often assigned to the Ga_{As} antisite [3], however, there is also evidence that this level is due to B_{As} [4]. Recently we have shown how to create Ga_{As} antisites in GaAs in a controlled way by implanting radioactive ^{71}As which transmutes to stable ^{71}Ga [5]. In addition, this approach offers the possibility to use the nuclear life-time of the involved isotopes as element specific labels to identify the levels of the Ga_{As} antisite. Remarkably, the PL spectra of all Ga_{As} doped samples did not differ from spectra of samples which have been only annealed and not implanted. In particular we did not observe a PL line at 1.441 eV.
In this work we report on additional experiments to clarify the enigma that no additional PL emission due to the creation of Ga_{As} is observed.

Experimental details

To create Ga_{As} antisite defects we implanted radioactive ^{71}As into semi-insulating LEC grown GaAs at the on-line mass separator ISOLDE at CERN with an energy of 260 keV and a dose of 3×10^{12} cm^{-2}. The implanted ^{71}As ions end up within a Gaussian shaped profile centered at 110 nm

depth with a width of 50 nm and a peak concentration of 2×10^{17} cm^{-3}. The implantation damage was removed by annealing at 1123 K for 10 min in evacuated quartz ampoules under As atmosphere. To reduce any possible contamination during the annealing the implanted GaAs surface was protected by a second GaAs wafer acting as proximity cap. This strongly reduces the Cu contamination observed in our previous work [5]. ^{71}As transmutes via the decay chain $^{71}As_{As}$ (64 h) $\rightarrow$ $^{71}Ge_{As}$ (11.2 d) $\rightarrow$ $^{71}Ga_{As}$ to stable ^{71}Ga. The half-lives of the isotopes are given in brackets. The resulting concentrations of these isotopes as function of time can be calculated from the decay laws and are shown in Fig. 1. This transmutation was monitored by PL spectroscopy at 4.2 K where PL was excited with 690-nm light from a laser diode with a power of 5 mW (50 Wcm^{-2} excitation density).

Results and discussion

Annealing the sample immediately after the ^{71}As implantation results in the placement of all ^{71}As nuclei on As lattice sites in GaAs. During the first days after the implantation the concentration of ^{71}As is decreasing with a half-life of 64 h (Fig. 1, dashed line) and the concentration of its daughter isotope ^{71}Ge is increasing (Fig. 1, solid line). After about 5 days the concentration of ^{71}Ge starts to decrease again and after 20 days its decrease is an almost pure exponential function with a half-life of 11.2 days. Provided that the lattice site of the nucleus does not change during its chemical transmutation, $^{71}Ga_{As}$ antisite defects are formed in GaAs and their concentration increases with time as shown in Fig. 1 (dotted line). As has been shown in detail in our previous work [5], the main difference between the PL spectrum taken from an unimplanted part of the sample and the spectra of the ^{71}As doped part is the peak (e,$^{71}Ge_{As}$) at 1.479 eV due to the recombination of electrons into Ge acceptor states [6] and its LO phonon replicas. The same is the case in our new experiment (see Fig. 2). These $^{71}Ge_{As}$ acceptor states have been created by the transmutation of $^{71}As_{As}$ to $^{71}Ge_{As}$. As a reference the result of our first experiment [5] is shown in Fig. 1 where the intensity of the (e,$^{71}Ge_{As}$) recombination as function of time after doping with ^{71}As is plotted (solid circles). Within the first days after doping with ^{71}As the intensity of (e,$^{71}Ge_{As}$) increased and after 5 days it started to decrease with a half-life of 11.2 days due to the transmutation of $^{71}Ge_{As}$ to $^{71}Ga_{As}$. After 100 days practically all $^{71}Ge_{As}$ has transmuted to $^{71}Ga_{As}$ and the (e,$^{71}Ge_{As}$) intensity was as low as in the part of the sample not doped with ^{71}As which is probably due to a small contamination of the sample with stable Ge isotopes.

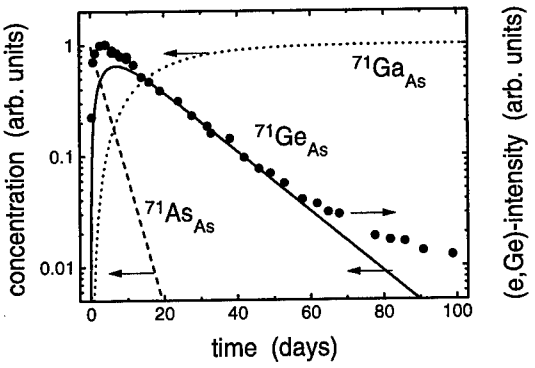

Fig. 1: Concentration of ^{71}As, ^{71}Ga, and ^{71}Ge as function of time (dashed, solid, and dotted line, respectively) resulting from the radioactive decay chain $^{71}As \rightarrow {}^{71}Ga \rightarrow {}^{71}Ge$. PL intensity of (e,Ge) recombination (solid dots) in a ^{71}As doped GaAs sample as function of time (from Ref. [5]).

The fact that the (e,$^{71}Ge_{As}$) line disappears almost totally after 100 days, both, in our first [5] and in our new experiments (Figs. 2 and 3), shows that finally all $^{71}Ge_{As}$ acceptors have transmuted to $^{71}Ga_{As}$ antisite defects. In all cases at the final state no PL line at 1.441 eV can be observed which is present in GaAs crystals grown from a Ga-rich melt [2]. This line and the corresponding 78-meV acceptor level is often assigned to Ga_{As} antisite defects. However, our results show, that this assignment is not correct and that the 78-meV acceptor level in Ga-rich GaAs belongs to another defect (a possible candidate might be B_{As} [4]). Another PL line that is also often related to Ga_{As} antisite defects and that we do not see in our samples is the 1.36-eV line [3]. Therefore, we can exclude that any of these defect lines is caused by an isolated Ga_{As} antisite.

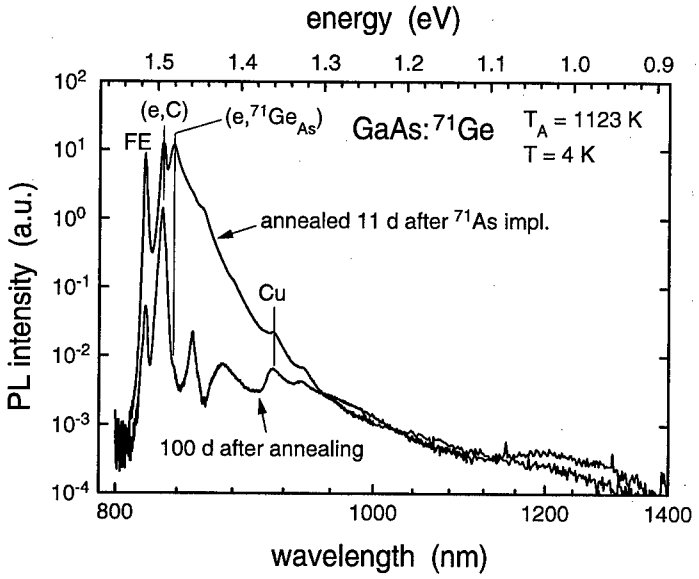

***Fig. 2:** PL spectra measured at GaAs annealed at 1123 K 11 d after ^{71}As implantation and 100 d after the annealing treatment.*

Even more puzzling is the fact, that we do not observe any new PL line appearing between 0.9 eV and 1.515 eV during the population of the Ga_{As} sites (see Fig. 2). One possible explanation is that the emission related to Ga_{As} is very weak or very broad and therefore difficult to discriminate against the background due to contaminations present in the sample, mainly C and Cu. Compared to our previous experiments [5], we have been able to enhance the annealing procedure resulting in a reduction of the PL emission due to Cu (1.36 eV) by at least a factor of 20. However, the new experiments show also no evidence for any new PL line correlated to the creation of Ga_{As}. The line at 1.425 eV which becomes visible 100 d after annealing (Fig. 2) is also seen in not implanted but annealed GaAs samples. Therefore, we attribute it to some damage due to the implantation and/or annealing procedure. A similar line (there labeled 'Q') is reported in Ref. [7] to appear after Ge implantation and annealing.

In Fig. 3a the intensity of the prominent PL lines recorded as function of time after the annealing of a GaAs sample implanted with ^{71}As is shown. This sample was annealed 8 h and the first PL spectrum was recorded 25 h after the implantation. For times longer than 20 d only the intensity of the (e,$^{71}Ge_{As}$) line shows a significant decrease with time which is due to the decay of ^{71}Ge. Surprising is the observation that the intensity of all lines is decreasing drastically within the first few days after the ^{71}As implantation. This decrease is not accompanied by the appearance and increase of any new lines. That means, new recombination pathways must have been created which either have an

energy below 0.9 eV – i.e are not observable with our setup – or which allow non-radiative transitions.

Defects responsible for such non-radiative transitions may be created by the sequence of β-decays occurring during the decay chain of ^{71}As. To check this assumption, we performed a similar experiment as shown in Fig. 3a with the only difference that the sample implanted with ^{71}As was annealed 11 d after the implantation where almost all ^{71}As atoms have already decayed to ^{71}Ge. As can be seen clearly in Fig. 3b, there is no strong reduction of the PL intensity within the first days after the annealing. This proves that the decay of ^{71}As is responsible for the previously described drastic reduction of the PL intensity.

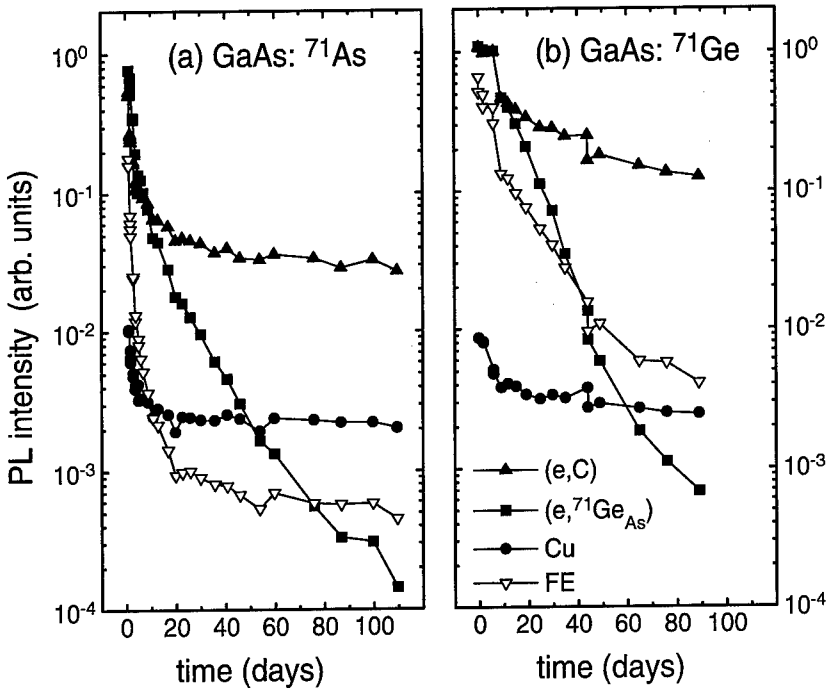

Fig. 3: (a) Intensity of the prominent PL lines as function of time after the annealing at 1123 K of a GaAs sample implanted with ^{71}As. The sample was annealed 8h and the first PL spectrum was recorded 25 h after the implantation. (b) Same as (a) but with the annealing performed 11 d after the ^{71}As implantation.

One possible explanation is the creation of lattice defects due to the emission of positrons during the decay of ^{71}As to ^{71}Ge. These positrons have a continuous energy spectrum with a maximum energy of 0.81 MeV [8]. The threshold energy for the displacement of a Ga or As atom away from its lattice site by electrons (or by the equally heavy positrons) is about 10 eV [2] which can be reached with a positron of an energy of 0.25 MeV performing a head-on collision. Such a collision can result in the creation of vacancies and interstitial atoms and there is also a certain chance to create antisite defects on both sublattices [9,10]. The emission of positrons happens for 32% of all ^{71}As decays, so the maximum total positron fluence is 1/3 of the implanted ^{71}As dose, i.e. 1×10^{12} cm^{-2}. Due to the low collision cross-section of positrons, the created defects are distributed within a depth of the sample much larger than the few microns probed by PL. The introduction rate for all kinds of defects by 1 MeV β-particles is about 5 cm^{-1} [11]. As a result of this the concentration of defects created by the positrons during the ^{71}As decay is far below the detection limit.

The other possibility for defect creation during the decay of ^{71}As is given by the fact that 68% of these decays happen by electron capture. This means that the energy gained by the decay (Q = 2.01 MeV) is totally transmitted to the simultaneously emitted neutrino. This results in a recoil energy of 30 eV transferred to the ^{71}Ge nucleus which is large enough to displace the atom from its lattice site leading to the creation of defects responsible to the observed decrease in PL intensity as shown in Fig. 3a. This kind of defect creation by neutrino recoil due to an electron capture decay has been shown by Mössbauer spectroscopy in InSb using the decay of ^{119}Te to ^{119}Sb [12] and in Ge by perturbed $\gamma\gamma$ angular correlation spectroscopy using the decay of ^{111}Sn to ^{111}In [13]. Annealing the sample directly after the ^{71}As implantation leads to the incorporation of all ^{71}As atoms on As lattice sites. However, the recoil during the decay of ^{71}As to ^{71}Ge leads to defects. On the other hand, waiting with the annealing treatment till most of the ^{71}As has decayed to ^{71}Ge allows the ^{71}Ge to be incorporated either on Ga or on As sites. If ^{71}Ge is incorporated on Ga sites it will act as donor and the resulting ^{71}Ga atoms end up on Ga sites which will have no influence on the PL spectrum. As can bee seen in Fig. 2, a large fraction of the ^{71}Ge is indeed incorporated on As sites acting as acceptors because the observed high intensity of the (*e*,Ge) line roughly corresponds to the one expected if the majority of the implanted ions ends up as ^{71}Ge acceptors.

In contrast to the results shown in Fig. 3a, the free exciton line (FE) decreases in intensity during the period of 100 d (Fig. 3b). In this experiment, the amphoteric ^{71}Ge could also occupy Ga lattice sites and acting there as donor. The (*e*,D) transition related to this level appears at almost the same energy as the free exciton line [6] and can not be separated due to the resolution of our PL setup. The decrease in intensity of the superposition line is than caused by the decay of ^{71}Ge to ^{71}Ga on Ga sites.

Finally, the recoil energy that can be transferred to the ^{71}Ga nucleus during the electron capture decay of ^{71}Ge to ^{71}Ga (Q = 0.24 MeV [8]) is 0.4 eV. This is much less then the energy necessary to displace a atom from a regular lattice site. Therefore it can be excluded that the lattice site of the nucleus changes during this decay. This together with the fact that most of the implanted ions form $^{71}Ge_{As}$ acceptors proves that after 100 d the implanted layer is doped with Ga_{As} antisite defects distributed in a Gaussian shaped profile centered at 110 nm depth with a width of 50 nm and a peak concentration of about 2×10^{17} cm^{-3} which should be easily visible by PL if they cause any PL transitions between 1.515 eV and 0.9 eV.

Conclusion

In conclusion, we have proven that implanting radioactive ^{71}As into GaAs and choosing the right timing for annealing the implantation induced defects leads to the formation of isolated $^{71}Ga_{As}$ involving most of the originally implanted ions. One explanation why we do not observe an increase in intensity of any peak due to the increase of the Ga_{As} antisite concentration with time is that Ga_{As} does not cause any PL emission between 1.515 and 0.9 eV. Another possible explanation is that the emission is either very weak or very broad making it difficult to detect. Other spectroscopic techniques like DLTS in combination with radioactive isotopes might be necessary to detect and identify the levels of Ga_{As}.

Acknowledgement

This work has been supported by the Bundesminister für Bildung, Wissenschaft, Forschung und Technologie under Grant No. 03-RE4KO1-5.

References

1. R. Magerle, A. Burchard, M. Deicher, T. Kerle, W. Pfeiffer and E. Recknagel, Phys. Rev. Lett. **75**, 1594 (1995).
2. for a short review, see J. C. Burgoin, H. J. Bardeleben, and D. Stievenard, J. Appl. Phys. **64**, R65 (1988), Section III. H, and references therein.
3. See, e.g., P. W. Yu, D.W. Fischer, and J.R. Sizelove, Semicond. Sci. Technol. **7**, 556 (1992).

4. R. C. Newman, B. R. Davidson, R. Addinall, R. Murray, J. W. Emmert, J. Wagner, W. Götz, G. Roos and G. Pensl, in: *Proc. of the 17th Intl. Conf. on Defects in Semiconductors,* ed. H. Heinrich and W. Jantsch (Mat. Sci. Forum **143-147**, Trans Tech Publications, Aedermannsdorf, 1994) p. 229.
5. R. Magerle, in: *Defects in Electronic Materials II*, ed. J. Michel, T. Kennedy, K. Wada and K. Thonke (Met. Res. Soc. Symp. Proc. Vol. **442**, Pittsburgh, 1997) p. 3.
6. *Properties of Gallium Arsenide*, EMIS Data Reviews Series No. 2, (INSPEC, The Institute of Electrical Engineers, London, 1990).
7. K.J. Keefer, Y.K. Yeo and R.L. Heneghold, J. Appl. Phys. **70**, 4634 (1991).
8. *Table of Isotopes, 7. Edition*, ed. C. M. Lederer and V. S. Shirley (Wiley, New York, 1978).
9. C,. Corbel, F. Pierre, K. Saarinen, P. Hautojärvi and P. Moser, Phys Rev. B **45**, 3386 (1992).
10. K. Krambrock, J.-M. Spaeth, C. Delerue, G. Allan and M. Lannoo, Phys. Rev. B **45**, 1481 (1992).
11. D.C. Look and J.R. Sizelove, J. Appl. Phys. **62**, 3660 (1987).
12. R. Sielemann, L. Wende and G. Weyer, Phys. Rev. Lett. **75**, 1524 (1995).
13. R. Sielemann, H. Hässlein, M. Brüssler and H. Metzner, in: *Proc. of the 16th Intl. Conf. on Defects in Semiconductors,* ed. G. Davies, G.G. DeLeo and M. Stavola (Mat. Sci. Forum **83-87**, Trans Tech Publications, Aedermannsdorf, 1992) p. 1109.

Materials Science Forum Vols. 258-263 (1997) pp. 951-956

DEFECT CONTROL IN As-RICH GaAs

P. Specht, S. Jeong*, H. Sohn, M. Luysberg, A. Prasad, J. Gebauer, R. Krause-Rehberg**, E.R. Weber**

Department of Materials Science and Mineral Engineering &
*Department of Electrical Engineering,
University of California, Berkeley. CA94720, USA

**Fachbereich Physik, Martin-Luther-Universität, D-06108 Halle, GERMANY

key words: non-stoichiometric GaAs, LT-GaAs, antisite defects, Ga vacancies, ultrafast, thermal stability

Abstract

The incorporation of excess As in GaAs, grown by MBE at low tempertures, produces native defects such as As antisites (As_{Ga}), As interstitials (As_i) or Ga vacancies (V_{Ga}). These point defects dilate the lattice. Their concentrations increase with decreasing growth temperature and can be well reproduced by a careful control of the substrate temperature and the As/Ga flux ratio. The ionized [As_{Ga}^+] equals three times the [V_{Ga}]. Therefore, V_{Ga} triple acceptors are the dominant native acceptors in LT-GaAs. The ultrafast electron trapping time, measured in LT-GaAs (< 1ps below T_G=230°C) was reported to correlate to [As_{Ga}^+]. In undoped LT-GaAs, however, the [As_{Ga}^+] does not exceed 10% of the total concentration of As_{Ga}.

We studied high p-doping with Be acceptors in order to achieve a larger ionization fraction of the As_{Ga}. As a result we developed thermally stable, non-stoichiometric GaAs with subpicosecond trapping times, grown at T=275°C. The ratio [As_{Ga}^+]/[As_{Ga}] was found to exceed 50%. However, in LT-GaAs:Be carrier capture at As_{Ga}^+ is not the only trapping mechanism, it´s concentration is neither correlated to the [Be] nor to the measured trapping times.It is suggested that additional carrier capture by doubly ionized As_{Ga}^{++}, is taking place, caused by the lowered Fermi level due to Be-doping. The strain compensation of the large As_{Ga} defects with the small Be_{Ga} acceptors enhances the thermal stability of the native point defects. Therefore, the thermally more stable LT-GaAs:Be offers new prospects for the application of As-rich GaAs in ultrafast optoelectronics.

Introduction

In 1988 Smith et al. were the first to report the growth of GaAs at low temperatures (200°C) for buffer layer application [1]. This highly non-stoichiometric GaAs offers as well unique applications in optoelectronic devices, because the material exhibits ultrafast trapping characteristics. This materials property relates to a supersaturation of native defects that increases the lattice constant with decreasing MBE growth temperature. In GaAs grown by MBE at temperatures near 200°C (LT-GaAs) we found with magnetic resonance and optical absorption spectroscopies neutral As_{Ga}^0 and ionized As_{Ga}^+ in concentrations up to $10^{20}cm^{-3}$ and $10^{18}cm^{-3}$ respectively [2]. As a result homoepitaxially grown LT-GaAs is tetragonally distorted (pseudomorphic growth) [3]. The incorporation of excess As can reach 1.5% [4]. The crystal quality of the highly non-stoichiometric layers is remarkably good, no extended defects (dislocations, stacking faults, precipitates) are usually found in the as-grown material [2], as long as a certain critical layer thickness that depends on the growth temperature is not exceeded. The lattice expansion was described by a linear relation between the antisite concentration [As_{Ga}^0] and the lattice mismatch $\Delta d/d$ [5].

Most of the excess As precipitates to form As clusters or diffuses out of the layer upon annealing at temperatures above 400°C [6,7] and the lattice mismatch to the substrate vanishes. This thermal

instability entails the necessity of growing diffusion barrier layers, because the As outdiffusion may be detrimental for neighbouring layers in device structures. Non-stoichiometric GaAs shows ultrashort trapping times (< 1ps) below a growth temperature of T_G=230°C. Because the trapping times correlate with the concentration of ionized As_{Ga}^+ [8], we introduced high Be-doping (> $10^{19}/cm^3$) in order to enhance the amount of As_{Ga}^+.

Experimental

As-rich GaAs layers were grown by molecular beam epitaxy using a Varian Gen II MBE system. (100) n^+-GaAs substrates (AXT, epi-ready) were wire mounted to a specific molybdenum block. The substrate temperature reading for the low temperature range was realized by a precision temperature measurement system (Thermionics). The system utilizes the diffused reflectance spectroscopy (DRS). Details are given elsewhere [9].All growth temperatures quoted in this paper were established by DRS. 1.5μm to 2.0μm thick LT-GaAs layers were deposited at a growth rate of 1μm/h. The beam equivalent pressure (BEP) ratio was kept at a value of 20 (As/Ga flux ratio ≈ 1.7).

Be concentrations were measured by SIMS. Native point defect concentrations were obtained by near-infrared absorption (NIRA: $[As_{Ga}^0]$), magnetic dichroism of absorption (MCDA: $[As_{Ga}^+]$) and slow positron annihilation ($[V_{Ga}]$) (see [10,11] for details). The lattice mismatch parallel to the growth direction (Δd/d) was measured by x-ray diffraction (XRD) using the (004) reflection. A TEM analysis was performed on as-grown and annealed material to study the structural properties. The time resolved reflectivity transients were recorded in a pump-probe laser pulse experiment. The used laser operated at a wavelength of 800nm, 100fs short pulses were repeated at a frequency of 100MHz. The recorded data could be modeled by two exponential decays, providing two time constants. The shorter time constant is influenced by the experimental resolution, but may contain as well carrier thermalization effects in the conduction band. Carrier trapping times, given in this paper, referred to the longer time constant. Carrier trapping times above 0.1ps can be reliably resolved.

Results

GaAs and LT-GaAs

The $[As_{Ga}^0]$ amounts to $10^{20}/cm^3$ in a sample grown at 200°C. This causes a lattice mismatch of Δd/d=0.12%. In contrast the lattice constant of a Be-doped sample, $[Be]=7*10^{19}/cm^3$, grown at T_G=600°C amounts to Δd/d= -0.032%. Therefore the incorporation of excess As in LT-GaAs causes a lattice expansion, while a Be incorporation in GaAs contracts the lattice. Consequently an incorporation of Be into LT-GaAs should compensate strain.

Figure 1 shows the concentration of Gallium vacancies $[V_{Ga}]$ in as-grown LT-GaAs, measured by slow positron annihilation, compared with the $[As_{Ga}^+]$. A factor 3 takes into account that each V_{Ga} can accommodate three electrons. The concentrations are equal within experimental errors. The $[V_{Ga}]$ decreases with increasing growth temperature similarly to the $[As_{Ga}]$ [4]. It is evident, that after annealing at 600°C, single V_{Ga} cannot be detected any longer. However, vacancy clusters may still be present.

LT-GaAs:Be

Figure 2 depicts the lattice mismatch in LT-GaAs:Be, grown at two different temperatures and a Be concentration between $7*10^{19}/cm^3$ and $5*10^{20}/cm^3$. We compare as-grown samples (full columns) with samples that were post-growth annealed at 600°C for 10 minutes (textured columns). In all cases the Be-doping levels were large enough to compensate the positive lattice mismatch, caused by the presence of the As_{Ga} defects. Upon thermal annealing the lattice mismatch in LT-GaAs is been

completely removed. In contrast, the annealing procedure has hardly any effect on the lattice constant of LT-GaAs:Be, just a slight increase of the (negative) $\Delta d/d$ is observed in the layer structure, grown at 240°C with [Be]= $7*10^{19}/cm^3$. Small precipitates were observed in all samples, grown at 240°C, upon thermal annealing, but no precipitate formation occurred in the Be-doped sample, grown at 275°C.

In Fig. 3 the neutral and singly charged antisite concentrations are given for LT-GaAs (white columns) and LT-GaAs:Be (gray columns) with a [Be]= $7*10^{19}/cm^3$ (as-grown: full columns, annealed: textured columns). These concentrations dropped below the detection limit, when the Be concentration exceeded $10^{20}/cm^3$. We assume that the As_{Ga} in these cases are doubly charged, however, for the time being we cannot determine the [As_{Ga}^{++}]. Therefore in Fig. 3 the total amount of As_{Ga} consists of [As_{Ga}^{0}] and [As_{Ga}^{+}] only. A steep increase in the antisite concentration was observed upon Be-doping in both the ionized [As_{Ga}^{+}] and the total [As_{Ga}]. The fraction of [As_{Ga}^{+}] / [As_{Ga}] increased from about 5% in undoped layers to more than 50% in the Be-doped layers. In the sample, grown at 275°C, both concentrations remained constant upon thermal annealing.

Ultrashort carrier trapping times were expected in LT-GaAs:Be because of the high concentration of ionized antisites. In Fig. 4 the trapping times obtained from time resolved reflectivity transients are shown for as-grown samples of different Be concentrations (T_G=240°C). We observed a strong reduction in carrier trapping time with increasing [Be]. The carrier trapping did not change significantly upon thermal annealing. The response time of the thermally stable Be-doped LT-GaAs, grown at 275°C, was determined to be

$$\tau = (0.3 \pm 0.1)\ ps$$

This result shows that subpicosecond carrier trapping times can be achieved at higher growth temperatures than T_G=230°C. Furthermore, highly non-stoichiometric GaAs could be thermally stabilized by Be-doping and no precipitates are found upon annealing.

Discussion

Mechanical compensation

Strain induced by substitutional point defects can be expressed by the following equation:

$$\varepsilon = \mathbf{b}\,C \qquad \text{(Vegard's law, Eq. 1)}$$

Here $\varepsilon=\Delta a/a=\Delta d/d$ for an isotropically expanded or compressed lattice, C stands for the point defect concentration and the coefficient b can be derived to be

$$\mathbf{b = 1/3\ [(r_S/r_H)^3 - 1]\ N^{-1}} \qquad \text{([12], Eq. 2)}$$

, with N: number of lattice sites in the observed lattice, r_H: covalent radius of host atom, r_S: covalent radius of solute atom.

For the pseudomorphically grown thin layers the tetragonal distorted lattice mismatch $\Delta d/d$ has to be corrected by a factor p, including the elastic constants of the lattice. The isotropic lattice mismatch $\Delta a^*/a^*$ corresponds to the measured $\Delta d/d$ according to:

$$\mathbf{\Delta d/d = 1/p * \Delta a^*/a^* = \varepsilon^*/p} \qquad \text{(Eq. 3)}$$

with $p(GaAs_{001}) = c_{11}/[c_{11} + 2\ c_{12}] = 0.524$, using the elastic constant measurements in [13]. It is worth noting that this calculation for the radius of the solute atom does not consider the concept of volume conservation, but involves the elastic response of the lattice. With $N = 2.2*10^{22}/cm^3$ for the number of sites in the Ga-sublattice and $r_H = 0.245nm$, we calculated the bond lengths of As_{Ga}-As and Be_{Ga}-As to

$$\mathbf{r_{As(Ga)} = 0.275nm} \quad \& \quad \mathbf{r_{Be(Ga)} = 0.231nm}$$

These values were calculated with the assumption, that the elastic constants and the thermal expansion coefficients of LT-GaAs are equal to them for GaAs. The difference of the As_{Ga}-As to the

Ga-As bond length amounts to 12%. Landman et al. obtained in recent first principle calculations the increase in bond length to 9% for the As antisite and to 12% for an As split interstitial [14], which is in reasonable agreement with our experimental data. With the known lattice expansion and contraction, caused by the As_{Ga} and Be_{Ga}, respectively, the lattice mismatch, observed in highly Be-doped LT-GaAs cannot be described. An obvious explanation is to assume a different covalent radius for the different charge states of the As antisites and a considerable amount of As_{Ga}^{++} to be present in the highest doped LT-GaAs:Be. Because of their small fraction, ionized antisite defects will not influence the lattice constant in LT-GaAs, but can explain the effects in LT-GaAs:Be. Of course, defect complexes might have to be taken into consideration as well. Further investigations are necessary to describe the observed effects in highly doped LT-GaAs:Be.

The thermal stabilization of the As antisites seems to be promoted by strain compensation. The compensation leads to an increase in the incorporation of both As_{Ga} and Be. In GaAs, grown at standard temperatures, a surface roughening, accompanied by a transition from 2D to 3D growth mode is observed, when the [Be] exceeds $2*10^{20}/cm^3$. In contrast, LT-GaAs:Be was grown with twice that concentration without any signs of growth mode transition. In this way the LT-GaAs is an ideal material for achieving highest doping levels. However, the electrical activity might remain poor because of electrical compensation effects from the high native point defect concentration. However, the controlled introduction of impurities can be exploited to achieve specific material properties like the carrier trapping time.

Electrical compensation

In contrast to the native V_{Ga} acceptors, the Be acceptors change the ratio of ionization for As_{Ga} drastically as described above. Assuming full compensation we expect that in the stabilized LT-GaAs:Be a fraction of $[As_{Ga}^{++}]$ must be present as well to account for the difference between [Be] and $[As_{Ga}^{+}]$ in the sample, grown at 275°C. The effect of electrical compensation on the thermal stabilization is unclear because at present we cannot distinguish it from strain compensation effects. With the increased ionization, however, we achieved ultrashort trapping time in LT-GaAs:Be, grown at 275°C. The ultrashort trapping times do not correlate with $[As_{Ga}^{+}]$ or [Be], which is to be expected when assuming a second trapping mechanism by As_{Ga}^{++}. Therefore, a more complex model for the carrier trapping has to be developed for non-stoichiometric GaAs:Be.

Acknowledgments

This work was supported by the Air Force Office of Scientific Research under grant No. F49620-95-100091. For the MBE growth the facilities of the integrated materials laboratories, IML of the UC Berkeley were used. The authors thank A. Mueck for performing the SIMS measurements as well as R. Lutz and C. Kisielowski for fruitful discussions.

References

1. F. Smith, A. Calawa, Appl. Phys. Lett. **42**, 818 (1988)
2. M. Luysberg, H. Sohn, A. Prasad, P. Specht, Z. Liliental-Weber, E.R. Weber, submitted to J. Appl. Phys.
3. C.R. Wie, K. Xie, D.C. Look, K.R. Evans, C.E. Stutz, in "Proc. of Semi-Insulating III-V Materials", eds. A. Milnes & C.J. Miner (Hilger, Bristol, 1990) p.71
4. K.M. Yu, M. Kaminska, Z. Liliental-Weber, J. Appl. Phys. **72**, 1850 (1992)
5. X. Liu, A. Prasad, J. Nishio, E.R. Weber, Z. Liliental-Weber, W. Walukiewicz, Appl. Phys. Lett. **67**, 279 (1995)

6. Z. Liliental-Weber, A. Claverie, J. Washburn, F.W. Smith, A.R. Calawa, Appl. Phys. A **53**, 141 (1991)
7. K. Mahalingam, N. Otsuka, M.R. Melloch, J.M. Woodall,A.C. Warren, J. Vac. Sci. Technol. B **9**, 2328 (1991)
8. Z. Liliental-Weber, J. Ager III, D. Look, X.W. Lin, X. Liu, J. Nishio, K. Nichols, W. Schaff, W. Swider, K. Wang, J. Washburn, E.R. Weber, J. Whitaker, in: "Proc. of the 8th Conf. on Semiinsulating III-V Materials", ed. M. Godlewski (World Scientific, 1994) p.305
9. P. Specht, H. Sohn, M. Luysberg, E.R. Weber, to be published
10. X. Liu, A. Prasad, W.M. Chen, A. Kurpiewski, Z. Liliental-Weber, E.R. Weber, Appl. Phys. Lett. **65**, 3002 (1994)
11. J. Gebauer, R. Krause-Rehberg, S. Eichler, M. Luysberg, H. Sohn, E.R. Weber, submitted to Appl. Phys. Lett.
12. C. Kisielowski, J. Krueger, S. Ruvimov, T. Suski, J.W. Ager III, E. Jones, Z. Liliental-Weber, M. Rubin, E.R. Weber, M.D. Bremser, R.F. Davis, Phys. Rev. B **54**, 17745 (1996)
13. M. Krieger, H. Sigg, N. Herres, K. Bachem, K. Koehler, Appl. Phys. Lett. **66**, 682 (1995)
14. J.I. Landman, C.G. Morgan, J.T. Schick, P. Papoulias, A. Kumar, Phys. Rev. B, accepted for publication
15. D.E. Bliss, W. Walukiewicz, K.T. Chan, J.W. Ager III, S. Tanigawa, E.E. Haller, Mat. Res. Soc. Symp. Proc. **241**, 93 (1992)

Figures

Fig. 1: Vacancy concentration in As-rich GaAs, determined by slow positron annihilation compared to 1/3 of the [As_{Ga}^{+}] concentration

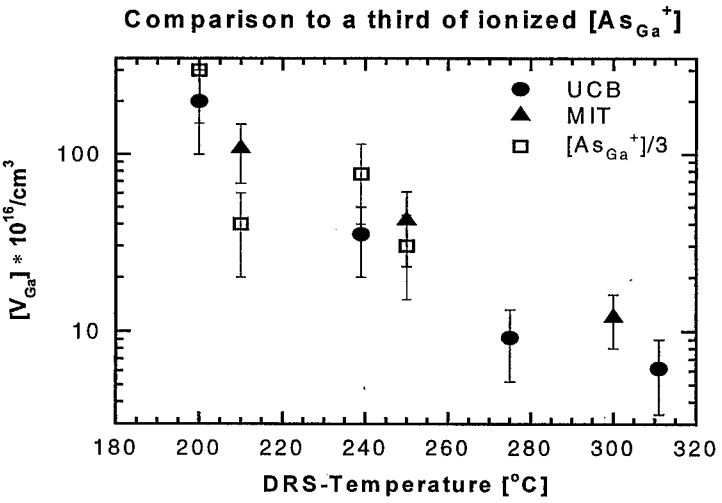

Fig. 2: Lattice Mismatch of LT-GaAs:Be

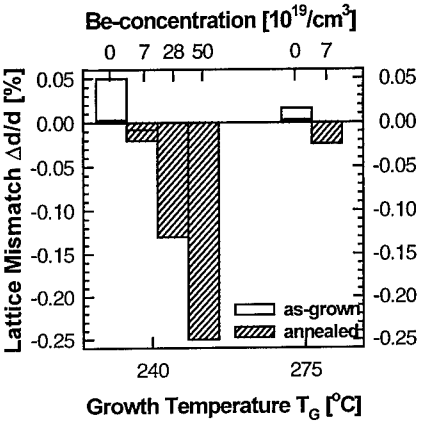

Fig. 4: Reduction in trapping time versus [Be] measured by time-resolved reflectivity

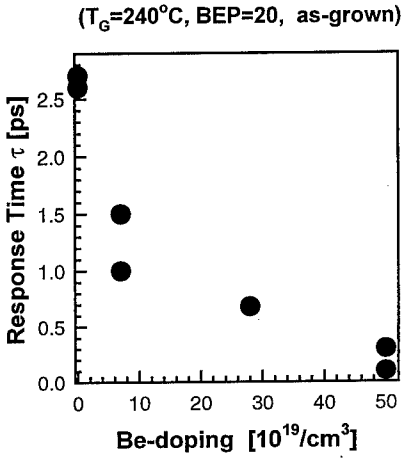

Fig. 3: $[As_{Ga}]$ and $[As_{Ga}^{+}]$ dependent on [Be] and growth temperature T_G

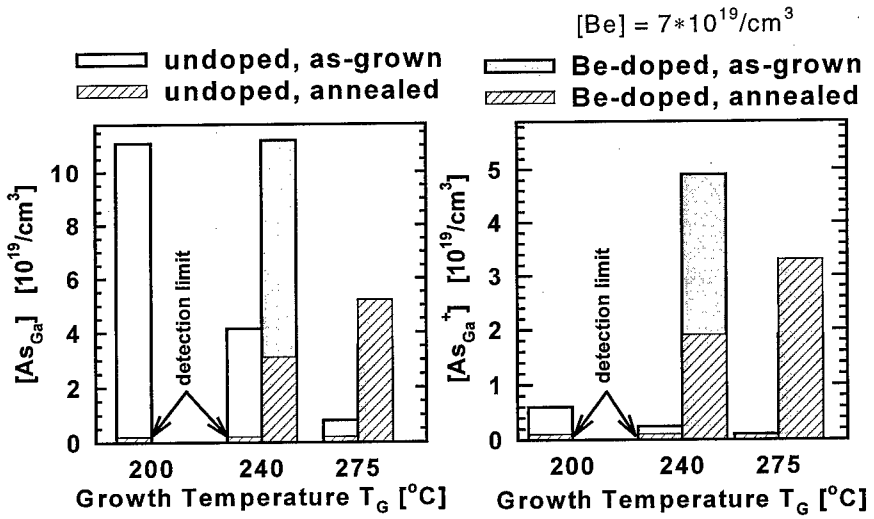

Materials Science Forum Vols. 258-263 (1997) pp. 957-962

As ANTISITE-RELATED DEFECTS DETECTED BY SPIN-DEPENDENT RECOMBINATION IN DELTA-DOPED (Si) GaAs GROWN BY MBE AT LOW TEMPERATURE

K. Krambrock, M.V.B. Pinheiro and S.M. Medeiros

UFMG, Departamento de Física, ICEx, C.P. 702, 30161-970 Belo Horizonte, MG, Brasil

Key words: intrinsic defects, antisite, GaAs, MBE, EDMR, SDR

Abstract

Investigations of electrically detected magnetic resonance (EDMR) in a delta-doped (Si) GaAs sample grown by the molecular beam epitaxy at 300^{0}C (LT-MBE) in a (311)-A direction have shown the signals due to an arsenic antisite-related defect. The sample consists of a planar-doped region with a two dimensional Si concentration of about N_{2D} = 3.4 x 10^{12} cm^{-2} buried within a 1.2 μm thick MBE GaAs layer grown at 300^{0}C. The observed EDMR spectrum shows the well-known quartet hyperfine split spectrum of an As antisite-related defect with a g-factor of 2.045 ± 0.01 and an isotropic hyperfine interaction due to ^{75}As (I = 3/2) with a magnitude of (2600 ± 100) MHz. The spin Hamiltonian parameters are very similar to those for the EL2 defect observed in bulk GaAs, however, like the As antisite-related defects measured by optically detected magnetic resonance (ODMR) in LT-MBE GaAs, the metastable defect transition induced by light of energy below the bandgap is suppressed. We propose a spin-dependent hopping process between the As antisite-related defects to explain the observation of the EDMR signal.

Introduction

Delta doping of semiconductors that is now possible by epitaxial growth using molecular beams, has attracted much interest because of the study of low dimensional structures which show a quasi two-dimensional electron gas with new interesting physical applications [1,2]. Some of the applications are, for example, new tunable laser systems [3] or delta doped FET structures [4].

MBE GaAs grown at low substrate temperatures is known to contain high concentrations of As antisite-related defects. In samples grown at 200^{0}C, concentrations up to 10^{20} cm^{-3} have been observed by various experimental techniques such as optical absorption [5], conventionally detected EPR [6] and optically detected EPR (ODEPR) [7]. In all these studies it has been found that the metastable transition of the As antisite defects under sub-bandgap light is suppressed. In contrast to these studies, electrical transport measurements under illumination have detected huge metastable effects using below sub-bandgap light in delta-doped MBE GaAs [8,9]. The origin of these illumination effects is not yet clear and is still controversial.

Motivated by the discussion about the origin of the strong effect of below bandgap light in the electrical transport properties of delta-doped GaAs, we have studied a delta-doped MBE GaAs sample grown at 300^{0}C with a nominal two-dimensional Si concentration of 3.4 x 10^{12} cm^{-2} by electrically detected electron paramagnetic resonance (EDMR) in order to find whether or not As antisite-related defects could be responsible for the observed

metastable effects at low temperatures observed in photo-conductivity and photo-Hall experiments [8,9].
Another motivation for our work is that there are only a few published studies about the application of EDMR in semiconductor compounds with a direct energy gap [10,11]. The first electrical detection of electron paramagnetic resonance goes back to 1966, involving a study of phosphorus donors in the indirect gap semiconductor silicon [12]. In the following years this technique has been applied to a variety of different semiconductors and semiconductor devices [13]. However, there is no conclusive model about the recombination mechanisms involved in the electrical detection of EPR. In this paper we report about the detection of an As antisite-related defect by EDMR in a delta-doped (Si) LT-MBE GaAs sample and compare our results with ODEPR measurements of As antisite-related defects in LT-MBE GaAs layers grown at different temperatures.

Experimental Setup

To measure EDMR we used a modified EPR X-band spectrometer working at 9.3 GHz and a continous flow He cryosystem (Oxford). A cylindrical cavity with optical windows allowed in-situ illumination of the samples. The modulation frequency for the magnetic field could be varied between 0.5 and 120 kHz. Instead of a magnetic field modulation, the microwave amplitude could be modulated by a PIN diode in the same frequency range. For the electrical measurements a constant current was applied to the sample and the change of the voltage or photo-voltage was measured under resonant microwave transitions with a home-made variable gain amplifier and lock-in detection.

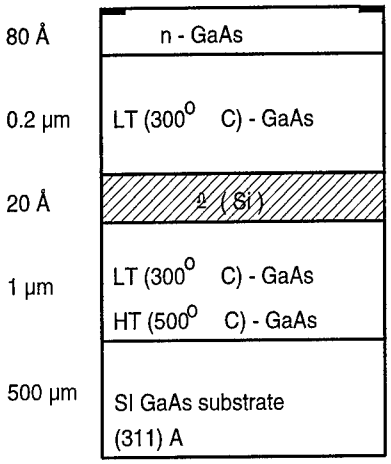

Fig. 1: Delta doped LT-MBE GaAs with a nominal Si concentration of 3.4 10^{12} cm^{-2}. The delta doped region is embedded in 1.2 µm of MBE GaAs grown at 300°C.

The investigated delta doped GaAs sample was grown by MBE on a semi-insulating (SI) GaAs substrate with a (311)-A orientation (fig. 1). The starting temperature for the MBE growth was 500°C, but it was then reduced to 300°C until completed about a 1 µm undoped GaAs layer had been grown. After that, without interrupting the growth process, a 20 Å thick Si delta doped layer was grown and an additional 0.2 µm layer of undoped GaAs at 300°C. Finally, the growth was terminated with a 80 Å thick n^+-type cap layer.
Electrical contacts were produced by soldering In at 200°C on two corners of the sample without diffusion of the In at higher temperatures, in order not to alter the characteristics of the LT-MBE sample.

Experimental Results

At 5 K, a four-line spectrum was observed by electrically detected EPR which is shown in fig. 2. The EDMR signal was detected under continous illumination with white light. By applying a constant current in the range of 0.5 - 5 µA, with a magnetic field modulation of 2

kHz we were able to detect the EDMR signal. The EPR resonance is the typical quadruplet fingerprint of an As antisite-related defect with an isotropic g-factor of 2.045 ± 0.01 and a hyperfine splitting of a = 2600 ± 100 MHz due to ^{75}As with I = 3/2 and 100% abundance, as for the EL2 defect observed in bulk GaAs. However, the EPR signal is stable for hours under white light illumination, indicating that the metastable transition of the As antisite-related defect is suppressed.

The EDMR resonance has been detected as a relative change of the photo-voltage of the order of $\Delta V/V$ about 10^{-6} in agreement with earlier studies done in LT-MBE GaAs [10]. However, in contrast to these studies the EDMR resonance is observed as an enhancement of the photo-voltage. The lineshapes of the resonance lines are not derivative-like as expected for a field modulation of EPR. Reasons for this might be the low modulation field amplitude available at 2 kHz and fast spin-lattice relaxation times.

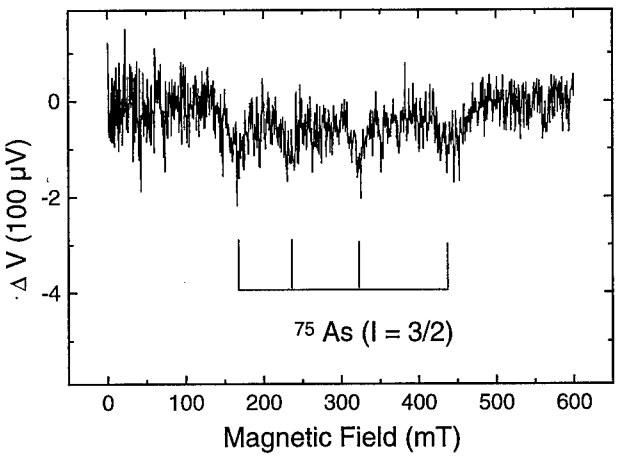

Fig. 2: EDMR spectrum of the delta doped LT-MBE GaAs sample measured at 5 K and 9.4 GHz with a microwave power of about 100 mW under illumination with white light. The spectrum was recorded with a field modulation of 2 kHz and an applied constant current of 2 μA. The observed signal was measured as a change of the photo-voltage with a relative change of the order 10^{-6}.

However, with a standard 100 kHz modulation the As antisite resonance was not observed. The reason is not yet clear. ODMR experiments via the magnetic circular dichroism in LT-MBE GaAs have shown that the spin lattice relaxation times of the As antisite-related defects are shorter than 20 ms at 1.5 K and 4.2 K, i.e. strongly reduced compared with the native EL2 defects which have relaxation times of 5 s at 1.5 K [7].

Fig. 3 shows the ODMR spectra of two LT-MBE GaAs samples grown at 200^{0}C and 400^{0}C without delta doping measured via the MCDA in a K-band (24 GHz) spectro-meter at 1.5 K. The ODMR spectrum observed in the sample grown at 200^{0}C is identical to the one observed by EDMR in the delta doped sample grown at 300^{0}C (fig. 2). In ODMR experiments the sample grown at higher temperatures (400^{0}C) shows another As antisite-related defect with a reduced ^{75}As hyperfine structure. The g-factor is 2.03 ± 0.01 and the isotropic hyperfine constant a is (2300 ± 70) MHz, i.e. 12 % reduced in comparison to the As antisite-related defect measured in the sample grown at 200^{0}C. The As antisite-related defects with the reduced hyperfine structure do not show any metastable transfer under sub-bandgap illuminations at low temperature. Optical absorption measurements of the MBE layer grown at 400^{0}C did not show conclusive evidence for the presence of As antisite-related defects in

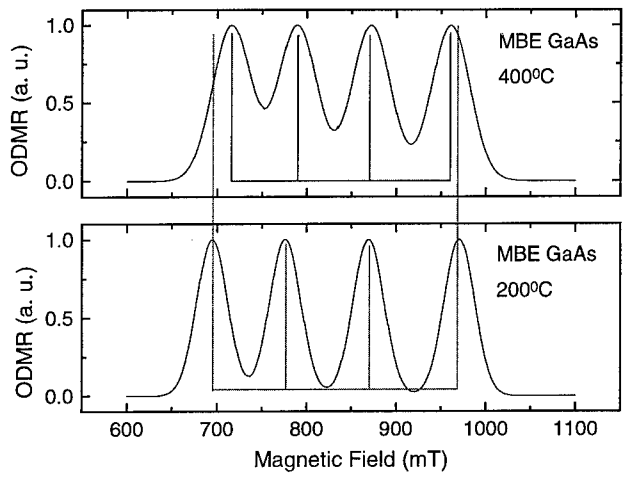

Fig. 3: ODEPR spectra of LT-MBE grown at 200°C and 400°C undoped GaAs Layers measured at 24.0 GHz and 1.5 K.

their neutral charge state. If As antisite-related defects are present their concentrations must be lower than 1 x 10^{18} cm^{-3}, the detection limit for a 2 μm thick layer, i.e. at least two orders of magnitude lower than in the samples grown at 200°C. Arsenic antisite-related defects with reduced hyperfine structure were only observed in samples where the Fermi level is close to the conduction band [7].

Discussions

The epitaxial growth of MBE GaAs can be separated in three temperature regions: (I) low temperature (200 - 300°C), (II) intermediate temperature (300-450°C) and (III) the normal high temperature growth (450 - 600°C). From ODMR investigations the first class of samples (I) shows high concentrations up to 10^{20} cm^{-3} of As antisite-related defects [10]. Their EPR parameters are practically identical to native EL2 defects observed in bulk GaAs. However, some properties are different to native EL2, that is the non-observation of the metastable defect transition at low temperatures under sub-bandgap light, the failure to detect the ZPL (zero phonon line) in optical absorption measurements and the strongly reduced spin lattice relaxation time. All these differences have been explained by the high concentration of these defects and strains in the samples [6,7]. Hall effect measurements showed that the dominant deep donor is located at 0.65 eV below the conduction band, i.e. 100 meV closer to the conduction band compared to native EL2 defects [14]. Hopping transport within the As antisite-related defects has been observed of both types with nearest neighbor hopping at higher temperatures and variable range hopping at lower temperatures [15].

The second class (II) of samples belong to intermediate growth temperatures. In these samples ODMR investigations revealed an As-antisite-related defect with a strongly reduced hyperfine structure compared to native EL2 defects [7]. Hall effect measurements have shown that the Fermi level in these type of samples lies closer to the conduction band in comparison to type (I) samples. Also, these type of As antisite-related defects with the reduced hyperfine structure are detected when the Fermi level is closer to the conduction band [7]. About the third class of HT-growth (III) only little is known about the presence of intrinsic defects. Their concentrations are strongly reduced, i.e. about 10^{12} cm^{-3} [14].

The delta-doped (Si) GaAs sample studied in this work belongs to type (I) samples, i.e. samples grown at low temperatures. The defect properties in the layer around the delta doped region should not be different from samples without the planar-doped region. In fact, our EDMR results demonstrate that As antisite-related defects are present, with properties similar

to the ones observed by ODMR via the MCDA, i.e. the same EPR parameters as for native EL2 defects. Like the ODMR detected As antisite-related defects in MBE samples of type (I), the metastable defect transition as known for native EL2 defects is suppressed for the EDMR detected As antisite - related defects in the delta-doped samples.

These results have an important influence on the interpretation of photo-conductivity and photo-Hall measurements in the same type of samples [8, 9], where huge metastable effects have been observed by sub-bandgap light illuminations at low temperatures. From the present data it seems very unlikely that the observed metastable effects in the transport measurements are related to a metastability of the antisite defects. More likely is a model in which the persistent effects under sub-bandgap light at low temperatures are related to the spatial separation of free carries, a model which have been proposed by the same authors to explain the n to p-type transition in these type of delta doped MBE GaAs samples [8]. In this model one channel is formed by the n-type delta-doped region and the other by a p-type channel near the surface [8]. Our observations suggest that also the metastable effects under below bandgap light illuminations are related to the spatial separation of free carriers which cannot recombine at low temperatures. However, a careful analysis of the sample and electrical contact preparations should be carried out because it is known that annealing of LT-MBE samples can alter the electrical properties strongly as well as metastable effects under illuminations. Further, if we assume a concentration of As antisite-related defects of the order 10^{20} cm^{-3}, the antisite-defects in the LT-GaAs layer should still dominate the electrical properties of the LT-MBE sample and not the delta-doped region. Scaling of the nominal two-dimensional Si concentration for three dimensions according to $N_{3D} = (N_{2D})^{3/2}$ lead to a concentration of 6.3 x 10^{18} cm^{-3}, i.e. still a factor of 50 lower than the concentration of antisite defects. More theoretical work and carefully planned experiments seem necessary to understand such persistent effects. It is certain, that the As anitiste-related defects can act as sources for electrons and holes under illumination, depending on the compensation of the samples, i.e. more electrons are produced in low compensated samples and more holes in highly compensated samples [16].

Other discussion is related to the observation of the As antisite-related defects by the electrically detected EPR. The results indicate that the As antisite-related defects are involved in the recombination processes, which should be spin-dependent. A deep donor -acceptor recombination is not very likely to explain the observation of As antisite resonance by EDMR, as found for an As antisite-related defect in electron irradiated GaAs via the deep photo-luminescence signal [17]. For the observation of the EDMR signal in LT-MBE GaAs we suggest a model in which spatial separated As antisite-related defects are responsible for the electrical detection via a hopping process in the deep donor band. Hopping conduction via As antisite-related defects has been observed in LT-MBE GaAs either as nearest neighbor hopping, which causes the low resistivity of the samples at 300 K or as variable range hopping [15]. In both cases, two spatially separated antisite defects, one in the neutral, the other in the paramagnetic charge state could lead to the spin-dependent recombination process. Under illumination by white light, both photoionization processes $As_{Ga}^{0} + h\nu \Rightarrow As_{Ga}^{+} + e^{-}_{cb}$ and $As_{Ga}^{+} + h\nu \Rightarrow As_{Ga}^{0} + h^{+}_{vb}$ can occur. Whether spin-polarization effects play a role in the detection mechanism, which could account for the relatively small photo-conductivity change, is not clear at the moment. Here, the EDMR signal amplitude should be proportinal to $(B/T)^2$. Further studies in different samples are planned to clarify the detection mechanism of EDMR in LT-MBE GaAs.

Conclusions

EDMR experiments in a delta-doped (Si) LT-MBE GaAs sample grown at 300^0C revealed spectra due to an arsenic antisite-related defect. The sample consisted of a planar-doped region with a two dimensional Si concentration of about $N_{2D} = 3.4 \times 10^{12}$ cm^{-2} buried within a 1.2 μm thick MBE GaAs layer grown at 300^0C. The spin Hamiltonian parameters were very similar to those for the EL2 defect observed in bulk GaAs, however, as for the As antisite-related defects measured by optically detected magnetic resonance (ODMR) in LT-MBE GaAs, the metastable defect transition induced by light of energy below the bandgap was suppressed. We suggest a spin-dependent hopping process between the As antisite-related defects to explain the observation of the EDMR signal.

Acknowledgments

We are grateful to acknowledge A.G. de Oliveira and M.V.Baeta Moreira for providing the delta doped LT-MBE sample and J.G. de Nascimento for development of the high impdedance amplifier. This work has been partly be supported by the Brazilian Foundations FAPEMIG and CNPq and the German Agency Deutsche Forschungsgemeinschaft in project no. Kr 1426/3-1.

References

[1] A. Zrenner, H. Reisinger, F. Koch and K. Ploog, in *Proc. 17th Int. Conf. on Phys. of Semicond.*, eds. J.D. Chadi and W.A. Harrison, Springer Berlin, p. 325 (1985).
[2] T.E. Whall, in *Contempory Physics*, vol. 33, p. 369 (1992).
[3] E.F. Schubert, Surf. Sci., 228, 240 (1990).
[4] K. Ploog, M. Hauser and A. Fischer, Appl. Phys. A, 45, 233 (1988).
[5] M.O. Manasreh, D.C. Look, K.R. Evans and C.E. Stutz, Phys. Rev. B, 41, 10272 (1990).
[6] M. Kaminska, Z. Liliental-Weber, E.R. Weber, E. George, J.B. Kortright, F.W. Smith, B.-Y. Tsaur and A.R. Calawa, Appl. Phys. Lett., 54, 1881 (1989).
[7] K. Krambrock, M. Linde, J.-M. Spaeth, D. C. Look, D. Bliss and W. Walukiewicz, Semicond. Sci. Technol., 7, 1037 (1992).
[8] A.G. de Oliveira, G.M. Ribeiro, D.A.W. Soares, J.A. Corrêa Filho, M.I.N. da Silva and H. Chacham, J. Appl. Phys., 78, 2659 (1995).
[9] M.I.N. da Silva, A.G. de Oliveira, G.M. Ribeiro, R.M. Rubinger, J.A. Corrêa F. and M.V. Baeta Moreira, submitted to J. Appl. Phys. (1997).
[10] N.M. Reinacher, M.S. Brandt and M. Stutzmann, Mat. Sci. Forum, vol. 196-201, p. 1915 (1995).
[11] M. Dobers, K.v. Klitzing, J. Schneider, G. Weimann and K. Ploog, Phys. Rev. Lett., 61, 1650 (1988).
[12] J. Schmidt and I. Solomon, Comptes Rendus, 263 B, 169 (1966).
[13] S. Greulich-Weber, Mat. Sci. Forum, vol. 143-147, 1337 (1994).
[14] D.C. Look, Thin Solid Films, 231, 61 (1993).
[15] D.C. Look, Z.-Q. Fang, J.W. Look, J.R Sizelowe, J. Electrochem. Soc., vol. 141, p. 747 (1994).
[16] K. Krambrock, C. Corbel and J.-M. Spaeth, submitted to Phys. Rev B (1997).
[17] J. Weber and G.D. Watkins, J. Phys. C, 18, L269 (1985).

Materials Science Forum Vols. 258-263 (1997) pp. 963-968

ELECTRICALLY DETECTED MAGNETIC RESONANCE AT DIFFERENT MICROWAVE FREQUENCIES

M. S. Brandt, M. W. Bayerl, N. M. Reinacher, T. Wimbauer, M. Stutzmann

Technical University of Munich, Walter Schottky Institute, Am Coulombwall, D-85748 Garching, Germany

Keywords: electrically detected magnetic resonance, a-Si:H, GaAs

ABSTRACT

Using microwave frequencies of 434 MHz, 9 and 34 GHz, the signal intensity of electrically detected magnetic resonance (EDMR) in amorphous hydrogenated silicon (a-Si:H) is found to be independent of the size of the Zeeman-level splitting. Taking into account the broadening of the resonance linewidth under strong saturation, the signal intensity follows the same dependence on the microwave field H_1 irrespective of the frequency used. In GaAs, both the microwave power dependence and the temperature dependence of EDMR (As_{Ga} antisite and Cr) has been investigated at 9 GHz. Below 10K, no significant dependence of the signal intensity on temperature was found. At higher temperatures, the signal intensity rapidly decreases due to the changes in the spin relaxation.

INTRODUCTION

The use of electrically detected magnetic resonance (EDMR) is being extended from its application to bulk semiconductors to the study of actual devices, as witnessed by invited contributions to this conference series over the last years [1-3]. Although important information is obtained on the identity of defects acting as recombination centers, the determination of defect concentrations with EDMR is not straightforward. While transitions between the Zeeman-levels of the defect are measured in conventional spin resonance, two paramagnetic species (typically a charge carrier and the defect) are involved in the spin-dependent recombination process monitored in EDMR.

A priori, the exact interaction of these two spins is not known. Various models have been proposed to describe this interaction. The two limiting cases are the Lepine-model, which invokes the interaction of the polarisations of the two spin ensembles, and the Kaplan-Solomon-Mott model (KSM) which assumes the formation of a spin-pair prior to the actual recombination [4,5]. The two models differ in particular in their predictions for the dependence of the EDMR signal $\Delta\sigma/\sigma$ on the Zeeman energy $h\nu$ and the temperature T. The Lepine-model predicts a very strong dependence $\Delta\sigma/\sigma \propto (h\nu/T)^2$, while the KSM-model predicts that $\Delta\sigma/\sigma$ is independent of these experimental conditions. It is a prerequisite for a quantitative understanding of EDMR that the microscopic origin of this interaction and the ensuing dependencies are determined. Since changing temperature over a large range often leads to changes in the dominant conductivity path and in the spin relaxation, experiments using different microwave frequencies or magnetic fields are more suited for such a fundamental study.

While experiments on materials with highly different atomic charge numbers Z (such as C_{60} and GaAs) are currently under way to determine the influence of the spin-lattice relaxation on these properties, we present here a detailed comparison of the EDMR signal intensities observed in one of the materials most intensively studied by EDMR, amorphous hydrogenated silicon (a-Si:H), at microwave frequencies of 434 MHz, 9 and 34 GHz. In addition, we briefly mention our first results on the temperature dependence of the EDMR in GaAs. Although similar experiments have been performed before [6,7], the results presented here cover an extended range of microwave power (6 orders of magnitude) allowing to study EDMR in the unsaturated and in different saturated regimes.

EXPERIMENTAL DETAILS

The measurements were performed in three electron spin resonance spectrometers. The 9 GHz setup is a commercial Bruker spectrometer with a standard TE_{102} cavity. In addition, the spectrometer is equipped with a 2 Watt solid state power amplifier. The 34 GHz apparatus is based on a microwave synthesizer (HP 8360). A power amplifier (DBS microwave) provides 250 mW over the whole 26.5 to 40 GHz Ka-band. A cylindrical cavity (TE_{011}) operating at 34 GHz was used in this study. Finally, the 434 spectrometer MHz uses ham radio equipment (Yaesu FT 790 RII transceiver and Tokyo High Power HL 130 U amplifier) to provide up to 100 Watt of radio frequency to a helical resonator. Microwave power modulation was used in general, with the exception of the 434 MHz system, where magnetic field modulation was employed. However, using overmodulation with $H_{mod}>>\Delta H_{pp}$, amplitudes $\Delta\sigma/\sigma_{om}$ are obtained which can be directly related to the corresponding amplitude $\Delta\sigma/\sigma_{pm}$ obtained by power modulation via $\Delta\sigma/\sigma_{om}=2\Delta\sigma/\sigma_{pm}$.

A particular problem with a quantitative comparison of the EDMR intensities at different microwave frequencies is the correct determination of the microwave magnetic field at the sample position, H_1. Since experimental determinations of H_1 in the resonator cavities have failed, the microwave field was calculated using

$$H_1 = \left(10^{-3} Q \eta \frac{V_W}{V_S} P\right)^{1/2} \tag{1}$$

with the quality Q, the filling factor η, the volume of the waveguide per wavelength V_W, the volume of the sample V_S, and the incident microwave power P. For cylindrical cavities

$$\eta = \frac{12.33}{1+(a/d)^2}\frac{V_s}{V_c} \tag{2}$$

with the cavity diameter d, the cavity length a and the cavity Volume V_C [8]. In the case of rectangular resonators, a corresponding relation holds. For the 34 GHz cylindrical cavity used for most of this study, an H_1 of 1.45 G at P_{max} of 250 mW was determined. Similarly, the X-band cavity yields H_1=2.3 G at 2 W incident power, in agreement with the results obtained via ENDOR experiments [9]. The microwave field in the 434 MHz helical resonator was determined from power broadening of the narrow a-Si:D EDMR resonance to 0.8 G at 30 W [10]. It should however be stressed that these figures carry an error margin of at least about a factor of 2.

AMORPHOUS SILICON

Spin-dependent photoconductivity experiments on standard amorphous hydrogenated silicon (a-Si:H) with a hydrogen concentration of 10 at. % were performed at room temperature in the three different spectrometers. Figure 1 shows the dependence of the linewidth on the microwave frequency. It is obvious that an inhomogeneous broadening is observed, which is due to g-factor anisotropy. The 434 MHz linewidth given in Fig. 1 is that of a-Si:D, since the large concentration of hydrogen leads to a noticeable broadening of the low-frequency linewidth of a-Si:H due to hyperfine interaction [10-12].

Figure 1: Dependence of the linewidth ΔH_{pp} of amorphous hydrogenated silicon as a function of the microwave frequency.

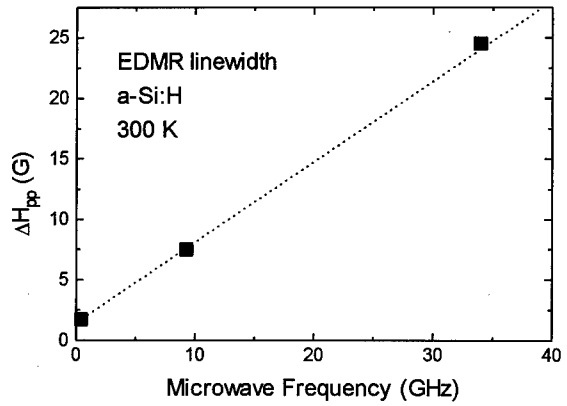

Figure 2 shows the EDMR signal intensity $\Delta\sigma/\sigma$ at the center of the resonance as a function of the microwave field H_1 for the three different spectrometers. Although it is known that the signal intensity $\Delta\sigma/\sigma$ is nearly independent of the photocarrier generation rate [10], care has been taken to use the identical light intensities in all three experiments, keeping the positions of the quasi-Fermi levels constant. Below H_1=0.1 G, all signal intensities are identical within the accuracy of the H_1 determination discussed above. In this regime, $\Delta\sigma/\sigma$ is proportional to H_1^2. For higher powers, two different behaviours are observed: In the case of the low-frequency EDMR, immediate saturation occurs with a maximum $\Delta\sigma/\sigma\approx10^{-5}$. In the inhomogeneously broadened cases at higher frequencies, a different, weak saturation regime is observed, with $\Delta\sigma/\sigma\propto H_1$. At 9 GHz, using a particular thin-film-transistor structure which led to an additional enhancement of the microwave field, the EDMR intensity dependence could even be observed for microwave fields greater than the inhomogeneous linewidth [13]. In this case, again strong saturation at $H_1>\Delta H_{pp}$ is found, as in the case of the homogeneous line.

The three different regimes observed at 9 GHz have been discussed in detail by Kawachi et al. [13], who have demonstrated that for an inhomogeneous line in the weak saturation regime ($\gamma^2 H_1^2 T_1 T_2>1$ and $(T_2/T_1)^{1/2}>H_1\gamma T_2^*$), the EDMR signal intensity increases as $\Delta\sigma/\sigma\propto H_1$ while the linewidth remains constant, ΔH_{pp}=const. In contrast, in the strong saturation regime ($H_1\gamma T_2^*>(T_2/T_1)^{1/2}$), $\Delta\sigma/\sigma$=const. and $\Delta H_{pp}\propto H_1$ is found. The latter behaviour also holds for a homogeneous line under saturation. Correcting the plotted EDMR signal intensities for the increasing linewidth by multiplying with $(\Delta H_{pp}(H_1)/\Delta H_{pp}(H_1\rightarrow0))$ eliminates this apparent saturation. In this case, all curves in Fig. 2 show the same H_1-dependence within the experimental error. The EDMR signal intensity in a-Si:H therefore does not depend of the size of the Zeeman level splitting induced. It should, however, be noted that this only applies because the relaxation times T_1 and T_2 do not depend on the Zeeman splitting, as shown by the values obtained for $(T_1T_2)^{1/2}$ included in Fig. 2.

Two experimental observations have for a long time argued against the applicability of the Lepine-model to EDMR of amorphous silicon. First, the room temperature signal intensity easily surpasses the maximum value of about $\Delta\sigma/\sigma=3\times10^{-6}$ predicted by Lepine. Second, no significant temperature dependence of $\Delta\sigma/\sigma$ was found at least down to 100 K. Here, the independence of $\Delta\sigma/\sigma$ on the size of the microwave frequency or the magnetic field, is a further argument against the Lepine-model in a-Si:H.

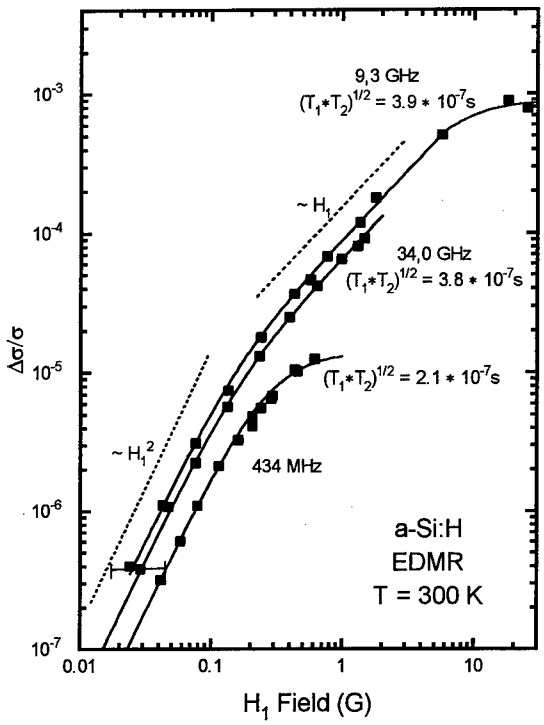

Figure 2: EDMR signal intensity $\Delta\sigma/\sigma$ as a function of the microwave magnetic field H_1 for three different microwave frequencies. The error bar represents the uncertainty in the determination of the H_1 fields.

GaAs

Materials with high nuclear charge Z generally exhibit very short spin relaxation times. If these are considerably shorter than typical recombination lifetimes, the Lepine-model should actually provide a good quantitative description of EDMR in these systems. We have recently been able to show that GaAs/AlGaAs-heterostructures can be studied with EDMR obtaining the sensitivity previously known only for light-element semiconductors [14]. In particular, surface defects, intrinsic defects such as the Ga interstitial and the As_{Ga} antisite defects as well as transition metal ion impurities can be detected. While a comparative study of EDMR in GaAs similar to the one presented above is currently under way, we show in Fig. 3 the EDMR spectrum observed in neutron-irradiated GaAs bulk crystals at 9.3GHz and 4.5 K. Figure 4 shows the corresponding power dependence of the conventional ESR and EDMR of the As antisite defect. The ESR signal intensity exhibits the expected $\chi'' H_1$ dependence at low fields and shows strong saturation at $H_1\approx0.5$ G, corresponding to a $(T_1T_2)^{1/2}\approx2\times10^{-7}$ s at this temperature. The EDMR shows a stronger dependence on H_1 at very low microwave fields and saturates to $\Delta\sigma/\sigma$= const. Included in Fig. 4 is the ratio of the EDMR to ESR signal intensities, which should be proportional to

H_1 over the whole range [13]. The deviation from this expected behaviour is due to the less than H_1^2 dependence of the EDMR signal at low H_1.

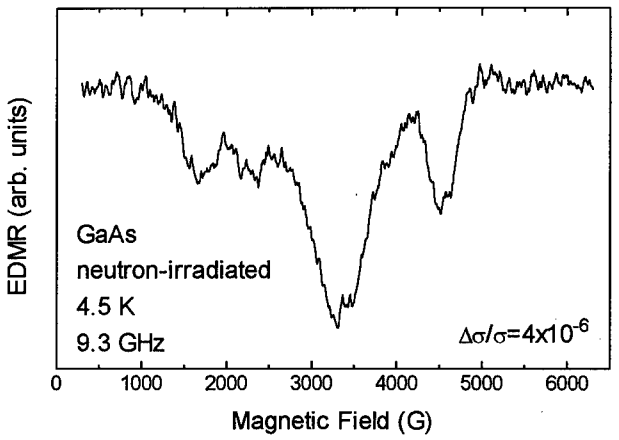

Figure 3: EDMR spectrum of neutron-irradiated GaAs showing the well known As_{Ga} anitsite defect and an additional g=2.00 resonance, possibly due to Cr^{4+}.

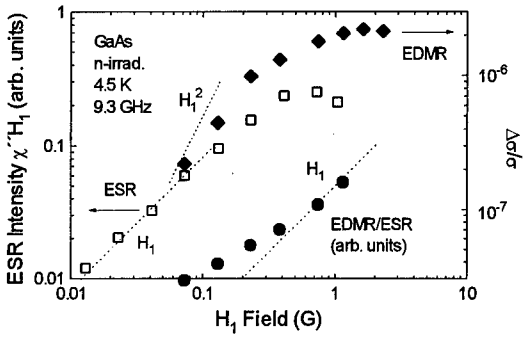

Figure 4: ESR signal intensity $\chi''H_1$ and EDMR signal intensity $\Delta\sigma/\sigma$ as a function of the microwave magnetic field H_1 for neutron irradiated GaAs.

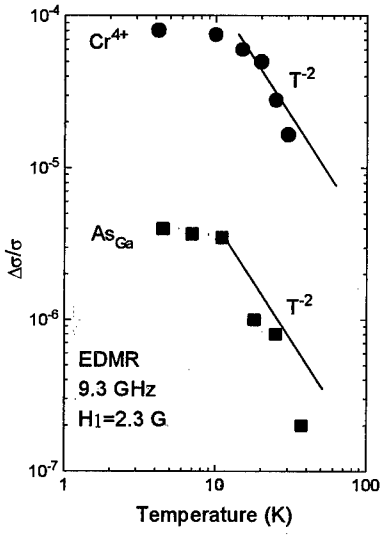

Figure 5: Temperature dependence of the EDMR signal intensities in Cr-doped and neutron-irradiated GaAs.

More informative is the temperature dependence of the EDMR signal keeping the microwave power at 2 W (corresponding to $H_1 \approx 2.3$ G). The results of EDMR experiments on two different GaAs samples are compared in Fig. 5: a Cr-doped semiinsulating substrate as well as the neutron-irradiated GaAs crystal of Fig. 3. Both samples show a virtually identical temperature dependence of the EDMR signal intensity: Below 10 K, no significant dependence is observed, while at higher temperatures a strong decrease of the signal intensity is evident ($\Delta\sigma/\sigma \approx T^{-a}$ with $a>2$). This behaviour can be understood with

the help of Fig. 4. Increasing the temperature leads to faster spin relaxation and a shift of the saturation regime to higher microwave fields. As long as saturation can still be achieved with the power levels available (i.e. the induced spin-flip rate is greater than the relaxation rate), no change occurs. Once relaxation becomes significantly faster, the EDMR amplitude cannot saturated even at the highest available microwave powers and $\Delta\sigma/\sigma$ decreases rapidly as the temperature is increased. The exact temperature dependence will in this case be determined by the temperature dependence of the relaxation times, which can be very strong, depending on the relaxation mechanism. This poses a practical limit on the temperature range relevant for EDMR experiments in GaAs: Using a conventional ESR spectrometer with typically 400 mW at 9 GHz, EDMR should be performed below 20 K. Higher powers or specific sample structures leading to an enhancement of the microwave magnetic field would extend this range to temperatures better suited for the study of GaAs devices.

CONCLUSIONS

We have presented here detailed investigations into the different dependencies of the EDMR signal intensity $\Delta\sigma/\sigma$ on experimental conditions. In particular, we have shown that the signal intensity in a-Si:H (as a model substance with long spin-lattice relaxation times) is indeed independent of microwave frequency or static magnetic field used for the experiment, as suggested by the Kaplan-Solomon-Mott model. In addition, we have shown that due to the limited microwave power available in conventional ESR systems, quantitative EDMR studies on GaAs should be performed at temperatures below 20 K. These investigations could help to obtain a better understanding of EDMR, with the ultimate goal to be able to deduce defect densities from spin-dependent transport measurements.

ACKNOWLEDGMENTS

The authors would like to thank the Deutsche Forschungsgemeinschaft for financial support (SFB 348).

REFERENCES

1. S. Greulich-Weber, Mat. Sci. Forum **143-147**, 1337 (1994)
2. N. M. Reinacher, M. S. Brandt, M. Stutzmann, Mat. Sci. Forum **196-201**, 1915 (1995).
3. W. E. Carlos, these proceedings.
4. D. J. Lepine, Phys. Rev. B **6**, 436 (1972)
5. D. Kaplan, I. Solomon, N. F. Mott, J. Phys. (Paris) **39**, L51 (1978)
6. V. S. L´vov, L. S. Mima, O. V. Tretyak, Sov. Phys. JETP **56**, 897 (1983)
7. B. Stich, S. Greulich-Weber, J.-M. Spaeth, J. Appl. Phys. **77**, 1546 (1995)
8. C. P. Poole, *Electron Spin Resonance* (Wiley, New York, 1983), p. 171
9. M. Stutzmann, D. K. Biegelsen, Phys. Rev. B **34**, 3093 (1986)
10. M. S. Brandt et al., to be published.
11. H. Dersch, L. Schweitzer, J. Stuke, Phys. Rev. B **28**, 4678 (1983)
12. U. Voget-Grote, J. Stuke, J. Electr. Mater. **8**, 749 (1979)
13. G. Kawachi, C. F. O. Graeff, M. S. Brandt, M. Stutzmann, Jpn. J. Appl. Phys. **36**, 121 (1997)
14. T. Wimbauer et al., these proceedings.

Materials Science Forum Vols. 258-263 (1997) pp. 969-974

METASTABLE ANTISITE PAIR IN GaAs

S. Pöykkö, M. J. Puska and R. M. Nieminen
Laboratory of Physics, Helsinki University of Technology,
FIN-02015 HUT, Finland

Keywords: Gallium arsenide, metastability, antisite defects

Abstract. Metastable arsenic-antisite–gallium-antisite pair in GaAs has been studied using self-consistent, parameter-free total energy methods. The metastability of this defect is similar to that of the isolated arsenic-antisite. The anti-structure pair has ionization levels in the band gap in the metastable configuration, unlike the isolated arsenic-antisite. These ionization levels enable absorption of infrared light in the metastable state. The results presented are in good agreement with recent experimental results for electron-irradiated GaAs.

Introduction

The introduction of As-antisite related defects in electron [1] and neutron [2] irradiation as well as during plastic deformation [3] has been actively studied during the last years. Recently, three different electron-irradiation-induced As_{Ga}-related defects possessing metastability have been observed by magnetic circular dichroism of absorption (MCDA) [4]. One of these is obtained after subsequent thermal annealing at room temperature. This defect has been studied with the optically detected electron nuclear double resonance (ODENDOR) technique and suggested to be an anti-structure defect, which is an As_{Ga} defect with a Ga-antisite (Ga_{As}) defect located in the next-nearest As shell of the As-antisite [5]. The structure is given schematically in Fig. 1. Positron lifetime measurements indicate that the defect has an associated vacancy in its metastable state [6]. The defect seen in the positron lifetime measurements is associated with that detected in MCDA, i. e. to the anti-structure pair [7].

The metastability of the famous EL2 defect is generally accepted to be connected to the movement of arsenic antisite. Many properties of the irradiation-induced As_{Ga}-related defects are quite similar to the ones of the EL2-defect, but some properties differ crucially from those of the native EL2-defects. For example, the existence of the metastability has not always been detected. The main difference between the EL2 defect and the irradiation-induced anti-structure defect is that the latter absorbs infrared light in the metastable configuration, suggesting that it has an ionization level in the band gap in the metastable configuration [7]. The stable state of the irradiation-induced As_{Ga}-defect can be optically recovered with 0.85 or 1.3 eV photons at 20 K, while this is not possible for the native EL2 defect [4,7]. Another interesting difference is that the metastable state of the irradiation-induced defect may be paramagnetic [4].

In our recent study of antisite pairs in GaAs [8] we have shown that neither the nearest- nor third-nearest-neighbor antisite pair models are capable to explain the above mentioned experimental findings. The nearest-neighbor antisite pair does not have any ionization level in the band gap in metastable configuration and thus it cannot effectively absorb infrared light. In the case of the third-nearest-neighbor antisite pair the two antisites interact only weakly and the arsenic antisite end of the defect behaves like an isolated As_{Ga}, which does not have any ionization level in the band gap in the metastable configuration.

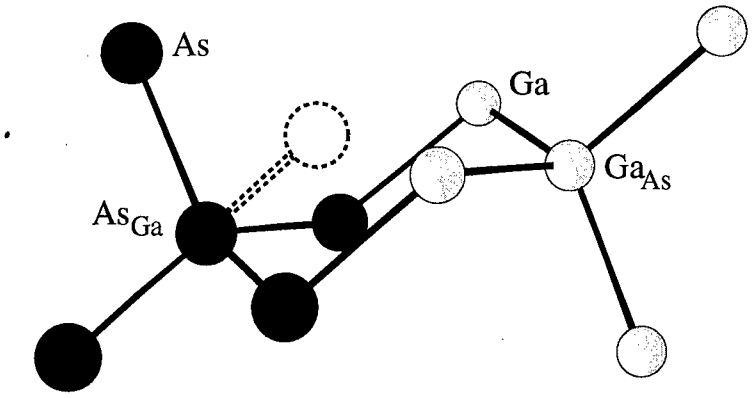

FIG. 1. Schematic view of the next-nearest-neighbor anti-structure pair in GaAs. The metastable interstitial position of the As_{Ga} antisite is shown by dashed lines.

Methods

In this paper we report studies of the anti-structure pair using first-principles electronic-structure methods [9]. Our calculations are based on the density-functional theory where the electron exchange-correlation energy is calculated within the local-density approximation (LDA) [10]. We use first-principles norm-conserving pseudopotentials [11] for both Ga and As. Calculations are performed with the supercells containing 32 or 64 atoms. We have also made calculations employing the local mass approximation [12] in order to esitimate optical energies needed to excite antistructure defect in substitutional and in metastable interstitial configurations. Local mass approximation is an attempt to develop a density functional capable to predict both quasiparticle energies and ground-state properties. Further computational details can be found from Ref. [8].

Results and discussion

The anti-structure defect has neutral and negative charge states (0, 1−, 2−, 3−). In the neutral state the highest occupied electron states are in the band gap close to the top of the valence band. They are related to the deep levels induced by an isolated Ga_{As} antisite. In the doubly negative charge state the highest states are related to those of an isolated As_{Ga} antisite. Our total energy calculations show that the defect has a metastable configuration similar to the large-lattice relaxation (LLR) [13] model for the EL2 defect: The metastable state is achieved when the arsenic antisite moves from the Ga-site to the open [111] direction by $\sim$ 60 percent of the bulk bond length (See Fig. 1). A vacancy in the metastable state of the anti-structure defect is thus created. The presence of a vacancy in the metastable state of the anti-structure defect is also directly probed by positron lifetime measurements [6]. The movement of the As_{Ga} antisite in the [111] direction in which the distance between the As_{Ga} and Ga_{As} antisites decreases is favoured. This is because the defect pair gains in the Coulomb attraction. The evaluation of the total energy, when the As ion is displaced in this direction from the substitutional Ga site is shown in Fig. 2 for the charge states 0, 1−, and 2−. The metastability exists for *all* of these charge states. In comparison, the isolated As_{Ga} antisite exhibits metastability *only* in the neutral charge state when the deep levels in the band gap are occupied with two electrons [13]. The corresponding charge state of the anti-structure defect is 2−.

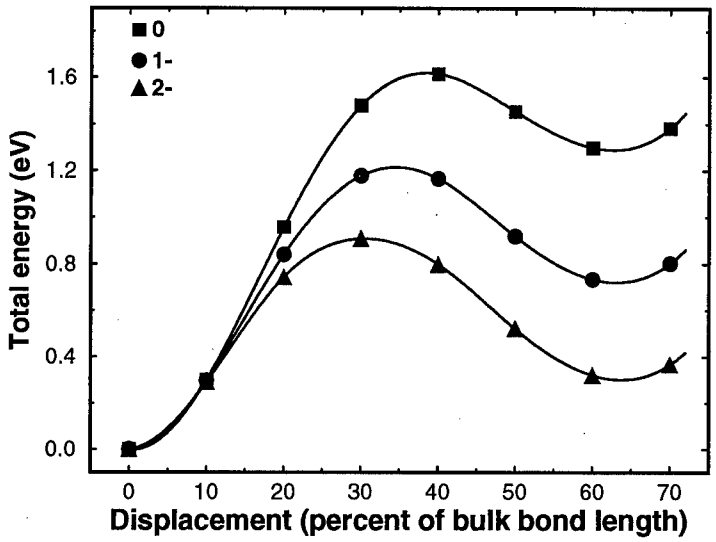

FIG. 2. Total energy of the anti-structure defect as a function of the As-ion displacement from the Ga substitutional position along the open [111] direction. The distance between the antisites decreases with increasing displacement. The zero of the energy corresponds to the total energy in the substitutional ionic configuration. No other ionic relaxations have been allowed. The three curves correspond to different charge states (0, 1−, 2−). The local minima in the total energy curves at ~ 60 percent displacement indicate the existence of metastable ionic configurations.

We have calculated the atomic relaxations for each energy minimum shown in Fig. 2. The calculated total energy difference between the substitutional and the metastable interstitial states for fully relaxed structures is between 0.24-0.95 eV, depending on the charge state of the defect. The energy difference is smallest for the 2− charge state and highest for the neutral charge state.

In the substitutional configuration of the anti-structure defect the interaction between the two antisites is rather weak. The distance between the two antisites is too large for a direct covalent bonding and thus the interaction is mainly Coulombic. With respect to the isolated As_{Ga} antisite the main effect of the Ga_{As} antisite in the defect complex is to change the total charge state of the complex, but the ionization levels and also the other properties of the *substitutional* As_{Ga} antisite do not differ significantly from those of the isolated antisite.

In the case of the chosen [111] direction for the movement of the As_{Ga} antisite, the distance between the two antisites in the metastable *interstitial* configuration is ~ 30 percent less than in the substitutional configuration. Thus the interaction between $V_{Ga}As_i$ and Ga_{As} in the metastable configuration is much stronger and the properties of the $V_{Ga}As_i$ in a pair differ to a great extent from an isolated $V_{Ga}As_i$. The fact that one As ion is substituted around the metastable position of the As_i by a Ga ion with a smaller valence charge pushes the $V_{Ga}As_i$-derived deep level higher in energy. This makes its partial occupancy or even its emptying possible and introduces ionization levels into the band gap. Moreover, the interaction pulls a state from the conduction band to the band gap and a triply negative charge state is possible for the anti-structure defect in the metastable configuration.

The $(V_{Ga}As_i)^0$ defect arising from an isolated As_{Ga} antisite does not have ionization levels in band gap in its metastable configuration. This is because there are no empty deep levels available in the band gap and the emptying of the occupied deep level by one electron leads

to the lowering of the level into the valence band and its refilling. The lack of the ionization levels means that light absorption for this defect is very low. According to the experiments for the EL2 defect an applied pressure brings an ionization level from the conduction band to the band gap, resulting in strong light absorption [14]. The ionized defect may capture a photocreated hole so that an excited neutral EL2 defect in the metastable state results [14]. In this state there is no energy barrier towards the substitutional configuration and therefore the pressure enables a photorecovery process. This pressure behaviour has been theoretically predicted also for the isolated As_{Ga} antisite [15]. In the case of the metastable configuration of the anti-structure defect ($V_{Ga}As_iGa_{As}$) there are, due to the the interaction between the $V_{Ga}As_i$- and Ga_{As}-derived states, ionization levels in the band gap already without applied pressure. The ionization levels cause the defect to absorb light strongly.

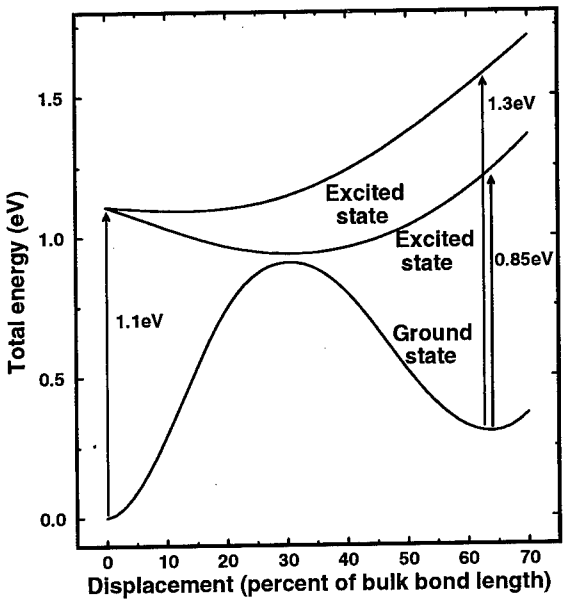

FIG. 3. Schematic model of possible optical excitation processes for the anti-structure defect. The experimental values [7] for the photon energies are shown in the figure. The lowest unoccupied single particle levels of the anti-structure defect are degenerate in the substitutional configuration of the defect. In the interstitial configuration the lowest normally empty single particle levels of the anti-structure defect are nondegenerate. Two empty single particle levels in the band gap explain the observed two possible photon energies for the photorecovery of the defect.

The illumination of the anti-structure defect by 1.1 eV light triggers the transition to the metastable state [4,7]. This is analogous to the EL2 defect. However, an important difference between the EL2 and the anti-structure pair is that the latter cannot be excited to the metastable state using unfiltered white light [4]. The optical properties of the anti-structure defect can be explained by the model given in Fig. 3. In the excited states one electron is shifted to a higher, originally unoccupied energy level leaving a hole behind. For the stable substitutional configuration the only unoccupied electron level in the band gap is in practice degenerate in the case of 1− and 2− charge states. Thus the excitation energy is unique. The degeneracy of these levels is due to the symmetry; these states correspond to the degenerate

e state of the As_{Ga}. The symmetry lowering due to the Ga_{As} in the next-nearest neighbor position is not strong enough to lift the degeneracy. Then, in the resulting excited state the total energy is lowered by the Jahn-Teller effect when the As_{Ga} antisite is displaced in the [111] direction. This causes the shift to the metastable state similarly to the LLR model for the EL2 defect [13]. For the anti-structure defect in the metastable interstitial configuration this level is split into two in the band gap and there are two possible excited states. The total energy of these states is lowered when the As_{Ga} antisite moves back towards to the substitutional configuration, resulting in the recovery to the stable state.

We have calculated estimates for the photon energies needed to excite an electron from the highest occupied defect levels to the lowest unoccupied ones by calculating the energy eigenvalue difference between the corresponding Kohn-Sham eigenstates, in these calculations a very high kinetic energy cut-off (27 Ry) and local mass approximation [12] have been used. The single-particle energy differences give for the substitutional configuration the photon energy of 1.2 eV and for the metastable configuration two energies of 0.7 eV and 1.1 eV. These energies correspond well to the experimental energies shown in Fig. 3. Thus the model explains all the processes activated by monochromatic light.

The anti-structure gallium antisite is in a diamagnetic state (Ga_{As}^{2-}), in agreement with experiments [5] for the stable state of the anti-structure defect. This assignment of diamagnetism for Ga_{As} is valid for all charge states of the anti-structure defect. Our calculations also predict, in accordance with the experiments [5], the existence of the paramagnetic charge state (1-) for the anti-structure defect both in the stable and metastable states when the Fermi level is near the mid-gap.

Conclusions

In conclusion, we have made calculations for the next-nearest-neighbor anti-structure pair in GaAs. The calculated properties are in excellent agreement with experimental results for electron-irradiated samples [4–7]. The observed metastability is connected to the large lattice relaxation of the arsenic-antisite. A gallium vacancy is created in the complex during the transition to the metastable interstitial configuration. The main difference between the isolated arsenic-antisite and the anti-structure defect is that the isolated antisite does not have any ionization levels in the band gap in the metastable state, whereas the anti-structure defect has ionization levels in the gap both in the stable and in the metastable state. Furthermore, the optical recovery of the anti-structure defect from the metastable state is possible at two photon energies. The optical recovery of the anti-structure defect also explains the inefficiency of the illumination by unfiltered white light to excite the defect from the stable state to the metastable one. Our results confirm the microscopic next-nearest-neighbor pair as the observed metastable defect induced by electron irradiation.

Acknowledgements. The authors wish to thank K. Saarinen, P. Hautojärvi, A. P. Seitsonen and T. Mattila for many valuable discussions. We also acknowledge the generous computing resources from the Center for Scientific Computing (CSC).

References

[1] A. Pillukat, P. Ehrhart, Appl. Phys. Lett. **60**, 2794 (1992); K. Krambrock, J.-M. Spaeth, C. Delerue, G. Allan and M. Lannoo, Phys. Rev. B **45**, 1481 (1992); E. Christoffel, A. Goltzene and G. Schwab, J. Appl. Phys. **66**, 5648 (1989); M. O. Manasreh, D. W. Fisher, Appl. Phys. Lett. **53**, 2429 (1988).

[2] A. Goltzene, B. Meyer and C. Schwab, Appl. Phys. Lett. **54**, 907 (1989); M. O. Manasreh, D. W. Fisher and B. C. Covington, Phys. Rev. B **37**, 6567 (1988).

[3] P. Omling, E. R. Weber and L. Samuelson, Phys. Rev. B **33**, 5880 (1986); M. Hoinkis and E. R. Weber, Phys. Rev. B **40**, 3872 (1989).
[4] M. Hesse, F. K. Koschnick, K. Krambrock, J.-M. Spaeth, Solid State Commun. **92**, 207 (1994).
[5] K. Krambrock and J.-M. Spaeth, Phys. Rev. B **47**, 3987 (1993).
[6] K. Saarinen, S. Kuisma, J. Mäkinen, P. Hautojärvi, M. Törnqvist and C. Corbel, Phys. Rev. B **51**, 14 152 (1995).
[7] S. Kuisma, K. Saarinen, P. Hautojärvi and C. Corbel, Phys. Rev. B **53**, 7588 (1996); Phys. Rev. B **55**, 9609 (1997).
[8] S. Pöykkö, M. J. Puska, and R. M. Nieminen, Phys. Rev. B **55**, 6914 (1997).
[9] R. Car and M. Parrinello, Phys. Rev. Lett. **55**, 2471 (1985).
[10] D. M. Ceperley and B. J. Alder, Phys. Rev. Lett. **45**, 566 (1980); J. Perdew and A. Zunger, Phys. Rev. B **23**, 5048 (1981).
[11] G. B. Bachelet, D. R. Hamann, and M. Schlüter, Phys. Rev. B **26**, 4199 (1982); R. Stumpf, X. Gonze and M. Scheffler, (unpublished).
[12] G. E. Engel, and W. E. Pickett, Phys. Rev. B **54**, 8420 (1996).
[13] J. Dabrowski and M. Scheffler, Phys. Rev. Lett. **60**, 2183 (1988); D. J. Chadi and K. J. Chang, Phys. Rev. Lett. **61**, 2187 (1988).
[14] M. Baj, P. Dreszer, and A. Babinski, Phys. Rev. B **43**, 2070 (1991); P. Dreszer, M. Baj, and K. Korzeniewski, Mater. Sci. Forum **83-87**, 875 (1992); T. W. Steiner, M. K. Nissen, S. M. Wilson, Y. Lacroix, and M. L. W. Thewalt, Phys. Rev. B **47**, 1265 (1993).
[15] C. Ziegler, U. Scherz, and M. Scheffler, Phys. Rev. B **47**, 16624 (1993).

Materials Science Forum Vols. 258-263 (1997) pp. 975-980

THEORETICAL STUDY OF ANTISTRUCTURE DEFECTS IN GaAs

A. Janotti[1], A. Fazzio[1], P. Piquini[2] and R. Mota[2]
[1] Instituto de Física, Universidade de São Paulo, Cxp 66318, 05389-970, São Paulo, SP, Brazil
[2] Departamento de Física, Universidade Federal de Santa Maria, 97119-900, Santa Maria, RS, Brazil

Keywords: electronic structure, defect complexes, GaAs

Abstract. We investigated the electronic and structural properties of the antistructure pairs (As_{Ga}+Ga_{As}), both nearest neighbor and next-nearest neighbor cases, and the vacancy-antisite-interstitial complex in GaAs. An ab initio density functional-pseudopotential theory is used. For the antistructure pairs acceptor levels are observed in the energy band gap. In the case of the nearest neighbor pair a metastable configuration is obtained similar to the isolated As_{Ga}. For the complex V_{Ga} + Ga_{As} + As_i different regimes are observed, related to their stabilities, depending on the interstitial positions.

Introduction.

Light ion or electron irradiation has been showed to be a powerful technique for inducing defects in semiconductors. With proper dose and appropriate particle, electron or ion, it is possible, to some extent, to control the type and the amount of created defects. It is possible to create point defects as well as amorphous regions. An important potential application of this technique is the electrical isolation between devices in integrated circuits. Using light ions, it is shown that irradiating with proper dose it is possible to transform a semi-insulating layer of GaAs into a highly resistive one [1,2]. However, the detailed structure and consequently the electronic properties of these defects are unknown.

Recent experiments with electron irradiated GaAs crystals have indicated the presence of the antistructure pairs [3] with interesting characteristics. In particular, the infrared optical absorption, even in a possible metastable configuration [4], has to be studied and compared with the isolated As_{Ga} which does not present an ionization level in the band gap in the metastable configuration.

Theoretical results have showed that the antistructure pairs present ionization levels in the energy gap [5,6]. Our aim in this work is to study the electronic and structural properties of the antistructure pairs and the complexes V_{Ga} + Ga_{As} + As_i and V_{As} + As_{Ga} + Ga_i ,which are possible irradiated induced defects.

Basic Computational Methods.

We use an ab initio pseudopotential method [7] with density functional theory within the local density approximation. The pseudopotential is taken in the Kleinman-Bylander form [8]. A supercell with 128 atoms is adopted with periodic boundary conditions. Plane wave basis set expansion up to 10 Ry is used. The Kohn-Sham equations [9] are solved in the Car-Parrinello scheme [10] with the exchange-correlation term taken in the Ceperley-Alder form as parametrized by Perdew and Zunger [11]. The special point method is taken through the Γ point for Brillouin zone sampling. The systems studied are fully relaxed in the directions of the Hellmann-Feynman forces down to 0.005 eV/Å.

Results and Discussion.

The antistructure pair is an interesting induced irradiation defect in GaAs. It is composed of two related antisites, As_{Ga}+Ga_{As}. We studied the cases in which they are in the nearest neighbor (nn) and next nearest neighbor (nnn) configurations. In the nn configuration the antisites are directly bonded, and in the nnn case the antisites belong to different planes. For the nn pair a metastable configuration is found when the As_{Ga} is moved away from Ga_{As} in the <111> direction. Figure 1

shows the total valence charge densities in the (110) plane for the nn pair in the stable (Fig. 1a) and metastable (Fig. 1b) configurations. In the stable configuration we can see a strong bond between the two As atoms. In the metastable configuration the antistructure bond (As-Ga) is broken and the As-As bond becomes stronger. In Fig. 2 we can see the total energy curve versus As displacement along the <111> direction away from the Ga antisite. It is interesting to observe that even in the presence of Ga antisite, the curve shows a metastable state very similar to the isolated As antisite [12]. The existence of this metastabitlity can explain the observed infrared absorption in the experiments of Kuisma *et al.* [4].

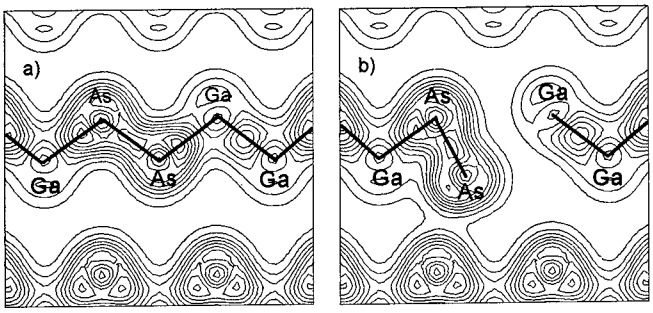

Fig. 1. Total charge densities for the As_{Ga} + Ga_{As} (nn) for the (a) stable and (b) metastable configurations in the (110) plane (0.01 e/a_0^3)

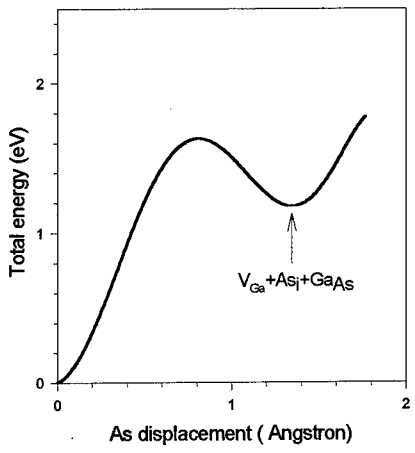

Fig.2. Total energy versus As_{Ga} displacement away from Ga_{As} along the <111> direction. The origin corresponds to the stable As_{Ga}+Ga_{As} (nn).

In Fig. 3 the charge densities for the the lowest unoccupied (a_1^*-orbital) and highest occupied (e-orbital) are showed. The left side of the Fig. 3 (a and b) refers to the (nn) and the right side (c and d) to the (nnn) antistructure pairs. In the (nn) case the planes are the same and in the (nnn)

case the planes are different. Observe that, although the different distances between the antisites, the charge distributions are very similar, with the a_1^*-orbital localized on the As_{Ga} and the e-orbital on the "wrong" Ga_{As}-Ga bond.

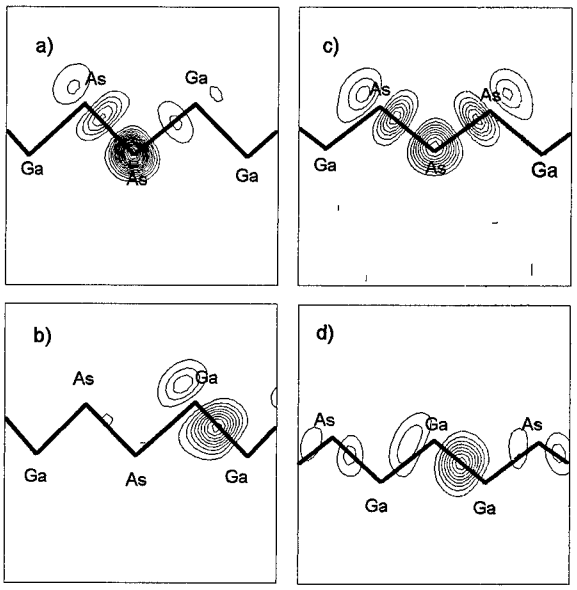

Fig.3. Charge densities for (a) the lowest unoccupied a_1^*-orbital and (b) the highest occupied e-orbital for the (nn) antistructure in the (110) plane and (c) the lowest unoccupied a_1^*-orbital and (d) the highest occupied e-orbital for the (nnn) antistructure pair (0.0016 e/a_0^3).

For the negative charge state, the additional electron occupies the a_1^*-orbital, which is close in energy to the fully occupied e-orbital in the energy gap. Although close in energy, their charge distribuition are spatially separated, resulting in a weak Coulomb repulsion between them.
From the total energy calculations, we obtain for the (nn) antistructure pair a first donor level (0/+), a first acceptor level (0/-), and also a second acceptor level (-/- -), located at 0.29 eV, 0.45 eV, and 0.71 eV above the valence band, respectively, as shown in Fig. 4(a) . For more details of the calculations see Ref. [5]. A comparison with Baraff and Schlüter [13] shows a good agreement for the first donor level (they calculated 0.30 eV), while the first acceptor level was not predicted by them. In our case we obtain the Mott-Hubbard U, E(0/-) - E(+/0) = 0.16 eV and E(--/-) - E(-/0) = 0.26 eV.
For the (nnn) case a first donor level, a first and second acceptor levels are similarly obtained, as shown in Fig. 4(b).

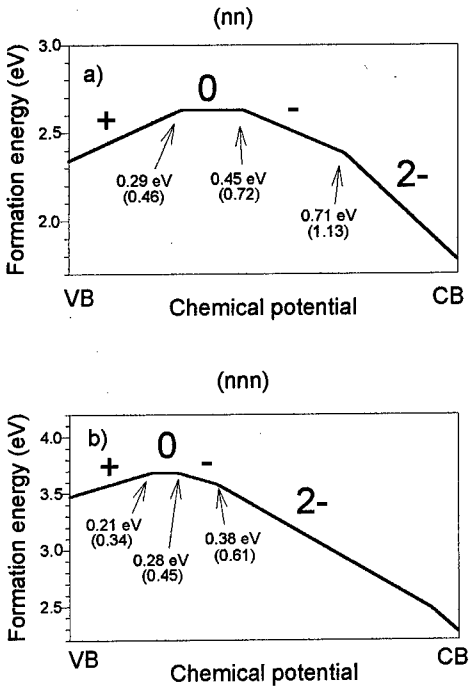

Fig. 4. Absolute formation energies for the (nn) and (nnn) antistructures, (a) and (b) respectively, as a function of the chemical potential. The numbers in parenthesis represent the ionizations levels relative to the experimental energy gap.

For the vacancy-antisite-interstitial complex (V_{Ga}+Ga_{As}+As_i), with the starting configuration presenting the Ga atom at the As site and the As atom kept at the nearest tetrahedral interstitial position, considering lattice relaxation both atoms return to their original positions, corresponding to a spontaneous recombination [5]. Nevertheless, with the As atom at the next-nearest tetrahedral interstitial position, surprisingly, the system changes its behavior. The Ga and As atoms get closer to each other and apart from the vacancy. It is interesting to observe that in the first configuration, with the As_i at the nearest position, the forces on As and Ga atoms are both in direction to recover their original positions (spontaneous recombination). In the next configuration, the force acting in Ga atom changes orientation avoiding the vacancy and with a small displacement in direction to As atom. In this sense, a stability of this defect can be established and allowing a possible vacancy diffusion. On the other side, considering, as an extreme case, the As_i moving too apart from the Ga_{As}, it is well known that the Ga atom will again be attracted by the vacancy and a recovery will take place with the Ga atom occupying its original site. Then this would correspond to a third regime for this particular defect complex. The other vacancy-interstitial-antisite complex studied is V_{As}+As_{Ga}+Ga_i. This defect is energetically stable even with the Ga_i in the nearest tetrahedral interstitial position [5], showing that this complex is easier to form than the V_{Ga} +Ga_{As}+As_i in which the transferred energy during irradiation should be sufficient to displace the As_i to the next nearest interstitial position.

Acknowledgments.
This work has been supported by brazilian agencies CNPq, FAPESP and FAPERGS.

References.

1. J. P. de Souza, I. Danilov, and H. Budinov, Appl. Phys. Lett. **68** (4), 535 (1996).
2. S. J. Pearton, Mater. Sci. Rep. **4**, 313 (1990).
3. K. Krambrock and J. M. Spaeth, Phys. Rev. B **47**, 3987 (1993).
4. S. Kuisma, K. Saarinen, P. Hautojärvi, and C. Corbel, Phys. Rev. B **53**, 7588 (1996).
5. A. Janotti, A. Fazzio, P. Piquini, and R. Mota, to be published in Phys. Rev. B.
6. S. Pöykkö, M. J. Puska, and R. M. Nieminen, Phys. Rev. B **55**, 6914 (1997).
7. G. B. Bachelet, D. R. Hamann, and M. Schlüter, Phys. Rev. B **26**, 4199 (1982).
8. L. Kleinman and D. M. Bylander, Phys. Rev. Lett. **48**, 1425 (1982).
9. P. Hohenberg and W. Kohn, Phys. Rev. **136**,B864 (1964);W. Kohn and L. J. Sham, Phys. Rev. **140**, A1133 (1965).
10. R. Car and M. Parrinello, Phys. Rev. Lett. **55**, 2471 (1985).
11. J. Perdew and A. Zunger, Phys. Rev. B **23**, 15048 (1981).
12. M. J. Caldas, J. Dabrowski, A. Fazzio, and M. Sheffler, Phys. Rev. Lett. **65**, 2046 (1990).
13. G. A. Baraff and M. Schlüter, Phys. Rev. B **33**, 7346 (1986).

Materials Science Forum Vols. 258-263 (1997) pp. 981-986

STUDY OF PLASTICALLY DEFORMED SEMICONDUCTORS BY MEANS OF POSITRON ANNIHILATION

H. S. LEIPNER, C. G. HÜBNER, J. KRÜGER[1], R. KRAUSE-REHBERG

Fachbereich Physik, Friedemann-Bach-Platz 6,
Martin-Luther-Universität Halle-Wittenberg, D-06108 Halle, Germany
(leipner@physik.uni-halle.de)
[1]Center for Advanced Materials, Lawrence Berkeley National Laboratory,
University of California, Berkeley, CA 94720, USA

Keywords: plastic deformation, positron annihilation, vacancies, antisites, dislocations

Abstract. Deformation–induced defects have been studied by means of positron annihilation. Temperature–dependent positron lifetime spectroscopy indicates the presence of dislocations acting as shallow positron traps. The decomposition of the lifetime spectra provides positron lifetime components related to vacancy clusters and mono– or divacancies. The correlation between positron measurements and electron paramagnetic resonance gives evidence that the Ga_{As} antisite is formed during plastic deformation. The density of point defects is estimated for different deformation conditions.

Introduction

The defect spectrum formed during plastic deformation of semiconductors is much more complex than that after irradiation with high–energy particles. The movement and the interaction of dislocations as the primary defects is thought to be responsible for the generation of various point defects. Different mechanisms have been discussed, depending on extrinsic parameters, e. g. the deformation temperature and the impurity level, and on intrinsic parameters, e. g. the stacking fault energy or the self–diffusion coefficient. These mechanisms are related to different stages of dynamic recovery of the stress–strain curve. For instance, a cross–slip mechanism was proposed for stage V. The model of Barrett and Nix [1], describing the dragging of jogs along screw dislocations, which results in a high number of vacancies at low or medium deformation temperatures, seems to play a special role. So far, the analysis of the different deformation stages was carried out with empirical power laws. First attempts have been made to phenomenologically calculate the density of deformation–induced vacancies [2].

Several spectroscopic or microscopic methods have been applied to characterize the point defects and dislocations present after plastic deformation. As early as 1969, positron annihilation was used to study plastically deformed silicon and germanium [3]. Saarinen et al. [4] and Krause-Rehberg et al. [5] analyzed the point defect spectrum in plastically deformed compound semiconductors using positron lifetime spectroscopy (POLIS). Dannefaer et al. [6] were the first to deal with dislocations in semiconductors as shallow positron traps. However, the interaction of positrons with dislocations seems to be rather complicated. It is not clear, whether positron trapping in dislocations is limited by the positron diffusion to the defect or by the transition rate. Both mechanisms provide in metals [7] a trapping rate approximately $\propto T^{-1/2}$ (T sample temperature). The favored model of positron capture in dislocations is a cascade process. The undisturbed dislocation line acts as a shallow precursor state, before the positron is trapped in a deep level related to a vacancy bound to the dislocation (Fig. 1). The transition to the deep level of the bound vacancy is very fast, so that the detrap-

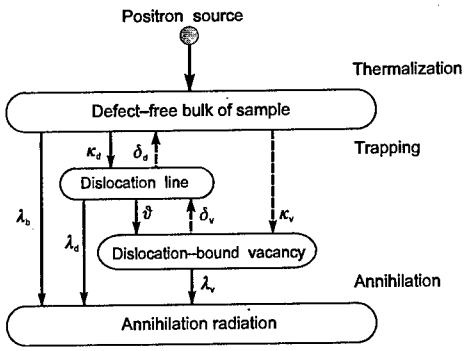

Fig. 1. Cascade trapping process in dislocations. The positron is trapped after thermalization in a shallow level related to the undisturbed dislocation line and transferred to a deeper level associated with a vacancy bound to the dislocation core. λ_i are the annihilation rates, κ_i the trapping rates, and δ_i the detrapping rates (i—dislocation d, vacancy v, bulk b). ϑ is the transition rate from the shallow to the deep state. The processes marked by dashed lines may be neglected for neutral dislocations.

ping rate from the shallow level, δ_d, may be neglected for neutral dislocations. The annihilation rate of the shallow level of the dislocation line, λ_d, is not very different from the bulk annihilation rate λ_b, $\lambda_d \approx \lambda_b$. Further approximations neglect the direct trapping in the bound vacancy κ_v and the detrapping rate δ_v, so that the solution of the set of rate equations of the scheme in Fig. 1 can be easily given [7]. Dislocations in n–type or undoped semiconductors are usually negatively charged. This leads to the formation of extended shallow Rydberg states. For simplicity, the same shallow level as for uncharged dislocations is assumed, but the detrapping rate δ_d cannot be neglected any more. Manninen and Nieminen [8] calculated in a thermodynamic approach the ratio of the detrapping and trapping rate,

$$\frac{\delta_d}{\kappa_d} = \frac{m^* k_B T N^{2/3}}{2\rho\hbar^2} \operatorname{erf}^{-1}\left(\sqrt{\frac{E_d}{k_B T}}\right) \exp\left(-\frac{E_d}{k_B T}\right)$$

(m^* effective positron mass, k_B Boltzmann constant, N number of atoms per unit volume, ρ dislocation density, E_d positron binding energy to the shallow dislocation level).

However, it is rather difficult to separate the dislocation signal from the contributions of point defects to the positron lifetime spectrum. In addition to dislocation–related defects, there are other positron traps, such as vacancies, vacancy clusters. A further complication arises in compound semiconductors with the appearance of point defects acting as shallow positron traps. It is hardly possible to separate more than two defect–related components from the decomposition of a positron lifetime spectrum. More information can be obtained from temperature–dependent positron lifetime measurements in conjunction with annealing experiments. In this study, the influence of the variation of deformation conditions (strain, strain rate, sample orientation, deformation temperature) on the defect densities in plastically deformed undoped gallium arsenide was investigated.

Experimentals

Prismatic single–crystalline samples ($12\times4\times5$ mm^3) were prepared from a nominally undoped GaAs ingot grown by liquid encapsulated Czochralski technique (Freiberger Compound Materials). The specific resistivity was $> 1\times10^7$ Ωcm. The samples were deformed in protective argon atmosphere by uniaxial compression at constant strain rates ranging from of 9×10^{-6} to 6×10^{-3} s^{-1}. [100], [110], and [213] deformation axes were chosen. The deformation temperatures were between 350 to 800 °C. The deformed bar was rapidly cooled after deformation to room temperature with about 3 K s^{-1}. Samples from the central part of the deformed bar were cut and polished for the spectroscopic analysis. Two adjacent slices were used for the positron annihilation measurements.

The positron lifetime was measured using a standard fast–fast coincidence spectrometer with a time resolution (FWHM) of 245 ps. A pair of samples was sandwiched with a 8×10^5 Bq source of

^{22}Na on an Al foil. About 2×10^6 counts were collected during 2 h. A closed–cycle He cryostat was used to vary the temperature from 10 to 600 K. A positron lifetime experiment was carried out with placing the samples in a magnetic field of 1.3 T in order to check for the formation of positronium.

In addition to the positron annihilation experiments, electron paramagnetic resonance (EPR) investigations were carried out with a modified Bruker ER-200 D SRC X band spectrometer at a temperature of 6.5 K in order to get information about the formation of antisite defects.

Results and discussion

The average positron lifetime is plotted in Fig. 2 as a function of the sample temperature. The decomposition of the positron lifetime spectra at room temperature results in three components: a reduced bulk lifetime and two defect–related lifetimes of $\tau_{d1} = (301 \pm 16)$ ps and $\tau_{d2} = (490 \pm 24)$ ps. The shorter positron lifetime τ_{d1} lies between the value of 295 ps experimentally found for monovacancies [9] and the value of 321 ps theoretically predicted for divacancies [10]. It was observed that this component nearly vanished after heat treatment of the deformed sample at 725 K for 30 min. The annealing of a defect band at 0.99 eV related to the EL6 center was found in infrared absorption measurements in the same temperature range [11]. A divacancy character of the EL6 defect has been discussed [12] and it is thus likely that this center gives a contribution to the lifetime τ_{d1}. However, other open–volume defects, such as monovacancies and dislocation–bound vacancies, the positron lifetime of which cannot be further resolved, may contribute to τ_{d1}.

The long–lived positron lifetime component τ_{d2} can be attributed to vacancy clusters. It can be deduced from the theoretical calculation of the positron lifetime as a function of the cluster size [13] that a saturation around 500 ps is reached for clusters containing at least ten vacancies. So, the actual size of the vacancy clusters cannot be given from τ_{d2}. However, the size can be estimated from the temperature dependence of the trapping rate of the vacancy clusters [6]. The trapping rate is calculated in the propagation model as $\kappa = v\sigma C$, where v is the thermal velocity of the positron and C the defect concentration. The temperature–dependent trapping cross section is given by $\sigma = \pi(r + 1/k)^2\xi$, with the radius of the defect r, the thermal wave number of the positron k, and the transmission coefficient ξ. The trapping in the vacancy–type defects d1 and in the vacancy clusters d2 dominates the temperature dependence above about 200 K. With the temperature dependencies for different void sizes given by Dannefaer et al. [6], it can be estimated that the radius of the vacancy clusters is about 2 nm.

It is conceivable that the size of the vacancy clusters is sufficient for the formation of positro-

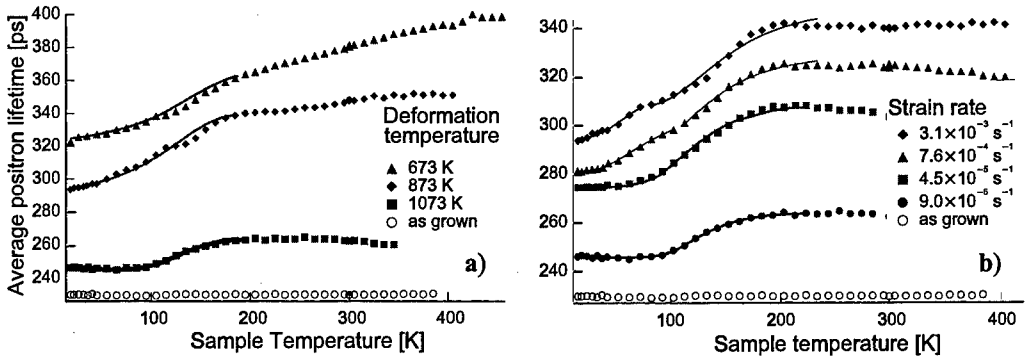

Fig. 2. Average positron lifetime as a function of the sample temperature in undoped GaAs plastically deformed in [110] direction up to 10 % strain **a)** at different temperatures (9×10^{-6} s^{-1} strain rate) and **b)** at different strain rates (800 °C deformation temperature). The full lines are fits as described in the text.

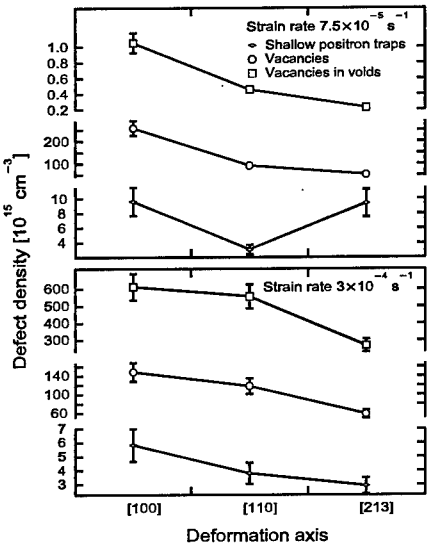

Fig. 3. Defect densities determined by temperature–dependendent positron lifetime measurements in undoped GaAs deformed up to 3 % in [100], [110], and [213] directions, respectively. The strain rates were 7.5×10^{-5} s^{-1} (upper panel) and 3×10^{-4} s^{-1} (lower panel), the deformation temperature 500 °C. The number of vacancies in voids was calculated from the obtained void radius of 2 nm. The lines are drawn to guide the eye.

nium. However, no modification of the lifetimes due to the reduction of the ortho–positronium fraction was observed in a magnetic quenching experiment exposing the sample to a magnetic field of 1.3 T during the positron lifetime experiment. It is thus concluded that no measurable fraction of positronium is formed in the vacancy clusters.

No reasonable decomposition of the positron lifetime spectra could be carried out for temperatures below 200 K. The strong decrease in the average lifetime can be explained by the occurrence of shallow positron traps. The solid lines in Fig. 2 are fits to the experimental data with the trapping model and including the temperature dependence of the detrapping rate to shallow traps [8]. The fitting procedure providing the densities of shallow traps, vacancies and vacancy clusters (Fig. 3) is the same as applied for tellurium–doped GaAs [5]. A kink in the curves, which is more remarkable for higher strain rates, occurs at about 100 K (Fig. 2b). This kink may be explained by two different types of shallow positron traps *d* and *p*. The curves were fitted in the low and high temperature parts separately. Two positron binding energies of 38 ± 13 meV and 12 ± 7 meV, respectively could be obtained. The former value is due to a point defect and corresponds to that assigned to the negatively charged Ga_{As} antisite defect [14]. The most likely candidate for the latter shallow trap is the dislocation line (Fig. 1). At high strain rates, dislocations cannot surmount obstacles by climbing and a strong dislocation multiplication occurs resulting in a higher dislocation density in samples deformed with a higher strain rate. The signals of both types of shallow traps can be separated. After isochronal annealing at 1070 K only the shallow traps *d* related to dislocations remained. The rearrangement of the dislocation network during annealing gave rise to a slight increase in the positron binding energy. The spectra decomposition at room temperature showed that only the component related to vacancy clusters remained after annealing.

The identification of the Ga_{As} antisite is still a matter of controversy. In order to be attractive for positrons, non–open volume defects must carry a negative charge. There is a number of candidates for negatively charged non–open volume defects in as–grown GaAs. Under discussion are on the one hand impurities such as boron or oxygen, and on the other hand interstitials. There is however clear evidence that the concentration of the shallow positron trap *p* is related to the parameters of the plastic deformation. The density of the *p* defect was as high as 1×10^{17} cm^{-3} after 10 % deformation at 400 °C with a strain rate of 4×10^{-4} s^{-1}. This density is well above the level of residual impurities. It is thus concluded that the shallow positron trap *p* is an intrinsic defect.

In order to get more information about the nature of this shallow positron trap, investigations by electron paramagnetic resonance were carried out at the very same samples studied by positron annihilation. The formation of cation antisites during deformation of GaAs has been proved in a former study by Krüger and Alexander [15]. The Ga_{As}^{-} center exhibits in accordance with theoretical models a trigonal symmetry. The quadruplet lines of this defect can be separated from the As_{Ga} antisite by the saturation of the latter signal at a microwave power of 200 mW. Fig. 4 shows the density of Ga_{As}^{-} defects in GaAs deformed at different temperatures as obtained from the EPR measurements. The density of the shallow positron trap p obtained from the fit of the temperature–dependent average positron lifetime is also sketched in Fig. 4. Both densities lie close together. Moreover, the same relative changes of the concentrations $[Ga_{As}^{-}]$ and $[p]$ were found as functions of the deformation temperature, the strain rate, and of the orientation of the deformation axis (the latter two not shown here). Thus it is likely that the same defect type is both detected in EPR and positron lifetime spectroscopy. From the characterization of this defect by electron paramagnetic resonance it is inferred that it is the negatively charged Ga_{As} antisite.

With the independent determination of $[Ga_{As}^{-}]$ by EPR, the trapping coefficient μ_p for the shallow positron trap p as the proportionality constant between the trapping rate and the defect concentration ($\kappa = \mu_p C$) can be given. A value of $(2.6 \pm 0.3)\times10^{16}$ s^{-1} was obtained for temperatures below 200 K.

The densities of defects were determined for deformation axes in [100], [110], and [213] directions, respectively (Fig. 3). These orientations correspond to a different number of equivalent slip systems: one dominant slip system for [213], four systems for [110], and eight for [100]. With a higher number of equivalent slip systems, the frequency of dislocation cutting is higher. The intersection of dislocations leads to the formation of jogs or kinks depending on the Burgers vector, the glide direction, and the line vector. The resulting jogs may not be glissile and a further motion requires the emission of point defects. Their concentration can be calculated [16] as

$$C = \frac{1}{\Omega}\frac{\mathbf{e}_1 \cdot \mathbf{u}\times\mathbf{e}_2}{|\mathbf{e}_1 \cdot \mathbf{u}\times\mathbf{e}_2|}\mathbf{b}_1 \cdot \mathbf{u}\times\mathbf{b}_2 .$$

(Ω atomic volume, $\mathbf{u}$ direction of the motion of the dislocation with the Burgers vector $\mathbf{b}_1$ and the line vector $\mathbf{e}_1$. $\mathbf{b}_2$ and $\mathbf{e}_2$ are the Burgers vector and the line vector of the static dislocation.) The first term determines the sign, i.e. whether interstitials or vacancies are formed, the second one gives the number of point defects emitted.

The monovacancies emitted by the dragging of jogs are not stable at the deformation tempera-

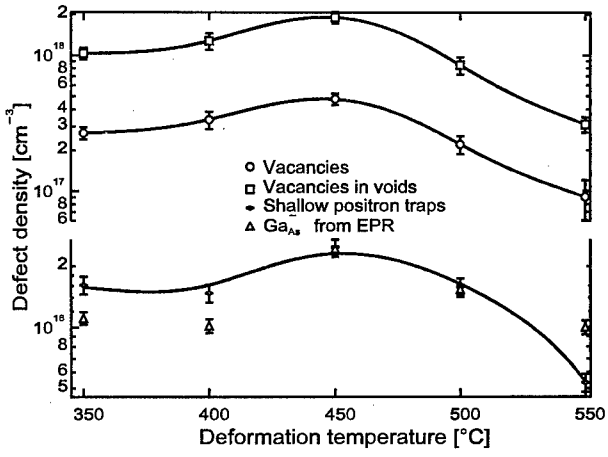

Fig. 4. Densities of defects after plastic deformation of undoped GaAs as a function of the deformation temperature for a [100] deformation axis. The strain was 3 % and the strain rate 7.7×10^{-6} s^{-1}. The number of vacancies in voids was estimated taking a void radius of 2 nm. The density of shallow positron traps is compared to the density of Ga_{As} antisites determined by electron paramagnetic resonance (EPR). The lines are drawn to guide the eye.

ture and clustering reactions to stable configurations occur. The interstitials formed are not visible by positron annihilation, but antisite defects are formed in secondary reactions between interstitials and vacancies.

Strain rate and deformation temperature dependencies of the densities of vacancy–type defects and antisites can be understood in the framework of the quantitative model of vacancy formation during plastic deformation by Militzer et al. [2]. From the balance of the vacancy concentration

$$\dot{C} = \frac{\sigma_p \dot{\varepsilon}}{E_j} - \frac{D}{\Lambda^2}\Delta C$$

(σ_p plastic strain, $\dot{\varepsilon}$ strain rate, E_j vacancy formation energy for jog dragging, D vacancy diffusion coefficient, $\Lambda = \rho^{-1/2}$ mean spacing between dislocations as sinks of vacancies), the excess vacancy concentration ΔC can be calculated in the stationary case. A higher concentration of excess vacancies with a higher strain rate follows immediately, what is also found in the experiments. From the model, a temperature dependence of $\ln C \propto T^{-1}$ is deduced. It was observed however that the defect density increased in the low temperature range (Fig. 4). In this range, the annihilation rate of vacancies at sinks is higher than the production rate due to the low frequency of dislocation intersections. Above a critical temperature, the expected decrease is observed. The exponent of the dependence of C from the strain rate is found to be smaller than one, what is also obtained in the model of Militzer et al. [2].

Acknowledgments. We would like to thank Eicke Weber (Berkeley) for valuable discussions and for enabling the stay of CGH at the University of California in Berkeley. Special thanks are due to Isabelle Billard (Strasbourg) for the positronium investigations. The study was supported by the Deutsche Forschungsgemeinschaft.

References

1. C R Barrett, W D Nix: Acta Metall. **13** (1965) 1247.
2. M Militzer, W P Sun, J J Jonas: Mater. Sci. Forum **113–115** (1993) 163.
3. I Y Dekhtyar, V S Mikhalenkov, S G Sakharova: Fiz. Tverd. Tela **11** (1969) 3322.
4. K Saarinen, C Corbel, P Hautojärvi, P Lanki, F Pierre, D Vignaud: J. Phys.: Cond. Mat. **2**(1990) 2453.
5. R Krause-Rehberg, H S Leipner, A Kupsch, A Polity, T Drost: Phys. Rev. B **49** (1994) 2385.
6. S Dannefaer, P Mascher, D Kerr: J. Appl. Phys. **69** (1991) 4080.
7. K Petersen, I A Repin, G Trumpy: J. Phys.: Cond. Mat. **8** (1996) 2815.
8. M Manninen, R M Nieminen: Appl. Phys. A **26** (1981) 93.
9. C Corbel, F Pierre, K Saarinen, P Hautojärvi, P Moser Phys. Rev. B **45** (1992) 3386.
10. M J Puska, S Mäkinen, R M Nieminen: Phys. Rev. B **39** (1989) 7666.
11. H S Leipner, C Hübner, O Storbeck, A Polity, R Krause-Rehberg in: *Semiconducting and insulating materials 1996*. IEEE: Piscataway (1996) p. 283.
12. C V Reddy, S Fung, C D Beling: Phys. Rev. B **54** (1996) 11290.
13. M J Puska, C Corbel: Phys. Rev. B **38** (1988) 9874.
14. K Saarinen, P Hautojärvi, A Vehanen, R Krause, G Dlubek:. Phys. Rev. B **39** (1989) 5287.
15. J Krüger, H Alexander: Mater. Sci. Forum **83–87** (1992) 899.
16. S Amelinckx in: *Dislocations in solids*, F R N Nabarro, Editor. North Holland: Amsterdam (1979) p. 67.

Materials Science Forum Vols. 258-263 (1997) pp. 987-992

THE MICRO STRUCTURE OF THE EL2 DEFECT IN GaAs - A DIFFERENT LOOK TO FORMER SPIN RESONANCE DATA

F. Wirbeleit and J.R. Niklas

Technical University Bergakademie Freiberg, Institute of Experimental Physics, Silbermannstr. 1, GER. - 09596 Freiberg / Sachsen

Keywords: EPR ENDOR ODENDOR GaAs EL2 DEFECT

Abstract. The As(Ga)-As(i) model for the antisite defect in GaAs as derived from former ODENDOR and ODMR experiments [1] was checked by simulating X-band and K-band EPR spectra using the ODENDOR data for the four nearest As neighbours and the As [111] interstitial according to [1]. The calculations are based on a full diagonalisation of the spin Hamiltonian taking into account also all forbidden transitions with their individual intensities which turned out to be essential. It clearly followed that the simulated EPR spectrum is significantly broader than the corresponding experimental ODEPR spectrum. To facilitate also the simulation of conventional X-band EPR spectra of different authors a computer time efficient new way of handling large spin matrices, termed "reduced procedure", was introduced and tested. Again, considering the interstitial As turned out to be inconsistent with these spectra. Apparently there were more neighbour nuclei with large interaction constants extracted from the ODENDOR experimental data than are consistent with ODEPR or conventional EPR. It is concluded that the ODENDOR data must no longer be taken as evidence for the existence of the As [111] interstitial as an integral part of the EL2 as claimed. By omitting the As interstitial both the ODEPR and the conventional EPR spectrum can be fitted using the same input data providing evidence that the same defect was investigated by conventional and optically detected EPR.

I. Introduction

Despite of more than one decade of research activities, the microstructure of the EL2 antisite defect in GaAs is still a matter of discussion [2]. The open question is whether or not the As atom on Ga site, As(Ga), is accompanied by an As interstitial, As(i), in the [111] direction. The As(Ga)-As(i) model was developed on the basis of former ODENDOR experiments claiming for the As interstitial ligand hyperfine interaction constants in the same order of magnitude as for the four first shell As neighbour nuclei [1]. This model is illustrated in Fig.1.

There are many arguments against this As(Ga)-As(i) model but also some arguments supporting it. As an example, the As(Ga)-As(i) model is supported by DLTS experiments [3], and the metastability of the EL2 defect can be explained [4]. From conventional experiments it was first concluded that the EL2 should consist of a pure As(Ga) without an interstitial As [5]. The question became more and more important whether or not the different experiments are really dealing with exactly the same defect. In particular, it was not even unambiguously clear, whether or not conventional EPR and ODMR/ODENDOR are looking at the same defect. In fact,

valuable additional pieces of information can be obtained by cross-checking the consistency between conventional EPR spectra, ODMR spectra, and ODENDOR results. Up to now, this was not yet followed in a suitable way for the EL2 defect, apparently mainly due to computational problems when handling large spin Hamiltonian matrices. As it is well known (see e.g. [6]), EPR spectra and ENDOR spectra are governed by the same spin Hamiltonian only different spin transitions are detected by both experimental methods. This means, if all Zeeman, hyperfine, ligand hyperfine and quadrupole interactions for each individual neighbour nucleus are correctly determined with ENDOR, then, after addition of the electron Zeeman term (S=1/2 for As(Ga)), the corresponding experimental EPR spectrum can be precisely reproduced theoretically. There are no free parameters, except for the amplitude of the EPR spectrum which is trivial. E.g., for the old example of Te^+ in Si [7,6], this was demonstrated in detail. If the lines in the simulated EPR spectrum are smaller than the experimental ones, then neighbour nuclei might have been overseen or purposely not been included in the ENDOR analysis. The latter is usually the case for very distant neighbour shells. If, however, the lines in the simulated EPR spectrum are broader than the experimental ones, then the ENDOR analysis is simply wrong. In this case there were more neighbour nuclei extracted from the ENDOR data than are consistent with the corresponding EPR spectrum or wrong interaction constants were determined. (The latter case is usually less probable). In principle, it can also not generally be excluded that, due to some experimental accident, in fact different defects are investigated by EPR and ENDOR. Due to the lack of resolution, EPR spectra particularly for defects in semiconductors usually do not provide very much detailed information. If, however, the details are known from ENDOR, the shape of the corresponding EPR spectrum provides a surprisingly crucial test whether or not the ENDOR analysis is correct. This is applied in the following to the problem of As(Ga) models.

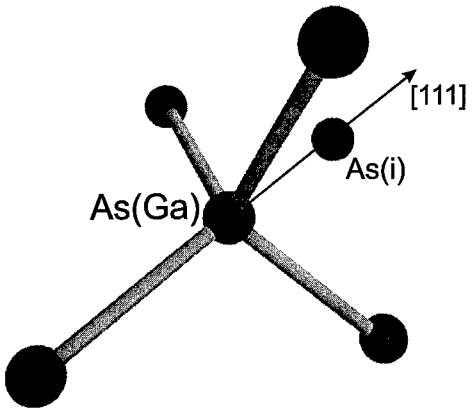

Figure 1: As(Ga)-As(i) model after [1].

2. EPR Simulation Technique

Simulating EPR spectra is rather difficult for the As(Ga) and As(Ga)-As(i) models due to relatively large anisotropic and quadrupole interaction contributions causing significant off-diagonal elements in the spin Hamiltonian. This, in turn, leads to many, in first order, forbidden transitions with intensities comparable to allowed ones. Taking these transitions, however, into account turned out to be essential. Often used perturbation theory approaches for an efficient calculation of these transitions are therefore inadequate. The EPR results were obtained by a full diagonalisation of the

entire Hamiltonian for the model shown in Fig. 1. The effect of higher shells was neglected, the calculated EPR lines should therefore exhibit a smaller width than the experimental ones. One Hamiltonian was diagonalised for each magnetic field step of the EPR spectrum. From the diagonalised Hamiltonian at a given magnetic field all those transitions were then selected which fall into a small frequency interval (e.g. +- 50 MHz) around the fixed microwave frequency of the spectrometer. As the EPR signal at a given magnetic field, all these transitions were summed up taking into account their individual calculated intensities. It was carefully checked that the width of the simulated EPR spectrum was not visibly influenced by the width of the chosen frequency interval. The Hamilton matrix for the six As nuclei with spin 3/2 and with electron spin 1/2 (compare with Fig. 1) is of the rank 8192. A diagonalisation of this matrix is feasible with modern high power computers, however, for all EPR spectra simulations several hundreds of these matrices must be diagonalised, which is impossible using standard techniques. It turned out, however, that the spin Hamilton matrices can be constructed in a way where off-diagonal elements from far outside the diagonal are very small compared to off-diagonal elements in the vicinity of the diagonal and compared to the diagonal itself and where the great majority of all off-diagonal elements is zero. Such an occupation pattern is known in mathematics as "diagonal dominant". An example is illustrated in Fig. 2. For such a matrix it can be verified that the small off-diagonal elements far from the diagonal exhibit only a negligible influence on the eigenvalues of the matrix. This effect is more pronounced the larger the matrix. If distant off-diagonal elements have only a small effect on the eigenvalues of the matrix they can be replaced by zero as well. As a consequence, the large matrix divides into smaller independent blocks which can be diagonalised individually. Particularly for very large matrices, this procedure saves orders of magnitude of computer time with only little degradation of accuracy. The degree of accuracy is determined by the block size selected which, in turn, is a question of computer time available. For practical cases, the computational errors can be kept well below the experimental uncertainties. Details of this procedure, which will be referred to as "reduced procedure" in the following, will be published elsewhere [8].

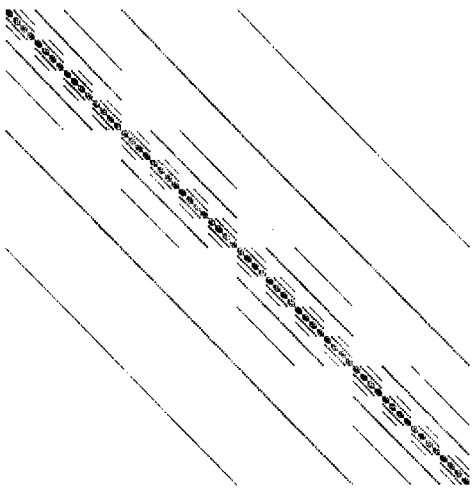

Figure 2: Occupation pattern of a large spin Hamilton matrix. Elements different from zero are indicated by points.

3. Simulation Results

The EPR spectrum of the $EL2^+$ is split into four broad lines due to the large isotropic hyperfine interaction of the As on the Ga site. It can be easily verified and understood that the width of each of these four lines does not noticeably depend on the spin state of the central As (I=3/2). In the simulations, the same width of such a line is obtained even when leaving out the central nucleus. The rank of the spin Hamilton matrix then reduces to 2048 (compare again Fig. 1). Results of such a simulation are summarised in Fig. 3 taking as input parameters the results from the ODENDOR analysis [1]. The inner part of the spectrum corresponds to a simulation without the [111] As interstitial, As(i), where four nearest As neighbours were taken into account. The calculations took place via an exact diagonalisation of spin matrices with rank 512. The resulting half width of the spectrum is in agreement with the experimentally obtained ODEPR line width [1] as indicated. The outer part of the spectrum does include the As(i). The calculation mainly made use of the reduced procedure. The open circles correspond to results obtained for an exact diagonalisation of matrices with rank 2048 agreeing well with

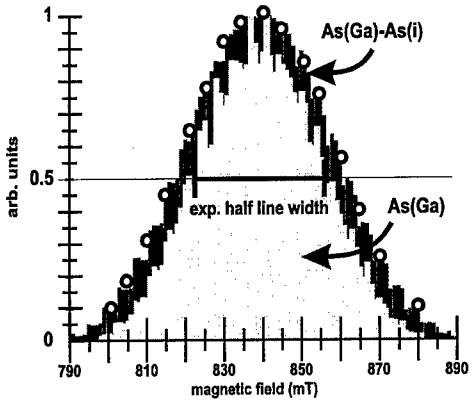

Figure 3: Simulated ODEPR spectra based on ODENDOR data [1] for the As(Ga) and the As(Ga)-As(i) model, respectively. The experimental ODEPR half width (33.5 mT [1]) is indicated by the horizontal line. For further details see text.

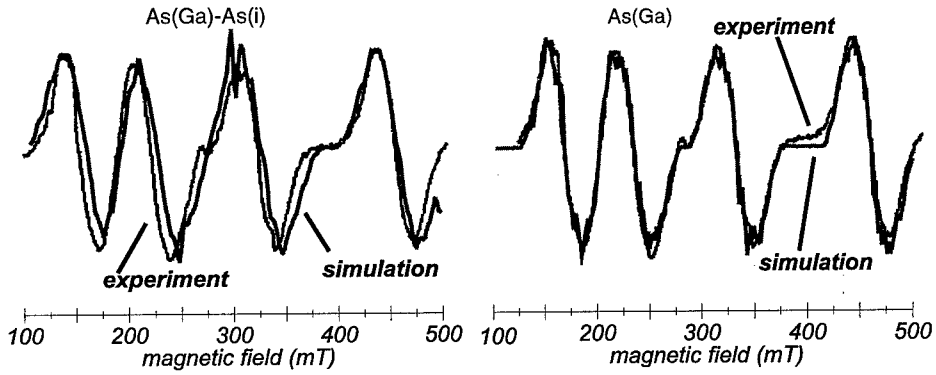

Figure 4: Comparison of conventional X-band EPR spectrum [5] with the simulated ones using ODENDOR interaction parameters [1], reduced procedure applied.
left part: As(Ga)-As(i) defect model; right part: As(Ga) model

the results by the reduced procedure. It is evident that the simulated EPR spectrum for the As(Ga)-As(i) model is significantly broader than the experimental one. According to the statements in section 1, this means, that the ODENDOR analysis [1] claiming the existence of the As(i) as an integral part of EL2 must be wrong. Again using the ODENDOR data, the conventional X-band EPR spectrum of a different author [5] was also simulated for the As(Ga) and the As(Ga)-As(i) model, respectively. (Calculations were made with the reduced procedure, rank of matrix 8192). As can be clearly seen from Fig. 4, only the As(Ga) model without the interstitial As is in agreement with the experimental EPR data. It follows at the same time, that for the As(Ga) model without the interstitial As, the ODEPR and the conventional EPR spectrum can both be nicely fitted by the same data. This provides evidence that the same defect was investigated with ODEPR and with conventional EPR.

4. Discussion

It turned out to be very probable that with ODEPR and with conventional EPR the same $EL2^+$ defect was investigated. However, the ODENDOR analysis [1] must no longer be regarded as evidence for the existence of an As interstitial, As(i), as integral part of the As(Ga) defect as claimed. The EPR spectra available (ODEPR, conventional EPR) are consistent with the pure As(Ga) model with T_d symmetry. Further details of the $EL2^+$ structure are beyond the scope of the above investigation. This could be made the subject of a revised ODMR investigation comprising improved experimental methods.

5. Acknowledgement

The authors wish to thank J. Monecke, Dept. for Theoretical Physics and M. Eiermann, Dept. for Mathematics of the Technical University Bergakademie Freiberg for stimulating and valuable discussions.

6. References

[1] B.K. Meyer, D.M. Hofmann, J.-M. Spaeth, *Mat. Sci. Forum,* **10-12**, 311 (1986)
[2] C. Ziegler, U. Scherz, and M. Scheffler, *Mat. Sci. Forum,* **143-147**, 995 (1994)
[3] D. Stievenard, H.J. von Bardeleben, J.C. Bourgoin, and A. Huber, *Mat. Sci. Forum*, **10-12**, 305 (1986)
[4] C. Delerue, M. Lannoo, D. Stievard, H.J. v. Bardeleben, and C.J. Bourgoin, *Phys. Rev. Lett.*, **59**, 2875 (1987)
[5] R.J. Wagner, J.J. Krebs, G.M. Strauss, and A.M. Withe, *Solid State Commun.*, **36,** 15 (1980)
[6] J.-M. Spaeth, J.R. Niklas, and R.H. Bartram, "Multiple Magnetic Resonance Spectroscopy for Structural Analysis of Point Defects in Solids", Springer (Heidelberg) 1991
[7] J.R. Niklas and J.-M. Spaeth, *Solid State Commun.*, **46**, 121 (1983)
[8] F. Wirbeleit and J.R. Niklas, *J. Magn. Res.*, (1997) to be published

Materials Science Forum Vols. 258-263 (1997) pp. 993-996

DETECTION AND IDENTIFICATION OF THE EL2 METASTABLE STATE IN GaAs

J.C. Bourgoin

Groupe de Physique des Solides, Université Paris 7, C.N.R.S., Tour 23, 2 place Jussieu, 75251 Paris Cedex 05, France

Keywords : *GaAs, EL2, metastable, antisite, excited state.*

ABSTRACT – We present experimental data, giving the temperature dependence of filled EL2 metastable states in GaAs under photo-excitation, which demonstrate that the associated level is located around 40 meV below the conduction band. This result combined with previously published observations, allows us to conclude that the metastable state is the first excited EL2 state, linked to the L band. The reason this state is metastable is then derived and successfully confronted with experimental data describing the rate of the metastable to stable transformation.

I. INTRODUCTION

The defect labelled EL2 present in bulk GaAs has been the subject of extensive studies (for a review, see refs. [1 and 2]). Its electronic and optical characteristics have been determined and it has been demonstrated that this defect is related to an As atom on a Ga site. A few years ago, the study of the EL2 defect was practically abandoned when semi-insulating materials, which owe it their semi-insulating character, reached a satisfactory state for micro-electronics applications. However, the physics of this defect are far from being fully understood. In particular, it possesses a so-called metastable state which has, up to now, escaped detection and whose nature is unknown. The aim of this communication is to suggest a simple means to realize this detection and to perform it. We will then identify the nature of the metastable state which allows us to deduce the physical reason for the metastability.

II. THE METASTABLE STATE

The existence of a metastable state associated with the EL2 defect has been demonstrated [3] early, by monitoring the time dependence of the capacitance under photo-lumination of a reverse biased p^+-n junction in GaAs material containing EL2 defects.

Let C_0 be the capacitance of a p^+- n junction which contains filled EL2 defects in its space charge region (developed on the n side). The filling is realized by cooling down the material in dark (below typically 100 K) and applying subsequently the bias. As sketched in Figure 1,

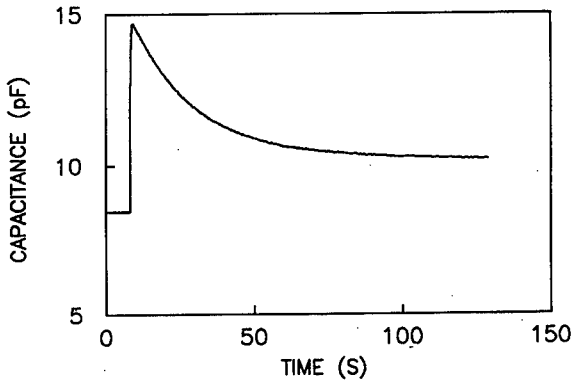

Fig. 1 – Time dependence of the capacitance induced by photo-excitation with white light, measured at 109 K.

when light illumination is then turned on, the capacitance increases to a value C_{max} and then further decreases to a value C_{min}. The change from C_0 to C_{max} is due to the fact that electrons are ionized from EL2 defects and leave the space charge region. As a result, the difference $C_{max} - C_0$ corresponds to the concentration of EL2 defects. The decrease from C_{max} to C_{min} corresponds to the creation of new states which have the same charge as filled EL2 ones. It has been demonstrated [3] that these new states, usually labelled EL2*, are directly related to EL2 defects. They are metastable because they persist once the light is turned off and because the transformation EL2* → EL2 occurs only when the temperature is increased (above typically 120 K).

Since an EL2* state localizes an electron, it should possess an energy level, E_T^*, located in the gap. Thus the capacitance difference $C_{max} - C_{min}$ corresponds to the concentration of filled EL2* states. When all the EL2 are transformed into filled metastable states, C_{min} is equal to C_0.

The obvious reason for which this metastable state has not been detected is that electron emission from E_T^* to the conduction band (E_C) occurs at a temperature higher than the temperature at which the EL2* → EL2 transformation takes place. However, it is perhaps possible to get an estimate of $E_C - E_T^*$ from the temperature dependence of the electron occupancy of the EL2* state, given by C_{min}, since it obeys the Fermi statistics. This EL2* occupancy f being: $f = (C_{max} - C_{min})/(C_{max} - C_0)$, the determination of $E_C - E_T^*$ consists in monitoring the capacitance versus time under illumination at different temperatures. The variation of C_{min} versus T gives f(T), from which one should deduce $E_C - E_T^*$ as the slope of the plot ln f (T^{-1}).

III. RESULTS

The experiment has been performed using $p^+ - n$ junctions realized by p^+ diffusion on a Czochralski grown material, slightly Si doped. The diodes, of area 2.5×10^{-3} cm^2, are mesa etched; the ohmic contacts are made by Au-Ge alloying on the back of the wafer and by gold evaporation on the p^+ layer. The gold layer is semi-transparent to allow photo-illumination.

Deep Level Transient Spectroscopy (DLTS) detects the EL2 defect at a concentration of 2.8×10^{16} cm^{-3}. The junction capacitance under a reverse bias of 2.5 V is $C_0 = 8$ pF when the EL2 defects are filled. The maximum capacitance C_{max} reached under illumination, 15 pF, is such that $C_{max} - C_0$ corresponds to the concentration of the EL2 traps detected by DLTS. This value C_{max} is temperature independent, as expected. It varies neither with the flux ϕ of illumination nor with the wavelength λ of the light (1.1 μm or visible lights have been used). Only the time constants, associated with the emptying of the EL2 defects and the formation of the EL2* defects, depend on ϕ and λ, but they are both temperature independent.

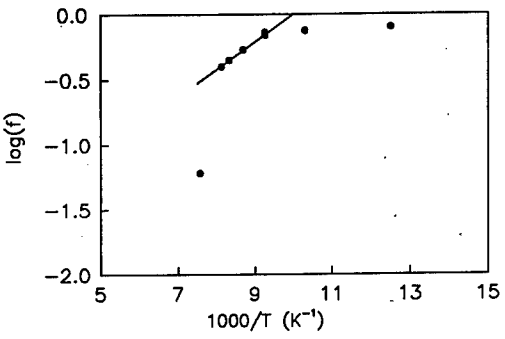

Fig. 2 – Arrhenius plot of the filling factor f of the metastable state. The line indicates an activation energy of 40 meV.

However, we observe that C_{min} varies with temperature suggesting that the temperature is high enough to modify the filling of the metastable state. From C_{min}, we

calculate f to get the temperature dependence of f, given in Figure 2. As seen on this figure, in the intermediary temperature range (100 – 120 K), the slope of this curve is 40 ± 10 meV. Since the Fermi level is located at 0.4 meV below the conduction band, this allows us to deduce that the energy level E_T^* is located 40 ± 10 meV from E_C. Below 100 K, electron ionization from the EL2* states is too small to be evaluated, and above 120 K the equilibrium is perturbed by the transformation of EL2* into stable EL2 states.

IV. THE NATURE OF THE METASTABLE STATE

We identify the EL2* state with an excited state of the stable EL2 state. There are indeed observations which indicate the existence of an EL2 related excited state [4]. Time resolved photoluminescence of the 0.635 eV band, known to be associated with EL2, suggests that this band corresponds to an internal transition, i.e. to the de-excitation of an electron from an excited state down to the fundamental state. Moreover, this same band exhibits sharp resonances for a photo-excitation a few tenth of an meV below the band gap energy.

There are three sets of excited states each linked to a different (Γ, L, X) conduction band. We identify the EL2* state with the L excited state, because the absorption lines associated with EL2 correspond to an internal $A_1 - T_2$ transition [5], where the zero phonon line exhibits the same hydrostatic pressure derivative as the L band [6]. The L excited state is lowest in energy although the L band is located at Δ = 0.30 eV above the (Γ) bottom of the conduction band. This occurs because the effective mass state is deepened by intervalley mixing [7] and is splitted as a result of a Jahn Teller distortion. Indeed, the T_2 state being threefold degenerate, its occupancy by one electron induces a Jahn Teller distortion.

In conclusion, we identify the EL2 metastable state as a neutral donor state of EL2, where the electron is localized on a shallow orbital corresponding to an L effective mass like state, T_2^L. The transition EL2 → EL2* corresponds, therefore, to the transfer of an electron from the fundamental EL2 state to the first excited L state (see Fig. 3).

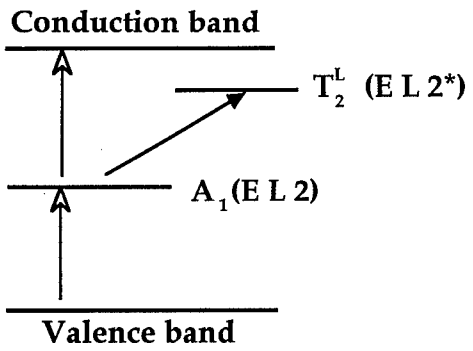

Fig. 3 – Representation of the electron transitions leading to the filling of the T_2^L excited state of EL2.

V. THE CAUSE OF METASTABILITY

The above identification provides a simple explanation for the origin of the metastability of the EL2* state. An electron occupying a T_2 excited state linked to the L band (EL2*) cannot decay directly on the A_1 ground state (EL2) simply because of the change in electron localization around the defect, hence the change in the electron-electron interaction, must be accompanied by a modification in the atomic configuration. The energy E corresponding to this modification of configuration has been estimated at 150 meV [8]. Consequently, electron capture on the EL2 state takes place only when the thermal energy is sufficient to induce this modification of configuration.

The rate for the transformation EL2* → EL2 is limited by the rate of electron capture from the L excited state to the ground state, because the thermal rate :

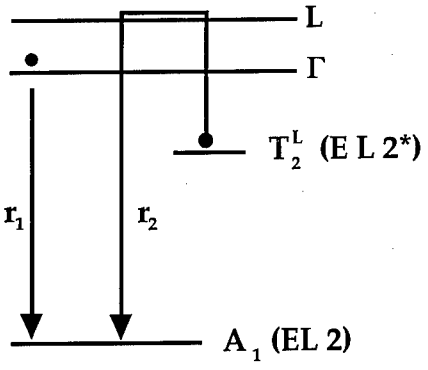

Fig. 4 – Processes for electron capture on the EL2 ground state.

$$r_{th} = \nu_{ph} \exp(-E/kT)$$

where $\nu_{ph} \sim 10^{12}$ s^{-1} is much faster. For this capture to occur, the excited electron must first reach the L band (see Fig. 4), and the rate r_2 of capture is thermally activated :

$$r_2 = r_0 \exp(-A/kT)$$

where $A = \Delta + (E_C - E_T^*)$, i.e. A = 0.34 eV. The rate of transformation observed experimentally is indeed thermally activated with an energy in the range 0.34 – 0.26 eV [3, 9-12]. In case free electrons (in concentration n) are present, electron capture and, consequently, the EL2* → EL2 transformation take also place with an additional rate :

$$r_1 = \sigma_0 \, v \, n \exp(-B/kT)$$

where σ_0 (10^{-14} to 10^{-16} cm^3 according to refs. [13-15]) is the capture cross section for electrons on the EL2 state and B (80 – 100 meV according to refs. [13-15]) the associated barrier. This process is also observed and fits quantitatively r_1.

V. CONCLUSION

In conclusion, we have detected the energy level associated with the metastable state of EL2. It is the first excited state of this defect, linked to the L band, located at 40 meV below the conduction band. This identification allows us to explain quite naturally the origin of the metastable character of this defect in terms of a barrier for electron capture due to the fact that an electron localized on the excited EL2* state must first reach the L band to be captured on the EL2 ground state.

REFERENCES

1. J.C. Bourgoin, J. von Bardeleben and D. Stievenard, J. Appl. Phys. **64**, R65 (1988).
2. G.M. Martin and S. Makram Ebeid, *in* Deep Centers in Semiconductors, ed. S.T. Pantelides (Gordon and Breach, N.Y.), **Chap. 6** (1986).
3. G. Vincent, D. Bois and A. Chantre, J. Appl. Phys. **53**, 3643 (1982).
4. B.V. Shanobrook, P.B. Klein, E.M. Swiggard and S.G. Bishop, J. Appl. Phys. **54**, 336 (1983).
5. H.J. von Bardeleben, Phys. Rev. B **40**, 12546 (1989).
6. M. Baj and P. Dreszer, Phys. Rev. B **39**, 10470 (1989).
7. A. Mauger and J.C. Bourgoin, Phys. Rev. B **46**, 12278 (1992).
8. J. Dabrowski and M. Scheffler, Phys. Rev. Lett. **60**, 2183 (1988).
9. A. Mitonneau and A. Mircea, Solid State Comm. **30**, 157 (1979).
10. Y.N. Mohapatra and V. Kumar, J. Appl. Phys. **64**, 956 (1988).
11. G. Vincent and D. Bois, Solid State Comm. **27**, 731 (1978).
12. X. Boddaert, D. Stievenard and J.C. Bourgoin, Phys. Rev. B **40**, 1051 (1989).
13. A. Mircea, A. Mitonneau, J. Hallais and M. Jaros, Phys. Rev. B **16**, 3665 (1977).
14. T. Matsumoto, P.K. Bhattacharya and M.J. Ludowin, Appl. Phys. Lett. **41**, 662 (1982).
15. A. Mitonneau and A. Mircea, G.M. Martin and D. Pons, Rev. Phys. Appl. **14**, 853 (1979).

Materials Science Forum Vols. 258-263 (1997) pp. 997-1002

DEFECTS IN THICK EPITAXIAL GaAs LAYERS

H. Samic° and J.C. Bourgoin

Groupe de Physique des Solides, Université Paris 7, C.N.R.S.,
Tour 23, 2 place Jussieu, 75251 Paris Cedex 05, France

Keywords: *Growth, GaAs, VPE, Hall effect, SIMS, IR absorption, EL2, luminescence.*

ABSTRACT. Thick (100 μm or more) layers of GaAs have been grown using various growth rates by Close Space Vapor Transport. We describe the results obtained by Hall effect, photoluminescence, IR absorption and secondary ion mass spectroscopy which allow the characterization of the impurities and defects they contain. The data provide in particular the variation of the concentration of EL2 defect versus the growth rate.

I. INTRODUCTION

Epitaxial growth is classically used to produce thin layers and heterostructures of good quality for micro- and opto-electronics. The up-to-date techniques, i.e.molecular beam and chemical vapor phase deposition techniques, are expensive, often polluting and do not allow the growth of layers more than few microns thick. However, there are many fields, such as high power electronics, optics, nuclear detection, for which the use of thicker epitaxial layers is required. Such thick layers cannot be produced by the above mentioned techniques.

However, we have used a simple, inexpensive and non polluting technique that allows the growth of very thick layers (from typically few microns to millimeters). This is a vapor phase technique with which the growth rate can be varied in a very large range (from 1 μm per hour to 50 μm per minute). Using this opportunity, we have grown thick (more than hundred microns) GaAs layers. The aim of this communication is to describe the electrical and optical characteristics of these layers in order to evaluate their potentialities for specific applications. We shall describe in particular how all these properties, which depend on the presence of impurities and lattice defects, vary with the conditions of growth.

II. THE GROWTH TECHNIQUE AND RESULTS

The technique is called Close Space Vapor Transport [for a recent review on the technique, see ref. 1]. It has already been used to grow thin epitaxial layers of various II-VI and III-V semiconductors, in particular GaAs [2], InP [3] and GaP [4]. It is based on the decomposition of a source material, here GaAs, by chemical reaction with an hydride, here H_2O. The gaseous products of this reaction are then transported in the concentration gradient of the gases to a substrate at a lower temperature where the reverse reaction takes place. The parameters which govern the growth are the source and substrate temperatures and the partial pressure of water in the transporting gas (H_2). The substrate and the source are placed face to face, separated by a short distance (of the order of few millimeters) so that the transport of matter, and hence the growth rate, is not limited

° *Permanent address:* Saobracajni Fakultet, Skenderija 35, 71000 Sarajevo (Bosnia-Herzegovina).

by diffusion but by the rate of the chemical reaction. The growth rate Vg can therefore be very large compared to the rates (1 μm per hour) of conventional techniques and it has been shown [1,5] that rates above 10 μm per minute can be reached easily.

In this communication we exploit the fact that high Vg values allow the growth of thick layers in a reasonable time, to grow layers with thicknesses of several hundred microns. Since such layers can find applications in many areas, we characterized their electronic and optical properties and the defects they contain to assess their potentialities.

III. CHARACTERIZATION OF THICK GaAs LAYERS

We performed optical and electrical studies of layers, 100 μm thick or more. We investigated in particular the variations of these properties, and of the nature and concentration of the defects they contain, with the growth rate. Structural characterizations have also been performed [6]. Briefly, X-ray topography demonstrates that the layers are free of dislocations and stacking faults. Double X-ray diffraction shows that the variation of the lattice parameter, compared to that of the substrate, is of the order of 10^{-5} to 10^{-3}. It varies with the growth rate, suggesting that the stoechiometry is rate dependent and, perhaps, with the thickness because the lattice strain depends on this thickness.

Hall effect measurements show that the free carriers are holes in the range $10^{15} - 10^{16}$ cm^{-3} (see Fig. 1) when the source is a semi-insulating, i.e. undoped Czochralski grown, material. This is in agreement with the fact that the source contains p-type dopants at a level of 10^{16} cm^{-3} compensated by n-type ones at a lower level (see below). The value of the hole mobility, as well as its temperature dependence (Fig. 2), indicates that the mobility is limited by phonons showing that

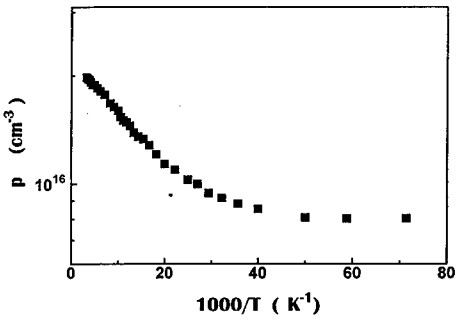

Fig. 1 – Temperature dependence of the free hole concentration in a 62 μm thick layer grown at 750° C with a growth rate of 1.7 μm.min^{-1}.

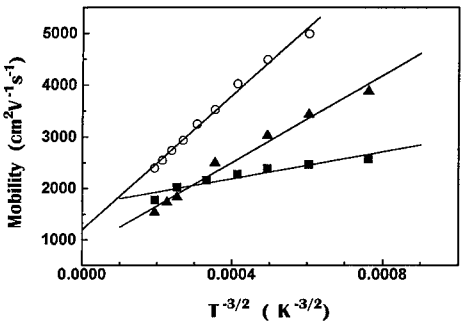

Fig. 2 – Temperature dependence of the hole mobility for three layers grown at 750 (○) and 800 (▲,■) °C with growth rates 1.7 (○), 3 (■) and 6.6 (▲) μm.min^{-1}. Their thicknesses are 62 (○), 30 (■) and 66 (▲) μm.

the layers contain a low level of charged defects. These conclusions are in agreement with the data provided by secondary ion mass spectroscopy (SIMS) (see Table I) and with photoluminescence observations. From SIMS analysis, it is found that the layers contain H at a level of $10^{16} - 10^{17}$ cm^{-3}, Si at a level of $10^{15} - 10^{16}$ cm^{-3} and C at $10^{16} - 10^{17}$ cm^{-3}; S exists also at a level ten times smaller than that of Si. The other impurity at a high level is O ($10^{17} - 10^{18}$ cm^{-3}) which is known to be inactive in GaAs (see Table II). The substrate temperature, as well as the growth rate, appears to have a negligible – if any – influence on the level of all these impurities as well as on

impurities which give rise to deep levels, given in Table II. These last impurities (Cr, Fe, Mn, Ni) are at the same level as in the source material.

Table I

Concentrations of the doping impurities detected by SIMS in layers grown from semi-insulating substrates.

Layer		**Impurity concentration** (cm^{-3})						
Growth rate ($\mu m.min^{-1}$)	*Substrate temperature* (°C)	*Al*	*C*	*H*	*Si*	*S*	*P*	*B*
5.4	800		3×10^{16}	7×10^{17}	5×10^{15}	1.2×10^{15}	$<10^{14}$	
0.5	720		2×10^{16}	5×10^{16}	2×10^{16}	6×10^{15}	1×10^{15}	
4	750		9×10^{16}	6×10^{16}	2×10^{16}	1×10^{16}	$<10^{14}$	
6.6	800	2×10^{15}			3×10^{15}			$\leqslant 10^{13}$
2	700	3×10^{15}			2×10^{16}			

Table II

Concentrations of the deep level impurities detected by SIMS in layers grown from semi-insulating substrates.

Layer		**Impurity concentration** (cm^{-3})										
Growth rate ($\mu m.min^{-1}$)	*Substrate temperature* (°C)	*O*	*Cl*	*Cr*	*Mn*	*Fe*	*Ni*	*Ti*	*Zn*	*Mg*	*Ca*	*Na*
5.4	800	7×10^{17}	2×10^{15}									
0.5	720	2×10^{17}	9×10^{14}									
4	750	4×10^{17}	3×10^{15}									
6.6	800			$\leqslant 10^{13}$	$\leqslant 10^{13}$	4×10^{13}	$\leqslant 10^{13}$	8×10^{14}	3×10^{15}	1×10^{14}	1×10^{15}	5×10^{14}
2	700			$\leqslant 10^{13}$		1×10^{14}		1×10^{15}	1×10^{15}	$\leqslant 10^{13}$	3×10^{14}	1×10^{15}

Photoluminescence confirms these observations. A typical photoluminescence spectrum (see Fig. 3) exhibits a strong band associated with the bond exciton, followed by the donor-acceptor and a phonon replica, which indicates that the material contains few deep defects. In the donor-acceptor recombination, the acceptor is Ga on As site, Ga_{As}. Another band of lower intensity corresponds to the transition from Si_{As} and Ga_{As} to the conduction band.

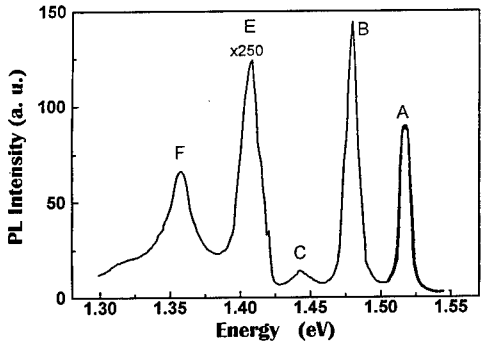

Fig. 3 – Typical photoluminescence spectrum exhibiting the bound exciton line (A), the acceptor (Si_{As})-conduction band transition (B) and the donor-acceptor (Ga_{As}) transition (C). The E band is a LO phonon replica of band C. The F band associated with the transition Cu-conduction band has only been observed once, obviously as a result of an accidental contamination.

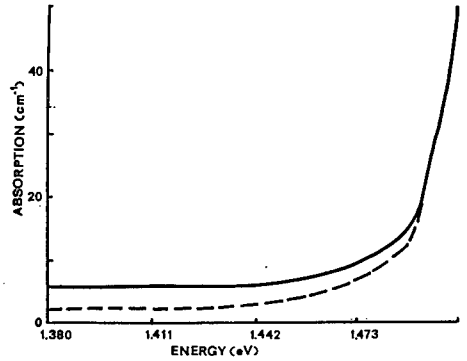

Fig. 4 – IR absorption spectra monitored at 4 K for a 180 μm thick layer (full line) and for the 680 μm thick substrate (dashed line). Absorption around 1 μm demonstrates that the substrate contains 3×10^{16} cm^{-3} EL2 defects, while the layer contains 4×10^{17} cm^{-3} of the same defect, as a result of a large growth rate.

The existence of the EL2 defect has been investigated by IR absorption. A typical spectrum contains a tail extending from the conduction band down to 1.3 eV and below, associated with EL2. In a thick layer, made with a large growth rate, this defect is found at a rather high level. As illustrated in Figure 4, the absorption at 1 μm, for a 170 μm thick layer grown at 5.8 $\mu m.min^{-1}$, gives a concentration of 4×10^{17} cm^{-3}, following the calibration of Martin *et al.* [7,8]. The increase of the EL2 concentration, C, versus the growth rate has not yet been quantitatively studied. Typically, for a substrate temperature of 800° C, at 1 $\mu m.min^{-1}$, C is of the order of 10^{14} cm^{-3}, while $C = 4 \times 10^{17}$ cm^{-3} at 6 $\mu m.min^{-1}$. It is also known that $C \sim 10^{13}$ cm^{-3} in a layer grown by a classical VPE technique, i.e. at a rate lower that 0.1 $\mu m.min^{-1}$. Preliminary data [5,9] suggested that C depends also on the substrate temperature θ. As shown in ref. [5], the variation of C versus Vg (or indirectly versus θ) is given by

$$C = C_0 \exp\left(\frac{-Ka}{Vg}\right)$$

where a is the lattice parameter, and

$$K = K_0 \exp\left(-\frac{E}{k\theta}\right)$$

the rate at which As antisite anneals on the surface during the time necessary to grow a layer. Using the available data, we can deduce from the plot of Figure 5 the concentration of the antisites (related to EL2 defects) initially deposited on one layer : $C_0 \simeq 1 \times 10^{18}$ cm^{-3} and $Ka \simeq 10^3$ Å s^{-1}. Taking for K_0 the frequency of lattice vibrations (10^{11} s^{-1}), we get : E = 2.2 eV.

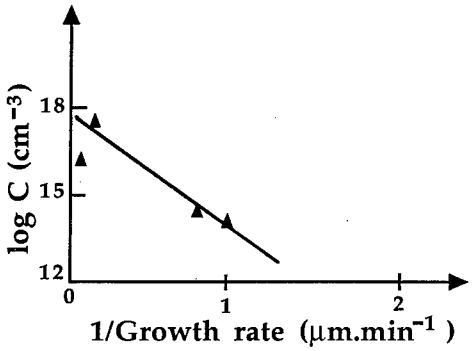

Fig. 5 – Growth rate dependence of the concentration of EL2 defects.

IV. CONCLUSION

We have characterized thick epitaxial GaAs layers which have been grown using a specific vapor phase technique allowing to reach very high growth rates. The results of Hall effect, photoluminescence, IR absorption and secondary ion mass spectroscopy demonstrate that these layers could be used for electronic and optical applications. Doping has been achieved and will be reported elsewhere [10]. These layers exhibit interesting features such as the variation of the EL2 concentration with the growth rate, which allows to adjust some of their properties for given applications. For instance, the concentration of EL2 defects can be adjusted to render a layer semi-insulating or to adjust its lifetime for use as fast photodetector.

ACKNOWLEDGMENTS

We thank K. Khirouni (University of Monastir, Tunisia), R. Bisaro, C. Grattepain (Laboratoire Central de Recherche, Thomson, France), N. Burle, M. Putero (Laboratoire Matériaux Organisation et Propriétés (MATOP)), Université Aix-Marseille III, France), B. Pajot (Groupe de Physique des Solides, Université Paris 7, France) for their contribution. The materials used as sources and substrates have been provided by Y. Otoki (Advanced Research Center Hitachi Cable Ltd., Japan).

REFERENCES

1. J.C. Bourgoin and H. Samic, *in* Properties of Gallium Arsenide, Emis Datareview serie n° 16 (INSPEC Publ.), eds. M.R. Brozel and G.E. Stillman, 1996, p. 639.
2. F. Chavez, J. Mimila-Arroyo, F. Bailly and J.C. Bourgoin, J. Appl. Phys. **54**, 6646 (1983).
3. J. Mimila-Arroyo, J. Diaz, A. Lusson, C. Grattepain, R. Bisaro and J.C. Bourgoin, Mat. Sci. Technol. **12**, 178 (1996).
4. J. Mimila-Arroyo, J. Diaz, M.B. Derbali, H. Maaref, S. Alaya, D. Stievenard and J.C. Bourgoin, J. Electron. Mat. **25**, 1851 (1996).
5. R. Castenedo, J. Mimila-Arroyo and J.C. Bourgoin, J. Appl. Phys. **68**, 6274 (1990).
6. H. Samic, J.C. Bourgoin, B. Pajot, R. Bisaro, C. Grattepain, K. Khirouni, M. Putero and N. Burle, 24th Int. Symp. on Compound Semiconductors Proc. (San Diego, 1997), *to be published.*
7. G.M. Martin, Appl. Phys. Lett. **39**, 747 (1981).
8. M. Skowronski, J. Lagowski and H.C. Gatos, J. Appl. Phys. **59**, 2451 (1986).
9. B.A. Lombos, J.A. Dodelet, A. Jean, T. Bretagnon, R. Le Van Mao and D. Cossement, *in:* Crystal Properties and Preparation, **Vol. 32-34**, (Transtech Publ., Switzerland, 1991), p. 424.
10. H. Sandoval, J. Mimila-Arroyo and J.C. Bourgoin, J. Appl. Phys. **77**, 5418 (1995).

Materials Science Forum Vols. 258-263 (1997) pp. 1003-1008

EFFECTS OF COPPER DIFFUSION ON THE NATIVE DEFECT EL2 IN GaAs

D. Seghier and H.P. Gislason
Science Institute, University of Iceland, Dunhaga 3, IS-107 Reykjavik, Iceland

Keywords : GaAs, Cu, EL2, photoquenching, photoconductivity, DLOS.

Abstract. In this work, diffusion of copper in GaAs is shown to produce changes in the EL2 defect similar to those observed in low-temperature MBE materials. A deep center found in copper-diffused n-type GaAs samples is investigated by means of the quenching of photoconductivity and by deep level optical spectroscopy (DLOS). Its thermal activation energy is 0.70 eV, lower than the EL2 value of 0.78 eV. Photoconductivity quenching at low temperature and recovery are observed from this new center and are similar to those usually observed for EL2. Furthermore, the spectral shape of the optical capture cross section measured by DLOS for the center is close to that of EL2. Thus, we conclude that this new defect is a complex center involving As_{Ga} and a defect probably induced by the copper diffusion.

Introduction

Copper is a common transition metal impurity in III-V compounds. It diffuses rapidly even at low temperatures, and is present in different quantities in every processing environment. Despite much work on copper in III-V compounds [1-4], no coherent picture of the Cu-related defects and their microscopic structure has been presented yet. In previous work [4] we reported observation of a deep electron trap referred to as T3 at E_c - 0.7 eV in addition to the well known copper acceptor levels at E_v + 0.14 and E_v + 0.4 eV (Fig. 1). These traps were observed in n-type GaAs:Cu using optical DLTS and in semi-insulating (s.i.) GaAs:Cu samples using photo-induced current spectroscopy (PICS). The s.i. samples were produced by diffusion of Cu in n-type, undoped GaAs starting materials. No signal from EL2 was detected in the copper-diffused n-type or s.i. samples. The nature of the deep electron trap T3 is not known. In this work, we observe that photoquenching and thermal recovery of photoconductivity (PC) are observed in GaAs:Cu. Their effects are found to be similar to those attributed to EL2. In addition, measurements of the electron optical cross section of T3 using deep level optical spectroscopy (DLOS) give values close to those measured for EL2. We deduce that T3 is a complex center, presumably including As_{Ga} and a defect induced by the copper diffusion. This demonstrates that doping with copper results in a transformation of EL2 similar to that observed in low-temperature MBE materials.

Experimental

Diffusion of copper was performed in an open tube system with the GaAs samples immersed in a Cu doped Ga solution saturated with As and equilibrated for several hours in an argon gas ambient. The starting materials were cut from undoped horizontal Bridgman n-type GaAs with n = 1.5×10^{16} cm.$^{-3}$ The dopant was added to the melt in the form of 99.99 % Cu metal and diffusion was carried out at 750 °C. After Cu-diffusion the samples were cooled to room temperature in Ar ambient. About 50 μm were removed from the as-diffused sample surface.

For PC measurements a sandwich structure was used which consisted of a semi-transparent ohmic contact made by evaporating Al on the front side of the samples, and another ohmic contact made on the back side by welding Zn-coated gold wire to the surface. For DLOS measurements, a semi-transparent dot of Au was evaporated on the front face of n-type Cu-diffused samples to obtain Schottky diodes and the same ohmic contact as for the PC measurements on the back side. The light source was a mercury lamp with a set of appropriate lenses enabling a wide range of photon flux densities (10^{11}- 10^{16} cm^{-2} s^{-1}). The wavelength was chosen by filtering through an appropriate filter. The sample was placed in a Joule-Thompson cryostat operating with nitrogen gas at 120 bar. The PC signal was measured under a bias of 10 V where metallic contacts show good ohmic behavior. The DLOS equipment used here is similar to that described in Ref. 5. Details on the photocapacitance techniques are reported elsewhere [5,6].

Results and Discussion

We illuminated the sample at 80 K with a sub-bandgap light using a 1.1 eV silicon filter. The time evolution of the PC signal during the illumination is shown in Fig. 2 for a variety of light intensities. For weak photon flux the PC signal increases and reaches a saturation value which does not change even after prolonged illumination. However, with stronger photon flux densities a quenching of the PC is observed. The PC decreases with time with a rate depending on the photon flux. For the highest light intensity used here (density of about 5×10^{16} cm^{-2} s^{-1}) the quenching is down by more than two orders of magnitude. In Fig. 2 is also shown the PC signal from a n-type GaAs reference sample (not diffused with copper) measured with the same highest light intensity. The applied bias was kept constant for comparison. The quenching of the photoconductivity curves from the two samples are similar. Illumination with weaker light intensities also give similar evolution of the PC signal from the GaAs:Cu and the reference samples.

Previous studies have shown that the photoquenching process in ordinary GaAs is due to EL2 centers changing from their stable to metastable state, as will be discussed later. It is also known that the PC signal can be fully recovered to the nonquenched value if the sample is heated over 125 K. We heated the Cu-doped samples to different temperatures, measuring each time the corresponding PC. These experiments involved the following steps:

(a) Quenching of the PC at low temperature (80 K) by prolonged illumination at 1.2 eV with high light intensity (5×10^{16} $cm^{-2}s^{-1}$)

(b) Heating to a given temperature, annealing for 30 s, and measuring the PC.

(c) cooling down again and starting at (a) using another annealing temperature.

The results show that the PC signal is completely recovered after heating to around 125 K (Fig. 3). The transition from quenched to non-quenched PC is abrupt.

We conclude that the Cu-diffused materials exhibit similar photoquenching and recovery of PC as the GaAs reference samples.

We also measured the activation energy E_b of the thermal regeneration rate of the center T3 from the metastable state to the normal state. After cooling the sample down to 80 K, it is illuminated at 1.2 eV with the strongest light intensity to achieve maximum photoquenching. Then the sample is heated with a linear heating rate under constant illumination of above-bandgap light. The photocurrent in recorded as a function of temperature. The results show that the photocurrent decreases exponentially with increasing temperature.

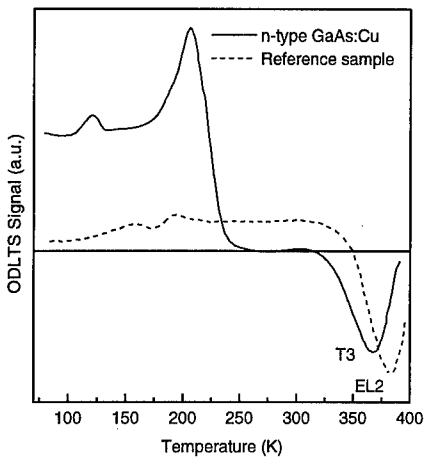

Fig. 1: Optical DLTS spectra from n-type GaAs.

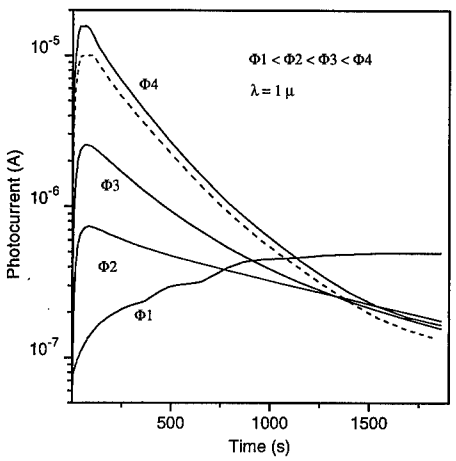

Fig. 2: Time evolution of PC at 80 K, with illumination with photons at 1.2 eV, for different photon flux densities (Φ). For comparison, quenching of PC from a reference n-type GaAs sample is presented as a dashed line.

In order to determine E_b we used calculations from Mohaparta et al. [9]. Values of E_b measured from different GaAs:Cu samples range between 0.22 - 0.26 eV. A value of E_b equal to 0.26 ± 0.01 eV has been reported for EL2 in Ref. 9. Thus, again there is a strong similarity between the metastability recovery kinetics of EL2 and the new center T3 in our Cu-diffused samples.

Fig. 4 shows the electron optical cross sections for T3, measured at 80 K. The basis of our DLOS experiments is to analyze the derivative at $t=0$ of the photocapacitance transient due to the change of the level occupancy induced by photon energy. For comparison, we also include data obtained by Silverberg et al. [7]. Comparison shows that the spectral shape of the cross section arises from similar defects in both materials. These results also illustrate that T3 is closely related to EL2.

Several authors have observed quenching of the PC in GaAs at low temperature after illumination with high-intensity below-bandgap photons [8-9]. The generally accepted explanation for the photoconductivity quenching is the optically induced transformation of EL2 centers into their metastable states, EL2* [8-9]. Since the metastable state EL2* interacts very weakly with light, this interrupts the main path of electron transfer from the valence band to the conduction band, which decreases the generation rate of free carriers with a consequent photoconductivity quenching. In addition, the sharp PC recovery after an annealing at 125 K is known to be caused by the recovery of EL2 centers from their metastable to stable state. In our samples, EL2 is suppressed by the copper diffusion, and the labeled T3 deep electron trap is observed instead. The fact that we observe the same PC quenching and recovery in these samples as in the reference samples suggests that T3 has the same optical properties as EL2. Also, the optical cross sections measured for T3 at 80 K and their dependence on the photon energy are similar to those measured for EL2 at the same temperature.

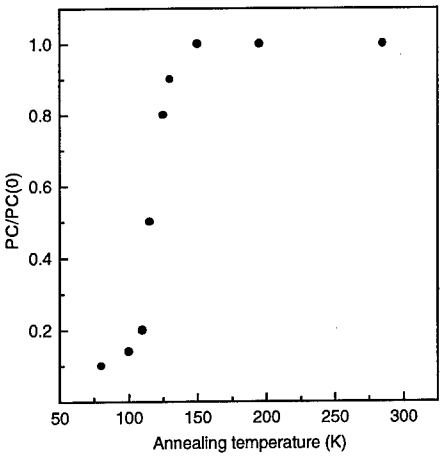

Fig. 3: Thermal recovery of PC at different annealing temperatures. PC(0) is the non-quenched value of PC.

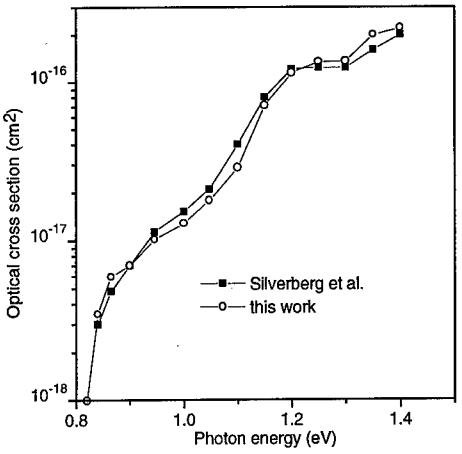

Fig. 4: The optical cross sections of T3 versus wavelength at 80 K. For comparison, data for EL2 reported by Silverberg et al. [7], is also presented.

Since T3 is very similar in many respects to EL2 it is likely that this center involves As_{Ga}. The similarities evidently result from measurements which are primarily influenced by the As_{Ga} core, while the differences (such as the apparent activation energy and the electron capture cross section) are deduced from experiments sensitive to the local environment. At this stage, speculation on the exact microscopic structure of T3 is unwarranted. A possible structure is a complex involving As_{Ga}. Mochizuki et al. [10] reported small variations in some properties of EL2, usually referred to as the EL2 family of defects. This may be especially true if pairing interaction is weak and only slightly perturbs the properties of EL2. Variations have been observed in the EL2-related DLTS signal [11]. In that study, annealing-induced transformation of EL2 into different defects ETX1 and ETX2, with distinct energies, is reminiscent of our hypothesis [11]. Also, a defect center has been observed in low-temperature MBE samples at E_c - 0.65 eV [12]. The properties of this center are close to those of EL2 in a similar way as we observed for T3. The authors assigned it to a defect involving As_{Ga} and V_{Ga} which forms via coulomb attraction. Due to the similarities between this defect and T3, the latter may also originate from a complex involving As_{Ga} and V_{Ga}. Since T3 is observed only in the GaAs:Cu samples, this would indicate that the copper diffusion enhances the creation of As_{Ga} and V_{Ga} complexes.

Conclusion

In summary, quenching of the PC at low temperature (80 K) and thermal recovery of the PC have been observed from GaAs samples diffused with copper after illumination with below-bandgap energy photons. The mechanism of quenching and recovery is very similar to that commonly observed in GaAs and attributed to EL2. In previous work we reported that diffusion of copper suppresses EL2 while an electron trap called T3 at E_c -0.7 eV appears. Measurements of the electron optical capture cross section of T3 at low temperature give values and a spectral shape very similar to those measured

from EL2. Hence, we deduce that T3 may be a defect complex including EL2 and probably a defect induced by the Cu diffusion process.

Acknowledgments
This research was supported by the Icelandic Research Council and the University Research Fund.

References

1. A. G. Milnes Advances in Electronics and Electron Physics **61**, 63 (1983).
2. D.V. Lang and R.A. Logan J. Electron. Mater. **4**, 1053(1975).
3. P.O. Fagerström, H.G. Grimmeiss and H. Titze, J. Appl. Phys. **49**, 3341 (1978).
4. B.H. Yang, D. Seghier and H.P. Gislason, in *Semi-insulating III-V Materials,* ed. Ch. Fontaine (IEEE, Toulouse, France, 1996) p.163.
5. G. Brémond, G. Guillot, A. Nouailhat and G. Picoli, J. Appl. Phys. **59**, 2038(1986).
6. H.G. Grimmeiss and C. Ovrén J. Phys. **E14**, 1032(1982).
7. P. Silverberg, P. Omling and L. Samuelson *Semi-insulating III-V Materials,* ed. G. Grossman and L. Ledebo (Adam Hilger, Malmo, Sweden 1988), p.369
8. U.V. Desnica, Dunja I. Desnica and B. Santic, Appl. Phys. **A51**, 379(1990).
9. Y.N. Mohaparta and V. Kumar J. Appl. Phys. **64**, 956(1988).
10. Y. Mochizuki and T. Ikoma, Revue de Phys. Appl. **23**, 747(1988).
11. M. Taniguchi and T. Ikoma, J.Appl. Phys. **54**, 6448(1983).
12. D.C. Look, Z-Q Fang, J.R. Sizelove and C.E. Stutz Phys. Rev. B **70**, 465(1993).

Materials Science Forum Vols. 258-263 (1997) pp. 1009-1014

EL2 INDUCED ENHANCEMENT OF THE DONOR ACCEPTOR PAIR LUMINESCENCE IN GaAs

Volker Alex and Jörg Weber
Max-Planck-Institut für Festkörperforschung, Heisenbergstr. 1, 70569 Stuttgart, Germany
Electronic mail : valex@vaxff1.mpi-stuttgart.mpg.de

Keywords : GaAs, EL2, photoluminescence, metastability, data storage

Abstract

In bulk-grown semi insulating GaAs the photoluminescence and the selectively excited donor acceptor pair luminescence are influenced by the characteristic metastability of the EL2 defect. In the metastable state the EL2 quenches the photoluminescence and the excitation of the selective pair luminescence. The excitation of the photoluminescence leads to a regeneration of the EL2 from the metastable state. The increase of the photoluminescence intensity is caused by the decrease of non-radiative losses of charge carriers. The selective pair luminescence is affected by the capture of holes at shallow acceptors, which are photoionized from the EL2 during the transition to the metastable state. We demonstrate, that the optical on-off switching of the SPL, which is initiated by the EL2 metastability can be used for optical data storage. An enhancement of the PL intensity and especially donor acceptor pair (DAP) transitions by the simultaneous excitation with below and above gap light is related to the electron photoionization of the EL2.

Introduction

In a recent publication we reported on the excitation of the near band edge photoluminescence (PL) by below band gap light [1]. The so called upconversion photoluminescence (UPL) is a two step process via the EL2 defect and reveals the characteristic photoquenching behavior of the EL2 donor state. Excitation of the UPL at around 1050 nm leads to a quenching of the UPL by the well known photoquenching of the EL2 donor state to the metastable EL2* state. Excitation in the range between 850 nm to 900 nm completely reactivates the EL2 donor state and the UPL is maximized. The regeneration mechanism was explained by the population of the $EL2^*$-acceptor level with hot electrons. This mechanism was first found to provide an efficient recovery channel under hydrostatic pressure [2] and was later also proposed to be responsible for the recovery with above band gap light [3]. We modeled the luminescence transients during the photoquenching and -recovery under the assumption that the hot electrons are provided in the two step process by the EL2 itself. In the present paper we study the excitation regime close to and above the band gap. We observe effects of the EL2 state on the luminescence, that strongly resemble our observations in the UPL excitation region, but are caused by different mechanisms. We demonstrate, that the observed quenching and regeneration of the donor acceptor pair excitation enables us to use semi-insulating GaAs as an erasable optical data storage and processing material.

Experimental

We investigate undoped semi-insulating GaAs, grown by the liquid encapsulated Czochralski (LEC) or vertical gradient freeze (VGF) technique with EL2 concentrations in the range of 2-3×10^{16} cm^{-3}. The samples are cooled by liquid helium to a temperature of 2K. The PL spectra and transients are measured by a cooled photomultiplier with GaAs cathode in combination with a SPEX 1704 double monochromator and a multichannel counter (EG&G). A cw-Ti:sapphire laser,

with different mirror sets and pumped by an all-line Ar^+-laser is used as a tunable excitation source in the region of 700 nm and 1000 nm and a 1064 nm cw-Nd:YAG laser is used to quench the EL2.

Selective Pair Luminescence

The emission photon energy of a donor acceptor pair (DAP) transition is given by

$$h\upsilon_{em} = E_G - E_D - E_A + \frac{e^2}{\varepsilon R}$$

where E_G is the band gap energy, ε the dielectric constant, E_D and E_A denote the donor and acceptor ground state energies and R the separation of the pair. The width of the DAP band results from the large variation of possible DAP separations in the crystal. Below-band-gap light with energies higher than the DAP-luminescence band can resonantly excite an electron from an excited state of the acceptor to a donor. The energy relation holds for an excited state of the acceptor at a certain distance from the donor R^*. Subsequent to the excitation the acceptor relaxes to its ground state. The recombination of the donor electron with the acceptor at the distance R^* then leads to luminescence, that is red-shifted to the excitation by the excited-state energy of the acceptor. The donor electron can however also recombine with acceptors at other distances, but the non-statistic distribution of DAP distances leads to sharp luminescence lines from DAP at distances R^*, that are superimposed on a broad background. The experimental technique of this so called selective pair luminescence (SPL) and its application for the determination of the excited energy levels is reviewed in the literature [4-6]. The total luminescence intensity of the SPL spectrum of our samples exceeds the conventional excited luminescence intensity and it is concentrated in narrower lines. Smaller non-radiative losses for electrons and holes, that are bound to donors or acceptors than for charge carriers in the band account for the high efficiency of the SPL.

Figure 1 shows a SPL spectrum, obtained with an excitation at 821nm. The sharp peak can be identified by its energetic position relative to the excitation photon energy as being due to the $2S_{3/2}$ excited state of the carbon acceptor. The visibility of different sharp lines from the various excited

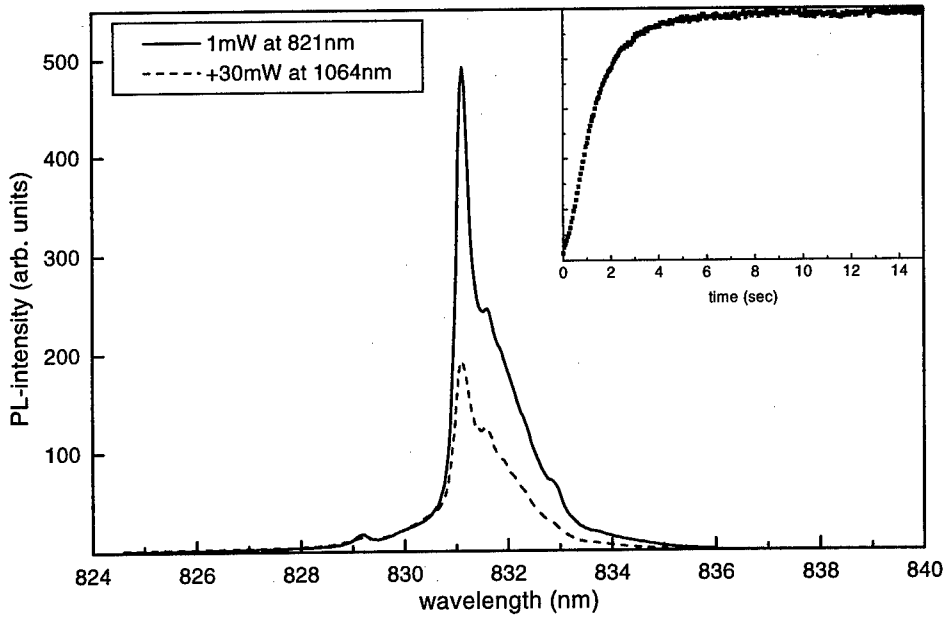

Figure 1: Photoquenching and recovery of the selective pair luminescence

states depends on the excitation wavelength. In Fig. 1 transitions from other excited acceptor states of carbon and zinc are hidden in the SPL broad band. The dashed spectrum with reduced intensity is obtained by the superposition of a 30mW 1064nm Nd:YAG laser to the 821nm excitation. If the Nd:YAG laser is not superimposed, but the sample is illuminated with the Nd:YAG alone, no steady state luminescence can be measured and the subsequent illumination at 821nm leads to the luminescence transient shown in the insert of Fig. 1.

Although this behavior looks very similar to what we have found for the UPL, a two step process via the EL2 could never excite the SPL. We explain the quenching of the SPL by the charge carrier compensation mechanism in semi insulating material. The shallow acceptors are compensated by electrons from the EL2, that thereby get positively charged. The excitation of the SPL requires these compensated acceptors. Only neutral EL2 can be transferred to the metastable state and positively charged EL2 have to be neutralized first by hole photoionization. These holes are captured by the shallow acceptors, which lose thereby their compensation [7]. This leads to a quenching of the SPL excitation. The regeneration of the EL2 from the metastable state and the restoration of the compensation happens via the occupation of the $EL2^*$-acceptor level as in the recovery of the upconversion luminescence. Sources of hot electrons in the region of SPL can be excitation processes from the ground state, instead of the excited states of the acceptors. The regeneration can start with acceptors, that are compensated by shallow donors and whose compensation is therefore not affected by the EL2 state. The small intensity level at the beginning of the regeneration transient however indicates, that this accounts only for a small number of acceptors.

The luminescence, that remains during the simultaneous excitation with the Nd:YAG laser is caused by the competition between the photorecovery and the photoquenching of the EL2 and shows the high efficiency of the regeneration process

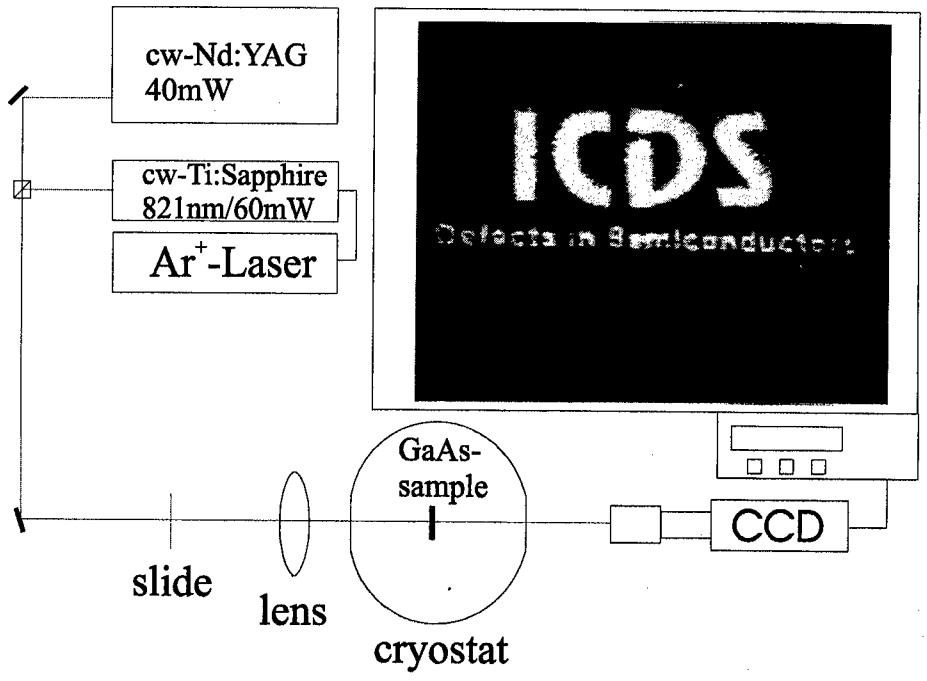

Figure 2: Setup for optical data storage in GaAs

Image Storing

The excitation process of the SPL is the dominant absorption process for wavelengths higher than the DAP luminescence band and below the band gap. The absorption in that region is higher than the sub-band gap absorption of the EL2 itself. It shows however a similar optical metastability. We therefore tried to exploit the quenching and regeneration of the selective pair excitation to use semi insulating GaAs as a regenerative material for optical data storage. Figure 3 shows the simple setup for the demonstration of the image storage process. A slide is illuminated by the Nd:YAG laser beam for several seconds at approximately 50 mW. The image is projected by a lens in a 1:1 ratio onto the sample, that is mounted in the cryostat. The Nd:YAG beam is then switched off and the slide removed. In order to read out the stored image, the sample is illuminated by the Ti:sapphire laser at 821nm. The absorption in those parts of the sample, in which the EL2 was quenched by the Nd:YAG laser is strongly reduced and the stored image can be seen easily in the transmitted laser beam. We record this image by an ordinary (i.e. not infrared enhanced) CCD-video camera with a macro zoom lens.

The image, shown in Fig. 2 is obtained by this method. Its original size is about 3.5mm×3mm. A disadvantage of the method is, that the image is erased by the same wavelength, that is required for the readout procedure. Our method shares this disadvantage however with other materials and methods, that are considered for applications. The laser intensity has to be set at a level, that gives a bright and clear image with our CCD-camera and at the same time avoids a too fast regeneration of the EL2. The image disappeared at the used intensity levels within about 10 seconds. The sample, that we used for storing the image in Fig. 2 was about 300μm thick. Assuming a typical shallow acceptor concentration of 10^{15} cm^{-3}, this shows, that about 3000 acceptors are sufficient to give a high contrast. With a line resolution target instead of the slide a lateral resolution of up to 40 lines/mm could be achieved. We believe however, that this resolution is at least partially determined by the simplicity of our optical setup. The maximum resolution should be given by the localization of the electrons, that participate in the compensation and excitation process around the EL2 or by the 1μm wavelength of the light, that is needed to quench the EL2.

The image presented in Fig. 2 was measured at liquid helium temperature. With an adjustment of the read-out wavelength and a slightly reduced contrast, also liquid nitrogen temperature turned out to be sufficient. At this temperature, SPL is not observed any more, because of the thermal ionization of the shallow donors. The excitation process however is only limited by the ionization of the deeper shallow acceptors. At 77K the metastable state of the EL2 is still stable enough to store the image for a very long time. Assuming the lowest reported value for the thermal barrier of the $EL2^*$ to the fundamental state, one calculates a regeneration rate of 2.4×10^{-9} s^{-1}.

Above gap excitation

Figure 3 shows the behavior of conventionally excited PL under the same conditions as was shown for the SPL in Fig. 1. The PL consists of an excitonic band at about 820nm and a broader band which contains the recombination of conduction band electrons or shallow donors with shallow acceptors (and DAP transitions). After the photoquenching of the EL2 with the Nd:YAG laser the luminescence intensity rises by about a factor of four within some seconds. Such luminescence transients are found in all regions of the PL-spectrum, the relative intensity increase on the DAP side of the spectrum is however slightly larger than on the e-A^0 transition or in the excitonic region. The luminescence change by the simultaneous excitation with the Nd:YAG laser is completely different from the behavior of the UPL or SPL: The luminescence intensity, especially the DAP luminescence rises strongly. It is tempting to ascribe this to the presence of EL2 in the metastable state. We investigated the wavelength dependence of this "sum-effect" by using a HeNe laser (633nm) as above band gap source and superimposed the Ti:sapphire laser in the range between 850nm and 1000nm. The strongest luminescence increase is obtained at 850nm, where no

photoquenching occurs and the electron photoionization cross section of the EL2 is largest. We therefore conclude, that the "sum-effect" is caused by the EL2 donor state and only the simultaneous recovery by the above gap excitation, that keeps a fraction of the EL2 in the fundamental state, makes it possible to observe the "sum-effect" for wavelengths within the EL2-photoquenching band.

The increase of the PL intensity after a previous photoquenching of the EL2 (and during its regeneration) is most likely caused by a decrease of non-radiative losses. If the dominant non-radiative loss of excess charge carriers is due to Shockley-Read-Hall (SRH) recombination, the SRH lifetime will be longest for the Fermi-level at mid-gap. The increase in PL intensity then results from the shift of the Fermi-level from close to the valence band, when the EL2 is in the metastable state, to mid-gap. Another possibility to explain the luminescence transients are non-radiative losses of charge carriers by the EL2 regeneration process itself: The recovery via the $EL2^*$ acceptor level is initiated by the non-radiative decay of excitons, that are bound to the negatively charged $EL2^*$. Probably both mechanism contribute to the luminescence increase.
Both mechanism are however not able to explain the stronger increase of the DAP luminescence in the transients or the "sum-effect". Our experiments have shown, that the "sum-effect" is related to the photoionization of the EL2 fundamental state. Because this photoionization takes place also for above gap excitation - however with reduced efficiency compared to below gap excitation - the stronger increase of the DAP transitions in the transients, is explained by the additional onset of the photoionisation of the regenerated EL2.
The preferential excitation of DAP transitions is also found in the UPL [1]. We explained it by the low excitation density due to the large penetration depth of the sub band gap light, which gives a complete relaxation of the electrons in the conduction band to the shallow donors before

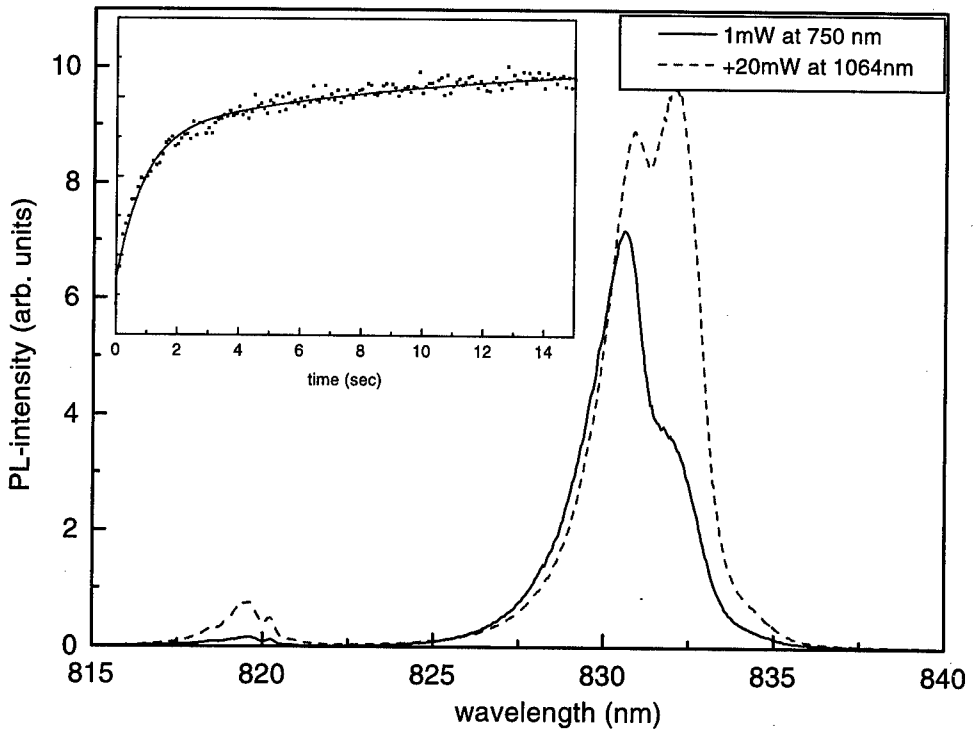

Figure 3: EL2 induced enhancement of the above gap excited luminescence.

recombination. The "sum-effect" is however limited to the penetration depth of the above gap source and low excitation conditions do not exist. If it is not caused by a more complete relaxation of electrons in the conduction band to a fixed number of shallow donors, an increase of DAP relative to free to bound transition is most easily explained by an increase of the shallow donor concentration. The EL2 defect itself exhibits a shallow-donor-like hydrogenic excited state $EL2^0(n=2)$, that can be populated by the photoionization of the EL2 ground state . The optical decay from this excited state to the EL2 ground state was correlated recently to the 0.63eV photoluminescence [9]. At present, however our interpretation of the involvement of this EL2 state in the excitation of DAP luminescence is speculative.

Conclusions

The transition of the EL2 to the metastable state leads to an on-off switching of the selective pair excitation in semi insulating GaAs. We demonstrate, that this can be used for the read-out of images, that are stored by the quenching of the EL2 donor state. This process works at least up to liquid nitrogen temperatures and with a spatial resolution better than 25 μm. The case of the EL2 defect might serve as model for the application of similar metastable defects for optical data storage.

The EL2 state also influences conventionally excited photoluminescence. This behavior can be understood by the possible change of non-radiative losses of charge carriers with the Fermi level position. The close relation of the EL2 to a shallow donor state, that was seen in several experiments [9,10] and the excitation of DAP luminescence however requires further investigations.

Acknowledgments

We gratefully acknowledge the continuous support and encouragement of Prof. H.-J. Queisser. We thank T. Iino from Sumitomo Metal Mining Co. for the supply of the samples and W. Heinz and W. Krause for technical assistance.

References

[1] V. Alex, T. Iino, and J. Weber, Mat. Res. Soc. Symp. Proc. 442, 411 (1997).
[2] M.Baj, P. Dreszer, and A. Babinski, Phys. Rev. B**43**, 2070 (1991).
[3] K. Khachaturyan, E.R. Weber, and J. Horigan, Phys. Rev. B**46**, 1365 (1992).
[4] H.Tews and H. Venghaus, Sol. State Comm. **30**, 219 (1979).
[5] D.W. Kisker, H. Tews, and W. Rehm, J. Appl. Phys. **54**, 1332 (1983).
[6] T. Iino, M. Tajima, and K. Ishida, J. Appl. Phys. **63**, 5454 (1988).
[7] R. Bray, K. Wan, and J.C: Parker, Phys. Rev. Lett. **57**, 2434 (1986).
[8] Y.N. Mohapatra and V. Kumar, J. Appl Phys. **64**, 956 (1988).
[9] M.K. Nissen, T. Steiner, D.J.S. Beckett, and M.L.W. Thewalt, Phys. Rev. Lett. **65**, 2282 (1990)
[10] T. Ohyama, T. Shimizu, H. Kobori, and E. Otsuka, Jpn. J. Appl. Phys. **32**, 1889 (1993).

Materials Science Forum Vols. 258-263 (1997) pp. 1015-1020

OBSERVATION OF PERSISTENT ELECTRON CAPTURE IN N-TYPE GALLIUM ARSENIDE STUDIED BY OPTICALLY DETECTED MAGNETIC RESONANCE

K. Krambrock[1,2], M. V. B. Pinheiro[1,2], K.-H. Wietzke[2] and J.-M. Spaeth[2]

[1]UFMG, Departamento de Física, ICEx, CP 702, 30.161-970 Belo Horizonte, Brazil
[2]Universität Paderborn, Physik, Warburger Str. 100A, 33098 Paderborn, Germany

Key words: intrinsic defects, GaAs, metastability, ODMR, EL2

Abstract

A set of slightly n-type GaAs crystals ($10^{14} < n < 10^{16}$ cm^{-3} at 300 K) grown by different techniques have been studied by optical absorption and optically detected electron paramagnetic resonance (ODEPR) via the magnetic circular dichroism of optical absorption (MCDA). In all samples the spectrum of neutral EL2, $EL2^0$, has been measured by optical absorption. By using a weak measurement light intensity at 0.85 eV or 0.94 eV with a photon flux of about 10^{14} cm^{-2} s^{-1} a metastable population of paramagnetic EL2, $EL2^+$, has been created within a few minutes monitored by MCDA at 1.5 K. The photon energy used in these experiments (<1.0eV) was below the threshold energy for bleaching of EL2 centers (>1.0eV) . As expected by extrapolation of the measurement light intensity to zero, no paramagnetic $EL2^+$ could be observed in darkness in these slightly n-type GaAs samples. The population of paramagnetic $EL2^+$ is metastable in the sense that a thermal barrier of 120 K exists for recapture of electrons by $EL2^+$. In addition, MCDA and ODEPR have shown the spectrum of an intrinsic defect of unknown origin, previously called D1. However, the signals due to D1 were not affected by the metastable population of $EL2^+$. The observations suggest that electron traps with high capture cross sections different from EL2 exist in n-type GaAs with energy levels in the upper part of the bandgap. A paramagnetic charge state of these traps has not been observed. We propose an As vacancy-related defect as the origin of the persistent electron capture.

Introduction

The EL2 defect in GaAs has been extensively studied because of its technological importance and its untypical properties, as for example the fact that it undergoes a metastable transformation under illumination with light of energy between 1.0 and 1.4 eV at low temperatures. Apart from the metastability of EL2, metastable transformations of other defects in semi-insulating (SI) and n-type GaAs have been discussed because of (i) the observation of enhanced photocurrent effects (EPC) which seems to be anti-correlated with EL2 [1] and of (ii) an activated state responsible for the EPC effect which recovers at lower temperatures than the EL2 defects from their metastable state [1] and of (iii) the bleaching and recovery characteristics of near band-edge absorptions, the so-called reverse contrast (RC), which anti-correlates with total and neutral EL2 concentrations [2]. A great problem in all these studies is the fact that the experimental techniques available could not detect both charge states of EL2 simultaneously or they were only sensitive for released free carriers by the photo-quenching experiments.
The magnetic circular dichroism of the absorption (MCDA) measurements are very suitable to identify different defects in different charge states in GaAs because the defects can be distinguished by their optical spectra. In particular, with the MCDA the paramagnetic charge state of EL2, $EL2^+$, can be detected with high sensitivity. Parallel optical absorption and MCDA allow us to observe the signals of both charge states of EL2 and other defects during

photo-quenching and thermal recovery processes. In a recent study [3] we showed that a trigonal acceptor (TA) pair defect, observed by MCDA detected EPR, previously attributed to a Ga antisite-related defect [4], can explain most of the observed features during transfer of EL2 to its metastable state and its recovery in highly compensated SI GaAs. The situation is quite different in n-type GaAs with low compensation. In this report we present the experimental results for n-type GaAs studied by the combination of optical absorption and MCDA/ODEPR. The sample characteristics are listed in table 1.

Tab. 1: Characteristics of the GaAs samples used in this study: growth, free carriers at room temperature and concentrations of neutral $EL2^0$.

	Sample	Growth	[n] at 300 K	[$EL2^0$]
#1	GaAs: Te	LEC	3×10^{14} cm^{-3}	1.0×10^{16} cm^{-3}
#2	GaAs: Te	LEC	5×10^{15} cm^{-3}	0.8×10^{16} cm^{-3}
#3	GaAs	VGF	1×10^{16} cm^{-3}	-
#4	GaAs	HB	5×10^{15} cm^{-3}	1.2×10^{16} cm^{-3}

Experimental results

The GaAs samples used in this study were all slightly n-type grown by either liquid encapsulated Czochralski (LEC) doped with Te, horizontal Bridgman (HB) or vertical Gradient Freeze (VGF) with no intentional doping. Therefore, all samples belong to lowly compensated GaAs where the Fermi level is in upper part of the bandgap. Figure 1a shows the MCDA spectra before and after bleaching of EL2 defects in GaAs: Te (#1, n at 300 K about 10^{14} cm^{-3}).

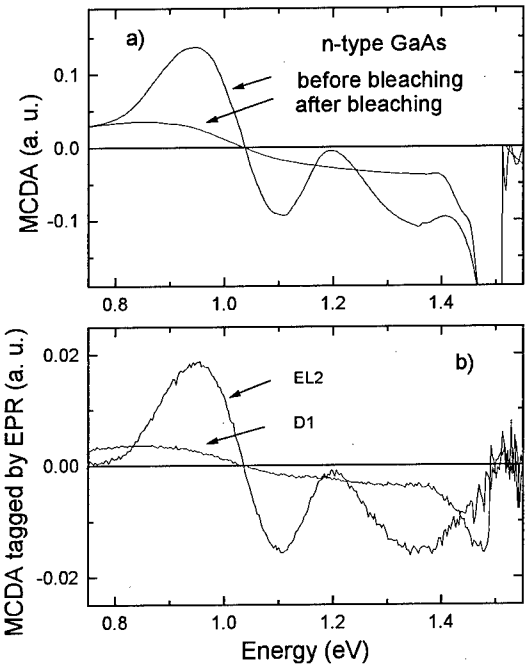

Fig. 1: MCDA of the slightly n-type GaAs: Te sample #1 (a) before and after bleaching of EL2) and (b) ODEPR excitation spectra of $EL2^+$ and D1.

Before bleaching of the EL2 defects with 1.2 eV light at low temperatures we observe the ODEPR spectra of $EL2^+$ and an intrinsic defect of unknown origin, previously called D1 [5]. Their respective ODEPR excitation spectra are shown in fig. 1b. From these spectra it is obvious that the D1 defect is present before and after bleaching of EL2 with no change in its signal amplitude. However, it was a great surprise to detect paramagnetic $EL2^+$ because the Fermi level in the n-type GaAs: Te lies in the upper part of the bandgap. The MCDA transition near the bandgap energy originates form a diamagnetic level (fig. 1a), i.e. it is not temperature dependent [15].

In order to verify the appearance of paramagnetic $EL2^+$, the sample was

heated up to 300 K with subsequent cooling down to low temperatures in dark. At 1.5 K we measured the time evolution of the MCDA signal using the weak measurement light at 0.94 eV, the low energy peak of the MCDA of $EL2^+$ (photon flux about 10^{14} cm^{-2} s^{-1}). It should be noted that the energy of the measurement light was below that of the transformation of EL2 defects to its metastable state EL2* (< 1.0 eV). Figure 2a shows the time evolution of the MCDA caused by the weak measurement light at an energy of 0.94 eV. The initial step in the transient MCDA, when the measurement light is switched on, belongs to the stationary signal of D1, thereafter we observe the population of paramagnetic $EL2^+$ defects building up within ten minutes. It was established that D1 was already populated in dark by doing the same experiment at 0.78 eV where the MCDA of paramagnetic $EL2^+$ is zero. Once $EL2^+$ is populated, it remains persistent for temperatures below 120 K (fig. 2b and 2c). This temperature range is only a little below the recovery temperature of neutral EL2 after bleaching, which is about 130 K for this n-type GaAs sample #1.

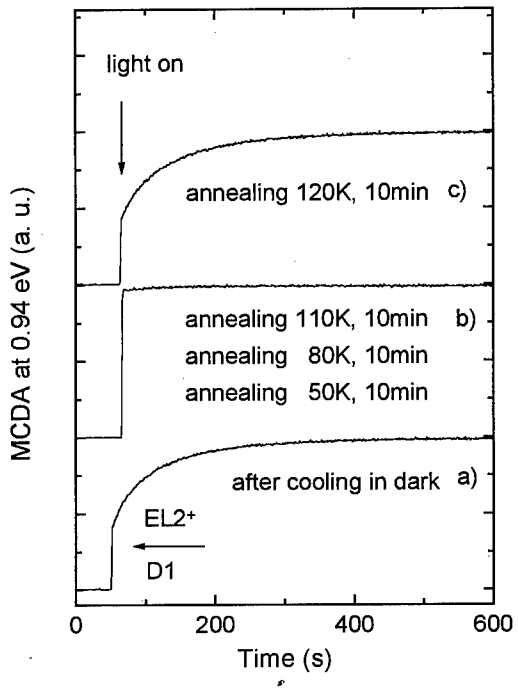

Fig. 2: Transient MCDA signal measured at 1.5K and 2T at 0.94 eV by weak measurement light before bleaching of EL2 (a) after cooling in dark, (b) after annealing at 110K for 5 min. and (c) after annealing at 120 K for 10 min. in sample #1.

The MCDA and ODEPR signal intensities of D1 are not affected by the persistent population of $EL2^+$. With a calibration of the MCDA intensity by EPR [6] for the concentration of paramagnetic $EL2^+$ we calculate that about 1 x 10^{15} cm^{-3} $EL2^+$ have been populated. The most obvious explanation of these results is that neutral $EL2^0$ is transformed to $EL2^+$ by liberating an electron to the conduction band by the process $EL2^0 + h\nu \Rightarrow EL2^+ + e_{cb}$ which has been observed by the absorption and subsequent capture of electrons by a another defect which has empty states. It can be an empty donor state or multiple acceptor state close to the conduction band. However, the unknown defect is not D1. Further the new defect should have its ionization level above the $EL2^{0/+}$ level in the upper part of the bandgap, i.e. more than 0.76 eV above the valence band. Furthermore, the observed persistent population of paramagnetic $EL2^+$ can only be explained by a persistent population of the unknwon defect in the sense that recapture of electrons by $EL2^+$ takes only place above 120 K. The metastable state of EL2 cannot be involved since illuminations with photon energies between 0.78 and 0.95 eV are far from the metastable transition of $EL2^0$ which occurs between 1.0 and 1.4 eV.

Discussion

The electrons liberated from $EL2^0$ via the process $EL2^0 + h\nu \Rightarrow EL2^+ + e^-_{CB}$ must be captured by unknown defects. The persistent capture of electrons by these defects is metastable in the sense that the depopulation takes place only by heating the samples above 120 K, a temperature near to the recovery temperature for metastable EL2 (130 K). However, illuminations with energies below the threshold for bleaching of EL2 defects (< 1.0 eV) lead to the capture of electrons by unknown defects detected indirectly via the persistent population of paramagnetic $EL2^+$ defects. The results in the different samples show that the electron capture is not related to the concentration of EL2, neither to total EL2 nor to neutral $EL2^0$. From the determination of the maximum concentration of the persistent population of paramagnetic $EL2^+$ we estimate a concentration of electron capture centers of the order of 10^{15} cm^{-3} in the different samples. For sample #1 the concentration is higher than the n-type doping, suggesting that an intrinsic defect is involved in this process. The existence of defects with metastable properties in GaAs other than EL2 have been demonstrated for the oxygen defect [7, 8] and probably for defects which belong to reverse contrast [9]. Our samples do not contain any oxygen-related defects.

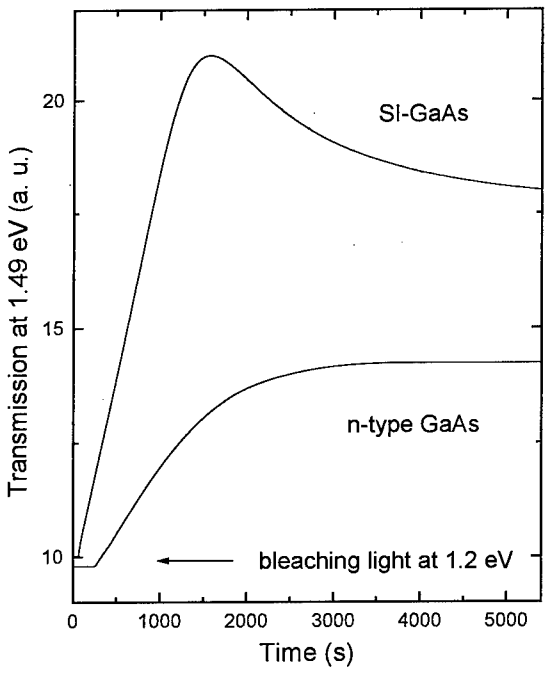

Fig. 3: Transient behaviors of the near band-edge transmissions under additional bleaching light of 1.2 eV measured at 1.5 K in SI and n-type GaAs.

In a combined optical absorption study with positron annihilation, a correlation between the concentration of RC centers and a native vacancy has been found. The RC centers have been attributed to As vacancy-related defects [10].

Fig. 3 shows the transient behaviors of near band-edge absorptions of a usual highly compensated GaAs sample in comparison to a lowly compensated n-type GaAs sample. The transients of transmission are different in the two types of GaAs. The n-type GaAs sample shows a nearly mono-exponentional behavior, whereas the SI GaAs sample shows a more complex behavior.

In a recent publication [3] we have demonstrated, that the complex behavior of highly compensated SI GaAs can be explained by a trigonal acceptor defect pair (TA), attributed to a distorted Ga_{As}-related defect [4], which captures the holes liberated from $EL2^+$ during the photo-quenching process of EL2. The TA defect has ionization levels at about 0.1 and 0.6 eV above the valence band. In addition, TA defects influence strongly the near-band edge absorptions in SI GaAs, which is also in the region

of reverse contrast (RC). In the case of n-type GaAs, all EL2 defects are in the neutral charge state. Therefore, there are no holes released from $EL2^+$ during bleaching which can be captured by TA defects and change their charge state. TA acceptors, if present in these n-type GaAs samples, cannot be observed by MCDA/ODEPR. From our experiments it seems clear that RC absorptions are not well defined because of superposition of different defects in this near band-edge energy range.

Our results in n-type GaAs by MCDA/ODEPR suggest that defects exist with ionization energies in the upper part of the bandgap. Before they capture electrons from neutral $EL2^0$ via the process $EL2^0 + h\nu \Rightarrow EL2^+ + e^-_{CB}$ (> 0.76 eV) these centers should be in a diamagnetic charge state. In n-type GaAs there have no conventionally detected EPR signals yet been observed in the dark. By optically detected EPR an intrinsic defect D1 has been observed. However, D1 has no influence on the persistent electron capture. After releasing electrons from EL2, they are captured by unknown defects. Because we do not detect any new MCDA/ODEPR signal we suggest that the new charge state should also be diamagnetic. Therefore, we suggest a process of the form $D^+ + 2e^- \Rightarrow D^-$, where the neutral state is not stable (fig. 4). Whether it can be a negative U configuration is not clear at the moment. It could rise an objection that the concentrations of these unknown defects are low and therefore not observed by EPR neither that these defects do not show a MCDA transition in the measured spectral range. A strong argument for the proposed model could be positron annihilation experiments which showed that a a negatively charged vacancy could be observed under illumination in SI GaAs [10].

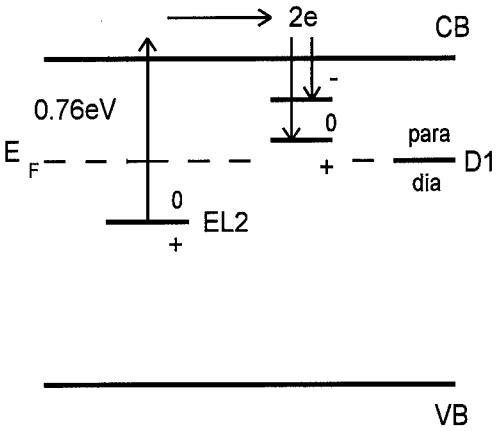

Fig. 4: Energy level scheme for electron capture in n-type GaAs. D1 is paramagnetic before and after electron capture. The capture process is metastable up to temperatures of 120 K.

The described model is very similar to the substitutional off-center oxygen defect [11], where the two diamagnetic states were called A and B. However, in contrast to our oxygen-free n-type samples the neutral paramagnetic charge state B´ [7] of the off-center oxygen defect has been observed by MCDA/ODEPR as a metastable state. Arsenic vacancy-related defects could be responsible for the electron capture centers. Also for the off-center oxygen defect an As vacancy is involved in the defect model. From theoretical calculations it is not very clear whether the As vacancy is a donor with an A_1 ground state and an energy level near the valence band [12] or if it is a multiple acceptor with a T_2 ground state and ionization levels in the upper part of the bandgap [13].

Calculations which included the Jahn-Teller effect in the degenerated states [14] showed that negative U configurations are possible which may suppress the stability of paramagnetic charge states of the As vacancy. Further experiments by MCDA/ODEPR in combination with positron annihilation are in progress to prove the proposed model.

Conclusion

In conclusion the present work gives new interesting results about intrinsic defects in n-type GaAs with metastable properties different from those known of EL2 defects. These defects have their ionization levels in the upper part of the bandgap. The persistent electron capture

was observed indirectly via population of paramagnetic $EL2^+$ centers by the magnetic circular dichroism of absorption and optically detected magnetic resonance, with a recovery temperature of about 120 K. The metastability can be created by light of energy below 1 eV, i.e. below the threshold for conversion of EL2 defects to its metastable state EL2*.
Our results suggest that electron centers in n-type GaAs exist with high capture cross sections, i.e. a good candidate for the non-radiative defects like RC. Their paramagnetic charge states are not observed. As vacancy-related defects could explain the observations. The concentrations of the unknown intrinsic defects estimated by the persistent population of paramagnetic $EL2^+$ are of the order of 10^{15} cm^{-3}.
The behavior of near band-edge absorption under additional bleaching light for EL2 defects of 1.2 eV in n-type GaAs is different from that in SI GaAs. In SI GaAs, the metastability under illumination at low temperature can be explained by the EL2 defects interacting with a trigonal acceptor pair defect (TA) which has its energy levels in the lower part of the bandgap. In contrast to n-type GaAs, SI GaAs does not show metastable effects by illumination below 1eV, i.e. the threshold for bleaching of EL2 defects.

Acknowledgments

We would like to thank M. Brozel for providing one of the slightly n-type Te-doped GaAs samples. We are grateful to C. Corbel and S. Tüzemen for fruitful discussions. This work has been supported by the German Agency Deutsche Forschungsgemeinschaft in project number Kr 1426/1-3 and the Brazilian agencies FAPEMIG and CNPq.

References

[1] W.C. Mitchel and J. Jiménez, J. Appl. Phys., 75, 3060 (1994).
[2] S. Tüzemen and M. Brozel, in Non-Stoichiometry in GaAs, eds. K.J. Bachman, H.L. Hwang and C.Schwab, Elsevier, Ne York, p. 211 (1992).
[3] K. Krambrock, M.V.B. Pinheiro, K.-H. Wietzke, J.-M. Spaeth and C. Corbel, submitted to Phys. Rev. B. (1997).
[4] K. Krambrock, B.K. Meyer and J.-M. Spaeth, Phys. Rev. B, 39, 1973 (1989).
[5] M. Jordan, M. Linde, T. Hangleiter and J. - M. Spaeth, Semicond. Sci. Technol., 7, 731 (1992).
[6] D.M. Hofmann, K. Krambrock, B.K. Meyer and J.-M. Spaeth, Semicond. Sci. Technol., 6, 170 (1991).
[7] M. Linde, J. - M. Spaeth and H. Ch. Alt, Appl. Phys. Lett., 67, 662 (1995).
[8] F.K. Koschnik, M. Linde, M.V.B. Pinheiro and J.-M. Spaeth, submitted to Phys. Rev B (1997).
[9] S Tüzemen, L. Breivik and M. R. Brozel, Semicond. Sci. Technol., 7, A36 (1992).
[10] C. Le Berre, C. Corbel, R. Mih, M. R. Brozel, S. Tüzemen, S. Kuisma, K. Saarinen, P. Hautojärvi and R. Fornari, Appl. Phys. Lett., 66, 2534 (1995).
[11] H. Ch. Alt, Semicond. Sci. Technol., 6, B121 (1991).
[12] G. A. Baraff and M. Schlüter, Phys. Rev. Lett., 55, 1327 (1985).
[13] C. Delerue, Phys. Rev. B, 44, 10525 (1991).
[14] M. Lannoo, Phys. Rev. B, 36, 9355 (1987).
[15] J.-M. Spaeth, J.R. Niklas and R.H. Bartram in *Structural Analysis of Point Defects in Solids*, vol. 43 Solid State Science, Springer (1992).

Materials Science Forum Vols. 258-263 (1997) pp. 1021-1026

ODMR INVESTIGATION OF PROTON IRRADIATED GaAs

S.A. Goodman*, F.K. Koschnick, Ch. Weber**, J.-M. Spaeth**, and F.D. Auret***
***Physics Department, University of Pretoria, Pretoria, South Africa**
****Fachbereich Physik, Universität GH Paderborn, Paderborn, Germany**

Keywords : GaAs, MCDA-EPR, defects, arsenic antisite, EL2, proton irradiation

Abstract. We have investigated, using electron paramagnetic resonance (EPR) detected via the magnetic circular dichroism of the optical absorption (MCDA) the defects introduced in bulk Te-doped and semi-insulating (SI) GaAs during 2.3 and 6.0 MeV proton irradiation at 300 K. We conclude that high energy proton irradiation of Te-GaAs introduced the anti-structure pair ($As_{Ga} - Ga_{As}$ (nnn)) and As_{Ga} - V_{As}. This is similar to the situation in the same material irradiated with high-energy electrons. Contrary to what is observed in electron irradiated SI-GaAs, the EL2 ($EL2^0$ and $EL2^+$) defect is introduced during proton irradiation at 300 K, the total introduction rate being of the order of 50 ± 25 cm^{-1}. Annealing to 600 K did not influence the concentration of EL2. Apart from the $As_{Ga} - Ga_{As}$ (nnn) and the EL2 defects, a new defect was detected after proton irradiation of SI-GaAs. This isotropic defect which has a Gaussian EPR line shape, g = 2.02 and a FWHM of 90 mT is believed to be an acceptor like defect.

Introduction

Electron irradiation produces intrinsic point defects in GaAs. One set of these defects is the antisite type defects, which have wide technological interest because of their electrical properties. It was the purpose of this investigation to examine whether proton irradiation produces the same kind of intrinsic point defects as were observed after electron irradiation and whether the same differences are observed between n-type and semi-insulating (SI) GaAs. Proton irradiation is used for device processing and therefore the radiation damage caused is very important. In GaAs four arsenic antisite (As_{Ga}) type defects have been observed after electron irradiation [1,2]. Using electron paramagnetic resonance (EPR) the hyperfine (hf) interaction with the central nucleus is resolved for these defects. This interaction results in a typical four-line split spectrum (nuclear spin of ^{75}As, I = 3/2 with 100 % abundance) without further superhyperfine (shf) splittings, thus preventing a detailed microscopic structure identification of each antisite type defect. To resolve the interactions with neighboring nuclei electron nuclear double resonance (ENDOR) measurements are necessary. In GaAs the optical detection of EPR and ENDOR via the magnetic circular dichroism of the absorption (MCDA) has enhanced sensitivity and is able to resolve shf interactions from neighboring nuclei. The MCDA is the differential absorption of right and left circularly polarised light in a longitudinal magnetic field and consists of a diamagnetic and paramagnetic part. If resonant microwave transitions between the Zeeman levels of the ground state (EPR transitions) reduce the spin polarisation under saturation conditions, the MCDA is reduced which is used to detect the electron paramagnetic resonance transitions (MCDA-EPR). Two As antisite defects, the isolated As_{Ga} and the so-called anti-structure pair ($As_{Ga} - Ga_{As}$ (nnn)), an antisite with a Ga antisite in the next nearest neighbor shell have similar ^{75}As hyperfine splittings in their paramagnetic charge state as the EL2+ [1]. The fourth member, $As_{Ga} - V_{As}$, an arsenic antisite defect with an As vacancy in the first neighbor shell, has a reduced hyperfine splitting in comparison to the former three As_{Ga}- type defects [3]. The members of the As_{Ga} family of defects have different microscopic structures which all contain As_{Ga} as a constituent [1]. By recording MCDA spectra it is possible to discriminate between these different defects, for example, the zero-phonon

line (ZPL) observed with MCDA at 1.13 eV with replicas separated by 11 meV is typical of the anti-structure pair (As_{Ga} - Ga_{As}, (nnn)) [4]. The diamagnetic charge state of EL2 ($EL2^0$) has a ZPL in optical absorption at 1.039 eV with a similar phonon replica structure [5]. The higher symmetry of the isolated As_{Ga} compared to the more complex EL2 situation is illustrated in their respective MCDA spectra [4]. The four members of the As_{Ga} family also exhibit different metastable properties [6]

Accordingly, the different antisite - related defects show pronounced differences in bleaching and recovery processes, which can also be used to identify their formation. Another technique which allows a selective measurement of the MCDA in the "MCDA tagged by EPR" a kind of MCDA excitation spectrum of a particular EPR line. For further details see [7].

Experimental

Undoped semi-insulating (SI) and Te-doped n-type GaAs were irradiated with 2.3 and 6.0 MeV protons at 300 K. The incident fluence ranged between 4×10^{14} and 1×10^{15} cm^{-2}. According to transport of ions in matter (TRIM) calculations, the penetration depth of 2.3 and 6.0 MeV protons in GaAs is of the order of 40 and 200 microns respectively [8]. In order to reduce the signal from the unirradiated material to the measured MCDA and EPR signals, the samples were thinned prior to irradiation to approximately 0.13 and 0.4 mm for the 2.3 and 6.0 MeV conditions, respectively. After polishing both surfaces of the samples to reduce light scattering, the material was irradiated on both sides with 2.3 MeV protons under identical conditions at 300 K using a Van de Graaff accelerator. Due to the much deeper penetration depth of 6.0 MeV protons the samples were only irradiated on one side. It must be noted that during the proton irradiations at both energies there was not an appreciable increase in the temperature of the samples. All crystals were investigated with MCDA and MCDA-detected electron paramagnetic resonance (MCDA-EPR). The MCDA and MCDA-EPR measurements were performed with a computer controlled K-band (24 GHz) spectrometer at a temperature of 1.5 K.

To investigate the defect metastability, two beam experiments were performed. One light beam of low intensity was used to monitor the MCDA as a measure of the concentration of the defect in its paramagnetic state. The second beam, which was oriented perpendicular to the optical axis of the spectrometer, was used for bleaching and recovery of the defects.

Results

Te-GaAs

The MCDA spectra of the unirradiated (curve (a)) material and 6.0 MeV proton irradiated (curve (b)) Te-GaAs are shown in Fig. 1. The spectrum after proton irradiation is similar to that measured after 5×10^{17} cm^{-2} 2 MeV electron irradiation of similar Te-GaAs [3]. It is known that As_{Ga} - Ga_{As} (nnn) is detected after high fluence electron irradiation. After lower electron fluence (1×10^{17} cm^{-2}) irradiation, the $As_{Ga} - V_{As}$ defect is detected, which is stable up to 520 K and has a hyperfine interaction of 1970 MHz, its +/++ level is approximately 1.2 eV above the valence band [3]. The reason for the detection of different arsenic antisite type defects after different incident electron fluences is due to Fermi level considerations [3]. Our MCDA measurements also showed the characteristic ZPL of the anti-structure pair. In order to confirm the presence of the different arsenic antisite type defects after proton irradiation, MCDA-EPR measurements were conducted. Figure 2 shows the MCDA-EPR spectra for the As_{Ga} - V_{As} (curve a, measured at 932 nm) and the $As_{Ga} - Ga_{As}$ (nnn), (curve b, measured at 1190 nm) defects. Further

proof that it is the anti-structure pair that is observed could be obtained by performing bleaching and recovery experiments. It was seen that the recovery of the As-antisite type defect in proton irradiated material was the same as that previously measured for $As_{Ga} - Ga_{As}$ (nnn). Hence, from the MCDA spectra, MCDA-EPR measurements, modeling and the metastable character we conclude that as is the case with electron irradiation, the As_{Ga} - V_{As} and the As_{Ga} - Ga_{As} (nnn) defects are observed after proton irradiation. The reason why both As_{Ga} - V_{As} and the As_{Ga} - Ga_{As} (nnn) are observed in the proton irradiated material may be explained as follows: Due to the shallower penetration depth of the protons versus electrons there are regions of the proton irradiated sample which are converted from n-type to semi-insulating (SI) and other regions which are not quite converted. This would in effect result in an uneven carrier concentration distribution in the material.

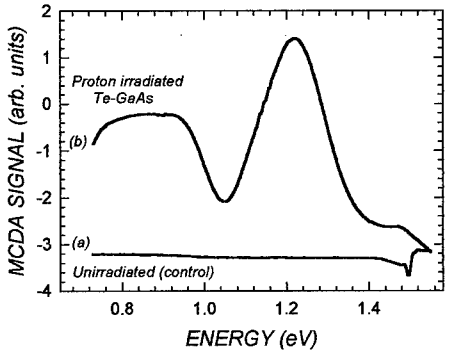

Figure 1. MCDA spectra of a Te-GaAs measured at 1.5 K and 2 T. Curve (a) is prior to irradiation. Curve (b) is after 6.0 MeV proton irradiation at 300 K (fluence = 1 x 10^{15} cm^{-2}).

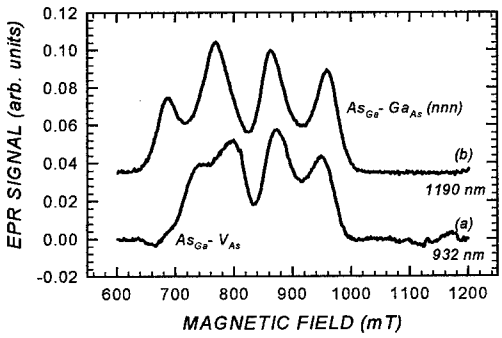

Figure 2. MCDA-EPR spectra recorded at 24.6 GHz and 1.5 K of a Te-GaAs after 6.0 MeV proton irradiation at 300 K (fluence = 1 x 10^{15} cm^{-2}). Curve (a) measured at 1.33 eV is the $As_{Ga} - V_{As}$ and curve (b) measured at 1.04 eV is the $As_{Ga} - Ga_{As}$ (nnn).

SI-GaAs

The defects introduced by 2.3 and 6.0 MeV protons are similar, however, the higher energy irradiation facilitated the separation of the different defect contributions to the observed signal. The unirradiated samples contained both charge states of the well known EL2 defect ($As_{Ga} - As_i$). Upon inspection of the MCDA spectra in Fig. 3 (curve (a), unirradiated and curve (b), 6.0 MeV proton irradiated to a fluence of 1 x 10^{15} cm^{-2}) it would appear that there was little change in the shape of the observed MCDA signal prior to and after irradiation. The observed MCDA spectrum is typical of the EL2 defect. However, the ZPL of the $As_{Ga} - Ga_{As}$ (nnn) at 1.13 eV could be resolved, therefore the MCDA signal consists of at least two superimposed bands, with the EL2+ being the dominant contribution and the anti-structure pair the lesser. The EL2 defect could not be bleached completely with light after proton irradiation. In an attempt to gain further knowledge into the nature of this defect, MCDA-EPR measurements were done. The MCDA-EPR spectrum recorded after 6.0 MeV proton irradiation is depicted in Fig. 4. A four line EPR spectrum is observed with the same splitting as that of the EL2+ spectrum. But the relative peak heights are not the same as would be expected. To establish if there was a superposition of two EPR signals resulting in the unexpected change in relative peak intensities, "MCDA tagged by EPR" spectra were recorded in the middle of the spectrum (810 mT) and in the outer lines (693 mT). Subtracting these two spectra from each other would then yield the signal responsible for the deviation in peak intensities and hf splitting.

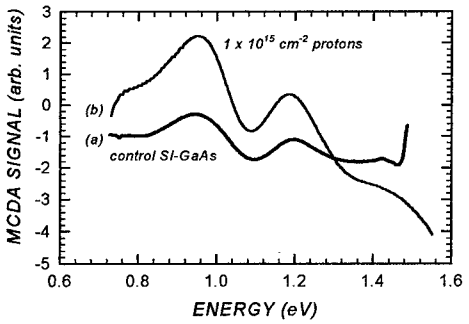

Figure 3. MCDA spectra of SI-GaAs measured at 1.5 K and 2 T. curve (a) is prior to irradiation. Curve (b) is after 6.0 MeV proton irradiation at 300 K (fluence = 1 x 10^{15} cm^{-2}).

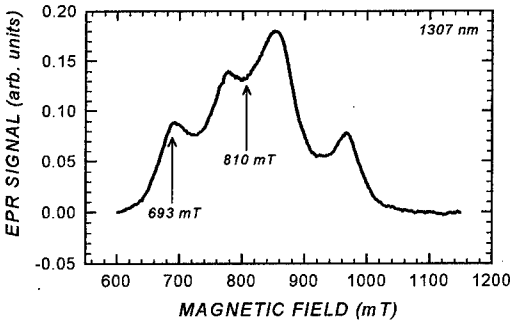

Figure 4. MCDA-EPR spectra recorded at 24.8 GHz and 1.5 K of SI-GaAs after 6.0 MeV proton irradiation at 300 K (fluence = 1 x 10^{15} cm^{-2}). The photon energy was 0.95 eV

Figure 5 depicts the "MCDA tagged by EPR" spectra recorded after bleaching the EL2 component of the 6.0 MeV proton irradiated material. Comparing spectra recorded at 810 and 693 mT and subtracting the spectrum recorded at 693 mT from the 810 mT spectrum, it would appear that there is an MCDA band in the low energy regime between approximately 0.7 and 1.4 eV. Performing EPR and "MCDA tagged by EPR" measurements it was seen that there was a new defect superimposed on the As_{Ga} type defects (EL2+ and a small contribution of anti-structure pair). The MCDA-EPR spectrum of this unknown defect was measured at a photon energy of 1.04 eV where the MCDA band of the EL2+ is zero. The measured MCDA-EPR spectrum of this unknown defect is depicted in Fig. 6. The unknown defect which has an EPR line shape superimposed on the antisite type defects is isotropic and has a Gaussian form, with a FWHM of approximately 90 ± 3 mT and $g = 2.02$. The spectrum in Fig. 4 could be explained assuming a superposition of the EPR spectrum of this unknown defect and of the EL2+ with a small contribution of the As_{Ga} - Ga_{As} (nnn) defect. The modeled data was generated assuming saturation broadening due to high microwave power (100 mW into cavity) and the Gaussian is measured at 1.04 eV, where the EL2+ MCDA is zero. The allowed and forbidden transitions of EL2+ were also used in this modeling. The two small depressions in the simulated spectrum in Fig. 6 are due to a small contribution from EL2+. The shape of the MCDA spectrum of this defect (see Fig. 5, subtracted spectrum) looks like a "hole" transition to the valence band. The energetic distance of the peaks of the MCDA spectrum is approximately 0.4 eV, which is similar to the 0.34 eV splitting of the valence band [9]. The low energy onset of the MCDA band of the unknown defect is between 0.6 and 0.7 eV. Assuming a Frank-Condon shift between 0.1 – 0.2 eV, then the unknown defect level must be approximately 0.4 – 0.6 eV above the valence band. The unknown defect is thus below the EL2 (o/+) level. It is believed that it is related to an acceptor like defect. The MCDA of this defect is considerably different from that reported for the trigonal acceptor, which is reported to be a Ga antisite [10]. The fact that it is not detected in n-GaAs which has been irradiated under similar conditions leads us to believe that it is not related to the As-sub lattice. The actual structure and formation mechanism of this defect is not yet resolved.

Using a direct correlation between the signal intensities of the two diamagnetic MCDA bands located at 0.93 and 1.19 eV and the concentration of neutral diamagnetic $EL2^0$ centers as well as the correlation for the paramagnetic MCDA band of $EL2^+$ in different GaAs samples it is possible to determine absolute calibration factors [11]. These calibration factors for the diamagnetic and paramagnetic contributions opens the

possibility to measure the concentrations of $EL2^0$ and $EL2^+$. Using this correlation, the absolute concentrations of the two charge states of EL2 were determined prior to and after proton irradiation. From these measurements it was seen that as a consequence of both charge states ($EL2^+$ and $EL2^0$) are present after proton irradiation and that EL2 was definitely introduced during proton irradiation at 300 K with an introduction rate of approximately 50 ± 25 cm^{-1}. This is opposite to the situation with electron irradiation of SI-GaAs, where the EL2 is only detected after annealing to 520 K [12]. Annealing the proton irradiated material to 500 and 600 K had no influence on the concentration of EL2 unlike the situation with electron irradiation where EL2 is detected after annealing to 520 K . The fact that the paramagnetic charge state of the unknown defect with its level below that of the $EL2^+$ was observed is probably caused by the inhomogenous radiation defect distribution in the sample due to the small penetration depth of the protons.

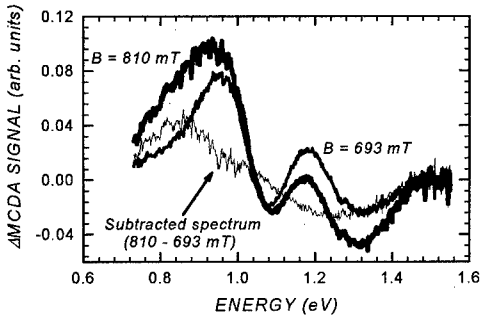

Figure 5. "MCDA tagged by EPR" spectra of 6.0 MeV proton irradiated SI-GaAs measured at 810 and 693 mT. Spectra were recorded at 24.75 GHz and 1.5 K.

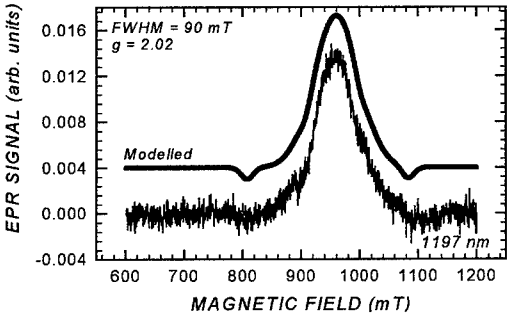

Figure 6. MCDA-EPR spectra of 6.0 MeV proton irradiated SI-GaAs. The simulated spectrum is offset only for illustrative purposes. Spectra were recorded at 1.5 K, 1.04 eV and 24.75 GHz.

Conclusions

It has been shown that high energy proton irradiation of n-type (Te-doped) GaAs introduces members of the arsenic antisite family of defects. The anti-structure pair ($As_{Ga} - Ga_{As}$, (nnn)), and to a lesser extent the $As_{Ga} - V_{As}$ defect are detected in proton irradiated n-type material. These defects are also detected in material irradiated with high energy electrons at "low" and "high" fluences. The presence of As_{Ga} - Ga_{As},(nnn) was confirmed by an investigation of its metastable character, from MCDA measurements, including a zero phonon line (ZPL) at 1.13 eV and by simulating the MCDA-EPR spectrum.

High energy proton irradiation of SI-GaAs resulted in a more complex situation. As was the case with n-type GaAs the anti-structure pair is detected. However, a second member of the As-antisite family, namely the $EL2^+$ is also detected. Normally, in electron irradiated SI-GaAs this defect is only detected after annealing to approximately 520 K, the mechanism being that Arsenic interstitials (As_i) become mobile at these temperatures. It is seen that EL2 is introduced during proton irradiation at 300 K, the introduction rate being of the order of 50 ± 25 cm^{-1}. This is in sharp contrast to the introduction rate by electrons, which has been reported to be of the order of 0.1 cm^{-1} after annealing to 520 K [11]. DLTS studies [13] have shown that the introduction rate of the major defects in n-GaAs by protons is approximately 500 times higher than for electron irradiation. Thus, the ratio of the introduction rate of $EL2^{+/0}$ for protons and electrons is of the same order as the major electron traps (E1 - E3) [14]. Annealing the proton irradiated material to 500 K and 600 K had very little influence on the

concentration of both charge states of the EL2 defect. Hence, we conclude that $EL2^+$ is created by high energy proton irradiation of SI-GaAs at 300 K. The mechanism responsible for this formation, is not yet understood.

Superimposed on these two EPR signals is a third unknown isotropic defect with g = 2.02 and a FWHM of 90 mT. This new defect is not detected after high energy electron irradiation of the same material. This defect cannot be attributed to either an antisite like defect or an interstitial because the line shape is Gaussian. In the situation where there was indeed a central nucleus with I = 3/2 and the line shape was unresolved it would not have a Gaussian shape. The MCDA band is typical of what would be expected for a hole transition to the valence band [15]. Also, this defect is not detected in n-type material irradiated under similar conditions. Thus we conclude that apart from introducing the EL2 defect and the anti-structure pair, proton irradiation of SI-GaAs also introduces an acceptor like defect, the structure of which has yet to be resolved.

Acknowledgments

One of the authors, S.A. Goodman would like to thank the Alexander von Humboldt stiftung for financial support. The authors would also like to thank M. Hayes for the 6.0 MeV proton irradiations and T. Hauser for the 2.3 MeV proton irradiations.

References

1. J.-M. Spaeth and K. Krambrock, Adv. Solid State Phys. **33**, 111 (1993).
2. K. Krambrock, J.-M. Spaeth, C. Delerue, G. Allan and M. Lannoo, Phys. Rev. B. Rapid Comm. **45**, 1481 (1992).
3. K.-H. Wietzke, F.K. Koschnick and J.-M. Spaeth, Mat. Sci. Forum **196-201**, 1061 (1995).
4. K. Krambrock and J.-M. Spaeth, Phys. Rev. B **47**, 3187 (1993).
5. M. Kaminska, Rev. Phys. Appl. **23**, 793 (1988).
6. M. Hesse, F.K. Koschnick, K. Krambrock and J.-M. Spaeth, Solid State Comm. **92**, 207 (1994).
7. J.-M. Spaeth, J.R. Niklas and R.H. Bartram, in *Structural Analysis of Point Defects in Solids*, edited by H.J. Queisser (Springer Series vol. 43, Springer Verlag, 1992).
8. J.F. Ziegler, J.P. Biersack and U. Littmark, in *The Stopping and Range of Ions in Solids*, Vol. 1, edited by J.F. Ziegler (Pergamon Press, New York, 1985).
9. M. Guzzi, J.L. Staehli, Solid State Phenomena **10**, 25 (1989).
10. K. Krambrock, B.K. Meyer and J.-M. Spaeth, Phys. Rev. B Rapid Comm. **39**, 1973 (1989).
11. K.-H. Wietzke, K. Krambrock and F.K. Koschnick, Submitted: Appl. Phys. Lett. 1997.
12. A. Pillukat and P. Erhart, Appl. Phys. Lett., **60**, 2794 (1992).
13. F.D. Auret, S.A. Goodman, M. Hayes, G. Myburg, W.O. Barnard and W.E. Meyer, S. Afr. J. Phys., **16**, 153 (1993).
14. D.V. Lang and L.C. Kimerling, Inst. Phys. Conf. Ser. **23**, 581 (1975).
15. K. Krambrock and J.-M. Spaeth, Solid State Comm. 95, 667 (1995).

Materials Science Forum Vols. 258-263 (1997) pp. 1027-1032

UNIAXIAL-STRESS SYMMETRY STUDIES ON THE E1, E2 AND E3 IRRADIATION-INDUCED DEFECTS IN GALLIUM ARSENIDE

S J Hartnett and D W Palmer

Physics and Astronomy Subject Group, University of Sussex, Brighton BN1-9QJ, UK

Keywords : GaAs, irradiation, E1, E2, E3, uniaxial stress, DLTS, defect symmetries

Abstract. To obtain information on the crystallographic symmetries of the E1, E2 and E3 irradiation-induced defects in n-GaAs we have investigated the effects of uniaxial-stress upto 0.4 GPa on the DLTS spectra of epitaxial n-GaAs irradiated by 1.0 MeV protons. We find that for each of those three defect levels, uniaxial stress applied along a <100> direction of the GaAs caused increase but no broadening of the DLTS-measured electron ionisation energy, but that <110> applied stress produced both broadening of the DLTS peaks and increase in the mean ionisation energy of each defect. For the E1 defect the effect of 0.4 GPa <110> stress was to produce clearly observable splitting of its peak into two peaks. By detailed analysis of the DLTS peak shapes we deduce that <110> stress causes splitting of each of the E1, E2 and E3 electronic energy levels into two levels of equal populations. These data strongly suggest that the E1, E2 and E3 defects each have C_{3v} (trigonal) crystallographic symmetry, ie that each is an atomic arrangement that contains a single <111> symmetry axis. The data do not support the identification of the E1 and E2 defects as simple arsenic vacancies of T_d symmetry, but are consistent with a previous proposal that E3 defects are arsenic Frenkel pairs. We believe these to be the first uniaxial-stress studies on any irradiation-induced defect in GaAs.

1. Introduction

Irradiation of n-GaAs by high energy electrons or light ions produces lattice defects, stable at room temperature, that give rise [1-3] to a series of electron traps, E1-E5, that have electronic levels in the upper half of the energy bandgap and can be observed by majority-carrier deep level transient spectroscopy (DLTS). There is good evidence [4, 5] that the E1, E2 and E3 defects are each produced by the initial displacement of one atom from its lattice site, and it has been proposed [6] that the E1 and E2 defects are different charge states of the single arsenic vacancy V_{As} and that the E3 defect is an arsenic Frenkel pair, V_{As}–i_{As}. It is clear that those suggested defect structures would have characteristic crystallographic symmetries. We present here the results [7] of combined deep level transient spectroscopy (DLTS) and uniaxial stress experiments that we have performed to investigate the symmetries of the irradiation-induced lattice defects E1, E2 and E3.

Considering any individual lattice defect in a single crystal solid, applied uniaxial stress can be expected to change anisotropically the local atomic positions at and near the defect and, in consequence, the energies of the defect-associated electrons. Because GaAs has a cubic Bravais lattice, all the individual defects of a defect species of a particular crystallographic symmetry axis can have the same electronic energy level, ie be orientationally degenerate, in the absence of uniaxial stress; but application of uniaxial stress can remove that degeneracy [8, 9], since the previously equivalent defect symmetry axes can be inclined at different angles to the direction of the applied stress. Investigations of the effects of uniaxial stress on the defect energy levels can therefore give information on the crystallographic symmetries, and hence on the structures and identities, of the defects. Even if uniaxial stress does not produce energy-level splitting, it may, because of stress-induced increase of the GaAs energy gap, raise the energy interval between the electronic level of the defect and the conduction band, ie increase the defect ionisation energy.

2. Experimental Procedures

The samples in this work were epitaxial silicon-doped n-GaAs layers having thicknesses of 4.0 μm and carrier concentration values of 4.5×10^{15} cm^{-3}, grown by MOVPE on (100) N^+-GaAs substrates of thickness 2.0mm. The substrate/layer combination was then cut into accurately rectangular blocks of dimensions 2.0 mm x 2.0 mm x 6.0 mm such that each 6.0 mm length was parallel to either a <100> or a <110> crystallographic axis to a precision of ±0.1°. On each sample block an ohmic contact was made by tin alloying on the substrate side, and one or two aluminium Schottky-barrier diodes of 1.0 mm diameter were formed on the epitaxial n-GaAs layer by vacuum evaporation.

The experimental investigations were made using a special uniaxial-stress cryostat installed in a high vacuum chamber on a beam-line of the University of Sussex 3MV Van de Graaff Ion Accelerator. The n-GaAs sample block was mounted in the cryostat with its 6 mm length vertical and with its 2 mm x 2 mm end-faces in contact with horizontal sapphire disks by which the sample was cooled and by which vertical loads were applied to produce the required uniaxial stresses. The equipment allowed irradiation of the sample through the Schottky layer at any sample temperature from 10K to 450K, and in-situ capacitance-mode Deep Level Transient Spectroscopy measurements over the same temperature range. The load applied to the sample was determined by use of a calibrated strain gauge. The irradiations were made by 1.0 MeV protons to doses of about 4×10^{11} cm^{-2} with the samples at 295K at essentially zero applied uniaxial stress. Since the thickness of the aluminium Schottky layer was less than 0.1 μm and the range of 1.0 MeV non-channelled protons in gallium arsenide is approximately 12 μm, the irradiation-induced lattice defect concentration can be assumed to be essentially uniform throughout the region of the epitaxial layer, from its surface to the distance of about 2 μm, investigated in our measurements.

The DLTS information on the lattice defects was obtained by the standard double-boxcar method applied to majority-carrier capacitance transients from the Schottky diode samples or by capture of the whole of such transients in a digital data recorder and subsequent analysis. The computer-stored experimental DLTS data from samples without and with applied uniaxial stress were compared in detail with theoretical spectra calculated as described in the next section.

3. Analysis of DLTS Peak Shapes

As shown below, we find that applied uniaxial stress can cause broadening of the DLTS peaks of the E1, E2 and E3 lattice defects created by irradiation of the n-GaAs sample layers, and, for the E1 peak, formation of a clearly observable doublet. For analysis of the data we calculate theoretical DLTS spectra for quantitative comparison with the experimental spectra. Since GaAs has a direct band-gap and uniaxial stress causes no splitting of the conduction band in such semiconductors, we interpret the <110>-stress induced changes in the DLTS spectra in terms of splitting of the electronic energy levels of the respective defects.

When a defect has one sharp ground-state electronic level in the energy gap of the semiconductor and is present at low concentration relative to the carrier concentration, the capacitance transient $\Delta C(t)$, for the thermal excitation of an electron to the conduction band edge, has the form

$$\Delta C(t) = \Delta C(t=0).\exp(-e_n t), \text{ where } \Delta C(t=0) = C(t=\infty) - C(t=0), \quad (1),$$

characterised by an electron-emission rate e_n (in s^{-1}) given [10] for GaAs by

$$e_n = 2.28 \times 10^{20} T^2 \sigma_n \exp(-E_n/(k_B T)) \quad (2),$$

in which E_n and σ_n are, respectively, the thermal activation energy for the electronic transition to the conduction band and the cross-section (in cm^2) for electron capture by the empty level. The DLTS spectrum as a function of temperature then shows a peak of shape given by $[\Delta C(t_2)-\Delta C(t_1)]$. If, however, the electronic level of a defect becomes split, the capacitance transient is the sum

$\Delta C_S(t)$ of two or more overlapping exponentials and the DLTS peak shape is broader than previously, if the component energy levels are close to each other, or observably comprises two or more separate peaks if the levels are very different in energy.

In this experimental situation we calculate, for each of the E1, E2 and E3 lattice defects, theoretical DLTS peaks $[\Delta C(t_2)-\Delta C(t_1)]$ or $[\Delta C_S(t_2)-\Delta C_S(t_1)]$, where t_1 and t_2 are the signal sampling times, for many assumed electronic level schemes comprising, respectively, one or more levels having a variety of E_n and σ_n values and electron-population ratios. By use of least-square-deviation fitting, we then find which level scheme produces the best fit to the experimental DLTS data, for all of the five or more electron-emission rate-windows employed in the measurement. By that means we have deduced, for the E1, E2 and E3 lattice defects, the effects of applied <100> and <110> uniaxial stress on the transition energies E_n of electrons from the respective electronic ground states to the conduction band.

4. Results and Discussion

Majority-carrier DLTS spectra of the n-GaAs sample layers on their respective sample blocks were measured before and after irradiation by 1.0 MeV protons. The spectra from the irradiated samples showed peaks at the temperatures of about 30K, 70K and 200K expected, respectively, for the E1, E2 and E3 irradiation-induced defects, for the DLTS emission rate-window employed in the measurements. In our experiments to study the E3 defect the irradiated samples were cooled quickly from the irradiation temperature of about 295K to below 250K in order to prevent the production of an irradiation-related DLTS peak, called E3a [11] or Eα3 [12, 13], that forms in irradiated silicon-doped n-GaAs in times of a few tens of hours at room temperatures; the E3a/Eα3 DLTS peak is centred near 180 K, and, if present, its overlapping of the E3 peak causes difficulty for detailed analysis of the E3 peak shape.

Figures 1(a), 2(a) and 3(a) show, as data points, experimental DLTS spectra (in all cases, V_R=3.0V, V_{PH}=2.0V) of the E1, E2 and E3 defects for zero uniaxial stress and for 0.4 GPa uniaxial stress applied across the 6 mm length of irradiated sample blocks in which that length was a <100> direction; figures 1(b), 2(b) and 3(b) show the corresponding spectra for irradiated sample blocks in which the 6mm length was a <110> direction. Experiments on several sample blocks of each orientation gave confirmatory data. The differing DLTS peak-heights in the Figures for a given defect in <100> and <110> samples are due to the use of different analogue-to-digital conversions.

Figures 1 and 2 show that for each of the defect species E1 and E2, uniaxial stress applied along a <100> direction produced shift of the respective DLTS peak to higher temperature but no peak broadening; in fact, the E1 peak was slightly narrowed by the <100> stress, as is seen in Fig. 1(a) by the larger height of that peak. In strong contrast, applied <110> stress caused also significant broadening of the peaks; Fig. 1(b) shows, indeed, that 0.4 GPa <110> stress caused formation of a clearly observable E1 doublet peak. The peaks that are indicated in Fig. 1 and Fig. 2 by continuous lines are the best-fit theoretical DLTS spectra calculated as described above in Section 3.

For the E1 defect all the best-fit spectra required the assumption of two electronic energy levels; even for zero applied stress we could find no single level that produced a reasonable match to the experimental E1 spectra. The mean value of the ionisation energy E_n of 0.043±0.003eV that our analysis gives for zero applied stress is in agreement with values reported previously [1-3] for this defect from measurements using the dependence of the temperature of the peak maximum on the emission-rate window.

A possible interpretation of the doublet nature of the E1 electronic level for zero applied stress is that the E1 defects are being affected by internal stress within the n-GaAs sample material; such stress might be due to the presence of one or more impurity atoms near to each E1 defect. The sharpening of the E1 DLTS peak by applied <100> stress, as seen in Fig. 2(a), could then be understood qualitatively in terms of the combined effect of the internal and externally applied

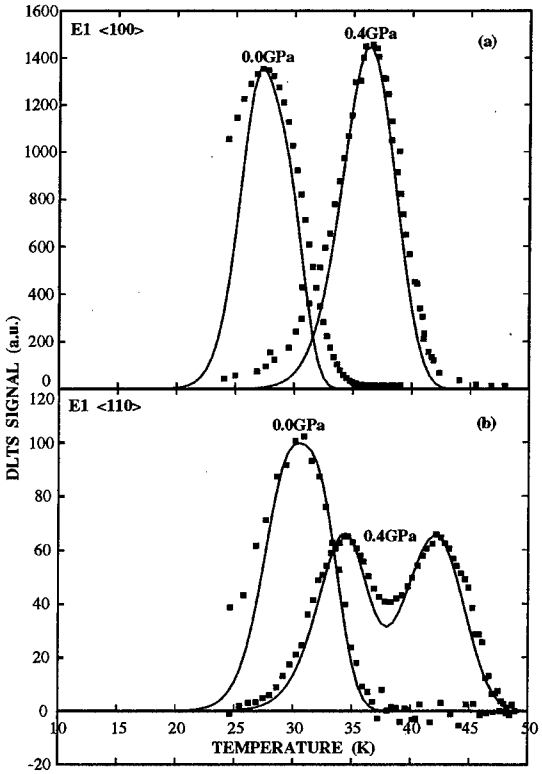

Fig. 1 : Experimental DLTS spectra (squares) of the E1 lattice defect for 0.0 and 0.4 GPa applied stresses: (a) for <100> stresses (t_1=21ms, t_2=86ms, e_n= 21.8 s^{-1}), (b) for <110> stresses (t_1= 10ms, t_2=40ms, e_n=46.2 s^{-1}) , compared to the simulated spectra (solid lines, for the same respective t_1 and t_2 times, and for the E_n and σ_n values stated below) that give the best fits :

(a) Experiment: 0.0 GPa; Simulation: two sharp levels, 0.040eV, $9x10^{-15}cm^2$, 50% and 0.047eV, $9x10^{-15}cm^2$, 50%. Experiment: 0.4 GPa along <100>; Simulation: two sharp levels, 0.057eV, $9x10^{-15}cm^2$, 50% and 0.061eV, $9x10^{-15}$ cm^2, 50%.

(b) Experiment: 0.0 GPa; Simulation: two sharp levels, 0.041eV, 9 $x10^{-15}cm^2$, 50% and 0.045eV, $9x10^{-15}cm^2$, 50%. Experiment: 0.4 GPa along <110>; Simulation: two sharp levels, 0.050eV, $9x10^{-15}cm^2$, 50% and 0.058eV, $9x10^{-15}cm^2$, 50%.

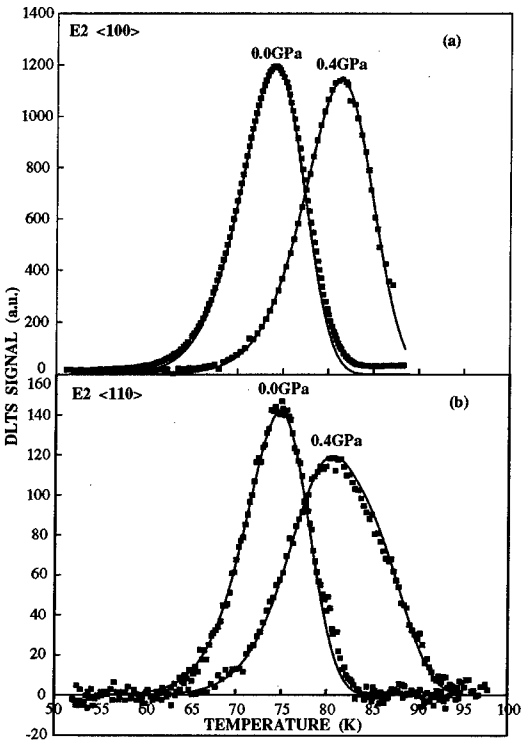

Fig. 2 : Experimental DLTS spectra (squares) of the E2 lattice defect for 0.0 and 0.4 GPa applied stresses: (a) for <100> stresses (t_1=21ms, t_2=86ms, e_n=21.8 s^{-1}), (b) for <110> stresses (t_1=10ms, t_2=40ms, e_n=46.2 s^{-1}) , compared to the simulated spectra (solid lines, for the same respective t_1 and t_2 times, and for the E_n and σ_n values stated below) that give the best fits :

(a) Experiment: 0.0 GPa; Simulation: single sharp level, 0.140eV, $7x10^{-14}cm^2$. Experiment: 0.4 GPa along <100>; Simulation: single sharp level, 0.154eV, $7x10^{-14}cm^2$.

(b) Experiment: 0.0 GPa; Simulation: single sharp level of 0.140eV, $7x10^{-14}cm^2$. Experiment: 0.4 GPa along <110>; Simulation: two sharp levels, 0.148eV, $7x10^{-14}cm^2$, 50% and 0.160eV, $7x10^{-14}cm^2$, 50%.

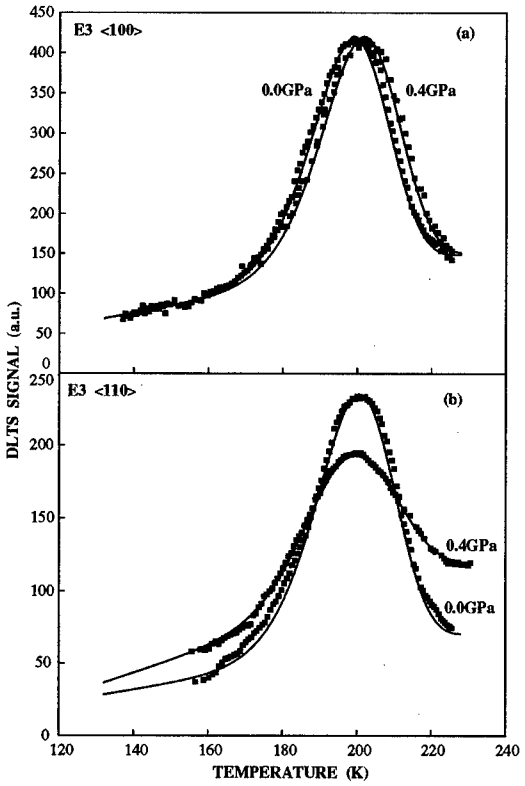

Fig. 3 : Experimental DLTS spectra (squares :t_1=21ms, t_2=86ms, e_n=21.8s^{-1}) of the E3 lattice defect for 0.0 and 0.4 GPa applied stresses: (a) for <100> stresses; (b) for <110> stresses, compared to the simulated spectra (solid lines, for the same t_1 and t_2 values and the E_n and σ_n values stated below) that give the best fits :

(a) Experiment: 0.0 GPa; Simulation: single level, 0.340eV, $1.0x10^{-15}$ cm^2. Experiment: 0.4 GPa along <100> ; Simulation: single sharp level, 0.352eV, $1.0x10^{-15}cm^2$.

(b) Experiment: 0.0 GPa; Simulation: single level of 0.340eV, $1.0x10^{-15}cm^2$. Experiment: 0.4 GPa along <110>; Simulation: two levels, 0.348eV, $1.0x10^{-15}cm^2$, 50% and 0.354eV, $1.0x10^{-15}cm^2$, 50%.

stresses. An alternative possibility is that, even for zero applied stress, the defect called E1 is actually a mixture of two defects having slightly different atomic arrangements.

As shown in Fig. 1(b) and noted above, applied <110> stress of 0.4 GPa caused the E1 DLTS peak to be become a clearly observable doublet; the continuous double-peaked line in Fig. 1(b) is the calculated spectrum for equally populated electronic levels having E_n values of 0.050eV and 0.058eV respectively.

In contrast to the E1 defect, the DLTS data for the E2 defect in the condition of zero applied stress were very well fitted by theoretical spectra calculated for a single sharp electronic level; the E_n value of 0.140±0.002eV deduced from the fitting is completely consistent with previously reported values [1-3] . As seen in Fig. 2(a), we find that for applied <100> stress the E2 peak continues to correspond very well to electron emission to the conduction band from a single sharp electronic level (with E_n value of 0.154±0.002eV for 0.4 GPa), but that for applied <110> stress the E2 DLTS peak is a doublet; our data analysis indicates E_n and population values of 0.148±0.002eV, 50±5% and 0.160±0.002.eV, 50±5% respectively for the two energy levels for 0.4 GPa <110> stress.

The experimental and best-fit theoretical DLTS spectra for the E3 defect are shown in Fig. 3 for zero stress and for <100> and <110> 0.4 GPa applied stresses. We deduce that for zero applied stress the E3 defect has a single sharp electronic level of E_n value equal to 0.340±0.002.eV (in agreement with previous reported data [1-3]), that applied <100> stress causes no broadening of the E3 peak but an increase of its E_n value, and that applied <110> stress produces broadening of the DLTS peak consistent with stress-induced splitting of the E3 level into two levels of respective populations 50±5% and 50±5% together with a mean E_n value that is higher than for zero stress. These stress-induced changes in the elcctronic level of the E3 defect are qualitatively the same as for the E2

defect, but the energy splitting of the E3 level is significantly smaller and its mean energy shift seems to be somewhat smaller.

Our experiments thus show that uniaxial stress applied along a <100> direction causes energy change but no splitting of the single sharp electronic levels of the E2 and E3 defects, but that <110> stress produces also splitting of each of those single levels into two levels whose DLTS peaks are consistent with their having equal electron populations. We find that the E1 defect level is not a singlet even for zero applied stress, but that applying <100> and <110> stresses causes qualitatively the same effects on the E1 defect as on the E2 and E3 defects.

These results give particular information on the crystallographic symmetries of the defects and strongly suggest that each individual E1, E2 and E3 defect is an atomic arrangement that has a <111> symmetry axis (ie, is of C_{3v} (trigonal) symmetry). In the situation of uniaxial stress applied along the <100> direction the four individual <111> crystal axes of such defects are equally inclined (at angles of 54.74°) to the stress direction and therefore such stress has equal effect on all the defects. But for applied <110> stress, two of the four <111> crystal directions are equally inclined (at angles of 35.26°) and two are perpendicular to the stress direction, thus removing the previous orientational degeneracy; <110> stress is therefore expected to change the singlet electronic levels of C_{3v}-symmetry defects into doublets of 50%, 50% population ratio, and that is indeed what we observe for the E1, E2 and E3 defects.

Analysis of data on the diffuse X-ray scattering from irradiated GaAs has suggested the presence in such material of Frenkel pair defects in which the dominating vacancy-interstitial orientations are <111> directions [14, 15]. It has been previously proposed [6] that E3 defects are arsenic Frenkel pairs, and the present uniaxial-stress results strengthen that proposal. Concerning the E1 and E2 defects, it has been suggested [2, 6] that these are different charge states of the arsenic monovacancy V_{As}; the present uniaxial-stress results are not consistent with such identification for a simple undistorted monovacancy, since the latter has Td symmetry and so would not show the <110>-stress-induced energy level splitting that we observe. It seems possible that E1 and E2 are also arsenic Frenkel pairs, but with V_{As}–i_{As} separations that our different from that in E3 defects.

We are grateful for financial support from the UK Engineering and Physical Sciences Research Council for this research and for a studentship bursary to one of us (SJH) by the University of Sussex. We express our thanks to Mr B. W. Farmery for technical assistance.

References

[1] D V Lang and L C Kimerling, Phys. Rev. Lett. **33,** 489 (1974)
and in "Lattice Defects in Semiconductors", Inst. Phys. Conf. Ser. 23, page 589 (1975)
[2] D. Pons and J. C. Bourgoin, J.Phys. C: Solid State Phys. **18,** 3839-3871 (1985)
[3] A. C. Irvine and D. W. Palmer, Phys. Rev. B **49,** 5695 (1994)
[4] D. Pons, P. M. Mooney and J. C. Bourgoin, J. Appl. Phys. **51,** 2038 (1980)
[5] D. Pons, Physica (Amsterdam) **116B,** 388 (1983)
[6] D. Stievenard, X. Boddaert, J. C. Bourgoin & H. J. von Bardeleben Phys. Rev. B **41,** 5271 (1990)
[7] S . J. Hartnett, D.Phil Thesis, University of Sussex (1997)
[8] A. A. Kaplyanskii, Optics and Spectroscopy (USSR) **10,** 83 (1961)
[9] L. C. Kimerling, NATO ASI Series B: Physics **Vol. 202** ("Point and Extended Defects in Semiconductors": Ed. by G. Benedek, A. Cavallini and W. Schröter; Plenum 1988) p. 1
[10] G. M. Martin, A. Mitonneau and A. Mircea, Electronics Letters **13,** 191 (1977)
[11] A. C. Irvine, D.Phil Thesis, University of Sussex (1993)
[12] F. D. Auret, R. M. Erasmus, S. A. Goodman and W. E. Meyer, Phys.Rev. B **51,** 17521 (1995)
[13] F. D. Auret, S A Goodman and W E Meyer, Materials Science Forum **196-201** (1995) 1067.
[14] A. Pillukat, K Karsten and P Ehrhart, Phys. Rev. B **53,** 7823 (1996)
[15] K. Karsten and P. Ehrhart, Materials Science Forum **143-147,** 365 (1994)
(Proc. 17th International Conference on Defects in Semiconductors, Austria 1993).

Materials Science Forum Vols. 258-263 (1997) pp. 1033-1038

MAGNETIC RESONANCE AND POSITRON ANNIHILATION OF INTRINSIC ACCEPTORS IN ITC-TREATED GaAs

K. Krambrock[1,2,3], C. Corbel[2] and J.-M. Spaeth[3]

[1]UFMG, Departmento de Física, ICEx, 30161-970 Belo Horizonte, MG, Brasil
[2]CE - Saclay I.N.S.T.N. UEPEM, 91191 Gif sur Yvette Cedex, France
[3]University of Paderborn, Physik, Warburger Str. 100, 33098 Paderborn, Germany

Keywords: intrinsic defects, GaAs, positron annihilation, ODMR, EPR, acceptors, ITC

Abstract

Thermal treatment near the melting point followed by a rapid quench to room temperature in semi-insulating GaAs destroy nearly all of the EL2 defects present in the as-grown material as shown previously by DLTS measurements. Two different structure-sensitive methods, i.e. positron annihilation (PAS) and optically detected magnetic resonance (ODMR) have been used to study the defects produced by such thermal treatments. In positron annihilation a new negatively charged mono-vacancy defect with a lifetime of 273 ps has been observed in addition to negatively charged ion-type defects. Both are acceptor-like defects. We attribute the higher lifetime of the vacancy, compared to Ga vacancy-related defects observed in as-grown material, to a higher open volume of this vacancy-related defect. In optically detected magnetic resonance experiments three acceptor-like defects have been observed. Two of them have been related to intrinsic defects, whereas the third was ascribed to a Cu-related defect which has been incorporated during the heating processes. We suggest that one of the acceptor-like defects is the Ga vacancy - related defect with the PAS lifetime of 273 ps.

Introduction

The quality of semi-insulating (SI) GaAs is strongly influenced by thermal treatments. Heat treatment of SI GaAs near the melting point , i.e. 1200^{0}C for 16 hours, followed by a rapid quench to room temperature, the so-called inverted thermal conversion (ITC), destroys almost all of the EL2 defects that were found previously in the as-grown material [1, 2]. After the ITC treatment the samples become slightly p-type. Furthermore, an additional annealing at 800^{0}C for 1h regenerates approximately 75 % of the EL2 defects and changes the sample to SI. In contrast, standard GaAs samples annealed to about 850^{0}C change from SI to low resistivity material.

The aim of the present work is to compare the results of different structure-sensitive experiments, i.e. positron annihilation spectroscopy (PAS), conventional electron paramagnetic resonance (EPR) and optically detected electron paramagnetic resonance (ODEPR) via the magnetic circular dichroism of the optical absorption (MCDA), in order to have a better insight on the formation and nature of intrinsic defects in GaAs.

In a previous work ODEPR measurements on ITC-treated GaAs have detected three new acceptor-type defects, called A1, A2 and A3 [3], which had never been observed in standard as-grown material. The main questions were whether these defects belong to Ga antisite-related defects or vacancy-type defects and how their formation occurs during the heating and quenching processes.

Experimental results

The investigated samples of this study are listed in tab. 1. Optical absorption and MCDA after calibration by conventionally detected EPR have been used to determine the concentrations of neutral EL2, $EL2^0$, and paramagnetic EL2, $EL2^+$, respectively [4].

Tab. 1: GaAs samples with different thermal treatments studied in this work. Concentrations of EL2 have been determined by optical absorption at 1.2 eV [$EL2^0$] and MCDA [$EL2^+$].

Samples	thermal treatment	ρ [Ω cm]	p/n [cm^{-3}, 300K]	$EL2^0$ [cm^{-3}]	$EL2^+$ [cm^{-3}]
#1	as-grown	$3\ 10^7$	n	$2.5\ 10^{16}$	$5\ 10^{15}$
#2a	ITC	$3\ 10^5$	p	$< 1\ 10^{15}$	$9\ 10^{15}$
#2b	ITC	10^4	p: $2\ 10^{11}$	$< 1\ 10^{15}$	$2\ 10^{15}$
#3	ITC+655°C	n.m.	p: $3\ 10^{15}$	$< 1\ 10^{15}$	$< 1\ 10^{15}$
#4	ITC+800°C	$2\ 10^8$	p: $2\ 10^{10}$	$1.0\ 10^{16}$	$14\ 10^{15}$

Positron annihilation

Positron lifetimes were measured conventionally with a time resolution of 220 ps. The average positron lifetimes in the samples τ_{av} and the annihilation times in the lattice τ_b and at vacancy-related defects τ_2 were determined from an analysis of the experimental lifetime spectra [5]. The average lifetime of the as-grown sample #1 decreases continuously from 20 to 300 K [6]. It can be decomposed into two exponential components with a mean value for the longer component τ_2 of 256 ± 5 ps, a typical value for a negatively charged mono-vacancy in as-grown material [6]. These vacancies have been attributed to Ga vacancy-related defects.
In the ITC-treated GaAs sample #2a the behavior of the average lifetime is different as shown in fig. 1a. In the low temperature region it increases, goes through a maximum at about 230 K and then decreases monotonically. However, at 450 K the average lifetime is still above the value that has been observed in vacancy-free material by 6 ps (GaAs: Zn, dashed line in fig. 1a). The decomposition of the spectrum is only possible above 200 K, where the one-defect trapping model is valid [5]. It shows a mean value for τ_2 of 273 ± 5 ps (fig. 1b) which is constant until 450 K. This lifetime is typical for a mono-vacancy.
The positron trapping rate at the vacancy κ_v can be calculated using the relation $\kappa_v = (\tau_{av} - \tau_b) / [\tau_b (\tau_2 - \tau_{av})]$ as long as the one-defect trapping model can be used [5]. The positron trapping rate as a function of temperature on a logarithmic scale is shown in fig. 2. It decreases monotonically and can be described by the relation $\kappa_v \sim T^{-1.54}$. Theoretical calculations have shown that this temperature dependence is what one expects for detrapping of positrons from a negatively charged vacancy [7]. The defect lifetime is constant above 200 K, only the intensity decreases from 90 to 50 %.
The positron trapping coefficient at the vacancy μ_v is related to the concentrations of vacancies c_v by the equation: $\mu_v = \kappa_v / c_v$. The trapping coefficient of native Ga vacancy-related defects in as-grown GaAs has been determined to $\mu_v = 3 \times 10^{15}$ at s^{-1} at 300 K [6]. This value is of the same order as the estimated value for the introduction rate of the vacancy [5]. Assuming $\mu_v = 2 \times 10^{15}$ at s^{-1}, knowing that κ_{exp} (300 K) = 1.6×10^9 s^{-1} and N = $4.43\ 10^{22}$ at cm^{-3} one gets the concentrations of vacancy-related defects of 3.5×10^{16} cm^{-3} for ITC-treated GaAs. This value for vacancy-related defects is about one order of magnitude higher than in as-grown material. Whether these negatively charged vacancy-related defects belong to Ga or As vacancy-related

defects is, however, not clear at the moment. Assuming the same arguments previously used for as-grown GaAs [6] and taking into account that the Fermi level is below midgap, the vacancy-type defects should be Ga vacancies. However, there is a clear difference in the defect lifetime τ_2 with 273 ps compared to native vacancies with 256 ps.

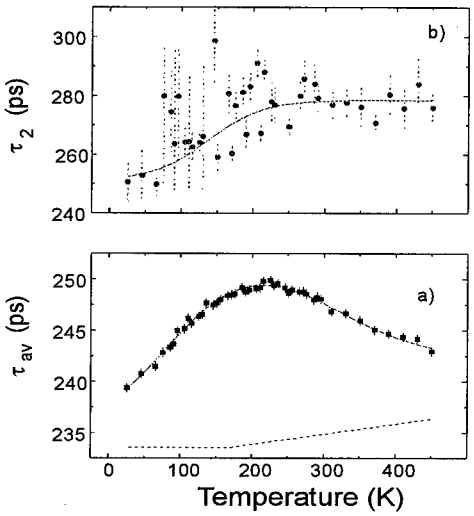

Fig. 1: (a) Average positron lifetime τ_{av} and (b) defect lifetime τ_2 as a function of measurement temperature for the ITC-treated GaAs sample #2a. Dashed line corresponds to a sample without negatively charged vacancies (GaAs: Zn).

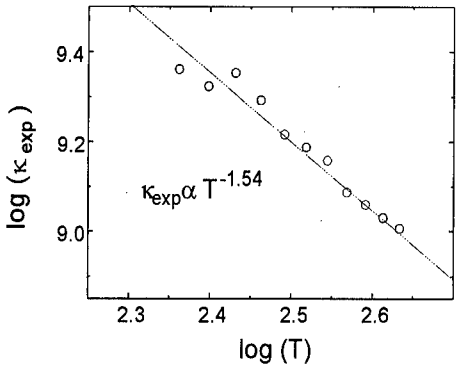

Fig. 2: Positron trapping rate κ in sample #2a as a function of measurement temperature in a double logarithmic plot.

At lower temperature (< 200 K, fig. 1) the trapping of positrons at the vacancies is in competition with trapping at negative ions which have a defect lifetime near to that of the bulk τ_b of 232 ps at 20K. A decomposition at low temperatures is not possible as seen by the large error bars in this range. Thus, the one-defect trapping model cannot be applied. At higher temperatures the trapping at these defects is inefficient which is typical for negative ion-type defects [6]. The traps of these negative ion defects are much shallower for the positrons than that of the vacancy-type defects. The positron trapping rate at the negative ions κ_{st} (at 20 K) could be calculated to be 1.8×10^{10} s^{-1} assuming that κ_{st} varies with temperature proportional to $T^{-0.5}$. In as-grown GaAs the trapping coefficient μ_{st} at the negative ions at 20K has been determined to be 2×10^{16} at s^{-1}. Using this value one gets for the concentration of negative ions $c_{st} = 4 \times 10^{16}$ cm^{-3}, the same order as the concentrations of vacancy-related defects.

Optical Absorption, EPR, MCDA and ODEPR

Figure 3 shows the optical absorption spectra of the as-grown GaAs sample #1 and the ITC-treated sample #2a (1200°C, 16h followed by a rapid quench) and fig. 4 their respective MCDA spectra. After the ITC treatment $EL2^0$ could not be detected anymore in optical

absorption in agreement with Lagowski et al [1]. However, depending on the sample, a small concentration of $EL2^+$ could be detected by MCDA and ODEPR.

Tab. 2: ODEPR parameters of three new acceptor-type defects observed in the ITC-treated GaAs samples: g g-factor, T_1 spin-lattice relaxation time and $\Delta B_{1/2}$ full linewidth at half maximum (FWHM) for B || [100]. The ODEPR spectra of A1 and A2 are anisotropic. A3 did not show any ODEPR line, although the corresponding MCDA spectrum is paramagnetic after [3].

		g [001]	T_1 (ms)	$\Delta B_{1/2}$ (mT)
A1	intrinsic defect	2.07	3000	40
A2	intrinsic defect	2.09	< 20	60
A3	Cu-related	-	-	-

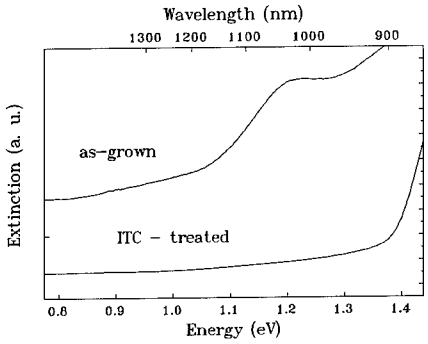

Fig. 3: Optical absorption spectra of GaAs as-grown #1 and ITC-treated #2a measured at 1.5 K.

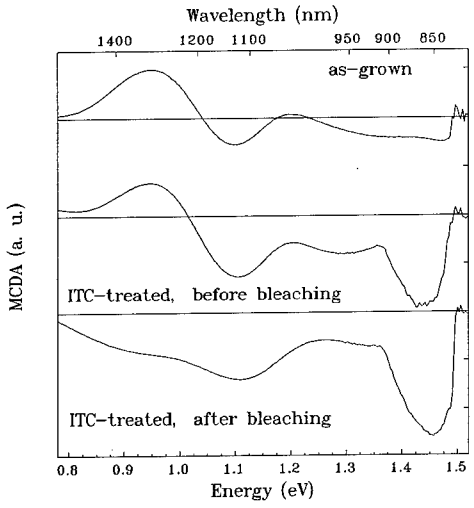

Fig. 4: MCDA spectra of GaAs as-grown #1 and ITC-treated #2a measured at 1.5 K and 2T before and after bleaching of EL2.

$EL2^+$ could be observed by MCDA and ODEPR. In addition to paramagnetic $EL2^+$, three new acceptor-type defects were detected by the MCDA/ODEPR technique, labeled A1, A2 and A3 [3]. They have never been observed before in as-grown GaAs. Their ODEPR parameters are listed in table 2.

In some of the thermally treated samples a small amount of Fe^{3+} was observed by optically detected EPR. Sample #2a showed the MCDA / ODEPR spectra of $EL2^+$, whereas in sample #2b $EL2^+$ could not be observed. All three new acceptor-type defects were observed simultaneously with $EL2^+$, indicating that their paramagnetic levels are below that of the $EL2^+/EL2^{++}$ at 0.54 eV above the valence band. The result of bleaching of $EL2^+$ at low temperaures is that the signal intensities of the new defects are increased (fig. 4 before and after bleaching). The MCDA of A3 starts at 1.36 eV and is paramagnetic. However, an ODEPR spectrum could not be detected with the available microwave power of 50 mW. It has been attributed to a Cu-related defect [8] which is introduced by the annealing experiments.

The other two defects, A1 and A2, have been associated with acceptors of intrinsic origin, i.e., Ga_{As} antisite-related or Ga vacancy-related defects. A1 is more likely associated with a Ga_{As} - related defect because of its MCDA lineshape compared to that of other intrinsic cation antisite-related defects measured in as-grown material [9]. However, the resolution in the ODEPR spectra is poor.

Conventionally detected EPR in ITC-treated GaAs samples normally show only weak signals of $EL2^+$ in its paramagnetic state. After illumination with white light or monochromatic light at about 1.1 eV at low temperatures the BE1 defect (same as FR1 [12]) has been observed, which is persistent until 90 K [10, 11]. The BE1 EPR intensity is two orders of magnitude higher than in the as-grown samples and one order of magnitude higher than in the ITC-GaAs + 800^0C samples. The BE1 defects have an annealing step near 450^0C. The EPR resonance has a g-factor of 1.87, the signal is slightly anisotropic and has a peak-to-peak linewidth of 65 mT [10]. The EPR spectrum consists of several broad lines at low temperature due to unresolved hyperfine interactions. However, the EPR intensity of this defect is strongly influenced by the electric field in the microwave-cavity which does not allow a quantitative analysis of the concentration of this defect. In addition some Fe^{3+} and EPR lines at g = 0.8 and g = 4.4 have been detected [11].

Discussion

In agreement with Lagowski et al. [1] our experiments on ITC-treated GaAs show that EL2 can be destroyed by high temperature annealings and rapid cooling to room temperature. However, some of these samples still show some paramagnetic $EL2^+$. That EL2 defects have not been observed or at least in much lower concentrations after the ITC treatments may be explained by the fact that near the melting point only primary defects, i.e., vacancies and interstitials, are in equilibrium. The quenching from the high temperature does not allow the formation of EL2 defects, only primary defects are frozen in the crystal. Additional annealings at about 800^0C allows the migration of those primary defects by formation of EL2 and other acceptor-type defects.

Earlier positron studies of ITC-GaAs showed that a vacancy-related defect annealed out at about 450^0C [13] suggesting that the BE1 center is the vacancy-related defect. In the present study we found a new vacancy-related defect with a lifetime of 273 ps in the ITC samples. The vacancy is negatively charged and a mono-vacancy. This lifetime is clearly different from the observed lifetime in as-grown GaAs where a negatively charged mono-vacancy shows a lifetime of 256 ps [6, 7] and also different from the metastable Ga vacancy of the EL2 defect in its metastable state which is about 245 ps. Hall measurements have shown that the samples are slightly p-type with p about 2×10^{11} cm^{-3}.

A correlation between PAS and MCDA/ODEPR experiments is difficult in the case of ITC-treated GaAs because of the superposition of different defects. However, both techniques show new acceptor-type defects. A1 and A3 may be associated with a Ga antisite-related defect and a Cu-related defect, respectively, which correspond to the negative charged ion-type defects in the PAS experiments. A1 had been attributed to a Ga antisite-related defect because of its MCDA and ODEPR lineshapes. Therefore, A2 may be tentatively related to the Ga vacancy-related defects with the new positron lifetime of 273 ps, which has been attributed to a higher open volume than native Ga vacancy-related defects observed in as-grown GaAs and the vacancy of the metastable state of EL2. The concentrations of both the Ga vacancies and the negative ion-type defects are in the mid 10^{16} cm^{-3}.

Conclusion

Positron annihilation in ITC-treated GaAs showed the formation of a new negatively charged mono-vacancy with a defect lifetime of 273 ps, which is likely attributed to a Ga vacancy-related defect. The higher lifetime compared to Ga vacancies in as-grown material is interpreted as being due to a higher open volume of the vacancy, but much less than a divacancy for which we expect a lifetime of 320 ps [7]. In ODEPR measurements three new acceptor-type related defects could be detected from which we attribute the A2 defect with the Ga vacancy observed by PAS. A1 and A3 may be associated to the negatively charged ion-type defects measured by PAS. The PAS results show that high acceptor concentrations are formed by the ITC treatment.

Acknowledgments

We are grateful to J. Lagowski for providing the ITC-treated GaAs samples and M. Lübbers for the Hall effect measurements. This work has been supported by the German agency DFG in project number Kr 1426/1-3, the French agency INSTN and the Brazilian agency FAPEMIG.

References

[1] J. Lagowski, H. C. Gatos, C. H. Kang, M. Skowronski, K. Y. Ko and D. G. Lin, Appl. Phys. Lett., 49, 892 (1986).
[2] C.H. Kang, J. Lagowski and H.C. Gatos, J. Appl. Phys., 62, 3482 (1987).
[3] M. Jordan, T. Hangleiter and J.-M. Spaeth, Semicond. Sci. Technol., 7, 725 (1992).
[4] D.M. Hofmann, K. Krambrock, B.K. Meyer and J.-M. Spaeth, Semicond. Sci. and Technol., 6, 130 (1991).
[5] P. Hautojärvi, in *Positrons in Solids*, Springer Series, 12, (1979).
[6] C. Le Berre, C. Corbel, R. Mih, M.R. Brozel, S. Tüzemen, S. Kuisma, K. Saarinen, P. Hautojärvi and R. Fornari, Appl. Phys. Lett., 66, 2534 (1995).
[7] M.J. Puska, C. Corbel, R.M. Nieminen, Phys. Rev. B, 41, 9980 (1990).
[8] M. Jordan, Doctoral thesis, University of Paderborn (1991).
[9] K. Krambrock, B.K. Meyer and J.-M. Spaeth, Mat. Sci. Forum, 38-41, 863 (1989).
[10] E. R. Weber and P. Omling, Festkörperprobleme, Advances in Solid State Physics XXV, Vieweg, 623 (1985).
[11] M. Hoinkis, Doctoral thesis, Lawrence Berkely Laboratory (1987).
[12] M. Baeumler, U. Kaufmann and J. Windscheif, in Conf. on Semi-Insulating III-V Materials, eds. H. Kukimoto and Miyazawa, Hakone, p. 361 (1986).
[13] S. Dannefaer, P. Mascher and D. Kerr, in *Defect Recognition and Image*, III-V compounds, ed. E.R. Weber, Elsevier, vol. II (1987).

Materials Science Forum Vols. 258-263 (1997) pp. 1039-1044

DEFECTS IN NEUTRON IRRADIATED, LEC SEMI-INSULATING GaAs

B.K. Jones, J.M. Santana and T. Sloan
School of Physics and Chemistry, Lancaster University,
Lancaster, LA1 4YB, UK
b.jones@lancaster.ac.uk

Keywords : Semi-insulating, GaAs, compensation, radiation damage, α-DLTS, PICTS

Abstract. The activation energy and capture cross-section of traps produced by neutron irradiation in LEC GaAs have been measured by a variety of techniques. The results have been compared with those from non-irradiated material.

Introduction.

The experiments reported here were obtained as part of a project to develop diodes for use as high energy particle detectors. These detectors are required to withstand considerable radiation damage and to preserve their DC and charge collection properties. The material used was Liquid Encapsulated Czochralski (LEC), semi-insulating (SI) GaAs from a variety of sources. Prototype Schottky-Ohmic diodes were irradiated with fast neutrons up to 1.9×10^{15} Ncm^{-2}, which is the expected annual dose that the detectors will receive near the interaction point at the Large Hadron Collider at CERN. The neutron irradiated material was studied in order to identify the traps that are introduced by irradiation and their relation with the Charge Collection Efficiency (CCE) of the diodes when used as high energy particle detectors. The ionisation created by the particles to be detected is collected by a charge amplifier after being swept from the depletion region of a reverse bias diode. Some charges can be trapped for the lifetime of the pulse and hence lost to the detector signal.

Experimental Methods.

The diodes were characterised by several techniques over a range of temperatures between 77 and 340K. The current-voltage (I-V) and capacitance-voltage (C-V) characteristics were measured. The latter at a range of frequencies.

The traps were studied using three different techniques, namely: α-DLTS [1,2], PICTS [3] and capacitance-voltage [4,5,6] measurements. The measurement techniques require special consideration because the material is highly compensated and is 'relaxation-like' so that the use of conventional semiconductor analysis needs care [7,8,9,10].

Materials where the dielectric relaxation time $\tau_D=\rho\varepsilon\varepsilon_0$ (ρ is the resistivity of the material, ε is the relative dielectric constant of the material and ε_0 is the permitivity of free space) exceed the carrier recombination lifetime τ_0 ($\tau_D >> \tau_0$) are called *relaxation materials*. The other type of materials where the carrier recombination lifetime τ_D exceeds the dielectric relaxation time ($\tau_0 >> \tau_D$) are called *lifetime materials* which encompass most of the more common semiconductor materials and applications. The relaxation limit is reached in materials with high resistivity due to low carrier density and those which have a fast electron-hole pair recombination rate due to high density of generation-recombination centres. Examples of this are poor quality Silicon at low temperatures or irradiated Silicon. Semi-insulating compound semiconductors such as GaAs are also very good candidates for the relaxation regime. The typical resistivity of GaAs is of the order of 10^8

Ωcm yielding a relaxation time of ~10^{-4} sec, while recombination lifetimes are estimated to be near or below 10^{-8} sec.

The first measurement technique uses alpha particles to create electron-hole pairs in a reverse biased diode and to collect them using a charge sensitive preamplifier. The charge transient produced has a "fast" component with time constant which is related to the trapping of the charge and one or more "slow" components with time constant τ_{Di} which is related to the detrapping of the charge carriers. A temperature scan produces a change of the detrapping time constant τ_{Di} which is fitted to a multi-exponential function and the activation energies and capture cross sections are obtained from an Arrhenius plot. The concentration of the trapping centres is found from the amplitude of the transient.

In the second technique the capacitance of the diode is measured as function of voltage, frequency and temperature. The time constant of the trapping centres, as well as the concentrations can be obtained from the fitting to a Debye curve of Capacitance-Frequency data as function of temperature. In normal lifetime material the free carriers are moved by the voltage to reveal the donor space charge. Here some traps are deep so that their emission time is slow and they do not respond to the AC field.

Finally the diodes were studied using Photo-Induced Current Transient Spectroscopy (PICTS). A pulse of sub-bandgap light is shone onto the diode and the current transient analysed using the high resolution multi-exponential fitting function already mentioned.

Results.
Several traps were identified. There was reasonable consistency between the results obtained from the different methods. This is shown in Figure 1 where the Arrhenius plots are shown for the three methods on one sample which showed four traps.

One of the outcomes of the project was the realisation that the analysis of many of the properties of these diodes made from semi-insulating GaAs has to be carried out assuming that it is a *relaxation* material. The material becomes more relaxation-like after irradiation. It is thought that such analysis does not affect the measured activation energy and cross section (which have been analysed in the usual way) but that the density values may not be so reliable since a conventional analysis, appropriate to lifetime material has been used.

For the irradiated diodes well known traps such as EL14 and EB10 were identified using the above mentioned techniques although a broad spectrum of traps was found in the different samples. No relation between a specific trap and the CCE of the diodes was found. Some of the diodes have traps that were not observed in other samples although the starting material is nominally the same. Most of the observed traps are electron traps but hole traps were also found.

Because of the variability of the results further investigations were made of the traps in the starting material and material from similar sources. Condiderable variation was found between samples, with little consistency even though a single (PICTS) was used and the samples were of similar construction. Some of the results are shown in Table 2 as well as Figure 1.

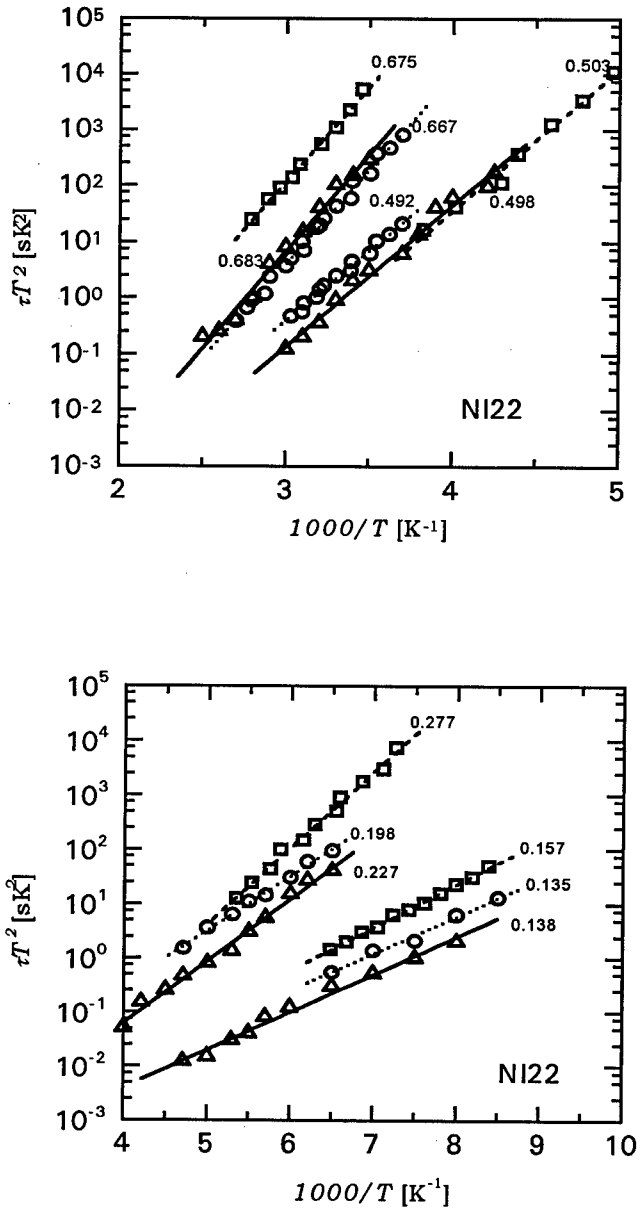

Figure 1. Arrhenius plot of the traps found in non-irradiated sample NI22 using different techniques. The *activation energies, concentration* and *capture cross sections* found using the different techniques are consistent.
Δ α-DLTS (solid), □ PICTS (dashed), ○ Capacitance-Voltage (dotted).

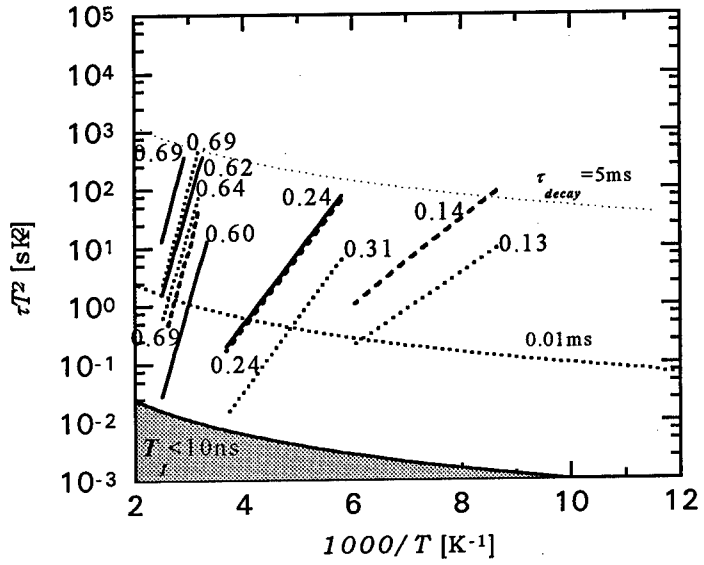

Figure 2. The properties of traps in irradiated LEC GaAs measured using the α-DLTS method. The 5ms and 0.01ms lines indicate the limits to the range of the apparatus.
B27S1 (solid line),
B27S6 (dashed line)
B20S6 (dotted line).

Table 1. The properties of traps in irradiated LEC GaAs, shown in Figure 1 above.

Sample and Neutron Dose ($\times 10^{14}$ N/cm^2)	E_A (eV)	σ ($\times 10^{-14}$cm^2)	N_T ($\times 10^{14}$cm^{-3})
B27S6 (4.8)	0.13	0.02	7.0
	0.31	0.11	0.20
	0.62	43	100
	0.69	85	125
B27S1 (14)	0.24	0.73	8.0
	0.60	46	9.0
	0.64	48	10
	0.69	52	200
B20S6 (19)	0.14	0.06	0.20
	0.24	0.74	10
	0.69	62	25

Table 2. The trap parameters measured in NON-irradiated LEC GaAs using PICTS. The charge collection efficiencies (CCE) for a-particles is shown but no correlation was found with the trap concentrations. Tentative assignments to established traps has been made.

Sample	E_A (eV)	σ ($\times 10^{-14}$cm^2)	N_t ($\times 10^{14}$ cm^{-3})	Trap family	associated defect	%CCE (alphas)
W2	0.15	0.2	0.2	EL10/EL11		45
	0.50	83	0.9			
	0.60	400	4.7	EL3	O_{As}	
	0.80	3900	13	EL2 group	As_{Ga}	
	0.82	1050	30	EL2 group	As_{Ga}	
W1.f	0.35	59×10^7	0.2	EL6	As_{Ga}-V_{As}	40
	0.44	430	12			
	0.58	1800	5.4	EL3	O_{As}	
	0.70	52.6	17	EL18	V_{Ga}/As_{Ga}	
	0.72	6.3	5	EL2 group	As_{Ga}	
WM4	0.16	84	3.5	EL10/EL11		38
	0.22	0.02	1.5			
	0.77	0.40	25	EL2 group	As_{Ga}	
WM1	0.21	1.12	1.5	EL17		51
	0.52	6010	8.0			
	0.75	4930	5.2	EL2 group	As_{Ga}	
	0.77	1040	6.8	EL2 group	As_{Ga}	
	0.81	1210	19	EL2 group	As_{Ga}	
C252-2	0.24	25	15	EL8		34
	0.50	6700	1.2	EB5		
	0.58	1300	5.3	EL3	O_{As}	
	0.60	45	5.9			
Dei-3	0.17	18	4.2	EL10/EL11		37
	0.25	92	12	EL8		
	0.30	3.5	5.8			
	0.61	2890	5.7			
	0.72	590	2.5	EL2 group	As_{Ga}	
C109	0.14	78	3.7	EL9	V_{Ga}	35
	0.25	4.2	2.5	EL6	As_{Ga}-V_{As}	
	0.60	2.2	14	EL5/HB5	V_{Ga}-V_{As}	
	0.69	12	12	EL3	O_{As}	
		14	4.2	EL2 group	As_{Ga}	
SL69	0.18	76	4.6	EL9	V_{Ga}	57
	0.32	4.5	5.9	EL6	As_{Ga}-V_{As}	
	0.41	2.4	18	EL5/HB5	V_{Ga}-V_{As}	
	0.56	15	1.1	EL3	O_{As}	
	0.80	18	2.7	EL2 group	As_{Ga}	

Conclusions.
The parameters determined for the traps in the three samples using the three different measurement techniques produced consistent results although this was better for the deeper traps.

In the *irradiated* diodes, only one trap may be clearly attributed to irradiation. The EL14 trap is present in B27S1 and B20S6 and coincides with a trap reported by Jorio et al [11].

In the *non-irradiated* material the variety of trapping centres found in different samples show that, although the material used to make the diodes is nominally the same, there are traps which are present in some samples but not in others.

More consideration is needed of these results, especially the calculation of the concentration of the traps' since the material is relaxation-like whereas the analysis theory has been developed for lifetime semiconductors

References.
1. A. Albergi-Quaranta, G. Casadei, M. Martini, G. Ottaviani and G. Zanarini, "On the information available from the rise-time of the charge pulse supplied by semiconductor particle detectors", Nucl. Inst. and Meth. **35**, 93-9 (1965).
2. B.K. Jones, J.Santana, T. Sloan et.al., "Gallium Arsenide Charged Particle Detectors; Trapping Effects", Nuclear Instruments and Methods in Physics Research **A342** 83-9, (1994).
3. J.C. Abele, R.E. Kremer and J.S. Blakemore "Transient conductivity measurements in semi-insulating GaAs, II. A digital approach," J.Appl. Phys. **62**, 2432-8, (1987).
4. R. Darvas, M. Mudrik, A. Seidman, M. Zilberstein and N.Croitoru, "Effect of radiation induced defects on the capacitance of silicon detectors," J. Appl. Phys. **71**, 1517-21 (1992).
5. G.L. Miller, D.V. Lang and L.C. Kimerling, "Capacitance Transient Spectroscopy", Ann. Rev. Mater. Sci, 377-448(1977)
6. C.T. Sah, L. Forbes, L.L. Rosier and A.F. Tasch Jr, "Thermal and optical emission and capture rates and cross sections of electrons and holes at imperfection centers in semiconductors from photo and dark junction current and capacitance experiments", Solid State Electron. **13**, 759-88 (1970).
7. W. Van Roosbroeck and H.C. Casey Jr, "Transport in relaxation semiconductors", Phys. Rev. **B5**, 2154-75 (1972).
8. K. Zdansky, B.K. Jones, J. Santana and T. Sloan, "Numerical Analysis of Charge Transport in Semi-insulating GaAs with Two Contacts", J. Appl. Phys. **79** 3611-8 (1996).
9. B.K. Jones, K. Zdansky, J. Santana and T. Sloan. "Relaxation Semiconductor Devices", Proc. GaAs and Related Compounds, San Miniato, March 1995, ed P.G.Pelfer, J. Ludwig, K. Runge and H. S. Rupprecht. 73-77.
10. B.K. Jones, J. Santana and M. McPherson, "Semiconductor detectors for use in high radiation damage environments-Semi-insulating GaAs or Si?", Nucl. Instrum. and Methods in Physics Research A **394** (1997) to be published.
11. A. Jorio, C. Rejeb, M. Parenteau and C. Carlone, "Radiation induced carrier enhancement and intrinsic defect transformation in n-GaAs", J. Appl. Phys. **74**, 2310-7 (1993).

Materials Science Forum Vols. 258-263 (1997) pp. 1045-1050

ELECTRICAL CHARACTERIZATION OF DEFECTS INTRODUCED DURING PLASMA-BASED PROCESSING OF GaAs

F. D. Auret[*], S. A. Goodman[*], G. Myburg[*], W. E. Meyer[*] and P. N. K. Deenapanray[*]
M. Murtagh[**], Shu-Ren Ye[**], H. J. Masterson[**], J. T. Beechinor[**], and G. M. Crean[**]
[*] Physics Department, University of Pretoria, Pretoria 0002, South Africa
[**] National Microelectronics Research Centre (NMRC), Lee Maltings, Cork, Ireland

Keywords: He-plasma processing, $SiCl_4$ reactive ion etching, Schottky barrier diodes, defects, DLTS

Abstract. Dry etching is a key processing step in microelectronics manufacturing. Both reactive and non-reactive ions, as well as combinations of these, are used to achieve the desired etch rate and semiconductor surface morphology. Dry etching does, however, introduce electrically active defects in semiconductors, which alter their properties and hence influence the quality of devices fabricated on them. We report the results of experiments during which epitaxially grown n-GaAs was exposed to He- and $SiCl_4$-plasmas at similar r.f. powers and pressures. To study the defects introduced during these plasma-exposures, we employed deep level transient spectroscopy (DLTS). The effect of the plasma induced defects on the GaAs free carrier concentration and the performance of Schottky barrier diodes (SBDs) fabricated on it was evaluated by capacitance-voltage (C-V) and current-voltage (I-V) measurements, respectively.

DLTS revealed that He- and $SiCl_4$-plasma processing introduced different sets of defects. The EHe1 and EHe2 introduced by He-plasma processing, and the ER3 introduced during $SiCl_4$ etching, have the same "signatures" as the Eα1 - Eα2 pair, and the metastable Eα3, respectively, introduced during α-particle irradiation of the same GaAs. I-V measurements demonstrated that the characteristics of SBDs fabricated on He-ion processed surfaces were very poor compared to those fabricated on GaAs etched with $SiCl_4$, which had almost ideal characteristics. C-V measurements revealed that He-plasma processing resulted in a more severe free carrier concentration reduction than $SiCl_4$ etching, which extended as deep as one micron below the surface for some processing conditions. The origin of the free carrier reduction is speculated to be electron traps with energy levels below midgap.

Introduction

Dry etching, using noble gas ions, reactive ions or mixtures of these, plays an important role in semiconductor device fabrication. It has several advantages over wet chemical etching, including increased anisotropic etching and the ability to obtain very narrow linewidths during microelectronics processing [1]. Whereas dry etching using noble gas ions occurs via sputtering, reactive ion etching (RIE) mainly proceeds through surface adsorption, chemical reactions and desorption [1], and thus requires much lower particle energies. During dry etching, particles from the plasma impinge on the semiconductor where they produce crystal damage. Most of this damage is continuously removed if the etch rate is high enough, but will accumulate for lower etch rates. The crystal disorder introduced in semiconductors by dry etching affects their electro-optical properties [2] and the characteristics of devices fabricated on them, such as the barrier height of Schottky barrier diodes (SBDs) [3,4]. Deep level transient spectroscopy (DLTS) [5] revealed that the reason for this modification of material and device properties is due to the introduction of electrically active defects during dry etching.

Noble gas ions are sometimes mixed with reactive ions to regulate the etch rate and uniformity [6]. Up to now, most investigations regarding the etching of GaAs with mixtures of noble gas and reactive ions, involved Ar and focused on etch rates, surface morphology and the effect of etching on SBD properties [6,7]. Little is yet known about the structure of the electrically active defects

introduced during dry processing of GaAs. Furthermore, the individual contributions of noble and reactive ions to the modification of GaAs materials and device properties are still unknown.

As a first step towards systematically investigating the defects introduced by different noble gas dry-etch constituents and evaluating the effects of these defects on materials properties and device performance, we present results for He- and $SiCl_4$-plasma processing of n-GaAs. We show that the free carrier reduction of n-GaAs thus processed, the characteristics of SBDs fabricated on it and the defects introduced therein, are different, even though the same processing conditions were used.

Experimental procedure

For this experiment we used an n-GaAs layer, doped with Si to 1.3×10^{16} cm^{-3}, grown by organo-metallic vapor phase epitaxy (OMVPE) on an n^+–substrate. Ni/AuGe/Au ohmic contacts were formed on the n^+–substrates. For control purposes, Pd Schottky contacts were fabricated on the epilayers cleaned by conventional wet chemistry, but not plasma processed. He-plasma processing [8,9] was performed for 10 minutes at pressures of 30 mTorr, 60 mTorr and 90 mTorr, and r.f. powers of 80 W, 140 W and 200 W. After plasma processing, the samples were once again chemically cleaned before depositing Pd Schottky contacts, 60 nm thick and 0.77 mm in diameter, by resistive evaporation through a metal contact mask.

The rectifying quality of the SBDs and GaAs free carrier concentration (N_D) were assessed by current-voltage (I-V) and capacitance-voltage (C-V) measurements, respectively. DLTS in a lock-in amplifier based system was employed to analyse the plasma processing-induced defects. The energy level of an electron trap (E_t) and its apparent capture cross-section (σ_n), the combination of which is referred to as its DLTS "signature", were determined from Arrhenius plots of ln (T^2/e) vs $1/T$, where e is the emission rate at a peak temperature T.

Results and discussion

I-V measurements

SBDs fabricated on unprocessed surfaces had ideality factors below 1.02 over at least 6 decades of current and saturation currents of $2\text{-}3\times10^{-12}$ A. In Figs. 1 and 2 we show that the I-V characteristics of SBDs fabricated on surfaces processed in He and $SiCl_4$ plasmas are vastly different. SBDs fabricated on He-ion processed surfaces exhibit high saturation currents and non-

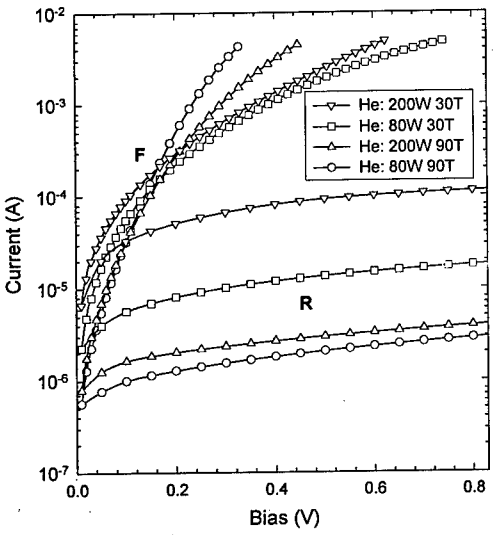

Fig. 1. I-V characteristics of Pd SBDs on n-GaAs processed in a He plasma at the pressure and r.f. power conditions indicated in the legend.

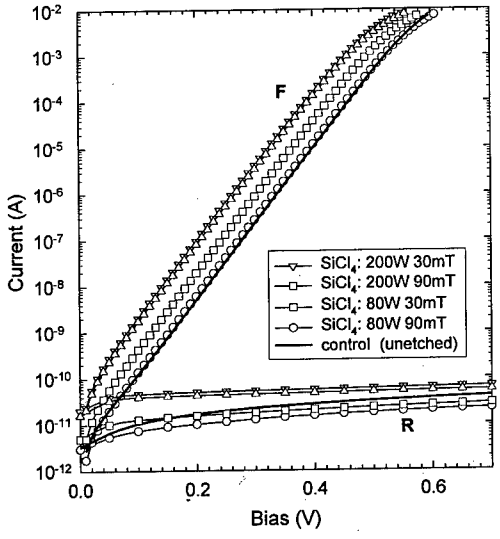

Fig. 2. I-V characteristics of Pd SBDs on n-GaAs etched with $SiCl_4$ at the plasma pressure and r.f. power conditions indicated in the legend.

linear forward characteristics, the degree of which strongly depends on deposition power and plasma pressure. In contrast, high quality SBDs could be fabricated on GaAs etched in a $SiCl_4$-plasma under identical power and pressure conditions. Figure 2 shows that some $SiCl_4$ etching conditions yielded SBDs with characteristics superior (higher barrier heights and lower reverse leakage currents) to those of the unetched samples. These SBDs have ideality factors of between 1.01 and 1.02, indicating that charge transport across the barrier takes place predominantly via thermionic emission. Figures 1 and 2 also show that for both He- and $SiCl_4$-plasma processing at a fixed r.f. power (e.g. 200 W), the lowest and highest saturation currents, I_s, were obtained for pressures of 90 mTorr and 30 mTorr, respectively. We observed the same trends for diodes on GaAs processed at powers of 140 W and 80 W. We also found that for a constant pressure (e.g. 30 mTorr), I_s increases with increasing r.f. power. We stress that, although the SBD quality depends on $SiCl_4$ processing conditions, *this dependence is much weaker than for He processing.*

The poor diode quality obtained after processing at low pressures and high power can be understood by noting that, as the pressure is reduced, both the (self) bias across the extended sheath region and the mean free path of ions in this region increase, resulting in increased incident ion energy impacting the GaAs. Similarly, as the power is increased, the energy of the particles reaching the substrate also increases. Since the total number of defects introduced increases with increasing ion energy, it follows that the total defect concentration increases with decreasing plasma pressure and increasing r.f. power, resulting in non-ideal SBD characteristics.

In order to gain some insight into the origin of the poor SBD characteristics on He-processed GaAs, we modelled the I-V data by assuming that the forward current, I, consists of thermionic emission (TE) and recombination-generation (RG), including the effect of series resistance, R_s [10]:

$$I = I_s\,[\exp\{(V - I\,R_s)/nkT\} - 1] + I_g\,[\exp\{(V - I\,R_s)/2kT\} - 1], \qquad (1)$$

where I_s and I_g are the saturation TE and RG currents and n is SBD ideality factor. Our analysis indicated that Eq. (1) did not yield a satisfactory fit to the experimental data. Good fits (solid lines in Fig. 1) could, however, be obtained by using only the TE term in Eq. (1) and by assuming that n depends on forward bias via constants n_0 and n_1:

$$n\,(V) = n_0 + n_1\,V, \qquad n_0 > 1\,,\, n_1 > 0 \qquad (2)$$

The $n\,(V)$ dependence observed here suggests that the barrier height is bias dependent to a much stronger degree than due to normal image force lowering, but to a degree which depends on the processing conditions, i.e. on the concentration of process induced defects.

C-V measurements

The free carrier concentration (N_D) profiles in Figs. 3 and 4, constructed from C-V measurements, show that both He- and $SiCl_4$-plasma processing significantly reduce N_D in the first micron below the interface. It is evident that the degree of N_D reduction is more severe for He than for $SiCl_4$ processing and that the extent of this carrier reduction depends on the processing conditions. For He, a clear trend is observed: at a given r.f. power, the carrier reduction increases with increasing plasma pressure, while for a given plasma pressure the carrier reduction is more or less independent of the r.f. power. The increase in carrier reduction with increasing pressure can be understood by noting that for increased plasma pressures, the number of He ions penetrating the GaAs, and therefore the number of point defects diffusing into it, also increases. For $SiCl_4$-plasma processing, the carrier reduction is not as severe as for He because the defects close to the surface are continuously being removed by $SiCl_4$ etching. The high etch rate of $SiCl_4$ [9] is evidenced by Fig. 4 (c) which shows that after etching for 10 min at 200 W and 90 mTorr, the etch "front" has reached the n^+ substrate. It is evident from Figs. 3 and 4 that the traps responsible for carrier depletion are present at depths which are orders of magnitude larger than the penetration depth (maximum: tens of nm, from TRIM [11]) of He ions or any $SiCl_4$-related plasma constituent. These traps are therefore mobile defects which diffuse into the GaAs from the highly damaged near-surface region (ahead of the etch "front" in the case of $SiCl_4$).

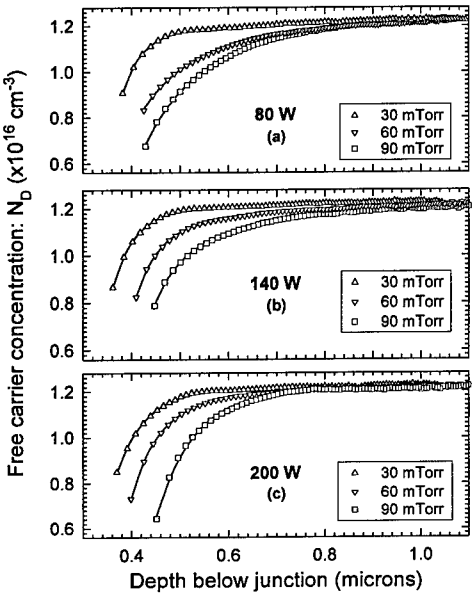

Fig. 3. Free carrier concentration profiles of n-GaAs processed in a He plasma at the pressure and r.f. power conditions indicated in the legend.

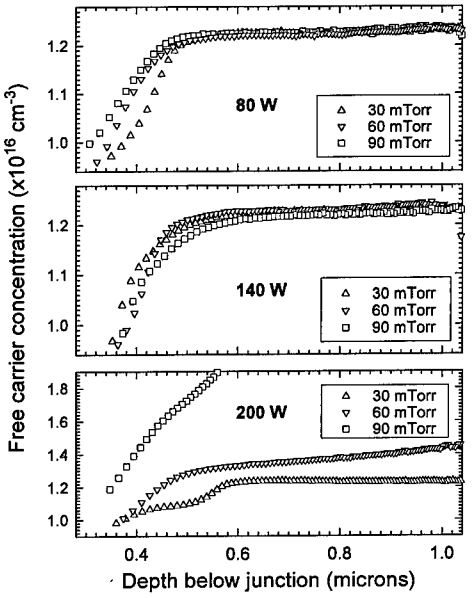

Fig. 4. Free carrier concentration profiles of n-GaAs etched in a $SiCl_4$ plasma at the pressure and r.f. power conditions indicated in the legend.

For He processing, we could account for the strong carrier reduction by assuming the presence of two electron traps with surface concentrations $N_{Ti}(0)$ ($i = 1, 2$) of which the concentrations decrease exponentially into the GaAs. The reduced free carrier concentration $N_D(x)$ thus becomes:

$$N_D(x) = N_D(\infty) - N_{T1}(0)\, exp(-x/\lambda_1) - N_{T2}(0)\, exp(-x/\lambda_2), \quad (3)$$

with $N_D(\infty)$ the uncompensated carrier concentration and λ_i the characteristic trap distribution depths. The lines in Fig. 3 were obtained by fitting Eq. (3) to the experimental data and by varying $N_{Ti}(0)$ and λ_i to obtain the best fit. For all the processing conditions investigated, we found that $N_{T1}(0)$ is of the order of 10^{18} cm^{-3} and $N_{T2}(0)$ is at least two orders of magnitude lower, while λ_1 and λ_2 typically range from 0.03 μm to 0.05 μm and 0.3 μm to 1.1 μm, respectively. Because $N_{T1}(0) > N_D(\infty)$, and since $N_{T1}(0) >> N_{T2}(0)$, it follows from Eq. (3) that complete carrier compensation will occur up to a distance x_c below the interface, given by:

$$x_c = \lambda_1 [\log \{N_{T1}(0)\}/\log \{N_D(\infty)\}] \quad (4)$$

Since $N_{T1}(0) \approx 10^{18}$ cm^{-3} and $N_D(\infty) \approx 10^{16}$ cm^{-3}, Eq. (4) yields $x_c \approx 1.1\ \lambda_1$.

DLTS measurements

The only defect detected in the control samples was the EL2 with a DLTS peak at 385 K (at a lock-in amplifier frequency of 46 Hz). It could not be positively identified after He-ion processing due to the low barrier height of SBDs on these surfaces [12]. Curve (a) in Fig. 5 reveals that He-ion processing introduced several prominent electron traps (EHe1 - EHe7) of which the concentrations depend on the processing conditions. For determining the defect "signatures", we used a small pulse to minimise electric field enhanced emission and to monitor only emission from defects (concentration N_T) in a narrow region so that $N_T/N_D < 0.1$. From the signatures that we determined for EHe1 and EHe2, we conclude that they are the same as Eα1 and Eα2, introduced during α-particle bombardment [Fig. 5, curve (c)] [13], and the EHe1 and EHe2 introduced by 5 keV He-ion bombardment [14] of the same material. Eα1 and Eα2 have energy levels at 0.04 eV and 0.14 eV, respectively, below the conduction band and are thought to be two charge states of the V_{As} - As_I pair [15]. We further note that the ratio of the EHe1 to EHe2 peak height is far less than unity, as

may be expected for two charge states of the same defect. We suggest that this is caused, firstly, by incomplete filling of EHe1 due to stress fields of extended defects in its vicinity (similar to the divacancy in Si [16]) and, secondly, because electron emission from EHe1 is more strongly influenced by an electric field than from EHe2 [17]. EHe7 has approximately the same energy level as EL2, but almost an order of magnitude higher capture cross section. The broad peak, EHeX, seems to consist of more than two superimposed peaks and it was not possible to separate their "signatures". However, by comparing curve (a) to (c) in Fig. 5, it appears that EHeX may consist of, among others, Eα3 and Eα4 [13].

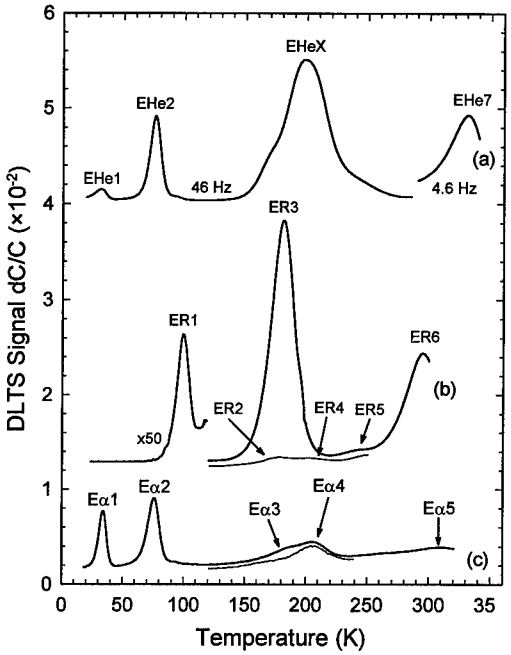

Fig. 5. DLTS spectra of n-GaAs: (a) processed in a He plasma; (b) etched with $SiCl_4$; and (c): bombarded with α-particles. For curves (a) and (b) the pressure and r.f. power were 200 W and 30 mTorr.

$SiCl_4$ processing did not noticeably affect the EL2 concentration. Curve (b) in Fig. 5 reveals that $SiCl_4$ etching introduced two prominent (ER3 and ER6) and some minor (ER1, ER2, ER4 and ER5) electron traps of which the properties are given in Table I. ER3 has the same electronic properties as the Eα3 introduced in GaAs by high energy He-ion bombardment [Fig. 5, curve (c)] [13], and is metastable. It can be reversibly removed [Fig. 5 (b), thin line] by hole injection below 120 K and re-introduced [Fig. 5 (b), thick line] by annealing above 200 K. The ER3 transformation kinetics are the same as those of previously reported for Eα3 [18].

Our DLTS results contrast those of Lootens *et al* [19] who reported that $SiCl_4$ etching removed some defects in epitaxially grown n-GaAs, but did not introduce new defects. These different observations may be due to the different processing conditions used.

Due to the high free carrier compensation, defect concentrations profiles could not be determined accurately. However, we estimate that, e.g. for processing at 200 W and 30 mTorr, the EHe2, EHeX and ER3 concentration decrease exponentially away from the surface, reaching values of approximately 10^{15} cm^{-3} and 10^{13} cm^{-3} at (0.20 - 0.25) μm and (0.55 - 0.60) μm below the surface, respectively. Processing at higher pressures and lower r.f. powers resulted in a decrease of the main

Table I. Electronic properties of defects introduced in n-GaAs by He- and $SiCl_4$-plasma processing

Etchant	*Defect*	E_t (eV)	σ_a (cm^2)	T_{peak} [(a)] (K)	*Similar defects*
He	EHe1	0.026	1.3×10^{-17}	30	Eα1 [13]
	EHe2	0.117	1.7×10^{-14}	72	Eα2 [13]
	EHe7	0.794	7.7×10^{-13}	354	EL2?
$SiCl_4$	ER1	0.190	6.5×10^{-14}	105	–
	ER3	0.354	7.1×10^{-14}	184	Eα3 [13, 18]
	ER6	0.630	1.8×10^{-13}	302	–

(a) Peak temperature at a lock-in amplifier frequency of 46 Hz, i.e. a decay time constant of 9.23 ms.

defect concentrations. These trends regarding the dependence of defect concentration on processing conditions are the same as those inferred from I-V measurements, despite the fact that DLTS and I-V measurements provide information about defects located at different depths below the junction.

Conclusions

I-V measurements showed that SBDs fabricated on $SiCl_4$-etched GaAs, exhibited excellent rectification behaviour while those on GaAs processed in a He plasma under similar conditions had poor characteristics. Since $SiCl_4$ plasmas etch GaAs at between 180 and 380 nm min^{-1} while the etch rate of He is negligible, we conclude from the I-V results that the plasma-induced damage which affects the I-V characteristics, resides close to the GaAs surface and can be removed if the etch-rate is high enough. C-V measurements showed that both He- and $SiCl_4$-plasma processing reduce N_D to distances of up to one micron below the surface. This implies that the defects responsible for free carrier trapping are mobile and diffuse into the GaAs during processing. DLTS revealed that He and $SiCl_4$ plasmas introduces different sets of defects. The ER3 introduced during $SiCl_4$-etching and the EHe1 - EHe2 pair have the same "signatures" as Eα3 and the Eα1 - Eα2 pair introduced during α-particle irradiation of the same GaAs. Simple calculations show that the emission rates of the main defects characterised here are, however, too high to account for carrier trapping at room temperature and thus to account for the reduction in N_D. Therefore, we conclude that the origin of the free carrier reduction are defects with levels well below midgap.

References

[1] S. J. Fonash, J. Electrochem. Soc. **137**, 3885 (1990).
[2] M. B. Johnson, T. C. McGill and N. G. Paulter, Appl. Phys. Lett. **54**, 2424 (1989).
[3] F. D. Auret, S. A. Goodman, G. Myburg and W. E. Meyer, J. Vac. Sci. Technol. B **10**, 2366 (1992).
[4] Y. G. Wang and S. Ashok, J. Appl. Phys. **65**, 2371 (1989).
[5] D. V. Lang, J. Appl. Phys. **45**, 3014 (1974).
[6] S. J. Pearton, U. K. Chakrabarti, W. S. Hobson and A. P. Kinsella, J. Vac. Sci. Technol. B **8**, 607 (1990).
[7] M. Meyyappan, H. S. Lee, D. Eckart, M. Namaroff and J. Sasserath, J. Vac. Sci. Technol. B **10**, 1215 (1992).
[8] F. D. Auret, G. Myburg, W. E. Meyer, P. N. K. Deenapanray, H. Nordhoff, M. Murtagh, Shu-Ren Ye, H. J. Masterson, J. T. Beechinor and G. M. Crean, , Mat. Res. Soc., Proc. 442, 51 (1997).
[9] M. Murtagh, Shu-Ren Ye, H. J. Masterson, J. T. Beechinor, G. M. Crean, F. D. Auret, G. Myburg, W. E. Meyer, P. N. K. Deenapanray and H. Nordhoff, Mat. Res. Soc., Proc. 442, 75 (1997).
[10] D. Donoval, J. de Sousa Pires, P. A. Tove and R. Harman, Solid-State Electronics **32**, 961 (1989).
[11] J. F. Ziegler, J. P. Biersack and U. Littmark, in *The Stopping and Range of Ions in Solids*, Vol. 1, edited by J. F. Ziegler (Pergamon Press, New York, 1985).
[12] Q.Y. Ma, M.T. Schmidt, X. Wu, H.L. Evans and E.S. Yang, J. Appl. Phys. **64**, 2469 (1988).
[13] F. D. Auret, S. A. Goodman, G. Myburg and W. E. Meyer, Appl. Phys. A**56**, 547 (1993).
[14] F. D. Auret and S. A. Goodman, Appl. Phys. Lett. **68**, 3275 (1996).
[15] B. Ziebro, J. W. Hemsky and D. C. Look, J. Appl. Phys. **72**, 78 (1992).
[16] B. G. Svensson, B. Mohadjeri, A. Hallen, J. H. Svensson and J. W. Corbett, Phys. Rev **B 43**, 2292 (1991).
[17] S. A. Goodman, F. D. Auret and W. E. Meyer, Jap. J. Appl. Phys. **33**, 1949 (1994).
[18] F. D. Auret, R. M. Erasmus, S. A. Goodman and W. E. Meyer, Phys. Rev. **B 51**, 17 521 (1995).
[19] D. Lootens, P. Van Daele and P. Demeester, J. Appl. Phys. **70**, 221 (1991).

Materials Science Forum Vols. 258-263 (1997) pp. 1051-1056

METASTABLE CHARGE RECOVERY IN PLASMA-IRRADIATED *n*-GaAs

K. WADA and H. NAKANISHI[1]

NTT System Electronics Laboratories,
3-1 Morinosato-Wakamiya, Atsugi, Kanagawa 243-01, Japan.
[1] Kochi University,
2-5-1 Akebono, Kochi 780, Japan

Keywords: GaAs, Metastability, Plasma-induced defects, Bias-annealing, Injection-annealing

Abstract. Photoinduced recovery and thermal reduction of charge densities has been found in Ar-plasma irradiated n-GaAs:Si. DLTS measurements reveal new metastable deep levels, A and B, but it is found that they are not responsible for the metastable behavior of charge densities. The present findings should be a first step for realizing optical nonlinear devices operating at room temperature.

Introduction

Optical nonlinearity is a unique application field for defects in compound semiconductors [1]. Indeed, the persistent photoconductivity due to DX centers and photocapacitance quenching due to EL2 in GaAs have been successfully applied to modulate the Fermi level of AlGaAs and GaAs by light illumination [2,3]. One of the problems with such applications is that metastable states of these defects are only attainable at low temperatures, typically near 100 K. We therefore need photosensitive metastable defects that persist at or above room temperature.

Since the reports on M3 and M4 in GaAs [4], there have been many reports on metastable defects in this material. Although the deep levels can be kept metastable even at room temperature by controlling bias voltages, it is so far unclear if they can be used to modulate the Fermi level [5]. We recently reported that Si donors in GaAs, once deactivated by plasma irradiation, can be reactivated by reverse-bias annealing under laser irradiation and can then be deactivated again by thermal annealing [6]. The present paper reports the characteristics of defects in Ar-plasma-irradiated GaAs and correlation of metastable deep levels.

Experimental procedures

Horizontal Bridgman-grown *n*-GaAs:Si wafers with a donor density of 2.5×10^{17} cm^{-3} were used. Irradiating the wafers with Ar plasma at 10 Pa for 1 min. in a reactive-ion-etching chamber with a parallel-plate reactor operated at 50 W produced a donor-deactivated zone in the surface layer. A typical zone was 150 nm thick. Semitransparent Ti metal dots 20 nm thick and 1 mm in diameter

were deposited on the irradiated wafers after 20 nm of the surface layer was chemically etched to minimize Schottky barrier height drift and current leakage. After Ti deposition the wafers were pre-annealed at 100°C for 12 min to produce what are called here the starting samples. For reverse-bias *injection* annealing (RBIA), these samples were irradiated by an Ar^+ ion laser (48 mW/cm^2), while the Schottky diodes reverse-biased at 4 V at temperatures between -20 and 100°C. For comparison, similar reverse-bias annealing (RBA) without laser irradiation was performed at 150°C. Thermal annealing (TA), which is the annealing but without bias application, was performed at 100°C for 12 min.

Deep level transient spectroscopy (DLTS) measurements were performed to study signatures and behavior of deep levels. To suppress "RBA" during DLTS measurements and avoid change in charge density profiles, a quiescent reverse bias of only 1 V was employed and the wafer temperature was kept below 100°C.

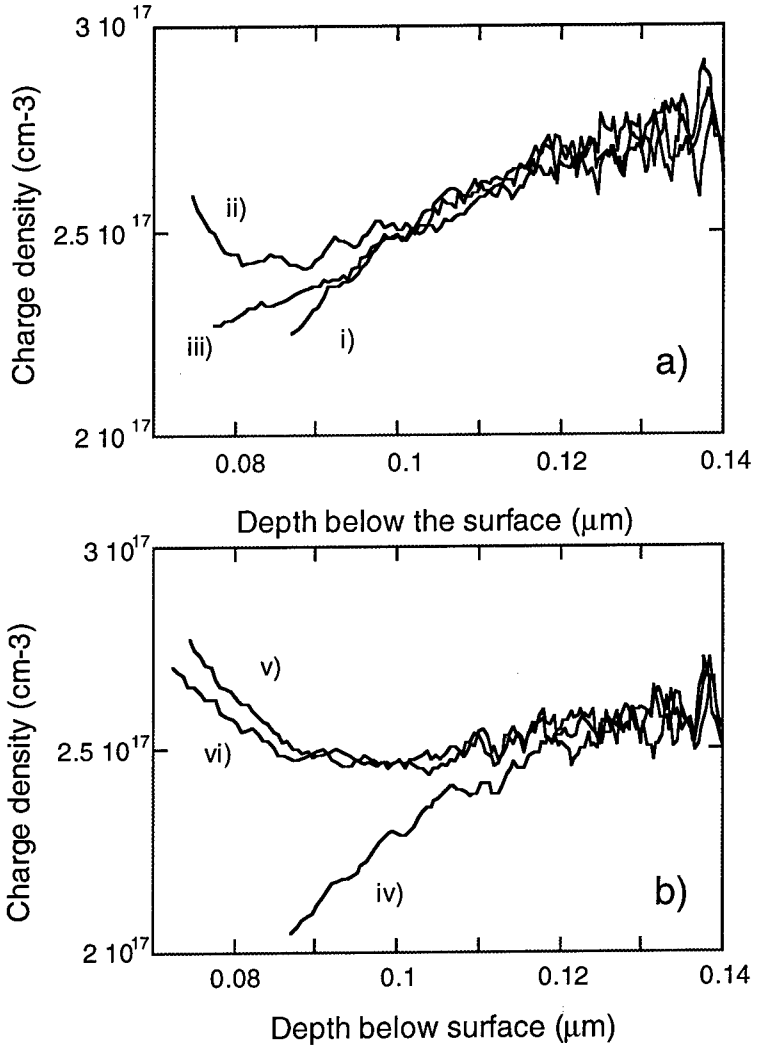

Fig. 1. Charge density changes induced by a) RBIA at 100°C and b) RBA at 150°C:
i) starting sample, ii) after 5-min. RBIA, iii) after (RBIA+TA); iv) starting sample, v) after 30-min. RBA, and after (RBA+TA).

Results

Charge density.

Figure 1 (a) shows charge density profiles in the surface layer of plasma-irradiated GaAs before and after RBIA at 100°C for 4 min. This RBIA clearly induced the

same kind of recovery of the charge density which has been reported to be recovered by RBA at a temperature higher than 150°C [7]. Because such recovery could not be observed after RBA at 100°C or after TA at 100°C , laser irradiation is essential to induce such recovery. The charge recovery reaction showed first-order kinetics with an activation energy, between -20 and 100°C, of 0.1 eV [6]. Since the recovery induced by RBA without laser irradiation had an activation energy of 0.7 eV, it is clear that the charge recovery should not be induced by temperature elevation due to laser irradiation. The mechanism of enhanced charge recovery is discussed later.

It is interesting to note that the charge density near the surface region, which was increased by RBIA, decreased after TA. Also shown in Fig. 1(a) is a typical example, obtained when the wafer was subjected first to RBIA at 100°C for 4 min. and then to TA. The profile after TA is similar to that of the starting samples. It seems that charges recovered by RBIA disappear during TA. This charge density recovery and reduction were repeatedly induced by alternating RBIA and TA.

The effects of TA on recovered charges differ markedly between the RBIA-treated samples by and the RBA-treated samples. A typical example is shown in Fig. 1(b), which shows that the charge density recovered by RBA shows only a slight reduction after TA. This difference suggests that the charge recovery phenomenon in RBIA is not the same as that in RBA.

Deep levels. DLTS measurements detected four deep levels in the samples subjected to RBIA, RBA, or TA. Figure 2 shows Arrhenius plots of these deep levels and of those hitherto reported [4, 8-10]. Deep levels A, B, and D were detected in the samples subjected to RBIA, while A and D were only detected in the samples subjected to RBA. Deep levels C and D were detected in the samples subjected to TA. The deep level D well corresponds to EL2, and the signature of C is similar to those of M3 [4] and E3 [9]. Furthermore, C disappeared upon RBA and reappeared upon TA, which is qualitatively identical to the reported behavior of M3 and E3. This similarity indicates

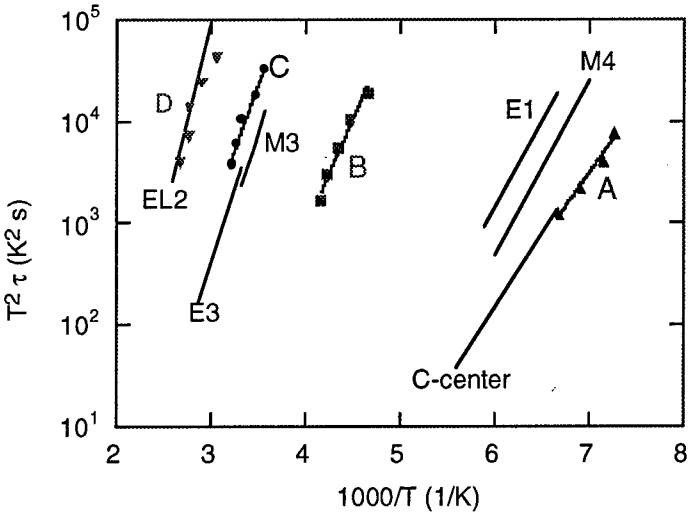

Fig. 2 . Arrhenius plots of deep levels A, B, C and D. M3 and M4 denote the metastable deep levels reported in Ref. 4. E1 and E3 denote those reported in Ref. 9. C-center denotes that reported in Ref. 8. The capture cross sections of A and B are 2.2 x 10^{-17} and 3 x 10^{-15} cm^2 and their depths are 0.24 and 0.52 eV.

that C corresponds to the metastable deep levels M3 or E3. The deep level A has a signature identical to that of the metastable deep level C-centers induced by high energy electron beam irradiation of n-GaAs:Te [8]. The signature B corresponds to none of the deep levels so far reported.

The only deep level detected in as-grown samples was EL2. This means that A, B, and C were induced by Ar plasma irradiation. B, C, and EL2 were present in the starting sample, but A was not. Figure 3(a) shows the changes in DLTS signal intensities of A, B, and EL2 that were produced by RBIA and TA. Under RBIA at 100°C for 4 min, A appears and B increases substantially:

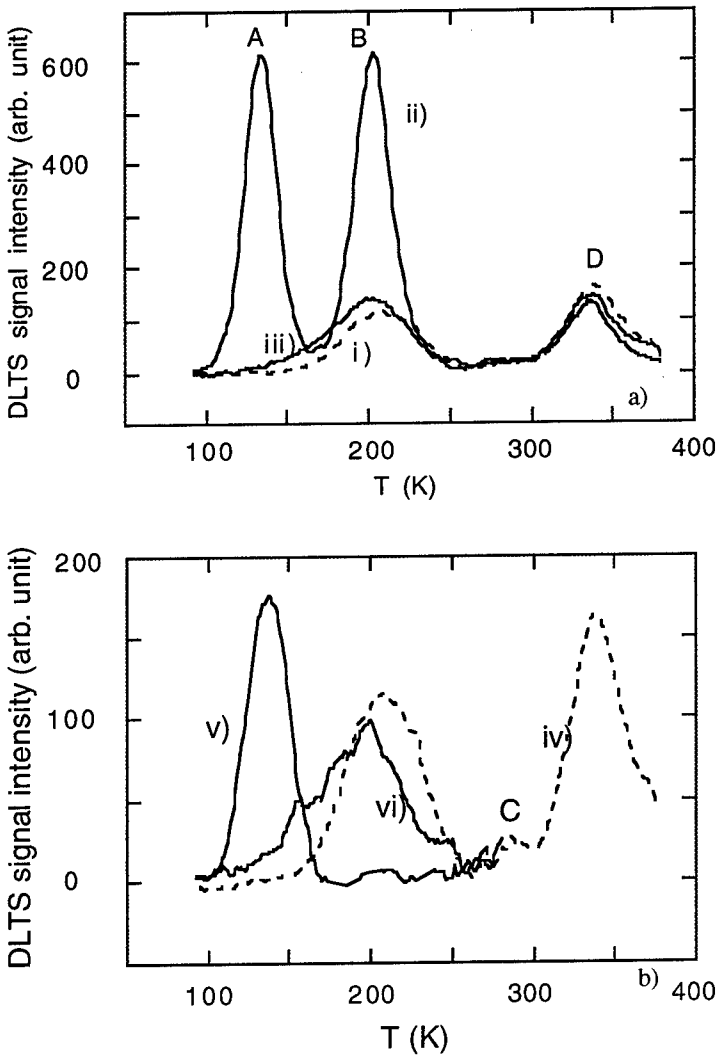

Fig. 3. Behavior of the deep levels by RBIA, RBA, and TA: i) starting sample, ii) after RBIA, iii) after (RBIA+TA); iv) starting sample, v) after RBA, and vi) after (RBA+TA).

After TA, both these deep levels are restored to the state in the starting samples. The reappearance and disappearance of A and the increase and decrease of B were reproduced by alternating RBIA and TA. We thus conclude that A and B are metastable defects and are independent each other. Furthermore, the behavior of A is identical to that of C-centers [8]. This, together with similarity in signature, indicates that A is indistinguishable from C-centers. It is also suggested that there should be some sources in the plasma-irradiated samples, which are invisible by conventional DLTS, and from which A is induced and B is increased during RBIA.

As shown in Fig. 3(b), RBA causes A to appear and B to disappear, and subsequent TA causes A to disappear and B to reappear . Thus, it is confirmed that TA restores the defect system to that in

the starting samples. This disappearance and reappearance behavior was also reversible by alternating RBA and TA. This confirms that A and B are metastable and independent defects.

Discussion

First, consider the model for the RBA-induced charge density increase proposed in Ref. 7. The reaction is

$$(\mathrm{Si}\ Y) \rightarrow \mathrm{Si}^{+} + Y^{+} + 2e^{-}. \qquad (1)$$

Here Y denotes an Ar-plasma-irradiation-induced defect which deactivates Si donors. Charge decrease upon plasma irradiation would be induced by complex formation between Si^{+} donor and Y^{-}. Charge recovery would be due to dissociation of Y^{-} from the complexes and due to its charge reversal to positive, Y^{+}. Thus, the mechanism of the enhanced recovery is proposed to be structual instability in terms of charge state change. As shown in Fig. 1 (b), the reaction (1) is irreversible.

During RBIA, minority carriers (here holes) are injected. Under the assumption that phenomena governing the charge recovery during RBIA are basically the same as those governing charge recovery during RBA, the reaction proposed here is

$$(\mathrm{Si}\ Y) + 2h^{+} \longleftrightarrow (\mathrm{Si}^{+} \cdot Y^{+}) \rightarrow \mathrm{Si}^{+} + Y^{+}. \qquad (2)$$

According to this reaction, the dissociation reaction would occur by hole capture instead of the electron emission shown in reaction (1). The complexes ($Si^{+} \cdot Y^{+}$) are introduced, in order to express metastable natures of the charge density. The reaction path to the complete dissociation of Y may be available, since the charge density is not completely restored to that of the starting materials, as shown in Fig. 1(a).

Metastable behavior of the deep level A agrees well with the changes in charge density, as observed in RBIA and TA. This is well explained by assuming that A are responsible for the charge increase induced by RBIA, i.e., Y = A. In TA after RBA, however, the reduction of A is not accompanied by large reduction in the charge density. This is inconsistent with the assumption. Therefore, it is concluded that the deep level A is not responsible for the change in charge density and that Y is not detected by conventional DLTS. It has been reported that hydrogen plays a decisive role for donor deactivation even in n-GaAs irradiated by nominally non-hydrogen plasma [12]. However, it is less probable in this particular experiment, because the intensity of M3 is quite small and no signal related M4 are detected, which were reported to be hydrogen-related [13]. This is further supported by the fact that the charge recovery occurs only near the surface, as shown in Fig. 1. It was reported that charge reduction occurs toward a deeper region in the bulk in hydrogenated *n*-GaAs during RBA [14]. Further studies are necessary to clarify the nature of Y which governs the charge density decrease and increase.

It is likely that the deep level A involves intrinsic point defects, since the signature and behavior is almost identical to those of C-centers. C-centers have been found in GaAs:Te after it was irradiated by a 3 MeV electron beam, and it is well known that Frenkel pairs are created by such high-energy electron irradiation [14].

We have first found metastability in the charge density change, which lasts at relatively high temperatures. Since this change in charge density should be accompanied by Fermi level modulation, the present findings will be an important mean to realize optical nonlinearity functioning at room temperature.

Conclusion

Metastability of charge density change is discovered in Ar-plasma-irradiated *n*-GaAs:Si. DLTS measurements unveil metastable deep levels named as A and B, whose signatures are different from those of the metastable deep levels M3 and M4. It is clearly shown that none of deep levels detected by DLTS governed the metastability of the charge density changes.

Since the metastability in charge density change occurs even at room temperature, it is potentially applicable for Fermi level modulation at relatively high temperatures.

References

[1] D.D. Nolte, in Photorefractive Effects and Materials (Kluwer Academic Pub. 1995).

[2] R.A. Linke, T. Thio, D.J. Chadi, and G.E. Devlin, Appl. Phys. Lett. 65, 16, 1994.

[3] D.D. Nolte, D.H. Olson, and A.M. Glass, Phys. Rev. B40, 10650, 1989.

[4] W.R. Buchwald, N.M. Johnson, and L.P. Trombetta, Appl. Phys. Lett. 50, 3023 (1987). W.R. Buchwald, G. J. Gerardi, E.H. Poindexter, N.M. Johnson, L.P. Trombetta, H.G. Grimmeiss, and D.J. Keele, Phys. Rev. B40, 1940 (1989).

[5] F.D. Auret, R.M. Erasmus, S.A. Goodman, and W.E. Meyer, Phys. Rev. B51, 17521, 1995. They reported free carrier concentration is changed by 2 x 10^{14} cm^{-3} which is comparable for Eα3 in GaAs:Si (n=1 x 10^{16} cm^{-3}). The Eα3 density may not be high enough to modulate the Fermi Level.

[6] H. Nakanishi and K. Wada, Appl. Surf. Sci. 117/118, 605, 1997. K. Wada and H. Nakanishi, Mater. Research Soc. 442, 69, 1997.

[7] K. Wada, H. Nakanishi, and L.C. Kimerling, Materials Science Forum 196-201 1401, 1995.

[8] T.I. Kol'chenko and V.M. Lomakoi, Semiconductors 28, 501, 1994.

[9] A.S. Tabata, M.A.A. Pudensi, and A.M. Machado, J. Appl. Phys. 65, 4076,1989.

[10] T. Shinagawa and T. Okumura, Mater. Research Soc. 442, 419, 1997.

[11] S.J. Pearton, C.R. Abernathy, and J. Lopata, Appl. Phys. Lett., 59, 3571,1991.

[12] Y. Mochizuki, T. Ishii, M. Mizuta, A. Mochizuki, and J.M. Langer, Phys. Rev. B77, 3601, 1996.

[13] A.W.R. Leitch, Th. Prescha, and J. Weber, Phys. Rev. B45, 14400, 1992.

[14] D. Pon, Physica 116B, 388, 1983.

Materials Science Forum Vols. 258-263 (1997) pp. 1057-1062

METASTABLE AMORPHOUS STRUCTURE IN ION IMPLANTED GaAs

I.D. Desnica-Franković, U.V. Desnica, M. Ivanda, D. Gracin and T. E. Haynes[1]
R. Bošković Institute, Physics Department, Bijenička 54, 10000 Zagreb, Croatia
[1]Solid State Division, Oak Ridge National Laboratory, Oak Ridge, TN 37831, USA

Key Words: GaAs, implantation, amorphous structures, order/disorder, boson peak

Abstract
Disorder was introduced into GaAs by implantation of $^{30}Si^{+}$ ions and studied by Raman scattering, RS. A very wide range of ion doses ($8x10^{12}$ - $3x10^{16}/cm^2$), dose rates, and implant temperatures was used. RS spectra were deconvoluted in a novel way so that the apparent 'background' signal was also included in the analysis. New arguments are given that: a) this 'background' is in fact a low frequency peak and hence a meaningful signal, equivalent to the analogous 'boson peak' (BP) regularly observed in glassy solids, and b) represents a specific amorphous phase, different than a well known continuous-random-network amorphous phase, a-CRN.
A systematic and self-consistent behavior of the BP signal is observed in all studied implantation conditions. The a-BP is the only component of RS spectra whose relative intensity was always proportional to the total disorder, as evaluated by RBS, regardless as to whether higher disorder is produced by higher dose, or higher rate or lower implant temperatures. The amorphous phase in GaAs is thus envisioned as a two-phase composite of strained nanometer-size regions within relaxed continuous random network. The a-BP can be converted in a controlled way into a-CRN (by thermal relaxation) and *vice versa,* a-CRN into a-BP (by additional implantation). This establishes a-BP as a metastable structure of amorphous phase that has higher free energy than the regular a-CRN.

Introduction
Traditionally, tetrahedrally coordinated amorphous semiconductors have been envisioned as a continuous-random-network (a-CRN) of host atoms, which was assumed to be the only amorphous phase[1-5]. However, based on the re-interpretation of the observed 'background' signal in Raman spectra, it has been proposed that in a-Si[6] and a-GaAs[7,8] there exists an additional amorphous structure, which has a specific, possibly medium range order. This peculiar structure, common in glassy materials, causes an excess in the vibrational density of states (in comparison to the expected Debye value), resulting in a broad band, the so-called boson peak (BP) in Raman spectra[7,8].
In this paper, results of Raman and ion channeling studies of the a-CRN and a-BP amorphous structures in Si implanted GaAs are presented. We have used recently developed procedure in analysis of Raman spectra with the inclusion of BP[7,8], which establishes clear correspondence between Raman and RBS detected damage[8] and allows monitoring the kinetics and morphology of disorder.

Experimental techniques
The starting material was Liquid Encapsulated Czochralski (LEC) grown, undoped, semi-insulating, (100) oriented GaAs, with dislocation density in the $10^4/cm^2$ range. $^{30}Si^{+}$ was implanted at an energy of 100 keV into substrates tilted 7^{o} with respect to the incident beam to minimize channeling effects. Precautions were taken to control the implantation temperature, as described previously[9,10,11]. Samples were implanted by varying ion doses (in the range $8x10^{12}/cm^2$ - $3x10^{16}/cm^2$), dose rates (in the range 0.05-1.0 $\mu A/cm^2$), or substrate temperature (-190°C to +40°C range). Annealings were performed on previously completely amorphized samples, starting from RT, in 40°C steps; with 30 min annealing at each step.
First order, dipole-allowed Raman spectra were obtained at room temperature (RT) by excitation with the 2.57 eV (514.5 nm) line from an Ar-ion laser, with low laser power (0.4 W) to avoid

heating. The probing depths for both crystalline and amorphous GaAs are shallower than the thickness of the implanted layer, which is approximately 100 nm, so that the undamaged, underlying substrate does not contribute to the Raman spectra. The scattered light was filtered with a triple spectrometer (DILOR Z-24). Some Raman spectra were taken in the wide 30-1000 cm^{-1} range, but most measurements were done in 190 to 320 cm^{-1} range, since in this range all RS signals characteristic for implanted GaAs can be observed, including two crystalline modes (longitudinal optical LO(Γ) peak at 290 cm^{-1}, and transversal optical TO(Γ) at 268 cm^{-1}), the most prominent amorphous band (centered at 250 cm^{-1}), and also a part of the very broad BP. This or similarly limited frequency range is often used in Raman analysis[1-3,8,12,13]
In ion channeling (RBS), backscattered ions from a 2 MeV He+ beam were detected at a scattering angle of 160°. The probing beam was aligned with the <100> axis of the crystal. Damage profiles were extracted from the RBS spectra by subtracting the dechanneling portion of the yield, and correcting for the dechanneled fraction of the beam as a function of depth[14].

Results

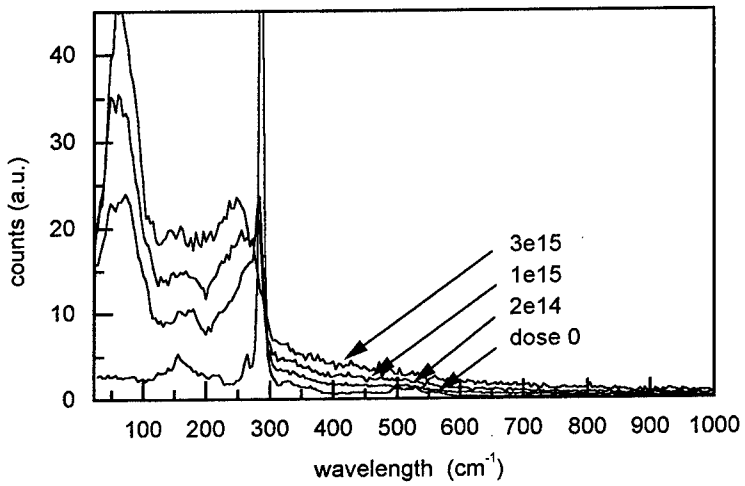

Figure 1. *Raman spectra of 100 keV $^{30}Si^{+}$ -implanted GaAs, obtained using 2.41 eV excitation line. Implantation doses are indicated in the figure, the implant current density was 50 nA/cm^2*

An example of Raman spectra depicting ion dose effects on representative samples are presented in Fig. 1. In the unimplanted sample (1.A), a sharp LO(Γ) line at 290 cm^{-1} is absolutely dominant.
With increasing dose other contributions become important, particularly TO(Γ) peak at 268 cm^{-1}, and 3 amorphous peaks - TA(K,X) at 80 cm^{-1}, IIA(K) at 170 cm^{-1} and TO(X,L) at 250 cm^{-1}, which are generally accepted to originate from the continuous-random-network structure of the amorphous phase (a-CRN) [1]. The BP ('background') signal also continuously increases with the dose. Above doses around $3x10^{15}/cm^2$ (CA-dose) both crystal-related peaks disappear, indicating complete amorphization of the layer. An example of temperature-reduced spectra, with deconvolution to both crystalline components LO and TO, and both amorphous components (all three CRN peaks, and broad BP peak with maximum close to 200 cm^{-1}) is given in the Figure 2.
The change of the morphology of the amorphous component in implanted GaAs is presented in Fig. 3. by the ratio of I_b/I_a (where I_a denotes the integral of the most important a-CRN peak at 250 cm^{-1}, and I_b denotes the integral of the BP component). Numerical values refer to the frequency range 190-320 cm^{-1}. Fig. 3a shows the change of this ratio with ion dose. I_b/I_a ratio remains practically constant for lower doses, and increases continuously for higher doses, indicating a significant change in the morphology of the amorphous phase. This morphology change begins even

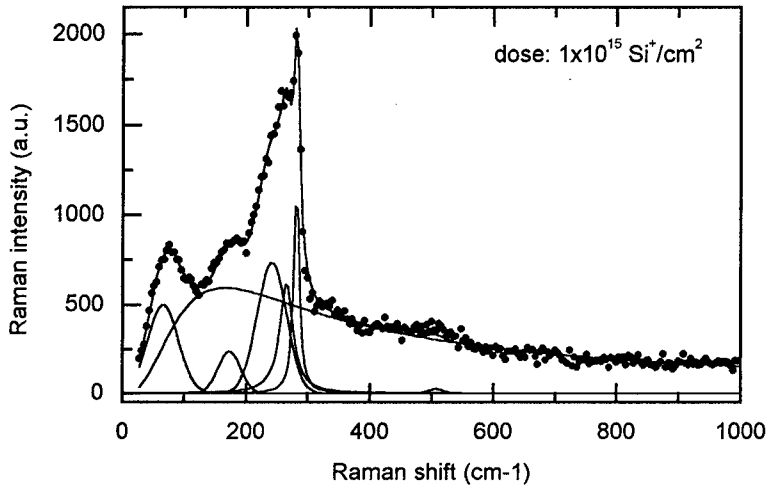

Figure 2. *Reduced Raman spectra, deconvoluted in the crystalline and amorphous contributions. The fitting procedure and decomposition is explained in the text.*

before than the RBS (lower part of Fig. 3a) detects complete amorphization, and moreover continues thereafter.

The same ratios are presented in Fig. 3b for a series of samples that were all implanted with the same dose but with different ion dose rates. Again, the I_b/I_a ratio increases with rate. The increase of the RBS signal clearly shows that total disorder increases drastically with ion dose rate. In addition, a similar rate-effect experiment was done by implanting $^{12}C^+$ into GaAs, since (for a given total damage) rate effects should be more pronounced for lighter ions. The results of $^{12}C^+$ have also been included in Fig.3b.

The effect of substrate temperature on the disorder is presented in Fig. 3c for three series of samples implanted with 3 different ion doses but at different temperature of implantation. The temperature range where the strongest increase of I_b/I_a ratios occurs, corresponds to the range of the most dramatic increase of RBS detected damage with the decrease of implant temperature. The effect increases for higher doses.

Fig. 4 shows effects of annealing on I_b/I_a ratio in a sample which was first implanted with a dose of $1x10^{16}/cm^2$ and then isochronally annealed (30 min, 40°C step). The dose was more than enough to completely amorphize the implanted layer (no crystalline-phase-related LO or TO peaks in Raman spectra, and 100% of disorder in RBS spectra, Fig 3a). The I_b/I_a ratio decreases with annealing. At 160°C and higher, gradual recrystallization begins, with reappearance of both LO(Γ) and TO(Γ) crystalline peaks.

Discussion

In all of above experiments (except for very low doses) there is a clear linkage between the increase of total disorder and the increase of I_b/I_a ratio, indicating a change in morphology of the amorphous phase. In dose effects, the most interesting finding is the continuation of the strong increase of I_b/I_a ratio for additional implantation into the layer which was already completely amorphized (doses above $3x10^{15}/cm^2$). This means that extended implantation continues to change the morphology of the amorphous phase, and that a-CRN fraction gradually converts into the a-BP fraction. Very high I_b/I_a ratio at the highest applied dose suggests that the composite mixture of BP and CRN amorphous phases is progressively being replaced with a network of strained regions connected through the remnants of a-CRN. Such a picture agrees with analogous interpretations of

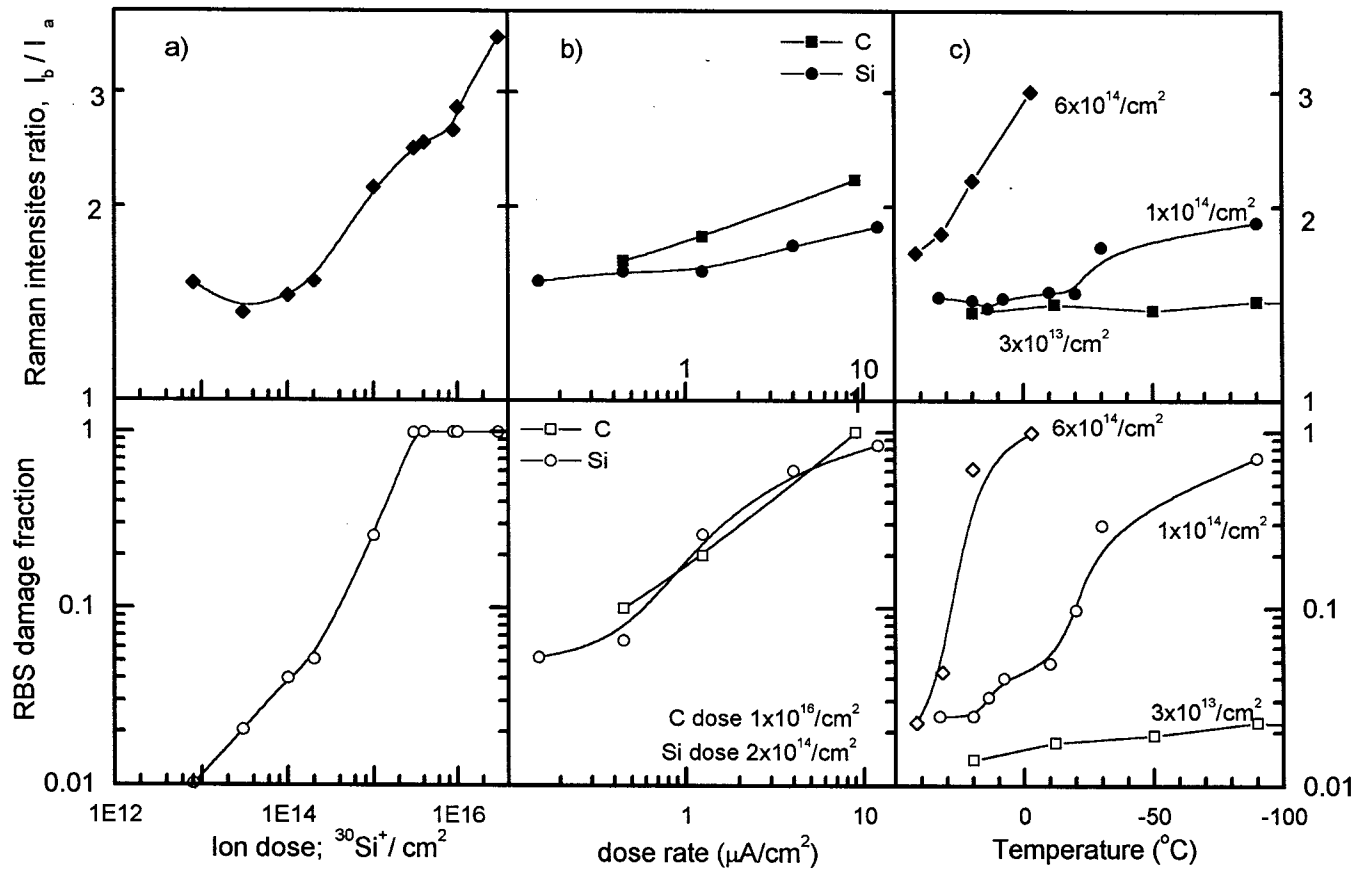

Figure 3a. *Ion dose dependence of I_b/I_a Raman intensity ratio of boson amorphous to random amorphous components (upper part of Fig.3a) and the fraction of displaced atoms in implanted layer, as determined with RBS (lower part). 3b. Dose rate dependence of I_b/I_a (upper part) and RBS determined total damage fraction (lower part). Twotypes of implanted ions were used, Si^+ and C^+; the doses were chosen such as to produce approximately equal amounts of damage. 3c. I_b/I_a, ratio (upper part) and RBS damage fraction (lower part) as a function of implant temperature, for 3 different doses indicated in the figure.*

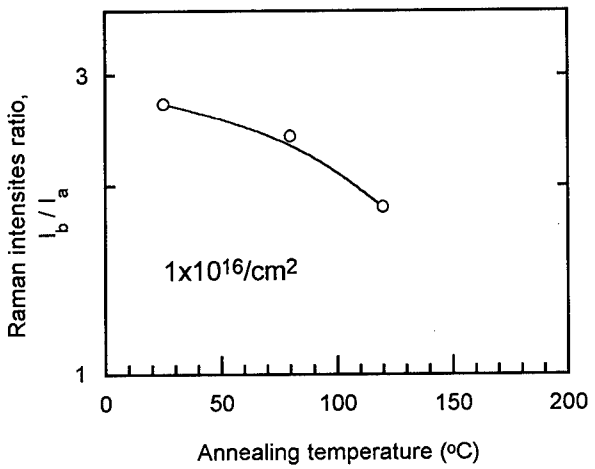

Figure 4. *The decrease of I_b/I_a Raman intensity ratio (boson amorphous to random amorphous components) due to thermal relaxation. The annealing time was 30 min in 40°C steps.*

experimental results in glassy materials and suggests an important link with this very different class of materials.

Rate effects cause an increase of the total damage, which is again accompanied by an increase (although more modest) of I_b/I_a ratio. Both the I_b/I_a and its increase with rate were stronger when C ions were implanted instead of Si. Since C ion has a smaller atomic mass than Si ion, a larger C dose was needed to produce comparable total damage (lower part of Fig. 3b). A larger I_b/I_a ratio was obtained with C^+ than with Si^+ implants for any rate as well as larger increase of ratio with ion rate. Since a larger dose means more overlaps between different cascades, larger effects for C ions again indicate that BP component is created more easily from the material that is already disordered.

A change of implant temperature drastically alters morphology of the amorphous phase, and even more so if the dose is higher. The observed strong increase of I_b/I_a for the same doses, but lower implant temperatures, indicates more efficient production, growth, and accumulation of the BP structure for conditions where implanted ions enter into crystal that is already disordered. This seems to be an universal and important property of the a-BP. The same effect is observed in dose effects (Fig. 3a) and rate effects (Fig. 3b) as well. Hence, independently of the type of disorder and how it is produced, the a-BP structure is formed preferentially over a-CRN component from pre-disordered GaAs, rather than directly from the perfect crystal. This finding also explains why at very low doses, where there are no overlaps of different cascades, I_b/I_a ratios becomes independent of dose and implant temperature and have relatively lowest values.

The strong inverse dependence of the I_b/I_a ratio on implant temperature indicates that the BP component is thermally less stable than a-CRN component of the disorder. This means that the free energy of the CRN structure is lower than the free energy of the BP structure. The reduction of I_b fraction with annealing in favor of I_a fraction (Fig. 4) in the layer which is still completely amorphous, indicates the return of a-BP type of the disorder back to a-CRN.

Conclusion

GaAs crystals were implanted in a wide range of ion doses, ion-dose rates and implant temperatures and analyzed with Raman scattering (RS) and Ion channeling (RBS). It has been shown that the amorphous phase consists of two components: continuos random network component a-CRN, and

non-random amorphous component, a-BP. The a-BP strongly depends on the total disorder in the implanted layer independently in which way the disorder is obtained. The fraction of a-BP (relative to a-CRN) can be increased either by increasing ion dose, increasing dose rates or decreasing implant temperature. On the other hand, the a-BP fraction can be decreased also in a controlled, reversible way by thermal annealing (relaxation). This establishes a-BP as a metastable structure of amorphous phase that has higher free energy than the regular a-CRN.

Acknowledgments

This research was supported by the Ministry of Science and Technology of Croatia. A portion of this research was performed at Oak Ridge National Laboratory, sponsored by U.S. Department of Energy, Division of Materials Science, under contract DE-ACO5-960R22464 with Lockheed Martin Energy Research Corp.

References

1. R. Zallen; J. Non-Cryst. Solids **141**, 227 (1992) and R. Zallen, *The Physics of Amorphous solids*, (Wiley, New York, 1983).
2. M. Holtz, R. Zallen, O. Brafman, S. Matteson; Phys. Rev. **B37**, 4609 (1988).
3. R. Ares, Y.B. Trudeau, J.L. Brebner, G.E. Kajrys, M. Jouanne; Nuc. Instr. and Methods **B90**, 419 (1994).
4. K.K. Tiong, P.M. Amirtharaj, F.H. Pollak, D.E.Aspnes; Appl. Phys. Lett. **44**, 122 (1984).
5. T. Nakamura and T. Katoda, J. Appl. Phys. **53**, 5870 (1982)
6. M. Ivanda; Phys. Rev. **B 46**, 14893 (1992)
7. M. Ivanda, I. Hartman and W. Kiefer, Phys. Rev. B, **51**, 1567 (1995)
8. U.V. Desnica, I.D. Desnica-Franković, M. Ivanda, K. Furić, T.E. Haynes, Pys. Rev. B, June 15 issue (1997)
9. U.V. Desnica, J. Wagner, T.E. Haynes, O.W. Holland; J. Appl. Phys. **71**, 2591 (1992).
10. T. E. Haynes, R. Morton, and S. S. Lau, p. 311 in III-V *Electronic and Photonic Device Fabrication and Performance*, edited by K. S. Jones, H. Kanber, and S. J. Pearton, Materials Research Society, Pittsburgh, PA (1993).
11. T. E. Haynes, R. Morton, S.S. Lau; Appl. Phys. Lett. **64**, 991 (1944)
12. G. Burns, F.H. Dacol, C.R. Wie, E. Burnstein, M. Cardona; Solid State Comm. **62**, 449 (1987)
13. G. Braunstein, D. Tuschel, S. Chen, S-T. Lee; J. Appl. Phys. **66**, 3515 (1989).
14. F.H. Eisen, pp. 417-9 in *Channeling*, ed. D.V. Morgan (Willey, New York, 1973).

Materials Science Forum Vols. 258-263 (1997) pp. 1063-1068

THEORY OF NITROGEN-HYDROGEN COMPLEXES IN GaP

V. J. B. Torres*, S. Oberg** and R. Jones***

* Departamento de Física, Universidade de Aveiro, 3810 Aveiro, Portugal.
** Department of Mathematics, University of Lulea, Lulea, S95187, Sweden.
*** Department of Physics, University of Exeter, Exeter, EX4 4QL, UK

Keywords: N-H, defects, passivation, GaP, semiconductors, LED

Abstract. Nitrogen in GaP is an isoelectronic acceptor. Due to its much higher electronegativity than phosphorus, nitrogen forms bound excitons. This had made possible the fabrication of LEDs from an indirect band gap material. A spectrocopic study of N-H complexes in GaP grown by LEC technology shows that two hydrogens and one nitrogen are involved, existing in three different states; two of them corresponding to different charged states. One of this centres does not show gallium isotope shift, resulting that both hydrogens are bonded to the nitrogen, the nitrogen being five fold coordinated. We investigated this new NH_2 configuration using *ab-initio* calculations on a $HNHGa_{22}P_{21}H_{42}$ cluster. As this centre has C_{3v} symmetry, nitrogen is positioned in a phosphorus site, one hydrogen is antibonding on nitrogen and the other at bond centre, both along a <111> direction. We found the hydrogen at bond centre prefers to bond to nitrogen for the double positive charged state, with the nitrogen five folded coordinated. This configuration is metastable for the singly positive charged state. The last two states have very similar configurations, being the plane formed by the three Ga atoms and nitrogen perpendicular to the H-N-H direction, very similar to the NH_5^{+2} molecule. A vibrational analysis of the $NHNGa_3^{+2}$ cluster is in a good agreement with experiment.

Introduction.

Hydrogen is unintentionally incorporated in semiconductors, during its growth. Hydrogen interacts with the perfect lattice atoms and vacancies, changing the electronic and/or optical properties of semicondutors. Hydrogen passivates acceptor and donor electronic levels in silicon, III-V, including nitrates, and II-VI materials, appearing in a bond centre or an antibonding position. Two hydrogens may form different complexes, like H_2 molecule or the H_2* defect, where one hydrogen atom is in an bond centre position and bonded to an lattice atom, while the other hydrogen is an anti bonding position and bonded to a nearest neighbour lattice atom of the first hydrogen, in a C_{3v} symmetry configuration. Hydrogen might also combine in larger numbers forming voids, as observed in silicon.

TABLE 1. Experimental Local Vibrational Modes (LVM) [4] of the NH2 defect in GaP, showing ^{14}N-^{15}N isotope shift but no ^{69}Ga-^{71}Ga isotope shift.LVMs in cm^{-1}.

^{14}N	^{15}N	Nitrogen isotope shift	Type
2885.5	2879.7	5.8	Stretch mode
2054.1	2052.4	1.7	Stretch mode
1049.8	not resolved		Transverse mode

Nitrogen is an isoelectronic acceptor in GaP. Due to its much higher electronegativity than phosphorus, nitrogen forms bound excitons. After plasma hydrogenation a reduction of the nitrogen excitonic luminescence occurs [1-2], showing that hydrogen and nitrogen interact in GaP. A spectrocopic study of the nitrogen excitonic photoluminescence of GaP growth by LEC technology has shown three different centres, involving two hydrogens and one nitrogen atom, two of them in a different charge state [3]. For one of these centres, absorption Infra Red measurements show that the Local Vibrational Modes (LVM) [4], table 1, shift with ^{14}N-^{15}N isotope, but not with gallium isotopes. The insensitivity of the IR lines to Ga isotopes shows that no hydrogens are bonded, or weakly bounded, to gallium atoms. In contrary, the nitrogen isotope reveals that the two hydrogens are bonded to nitrogen atom. As uniaxial stress experiemts on the LVMs determine C_{3v} symmetry, the two hydrogens are tentatively positioned along <111> direction, and bonded to nitrogen. One hydrogen is an antibonding position, H(ab), being the other at the bond centre, H(bc). We call this model by HNH model. A spring HNH model fits well the IR modes and the nitrogen isotope shifts of table 1 [4]. In this model one N-Ga bond was broken and two new N-H bonds were formed, the nitrogen being five-fold coordinated. To our knowledgement a five fold coordinated nitrogen had not been found in molecules and in defects in semiconductors.
The aim of this paper is to study by first principles the NH_2 defect in GaP by inspecting the five fold coordination of nitrogen. We have also looked at the NH_5 molecule.

Theory.
We have performed calculations using the Density Functional Theory, with norm-conserving pseudo potentials in a large hydrogen terminated cluster [5]. The wave function and the charge density were expanded in *s* and *p* type gaussians atomic orbitals. Gaussians in the bond centres were also considered for all bulk bonds.
The forces on the atoms were calculated by the Hellman-Feynman theorem. A gradient conjugated algorithm were used to relax all the atoms, in order to find the configuration with the lowest total energy.
Second derivatives of the total energy in respect to the atomic positions were calculated numerically. When inserted into the dynamical matrix the vibrational modes can be obtained. A Musgrove-Pople potential for GaP were used to calculate the second derivatives for bulk atoms.

TABLE 2: Bond Lengths in Angstrom. In brackets ab means antibonding on nitrogen and bc bond centre at N-Ga bond. lel is the absolute electric charge of the electron.

Electric	**HNH** CONFIGURATION			H_2* CONFIGURATION	
charge (lel)	H(ab)-N	N-H(bc)	H(bc)-Ga	H(ab)-N	H(bc)-Ga
+2	1.03	1.05	2.48	1.03	1.51
+1	1.07	1.11	2.31	1.03	1.48
0	none			1.00	1.50
-1	none			0.99	1.49
-2	none			none	

Results.

NH_2 Defect: As there is no experimental information about the charged stateof the NH_2 complexes and we want to test the five fold coordination of nitrogen, we have investigated where the hydrogen, placed initially between the nitrogen and the gallium atom, prefers to bond, with nitrogen or to gallium, being the other hydrogen at antibonding at nitrogen. The calculations were performed for five charged $HNHGa_{22}P_{21}H_{42}q$ clusters (q = 2,1,0,-1,-2). For the double positive charged we found that the HNH configuration is 0.8 eV lower total energy that the H_2*. In the HNH configuration the N-H bond lengths are 1.03 and 1.07 Å, for the antibonding and bond centre respectivity, table 2. The three Ga-N-Ga angles, where Ga are first neighbour of nitrogen, are 118.7°, being the angles formed by H(bc)-N-Ga 96.7°. This means that the N and its first Ga neighbours are very close to a plane perpendicular to the H-N-H direction. For the positive charged we obtained the HNH configuration to be 1.2 eV higher than the H_2*. The HNH configuration is very similar to the double positive charged.

For the neutral and the single negative charged we determined only the H_2* configuration. For the double negative charged none of the HNH and H_2* configurations where found. Instead the hydrogen at bond centre is at 1.42 and 1.72 Å from the nitrogen and gallium, respectively.

NH_5 Molecule: To visualize the NH_5 molecule we consider a NH_3 molecule with two more hydrogen atoms, H_a and H_b, at each side of nitrogen along the C_3 axis. We looked at NH_5 in neutral, positive and double positive charge. We found that the NH_5^{+2} is the only stable molecule among the investigated ones. This molecule has D_{3d} symmetry, the three H from ammonia lying with N on σ plane perpendicular to the H_a-N-H_b direction. The H-N-H angles for the hydrogen atoms on σ plane are 120°. The N-H bond lengths are 1.08 and 1.11 Å, for the H on plane σ and for H along C_3 axis, respectively, being longer than for the ammonia molecule. This configuration is very similar to those obtained for the double and singly positive charged NH_2 defect. We have tested this method to the existing NH_4^+ molecule. We obtained a perfect tetrahedral structure in agreement with experiment [6]. We have calculated the vibrational modes (VM), as it may be seen in

TABLE 3. Vibrational modes for NH_5^{+2} molecule and $HNHGa_3^{+2}$ cluster, in cm^{-1}.

NH_5^{+2}	$H^{14}NHGa_3^{+2}$	$H^{15}NHGa_3^{+2}$	N isotope shift	Type
2826				stretch
2717				wag
2426	2429	2429	0	symmetric stretch
2324	2422	2413	9	asymmetric stretch
1906	1065	1031	34	wag
1024				stretch

table 3. The highest VM are smaller than those of ammonia, which are 3846 and 3706 cm-1, for stretch and wag modes, respectively. When the hydrogen mass for those on σ plane is replaced by the gallium mass, we obtain the VMs listed in column 2 of table 3. The symmetric stretch mode is infra red inactive and does not shift with ^{14}N-^{15}N isotope. When we increase the strength of one H-N bond, the molecule symmetry decreases to C_{3v}, the symmetric VM decreases and the assymmetric increases, leaving the wag mode unchanged. Now the symmetric mode is IR active and shows a small ^{14}N-^{15}N isotope shift. The asymmetric mode is IR active and shows a larger nitrogen isotope shift. In the crystal the proximity of one gallium atom in <111> direction will push the hydrogen at bond centre to nitrogen, increasing it bond strength. This effect tends to move the $HNHGa_3^{+2}$ VMs to the LVM data of NH2 defect in GaP.

Conclusion.

Using a first principles method we have shown that the NH_2 defect in GaP may exist in HNH and H_2* configurations, depending on charge state, and shows metastability for the double and singly positive charge complexes. We also show that the hydrogen at bond centre prefers to bond to nitrogen instead of gallium, becoming nitrogen five-folded coordinated for the double positive charged, supporting the HNH model. This configuration was also found to be metastable for the single positive charged.

We also obtained a structure for a five fold nitrogen molecule. The only stable NH_5 molecule was the double positive charged, in a configuration very similar to the NH_2 defect. When the masses of the three hydrogens on the plane are replaced by gallium mass, like for the NH_2 defect, we obtained VM in the range of the experimental LVM of the defect. If we consider a gallium atom nearby one hydrogen, in a way to simulate better the NH_2 defect, the gallium pushes the hydrogen to nitrogen, strengthening their bonding. This effect tends to move the stretch modes and the nitrogen isotope shifts of the $NHNGa_3^{+2}$ cluster close to the experimental NH_2 defect. The wag mode is in agreement with the experimental one.

We have produced a qualitative agreement with LVM data. To identify this NH_2 defect experiments on deuterium doped samples are needed and LVMs of the defect have to be calculated.

Acknowledgements.
V. J. B. Torres thanks PRAXIS XXI for its financial support, contract PBIC/C/CTM/1925/95.

References:

[1] J. Weber and M. Singh, Mater. Res. Soc. Symp. Proc. **104**, 325 (1988).
[2] M. Singh and J. Weber, Appl. Phys. Lett. **54**, 424 (1989).
[3] W.-S. Hahn, B. Clerjaud, D. Cote, F. Gendron, C. Porte, W. Ulrici, D. Wasik, and W. Wilkening, Materials Science Forum **143-147**, 277 (1994).
[4] B. Clerjaud, F. Gendron, W.-S. Hahn, W. Ulrici, and D. Wasik, Physical Review Letters **77**, 4930 (1996).
[5] R. Jones, Phil. Trans. Roy. Soc. London Ser. A 341, **351** (1992).
[6] R. McWeeny, Coulson's Valence, Oxford, 3rd edition (1979).

Materials Science Forum Vols. 258-263 (1997) pp. 1069-1074

PHOTOLUMINESCENCE, OPTICAL ABSORPTION, AND EPR STUDIES OF THE Co^{2+}-S_P PAIR DEFECT IN GaP

R. Göser[1], J. Kreissl[2], K. Thonke[1], and W. Ulrici[3]

[1]Abt. Halbleiterphysik, Universität Ulm, D-89069 Ulm, Germany
[2]Institut für Festkörperphysik, Technische Universität Berlin, D-10623 Berlin, Germany
[3]Paul-Drude-Institut für Festkörperelektronik, D-10117 Berlin, Germany

Keywords: GaP:Co^{2+}:S, pair defect, PL, EPR

Abstract

In the photoluminescence spectrum of GaP:Co containing sulphur impurities two zero-phonon lines at 3977.9 cm^{-1} and 3968.0 cm^{-1} have been detected. Both lines split linearly under uniaxial stress **X** || <111> and || <110>, but do not split for **X** || <100>. The intensity ratios and the polarisation properties of the lines under stress reveal that they arise from a centre of trigonal symmetry. In the EPR spectrum of these samples resonances are measured with an angular dependence indicating a Co^{2+} centre of trigonal symmetry. Both the photoluminescence and the EPR spectra are consistently interpreted as being due to a Co_{Ga}^{2+}-S_P nearest neighbour pair defect.

Introduction

The formation of pairs consisting of a substitutional transition metal (TM_{Ga}) acceptor and a shallow donor has been investigated in the host material GaP for several TM_{Ga} like Ti, V, Cr, Mn, Fe, and Ni, and in the GaAs host lattice for the TM ions Mn, Co, and Ni (see [1 - 3] and references therein). Most of the investigated pair centres were found with the sulphur (S_P) shallow donor, and the symmetry of the TM_{Ga}-S_P pair centres was found to be trigonal from electron paramagnetic resonance (EPR) measurements or by uniaxial stress experiments on photoluminescence (PL) lines.

Isolated substitutional Co_{Ga}^{2+} in GaP is well investigated by optical absorption and PL including Zeeman- and uniaxial stress experiments [4,5] as well as by EPR [6]. The $^4A_2 \leftrightarrow {}^4T_2$ transition of Co_{Ga}^{2+} giving rise to an intense zero-phonon-line (ZPL) at 4509.2 cm^{-1} observed by optical absorption and PL can serve as an indicator for the complexing of Co_{Ga}. The EPR spectrum of Co_{Ga}^{2+} consists of one weakly anisotropic resonance line at $g = 2.164$ [6] and in the case of pair formation a strongly angular dependent spectrum should be observed. Co_{Ga} as a constituent of an acceptor-donor pair is of particular interest because the neutral state Co_{Ga}^{3+} has in GaP a low-spin ground state and is the only TM_{Ga} in III-V materials for which this behaviour has been shown unambiguously [7]. This paper presents evidence that in GaP:Co pairs of Co_{Ga}^{2+}-S_P exist and are formed with sulphur as a residual impurity. We find fingerprints of this pair centre of trigonal symmetry in the PL, optical absorption, and EPR spectra.

Experimental

The samples investigated here were taken from the tail end of a GaP boule grown by the liquid encapsulation Czochralski (LEC) technique and doped with metallic Co in the melt. They are of high-resistivity p-type with the Fermi level pinned by the Co^{2+}/Co^{3+} acceptor level. The content of Co is estimated to be about 10^{17} cm^{-3}. Sulphur is the dominant residual impurity in GaP grown by this technique and is introduced with the used phosphorous during the synthesis of GaP. The content of

sulphur in the samples amounts to about 1-3 x 10^{16} cm^{-3}. The oriented samples used for PL with uniaxial stress have the dimensions 1×1×10 mm^3 and 7×6×3 mm^3 where on the latter ones also the optical absorption was measured. The oriented samples for the EPR experiments have the dimensions 12×3×3 mm^3.

Optical absorption was measured with a Fourier transform spectrometer Bruker IFS 120 HR. For PL measurements the samples were cooled in a gas flow cryostat and excited by the 514 nm line of an Ar^+ ion laser (typ. 50 mW on a spot of 1 mm^2). The emission light was recorded with a Fourier transform spectrometer (Bomem DA8 or Bruker IFS66v) using an InAs or InSb detector. The EPR spectra were measured at T = 4 K with a Bruker ESP 300 E spectrometer and the microwave frequency of 9.47 GHz.

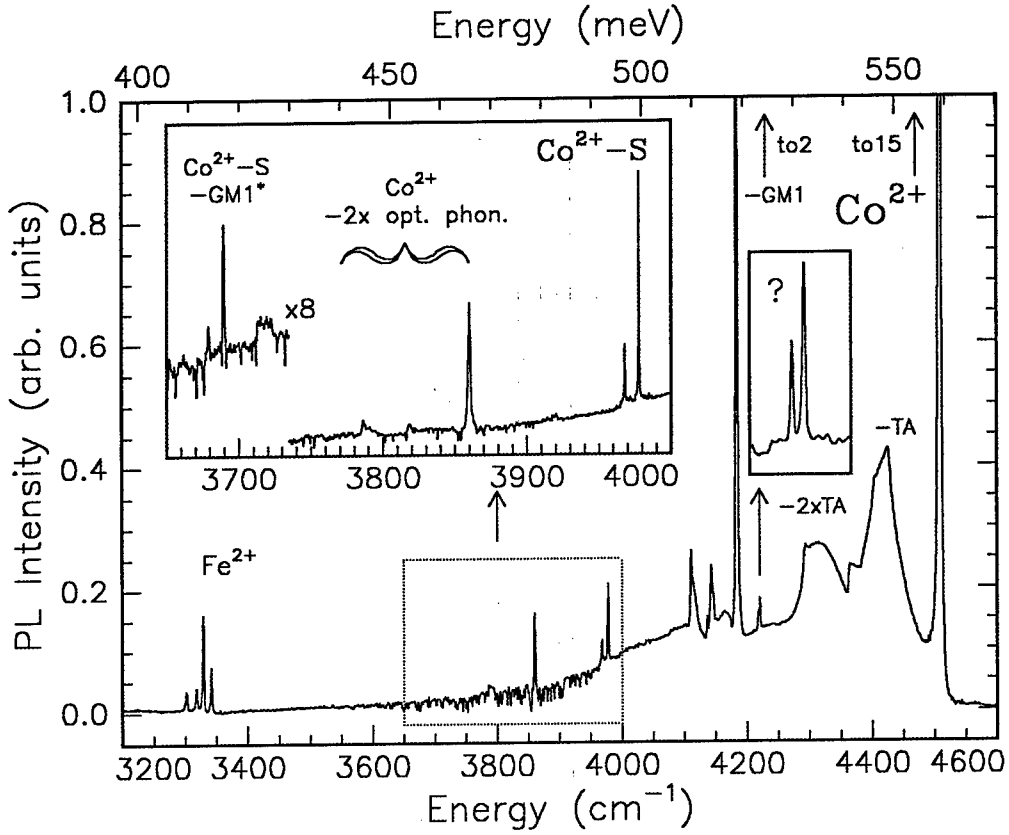

Fig. 1: PL spectrum of GaP:Co:S recorded at 5 K with a resolution of 0.5 cm^{-1} (inset: 0.3 cm^{-1}). Besides the dominant Co^{2+}_{Ga} lines new Co related defect ZPLs show up at ~ 3980 cm^{-1} (assigned to Co-S) and at ~ 4220 cm^{-1} (origin yet unknown).

Optical experiments

The PL spectra of the GaP:Co:S co-doped samples are dominated by the strong ZPL emission at 4509.2 cm^{-1} and its associated phonon replica band [5]. Much weaker, we observe in PL another close doublet group of ZPLs at 3977.9 cm^{-1} and 3968.0 cm^{-1}, the high energy line being more intense by a factor of 3.8, independent of temperature (see Fig. 1, inset). The dominant gap mode phonon replica $GM1^*$ for this new ZPL set is located in the PL spectra at 3679.5 cm^{-1} and 3689.4 cm^{-1}, i.e. shifted by 288.5 cm^{-1}. This phonon replica energy is ≈ 36 cm^{-1} lower than the 324.6 cm^{-1} observed for the isolated Co^{2+}. In absorption experiments, the stronger one of the new absorption lines is observed at T = 7 K with α_{peak} = 0.05 cm^{-1} and half width Γ= 0.15 cm^{-1}. When assuming

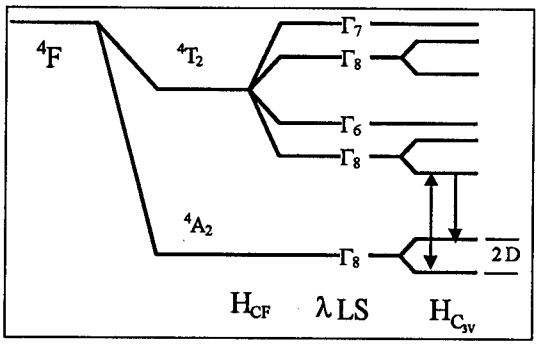

Fig. 2: Energy level scheme derived for the Co^{2+} ion in trigonally distorted environment. The arrows indicate the two transitions observed in PL and absorption.

equal oscillator strength for this new Co related defect ZPLs and for the isolated Co^{2+}, we estimate from the ratio of the absorption lines, that ≈ 2% of the Co is bound in the new complexes. Since the new defect lines are observed only in GaP crystals containing both Co and S, and since these lines are located close to the transition of the isolated Co^{2+}, we ascribe the new transitions tentatively to a Co_{Ga}-S_P complex, in accordance with the finding of our stress measurements. Based on these data and assumptions, the level scheme shown in Fig. 2 is derived.

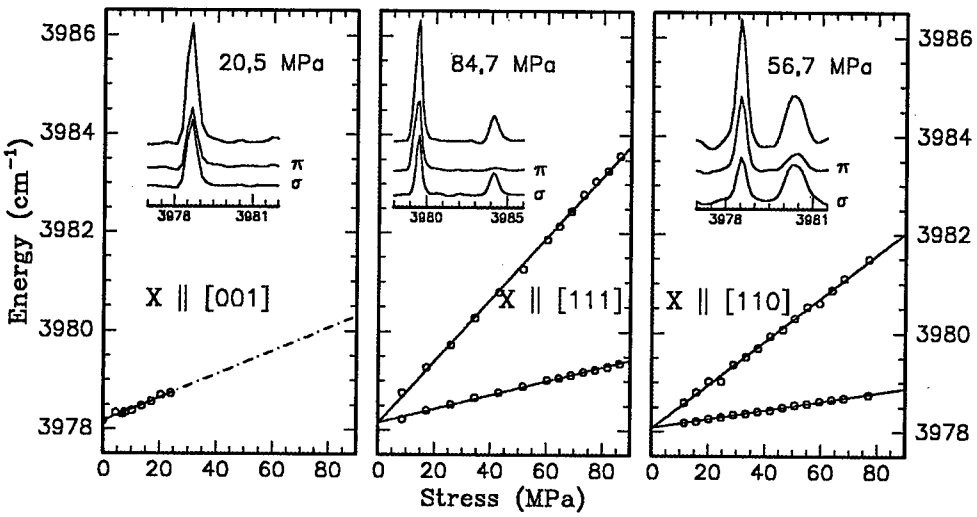

Fig. 3: Splitting of the new Co_{Ga}-S_P defect line under uniaxial stress. The PL spectra shown in the insets were recorded polarized und unpolarized at T = 5 K with a resolution of 0.25 cm^{-1} – 0.4 cm^{-1}. Lines are guides to the eye.

Uniaxial stress experiments on the new ZPL lines reveal clearly trigonal symmetry of this defect (see Fig. 3). This is readily seen for stress **X** || [111], where both ZPLs split with an intensity ratio of 4:1, the weaker line being totally polarized **E** ⊥ **X**. This is what theory predicts for a so-called σ-Oscillator with trigonal Symmetry in T_d crystals [8]. The results for stress **X** parallel to the other two major crystal directions also closely obey the predictions for this simple case: No splitting for **X** || [001] (unpolarized line), and twofold splitting for **X** || [110] with mixed polarizations depending on the observation direction. The complete splitting pattern can be described by two parameters only[8]: A_1 for the hydrostatic shift, and A_2 for the uniaxial response. Uniaxial stress measurements are often hampered by poor controllability of the absolute stress. In our case, we find slightly different sets of parameters for the three major directions, the differences of which we believe to be due to experimental deficiencies. For **X** || [111], we find A_1 = 29.5 cm^{-1}/GPa and A_2 = 20 cm^{-1}/GPa; for **X** || [100] A_1 = 23.6 cm^{-1}/GPa; for **X** || [110] A_1 = 26.5 cm^{-1}/GPa and A_2 = 17.5 cm^{-1}/GPa. An alternative cause of deviations from the simple Kaplyanskii equations could be sought in the interaction of the upper PL level with adjacent states of the $^4T_2$ multiplicity. Since the polarizations and intensities are still ideal for both ZPLs, we consider the stress responses as reliable proof of trigonal

symmetry of the defect, thus supporting the microscopic model of a nearest neighbour Co_{Ga}-S_P (C_{3v}) pair defect. The hydrostatic response of the new defect lines comes close to that of the isolated Co^{2+}, which we find to be 24 cm^{-1}/GPa. Indeed, an estimate of the pressure induced change in 10Dq based on elasticity theory [9] predicts a 0.6 % change in energy per GPa, i.e. ≈ 30 cm^{-1}/GPa.
In some of our samples, we find amongst the Co^{2+} phonon replica lines another close doublet set of ZPLs at 4218 cm^{-1} and 4220.8 cm^{-1} plus their gap mode phonon replicas shifted by 300 cm^{-1}. Again, the intensity ratio 1:2 of these lines is temperature independent. Possibly, these lines are linked to a Co^{2+} defect complex with another constituent instead of sulphur, or a complex with lower symmetry. Unfortunately, these lines are too weak to perform uniaxial stress measurements.

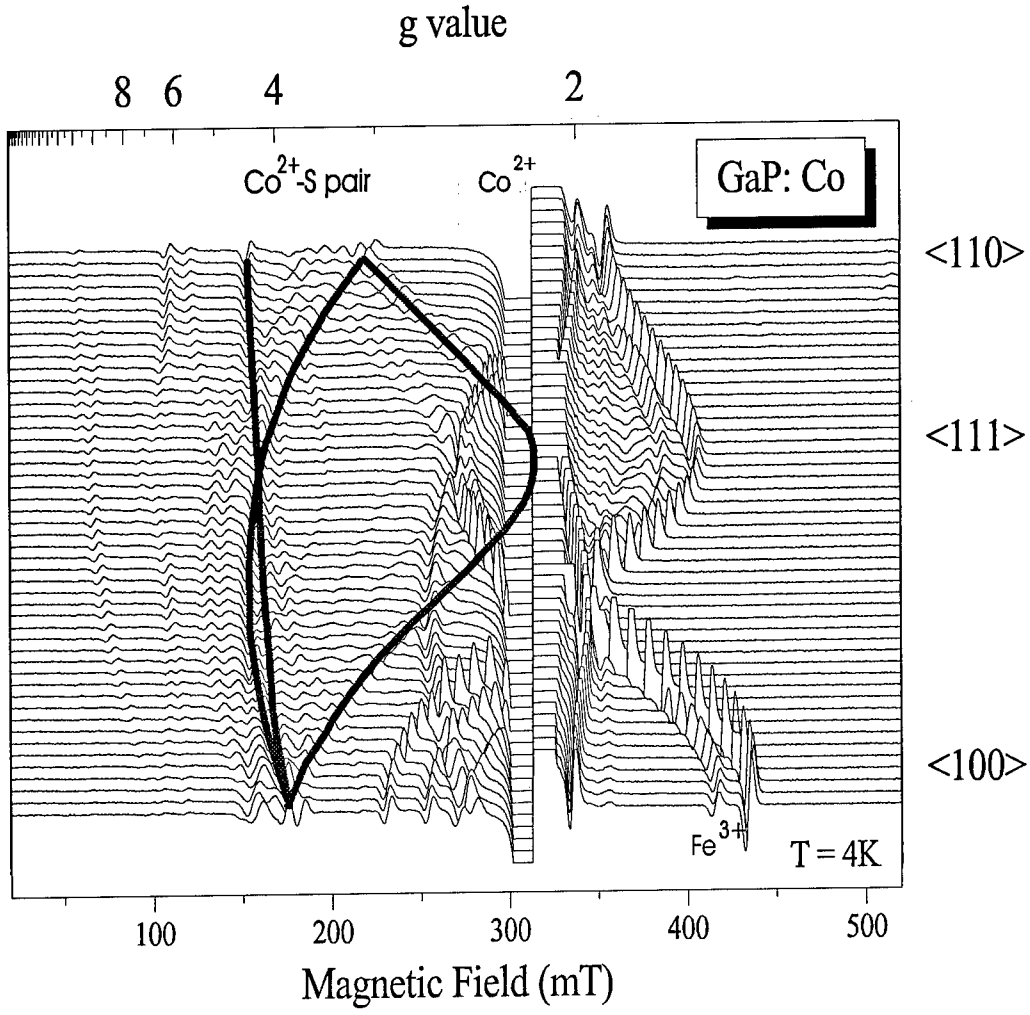

Fig. 4: Stack plot of the EPR spectra measured on GaP:Co. The magnetic field is rotated in a {110} crystal plane. The transitions between the |±1/2> levels belonging to the trigonal Co_{Ga}^{2+}-S_P pair have been linked by a solid line demonstrating their angular dependence.

Electron Paramagnetic Resonance

The EPR spectra measured on the GaP:Co samples show a superposition of resonance lines due to various centres (see Fig. 4). The spectra are dominated by the slightly anisotropic line at g = 2.164 due to isolated Co^{2+} on Ga site. Furthermore, the well-known Fe_{Ga}^{3+} spectrum is measured resulting from iron as residual impurity. The remaining angular dependent lines seem to arise from Co-related centres. Here we will give an analysis of that part of these lines assigned to a trigonal Co centre while the other ones (due to a Co centre of orthorhombic symmetry) are still under investigation. As in the case of the isolated Co_{Ga}^{2+} centre, the expected eight-line hyperfine structure due to ^{59}Co (I = 7/2) could not be resolved because of the large EPR line width in III-V materials. The angular dependence exhibits the typical pattern of a trigonal centre with an effective spin S'= ½ and is marked in Fig. 4 by solid lines. The assignment of this spectrum to a Co_{Ga}^{2+} related defect is based on the following observations: it occurs exclusively in Co-doped GaP samples and its g-values are characteristic for a centre with d^7 configuration as will be shown below.

The ground state of Co^{2+} on a site with tetrahedral symmetry is $^4A_2(F)$ and this spin quartet splits in trigonal symmetry into the two Kramers doublets $|\pm 1/2\rangle$ and $|\pm 3/2\rangle$ separated by 2D see Fig. 2). The energy levels of such a system can be described by the spin Hamiltonian with S = 3/2

$$\mathcal{H} = g_{\parallel}\mu_B B_z S_z + g_{\perp}\mu_B(B_x S_x + B_y S_y) + D[S_z^2 - 1/3\ S(S+1)]\ . \qquad (1)$$

All symbols have their usual meanings. The z axis of the coordinate system (x,y,z) coincides with the trigonal C_3 symmetry axis parallel to <111>. According to the four C_3 directions there are four different centre positions, two of which are always magnetically equivalent under rotation around a <110> axis as it was done in our experiments and shown in Fig. 4.

If the trigonal zero-field splitting of the $^4A_2$ ground state is large compared to the microwave energy (D>> hν, i.e. our investigated system), the detectable EPR transitions occur only within the $|\pm 1/2\rangle$ doublet and can be described by an effective S'= ½ formalism. The angular dependence has been fitted by the effective g-values given in Table 1 (see Fig. 4). Calculating the Zeeman correction to the fine structure energies by perturbation theory using the spin Hamiltonian (1) for the total $^4A_2$ ground state, one obtains the principal values of the g'-tensor related to the parameters of the S = 3/2 manifold ($^4A_2$ ground state) by [10] $g_{\perp}' = (S+1/2)g_{\perp}$ and $g_{\parallel}' = g_{\parallel}$ (see Table 1). The resulting g-values differ only slightly from the known g-value of the isolated Co_{Ga}^{2+}. Indeed, we expect approximately the same g-values for both the isolated Co_{Ga}^{2+} and the Co_{Ga}^{2+} in the pair because the cubic crystal-field splitting Δ, that mainly determines the g-shift from the free electron value, should be similar for both defects. The g-values show the typical shift for $3d^7$ ions in a tetrahedral crystal field supporting the assignment of the spectrum to a Co_{Ga}^{2+} related defect. According to the relation $g = g_e - 8k\lambda_0/\Delta$ we get a reasonable value k = 0.5 for the covalency reduction factor if we use the free-ion spin-orbit coupling constant of Co^{2+} $\lambda_0 = -180\ cm^{-1}$ [10] and $\Delta = 4509\ cm^{-1}$ ($^4A_2$ - $^4T_2$ distance).

Table 1: Parameters of the ground state spin Hamiltonian for the Co_{Ga}^{2+}-S_P pair in GaP. The value of D is taken from the optical spectra.

Effective S' = ½ description	$^4A_2$ ground state
$g_{\parallel}' = 2.16$ $g_{\perp}' = 4.391$	$g_{\parallel} = 2.16$ $g_{\perp} = 2.164$ $\lvert D\rvert = 5.0\ cm^{-1}$

Conclusions

We find both in optical and EPR experiments on GaP containing Co and S signatures of a trigonal defect, which we believe to be due to a next neighbour Co^{2+}_{Ga}-S_P pair. The concentration of this defect is enhanced over the pure statistical probability by Coulomb attraction of both constituents during crystal growth. In EPR, the paramagnetic behaviour of Co_{Ga}^{2+} determines mainly the characteristics of the Co_{Ga}^{2+}-S_P pair spectrum. Therefore, we conclude that the S donor is in its empty charge state. In this state the S donor is not paramagnetic and is only responsible for the observed lowering of symmetry.

Acknowledgements

We thank K. Kornitzer for experimental assistance and for helpful discussions. The steady support of R. Sauer is gratefully acknowledged.

References

[1] H. Ennen, U. Kaufmann, J. Schneider, Appl. Phys. Letters **38**, 355 (1981)
[2] J. Kreissl, W. Ulrici, U. Rehse, W.Gehlhoff, Phys. Rev. B **45**, 4113 (1992)
[3] S. Steck, G. Rückert, K. Thonke, W. Ulrici, R. Sauer, Mater. Sci. Forum **196-201**, 725, (1995)
[4] J. Weber, H. Ennen, U. Kaufmann, J. Schneider, Phys. Rev. B **21**, 2394 (1980)
[5] W. Hayes, J.F. Ryan, C.L. West, P.J. Dean, J. Phys. **C 13**, L149 (1980)
[6] U. Kaufmann, J. Schneider, Sol. State Commun. **25**, 1113 (1978)
[7] D. Ammerlahn, R. Heitz, D. Bimberg, D. Côte, B. Clerjaud, W. Ulrici, Proceed. 23. ICPS, World Scient. Publ. Co., p. 2825 (1996)
[8] A.A. Kaplyanskii, Opt. Spectrosc. **16**, 329 (1964)
[9] D.W. Jenkins, S.Y. Ren, J.D. Dow, Phys. Rev. B **39**, 7881 (1989)
[10] A. Abragam, B. Bleaney, Electron Paramagnetic Resonance of Transition Ions, Clarendon, Oxford (1970)

Materials Science Forum Vols. 258-263 (1997) pp. 1075-1080

RESONANCE-MODE PHONON REPLICA IN THE OPTICAL SPECTRA OF TRANSITION-METAL IMPURITIES IN GaP

C. Schrepel, U. Scherz, W. Ulrici*, and K. Thonke**

Inst. f. Theor. Physik, TU-Berlin, Hardenbergstr. 36, D-10623 Berlin, Germany
*Paul-Drude-Inst. f. Festkörperelektronik, Hausvogteiplatz 5-7, D-10117 Berlin, Germany
** Abt. Halbleiterphysik, Univ. Ulm, Albert-Einstein-Allee 45, D-89069 Ulm, Germany

Keywords: local vibrations, Keating-Kane model, photoluminescence, optical absorption.

Abstract. The optical absorption and photoluminescence spectra of transition-metal impurities (TM) in GaP, originating from internal *d-d* transitions, show sharp (linewidth $\approx 120\mu eV$) phonon replica of the zero-phonon lines. For the energy of the phonon we found $\hbar\omega = (40.30 \pm 1.23)$ meV for all of the investigated TMs Ti, V, Cr, Mn, Fe, Co, Ni and no correlation with the impurity mass. To explain this, we used a method based on the valence-force model of Keating and Kane [1,2] to calculate the vibration frequencies and amplitudes of local vibrational modes (LVMs) at the impurity. The validity of the model is tested by calculating LVMs for $^{11}B_{Ga}$ and $^{10}B_{Ga}$ impurities in GaP which gives good agreement with our IR-absorption measurements. Our calculations for GaP:TM show intensive LVMs of T_2 and A_1 symmetry at $\approx$ 40 meV for all of the TMs. We calculated the energy shift of these LVMs with respect to different TM masses and found it to be small compared with the deviation range of ± 1.23 meV. This explains the absence of a correlation between the observed phonon energy and the TM mass. The phonon replica are therefore interpreted as resonance modes at the bottom of the optical phonon branch.

Introduction

First-row transition metal (TM) ions ($3d^n$), as substitutional impurities in III-V semiconductors, have been intensively investigated by spectroscopical techniques during the last decades. The transitions between the ground state and the excited state, arising from the splitting of the free ion levels due to the cubic crystal field of tetrahedral symmetry, manifest itself in the optical spectra (absorption, photoluminescence) by zero-phonon lines (zpl) accompanied by broad phonon side bands due to the coupling of the electronic states with lattice phonons. These side bands often reflect the one-phonon density of states of the undoped material. Already in the first papers on Ni^+, Co^{2+} and Fe^{2+} in GaP [3-6], additional quite sharp and intense phonon replica were reported and interpreted as localized vibrational modes (LVMs) which are located near the gap between acoustical and optical modes.

Experiments

To check whether these sharp phonon replica occur generally in the optical spectra of TM_{Ga} in GaP we have measured optical absorption and photoluminescence of the impurities Ti^{3+}, V^{3+}, Cr^{3+}, Cr^{2+}, Mn^{2+}, Fe^{2+}, Co^{3+}, Co^{2+}, and Ni^+ in GaP with Fourier-transform spectrometers at $T \approx 6K$. The results of these experiments are collected in Table 1 and can be summarized as follows. For all investigated transitions, a narrow phonon side band with a half width of $\Gamma_{ph} \approx 120\mu$eV was found in the spectra of absorption or luminescence or both of them. The energy of the phonon is approximately the same for all transitions and shows only small deviations within the range $\hbar\omega = (40.30 \pm 1.23)$ meV. This phonon energy is near the bottom

Table 1. Positions E_{zpl} of the zero-phonon lines and the energy $\hbar\omega$ of the resonance mode replica measured at $T \approx 6K$ in absorption and photoluminescence for the indicated transitions of substitutional transition metal impurities in GaP. I_{RM}/I_{zpl} is the intensity ratio of the phonon replica related to that of the zpl. n.m. means not measured; 2x,3x means that also the replica at $2\hbar\omega$ and $3\hbar\omega$ could be detected. References are given for those systems for which the resonance mode replica have already been reported.

		Optical Absorption			Photoluminescence		
transition	E_{zpl}(meV)	$\hbar\omega$(meV)	$\frac{I_{RM}}{I_{zpl}}$	remarks	$\hbar\omega$(meV)	remarks	ref.
$Fe^{2+}(^5E \leftrightarrow {}^5T_2)$	414.35	39.84	0.11	2x,3x	40.11	2x	[3]
$Co^{2+}(^4A_2 \leftrightarrow {}^4T_2)$	559.07	39.94			40.23	2x,3x	[4,5]
$Ni^{+}(^2T_2 \leftrightarrow {}^2E)$	663.53	41.20	0.24	2x,3x	41.14	2x	[6]
$Mn^{2+}(^6A_1 \leftrightarrow {}^4T_1)$	1533.9			n.m.	39.50	2x,3x	[7,8]
$Co^{3+}(^3T_1 \leftrightarrow {}^5E)$	304.62	39.48	0.13			n.m.	
$Cr^{2+}(^5T_2 \leftrightarrow {}^5E)$	871.89	39.07	0.23			n.m.	[10]
	872.46	39.10	0.23	2x		n.m	
$Cr^{3+}(^4T_1 \leftrightarrow {}^4T_2)$	1029.81	39.37	0.02			n.m	
$V^{3+}(^3A_2 \leftrightarrow {}^3T_2)$	791.21	41.50	0.8		41.20	weak	
	793.14	41.53	1.9		41.20	weak	
$Ti^{3+}(^2E \leftrightarrow {}^2T_2)$	604.18			n.m.	41.30	weak	

of, but still within the optical phonon branch of GaP and is therefore called a resonance mode which is probably localized around the TM_{Ga} . However, no correlation of the phonon energy with the mass of the transition metal could be found. Fig. 1 shows as an example the zpl due to the $^3T_1(\Gamma_1) \rightarrow {}^5E(\Gamma_2)$ transition of Co^{3+}_{Ga} [9] and the corresponding phonon side band at 39.48 meV distance. Several of the transitions listed in Table 1 show more than one zpl according to the splitting of the ground state and/or the excited states due to additional interactions. If their distances are large enough compared to the half width Γ_{ph}, phonon replica to each of the zpls were found. In Table 1 the values for V^{3+} and Cr^{2+} are given as examples.

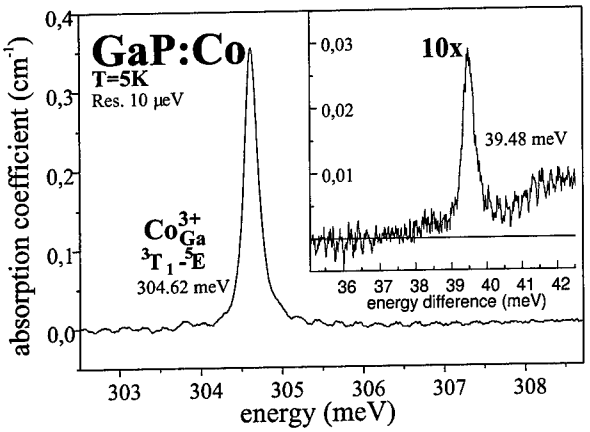

Fig. 1. Co^{3+} absorption in GaP observed at temperature 5K in the spectral region of the $^3T_1 \rightarrow {}^5E$ transition [9]. The dominating zpl is assigned to the $^3T_1(\Gamma_1) \rightarrow {}^5E(\Gamma_5)$ transition. The insert shows the local vibrational mode replica of the zpl at 304.62 meV, corresponding to an energy $\hbar\omega = 39.48$ meV of the LVM.

To clarify the origin of the phonon replica we performed calculations of vibration frequencies and amplitudes of LVMs at TM_{Ga} impurities using the valence-force model of Keating and Kane [1,2].

Valence-Force Model

The interatomic forces of cubic semiconductors have been parametrized in consideration of symmetry requirements by Keating [1]. The simple model for bond stretching and bond bending forces was extended by Kane [2] to include up to the third nearest neighbour interactions. He demonstrated that the phonon dispersion curves of various crystals can be well reproduced by a small number of parameters including an effective atomic charge to take the long-range Coulomb interaction into account. We used this model to set up the dynamical matrix, the eigenvalues of which are the squares of the vibration frequencies. The valence-force parameters for the perfect GaP crystal were obtained by fitting the phonon dispersion curves to neutron scattering experiments [11]. Our fit reproduces the optical phonon branch quite well whereas there are some discrepancies in the acustic phonon branch. In order to apply the Keating-Kane model to the calculation of LVMs at point defects in semiconductors we used a cluster of 281 vibrating atoms around the defect which is embedded in the non vibrating crystal. We adopted the scaling-factor approximation (SFA) [12] to describe the change of the interatomic forces in the vicinity of the defect. The scaling factor s is defined by $p_d = p + sp$, where p is any of the valence-force parameters α and β of the perfect crystal and p_d the corresponding parameter at the defect site. This approximation assumes an equal relative change of the forces at the defect with respect to the perfect crystal values. For a given impurity mass and scaling factor the vibration frequencies were obtained from a numerical diagonalization of the dynamical matrix and the local vibrational modes were selected from the large vibration amplitudes of the atoms in the vicinity of the defect. In case the energy of the LVM lies in the forbidden gap or above the optical phonon band, they are usually strongly localized at the defect. In case the energy of the LVM is in a region of large density of phonon states, these modes hybridize with crystal phonons, and are therefore often called resonance modes. We tested the SFA and the valence-force parameters by a calculation of the energies and isotope shifts of the LVMs at boron impurities in GaP. The IR-absorption spectra show two LVMs at 73.46 (73.46) meV and 35.27 (32.4) meV for ^{10}B and well resolved isotope shifts $^{10}\mathrm{B} \rightarrow {}^{11}\mathrm{B}$ of 2.81 (2.85) meV and 0.170 (0.115) meV, respectively. The values in parantheses are the corresponding values from a calculation with a scaling factor $s = -0.10$, which is obtained by fitting the energy of the LVM at 73.46 meV to the experiment. The isotope shift of the split-off LVM above the optical phonons can be well reproduced, whereas the energy and the calculated isotope shift for the LVM in the phonon gap are to small. This is most probably due to the discrepancies in the calculated phonon dispersion curves in the region of acustical phonons. Nevertheless, we are confident that our model describes the energy and isotope splitting of LVMs near or within the region of optical phonons with good accuracy.

Results

We here describe as an example our calculations of GaP:Cr^{3+}. Figure 2 shows the density of phonon states of the perfect crystal together with the change of the density of phonon states due to the Cr impurity. The scaling factor of $s = -0.30$, which corresponds to a softening of the interatomic forces at the defect by 30%, was obtained by fitting the the energy of the T_2 mode to the observed phonon energy. It can be seen, that two LVMs with symmetries T_2 and A_1 appear at the bottom of the optical phonon branch. The insert of Fig. 2 shows the energy of these LVMs as a function of the scaling factor. An increase of the scaling factor to $s = -0.1$ increases the energy of the LVM, shifting it into the optical phonon band, which results in

a hybridization with crystal phonons and a large delocalization. This is demonstrated in Fig. 3. The characteric LVMs of T_2 and A_1 symmetry also appear for all other TMs. We fitted the energy of either the A_1 LVM or the T_2 LVM to the phonon energy, observed in emission (GaP:Mn^{2+}, GaP:Ti^{3+}) or absorption. The resulting scaling factors S_{A_1} and S_{T_2}, summarized in Table 2, are within a

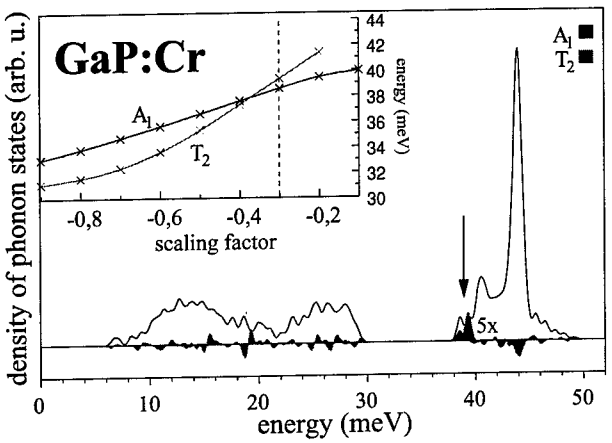

Fig. 2. Density of phonon states of the perfect GaP crystal (full line) and the change due to the Cr impurity (filled curve), enlarged by a factor of 5) using a scaling factor of $s = -0.30$. The insert shows the energies of the LVMs of T_2 and A_1 symmetry as a function of the scaling factor.

narrow range $-0.31 \leq S_{T_2} \leq -0.14$ and $-0.24 \leq S_{A_1} \leq -0.10$ for the T_2 LVM and the A_1 LVM respectively. Thus, the results are quite similar and Figures 2 and 3 hold without significant changes for all the TMs.

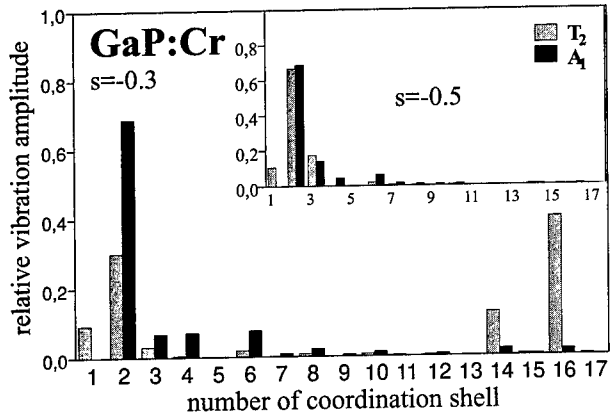

Fig. 3. Relative vibration amplitudes of the atoms for the LVMs of A_1 and T_2 symmetry calculated with scaling factors $s = -0.30$ and $s = -0.50$ (insert). The bars indicate the sum of the squares of the vibration amplitudes times $\sqrt{M}$ of all atoms (mass M) in a particular coordination shell, having the same distance to the defect site. The delocalization for increasing scaling factor due to hybridization with crystal phonons is clearly seen.

The small energy difference $\Delta\hbar\omega$ of the phonon energy for two specific TMs with masses M and $M + \Delta M$ is due to a different nuclear mass at the defect site and due to a change of the electron density, resulting in changes of the interatomic forces in the vicinity of the defect. In first order approximation this means in our two parameter model

$$\Delta\hbar\omega \approx \frac{\partial\hbar\omega}{\partial M}\Delta M + \frac{\partial\hbar\omega}{\partial S}\Delta S \qquad (1)$$

where ΔS is the change of the scaling factor due to the different TMs which can be taken from Table 2. Irrespective of the validity of a VFM, there exists a simple way to calculate the derivative of the energy $\hbar\omega$ of a LVM with respect to the impurity mass M from the corresponding eigenvector of the dynamical matrix. Let A^2 be the sum of the squares of the

transition	$\hbar\omega$(meV)	S_{T_2}	S_{A_1}	$\frac{\partial\hbar\omega}{\partial M}(\frac{\mu eV}{\text{nucl.}})$
$Fe^{2+}(^5E \leftrightarrow {}^5T_2)$	39.84	-0.26	-0.13	-62
$Co^{2+}(^4A_2 \leftrightarrow {}^4T_2)$	39.94	-0.24	-0.10	-55
$Ni^{+}(^2T_2 \leftrightarrow {}^2E)$	41.20	-0.18	-	-24
$Mn^{2+}(^6A_1 \leftrightarrow {}^4T_1)$		-0.28	-0.19	-65
$Co^{3+}(^3T_1 \leftrightarrow {}^5E)$	39.48	-0.27	-0.19	-59
$Cr^{2+}(^5T_2 \leftrightarrow {}^5E)$	39.07	-0.31	-0.24	-44
	39.10	-0.31	-0.23	-42
$Cr^{3+}(^4T_1 \leftrightarrow {}^4T_2)$	39.37	-0.30	-0.21	-35
$V^{3+}(^3A_2 \leftrightarrow {}^3T_2)$	41.50	-0.14	-	>-8
	41.53	-0.14	-	>-8
$Ti^{3+}(^2E \leftrightarrow {}^2T_2)$		-0.23	-	-32

Table 2. The scaling factors S_{A_1} and S_{T_2} for the various TMs in GaP. In some cases, the observed phonon energy could not be reproduced for any scaling factor S_{A_1}. The shift $\frac{\partial\hbar\omega}{\partial M}$ of the energy with respect to mass of the impurity for the LVM of T_2 symmetry is also given. For the LVM of A_1 symmetry it is $\frac{\partial\hbar\omega}{\partial M} = 0$.

three corresponding components of the eigenvector of the dynamical matrix, then $A/\sqrt{M}$ is the relative vibration amplitude of the TM and we have

$$\frac{\partial\hbar\omega}{\partial M} = -\frac{1}{2}\frac{\hbar\omega}{M}A^2 \quad \text{with} \quad 0 \leq A^2 \leq 1. \tag{2}$$

As an example we have for the T_2 LVM in GaP:Cr^{3+} $\frac{\partial\hbar\omega}{\partial M} = -35\frac{\mu eV}{\text{nucl.}}$ corresponding to $A^2 = 9.3\%$ which is the height of the first bar in Fig 3. In tetrahedral symmetry only LVMs of T_2 character can have $\frac{\partial\hbar\omega}{\partial M} \neq 0$ because only in this case the central impurity ion is moved. As can be seen from Table 2, the values $\frac{\partial\hbar\omega}{\partial M}\Delta M$ for the T_2 LVM are small compared to the deviation range ± 1.23 meV of the observed phonon energy, thus the term $\frac{\partial\hbar\omega}{\partial S}\Delta S$ in Eq. 1 dominates. This is also true in case of the A_1 LVM because of $\frac{\partial\hbar\omega}{\partial M} = 0$ and explains the absence of a correlation between the observed phonon energy and the mass of the TM in both of the possible cases where the phonon replica are either due to the A_1 LVM or due to the T_2 LVM.

Discussion

So far, it is not clear whether the resonance mode phonon replicas are due to the A_1 LVM or due to the T_2 LVM. We present here some arguments for both of the possible assignments.

1. Possible isotope effect in the phonon satellite line of a specific zpl.
In case of the T_2 LVM the energy of the resonance mode for two specific isotopes of a TM with masses M and $M + \Delta M$ is different. For a particular zpl this is manifested in the optical spectra as an isotope splitting with magnitude $\Delta\hbar\omega \approx \frac{\partial\hbar\omega}{\partial M}\Delta M$ of the corresponding phonon satellite line. However, in none of the absorption and photoluminescence spectra such isotope splittings could be observed. This could be either due to the experimental linewidth of 120μeV, which is nearly equal or larger than $\Delta\hbar\omega$, see Table 2, or due to coupling of the electronic states to the A_1 LVM. In the latter case there is no isotope splitting because the A_1 LVM does not move the TM and therefore does not change its energy with respect to different isotopes.

2. Jahn-Teller-Effekt in the optical spectra.
Some of the spectra are influenced by Jahn-Teller interactions of the electronic states with other LVMs of T_2 symmetry. This can be seen from the phonon side bands or from additional isotope effects of the zero phonon lines, which could be observed in some cases. Such isotope splittings of the optical fine-structure transitions result from different isotope shifts of the excited and ground-state vibronic energy levels. Their dependence on the impurity mass is

a consequence of the coupling of the electronic defect states to LVMs of T_2 symmetry. For the T_2 LVM at $\approx$ 40 meV we expected non-vanishing linear Jahn-Teller coupling constants because of its strong localization to the vicinity of the defect. This is in contradiction with the assumption that the resonance mode replica are due to this particular T_2 LVM.

3. Stronger hybridization effect for the A_1 LVM

As can be seen from Fig. 2, for an increasing scaling factor the hybridization with crystal phonons leads to a delocalization of the A_1 LVM, resulting in a smaller shift of the energy with respect to the scaling factor and a convergence of the energy to $\approx$ 40 meV. Therefore, in some cases, the observed phonon energy could not be reproduced for any scaling factor, see Table 2. This could be either due to resonance modes of T_2 symmetry or due to the following problem of our calculation. The calculation shows a mode of A_1 symmetry which is mainly located to the surface of the cluster and therefore is an artificial effect of our model. This surface mode with energy at the bottom of the optical phonon branch hybridizes with the A_1 LVM and possibly results in additional unphysical hybridization effects.

To summarize, our model explains the occurrence of LVMs of A_1 and T_2 symmetry with an energy of $\approx$ 40 meV for all investigated TM_{Ga}s independent of their mass. However, at present, we are not able to decide between the two possible symmetries. Further measurements and more detailed calculations are necessary to clarify this situation. As an example an additional crystal field of C_{3v}-symmetry splits the T_2 LVM in an A_1 and a E component which should be observable as a doublet structure of the resonance mode satellite lines. It should also be noted that from the data available in the literature on InP:TM_{In} (TM=V^{3+}, Fe^{2+}, Co^{2+}, Ni^{+}) a sharp phonon replica of energy $\hbar\omega = (37.2 \pm 1.2)$ meV appears in InP, which has probably the same physical origin as discussed here for GaP.

Acknowledgments

We thank the Zentraleinrichtung Rechenzentrum of the Technische Universität Berlin for their support and the provision of computing facilities.

References

1. P.N. Keating, Phys. Rev. **145**, 637 (1966).
2. E.O. Kane, Phys. Rev. B **31**, 7865 (1985).
3. G. Rückert et al., Phys. Rev. B **46**, 13207 (1992).
4. J. Weber, H. Ennen, U. Kaufmann, and J. Schneider Phys. Rev. B **21**, 2394 (1980).
5. W. Hayes, J.E. Ryan, C.L. West, and P.J. Dean, J. Phys. C **13**, L149 (1980).
6. U. Kaufmann et al., Phys. Rev. B **19**, 3343 (1979).
7. A. T. Vink, G.G.P. Van Gorkom, J. Lumin. **5**, 379 (1972).
8. G. Hofmann, A. Keckes, and J. Weber, Semicond. Sci. Technol. **8**, 1523 (1993).
9. D. Ammerlahn et al., Proceed. 23. ICPS, World Scient. Publ. Co., 2825 (1996).
10. W. Ulrici, J. Kreissl, Proceed. 23. ICPS, World Scient. Publ. Co., 2833 (1996).
11. Landoldt-Börnstein, new series, volume **22a**, 306 (1987).
12. R.M. Feenstra, R.J. Hauenstein, and T.C. McGill, Phys. Rev. B **28**, 5793 (1983).

Materials Science Forum Vols. 258-263 (1997) pp. 1081-1086

GaN GROWN USING TRIMETHYLGALLIUM AND TRIETHYLGALLIUM

A. Saxler, P. Kung, X. Zhang, D. Walker, J. Solomon[1], W. C. Mitchel[1], and M. Razeghi

Center for Quantum Devices, Department of Electrical and Computer Engineering, Northwestern University, Evanston, IL 60208

[1]Air Force Research Laboratory, Materials Directorate, Wright-Patterson AFB, OH 45433-7707

Keywords: GaN, trimethylgallium, triethylgallium, MOCVD

Abstract. GaN films grown by low pressure metalorganic chemical vapor deposition using trimethylgallium and triethylgallium as gallium precursors are compared. The films were characterized by x-ray diffraction, Hall effect, photoluminescence, secondary ion mass spectroscopy, and etch pit density measurements. GaN layers grown using triethylgallium exhibited superior electrical and optical properties and a lower carbon impurity concentration.

Introduction.

GaN and related III-Nitride compounds are wide bandgap semiconductors with many important applications. They have utility for electronics operating at high-power in high-temperature environments [1], solar-blind ultraviolet photodetectors [2,3], and for blue and ultraviolet light emitting and laser diodes [4]. However, further improvement in device performance is largely dependent on improvement of the material quality.

We have already reported on the growth [5-7] of III-Nitrides, their characterization [8,9], and photodetectors [2,10] made from these materials. The choice of gallium precursors has recently been shown to influence the deep levels [11] and impurities [12] in GaN films. In this paper, we compare trimethylgallium (TMGa) and triethylgallium (TEGa) as gallium precursors for the metalorganic chemical vapor deposition (MOCVD) growth of GaN.

Experimental.

The GaN films were grown in a horizontal low-pressure (10 mbar) MOCVD reactor using a high temperature AlN buffer layer. Film thicknesses were typically about 0.7 μm. The organometallic gallium sources used were special grade TMGa, purified grade TMGa, and oxygen reduced grade TEGa from Morton, and adduct grade TEGa from Epichem. No significant differences were observed in the GaN layers as a function of the grade or supplier of these high purity organometallic sources. For purposes of comparison, the films were grown on identical (00·1) sapphire substrates, with identical AlN buffer layers, and with identical growth conditions except for the choice of the gallium source.

Results and Discussion.

Figure 1 shows the (00·2) GaN open-detector x-ray diffraction rocking curves for samples grown using TMGa and TEGa. The full width at half maximum (FWHM) for the TEGa grown film was 33 arcseconds while the TMGa grown film had a FWHM of 62 arcseconds. The linewidth and tails were somewhat narrower for the film grown using TEGa. Pendellösung oscillations for the TEGa grown film are visible even in the open-detector rocking curve as shown in Fig. 1(b). Typically, the linewidths are approximately equivalent for films grown using TEGa and TMGa.

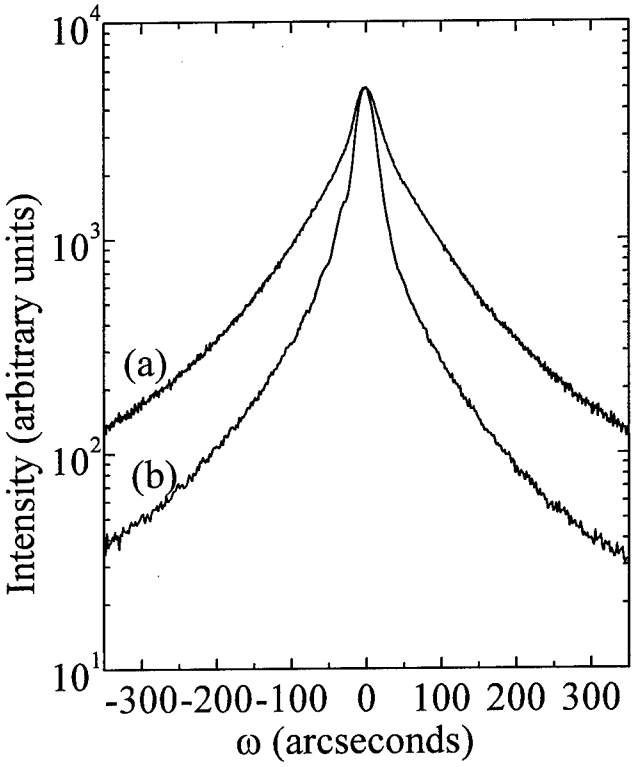

Fig. 1. Open-detector x-ray rocking curves of the (00·2) GaN peak of (a) a sample grown with TMGa and (b) a sample grown with TEGa under otherwise identical growth conditions.

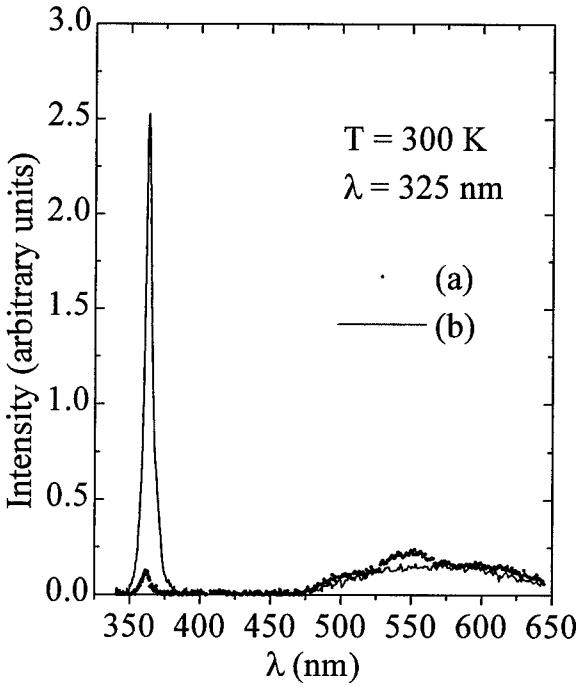

Fig. 2. Room temperature photoluminescence spectra of (a) a sample grown with TMGa and (b)a sample grown with TEGa under otherwise identical growth conditions.

Figure 2 shows the room temperature photoluminescence (PL) spectra measured using a 325 nm He-Cd laser for samples grown using TMGa and TEGa. Typically, the near bandgap luminescence was much stronger for the samples grown using TEGa, although the yellow luminescence was approximately the same as illustrated in Fig. 2. From these results, it is clear that the films grown using TEGa have better optical quality than films grown using TMGa.

Figure 3 shows the variation of the electron mobility and carrier concentration as a function of the dopant flow rate of dilute SiH_4 for GaN films grown using TMGa and TEGa. The mobility of TEGa grown films was typically much higher than in TMGa grown films for the same carrier concentration as seen in Fig. 3. Undoped films were typically insulating for films grown using either TMGa or TEGa. The TMGa grown films required a higher flow rate of dilute SiH_4 in order to achieve conduction, and the resulting mobility was extremely low indicating that the TMGa grown films are heavily compensated. The TEGa grown films were easier to dope and had higher mobilities as seen in Fig. 3.

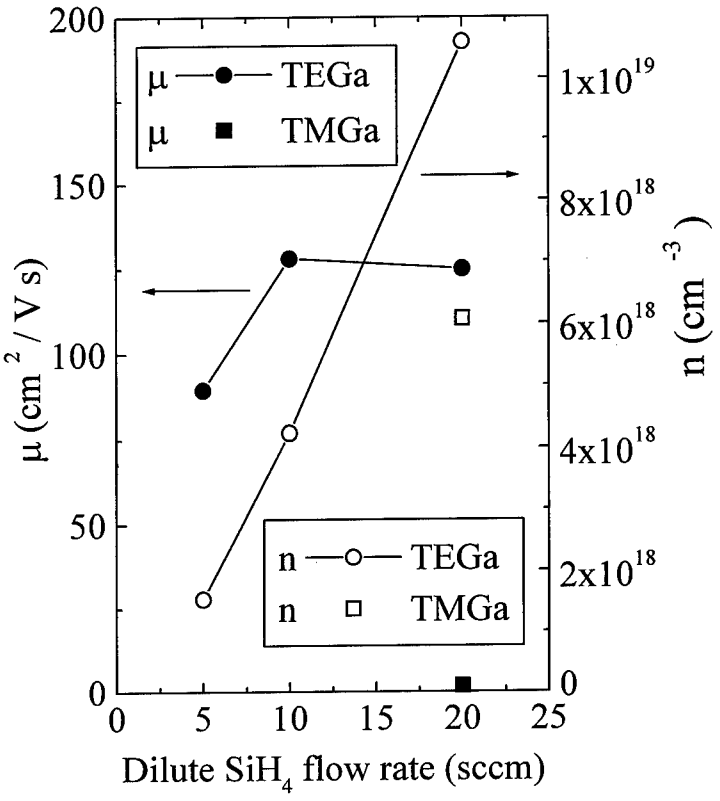

Fig. 3. Room temperature electron mobility and n-type carrier concentration for TMGa and TEGa grown samples as a function of the doping level using otherwise identical growth conditions.

Fig. 4 shows the secondary ion mass spectroscopy (SIMS) depth profiles for typical samples grown using TMGa and TEGa using cesium for the primary ions. At a depth of about 400 nm, the oxygen concentration was 7 times higher, and the carbon concentration was 50 times higher in the TMGa grown film compared to the TEGa grown film. The higher concentration of carbon and oxygen in the GaN layers grown using TMGa may be responsible for the poorer electrical and optical properties of those films.

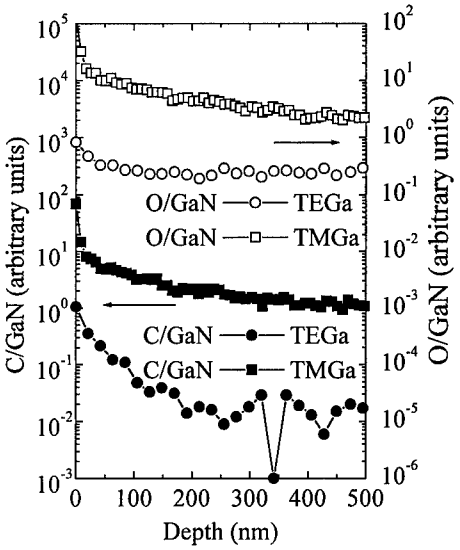

Fig. 4. SIMS depth profiles of oxygen and carbon normalized to the GaN signal in a sample grown with TMGa and a sample grown with TEGa under otherwise identical growth conditions.

In order to further assess the material quality, hot phosphoric acid (H_3PO_4) was used to attack the GaN films. A scanning electron microscope (SEM) with a field emission gun was used to examine the surface.

The etch pits in the GaN films exhibited hexagonal symmetry. The bases of the hexagons were determined to be along the [[11·0]] directions through x-ray diffraction measurements. The walls appear to be nearly vertical, so the etched faces correspond to the {10·0} planes. The etch pit density (EPD) was approximately 10^4 cm^{-2} for these films. The typical size of the etch pits ranged from 2 to 40 μm. (This EPD compares favorably with an EPD of over 10^7 cm^{-2} that was revealed in early GaN films by Shintani and Minagawa with this etching technique [13].)

Although the density of the large etch pits was approximately equal in the films grown using TMGa and TEGa, the borders were very different. The TEGa grown film had sharp borders but the TMGa grown film had irregular borders. In addition to these large pits with a density of 10^4 cm^{-2} in the TMGa grown film, smaller pits were present with a density of 10^9 cm^{-2} and sizes of about 0.05 to 0.1 μm. It is possible that when these small pits are present near the edge of the large pits, the border extends to envelop them, creating an irregular border. None of these small pits were present in the TEGa grown film that was grown under identical conditions. It is possible that the difference in the shape of the etch pits for TMGa grown films is due to the higher carbon and oxygen impurity concentration which enhances the etching rate in the vicinity of defects.

In summary, we grew GaN layers using high purity TMGa and TEGa and found that the properties of GaN films depend strongly on the gallium precursor chosen for the MOCVD growth. Films grown using TEGa showed stronger near-bandedge photoluminescence and higher mobilities. SIMS measurements indicated higher carbon and oxygen concentrations in the films grown using TMGa. Hot phosphoric acid was used to measure the EPD to be 10^4 cm^{-2} for large pits in films grown with either TMGa or TEGa. The edges of the large etch pits in the TEGa grown films were generally sharp while the borders of the etch pits in the TMGa grown films were irregular. The TMGa film also had small pits with a density of 10^9 cm^{-2} which were not present in the TEGa grown film. We conclude that TEGa is the superior gallium source for the MOCVD growth of GaN for the experimental conditions studied.

Acknowledgements.

The authors would like to thank M. Yoder, Y.-S. Park, and C. Wood of ONR, A. Husain of DARPA, and P. Shu, B. Mott, and Z. C. Huang of NASA for their support and encouragement. Funding for this work was received under ONR/BMDO Grant N00014-93-1-0235 and DARPA/ONR Grant N00014-96-1-0714.

References.

1. O. Aktas, Z. F. Fan, S. N. Mohammed, A. E. Botchkarev, and H. Morkoç, Appl. Phys. Lett. **69**, 3872 (1996).
2. D. Walker, X. Zhang, A. Saxler, P. Kung, J. Xu, and M. Razeghi, Appl. Phys. Lett. **70**, 949 (1997).
3. M. Razeghi and A. Rogalski, J. Appl. Phys. **79**, 7433 (1996).
4. S. Nakamura, M. Seno, S. Nagahama, N. Iwasa, T. Yamada, T. Matsushita, Y. Sugimoto, and H. Kiyoku, Appl. Phys. Lett. **69**, 4056 (1996).
5. P. Kung, A. Saxler, X. Zhang, D. Walker, T. C. Wang, I. Ferguson, and M. Razeghi, Appl. Phys. Lett. **66**, 2958 (1995).
6. A. Saxler, P. Kung, C. J. Sun, E. Bigan, and M. Razeghi, Appl. Phys. Lett. **64**, 339 (1994).
7. P. Kung, A. Saxler, X. Zhang, D. Walker, R. Lavado, and M. Razeghi, Appl. Phys. Lett. **69**, 2116 (1996).
8. A. Saxler, M. A. Capano, W. C. Mitchel, P. Kung, X. Zhang, D. Walker, and M. Razeghi, MRS Symposium Proceedings **449**, 477 (1997).
9. X. Zhang, P. Kung, D. Walker, A. Saxler, and M. Razeghi, MRS Symposium Proceedings **395**, 625 (1996).
10. X. Zhang, P. Kung, D. Walker, J. Piotrowski, A. Rogalski, A. Saxler, and M. Razeghi, Appl. Phys. Lett. **67**, 2028 (1995).
11. J.-F. Chen, N.-C. Chen, W.-Y. Huang, W.-I. Lee, and M.-S. Feng, Jpn. J. Appl. Phys. **35**, L810 (1996).
12. A. Ishibashi, H. Takeishi, M. Mannoh, Y. Yabuuchi, and Y. Ban, J. Electron. Mater. **25**, 799 (1996).
13. A. Shintani and S. Minagawa, J. Electrochem. Soc. **123**, 706 (1976).

Materials Science Forum Vols. 258-263 (1997) pp. 1087-1092

ODMR STUDIES OF AS-GROWN AND ELECTRON-IRRADIATED GaN AND AlN

G.D. Watkins, M. Linde, P.W. Mason, H. Przybylinska, C. Bozdog, S.J. Uftring, V. Härle[1], F. Scholz[1], W.J. Choyke[2], and G.A. Slack[3]
Department of Physics, Lehigh University, Bethlehem, PA 18015, USA
[1] 4. Physikalisches Institut, Universität Stuttgart, D-70550 Stuttgart, Germany
[2] Department of Physics, University of Pittsburgh, Pittsburgh, PA 15620, USA
[3] Department of Physics, Rensselear Polytechnic Institute, Troy, NY 12180, USA

Keywords : GaN, AlN, PL-ODMR, electron irradiation.

Abstract. In a thin epilayer of wurtzite GaN grown on sapphire, electron irradiation strongly quenches the visible luminescence, producing a set of new overlapping bands in the infrared at ~ 0.85 and ~ 0.93 eV. Four new ODMR signals are detected in these bands, one of them, LE3, displaying resolved "hyperfine-like" structure. The origin of this structure is presently not understood, however. In as-grown small single crystals of AlN, many well resolved strongly anisotropic ODMR signals are detected. The main effect of electron irradiation is to enhance one of signals, an S = ½ signal near g ~ 2, whose flat-topped shape suggests possible unresolved hyperfine interaction with a single nucleus.

Introduction

There is considerable current interest in the role of point defects in the III-V nitrides, stimulated by their successful application in blue light emitting and laser devices, and their potential for high temperature electronic device applications. We here describe optical detection of magnetic resonance studies via photoluminescence (PL-ODMR) in GaN and AlN before and after 2.5 MeV electron irradiation. This first such study of electron irradiation in these materials has been initiated because it may shed light on the properties of their intrinsic defects about which little is presently known.

Experiment

The GaN sample investigated was a 1 μm-thick wurtzite layer grown by metalorganic vapor phase epitaxy (MOVPE) on a sapphire substrate with a thin AlN buffer layer [1]. It was not intentionally doped, the net n-type carrier concentration being in the mid-10^{16} cm^{-3} range. The AlN samples were small, ~ $(0.5\ mm)^3$, single crystals, grown several years ago by vapor transport at Westinghouse (WJC) and at General Electric (GAS) Research Laboratories. They also were not intentionally doped. After first PL-ODMR characterization in the as-grown state, the samples were subsequently irradiated at room temperature by 2.5 MeV electrons from a Van de Graaff accelerator to doses of 0.5-2 $\times 10^{18}$ cm^{-2}. The luminescence was excited by either the 351 nm or 458 nm line of an Argon laser, or the 325 nm line of a HeCd laser (~15 mW). PL-ODMR was studied at 1.5 K in a 35-GHz spectrometer, the details of which have been previously described [2]. Annealing studies of the GaN sample were performed in a nitrogen atmosphere.

GaN Results

Before irradiation, the PL bands at 3.47 eV (exciton-related [3]), 3.27 eV (shallow donor to shallow

acceptor recombination [4]) and 2.2 eV (not established), typical of high quality *n*-type GaN layers, were observed. Our PL-ODMR studies of the broad 2.2 eV band revealed the same two ODMR signals reported by other workers, one attributed to the shallow donor with $g_{\|} = 1.951$, $g_{\perp} = 1.949$. the other, unidentified, with $g_{\|} = 1.989$, $g_{\perp} = 1.992$ [5-9]. After electron irradiation to 1×10^{18} cm^{-2}, the two higher energy bands vanished completely and the 2.2 eV band decreased by a factor of ~15. At the same time, two new overlapping broad PL bands emerged in the infrared, not present before irradiation, at ~ 0.85 and ~0.93 eV. The lower energy one revealed sharp phonon structure. Separating the two bands with low pass (<0.83 eV) and high pass (>0.88 eV) filters, four new S = ½ ODMR signals were observed, labeled LE1-4, whose g-values (~2) we have previously published in a preliminary report [10].

In Fig. 1, we show part of the angular dependence of three of the spectra, labeled LE1, LE2, and LE3, observed in the higher energy (>0.88 eV) band. Of particular interest is LE3 which displays well resolved structure to either side of the central region. Shown also is a simulation of its spectrum, with the magnetic field, **B**, 80^0 from the c-axis, as arising from the simple four-line structure predicted for hyperfine interaction with a single gallium atom, with the 60% - 40% natural isotope abundance ratio of the I=3/2 ^{69}Ga and ^{71}Ga nuclei. On the basis of this very close agreement, we previously suggested that the defect was a displaced Ga atom of some kind [10]. However, we must now modify that simple interpretation as a result of subsequent annealing studies. In Fig. 1, we also show by the lighter curves the spectra after a 30 min 400 °C anneal, where LE3 has almost completely disappeared. In Fig. 2, we plot the difference in the spectra between the before and after anneals, in order to reveal what has annealed out. It is apparent that the interpretation of what appeared to be closer spaced inner satellite lines in Fig. 1 as arising from the Ga m = ±1/2 hyperfine lines cannot be correct because they are no longer apparent in sufficient intensity in the difference spectra of Fig. 2. Instead, there is a strong suggestion that a component in the

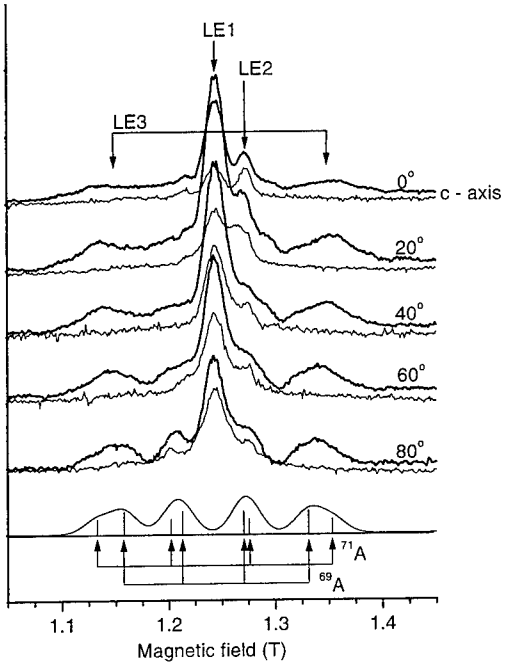

Fig. 1. ODMR spectra (bold) detected in the higher energy IR band (>0.88 eV) *vs* orientation of **B** with respect to the c-axis. Shown below is a comparison to the 80^0 spectrum of a simulated spectrum for hyperfine interaction with the naturally abundant ^{69}Ga and ^{71}Ga isotopes of a single Ga atom, as proposed in Ref. 10. Also shown (light) are the spectra after 400°C anneal.

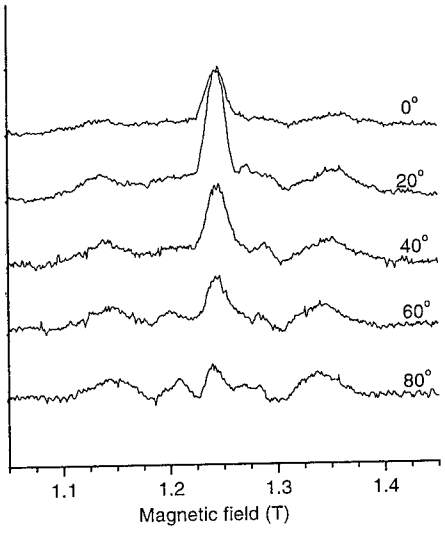

Fig. 2. The difference between the ODMR spectra of Fig. 1, before and after the 400 °C anneal, revealing the LE3 spectrum.

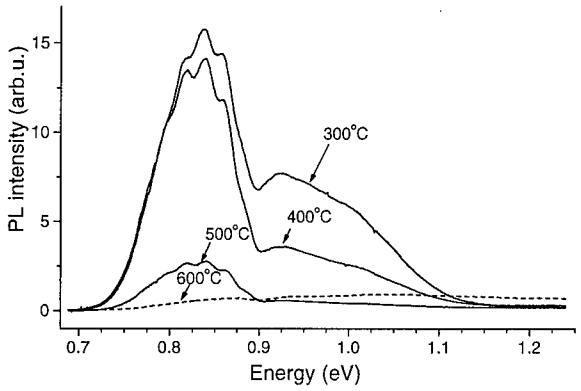

Fig. 3. IR luminescence *vs* 30 min. isochronal anneals.

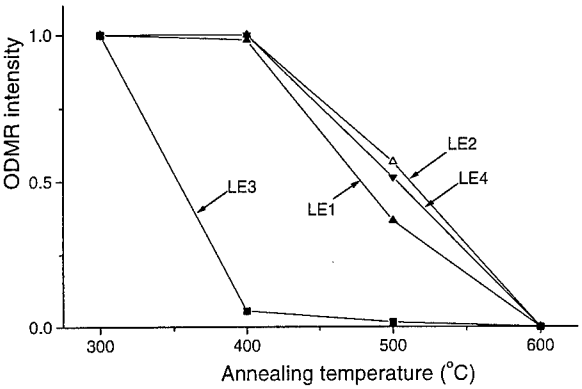

Fig. 4. Normalized intensity for the four irradiation-produced ODMR spectra *vs* 30 min isochronal anneals.

central region, whose intensity varies *vs* orientation may actually be part of LE3, accidentally superposing on LE1, which remains after the anneal. (LE1 can also be followed in the lower energy PL band where LE3 is absent, and it does not anneal at this temperature, see Fig. 4).

And so, spectrum LE3 remains exciting, because it is the first ODMR-observed defect in GaN with resolved structure. This, in turn, clearly contains potential chemical and structural information concerning the defect identity. Unfortunately, however, at this stage, it is not clear what this information is telling us. We are inclined to believe that the structure still is that of a Ga hyperfine interaction, but reflecting the result of a large quadrupole interaction, but this remains to be tested.

The other spectra, LE1, LE2, and LE4 are also important, of course, having also been produced by the irradiation, and therefore quite likely also related to intrinsic defects. The absence of resolved structure for them, however, makes them less promising as regards identification. In Figs. 3 and 4, we present isochronal annealing results for the infrared luminescence and all four of the irradiation-produced ODMR spectra. After the last anneal at 600 °C, the infrared luminescence and the four ODMR signals have completely disappeared. At this point, the 2.2 eV band has returned to approximately 1/3 of its original intensity.

AlN Results

In Fig. 5, we show the PL spectrum observed in a Westinghouse as-grown slightly greenish-gray crystal of AlN under photo-excitation at 351 nm and 458 nm. Monitoring this luminescence, at least six distinct, strong, well resolved ODMR spectra are observed, as illustrated in Fig. 6. Here, under 351 nm excitation, the spectrum is dominated by two S = 1 centers, labeled D1 and D2. Under 458 nm excitation, these two centers are absent revealing two additional S = 1 centers (also evident under 351 nm excitation but swamped by D1 and D2), labeled D3 and D4. All four show well resolved angular dependent fine structure splittings. In addition, present under both excitation conditions, are two S = ½ centers with small but measurable anisotropy in their g-tensors, which are shown under higher magnetic field resolution in the central field g~2 region. All of these centers have been observed in most of the samples studied and therefore arise from common defects. An exception is one sample from General Electric which had been judged to be of particularly high chemical purity

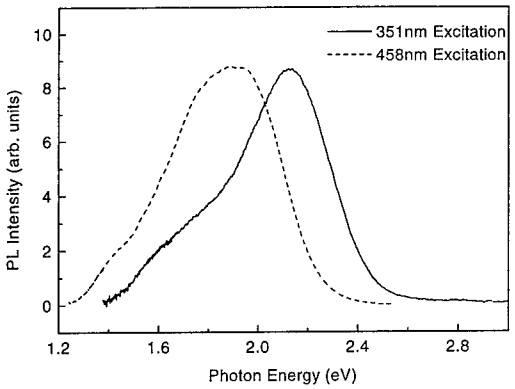

Fig. 5. Photo-luminescence in an as-grown single crystal of AlN under excitation at two different Argon laser wavelengths.

from its superior optical and thermal conductivity properties [11]. In it, other ODMR centers appear to dominate. In no case, however, has resolved hyperfine structure been detected, so that chemical identification has not yet been possible. The spectra of these interesting defects have been fully analyzed, their polarization and spectral dependencies determined, etc. They will be the subject of a subsequent publication. We here will discuss only D5.

D5 is an S = ½ center with $g_{\|}$ = 2.0011(10) and $g_{\perp}$ = 2.0065(10). Its FWHM width varies from ~105 G for **B** perpendicular to the c-axis to ~210 G for **B** parallel to the c-axis, where its shape is somewhat flat-topped, suggesting perhaps unresolved hyperfine interaction with a single nucleus. The spectrum is easy to miss at the microwave modulation frequency of ~ 500 Hz used in studying most of the other ODMR signals. However, its intensity increases dramatically as the microwave modulation frequency is decreased. In fact, if one simply follows the average intensity of the luminescence, with or without microwave modulation, the intensity increase at resonance can be as large as ~1%, representing by far the largest contributor to the ODMR effect in the sample. This tells us that the radiative lifetime associated with its contribution to the luminescence is very long, most likely indicating distant donor-acceptor-like recombination. It makes it also very easy to detect because in all of our studies the total average luminescence is automatically recorded for each magnetic field sweep run, and its presence and intensity are immediately observed even in the higher modulation frequency runs. In most of the Westinghouse samples studied, it was present in the as-grown state. In one of the Westinghouse samples, however, it was absent, even though the D1 - D4 signals were prominent.

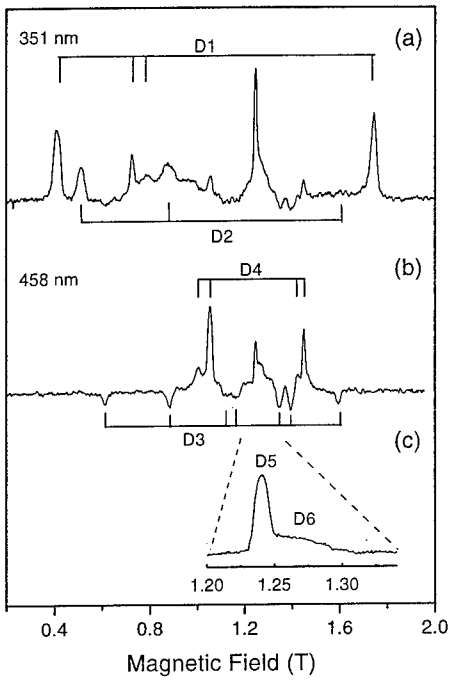

Fig. 6. ODMR spectra in AlN under (a) 351 nm, and (b) 458 nm excitation, for **B** || [$\bar{1}$100]. (c) Additional centers near g ~ 2 under expanded magnetic field resolution.

This sample was then subsequently irradiated by 2.5 MeV electrons in three stages, to total doses of 0.5, 1.0 and 2.0 $\times 10^{18}$ cm^{-2}. There was little change in the luminescence and in the strength of the D1 - D4 ODMR spectra. However, the D5 spectrum, absent before and after the first irradiation, emerged strongly after the 1.0×10^{18} cm^{-2} dose, and doubled to ~1% after the last. As well as we can determine, this is the same defect as observed in the other as-grown samples, with the same long radiative

lifetime characteristics, the same g-values, and similar linewidth changes *vs* orientation of **B.**

This suggests that the D5 defect may be being produced by the electron irradiation and therefore related to a primary defect such as a vacancy or interstitial. The D5 spectrum bears an intriguing similarity to one observed by EPR in neutron- and electron-irradiated polycrystalline AlN, and attributed to a nitrogen vacancy [12]. It is, however, broader. Of course, centers at g ~ 2 are not distinctive, and the one reported here could be entirely different. Preliminary attempts to detect ENDOR in the spectrum have been unsuccessful, but will be pursued.

Finally, let us emphasize that the excitation that we have used in this study is well below the AlN bandgap (6.28 eV) and therefore quite likely directly exciting the defects. Therefore the failure to significantly quench the luminescence or the ODMR signals by the electron irradiation does not necessarily mean that the luminescence efficiency from free electron and hole recombination is unaffected. Indeed, this efficiency, relevant to light emitting and laser diode operation, may well be significantly reduced, as we have found from our studies here for GaN, where above bandgap excitation was possible.

Summary

In electron-irradiated GaN, the visible luminescence is strongly quenched. New luminescence bands are produced in the near infrared, and, in them, four new ODMR signals are observed. One of these, LE3, displays the first resolved "hyperfine-like" structure found for an ODMR signal in this material, the origin of which, however, is not clear at present. The infrared luminescence and the four ODMR signals disappear in discrete stages between 400 and 600 °C. In single crystals of AlN, on the other hand, many strong well resolved anisotropic ODMR signals are observed in visible luminescence in the as-grown materials. The main effect of electron irradiation for AlN appears to be a strong increase in an ODMR signal near g=2, which is not as yet identified.

Acknowledgments

The ODMR studies at Lehigh University were supported jointly by the Office of Naval Research under Grant No. N00014-94-1-0117 and the National Science Foundation under Grant No. DMR-92-04114.

References

1. F. Scholz, V. Härle, H. Bolay, F. Steuber, B. Kaufmann, G. Reyher, A. Dörnen, O. Gfrörer, S.-J. Im, and A. Hangleiter, Sol. State Electronics, in press.
2. M.H. Nazare, P.W. Mason, G.D. Watkins, and H. Kanda, Phys. Rev. B **51**, 16741 (1995).
3. R. Dingle, D.D. Sell, S.E. Stokowski, and M. Ilegems, Phys. Rev. B **4**, 1211 (1971).
4. R. Dingle and R. Ilegems, Sol. Stat Commun. **9**, 175 (1971).
5. E.R. Glaser, T.A. Kennedy, K. Doverspike, L.B. Rowland, D.K.Gaskill, J.A. Freitas, M. Asaaf-Khan, D.T. Olson, J.N. Kuznia, and W.K. Wickenden, Phys. Rev. B **51**, 13326 (1995).
6. F.K. Koschnick, J.-M. Spaeth, E.R. Glaser, K. Doverspike, L.B. Rowland, D.K. Gaskill, and D.K. Wickenden, Mat. Sci. Forum **196-201**, 37 (1995).
7. U. Kaufmann, M. Kunzer, C. Merz, I. Akasaki, and H. Amano, in *Gallium Nitride and Related Materials*, eds. F.A. Ponce, R.D. Dupuis, S.Nakamura, and J.A. Edmond, (Pittsburgh: Materials Research Soc. Symp. Proc. No.395) p. 633 (1996).
8. D.M. Hoffmann, D. Kovalev, G. Steude, D. Volm, B.K. Meyer, C. Xavier, T. Monteiro, E. Pereira, E.N. Mokov, H. Amano, and A. Akasaki, in *Gallium Nitride and Related Materials*,

eds. F.A. Ponce, R.D. Dupuis, S.Nakamura, and J.A. Edmond, (Pittsburgh: Materials Research Soc. Symp. Proc. No.395), p. 619 (1996).
9. P.W. Mason, A. Dörnen, V. Härle, F. Scholz, and G.D.Watkins, in *III-V Nitrides*, eds. F.A. Ponce, T.D. Moustakas, I. Akasaki, and B.A. Monemar, (Pittsburgh: Materials Research Society Symp. Proc. No. 449), p. 793 (1997).
10. M. Linde, S.J. Uftring, G.D. Watkins, V. Härle, and F. Scholz, Phys. Rev. **55**, R10177 (1997).
11. G.A. Slack and T.F.McNelly, J. Crystal Growth **42**, 560 (1977).The sample we refer to here is the higher purity sample listed as W-154 in the above reference.
12. M. Honda, K. Atobe, N. Fukuoka, M. Okada, and Masuo Nakagawa, Jap. J. Appl. Phys. **29**, L652 (1990).

Materials Science Forum Vols. 258-263 (1997) pp. 1093-1098

ELECTRICAL AND OPTICAL CHARACTERIZATION OF DEFECTS IN GaN GENERATED BY ION IMPLANTATION

D. Haase, M. Burkard, M. Schmid, A. Dörnen, H. Schweizer, H. Bolay, F. Scholz

4. Physikalisches Institut, Universität Stuttgart, 70550 Stuttgart, Germany

Keywords: GaN, implantation, DLTS, PL

Abstract. Radiation damage of n-GaN by ion implantation is studied in this paper. Deep level transient spectroscopy (DLTS), supported by capacitance voltage (CV) and Hall analysis as well as photoluminescence spectroscopy (PL) were performed to investigate deep levels. The samples were analyzed as-implanted and after implantation with subsequent rapid thermal annealing (RTA). To generate radiation damage in GaN we implanted the noble gas atom neon and the intrinsic atoms nitrogen and gallium. The investigation of GaN implanted with the group I, II and IV elements potassium, magnesium, and carbon was motivated by the search for typical fingerprints in DLTS and optical spectra to identify deep levels according to impurities.

Introduction

Gallium nitride has recovered great interest in research and development of opto-electronic devices and materials since Akasaki et al. [1] showed that p-type doping is achievable. The direct bandgap energy of $E_G = 3.4$ eV at room temperature allows the realization of blue-light-emitting devices [2]. Although the development of devices for optical and electrical applications achieves excellent success, little is known about impurity and defect levels in the band gap and their origin.

To investigate the defect levels due to intrinsic defects and impurities we studied the effects of N, Ne, Ga and K ion implantation in n-type GaN. The samples were analyzed by Hall measurements utilizing van der Pauw geometry. Photoluminescence spectroscopy (PL) was performed in a liquid helium cryostat, excitation was obtained by an Ar gas laser (emission line 300nm at 50mW). Deep level transient spectroscopy (DLTS) was performed with a commercial PO-LARON DL 4600 equipment. All DLTS spectra shown in this paper were recorded with the rate window set to 200/s.

Implantation of the different ions was performed with energies between 270 and 320 keV and ion doses between $I = 1.1 \cdot 10^{10}$ cm^{-2} and $I = 1 \cdot 10^{15}$ cm^{-2}. The beam direction was shifted 7° out of the [0001] direction for all samples to avoid channelling. During rapid thermal annealing (RTA) the samples were covered by a silicon wafer to form proximity caps. Schottky and ohmic contacts were fabricated as published by Hacke et al. [3]. To ensure a reliable probe contact to the measurement equipment all samples were fixed on a submount and the contacts were bonded with Au wires. The performance of the Schottky contacts (max. reverse bias $U_R < -10$ V, reverse current density $I_R < 7 \cdot 10^{-4}$ A/cm^2, threshold voltages $U_{th} \approx +0.5$ V) was almost identical for all samples.

The samples were grown by metal-organic vapour-phase epitaxy (MOVPE) on sapphire substrate oriented along the [0001] direction using an AlN buffer. The growth parameters were $T_G = 1000$°C and $P_G = 100$ mbar. The as-grown samples were characterized by X-ray diffraction and photoluminescence (PL) measurements. Both methods indicate a good crystal quality. Full width at half maximum (FWHM) of X-ray diffraction was between 50 and 100 arcsec. The carrier concentration of the as-grown samples was between $5 \cdot 10^{16}$cm^{-3} and $3 \cdot 10^{17}$cm^{-3}. The electron mobility at room temperature was found to be between 70 and 300 Vs/cm^2. The intense PL signal of the dominant excitonic luminescence at T=4.2 K showed a FWHM between 3.6 meV and 5 meV.

Implantation of N, Ga and Ne

The typical DLTS spectrum of an as-grown MOCVD n-type GaN sample is shown on bottom of Fig. 1. The defect level D2 is common to all samples which have good crystal quality in terms of PL FWHM, carrier concentration and mobility. The level D1 is in low concentration common to most of the good quality samples, the parameters (table 1) are comparable to those of E1 in Ref. [3] and E2 in Ref. [4]. Levels D4 and D5 were not yet published to our knowledge, they are only detectable in some samples.
The DLTS results of GaN implanted with N, Ne and Ga with identical doses of I=10^{11} cm^{-2} are shown in Fig. 1. Implantation of N introduces level D3 which dominates the DLTS spectra. After Ne implantation a DLTS spectra is detected which is a superposition of D2 and D3. With Ga as the implantation species the DLTS spectra shows D2 clearly as a shoulder of level D3. Level D1 is reduced in all as-implanted samples.
Figure 2 shows the spectra after RTA at 900°C for 60 s of implanted and as-grown samples. For defect level D1 the strong effect of RTA in all implanted samples is obvious, for the N- and Ga-implanted samples D1 is the dominating level after RTA. Level D2 shows little reaction on RTA for the N- and Ne-implanted samples, but is reduced after RTA of the Ga-implanted sample. Level D3 disappears after RTA in case of the N and Ne implanted samples. For the Ga-implanted sample D3 remains with reduced concentration. The defect level labelled C is detectable in the annealed Ne- and Ga-implanted samples. The parameters of all levels are given in Table 1.

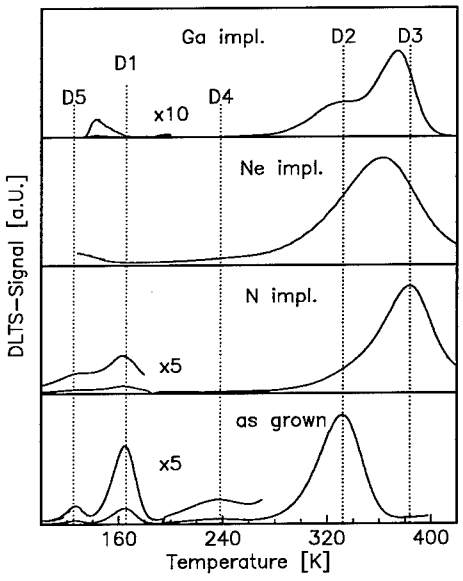

Figure 1: *DLTS spectra of MOCVD GaN after growth and subsequently implantation of N, Ne and Ga. Implantation doses were I=10^{11} cm^{-2}. All DLTS spectra shown here and in following figures are recorded with a rate window of 200/s .*

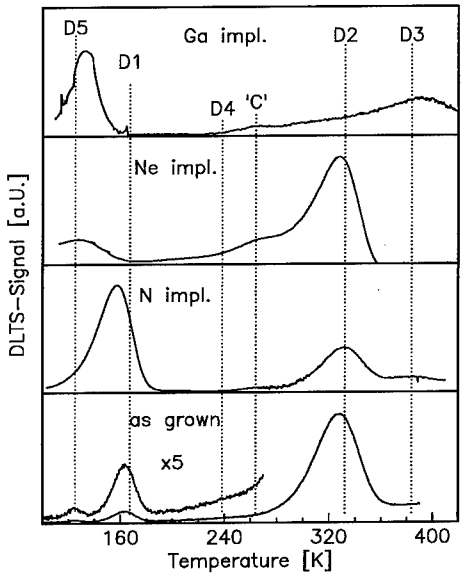

Figure 2: *DLTS spectra of the samples of Fig. 1 analyzed after RTA at 900°C for 60s. Arrhenius plots of defect levels D1 to D5 are shown in Fig. 5, parameters are given in table 1.*

Implantation of K and C

After implantation of K and C, the DLTS spectra shown in Fig. 3 and 4 resemble the spectra of the as-implanted samples shown in Fig. 1. The spectra are dominated by D3. After RTA the defect C shows up more clearly in the carbon-implanted sample than in the other samples after RTA. For the annealed K-implanted sample, DLTS spectra are depicted in Fig. 4, the defect level K is detectable. We note, that the K-implanted sample is not annealed like the samples in Fig. 2 and 3, therefore the resistance against annealing of D3 in the K-implanted sample is not necessarily comparable to the other annealed samples. The parameters of defect levels C and K are given in Fig. 6 and Table 1.

Discussion

The results shown in Fig. 1 to 4 represent typical features of the defect levels D1 to D5. The levels D1, D4 and D5 are not detectable in all as-grown samples, their concentration varies significantly. If levels D1 and D5 are present in the as-grown samples, their concentrations increase after implantation and subsequent annealing. This behaviour would be expected for an impurity, which is partially activated during growth and further activated after RTA. On the other hand D1 and D5 are detected in higher concentration after implantation and subsequent annealing compared to exclusively annealed samples. The enhancement of D1 (and D5) after implantation and subsequent RTA is most effective for the C and N implantation. It seems to be reasonable that a correlation of an impurity and radiation damage is responsible for the behaviour of D1. For example, the higher concentration of vacancies can increase the probability of the recombination of an impurity interstitial. Defect D2 is omnipresent in the good quality GaN samples. It is less affected by annealing of the as-grown samples. Level D2 is much less reduced in the annealed and implanted samples than D3 for the N and Ne implantation. The

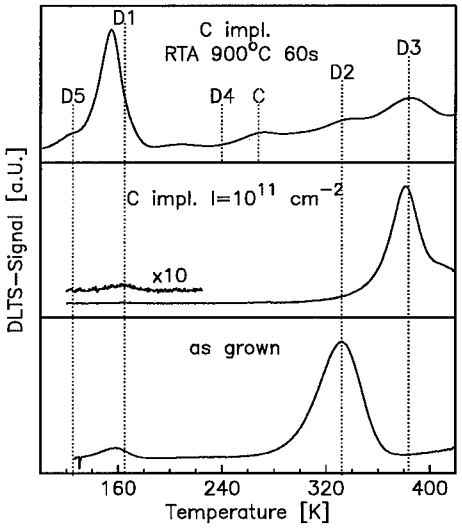

Figure 3: *DLTS spectra of as-grown, carbon implanted and subsequent annealed GaN. Dose 10^{11} cm^{-2} . RTA 900°C, 60s. Arrhenius plot see Fig. 6 .*

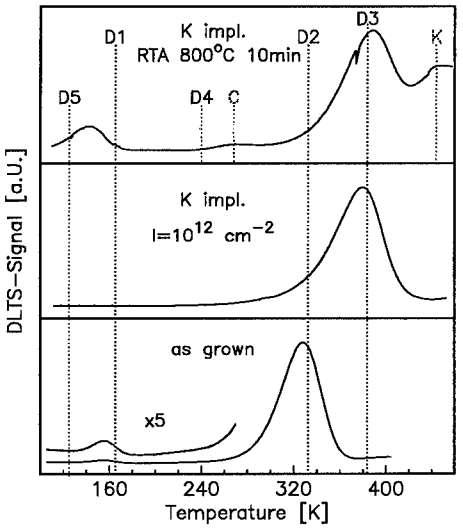

Figure 4: *DLTS spectra of as-grown, potassium implanted and subsequent annealed GaN. Dose 10^{12} cm^{-2} . RTA 800°C, 10min. Arrhenius plot see Fig. 6 .*

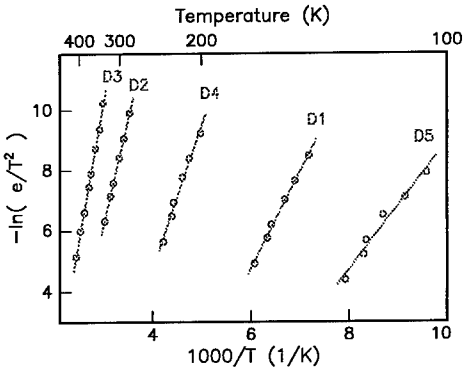

Figure 5: *Arrhenius plots of the rate window series of defect levels D1 to D5. Fit-parameters see table 1.*

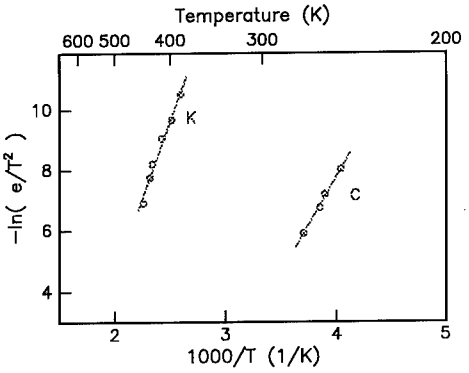

Figure 6: *Arrhenius plot of rate window series of traps C and K. Fit-parameters see table 1.*

parameters for D2 resemble those given for E2 in Ref. [3], where the N antisite is suggested as explanation of D2.

The annealed Ga-implanted sample shows both D2 and D3 significantly reduced. This could be due to the fact that Ga has a much higher atomic mass. This causes a shorter penetration path during implantation and therefore the generation of cluster defects is more probable. This should lead to a different defect distribution. Further investigations are scheduled to clear this point.

Defect D3, which was never detected in the as-grown MOCVD samples but is probably identical with E3 in as-grown HVPE GaN Ref. [3], shows up after implantation of any element in our experiments. Although the temperature corresponding to the maximum DLTS signal (T_{max}) does not change much, a certain range of evaluated trap energies $E_T(D3)$ from sample to sample is evident. Values between $E_T(D3)$=640 meV up to $E_T(D3)$= 840 meV have been obtained from Arrhenius plots for different samples. Due to the similarity in their behaviour, these defects were all labelled D3. It seems reasonable that a family of D3-type defects exists, because the variant values differ more than even very large error assumptions. In Fig. 5 only one representative data set for a D3-related level is included to preserve the clarity of the plot. In comparison the fluctuations of $E_T(D2)$ of level D2 evaluated from different samples are with ±15 meV well

Table I: Parameters of defect levels reported in this paper

	D1	D2	D3	D4	D5	C	K
T_{max}[K] (rw 200/s) (1)	165	335	383	238	125	270	440
E_C-E_T [meV] (2)	270	603	770	412	180	550	881
σ [10^{-15} cm^2] (3)	4	5	40	4	0.3	30	20

(1) T_{max}: Temperature of maximum DLTS signal, rw: rate window=200/s

(2) Error for the values of E_T is assumed to be ±5%

(3) The capture cross sections σ are assumed to be temperature independent

within the 5% error assumed for the energy values. The efficient generation and the strongly decreasing concentration after annealing of D3 in the implanted samples are good arguments to identify them as point-defect related as suggested in Ref. [6] or traps defined by a simple point defect complex. The resistance against annealing of D3 in the K-implanted sample is not necessarily comparable to the other samples because of the lower RTA temperature, further investigations are scheduled to clear this point.
The correlation of defect level C after carbon-implantation and annealing is not that clear like the correlation of defect level K after potassium implantation. Trap C is detectable in various implanted and annealed samples, but at highest concentration in the annealed carbon-implanted sample. Trap K is only detected in the annealed potassium-implanted sample.

Implantation of Mg

Implantation of Mg in GaN has been reported to achieve p-type GaN [7]. The competition between active Mg on the Ga lattice site and the stabalizing of the nitrogen vacancy V_N after implantation due to p-type conditions [8] makes it interesting to investigate lower annealing temperatures than in Ref. [7]. Our experiment did not lead to p-type conductivity, the samples remained clearly n-type in Hall measurements and optical spectra after implantation and annealing.
For the sample with the lower dose of I=10^{13} cm^{-2}, spectra depicted left in Fig. 7, a significant change in the intensities of the yellow luminescence band and the donor-acceptor-pair transition is observable. Their intensities increase while the excitonic peak decreases. The excitonic PL does not recover completely after the annealing steps.
A distinctive change in the PL spectra is the result of the Mg implantation at the higher dose of I=10^{15} cm^{-2}, the spectra are depicted in the middle section of Fig. 7. The yellow luminescence band decreases after implantation and vanishes completely after RTA. In the band edge region the excitonic peak vanishes and is replaced by a intense PL peak labelled L3 and a weak peak labelled L4. The peak L3 is found at 3.364 eV with a FWHM of 6.36 meV. After annealing at

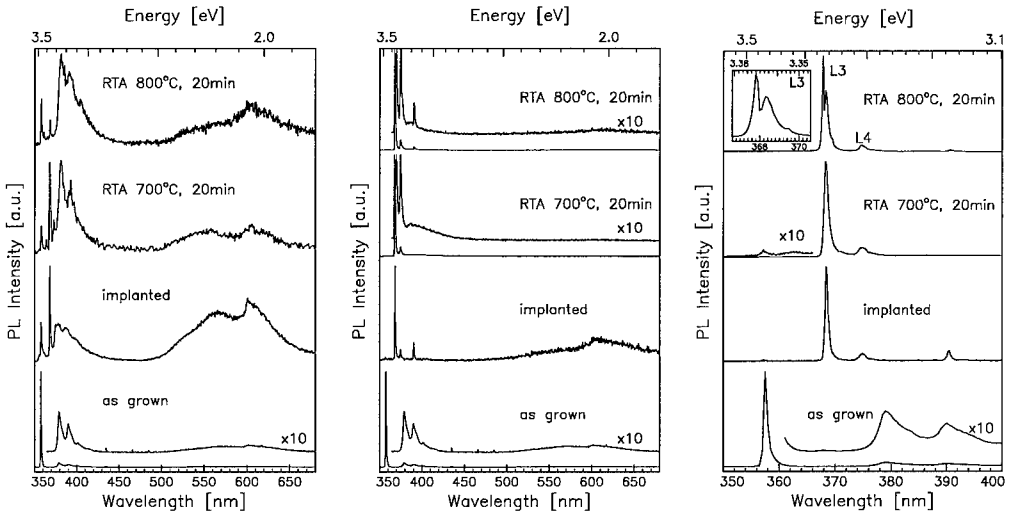

Figure 7: PL Mg implantation series, all figures from bottom to top: as grown, implanted, impl. + annealed 700°C, 20min, impl. +annealed 800°C, 20min. Left: dose 10^{13} cm^{-2}. Middle: dose 10^{15} cm^{-2}. Right: near band edge PL, dose 10^{15} cm^{-2}. All spectra T=4.2 K

800°C this peak develops a three fold substructure. This structure shows an energy difference of 14 meV between the dominant line and the least intense peak. The peak energy of L3 is close to that of a frequently found PL line, e.g. Ref. [9], and close to the peak L3 reported by Götz et al. [5]. In Ref. [5] L3 (and L4) are found only in Mg-doped or Mg-contaminated GaN samples. Wetzel et al.[10] identified this peak as a deeply bound exciton. This line shows up after implantation of Mg in MOCVD GaN, but it has to be pointed out, that Ga implantation has also lead to a PL peak close to the energy of L3 [11]. This can be a hint that at least L3 is a PL peak related to radiation induced defects which might be comparable to the extended defects Wetzel et al. suggested to explain the strongly localized exciton I3 in Ref. [10]. It can not be decided weather the three fold structure is correlated with Mg.

Conclusion

As we have shown in this paper, implantation and annealing of GaN with different chemical elements leads to distinctive changes in DLTS spectra. Intrinsic, radiation induced and impurity related levels have been identified and its parameters have been evaluated. D1, D4 and D5 have been discussed as impurity related traps, for D2 and D3 arguments were found which make it reasonable to identify these traps as point defect related. Carbon and potassium implantation introduce new traps which were characterized in this paper. The results of Mg implantation and annealing at low temperatures have been presented. The origin of PL lines which are related to the radiation and annealing treatment have been investigated.

We acknowledge Prof. M. H. Pilkuhn for encouraging our work on defects in GaN.

References

[1] H. Amano, M. Kito, K. Hiramatsu, I. Akasaki, Jpn. J. Appl. Phys. **28** L2112-14 (1989)

[2] S. Nakamura, M. Senoh, T. Mukai, Jpn. J. Appl. Phys. **32** L8-L11 (1993)

[3] P. Hacke, T. Detchprohm, K. Hiramatsu, N. Sawaki, J. Appl. Phys. **76**, 304 (1994)

[4] W. Götz, N. M. Johnson, H. Amano, I. Akasaki, Appl. Phys. Lett. **65**, 463 (1994)

[5] W. Götz, N. M. Johnson, J. Walker, D. P. Bour, R. A. Street Appl. Phys. Lett. **68**, 667 (1996)

[6] D. Haase, M. Schmid, W. Kürner, A. Dörnen, M. Burkard, H. Schweizer, F. Scholz Appl. Phys. Lett. **69**, 2525 (1996)

[7] S. J. Pearton, C. B. Vartuli,J. C. Zolper, C. Yuan, R. A. Stall, Appl. Phys. Lett. **67**, 1435 (1995)

[8] J. Neugebauer, C. G. Van de Walle, Phys. Rev. B **50**, 8067 (1994)

[9] J. I. Pankove, J. E. Berkeyheiser, H. P. Maruska, J. Wittke, Solid State Commun. **8**, 1051 (1970)

[10] C. Wetzel, S. Fischer, J. Kruger, and E. E. Haller, R. J. Molnar, T. D. Moustakas, E. N. Mokhov P. G. Baranov Appl. Phys. Lett. **68**, 2556 (1996)

[11] to be published

Materials Science Forum Vols. 258-263 (1997) pp. 1099-1104

IMPLANTATION DOPING AND HYDROGEN PASSIVATION OF GaN

A. Burchard [1], M. Deicher [1], D. Forkel-Wirth [2], E.E. Haller [3], R. Magerle [1], A. Prospero [1], A. Stötzler [1] and the ISOLDE-Collaboration [2]

[1] Fakultät für Physik, Universität Konstanz, D-78457 Konstanz, Germany
[2] CERN / PPE, CH-1211 Geneva 23, Switzerland
[3] Dept. of Materials Science, University of California Berkeley, Berkeley CA 94270, U.S.A.

Keywords: GaN, hydrogen passivation, Cd acceptors, ion implantation, PAC spectroscopy

Abstract. The possibility of p-type doping of GaN with Cd by ion implantation has been studied using the perturbed $\gamma\gamma$ angular correlation spectroscopy (PAC). To determine the lattice site of the implanted ions and to discriminate between defects created by the heavy ion implantation and their interaction with implanted Cd-acceptors, both the group-III atom ^{111}In and the group-II acceptor ^{111m}Cd have been implanted. The annealing of the implantation damage has been studied up to annealing temperatures of 1300 K. We also report on the atomic-scale observation of the formation of Cd-H pairs in GaN using the radioactive acceptor ^{111m}Cd. This pair formation requires the electrical activation of the implanted acceptors.

Introduction

Ion implantation into crystalline compound semiconductors is one of the main methods for selective introduction of dopant atoms. It offers control on concentration, depth and lateral distribution of the dopants. However, the use of ion implantation is always accompanied by undesirable structural damage to the crystal. The initial damage level depends on many factors such as substrate temperature, mass and energy of the implanted ion, dose and dose rate. Even under optimum implantation conditions thermal annealing is necessary to achieve electrical activation of the implanted dopant atoms. The understanding and control of the implantation induced defects and their interaction during the annealing process may become crucial for the realization of advanced devices based on GaN. Most of the work published on ion implantation into GaN [1,2] deal with the electrical or optical characterization of the implants but very little is known on the nature of the created damage and its evolution during annealing. It has been shown that GaN behaves significantly different from other III-V semiconductors: Its threshold for ion beam induced amorphization is very high (about 10^{16} cm^{-2}) [3] and its high melting point of about 2800 K makes it difficult to remove completely the implantation damage at temperatures achievable with standard furnaces or rapid thermal annealing equipment. It has been shown by Rutherford backscattering measurements [4] that even after annealing at 1370 K a significant amount of damage remains in the material. This high thermal stability of defects is also reflected by the high thermal stability of implanted impurity ions [5].
In this work we report on the observation of implantation induced defects using the perturbed $\gamma\gamma$ angular correlation spectroscopy (PAC) [6]. This technique probes the immediate vicinity of a suitable radioactive dopant. To determine the lattice site of the implanted ions and to discriminate between defects created within the own defect cascade by the heavy ion implantation and their possible interaction with implanted Cd-acceptors, both the group-III probe atom ^{111}In and the group-II acceptor ^{111m}Cd have been implanted. We also report on the atomic-scale observation by PAC of the formation of Cd-H pairs in GaN using the radioactive acceptor ^{111m}Cd. The sensitivity of PAC for detecting dopant-hydrogen interaction has been demonstrated for many III-V semiconductors [7].

Experimental details

N-type GaN layers grown on sapphire have been implanted either with ^{111}In (E = 350 keV, 3×10^{12} cm^{-2}) at the Konstanz ion implanter or with ^{111m}Cd ions at the on-line mass separator ISOLDE at CERN (E = 60 keV, 5×10^{11} cm^{-2}). The evolution of the implantation induced damage has been followed by annealing the samples for 600 s at increasing temperatures up to 1300 K in a closed quartz ampoule under N_2 atmosphere. An additional set of samples implanted with ^{111m}Cd and annealed at 1100 K was loaded with hydrogen at 323 K by using a low energy implanter that provides a mass separated H^+ beam with an energy of 100 eV and doses up to 1×10^{16} cm^{-2}. This procedure allows a quantitative control of the introduced amount of H and avoids the contamination by other impurity atoms and the creation of native lattice defects.

The immediate neighborhood of the radioactive probe atoms was monitored with the perturbed $\gamma\gamma$ angular correlation spectroscopy (PAC) [6]. The PAC technique is sensitive to electric field gradients (EFG) present at the site of the probe atom, in our case ^{111}In ($t_{1/2}$ = 2.8 days) or ^{111m}Cd ($t_{1/2}$ = 48 min), both decaying via the same intermediate nuclear state of ^{111}Cd. An EFG causes a threefold hyperfine splitting of an excited state of the ^{111}Cd nuclei populated either via the electron capture decay of ^{111}In to ^{111}Cd or by the γ decay of the isomeric state ^{111m}Cd. This splitting is observed by PAC and is characteristic for the presence or absence of defects in the immediate neighborhood of the probe atom. The EFG is described by the quadrupole coupling constant $\nu_Q = eV_{zz}/h$ (Q denotes the nuclear quadrupole moment and V_{zz} the largest component of the diagonalized EFG tensor) and the asymmetry parameter η. These quantities are unique for specific defects and both, the symmetry of a formed probe-atom-defect complex and the fraction of probe atoms involved in this complex, can be determined from the characteristic modulation of the PAC spectrum R(t) generated by this hyperfine interaction. A possible damping of the observed modulation due to the superposition of many different EFGs caused by the presence of many different defect configurations is described by the width $\Delta\nu_Q$ assuming a Lorentzian distribution of these EFGs. The short half-life of ^{111m}Cd allows to record only two PAC spectra per implanted sample.

Results and discussion

Implantation induced defects

Isoelectronic group-III atoms like ^{111}In should occupy substitutional Ga sites in GaN and should have no attractive interaction to migrating defects. So PAC measurements with ^{111}In probe the annealing behavior of defects created by its own collision cascade. Figure 1 shows a series of PAC spectra recorded after ^{111}In implantation with an energy of 350 keV (dose 3×10^{12} cm^{-2}) at room temperature (a) and after annealing at 1100 K (b) and 1300 K (c). All spectra have been recorded with the c-axis of the GaN layer oriented in the detector plane with an angle of 45 degrees between two detectors. Immediately after the implantation at room temperature all probe atoms are surrounded by a high defect concentration which is reflected by the superposition of many different EFGs leading to a strong damping of the spectrum (Fig. 1a). Annealing at 1100 K (Fig. 1b) shows a partial recovery of the damage. Now 50% of the probe atoms are exposed to an EFG with ν_Q = 6.0(5) MHz which exhibits only a small damping ($\Delta\nu_Q$ = 0.2 MHz). This EFG is axially symmetric (η = 0) and its symmetry axis is oriented along the c-axis of the hexagonal wurtzite structure of GaN. Both the symmetry and the small value of this EFG favors its association with the intrinsic EFG detected by probe atoms located on Ga lattice sites with a defect free nearest surrounding. Annealing at temperatures above 1200 K changes the situation once more. Now the fraction of probe atoms with defect free surroundings decreases and new defect structures are building up. These defects are characterized by a broad EFG distribution which is centered at much smaller values than the one observed at annealing temperatures below 900 K.

In Fig. 2, these results are summarized. Annealing above 400 K leads to an increase of the fraction of ^{111}In atoms with no defects in the immediate neighborhood (Fig. 2a, closed circles) which is reflected by the accompanying reduction of the fraction residing in highly defective surroundings (Fig. 2a, open circles). At 750 K, about 65% of the probe atoms observe the intrinsic lattice EFG

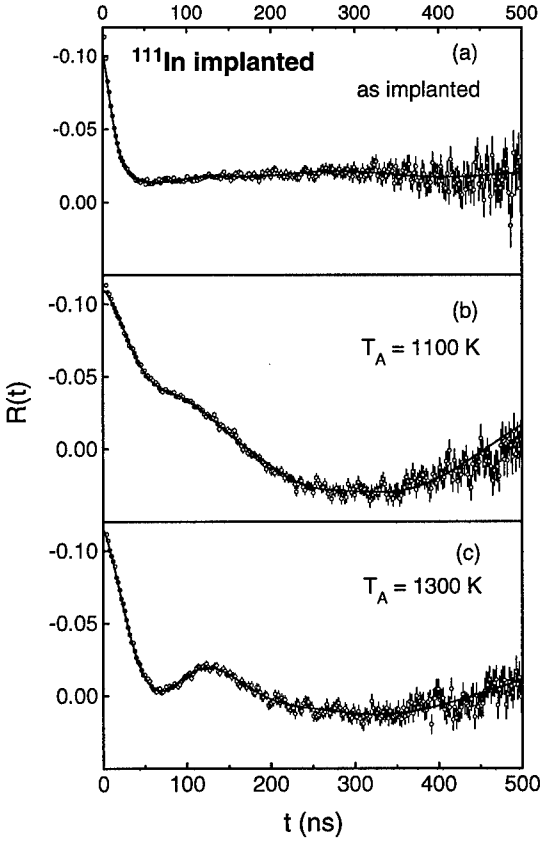

Fig. 1: PAC spectra of GaN implanted with ^{111}In (350 keV, 3×10^{12} cm^{-2}) at 295 K (a), after annealing at 1100 K (b) and 1300 K (c), respectively.

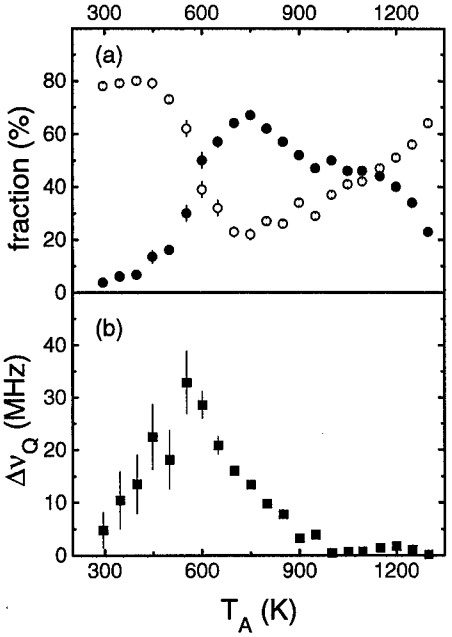

Fig. 2: (a) Fractions of ^{111}In atoms implanted into GaN (350 keV, 3×10^{12} cm^{-2}) as function of the annealing temperature corresponding to two different local environments of the probe atoms: ^{111}In atoms residing within a highly defective region (open circles) and ^{111}In atoms with a defect free neigborhood (solid circles). ((b) Width $\Delta\nu_Q$ of EFG around the EFG caused by the wurtzite structure of GaN at the ^{111}In / ^{111}Cd atoms residing on Ga lattice sites as function of the annealing temperature.

but the rather broad distribution of $\Delta\nu_Q$ = 20 MHz indicates the presence of more distant defects. As shown in Fig. 2b, the width of this distribution becomes more narrow with increasing annealing temperatures indicating the removal of defects in the vicinity of the probe atoms. Annealing between 950 K and 1200 K leads to 50% of the ^{111}In atoms on almost unperturbed lattice sites characterized by a minimum of the damping of $\Delta\nu_Q$ = 0.5 MHz associated with ν_Q = 6 MHz. This small residual damping may be caused by the high dislocation density present in the layer due to the large lattice mismatch of about 12% between GaN and sapphire [8]. In the same range of annealing temperatures a significant electrical activation of implanted Si and Mg dopants has been observed [10]. The fact that at these temperatures 50% of the implanted species still reside in highly perturbed surroundings is consistent with results obtained by Rutherford backscattering measurements and XTM images [4] of Si implanted GaN which both show the presence of implantation induced defects and an electrical activation of about 50% of the dopants at these annealing temperatures. On the other hand, using the emission channeling technique it has been shown [9] that after ^{111}In implantation at room temperature already about 90% of the implanted ions occupy substitutional sites with almost no displacement (< 0.01 nm) of the ^{111}In atoms caused

by the presence of defects in the neighborhood of the probe atoms. This fraction stays unchanged for annealing temperatures up to 1300 K. The PAC results show, that annealing above 1200 K leads to a reduction of the number of ^{111}In atoms on defect free sites to about 25% at 1300 K. This corresponds to the formation of defects in the neighborhood of the probe atoms with a different PAC signature as the one observed below 1200 K. These defects are characterized by a broad distribution of EFGs centered around ν_Q = 22(2) MHz which in contrast to the defect related EFGs observed below 1250 K show a symmetry along the c-axis of the crystal. The implanted probe atoms are located in a mean depth of about 80 nm and the observed defects may be related to the onset of N loss from the near surface region at annealing temperatures around 1200 K which has been shown to drastically reduce the optical activation of implanted Zn impurities [11].

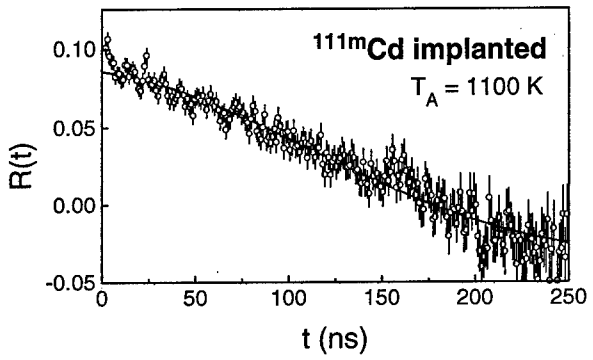

Fig. 3: PAC spectrum of a GaN layer implanted with ^{111m}Cd (60 keV, 5 × 10^{11} cm^{-2}) and annealed at 1100 K.

Figure 3 shows a PAC spectrum after ^{111m}Cd implantation (5×10^{11} cm^{-2}) with 60 keV and annealing at 1100 K. The observed reduction of the R(t) signal with increasing time corresponds to the same slow modulation which has been observed after implantation of ^{111}In and annealing at this temperature. This proves that Cd occupies the same lattice site as In. ^{111}In which is an impurity isoelectronic to Ga should occupy Ga sites in GaN. The similarity between this spectrum and the one recorded at the same annealing temperature with ^{111}In shows that no defect complexes with lattice defects are formed due to a possible attractive interaction with the acceptor ^{111}Cd.

Cd-H interaction

In a previous work [12] we have shown, that hydrogen forms Cd-H pairs in GaN and we determined the stability of these pairs which was in good agreement with theoretical calculations [13,14]. In Fig. 4a, a PAC spectrum after H implantation at 323 K (1×10^{15} cm^{-2}) with 100 eV into GaN implanted with ^{111m}Cd and annealed at 1100K is shown. The details of the observed modulation can be seen in the Fourier transform of the same spectrum (Fig. 4b). The two observed frequency triplets correspond to two different configurations of Cd-H pairs which both possess axial symmetry (η = 0.0(1)) and are characterized by ν_Q = 360(2) MHz and ν_Q = 572(2) MHz, respectively. The observed amplitudes correspond to a fraction Cd acceptors involved in these defects of about 30%. Varying the implanted hydrogen dose between 3×10^{14} cm^{-2} and 1×10^{16} cm^{-2} always creates the same defects and no other complexes with a fraction larger than 2% are formed. This strongly indicates that the observed defects involve only one hydrogen atom, i.e., electrically neutral Cd-H pairs are formed. Moreover, this variation of the hydrogen dose over almost two orders of magnitude always results in the same concentration of Cd-H pairs involving about 30% of the Cd acceptors. This is in contrast to GaAs and InP where more than 80% of the Cd acceptors form Cd-H pairs under similar conditions [7]. Because the acceptor-hydrogen pair formation is driven by the Coulombic attraction between the two species, the electrical activity of the implanted ^{111m}Cd acceptors is a pre-

requisite for the pair formation. This activation requires for the implanted species to occupy the correct lattice sites and at least the immediate neighborhood to be free of defects. As has been discussed in the previous chapter, for the annealing temperatures and conditions used in this work these conditions can only be fulfilled for about 50% of the implanted In or Cd ions.

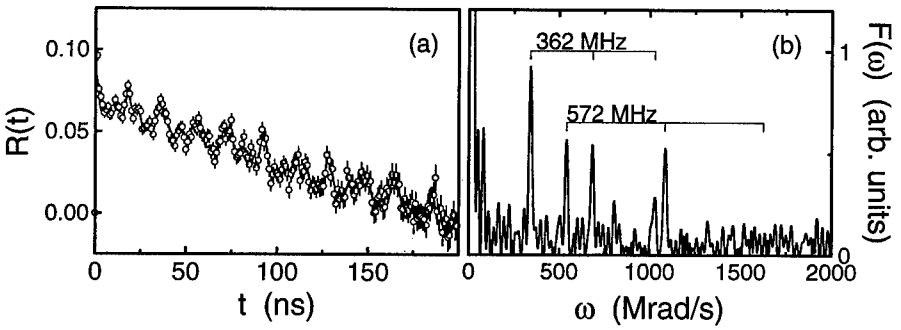

Fig. 4: (a) PAC spectrum of a GaN layer implanted with ^{111m}Cd (60 keV, 5 x 10^{11} cm^{-2}) and annealed at 1100 K after H implantation (100 eV, 1x10^{15} cm^{-2}) at 323 K. The corresponding Fourier transform (b) shows the formation of two different Cd-H configurations.

Conclusions

In conclusion, the evolution of the defects created by implantation of In and Cd ions into GaN has been studied up to annealing temperatures of 1300 K. It has been shown on an atomic scale, that up to 50% of the implanted species occupy lattice sites with a defect free environment after annealing between 950 K and 1200 K. The electrical activity of Cd acceptors implanted under these conditions has been confirmed by the observation of the formation of a large number Cd-H pairs. Increasing the annealing temperatures above 1200 K leads to the build-up of new defects in the neighborhood of the impurity atoms which may be correlated to the onset of N loss from the surface region of the GaN layer.

Acknowledgements

We acknowledge the Hewlett-Packard Optoelectronics Division for supplying the GaN samples. This work has been supported by the Bundesminister für Bildung, Wissenschaft, Forschung und Technologie under Grant No. 03-RE4KO1-5.

References

1. J.C. Zolper, S.J. Pearton, J.S. Williams, H.H. Tan, R.J. Karlicek and R.A. Stall, Mat. Res. Soc. Symp. Proc. **449**, 981 (1997).
2. J.C. Zolper and R.J. Shul, MRS Bulletin **22(2)**, 36 (1997).
3. H.H. Tan, J.S. Williams, J. Zou, D.J.H. Cockayne, S.J. Pearton and R.A. Stall, Appl. Phys. Lett. **69**, 2364 (1996).
4. J.C. Zolper, H.H. Tan, J.S. Williams, J. Zou, D.J.H. Cockayne, S.J. Pearton, M. Hagerott Crawford and R.F. Karlicek, Appl. Phys. Lett. **70**, 2729 (1997).
5. R.G. Wilson, S.J. Pearton, C.R. Abernathy and J.M. Zaveda, Appl. Phys. Lett. **66**, 2238 (1995).
6. Th. Wichert, N. Achtziger, H. Metzner, and R. Sielemann, in: *Hyperfine Interactions of Defects in Semiconductors*, ed. G. Langouche (Elsevier, Amsterdam, 1992) p. 77.
7. M. Deicher and W. Pfeiffer, in: S.J. Pearton (ed.), *Hydrogen in Compound Semiconductors*, (Materials Science Forum Vol. **148-149**, Trans Tech Publications, Zürich, 1994), p. 481.

8. S.D. Lester, F.A. Ponce, M.G. Craford and D.A. Steigerwald, Appl. Phys. Lett. **66**, 1249 (1995).
9. C. Ronning, M. Dalmer, M. Deicher, M. Restle, M.D. Bremser, R.F. Davis and H. Hofsäss, in: *Gallium Nitride and Related Materials II*, ed. C.R. Abernathy, H. Armano and J.C. Zolper (Mat. Res. Soc. Symp. Proc. Vol. **468**, Pittsburgh, 1997) in press.
10. S.J. Pearton, C.R. Abernathy, C.B. Vartuli, J.C. Zolper, C. Yuan and R.A. Stall, Appl. Phys. Lett. **67**, 2435 (1995).
11. A. Pelzmann, S. Strite, A. Dommann, C. Kirchner, M. Kamp, K.J. Ebeling and A. Nazzal, MRS Internet J. Nitride Semicond. Res. **2** (4) (1997).
12. A. Burchard, M. Deicher, D. Forkel-Wirth, E.E. Haller, R. Magerle, A. Prospero and A. Stötzler, in: *III-V Nitrides*, ed. F.A. Ponce, T.D. Moustakas, I. Akasaki and B.A. Monemar (Mat. Res. Soc. Symp. Proc. Vol. **449**, Pittsburgh, 1997) **p. 961**
13. J. Neugebauer and C.G. Van de Walle, Phys. Rev. Lett. **75**, 4452 (1995).
14. J. Neugebauer and C.G. Van de Walle, Appl. Phys. Lett. **68**, 1829 (1996).

Materials Science Forum Vols. 258-263 (1997) pp. 1105-1112

ELECTRICALLY AND OPTICALLY DETECTED MAGNETIC RESONANCE IN GaN-BASED LEDS

W.E. Carlos
Naval Research Laboratory, Washington, D.C. 20375, USA

KEYWORDS: Gallium Nitride, Magnetic Resonance, EDMR, ODMR, LED

ABSTRACT

Electrically detected magnetic resonance (EDMR) has emerged as a highly sensitive probe of defects in semiconductor device structures. In this work EDMR is combined with electrically excited, optically detected magnetic resonance (i.e., electroluminescence detected magnetic resonance - ELDMR), and optical excitation and quenching of EDMR to study and compare radiative and non-radiative recombination in GaN-based single quantum well (SQW) LEDs. The dominant feature detected by any of these techniques is a broad resonance ($\Delta B \approx 13$ mT) at $g \approx 2.01$. ELDMR measurements show that, depending on bias, this defect is predominately associated with either an increase or a decrease in electroluminescence at resonance while our EDMR measurements show that this resonance is associated with an increase in current at resonance. This center is also observed as photocurrent-enhancing resonance and the EDMR can be quenched by optical absorption in the quantum well. It is suggested that this center is associated with a non-radiative recombination path, in parallel with the radiative recombination path and with recombination in the depletion region of a contact. A second resonance, with $g \approx 1.98$ and $\Delta B \approx 7$ mT, is very similar to the deep donors, previously observed in GaN films and is associated with a decrease in both the current and electroluminescence at resonance but is not observed in the optical excitation experiments.

INTRODUCTION

Electro-optic GaN-based devices have a range of promising and, in some cases already partially realized, applications.[1] Advances in materials growth[2] have led to devices such as efficient blue and green light emitting diodes (LEDs).[3,4] Recently, GaN-based LEDs whose electroluminescence (EL) is due to near bandedge emission from a single quantum well (SQW) of undoped InGaN have been introduced.[5] These diodes have more intense, sharper electroluminesence than the earlier double heterostructure (DH) diodes. Multi-quantum well laser diodes are now under development[6] and it can be argued that many of the basic emission and loss mechanisms in the SQW diodes are very similar to those in the laser diodes. However, the details of the luminescence and transport mechanisms are not fully resolved. For example, Perlin and coworkers[7] (based on their observation that the pressure dependence of the emission is much weaker than that of the bandgap) have argued that a localized or bandtail state must be involved in the luminescence process. They have also maintained that the electrical transport mechanism is electron-hole tunneling.[8] Chichibu and coworkers[9] have argued that the luminescence is due to exitons trapped at potential minima in the quantum well, which result from alloy fluctuations in InGaN.

Optical and magnetic resonance spectroscopies have yielded a number of insights into the basic materials properties and defects in the nitrides.[10-15] ESR and ODMR (optically detected magnetic resonance in which changes in photoluminescence are monitored)

have been applied to doped and undoped wurtzite GaN thin films. Several resonances are observed,[12-14] including an effective mass (EM) donor, a deep double donor and Zn- and Mg-related acceptor states (in doped films).

Magnetic resonance techniques based on spin-dependent processes in semiconductor devices are finding increasing application in a number of materials systems. Such techniques are especially well suited to the problem of defects in small device structures in that measurement sensitivity is determined by the density of resonance centers rather the absolute number of centers; furthermore, the measurements are primarily sensitive to defects involved in the electrical and/or optical properties of the device. ELDMR has been applied to organic semiconductor-based[16] and amorphous Si-based[17] LEDs and EDMR has been applied to a number of devices and materials.[18,19] The application of magnetic resonance techniques to the SQW LEDs[20,21] as well as to the DH LEDs[22] have been discussed previously. In previous work on SQW devices[16] two resonances were resolved, one of which was attributed to a deep defect and the other to a somewhat shallower donor. Neither of these resonances was attributed to a defect directly involved in the radiative recombination process but rather to centers involved in nonradiative recombination paths either in parallel or in series with the radiative channel. In a previous paper[21] it was shown that high current stressing could have significant effects on the resonance signals. In this paper previously published results are briefly reviewed and new work comparing results for the blue and green (unstressed) diodes in more detail and exploring the effects of magnetic resonance on photocurrents and the effect of optical absorption on the EDMR signal are presented.

The structure and manufacture of the single quantum well AlGaN/InGaN LEDs used in this work have been discussed in detail in previous publications.[5] These devices are now available commercially in both blue (λ_{peak}=450 nm) and green (λ_{peak}=520 nm) colors. The optically active region is a 2 nm thick layer of undoped $In_xGa_{1-x}N$ (x=0.43 for the green LEDs and x=0.20 for blue LEDs). The magnetic resonance apparatus is based on a Varian E9 X-band (9.25 GHz) ESR spectrometer. Samples were cooled using a liquid helium flow cryostat and current was applied from a constant current source through a ~1 mm diameter coaxial cable. The c-axis of the thin film LED was always perpendicular to the magnetic field and light was extracted or introduced using a quartz light pipe. Optical excitation was accomplished with the blue and green lines (458 nm. - 514 nm.) of an Argon laser. The EL was detected by a UV-enhanced Si photodiode. Electroluminescence spectra were measured using a 0.22 m single grating spectrometer. The magnetic resonance

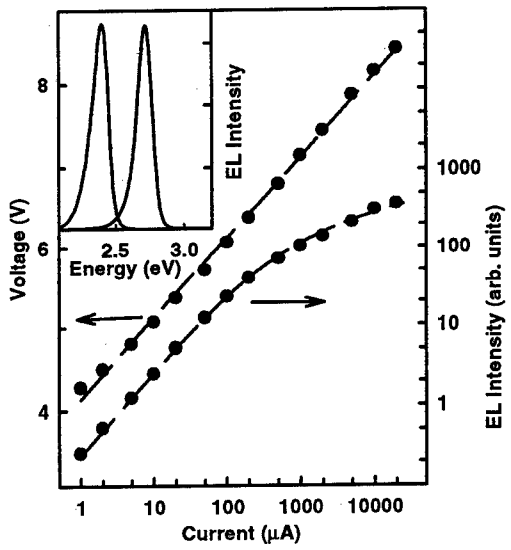

Figure 1. The DC V-I and EL-I characteristics of a green SQW LED. The spectral dependence of the EL for the green (left peak) and blue (right peak) is shown in the inset.

results presented here were obtained by detecting the AC component of the voltage across the sample, the current through it or the EL in phase with magnetic field modulation. (Modulation frequencies were 10 Hz - 10 kHz.) While there are interesting effects which can be observed by detecting the signal in quadrature with the field modulation, the discussion in this paper will be restricted to the low frequency limit in which only the signal in phase with the modulation is of concern.

RESULTS WITHOUT OPTICAL EXCITATION

This section is devoted to results for blue and green diodes which are not subjected to any external illumination. Figure 1 shows the DC characteristics for a typical green diode at T=4.2K. As most of our results are for liquid helium temperatures, it is necessary to examine the characteristics at such temperatures and their differences from room temperature characteristics. One important difference is the dependence of the electroluminescence intensity on current. At higher temperatures there is a much stronger bias dependence, particularly at higher currents (I>100 μA) where the approximately linear bias dependence is maintained up to about 10 mA. At low temperatures the voltage across the sample is significantly higher, presumably due to the increase in contact resistance. However the derivative of the curve shows little temperature dependence, suggesting tunneling processes in agreement with Perlin and coworkers.[8] The spectral dependence of the EL is shown in the inset. The peak is very similar in width and intensity to that observed at room temperature. No significant bias dependence to the peak position or width was observed, although others have observed such shifts at room temperature.[7]

In Figure 2 the EDMR spectra is plotted for the blue and green diodes at a relatively low

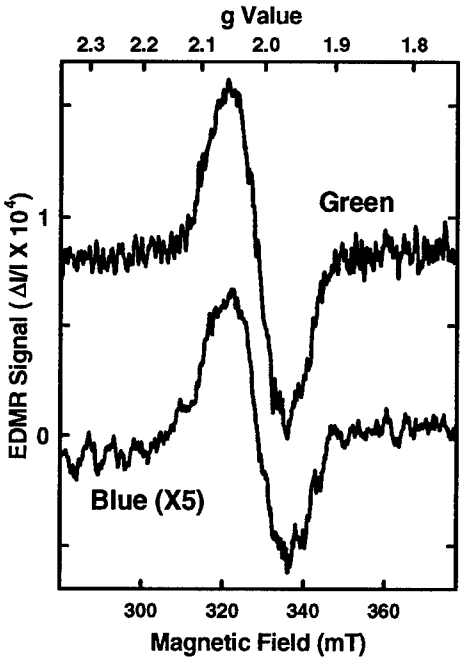

Figure 3. The EDMR spectra of a blue and a green LED at I=10 μA and T=4 K.

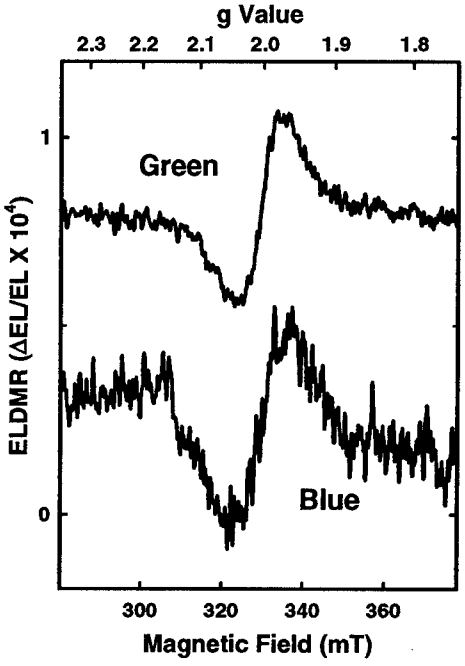

Figure 2. The ELDMR spectra of a blue and a green LED at I=10 μA and T=4 K.

bias current. In this and subsequent figures a derivative signal which is first positive then negative (i.e., integrates to a positive signal) is due to a current-enhancing resonance and one which is negative and then positive is due to a current-quenching resonance. The measurements are taken at constant current so the relative change is related to the measured change in voltage across the sample by;

$$\frac{\Delta I}{I} = -\Delta V \frac{d(\ln I)}{dV} \quad . \tag{1}$$

The ELDMR spectra for the same two diodes at the same bias as in Figure 2 are shown in Figure 3. Here the relative signal is simply the ratio of the AC signal to the DC electroluminescence, i.e., $\Delta EL/EL$. Before discussing differences in the measurements and samples, it should be noted that the linewidths ($\Delta B \approx 13$ mT), positions ($g \approx 2.01$) and amplitudes ($\sim 10^{-5}$-10^{-4}) are quite similar for the two measurements. Note, however, that the intensities for the blue diodes are generally somewhat lower than that for the green diodes. This is generally true for the several samples studied and across the range of biases employed. While the spectra are dominated by a broad line over most of the bias range, at higher biases a weak second line begins to emerge[23] and will be discussed below. The most obvious difference between the EDMR and the ELDMR is in the phase; the EDMR shows a current enhancement at resonance while the ELDMR shows a quenching of the EL at resonance. As discussed in previous work[20,21] the ELDMR of the green diodes goes from an EL-quenching signal at low biases to an EL-enhancing signal at higher biases; however, this effect has not been observed in the blue diodes.

The integrated intensities of the EDMR and ELDMR spectra of a green diode are shown in Figure 4 for a range of currents. Note that while the two signals have approximately equal magnitudes at I=1 μA, the magnitude of the EDMR signal remains relatively constant up to about 20 μA but the magnitude of the ELDMR is nearly zero at that bias. The current-enhancing signal seen in EDMR under the same conditions as an EL-quenching signal is observed is due to an increase in the non-radiative recombination rate. The EDMR measures the total $\Delta I/I$ and thus shows an increase in recombination current at resonance. In contrast, as more current flows through the non-radiative channel the current flowing through the radiative channel decreases. Hence, an EL-quenching signal is seen in the ELDMR. However, as seen in Figure 4, the EDMR and ELDMR are not mirror images of each other. This is the result of detection of this defect in another region of the device, such as the depletion width of one the contacts, in series with the optically active region of the device.[20,21] The measurement is made at a constant current so a resonance in a part of the device in series with the quantum well region does

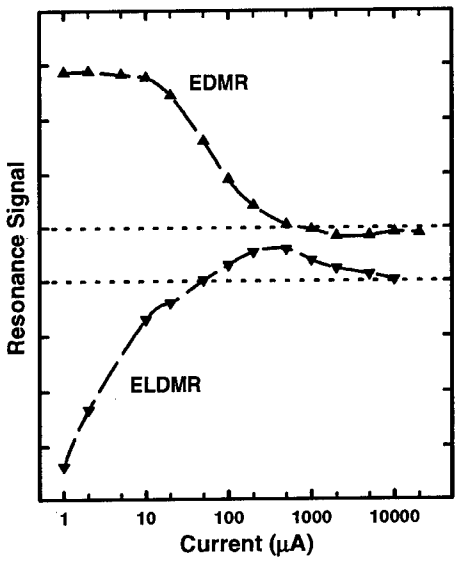

Figure 4. The intensities of the EDMR (top) and the ELDMR (bottom) signal of a green diode. The dotted lines indicate the zero levels of he two curves.

not affect the ELDMR but does change the total voltage across the device and thus contributes to the EDMR signal.

At high bias currents (I~1 mA), a second sharper ($\Delta B \approx 7$ mT) resonanceis observed in both techniques for the green diode and only with EDMR in the blue dioded, as illustrated in Figure 5. The relative intensity of the resonance is enhanced at lower temperatures and high magnetic field modulation frequencies. (1 - 10 kHz) The g value is a weak function of current bias, with $g \approx 1.98 \pm 0.01$. The g values are similar to those of donor resonances observed in ODMR[12,24] and in EDMR.[22] Götz and coworkers[25] have suggested that there is a range of deep levels in GaN and the weak bias dependence observed here as well as the other resonance results tend to support that argument. Both EDMR and ELDMR give a quenching resonance, suggesting that this may be the result of recombination in either the lightly In-doped layer on which the InGaN quantum well is grown or conceivably in an AlGaN barrier layer. This would take carriers away from the EL process and result in a quenching of the EL as well as quenching of the current. The fact that a similar resonance in both blue and green SQW diodes is observed, may argue that this defect is located in the low x $In_xGa_{1-x}N$ layer (x=0.02 for the blue diode and x=0.04 for the green diode[4]). That is, one might expect a difference in the g value for this relatively shallow defect in another layer where the alloy concentrations are significantly different for the blue and green diodes but not for this layer which very similar for the two diodes.

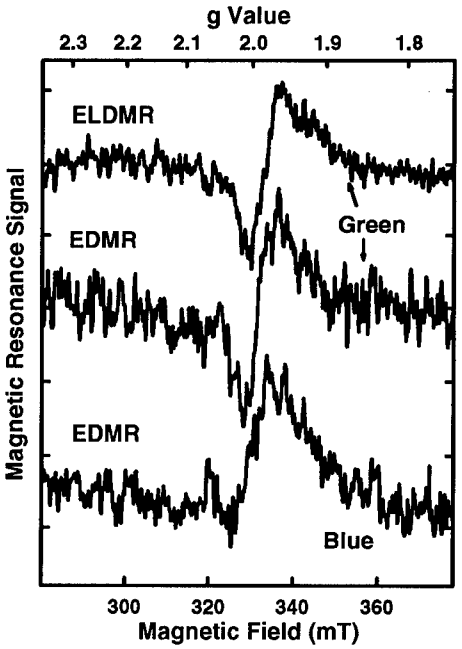

Figure 5. The EDMR and an ELDMR spectra for green and blue LEDs (as indicated)) at currents near 1 mA. The parameters have been adjusted to best resolve the sharp donor line in each of the three spectra.

RESULTS WITH OPTICAL EXCITATION

The effects of spin dependent processes can also be detected by monitoring changes in the photocurrent under short circuit conditions and as optically induced changes in the EDMR under forward bias. These effects are only observed with the green LEDs, primarily because the blue diode does not have appreciable absorption[9] in the available spectral range (458 nm - 514 nm). In the case of photocurrent-detected magnetic resonance (PCDMR) the short circuit current is, of course, negative and an enhancement of this current at resonance is observed. This is illustrated in the lower trace of Figure 6. This effect is most strongly observed with λ_{excit}=458 nm, the shortest wavelength available and the most strongly absorbed. It is also more weakly detectable for longer wavelengths such as 476 nm and 488 nm, which are less strongly absorbed. The magnetic resonance signal intensity approximately tracks the DC photocurrent amplitude which was less than 1 μA for the spectrum illustrated. The effect of optical excitation can also be observed as a photo-quenching of the EDMR signal at low bias currents as is also shown in Figure 6. This effect is very bias and temperature dependent. No detailed study of the parameter

dependence of the quenching effect was undertaken; however, this effect was strongest for I=2 μA and T= 20 K, for the sample used in the data presented. Only the broad resonance is observed, as might be expected given that both are low bias experiments and the noise (due to the laser) is higher, obscuring weaker signals.

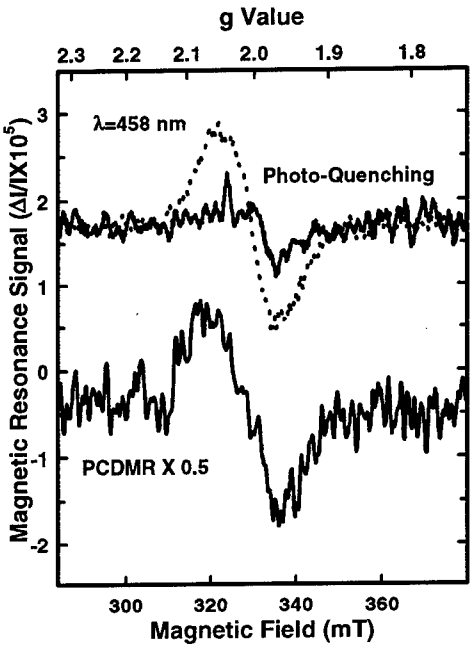

Figure 6. The top traces illustrate the photoquenching of the EDMR signal with the dotted line being the signal in the dark and the solid line the signal under illumination. The photocurrent detected magnetic resonance is shown in the lower trace.

The null result for the blue diode indicates band-to-band absorption in the quantum well region rather than a defect-to-band process in another layer in the green diode. There are two phenomena important to these effects: a spin dependence to the photogeneration mechanism and a reduction in the spin dependence in the nonradiative channels in the quantum well region. The absorption, of course, generates electron-hole pairs in the quantum well, some of which recombine and some of which are swept out by the built-in field giving rise to the photocurrent. Spin dependent generation has been previously observed in Si MOSFETs[26] and it is suggested that a spin dependence to the photo-generation process enhances the current at resonance in these diodes, giving rise to the PCDMR. In forward bias, the EDMR signal can be quenched by greatly increasing (absorbed photon flux>>Injected carrier density) the electron-hole population in the quantum well. While this decreases the DC voltage across the diode it also reduces the spin dependence of the non-radiative recombination channel. This effect is also important in the PCDMR in that it reduces the effects of spin dependence of the recombination in the non-radiative channels. Without this effect the PCDMR signal would be reduced. These effects are illustrated in a simple circuit model for a diode in Figure 7. Under intense illumination the non-radiative recombination channels, illustrated by $R_{||}$, become more conducting due to the increased carrier concentration. This also makes this channel much less spin-dependent. Under short circuit conditions the spin dependence of the generation current, I_G, is then revealed. At low forward biases the spin dependence is dominated by $R_{||}$ in the dark and this effect is then queched by the optical absoption. Note,

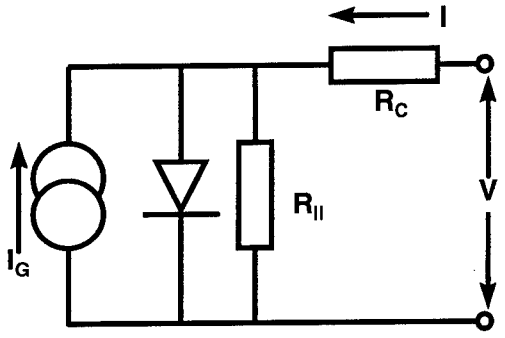

Figure 7. A simple circuit model for a nonideal diode. $R_{||}$ and R_C reprensent the non-radiative recombination channels in parallel and series with the ideal diode. Under illumination a current I_G is generated.

also that an enhancement in I_G at resonance will also decrease the total current. So, the two effects both contribute to both of the photo-excitation effects. At higher biases R_C does become important as seen in the previous section.

SUMMARY AND CONCLUSIONS

A number of probes based on spin dependent recombination/generation have been applied to GaN-based single quantum well LEDs. The spectra are dominated by a broad resonance at g≈2.01 which is apparently due to a deep defect present in both the non-radiative recombination channels in the optically active region of the diode and in at least one of the contact depletion widths. The various techniques permit us to focus on this defect's role under various bias and illumination conditions. A second resonance is attributed to a deep donor. While the dependencies of the electrically and optically detected resonances and a comparison of their amplitudes and phases provides some understanding of the location of these defects and their role in recombination processes, their chemical identity is still elusive. However a number of groups continue to apply more powerful spectroscopic probes such as double resonance techniques to the problem of understanding the structure of defects which limit GaN device performance.

ACKNOWLEDGMENTS

I wish to thank Shuji Nakamura for supplying the devices used in this and previous work. I am also very grateful to E.R. Glaser, T.A. Kennedy and J.A. Freitas, Jr. for many helpful discussions regarding GaN and many aspects of this study. This work was funded by the Office of Naval Research and Defense Advanced Research Projects Agency.

REFERENCES

1. For an overview of work in the Group III Nitrides see *The Blue Laser Diode* by Shuji Nakamura and Gerhard Fasol (Springer-Verlag, Berlin, 1997).
2. H. Amano, N. Sawaki, I. Akasaki and Y. Toyoda, Appl. Phys. Lett. **48**, 353 (1986); H. Amano, M. Kitoh, K. Hiramatsu and I. Akasaki, J. Electochem. Soc. 137, 1639 (1990); S. Nakamura, M. Senoh and T. Mukai, Jpn. J. Appl. Phys. **30**, L1708 (1991).
3. Shuji Nakamura, Takashi Mukai and Masayuki Senoh, Jpn. J. Appl. Phys. **30**, L1998 (1991).
4. Shuji Nakamura, Takashi Mukai and Masayuki Senoh, Appl. Phys. Lett. **64**, 1687 (1994).
5. Shuji Nakamura, Masayuki Senoh, Naruhito Iwasa and Shin-ichi Nagahama, Jpn. J. Appl. Phys. **34**, 797 (1995); Appl. Phys. Lett. **67**, 1868 (1995).
6. Shuji Nakamura, M. Senoh, S. Nagahama, N. Iwasa, T. Yamada, T. Matsushita, H. Kiyoku and Y. Sugimoto, Jpn. J. Appl. Phys.. **35**, L74 (1996); Shuji Nakamura, Masayuki Senoh, Shin-ichi Nagahama, Naruhito Iwasa, Takao Yamada, Toshio Matsushita, Yasunobu Sugimoto, and Hiroyuki Kiyoku, Appl. Phys. Lett. **70**, 1417 (1997).
7. Piotr Perlin, Valentin Iota, Bernard A. Weinstein, Przemek Wiśniewski, Tadeusz Suski, Petr. G. Eliseev and Marek Osiński, Appl. Phys. Lett. **70**, 2993 (1997).
8. Piotr Perlin, Marek Osiński and Petr G. Eliseev, III-V Nitrides, ed. by F.A. Ponce, T.D. Moustakas, I. Akasaki and B.A. Monemar (Materials Research Society, Pittsburgh, 1997), p. 1173.

9. S. Chichibu, T. Azuhata, T. Sota and S. Nakamura, Appl. Phys. Lett. **69**, 4188 (1996).
10. For a review of recent optical and magnetic resonance results see; U. Kaufmann, M. Kunzer, C. Merz, I. Akasaki and H. Amano, *Gallium Nitride and Related Materials*, ed. by F.A. Ponce, R.D. Dupuis, S. Nakamura and J.A. Edmond (Materials Research Society, Pittsburgh, 1996), p. 633.
11. W.E. Carlos, J.A. Freitas, Jr., M. Asif Khan, D.T. Olson and J.N. Kuznia, Phys. Rev. B**48**, 17878 (1993).
12. E.R. Glaser, T.A. Kennedy, K. Doverspike, L.B. Rowland, D.K. Gaskill, J.A. Freitas, Jr., M. Asif Khan, D.T. Olson, J.N. Kuznia, and D.K. Wickenden, Phys. Rev. B**51**, 13326 (1995).
13. M. Kunzer, U. Kaufmann, K. Maier, J. Schneider, N. Herres, I. Akasaki, and H. Amano, Mat. Sci. Forum **143-147**, 87 (1994); K. Maier, M. Kunzer, U. Kaufmann, J. Schneider, B. Monemar, I. Akaski and H. Amano, Mat. Sci. Forum **143-147**, 93 (1994). M. Kunzer, J. Baur, U. Kaufmann, J. Schneider, H. Amano and I. Akasaki, Solid State Elect. **41**,189 (1997).
14. D.H. Hofmann, D. Kovalev, G. Steude, B. K. Meyer, A. Hoffmann, L. Eckey, R. Heitz, T. Detchprom, H. Amano and I. Akasaki, Phys. Rev. B**52**, 16702 (1995).
15. M. Ramsteiner, J. Menniger, O. Brandt, H. Yang and K.H. Ploog, Appl. Phys. Lett. **69**, 1276 (1996).
16. L.S. Swanson, J. Shinar, A.R. Brown, D.D.C. Bradley, R.H. Friend, P.L. Burn, A. Kraft and A.B. Holmes, Phys. Rev. B**46**, 15072 (1992).
17. K.P. Homewood, B.C. Cavenett, I.G. Austin, T.M. Searle, W.E. Spear and P.G. Lecomber J. Phys. C**17**, L103 (1984).
18. D.J. Lépine, Phys. Rev. B**6**, 436 (1972); I. Solomon, Solid State Commun. **20**, 215 (1976); F.C. Rong, G.J. Gerardi, W.R. Buchwald, E.H. Poindexter, M.T. Umlor, D.J. Keeble and W.L. Warren, Appl. Phys. Lett. **60**, 610 (1992); B. Stich, S. Greulich-Weber and J.-M. Spaeth, J. Appl. Phys. **77**, 1546 (1995).
19. N.M. Reinacher, M.S. Brandt and M. Stutzmann, Materials Science Forum **196-201**, 1915 (1995); M.W. Bayerl, M.S. Brandt, M. Stutzmann, Phys. Stat. Sol. A**159**, R5 (1997).
20. W.E. Carlos and Shuji Nakamura, Appl. Phys. Lett., **70**, 2019 (1997).
21. W.E. Carlos, E.R. Glaser, T.A. Kennedy and S. Nakamura, *III-V Nitrides*, ed. by F.A. Ponce, T.D. Moustakas, I. Akasaki and B.A. Monemar (Materials Research Society, Pittsburgh, 1997), p. 757.
22. W.E. Carlos, E.R. Glaser, T.A. Kennedy and S. Nakamura, Appl. Phys. Lett. **67**, 2376 (1995).
23. W.E. Carlos, E.R. Glaser, T.A. Kennedy and S. Nakamura, in *The Physics of Semiconductors*, ed. by M. Scheffler and R. Zimmermann (World Scientific, Singapore, 1996) p. 2921.
24. E.R. Glaser, T.A. Kennedy, A.E. Wickenden, D.D. Koleske and J.A. Freitas, Jr., *III-V Nitrides*, ed. by F.A. Ponce, T.D. Moustakas, I. Akasaki and B.A. Monemar (Materials Research Society, Pittsburgh, 1997), p. 543.
25. W. Götz, N.M. Johnson, H. Amano and I. Akasaki, Appl. Phys. Lett. **65**, 463 (1994); W. Götz, N.M. Johnson, R.A. Street, H. Amano and I. Akasaki, Appl. Phys. Lett. **66**, 1340 (1995).
26. Brian Henderson, M. Pepper and R.L. Vranch, Semicond. Sci. Technol. **4**, 1045 (1989).

Materials Science Forum Vols. 258-263 (1997) pp. 1113-1118

DONOR-ACCEPTOR PAIR TRANSITIONS IN GaN

K. Kornitzer, M. Mayer[§], M. Mundbrod, K. Thonke, A. Pelzmann[§], M. Kamp[§], R. Sauer

Abt. Halbleiterphysik, Universität Ulm, D-89069 Ulm, Germany
[§]Abt. Optoelektronik, Universität Ulm, D-89069 Ulm, Germany

Keywords: GaN, donor-acceptor transitions, Photoluminescence

Abstract

We report the observation of several new photoluminescence bands in the near-bandedge energy range of GaN. The 6H GaN layers were grown by MBE at temperatures around 700°C on sapphire substrates with an intermediate AlN/GaN nucleation layer. In addition to the well-known donor-bound exciton line at 3.475 eV and the oxygen-related 3.418 eV line (at 4 K), we find weaker defect-related lines in the energy range extending to 400 meV below the bandgap, but no "yellow band".
Variation of the sample temperature between 4 K and room temperature and variation of the excitation power allows us to identify a line at 3.345 eV as donor-acceptor pair transition. The estimated binding energy of the acceptor involved is no more than 150 meV. Further lines at 3.365 eV and 3.21 eV are studied as well, but not finally assigned.

Introduction

Despite impressive progress in the production of blue light emitting GaN optical devices, the control of unintentional doping species still remains a problem to solve. Since the first reports of photoluminescence from GaN about 40 years ago, all spectra show strong contributions of donor- and acceptor-bound excitons, and most of them show bands originating from donor-acceptor pair (DAP or (D^0,A^0)) recombination. Commonly reported is a DAP band located around 3.26 eV [1, 2], but the acceptor involved remains unidentified. Later work reports similar DAP bands along with strong LO phonon replicas at 3.284 eV [3]. Recently, Kaufmann et al. [4] interpreted some weak sharp lines at ≈ 3.35 ... 3.37 eV as distant (D^0, A^0) transitions of donors and acceptors with energies of 35 meV and 116 meV, respectively. Broader bands with onsets at 3.3 eV in GaN:Mg and at 3.15 eV in GaN:Zn were ascribed to DAP transitions from closer pairs. The "yellow band" emitted at ≈ 2.2 eV from samples with inferior quality was also interpreted as DAP transition [5].

Experimental

The samples investigated were grown by MBE at ≈ 700 °C on (0001) sapphire substrate. After a low temperature AlN/GaN buffer layer of 4 nm to 20 nm thickness a nominally undoped GaN layer of 2 – 3.7 μm thickness was grown [6]. X-ray analysis shows good crystal quality with diffraction peak of 500" - 590" (ω scan, (0002) reflex, Cu $K_{\alpha 1}$). Carrier concentrations as determined by room temperature Hall experiments were $(1.4 - 4.3)\cdot 10^{17}$ cm^{-3} n-type, with mobilities in the range of (170 ... 210) cm^2/Vs.
For the optical studies the samples were cut into ≈ 3 x 3 mm^2 pieces, cooled in a gas-flow cryostat. The excitation source was a HeCd laser (λ = 325 nm) with a maximum power of 20 mW (typically 1 mW) on a sample spot of ≈ 1 mm^2. The emitted light was dispersed by either a 0.27 m or a 1 m monochromator and detected with a LN_2-cooled CCD camera. The spectra shown here are not normalized to the response of the spectral apparatus (which is essentially flat).

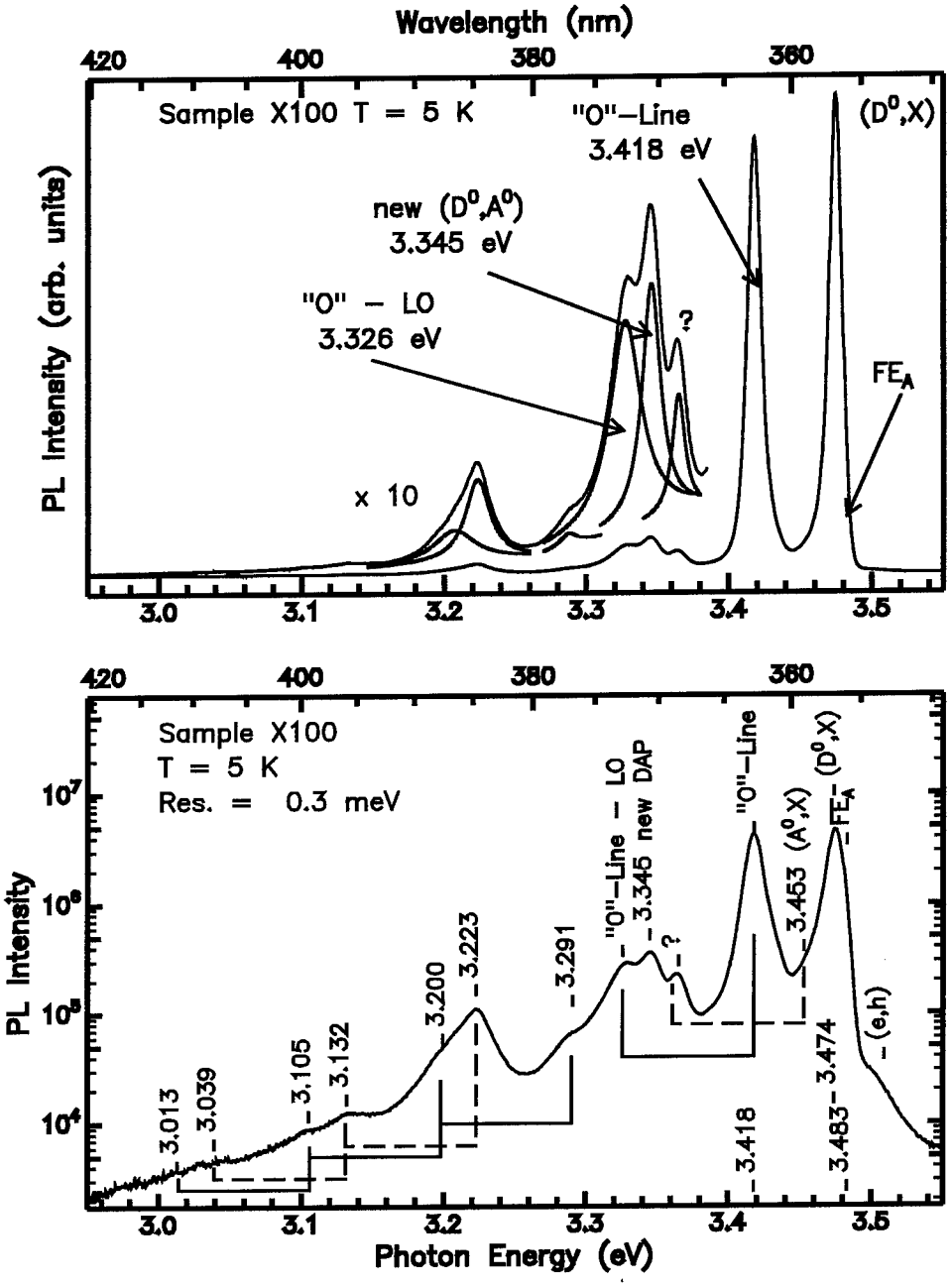

Fig. 1 a): PL overview spectrum recorded at T = 5 K in linear presentation. Besides the dominant (D^0,X) and oxygen defect related emissions "O" several new weaker bands show up. The line at 3.345 eV is identified as a new DAP transition. For the weak lines a deconvolution into Lorentzian components is shown. Spectral resolution was 0.03 meV.

Fig. 1 b): The same spectrum on logarithmic intensity scale. The rectangular indication lines connect transitions with their (multiple) LO replicas (LO energy = 92 meV).

Results

Figure 1 shows a photoluminescence (PL) spectrum which is typical for a set of our MBE samples investigated closer here. The "yellow band" emission around 2.2 eV (region not shown here) is by at least 3 orders of magnitude lower than the dominant peaks in the bandgap region. Thus the overall material quality is believed to be good. The dominant emission at low temperatures is the line at ≈ 3.480 eV (full width at half maximum FWHM ≈ 10 meV), which reveals a twofold structure at closer inspection: Superimposed on the dominant line at 3.474 eV due to the decay of neutral donor bound excitons (D^0,X), there is a high energy shoulder around 3.483 eV which we ascribe to the ground state of the A free exciton $FE_A^{n=1}$. At temperatures around 100 K these two contributions are comparable in intensity, and a third higher energy line at 3.495 eV (hardly resolvable) comes up. This line is due to the B free exciton $FE_B^{n=1}$ [7]. On the low energy tail of the (D^0,X) line at 3.457 eV an additional weak contribution possibly due to acceptor bound excitons (A^0,X) or donor-bound exciton two-electron transitions (D^0,$X_{n=2}$) is observed. The second dominant line in Fig. 1 at 3.418 eV was recently ascribed to a (D^0,h) transition at an oxygen-related defect [8, 9].
Down from these intense, relatively well-studied peaks we observe in our samples several new features. The major part of this paper will be concerned with the line at 3.345 eV. Arguments are given that it is due to donor-acceptor transitions between a shallow donor with $E_d \approx 35$ meV and a (relatively) shallow acceptor with $E_a \approx$ of 150 meV. Next to this line is a relatively strong transition at 3.330 eV spaced 92 meV from the "O"-defect line; it is therefore interpreted as a LO phonon replica of the latter line. Spectra recorded at increasing temperature show a simultaneous decrease of these two lines confirming this interpretation. The last transition in the triplet-like structure at 3.364 eV marked with "?" is hitherto unexplained. Its energy could hint to an interpretation as LO phonon replica of the weak (A^0,X) transition on the low energy tail of (D^0,X). However, a logarithmic plot of the PL spectrum shows, that the $2 \cdot$ LO –replica is totally absent, which then would be expected to have ≈ 0.5 relative intensity. Thus the nature of this line remains unclarified at present.

The weak hump at 3.292 eV could be an independent no-phonon transition. Then three low-energy peaks at 3.195 eV, 3.105 eV, and 3.01 eV mutually equispaced be $\hbar\omega$(LO) ≈ 90 meV and with progressively decreasing intensities could be interpreted as multi-LO replicas. Although shifted to slightly higher energy in our thin layers, we believe the peak at 3.292 eV to be the same DAP band as observed earlier by Dingle et al. [1] or by Lagerstedt et al. [2].

The next twofold group in Fig. 1 contains a line at 3.223 eV which can be assigned as a no-phonon transition with a sequence of LO phonon replicas. The origin of this spectrum is again unknown. When strong phonon replicas are observed, it is commonly concluded, that acceptor states are involved, as these can couple through their hole orbital momentum to the phonons. The weaker partner in the twofold group at 3.195 eV also has a sequence of LO phonon replicas associated with it as shown in Fig. (1b), thus hinting to a transition similar in nature as the DAP bands above.

The line at 3.345 eV (for T = 5 K) was investigated in more detail (Fig. 2). When varying the sample temperature between 5 K and room temperature, we find a luminescence take over at around T = 100 K from this emission to a ≈ 31 meV higher energy band. The donor with ≈ 30 meV binding energy involved in the (D^0,A^0) transition is apparently thermally ionized, thus giving rise to a free electron → acceptor-bound hole transition (e,A^0) instead of (D^0,A^0). We performed for all spectra lineshape fits to identify the individual contributions of the ("O"-LO)-line, the (D^0,A^0) transition, and the (e,A^0) peak in the group centered at 3.345 eV. When the ratios of the latter two transitions are drawn in an Arrhenius plot (Fig. 3), they yield a straight line between 50 K and 160 K, with a slope according to an activation energy of 15 meV. Both Hall measurements on the same sample and theoretical simulations show, that for a donor concentration N_D of a few 10^{17} saturation of the free electron concentration n is not reached for $T_s \leq 200$ K. Thus in the temperature range $T < T_s$, where $n << N_D^0$ (number of neutral donors) ≈ const., the ratio n to N_D^0 is roughly equal to the number of

free electrons and is governed by an exponential law $\exp(-E_d/2)$, with E_d being the donor ionization energy. The donor involved here must have an ionization energy of $2\cdot(15.5 \pm 2)$ meV = (31 ± 4) meV in accordance with recent literature data [10].

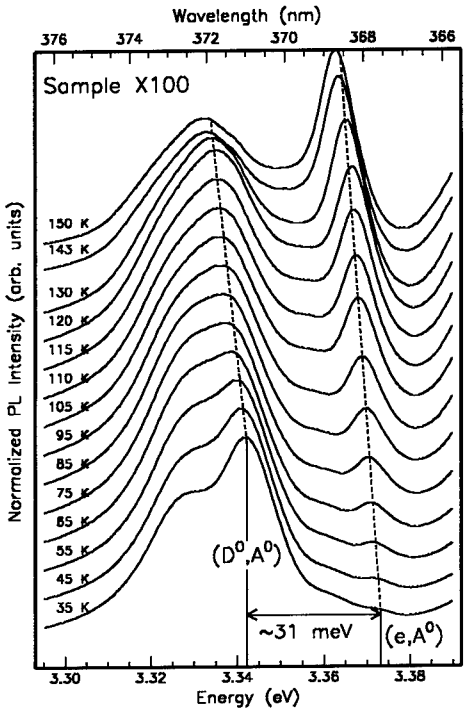

Fig. 2a: With increasing temperature luminescence from the (D^0,A^0) transition at 3.345 eV is taken over by the (e,A^0) transition $\approx$ 30 meV higher in energy. Excitation density was about 30 mW/mm².

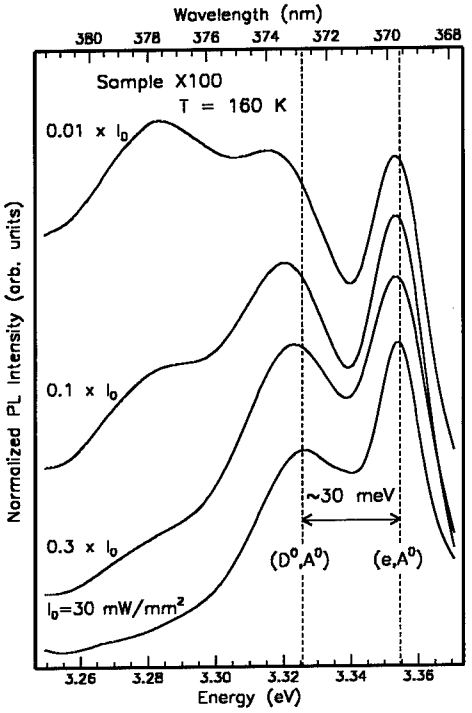

Fig. 2b: The same spectral region as in Fig. 2a at 160K sample temperature, recorded with varying excitation density.

The other feature for the identification of (D^0, A^0) transitions is that such a band shifts towards higher energy with increasing excitation density, since then there are more close pairs occupied, which have high recombination probability. Fig. 2b) shows our findings for the 3.345 eV band (which is shifted to $\approx$ 3.325 eV for T = 160 K). When the excitation density is varied over two decades, the (D^0, A^0) band indeed shifts by roughly 10 meV, whereas the (e, A^0) band remains at constant energy as expected.

We will now estimate the ionization energy of the acceptor involved in this new 3.345 eV transition. According to Fischer et al. [11] the (D^0, A^0) peak energy can be described by the relation

$$E_{D-A,peak} = E_{gap} - E_d - E_a + \alpha \cdot n^{1/3}, \qquad (1)$$

where α is an empirical constant of $(2.1 \pm 0.1)\cdot 10^{-8}$ eVcm. The carrier concentration for the specific sample used in Fig. 1 was $n = 4.3\cdot 10^{17}$ cm^{-3}, thus the average distance of donors is $n^{-1/3} \approx 13$ nm and the last term in eq. (1) yields ≈ 16 meV. Our measurements on the A-exciton in the same sample yield the excitonic bandgap as 3.483 eV for $T \rightarrow 0$ from a Varshni fit. Adding the excitonic Rydberg of 26 meV [7], the direct gap amounts to 3.509 eV. Thus we calculate

$$E_a = E_{gap} - E_d - E_{D-A,peak} + \alpha \cdot n^{1/3} = (3.509 - 0.030 - 3.345 + 0.016)\text{eV} = 150\text{meV}. \qquad (2)$$

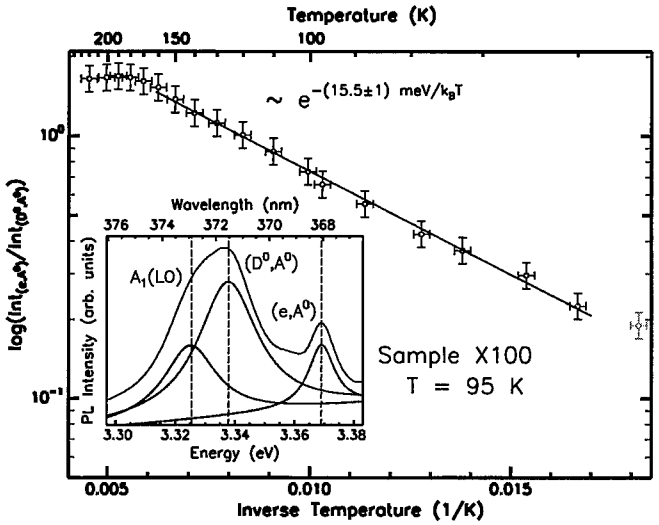

Fig. 3: Ratio of the intensities of the (e,A^0) and (D^0,A^0) transitions. The inset shows the deconvolution of the spectrum recorded at 95 K.

This is considerably less than quoted in the literature for the technologically established acceptor magnesium (280 meV) or for carbon (230 meV) [11]. A chemical identification of the involved acceptor can only be speculative with our present knowledge. Since we see this transition strongly in samples, where the 3.418 eV ("O"-)line is also strong, oxygen could be related to our acceptor state provided the assignment of the 3.418 eV line to an oxygen containing defect is right.

Since there is some ambiguity in literature about the nature of the decay process responsible for the 3.418 eV ("O"-) line, we analysed the behaviour of this line under variation of excitation density as well. For the range of excitation from low 6 $\mu W/mm^2$ up to 30 mW/mm^2 we find within an error of $\pm$ 0.5 meV absolutely no shift or change in lineshape for this line. This is unlike the finding of Smith et al. [9], who found a shift of $\approx$ 10 meV during the decay after pulsed excitation. Possibly this is due to the fact, that our cw excitation density is much lower than their peak pulse power and corresponds just roughly to their averaged power. We observe only an increase of the "O"-line intensity relative to the (D^0,X) by a factor of two over this ≈ 4 orders of magnitude change in excitation density. This is surely due to different absolute numbers of recombination centers and to different recombination rates involved. When raising the sample temperature from 5 K to $\approx$ 200 K, no new line $\approx$ 30 meV above the "O"-Line comes up, but the high-energy tail seems to broaden according to a Boltzmann-law. We thus definitely can rule out a (D^0,A^0) recombination mechanism for this line. The proposed (D^0,h) recombination seems to be the likeliest model. Alternatively, a recombination of an exciton bound with $\approx$ 66 meV localisation energy to an isoelectronic impurity (or a complex which is overall isoelectronic) could be considered. In case of an acceptor bound exciton, an unlikely deep acceptor would be required.

There are no apparent correlations between literature reports and the Lorentzian-shaped band at 3.223 eV followed by progressively weaker (factor $\approx$ 1/10) LO replicas. Basically, it could also be (D^0,A^0) recombination. In such a case eq. 2 would yield $E_a \approx 300$ meV as acceptor binding energy. This is not too different from the ionization energy of the Mg acceptor. But the very weak coupling strength to the LO replicas, and mainly the total absence of associated (e,A^0) transitions in our PL spectra expected to emerge at $\approx$ 30 meV higher energy when the sample temperature is raised, rules out such an assignement to (D^0,A^0) transitions. Alternatively, an exciton deeply bound to an unknown acceptor could lead to this emission.

Conclusions

In the energy range 3 ... 3.45 eV we observe several new bands in low-temperature PL measurements. A transition at 3.345 eV was definitively assigned to a (D^0,A^0) pair transition between a donor with (31 ±2) meV and a relatively shallow acceptor with 150 meV. The defect related line at 3.418 eV is not due to (D^0,A^0) recombination.

Acknowledgements

We thank A. Pelzmann for pre-characterization of the samples. W. Limmer provided expert assistance in the temperature-dependent Hall measurements.

References

[1] R. Dingle, M. Illegems, Sol. Stat. Comm. **9**, 175 (1971)
[2] O. Lagerstedt, B. Monemar,, J. Appl. Phys. **45**, 2266 (1974)
[3] Gyu-Chul Yi, B. Wessels, Proc. of the ICDS18, Ed.: M. Suezawa, H. Katayama-Yoshida, p. 49, Trans Tech Publ., Zürich, (1995)
[4] U. Kaufmann, M. Kunzer, C. Merz, I. Akasaki, H. Amano, Proc. of "Gallium Nitride and Related Materials. First International Symposium" , Ed.: Ponce, F.A.; Dupuis, R.D.; Nakamura, S.; Edmond, J.A., Pittsburgh, PA, USA: Mater. Res. Soc, 633 (1996)
[5] T. Ogino, M. Aoki, Jap. J. Appl. Phys. **19**, 2395 (1980)
[6] M. Kamp, M. Mayer, A. Pelzmann, K.J. Ebeling, Mat. Res. Soc. Symp. Proc. **449**, 161 (1997)
[7] B.J. Skromme, H. Zhao, B. Goldenberg, H.S. Kong, M.T. Leonard, G.E. Bulman, C.R. Abernathy, S.J. Pearton, Mat. Res. Soc. Symp. Proc **449**, 713 (1997)
[8] B.C. Chung, M. Gershenzon, J. Appl. Phys. **72**, 651 (1992)
[9] M. Smith, G.D. Chen, J.Y. Lin, H.X. Jiang, A. Salvador, B.N. Sverdlov, A. Botchkarev, H. Morkoc, Appl. Phys. Lett. **66**, 3474 (1995)
[10] S. Fischer, D. Volm, D. Kovalev, B. Averboukh, A. Graber, H.C. Alt, B.K. Meyer, Materials Science & Engineering B (Solid-State Materials for Advanced Technology) B **43**, 192 (1997)
[11] S. Fischer, C. Wetzel, E.E. Haller, B.K. Meyer, Appl. Phys. Lett. 67, 1298 (1995)

Materials Science Forum Vols. 258-263 (1997) pp. 1119-1124

AB INITIO STUDIES OF ATOMIC-SCALE DEFECTS IN GaN AND AlN

T. Mattila[1] and R. M. Nieminen[2]
Laboratory of Physics, Helsinki University of Technology,
P.O. Box 1100, FIN-02015 HUT, Finland

Keywords: GaN, AlN, donor impurities, cation vacancies, broadband luminescence

Abstract. The plane-wave pseudopotential method is applied to study point-defects and their complexes in GaN and AlN. The calculations reveal a qualitative difference in the donor behavior between the two materials: the oxygen and silicon impurities act as shallow donors in GaN while in AlN they have a deep character, in good agreement with the experimentally measured conductivity. Therefore a DX-behavior is predicted for these donor defects in $Al_xGa_{1-x}N$ alloys with sufficient Al concentration. Effective compensation through cation vacancies (V_{Ga}, V_{Al}) and related defect complexes is shown to occur in both materials. We present evidence that the broadband luminescence (yellow in GaN and violet in AlN) originates from electronic transitions between the donor and acceptor levels induced by the defects mentioned above.

Introduction

GaN and AlN are two III-V nitride materials which have recently gained extensive interest due to their optoelectronic materials properties. Typical for both materials is the wide bandgap, ranging from 3.4 eV for w-GaN to 6.2 eV for w-AlN. Nitrogen as the other major constituent favors short bondlengths. This results in high structural stability of the materials, which is advantageous e.g. for laser applications.

A characteristic difference in the properties of GaN and AlN is their electrical conductivity: while undoped GaN is normally n-type, AlN remains insulating. This observation suggests a fundamental difference in the donor behavior between the two materials. In this paper we theoretically investigate the dominant donors and predict their properties in both materials in order to explain the observed difference in conductivity.

If positively charged donors are present in the material, formation of compensating acceptor defects is likely to occur. Our calculations give evidence that vacancies in the cation sublattice (V_{Ga}, V_{Al}) and related defect complexes act as efficient compensating acceptors in both materials. These defects are also shown to induce deep electronic levels in the bandgap, and are suggested to take part in the broadband luminescence processes typical for both materials.

Method

Our plane-wave pseudopotential (PWPP) approach is based on the density-functional theory (DFT) in the local density approximation (LDA). The Kohn-Sham equations are solved self-consistently for the electronic ground state and, using the calculated Hellmann-Feynman forces, the atomic degrees of freedom are successively allowed to relax until the optimum geometry is reached. No symmetry constraints are assumed in the calculations. The calculations have been principally performed with a 72 atom supercell in the wurtzite structure. A $2 \times 2 \times 2$ Monkhorst-Pack special k-point mesh [1] has been used for the Brillouin zone sampling. Further details of our PWPP method can be found in earlier publications [2, 3].

Behavior of O and Si donors

For GaN our calculations show that oxygen impurities are easily incorporated into the nitrogen sublattice, and correspondingly silicon atoms readily occupy the gallium sites. Both defects act as shallow donors i.e. the only stable charge state for all Fermi-level positions in GaN is the singly positive one. The calculated formation energy for nitrogen vacancy is more than 2 eV higher than for oxygen and silicon impurities. This corroborates the earlier suggestion by Neugebauer and Van de Walle [4] that the n-type conductivity of nominally undoped samples is caused rather by the easily incorporated impurities than the vacancies in nitrogen sublattice.

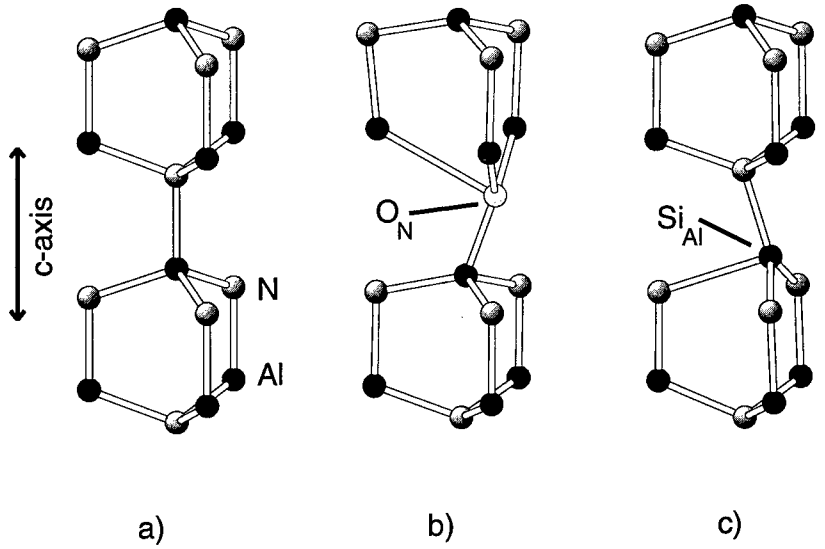

Figure 1: The symmetry lowering atomic relaxations associated with the deep state of impurity donors in AlN. In a) the ideal wurtzite structure is illustrated, b) and c) correspond to the ground state geometries found for O and Si donors, respectively. The hexagonal c-axis is vertically oriented.

In AlN the oxygen and silicon donors are found to act as *bistable* centers: in addition to the shallow state a deep state is stable. This behavior is due to the wide bandgap of AlN which allows trapping of two electrons to a localized deep level in the negatively charged configuration. In GaN the corresponding electron level resides in the conduction band, which prevents the stabilization of the negative charge state. Characteristic for the deep state in AlN is that its atomic configuration differs considerably from the one for the shallow state. Our calculations performed with the 72 atom wurtzite AlN supercell clearly reveal that the lowest energy configuration in the deep state of both O and Si donors occurs when the impurity atom resides in one of the three equivalent interstitial regions perpendicular to the hexagonal c-axis (see Fig. 1). With respect to the substitutional site we find this configuration to be 0.2 (0.15) eV lower in energy in the case of O (Si). In the displaced configuration the induced donor level resides deep in the band gap: for oxygen the level is about 2.0 eV below the conduction band edge, while for silicon the highest eigenvalue is found to be about 0.5 eV higher i.e. 1.5 eV

below the conduction band minimum.

The predicted deep character of the dominant donors in AlN is in excellent agreement with experimental observations: despite large impurity concentrations AlN remains insulating with a high activation energy (1.5 - 2.5 eV) necessary for electrical conductivity [5, 6]. Since the same donors have only a shallow character in GaN, our calculations predict a DX-behavior, well known to occur e.g. in $Al_xGa_{1-x}As$-alloys [7, 8], to exist also in $Al_xGa_{1-x}N$ with sufficient Al-concentration. By assuming that the bandgap increases linearly as a function of Al-concentration, we estimate that the stabilization of deep levels should start at $x = 0.2 - 0.3$ for oxygen and at $x = 0.4 - 0.5$ for silicon. These values correlate well with the available experimental data concerning the free carrier concentration as a function of Al_xGa_{1-x}-composition [9, 10] or applied external pressure on GaN [11, 12, 13]. However, in the high-pressure studies for intentionally Si-doped GaN samples [13] the shallow-deep transformation could not be verified. We associate this somewhat puzzling issue to the fact that the oxygen DX-level resides about 0.5 eV deeper in the bandgap than the one for silicon, and thus the stabilization of the deep level occurs at much higher bandgap values. In the high-pressure studies the DX-transition for oxygen was observed at 20 GPa [13]. Therefore it seems possible that applied pressure range up to 25 GPa is not necessarily high enough to lead to the stabilization of the silicon induced deep level.

Cation vacancies and broadband luminescence

We find the formation energies for V_{Ga} in GaN and V_{Al} in AlN to be to very low when the Fermi-level resides above midgap (n-type conditions). The principal charge state for these cation vacancies is the triply negative one, and the induced deep acceptor level is roughly 1 eV above the valence band maximum. The easy formation of the vacancies in the cation sublattice suggests that they should act as efficient compensating centers in materials containing silicon and oxygen donors. Indeed, recent experimental positron annihilation studies have revealed the presence of negatively charged gallium vacancies in GaN [14].

We have also investigated the possibility for the formation of defect complexes between the negatively charged cation vacancies and positively charged donor impurities. For the nearest-neighbor $V_{Ga} - O_N$ ($V_{Al} - O_N$) defect pair we find binding energies over 1 eV in both materials, which makes the formation of such defect complexes a likely process. Since the silicon donors cannot exist as nearest-neighbors for the cation vacancies, this results in considerably lower binding energies for such defect pairs.

Both GaN and AlN commonly exhibit broadband luminescence emission at energies well below the band gap. In GaN this emission is centered in the yellow part of the spectrum (at 2.2 - 2.3 eV) while in AlN the band is located in the violet region (at 3.2 - 3.3 eV). There is accumulating evidence in GaN that this yellow luminescence originates from shallow donor to deep acceptor transition. In experimental studies the acceptor level has been determined to lie about 1 eV above the valence band [15]. In the light of present and other computational results [16] the gallium vacancies and related defect complexes act as the most likely candidates inducing the deep acceptor level. Furthermore, a recent combined positron annihilation–photoluminescence study revealed a clear correlation between the gallium vacancy concentration and the yellow luminescence intensity in GaN [14]. The initial states in the luminescence process are likely to be induced by the dominant donors. This is corroborated by the experimental data which show that pressure-dependence of the yellow luminescence transition agrees with predicted behavior for shallow levels following rather closely the rising conduction band edge [17]. In addition, the pressure-induced blue-shift was found to saturate at very high pressures [17], which closely correlates with the DX-behavior described above.

In AlN the incorporation of oxygen is experimentally observed to bear a clear connection to the violet broadband luminescence [5]. In analog with GaN we suggest that the oxygen

induced deep donor level about 2 eV below the conduction band acts as the initial state for the luminescence transition (Fig. 2). Correspondingly, the aluminium vacancy-oxygen complex induced deep acceptor level about 1 eV above the valence band maximum is a likely candidate for the final state in the transition. The energy difference between these donor and acceptor levels agrees closely with the center of the experimental luminescence spectrum. Thus the broadband luminescences in GaN and AlN appear to have a similar origin: the initial state in the transition is a donor-induced level, which is shallow in GaN and deep in AlN. The final state is the deep acceptor state induced by a cation vacancy or related complex.

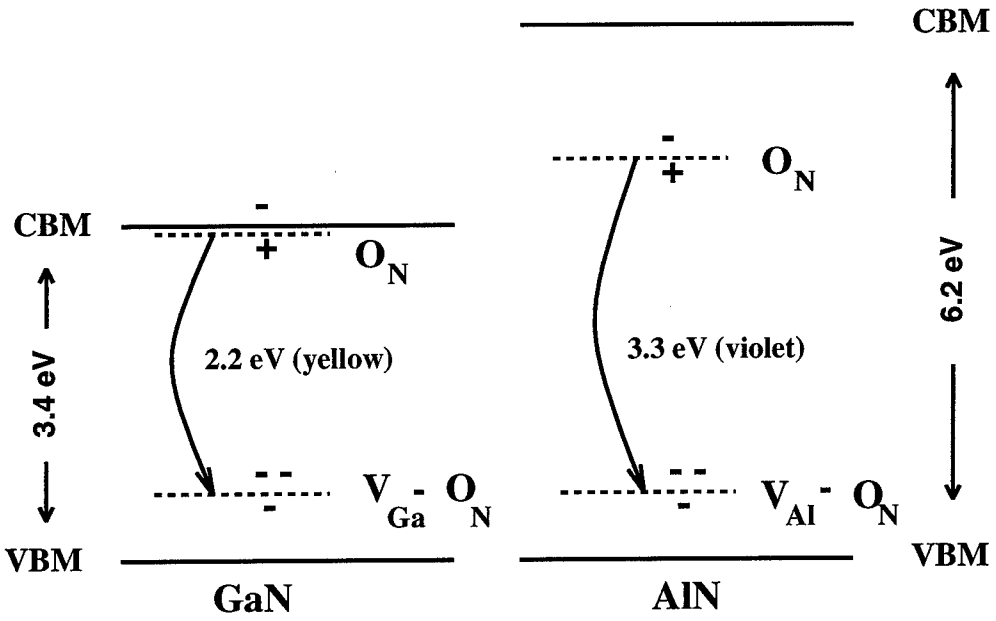

Figure 2: A schematic diagram of the yellow/violet luminescence mechanism in GaN and AlN.

Further evidence for the donor-acceptor pair transition behind the two luminescence phenomena is provided with comparison with other rather ionic materials. For instance, in ZnS or ZnTe transitions from donor levels to zinc-vacancy-halogen-impurity-complex acceptor levels are known to induce broad luminescence bands with a Gaussian lineshape [18].

Conclusion

The presented results show that modern *ab initio* calculations provide an efficient tool to predict defect related phenomena in GaN and AlN. Oxygen and silicon impurities are shown to act as dominant shallow donors in GaN while in AlN they have a bistable *DX*-like character. Cation vacancies and their complexes with oxygen impurities are predicted to be likely compensating acceptors in both materials. The presence of these deep acceptor levels can be used to explain the origin of the commonly observed broadband luminescence: in both GaN and AlN the luminescence transition is suggested to occur from the donor state to cation-vacancy related acceptor state.

Acknowledgments

We are grateful for useful discussions with A. P. Seitsonen, K. Laasonen, S. Pöykkö, K. Saarinen and K. Hjelt. The generous computing resources provided by CSC (Center for Scientific Computing, Finland) are gratefully acknowledged.

References

[1] H. J. Monkhorst and J. D. Pack, Phys. Rev. B **13**, 5188 (1976). J. D. Pack and H. J. Monkhorst, Phys. Rev. B **16**, 1748 (1977).

[2] T. Mattila and R. M. Nieminen, Phys. Rev. B **54**, 16676 (1996).

[3] T. Mattila and R. M. Nieminen, Phys. Rev. B **55**, 9571 (1997).

[4] J. Neugebauer and C. G. Van de Walle, in *Proceedings of the 22nd International Conference on the Physics of Semiconductors*, edited by D. J. Lockwood (World Scientific, Singapore, 1994), Vol. III, p. 2327.

[5] R. A. Youngman and J. H. Harris, J. Am. Ceram. Soc. **73**, 3238 (1990) and references therein.

[6] W. A. Groen, J. G. van Lierop, and A. Roosen, J. Mat. Sci. Lett. **12**, 1224 (1993).

[7] *Physics of DX Centers in GaAs Alloys*, edited by J. C. Bourgoin, (Sci-Tech, Lake Isabella, CA, 1990).

[8] D. J. Chadi and K. J. Chang, Phys. Rev. Lett. **61**, 873 (1988), Phys. Rev. B **39**, 10063 (1989).

[9] M. D. Bremser *et al.*, MRS Internet J. Nitride Semicond. Res. **1**, 8 (1996).

[10] S. Yoshida, S. Misawa, and S. Gonda, J. Appl. Phys. **53**, 6844 (1982).

[11] P. Perlin *et al.*, Phys. Rev. Lett. **75**, 296 (1995).

[12] C. Wetzel *et al.*, Phys. Rev. B **53**, 1322 (1996).

[13] C. Wetzel *et al.*, Phys. Rev. Lett. **78**, 3923 (1997).

[14] K. Saarinen *et al.*, submitted to Phys. Rev. Lett.

[15] N. M. Reinacher *et al.*, in the Proceedings of the 23rd International Conference on the Physics of Semiconductors, edited by M. Scheffler and R. Zimmermann (World Scientific, Singapore, 1996), Vol. 4.

[16] J. Neugebauer and C. G. Van de Walle, Appl. Phys. Lett. **69**, 503 (1996).

[17] T. Suski *et al.*, Appl. Phys. Lett. **67**, 2188 (1995).

[18] R. K. Watts, *Point Defects in Crystals*, Wiley, New York, 1977.

Materials Science Forum Vols. 258-263 (1997) pp. 1125-1130

PHOTOLUMINESCENCE DYNAMICS IN THE NEAR BANDGAP REGION OF HOMOEPITAXIAL GaN LAYERS

K. P. Korona[1], J. P. Bergman[2], B. Monemar[2], J. M. Baranowski[1], K. Pakuła[1], I. Grzegory[3], S. Porowski[3]

1. Institute of Experimental Physics, Warsaw University, ul. Hoża 69, 00-681 Warszawa, Poland
2. Department of Physics and Measurement Technology, Linköping University, S - 581 83 Linköping, Sweden
3. High Pressure Research Center, Polish Academy of Sciences, ul. Sokołowska 29/37, 01-142 Warszawa, Poland

Keywords: GaN, MOCVD, photoluminescence, time-resolved PL, donors, acceptors.

Abstract. Homoepitaxial MOCVD-grown gallium nitride (GaN) layers have been studied by photoluminescence (PL) measurements and picosecond (ps) time-resolved photoluminescence spectroscopy (TRPL). The TRPL has shown that the free excitons have the fastest dynamics (decay time of a few picoseconds for FE_B and of about 100 ps for FE_A). Then, the 3.472 eV DBE emission rises (with the rise time similar to the free excitons decay time). The 3.467 eV ABE has the slowest decay (about 0.7 ns). The identification of the two-electron transition DBE $\rightarrow$ D* at the energy E_{DBE} - 22 meV has been confirmed by TRPL measurements. The PL emission of an exciton bound to a second acceptor A_2BE at ~3.457 eV is reported. An analysis of the long living part of the DBE emission is also presented.

Introduction

Gallium nitride is a very promising material for optoelectrical devices. The performance of such devices depends upon the dynamics of band to band recombination processes, so the information about photoluminescence kinetics in the near bandgap region of GaN is of great interest. Since the position and intensities of the photoluminescence peaks, and also the observed decay times depend upon the growth technique, it is of interest to study the bulk material or homoepitaxial layers as a reference. The excitonic luminescence spectrum of GaN has been widely studied both for heteroepitaxial [1, 2] and for homoepitaxial layers [3, 4]. It consists mainly of two strong lines caused by recombination of excitons bound to donors (DBE) and acceptors (ABE), respectively. The recombination times in GaN are very fast, in the range of few hundred picoseconds[5, 6]. In this work the luminescence dynamics of the free and bound excitons and two other peaks connected with excitons is analysed.

Experimental techniques

The GaN samples used in our experiments were homoepitaxial layers grown by metalorganic chemical vapour deposition (MOCVD) on GaN single crystals. Their thickness was about 1μm. In order to analyse donor-acceptor interaction some samples with different donor to acceptor ratios have been selected. Most of them were nominally undoped. Since in the undoped MOCVD GaN layers the concentration of donors is always higher than the acceptor concentration, some of the layers (for example sample #3 on Fig. 1.) has been doped with magnesium by adding Cp_2Mg during growth.

Measurements have been done at the temperature 1.8 K. A mode locked solid state Ti:sapphire laser has been used as an excitation source. This produces 300 fs or 2 ps pulses, which are frequency doubled with a BBO crystal to an energy of about 3.53 eV. For spectral measurements the emitted PL has been detected with a cooled CCD camera, while the time resolved measurements have been performed with a synchroscan streak camera.

Results and discussion

The cw-excited photoluminescence spectra of some homoepitaxial GaN layers have been measured. Three of them are plotted in Fig.1. The spectra consist mainly of two strong lines connected with recombination of excitons bound to donors (DBE) and to acceptors (ABE). Their energies are hν = 3.472 eV for DBE and hν = 3.467 eV for ABE. The PL lines has a full width at half maximum (FWHM) of about 1 meV. The ratios of the DBE to ABE intensities are 20, 5 and 0.15 for samples #1, #2 and #3, respectively. All samples show the free exciton lines FE_A and FE_B. Due to the momentum conservation rule, the photon emission by the free exciton is less probable than by the bound exciton, so the FE lines are very weak. The FX_A peak is split by the polariton effect. The energies of free excitons are in agreement with the values previously reported for homoepitaxial GaN: E_A = 3.478 eV, E_B = 3.483 eV[4].

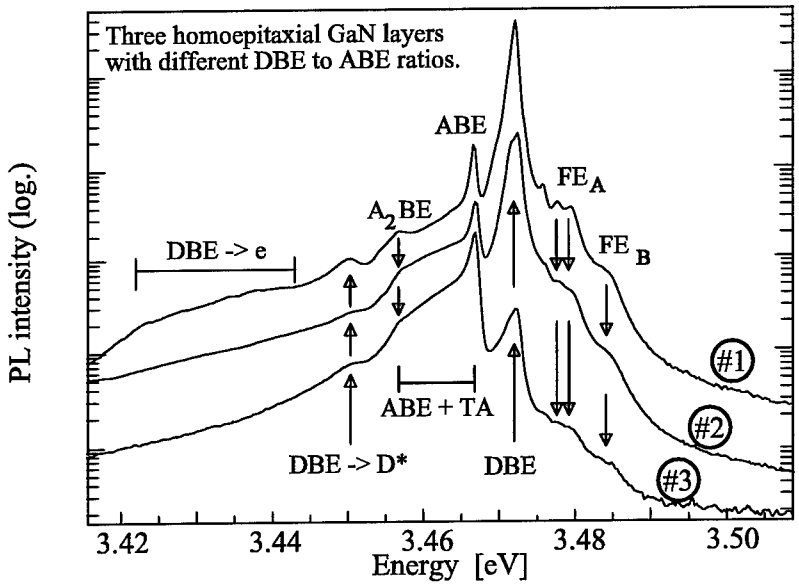

Fig.1. Comparison of cw-excited PL spectra of three GaN layers. Spectra #2 and #3 are shifted down in order not to cross each other.

At the energy 3.450 eV a weak peak is observed. Taking into account that the intensity of this peak correlates with the intensity of the DBE emission, we assigned it as a two-electron replica of the donor bound exciton (DBE → D*). The DBE → D* process consists of the bound exciton recombination with simultaneous excitation of the donor to the n = 2 state. This identification is supported by results of the time-resolved photoluminescence spectroscopy. Figure 2 shows that the DBE → D* feature is best visible just a short time after the laser impulse (when the DBE is strongest) and it nearly vanishes for longer times. In fact the decay process of the DBE → D* is very similar to the DBE decay (see Fig. 4A), it is biexponential, and both decay constant are within experimental error the same as for the DBE emission. For example, for sample #3 t_f = 0.10 ns and

t_s = 0.53 ns for the fast and slow component, respectively. The ABE has probably no direct influence on this emission since the ABE decay is single exponential. The difference between the energy of the DBE → D* and the DBE gives the energy of the donor 1s → 2s transition ΔE = 22 meV. Considering a simple hydrogenic model (neglecting chemical shift and other effects) we obtain a donor ionization energy E_D = 29 meV, in agreement with the numbers reported for heteroepitaxial layer[2].

Interaction of the ABE with transverse acoustic phonons leads to creation of the characteristic ABE+TA band (Fig.1). On the edge of this band (at the energy hν = 3.457eV) a peak, which was by some authors connected with the ABE+TA band, exists. Our TRPL results show that it is a quite independent peak. It has a long lifetime t = 0.7 ns (similar to the ABE lifetime). Figure 2A shows that it is best visible for the longest delay time which means that it rises very slowly, with a rise time about two times longer than the ABE and DBE rise time. In fact, its maximum is delayed about 70ps after the maximum of the ABE (see Fig.3. and Fig. 4B). The slow evolution suggests that the emission comes from an exciton bound to a centre which has a small cross-section for the FE capture, probably caused by a small polarizability of these acceptors. Its dipole moment can be small due to the small radius (r_A<1nm) and can be difficult to induce due to a high ionisation energy. It means that the A_2BE is stronger localised than the shallow acceptors related to the 3.467 eV ABE. Also the high binding energy E_b = 21 meV, suggests that this peak is connected with the exciton bound to a deep acceptor. This peak appears in many samples and is not correlated neither with the other ABE nor the DBE peaks, nor with the doping of the sample. It might be connected with some intrinsic defect which is stronger localised than the shallow acceptors. It could be for example the gallium vacancy, which is expected to be an intrinsic acceptor[7].

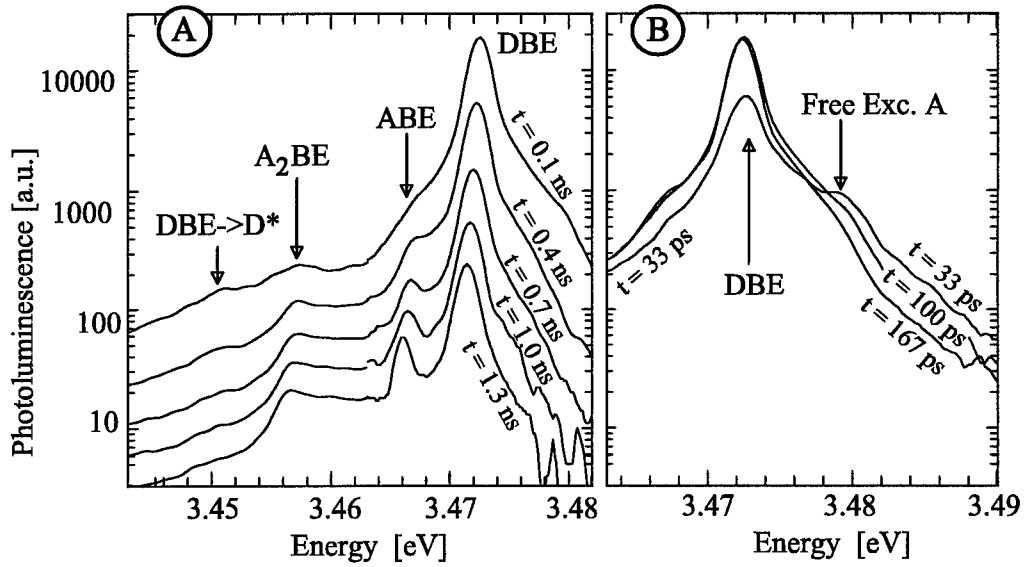

Fig.2. Delayed spectra of GaN photoluminescence (sample #1). The time 't' given on the plots indicates the delay between the laser impulse and the measurement of the spectrum. Note that the times in Fig. B are shorter than in Fig. A.

The time evolution of the excitonic lines is qualitatively similar in all samples with different donor to acceptor ratios. However quantitative differences have been observed. These are caused by the dependence of a nonradiative recombination rates on the defect concentration. It has been found that the fastest kinetics are connected with the free exciton luminescence. The typical process is presented on Fig. 2B. It is observed that for very short time, t = 33 ps, the free exciton

line is strong, then it rapidly vanishes (note that the times in Fig. 2B are shorter than in Fig. 2A). The decay of the free exciton B is very fast, of the order of few picoseconds. So the short lifetime can cause a lifetime broadening of the B exciton line, which has been observed in reflection experiments[8]. This fast decay is probably due to efficient thermalisation of the B to the A polariton state. The free exciton A lives longer, long enough to be well visible on Fig. 3, however its lifetime is still very short. Figure 3 shows that the free exciton emission nearly vanishes even before the DBE emission reaches its maximum. The FE_A decay time is sample-dependent, for example in the layer #1, it is $t_X = 0.10$ ns and in the layer #2 $t_X = 0.03$ ns which is much shorter than the bound exciton lifetime. It is expected that the radiative recombination rate for free excitons should be smaller than (or comparable to) for bound excitons, so the fast recombination of the FE_A is caused by a nonradiative process, for example capture by defects. This conclusion explains also why t_X is sample dependent. The bound exciton PL evolution has been fitted with the exponential rise and decay curve. The obtained rise time t_R of the DBE and the ABE is very similar to the free exciton decay time and is much longer than the hot carrier lifetime. It is $t_R = 0.09$ ns and $t_R = 0.036$ ns, for the DBE in the samples #1 and #2, respectively. This fact suggests that the DBEs are formed rather by binding of free excitons than by independent capture of holes and electrons.

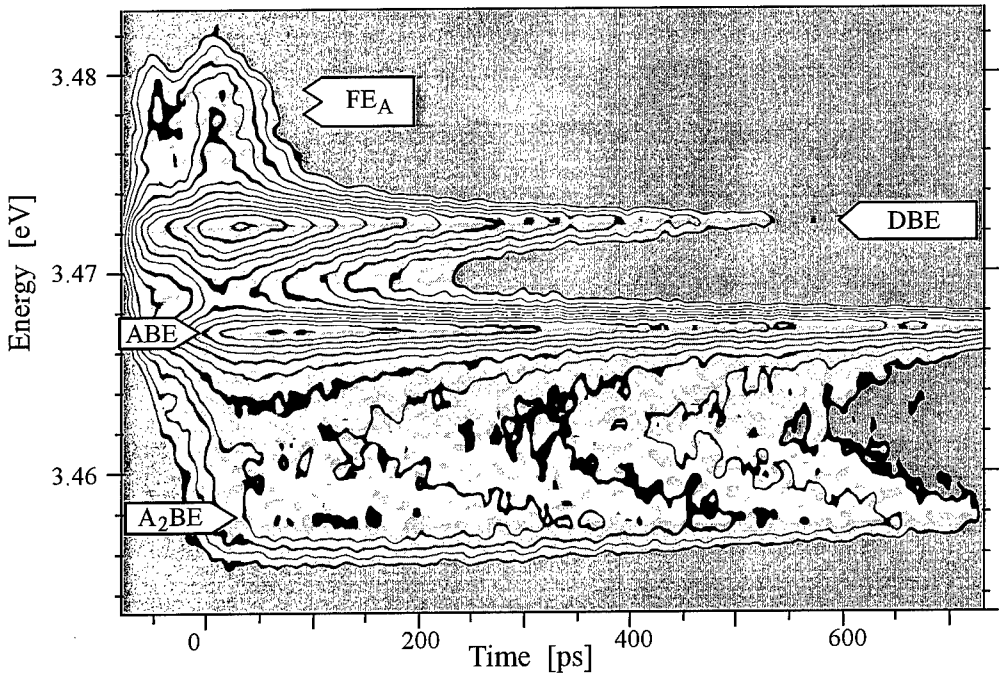

Fig. 3. Contour plot (logarithm of PL intensity versus photon energy and time) of PL evolution of the GaN layer #2. The zero time value has been taken for the maximum of the laser impulse.

One can see (Fig. 3 and Fig. 4) that the DBE recombination is faster than the ABE one. For example on the spectrum of the sample #3 (Fig. 4B), for very short times the DBE emission is stronger then the ABE emission, but for longer times one can observe the opposite proportions. Since the ratio of TRPL amplitude to the time-integrated PL amplitude is reciprocally proportional to the decay time, the TRPL amplitude of the DBE peak is higher than for the ABE even for the layer where the time-integrated PL amplitude of the DBE is lower than the ABE.

Detailed studies show that the DBE decay curve is composed of at least two exponentials (see Fig. 4). The decay times differ between samples, which means that even at the 1.8 K the

nonradiative processes are significant. For example for the sample #1 (high DBE) the faster component has time t_{DBEf} = 0.19 ns and the slower component t_{DBEs} = 1.0 ns, whereas for the sample #3 (low DBE) we obtain t_{DBEf} = 0.10 ns and t_{DBEs} = 0.53 ns.

The rise time of the ABE emission is similar to the DBE, but the maximum of the ABE is always delayed after the DBE. For example on sample #2 (see a contour plot of the streak camera image on Fig. 3) the delay is Δt = 50 ps. It is an effect of a slow decay of the ABE. Contrary to the DBE the ABE decay is a single exponential. It has been checked that even in the sample #1, which has a very strong DBE peak (masking the ABE peak), the ABE emission decay is monoexponential, because the decay of the LO phonon replica of the ABE is monoexponential. The decay time of the ABE does not change significantly between samples and is in the range from 0.6 ns up to 0.8 ns. We can conclude that the time t_{ABE} = 0.7 ns is a good approximation of the ABE radiative decay time.

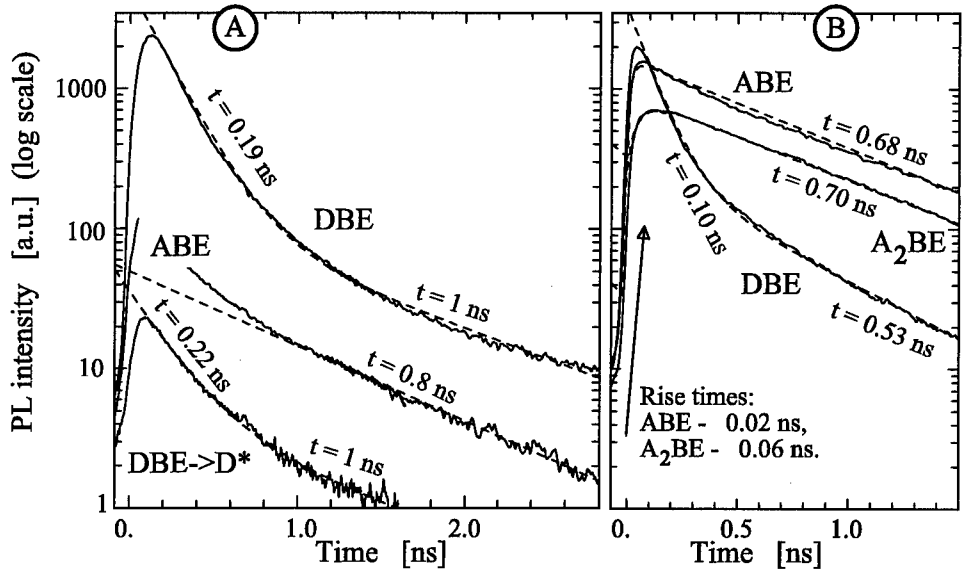

Fig. 4. The PL temporal evolution of the exciton related emission of (A) the sample #1 which has very high time integrated intensity of the DBE, and (B) the sample #3 which has a high ABE peak. The fitted curves (dashed lines) are single exponential for the ABE curve in Fig. A, but double exponential decay for the DBE, and for the DBE → D* curves. The exponential rise and decay curves are fitted for the A_2BE and the ABE in Fig. B.

The slow component of the DBE decay is surprisingly similar to the ABE decay, which may be a coincidence. We believe, however, that there is a strong energy transfer between donors and acceptors by means of exciton tunnelling from donor to acceptor. The shallow donor concentration in our layers is of the order of 10^{17}cm^{-3} what means that the average distance between donor and acceptor is about 10nm what is few times the radius of the exciton bound to a donor. So the exciton tunnelling from donor to acceptor should be possible. Due to low temperature, the transition in the opposite direction is $\exp((E_{DBE}-E_{ABE})/kT) \sim 10^{15}$ times less probable.

The probability of the donor to acceptor tunnelling of exciton depends exponentially upon donor to acceptor distance. So for the donors lying near an acceptor the decay is very fast. This contributes to the fast process which is characteristic for the beginning of the transient and which is stronger in samples with a high ABE peak. But we believe that there are additional nonradiative processes that contribute to the sample-dependent fast initial decay of the DBE (as well as the FE).

The slow decay component observed at long delay times for the DBE is present in all our samples, and also has been reported for heteroepitaxial layers[9]. It decay time is similar to the ABE one, but its amplitude is not correlated with the ABE. We tentatively suggest that this long living tail might be due to a crystal field split component of the DBE line, which has a long lifetime (forbidden optical transition). Such a state could nevertheless obtain an initial occupation, and subsequently transfer the DBE to the radiative DBE states, which are expected to have a fairly short radiative lifetime (about 250 ps [9]). The slow decay component of the DBE then would correspond to the decay of the optically forbidden DBE component. The second possibility is a direct emission from another DBE (may be bound to another kind of donor). In this case the long living component of the DBE emission should have a different energy. However, the spectral resolution in our equipment (1meV) is not sufficient to verify this suggestion.

Conclusions

In summary, the spectral and time resolved photoluminescence of exciton related emissions in homoepitaxial GaN has been analysed. The TRPL has shown that the free excitons have fast, sample dependent dynamics (decay time of a few picoseconds for FE_B and of about 100 ps for FE_A) which indicates a contribution of a nonradiative recombination. The DBE emission rises with the rise time similar to the free excitons decay time, which suggests that the DBEs are formed rather by binding of the free excitons than by independent capture of holes and electrons. It has been found that the ABE has a slow decay. Its radiative recombination time is about 0.7 ns. It has been proposed that the exciton tunnelling from donor to acceptor contributes to the nonexponential character of the DBE decay. The identification of the two-electron transition DBE $\rightarrow$ D* at the energy E_{DBE} - 22 meV has been confirmed by TRPL measurements. The PL emission at $h\nu$ = 3.457eV has been assigned to an exciton A_2BE bound to a second acceptor.

References:

[1] See e.g. O. Lagerstedt and B. Monemar, J. Appl. Phys. **45**, p. 2266 (1974)
[2] B.J. Skromme, H. Zhao, B. Goldenberg, H.S.Kong, M.T. Leonard, G.E. Bulman, C.R. Abernathy, S.J. Pearton, MRS Proc. 449, p. 713, ed. F.A. Ponce, T.D. Moustakas, I. Akasaki, B. Monemar, (MRS, Pittsburgh, 1997)
[3] K.Pakuła, A.Wysmołek, K.P.Korona, J.M.Baranowski, R.Stępniewski, I.Grzegory, B.Łucznik, M.Wróblewski, S.Porowski, Solid State Commun. **97**, p. 919 (1996)
[4] K.P.Korona, A.Wysmołek, K.Pakuła, R.Stępniewski, J.M.Baranowski, I.Grzegory, B.Łucznik, M.Wróblewski, S.Porowski, Appl. Phys. Lett. **69**, p. 788 (1996)
[5] J.P. Bergman, B. Monemar, H. Amano, I. Akasaki, T. Detchprohm, K. Hiramatsu and N. Sawaki, Proc. ICSCRM'95, Kyoto 1995, IOP Conference Proceedings **142**, p. 931 (1996).
[6] M. Godlewski, A. Wysmolek, K. Pakula, J.M. Baranowski, I. Grzegory, J. Jun, S.Porowski, J.P. Bergman, B. Monemar, Proc. Int. Symposium of Blue Laser and Light Emitting Diode, Ed. by A.Yoshikawa, K.Kishino, M. Kobayashi, T.Yasuda, p.356, (Omsha Ltd, Tokyo, 1996)
[7] J. Neugebauer and C. G. Van de Walle, Phys. Rev. **B50**, p. 8067 (1994)
[8] R. Stępniewski, K.P. Korona, A. Wysmołek, J.M. Baranowski, K. Pakuła, M. Potemski, G. Martinez, I. Grzegory, S. Porowski, to be published (submitted to Phys. Rev. 1997)
[9] B. Monemar, J.P. Bergman, H. Amano, I. Akasaki, T. Detchprohm, K. Hiramatsu, N. Sawaki, Proc. Int. Symposium of Blue Laser and Light Emitting Diode, Ed. by A.Yoshikawa, K.Kishino, M. Kobayashi, T.Yasuda, p. 135-140, (Omsha Ltd, Tokyo, 1996)

Materials Science Forum Vols. 258-263 (1997) pp. 1131-1136

ZEEMAN STUDY OF THE 0.9 eV EMISSION IN AlN AND GaN

P. Thurian, I. Loa, P. Maxim, K. Pressel*, A. Hoffmann, and C. Thomsen
Institut für Festkörperphysik, TU-Berlin, Hardenbergstr. 36, 10623 Berlin, GERMANY
***Inst. for Semiconductor Physics, Walter-Korsing Str. 2, 15230 Frankfurt (Oder), GERMANY**

Keywords: AlN, GaN, transition metals, V^{3+}, photoluminescence, Zeeman effect

Abstract: We investigate the magnetooptical properties of the 0.9 eV luminescence in AlN and GaN. The zero-phonon lines at 0.943 eV in AlN and at 0.931 eV in GaN are attributed to transitions within a d^2-configuration, because of a characteristic threefold ground-state splitting in magnetic fields. For AlN we determine a g-value of 1.96±0.07 and a zero-field splitting of 120±30 μeV for the $^3A_2(F)$ ground state. On the basis of the temperature dependence in a magnetic field, we attribute the 0.943 eV zero-phonon line in AlN to the $^1E(D)$-$^3A_2(F)$ transition and the 0.931 eV zero-phonon line in GaN to the $^3T_2(F)$-$^3A_2(F)$ transition of isolated V^{3+}. The different fine-structure of the excited state in AlN and GaN is explained in a Tanabe-Sugano diagram.

Introduction

Despite the enormous progress in growth and device technology there is only little information about deep defects in group III-nitrides. Transition metals (TMs) form deep defects and can be expected to be common contaminations of these materials which are grown at very high temperatures. In spite of their technological relevance for growing high resistivity material, not much detailed information on TM defects is available up to now.
Usually, the TMs are incorporated substitutionally on the metal-cation site in III-V compounds. Thus, the neighborhood of the TM is given by four nitrogen atoms. Because of the localized wavefunction of the deep impurity and the similar lattice constants of GaN and AlN together with their large bandgaps, it is expected that internal transitions of the same transition metal element appear at about the same energy. Up to now, five TM luminescence bands have been reported for both GaN and AlN and they are compared in [1] .
On the basis of magnetooptical measurements, the electronic configurations of the 1.30 eV and 1.19 eV TM defects in GaN were identified. The 1.30 eV luminescence is unambiguously attributed to the $^4T_1(G)$-$^6A_1(S)$ transition of Fe^{3+} ($3d^5$-system) [2,3], whereas the 1.19 eV zero-phonon line (ZPL) is attributed to the $^1E(D)$-$^3A_2(F)$ transition of a d^2-system [4]. Ti^{2+} and Cr^{4+} are discussed as luminescence centers [4,5]. No other magnetooptical measurements have been performed so far. For GaN, the ZPLs at 0.931 eV and 0.82 eV are attributed to V^{3+} [5] or TM-complex centers [1]. Analogous assignments have been performed for the ZPLs at 1.297 eV, 1.201 eV, 1.043 eV, 0.943 eV and 0.797 eV in AlN [1]. No Zeeman data were published for AlN up to now. In this paper we report on the first Zeeman study of the 0.943 eV ZPL in AlN and the 0.931 eV ZPL in GaN.

Experimental Results

The AlN samples were grown by mixing Al and N at very high temperatures (1900°C). Small AlN crystalline needles were obtained with a typical length of 3 mm and a diameter of about 100 μm. The GaN sample investigated here was epitaxially grown on (0001) sapphire by Hydride Vapour Phase Epitaxy. The sample was 400 μm thick and has n-type conductivity. Photoluminescence (PL) was excited by various lines of an Ar^+ or Kr^+ laser. The Zeeman PL experiments were carried out using a superconducting 15 T magnet built in split-coil configuration. All Zeeman

measurements were done in Faraday configuration (H||k). The luminescence was detected by a cooled Ge photodiode.

Figure 1 shows typical luminescence spectra of the AlN and GaN samples at T= 1.8 K. For GaN, the 1.30 eV, the 1.19 eV and the 0.93 eV emission bands are observed, when exciting the samples with the 2.61 eV emission line of the Ar^+ laser. For AlN, only the 0.94 eV and the 0.79 eV luminescence is detected using the blue/green lines of the Ar^+ laser for excitation. With 1.92 eV excitation, the 1.2 eV and the 1.05 eV luminescence are also observed in AlN. The 1.297 eV ZPL is not observed in our AlN samples. This indicates a different impurity content of the AlN samples compared to the AlN ceramics investigated by Baur *et al.* [5].

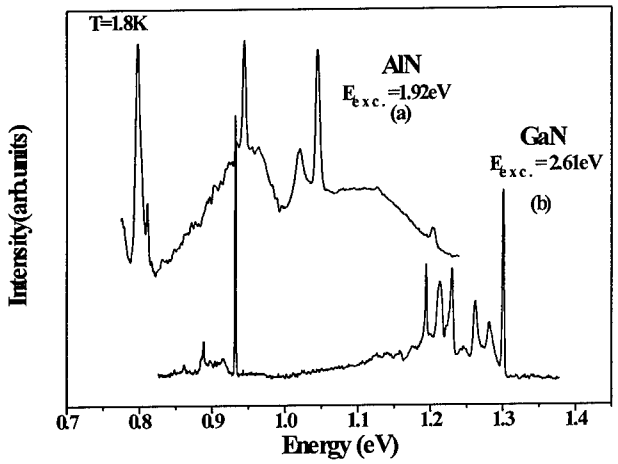

Figure 1: Photoluminescence spectra of AlN and GaN at T=1.8 K. The samples were excited at 1.92 eV (a) and at 2.61 eV (b), respectively.

The 0.9 eV ZPL in GaN and AlN

In order to investigate the fine-structure of the 0.9 eV ZPLs in AlN and GaN, we performed temperature dependent PL studies. Only for GaN a hot line 1.6 meV above the main peak at 0.931 eV is observed, whereas for AlN no hot lines could be detected. This indicates, that the excited state is a singulet for AlN and a doublet for GaN. No polarization effects could be detected. These results are in accordance with those of Pressel *et al.* [1] and Baur *et al.* [5].

High resolution spectra of the 0.943 eV ZPL in AlN for magnetic fields of 0 T, 9 T and 15 T are shown in figure 2. For 0 T, in addition to the main peak at 0.943 eV, a weak shoulder is detected on the low energy side. These structures can be fitted with two Gaussian lineshapes peaking at 0.94255 eV and 0.94170 eV. The full width at half maximum (FWHM) is 1.5±0.1meV for the main peak and 1.9±0.5 meV for the weak structure.

With increasing magnetic field, a threefold splitting of the main ZPL is observed above B= 7 T in the configuration H⊥c. The intensity ratio of the three lines does neither depend on the temperature nor on the magnetic field. This indicates that the splitting occurs in the ground state of the impurity. The splitting can be fitted with three Gaussian lineshapes with a FWHM of 1.5 meV for each peak. It is observed, that the energy splitting between the two high energy ZPLs of the three ZPLs is slightly larger than that of the two low energy ZPLs. This behavior indicates a zero-field splitting.

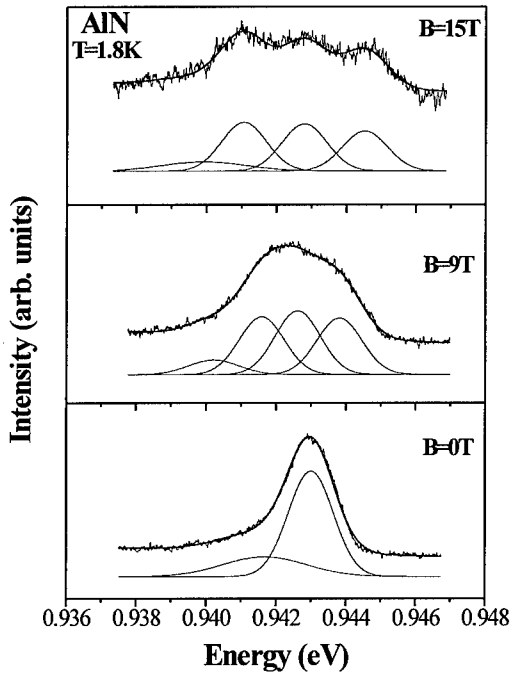

Figure 2: Zero-phonon line region of the 0.943 eV emission in AlN for different magnetic fields at T=1.8 K. The threefold splitting of the main ZPL is caused by the magnetic behavior of the $^3A_2(F)$ ground state.

The weak structure at 0.9417 eV, observed in spectrum at 0 T exhibits a broadening up to a FWHM of 2.8±0.5 meV at 15 T. This broadening corresponds to a g-value of 1.0±0.2, which indicates a different Zeeman-behavior compared to the main ZPL. However, due to the signal to noise ratio, the broadening could be larger, too. Possibly this shoulder is caused by internal strain or a disturbance in the neighborhood of the luminescence center.

The energy positions of the three fitted peaks in dependence on the magnetic field are summarized in Fig. 3. By fitting the data points in dependence on the magnetic field, it is clearly observed that a zero-field splitting of the ground state exists ($|D|=120\pm30$ μeV). Such a Zeeman behavior is a typical fingerprint for $^3A_2$ ground state of a d^2 configuration in trigonal symmetry usually detected by EPR measurements [10].

In order to check whether the spectra are isotropic, we rotated the AlN needle at B = 14 T from $H\perp c$ to $H\|c$. Within the margin of error, the Zeeman pattern did not depend on the rotation angle θ. Together with the almost symmetric Zeeman pattern (Fig. 3), this indicates that there is no Zeeman splitting of the excited state.

For GaN, only a broadening of the ZPL is observed in dependence on the magnetic field. This is mainly due to the larger FWHM of the ZPL (3 meV) in comparison to AlN and leads to a larger error of detection for GaN. However, the broadening of the 0.931 eV ZPL in GaN can be simulated assuming a threefold symmetrical splitting and using three identical Gaussian lineshapes with constant FWHM for all magnetic fields. This procedure results in an estimated g-value of 2.0±0.5 in agreement with that of the 0.943 eV emission in AlN.

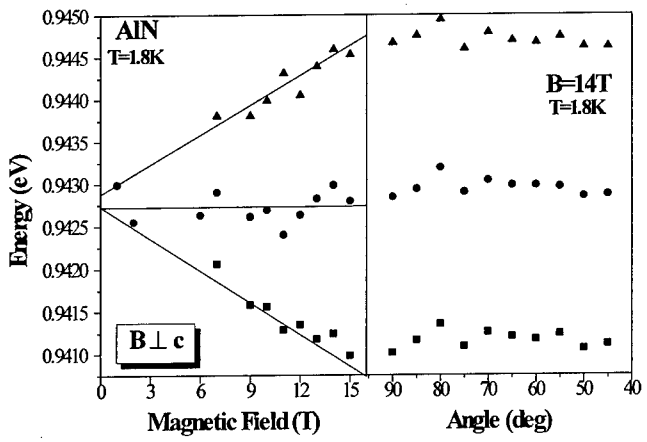

Figure 3: Zeeman behavior of the 0.943 eV ZPL for **B⊥c** (left) and angular dependence at B=14 T (right). The zero-field splitting of 120±30μeV together with the g-value of 1.96±0.07 is a fingerprint for the $^3A_2(F)$ ground state of V^{3+}.

Discussion

Taking into account the identical neighborhood of a TM impurity in both nitride compounds, one should expect similar ZPL energies in both compounds, if these ZPLs are due to the same TM. This is what we observed in the case of the 0.943 eV and 0.931 eV emissions in AlN and GaN, respectively. In the context of our results, cation-substitutional $V^{3+}(3d^2)$ is the most probable TM candidate for these ZPLs in AlN and GaN. However, the observed fine-structure of the impurity transition is slightly different for both host compounds (Fig. 4). For AlN, no hot line and no phonon sideband is observed for the 0.943 eV ZPL. Together with the isotropic threefold Zeeman splitting of the ground state it seems most probable to attribute this ZPL to a $^1E(D)$-$^3A_2(F)$ transition where the g-value of the excited state is smaller than 0.1. It is expected, that the electron-phonon coupling of such a transition is small for both the ground and excited state, explaining the missing of a phonon sideband. Such a weak phonon coupling is also observed for the 1.19 eV ZPL in GaN, which is caused by a $^1E(D)$-$^3A_2(F)$ transition [4]. As already mentioned by Baur *et al.* [5], a hot line 1.6 meV above the main ZPL at 0.931 eV is observed for GaN. For GaAs, GaP, and InP, vanadium correlated ZPLs between 0.73 and 0.83 eV have been assigned to the symmetry forbidden $^3T_2(F)$-$^3A_2(F)$ crystal field transition of V^{3+}. At higher sample temperatures hot ZPLs separated by 1.2 meV, 1.9 meV and 1.5 meV from the cold ZPL have been reported for these materials [7]. The analogy to the GaN PL data is obvious. The line position of the ZPL is mainly determined by the cubic crystal field strength (Dq), which increases with the ionicity of the host crystal. Therefore, the higher energy of the emission in GaN and AlN is not suprising. The hot ZPL in GaN can be explained by a moderately strong dynamic Jahn-Teller effect [7]: The first order spin-orbit interaction within the excited $^3T_2(F)$ state is quenched by electron-phonon coupling; thermal occupation of the upper level at elevated temperatures yields an additional hot ZPL. The splitting between the ZPLs is mainly determined by the spin-orbit coupling constant λ, which is characteristic for the incorporated impurity atom. The splitting of 1.6 meV in the GaN PL is in excellent agreement with the splittings observed for V^{3+} impurities in other III-V compounds. It is also expected that the electron-phonon coupling for the $^3T_2(F)$-$^3A_2(F)$ is stronger than for the $^1E(D)$-$^3A_2(F)$ transition, explaining the stronger phonon sideband in GaN.

The different fine-structures found for GaN and AlN can be explained in the context of a schematic Tanabe-Sugano diagram. For smaller crystal field strength (10 Dq), the $^3T_2$ state is below the $^1E(D)$ state (GaN-case), whereas for larger crystal fields, the $^1E(D)$ state is below the $^3T_2(F)$ state (AlN-case). Because of the smaller lattice constant of AlN compared to GaN, it is expected, that the crystal field strength (10 Dq) is slightly stronger in AlN. The crystal-field transition in both cases should be located near the crossover point of the $^3T_2(F)$ and $^1E(D)$ level in the schematic Tanabe-Sugano diagram.

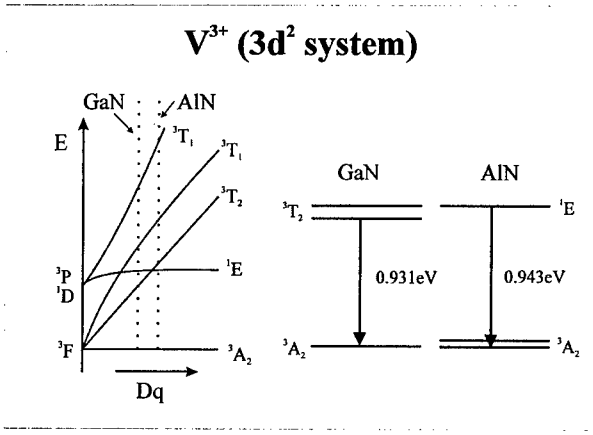

Figure 4: Schematic Tanabe-Sugano diagram for a $3d^2$-system together with the observed fine-structure for the V^{3+}-center in GaN and AlN. The larger crystal-field para-meter Dq for AlN is caused by the smaller lattice constant of AlN compared to GaN and explains the different fine structure of the excited states.

As mentioned above, the magnetoptical behavior (Fig. 3) of the 0.943 eV ZPL in AlN is a clear fingerprint for the $^1E(D)$-$^3A_2(F)$ transition. A zero-field splitting of $|D|=120\pm30$ μeV within the ground state is observed. In contrast to EPR, the sign of the splitting parameter D can be determined from the magnetooptical spectra. We obtain a positive sign for D and a g-value of 1.96 ± 0.07. These results are in good qualitative agreement with ZnO:V^{3+}. For ZnO:V^{3+}, a ground-state g-value of 1.93 and a zero-field splitting of D= +97 μeV were obtained [8,9]. The slightly larger D-value in GaN is due to the stronger covalent bonding compared to ZnO.

Similar trends for the zero-field splitting for the Fe^{3+} center in GaN compared to ZnO and ZnS are also known [3] (D=-8.84 μeV GaN, -7.38 μeV ZnO, -5.95 μeV ZnS). By comparing D for different d^2-systems in similar hosts, the spin-orbit coupling constant is the leading parameter for the magnitude of the zero-field splitting. A larger spin-orbit coupling constant λ should result in a larger D-value [10]. The free-ion value of λ increases from Ti^{2+} to V^{3+} and Cr^{4+} (λ=60 cm^{-1} (Ti^{2+}), 106 cm^{-1} (V^{3+}), 163 cm^{-1} (Cr^{4+})) due to the larger atomic number Z. It is expected, that the zero-field splitting is similar for identical TMs in AlN and GaN. It should be emphasized, that no zero-field splitting is observed for the magnetooptical measurements of the $^1E(D)$-$^3A_2(F)$ transition of the 1.19 eV luminescence in GaN which was attributed to Ti^{2+} [4] and Cr^{4+} [5] as well. As a consequence of the missing zero-field splitting, Ti^{2+} seems to be more probable than Cr^{4+} to explain the 1.19 eV ZPL in GaN. The observation of the zero-field splitting of the 0.943 eV ZPL in AlN is thus a further proof for the V^{3+} attribution in AlN and to the 0.931 eV ZPL in GaN. Unfortunately, the quality of Zeeman-data for GaN does not allow a direct estimation of a possible zero-field splitting of the 0.931 eV ZPL.

In order to prove the chemical nature of a defect, ion implantation of the corresponding TM is sometimes useful. However, the lattice damage and the creation of new defects during the implantation process makes the interpretation of the data difficult.

Recently, it was shown by Kaufmann *et al.* [6] that the implantation of vanadium in GaN followed by heat treatment gives rise to an intense PL emission at 0.82 eV. The center occurs in several

modifications caused by the radiation damage in the neighborhood of the impurity. No correlation between the 0.931 eV ZPL and the V doping is observed by these authors. This might indicate, that the charge state of the implanted V is different from the 3+ state. In the context of these results it is useful to compare these results with the properties of vanadium in ZnSe. Here, V^{3+}, V^{2+} and V^{+} can be observed in the same crystal, depending on the Fermi level position and on the excitation energy [11]. Thereby, the energy of the corresponding transition decreases from V^{3+} to V^{2+} and V^{+}. In this context it is also probable, that the 0.82 eV PL in GaN is related to V^{2+} or V^{+}. Also, V^{2+} with nearby radiation induced defects seems to be a reasonable interpretation for the 0.82 eV ZPL in GaN. Due to the fact, that our AlN needles also show the 0.797 eV ZPL, a vanadium correlation is also probable for these ZPLs. In summary, there is strong evidence to attribute the 0.943 eV ZPL in AlN and the 0.931 eV ZPL to recombinations within isolated V^{3+} centers.

Acknowledgements:
The authors are indepted to W. Pasternak for the supply of AlN samples and to K. Hiramatsu for the supply of GaN crystals.

References

[1] K. Pressel, R. Heitz, S. Nilsson, P. Thurian, A. Hoffmann, and B. K. Meyer, MRS, Boston, 1996, Symp. Proc. Vol. **395**, 613
[2] R. Heitz, P. Thurian, I. Loa, L. Eckey, A. Hoffmann, I. Broser, K. Pressel, B.K. Meyer, and E.N. Mokhov, Appl. Phys. Lett. **67**, 2822 (1995).
[3] K. Maier, M. Kunzer, U. Kaufmann, J. Schneider, B. Monemar, I. Akasaki, and H. Amano, Mat. Science Forum **143-147,** 93 (1994)
[4] R. Heitz, P. Thurian, K. Pressel, I. Loa, L. Eckey, A. Hoffmann, I. Broser, B.K. Meyer, and E.N. Mokhov, Phys. Rev. B **52**, 16508 (1995).
[5] J. Baur, U. Kaufmann, M. Kunzer, J. Schneider, H. Amano, I. Akasaki, T. Detchprohm, K. Hiramatsu, Mat. Science Forum **196-201**, 55 (1995)
[6] B. Kaufmann, A. Dörnen, V. Härle, H. Bolay, F. Scholz, and G. Pensl, Appl. Phys. Lett. **68**, 203 (1996)
[7] G. Aszodi and U. Kaufmann, Phys. Rev. B **32**, 7108 (1985)
[8] R. Heitz, A. Hoffmann, B. Hausmann, and I. Broser J. of Lum. **48&49**, 689 (1991)
[9] A. Hausmann and E. Blaschke, Z. Phys. **230**, 255 (1970)
[10] A. Abragam and B. Bleaney in EPR of Transition Ions, Oxford University Press, 1970,426 ff.
[11] G. Goetz, U. W. Pohl, H.-J. Schulz, and M. Thiede, J. Lumin. **60&61**, 16 (1994)

Materials Science Forum Vols. 258-263 (1997) pp. 1137-1142

A FIRST-PRINCIPLES STUDY OF Mg-RELATED DEFECTS IN GaN

K. J. Chang and Sun-Ghil Lee

Department of Physics, Korea Advanced Institute of Science and Technology, Taejon 305-701, Korea

Keywords: gallium nitride, deep level defect, photoluminescence

Abstract. We study the energetics of Mg-related defects in GaN through first-principles pseudopotential calculations. In *p*-type GaN, Mg_{Ga}^{-} acceptors are found to be compensated by V_N^{+} donors and also deactivated by the formation of complexes such as Mg_{Ga}-V_N and Mg_i-V_N. We suggest that a Mg_i-V_N complex, which consists of a Mg interstitial and a N-vacancy, is responsible for the blue luminescence observed in heavily Mg-doped GaN. Although this defect complex is easily passivated by three hydrogen atoms, thermal annealing recovers the activity of this complex and thereby increases the intensity of the blue luminescence.

Introduction.

It is achievable low resistive *p*-type GaN with hole concentrations up to 10^{18} cm^{-3} by doping with Mg impurities [1-3]. Since the hole carrier concentration is much lower than the total amount of incorporated Mg impurities, it is highly expected that the Mg acceptors are compensated for by some donors and passivated by hydrogens [3]. Recent experiments showed that heavily Mg-doped GaN films exhibit blue luminescences (BL) around 2.7 - 2.9 eV, the intensity of which increases with increasing of temperature [4,5], whereas the donor-acceptor pair peaks associated with the shallow Mg acceptors at about 3.2 eV are quenched. Nakamura and his coworkers reported that the intensity of the BL increases with increasing of annealing temperature up to 700°C and then quenches for further annealings, while the resistivity begins to decrease at about 400°C with an almost constant value above 700°C.

In this work, we perform first-principles theoretical calculations to study the energetics of Mg-related defects in GaN. Calculating the formation energies of various defects, we determine the defect stability which depends on growth condition and find that Mg_{Ga}^{-} impurities are deactivated by the formation of Mg_{Ga}-V_N and Mg_i-V_N complexes. To see the temperature dependence of the blue luminescence, we examine the hydrogen passivation and migration of a Mg atom in a Mg_i-V_N complex, which was recently suggested to be responsible for the blue luminescence band at about 2.7 - 2.9 eV [6].

Method.

Our calculations are based on the first-principles pseudopotential method within the local-density-functional approximation (LDA) [7]. The Wigner interpolation formula is used for the exchange and correlation potential [8]. Norm-conserving nonlocal pseudopotentials are generated by the scheme of Troullier and Martins and transformed into the separable form of Kleinman and Bylander [9]. For Ga pseudopotentials, it is known that the inclusion of the Ga $3d$ states in the core shell results in a poor description of the ground state properties for GaN. With partial core corrections, however, the bulk properties of GaN are much improved, as compared to the Ga potentials with the $3d$ electrons in the valence shell. We employ a supercell

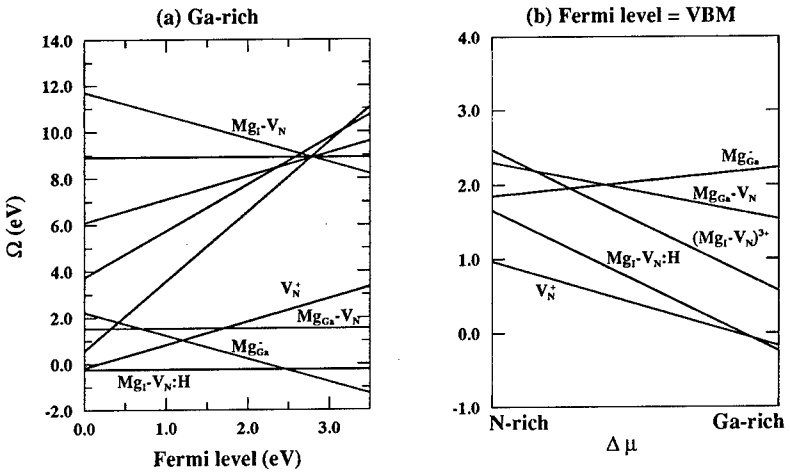

Fig. 1. (a) Defect formation energies (Ω) as a function of the Fermi energy for Ga-rich condition and (b) Ω vs $\Delta\mu$ for the Fermi energy equal to the valence band maximum, where $\Delta\mu$ represents the difference of the Ga and N chemical potentials (Ref. 12) and varies from the N-rich to the Ga-rich limit.

containing 72 host atoms for the wurtzite structure. The wave functions are expanded in a plane-wave basis set with a kinetic energy cutoff of 25 Ry throughout this work. We use one special **k** points to perform the Brillouin zone summation of the charge density. The energy functional is fully minimized by the modified-Jacobi relaxation method which has been employed successfully for a variety of systems [10]. We relax internal ionic positions by calculating the Hellmann-Feynman forces until the optimized atomic configuration is obtained [11]. The stability of a defect is determined by calculating the formation energy, which is well discussed in Ref. 12.

Results and discussion.

In GaN, a Mg atom behaves as a single acceptor by occupying a Ga-sublattice site. Since the atomic radius (1.301 Å) of the Mg atom is not very different from that of the Ga atom (1.225 Å), lattice relaxations of the Mg_{Ga} neighboring atoms are very small. Thus, the formation energy of a substitutional Mg_{Ga}^{-} is quite low as shown in Fig. 1. When a Mg atom occupies a N-sublattice site, it gives large lattice distortions for the neighboring Ga atoms and a high formation energy, thus, its existence is highly unlikely. Under Ga-rich condition, Mg_{Ga}^{-} has the same formation energy as that of V_N^+, when the Fermi level lies at 1.2 eV above the valence band maximum. The V_N^+ donors, which are believed to cause the intrinsic n-type conductivity of as-grown GaN without extrinsic impurities such as O and Si, are likely to compensate for Mg acceptors. Since V_N^+ and Mg_{Ga}^{-} are the most stable defects and attract electrostatically with each other, a pair of these defects is quite probable, with the binding energy of 0.52 eV with respect to their isolated configurations. The Mg_{Ga}-V_N complex is electrically inert via self-compensation and the defect levels are not much different from those of isolated Mg_{Ga} and V_N. We next consider the complexes composed of a Mg interstitial and vacancies, i.e., Mg_i-V_N and Mg_i-V_{Ga}. Previously, the V_{Ga} acceptor and its complex with oxygen were suggested to be

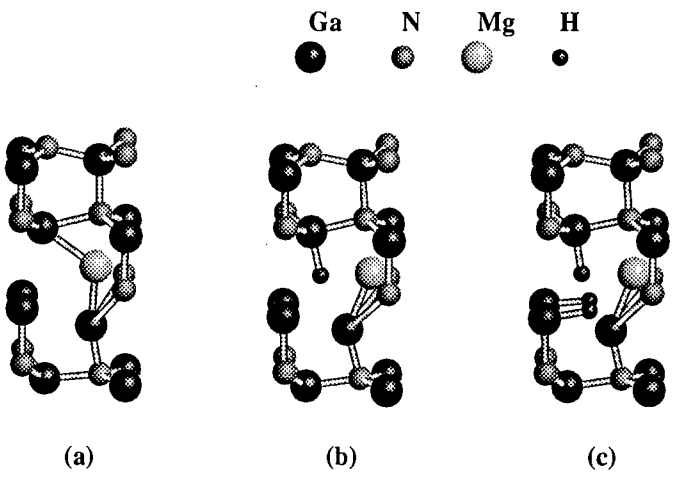

Fig. 2. Stable atomic geometries for (a) a Mg_i-V_N complex and complexes passivated by (b) one and (c) three hydrogen atoms.

the origin of the yellow luminescence in GaN [13,14]. However, we do not expect the existence of V_{Ga} due to its high formation energy, particularly, in *p*-type GaN. In addition, the Mg_i-V_{Ga} complex is highly unstable because the interstitial Mg atom is relaxed into the Ga-vacancy site. On the other hand, the Mg_i-V_N complex is a stable donor, especially, for Ga-rich limit (see Fig. 1). Investigating the transition levels, this defect complex was suggested to give rise to the blue luminescences around 2.7 - 2.9 eV [6]. When the Fermi level is close to the valence band maximum, the formation energies of V_N^+, Mg_{Ga}-V_N, and $(Mg_i\text{-}V_N)^{3+}$ become lower than that of Mg_{Ga}^-, deactivating the Mg acceptors. This behavior is more prominent as going to the Ga-rich limit, as shown in Fig. 1.

In Mg-dopd GaN, post-growth annealing and low energy electron beam irradiation increase the hole carrier concentration and pick up the intensity of the BL [1,3,4]. Since hydrogens are readily incorporated during growth, both the Mg_{Ga}^- acceptors and $(Mg_i\text{-}V_N)^{3+}$ donors are expected to be highly passivated by hydrogens. Recent theoretical calculations showed that hydrogen occupies an antibonding site of one of the acceptor neighbors to passivate the Mg_{Ga} acceptor [15]. In a neutral Mg_i-V_N complex, the Mg atom is strongly bonded to the two nearest Ga atoms of V_N and the remaining two Ga neighbors make a strong Ga-Ga bond with the bond length of 2.776 Å. In this complex, we find that a single H atom has the lowest energy when it is bonded to one of the two Ga atoms bonded to the Mg atom, as shown in Fig. 2(b), however, the formation energy is very high, exceeding 5 eV. When three H atoms are involved, the most stable geometry is that the H atoms and Mg interstitial are directly bonded to the four Ga neighbors of V_N [see Fig. 2(c)], and the Ga-Ga bond is nearly broken with the bond length of 3.021 Å. We find that the Mg_i-V_N complex passivated by three H atoms is very stable, as shown in Fig. 1. Recently, it was reported that hydrogens are easily dissociated upon annealing and mobile in *p*-type GaN, with the the barrier height of 0.7 eV for H^+ diffusion [15]. We also expect that thermal annealing activates the passivated Mg_i-V_N complex by releasing hydrogens, thus, it increases the intensity of the BL. Although the intensity of the BL was shown to increase with increasing of annealing temperature, it

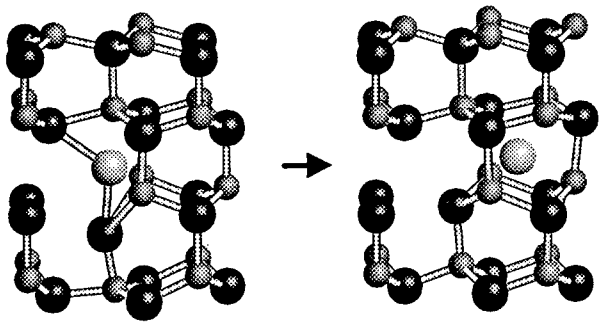

Fig. 3. A migration path of Mg_i^{2+} into a neighboring interstitial site in the $(Mg_i\text{-}V_N)^{3+}$ complex.

begins to quench as the annealing temperature increases above 700°C [4]. To see whether the weakening of the BL intensity is related to the dissociation of a Mg interstitial at very high annealing temperatures, we investigate the energy barrier for Mg migration from the Mg_i-V_N complex to a nearest interstitial site (see Fig. 3). Because of the small lattice volume of GaN, the migration of a neutral Mg atom costs very high energy when passing through the host lattice, while an ionized Mg^{2+} atom can diffuse rather easily due to the small ionic size and the attractive interaction with electrons distributed in the bonding regions. This diffusion is easily proceded, especially, for *p*-type GaN, similar to the H^+ diffusion. In the diffusion process of Mg shown in Fig. 3, the energy barrier is estimated to be about 1.4 eV. Considering such a moderate diffusion barrier, the Mg interstitial in the Mg_i-V_N complex is likely to diffuse out at very high annealing temperatures, decreasing the intensity of the BL. On the other hand, the resistivity of *p*-type GaN showed different behavior upon annealing; it decreases with increasing of annealing temperature and has an almost constant value above 700°C [4]. As the annealing temperature increases, the hydrogen atoms are released from both the Mg_{Ga} acceptor and Mg_i-V_N complex, thus, the activated Mg_{Ga} acceptors decrease resistivity. For further annealings, although the Mg interstitial in the Mg_i-V_N complex diffuse out easily, the Mg_{Ga} acceptor remains very stable. We calculate the energy barrier for the Mg diffusion from a Mg_{Ga} acceptor to an interstitial site to be about 7 eV, which is much higher than that for the Mg_i-V_N complex. Thus, the resistivity remains unchanged for annealing temperatures above 700°C.

Summary.

In summary, we have found that it is difficult to achieve very low resistive *p*-type GaN by doping Mg impurities because of the formation of the Mg_{Ga}-V_N and Mg_i-V_N complexes, which compensate for the Mg_{Ga}^- acceptors. The Mg_i-V_N complex, which gives rise to the blue luminescence in heavily Mg-doped GaN, is stabilized by hydrogen passivation. Upon annealing, the intensity of the blue luminescence increases while the resistivity decreases, because hydrogen dissociation increases the activity of both the Mg_{Ga}^- acceptor and Mg_i-V_N complex. However, at very high annealing temperatures, it is highly likely for the Mg interstitial in the Mg_i-V_N complex to diffuse out, reducing the intensity of the blue luminescence, while the Mg_{Ga}^- acceptor is very stable, keeping almost the same resistivity.

Acknowledgments.

This work was supported by the Ministry of Science and Technology, the CMS at KAIST, and the SPRC at Jeonbuk National University.

References.

1. S. Nakamura, M. Senoh, and T. Mukai, Jpn. J. Appl. Phys. **30**, L1708 (1991).
2. H. Morkoc, S. Strite, G. B. Gao, M. E. Lin, B. Sverdlov, and M. Burns, J. Appl. Phys. **76**, 1363 (1994).
3. M. S. Brandt, N. M. Johnson, R. J. Molnar, R. Singh, and T. D. Moustakas, Appl. Phys. Lett. **64**, 2264 (1994).
4. S. Nakamura, T. Mukai, M. Senoh, and N. Iwasa, Jpn. J. Appl. Phys. **31**, L139 (1992).
5. M. Smith, G. D. Chen, J. Y. Lin, H. X. Jiang, A. Salvador, B. N. Sverdlov, A. Botchkarev, H. Morkoc, and B. Goldenberg, Appl. Phys. Lett **68**, 1883 (1996).
6. S.-G. Lee and K. J. Chang, Appl. Phys. Lett., unpublished (1997).
7. W. Kohn and L. J. Sham, Phys. Rev. **140**, A1133 (1965).
8. E. Wigner, Trans. Faraday Soc. **34**, 678 (1938).
9. N. Troullier and J. L. Martins, Phys. Rev. B **43**, 1993 (1991): L. Kleinman and D. M. Bylander, Phys. Rev. Lett. **48**, 1425 (1982).
10. C. H. Park, I.-H. Lee, and K. J. Chang, Phys. Rev. B **47**, 15996 (1993).
11. H. Hellmann, *Einführung in die Quantenchemie,* (Deuticke: Leipzig 1937); R. P. Feynman, Phys. Rev. **56**, 340 (1939).
12. J. E. Northrup and S. B. Zhang, Phys. Rev. B **47**, 6791 (1993).
13. J. Neugebauer and C. G. Van de Walle, Appl. Phys. Lett. **69**, 503 (1996).
14. T. Mattila and R. M. Nieminen, Phys. Rev. B **55**, 9571 (1997).
15. J. Neugebauer and C. G. Van de Walle, Phys. Rev. Lett. **75**, 4452 (1995).

Materials Science Forum Vols. 258-263 (1997) pp. 1143-1148

IMPACT OF RADIATION-INDUCED DEFECTS ON THE YELLOW LUMINESCENCE BAND IN MOCVD GaN

V.V. Emtsev, V.Yu. Davydov, I.N. Goncharuk, E.V. Kalinina, V.V. Kozlovskii[1], D.S. Poloskin, A.V. Sakharov, N.M. Shmidt, A.N.Smirnov, and A.S. Usikov
Ioffe Physicotechnical Institute, Russian Academy of Sciences, 194021 St.Petersburg, RUSSIA
[1]Technical State University, 195251 St.Petersburg, RUSSIA

Keywords: gallium nitride, irradiation, native defects, luminescence

Abstract. Changes in a yellow luminescence band at ~ 2.2 eV were studied for n- and p-GaN subjected to electron and gamma-irradiation at room temperature. The intensity of the band strongly increases upon irradiation. Pronounced shifts of the band after irradiation is also observed. The experimental results obtained allow us to conclude that the gallium vacancy is involved in the yellow luminescence, in accordance with the recent theoretical predictions. It has been suggested that there is also another component in the luminescence band due to unidentified grown-in defects. Irradiation gives rise to strong changes in concentrations of charge carriers in n- and p-GaN.

Introduction

At present GaN finds ever increasing use in various electronic devices due to rapid progress in the growth techniques. However, a great success in technical applications of GaN based structures stands out sharply against slight knowledge of impurities and native defects in this material. From the other side, rigorous theoretical studies (see for instance [1-3]) present a striking contrast to tentative identification of most of impurity centers. Despite of many papers devoted to investigations of the yellow luminescence in GaN the origin of this band is a matter of controversy for a long time; see for instance [4,5]. Recently, the gallium vacancy has been suggested as a candidate for the appearance of the yellow luminescence [3]. It is well known that a convenient way of creating native defects in solids is to subject them to electron irradiation at energies of a few MeV. Elastic collisions of fast electrons with host atoms lead to production of vacancies and self-interstitials due to atomic displacement. Thus, it is possible to check up whether the centers responsible for the yellow luminescence are related to native defects.

The aim of the present work is to shed new light on this question and provide information on the electrical properties of native defects. So far this issue was touched in [6].

Experimental

Layers of hexagonal GaN were grown by the MOCVD technique using 6H-SiC and Al_2O_3 as substrates. The growth rate was about 2 μm/h and the thickness of layers ranged from 1 μm to 3 μm. Silicon and magnesium were used as dopants for n-GaN and p-GaN, respectively. Besides, some samples of undoped n-GaN were also studied.

Making use of the first-order E_2 phonon line in Raman spectra one can estimate internal stresses in GaN layers. The samples with low stresses (less than 0.1 GPa) were selected for irradiation. Photoluminescence spectra were recorded using a He-Cd (325 nm) or Ar laser (458 nm) for optical excitation at T=10 K and room temperature, respectively. Because of spatial variations of photoluminescence in GaN it is necessary to pick a reliable reference point for comparison studies. For this purpose one can use first-order Raman lines, as their

intensities were found to be not affected by irradiation over the dose range investigated. Electrical measurements were conducted with the aid of the Van der Pauw technique.

Samples were subjected to electron and gamma-irradiation. The energy of fast electrons was 0.9 MeV and the beam current was 5 $\mu A/cm^2$. Under air cooling the irradiation temperature didn't exceed T=50°C. Irradiation with ^{60}Co gamma-rays was carried out at T=280 K. The dose rate was $8 \cdot 10^{12}$ $cm^{-2} \cdot s^{-1}$. It might be well to recall that the gamma-irradiation used is equivalent to electron irradiation with fast electrons of about 0.6 MeV.

Results and Discussion

Electron irradiation of n-GaN

The initial photoluminescence spectrum over the spectral region of interest is shown in Fig. 1 (spectrum 1) for one of the samples. As is seen from the figure (spectrum 2), the band intensity strongly increases for the irradiated n-GaN. Evidently, the centers responsible for the yellow luminescence are associated with native defects. Along with this, the band maximum clearly shifted to a new position, from 2.23 eV to 2.28 eV.

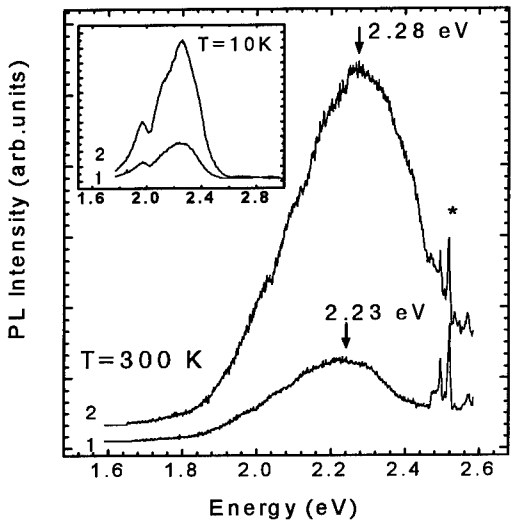

Fig. 1. Yellow luminescence band for doped n-GaN before and after electron irradiation. Dose: $1 \cdot 10^{17}$ cm^{-2}. Initial n-GaN, spectrum 1; irradiated n-GaN, spectrum 2. Spectrum 2 is slightly shifted along the ordinate axis for clarity. Arrows show the band maxima. Second-order phonon lines are marked with an asterisk.

Let us now turn to the electrical parameters of n-GaN before and after irradiation. The initial concentration of charge carriers at room temperature was about $7 \cdot 10^{17}$ cm^{-3}; see curve 1 in Fig. 2. At temperatures T<170 K the curve n(T) shows a plateau due to an impurity band. Because of this one can roughly estimate the ionization energy (E_d) and concentration (N_d) of shallow donors making their appearance at T>170 K, $E_d \geq 0.044$ eV and $N_d \geq 8 \cdot 10^{17}$ cm^{-3}. Most likely, these shallow donor states are Si-related; see for instance [7]. Curve 2 in Fig.2 shows a pronounced increase in the electron concentration due to irradiation. Interestingly, this increase can be traced down to T=125 K. It means that the radiation-induced donor states are closer to the conduction band than the Si-related ones. As a consequence, the calculated n(T) curve fits the experimental one at T>170 K setting the initial parameters of the deeper donors. However, it appears that the increase in the electron concentration is higher than that seen in Fig. 2. The initial concentration of ionized scattering centers is about $1 \cdot 10^{18}$ cm^{-3} and the electron mobility at room temperature (curve 1 in Fig. 3) correlates with most of the data reported so far; see for instance [8,9]. For the irradiated n-GaN the mobility of charge carriers decreased markedly; cf curves 1 and 2 in Fig. 3. This sizable decrease in the mobility corresponds to an effective increase in the concentration N_{ion} of ionized scattering centers by $\sim 1 \cdot 10^{18}$ cm^{-3} (cf [8,9]); the increase in N_{ion} seen in Fig. 2 couldn't have led to such an appreciable reduction in the electron mobility. It means that the total concentration of radiation-induced shallow donors is considerably higher than that derived from Fig. 2 and they are mostly compensated by radiation-induced acceptors.

At this point one can draw some conclusions concerning the nature of defects. Irradiation of GaN with fast electrons results in the production of Frenkel pairs as primary defects on both sublattices. A fraction of the primary defects can escape from spontaneous annihilation and give rise to the appearance of vacancies (V_{Ga} and V_N) and self-interstitials (Ga_i and N_i). These defects can be loosely bound in pairs or separated if mobile. We believe that most of them cannot migrate at room temperature taking into account the behaviour of native defects in other Ga-related binary compounds like GaP and GaAs to a certain extent; see for instance [10].

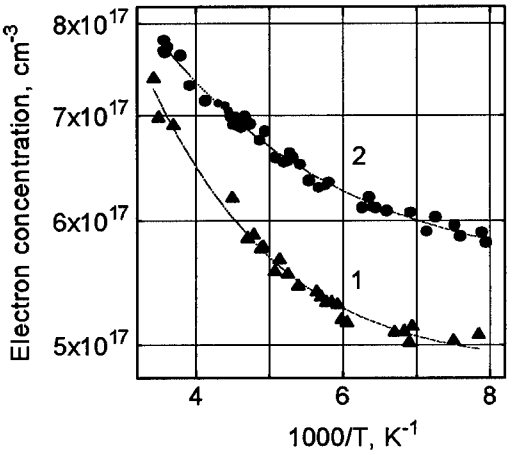

Fig. 2. Electron concentration *vs* temperature for doped n-GaN before and after electron irradiation. Dose: $1 \cdot 10^{17}$ cm^{-2}. Initial n-GaN, curve 1; irradiated GaN, curve 2.

Referring to [1-3] one can expect that the Ga vacancy is a triple acceptor in GaN. These defects V_{Ga}^{3-} are claimed to be responsible for strong compensation of n-GaN doped with Se during the growth [11]. The expected appearance of Ga vacancies in the irradiated n-GaN and the observed enhancement of the yellow luminescence in Fig. 1 are consistent with the idea of [3] that this luminescence band may be associated with V_{Ga}. However, the fact that the band maximum is moved in the course of irradiation invites us to suggest that the Ga vacancy is not the only deep center involved in the luminescence process. In such a case, the observed shift of the band maximum in Fig. 1 can be attributed to increasing contribution of the yellow luminescence associated with V_{Ga}. The results obtained for irradiated p-GaN seem to justify this suggestion; see below. The Ga vacancy, a "soft" defect, should be sensitive to stresses. It is felt that the data obtained in [12] for the yellow luminescence band *vs* pressure are related to another less sensitive defect if available in abundance. As to the Ga interstitial, it is expected to be a donor [2,13], possibly a shallow one [2]. Anyway, the production of Frenkel pairs on the gallium sublattice should result in strong compensation of shallow donors as well as effective scattering of charge carriers in irradiated n-GaN.

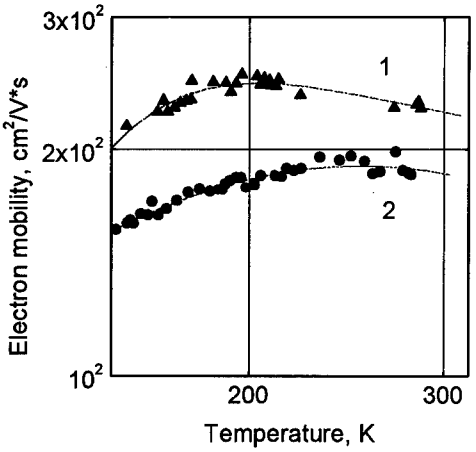

Fig. 3. Electron mobility *vs* temperature for doped n-GaN before and after electron irradiation. Dose: $1 \cdot 10^{17}$ cm^{-2}. Initial n-GaN, curve 1; irradiated GaN, curve 2.

Let us now get a look at the native defects on another sublattice. The nitrogen vacancy is claimed to be a shallow donor. This has been theoretically substantiated; see for instance [1,2]. The nitrogen interstitial appears to be amphoteric [1,2]. Again, one can conclude that the appearance of V_N and N_i in n-GaN couldn't contribute to increasing concentration of charge carriers upon irradiation. To reconcile this model with the experiment is possible by assuming that

either the N interstitial is a donor or it is mobile at room temperature and can form an electrically neutral complex at sinks (impurities, structural defects etc.).

Electron irradiation of undoped n-GaN

The initial concentration of electrons in the undoped n-GaN was about $3 \cdot 10^{16}$ cm^{-3} and the electron mobility ranged from 400 $cm^2/V \cdot s$ to 460 $cm^2/V \cdot s$ at room temperature telling us that the actual concentration of ionized scattering centers is in the low 10^{17} cm^{-3}. These electrical parameters are in line with the literature data available; see for instance [9].

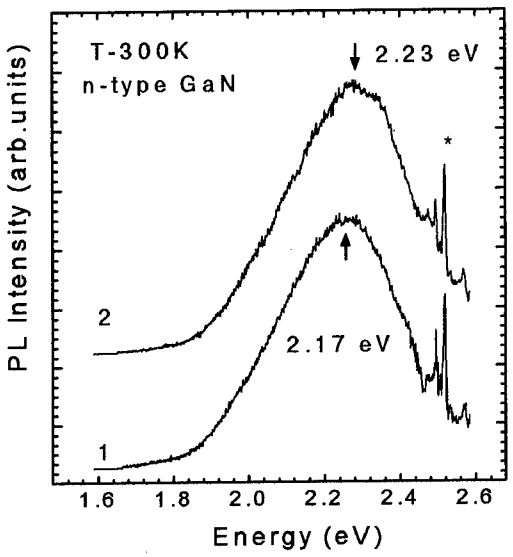

Fig. 4. Yellow luminescence band for undoped n-GaN before and after electron irradiation. Dose, $1 \cdot 10^{17}$ cm^{-2}. Initial GaN, spectrum 1; irradiated GaN, spectrum 2. Spectrum 2 is slightly shifted along the ordinate axis for clarity. Arrows show the band maxima.

In sharp contrast to what was observed for the yellow luminescence in doped n-GaN subjected to irradiation (see above), this luminescence band is little changed by the irradiation; cf Fig. 1 and 4. Nonetheless, a slight shift of the band maximum in the irradiated n-GaN is still observable. This behaviour seems to be puzzling in view of the fact that the concentrations of primary defects should be the same at the same irradiation dose. It appears that the fate of Frenkel pairs on the Ga sublattice, survive or annihilate, is different in both cases. Interactions of defects are strongly influenced by their charge states. One can speculate that the Ga interstitial may change its charge state from Ga_i^0 to Ga_i^+ when the Fermi level shifts by about 0.1 eV from the conduction band due to lower concentrations of charge carriers in the undoped n-GaN as compared to that in the doped one. The coulombically assisted interaction of V_{Ga}^{3-} with Ga_i^+ may enhance the annihilation of Frenkel pairs on the gallium sublattice, thus producing little effects on the yellow luminescence.

Electron and gamma-irradiation of p-GaN

The yellow luminescence in the initial p-GaN was found to be much weaker than that in the doped n-GaN; see Fig. 5. This observation corroborates the conclusion of [1-3] that the formation of Ga vacancies in p-GaN during the growth should be suppressed, in contrast to n-GaN, because of a large difference in the formation energies. Figure 5 also displays another interesting feature. The band maxima for n- and p-GaN are placed at the different positions on the energy scale. This lends additional support to the suggestion that two centers, V_{Ga} and X, are responsible for the yellow luminescence in GaN. Actually, it is plausible that low concentrations of Ga vacancies in p-GaN enhance the contribution of another component. As a result, the band maximum shifts to lower energies. This band may be related to the X defects only if the concentration of Ga vacancies is negligible. It is conceivable that the formation of these defects during the GaN growth is charge-state dependent, too.

Electron and gamma-irradiation of p-GaN produce strong effects on the yellow luminescence band. First, the intensity of the band markedly increased after irradiation; see Fig. 6. Second, the band maximum shifted to higher energies. Both features are similar to what is observed for n-GaN; cf Fig.1 and 6. Slight differences in the maximum position for n- and p-GaN after electron irradiation are most likely associated with disturbance of Ga vacancies by the parent self-interstitials in different charge states, say, Ga_i^0 and Ga_i^+, respectively. In addition, the mean distance between the constituent defects in Frenkel pairs is expected to be shorter for gamma irradiation as compared to that for electron irradiation.

The initial concentration and mobility of holes in the p-GaN at room temperature were found to be about $3 \cdot 10^{17}$ cm^{-3} and 7 $cm^2/V \cdot s$ respectively. These parameters are in line with those reported in the literature; see for instance [14]. The concentration of charge carriers decreases in the course of irradiation due to strong compensation of the Mg-related acceptor states. To take one example, the hole concentration at room temperature dropped from $3 \cdot 10^{17}$ cm^{-3} to $\sim 1 \cdot 10^{17}$ cm^{-3} at a dose of $1 \cdot 10^{17}$ cm^{-2}. However, one cannot explicitly derive the production rate of radiation-induced donors from the data obtained. The Mg-related acceptors whose ionization energy is about 0.18 eV are activated at T>300 K for the most part; see [14]. Rough estimates showed that the removal rate of holes is of order of 1 cm^{-1}.

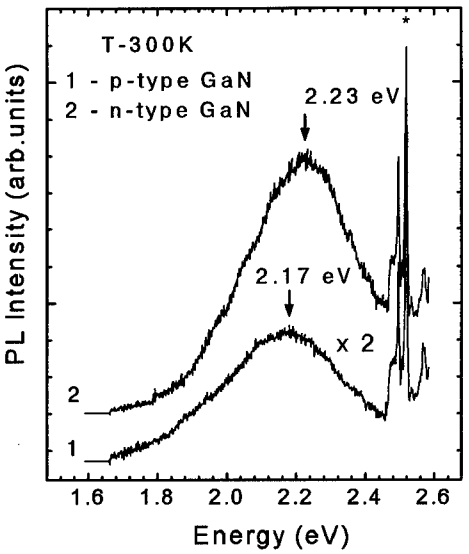

Fig. 5. Yellow luminescence band for doped n-GaN (spectrum 1) and p-GaN (spectrum 2) before irradiation. Spectrum 2 is slightly shifted along the ordinate axis for clarity. Arrows show the band maxima.

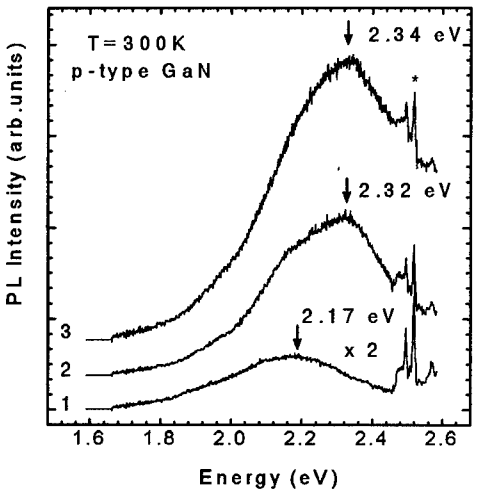

Fig. 6. Yellow luminescence band for doped p-GaN before (curve 1) and after electron (curve 2) and gamma-irradiation (curve 3). Dose: $1 \cdot 10^{17}$ electrons/cm^2, curve 2; $1 \cdot 10^{19}$ γ-quanta/cm^2, curve 3. Spectra 2 and 3 are slightly shifted along the ordinate axis for clarity. Arrows show the band maxima.

Conclusions

The present work provides conclusive evidence that the yellow luminescence in GaN is associated with native point defects. The experimental results have substantiated the suggestion of [3,13] that the gallium vacancy is involved in the luminescence process. However, it appears that there is also another defect contributing to this luminescence band. The production of native defects under irradiation leads to increasing concentration of electrons in doped n-GaN and decreasing concentration of holes in p-GaN.

References

1. J. Neugebauer and C.G. Van de Walle, Phys. Rev. B **50**, 8067 (1994).
2. P. Bogusławski, E.L. Briggs, and J. Bernholc, Phys. Rev. B **51**, 17255 (1995).
3. J. Neugebauer and C.G. Van de Walle, Appl. Phys. Lett. **69**, 503 (1996).
4. T. Ogino and M. Aoki, Jap. J. Appl. Phys. **19**, 2395 (1980).
5. E.R. Glaser, T.A. Kennedy, K. Doverspike, L.B. Rowland, D.K. Gaskill, J.A. Freitas, Jr., M.A. Khan, D.T. Olson, J.N. Kuznia, and D.K. Wickenden, Phys. Rev. B **51**, 13326 (1995).
6. C.H. Qui, M.W. Lecsono, J.I. Pankove, C. Rossington, and E.E. Haller in *MRS Symp. Proc.,* Vol. **449**, eds F.A. Ponce, T.D. Moustakas, I. Akasaki, and B.A. Monemar (Pittsburgh, Pennsylvania: MRS), pp. 585-590 (1997).
7. L.B. Rowland, K. Doverspike, and D.K. Gaskill, Appl. Phys. Lett. **66**, 1495 (1995).
8. V.W. Chin, T.L. Tansley, and T. Osotchan, J. Appl. Phys. **75**, 7365 (1994).
9. D.L. Rode and D.K. Gaskill, Appl. Phys. Lett. **66**, 1972 (1995).
10. D.V. Lang in *Radiation Effects in Semiconductors 1976,* Conf. Ser. No 31, eds N.B. Urli and J.W. Corbett (Bristol and London: The Institute of Physics), pp. 70-94 (1977).
11. G.-C. Yi and B.W. Wessels, Appl. Phys. Lett. **69**, 3028 (1996).
12. P. Perlin, T. Suski, H. Teisseyre, M. Leszczynski, I. Grzegory, J. Jun, S. Porowski, P. Bogusławski, J. Bernholc, J.C. Chervin, A. Polian, and T.D. Moustakas, Phys. Rev. Lett. **75**, 296 (1995).
13. J. Neugebauer and C.G. Van de Walle in *23rd Int. Conf. on the Physics of Semicond.,* Vols **1-4**, eds M. Scheffler and R. Zimmermann (Singapore-New Jersey-London-Hong Kong: World Scientific), pp. 2849-2856 (1996).
14. W. Götz, N.M. Johnson, J. Walker, and D.P. Bour in *MRS Symp. Proc.,* Vol. **423**, eds D.K. Gaskill, Ch. D. Brandt, and R.J. Nemanich (Pittsburgh, Pennsylvania: MRS), pp. 595-600 (1996).

Materials Science Forum Vols. 258-263 (1997) pp. 1149-1154

ON THE ORIGIN OF THE YELLOW DONOR-ACCEPTOR PAIR EMISSION IN GaN

M. Godlewski[1], V.Yu. Ivanov[1], A. Kamińska[1], H.Y. Zuo[2], E.M. Goldys[2], T.L. Tansley[2]
A. Barski[3], U. Rossner[3], J.L. Rouvicre[3], M. Arlery[3], I. Grzegory[4], T. Suski[4], S. Porowski[4]
J.P. Bergman[5] and B. Monemar[5]

[1]Inst. Phys., Polish Acad. Sci., 02-668 Warsaw, Al. Lotników 32/46, POLAND
[2]Semicond. Sci. & Technol. Lab., Macquarie Univ., North Ryde, 2109, NSW, AUSTRALIA
[3]CEA-Grenoble, DRFMC/SP2M, FRANCE
[4]High Pressure Res. Center, Polish Acad. Sci., 01-142 Warsaw, Sokołowska 29, POLAND
[5]Dept. Phys. & Meas. Technol., Linköping Univ., S-581 83 Linköping, SWEDEN

Keywords: GaN, photoluminescence, donor-acceptor pair recombination

Abstract. The "deep" yellow donor-acceptor pair (DAP) recombination is perhaps the most known but less understood photoluminescence (PL) emission of GaN. The origin of the "yellow" DAP emission was recently discussed based on the results of optically detected magnetic resonance (ODMR), stress and PL kinetics investigations. A deep donor-shallow acceptor transition was proposed based on the results of one ODMR study, whereas other ODMR experiments and stress and PL kinetics measurements were explained in terms of a shallow donor-deep acceptor transition model. The present PL investigations support the second model of the "yellow" DAP emission. However, the presence of an underlying second PL emission may explain the reasons for conflicting explanations of the results of the ODMR investigations by two different groups.

Introduction

Several deep emissions, attributed to donor-acceptor pair (DAP) transitions, have been observed in optical studies of wurtzite phase GaN (w-GaN). This we show in Fig. 1, which presents PL studies of visible PL of w-GaN epilayers grown by the low temperature laser induced chemical vapor deposition (LCVD) method [1]. For GaN epilayers grown by this method on lattice mismatched Si and GaAs substrates we observed broad PL emissions in the whole visible region. The PL spectrum shown in Fig. 1 is dominated by the blue (for epilayers grown on Si substrate), and the blue and green PL emissions, respectively. A DAP origin of these emissions was proposed by Tansley and Egan [2]. The model of DAP transitions is shown in the inset of Fig. 1. Of the three visible DAP transitions, shown in Fig. 1, only the yellow DAP PL, with maximum at 2.2-2.3 eV, is commonly observed. There are several indications that the intensity of the yellow PL anticorrelates with the strength of the 'edge' PL of GaN epilayers. Strong yellow PL is thus often associated with a reduced morphological quality of the GaN structure. This important observation, which needs further clarification, suggests that some native defect of the GaN lattice is involved in the yellow PL. The origin of this native defect is still disputed, but the DAP origin of the yellow PL is firmly established. It was also confirmed by recent ODMR investigations [3-6]. The first ODMR experiments explained the yellow emission by DAP transitions involving a deep donor related to a native defect (such as a gallium interstitial) and a shallow acceptor [3-5]. This interpretation agrees with the model shown in the inset of Fig. 1. An alternative interpretation of the yellow DAP PL was given from the recent ODMR studies of Hofmann et al. [6] and from the pressure investigations of Perlin et al. [7] and Suski et al. [8]. These authors relate the yellow PL to DAP transitions between a shallow hydrogenic donor, nitrogen vacancy related [7], and a deep acceptor, due to some native defect.

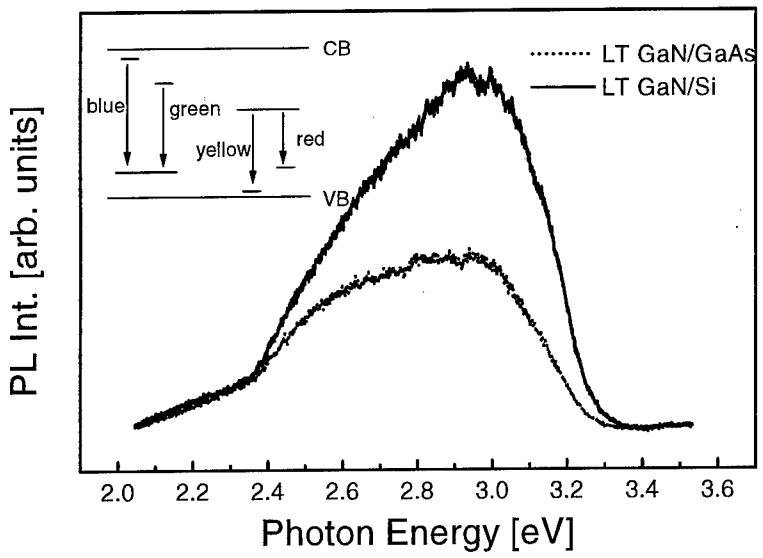

Figure 1. Visible PL of w-GaN epilayers grown by the low temperature LCVD method. A model of DAP transitions in w-GaN (after Ref. 2) is shown in the inset.

In this work we discuss properties of the yellow PL based on the results of PL and PL kinetics experiments performed for bulk GaN samples, and for w-GaN and cubic phase (c-GaN) epilayers grown by different methods. The present results confirm the shallow donor - deep acceptor origin of the yellow PL, which in the case of bulk n-type sample overlaps with free-to-bound (electron - deep acceptor) transitions. We also propose that the conflicting interpretation of the ODMR investigations may be related to an overlap of the yellow PL with some other deep DAP transition peaked at slightly lower energy.

Experimental

Three different types of GaN samples were measured. Most of the PL and also the ODMR experiments were performed on a bulk GaN sample grown in the High Pressure Research Center of the Polish Academy of Sciences, Warsaw, Poland. These investigations were supplemented by the studies of GaN epilayers grown by either the low temperature laser induced chemical vapor deposition (LCVD) method (wurtzite phase epilayers) or by molecular beam epitaxy (cubic phase epilayers). c-GaN epilayers were grown by molecular beam epitaxy on an (001) Si substrate, which prior to the growth process was annealed at 1300-1400 °C in propane. This annealing covered the Si substrate with a thin (~4nm thick) SiC layer acting as a buffer layer. Even though this SiC layer is very thin good quality cubic phase epilayers were obtained, showing only very weak deep DAP PL.

The PL and PLE experiments were performed on conventional set-ups. PL kinetics measurements were performed with a Hamamatsu synchroscan streak camera with a temporal resolution of about

20 ps. Pulsed excitation was provided by a mode locked Ti:sapphire solid state laser with a pulse length of 2 ps duration. The reported measurements were performed at 2 K in a He bath cryostat.

ODMR experiments were performed on a converted X-band electron spin resonance spectrometer (Bruker 200) equipped with an Oxford Instruments helium gas flow cryostat working in the temperature range of 2 - 300 K. A PIN diode was used for on-off modulation of the microwaves, which was driven by an external generator from the lock-in amplifier. The uv line of Ar+ laser was used for the PL excitation.

Experimental results

In Fig. 2 we show the PL spectrum and its temperature dependence for the yellow emission observed for the bulk GaN sample. With increasing temperature the yellow PL first decreases in intensity, but then, for temperatures above 175 K, starts to increase in intensity.

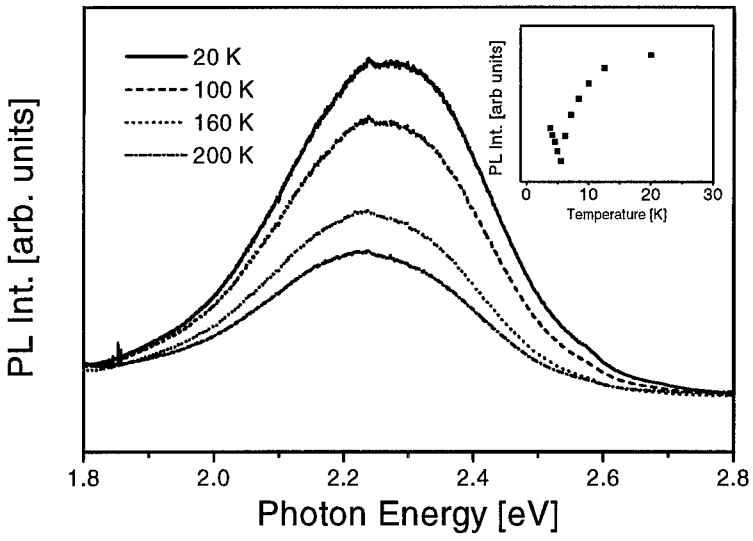

Figure 2: PL spectrum of a bulk GaN sample measured at four different temperatures. In the inset is shown the temperature dependence of the integrated intensity of the yellow DAP PL in the bulk GaN sample.

The increase of the integrated PL intensity is accompanied by a change of the PL line shape of the yellow emission. This we show in Fig. 3, in which we deconvolute the PL measured at 260 K to two Gaussian components peaked at about 2.23 eV and 1.85 eV. Fig. 3 also shows that the two PL emissions partly overlap in the spectral region of the 2.2-2.3 eV, i.e., where the yellow PL reaches its maximum. The observed decrease and then increase of the integrated PL we relate to the competition of two PL transitions, with the one at lower energy becoming more important at increased temperatures. The origin of the low energy PL is unknown, but it is likely due to DAP transitions. The 1.8 eV PL band was also observed in the previous ODMR studies [3-5], which indicated its DAP origin. This PL, for Mg doped samples, was assigned to a transition involving an electron on the 1 eV deep donor and a hole on the 0.5 eV deep acceptor (related to a perturbed Mg

center) [3-5]. The chemical origin of donor and acceptor species could not be determined due to the lack of a resolved hyperfine structure of the ODMR signals [3-5] .

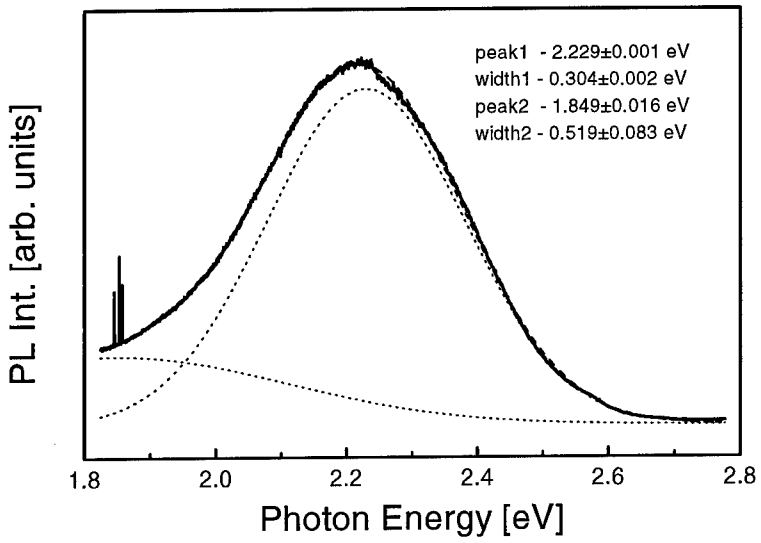

Figure 3: PL spectrum of a bulk GaN sample measured at 260 K. The deconvolution of the PL to two Gaussian PL bands is also shown.

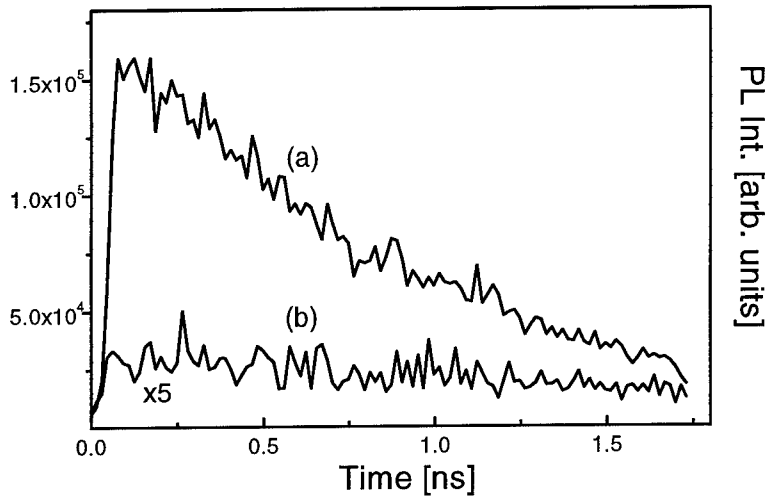

Figure 4: PL kinetics measured at 2 K under 2ps long pulse excitation and with the detection set at the maximum of the yellow DAP PL (a), and at the low energy wing of this PL (b).

We attempted ODMR investigations for the bulk GaN sample. Even though the strong yellow PL was observed, we could not detect any resonance signal via the change of the intensity of this PL.

The lack of the relevant ODMR signals will be explained below, based on the results of time-resolved PL investigations.

One of the arguments for the DAP origin of the yellow PL were PL kinetics investigations reported by Hofmann et al. [6]. A broad distribution of the PL lifetimes was observed, which is due to the distribution of the distances between donor and acceptor centers active in the radiative transitions [6]. Such a distribution of the PL decay times, the energy dependence of the decay times (a faster decay is observed for closer pairs, which recombine at the higher energy wing of the PL) and the long decay times observed (up to milliseconds) were consistent with the DAP origin of the yellow PL. This PL was related to radiative transitions involving shallow donors and deep acceptors [6].

We have also performed PL decay investigations for the bulk GaN sample. The results of the PL kinetics measurements, shown in Fig. 4, are dramatically different from those reported in Ref. 6. The observed PL decay times are energy independent, they are very short (about 1 ns) and show a contribution with a noticeable longer decay time, which becomes more pronounced at the low energy wing of the PL, where the PL investigations (see Fig. 3) show an overlap of the yellow PL with another PL. We propose that the component with a longer PL decay time is due to the overlap of the yellow DAP PL with another PL. This PL has much longer PL decay times.

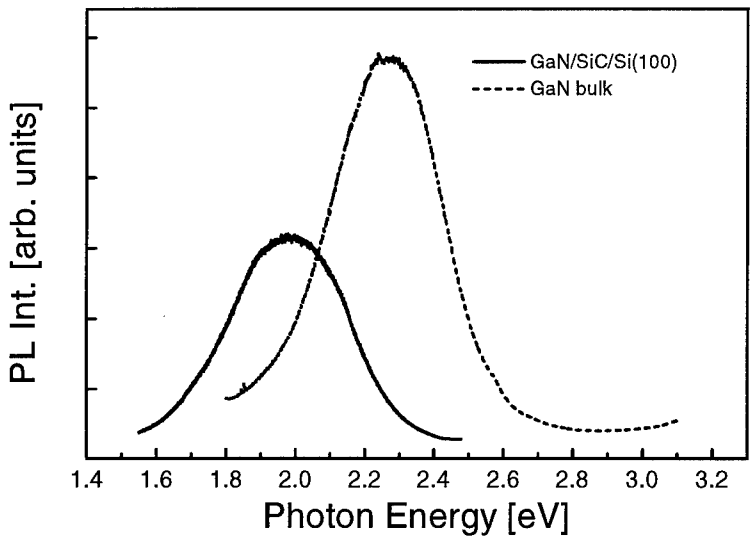

Figure 5: Comparison of the deep DAP PL emissions in wurtzite phase GaN (the bulk sample) and metastable cubic phase GaN, for the sample grown on (001) Si.

Discussion

The relevant question is how the present results contribute to solving the enigma of the yellow PL in w-GaN. In some points these results are significantly different from those reported in Refs. [3-6]. First of all, we failed to observe any ODMR signal even though a strong yellow PL was observed for the bulk GaN sample. The time-resolved PL investigations indicate however extremely short PL decay times observed for bulk GaN. For such short PL decay times we cannot expect any effect of a

magnetic resonance on recombination rates. Thus the lack of the ODMR signal does not exclude the DAP identification of the yellow PL.

We should, however, explain why so short PL decay times are observed in the present case. The very short PL decay times we relate to a strong contribution of free-to-bound transitions (electrons in the conduction band - acceptor and electrons in the shallow donor band - acceptor) expected for the case of a degenerate n-type sample. The latter means that our data clearly favor the shallow donor - deep acceptor origin of the yellow DAP PL and that the results of PL investigations cannot be explained by the alternative model of the yellow PL. The present results also indicate that the yellow PL overlaps with another PL, which is likely to be of the DAP origin. This deeper PL even for the degenerate n-type GaN sample shows much longer PL decay times. This suggests its deep donor - acceptor origin, but further investigations are necessary to make this identification less tentative. We postulate that the overlap of the two DAP emissions explains why two previous ODMR studies gave conflicting models of the yellow DAP PL.

We verified our conclusion on the origin of the yellow DAP PL by performing PL investigations of the c-GaN epilayers [9]. In Fig. 5 we compare two PL emissions observed for the wurtzite and cubic phases of GaN. The relevant emission in c-GaN is shifted down in energy by about 300 meV, i.e., by an energy similar to the difference of the band gap energies of the two phases of GaN. Such a shift is expected for the shallow donor - deep acceptor model of the yellow PL and of its equivalent in c-GaN and, in our opinion, not for the alternative model of the yellow DAP PL - i e the deep donor - "shallow" acceptor transition.

Concluding, our results confirm the shallow donor - deep acceptor origin of the yellow PL in w-GaN. For the degenerate n-type bulk sample free-to-bound transitions also contribute to this PL. The yellow PL overlaps with another broad PL, which we relate to a deep DAP transition. The overlap of these two DAP transitions may explain previous conflicting models from ODMR studies.

This work was partly supported by the joint project no. 76568 of KBN (Poland) and the Ministry of Foreign Affairs (France).

References:

1. B. Zhou, X. Li, T.L. Tansley, K.S.A. Butcher and M.R. Phillips, J. Cryst. Growth **151**, 249 (1995).
2. T.L. Tansley and R.J. Egan, Phys. Rev. **B45**, 10942 (1992).
3. E.R. Glaser, T.A. Kennedy, K. Doverspike, L.B. Rowland, D.K. Gaskill, J.A. Freitas, Jr., M. A. Khan, D.T. Olson, J.N. Kuznia and D.K. Wickenden, Phys. Rev. **B51**, 13326 (1995).
4. E.R. Glaser, T.A. Kennedy, H.C. Crookham, J.A. Freitas, Jr., M. A. Khan, D.T. Olson and J.N. Kuznia, Appl. Phys. Lett. **63**, 2673 (1993).
5. T.A. Kennedy, E.R. Glaser, J.A. Freitas, Jr., W.E. Carlos, M. A. Khan and D.K. Wickenden, J. of Electron. Materials **24**, 219 (1995).
6. D.M. Hofmann, D. Kovalev, G. Steude, B.K. Meyer, A. Hoffmann, L. Eckey, R. Heitz, H. Amano and I. Akasaki, Phys. Rev. **B52**, 16702 (1995).
7. P. Perlin, T. Suski, H. Teisseyre, M. Leszczynski, I. Grzegory, J. Jun, S. Porowski, P. Boguslawski, J. Bernholc, J.C. Chervin, A. Polian, and T.D. Moustakas, Phys. Rev. Lett. **75**, 296 (1995).
8. T. Suski, P. Perlin, H. Teisseyre, M. Leszczynski, I. Grzegory, J. Jun, M. Bockowski, S. Porowski, and T.D. Moustakas, Appl. Phys. Lett. **67**, 2188 (1995).
9. M. Godlewski, V.Yu. Ivanov, J.P. Bergman, B. Monemar, A. Barski and R. Langer, Acta Phys. Polonica (in press)

Materials Science Forum Vols. 258-263 (1997) pp. 1155-1160

BLUE EMISSION IN Mg DOPED GaN STUDIED BY TIME RESOLVED SPECTROSCOPY

R. Seitz*, C. Gaspar* , T. Monteiro*, E. Pereira*
M. Leroux,B. Beaumont**, P. Gibart****
***Departamento de Física, Universidade de Aveiro, 3810 Aveiro, PORTUGAL**
****Centre de Recherches sur l'Hétéro-Epitaxie et ses Applications – CRHEA-CNRS**
Rue B. Grégory, 06560 Valbonne, FRANCE

Keywords: GaN:Mg, blue emission, time resolved spectroscopy

Abstract.
A strong blue emission is present when GaN films are heavily doped with Mg. It is known that compensation by non-intended donors reduces the free hole density at least two orders of magnitude when compared with the Mg concentration. Previous work on the blue band in heavily Mg doped (10^{20} cm^{-3}) material shows that two main emissions contribute to the band. The dependence on excitation intensity shows a shift of the peak position of the emissions too large to be attributed to donor acceptor pair (DAP) recombination. In the present work we analyse by time resolved spectroscopy, in conditions of low excitation density, the temperature dependence of the blue emission and compare it with steady state data. From the data a model for this emission is proposed.

Introduction.

Wide band gap nitride semiconductors are currently of considerable interest due to their properties as blue light emitting and high temperature electronic devices. A major obstacle for the realisation of such devices from Metal-Organic Vapour Phase Epitaxy (MOVPE) grown GaN films is an apparent difficulty to achieve p-type material due to highly n-type residual conductivity. Several groups [1-3] have recently reported their ability to dope p-type GaN using Mg as dopant, in combination with post grow low energy beam irradiation (LEEBI) and thermal annealing in nitrogen environment to activate Mg dopants. During the growth Mg-H complexes are formed which give rise to local vibrational modes at 3125 cm^{-1} as observed by infrared absorption [4], in agreement with theoretical calculations [5,6]. The post growth activation treatment results in the dissociation of Mg-H complexes [1-4]. Also p-type GaN:Mg growth by Molecular Beam Epitaxy (MBE) without post growth treatment was recently achieved. This was tentatively attributed to the absence of H in the growth process [7,8].
It is known that Mg introduces shallow (effective mass like character) [9-16] and quasi deep [11,14,17-22] electronic levels in the band gap. In lightly doped samples the shallow level is responsible for the Mg-related DAP recombination at 3.27 eV [10,13-17]. With increasing doping photoluminescence (PL) bands broaden and deepen being dominated by a blue emission depending on doping and excitation intensity [10,16,22-24], but independent of the GaN growth technique. Previous work on the blue band in Mg heavily doped (10^{20} cm^{-3}) films shows that two main emissions contribute to the band with maximum at 2.9 and 2.7 eV [16,22]. The dependence of the peak position on excitation intensity shows a shift too large to be attributed to donor acceptor pair (DAP) recombination. In the present work we

analyse by time resolved spectroscopy, in conditions of low excitation density, the temperature dependence of the blue emission and compare it with steady state data. We are able to show that the blue emission is better explained by the overlapping of four emission bands, whose origin is discussed, giving further support to the idea that this emission is not due to DAP recombination.

Materials and Methods.

The samples used in this work were grown by MOVPE on (0001) sapphire substrates using bismethylcyclopentadienyl magnesium as precursor. The Mg doped sample is highly doped with p ~10^{18} cm^{-3} at 300 K. Time resolved photoluminescence (TR-PL) spectra and lifetime measurements were carried out with a 1934C Spex phosporimeter using a pulsed Xe arc lamp with a pulse width of 3 μs (tail after 10 μs accounts for 1% of initial intensity) as light source. Steady state photoluminescence spectra (SS-PL) were obtained after excitation above band gap by using a Xe arc lamp as light source in combination with a monochromator. In both cases the luminescence was dispersed by a Spex 1704 monochromator and detected by a photomultiplier. The samples were held in a cold tip of a closed cycle Air-Products He cryostat in a temperature range between 10 K and RT. All spectra were corrected for the experimental set up response.

Results and Discussion.

Figure 1 shows a comparison of a SS-PL spectrum, obtained by above band gap excitation, and TR-PL spectra for different time delays after the light pulse, at 10 K, both under low excitation intensity conditions.

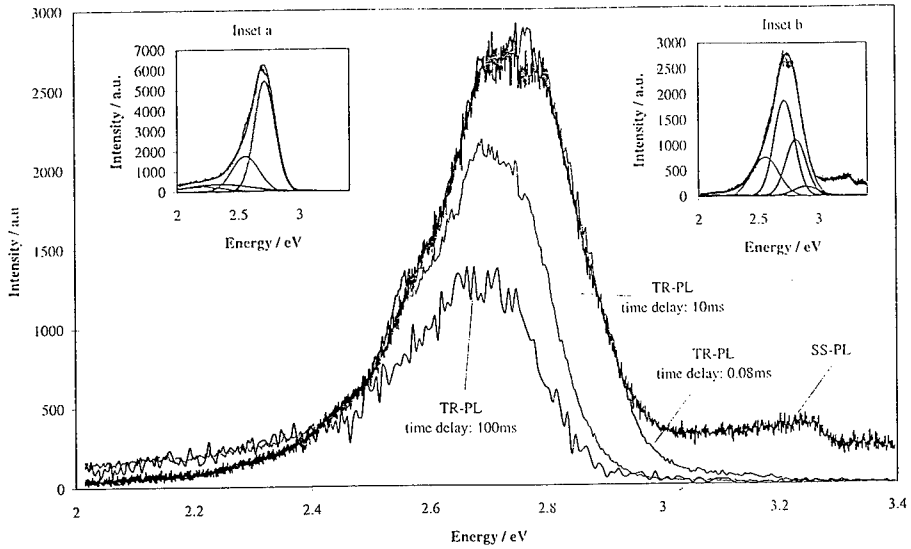

Fig. 1: Comparison of a SS-PL spectrum, obtained by above band gap excitation, and TR-PL spectra for different time delays after the light pulse, at 10 K under low excitation intensity conditions. Inset (a): TR-PL spectrum for a delay of 10 ms: fit with two gaussians peaked at 2.72 eV and 2.56 eV. Inset (b): SS-PL spectrum: fit with four gaussians peaked at 2.9 eV, 2.81 eV, 2.72 eV and 2.56 eV.

Beside the shallow 3.27 eV DAP recombination, shoulders at 2.9, 2.81, 2.72 and 2.56 eV are observed in the blue band of the SS-PL spectra. When the spectra are taken by TR-PL we can see that the band shape is different when different time delays and windows are used. The shoulder at 2.9 eV is missing indicating that the 2.9 eV band is a prompt emission with a lifetime shorter than tens of μs. While for shorter delays (0.08 ms) the maximum occurs at 2.81 eV, for longer delays (above 10 ms) the peak occurs at 2.72 eV indicating that this emission has a longer lifetime than the 2.81 eV emission. Increasing delays (above 100 ms) shows a higher contribution of the 2.56 eV band and on the low energy side the slow component of the well known yellow band common in the undoped samples appears [25]. There is a decrease in intensity of the low energy bands above 100 K, while the intensity of 2.9 eV band decreases above 175 K. Although the change in band shape is not important below 220 K above this temperature there is a marked change in band shape due to a particular strong decrease of 2.9 and 2.81 eV bands as shown in figure 2.

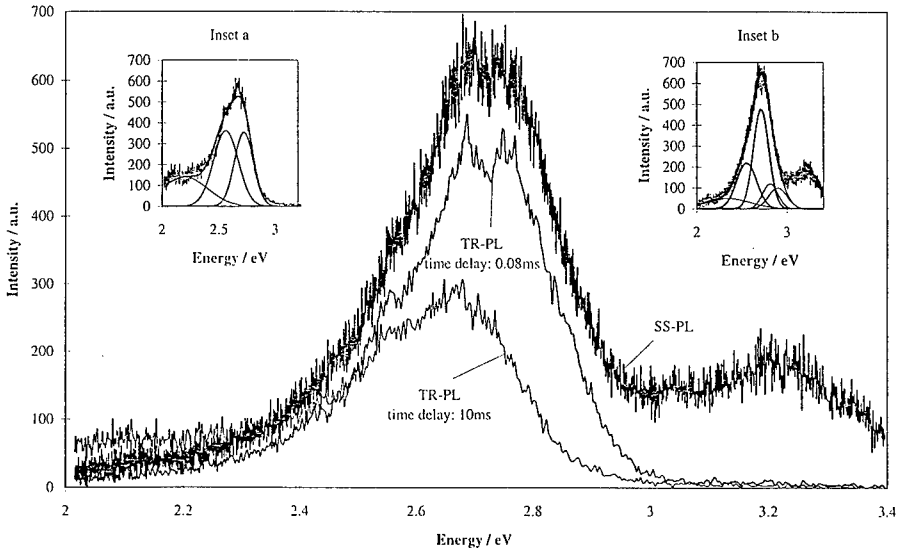

Fig. 2: Comparison of a SS-PL spectrum, obtained by above band gap excitation, and TR-PL spectra for different time delays after the light pulse, at 220 K under low excitation intensity conditions. Inset (a): TR-PL spectrum for a delay of 10 ms: fit with two gaussians peaked at 2.72 eV and 2.56 eV. Inset (b): SS-PL spectrum: fit with four gaussians peaked at 2.9 eV, 2.81 eV, 2.72 eV and 2.56 eV.

If this blue band were due to DAP recombination a progressive shift towards lower energies would be expected when the delays after the light pulse increase, in contrary to the experimental data. These results point to different contributions of overlaping bands at fixed energies. In order to test this hypothesis TR-PL spectra have been adjusted with gaussian bands, with fixed maxima and different relative intensities for different time delays. The results for a delay of 10ms are shown in inset (a). Using these results we were able to fit the SS-PL spectrum by including as well a contribution from gaussian bands with maxima at 2.81 and 2.9 eV, as shown in inset (b) of figure 1. A similar treatment is shown in figure 2. It can be seen that the spectrum can be fitted to the same gaussians, although as expected the relative intensities change.

Lifetime measurements were performed at different emission energies. As expected the faster transitions dominate in the high energy side of the spectrum. When the decays are analysed we see that they can be fitted with three exponential decays: 0.18 ms, that we assign to the 2.81 eV band, 3.3 ms corresponding to the 2.72 eV band and 19.5 ms for the 2.56 eV band. A typical decay curve is shown in figure 3 with the corresponding fit with three exponentials.

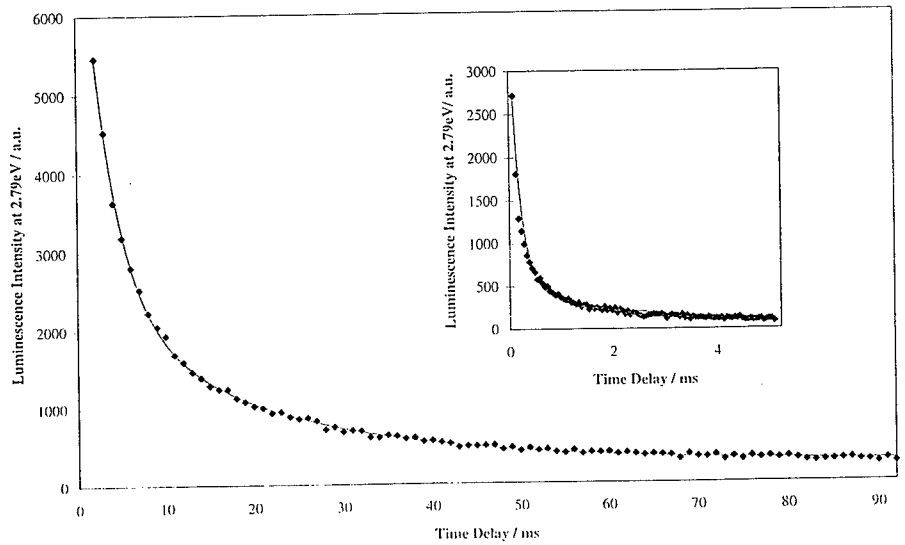

Fig. 3: Typical decay curve at 10 K and the corresponding fit (solid line) with 3 exponentials with lifetimes of 0.18 ms, 3.3 ms and 19.5 ms. The inset shows the decay in the short time delay range.

Temperature dependence of the intensities of the four band emissions is shown in figure 4. They present different thermal quenching parameters. The solid lines are best fits assuming that quenching processes follow an exponential law. The activation energies for deexcitation processes are 87, 92, 127 and 167 meV for the 2.56, 2.72, 2.81 and 2.9 eV bands respectively. The presence of exponential decay components and the absence of a progressive shift to lower energies with delay excludes a DAP recombination. The shift towards higher energies observed when the excitation

intensity increases [16,22] shows that under these conditions the fast transition is favoured due to saturation of the long lived transitions. This indicates that they cannot originate in emission from one excited level to different ground levels. This is supported by the different thermal quenching parameters of the four emissions.

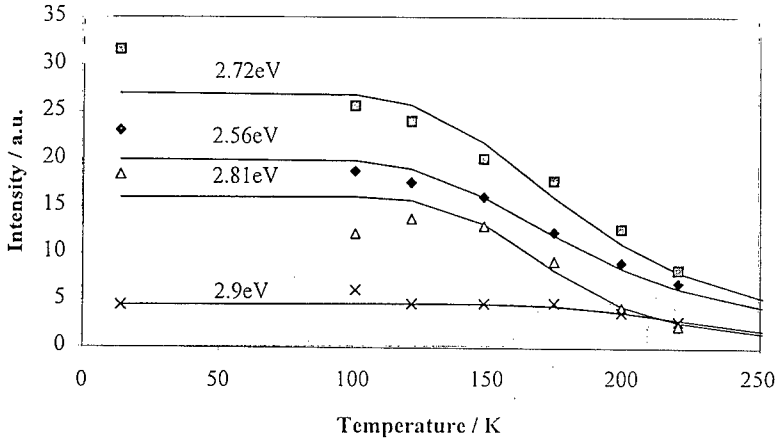

Fig. 4: Temperature dependence of the intensities of the 2.9, 2.81, 2.7 and 2.56 eV bands. Solid lines fits assuming that quenching processes follow an exponential law.

The studied blue emission bands are present only in Mg doped samples. It is known that several quasi deep levels are created by Mg doping [11,14,17-22]. The experimental results are compatible with the idea that the blue band originates in at least four different Mg related defects. Further work is under way in order to study samples with different Mg concentration and different carrier density in order to clarify the nature of the levels envolved in the transitions.

Conclusions.

From the present work we conclude that the blue emission typical for Mg doped GaN samples is composed of four different emissions, separated by TR-PL due to the different decays associated with each one.The different temperature quenching found for each conponent gives further support to this model. Thus the model of pair recombination must be excluded. Internal transitions in quasi deep defects related with Mg, that are known to be present in higher doping conditions, are most probably responsible for this emission.

References.

1. H. Amano, M. Kito, K. Hiramatsu and I. Akasaki, Jpn. J. Appl. Phys., **28**, L2112 (1989).
2. S. Nakamura, M. Senoh and T. Mukai, Jpn. J. Appl. Phys., **30**, L1708 (1991).
3. S. Nakamura, T. Mukai, M. Senoh and N. Iwasa, Jpn. J. Appl. Phys., **31**, L139 (1992).

4. W. Gotz, N. M. Johnson, D. P. Bour, M. D. McCluskey and E. E. Haller, Appl. Phys. Lett., **69**, 3725 (1996).
5. J. Neugebauer and C. G. van de Walle, Phys. Rev. Lett, **75**, 4452 (1995).
6. V. J. B. Torres, S. Oberg and R. Jones, MRS Internet J. Nitride Semicond. Res., (submitted).
7. M. S. Brandt, N. M. Johnson, R. J. Molnar, R. Singh and T. D. Moustakas, Appl. Phys. Lett., **64**, 2264 (1994).
8. M. Rubin, N. Newman, J. S. Chan, T. C. Fu, and J. R. Ross, Appl. Phys. Lett., **64**, 64 (1994).
9. T. Tanaka, A. Watanabe, A. Amano, Y. Kobayashi, I. Akasaki, S. Yamazaki and M. Koike, Appl. Phys. Lett., **65**, 593 (1994).
10. W. Kim, A. Salvador, A. E. Botchkarev, O. Aktas, S. N. Mohammad and H. Morçoc, Appl. Phys. Lett., **69**, 559 (1996).
11. W. Gotz, N. M. Johnson, D. P. Bour, C. Chem, H. Liu, C. Kuo and W. Imler, Mat. Res. Soc. Symp. Proc., **395**, 443 (1996).
12. N. M. Johnson, W. Gotz, J. Neugebauer and C. G. van de Walle, Mat. Res. Soc. Symp. Proc., **395**, 723 (1996).
13. M. Ilegems and R. Dingle, J. Appl. Phys, **44**, 4234 (1973).
14. E. R. Glaser, T. A Kennedy, K. Doverspike, L. B. Rowland, D. K. Gaskill, J. A. Freitas Jr., M. A. Khan, D. T. Olson, J. N. Kuzmia and D. K. Wickenden, Phys. Rev. B, **51**, 13326 (1995).
15. M. Leroux, B. Beaumont, N. Grandjean, P. Gibart, J. Massies and J. P. Faurie, MRS Internet J. Nitride Semicond. Res., **1**, 17 (1996).
16. M. Leroux, B. Beaumont, N. Grandjean, P. Lorenzini, S. Haffouz, P. Vennéguès, , J. Massies and P. Gibart, ICAM/E-MRS '97 spring meeting, Symposium L, L-III.1, Strasbourg, June (1997).
17. J. I. Pankove and J. A. Hutchby, J. of Appl. Phys., **47**, 5387 (1976).
18. J. W. Orton, Sem. Sci. Techn., **10**, 101 (1995).
19. G. C. Yi and B. Wessels, Appl. Phys. Lett., **68**, 3769 (1996).
20. P. Hacke, H. Nakayama, T. Detcprohm, K. Hiramatsu and N. Sawaki, Appl. Phys. Lett., **68**, 1362 (1996).
21. W. Gotz, N. M. Johnson and D. P. Bour, Appl. Phys. Lett., **68**, 3470 (1996).
22. M. Leroux, B. Beaumont, N. Grandjean, J. Massies and P. Gibart, Mat. Res. Soc. Symp. Proc (to be published).
23. W. Gotz, N. M. Johnson, J. Walker, D. P. Bour and R. A. Street, Appl. Phys. Lett., **68**, 667 (1996).
24. M. Smith, G. D. Chen, J. Y. Lin, H. X. Jiang, A. Salvador, B. N. Sverdlov, A. Botchkarev, H. Morçoc and B. Goldenberg, Appl. Phys. Lett., **68**, 1883 (1996).
25. R. Seitz, C. Gaspar, T. Monteiro, E. Pereira, M. Leroux, B. Beaumont and P. Gibart, EGW 2, 9-42, Valbonne, June (1997)

Acknowledgments.
This work has been performed under the auspices of the Commission of the European Communities, under contract BRPR-CT96-034 (DG 12 – RSMT). Also financial support by JNICT, contract PRAXIS XXI PBIC/C/CTM/1925/95 is acknowledged.

Materials Science Forum Vols. 258-263 (1997) pp. 1161-1166

GaN DOPED WITH SULFUR

A. Saxler, P. Kung, X. Zhang, D. Walker, J. Solomon[1], M. Ahoujja[1], W. C. Mitchel[1], H. R. Vydyanath[2], and M. Razeghi

Center for Quantum Devices, Department of Electrical and Computer Engineering, Northwestern University, Evanston, IL 60208

[1]Air Force Research Laboratory, Materials Directorate, Wright-Patterson AFB, OH 45433-7707

[2]Avyd Devices, Inc., Costa Mesa, CA 92626

Keywords: GaN, sulfur, doping

Abstract. GaN thin films were doped during metalorganic chemical vapor deposition with sulfur using dilute hydrogen sulfide in hydrogen. The effects of dopant flow and growth temperature were studied. The films were characterized by temperature electrical measurements, Auger electron spectroscopy, x-ray photoelectron spectroscopy, x-ray diffraction, photoluminescence, and scanning electron microscopy. The low resultant carrier concentrations indicate that sulfur has a limited solubility in GaN.

Introduction.

The III-Nitrides are wide bandgap semiconductors with many potential applications including solar blind photodetectors [1], blue light emitting and laser diodes [2], and high temperature and high power electronics [4]. We have previously reported on the growth [4-6] of III-Nitrides, their characterization [7,8], and photodetectors [9,10] made from these materials. There are still many materials issues, including doping, that need to be resolved before this system can be fully exploited. We have used n-type and p-type dopants such as germanium, silicon, and magnesium. Each of these dopants occupies the group III metal site. Another potential n-type dopant for the III-Nitrides is sulfur on the nitrogen site. Since sulfur is significantly less electronegative than the nitrogen host atom, it is expected to easily donate its extra electron. However, since the size of the sulfur atom is also quite different from the host atom, we expect it to be difficult to incorporate into the lattice. To date, only implantation studies of S into GaN have been performed [11,12]. An early photoluminescence study of implanted GaN did not find any transitions characteristic of sulfur in addition to the peaks attributable to annealing and implantation damage [11]. SIMS analysis showed redistribution of the sulfur implanted into mixed phase GaN after annealing at only 600 C [12]. Assuming that the redistribution and surface loss of sulfur also applies to single phase hexagonal GaN typical of metalorganic chemical vapor deposition (MOCVD) growth, there could be considerable difficulty successfully doping in-situ at the typical growth temperatures of approximately 1000 C. In fact, segregation to the GaN surface was seen in MOCVD in-situ doping using selenium [13], which has a similar chemistry and atomic size to sulfur. In this paper, we discuss the doping of GaN with sulfur by MOCVD.

Experimental.

The films were grown in a horizontal low pressure MOCVD reactor. Triethylgallium (TEGa), trimethylaluminum (TMAl), and ammonia (NH_3) were used as sources for gallium, aluminum, and nitrogen respectively. Hydrogen sulfide (H_2S) diluted to 200 ppm in hydrogen was used as the dopant source for sulfur. All of the films were grown on (0001) Al_2O_3 substrates with a high temperature AlN nucleation layer. The layer thickness was 0.7 μm. We have previously published the details of the growth of GaN [4].

Results and Discussion.

The x-ray diffraction linewidths are very narrow for low doping levels as shown in Fig. 1. As the dopant flow increases over 100 sccm, the linewidths dramatically increase to over 100 arcseconds. The higher dopant flow also results in increased near bandedge photoluminescence (PL) intensity as seen in Fig. 1. The morphology changed from smooth for lightly doped samples to rough for the heavily doped samples. The change in morphology for samples doped with more than 100 sccm corresponds to the increases in the x-ray full width at half maximum (FWHM) and the PL intensity. These results suggest that for high hydrogen sulfide flow rates the growth mechanism is disturbed, changing the basic material properties.

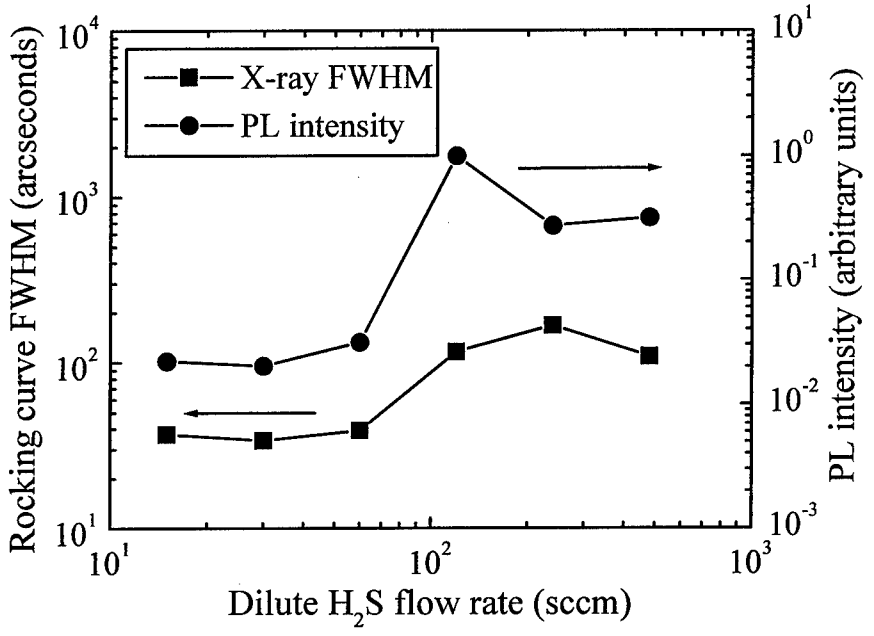

Fig. 1. Open detector (0002) GaN x-ray rocking curve FWHM and 77 K PL intensity as a function of the H_2S flow rate.

The room temperature electrical data is shown in Fig. 2 as a function of the hydrogen sulfide dopant flow rate. The n-type carrier concentration is nearly constant at 10^{17} cm^{-3} regardless of the flow rate. If we compare this to silicon or germanium doping using dilute silane or germane respectively, sulfur is a less efficient dopant for achieving a high n-type carrier concentration [14]. The lower carrier concentration may be due to a higher ionization energy for the sulfur levels or due to a lower rate of incorporation of the sulfur atoms into the GaN lattice.

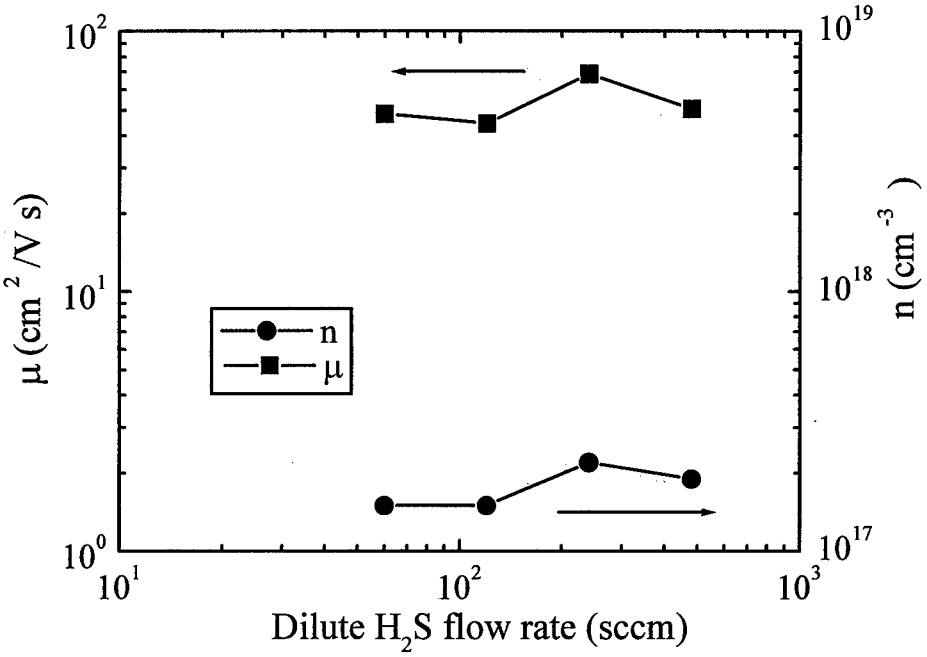

Fig. 2. Mobility and carrier concentration of GaN:S as a function of the H_2S flow rate.

The temperature dependent resistivity of the lightly doped samples is shown in Fig. 3. The activation energy was reduced as the H_2S flow was increased. The activation energies were 132 meV for the sample doped with 15 sccm and 50 meV for the sample doped with 30 sccm. The resistivity of the sample doped with 60 sccm was nearly independent of temperature.

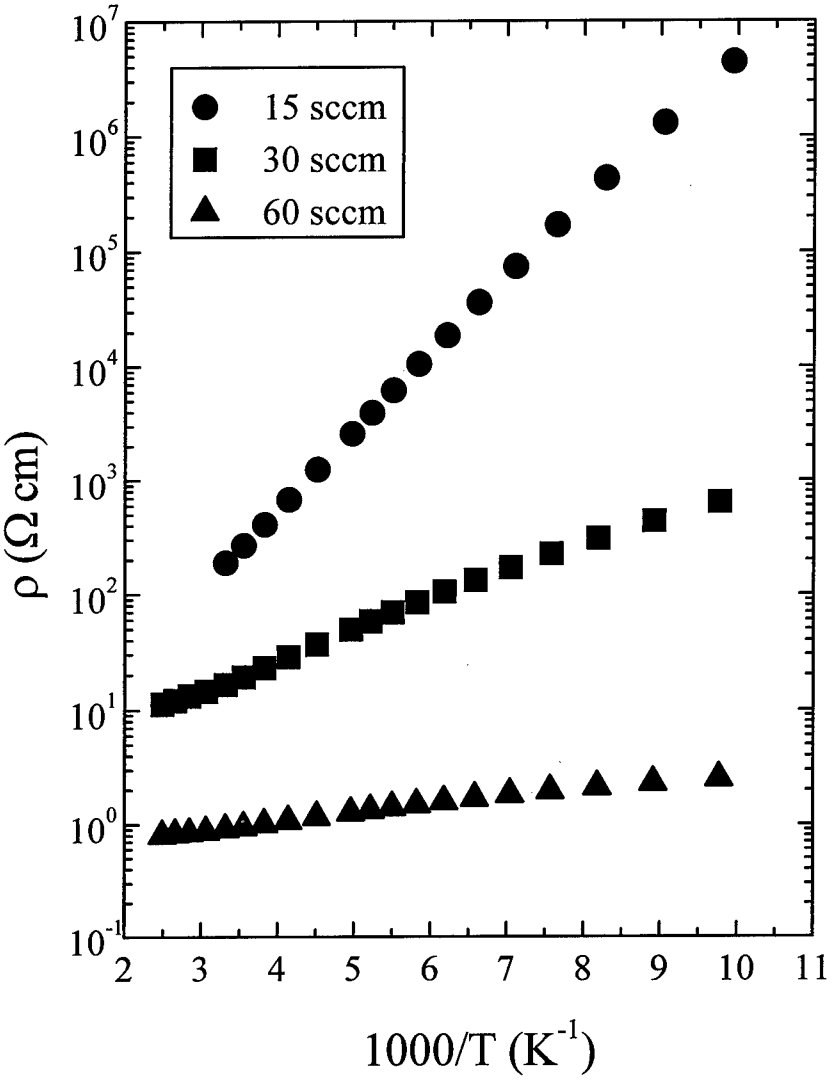

Fig. 3. Temperature dependent resistivity for GaN:S for several H_2S flow rates.

Sulfur was detectable on the surface of the samples by x-ray photoelectron spectroscopy (XPS) and by auger electron spectroscopy (AES). This indicates that higher quantities of sulfur are present at the surface than would be expected for a uniformly distributed shallow donor concentration on the order of 10^{17} cm^{-3}.

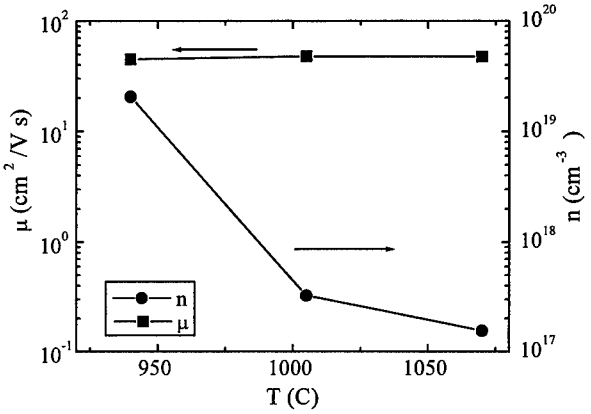

Fig. 4. Mobility and carrier concentration of GaN:S as a function of the growth temperature with the H_2S flow rate fixed at 60 sccm.

Figure 4 shows the effect of the growth temperature on the electrical properties. The dopant flow was fixed at 60 sccm while the growth temperature was decreased. The carrier concentration increased dramatically as the growth temperature was decreased. If we assume that the sulfur incorporation is saturated, we can fit the carrier concentration to the following equation: $n = A \exp(E_i/kT)$ where A is a constant, E_i is the activation energy of sulfur incorporation, k is Boltzmann's constant, and T is the absolute temperature. The resulting estimate of E_i is 2 to 8 eV. This result is similar to that seen for other III-V materials [15]. Figure 5 shows that the x-ray linewidth and the PL intensity also increased for the lower temperatures and higher carrier concentrations.

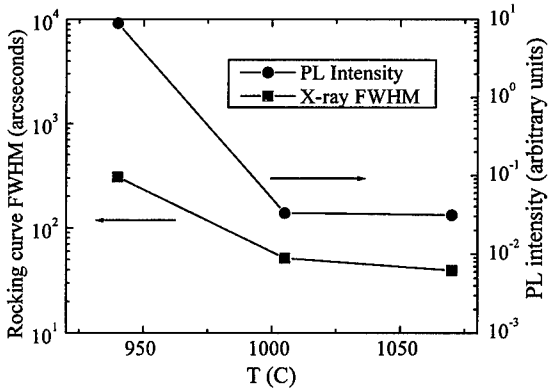

Fig. 5. Open detector (0002) GaN x-ray rocking curve FWHM and 77 K PL intensity as a function of the growth temperature with the H_2S flow rate fixed at 60 sccm.

In summary, sulfur is a difficult dopant to incorporate during the MOCVD growth of GaN. Reducing the growth temperature enabled the carrier concentration to be increased to over 10^{19} cm^{-3}.

Acknowledgements.

The authors would like to thank M. Yoder, Y.-S. Park, and C. Wood of ONR, A. Husain of DARPA, and P. Shu, B. Mott, and Z. C. Huang of NASA for their support and encouragement. Funding for this work was received under ONR/BMDO Grant N00014-93-1-0235 and DARPA/ONR Grant N00014-96-1-0714.

References.

1. M. Razeghi and A. Rogalski, J. Appl. Phys. **79**, 7433 (1996).
2. S. Nakamura, M. Seno, S. Nagahama, N. Iwasa, T. Yamada, T. Matsushita, Y. Sugimoto, and H. Kiyoku, Appl. Phys. Lett. **69**, 4056 (1996).
3. O. Aktas, Z. F. Fan, S. N. Mohammed, A. E. Botchkarev, and H. Morkoç, Appl. Phys. Lett. **69**, 3872 (1996).
4. P. Kung, A. Saxler, X. Zhang, D. Walker, T. C. Wang, I. Ferguson, and M. Razeghi, Appl. Phys. Lett. **66**, 2958 (1995).
5. A. Saxler, P. Kung, C. J. Sun, E. Bigan, and M. Razeghi, Appl. Phys. Lett. **64**, 339 (1994).
6. P. Kung, A. Saxler, X. Zhang, D. Walker, R. Lavado, and M. Razeghi, Appl. Phys. Lett. **69**, 2116 (1996).
7. A. Saxler, M. A. Capano, W. C. Mitchel, P. Kung, X. Zhang, D. Walker, and M. Razeghi, MRS Symposium Proceedings **449**, 477 (1997).
8. X. Zhang, P. Kung, D. Walker, A. Saxler, and M. Razeghi, MRS Symposium Proceedings **395**, 625 (1996).
9. X. Zhang, P. Kung, D. Walker, J. Piotrowski, A. Rogalski, A. Saxler, and M. Razeghi, Appl. Phys. Lett. **67**, 2028 (1995).
10. D. Walker, X. Zhang, A. Saxler, P. Kung, J. Xu, and M. Razeghi, Appl. Phys. Lett. **70**, 949 (1997).
11. J. I. Pankove and J. A. Hutchby, J. Appl. Phys. **47**, 5387 (1976).
12. R. G. Wilson, S. J. Pearton, C. R. Abernathy, and J. M. Zavada, Appl. Phys. Lett. **66**, 2238 (1995).
13. J. D. Guo, M. S. Feng, and F. M. Pan, Jpn. J. Appl. Phys. **34**, 5510 (1995).
14. S. Nakamura, T. Mukai, and M. Senoh, Jpn. J. Appl. Phys. **31**, 2883 (1992).
15. M. Razeghi, "The MOCVD Challenge, Volume 2: A survey of GaInAsP-GaAs for photonic and electronic device applications" (Institute of Physics Publishing, Bristol, UK) pp. 207-209 (1995).

Materials Science Forum Vols. 258-263 (1997) pp. 1167-1172

IDENTIFICATION OF IRON TRANSITION GROUP TRACE IMPURITIES IN GaN BULK CRYSTALS BY ELECTRON PARAMAGNETIC RESONANCE

P.G. Baranov, I.V. Ilyin and E.N. Mokhov
A.F. Ioffe Physico-Technical Institute, St.Petersburg, 194021 Russia

Keywords: galium nitride, manganese, nickel, electron paramagnetic resonance.

Abstract. We report on the observation of electron paramagnetic resonance of iron, manganese and nickel trace impurities in bulk GaN crystals grown by the sublimation sandwich method. The resolved hyperfine structure due to interaction with ^{55}Mn (I=5/2) nuclei has been observed in GaN, allowing unambiguous identification of the impurity . Manganese and nickel exist in Mn^{2+} ($3d^5$) and Ni^{3+} ($3d^7$) charge states with electron spin S=5/2 and S=3/2, respectively, and occupy gallium sites in the GaN lattice. For Mn^{2+} we found g=1.999, hyperfine structure constant A=70·10^{-4}cm^{-1} and fine structure parameter $|D| = 240 \cdot 10^{-4}cm^{-1}$. The EPR spectrum of Ni^{3+} in GaN had the characteristic anisotropy of an S = 3/2 system in a strong axial crystalline field. The effective g-factor values were found to be $g_{||}' = 2.10$ and $g_{\perp}' \cong 4.20$ for a system with an effective spin $S' = 1/2$. An analogy was revealed between the parameters of Mn^{2+} and Ni^{3+} in GaN and ZnO crystals. The zero-phonon line at 1.047 eV seems to belong to transition $^4T_2(F)$-$^4A_2(F)$ within 3d levels of Ni^{3+} ion with a $3d^7$ electronic configuration. In addition, EPR spectra of two new axial centres, labelled as ii1 and ii2 centres, have been observed.

Introduction

GaN is considered to be one of the most promising semiconductor materials for the construction of short-wavelength emitting devices, such as blue diodes and lasers [1]. In spite of impressive technological achievements of the last few years, there are still substantial gaps in our knowledge of the basic physical properties of GaN. One of them concerns the identification of transition metal impurities and related complexes in GaN. The EPR proved to be a powerful method for the identification of transition metal impurities in semiconductors. By now only Fe^{3+} ions were investigated in GaN using EPR [2,3].

The sublimation sandwich-method was used for growing GaN crystals as thick as 0.1 mm [4,5]. It was reported [6,7], that these crystals have good characteristics, no worse than in thin GaN layers grown by other techniques. These crystals have shown at least three zero-phonon lines of photoluminescence in infrared spectrum range: 1.3 eV, 1.19 eV, 1.047 eV [6,7]. It was supposed, that these lines belong to transitions within 3d levels of trace impurities of transition metal ions. The investigations of optically detected magnetic resonance have shown the correspondence between the EPR spectra, attributed to Fe^{3+}, and 1.3 eV luminescence line. The nature of other lines was widely discussed. The experimental results on the 1.047 eV emission [8] fit to a $^4T_2(F)$-$^4A_2(F)$ internal electronic transition of a transition metal with a $3d^7$ electronic configuration. It was suggested [9] that the best candidate was Co^{2+}, but the author could not completely exclude the Ni^{3+}. Thus, only correlation with the EPR seems can clarify this problem. It should be noted that the emission at 1.047 eV has not been observed as natural contaminant in GaN samples grown by metal organic vapour phase epitaxy and vapour phase epitaxy.

We report here EPR results for Fe^{3+}, Mn^{2+}, Ni^{3+} and EPR spectra of two new axial centres in GaN grown by the sublimation sandwich method. Preliminary reports have been published elsewhere [9].

Experimental results

In this work we investigated GaN crystals grown on 6H-SiC substrates by the sublimation sandwich method [4,5]. The thickness of GaN epitaxial layers was 0.1-0.2 mm and we can say with reasonable confidence that GaN was a bulk material in our experiments. Epitaxial layers on substrates and free-standing layers were used. No intentional doping of samples was performed. The samples were oriented for rotation in the $\{11\bar{2}0\}$ plane. The EPR spectra were studied on a conventional X-band (9.25 GHz) EPR spectrometer in the temperature range 4 - 150 K.

Figure 1 shows a part of the EPR spectrum of a GaN epitaxial layer on a 6H-SiC substrate, recorded at T=4 K for several angles (θ) between the applied magnetic field and the hexagonal axis (*c*-axis) of the sample (rotation in the $\{11\bar{2}0\}$ plane). In Fig. 1 a set of six equally intense lines can be seen on both sides of the central line. The strong signal near 3300 G contains, except the central fine-structure line of Fe^{3+}, a signal from the nitrogen donor impurity in the 6H-SiC substrate. The latter was nearly suppressed upon removing the substrate. In the orientations B || *c* and B⊥*c* these lines are marked by a set of vertical lines. The separations between the lines are about 70 G. We could observe other four groups with smaller intensities on both sides of central one, which proves that this spectrum belongs to an ion with electron spin S=5/2. All the groups have the same hf structure as the central one. Among the transition metal elements only manganese has a 100% abundant isotope with nuclear spin I=5/2 and the observed splitting corresponds to that of Mn^{2+} in $3d^5$ ($^6S_{5/2}$) state. The group in Fig. 1 belongs to the Mn^{2+} central fine structure transition (M_S= 1/2 ↔ M_S= -1/2), split by the hf interaction with nuclear spin I=5/2. This spectrum can be described by the spin Hamiltonian [10]

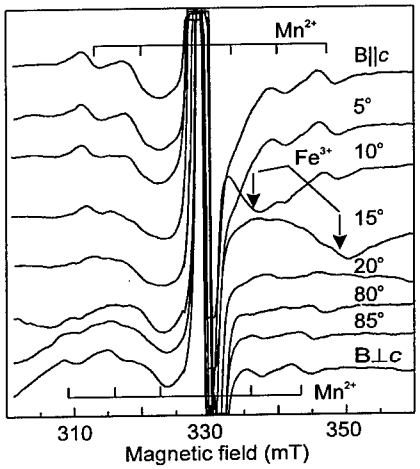

Fig. 1. EPR spectrum of Mn^{2+} ions in GaN in some orientations of crystal under rotation in $\{11\bar{2}0\}$ plane. In orientations B || *c* and B ⊥ *c* the positions of hf structure transition of Mn^{2+} (M_S=1/2 ↔ M_S=-1/2) are indicated. The arrows indicate positions of Fe^{3+} EPR signal.

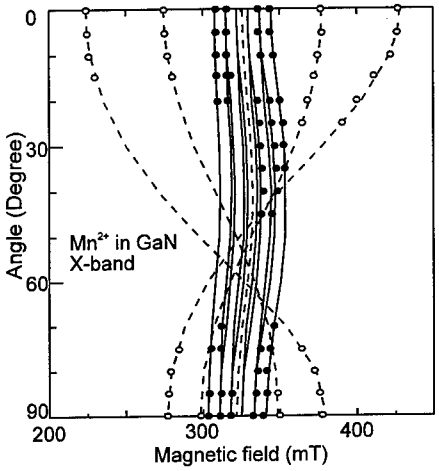

Fig. 2. The measured (open circles) and calculated (dashed lines) angular dependencies of fine-structure line positions of Mn^{2+} ions in GaN obtained at 9.25 GHz. The solid circles and solid lines represent the measured and calculated hf structure positions, respectively, which are plotted only for central transition (M_S = 1/2 ↔ M_S = -1/2).

$$H = \mu_B \boldsymbol{H}\cdot\boldsymbol{g}\cdot\boldsymbol{S} + 1/6\cdot a\{S_\xi^4+S_\eta^4+S_\zeta^4-1/5\cdot S(S+1)(3S^2+3S-1)\}+D\{S_z^2-1/3\cdot S(S+1)\}+ 1/180\cdot F\{35S_z^4-30S(S+1)S_z^2+25S_z^2-6S(S+1)+3S^2(S+1)^2\}+\boldsymbol{S}\cdot\boldsymbol{A}\cdot\boldsymbol{I}, \quad (1)$$

where $S=5/2$ and $I=5/2$ are the electron and nuclear spins, μ_B is the Bohr magneton, $\boldsymbol{g}$, $\boldsymbol{A}$ are tensors, describing the electron g-factor and the hf interaction with the impurity nucleus. Parameters D, F and a characterise the axial and cubic crystal fields.

An investigation of the angular dependence of the spectrum of Mn^{2+} allowed us to find the best-fit parameters for spin Hamiltonian of Eq. (1). The results are listed in Table 1 (the small parameters a-$F\cong 4\cdot10^{-4}cm^{-1}$ and $a\cong 5\cdot10^{-4}cm^{-1}$ are not pointed out in the table). The measured and calculated angular dependencies of fine-structure line positions of Mn^{2+} ions obtained at 9.25 GHz are plotted as open circles and dashed lines, respectively, in Fig. 2. The fine-structure positions have been estimated as the centre of gravity of the measured hf structure transitions. The solid circles and solid lines represent the measured and calculated hf structure positions, which are plotted only for central transition ($M_S = 1/2 \leftrightarrow M_S = -1/2$).

In Fig. 1 for the orientations $\theta = 10^0$ and 15^0 one can see intense broad EPR line, attributed [2] to one of the fine-structure transitions of Fe^{3+} with electron spin $S=5/2$. With increasing temperature EPR signals of Mn^{2+} and Fe^{3+} decrease in a similar manner. Fe^{3+} and Mn^{2+} EPR signals are detectable up to ~100 K.

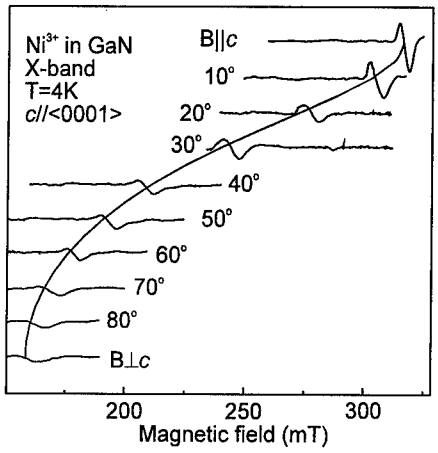

Fig. 3. Angular dependence of Ni^{3+} EPR line for rotation of the GaN crystal in $\{11\bar{2}0\}$ plane. Solid line have been calculated using spin Hamiltonian parameters of Eq. (2), listed in the article.

An intense anisotropic EPR line was observed in some GaN crystals. Fig. 3 shows an angular dependence of these line in GaN crystal at the X-band. The magnetic field applied was rotated in the $\{11\bar{2}0\}$ plane. This EPR spectrum has the characteristic anisotropy of an $S=3/2$ system in a strong axial crystalline field and positive g shift which is consistent with the electron configuration d^7 . The EPR line can be observed up to ~150 K and the linewidth is very sensitive to the orientation of the crystal in magnetic field. The intensities of the EPR signals for $\theta\neq0$ at 77 K are lower and depend more on the angle between magnetic field and c-axis then those at 4 K. Therefore it has not been possible to detect the signals at all angles at 77 K.

We attribute this spectrum to the trace impurity of nickel in the charge state Ni^{3+}. Isolated substitutional Ni^{3+} ion has a $3d^7$ electronic configuration. In GaN there are a combination of a trigonal and tetrahedral crystalline fields. The ^4F ground term of the free ion is split by a cubic tetrahedral part of crystalline field into two orbital triplets, $^4T_2$ and $^4T_1$, and a ground-state orbital singlet, $^4A_2$. The $^4A_2$ ground state is split into two Kramers doublets by the combined action of the trigonal field and the spin-orbit interaction. Omitting the hyperfine interactions, the EPR spectrum can be described by a spin Hamiltonian of the form

$$H = g_{||}\mu_B B_z S_z + g_\perp \mu_B (B_x S_x + B_y S_y) + D[S_z^2 - 1/3S(S+1)], \quad (2)$$

with S=3/2, z denotes the c-axis of the crystal, which is also the principal axis of the centre; D is the axial fine structure parameter. Since the magnitude of the zero-field splitting $2D$ is much larger than the microwave energy at the X-band (the strong zero-field limit), only the transitions within the M_S=±1/2 Kramers doublet can be detected. The spin Hamiltonian of Eq. (2) can be transformed as

$$H = g_{||}'\mu_B B_z S_z' + g_\perp'\mu_B (B_x S_x' + B_y S_y'), \quad (3)$$

where g' is the effective g-factor and S' is an effective spin $S' = 1/2$. The g values are listed in Table 1. Using the perturbation theory up to the third order, it was shown [11] that the experimental g' values of transition within the M_S=±1/2 Kramers doublet of an orbital singlet system with the spin 3/2 give $g_{||}' = g_{||}$, $g_\perp' = 2g_\perp[1-3/16(h\nu/2D)^2]$. Dividing $g_\perp'$ by two gives a rough approximation to $g_\perp$ which is very close to $g_{||}$. Figure 3 shows the theoretical angular dependence of Ni^{3+} EPR spectrum (solid line), calculated using spin Hamiltonian of Eq. (2) with following parameters: S=3/2, $g_{||} = g_\perp = 2.10$, D=2cm^{-1} (Table 1).

Table 1

	GaN					ZnO				
	$g_{\|\|}$	$g_\perp$	$\|D\|$ 10^{-4}cm^{-1}	A 10^{-4}cm^{-1}	Ref.	$g_{\|\|}$	$g_\perp$	D 10^{-4}cm^{-1}	A 10^{-4}cm^{-1}	Ref.
Fe^{3+} ($3d^5$)	1.990 1.995	1.997 1.995	713 715		[2] this work	2.006	2.006	-595		[2]
Mn^{2+} ($3d^5$)	1.999	1.999	240	70	this work	2.001	2.001	-236	74.1	[13]
Ni^{3+} ($3d^7$)	2.10 2.10	≅4.2 ≅2.1	≥1.5·10^4		this work S′=1/2 S=3/2	2.142 2.142	4.318 ≅2.16	+2·10^4		[12] S′=1/2 S=3/2

The g shift, $\Delta g = g - g_e$ (g_e is the free-electron g-factor), is given approximately by $\Delta g = -8\lambda/10Dq$, where λ is the spin-orbit coupling constant (for Ni^{3+} free-ion λ is approximately -238 cm^{-1}) and 10Dq is the energy splitting between $^4A_2$ and $^4T_2$. For tetrahedral symmetry additional terms cubic in spin operators and linear in the magnetic field should appear in the S=3/2 spin Hamiltonian of Eq. (2). However, these terms should be small and they will therefore produce small additional terms in the expression for the g' factor but will not modify the angular dependence predicted by the spin Hamiltonian of Eq. (3).

Practically, it is impossible at the X-band to determine all parameters of the spin Hamiltonian of Eq. (2) for a real magnetic field in the strong zero-field limit and our purpose at that moment was only to estimate the zero-field splitting parameter. In the magnetic field range available in our EPR experiments (0-16 kG), only the M_S=1/2 ↔ M_S=-1/2 transitions were observed. Our analysis has shown that $D \geq 1.5$ cm^{-1}. The zero-field splitting $2D$ was shown [12] to be positive and large for all $3d^7$ ions studied in the wurtzite lattice. This is comparable to the one reported for Ni^{3+} in ZnO [12] (Table 1).

Nickel has only one stable odd isotope, ^{61}Ni (natural abundance 1.13%), having nuclear spin I=3/2 and one normally expects a spectrum consisting of one intense main line and four equally intense

weak satellite lines. Their intensity, as a fraction of the main line, is expected to be about 0.25% only and the hf structure could not be observed.

In Ref. 2, an analogy was revealed between the parameters of Fe^{3+} ions in GaN and ZnO crystals. It was taken into account that both materials have the same hexagonal wurzite structure and close by similar physical parameters. We will follow this analogy in the case of Mn^{2+} and Ni^{3+} and the Table 1 lists corresponding values previously obtained for ZnO: Mn^{2+} [13] and ZnO: Ni^{3+} [12] (the parameters for Mn^{2+} in ZnO, a-F=5.2·10^{-4}cm^{-1} and a=6.2·10^{-4}cm^{-1}, are not pointed out in the Table 1). As illustrated in Table 1, a good correspondence is observed between the parameters of Fe^{3+}, Mn^{2+} and Ni^{3+} in GaN and ZnO. The small quantitative variation in the EPR parameters seems to reflect the changing degree of covalency. By analogy with Fe^{3+} in GaN we suppose that manganese and nickel occupy gallium sites in the GaN lattice. Since no hf structure for the line which we attributed to Ni^{3+} was observed we could not completely exclude some impurities which are isoelectronic to Ni^{3+} and have small concentration of odd isotopes or a very small value of nuclear magnetic moment, e.g., Fe^{+} or ions with $4d^7$ and $5d^7$ configurations.

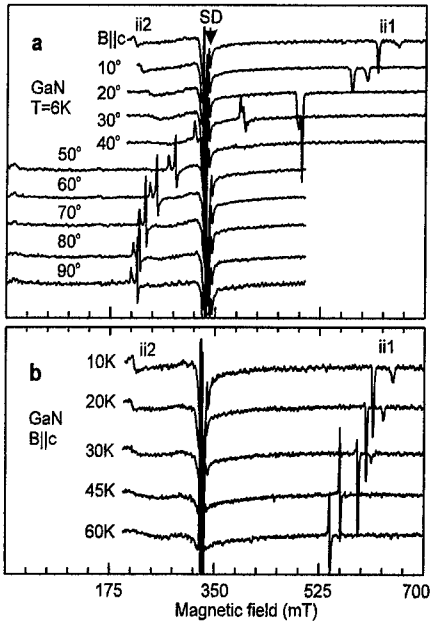

Fig.4. The EPR spectra observed in some GaN crystals (marked by ii1 and ii2). (a) Angular dependency, made at 4K in {11$\bar{2}$0} plane. (b) Temperature dependency in B||c orientation. The signal due to the shallow donors is marked by SD.

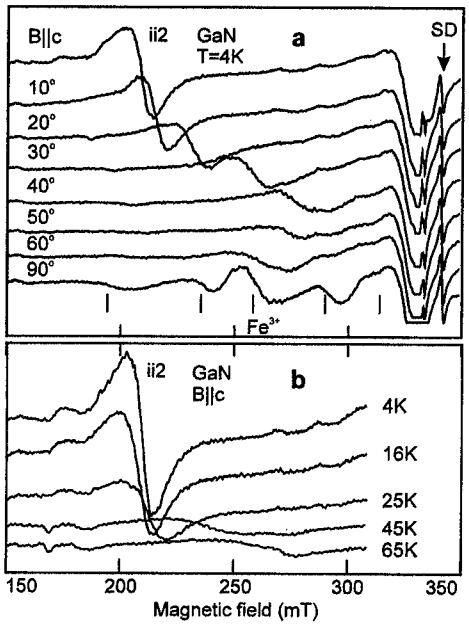

Fig 5. Orientational (a) and temperature (b) dependencies of the EPR spectra (marked ii2) observrd in some GaN crystals. Angular dependency was made at 4K in {11$\bar{2}$0} plane. Temperature dependency made for B||c direction.

According to our investigations we have every reason to think, that zero-phonon luminescence line at 1.047 eV belongs to transition $^4T_2(F)$-$^4A_2(F)$ within 3d levels of Ni^{3+} ion with a $3d^7$ electronic configuration. This luminescence line has been observed only in GaN samples grown by the sandwich technique and seems to correlate with EPR spectra of Ni^{3+}. This assumption is consistent

with the experiments of Ref. 8 in which photoluminescence results on the 1.047 eV emission fit to a $^4T_2(F)$-$^4A_2(F)$ internal electronic transition of a transition metal with a $3d^7$ electronic configuration. It should be noted that Fe^{3+} (the same charge state as Ni^{3+}) has the stable configuration in *n*-type GaN material and it's EPR spectra have been observed in the same samples in which the EPR spectra of Ni^{3+} were recorded.

In addition, EPR spectra of two new axial centres have been observed in some GaN crystals grown by the sandwich sublimation technique. Figure 4 (a) and Fig. 5 (a) show the orientational dependencies of the EPR spectra, labelled as ii1 (ii - Ioffe Institute) and ii2. The *g* -tensor for the EPR spectra of the both centres is nearly axial around *c* -axis and the positions of the groups of lines, in principle, can be fitted usual axial spin Hamiltonian. The principal values of the *g*-tensor at T=4.5 K was estimated to be $g_{||}$ = 1.07; 1.015 and $g_{\perp}$ = 3.00; 3.12 for each line of ii1 centre and $g_{||}$ =3.17 and $g_{\perp} \cong 2.0$ for ii2.

The *g* value for ii1 and ii2 centres was found to depend on temperature. Figure 4 (b) and Fig. 5 (b) show the temperature dependencies of the EPR spectra for the orientation B || *c*. Upon warming the crystal above 5 K, ii1 lines move to lower magnetic field with decreasing of the distance between lines for B|| *c* (for B⊥*c* they move in opposite direction) and to higher magnetic field for ii2 centre and decay above 60K for the both centres.

The ii1 centre is not stable at room temperature and it decreases to below 10% during about 100 days. We can only suggest that ii1 lines belong to hydrogen-related defect (two lines perhaps are due to hyperfine interaction with hydrogen) and the decay of this centre at room temperature can be result of hydrogen diffusion. The second ii2 centre seems to belong to deep state which can be related to yellow luminescence in GaN.

Acknowledgements - This work was partially supported by VW foundation under Grant No. I/70958, by NWO Grant No. 047.005.12.96 and by Russian Foundation for Basic Research under Grant No. 96-02-16927.

References

1. H.Morkoc, S.Strite, G.B.Gao, M.E.Lin, B.Sverdlov & M.Burns, *J.Appl.Phys.* **76**, 1363 (1994).
2. K. Maier, M. Kunzer, U. Kaufmann, J. Schneider, B. Monemar, I. Akasaki & H. Amano, *Mat. Sci. Forum* **143-147**, 93 (1994).
3. J. Baur, K. Maier, M. Kunzer, U. Kaufmann & J. Schneider, *Appl.Phys.Lett.* **65**, 2211 (1994).
4. Yu.A. Vodakov, E.N. Mokhov, A.D. Roenkov & Saidbekov D.T., *Phys.Stat.Sol.* A**51**, 209 (1979).
5. Yu.A. Vodakov, M.I. Karklina, E.N. Mokhov & A.D. Roenkov, *Inorganic Mater.* **17**, 537 (1980).
6. C. Wetzel, D. Volm, B.K. Meyer, K. Pressel, S. Nilsson, E.N. Mokhov & P.G. Baranov, *Mat. Res. Soc. Symp. Proc.* **393**, 453 (1994).
7. C. Wetzel, D. Volm, B.K. Meyer, K. Pressel, S. Nilsson, E.N. Mokhov & P.G. Baranov, *Appl. Phys. Lett.* **65**, 1033 (1994).
8. K.Pressel, S.Nilsson, R.Heitz, A.Hoffmann & B.K.Meyer, *J. Appl. Phys.* **79**, 3214 (1996).
9. P.G. Baranov, I.V. Ilyin and E.N. Mokhov, *Sol. St. Comm.* **101**, 8, 611 (1997).
10. A. Abragam & B. Bleaney, *Electron Paramagnetic Resonance of transition ions*, v.1, ch.7, Clarendon Press, Oxford (1970).
11. G.W. Ludwig & H.H. Woodbury, *Solid State Physics* vol. 13 ed F. Seitz and D. Turnbull (New York: Academic Press Inc.) p. 223 (1962).
12. W.C. Holton, J. Schneider & T.L. Estle, *Phys. Rev.* **133**, A1638 (1964)]
13. A. Hausmann, *Sol. St. Comm.* **6**, 457 (1968).

Materials Science Forum Vols. 258-263 (1997) pp. 1173-1178

LOCAL VIBRATIONAL MODES AT TRANSITION-METAL IMPURITIES IN HEXAGONAL AlN AND GaN CRYSTALS

C. Göbel, C. Schrepel, U. Scherz,
P. Thurian[1], G. Kaczmarczyk[1] and A. Hoffmann[1]
Inst. f. Theoretische Physik, TU-Berlin, Hardenbergstr. 36, D-10623 Berlin
[1]Inst. f. Festkörperphysik, TU-Berlin, Hardenbergstr. 36, D-10623 Berlin

Keywords: GaN, AlN, Transition Metals, Local Vibrational Modes, Isotope Shifts

Abstract. We present a detailed experimental and theoretical study of local vibrational modes (LVMs) at transition-metal (TM) impurities in wurtzite-type crystals. The energies of the LVMs of Fe^{3+} and Ti^{2+} in hexagonal GaN and Fe^{3+} in hexagonal AlN are calculated with a modified valence-force model of Keating and Kane, which was generalized for hexagonal symmetries including long-range Coulomb forces. The valence-force parameters of the perfect crystals are calculated by fitting the phonon dispersion curves to experimental Raman data of GaN and to ab-initio calculations of AlN. The valence-force parameters in the vicinity of the defect are determined using the scaling-factor approximation. The dynamical matrix is set up for a cluster of 295 vibrating atoms, which is embedded in the non-vibrating crystal, taking the TM as the central atom. The eigenvalues of the dynamical matrix give the vibration frequencies. The LVMs were selected due to their large vibration amplitudes of the atoms close to the defect as obtained from the eigenvectors of the dynamical matrix. The calculated energies of the LVMs are in good agreement with the results obtained by our photoluminescence and photoluminescence excitation measurements. We present the calculated impurity and the ligand induced isotope shifts of the LVMs. The energy differences with respect to different impurity isotopes were found to be smaller than 1 meV per nucleon and therefore could not been observed because of the experimental linewidth of 1.5 meV for the corresponding photoluminescence zero-phononlines. We also demonstrate the delocalization of LVMs with energy in the phononbands due to hybridization with crystal phonons.

Introduction

In the last few years the interest in the wide bandgap semiconductors, especially in the nitrides, has been strongly increased. With the nitride based semiconductors InN, GaN and AlN the band-gap can be varied between 1.9 eV (bandgap of InN) and 6.3 eV (bandgap of AlN). The aim of this paper is to give a comprehensive study on LVMs at various transition metal (TM) centers in these compounds. We here focus on the wurtzite-type crystals of AlN doped with Fe [5, 2], and GaN doped with Fe [3] or Ti [4], respectively.

The Energy of the local vibrational modes of the Fe^{3+} defect in GaN is determined experimentally by photoluminescence (PL). In the 1.2988 eV luminescence band LVMs at 37.3 meV, 39.2 meV, 85.5 meV and 88.9 meV are observed. The 1.2988 eV luminescence is attributed to the Fe^{3+} ($^4T_1$-$^6A_1$)-transition [1, 3].

Figure 1 shows a low-temperature photoluminescence-excitation spectrum of the Fe zero-phonon line for a Fe doped GaN crystal at 1.8 K [3]. There are several phonon satellites with a distance of 75 meV, coupled to the (Fe^{3+},e,h) transition [3].

A luminescence line at 1.1934 eV was detected with low-temperature photoluminescence measurements of a Ti and Cr doped GaN crystal at 1.8 K, which is attributed to the Ti^{2+} [4] center or to the Cr^{4+} center [2]. We attribute it to the (^1E-$^3A_2$)-transition of Ti^{2+} and not to Cr^{4+} [10].

A LVM at 87 meV has been observed in the photolumiscence spektrum of hexagonal AlN crystals [5] doped with Fe.

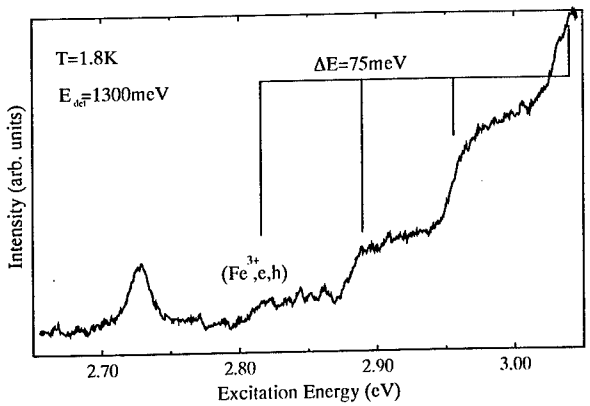

Figure 1: Low temperature photoluminescence excitation spektrum of a Fe doped GaN crystal at 1.8 K.

Theoretical Model

Our theoretical model is based on the harmonic approximation and the modified valence-force model of Keating and Kane, which was originally developed for crystals of cubic symmetry. The model for bond stretching and bond bending forces of Keating was extended by Kane to include up to third nearest neighbour interactions and long-range Coulomb forces. This model was generalized by us for hexagonal symmetry. In cubic crystals there are eight independent parameters. Because of the anisotropy in the direction of the c-axis there are fourteen independent parameters in crystals under hexagonal symmetry. To obtain the phonon-dispersion curves and the valence-force parameters of the perfect crystal, the long-range coulomb forces are calculated using the Ewald method.

For the calculation of the LVMs we used this model to set up the dynamical matrix of a cluster of 295 vibrating atoms, which is embedded in the non-vibrating perfect crystal and taking the TM as the central atom. The valence-force parameters in the vicinity of the defect are determined using the scaling-factor approximation which is defined by $p_d = p + ps$, where p is any of the valence-force parameters of the perfect crystal and p_d the corresponding parameter at the defect site, and s is the scaling factor which was varied between -0.2 and 1.0. A negative s indicates a local softening of the interatomic forces near the defect and a positive s means that the defect site is stronger bound than the atoms of the perfect crystal. The vibration frequencies were obtained from a numerical diagonalization of the dynamical matrix. The LVMs were selected from their large vibration amplitudes of the atoms in the vicinity of the defect as obtained from the corresponding components of the eigenvector of the dynamical matrix.

Based on the harmonic approximation the mass dependence of the energy of a LVM mode is associated with the sum of the squares of the three corresponding components of the eigenvector of the dynamical matrix A^2 and we have

$$\frac{\partial \hbar\omega}{\partial M} = -\frac{\hbar\omega}{2M} A^2. \tag{1}$$

This equation allows the determination of the shift of the energy of a LVM with respect to different impurity or ligand isotopes from the corresponding eigenvector of the dynamical matrix. In general three different isotope effects are possible in hexagonal crystals.

case a: The isotope shift depends on a different impurity mass.

case b: The ligand in the direction of the c-axis is replaced by a different isotope.

case c: One of the three other ligands is replaced by a different isotope. This causes a split of the otherwise twofold degenerated LVMs of E-symmetry.

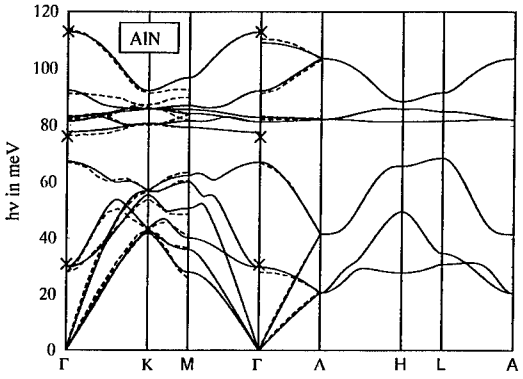

Figure 2: Calculated phonon-dispersion curves of AlN. The ab-initio calculated phonon-dispersion curves of Karch et al. are drawn with dashed lines. Some experimental values are shown with crosses [11].

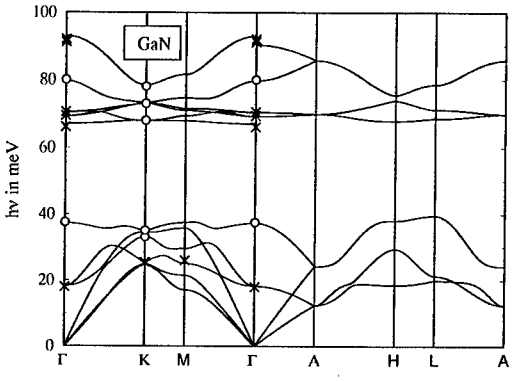

Figure 3: Calculated phonon-dispersion curves of GaN. The experimental energy values [8] are drawn with crosses and the additional used points due to the comparision with AlN are drawn with circles.

Results

The valence-force parameters of Keating and Kane for the perfect hexagonal AlN crystal were obtained from fitting to theoretical phonon-dispersion curves of Karch et al. [9]. Figure 2 shows the phonon-dispersion curves of AlN. Near the Γ-Point the fit is very good, but in the region of the boundary of the Brillouin zone the fit shows deviations up to 5 meV at the optical branches. This is in the energy region between 80 meV and 95 meV. The acustic phonon branches are well adapted.

The valence-force parameters for the perfect hexagonal GaN crystal were calculated from fitting to expertimental data [8]. Because of the nonexistence of neutron scattering data there are only a few values from Raman measurements [8] available, which are insufficient to obtain a unique determination of the parameters. To resolve this problem we suppose on the one hand a similarity between the Phonon-dispersion curves of GaN and AlN and on the other hand we assume that they are well adapted if the calculation of the local vibrational modes coincides with the experiments. The phonon-dispersion curves of GaN are shown in Fig. 3.

Figure 4 and Figure 5 show the dependence of the energy of the LVMs on the scaling factor for the Fe^{3+} defect in AlN and GaN. We selected the LVMS by the condition that the sum of the squared components of the eigenvector corresponding to the atoms in the first three shells around the defect is larger than 0.2. An agreement with the experimental values is achieved for a scaling factor of $s = 0.23$. This means the force constants in the vicinity of the defect are 23 % stronger than the force constants of the perfect crystal.

Ti behaves different in comparision to the Fe defect. There is an experimentally determined LVM with an energy close to the bottom of the optical phonon band. That gives reason to the assumption that the appropriate scaling factor is negative. We selected the LVMS by the condition that the sum of the squared components of the eigenvector corresponding to the atoms in the first five shells around the defect is larger than 0.3.

We obtained a sufficient agreement with the experimental values for an expected negative scaling factor of $s = -0.1$. The negative scaling factor indicates a softening of the forces at Ti in GaN. The vibration amplitudes of LVMs of the Fe-defect in AlN are shown in Fig. 6 and of the Fe-defect in GaN in Fig. 7.

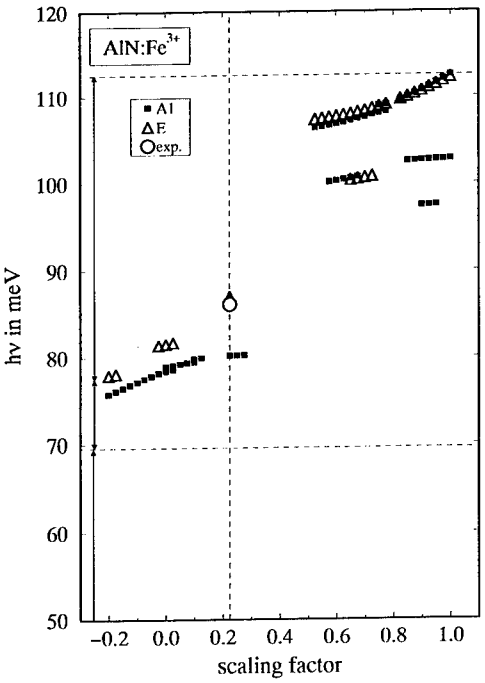

Figure 4: LVMs of AlN:Fe^{3+} in dependence on the scaling factor

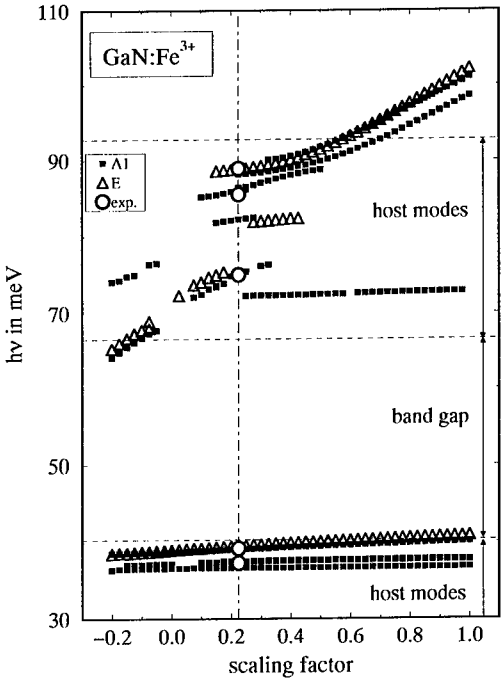

Figure 5: LVMs of GaN:Fe^{3+} in dependence on the scaling factor

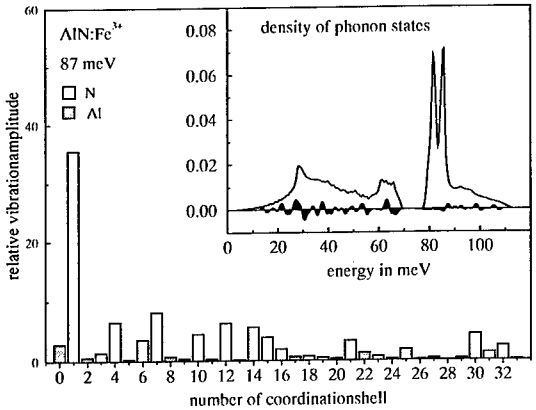

Figure 6: Vibrationamplitudes of the LVM with E-symmetry at 87.0 meV of hexagonal AlN and density of phonon states.

The bars indicate the sum of the squares of the vibration amplitudes of all the atoms in the various coordination shells, having the same distance to the central defect. The coordination shells are numbered zero for the TM to 33. The insets show the density of phononstates of the perfect crystals. The difference between the density of phonon states of the unperturbed and of the perturbed crystal multiplied by two is shown black filled. There are two effects responsible for the occurance of LVMs. A larger mass of the impurity leads to a shift of to lower energies and the modified binding properties of the defect give an additional shift of the energy. LVMs are expected to occur mainly in the energy region, where the density of phonon states of the perfect crystal is low. Due to hybridization, the localization of the LVMs decreases with the scaling factor if its energy is shifted from regions of low density of phonon states into regions of high density of phonon states.

The vibration amplitudes of the LVM at 87 meV of AlN:Fe^{3+} are shown in Fig. 6. The hybridization effects lead to a delocalisation of this mode. In contrast to this the Fig. 7 shows a

strong localized LVM of GaN:Fe^{3+} with an energy of 39.5 meV. Very large vibrationamplitudes are found within the first three shells around the defect.

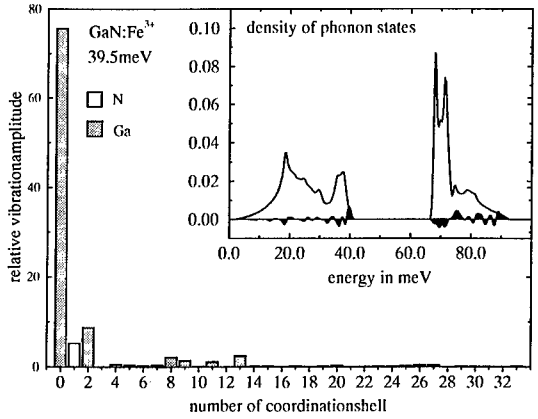

Figure 7: Vibrationamplitudes of the LVM with E-symmetry at 39.5 meV of hexagonal GaN and density of phonon states.

Local Vibrational Modes				Isotope Shifts		
	exp. [meV]	$\hbar\omega$ [meV]		case a $\left[\frac{\mu eV}{nucleon}\right]$	case b $\left[\frac{\mu eV}{nucleon}\right]$	case c $\left[\frac{\mu eV}{nucleon}\right]$
AlN:Fe^{3+}		80.2	A_1	-7	-103	-148
$s = 0.225$	86.1	87.0	E	-13	-8	-18 | -370
GaN:Fe^{3+}		36.7	A_1	-4	0	-1
$s = 0.225$	37.3	37.5	A_1	-19	-1	-1
	39.2	39.1	A_1	-49	-6	-2
		39.5	E	-85	-2	-12 | -2
	75.0	75.1	A_1	-25	-692	-55
($s = 0.175$)		75.3*	E			
		82.2	A_1	0	-105	-203
	85.5	86.0	A_1	0	-406	-194
		86.4	A_1	-1	-13	-213
		88.1	A_1	-16	-173	-122
	88.9	88.8	E	-21	-111	-99 | -267
GaN:Ti^{2+}		36.6	A_1	-7	0	-1
$s = -0.1$		38.9	A_1	-46	-1	-1
		39.3	E	-99	-2	-3 | -2
		67.0	A_1	-41	-1218	-131
	67.8	67.9	E	-11	-5	-14 | -531
	82.2	84.5	A_1	0	-42	-46
		88.2	E	-10	-131	-134 | -64

Table 1: Summary of the calculated LVMs in comparision to the experimental values. The isotope shifts due to the three possible isotope effects are also summarized.

In both semiconductors the Fe defect has a LVM in the optical phonon band. The LVM of AlN:Fe^{3+} has E-symmetry, whereas the LVM of GaN:Fe^{3+} has A_1-symmetry. Because of the similarity of the phonon-dispersion curves we expect in both materials a LVM of the same symmetry. If we regard the LVMS of GaN:Fe^{3+} at a scaling factor of s=0.175 we find a LVM of E-symmetry with an energy of 75.3 meV. Considering the uncertainties of the fit of the phonon-dispersion curves of GaN, our calculations a consistent with both E and A_1 modes

AlN and GaN exist also in the cubic modification. We suppose that there is a LVM at about 75 meV with T_2 symmetry in cubic GaN. This gives reason to the assumption that there also exists an A_1 mode at about 87 meV in hexagonal AlN and a LVM of T_2 symmetry in cubic AlN. We did not find the expected LVM of A_1 symmetry. A possible reason is an improper fit of the phonon-dispersion curves of AlN in the energy region between 80 meV and 90 meV. The highest optical phonon branch is about 5 meV too high, which leads to a large density of phonon states in the energy region of 87 meV. We therefore assume that the hybridization of the A_1 mode with host modes is very strong.
Our calculations of the impurity and ligand induced isotope shifts of the LVMs are based on Eq. 1. The results are listed in Table 1. There were no isotope shifts observed and the calculated isotope shifts were found to be smaller than 1.2 meV. Because of the dependence of the isotope shift on the vibration amplitude, the isotope shift is strongly affected by hybridization.

Conclusion

We present a detailed experimental and theoretical study of the local vibrational properties of the Fe^{3+} transition metal impurity in wurtzite type GaN and AlN and of the Ti^{2+} defect in hexagonal GaN. In spite of the uncertainties of the phonon-dispersion curves of the perfect crystals, our calculated energies of the LVMs are in good agreement with the results obtained by our photoluminescence and photoluminescence excitation measurements. The Fe^{3+} defect has in both semiconductors, GaN and AlN, a LVM in the optical phonon band which is strongly hybridized with host modes. The calculated isotope-shifts due to the impurity were found to be smaller than 1.2 meV per nucleon and therefore could not been observed because of the experimental linewidth of 1.5 meV.

References

[1] P. Thurian, G. Kaczmarczyk, H. Siegle, R. Heitz, A. Hoffmann, I. Broser, B.K. Meyer, R. Hoffbauer, U. Scherz, Material Science Forum **196-201**, 1571 (1995)

[2] J. Baur, K. Maier, M. Kunzer, U. Kaufmann, J. Schneider, H. Amano, I. Akasaki, T. Detchprohm and K. Hiramatsu, Appl. Phys. Lett. **64** 857 (1994)

[3] R. Heitz, P. Maxim, L. Eckey, P. Thurian, A. Hoffmann, I. Broser K. Pressel and B.K. Meyer, Phys. Rev. **B55** 4382 (1997)

[4] R. Heitz, P. Thurian, P. Pressel, I. Loa, L. Eckey, A. Hoffmann, I. Broser, B.K. Mayer and E.N. Mokhov, Phys. Rev. **B52** 16508 (1995)

[5] K. Maier, M. Kunzer, U. Kaufmann, J. Schneider, B. Monemar, I. Akasaki and H. Amano, Materials Science Forum 143-147, 93 (1994)

[6] P.N. Keating, Phys. Rev. **145**, 637 (1966)

[7] E.O. Kane, Phys. Rev. **B31**, 7865 (1985)

[8] H. Siegle, L. Eckey, A. Hoffmann, C. Thomson, B.K. Meyer, D. Schikora, M. Hankeln and K Lischka, Solid State Communications **96**, 943 (1995)

[9] K. Karch, G. Portisch, F. Bechstedt, P. Pavone and D. Strauch, Technical Digest of - ICSRM-95- (1995) 'Ab initio Calculation of Structural and Dynamical Properties of AlN'

[10] 'Transition Metal Luminescence in AlN Crystals', K. Pressel, S. Nilsson, R. Heitz, A. Hoffmann, B.K. Meyer, Material Research Soc., Fall Meeting **95** Boston (1995)

[11] L.E.McNeil, M. Grinsditd, R.H. French, J. Am. Ceram. Soc. **76**, 1132 (1993)

Materials Science Forum Vols. 258-263 (1997) pp. 1179-1184

LOCAL VIBRATIONAL MODES AT As_N IN CUBIC GaN: COMPARING AB-INITIO CALCULATIONS TO A SEMI-EMPIRICAL MODEL

K. Petzke, C. Göbel, C. Schrepel, P. Thurian*, and U. Scherz

Inst. für Theoretische Physik, Technische Universität Berlin, Hardenbergstr. 36, D-10623 Berlin
* Inst. für Festkörperphysik, Technische Universität Berlin, Hardenbergstr. 36, D-10623 Berlin

Key Words: cubic GaN:As, local vibrational mode, density-functional theory

Abstract

We present a study of the local vibrational modes (LVM) at the As_N impurity in cubic GaN. These are of interest, as in the growth of cubic GaN on a GaAs substrate, some As penetrate from the substrate into the layer. Such impurities might be the origin of a large number of sharp Raman modes, which can be observed at low temperatures and certain excitation wavelengths [4]. We focus on the As_N substitutional impurity in the GaN layer. The energies of the LVMs at those centres are calculated using two different approaches: first, a semi-empirical calculation is presented, then an ab-initio one. In the conclusion, we will show, that the results of both calculations produce similiar results. The Raman lines of ref. [4] can not be explained by LVMs at isolated As impurities in GaN.

Introduction

Layers of cubic GaN, grown on a GaAs substrate, show a large number of Raman lines, which can be observed at low temperatures and if green laser light is used for excitation [4]. Because those modes can only be found on GaN layers grown on GaAs, it is likely, that they are caused by As atoms diffusing into the GaN layer, or N atoms diffusing into the GaAs substrate. In this paper, we investigate the possibility, that isolated As impurities within the GaN layer are the cause for the observed Raman lines. We do so by calculating the energies of the possible local vibrational modes (LVMs) at this centre.

Semi-empirical calculations

Our theoretical model is based on the harmonic approximation and the valence-force model of Keating and Kane. The model for bond stretching and bond bending forces of Keating was extended by Kane to include up to third nearest neighbour interactions and long-range Coulomb forces. There is a total of eight independent parameters. To obtain the phonon-dispersion curves and the valence-force parameters of the perfect crystal, the long-range coulomb forces are calculated using the Ewald method.

For the calculation of the LVMs we use this model to set up the dynamical matrix of a cluster of 281 vibrating atoms, which is embedded in the non-vibrating perfect crystal. The central atom of the cluster is replaced with the impurity atom. The valence-force parameters in the vicinity of the defect are determined using the scaling-factor approximation. It is defined by $p_d = p + ps$, where p is any of the valence-force parameters of the perfect crystal and p_d the

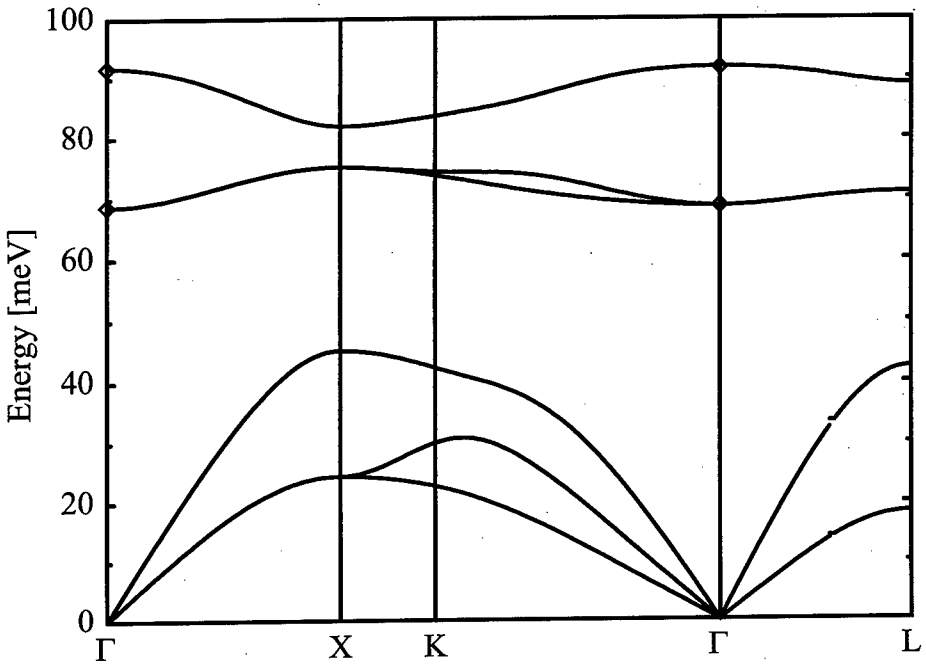

Figure 1: The phonon dispersion curves of the perfect GaN crystal, as fitted with the Keating and Kane model. The fit has been performed using the Raman frequencies at the Γ point and some qualitative data from the ab initio calculations.

corresponding parameter at the defect site. s is the scaling factor, which is varied between -0.3 and 1.0. A negative s indicates a local softening of the interatomic forces near the defect and a positive s means that the defect site is stronger bound than the atoms of the perfect crystal.

The vibration frequencies are obtained from a numerical diagonalization of the dynamical matrix. The LVMs are selected from their large vibration amplitudes of the atoms in the vicinity of the defect.

Ab initio calculations

All ab initio calculations have been performed with a modified version of the program fhi93cp respective fhi94md from the Fritz–Haber–Institute, Berlin [2]. In particular, we have ported the program to run on the massively parallel computer Cray T3D.

The program expands the wave function using a plane wave basis set. We have used Troullier-Martins pseudopotentials [3] for all three atoms (Ga, N and As). The 3d shell of electrons is treated as a valence shell for Ga, but only in the calculations for the perfect crystal. For the disturbed system, though, we have to use a Ga potential, that has the 3d electrons in the core, and use non-linear core correction (NLCC) instead. The latter potential has been generated using the Bachelet, Haman and Schlüter scheme [1].

We have choosen cut off energies of 40 Rydberg (in case of the Ga potential with non-linear core correction) or 80 Rydberg (in case of the Ga potential with 3d electrons as valence electrons).

The calculations for the perfect crystal are described in ref. [5]. The resulting density of phonon states is used to account for the hybridization of the local vibrational modes with host modes.

For the disturbed crystal, we use a supercell with 54 atoms, which is 3x3x3 times the size of the primitive cell. One Nitrogen atom is replaced by Arsenic. Relaxation of the first and second

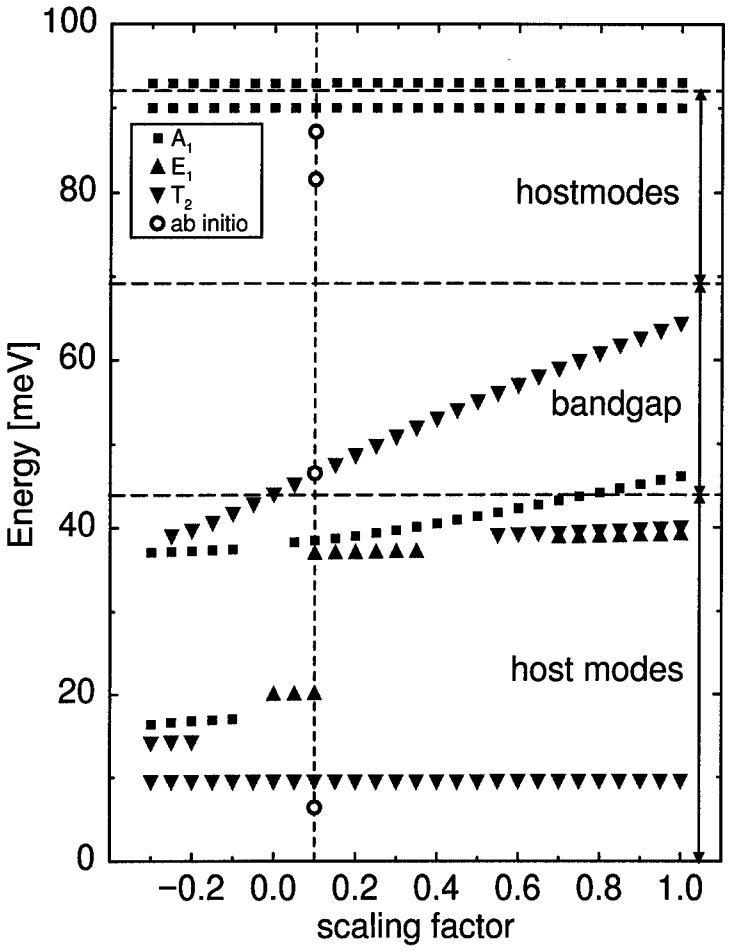

Figure 2: Plot of the LVM over the scaling factor. Those modes, that show a high hybridization with host modes have a low or now dispersion, while modes in the bandgap show a high dispersion.

nearest neighbors has been taken into account. We then determine all force constants between the defect atom and its relaxed first and second nearest neighbors.

The data of the impurity and the perfect crystal is used to set up a cluster of 441 vibrating atoms. We diagonalize the dynamical matrix for that cluster and determine the eigenstates, which are highly localized in the vicinity of the impurity.

Ab initio results

We obtain four localized vibrational modes: at 6.4 meV, 46.6 meV, 85.0 meV and 87.2 meV. The energy of the lowest mode decreases with increasing cluster size. At 441 atoms, it may not be fully converged, yet. As this mode shows an exponential decrease of the amplitude when going to outer shells, we identify it as a LVM. The mode at 46.6 meV in the bandgap is undoubtedly a LVM. The modes at 85.0 meV and 87.2 meV are highly hybridized with optical phonons. Most of the vibration energy is located at the twelve nitrogen atoms, which are second nearest neighbors of the impurity.

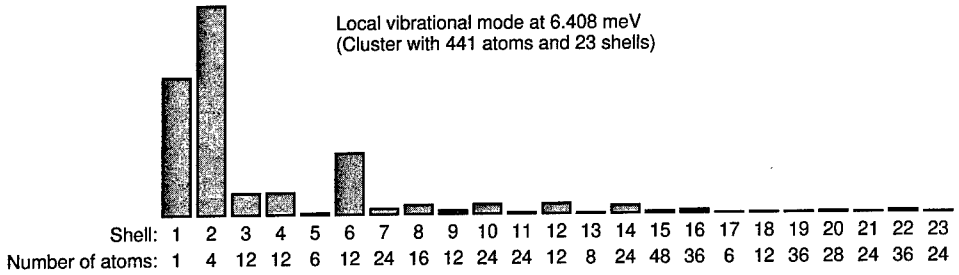

Figure 3: The LVM with the lowest energy, that was found by the ab initio calculation.

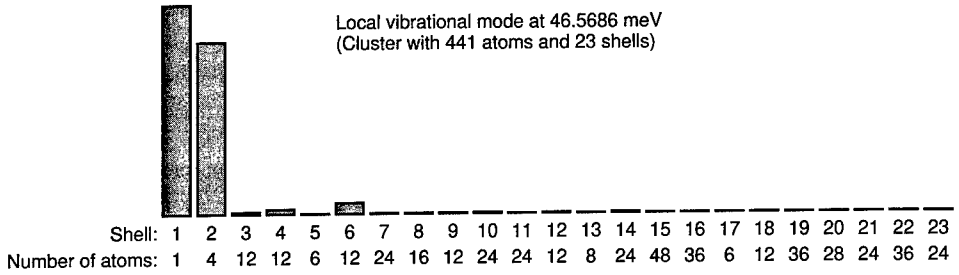

Figure 4: The LVM in the bandgap, that was found by the ab initio calculation.

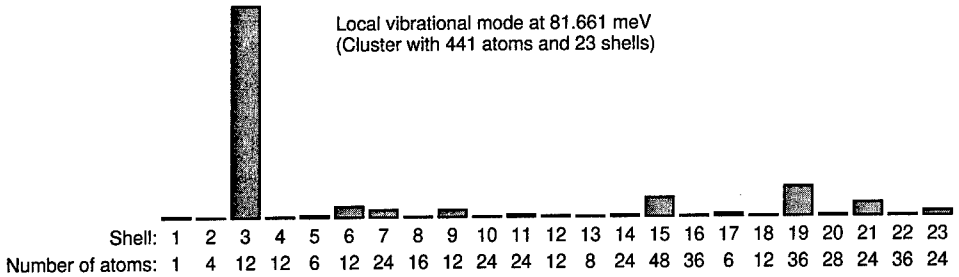

Figure 5: The first hybridized mode, that was found by the ab initio calculation.

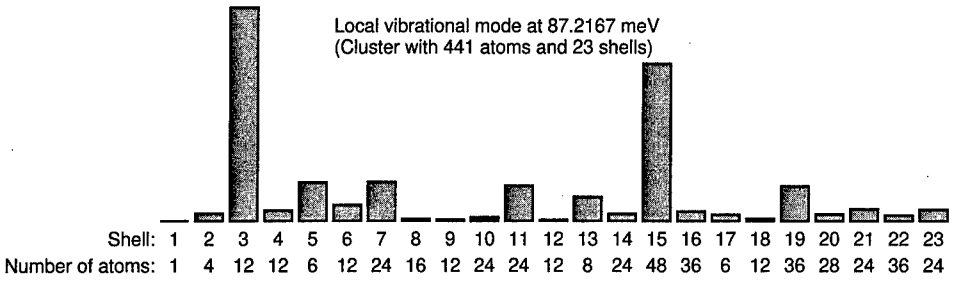

Figure 6: The second hybridized mode, that was found by the ab initio calculation.

Comparison

The results of the ab initio and semi-empirical calculations compare well. Both show two modes, that are highly hybridized with the optical phonons, one mode in the bandgap, and one at low accoustic energies. However, the ab initio calculations obtain lower energies for the hybridized modes than the semi-empirical calculations. This is consistent with the observation, that the ab initio results for GaN are about 4 meV too low for the optical phonons. There is also a difference of 3 meV in the energy of the lowest LVM. This difference can easily be explained by the different cluster sizes. At the 281 atoms of the cluster for the semi-empirical calculations, the results are not fully converged, yet.

It is very unlikely, that the Raman modes observed in ref. [4] can be attributed to LVMs of As_N in GaN. There is a minimum of 9 distinct Raman modes in the energy range from 7.4 to 31.0 meV, which all show the same temperature dependency. However, the semi-empirical calculation gives not more than two modes in that energy range. The ab initio calculations even finds no mode at all in that range.

Conclusion

The semi-empirical and the ab initio calculation give comparable results. These indicate, that the large number of Raman modes of cubic GaN layers on GaAs are not due to LVMs on As centres, that diffused into the GaN layer.

Acknowledgements

We thank the Fritz–Haber–Institut, Berlin, for providing their computer program fhi94md. We thank the Konrad–Zuse–Zentrum für Informationstechnik, Berlin for providing CPU time on a Cray T3D massive parallel system and for their support.

References

[1] G. B. Bachelet, D. R. Hamann, M. Schl"uter 1982, *Phys. Rev. B.* **26**, 4199.

[2] R. Stumpf und M. Scheffler 1994, *Computer Physics Communications* **79**, 447.

[3] N. Troullier, José Luís Martins 1991 *Phys. Rev. B.* **43**, 1993.

[4] H. Siegle et. al. 1997, *Z. Physik. Chemie* **201**, to be published.

[5] K. Petzke, C. Schrepel and U. Scherz 1997, *Z. Physik. Chemie* **201**, 317-322.

Materials Science Forum Vols. 258-263 (1997) pp. 1185-1190

A CODOPING METHOD IN GaN PROPOSED BY *ab initio* ELECTRONIC-STRUCTURE CALCULATIONS

T. YAMAMOTO [1,2] AND H. KATAYAMA-YOSHIDA [1,3]

[1] Department of Condensed Matter Physics, ISIR, Osaka University, Osaka 567, Japan.
[2] Department of Computational Science, Asahi Chemical Industry Co., Ltd., Fuji, Shizuoka 416, Japan.
[3] PRESTO, Japan Science and Technology Corporation, Kawaguchi, Saitama 332, Japan.

Keywords : GaN, self-compensation, wide-band-gap semiconductors, electronic-band structures, the Madelung energy, a codoping method.

Abstract. We propose a new type doping method, the " codoping method (doping *n*- and *p*-type dopants at the same time) " for the fabrication of high-conductivity *p*-type GaN with a wurtzite structure. *Ab initio* electronic-structure calculations predict that the co-incorporation of Be_{Ga} with O_N or Si_{Ga} in codoped *p*-type GaN produces high Be concentrations with stable ionic charge distributions markedly due to a decrease in the Madelung energy in contrast to *p*-type GaN doped with only Be.

Introduction.

GaN with a direct wide-band-gap energy of 3.44 eV has attracted widespread attention for producing highly-efficient blue-light emitting diodes and has potential for use in optoelectronic devices in the short wavelength range of the visible ultraviolet regions. While controlled *n*-type conductivity is commonly achieved by the incorporation of Si_{Ga} with an activation energy between 12 and 17 meV [1], difficulties in achieving high-conductivity *p*-type layers have hampered the applications of GaN in devices e.g. laser diodes. *P*-type doping of GaN is one of the crucial issues for large scale applications using this material. Various mechanisms which may limit the hole concentration in *p*-type doped GaN based on first-principle calculations have been proposed [2]. Several authors reported on obtaining high-conductivity *p*-type GaN films [3-6]. Very recently, Brandt *et al.* produced high-conductivity *p*-type GaN using acceptor dopants (Be) and donor dopants (O) [7]. Despite the rapid progress in the development of the GaN crystals, little is known about the relation between the cause of difficulty in fabricating high-conductivity *p*-type GaN and a change in the electronic band structure or in the nature of the chemical bonds of *p*-type doped GaN crystals.

The purpose of this work is to understand the role of *n*-type codopants, O_N or Si_{Ga}, in *p*-type GaN by (Be, O) or (Be, Si) codoping. Several effects of *p*-type doping of the acceptor-dopants, Be and Mg, on the electronic structures are described and discussed in order to understand the occurrence of the uni-polarity that both high conductivity *p*- and *n*-type crystals are difficult to fabricate in GaN crystals.

Methodology.

The calculations are based on the local-density-functional theory where we treat exchange and correlation effects using the parametrization of Hedin and Lundquist and von Barth and Hedin [8-10] and on the augmented spherical wave (ASW) formalism [11]. We adopt the atomic sphere approximation (ASA) with a correction term for the calculations. For valence electrons, we employ outermost *s* and *p* orbitals for each atom. We studied the crystal structures of doped and codoped GaN with periodic boundary conditions by generating supercells that contain the object of interest: (1) For doped GaN, we replace one of 16 sites of Ga or N atoms by a donor or an acceptor site in model supercells; (2) For codoped GaN:Be (Mg) and O, we replace two of 16 sites of the Ga atoms by the

Be (Mg) atom sites and one of 16 sites of the N atoms by the O site; (3) For codoped GaN:Be (Mg) and Si, we replace two of 16 sites of the Ga atoms by the Be (Mg) sites and one of 14 sites of the remaining Ga atoms by the Si site.

Results and Discussion.

The effects of *p*-type doping on the electronic structures. We show the total and site-decomposed density of states (DOS) of undoped GaN as a standard reference and those of GaN crystals doped with Be or Mg atoms in Fig. 1. Energy is measured relative to the Fermi level (E_F).

The site-decomposed DOS of undoped GaN in Figs. 1b and 1c show that the mixing between the 2*s* and 2*p* states of N and the 4*s* and 4*p* states of surrounding Ga shifts the center of gravity of the local density of states of the N atom towards lower energy. While an interaction between the N 2*p* and the Ga 4*s* orbitals causes the shift of the 4*s* states of Ga atoms towards lower energy, charge transfers from Ga 4*p* to N 2*s* and 2*p* give rise to an shift of Ga 4*p* levels towards higher energy regions above E_F. We noted that for GaN crystals the calculated Madelung energy, E_M, is 4.08 Ry (= 55.5 eV) in the unit cell with 4 atoms. The large E_M is due to the ionic features of the chemical bonds in GaN crystals.

Total and site-decomposed DOS for GaN:Be and GaN:Mg in Fig. 1d-Fig. 1g show that a hole in the unit cell is generated. We find that the electronic structures of the two *p*-type doped GaN crystals with higher concentrations, being on the order of 10^{21} cm^{-3}, have the same band shape as that of undoped GaN. The impurity states for those *p*-type doped crystals are in the energy region at the top of the valence band and are delocalized on sites of N atoms, as determined from site-decomposed DOS and dispersion relations. Thus, the *ab initio* calculations predict that both Be and Mg are shallow acceptors in GaN.

From Figs. 1e and Fig. 1g, we find that the *p*-type doping has a considerable effect on the electronic structures at N-sites close to the acceptor dopants as discussed below.

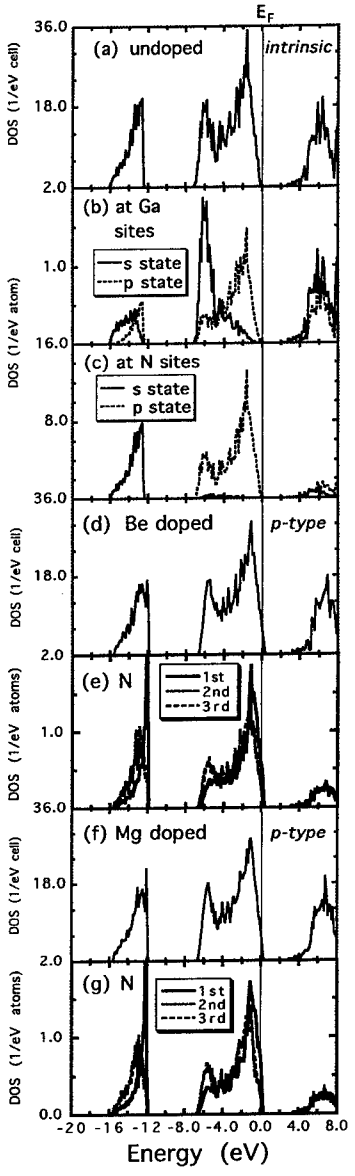

Fig. 1. (a) Total and (b), (c) site-decomposed DOS of undoped GaN, (d) total and (e) site-decomposed DOS of GaN:Be, and (f) total and (g) site-decomposed DOS of GaN:Mg.

Considering that the wurtzite structure tends to occur in semiconductors with high polarization, the understanding of the change in the stability of the charge distributions by *p*- or *n*-type doping is to recognize that the ion in the solid experience a strong electrostatic potential from the surrounding ions of opposite charge. The main contributor to the binding energy of crystals having ionic character is electrostatic energy and is called the Madelung energy, E_M.

In Table I, we summarize the centers of gravity of the bands given by the Hankel energies within the ASW formalism [11] and the differences in the calculated Madelung energy between undoped and the *p*-type doped GaN crystals. Table I indicates that the impurity states due to doped Mg are more localized on the neighboring N atoms than those due to doped Be. This suggests that Mg is a deeper acceptor than Be. Table I, Fig. 1e and Fig. 1g show that *p*-type doping of Be or Mg causes shifts of the *p*-levels of N atoms, close to the dopants, towards high energy regions compared with the other N atoms. The increase in the Madelung energy will inhibit higher doping concentrations of the Be or Mg atoms as acceptors due to the destabilization of the ionic charge distributions in the crystals or will lead to compensation of the acceptor-vacancy of N atoms. As a result, Be_3N_2 or Mg_3N_2 precipitates will be formatted, which gives rise to a loss of the crystal quality as well as the morphology. These are in good agreement with the theoretical report [12].

Table I. Energy positions of 2*p* orbitals of N atoms and the Madelung energies for undoped, Be-doped, and Mg-doped GaN crystals. The energy positions are measured relative to the Fermi level of each crystal. The 2nd row contains 2*p* levels of N atoms for undoped GaN crystals as a standard reference and those of N atoms close to the acceptor dopants for *p*-type doped GaN crystals. The 3rd row contains those of 2nd-neighbor N atoms. The 4th row, those averaged for the more distant N atoms. The last row contains energy differences in the Madelung energy between undoped and doped GaN crystals. units: eV

	undoped	Be-doped	Mg-doped
1st	-2.09	-1.08	-1.21
2nd	-	-1.73	-1.79
more distant	-	-1.84	-1.82
E_M	-	+16.3	+9.52

A codoping method. Suitable candidates for use as acceptor dopants can be Be atoms considering the above calculated results and the experimental data for the large (~ 200 meV) ionization energy for *p*-type GaN:Mg. However, Table I shows that the doping of Be affects the electronic structure of not only the 1st-neighbor N shells but also the 2nd-neighbor ones. In fact, from the total energy calculations for our modeling of supercells whose compositions are N:50.00, Ga:43.75, and Be:6.25 at. %, we verified a large distance of 6.09 Å between the two Be atoms (see Fig. 2 (a)) compared with that of 4.51 Å between the two Mg atoms, which may result in the low solubility of the Be atoms. On the other hand, in the previous study [13,14], we concluded that *n*-type doping of Si or O leads to the stabilization of the ionic charge distributions caused by a decrease in E_M and their impurity levels are shallow. Next, we investigate the roles of the simultaneous incorporation of the *n*-type dopants, Si and O, on the stability of the ionic charge distributions.

Figures 2 (b) and 2 (c) show the crystal structures of GaN doped with Be as the acceptor and O as the donor, in the ratio of 2 to 1 (GaN:2Be, O) and GaN:2Be, Si. We determined it under the condition that the total energy is minimized. At higher concentrations, the donor and acceptor orbitals will start to overlap with one another, to form the complex with Be-O-Be or Be-N-Si-N-Be.

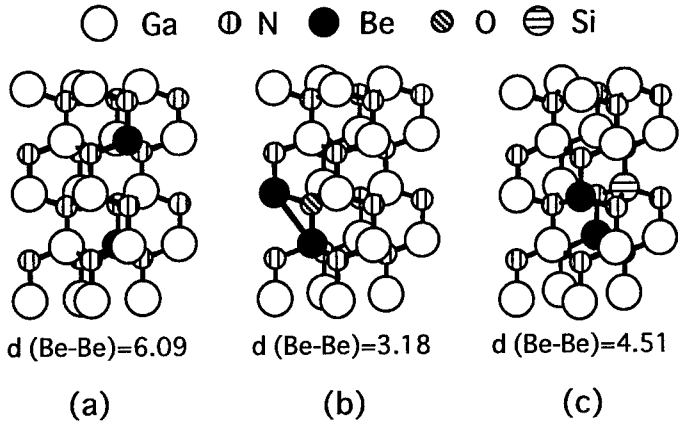

Fig. 2. Crystal structures of (a) GaN:2Be, (b) GaN: 2Be, O, and (c) GaN:2Be, Si. For an explanation, see text.

Figures 2a and 2b shows that the main role of the highly electronegative O atoms is to collect the Be atoms, to improve the crystal quality because of the inhibition of the formation of precipitates such as Be_3N_2 at higher Be concentrations. We present the total and site-decomposed DOS for GaN:2Be, O in Fig. 3 where we focus on the complex, Be-O-Be. The site-decomposed DOS in Figs. 3b and 3c indicate a strong interaction between the O $2p$ and Be $2s$ and $2p$ orbitals. We find that the co-incorporation of Be_{Ga} with O_N leads to a decrease in E_M compared with that of GaN:2Be as summarized in Table II.

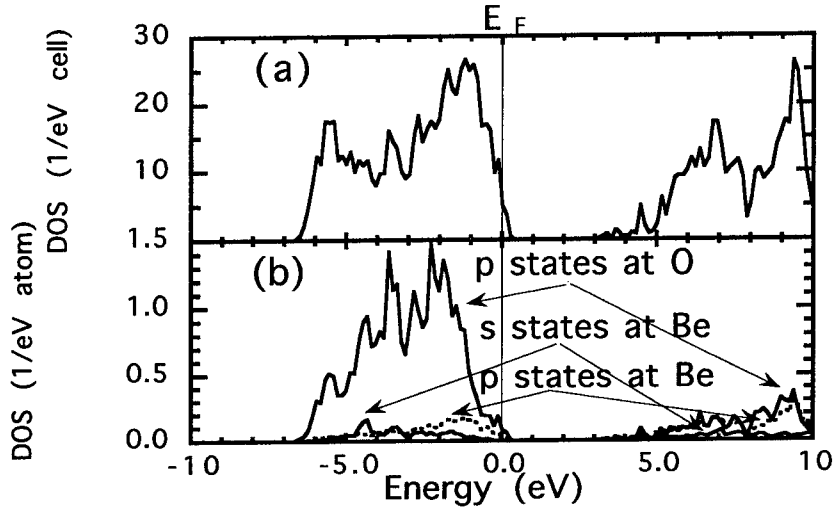

Fig. 3. (a) Total and (b) site-decomposed DOS of codoped GaN:2Be and O. Energy is measured relative to the Fermi energy.

We find a decrease in the Madelung energy using *n*-type dopants, Si, instead of the O atoms as shown in Table II. We show the total and site-decomposed DOS for the codoped GaN crystals in Fig. 4 where we focus on the complex, Be-N-Si-N-Be. Figure 4b indicates a strong interaction among the N 2*p*, Si 4*p*, and Be 2*p* orbitals. A sharp peak around -5.0 eV come from Si 4*s*-N 2*p* bonding. Analysis of state-decomposed DOS at the Si-sites and their dispersion relation indicate the delocalized impurity states of the Si atoms. Figure 4 shows a dip at E_F, which originates in the formation of the impurity band due to the strong interaction between the Si and N. We note that the main role of the *n*-type dopant, Si, on the charge distributions is to decrease the Madelung energy in *p*-type codoped GaN crystals as shown in Table II.

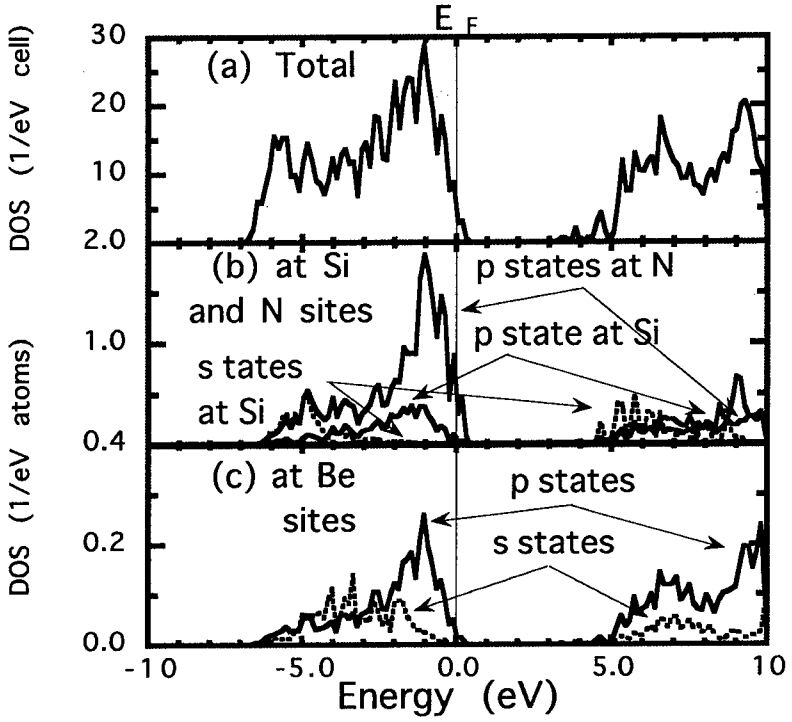

Fig. 4. (a) Total and (b) site-decomposed DOS for codoped GaN:2Be and Si. Energy is measured relative to the Fermi energy.

Table II. The difference in the Madelung energies (units: eV) between only Be-doped and codoped GaN crystals. For their crystal structures and compositions, see Fig. 2 and the text.

	p-type doped	*p*-type codoped	
dopants	2Be	2Be and O	2Be and Si
ΔE_M	-	-2.09	-7.93

Finally we note the advantage of the codoping method using the donors and acceptors at the same time as following: Enhancement of carrier concentrations and mobility. The acceptor-donor incorporation causes to higher concentrations of the acceptors, or can enhance the solubility due to its small formation energy. The complex such as Be-O-Be and Be-N-Si-N-Be has a short-range dipole scattering mechanism on the mobility considerably less than the Coulomb potential of isolated charged impurities. This gives rise to an enhanced carrier mobility.

Conclusions.

We have studied the influence of *n*-type codopants, O_N and Si_{Ga}, on the electronic structures for *p*-type GaN codoped with Be_{Ga} as acceptor dopants and O_N (Si_{Ga}) as donor ones. *Ab initio* total energy calculations show that the formation of Be-O-Be structures or Be-N-Si-N-Be ones is favorable in terms of energy and the *n*-type codopants lead to the stabilization of the ionic charge distributions due to a decrease in the Madelung energy compared with *p*-type doped GaN crystals which have larger distances between the acceptors. The codoping method would be effective for the materials design to fabricate high-conductivity *p*-type GaN with high Be concentrations.

Acknowledgments.

The authors would like to thank Dr. Jürgen Sticht of Molecular Simulations, Inc. for his technical support. Their sincere thanks are also due to Professors S. Gonda and H. Asahi of ISIR, Osaka university for fruitful discussions. Thanks are also offered to general manager Dr. T. Yamada and senior scientist Dr. Y. Ueshima (Asahi Chemical Industry Co., Ltd.) who gave their support and encouragement during the course of this study.

References.

1. W. Götz, N. M. Johnson, C. Chen, H. Liu, C. Kuo and W. Imler, Appl. Phys. Lett. **68**, 3144 (1996).
2. J. Neugebauer and C. G. Van de Walle, Appl. Phys. Lett. **68**, 1829 (1996).
3. H. Amano, M. Ito, K. Hiramatsu and I. Akasaki, Jpn. J. Appl. Phys. **28**, L2112 (1989).
4. H. Amano, M. Ito, K. Hiramatsu and I. Akasaki: Inst. Phys. Conf. Ser. **106**, 825 (1989).
5. S. Nakamura, T. Mukai, M. Senoh and N. Iwasa, Jpn. J. Appl. Phys. **31**, L139 (1992).
6. S. Nakamura, T. Mukai, M. Senoh and N. Iwasa: Jpn. J. Appl. Phys. **31**, 1258 (1992).
7. O. Brandt, H. Yang, H. Kostial and K. H. Ploog, Appl. Phys. Lett. **69**, 2707 (1996).
8. W. Kohn and L. J. Sham: Phys. Rev. **140**, A1133 (1965).
9. L. Hedin and B. I. Lundquist, J. Phys. **C4**, 3107 (1971).
10. U. von Barth and L. Hedin, J. Phys. **C5**, 1629 (1972).
11. A. R. Williams, J. Kübler, and C. D. Gelatt: Phys. Rev. **B19**, 6094 (1979).
12. V. Fiorentini, F. Bernardini, A. Bosin, and D. Vanderbilt, preprint.
13. T. Yamamoto and H. Katayama-Yoshida, Jpn. J. Appl. Phys. **36**, L180 (1997).
14. T. Yamamoto and H. Katayama-Yoshida in Proc. of The 1997 MRS SPRING MEETING in San Francisco, in press.

Materials Science Forum Vols. 258-263 (1997) pp. 1191-1196

PHOTOLUMINESCENCE OF DONOR ACCEPTOR PAIR TRANSITIONS IN HEXAGONAL AND CUBIC MBE-GROWN GaN

Joachim Krüger, Dorina Corlatan, Christian Kisielowski, Yihwan Kim, Ralf Klockenbrink, Sudhir G.S., Michael Rubin, and Eicke R. Weber

Materials Science Division, Lawrence Berkeley National Laboratory, and Department of Materials Science, UC Berkeley, Berkeley, CA 94720, USA
e-mail: joachim@socrates.berkeley.edu

Keywords: Luminescence, hexagonal/cubic GaN, Donor Acceptor Pair transition

Abstract

In this report we present photoluminescence results taken on MBE grown GaN. We identify and analyze two donor acceptor pair transitions (DAP) in the predominant hexagonal phase. These defect complexes are proven to involve the same acceptor but to differ in the thermal ionization energy for the donor. Also, we describe PL lines which we ascribe to the donor bound exciton and a donor acceptor pair transition of cubic inclusions within the predominant hexagonal matrix.

Introduction

As an opto-electronic material for UV-based applications, GaN has attracted a lot of scientific as well as technical interest within the last decade. Though light emitting devices have already been commercially available for more than 5 years [1], the fundamental nature and chemical identity of involved defects of many optical transitions in GaN is vastly unknown.

The low temperature photoluminescence spectra of GaN consist of the band edge related PL transitions at 3.40 to 3.48 eV, the Donor Acceptor Pair (DAP) transitions, typically in the regime between 3.0 to 3.3 eV, and the broad yellow band between 2.25 and 2.55 eV. Due to the smaller band gap of 3.302 eV (in respect to 3.503eV), the band edge related PL transitions of the cubic phase overlap with the DAP lines of the hexagonal phase but can be distinguished by variation of temperature.

In our previous publication [2], we identified and analyzed the donor bound exciton of cubic inclusions within the hexagonal matrix of MBE-grown GaN. In this study we investigate several donor acceptor pairs in the hexagonal as well as cubic phase.

Experimental

The undoped GaN films were grown using a rebuilt Riber 1000 chamber. Gallium was evaporated from a Knudsen effusion cell. The activated nitrogen species were provided by a Constricted Glow Discharge Plasma Source (for details see [3]). Prior to the growth, the (0001) sapphire substrate was nitridated for 10 minutes. Subsequently, a buffer layer of typically 25 nm thickness was grown. Other typical

growth conditions are: Ga source temperature: 1210 K, nitrogen flow rate: 35 sccm, buffer layer growth temperature: 800K, main layer growth temperature: 1000K, growth rate ≈ (0.2-0.5) μm/hr. For p-type doping, the Magnesium source temperature was 580K. The GaN main layers had a typical thickness of (0.5 - 2) μm. Hall effect measurements proved the free electron concentration of the nominally undoped GaN layers to be between [n] = 10^{16} and 10^{19}cm^{-3}, depending on the growth conditions.

Photoluminescence was excited using the 325 nm line of a 50mW cw HeCd laser. The luminescence light was then dispersed by a 0.85m double grating monochromator and detected with a photomultiplier using a lock-in technique. The sample temperature was varied between 4 K and 300 K.

Results

We have analyzed the low temperature photoluminescence spectra of MBE as well MOCVD grown samples.

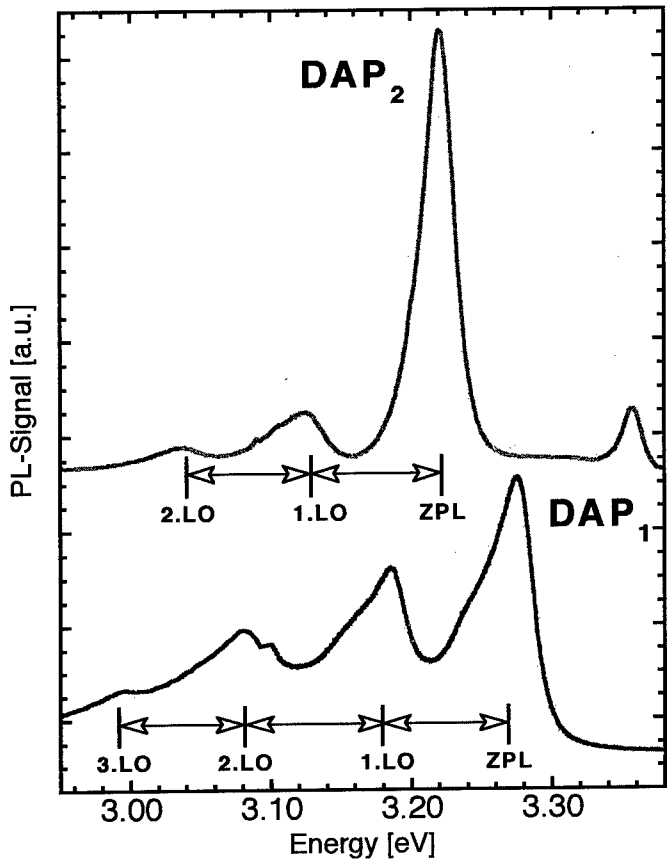

Figure 1: *PL spectra of the two DAP transitions in hexagonal GaN taken at 4.2 K*
DAP_1: MOCVD grown GaN sample
DAP_2: MBE-grown GaN (main layer deposited on room temperature grown GaN buffer layer)
(Note: To account for the different amount of stress in the GaN layers, the DAP_1 spectrum has been red-shifted by 7.8 meV and the DAP_2 spectrum blue-shifted by 12.0 meV, (D^0X = 3.468 eV, stress free value)).

Donor Acceptor Pair of the *Hexagonal* Phase

Figure 1 shows the PL spectra of two different MBE grown GaN samples in the typical energetic region of DAP recombination. For comparison the spectra have been shifted in energy to account for the different amount of stress in the epilayer. Spectrum 1 consists of the Donor Acceptor Pair transition DAP_1 which we frequently find in n-type as well p-type materials grown by either MBE or MOCVD. This transition is very well known since the work by Dingle and Ilegems [4] though the nature of involved donors and acceptors is entirely unknown yet [5]. We find the other spectrum DAP_2 to be the strongest in intensity for samples being under great tensile stress at helium temperatures. Contrary to all other MBE samples investigated, these epilayers have been deposited on buffer layers grown at temperatures significantly lower than the main layer, T_{buffer} = (20-350)°C as opposed to T_{main} = 725°C. This temperature difference has been shown [6] to result in tensile stress in the epilayer of up to 0.5 GPa, as indicated by a red shift of the donor bound exciton of up to 12 meV.

In order to determine the nature of the involved donors and acceptors and their respective thermal activation energies, temperature dependent PL measurements have been performed. Fitting the analytical relationship between temperature and PL intensity, eq. (1),

$$I(T) = I(T=0) * \frac{1}{1 + a\,T^{3/2}\exp(-E_{act.}/kT)} \approx I(T=0) * \exp(E_{act.}/kT)$$

one consistently finds for all investigated samples (figure 2) the activation energy of the acceptor's thermal ionization to be

$$E_{acc.,\,act.}(DAP_1, DAP_2) \doteq (125 \pm 3)\ \text{meV}$$

In particular it should be noted that the acceptor giving rise to the DAP_1 in Mg-doped p-type material (Sample B, [p] = $1 * 10^{17}cm^{-3}$ at 300K) has the same thermal activa-

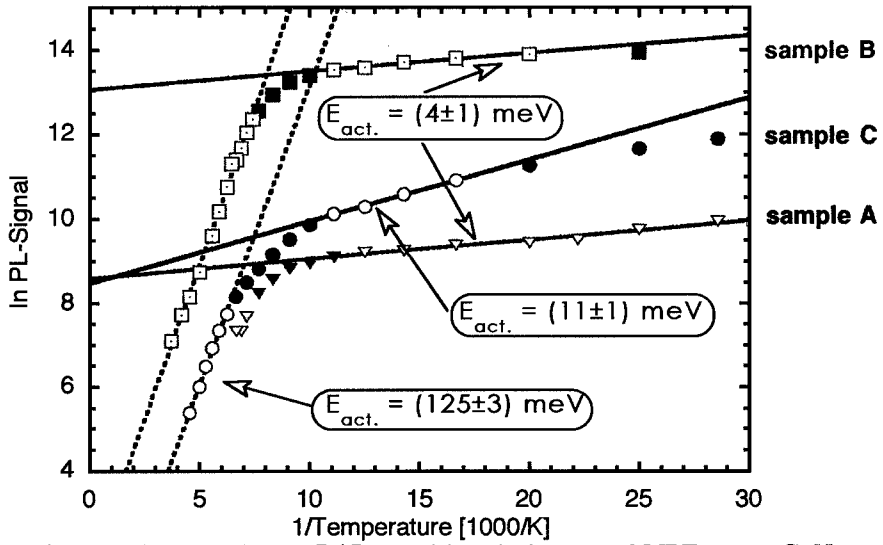

Figure 2: *Arrhenius plot of the two DAP transitions in hexagonal MBE-grown GaN*
Sample A: n-type undoped GaN (DAP_1)
Sample B: p-type Mg-doped GaN (DAP_1)
Sample C: n-type undoped GaN (DAP_2)

tion energy as the one in n-type undoped GaN. However, differences between the DAP_1 and DAP_2 spectra can be seen for the thermal ionization of the involved donor.

$$E_{donor,\ act.}(DAP_1) = (4 \pm 1)\ meV$$

and

$$E_{donor,\ act.}(DAP_2) = (11 \pm 1)\ meV$$

Donor Acceptor Pair of the *Cubic* Phase

In some of our MBE-grown GaN materials we observed by TEM spontaneous nucleation of cubic inclusions. They account for about 1% of the overall matrix volume [7] and can be found throughout the whole layer. A sharp PL transition at 3.261 eV has been identified as the donor bound exciton of the cubic phase[2, 8]. In one of the MBE crystals grown with Bi as a surfactant [10] we detect an additional signal structure consisting of one line at 3.148 eV (FWHM = 34 meV) followed by two weaker lines spaced by about 92 meV, figure 3 and table 1. Temperature dependent measurements being discussed in the next paragraph prove this group to be the zero phonon line (ZPL) of another donor acceptor pair transition accompanied by two phonon replica.

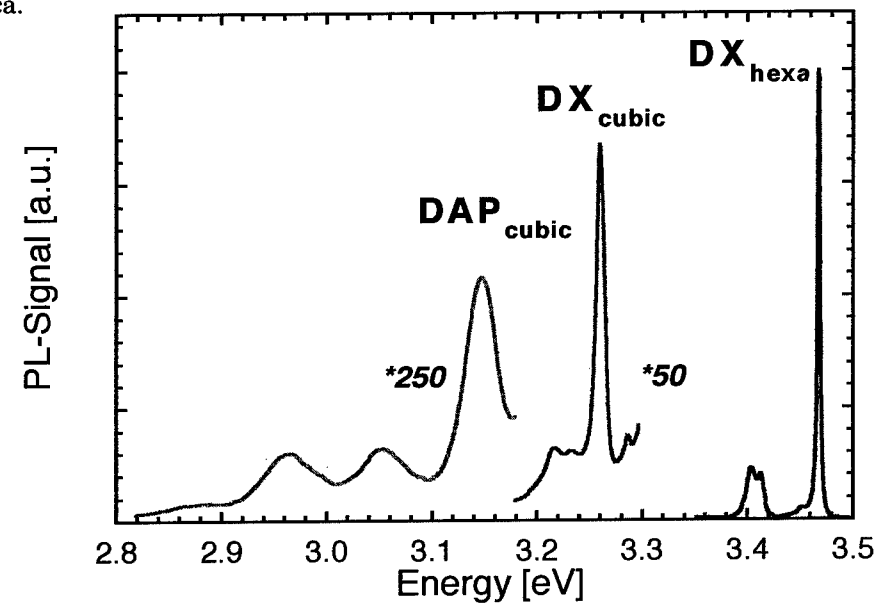

Figure 3: *4.2 K PL spectrum of the cubic and hexagonal phase*

Varying the temperature we note that all three lines show the same temperature behavior and collectively disappear at about 130 K. Though our measurements suffer from the low relative amount of the cubic phase and consequently low signal/noise ratio, one also realizes a collective blue shift with increasing temperature. This is another indication of a DAP transition.

Two recent publications report on similar PL lines in MBE grown GaN as we are describing here but come to diverse line assignments. J.Menninger *et.al.* [8, 9] performed spatially resolved cathodoluminescence measurements on cubic grown GaN.

PL Line	ZPL [eV]	1.LO [eV]	2.LO [eV]
DX (hexa.)	3.468		
DX (cubic)	3.261		
DAP_1(hexa.)	3.266	3.179	3.087
DAP_2(hexa.)	3.220	3.126	3.035
DAP (cubic)	3.148	3.054	2.964

Table 1: *Line positions of PL transition in the hexagonal and cubic phase*

From the different temperature behavior of the line positions the authors conclude that the dominant line is indeed the ZPL of a DAP transition, whereas the two smaller lines should be identified as a free-to-bound transition accompanied by first order phonon replica [9]. The nature of this impurity could not be determined. U.Strauss *et.al.* [11] analyzed cubic inclusion within the predominant hexagonal GaN layer by cw and time resolved PL. Based upon the luminescence lifetime and the correlation between line position and free carrier concentration they identify the lines at 3.15 and 3.06 eV as the ZPL and first phonon replica of a DAP transition in the cubic phase.

Discussion

The thermal acceptor activation energies for both kind of DAP transitions found here in n-type MBE as well as in MOCVD grown GaN are practically identical with the value determined for HTVPE GaN [5]. On the contrary, it is very striking, that one does not see any change of this acceptor energy for p-type Mg-doped MBE-grown GaN, though the Hall concentration of p-type carriers at 300K indicates a high incorporation of Mg, $[Mg] = 3 * 10^{19}cm^{-3}$.

Recent progress in the understanding of the stress-strain relationship in thin GaN layers grown on sapphire [12] has shown that the amount of stress in the epilayer can be determined by its stoichiometry. It can be altered by growing buffer layers of different thickness and morphology. The samples that exhibit the DAP_2 transition were grown in a nitrogen rich regime. On the other hand, the thermal donor activation energy of the DAP_2 is considerably higher than for the commonly observed DAP_1. Thus, we suggest that a stoichiometry-related donor, which is energetically deeper than the donor associated with the DAP_1, is involved in the defect structure of the DAP_2. Alternatively, we proprose that a deeper donor being omnipresent becomes visible resulting from the drop in the Fermi energy.

Summary

We describe two different donor acceptor pair recombinations in hexagonal GaN. The thermal activation of the acceptors are identical in both cases, whereas we find the donor's activation energies to differ by 7 meV. In the latter case we suggest the donor to be a stoichiometry-related defect. Also, the thermal activation energy of the

acceptor in undoped n-type GaN is identical with the one in Mg-doped p-type material. We also identified a donor acceptor transition which stems from cubic inclusions.

Acknowledgment

This work was supported by the Advanced Energy Projects and Technology Research Division, U.S. Department of Energy, under Contract No. DE-AC03-76SF00098.

References

[1] S.Nakamura, T.Mukai, and M.Senoh; Jap.J.Appl.Phys.(Lett.) **30**, L1998 (1991)
[2] J.Krüger, C.Kisielowski, R.Klockenbrink, Sudhir G.S., Y.Kim, M.Rubin, and E.R.Weber; to appear in Mat. Res. Soc. Symp. Proc (Proceedings of the MRS Spring Meeting, San Francisco '97)
[3] A.Anders and S.Anders; Plasma Sources Sci. Technol. **4**, 571 (1995)
[4] R.Dingle and M.Ilegems; Solid State Commun. **9**, 175 (1971)
[5] S.Fischer, C.Wetzel, and E.E.Haller, B.K.Meyer; Appl.Phys.Lett. **67**, 1298 (1995)
[6] R.Klockenbrink, Y.Kim, C.Kisielowski, J.Krüger, M.Rubin, E.R.Weber, et.al.; to be published
[7] M.S.H.Leung, R.Klockenbrink, C.Kisielowski, H.Fujii, J.Krüger, Sudhir G.S., A.Anders, Z.Liliental-Weber, M.Rubin, and E.R.Weber, Mat.Res.Soc.Symp.Vol. **449**, p. 221 (1997)
[8] J.Menniger, U.Jahn, O.Brandt, H.Yang, and K.Ploog; Phys.Rev.B **53**, 1881 (1996)
[9] J.Menniger, U.Jahn, O.Brandt, H.Yang, and K.Ploog; Appl.Phys.Lett. **69**, 836 (1996)
[10] R.Klockenbrink,Y.Kim, M.S.H. Leung, C.Kisielowski, J.Krüger, Sudhir G.S., M.Rubin, and E.R.Weber; same reference as [2]
[11] U.Strauss, H.Tews, H.Riechert, R.Averbeck, M.Schienle, B.Jobst, D.Volm, T.Streibl, B.K.Meyer, and W.W.Rühle; Semicond.Sci.Technol. **12**, 637 (1997)
[12] Sudhir G.S., Yann Peyrot, C.Kisielowski, J.Krüger, M.Rubin, E.R.Weber, *et.al.*; to be published

Materials Science Forum Vols. 258-263 (1997) pp. 1197-1202

RAMAN SCATTERING FROM DEFECTS IN GaN

H. Siegle, A. Kaschner, P. Thurian, A. Hoffmann, I. Broser, and C. Thomsen
Institut für Festkörperphysik, Technische Universität Berlin,
Hardenbergstraße 36, 10623 Berlin, Germany

Keywords: GaN on GaAs, Raman scattering, high-pressure measurements, defect modes

Abstract. We present results from Raman-scattering experiments on GaN layers grown on GaAs and sapphire. In the low-energy region between 95 cm^{-1} and 250 cm^{-1} a series of sharp lines appear which decreases exponentially in intensity with increasing temperature. The lines disappear when reaching room temperature. Wavelength-dependent measurements reveal that they are strongest under excitation at around 514.5 nm. Raman-scattering experiments at high pressures up to 6 GPa show that neither their energies nor their resonance profile vary remarkably with pressure indicating that they are not connected to the bandgap. Comparitive measurements on different substrates show that these lines are exclusively present in GaN layers grown on GaAs.

Introduction.

In the last few years the wide-bandgap semiconductor GaN has received increasing attention because of its application as the favorite basic material for optoelectronic devices working in the blue to ultraviolet spectral region [1]. One of the main problems which still restricts the growth of high-quality GaN layers is the high concentration of defects which yields high background carrier concentrations and the typical n-type conductivity of GaN layers. It is still unclear what kind of defects are responsible for these effects.

We present results of Raman-scattering experiments on predominantly cubic GaN layers grown on GaAs and hexagonal layers grown on sapphire. While the layers deposited on sapphire exhibit only the expected host phonon modes, we found a series of additional sharp lines in the range between 95 cm^{-1} and 250 cm^{-1} from the layers grown on GaAs. Four of these lines have already been observed by Ramsteiner et al. [2]. The lines show a strong temperature dependence. They decreases drastically in intensity when increasing the sample temperature and disappear when reaching room temperature. Wavelength-dependent measurements show that they have a broad resonance profile with its maximum around 514.5 nm. Ramsteiner et al. [2] attributed four of the observed lines to hydrogen-like transitions between the electronic states of a shallow donor in hexagonal and cubic GaN. In order to prove this model we performed a systematic Raman study on several series of GaN layers grown on GaAs and sapphire. We found that more lines appear than expected by hydrogen-like transitions of one donor [2, 3]. On the basis of the new experimental data including results of high-pressure Raman experiments we discuss possible candidates of defects.

Experimental Details.

The samples under study were series of predominantly cubic GaN layers grown on (001) GaAs using molecular beam epitaxy (MBE) and several hexagonal layers grown on sapphire by MBE,

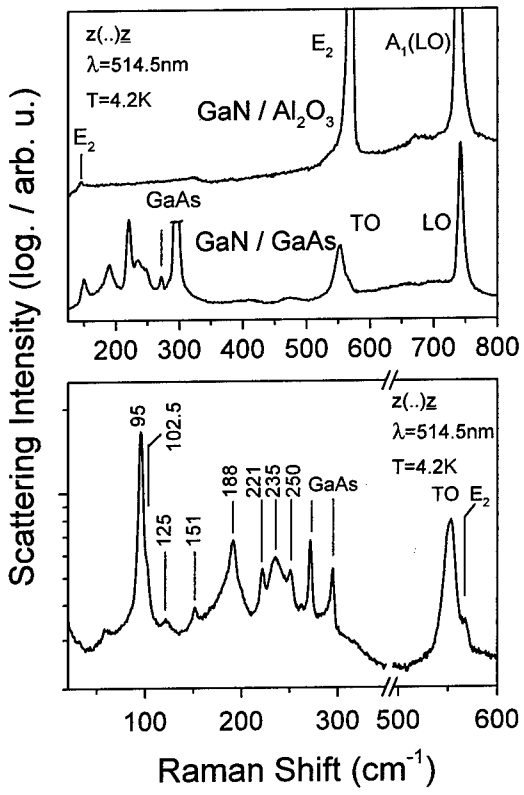

Fig. 1a: Comparison between the low-temperature (4.2 K) Raman spectra of a GaN layer grown on sapphire (upper curve) and on GaAs (bottom curve). While the spectrum of the hexagonal layer grown on sapphire exhibits only the phonon modes of the host material, a series of defect modes are present in the cubic layer grown on GaAs. Excitation was at 514.5 nm.
Fig. 1b: Low-temperature Raman spectra taken from GaN grown on GaAs after excitation at 514.5 nm on an enlarged spectral scale.

metal organic chemical vapor deposition (MOCVD) and hydride vapor phase epitaxy (HVPE). Thicknesses vary between 0.5 to 2 μm in case of the MBE samples and up to 400 μm in case of the HVPE samples.

The Raman-scattering experiments at ambient conditions were carried out in back-scattering geometry with a triple-grating spectrometer equipped with a cooled charge-coupled device (CCD) detector. An Ar^+/Kr^+ mixed-gas laser was used for excitation in the range between 458 nm and 647 nm. Parts of the experiments were performed with a microscope setup with a spatial resolution better than 1 μm. The sample temperature was varied in the range from 2 K to 300 K using either an Oxford microscope cryostat in case of micro-Raman measurements or an Oxford bath cryostat.

The high-pressure Raman experiments were performed in a gasketed diamon-anvil cell at low temperatures (10 K) using liquid helium as the pressure-transmitting medium. The shift of the

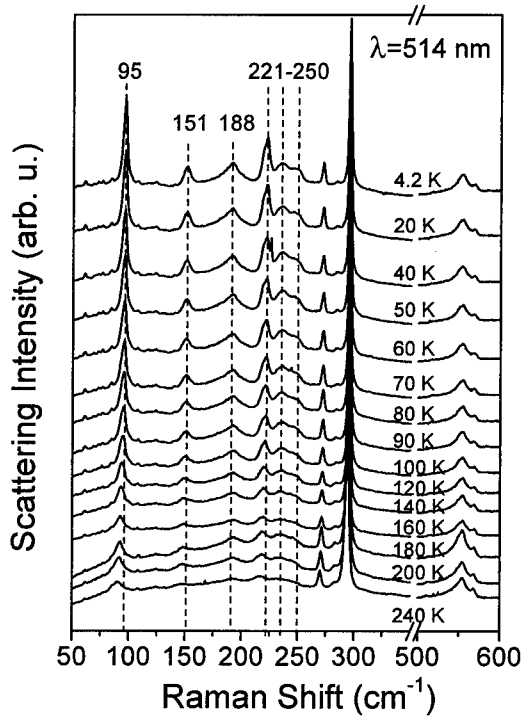

Fig. 2: Evolution of the Raman spectra taken from a GaN layer grown on GaAs with temperature. The defect modes show a strong decrease in intensity with increasing temperature.

ruby R-line luminescence was used to calibrate the pressure inside the cell. Prior to the experiment, the substrates of the samples were mechanically removed. Finally, the samples were cleaved and placed in the gasket hole of the diamond-anvil cell. The 488 nm, 502 nm and 514.5 nm lines of an Ar^+-ion laser were used for excitation. Like in the experiments at ambient conditions the scattered light was detected in back-scattering geometry and analyzed by a triple-grating spectrometer equipped with a CCD.

Results and Discussion.

In Fig. 1a typical low-temperature Raman spectra taken from a hexagonal GaN layer grown on sapphire (upper curve) and from a cubic layer grown on GaAs (lower curve) are compared. While the upper spectrum shows only the Raman modes of the hexagonal GaN phonons located at 145 cm^{-1} (E_2(low)), 569 cm^{-1} (E_2(high)) and at 735 cm^{-1} (A_1(LO)), the lower spectrum exhibits in addition to the host phonon modes of cubic GaN (TO at 555 cm^{-1} and LO at 740 cm^{-1}) a series of sharp lines in the low-energy part of the spectrum. In total we observe eight lines ranging from 95 cm^{-1} to 250 cm^{-1}, which are shown on an enlarged scale in Fig. 1b.

The temperature dependence of these modes is displayed in Fig. 2. The intensity of all the additional low-energy modes decreases drastically when increasing the sample temperature and finally disappear when reaching room temperature. This behavior cannot be explained by vibrational Raman scattering and indicates that these modes are caused by electronic Raman scattering from defects built in the host material [4].

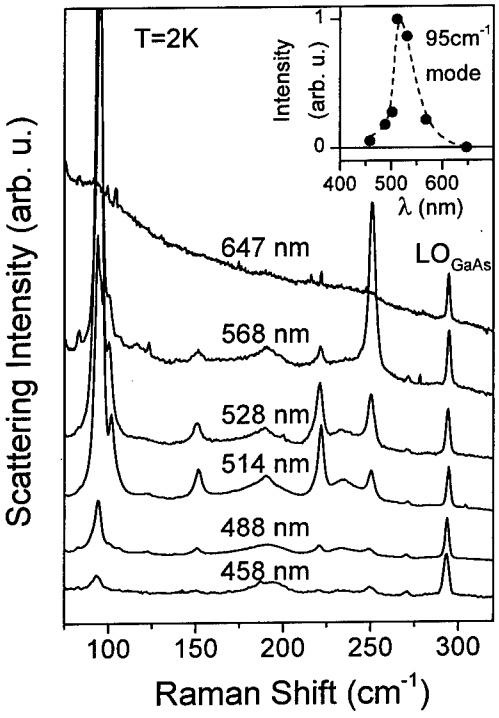

Fig. 3: Low-temperature Raman spectra obtained with different excitation wavelengths between 458 nm and 647 nm. The inset shows examplary the resulting resonance profile of the 95 cm^{-1} mode. The dashed line is only guide to the eye.

Four of these defect modes were also found by Ramsteiner et al. [2]. From the temperature behavior Ramsteiner et al. concluded that these four modes were caused by transitions between the hydrogen-like electronic states of a shallow donor in GaN. They ascribed the lines at 188 cm^{-1} and 235 cm^{-1} to inner transitions of one shallow donor in cubic GaN and the lines at 151 cm^{-1} and 221 cm^{-1} to a corresponding donor in the hexagonal modification which was present in their samples as a minority phase. We found a series of additional lines from which three (95 cm^{-1}, 102.5 cm^{-1} and 125 cm^{-1}) are located at lower energies and thus do not fit a hydrogen-like donor.

Figure 3 shows low-temperature Raman spectra of a GaN film excited at different wavelengths in the range from 458 nm to 647 nm. The intensities of the defect modes vary strongly and exhibit clearly a resonant behavior with a maximum around 514. 5 nm as can be seen for the 95 cm^{-1} mode in the inset of Fig. 3. All defect modes show a similar temperature and resonance behavior [3]. From this it seems clear that all these lines should either have a similar origin or the electronic states involved in the resonance mechanism should be the same. One single donor can be ruled out as an explanation.

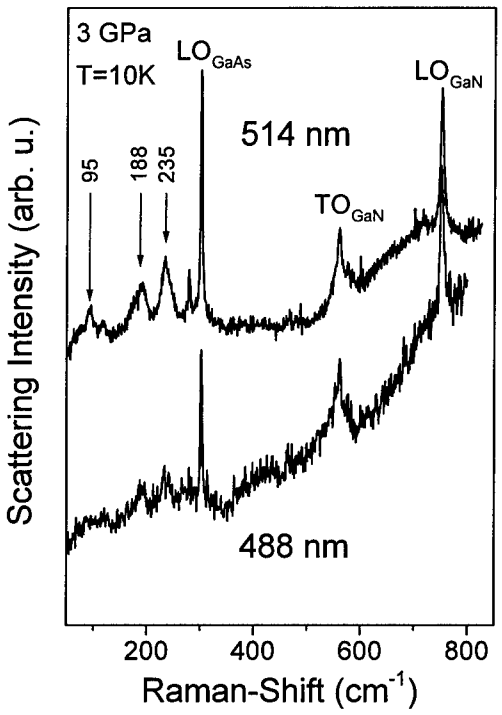

Fig. 4: Raman spectra taken at a hydrostatic pressure of 3 GPa and different excitation wavelengths.

It is in principle possible to determine activation energies of the defect modes by fitting their intensity as a function of temperature. We found that the activation energies ranging from 10 meV to 50 meV differ from mode to mode and depend strongly on the wavelength used for excitation [3, 5] confirming that the various modes could not belong to one single shallow impurity.

In order to get further information on the nature of the responsible defects we have performed magnetic-field dependent Raman-scattering experiments on our samples up to 13 T. Assuming an electronic origin one would expect a change in energy when applying a magnetic field, but we could not observe any shift of the lines [6].

In contrast, the application of high hydrostatic pressures on these samples changes the Raman spectra drastically as displayed in Fig. 4, in which two Raman spectra at 3 GPa with different excitation wavelengths are compared. One was excited at 514.5 nm the other at 488 nm. Both spectra were normalized to the intensity of the GaN LO phonon mode. When applying hydrostatic pressure the intensity of the sharp lines at 95 cm^{-1}, 151 cm^{-1}, 221 cm^{-1} and 250 cm^{-1} decreases strongly without changing their energy position remarkably. Finally these lines disappear for pressures higher than 3 GPa. As can be seen in Fig. 4 the strongest defect mode at 95 cm^{-1} could only weakly be observed. However, the broader lines at 188 cm^{-1} and 235 cm^{-1} seems not to be affected by pressure and they are still present in the spectra up to 6 GPa.

If the electronic states involved in the resonance mechanism were connected to the bandgap one would expect that the lines should be stronger in the spectrum excited at 488 nm than at

514.5 nm, because of the positive pressure coefficient of the GaN bandgap, which is about 40 meV/GPa [7]. Following this relation the resonance maximum at 3 GPa should be located 120 meV higher in energy, corresponding to a change from 514.5 nm to 488 nm. We found that the intensity ratio between the lines excited at these different wavelengths does not change, indicating that the defects responsible for the resonant behavior are not connected to the bandgap but form strongly localized states. Because additionally the energy positions of the defect modes do not change with increasing pressure, inner transitions between the electronic states of shallow impurities can also be ruled out as an explanation for the observed lines.

Probably, deep impurities are involved in the electronic resonance transitions but the chemical identification of these defects remains unclear from our results. However, they must be specific to the MBE growth process of GaN layers on GaAs substrates, because the defect modes were exclusively present in these films.

Conclusion.

Low-temperature Raman measurements were performed on several series of GaN films epitaxially grown on GaAs and sapphire by MBE, MOCVD and HVPE. Only those GaN layers which were deposited on GaAs exhibit a series of sharp lines in the low-energy range from 95 cm^{-1} to 250 cm^{-1}. The intensity of these defect modes increases drastically with decreasing temperature indicating an electronic scattering origin. Raman excitation spectra show a maximum around 514.5 nm. High-pressure Raman experiments reveal that the responsible defects are strongly localized. Their exclusive presence in GaN films on GaAs indicates that they are connected to the growth procedure and to the substrate.

Acknowledgements

The authors thank D. J. As, B. Schöttker, and D. Schikora for supplying the GaN / GaAs samples.

References.

1. For a review see e.g. R. F. Davis, Proc. IEEE **79**, 702 (1991); S. Strite and H. Morkoc, J. Vac. Sci. Technol. **B10**, 1237 (1992)
2. M. Ramsteiner, A. J. Menninger, O. Brandt, H. Yang, and K. H. Ploog, Appl. Phys. Lett. **69**, 1276 (1996)
3. H. Siegle, I. Loa, P. Thurian, L. Eckey, A. Hoffmann, I. Broser, and C. Thomsen, Appl. Phys. Lett. **70**, 909 (1997)
4. M. V. Klein, in: Light Scattering in Solids I, ed. M. Cardona (Springer, Berlin, Heidelberg 1983), pp. 147
5. H. Siegle et al., to be published
6. H. Siegle, I. Loa, P. Thurian, G. Kaczmarczyk, L. Filippidis, A. Hoffmann, C. Thomsen, D. Schikora, M. Hankeln, K. Lischka, Zeitschrift für Physikalische Chemie 200, **187** (1997)
7. T. Suski, P. Perlin, H. Teisseyre, M. Leszcynski, I. Grzegory, J. Jun, M. Bockowski, S. Porowski, and T. D. Moustakas, Appl. Phys. Lett. **67**, 2188 (1995)

Materials Science Forum Vols. 258-263 (1997) pp. 1203-1210

Structural and Electrical Properties of Threading Dislocations in GaN

J. Elsner and R. Jones[1], P. K. Sitch and Th. Frauenheim[2], M.I. Heggie[3], S. Öberg[4] and P. R. Briddon[5]

[1] Department of Physics — University of Exeter
Exeter, EX4 4QL, UK.
[2] Theoretische Physik III — TU Chemnitz
D–09107 Chemnitz, Germany
[3] CPES — University of Sussex
Falmer, Brighton, BN1 9QJ, UK
[4] Department of Mathematics — University of Luleå
Luleå, S97 187, Sweden
[5] Department of Physics — University of Newcastle upon Tyne
Newcastle, NE1 7RU, UK

Keywords: GaN, threading dislocations, density–functional theory

Abstract. The atomic structures and electrical properties for threading screw and threading edge dislocations of wurtzite GaN are calculated within the local–density approximation. Both dislocations are electrically inactive with a band gap free from deep levels. These results are understood to arise from relaxed core structures which are similar to $(10\bar{1}0)$ surfaces. The threading screw dislocations are found to be stable with an open–core whereas the threading edge dislocations possess filled cores.

1 Introduction

Device quality wurtzite-GaN (α) can be grown using metalorganic chemical vapour phase deposition (MOCVD) on (0001) sapphire substrates. Isolated threading dislocations, parallel to **c**, with densities $\sim 10^9$ cm^{-2} and Burgers vectors **c**, **a** and **c**+**a** persist beyond $\sim 0.5\mu$m above the interface [1, 2, 3] and thus cross the active region of the devices. An unexpected finding [4, 5] is that these dislocations do not lead to a pronounced reduction in the device-lifetime of the light-emitting diodes [6] or blue lasers [7]. This can be contrasted with GaAs where radiation enhanced dislocation motion [8] readily occurs and leads to an increase in non-radiative processes. Recent cathodoluminescence (CL) studies of the yellow luminescence (YL) centred at ~ 2.2 eV have shown that the YL is spatially non-uniform and can be correlated with extended defects and especially low angle grain boundaries which contain dislocations [9]. On the other hand, atomic force microscopy in combination with CL has led to the conclusion that threading dislocations act as non-radiative recombination centres and degrade the luminescence efficiency in the blue light spectrum of the epilayers [10].

The screw dislocations, occurring at a density $\sim 10^6$ cm^{-2} in α–GaN grown by MOCVD on (0001) sapphire have elementary Burgers vector $\pm$ **c** and are unusual in often being associated with nanopipes with diameters 50 - 250 Å [11]. The large range of diameters suggest that they originate from the coalescence of misaligned interfacial growth islands [2, 12] leading to pinholes which do not grow out. Pure edge dislocations lying on $\{10\bar{1}0\}$ planes are a dominant species of dislocation, occurring at extremely high densities of $\sim 10^8 - 10^{11}$ cm^{-2} in α–GaN grown by MOCVD on (0001) sapphire, and are also thought to arise from the collisions of islands during

2 Theoretical Methods

Here we explore the structure and electronic properties of screw and threading edge dislocations in GaN using an *ab initio* local density functional (LDF) cluster method, *AIMPRO*, and a density functional based tight binding method *DF–TB* which can be used for both clusters and supercells. *AIMPRO* uses norm-conserving pseudopotentials [13] and a basis of s and p-Gaussian orbitals for the pseudo-wavefunctions together with an ancillary basis to fit the charge density. The self-consistent energy and adiabatic forces acting on the atoms of the cluster are evaluated and the atoms moved by a conjugate-gradient algorithm to determine the relaxed structure [14, 15]. In the current application we use 5 (4) s and p-Gaussian orbitals with different exponents for each Ga (N) atom yielding a large real–space basis set of 20 (16) Gaussian orbitals on every Ga (N) atom. Applied to a 72 atom H-terminated stoichiometric cluster arranged as in wurtzite, gave GaN bond lengths within 4% of experiment and a maximum vibrational frequency of 729 cm^{-1} compared with 741 cm^{-1} experimentally found for the $E_1(LO)$ mode [16].

The *DF–TB* method uses a basis of numerically derived s, p and d confined atomic orbitals and all two-centre integrals of the LDF Hamiltonian and overlap matrix are evaluated. Thus in contrast to empirical TB schemes, interactions extending beyond the first shell of neighbours are taken into account. This is of crucial importance for GaN, because the second neighbour Ga-Ga distances (3.18 Å) are comparable to the distances between neighbouring atoms in bulk Ga which range from 2.45 Å to 2.71 Å. Charge transfer plays an important role, especially if bonds are broken as at surfaces and extended defects, since although GaN is a covalently bonded material, it has partial ionic character. The *DF–TB* code was modified to take this into account through the incorporation of a self–consistency (SC) scheme for the Mulliken charges based on a second order expansion of the Kohn-Sham ground state energy in terms of charge density fluctuations at a given proper input density. In this formalism the Mulliken charges for each atom are evaluated after each step of the SC cycle. The diagonal elements of the Hamilton matrix employed at the next iteration are then modified by charge dependent contributions in order to describe the change in the atomic potentials due to the charge transfer for that iteration. The off–diagonal entries have additional charge dependent terms coming from the Coulomb potential of the ions. They decay with $1/r$ and thus account for the Madelung energy of the system. The short range real space repulsive interatomic potential used in the *DF–TB* scheme was derived from the experimental value for the bulk modulus in the zinc–blende phase and its derivative with respect to pressure via the non–linear Murnaghan equation of state [17]. For further details of the *DF–TB* method see references [18, 19].

As an illustrative benchmark of the *DF–TB* method, we choose quantitative calculations for the non–polar GaN $(10\bar{1}0)$ surface, since very similar configurations occur in the dislocation cores. Fig. 1 and Table 1, give details of the calculated geometrical structure of the nonpolar GaN $(10\bar{1}0)$ surface along with the results of first–principles calculations by Northrup and Neugebauer [20]. The structures are very similar. Moreover, the calculated absolute surface energy of 121 meV/Å^2 agrees very well with the 118 meV/Å^2 given in [20]. We now apply these methods to dislocations in GaN. In the *DF–TB* case the dislocations are modelled in large clusters and in 576 atom $(12 \times 12 \times 1)$ supercells containing a dislocation dipole in each cell in order to calculate the local line energy of the dislocations. Isotropic elasticity theory was used to generate the initial positions of the atoms. Relaxations were then carried out using the conjugate gradient algorithm.

In the AIMPRO case, relaxations were carried out in 392 atom stoichiometric clusters,

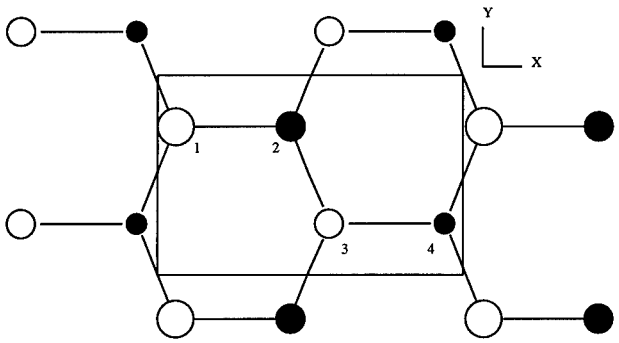

Fig. 1. Schematic top view of the $(10\bar{1}0)$ surface of wurtzite GaN. Atoms 1 and 2 form a dimer in the surface layer. Atoms 3 and 4 form the second layer.

Table 1. Atomic displacements in Å for the top two layers of atoms at the GaN$(10\bar{1}0)$ surface. Atom numbers refer to Fig. 1. Values in brackets are results of reference[20].

Atom	Δx	Δy	Δz
1 ($Ga_{3\times coord.}$)	-0.10 (-0.11)	0.0	-0.23 (-0.20)
2 ($N_{3\times coord.}$)	0.03 (0.01)	0.0	-0.01 (0.02)
3 ($Ga_{4\times coord.}$)	0.01 (0.05)	0.0	0.08 (0.05)
4 ($N_{4\times coord.}$)	0.04 (0.05)	0.0	0.07 (0.05)

where again isotropic elasticity theory was used to generate the initial positions of the atoms. *DF–TB* structures are given in the tables and diagrams, but *AIMPRO* structures are identical to within 5% for bond lengths and 2% for angles. LDF eigenvalues are also close, especially near the valence band maximum, but the conduction band is not best described by a minimal basis set, so *AIMPRO* eigenvalues are cited.

3 Threading Screw Dislocations

We consider first the screw dislocation ($b = \pm[000c]$) with a full core. Both methods found heavily distorted bond lengths (see Table 2) yielding deep gap states ranging from 0.9–1.6 eV above the valence band maximum, VBM, and shallow gap states at ~ 0.2 eV below the conduction band minimum, CBM. An analysis of these gap states revealed that the states above the

Table 2. Bond lengths, min-max (average), in Å and bond angles (min-max) in ° for the most distorted atoms at the core center of the full–core screw dislocation ($b = [0001]$).

Atom	bond lengths	bond angles
1 ($Ga_{4\times coord.}$)	1.85-2.28 (2.14)	68-137
2 ($N_{4\times coord.}$)	1.89-2.28 (2.13)	71-136

VBM are localised on N core atoms, whereas the states below CBM are localised on core atoms but have mixed Ga and N character. A calculation in a supercell containing a screw dipole consisting of two dislocations with $b = [000c]$ and $-[000c]$, which are symmetrically equivalent, confirmed these results.

A similar calculation was then carried out using the same supercell, but with the hexagonal core of each screw removed leading to a pair of open–core dislocations with diameters $d \approx 7.2$ Å. The relaxed structure (Fig. 2) preserved the hexagonal core character, demonstrating that the internal surfaces of the dislocation cores shown in (Fig. 3) are similar to $(10\bar{1}0)$ facets except for the topological singularity required by a Burgers circuit. It is instructive to compare the

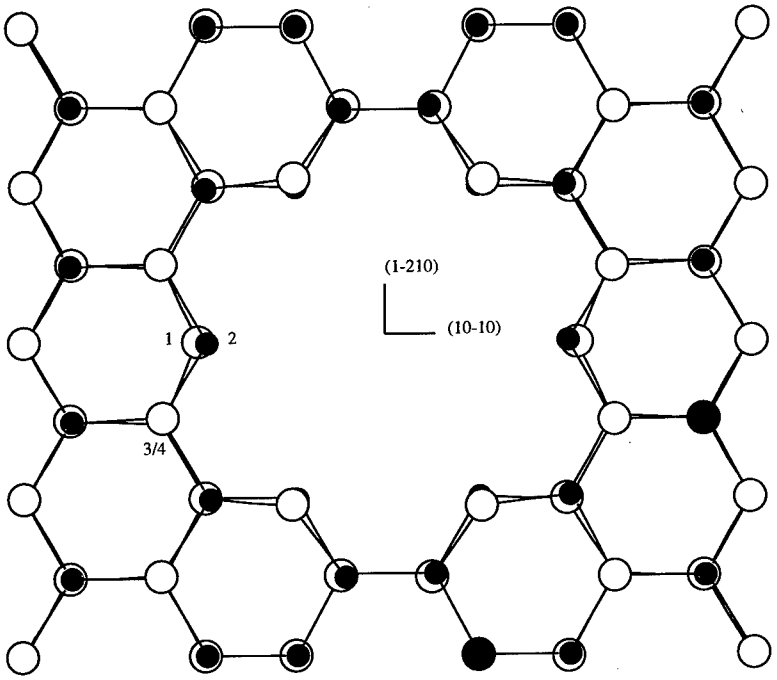

Fig. 2. Top view (in [0001]) of the relaxed core of the open–core screw dislocation (b = [0001]). The three fold coordinated atoms 1 (Ga) and 2 (N) adopt a hybridization similar to the $(10\bar{1}0)$ surface atoms.

distortions of the atoms situated at the wall of the open–core (Table 3) with the corresponding atoms at the $(10\bar{1}0)$ surface (Table 1). In both cases the three fold coordinated Ga (N) atoms

Table 3. Bond lengths, min-max (average) in Å and bond angles, min-max (average) in ° for the most distorted atoms at the wall of the open core screw dislocation (b = [0001]). Atom numbers refer to Fig. 2,3.

Atom	bond lengths	bond angles
1 ($Ga_{3x coord.}$)	1.86-1.89 (1.88)	107-123 (117)
2 ($N_{3x coord.}$)	1.88-2.05 (1.96)	102-111 (108)
3 ($Ga_{4x coord.}$)	1.89-2.07 (1.96)	100-122
4 ($N_{4x coord.}$)	1.93-2.03 (1.97)	98 -120

adopt sp^2 (p^3) like hybridisations which lower the surface energy and clean the gap [20]. Indeed, we find that unlike the full– core screw dislocation, the gap is free from deep states. There are, however, in contrast to the $(10\bar{1}0)$ surface, shallow gap states. Calculations were carried out for

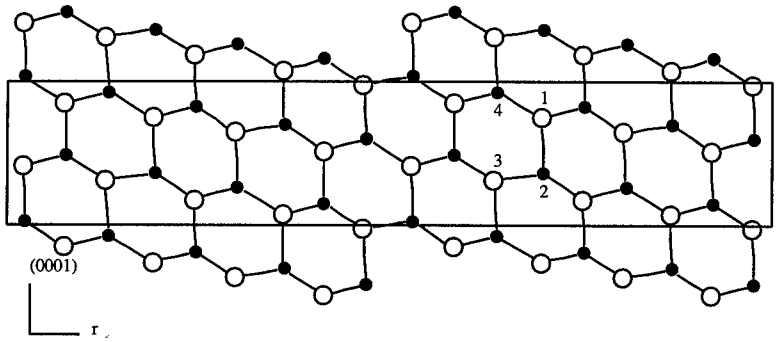

Fig. 3. Projection of the wall of the open–core (d=7.2 Å) screw dislocation (b = [0001]). The three fold coordinated atoms 1 (Ga) and 2 (N) adopt a hybridization similar to the $(10\bar{1}0)$ surface atoms.

Table 4. Bond lengths, min-max (average) in Å and bond angles, min-max (average) in ° for the top two layers of atoms at the GaN$(10\bar{1}0)$ surface. Atom numbers refer to Fig. 1.

Atom	bond lengths	bond angles
1 ($Ga_{3\times coord.}$)	1.83-1.88 (1.86)	116-117 (117)
2 ($N_{3\times coord.}$)	1.83-1.92 (1.89)	107-111 (108)
3 ($Ga_{4\times coord.}$)	1.91-2.02 (1.94)	107-112
4 ($N_{4\times coord.}$)	1.88-2.03 (1.93)	99-115

a distorted $(10\bar{1}0)$ surface, i.e. a $(10\bar{1}0)$ surface in a unit cell where the unit cell vectors were modified to give a distorted surface corresponding to that of the wall of the open–core screw dislocation with diameter d = 7.2 Å. We find that the distorted $(10\bar{1}0)$ surface has a spectrum with shallow states very similar to those of the open–core screw dislocation with d = 7.2 Å. We also calculated the spectrum for a nanopipe with d = 7.2 Å but without a dislocation core. This, like the undistorted $(10\bar{1}0)$ surface, possesses a gap free from deep states, although there are N (Ga) derived surface states lying slightly below (above) the VBM (CBM). These results indicate that the shallow states in the open–core screw dislocation with diameter d = 7.2 Å can be attributed to the distortion arising from the dislocation Burgers vector. Calculations for a series of different distortions of the $(10\bar{1}0)$ surface corresponding to open–core screw dislocations with different diameters also suggest that open–core screw dislocations with a diameter $d >\sim$ 20 Å should have no gap states at all. It is unlikely, that isotropic elasticity theory can describe the severely distorted full core dislocation which limits the usefulness of Frank's expression relating to the diameter of an open core dislocation [21]. Dislocations with large open diameters that are observed might arise from kinetic factors relating to the collision of GaN islands on the sapphire surface [12]. As the $\{10\bar{1}0\}$ facets of these open cores are low energy surfaces, they do not grow out during the initial growth process but thread through the crystal.

4 Threading Edge Dislocations

In the same way threading edge dislocations were modelled by relaxation of a cluster containing one dislocation with Burgers vector $a[11\bar{2}0]/3$ and a supercell with a dislocation dipole. The relaxed core is shown in Fig. 4. The corresponding bond–lengths and bond angles of the most

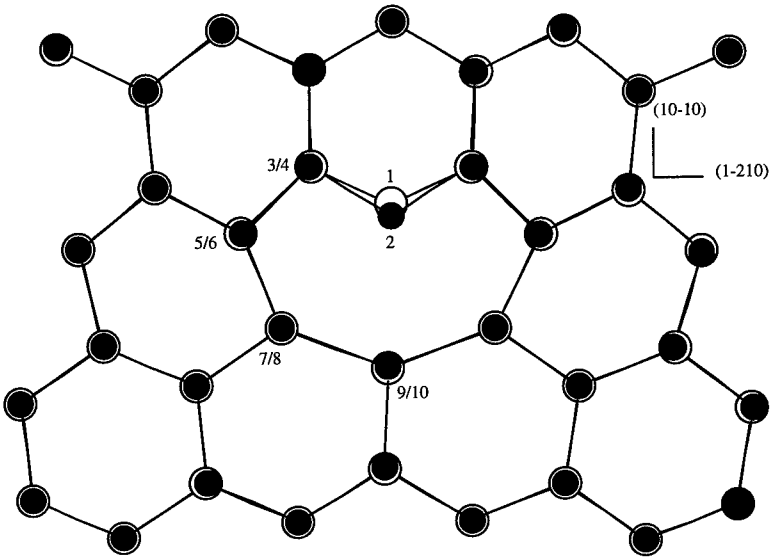

Fig. 4. Top view (in [0001]) of the relaxed core of the threading edge dislocation ($b = [11\bar{2}0]$). The three fold coordinated atoms 1 (Ga) and 2 (N) adopt a hybridization similar to the $(10\bar{1}0)$ surface atoms.

distorted atoms are given in Table 5. Again the three–fold coordinated Ga (N) atoms (no. 1

Table 5. Bond lengths, min-max (average) in Å and bond angles, min-max (average) in ° for the most distorted atoms at the core of the threading edge dislocation ($b = \frac{1}{3}[11\bar{2}0]$). Atom numbers refer to Fig. 4.

Atom	bond lengths	bond angles
1 ($Ga_{3x\,coord.}$)	1.85-1.86 (1.85)	112-118 (116)
2 ($N_{3x\,coord.}$)	1.88-1.89 (1.86)	106-107 (106)
3 ($Ga/N_{4x\,coord.}$)	1.86-1.95 (1.91)	97-119
4 ($Ga/N_{4x\,coord.}$)	1.92-2.04 (1.97)	100-129
5 ($Ga/N_{4x\,coord.}$)	2.01-2.21 (2.06)	94-125
6 ($Ga/N_{4x\,coord.}$)	2.00-2.21 (2.11)	100-122

and 2 in Fig. 4) relax towards sp^2 (p^3) leading to empty Ga lone pairs pushed towards the CBM, and filled lone pairs on N atoms lying near the VBM, in a manner identical to the $(10\bar{1}0)$ surface. Thus threading edge dislocations are also electrically inactive.

It is worth noting, that the core atoms 9 and 10 have very stretched bonds with bond–lengths ranging from 2.0 to 2.2 Å and thus give rise to a stress field which could act as a trap for intrinsic defects and impurities, *eg.*, the Ga vacancy O complex which could be responsible for the YL in n-type GaN [22]. Results on defect complexes in the stress field of dislocations is under current investigation and will be published in a forthcoming paper.

5 Summary

In conclusion, the density functional calculations reveal that the common threading screw and threading edge dislocations in wurtzite GaN are electrically inactive. It seems that the stress fields are sufficiently large that impurities might well be trapped. We suggest that the formation of dislocations in wurtzite GaN is radically different from those in Si or GaAs where mobile partial dislocations are to be found. The dislocations in GaAs and Si [23] are believed to contain cores composed of atoms which are fully four fold coordinated. These are then to be contrasted with those in GaN whose core atoms are three fold coordinated.

S. Öberg thanks NFR and TFR in Sweden for financial support. He also thanks PDC at KTH in Sweden, for computer time on the SP2. We also thank the HPCI committee of the EPSRC for computer time on the T3D (grant reference GR/K42301) and David Cherns for helpful discussions.

References

[1] X. H. Wu, L. M. Brown, D. Kapolnek, S. Keller, B. Keller, S. P. DenBaars, and S . J. Speck, J. Appl. Phys. **80**, 3228 (1996).

[2] X.J. Ning, F.R. Chien, and P. Pirouz, J. Mater. Res. **11**, 580 (1996)

[3] F.A. Ponce, D. Cherns, W.T. Young, and J.W. Steeds, Appl. Phys. Lett. **69**, 770 (1996).

[4] S. D Lester, F. A. Ponce, M. G. Cranford, and D. A. Steigerwald, Appl. Phys. Lett., **66**, 1249 (1996).

[5] L. Sugiura, J. Appl. Phys. **81**, 1633 (1997).

[6] Nakamura S., Mukai T., and M. Senoh, J. Appl. Phys., **76**, 8189 (1994).

[7] S. Nakamura, M. Senoh, S. Nagahama, N. Iwasa, T. Yamada, T. Matsushita, H. Kiyohu, and Y. Sguimoto, Jpn. J. Appl. Phys. **35**, L74 (1996).

[8] K. Maeda, and S. Takeuchi, J. Physique **44**, C4-375 (1983).

[9] F. A. Ponce, D. B. Bour, W Gotz, and P. J. Wright, Appl. Phys. Lett. **68**, 57 (1996). Recent combined cathodoluminescence and atomic force microscopy points to threading dislocations as as a source for these centers [10]

[10] S. J. Rosner, E. C. Carr, M. J. Ludowise, G. Girlami, and H. I. Erikson, Appl. Phys. Lett. **70**, 420 (1997).

[11] W. Qian, M. Skowronski, K. Doverspike, L. B. Rowland, and D. K. Gaskill, J. Cryst. Growth, **151** 396, (1995).

[12] D. Cherns, W. T. Young, and J. W. Steeds, F. A. Ponce, and S. Nakamura, J. Cryst. Growth, in press 1997.

[13] G. B. Bachelet, D. R. Hamann and M. Schlüter, Phys. Rev., **B26**, 4199 (1982).

[14] Jones, R.; *Phil. Trans. Roy. Soc. Lond. A* 1995, **350**, 189.

[15] Jones, R.; "The *ab initio* cluster method and the dynamics of defects in semiconductors"; *in* Willardson, R. K.; Beer, A. C.; Weber, E. R; Eds.; *Semiconductors and Semimetals: Identification of Defects in Semiconductors*; Ed. by M. Stavola, Academic Press: New York, 1997, *in press.*

[16] D. Behr, J. Wagner, J. Schneider, H. Amano, and I. Akasaki, Appl. Phys. Lett. **68**, 2404 (1996).

[17] F. D. Murnaghan, Proc. Natl. Acad. Sci. USA **30**, 244 (1944).

[18] D. Porezag, Th. Frauenheim and Th. Köhler Phys. Rev. B **51**, 12947 (1995).

[19] M. Elstner, D. Porezag, G. Jungnickel, Th. Frauenheim, G. Seiffert, to be submitted to PRL

[20] J. E. Northrup, and J. Neugebauer, Phys. Rev. B **53**, 10477 (1996).

[21] F. C. Frank, Acta. Crys. **4**, 497 (1951).

[22] J. Neugebauer, and C. Van de Walle, Appl. Phys. Lett. **69**, 503 (1996).

[23] S. Öberg, P. K. Sitch, R. Jones, M. I. Heggie, Phys. Rev. B., **51**, 13138 (1995).

This article was processed using the LaTeX macro package with TTP style

Materials Science Forum Vols. 258-263 (1997) pp. 1211-1216

DEFECTS ANALYSIS IN STRAINED InAlAs AND InGaAs FILMS GROWN ON (111)B InP SUBSTRATES

N. Bécourt, J. C. Ferrer, F. Peiró , A. Cornet and J. R. Morante
Departament de Física Aplicada i Electrònica, Universitat de Barcelona, Diagonal 645-647, E-08028 Barcelona, Spain
P. Gorostiza
Serveis Científico-Tècnics, Universitat de Barcelona, Lluís Solé i Sabarís, 1-3, 08028, Barcelona, Spain
G. Halkias
NCSR "Demokritos", Institute of Microelectronics (IMEL), P.O. Box 60228, Aghia Paraskevi 153 10, Greece
K. Michelakis and A. Georgakilas
FORTH, Institute of Electronic Structure and lasers (IESL), Microelectronics Research Group (MRG), P. O. Box 1527, Heraklion, Crete, Greece; and University of Crete, Department of Physics, Heraklion, Greece

Keywords : InAlAs, InGaAs, InP(111), step-bunching, strain, TEM, AFM.

Abstract. We have examined the structure of InGaAs and InAlAs strained monolayers grown by Molecular Beam Epitaxy on (111)B 1° off toward [$\bar{2}$11] InP substrates. Transmission Electron Microscopy and Atomic Force Microscopy observations have revealed the bunching of InAlAs surface steps. The film exhibits structural inhomogeneities and threading dislocations induced by the coalescence of misorientation steps. The characterizations performed on the InGaAs film have shown periodical contrasted domains developing in the direction of growth. From similar results obtained on InP(100)-based growth, we have interpreted these variations to be composition modulation involved in the tensile strains relaxation process. Also, InAs epitaxy performed on the InAlAs top-surface has demonstrated that the first stage of growth were proceeding at the bunched step edges following a 3D mechanism.

Introduction.

Nowadays, there are great interests in the optical and electronical properties of strained III-V compounds grown on InP substrates [1-5]. Depending on the crystallographic orientation, effects such as high electronic properties [1] or Quantum Confined Stark Effect [2-5] have already been demonstrated. Moreover, InP substrate utilisation presents the possibility for growing either tensilely either compressively strained InAlAs and InGaAs on it. In the past, a large quantity of works was devoted to the study of the defects present in heteroepitaxial mismatched layers of $In_xGa_{1-x}As$ or $In_xAl_{1-x}As$ grown on (100) oriented InP substrates [1,6-11]. Those studies showed that depending on the Indium composition and technological parameters, a network of misfit dislocations, the presence of islands due to the tridimensional growth, or composition inhomogeneities can contribute to the structure relaxation. Recently, for optical and electro-optical applications, technological efforts have been devoted to the obtention of strained InAlAs/InGaAs Multi Quantum Well (MQW) structures grown on (111) oriented InP substrates [2-4]. Nevertheless, few work has been performed in order to understand the mechanisms of relaxation along this direction of growth.

In this study, we present the characterization by Atomic Force Microscopy (AFM) and Transmission Electron Microscopy (TEM) of strained InGaAs and InAlAs monolayers grown by

Molecular Beam Epitaxy (MBE) on (111)B InP substrates. The observations have clearly revealed a bunching of the misorientation steps developed during the growth of InAlAs. We demonstrate the formation of strain inhomogeneities in the layer as well as extended dislocations relatively to the surface steps reconstruction. Periodical composition domains have been observed in the thickness of the InGaAs film along the direction of growth. The origin of these modulations is discussed and compared with similar results obtained on InP(100)-based growth. We have also experimented the growth of InAs on the bunched InAlAs surface. AFM and TEM results have shown that InAs was developing preferentially at the steps edge prior to expand on the (111) surface terraces.

Experimental details.

We have analysed three compressively strained $In_{0.56}Al_{0.44}As$ films grown at 0.3, 0.55 and 1.2μm (sample #A, #B and #C) and a tensilely strained $In_{0.51}Ga_{0.49}As$ film grown at 1.8μm on (111)B 1° off toward [$\bar{2}$11] InP substrates. From previous MBE experiments, the growth temperature (T_g) was fixed at 530°C and 500°C for InAlAs and InGaAs respectively [1, 12]. Prior to deposition, the substrates were supporting a thermal treatment at 530°C in order to remove the protective oxide and to activate surface steps reconstruction [13]. At the end of sample #B run, In and As shutters were left open for a few seconds in order to experiment InAs growth on the InAlAs surface. The sample characterizations have been performed by Tapping Mode AFM (TMAFM) using a Nanoscope III electronics. For TEM experiments, the structures were first mechanically thinned and then Ar+ ion milled in a liquid nitrogen cooled stage. The observations have been achieved at 200kV in a Hitachi 800 NA microscope, in bright-field (BF) two-beams imaging conditions.

Results.

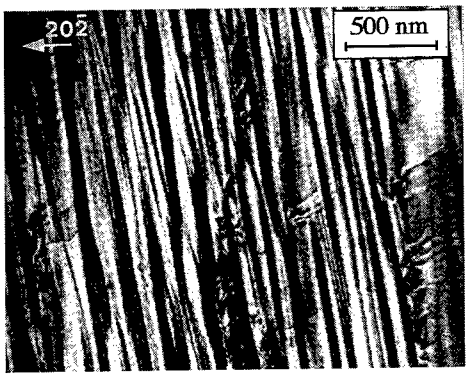

FIG. 1. PVTEM image of a (111) InGaAs film grown on InP substrate.

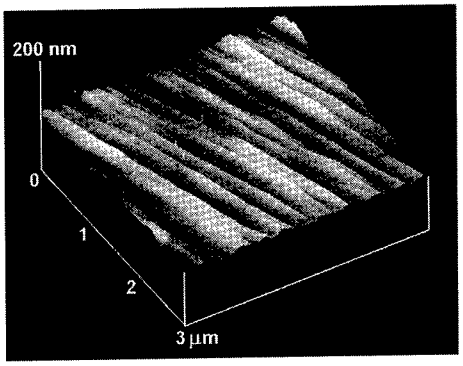

FIG. 2. 3D TMAFM image of a (111) InGaAs film grown on InP substrate. The wavy aspect of the surface is related to periodical composition domains in the layer.

$In_{0.51}Ga_{0.49}As$/InP(111) sample :

From PVTEM observations (Fig. 1), alternatively dark and clear straight parallel contrasts are seen running on the surface in the [$\bar{1}\bar{2}$3] direction. This topography is related to a periodical undulation of the sample top-surface as observed by AFM (Fig. 2).

Figure 3a shows the InGaAs layer near the film/InP substrate interface. It seems that the first 270nm of the film act as a transition region where the structure gradually evolves until it presents distinct domains along the direction of growth. The width of these domains is in average 60nm and corresponds to the period of the surface undulations. Such features have already been well described in strained InGaAs/InAlAs heterostructures grown on misoriented (100)InP substrate

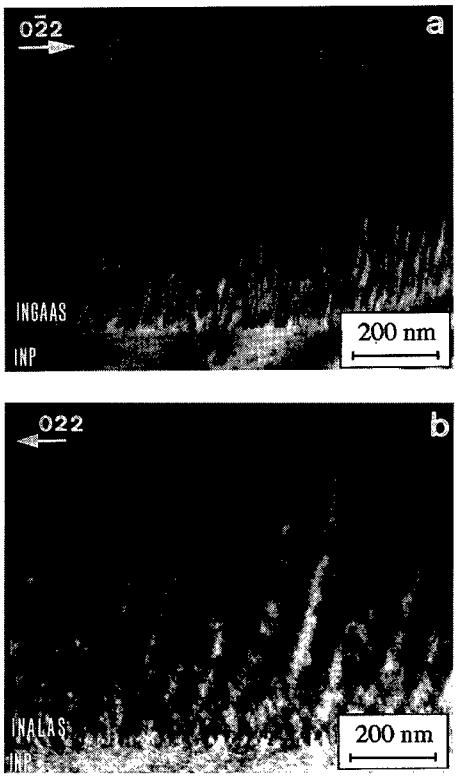

FIG. 3. BF images on cross-sectional view, (a) along [$\bar{2}11$] of a (111) InGaAs film and (b) along [$0\bar{1}1$] of a (100) InAlAs film, tensilely grown on InP substrate. Notice the periodical composition domains in both materials.

(Figure 3b) [14]. These previous studies have revealed that the periodical contrasts were composition variations in the InAlAs buffer layer, leading to In-rich and Al-rich regions. The high growth temperature of InAlAs (580°C) and the presence of misorientation steps on the substrate surface were found to be at the origin of these segregations. Also, XRD experiments performed on InAlAs tensilely strained layers have demonstrated the contribution of these modulations to the stress relaxation. The comparison between Figure 3a ($In_{0.51}Ga_{0.49}As$ (111)/InP) and Figure 3b ($In_{0.48}Al_{0.52}As$ (100)/InP) shows very well the similarity of the phenomena in both materials. This means that the periodical contrasts observed in the InGaAs film could be the result of a segregation of the III elements leading to In and Ga-rich domains. This mechanism is a thermally activated process and such result shows that, in InGaAs, it can occur at temperature even so low that 500°C. The growth rate of the InGaAs film will be different in the In-rich and in the Ga-rich domains. Two growth fronts will be distinguished in the layer, leading to a wavy aspect of the surface as observed in our sample (Fig. 2).

As illustrated on Figure 1, inhomogeneously distributed pairs of dislocations have developed in the [$\bar{1}\bar{2}3$] direction, in interaction with the composition domains. This observation, supported by the experiments performed on InAlAs/InP(100) [14], seems to confirm that the composition segregation is closely involved in the stress relaxation process of the (111) InGaAs film.

$In_{0.56}Al_{0.44}As$/InP(111) samples :

AFM observations have demonstrated the highly stepped topography of the three samples as shown on Figure 4. We can observe sequences of giant steps running on the surface of the 0.3, 0.55, and 1.2μm thick InAlAs films (Fig. 4a, b, and c, respectively). The step height and periodicity have been calculated from AFM and reported in Table 1.

Table 1. Average surface step height and terrace width, measured by AFM, for the three InAlAs-on-InP samples.

Sample reference	#A	#B	#C
Thickness (μm)	0.3	0.55	1.2
Step height (nm)	4.8	10.2	16.6
Terrace width (μm)	0.34	0.58	0.93
Calculated angle (°)	0.81	1	1.02

As illustrated for sample #B [Fig. 5], PVTEM performed on the InAlAs films shows the giant steps as dark linear contrasts on the surface [Fig. 5a and b, black arrows], while straight parallel

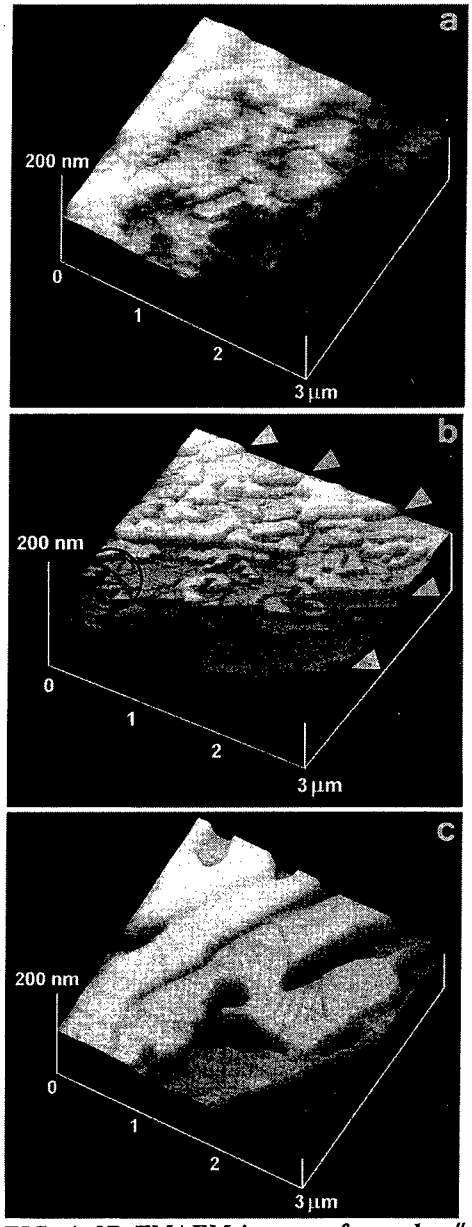

FIG. 4. 3D TMAFM images of samples #A (a), #B (b), and #C (c). A sequence of 5 consecutive steps is indicated with arrows for sample #B.

features are observed along [1$\bar{2}$1] and [11$\bar{2}$] directions [Fig. 5a, white arrows]. Transmitted Electron Diffraction (TED) pattern obtained in the [111] growth direction has revealed that the steps were running in the direction of misorientation [$\bar{2}$11]. Their profile is clearly seen on the

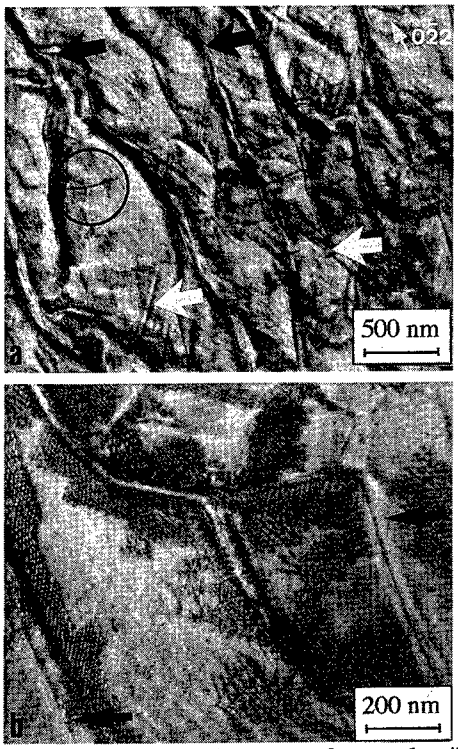

FIG. 5. PVTEM images of sample #B surface. Bunched steps and linear contrasts are respectively indicated with black and white arrows. (a) Dislocations are running from the bunched steps along [$\bar{3}$21] (circle). (b) Due to the lattice mismatch, InAs islands appear as Moiré domains mainly located at the step edges.

sample #B surface using CS analysis [Fig. 6a and b], with average height and periodicity equal to 10.92nm and 0.58µm respectively what agrees with the AFM results reported on Table 1. Furthermore, the film/InP substrate interface is revealed very flat as indicated on Figures 6a and b. This observation confirms that the surface stepped aspect of the InAlAs films is not a reproduction of the substrate topography but that the giant steps form during the growth. This is the first time from our knowledge that the bunching of misorientation steps is demonstrated in InP-based growth. The substrate off-cut angle deduced from the surface step height and periodicity of the 3 samples has been reported on Table 1. The calculated misorientation angle agrees very well with the 1° expected for

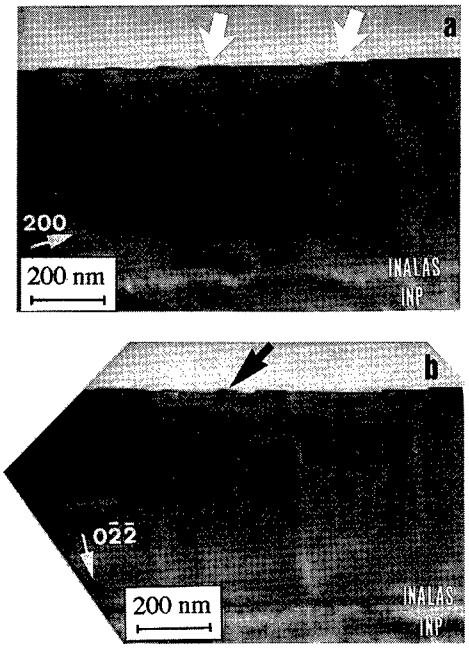

FIG. 6. BF images on cross-sectional view along [0$\bar{1}$1] direction of sample #B. The InAs islands (arrows) have nucleated preferentially at the step edges. (a) Groups of dislocations have developed through the film up to the surface step edges. (b) Structural inhomogeneities appear as curved clear contrasts.

samples #B and #C while a slight deviation appears for sample #A. As shown on figure 4, the step size and the terrace width increase with the film thickness, in agreement with similar observations performed on homoepitaxially grown GaAs [11].

Groups of straight dislocations are observed in the thickness of sample #B, originating approximatively at 40nm from the film/substrate interface and propagating through the layer up to the surface [Fig. 6a]. The dislocations end below the steps edge and their presence is clearly related to the formation of the bunched steps. PVTEM shows the dislocations running from the steps edge in the [$\bar{3}$21] direction [Fig. 5a, circle].

As illustrated on Figure 6b, the sample #B structure exhibits structural inhomogeneities appearing as fringes contrasts in the film thickness. A first relation can be established between such features and the straight parallel lines observed by PVTEM along [1$\bar{2}$1] and [11$\bar{2}$] directions [Fig. 5a, white arrows]. Similar linear contrasts have been observed in (100) InAlAs [15], and were found to be composition inhomogeneities.

InAs islands are seen by AFM all over the surface of sample #B, mainly located along the bunched steps as illustrated in the circle on Figure 4a. XTEM observation demonstrates clearly that InAs has developed preferentially at the steps edge prior to expand on the terraces, resulting in superficial faceted 3D-grown islands [Fig. 6a and b, arrows]. Due to the different lattice constant between $In_{0.56}Al_{0.44}As$ and InAs, the islands appear as Moiré domains by PVTEM observation [Fig. 5b]. The InAs clustering was also observed during the growth by in-situ Reflexion High Electron Energy Diffraction (RHEED).

Discussion and conclusion.

The MBE growth of tensilely strained (111) InGaAs on off-axis InP substrate has been investigated. We have demonstrated that the strain relaxation was proceeding by the segregation of In and Ga during the growth and the generation of dislocations. Homogeneously distributed periodical composition domains were observed in the layer, leading to a wavy aspect of the surface. This mechanism has been found to be very similar to the strain relaxation observed for (100) InP-based growth [14].

Our experiments have shown that the growth of compressively strained InAlAs on (111) off-axis InP substrate was followed by a bunching of misorientation steps. These results are a new demonstration of the bunching mechanism already well known in III-V semiconductors such as GaAs, GaSb, $In_{0.5}Ga_{0.5}P$ or $In_XGa_{1-X}As$ grown on GaAs [13, 16-18]. The reconstruction of the surface misorientation steps induces the formation of threading dislocations in the layer. structural inhomogeneities attributed to composition modulation are

also observed in the InAlAs film thickness. These features are related to the relaxation of the strains induced by the lattice-mismatched composition of the grown epilayer. Finally, we have shown that InAs nucleation on the InAlAs surface was proceeding at the giant step edge following a 3D-mechanism. The bunched topography of the (111) surface may be used for local deposition as a method for spontaneous formation of quantum wire structures.

InAlAs and InGaAs materials are involved in (111) multilayered heterostructures such as MQW and the observed defects are a limitation to the development of such applications. The composition modulation and the stepped/wavy topography will develop non uniformities in the device properties as well as planarity problems for surface technologies. This work shows that the growth conditions along the (111) orientation have to be optimised independently from the (100) orientation. Previous studies performed on InAlAs and InGaAs films grown on InP (100) have shown how critical was the growth temperature for the obtention of excellent quality material. For InAlAs (100), an optimum T_g was found to be the limit between a regime where crystalline defects were produced in the layer for low temperature, and a regime where composition segregation occurred for high T_g. If we assume the same mechanisms along (111) orientation, the growth temperature of InGaAs should be lowered in order to cancel the observed composition segregation. Although the present work concerns the growth of tensilely strained InAlAs and most of the observed defects are related to the strain relaxation, InAlAs is usually grown lattice-matched to the substrate for example as barrier layer in MQW structures. Further studies should focused on the careful control of the composition around the lattice-matched value in order to achieve better crystalline quality of the (111) InAlAs material.

This work has been supported by European Union contract CHRX-CT94-0428, HCM network "SQUAD".

References.

1. A. Georgakilas, G. Halkias, A. Christou, N. Kornilios, C. Papavassiliou, K. Zekentes, G. Konstantinidis, F. Peiró, A. Cornet, S. Ababou, A. Tabata and G. Guillot, J. Electrochem. Soc. 140, 1503 (1993).
2. K. Nishi and T. Anan, J. Appl. phys. 70, 5004, (1991).
3. H. C. Sun, L. Davis, Y. Lam, P. K. Bhattacharya, and J. P. Loehr, Inst. Phys. Conf. 129, 229 (1992).
4. H. Q. Hou and C. W. Tu, J. Appl. Phys. 75, 4673 (1994).
5. W. Q. Chen and S. K. Hark, J. Appl. Phys. 77, 5747 (1995).
6. F. Peiró, A. Cornet, J. R. Morante and A. Georgakilas, J. Vac Sci. Technol. B 13, 1006 (1995).
7. H. Ohno, C. E. C. Wood, L. Rathbun, D. V. Morgan, G. W. Wicks, and L. F. Eastman, J. Appl. Phys. 52, 4033 (1981).
8. J. Massies, J. F. Rochette, P. Ettienne, P. Delescluse, A. M. Huber, and J. Chevrier, J. Cryst. Growth 64, 101 (1983).
9. A. S. Brown, M. J. Delaney, and J. Singh, J. Vac. Sci. Technol. B7, 384 (1989).
10. J. P. Praseuth, L. Goldstein, P. Hénoc, J. Primot, and G. Danan, J. Appl. Phys. 61, 215 (1987).
11. M. Kasu and N. Kobayashi, J. Appl. Phys. 78, 3026 (1995).
12. A. Georgakilas, A. Christou, P. Lefebvre, J. Allegre, K. Zekentes, and G. Halkias, Appl. Phys. Lett. 61, 798 (1992).
13. F. Peiro, A. Cornet, A. Herms, J. R. Morante, A. Georgakilas and G. Halkias, J. Vac. Sci. Technol. 10, 2148 (1992).
14. F. Peiró, A. Cornet, J. C. Ferrer, J. R. Morante, G. Halkias and A. Georgakilas, Mat. Res. Soc. Symp. Proc. 417, 265 (1996).
15. F. Peiró, A. Cornet, and J. R. Morante, Mat. Res. Soc. Symp. Proc. 312, 131 (1993).
16. M. Aindow, T. T. Cheng, N. J. Mason, T.-Y. Seong and P. J. Walker, J. Cryst. Growth 133, 168 (1993).
17. A. Gomyo and T. Suzuki, J. Cryst. Growth 145, 126 (1994).
18. R. Beanland, A. Sacedon and E. Calleja, Inst. Phys. Conf. Ser. No 146, 169 (1995).

Materials Science Forum Vols. 258-263 (1997) pp. 1217-1222

IRRADIATION INDUCED LATTICE DEFECTS IN $In_{0.53}Ga_{0.47}As$ PIN PHOTODIODES

T. Kudou[1], H. Ohyama[1], J. Vanhellemont[2, 3], E. Simoen[2], C. Claeys[2], Y. Takami[4], A. Fujii[5] and H. Sunaga[6]

[1]Kumamoto National College of Technology, 2659-2 Suya Nishigoshi Kumamoto, 861-11 Japan
[2]IMEC, Kapeldreef 75, B-3001 Leuven, Belgium
[3]Present address: Wacker Siltronic AG, D-84479 Burghausen, Germany
[4]Rikkyo University, 2-5-1, Nagasaka Yokosuka Kanagawa, 240-01 Japan
[5]Kumamoto University, 39-1, Kurokami Kumamoto, 860 Japan
[6]Takasaki JAERI, 1233 Watanuki Gunma, 370-12 Japan

Key words : $In_{0.53}Ga_{0.47}As$ epitaxial layer, pin photodiodes, radiation damage, deep levels

Abstract. Results are presented of an extended study on the induced lattice defects and their effects on the degradation of $In_{0.53}Ga_{0.47}As$ pin photodiodes, subjected to a 20-MeV alpha ray irradiation. The difference in radiation damage between 1-MeV fast neutrons and 1-MeV electrons is discussed taking into account the energy transfer. The radiation source dependence of performance degradation is attributed to the difference of mass and the probability of nuclear collision for the formation of lattice defects.

Introduction

Extensive studies aiming at the development of semiconductor devices which can operate normally in a radiation environment have been undertaken, as there is an expansion in the utilization of hardened electronic circuits. The $In_{1-x}Ga_xAs_yP_{1-y}/InP$ semiconductor system has attained much interest for optoelectronic devices in the 950 to 1650 nm wavelength region [1-2]. Such detectors are good candidates for use in the telecommunication system of a spacecraft. Therefore, it is worthwhile to investigate the operation of such photodiodes in a radiation environment. Although several results on the degradation of and induced lattice defects in InGaAs p-i-n photodiodes by electron and neutron irradiation have been published [3-5], there are only a few reports available on the radiation damage and its recovery behavior after alpha ray irradiation.

In the present paper, the degradation of $In_{0.53}Ga_{0.47}As$ p-i-n photodiodes by 20-MeV alpha rays is studied together with the recovery of electrical and optical characteristics. The radiation source dependence is discussed by comparing 1-MeV fast neutrons and 1-MeV electrons. In order to examine the recovery behavior of the induced deep levels and the device performance, isochronal thermal annealing is carried out for temperatures ranging from 75 to 300 ^{o}C. Moreover, the effects of the induced lattice defects on the performance degradation is presented.

Experimental

p-i-n photodiodes are fabricated by deposition of $In_{0.53}Ga_{0.47}As$ epitaxial layers on S-doped high-resistivity (100) InP substrates, which had an approximately 300 nm n^+-InP buffer layer on top. A hydride ($Ga/In/HCl/AsH_3/H_2$) vapor phase epitaxy (VPE) system with dual-growth chamber reactor was. The InP substrate temperature was kept at 700 ^{o}C for the growth of $In_{0.53}Ga_{0.47}As$ epitaxial layers. The nominal thicknesses of the n-InP window layer and the n^--$In_{0.53}Ga_{0.47}As$ epitaxial layers used as a light absorbing layer are about 1 and 3 μm, respectively.

The p region was created by a Zn diffusion to a depth of about 200 nm. SiN_X of 200 nm thickness formed by chemical vapor deposition was used for passivation and as anti-reflection film. Au-Zn and Au-Ge/Ni with a thickness of 200 nm were then evaporated and alloyed for p and n contacts, respectively. After dicing in chips of 300 x 300 μm^2 size, diodes were encapsulated in TO-18 packages with Kovar glass windows of 0.3 mm thickness. More details on the diode process are described in a previous paper [6].

TO-18 packaged diodes with the Kovar glass removed were irradiated at room temperature by a 20-MeV alpha ray in the AVF cyclotron in TIARA at the Takasaki Radiation Chemistry Research Establishment. The fluence of the alpha ray was varied between 10^{10} and 10^{13} $1/cm^2$. The diodes were also irradiated by fast 1-MeV neutrons at room temperature in the irradiation tube of the Rikkyo University reactor (Triga Mark II). The neutron fluence was varied between 10^{12} and 10^{14} n/cm^2. Moreover, 1-MeV electron irradiations using the linear electron accelerator at the Takasaki JAERI (Dynamitron) were performed at room temperature. The electron fluence was varied from 10^{13} to 10^{15} e/cm^2. Electron and neutron irradiations were carried out through the Kovar glass and package.

Before and after irradiation, the current/voltage (I/V) characteristics of the diodes were measured at room temperature to examine the change of dark current (I_D) by irradiation. The photo current (I_L) as a function of the white light power (P_L) and wavelength (λ) was also measured at room temperature. The I_L/λ measurement were performed using a monochromator for wavelengths ranging from 700 to 1600 nm. The deep levels in the $In_{0.53}Ga_{0.47}As$ epitaxial layer were studied using the deep level transient spectroscopy (DLTS) method in the temperature range between 77 to 300 K. The emission rate window used in this measurement ranged from 1.18 to 26.51 msec. The applied filling pulse ranged from -2 to 0 V to observe electron capture levels in the n^--$In_{0.53}Ga_{0.47}As$ epitaxial layers. To investigate the recovery behavior and the difference in radiation damage, isochronal thermal anneals were carried out at temperatures between 100 and 300 °C under nitrogen flow and without bias. The annealing time was fixed at 15 min, and the temperature was varied in steps of 25 °C with an accuracy of 1 °C. I/V, I_L/P_L and I_L/λ characteristics and DLTS spectra were measured after each annealing step.

Results and discussion

Figures 1 (a) and (b) show typical DLTS spectra in the $In_{0.53}Ga_{0.47}As$ epitaxial layer for alpha rays and neutron irradiation for different fluences, respectively. Before irradiation native electron capture levels with energy level Ec - 0.58 eV are observed. The levels are thought to be formed during the growth of the $In_{0.53}Ga_{0.47}As$ epitaxial layer and are probably associated with a Ga vacancy [7, 8]. After irradiation, electron capture levels with Ec - 0.37 eV are induced. The density increase of deep level with increasing fluence and the appearance of new deep levels are not observed for the alpha ray irradiations, while levels E^{IGA}_{513N2} (Ec - 0.45 eV) are induced with E^{IGA}_{513N1} (Ec - 0.37 eV) for neutron irradiation. The damage coefficient of device performance for alpha ray irradiation is about three orders of magnitude larger than that for neutron irradiation as mentioned later. These results contradict each other. It has to be remarked that for the high fluence alpha ray irradiations the depleted area extends into the InP substrate so that one is no longer only measuring deep levels in the $In_{0.53}Ga_{0.47}As$ epitaxial layer.

Figure 2 (a) and (b) show the typical I/V and I_L/P_L characteristics, after irradiation by 20-MeV alpha rays, for different fluences, respectively. From figure 2a it is noted that both the reverse and forward currents increase. Also, the dark current (I_D) at V_R = -2 V increases by alpha ray irradiation. The reason for this might be an increased generation current due to the lattice defects induced in the $In_{0.53}Ga_{0.47}As$ epitaxial layer. Figure 2b shows the typical I_L/P_L characteristics under an applied reverse voltage of -2 V. It is also found from the figure that I_L decreases by irradiation. In this case, I_L is defined as the value of the photo current minus the dark current I_D. The capture of carriers by

defects introduced in the epitaxial layer is mainly responsible for the decrease of I_L. The performance degradation increases with increasing alpha ray fluence. Similar degradation of device performance is observed in electron-irradiated photodiodes [9]. Assuming a linear relationship between radiation damage and fluence, the damage coefficient of dark current and of photo current (K_D, K_L) are calculated. Table 1 (a) lists K for 1-MeV electrons, 1-MeV neutrons and 20-MeV alpha rays, respectively. As shown in this table, K_D for alpha ray irradiation is about 500 times larger than for neutron irradiation, while K_L is about 6 times larger. One can also calculate the number of knock-on atoms and nonionizing energy loss (NIEL) in the $In_{0.53}Ga_{0.47}As$ epitaxial layer (Table 1 (b)). N_d and NIEL values for alpha ray irradiation are about 20 times larger than those for neutron irradiation. The reason that K_D for the alpha ray irradiation is larger than the calculated one is thought to be due to the removal of the Kovar cover glass. Based on these consideration, the radiation source dependence of performance degradation is thought to be attributed to the difference of mass and the possibility of nuclear collision for the formation of lattice defects.

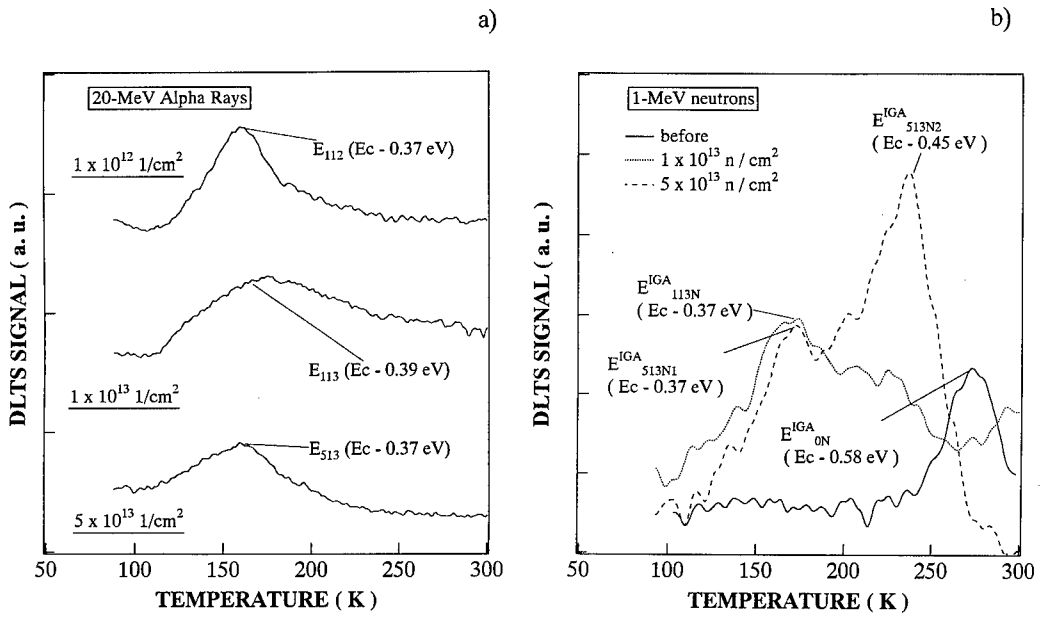

Figure 1 : DLTS spectra in the $In_{0.53}Ga_{0.47}As$ epitaxial layer for 20-MeV alpha rays (a) and 1-MeV fast neutron (b) irradiation.

The diode performance degraded by neutron or electron irradiation recovers by thermal annealing after irradiation. Figure 3 (a) and (b) show the result of 15 min isochronal anneals of the electric current and photocurrent characteristics for different alpha ray fluence, respectively. There is almost no recovery of the I_L/P_L characteristics. Annealing above 300 ^oC leads to a destruction of the contacts so that no diode performance was observed. To investigate the radiation source dependence of the recovery behavior, the unrecovered fraction of dark and photocurrent, which is defined as the ratio of recovery of performance after and before annealing, for 1-MeV electrons, 1-MeV fast neutrons and 20-MeV alpha rays as a function of annealing temperature is shown in figure 4 (a) and (b). As shown in those figures, the recovery behavior has a radiation source dependence, while the device performance degraded by irradiation recovers by thermal annealing and the recovery increases with increasing annealing temperature. After 300 ^oC thermal annealing, the photocurrent recovers to 47 % of the value before neutron irradiation, for a fluence of 1 x 10^{13} n/cm^2, while it recovers to 76 % for a fluence of 1 x 10^{15} e/cm^2. For the photo current in figure 4 (b), the amount of recovery at

300 °C for alpha ray irradiation is nearly the same as for neutron irradiation, while that for electron irradiation is much larger. The radiation source dependence of recovery behavior is thought to be due to the different type of induced radiation damage.

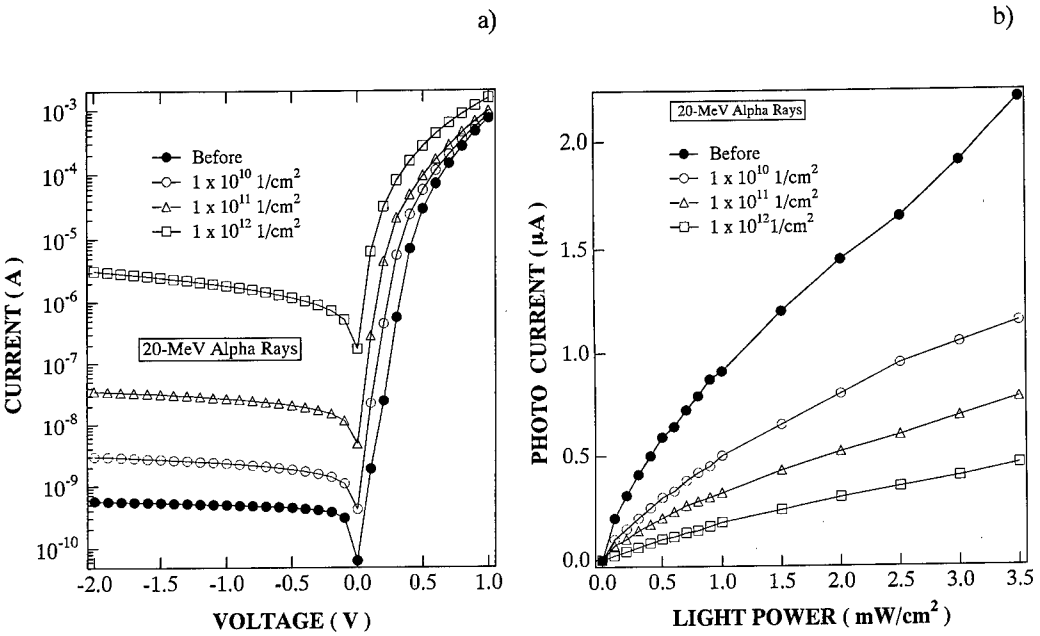

Figure 2 : Degradation of I/V (a) and I_L/P_L (b) characteristics of $In_{0.53}Ga_{0.47}As$ epitaxial by 20-MeV alpha ray irradiation.

Table 1 : Damage coefficient (a) and N and NIEL (b) for different radiation sources.

a)

	1-MeV Electrons	1-MeV Neutrons	20-MeV Alpha Rays
K_D	3.8×10^{-23} ($e^{-1}Acm^2$)	8.2×10^{-21} ($n^{-1}Acm^2$)	4.5×10^{-18} (Acm^2)
K_L	-3.5×10^{-22} ($e^{-1}Acm^2$)	-8.1×10^{-20} ($n^{-1}Acm^2$)	-5.5×10^{-19} (Acm^2)

b)

	1-MeV Electrons	1-MeV Neutrons	20-MeV Alpha Rays
N_d (cm^{-3})	3.0×10^{-2}	6.2	93
NIEL ($MeVcm^2g^{-1}$)	1.78×10^{-6}	0.83×10^{-3}	13×10^{-3}

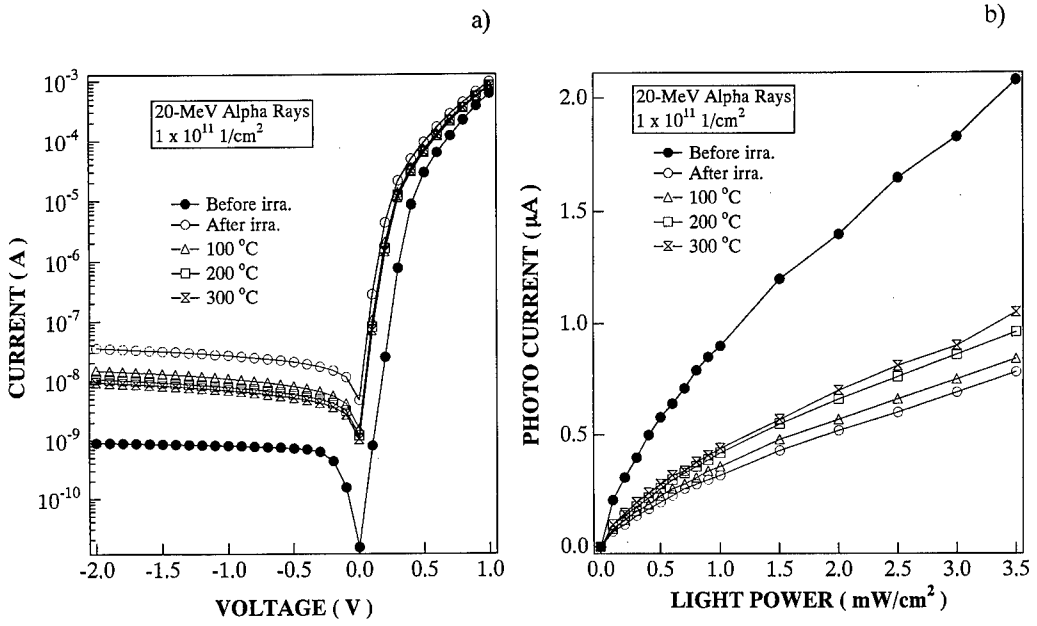

Figure 3 : Recovery behavior of I/V (a) and I_L/P_L (b) characteristics of $In_{0.53}Ga_{0.47}As$ epitaxial by 20-MeV alpha ray irradiation.

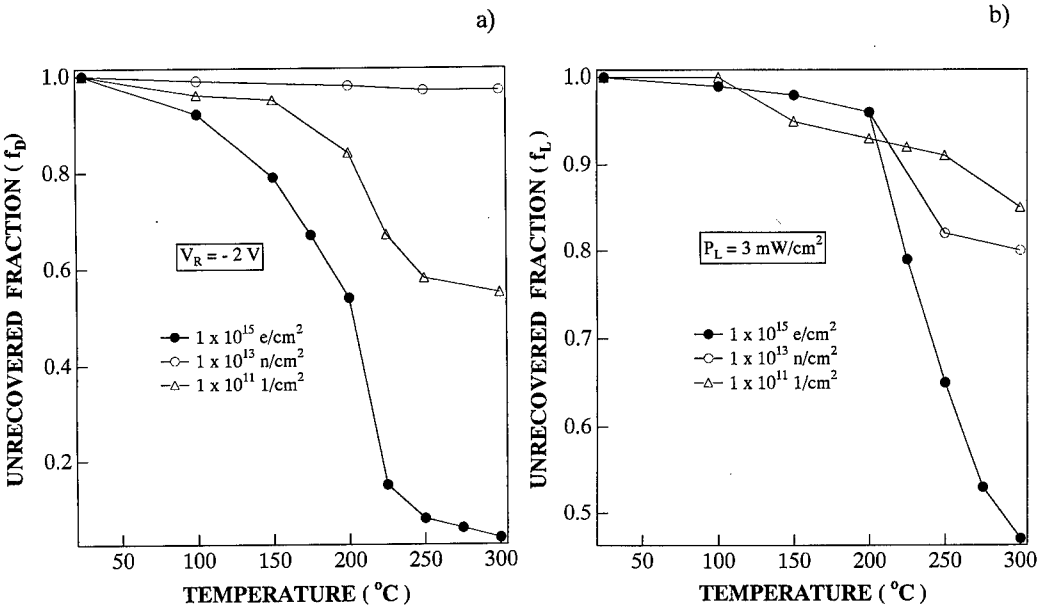

Figure 4 : Unrecovered fraction of dark (a) and photocurrent (b) as a function of annealing temperature for 1-MeV electrons, 1-MeV fast neutrons and 20-MeV alpha ray irradiation.

Conclusions

The main conclusions which can be made from the present study are:
1. The degradation of the electrical and optical performance of $In_{0.53}Ga_{0.47}As$ p-i-n photodiodes increases with increasing alpha ray fluence.
2. After irradiation, electron capture levels in the $In_{0.53}Ga_{0.47}As$ epitaxial layers are observed. The induced deep levels are mainly responsible for the increase of dark current and the decrease of photo current.
3. The damage coefficient is about one order of magnitude larger than that for neutron irradiation, and is about three orders of magnitude larger than that for electron irradiation. This difference is due to the different number of knock-on atoms, which is correlated with the difference of mass and the possibility of nuclear collisions for the formation of lattice defects.
4. The degraded performance recovers by thermal annealing for electron irradiation, while little recovery is observed for neutron and alpha ray irradiation.

Acknowledgments

Part of this work was supported by Giant-in-Aid for Scientific Research (No. 09045063) from the Japanese Ministry of Education for Science.

References

1. M. Capizzi, A. Polimeni, B. Bonanni, A. Frova, D. Marangio and F. Martelli, Semicond. Sci. Technol., **9**, 2233 (1994).
2. B. D. Evans, H. E. Hager and B. W. Hughlock, IEEE Trans. Nucl. Sci., **40**, 1645 (1993).
3. R. J. Walters, G. J. Shaw, G. P. Summers, E. A. Burke and S. R. Messenger, IEEE Trans. Nucl. Sci., **39**, 2257 (1992).
4. G. J. Shaw, R. J. Walters, S. R. Messenger and G. P. Summers, J. Appl. Phys., **73**, 1629 (1993).
5. G. J. Shaw, R. J. Walters, S. R. Messenger and G. P. Summers, J. Appl. Phys., **73**, 7244 (1993).
6. H. Ohyama, J. Vanhellemont, Y. Takami, K. Hayama, T. Kudou, H. Sunaga, Semicond. Sci. Technol., **11**, 1461 (1996).
7. S. R. Forrest and O. K. Kim, J. Appl. Phys., **53**, 5738 (1982).
8. M. Levinson and H. Temkin, Appl. Phys. Lett., **42**, 605 (1982).
9. H. Ohyama, J. Vanhellemont, Y. Takami, K. Hayama, H. Sunaga, J. Poortmans and M. Caymax, IEEE Trans. Nucl. Sci., **41**, 3019 (1994).

Materials Science Forum Vols. 258-263 (1997) pp. 1223-1228

ACCEPTOR-HYDROGEN INTERACTION IN InAs

A. Burchard [1], J. G. Correia [2], M. Deicher [1], D. Forkel-Wirth [2], R. Magerle [1], A. Prospero [1], A. Stötzler [1] and the ISOLDE Collaboration [2]

[1] Fakultät für Physik, Universität Konstanz, D-78457 Konstanz, Germany
[2] CERN / PPE, CH-1211 Geneva 23, Switzerland

Keywords: InAs, Cd-acceptors, hydrogen passivation, γ-ray spectroscopy, PAC spectroscopy

Abstract. The hydrogen passivation of the group IIB acceptor Cd in InAs was studied using the perturbed angular correlation spectroscopy. After low energy H^+ implantation up to three, different hydrogen correlated complexes are formed at the Cd probe atom. After H^+ implantation with an energy of 100 eV the well-known Cd-H pair, oriented along <111> lattice directions (ν_Q = 427 MHz, η = 0) and the complex C555 (ν_Q = 555 MHz, η = 0.19) were found. After H^+ implantation at 1 keV the Cd-H pair and a different complex C577 (ν_Q = 577 MHz, η = 0.09) are detected. Both, C555 and C577 transmute into Cd-H and the corresponding transformation energy is E_D = 1.0(1) eV. An interpretation of C555 and C577 in terms of Cd-H_x or Cd-H-defect complexes is possible. Besides these hydrogen correlated complexes a fourth one, C168, appeared after He^+ and hydrogen implantation. It is labeled by ν_Q = 168 MHz, η = 0.0 and its nature is not yet identified.

Introduction

Hydrogen represents one of the most interesting impurities in semiconductors [1,2], both from the technical and the scientific point of view. During various manufacturing process steps hydrogen is easily incorporated into the semiconducting material where it very efficiently interacts with other impurities or defects. Hydrogen appears ionized (H^+, H^-), atomic (H^0), stable molecular (H_2), metastable molecular (H_2^*) or precipitated (H-platelets) and this rather puzzling behavior poses problems in understanding processes like complex formation and hydrogen diffusion.
Since the late 80s perturbed angular correlation (PAC) spectroscopy experiments have been performed to study H in III-V semiconductors [3] and a considerable amount of new information could be provided concerning formation, microscopic structure and stability of acceptor hydrogen complexes. Recent successful PAC experiments on free hydrogen diffusion in III-V semiconductors for the first time opened a "microscopic" insight into this process by directly observing H [4].
In III-V semiconductors (GaN, GaAs, InAs, GaP, InP) the group IIB metal dopant Cd was employed to study the hydrogen passivation mechanism of acceptors[3,5,6,7]. In GaN two differently configured Cd-H pairs were observed as consequence of its wurtzite lattice structure [6,7], whereas only one Cd-H pair was detected in all the other, zincblende structured materials. In GaAs, InAs, InP and GaP the crystallographic orientation and the stability of the Cd-H pairs support a model proposed by Pajot [8] which favors H on the bond center site, forming H-P and H-As bonds instead of an acceptor-hydrogen bond.
In GaAs and InAs a second complex was found after plasma charging [9] and after low energy H^+ implantation[5,10]. Its formation, stability and microscopic structure was investigated in InAs as function of Cd concentration, H^+ implantation energy and the creation of radiation defects. The results clearly revealed, that hydrogen is a component of this complex [5], but a more detailed investigation required further experiments and the corresponding results are subject of the present contribution.

Experiment

Samples of undoped, LEC grown InAs were implanted with ^{111m}Cd ions at the PSB ISOLDE online mass separator at CERN. The implantation energy was 60 keV and the Cd doses 5×10^{11} cm^{-2}.

The projected range (R_p) as well as the straggling (ΔR_p) of the ions were calculated with the TRIM code [11] to be R_p = 25 nm and σ = 13 nm. In order to remove the radiation damage the samples were annealed at 923 K for 10 minutes in a sealed quartz ampoule under As overpressure. During the annealing process about 10% to 50 % of the Cd atoms diffused out of the crystals, resulting in a final Cd peak concentration of 1×10^{17} cm^{-3} within the implantation profile. After the annealing step the InAs crystals have been implanted at 300 K with H^+ ions at energies of 100 eV or 1 keV and a dose of 3×10^{14} cm^{-2}. This procedure allows a quantitative control of the introduced amount of H and avoids contamination by other impurities. For control experiments He^+ was implanted at an energy of 1 keV and a dose of 3×10^{14} cm^{-2}. Subsequent PAC measurements were performed at ambient temperature or 77 K.

The PAC technique [3] is based on the observation of the quadrupole hyperfine interaction between the nuclear quadrupole moment Q of a specific probe atom (here: $5/2^+$ state of ^{111}Cd) and the electric field gradient tensor (efg) the probe nucleus is exposed to. The efg is caused by the electrical charge distribution of the next nearest lattice surrounding of the probe atom and yields information on trapping and detrapping of impurities and defects at the Cd acceptor as well as on the microscopic structure of the formed complexes. Each complex is characterized by its specific quadrupole hyperfine interaction parameters: the strength of the interaction is described by the quadrupole coupling constant $\nu_Q = eQV_{zz}/h$, where V_{zz} represents the largest component of the efg tensor and the symmetry of the complex is reflected by the asymmetry parameter η of the efg tensor.

The quadrupole hyperfine interaction results in a three fold splitting of the $5/2^+$ state of ^{111}Cd which is detected by coincidence measurements of a γ-quantum populating the $5/2^+$ state and one depopulating it. These coincidence spectra are combined to form the R(t) spectra which in case of ^{111}Cd are composed by the superposition of three cosine functions. The frequency is proportional to ν_Q and the ratio of the three frequencies gives the asymmetry η of the efg. The relative amplitudes depend on the efg orientation with respect to the crystallographic axis, whereas the absolute amplitude is directly proportional to the total number of probe atoms, decorated by trapped defects or impurities.

Results and Discussion

After ^{111m}Cd implantation and annealing the radiation damage, more then 80% of the Cd probe atoms are located on unperturbed lattice sites in InAs. Subsequent hydrogen loading by low H^+ energy implantation results in the formation of various complexes. Figure 1a shows a PAC spectrum for samples implanted with ^{111m}Cd, annealed at 923 K and post-implanted with H^+ of an energy of 100 eV and a dose of 3×10^{14} cm^{-2}. The strong modulation of the R(t) spectrum clearly shows the existence of efg(s) at the probe nuclei and the corresponding Fourier transform of the R(t) spectrum reveals two frequency triplets. Each of them corresponds to a specific complex, in future named C427 and C555, respectively. C427 is characterized by a quadrupole coupling constant ν_Q = 427(2) MHz and an asymmetry parameter η = 0.00(1) whereas C555 is labeled by a quadrupole coupling constant ν_Q = 555(2) MHz and η = 0.19(1) (see Tab. 1). In total 70% of the Cd acceptors are involved in these complexes. Figure 1b gives PAC data for samples doped with ^{111m}Cd and annealed as described above but post-implanted with H^+ at an energy of 1 keV and a dose of 3×10^{14} cm^{-2}. The obtained results are very similar to those observed after H^+ implantation with 100 eV: the R(t) spectrum shows a clear time modulation and the corresponding Fourier transform shows two frequency triplets characterizing two complexes. One of them (C427) is identical to the one found after implantation with 100 eV, but configuration C577 differs from C555: it is specified by ν_Q = 577(2) MHz and an asymmetry parameter η close to zero (η = 0.09(1)). In total 70% of the Cd acceptors are involved in C427 and C577 after 1 keV H^+ implantation. After He^+ implantation at an energy of 1 keV and dose 3×10^{14} cm^{-2} none of these three complexes is observed (see Fig. 1c).

To determine the orientation of the efg tensors PAC measurements were performed under different orientations of the <100> InAs crystals with respect to the four γ-detectors. Figure 2 shows the Fourier transforms of the corresponding R(t) spectra for three different orientations (<100>, <110>,

<111>) [1] after H^+ implantation with 1 keV (Fig. 2a) and at 100 eV (Fig. 2b). An analysis of the Fourier transforms clearly proves that C555 and C577 are oriented into a <110> lattice direction whereas complex C427 is aligned into the <111> crystal direction. The characteristic PAC data of all observed complexes are listed in Table 1.

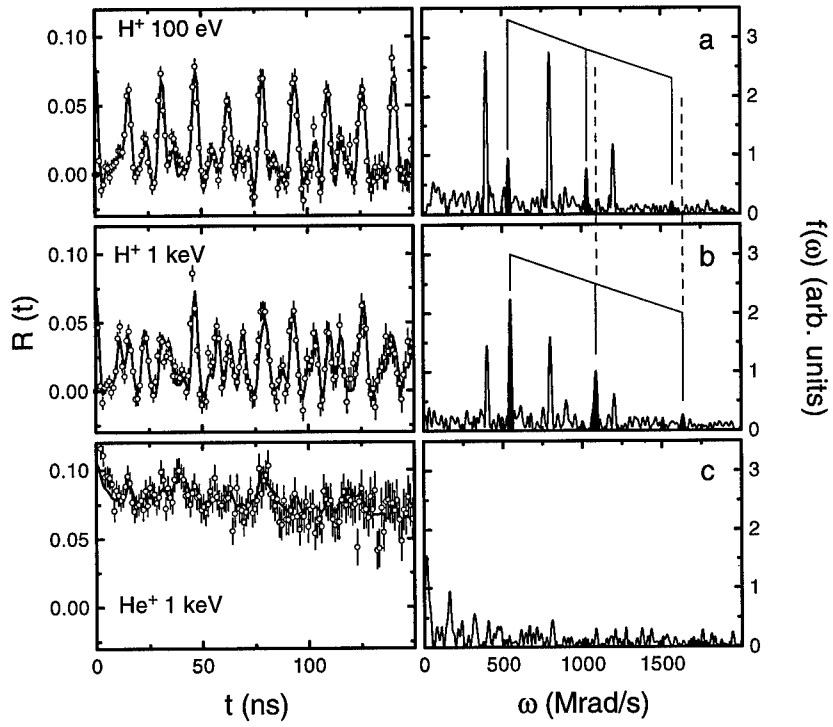

Fig. 1: PAC spectra and corresponding Fourier transforms of InAs implanted with ^{111m}Cd (60 keV, 5×10^{11} cm^{-2}) at 295 K, annealed at 923 K and post-implanted with a) H^+ (100 eV, 3×10^{14} cm^{-2}), b) H^+ (1 keV, 3×10^{14} cm^{-2}) and c) He^+ (1 keV, 3×10^{14} cm^{-2}). The Fourier transform a) shows two frequency triplets which correspond to the formation of two complexes C427 and C555 (black triplet) and b) shows two frequency triplets which correspond to the formation of C427 and C577 (black triplet).

Besides the characteristic PAC parameters like quadrupole coupling constants or asymmetry parameters the knowledge of the formation conditions and of the stability of the complexes is necessary to interpret the observed configurations. In previous experiments on plasma charged InAs crystals a decrease of fraction C577 accompanied by a simultaneous increase of fraction C427 was observed [12]. Consecutive PAC measurements on one sample at room temperature after H^+ implantation with 1 keV confirmed this trend: the concentration of C577 complexes is decreasing with increasing time whereas the number of C427 is increasing and the sum of both fractions remains constant [5]. This observation is confirmed by our present results of consecutive PAC measurements with a time interval of 10 min: immediately after the H^+ implantation with 1 keV both complexes, C427 and C577 are present at room temperature. With increasing time the fraction C577 decreases and the fraction of C427 increases, whereas the sum of both fractions remains constant within the experimental error. Assuming that this transmutation of C577 happens via a single jump mechanism a least square fit to the data yields a dissociation energy of E_D = 1.0(1) eV. The corre-

[1] The terminology <abc> describes the experimental set-up: each detector is pointing into the direction of a <abc> crystal axis.

sponding attempt frequency was assumed to be $\nu = 1\times10^{13}$ s^{-1}. In case of a 100 eV H^+ implantation similar observations were made: immediately after the hydrogen loading two complexes, C555 and C427 are formed. With increasing time, the fraction of C555 is disappearing and the one of C427 is increasing whereas the sum of both fractions remains constant (see Fig. 3). Under the same assumptions as in case of C577 a dissociation energy of $E_D = 1.0(1)$ eV for C555 is extracted.

Tab. 1: *PAC parameters for the three hydrogen correlated complexes C427, C555 and C577 as well as for complex C168 in InAs. ν_Q denotes the quadrupole coupling constant at 295 K, η describes the symmetry and <ijk> the orientation of the efg tensor. E_D gives the dissociation energy of the complex.*

Complex	ν_Q (MHz)	η	Orientation	E_D (eV)	Interpretation
C427	427(2)	0.00(1)	<111>	1.4(1)	Cd-H pair
C555	555(2)	0.19(1)	<110>	1.0(1)	Cd-H_x, Cd-H-defect
C577	577(2)	0.09(1)	<110>	1.0(1)	Cd-H_x, Cd-H-defect
C168	168(2)	0.0(1)	?	?	?

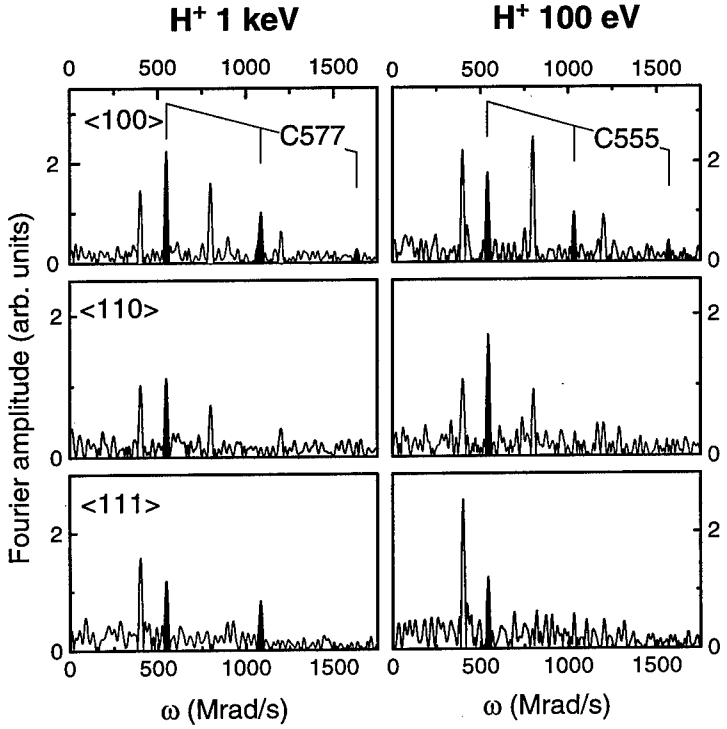

Fig. 2: *Fourier transforms of PAC spectra of InAs implanted with ^{111m}Cd and post-implanted with H^+ at 1 keV (left) and H^+ at 100 eV (right), respectively. The results for three different orientations of the crystal axis with respect to the 4 γ-detectors indicate, that C427 is oriented in <111> lattice direction, whereas C577 and C555 are oriented in <110> direction.*

The fact, that all three complexes (C427, C555, C577) cannot be produced by He^+ implantation (1 keV, 3×10^{14} cm^{-2}) but only if hydrogen is present clearly proves the involvement of H in all three configurations.
The symmetry of complex C(427) ($\eta = 0$, <111> lattice orientation) and its stability ($E_D = 1.4$ eV) already favored in a very early state of the investigations the assignment of the most simple hydrogen correlated configuration, the Cd-H pair to C427 [9,12]. Following the model of Pajot [8], we proposed that H^- is trapped by the Cd^+ acceptor due to Coulomb interaction, the bond between Cd and As is broken and H finally occupies the bond center site, establishing a bond to the next nearest As atom [3,9].

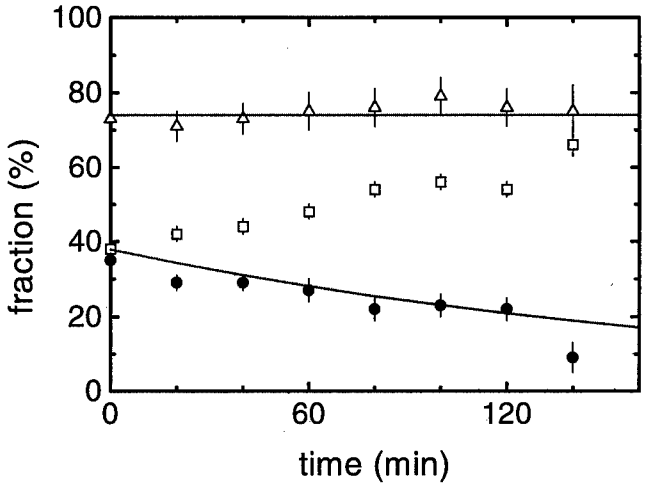

Fig. 3: Time development of the fractions of the two hydrogen correlated complexes C427 (open squares) and C555 (solid circles) measured at room temperature. The sum of both fractions (open triangles) remains constant, whereas the fraction of C427 increases and the one of C555 decreases.

Complex C(577) was observed after plasma charging and after H^+ implantation with an energy of 1 keV [5]. The orientation of the corresponding efg tensor into <110> direction indicates a more complicated microscopic configuration as the one of a Cd-H pair. This assumption is also supported by the observed transmutation of C577 into C427, which could be explained by a Cd-H-defect or Cd-H_x complex which decays into Cd-H pairs by releasing one of its partners, the defect or one of the hydrogen atoms. The fact that C555 and C577 transmute into C427 by dissociation supports the interpretation of C427 as Cd-H pair.
C555 can be produced by H^+ implantation at 100 eV and for its interpretation similar arguments hold as in case of C577. The orientation of the efg tensor in <110> direction together with an asymmetry parameter of $\eta = 0.19(1)$ points also to a more complicated microscopic structure. Since C555 also transmutes into Cd-H pairs and its characteristic PAC data are similar to those of C577 an interpretation in terms of Cd-H-defect or Cd-H_x complexes seems reasonable. The dissociation of C555 into C427 would also happen via the release of one or more of the partners involved in the complex.
Experiments on hydrogenated GaAs:Cd show the same trend as in InAs [10]. Besides the Cd-H pair additional, hydrogen correlated complexes are observed after 1 keV and 100 eV H^+ implantation.
Besides the hydrogen correlated complexes a fourth configuration C168 was found in InAs after He^+ implantation and more evident after H^+ implantation at 100 eV and 1 keV. C168 is characterized by $\nu_Q = 168(2)$ MHz and an asymmetry parameter $\eta = 0$. The fraction of C168 is rather small (~ 15% of the Cd probe atoms are involved in C168) compared to a fraction of 60% - 80 % of Cd probe atoms involved in the hydrogen correlated complexes. An interpretation in terms of radiation defects seems to be unlikely, since the maximum energy which can be transferred by a 100 eV H^+

ion to an In- or As atom (In: 3.5 eV, As: 5.2 eV) is lower than the displacement energy for these atoms as measured by Bäuerlein (In: 6.7 eV, As: 8.5 eV) [13]. At the moment we have no interpretation for this defect complex but the small efg would favor a more distant defect not located on a nearest interstitial site to the Cd.

Conclusion

After low energy H^+ implantation in total up to four different complexes formed at Cd acceptors in InAs (C427, C555, C577, C168) are observed. Three of them are unambiguously correlated with hydrogen and are interpreted as Cd-H pairs, oriented in <111> lattice direction (C427), and two more complicated complexes like Cd-H_x of Cd-H-defect configurations (C555, C577) with efg tensors oriented in <110> lattice directions. The dissociation energy of C555 and C577 is E_D = 1.0(1) eV and the process itself happens via releasing one partner (defect or H) and forming a Cd-H pair. The nature of the fourth complex C168 is not understood until now.
Our PAC studies clearly demonstrate that the hydrogen passivation mechanism in InAs is rather complicated and cannot be explained only by the formation of close acceptor-hydrogen pairs. We will continue the investigations of the passivation mechanism in InAs by employing D instead of H and by studying the formation and stability of the complexes in function of the Cd-, H and D concentration.

Acknowledgment

This work has been funded by the Bundesministerium für Bildung, Wissenschaft, Forschung und Technologie under contract number 03-RE4KO1-5.

References

1. *Hydrogen in Semiconcuctors*, ed. J. I. Pankove and N.M. Johnson, (Semiconductors and Semimetals Vol. 34, Academic Presss, San Diego,1991).
2. *Hydrogen in Compound Semiconductors*, ed. S.J. Pearton (Materials Science Forum Vol. 148 - 149, Trans Tech Publications, Aedermannsdorf, 1994).
3. M. Deicher, W. Pfeiffer in ref. [2], p. 481.
4. A. Burchard, M. Deicher, R. Magerle, A. Egenter, R. Spengler and D. Forkel-Wirth, in: *7th International Conference on Shallow Level Centers in Semiconductors*, ed. C.A. Ammerlaan and B. Pajot (World Scientific, Singapore, 1997), p. 185.
5. D. Forkel-Wirth, N. Achtziger, A. Burchard, J.G. Correia, M. Deicher, J. Grillenberger, H. Gottschalk, T. Licht, R. Magerle, U. Reislöhner, M. Rüb, M. Toulemonde and W. Witthuhn, in: *Proc. of the 18th Intl. Conf. on Defects in Semiconductors*, ed. M. Suezawa and H. Katayama-Yoshida (Mat. Sci. For. **196-201,** Trans Tech Publications, Zürich, 1995) p. 987.
6. A. Burchard, M. Deicher, D. Forkel-Wirth, E.E. Haller, R. Magerle, A. Prospero and A. Stötzler, in: *III-V Nitrides*, ed. F.A. Ponce, T.D. Moustakas, I. Akasaki and B.A. Monnemar (Mat. Res. Soc. Symp. Proc. Vol. 449, Pittsburgh, 1997) p. 961.
7. A. Burchard, M. Deicher, D. Forkel-Wirth, E.E. Haller, R. Magerle, A. Prospero and A. Stötzler, this conference.
8. B. Pajot, Inst. Conf. Ser. **95,** 437 (1989).
9. A. Baurichter, M. Deicher, S. Deubler, D. Forkel, H. Plan, H. Wolf andW. Witthuhn, Appl. Phys. Lett. **55,** 2301 (1989).
10. A. Burchard et al., to be published.
11. J.P. Biersack and I.G. Haggmark, Nuclear Instruments and Methods **174,** 257 (1980).
12. A. Baurichter, M. Deicher, S. Deubler, D. Forkel, J. Meier and W. Witthuhn, in: *Proc. of the 16th Intl. Conf. on Defects in Semiconductors*, ed. G. Davies, G.G. DeLeo and M. Stavola (Mat. Sci. For. **83-87,** Trans Tech Publications, Zürich, 1992) p.593.
13. R. Bäuerlein, Zeitschrift f. Physik **176**, 498 (1963).

Materials Science Forum Vols. 258-263 (1997) pp. 1229-1234

ELECTROLUMINESCENCE OF III-NITRIDE DOUBLE HETEROSTRUCTURE LIGHT EMITTING DIODES WITH SILICON AND MAGNESIUM DOPED InGaN

A. Saxler, K. S. Kim, D. Walker, P. Kung, X. Zhang, G. J. Brown[1], W. C. Mitchel[1], and M. Razeghi

Center for Quantum Devices, Department of Electrical and Computer Engineering, Northwestern University, Evanston, IL 60208

[1]Air Force Research Laboratory, Materials Directorate, Wright-Patterson AFB, OH 45433-7707

Keywords: InGaN, light emitting diode, doping, magnesium, silicon, electroluminescence

Abstract. GaN/InGaN/GaN double heterostructures were deposited by low pressure metalorganic chemical vapor deposition. Two different structures are studied: one with a silicon doped InGaN layer and the other with a magnesium doped InGaN layer. The electroluminescence spectrum is shifted to longer wavelengths in the structure with the magnesium doped InGaN layer. An additional red peak is seen in the electroluminescence spectrum of the magnesium doped structure. We believe this peak may be due to a transition metal (i.e. Cr) which absorbs in the green and emits in the red.

Introduction.

The III-Nitrides are wide bandgap semiconductors with many potential applications including solar blind photodetectors [1], blue light emitting and laser diodes [2], and high temperature and high power electronics [4]. We have previously reported on the growth [4-6] of III-Nitrides, their characterization [7,8], and photodetectors [9,10] made from these materials. In this paper we report on the electroluminescence of double heterostructure light emitting diodes as a function of the doping type of the active layer.

Experimental.

The films were grown in a horizontal low pressure metalorganic chemical vapor deposition reactor. Triethylgallium (TEGa), trimethylgallium (TMGa), trimethylindium (TMIn), biscyclopentadienylmagnesium (Cp_2Mg), dilute silane (SiH_4), and ammonia (NH_3) were used as precursors. All of the films were grown on (0001) Al_2O_3 substrates with a low temperature GaN buffer layer.

Figure 1 shows schematic diagrams of the two double heterostructure devices which were grown and fabricated. After the buffer layer was deposited, a 1 μm thick silicon doped GaN layer with an electron concentration of 5×10^{18} was grown. This was followed by a 2000 Å InGaN active layer and a 2000 Å magnesium doped GaN layer. In the first structure the active layer was silicon doped, while in the second structure the active layer was magnesium doped. After dry etching down to the n-type layer, Ti/Au contacts were deposited. The p-type contacts were Ni/Au.

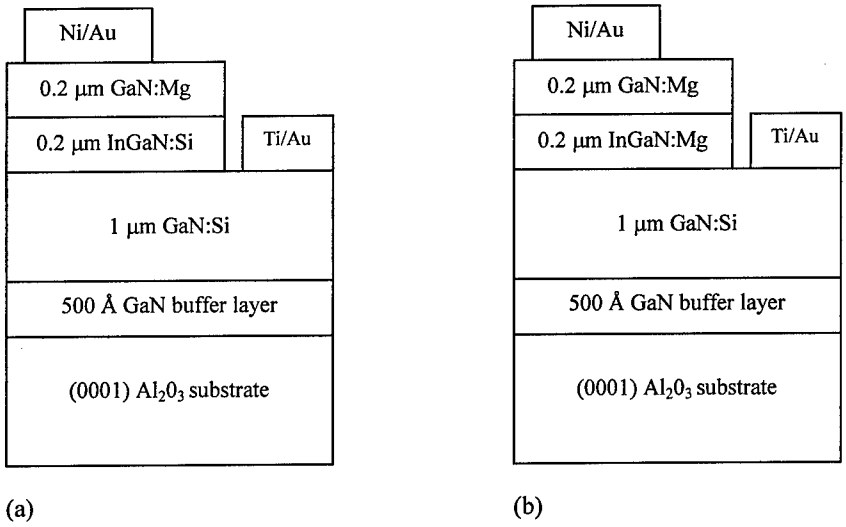

Fig. 1. Schematic drawing of double heterostructures with (a) n-type and (b) p-type active layers.

Results and Discussion.

The I-V curves of the two diodes are shown in Fig. 2. Both diodes exhibit low currents with reverse bias. The structure with the magnesium doped InGaN layer showed a lower turn on voltage than the structure with the silicon doped InGaN layer.

Figure 3 shows the electroluminescence curve of the double heterostructure with the silicon doped InGaN layer. A broad blue emission peak can be seen in the electroluminescence spectrum. The emission may be from magnesium related transitions in the GaN.

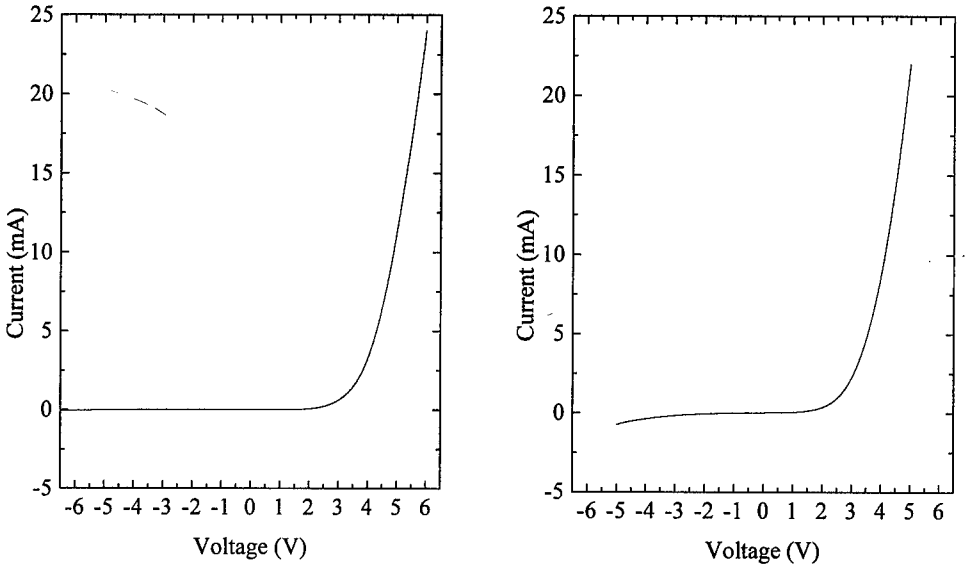

Figure 2. I-V curves of the double heterostructures with a (a) n-type and (b) p-type InGaN layer.

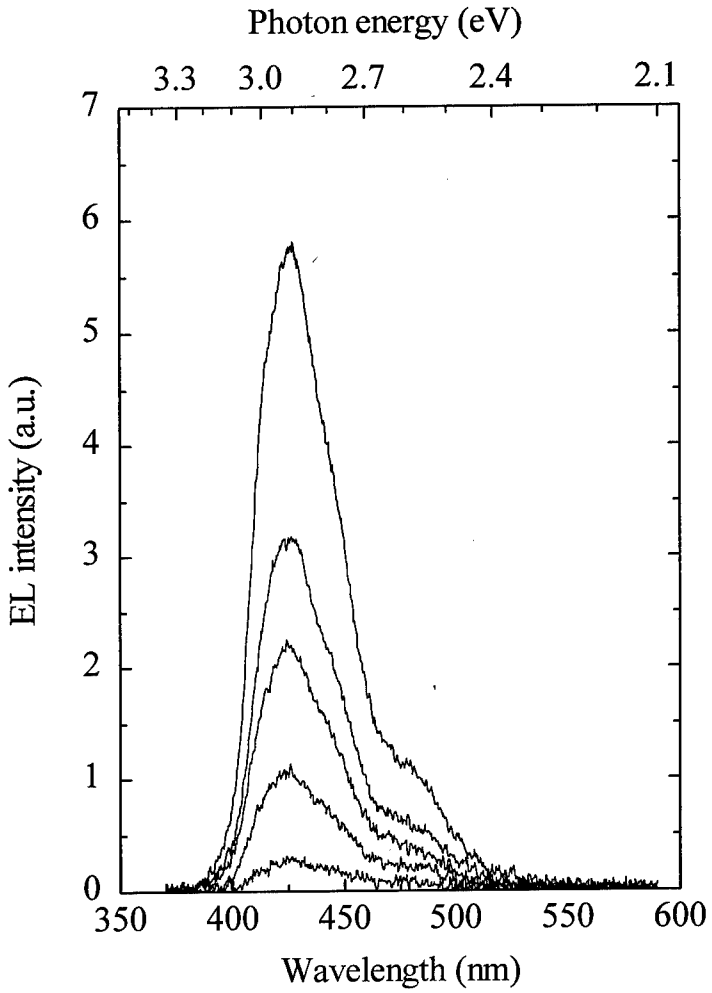

Fig. 3. Voltage dependent electroluminescence spectrum of the structure with a silicon doped InGaN layer.

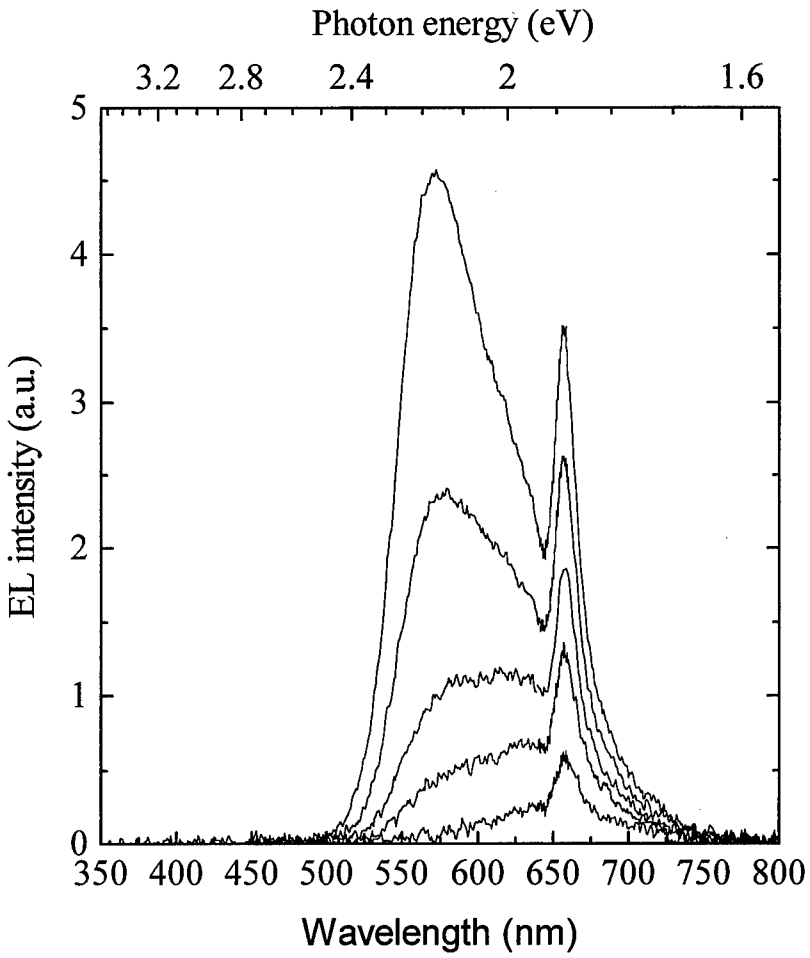

Fig. 4. Voltage dependent electroluminescence spectrum of the structure with a magnesium doped InGaN layer.

Figure 4 shows the electroluminescence of the structure with the magnesium doped InGaN layer. At low bias the red peak is dominant. As the bias is increased, the green peak begins to dominate. The green peak appears to be due to the magnesium related transition in the InGaN layer. The origin of the red peak is under further investigation. It is possible that the red peak

is due to a transition metal (i.e. Cr) which has an absorption band in the green and a red emmision band.

Acknowledgements.

The authors would like to thank M. Yoder, Y.-S. Park, and C. Wood of ONR, A. Husain of DARPA, and P. Shu, B. Mott, and Z. C. Huang of NASA for their support and encouragement. Funding for this work was received under ONR/BMDO Grant N00014-93-1-0235 and DARPA/ONR Grant N00014-96-1-0714.

References.

1. M. Razeghi and A. Rogalski, J. Appl. Phys. **79**, 7433 (1996).
2. S. Nakamura, M. Seno, S. Nagahama, N. Iwasa, T. Yamada, T. Matsushita, Y. Sugimoto, and H. Kiyoku, Appl. Phys. Lett. **69**, 4056 (1996).
3. O. Aktas, Z. F. Fan, S. N. Mohammed, A. E. Botchkarev, and H. Morkoç, Appl. Phys. Lett. **69**, 3872 (1996).
4. P. Kung, A. Saxler, X. Zhang, D. Walker, T. C. Wang, I. Ferguson, and M. Razeghi, Appl. Phys. Lett. **66**, 2958 (1995).
5. A. Saxler, P. Kung, C. J. Sun, E. Bigan, and M. Razeghi, Appl. Phys. Lett. **64**, 339 (1994).
6. P. Kung, A. Saxler, X. Zhang, D. Walker, R. Lavado, and M. Razeghi, Appl. Phys. Lett. **69**, 2116 (1996).
7. A. Saxler, M. A. Capano, W. C. Mitchel, P. Kung, X. Zhang, D. Walker, and M. Razeghi, MRS Symposium Proceedings **449**, 477 (1997).
8. X. Zhang, P. Kung, D. Walker, A. Saxler, and M. Razeghi, MRS Symposium Proceedings **395**, 625 (1996).
9. X. Zhang, P. Kung, D. Walker, J. Piotrowski, A. Rogalski, A. Saxler, and M. Razeghi, Appl. Phys. Lett. **67**, 2028 (1995).
10. D. Walker, X. Zhang, A. Saxler, P. Kung, J. Xu, and M. Razeghi, Appl. Phys. Lett. **70**, 949 (1997).

Materials Science Forum Vols. 258-263 (1997) pp. 1235-1240

EFFECT OF NEUTRON IRRADIATION ON Ga-BASED SEMICONDUCTORS

L.C. Damonte, F.J. Navarro[1], J.L. Ferrero[2], A.Segura[2] and V. Muñoz[2]

Dpto. Física, Fac. Ciencias Exactas, Universidad Nacional de La Plata, Argentina.
[1]Dpt. Física Aplicada, Universitat Politécnica de València, 46071-València, Spain.
[2] Inst. Ciència de Materials, Universitat de València, 46100-Burjassot, Spain.

Keywords: Neutron irradiation, positron annihilation, GaSe, GaS

ABSTRACT

Neutron irradiation GaS and GaSe single crystals have been investigated by positron lifetime and Doppler broadening measurements. The samples were irradiated at fluences yielding estimated Ge concentrations within $2.5x10^{15}$ and $2x10^{16}$ cm^{-3}. The positron annihilation parameters (average lifetime, τ_m, and parameter S) have shown a saturation effect with increasing radiation doses. A second lifetime component was found of 335 ps in GaSe and of 330 ps in GaS. These lifetimes have been associated to Ga-monovacancy related defects.

INTRODUCTION

Positron annihilation tecnique (PAT) has demonstrated its capability to detect defects in semiconductors materials [1]. However it seems that PAT has been scarcely applied to III-VI layered semiconductors [2-4]. These compounds have attracted much attention in the last years due to their electronic transport properties and non-linear optical coefficients. They have a structure formed by layers containing monoatomic planes stacked in a sequence Ga-Se-Ga-Se. The layers are bound by Van der Waals forces, while within a layer the binding between atoms is covalent. GaS and GaSe belong to this group and they have not been as extensively studied by PAS as InSe (the most representative). It may be expected that this two dimensional scheme yields similar positron annihilation characteristics in all this group.

Neutron Transmutation Doping (NTD) is a convenient method for semiconductor doping purpose when a precise amount and a homogeneous distribution of the impurities are required [5-7]. NTD relies on the capture of thermal neutrons by the host lattice nuclei. The process depends on the capture cross-sections and the natural abundance of each isotope. The main impurity introduced in GaSe and GaS by NTD is Ge, which comes from the transmutation of the ^{69}Ga (60%) and ^{71}Ga(39.9%) isotopes according to the following reactions:

$$^{69}Ga(n,\gamma)^{70}Ga \rightarrow ^{70}Ge+\beta^- \quad ; \sigma_c = 1.7 \text{ b}$$
$$^{71}Ga(n,\gamma)^{72}Ga \rightarrow ^{72}Ge+\beta^- \quad ; \sigma_c = 4.6 \text{ b}$$

where σ_c is the thermal neutron cross-section. The rest of the isotopes yield estimated concentrations of transmuted atoms of less than 10^{15} cm^{-3}, which are too low for the PAT sensitivity. During the NTD process some lattice defects are created due to the γ and β particles produced in the nuclear reactions and also due to the fast neutrons which

unavoidably accompany the thermal neutrons flux and cannot be completely eliminated. In this situation, the recoil energy transmitted to the involved atom through the β^- and γ decay can displace the resultant Ge-atoms from their initial Ga sites to interstitial positions [5-7]. PAT as a technique sensitive to vacancies, can be useful to investigate the nature and charge state of those vacancy related defects created during irradiation.

EXPERIMENTAL

The GaSe and GaS single crystals were irradiated at different fluences in order to obtain Ge transmuted concentrations in the range (2.5-20)x10^{15} cm^{-3} . Due to the low flux used $\phi \approx 4x10^{11}$ $n°cm^{-1}s^{-1}$ (En < 0.04 eV), the samples remained at room temperature during the irradiation.

Positron lifetime spectra were recorded at room temperature using a fast-fast lifetime equipment with a resolution of 300 ps (FWHM). The spectra were analyzed after subtracting a source correction of two components: Kapton foil contribution with a component of 382ps/13%, and a long lifetime component of 1ns/1%. The Doppler broadening energy measurements were carried out using a Ge(HP) detector with a resolution near to 1.30 keV in the region of the 477 keV line of ^{7}Be.

RESULTS AND DISCUSSION

Before irradiation, the lifetime spectra are well described in terms of one exponential component. The lifetime values obtained, 287±1 ps for GaSe and 291±2 ps for GaS, are slightly different from those reported by De la Cruz *et al.* [4] (293 ps for GaSe and 300 ps for GaS). These differences can be attributed to the different source and source corrections employed.

After irradiation, the lifetime spectra have been fitted with two exponential decay components. In both semiconductors, a second long lifetime component τ_2 is found, 335±4 ps (GaSe) and 330±4 ps (GaS), which indicates that certain lattice defects induced by thermal neutrons can be effective positron traps. The short lifetime component, τ_1, decreases with the Ge concentration from 174 to 160 ps (GaSe) and from 260 to 199 ps (GaS).

Figure 1 shows the evolution with the [Ge] concentration of the following positron annihilation parameters: the intensity I_2, the average positron lifetime τ_m calculated from the lifetime parameters as $\Sigma_i I_i \tau_i$, and the adimensional parameter S defined as the fraction of counts in a central region of the annihilation peak (511 keV). This last parameter is roughly related to the fraction of positrons annihilated with valence electrons [8].

The intensity I_2 increases with growing [Ge] concentrations to a constant value close to 90% ([Ge]=2x$10^{16}$$cm^{-3}$). Above an estimated Ge concentration of 5x10^{15} cm^{-3}, τ_m remains constant with a value of 311±5 ps (GaSe) and 310±6 ps (GaS). The evolution of the parameter S also shows a similar effect above the same concentration.

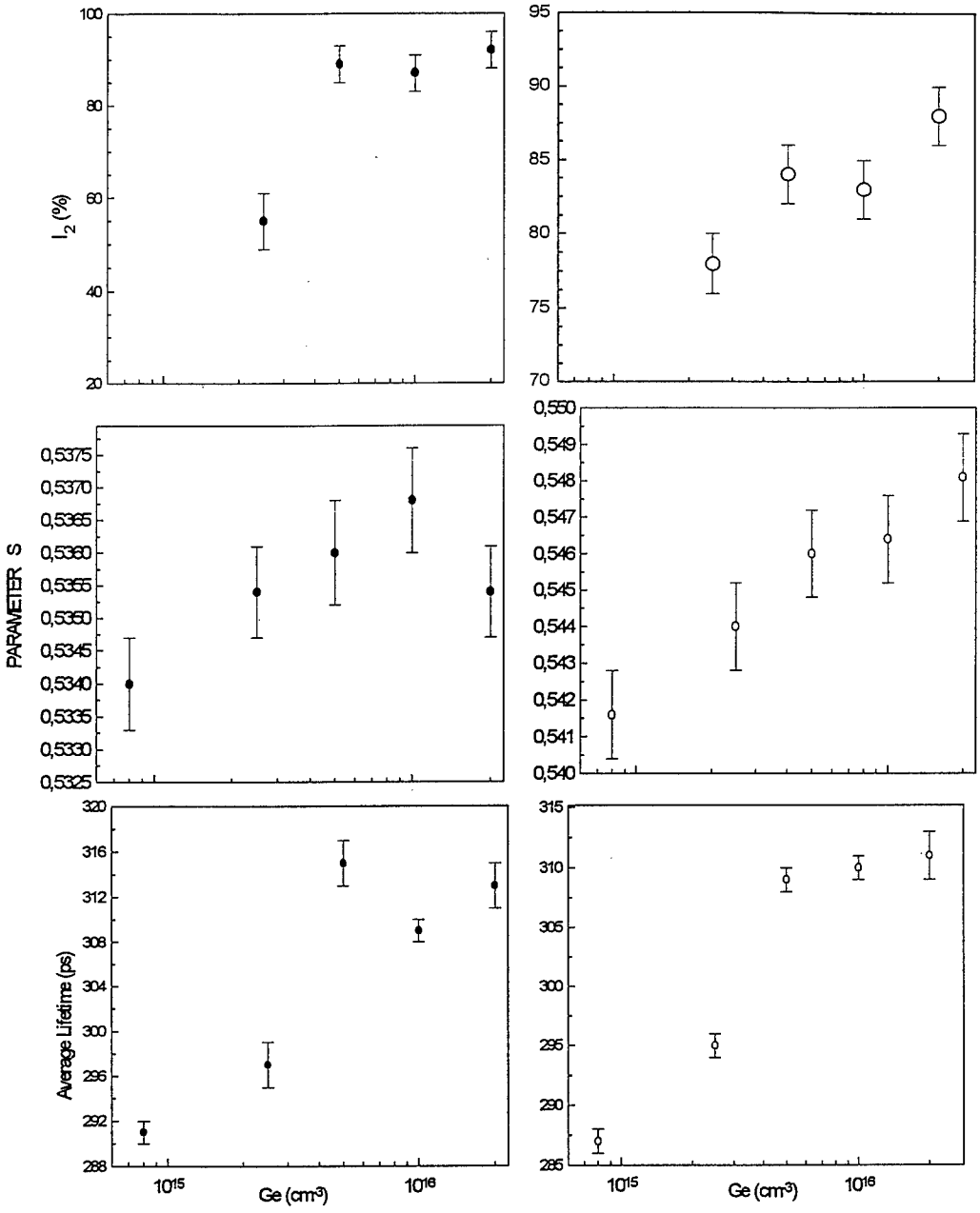

Fig. 1. Lifetime parameters for GaSe (empty circles) / GaS(full circles) versus Ge concentration (cm^{-3}). For comparison purposes, lifetime parameters obtained before irradiation are plotted at $8x10^{15}$ cm^{-3}.

The rise of the average positron lifetime, τ_m, above the bulk lifetime (287ps/GaSe; 291ps/GaS) and of the parameter S after irradiation, gives clear evidence of the positron trapping at vacancy-type defects. Positrons trapped at vacancy related defects annihilate with lifetimes longer than in bulk, because in the regions of the defect, positrons encounter electron densities lower than in the perfect lattice. The increase in τ_m (from 295 to 311 ps in GaSe; from 297 to 313 ps in GaS), and the value of τ_2 nearly constant in 335 ps (GaSe) and in 330 ps (GaS), with a change in lifetime relative to the bulk lifetime of $\Delta\tau_2$ in the range of 48 ps in GaSe and 39 ps in GaS, can be associated, according to theoretical calculations [9], to positron trapped at monovacancy related defects. In the absence of data for GaS and GaSe, we take the compound semiconductors GaP and GaAs for comparison, respectively. The lifetime rise associated with Ga-monovacancies (V_{Ga}) relative to bulk lifetime calculated by these authors is 40 ps in GaP and 36 ps in GaAs, while the increase is 39 ps for As-monovacancies (V_{As}). The values obtained in the present work were close to these values. So the observed τ_2 lifetimes might be associated with monovacancy related defects.

This explanation agrees well with the type of defect expected from the transmutation process where mainly points defects are produced by the γ and β particles involved in the doping process. In this process, vacancies can be formed in both sublattice and positrons can be trapped by one of both of them. Nevertheless, although it is expected that τ_2 was a mixture of defects produced in the two sublattices, at least an important contribution of the positron traps would be V_{Ga} related defects.

We can analyse the dose effects displayed in figure 1 in the framework of the one-state trapping model [10]. The positron trapping rate, K, is related to the defect concentration C_d attractive to positrons as:

$$K = \mu\, C_d \qquad \text{(Eq. 1)}$$

where μ is the specific trapping rate of defects. From the experimental lifetime parameters (τ_i,I_i), the trapping rate K can be given using:

$$K = I_2 \left(1/\tau_1 - 1/\tau_2 \right) \qquad \text{(Eq.2)}$$

Figure 2 shows the K values versus Ge estimated concentration. From this plot, the specific trapping rate can be roughly calculated using the equations 1 and 2. A linear fit yields a value of 4×10^{-17} cm^3 ns^{-1} (GaSe) and of 9×10^{-17} cm^3ns^{-1} (GaS). These values agree with the specific trapping rate of neutral monovacancy in GaAs (in absence of data for GaSe/GaS), 1×10^{-17} cm^3ns^{-1} estimated by Dannefaer *et al.* [11].

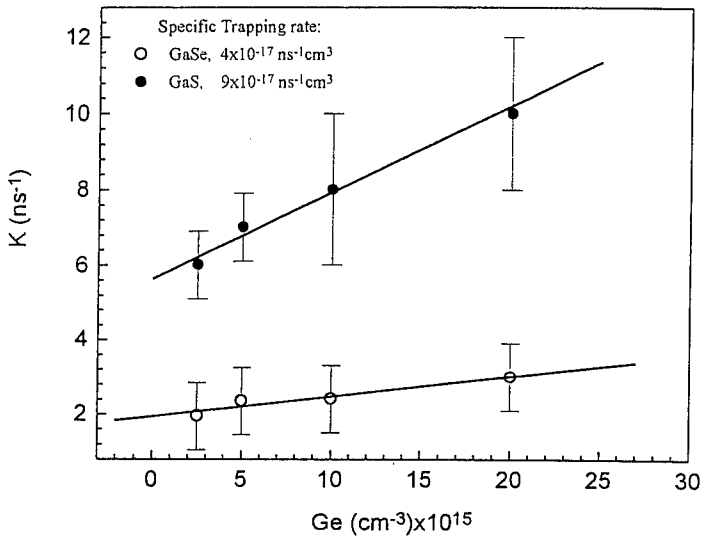

Fig. 2. Estimation of the specific trapping rate, μ , for GaSe and GaS according to the trapping model (Equation 1.).

CONCLUSIONS

After thermal neutron irradiation, a new second lifetime component τ_2 =335 ps for GaSe and 330 ps for GaS is found. These results show that certain lattice defects induced by irradiation act as effective positron traps. These defects are identified as gallium monovacancies related defects.

ACKNOWLEDGMENTS

The authors are grateful to Dr. A. Stampfler for the neutron irradiation at the Service de la Pile Universitaire (CRN, Strasbourg). They are grateful also to Dr. R. Pareja for their comments.

REFERENCES

[1] ICPA88. Positron Annihilation. Proceedings of the 8th International Conference on Positron Annihilation, Ghent, 1988, edited by L. Dorikens-Vanpraet, M. Dorikens and D. Segers. World Scientific, Singapore (1989).
[2] R.M. de la Cruz, R. Pareja, A. Segura and A. Chevy, J. Phys. C: Solid State Phys. **21**, 4403(1988).
[3] R.M. de la Cruz, R. Pareja, A. Segura, P. Moser and A. Chevy, Appl. Phys. **A54**, 147(1992).
[4] R.M. de la Cruz, R. Pareja, A. Segura, V. Muñoz and A. Chevy,

J. Phys:Condensed Matter **5**, 971(1993).
[5] M.A. Vesaghi, Phys. Rev. **B25**, 5436(1982).
[6] B.Lee, N.Pan, G.E.Stillman and K.L.Hess, J. Appl. Phys. **62** 1129(1987).
[7] B.Boudart, B. Marí, B. Prévot and C. Schwab, Nucl. Inst. Met. **B63**, 101(1992).
[8] R.N.West. Positron in Solids. Pgs:89-144.
Ed: P. Hautojärvi. Springer-Verlag Berlin Heidelberg New York (1979).
[9] M.J.Puska, S.Mäkinen, M. Manninen and R. Nieminen, Phys. Rev. **B39** 7666(1989).
[10] M.J. Puska and R.M. Nieminen, Rev. Mod. Phys. **66** 841(1994).
[11] S. Dannefaer, P. Mascher and D. Kerr, J.Phys:Condens. Matter **1** 3213(1989).

Materials Science Forum Vols. 258-263 (1997) pp. 1241-1246

POLARON COUPLING FOR SULPHUR IMPURITY IN GASB

[1]P. Kaczor, [1]A. Zakrzewski, [1]L. Dobaczewski, [1]Z. Kaliński,
[2]A. M. Gerrits and [2]J. Perenboom

[1]Institute of Physics, Polish Academy of Sciences
Al. Lotników 32/46 02-668 Warsaw, Poland
[2]High Field Magnet Laboratory - University of Nijmegen,
P.O. Box 9010 NL - 6500 GL,
Nijmegen, The Netherlands

Keywords: magnetopolaron effect, bound polaron, metastable defects, shallow-deep transition

Abstract. We present a detailed far infrared absorption study of the intra-center 1s-2p shallow donor transition in GaSb:S in high magnetic fields. From this study an information about the binding energy, polaron coupling strength and metastable transition mechanism could be obtained.

Introduction.

Although the DX centres in III-V semiconductors belong to the most investigated defect systems in last fifteen years there are still some unsolved problems. Among them there is a microscopic identification of processes leading to metastability effects observed for the sulfur donor in GaSb. This donor forms in GaSb the DX state possible to observe at ambient pressure [1][2]. Until recently [3] it was the only known case for a binary III-V compound.

The unusual features of GaSb:S - the persistent photoconductivity (PPC) effect at low temperatures and the photoinduced decrease of conductivity at elevated temperatures were known since the early seventies [1]. At that time they were attributed to the doping unhomogenities in the sample. Later [2] these memory effects were associated with the large lattice relaxation of the sulfur defect. In early nineties there has been shown [4] that the ground state of the sulfur defect has a negative correlation energy for electrons (negative-U system). The similarity of the effects related to sulfur in GaSb to that exhibited by the DX-type defects in e.g. CdF_2 [5] and AlGaAs [6] was striking.

In the present paper we investigate the metastable, photoinduced IR-absorption band related to a single shallow donor which is a characteristic feature of the shallow-deep bistability common to the DX-type defects. This band exhibits a Zeeman splitting in the magnetic field and can be identified as a 1s-2p internal transition. Additionally, a polaron pinning phenomenon can be observed and the polaron coupling constant $\alpha \sim 0.54$ can be derived from the experimental data. The implication of such a large plaron coupling constant on the mechanism of the shallow-deep transition for the sulphur defect in GaSb are discussed.

Experimental.

The samples used were n and p type Czochralski grown single crystals doped with sulfur with the net donor concentration (estimated from Hall effect at room temperature) of N_d-$N_a \sim 1*10^{16}$ cm^{-3} for the n type samples and net acceptor concentation of N_d-$N_a \sim 5*10^{15}$ cm^{-3} for the p type samples. In the course of temperature dependent Hall effect measurements the PPC phenomenon has been evidenced only for the n type samples samples.

The IR absorption measurements were carried out at T = 1.7 K with the Bruker 113A FTIR spectrometer coupled to a superconducting coil (B range: form 0 to 15 T). The resolution was 1 cm^{-1}. A mercury lamp was used for near-bangap illumination (creation of the matastable band) and it was filtered off with the back polyethylene filter during the experiment.

The intracenter absorption of the shallow sulfur donor.
The maximum of the photoinduced IR-absorption is observed at 68 cm^{-1}. In the magnetic field a Zeeman splitting into two bands can be measured. One of them shifts down in energy very slightly at low fields and then its position remains fixed over the entire range of the magnetic fields. The peak position of the other split-off band increases rapidly with magnetic field. For large magnetic fields its amplitude increases and that of the other one decreases with field (Fig. 1). Such behaviour is characteristic for an intracenter 1s-2p transition of a shallow hydrogenic donor [7]. The low energy

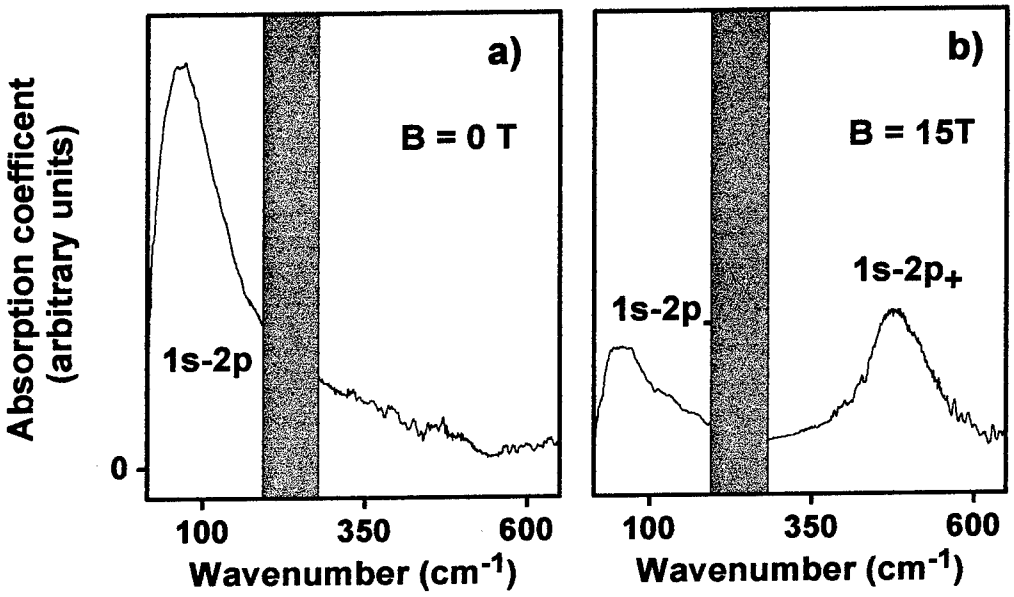

Fig.1 Differential absorption in far infrared of the sulfur sahallow metastable state. A transmission spectrum before illumination was taken as a reference. The shaded region represents the restrahlen band a) 1s-2p transition at zero field b) split-off bands at higher field.

split-off band can be identified with the 1s-2p- and the higher energy band with 1s-2p+ transition.

The magnetic field dependence of the peak positions of the bands is shown on Fig. 2. At low fields the splittinfg should be symmetrical relatively to the 1s-2p transition at zero field.

In the high field case (where the $2p_+$ levels follow the N = 1 landau level) the splitt off bands behave approximately as: $\frac{3}{2}\frac{\hbar e}{m_{eff}}B$ ($2p_+$) and $\frac{1}{2}\frac{\hbar e}{m_{eff}}B$ ($2p_-$), where m_{eff} is the effective mass of the bound electron. Both these limiting cases are indicated on Fig. 2. For all magnetic field strengths the Zeeman splitting should have the same value of $\Delta E_{Zeeman}(B) = \frac{\hbar e}{m_{eff}}B$. It is clear from Fig. 2 that the experimental magnetic field dependence of the split-off bands does not match the theoretical predictions for higher fields. Additionally, at fields of the order of 4-5T a large discontinuity in the B-dependence of the 1s-2p+ split-off band appears. This discontinuity can be associated with the so called "polaron anticrossing" or "polaron pinning" effect [7][8], where the $2p_+$ level of the donor interacts with the 1s+LO virtual state. The magnitude of this discontinuity can be connected (first order approximation) to the LO phonon energy via the simple formula [7]: $\Delta\nu_{disc.} = \alpha\nu_{LO}$, where α

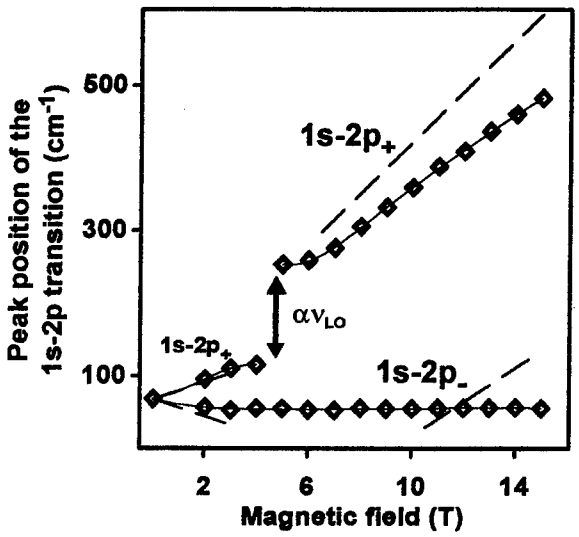

Fig.2 The peak positions of the split off bands vs. magnetic field. A thin line drawn through the experimental points is guide to the eyes. The broken line indicates the expected B dependence of the peakpositions in the limiting cases of low and high fields. The polaron "gap' in the field dependence of the 1s-2p+ transition is indicated by arrows.

the polaron coupling constant and ν_{LO} the energy of the LO phonon in cm^{-1}. From this the polaron coupling constant can be estimated: $\alpha = 0.54 \pm 0.08$.

For fields B > 7 T the Zeeman splitting vs. B can be plotted with great accuracy. From the linear dependence of this splitting on B the effective mass of the electron bound to the shallow center can be estimated: $m_{eff} = (0.037 \pm 0.01)m_0$, where m_0 - free electron mass. This value of the effective mass is of the order of the effective mass of the Γ minimum (m $0.0396m_0$ [9] or 0.043 [10]). After taking into account the polaron [11] and band nonparabolicity [12] corrections the obtained „bare" effective mass is $m_{eff} = 0.031m_0$ which is a significantly lower value than that found in literature (Fig. 3a). The reason for this discrepancy most probably is due to the (weak but significant) polaron interaction of the 1s+LO level with the 2p. level.

One can also attempt to find an upper bound of the polaron effective mass from the magnetic field dependence of the $2p_+$ level alone (Fig. 3b). After taking into account the band nonparabolicity corrections [12] one estimates $m_{eff} = 0.045m_0$. This polaron mass is larger than the

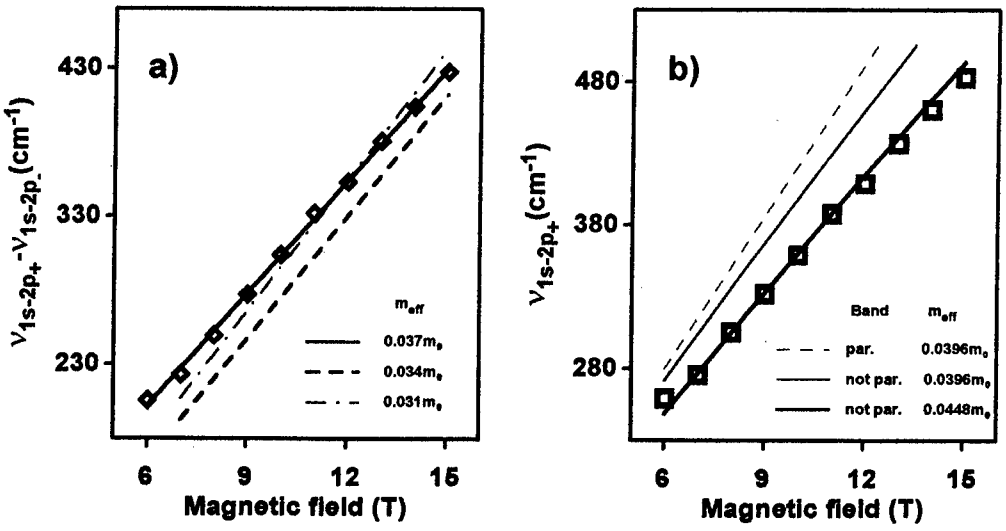

Fig. 3.

a) *Zeeman splitting of the 1s-2p+ transition for the sulfur donor in GaSb. From the straightforward fit to the data a $m_{eff\,(polaron)}$ value of $0.037m_0$ is obtained. Thick broken line is drawn for the "bare" mass $m_{eff(bare)} = 0.034m_0$. This line starting from the origin at B = 0T should creoss the experimental data. Only the straight line of $m_{eff} = 0.031m_0$ shows the expected behaviour.*

b) *Magnetic field dependence of the 1s-2p+ peak position for high fields. The data can be fitted only assuming correction for nonparabolicity and a polaron mass of $m_{eff(polaron)} = 0.0448m_0$.*

bare mass by a polaron correction factor $\left(1-\frac{\alpha}{6}\right)^{-1}$. Assuming that the value found in ref. [9] is most close to a "bare" effective mass for the Γ conduction band minimum, we can obtain an upper bound of the coupling constant $\alpha \sim 0.7$.

From the position of the intracenter absorption at zero field the binding energy of the shallow donor can be found. Assuming that the binding energy of the 2p level E_{B2p} at zero field can be exactly estimated from the effective mass theory the donor binding energy $E_B = E_{B2p} + E_{1s\text{-}2p}$ = 0,5 meV + (8,4 ± 0,6) meV = 8,9 ± 0,6 meV. This binding energy value agrees well with the shallow donor binding energy found in GaSb:S in the hydrostatic pressure experiments of ref. [2].

Discussion

The properties of the shallow sulphur donor which could be found in the present experiment are:

1. the donor can be regarded as a metastable state of the DX-type sulphur defect in GaSb.
2. the donor is bound to the Γ minimum ($m_{eff} \sim 0.03\text{-}0.04m_0$),
3. its binding energy is of about 9 meV.
4. the polaron coupling constant of the electron bound to the donor is of the order of 0.5-0.7.

Although the donor can still be considered as "shallow" its binding energy exceeds 4 times the binding energy predicted by the effective mass theory for the Γ minimum in GaSb ($E_B \sim 2$meV). One can expect a large central cell potential to be present. The polaron coupling constant exceeds nearly 20 times the Fröhlich value of α for GaSb (α = 0.025) estimated using the "usual" values of the static (ε_0) and high frequency (ε_∞) dielectric constants and a bare effective mass value of ref. [9].

It seems that properties 3 and 4 both have the same physical origin - the localized central cell potential. Unfortunately, there exists no theory coupling the large central cell effects with the polaron effects, which could explain consistently the observations for a kind of center found in GaSb:S. The theory of polaron effects as developed e.g. in ref [8] considers the defect potential as a simple Coulomb potential. To our knowledge there has been no attempt so far to incorporate polaron effects into the theory of "localised" centers [12]. Therefore one has to rely on extrapolations of the present knowledge to derive at least some approximate information about the changes of properties of the defect potential due to coupled central cell and polaron effects.

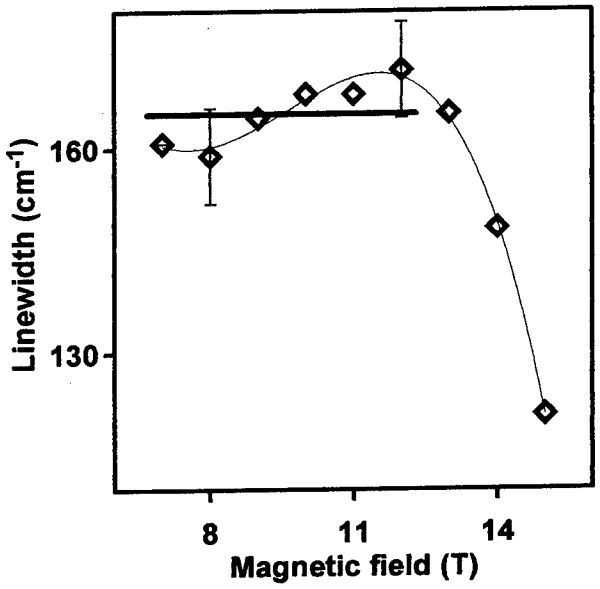

Fig 3. The magnetic field dependece of the 1s-2p+ transition linewidth.

To do this we will recall the Fröhlich's formula for the polaron coupling constant (valid for $\alpha < 1$):

$$\alpha = \frac{1}{2}\bar{\varepsilon}^{-1}\frac{1}{\hbar\omega}\frac{e^2}{r_p} = \frac{e^2}{\sqrt{2}\hbar}\bar{\varepsilon}^{-1}\sqrt{\frac{m_{eff}}{\hbar\omega}}$$

where $\bar{\varepsilon}^{-1} = \frac{1}{\varepsilon_\infty} - \frac{1}{\varepsilon_0}$, $\hbar\omega$ - phonon enregy and r_p the so called polaron radius [13].

One can see that there could be two possible reasons for the increase of α: 1) a decrease of the polaron radius due to binding of the electron to the donor potential, 2) changes in $\bar{\varepsilon}^{-1}$.

In the first case the donor potential seems not to be strong enough to affect the polaron radius r_p. The polaron radius for the above parameters of "bare" m_{eff} and L0 phonon energy

amounts to 60 Å the Bohr radius (r_B) is of the order of 100-120 Å for the $E_B \sim 9$ meV. The bound electron will loose its polaron properties only when its Bohr radius (electron orbit) will be smaller than the polaron radius (dimesion of the polaron, range of "phonon assisted" movement of the polaronic electron") i.e. the binding will be so strong that the elctron would not any longer interact with the phonon field. At zero and at low magnetic fields $r_B > r_p$. At higher fields (B > 12 T) this may not longer be true as one can see on Fig. 3. There, the broadening of the $1s\text{-}2p_+$ transition, being as it seems a "polaron broadening" [15], decreases rapidly for B > 12 T - the polaronic effects are suppressed by a strong reduction of the electron orbit due to magnetic field.

As at zero field the binding by the donor potential does not affect the value of r_p it seems that the entire increase in α should be attributed to the change in $\bar{\varepsilon}^{-1}$: $\frac{\alpha_{bound}}{\alpha_{free}} = \frac{\bar{\varepsilon}^{-1}_{bound}}{\bar{\varepsilon}^{-1}_{free}} \cdot \frac{r_{p\,free}}{r_{p\,bound}} \cong \frac{\bar{\varepsilon}^{-1}_{bound}}{\bar{\varepsilon}^{-1}_{free}} \sim 20$. The indices "bound" and "free" correspond to the electron bound and unbound (free) to the sulfur centre. As the value of $\bar{\varepsilon}^{-1}_{bound}$ differs from the $\bar{\varepsilon}^{-1}_{free}$ value the "effective" dielectric constants ε_{0bound} and $\varepsilon_{\infty bound}$ for the electron in the vicinity of the donor centre should take values different from the standard material parameters. Having the experimentally derermined ratio of $\frac{\alpha_{bound}}{\alpha_{free}}$ fixed one can express the effective dielectric constants by the value of $\eta = \frac{\varepsilon_{\infty bound}}{\varepsilon_{0bound}}$ which is also a convenient measure for the "polaronic susceptibility" of the system: $\varepsilon_\infty = \frac{1-\eta}{a}$ and $\varepsilon_0 = \frac{1}{a}\left(\frac{1}{\eta} - 1\right)$, where a = $\bar{\varepsilon}^{-1}_{free} \cdot \frac{\alpha_{bound}}{\alpha_{free}}$ and fixed.

One than sees immediately that maintaining the high $\frac{\alpha_{bound}}{\alpha_{free}}$ ratio determined from the experiment and taking the value of η of 0.92 (given by the material constants) one obtains both "effective" dielectiric constants to be of the order of 1 which would result in unreasonably large binding energy of the donor.

Applying some simple reasoning [14] the value of η can be approximated meeting the requirements of not too high value of the binding energy (~ 10 meV) and the fixed ratio $\frac{\alpha_{bound}}{\alpha_{free}} \sim 20$. The η value found in this way is of the order of 0,2-0,3 [14]. It then follows staightforwardly that the values of ε_0 and ε_∞ should not be so close to each other as in the case of free electron in the crystal. ε_{0bound} takes values larger than the ε_{0free} and for ε_∞ the reverse appiles.

The above described changes in the effective dielectric constants reflect changes in the defect potential when the sulfur impurity is put into the GaSb instead of Sb. For the sulfur there are less core electrons compared to the antimony and the screening electronic screening alone (lower effective ε_∞) would be not sufficent to account for the low binding energy in the shallow state. Thus the polaron screening is switched on - ε_0 felt by the electron bound to the sulfur centre is higher.

A higher value of the effective ε_0 at a low η value found in our experiment for the sulfur centre in GaSb means that the stability of the lattice at the sulfur donor site is decreased. High amplitudes of low frequency lattice vibrations can thus be achieved. They are necessary to provide a sufficient gain for the pseudo Jahn-Teller transition [15] which is resonsible for the transiton from the shallow to deep DX-like state. On the other hand the low value of η and the low dimensionality of the system (an electron bound in a defect potential is a "natural" realization of a quantum box) can be the reason for enhanced ability of the sulphur centre to attract and bind large bipolarons [16]. The transition to a deep DX state would thus be accompanied by capture of two electrons.

Acknowledgments
This work is supported in part by European Community grant № CIPA-CT94-0172.

References

1. A. Y. Vul, L. V. Golubev, L. V. Sharonova, Y. V. Shmartsev *Fiz. Tekh. Poluprowodn.* **4**, 2347 (1970); A. Y. Vul, A. Y. Shik *Sol. St. Commun.* **13**, 1049 (1973).
2. L. Dmowski, S. Porowski, M. Baj *Int. Conf. on High Pressure and Low Temperature Physics*, Cleveland, USA 1977, ed. C. W. Chu, J. A. Woollam, Plenum Press, New York 1978, p. 505; L. Dmowski, M. Baj, R. Piotrzkowski, S. Porowski *Proc. of the 14th Intern. Conf. on the Physics of Semiconductors*, Edinburgh, Scotland 1978, wyd. B. L. H. Wilson, IOP Bristol & London 1979, str. 417.
3. W. Jost, M. Kunzer, U. Kaufmann, H. Bender *Phys. Rev. B* **50**, 4341 (1994); P. Stallinga, W. Walukiewicz, E. R. Weber, P. Becla, J. Lagowski *Acta Phys. Pol.* **A88**, 1043 (1995).
4. L. Dobaczewski, P. Kaczor *Semicond. Sci. Technol.* **6**, B51 (1991).
5. U.Piekara, J. M. Langer *Sol. St. Commun.* 23, 583 (1977).
6. J. E. Dmochowski, L. Dobaczewski, J. M. Langer, W. Jantsch *Phys. Rev. B* **40**, 9671 (1989).
7. R. Kaplan *Proc. of the Int. Summer School on the Generation of High Magnetic Fields and Their Application in Solid State Physics,* Würzburg 1972, Universität Würzburg 1973, p. 278.
8. D. R. Cohn, D. M. Larsen, B. Lax *Phys. Rev. B* **6**, 1367 (1972); M. Grynberg, S. Huant, G. Martinez, J. Kossut, T. Wojtowicz, G. Karczewski, J. M. Shi, F. M. Peeters, J. T. Devreese *Phys. Rev. B* **54**, 1467 (1996).
9. D. A. Hill, C. F. Schwerdtfeger *J. Phys. Chem. Solids* **33**, 1533 (1974).
10. N. B. Brandt, V. V. Moshalkov, A. S. Rylik, S. M. Chudionov, D. G. Adrianov, E. P. Kolchina *Fiz. Tekch. Polupr.* **14**, 1704 (1980).
11. I. M. Cydlikovskij *„Elektrony i dyrki v poluprovodnikach"*, Izdatelstvo Nauka, Moskva 1972, p. 458 (in russian).
12. S. T. Pantelides *Rev. Mod. Phys.* **50**, 797 (1978).
13. H. Fröhlich in *„Polarons and Excitons"* ed. C. G. Kuper, G. D. Whitfeld, Oliver and Boyd, Edinburgh and London 1963, p. 1
14. J. T. Devreese in *„Polarons in Ionic Crystals and Polar Semiconductors"*, ed. J. T. Devreese, North-Holland, Amsterdam 1972, p. 83.
15. P. Kaczor PhD Thesis (1997).
16. G. Watkins *Semicond. Sci. Technol.* **6**, 111B (1991).
17. Emin, M. S. Hillery *Phys. Rev. B* **39**, 6575 (1989); J. Adamowski *Phys. Rev. B* **39**, 3649 (1989).

Materials Science Forum Vols. 258-263 (1997) pp. 1247-1252

RESONANT INTERACTION BETWEEN LOCAL VIBRATIONAL MODES AND EXTENDED LATTICE PHONONS IN AlSb

M.D. McCluskey[1], E.E. Haller, W. Walukiewicz, and P. Becla[2]
Lawrence Berkeley National Laboratory, MS 2-200, 1 Cyclotron Rd., Berkeley CA 94720, USA
[1]Present address: Xerox PARC, 3333 Coyote Hill Rd., Palo Alto, CA 94304
[2] Department of Materials Science and Engineering, Massachusetts Institute of Technology, Cambridge, MA 02139

Keywords: Local vibrational modes (LVM's), AlSb, DX centers, hydrogen

Abstract. Using infrared spectroscopy we have observed Se-H stretch and wag local vibrational modes (LVM's) in AlSb. The frequencies of the wag mode harmonics are explained by perturbation theory. In addition, there is evidence of a resonant interaction between LVM's and multi-phonon modes. This interaction leads to a splitting of the Se-H stretch mode into three peaks at 1606.3, 1608.6, and 1615.7 cm^{-1} at liquid-helium temperatures. As the temperature or pressure is increased, the stretch mode and multi-phonon modes show anti-crossing behavior.

Introduction.

In this paper, we report evidence of a resonant interaction between LVM's and extended lattice phonons that gives rise to a new collective excitation called a "localon." This resonance is similar to the Fermi resonance between wag and stretch local vibrational modes (LVM's) in donor-hydrogen complexes in silicon [1]. By varying the temperature and pressure to change the phonon energies, we have studied the evolution of the localon spectra in AlSb.

As we have noted previously [2], at liquid-helium temperatures, hydrogenated AlSb:Se has stretch mode peaks at 1608.6 and 1615.7 cm^{-1}, whereas the Se-D mode has only one stretch mode peak at 1173.4 cm^{-1}. In addition, there is a small Se-H peak at 1606.3 cm^{-1}. Hydrogenated and deuterated AlSb:Te have only one stretch mode peak each, at 1599.0 and 1164.4 cm^{-1} respectively. The ratio of the three Se-H peak areas is constant from sample to sample, which suggests that they are not due to additional impurity complexes. The details of the crystal growth, sample preparation, and hydrogenation techniques are given in Ref. 2.

Experimental details.

Variable temperature spectra were obtained with a Bomem DA8 spectrometer with a KBr beamsplitter and a mercury cadmium telluride (MCT) detector. Variable pressure spectra were obtained with a Digilab 80-E spectrometer with a KBr beamsplitter and an instrumental resolution of 1 cm^{-1}. To generate hydrostatic pressures up to 15 kbar, we used a modified Merrill-Basset diamond-anvil cell [3,4]. The liquid immersion-technique [5] was used to load the cell with liquid nitrogen. A light-concentrating cone focused the light through the diamonds and sample and into a Ge:Cu photoconductor mounted directly behind the sample. We used the pressure dependence of the AlSb:C_{Sb} LVM as a precise *in situ* calibration of the sample pressure [6].

Wag modes.

The splittings of the wag harmonics are consistent with a complex which possesses C_{3v} symmetry. In the plane perpendicular to the [111] axis, the C_{3v} potential is given by [7,8]

$$V(x,y)=\frac{1}{2}k(x^2+y^2)+B(xy^2-x^3/3)+C(x^2+y^2)^2+\cdots \quad , \tag{1}$$

where x and y are parallel to the $[1\bar{1}0]$ and $[11\bar{2}]$ crystallographic axes, respectively. For simplicity, we have omitted the wag-stretch coupling terms. The anharmonic terms in Eq. 1 lift the degeneracy of the wavefunctions for $N = n_x + n_y > 1$. The predicted splittings are shown in Fig. 1. The dipole allowed transitions are the $\Gamma_1 \rightarrow \Gamma_1$ and $\Gamma_1 \rightarrow \Gamma_3$ transitions. The higher harmonics give rise to weaker peaks, since they require higher order anharmonic terms in Eq. (1). The theoretical wag frequencies are calculated with perturbation theory to second order for the cubic term and to first order for the quartic term. By adjusting the parameters k, B, and C, a reasonable fit to experiment is obtained (Table I).

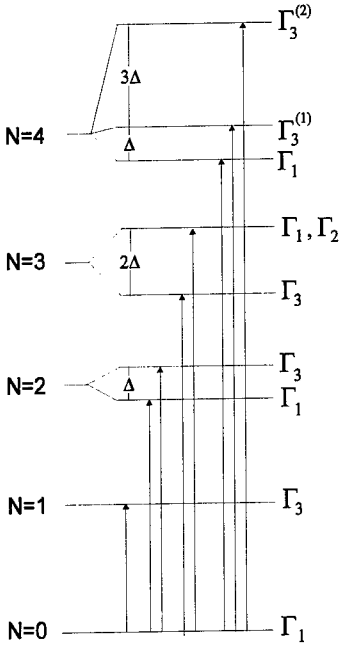

Figure 1. The splitting of the hydrogen/ deuterium wag modes in C_{3v} symmetry.

TABLE I. Theoretical and experimental values of Se-H and Se-D wag modes in AlSb.

N	Symm.	$0 \rightarrow N$ transition (cm^{-1})			
0	Γ_1	H (theory)	H (expt)	D (theory)	D (expt)
1	Γ_3	342	ND	247	ND
2	Γ_1	666	666	484	478
2	Γ_3	689	692	496	497
3	Γ_1	1040	1032	748	742
3	Γ_2	1040	*	748	*
3	Γ_3	994	993	724	718
4	Γ_1	1304	1316	955	948
4	$\Gamma_3^{(1)}$	1327	1333	967	957
4	$\Gamma_3^{(2)}$	1396	ND	1002	ND
5	Γ_1	1665	ND	1212	ND
5	Γ_2	1665	*	1212	*
5	$\Gamma_3^{(1)}$	1629	ND	1193	ND
5	$\Gamma_3^{(2)}$	1735	ND	1247	ND

*IR inactive
ND = not discovered

Temperature dependence.
The temperature dependence of the Se-H and Se-D stretch modes is shown in Fig. 2. The linewidth broadening and shift to lower frequency with increasing temperature are seen in numerous semiconductor systems and are caused by an anharmonic interaction between the localized mode and acoustic phonons [9,10]. In our case, this temperature dependent broadening causes peaks 0 and 1 to overlap such that they are not resolved for temperatures greater than 40 K. For variable temperature measurements, therefore, we refer to the superposition of peaks 0 and 1 as "peak 1."

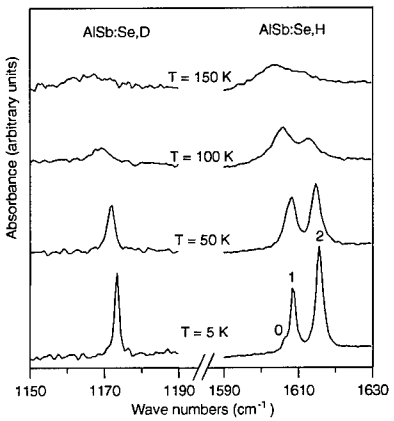

Figure 2. Temperature dependence of Se-D and Se-H stretch modes in AlSb.

To explain these observations, we propose a model in which the Se-H stretch LVM of energy ω_{LVM} interacts with a nearly degenerate multi-phonon mode of energy ω_{phonon}. The Hamiltonian is given by

$$H = H_{LVM} + H_{phon.} + H_{int.}, \tag{2}$$

where H_{LVM} and $H_{phon.}$ are the Hamiltonians for the local and extended phonons, respectively, and $H_{int.}$ is a weak interaction between these two systems. The phonon combinations that resonantly interact with the local mode are represented by a single energy ω_{phonon}.

Treating $H_{int.}$ as a small perturbation, we obtain the following matrix:

$$H = \begin{bmatrix} \omega_{LVM} & A \\ A & \omega_{phonon} \end{bmatrix}, \tag{3}$$

where $A = \langle LVM | H_{int.} | phonon \rangle$. The eigenvalues of this Hamiltonian are given by

$$\omega_{\pm} = \tfrac{1}{2}\left[\omega_{LVM} + \omega_{phonon} \pm \sqrt{\left(\omega_{LVM} - \omega_{phonon}\right)^2 + 4A^2} \right]. \tag{4}$$

The corresponding wavefunctions are given by

$$|\psi\rangle = a|LVM\rangle + b|phonon\rangle. \tag{5}$$

We refer to this linear combination of a local mode and a phonon as a *localon*. As explained below, the multi-phonon mode involves at least five phonons, and therefore has a negligible optical absorption cross section. The strength of the absorption peaks are determined by the LVM contribution to the wavefunction in Eq. (5), given by

$$|a|^2 = \frac{A^2}{(\omega_{LVM} - \omega_{\pm})^2 + A^2} \tag{6}$$

Experimentally, $|a|^2$ represents the normalized area of peak 1:

$$|a|^2 = A_1/(A_1+A_2), \tag{7}$$

where A_1 and A_2 are the areas of peaks 1 and 2, respectively.

In our model, the temperature dependence of the unperturbed stretch mode is given by

$$\omega_{LVM} = 1612.7 - 0.034\ U(T), \tag{8}$$

where $U(T)$ is the mean vibrational energy of the lattice [9,10] in cal/mole and ω_{LVM} is given in cm^{-1}. The frequency of the multi-phonon mode can be approximated by a constant independent of temperature,

$$\omega_{phonon} = 1611.2\ cm^{-1}, \tag{9}$$

where the parameters in Eqs. (8) and (9) were adjusted to fit the data. As the temperature increases, the area of peak 1 increases as it becomes more "LVM-like" (Fig. 3). Conversely, the area of peak 2 decreases as it becomes more "phonon-like." Fig. 3 shows a comparison between the theoretical calculations and experimental results. Using a value of $A = 3.45\ cm^{-1}$, we can explain the temperature dependence of the peak positions [Fig. 3(a)] as well as the relative absorption strengths of the peaks [Fig. 3(b)].

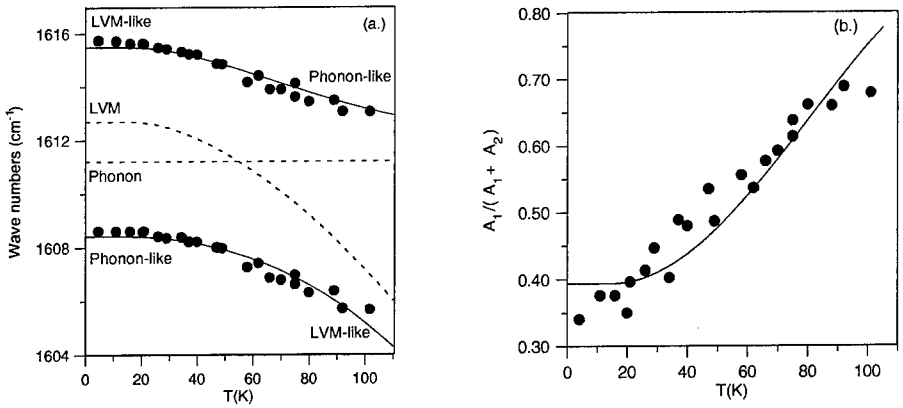

Figure 3. (a) Se-H stretch modes as a function of temperature. (b) Normalized area of Se-H peak 1 (lower-frequency peak). The solid lines are plots of the theoretical model.

This model also explains why we do not observe a splitting in the Se-D mode. The small interaction energy of $A = 3.45$ cm^{-1} means that a local mode must lie within a few wavenumbers of the multi-phonon mode to show an appreciable splitting. The Se-D stretch mode at 1173.4 cm^{-1} is much too far below the multi-phonon mode at 1611.4 cm^{-1} to significantly interact. The same is true for the Te-H stretch mode at 1599.0 cm^{-1}, which also does not show a splitting.

Pressure dependence.

To further probe the properties of this interaction, we used hydrostatic pressure to change the resonance conditions between the local and extended modes. Varying the pressure has an advantage over varying the temperature in that the lines do not broaden, so all three peaks are resolved. We find that the strength of peak 0, which is negligibly small at ambient pressure, increases rapidly at the expense of peaks 1 and 2. At pressures above 4.5 kbar, only peak 0 can be detected. The integrated absorption for all the peaks remains constant to within experimental error.

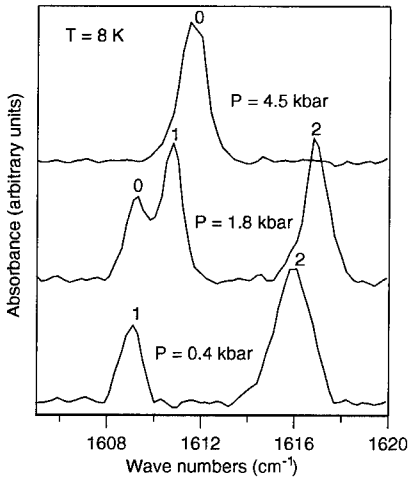

Figure 4. Se-H stretch mode peaks as a function of pressure.

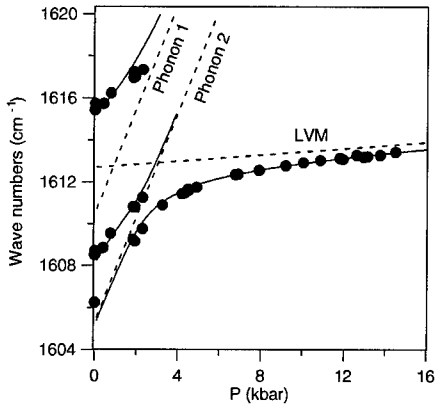

Figure 5. Se-H stretch mode peaks as a function of pressure. The dashed lines are the unperturbed LVM and multi-phonon modes and the solid lines are plots of the three-level theory.

To explain the pressure dependence of these peaks, we must consider the interaction of the LVM with two extended multi-phonon modes. The localon energies are given by

$$H = \begin{bmatrix} \omega_{LVM} & A & B \\ A & \omega_{phonon,1} & 0 \\ B & 0 & \omega_{phonon,2} \end{bmatrix}, \qquad (10)$$

where $A = \langle LVM|H_{int.}|phonon1\rangle$, $B = \langle LVM|H_{int.}|phonon2\rangle$, and for simplicity we have neglected the interaction between the multi-phonon modes. We use values of A = 3.45 cm^{-1}, as before, and B = 1 cm^{-1}. The pressure dependence of the LVM is given by

$$\omega_{LVM} = 1612.7 + 0.075\,P, \tag{11}$$

where the zero pressure value of 1612.7 cm^{-1} is the same as that used in Eq. 8. To estimate the pressure dependence of the multi-phonon modes, we use the Grüneisen parameter for the zone-center LO phonon, yielding a pressure derivative given by $d\omega/dP$ = 2.5 cm^{-1}/kbar. The eigenvalues of the Hamiltonian (10) are calculated numerically. We obtain very good agreement between the model and experiment (Fig. 5).

We propose that the multi-phonon modes are different combinations of five phonons, since, e.g., 5 X $\omega_{TO}(\Gamma) \sim 1610$ cm^{-1} is close to the observed frequencies. It has been suggested that the modes may be overtones of Se-H wag modes [11]. From perturbation theory, however, the N=5, Γ_1 wag mode has a predicted frequency of 1665 cm^{-1} (Table I), which is too far above the stretch mode (1610 cm^{-1}) to strongly interact. In addition, in C_{3v} symmetry there is only one N=5, Γ_1 wag mode, while we observe two "unknown" modes. However, we cannot exclude the possibility that the stretch mode resonantly interacts with a local vibrational mode of the Se-H complex that has not yet been discovered.

In conclusion, we have discovered evidence of a resonant interaction between local modes and phonons in AlSb. We propose that the Se-H stretch mode interacts with two different combinations of five phonons, resulting in anti-crossing between three distinct peaks. How a 5-phonon mode could have such a sharp resonance with the stretch mode, however, is an open question. One test of the 5-phonon model is to use temperature or pressure to tune a mode unrelated to the Se-H complex into resonance with the "unknown" mode. If the unknown mode is indeed a multi-phonon mode, then anti-crossing behavior should be observed.

We would like to thank L. Hsu for his assistance with the high-pressure work. This work was supported by in part by USNSF grant DMR-94 17763 and in part by the Director, Office of Energy Research, Office of Basic Energy Sciences, Materials Science Division of the U.S. Department of Energy under Contract No. DE-AC03-76SF00098.

References.

1. J.-F. Zheng and M. Stavola, Phys. Rev. Lett. **76**, 1154 (1996).
2. M.D. McCluskey, E.E. Haller, W. Walukiewicz, and P. Becla, Phys. Rev. B **53**, 16297 (1996).
3. L. Merill and W.A. Bassett, Rev. Sci. Instr. **45**, 290 (1974).
4. E. Sterer, M.P. Pasternak, and R.D. Taylor, Rev. Sci. Instr. **61**, 1117 (1990).
5. D. Schiferl, D.T. Cromer, and R.L. Mills, High Temp. High Pressures **10**, 493 (1978).
6. M.D. McCluskey, L. Hsu, L. Wang, and E.E. Haller, Phys. Rev. B **54**, 8962 (1996).
7. R.C. Newman, Adv. Phys. **18**, 545 (1969).
8. M. Dean Sciacca, A.J. Mayur, N. Shin, I. Miotkowski, A.K. Ramdas, and S. Rodqiguez, Phys. Rev. B **51**, 6971 (1995).
9. R.J. Elliot, W. Hayes, G.D. Jones, H.F. MacDonald, and C.T. Sennet, Proc. R. Soc. Lond. **A289** 1 (1965).
10. M.D. McCluskey, E.E. Haller, J. Walker, and N.M. Johnson, Phys Rev. B **52**, 11859 (1995).
11. B. Clerjaud and C. Van de Walle, private communication.

Materials Science Forum Vols. 258-263 (1997) pp. 1253-1258

DEFECT REACTIONS IN LOW TEMPERATURE ELECTRON IRRADIATED AlAs INVESTIGATED BY MEASUREMENTS OF THE LATTICE PARAMETER

A. Gaber[1,2], H. Zillgen[1], P. Ehrhart[1], P. Partyka[3], and R. S. Averback[3]
[1]IFF, Forschungszentrum Jülich GmbH, D-52425 Jülich, Germany
[2]Phys. Dept., Assiut University, Assiut 71516, Egypt
[3]Frederick Seitz Materials Research Laboratory, University of Illinois, Urbana, IL 61801

Keywords: AlAs, interstitial atoms, vacancies, electron irradiation, lattice parameter

Abstract. Pseudomorphic layers of AlAs on GaAs substrates were irradiated at 4.6K with 2.5 MeV electrons up to a total dose of $2 \cdot 10^{19}$ electrons/cm². X-ray diffraction was employed to investigate damage accumulation and the subsequent thermally activated annealing reactions. We observe an irradiation-induced increase of the lattice parameter which amounts to about half of the changes observed in the GaAs substrates. There is a major annealing step near room temperature, a rather continuous annealing up to 500K and a final recovery stage between 700K and 900K. The observed defect properties and defect reactions are compared to those of other III-V compounds like GaAs and InP.

1. Introduction.

Layered structures of AlAs and GaAs on GaAs substrates have gained technological importance for applications in electro-optical devices such as light emitting diodes and laser diodes. Although the control of defects is crucial for device production and application, the present knowledge of defects in AlAs is very limited. Of special interest here is the behavior of AlAs layers under ion implantation, as several studies have found an unusual resistance of $Al_xGa_{1-x}As$ to damage accumulation during ion irradiation [1-5]. Transmission electron microscopy showed that AlAs remains crystalline and nearly free of damage, even when subjected to ion fluences orders of magnitude greater than those required for complete amorphization of GaAs and other III-V compounds. This resistance to damage accumulation might quite generally be attributed to a high defect mobility and a subsequent high defect recombination rate even at low temperatures [6]. Additional X-ray diffraction measurements have, however, demonstrated that strain from radiation-induced defects in AlAs first increases with dose below some saturation value, Φ_s, reaches a plateau where the strain remains constant over a broad increment of dose, $\approx 100\ \Phi_s$, and finally diminishes upon additional irradiation Fig.1 [7,8]. These results suggest that the accumulation of strain during ion irradiation at 80 K will never cause amorphization of AlAs, simply because the strain never exceeds some critical value. In order to explain the observed strain relaxation it was assumed as an

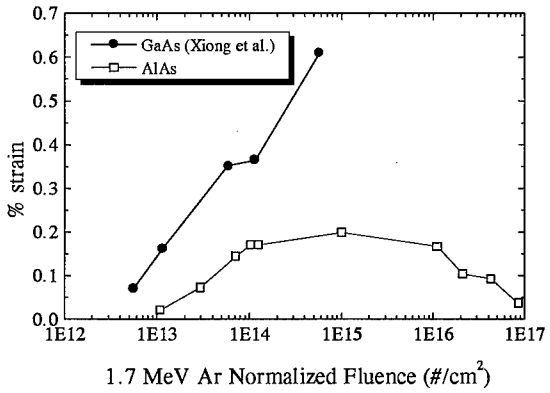

Fig.1: Change of the lattice parameter of the c-axis of pseudomorphic AlAs layers on GaAs substrates during irradiation with Argon ions. The lattice parameter of the a-axis is fixed by the GaAs substrate. The data for GaAs (from ref.9) end at the amorphization dose

alternative model that point defects and their small clusters induce large lattice strains, but as these clusters grow they become unstable and spontaneously relax by defect rearrangements, e.g. the formation of dislocation loops [7,8]. This model relies on the assumption that interstitial atoms and vacancies induce large lattice relaxations which can relax upon agglomeration. Such large relaxation volumes of the point defects were observed in GaAs [10], however, there are other compounds like InP [11] or the elemental semiconductors Si and Ge [12], in which there is nearly complete compensation of the strain fields from pairs of interstitials and vacancies.
As there are at present no results on the structure of Frenkel defects or their mobility in AlAs, which would provide support for one model or the other, we measured the changes of the lattice parameter after electron irradiation of AlAs at 4.6 K and after subsequent annealing up to 900 K. Electron irradiations are used here because they produce simple Frenkel pair defects. Hence, they should indicate whether unusually high defect mobility occurs in AlAs at low temperatures, that is, below 80 K, and what are the relaxation volumes of point defects in this material.

2. Experimental.

For this investigation we used AlAs layers of 180 nm thickness which were grown by metalorganic chemical vapor deposition (MOCVD) on 2 inch (001) GaAs substrates. A thick buffer layer of GaAs was first grown, followed by the layer of AlAs, and a cap layer of 100 nm GaAs. The AlAs films were initially under compressive stress due to the slight lattice mismatch. The growth process incorporated on the order of 10^{18} cm^{-3} carbon atoms in the AlAs films. Irradiations were performed at the irradiation facility in Jülich [13] with 2.5 MeV electrons at 4.7K up to a total dose of $1.6 \cdot 10^{19}$ cm^{-2}. The first sample was transferred to the X-ray diffractometer immediately following irradiation while still at 8 K and a second sample was examined only after warming to room temperature. The measurements were then repeated after different steps of an isochronal annealing program. Up to 300K holding times were 15 min while at higher temperatures the holding times were 30 min.
The study employed Cu-K_{α_1} radiation and utilized the (004), (006), (444) and (117) reflections in a setup which has been described elsewhere [10,11]. As expected, the different measurements confirmed the good epitaxy of the layer. Due to its higher sensitivity, the (117) reflection was used for quantitative analysis of the changes of the strain after the different treatments reported here. The lattice parameter of AlAs was obtained by referencing the centroid of the AlAs reflection to the measured position of the GaAs substrate reflection. An example of the well resolved peaks of the rocking curves is shown in fig.2. Before irradiation the Bragg angle for AlAs is smaller than that for GaAs by 0.8160° due to the larger lattice parameter of AlAs (a_0= 5.65826Å). By measuring the rocking curves for two different sample angles (corresponding to (1 -1 7) and (-1 1 7) reflections respectively) the inclination of the lattice planes due to the tetragonal distortion was eliminated and the lattice spacing, d_{hkl}, was determined from Braggs law.

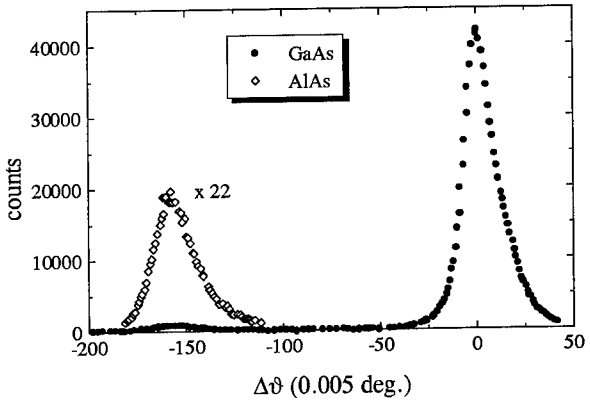

Fig.2: Distance of the (117) peaks of AlAs and GaAs. The width of the GaAs peak is determined by the experimental resolution.

Due to the large penetration length of the electrons, the GaAs substrate is damaged along with the AlAs and this change of the reference must be considered. Therefore the absolute value of the lattice parameter, a_{GaAs}, was determined using a modified Bond technique. This value was compared to a Si reference in order to correct for possible changes of the wavelength due to shifts of the monochromator. Taking the exact wavelength of the Cu-K_{α_1} radiation of λ=1.54050 Å a value of a = 5.42960 Å is deduced for silicon at the measuring temperature of 8K. The value of the unirradiaded GaAs was 5.64792Å at 8K. These measurements at the GaAs substrate yields the cubic lattice parameter of the substrate and the in-plane lattice parameter, a, of the epitaxial AlAs layer is identical to this lattice parameter of the substrate.
In combination with this in-plane lattice parameter the lattice parameter of the c-axis, c, can be determined from the (117)-lattice spacing of the tetragonally distorted AlAs layer. From the lattice parameters determined in this way, the average volume of the unit cell can be deduced: $V = a^2c$. This value, however, is affected by the size of the strain due to the substrate, and the hypothetical unconstrained lattice parameter of the corresponding cubic AlAs, a_0, can be deduced using the elastic boundary condition: i.e. there is zero stress perpendicular to the free surface of the film. This yields a relation between the strain perpendicular, $\varepsilon_{perp}=(a_{perp}-a_0)/a_0$, and parallel, $\varepsilon_{para} = (a_{para}-a_0)/a_0$, to the surface of our (001)-oriented samples [14]:

$$\varepsilon_{perp} = - \varepsilon_{para}\ 2\ c_{12}/c_{11} \qquad (1)$$

Using the elastic constants c_{11}= 12.02·10^{12} dyn cm^{-2}, and c_{12} = 5.70·10^{12} dyn cm^{-2} [15] we obtain:

$$a_0 = (\ 0.95\ a\ +\ c)\ /\ 1.95 \qquad (2)$$

as a final result for the lattice parameter of unconstrained AlAs.

3. Results.

After an irradiation with 1.6· 10^{19} e/cm^2 we observe a change of the lattice parameter, a, which corresponds to the cubic GaAs substrate as well as to the in-plane value of the tetragonally distorted

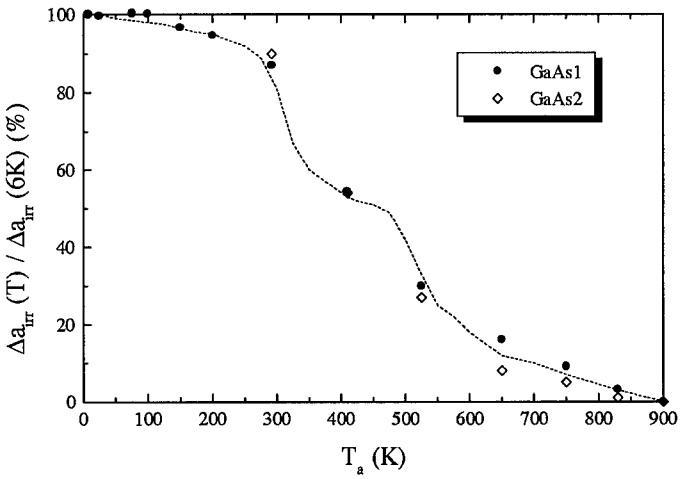

Fig.3: Annealing behavior of the irradiation induced changes of the lattice parameter of the GaAs substrate, which is identical to the in-plane lattice parameter of AlAs, after an irradiation with 2.5 MeV electrons to a dose of 1.6·10^{19} e/cm² and 1.3·10^{19} e/cm² respectively. The average values of ref.10 are shown for comparison.

AlAs layer, of $\Delta a/a = 1.54 \cdot 10^{-4}$. This value corresponds to a specific change of $\eta = (\Delta a/a)/(\Phi) = 9.6 \cdot 10^{-24}$ ($1/e^- cm^{-2}$) and is in reasonable agreement with earlier measurements on GaAs after 3 MeV irradiations [10], which yielded an average value of $\eta = 11.6 \cdot 10^{-24}$ ($1/e^- cm^{-2}$). The smaller value corresponds to the decrease in the displacement cross section, by about 15%, due to the lower electron energy used here.

Fig.3 summarizes the annealing of the lattice parameter, a, measured at the substrate. The annealing of the present samples reproduces the well documented annealing stages of GaAs, i.e. stage I, II around room temperature, stage III around 500K [16] and the final annealing stage between 600K and 850K [10] which are attributed to interstitial and vacancy mobility respectively.

The lattice spacing of the (117) planes includes major contributions of the c-axis and Fig.2 showed a typical rocking curve around the (117)-reflection of the layered sample. Fig.4 summarizes the change of the angular distance between the (117) Bragg reflections of GaAs and AlAs. After irradiation we observe first a small decrease of this distance, which indicates that the irradiation induced increase of the volume of GaAs is larger than that of AlAs. However, there must be an increase also for the AlAs as the expected decrease of the distance would be larger by a factor of $\approx$ 7 if we assume no volume change for the AlAs itself.

The variation of the lattice parameter of the c-axis of AlAs was deduced from the measured changes of the in plane lattice parameter and the spacing of the (117) planes and these changes are shown in Fig.5. These values as well as their changes during annealing are a superposition of changes due to the AlAs itself and changes of c which are induced by the changes of the substrate. As the total changes are larger for the a-axis of GaAs the corresponding annealing stages dominate also the c-axis variations of AlAs. Nevertheless, above 500K we observe that $\Delta\theta$ changes sign, which indicates that some defects in AlAs are stable up to higher temperatures than in GaAs.

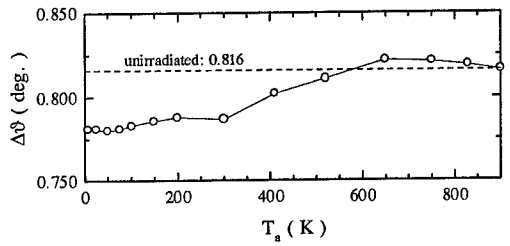

Fig.4: Annealing behavior of the angular separation of the (117) reflections

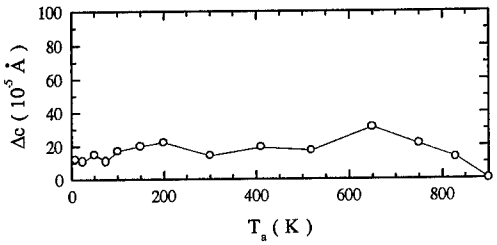

Fig.5: Annealing behavior of the lattice parameter of the c-axis of electron irradiated AlAs

Combining the results for the a-axis and the c-axis we obtain from eq.2 the change of the unconstrained lattice parameter of AlAs, i.e.: $\Delta a_0/a_0 = 0.81 \cdot 10^{-4}$ which is 52% of the change of GaAs. The annealing behavior of the two materials is summarized in Fig.6. Similar to the behavior in GaAs, there is no significant annealing of the lattice parameter in AlAs below 250K. Recovery in AlAs begins at around room temperature and this annealing stage seems to be rather broad and continuous up to about 500K. At this temperature there is a break in the annealing of AlAs, and the defect retention is higher than in GaAs. This behavior is also directly reflected in the experimental values of theta that become larger than before irradiation, simply because the substrate enforced change of the in-plane lattice parameter no longer compensates for the total volume increase. The final annealing step starts at about 750K and complete annealing is observed within the errors at 900K i.e. at about 70K higher temperatures than for GaAs.

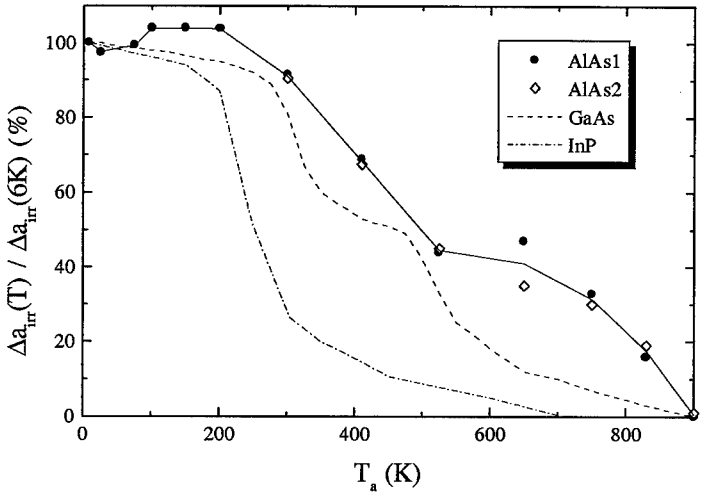

Fig.6: Annealing of the III-V compounds AlAs, GaAs and InP after low temperature electron irradiation to typical doses of $2 \cdot 10^{19}$ e⁻/cm². The major annealing stages are evidenced by changes of the lattice parameter for AlAs and GaAs; for InP the intensity of the HDS is shown as there is no change of the lattice parameter observed due to the cancellation of the contribution of vacancies and interstitial atoms. The data for AlAs present the stress free cubic lattice parameter as determined from equ.2. Circles refer to sample #1 (see fig.2,5) and diamonds to sample #2 ($\Phi = 1.3 \cdot 10^{19}$ e⁻/cm²) which was annealed to room temperature after irradiation (these data are normalized at the annealing temperature of 410K).

4. Discussion and Conclusion.

We investigated the irradiation induced changes of the lattice parameter in order to obtain information about the properties of interstitial atoms and vacancies in AlAs. In spite of the very different amorphization behavior the results for the basic point defects show remarkable similarities to GaAs.

The observed value of Δa_0 is determined by the defect concentration, c, and the relaxation volume of the interstititial atoms, V^i_{rel} , and vacancies, V^v_{rel} , i.e.:

$$\Delta a_0/a_0 = c\,(V^i_{rel} + V^v_{rel})/3\Omega \qquad (3)$$

Ω is the average atomic volume. Separation of the defect concentration and the relaxation volume of the Frenkel pair is not possible from the lattice parameter alone. Nevertheless, the increase of a_0 indicates that the interstitial atoms, which are expected to have a positive V_{rel} dominate over the vacancies which may have smaller negative values of the relaxation volume. A comparison to the relaxation volumes discussed for other semiconductors like GaAs [10], InP [11], or Si and Ge [12], indicates that a value of 1Ω should be considered as a maximum value for ($V^i_{rel} + V^v_{rel}$). Using this value of 1Ω, the measured change of the lattice parameter yields (equ.3) a minimum value for the defect concentration c of about $1 \cdot 10^{19}$ cm^{-3} for the present samples. Hence, Frenkel pairs in AlAs can be frozen in at low temperatures in large quantities.

There is no indication of an unusual high defect mobility as, similar to GaAs, there is no significant annealing below 250K. The broad annealing stage between 250K and 500K might have some fine structure which is not resolved in the present experiment, and may correspond to the stages I, II, and III observed in GaAs, i.e. to the migration of different types of interstitial atoms [10].

We attribute the final annealing to the thermally activated migration of the vacancies. Considering that the corresponding final annealing is observed at about 700K for InP , at 830K for GaAs and at 900K for AlAs (fig.6) there is a remarkable correlation with the melting temperature for these three III-V compounds.
The observations of high concentrations of point defects and high annealing temperatures indicate that neither spontaneous recombination nor low temperature thermally activated defect recovery can be the reason for the resistance of AlAs against amorphization. The observed defects, which are characterized by rather large distortion fields, therefore provide strong support for the model which attributes the special resistance of AlAs against amorphization to stress relaxation by rearrangements of small defect clusters [7,8].

Acknowledgments. We greatly acknowledge the experimental assistance by W. Bergs and the support of Dr. F. Dworschak, B. Schmitz, and F. Werges during the irradiations. We thank J.J. Coleman for supplying the samples. A. Gaber thanks the Deutschen Akademischen Austauschdienst (DAAD) for financial support. Work at the University of Illinois was supported by the U.S. Dept of Energy, Basic energy Sciences under grant, DEFG 02-91 ER 45439.

References.

1. A.G. Cullis, N.G. Chew, and C.R. Whitehouse, D.C. Jacobson, J.M. Poate, and S.J. Pearton, Appl.Phys. Lett. **55**. 1211 (1989)
2. A.G. Cullis, P.W.Smith, D.C. Jacobson, and J.M. Poate , J.Appl.Phys. **69**,1279 (1991)
3. I. Jencic, M.W. Bench, I.M. Robertson, and M.A. Kirk, J.Appl.Phys. **69**.1287 (1991)
4. D.J. Eaglesham, J.M. Poate, D.C. Jacobson, M. Cerullo, L.N. Pfeiffer, and K. West, Appl.Phys.Lett. **58**, 523 (1991)
5. J.L. Klatt, R.S. Averback, D. Forbes, and J.J. Coleman, Phys.Rev. **B 48**, 17629 (1993)
6. W. Wesch, Mat. Res. Soc. Symp. Proc. Vol. **300**, 297 (1993)
7. P. Partyka, R.S. Averback, D.V. Forbes, J.J. Coleman, P.Ehrhart, and W. Jäger, Appl. Phys. Lett. **65**, 421 (1994)
8. P. Partyka, R.S. Averback, D.V. Forbes, J.J. Coleman, P.Ehrhart, to be published
9. F. Xiong, C.J. Tsai, T. Vreelan, and T.A.Tombrello, J. Appl. Phys. **69**. 2964 (1991)
10. A. Pillukat, K. Karsten, and P. Ehrhart, Phys.Rev. **B 53**, 7823 (1996)
11. K. Karsten and P. Ehrhart, Phys. Rev. **B 51**, 10508 (1995)
12. St. Bausch, H. Zillgen, and P. Ehrhart, Mat.Sci. For. **196/201**, 1141 (1995)
13. J. Hemmerich, W. Sassin, and W. Schilling, Z.Phys. **29**, 1 (1970)
14. A.Segmüller and H. Murakami, in **Analytical Techniques for Thin Films,** (Vol. **27** of Treatease on Mat. Sci. and Tech., K.N. Tu and R .Rosenberg eds., Academic Press 1988) p.143-200
15. Landolt-Börnstein , New Series **III/22a** (1992) p.65
16. K. Thommen, Radiat.Eff. **2**, 201 (1970)

Materials Science Forum Vols. 258-263 (1997) pp. 1259-1264

TRANSITION FROM TUNNELING TO POOLE-FRENKEL TYPE TRANSPORT IN ALUMINUM-NITRIDE

R. Schwarz[1], J.J. Sun[2], R. Rocha[1], E. Morgado[3], P.P. Freitas[1,2]

[1] Physics Department, Instituto Superior Técnico, 1096 Lisboa, Portugal
[2] INESC, Instituto de Engenharia de Sistemas e Computadores, 1000 Lisboa, Portugal
[3] Center of Molecular Physics, Instituto Superior Técnico, 1000 Lisboa, Portugal

Keywords: AlN, tunneling transport, charged defects, interface traps

Abstract. Aluminum nitride (AlN) films, prepared by reactive sputtering, with thicknesses between 20 Å and 2 μm, were tested for different transport models. Perpendicular I-V characteristics showed tunneling behaviour for nominal thicknesses below 30 Å. The curves changed to activated behaviour in thicker samples indicating Poole-Frenkel type transport with reemission of charge from deep defects. Their presence could be confirmed indirectly in thicker films by taking optical absorption spectra and by C-V measurements which were performed on MIS structures with p-type silicon as the substrate.

Introduction.

AlN is an intensively studied nitride material with a large bandgap of 6.2 eV. It shows good insulating properties, a high break-down field, and a high thermal conductivity of about 2 W/cmK [1]. Low diffusivity for dopants makes it an excellent passivation material. Since it is lattice-matched to GaN a number of interesting heterostructures can be fabricated, like field effect transistors suitable for high temperature operation [2]. Another application was intensively studied after the discovery of giant magnetoresistance in so-called spin valves that include a thin layer of only a few tens of Ångstrøm thickness of insulating material like Al_2O_3 or AlN, which is sandwiched between permalloy layers [3]. Such structures are used for magnetic recording devices [4]. Deposition of nitrides can be achieved by a number of methods. MOCVD, for example, with NH_3 and Trimethylaluminium and substrate temperatures of 1300 °C lead to polycrystalline 2H-AlN films [5]. Reactive sputtering is a commonly used method and only requires high-purity Al targets and pure N_2 gas [6]. Basically the samples described below are prepared in the same manner.

It was not the purpose of this study to optimize the AlN film quality. Even on the contrary, a series of thin films with relatively large defect densities was prepared and then directly or indirectly characterized for transport processes and the possible role of deep defects in metal-insulator-metal (MIM) and metal-insulator-semiconductor (MIS) structures.

Sample structure.

The films were deposited by reactive sputtering in an Ar/N_2 plasma of an Al target (with 1% Si, and 0.5% Cu) at room temperature. Usually the AlN insulator films were sandwiched between ferromagnetic layers to study magnetoresistance effects in tunnel junctions [7]. The small amount of Cu serves as barrier against electromigration. For the purpose of testing transport models we also used glass substrates that were coated with a semitransparent Co bottom layer. The sandwich structure was terminated with a Cr top contact layer deposited by electron beam evaporation. I-V characteristics were measured in perpendicular direction from room temperature down to 20 K, while limiting the current to some ten mA/cm^2.

Thicker samples were deposited on p-type crystalline silicon wafers with a doping concentration of 10^{14} cm^{-3} forming MIS structures which allowed us to perform C-V measurements and to take capacitance transients.

Study of I-V characteristics.

In this chapter we mainly consider thin AlN films with a thickness from 20 to 400 Å. We measured I-V curves in MIM structures where the bottom metallic contact was either a FeNi ferromagnetic layer or a semitransparent Co layer. As far as basic assumptions about transport through the insulator layers are concerned, we show schematically the situation for tunneling and Poole-Frenkel type charge transport in Fig. 1.

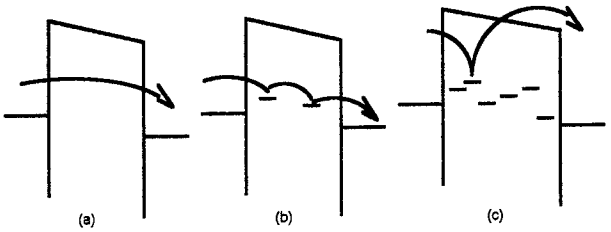

Fig. 1: Illustration of (a) direct tunneling, (b) sequential hopping, and (c) Poole-Frenkel transport through the AlN film.

Fig. 2 shows I-V curves taken on two different samples. Sample JUN-1 shows an excellent fit to tunneling theory [8] with an effective thickness $d = 22.3 \pm 0.1$ Å and a barrier height $\phi_0 = 1.18 \pm 0.01$ eV using the following formula:

$$I_{tunnel} = c_t \left[(\phi_0 - qV/2)\exp\{-b(\phi_0 - qV/2)^{1/2}\} - (\phi_0 + qV/2)\exp\{-b(\phi_0 + qV/2)^{1/2}\}\right] \quad (1)$$

with appropriate constants c_t and b. V is the applied voltage, q the electronic charge. Let us mention that there is no explicit temperature dependence in eq. (1). Figure 3 shows the temperature dependence of the conductivity of sample JUN-1 below room temperature. The curve is nearly flat in agreement with the tunneling hypothesis.

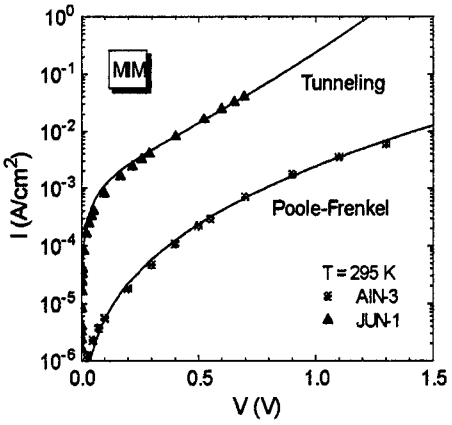

Fig. 2: Room temperature I-V curves of a thin AlN layer (sample JUN-1, 22 Å) with tunneling behaviour and a thick sample (AlN-3, 400 Å) with a good fit to the Poole-Frenkel model.

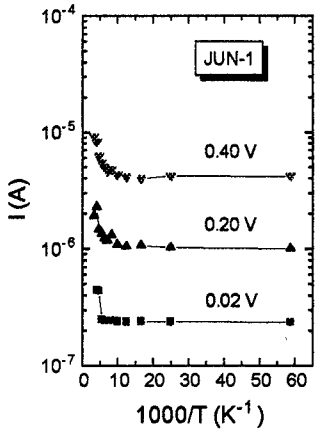

Fig. 3: Temperature dependence of the conductivity in sample JUN-1.

The 400 Å thick sample AlN-3 in Fig. 2 is not well described by eq. (1) at room temperature. The preparation conditions were probably not optimal for a low defect density film as evidenced by the large optical absorption coefficient of about 10^5 cm^{-1} in the visible region. So, we suspect a large defect density to be present in this film. Especially for such a sample we can expect that transport is controlled by defects and Poole-Frenkel type behaviour should be expected rather than tunneling currents. The dotted line in Fig. 2 confirms the good fit to the Poole-Frenkel formula [9,10]:

$$I_{Poole} = c_t F \exp\{-(\phi_0 - qF/\pi\varepsilon_i)^{1/2} q/kT\} \qquad (2)$$

where F is the applied field, ε_i the dielectric constant, and c_t an appropriate constant. The essential features in eq. (2) are the square-root dependence w.r.t. the electric field and a strong temperature dependence. Some of the thicker samples showed the transition from tunneling to Poole-Frenkel type transport when increasing the temperature from about 20 K to 300 K. To further characterize the defects in AlN we have performed measurements on thick films as described in the following section.

Areal defect density from C-V characteristics.

For capacitance measurements we used MIS structures with thick AlN films and we verified that the measurements were not affected by leakage currents. Also the optical absorption was negligible as expected for insulator films. An upper limit of 50 cm^{-1} for the absorption coefficient in the visible region could be inferred from photothermal deflection

and reflection spectroscopy. The variation of the capacitance in the semiconductor layer served as a sensor to monitor the charge transfer in the insulator layer.

Figure 4 shows C-V curves taken with different voltage ramp speeds. The overall trend is that negative voltage bias shifts the curve to negative bias values. The opposite is true for positive voltages. The hysteresis is small when the scan is fast which leaves less time for deep defects to recharge. Taking a voltage shift of 2 V and the insulator layer capacitance of 3 nF for a 2-mm-diameter contact, an estimate for the involved charge of 1.5×10^{12} cm^{-2} can be calculated.

Time-dependent capacitance measurements should reveal the energy scale involved. Fig. 5 shows a capacitance transient measured at zero bias in the 0.25 μm thick sample AlN-6 after a filling pulse at -5 V of 8 s duration is applied. The decay is obviously non-exponential indicating that a broad energetic distribution of trap levels is involved. From standard textbooks on DLTS techniques [11,12] the energetic level E_t of the traps that contribute most to the change of capacitance δC in the time window $\delta t = t_2 - t_1$ is given by

$$E_t = kT \ln\{ \ln(t_2/t_1) / (\nu_0 \delta t) \} \qquad (3)$$

where ν_0 is a typical phonon frequency. We have used a value of 10^{12} s^{-1} for the analysis below. Then a typical trap energy value of 0.7-0.8 eV follows from the time scale of the transients. Together with the charge estimate given in the preceding paragraph we can quite safely exclude that the defect density related to this charge is originating from the high-quality semiconductor substrate itself. In addition, the energetic level of the dopants that could be responsible for the shift is much shallower than the value of E_t given above.

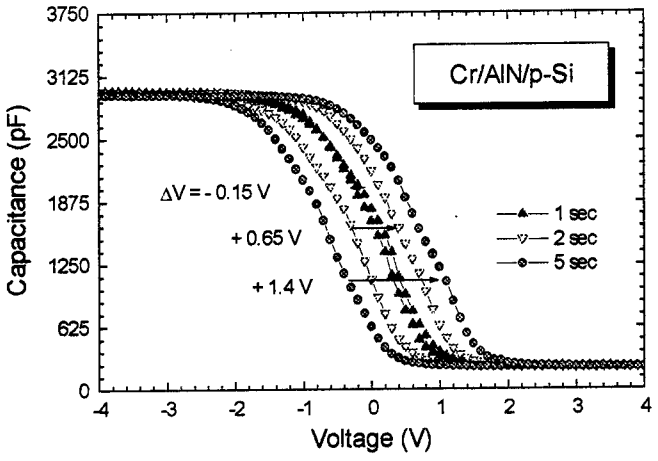

Fig. 4: Hysteresis in C-V curves (sample AlN-6, 0.25 μm) with different scan speed.

If we assume the defects to be located at the semiconductor-insulator interface then the equilibration of charge after the filling pulse would lead to current transients which are

related to the capacitance transients through $I(t) = dQ/dt = V\ \delta C/dt$. Then the areal density N_{area} of occupied traps is simply obtained from:

$$N_{area}(E) = tV_f/(qkT)\ \delta C/\delta t \qquad (4)$$

The result for sample AlN-6 is given in Fig. 5. Since we applied a negative filling pulse V_f and work with a p-type substrate it is most likely that the moving charges are holes being released from the insulator layer and swept into the substrate.

Discussion.

We have assumed so far that the AlN layers in the MIS samples have a large density of interface defects. It is, however, not possible from the analysis which leads to eqs. (3) and (4) to distinguish interface and bulk defects which both contribute to the areal density. One solution would be analyze a thickness series of AlN films deposited on crystalline silicon substrates, calculate the areal defect density as above, and then subtract the constant contribution from interface states. This procedure can also be followed for optical absorption data.

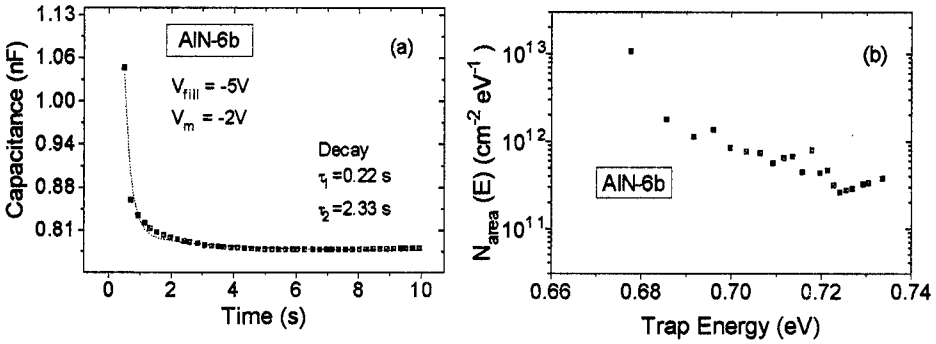

Fig. 5: (a) Capacitance transient and (b) areal defect density inferred from (a).

Another handicap in the above analysis is that the thin samples were deposited in a run different from the thick samples, so their defect densities are not directly comparable. This problem, however, cannot be solved even by preparing a thickness series spanning the whole range with different substrates as needed for the different types of experiments. Since, it is not clear whether films of only a few Ångstrøm are of exactly the same material quality than the bulk films. In addition, initial film growth might be different on different types of substrates.

The overall behaviour of the films studied here is summarized in the illustration of different types of transport in Fig. 1. Thin samples, essentially independent of the defect density present, will lead to tunneling currents (Fig. 1a) for thicknesses below about 30 Å. In thicker samples tunneling is still possible via sequential hopping if a certain defect density

is available (Fig. 1b). Finally, in thicker samples of modest defect density, where the tunneling contribution would be relatively small due to the large distances involved, or in samples of high defect density a Poole-Frenkel type current transport (Fig. 1c) is observed.

Conclusion.

Perpendicular transport measurements in MIM structures showed a transition from tunneling behaviour in extremely thin AlN films to Poole-Frenkel type transport in thicker insulator films indicating reemission of charge from deep defects. The presence of such defects was confirmed in thicker samples through optical absorption and C-V measurements. From the capacitance transients in MIS structures we could infer an areal density of 10^{11}-10^{12} $cm^{-2}eV^{-1}$ defects at an energetic level of 0.7 to 0.8 eV. We will need to include other complementary measurements in order to extract the energetic and spatial defect distribution also in the extremely thin AlN samples.

Acknowledgement: We want to thank U. Mardolcar, L. Pereira, and M. Schmidt for assistance with C-V measurements, M. Vieira, M. Fernandes, and J.P. Conde for support during the experimental set-up, A. Veloso, S. Cardoso, and F. Silva for sample preparation. Partial financial support for this work from the Portuguese Ministry of Science and Technology through project PRAXIS/PCEX/P/FIS/7/96 is gratefully acknowledged.

References.

1. H. Morkoç, S. Strite, G.B. Gao, M.E. Lin, B. Sverdlov, and M. Burns, J. Appl. Phys. **76** (1994) 1363.
2. M.A. Khan, M.S. Shur, J.M. Kuznia, Q. Chen, J. Burn, and W. Schaff, Appl. Phys. Lett. **66** (1995) 1083.
3. T. Miyazaki and N. Tezuka, J. Magn. Magn. Mater. **139** (1995) L231.
4. T.S. Plaskett, P.P. Freitas, N.P. Barradas, M.F. da Silva, and J.C. Soares, J. Appl. Phys. **78** (1994) 6104.
5. D. Prasad Beesabathina, K. Fekade, K. Wongchotigul, M.G. Spencer, and I. Salamanca-Riba, Mat. Res. Soc. Symp. Proc. **339** (1994) 363.
6. T.J. Kistenmacher, S.A. Ecelberger, and W.A. Bryden, Mat. Res. Soc. Symp. Proc. **339** (1994) 509.
7. T.S. Plaskett, P.P. Freitas, J.J. Sun, R.C. Sousa, F.F. da Silva, T.T.P. Galvão, N.M. Pinho, S. Cardoso, M.F. da Silva, and J.C. Soares, to be published in Mat. Res. Soc. Symp. Proc. (1997)
8. J.C. Simmons, J. Appl. Phys. **34** (1963) 1793.
9. J. Frenkel, Phys. Rev. **54** (1938) 647.
10. T. Muschik and R. Schwarz, Phys. Rev. **B51** (1995) 5078.
11. D.K. Schroder, *Semiconductor Material and Device Characterization,* (John Wiley & Sons, New York, 1990).
12. B.G. Streetman, *Solid State Electronic Devices*, (Prentice-Hall, 1990).

Materials Science Forum Vols. 258-263 (1997) pp. 1265-1274

GROWTH SURFACE DEPENDENCE OF CATHODOLUMINESCENCE OF CUBIC BORON NITRIDE

H.Kanda*, A.Ono**,Y.Suda** and K.Era***

*NIRIM, 1-1 Namiki, Tsukuba, Ibaraki 305, Japan

**Tokyo University of Agriculture and Technology, 2-24-16 Koganei, Tokyo 184, Japan

***Helios Optical Science Lab., Inc., 1-13-12 Sengen, Tsukuba, Ibaraki 305, Japan

Key words: Cubic Boron Nitride, Cathodoluminescence

Abstract

We have investigated cathodolumienscence(CL) of a type of commercially available cBN crystals. Four kinds of luminescence bands were seen in a given crystal. Three of them have been reported and named the O-center, the T-center and the UCL, but the other one, which has a broad peak around 350 nm, has not been documented. Clear growth surface dependence of the bands was seen; the O-center was present on nitrogen terminated {111}, the T-center and the undocumented broad band were on boron terminated {111} and the UCL was on {100}. The O-center and UCL were intensified with annealing at 1600 °C and 6 GPa.

1. Introduction

Cubic boron nitride(cBN) is a typical wide band gap semiconductor with ~6 eV of energy gap. However, little research work on impurity control or defect structure has been made for cBN, in contrast that diamond, which is a similar material to cBN, has a long history in such studies. Only a few group have studied on luminescence of cBN, and about 20 luminescence centers have been documented so far1-5). However, structures of them have not been identified definitely. As for distribution of the centers, only a brief description that four {111} surfaces of octahedron, i.e. boron terminated or nitrogen terminated one, exhibit bright luminescence has been given(6).

In the present study, we took cathodoluminescence(CL) spectra of a type of commercially available cBN crystals, and observed distribution of the CL centers.

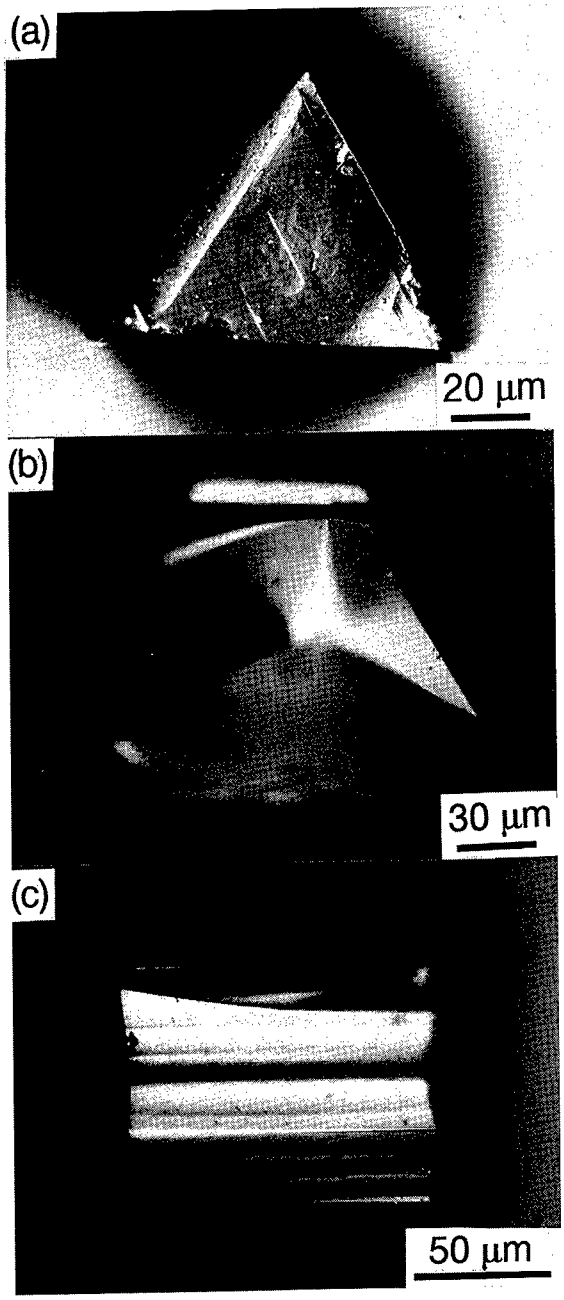

Fig.1 Morphology of (a) {111}B, (b) {111}N and (c) {110} of cBN crystal (Differential interference microscopy)

2. Experimental

Specimens examined in this study were commercially available cBN grains(SBN-M, SHOWA DENKO KK, Japan), which were 200 mm in diameter and exhibited amber color. Roughly speaking, each particle showed octahedral habit consisting of {111} surfaces, but small {100} surfaces sometimes truncated tops of the octahedron. Most of crystals, however, showed complicated or irregular shapes caused by twinning, agglomeration or chipping off. We selected crystals having a simple form for the CL investigation.

Main effort of the investigation was made for crystals annealed at 6GPa, 1600 °C for 5 to 30 hr, although as-grown crystals were also investigated, because the annealed crystals gave more intense luminescence. For annealing, the crystals were sandwiched between graphite discs placed in an NaCl pressure medium which was filled in a graphite heater of a belt type high pressure apparatus. Some crystals were annealed in CsCl powder so as to anneal in more isostatic environment, although influence of the environment on the CL property was not seen. The crystals recovered from the cell were cleaned in water or boiled mixture of H_2SO_4 and HNO_3 to remove CsCl and graphite. With annealing, color of the crystals slightly became paler, but their morphology did not change at al.

Cathodoluminescence spectra and images were taken using a TOPCON SX-40A scanning electron microscope. Accelerating voltage was 25 or 30 kV and beam current was ~10^{-8}A. The CL spectra were measured by a SPEX 1/3 m grating monochrometer and a Hamamatsu R1104 photomultiplier. The monochrometer has 300 nm and 500 nm blazed gratings. We used the former grating for measurement between 200 and 400 nm and the latter for measurements between 300 and 500 nm. The gratings have different spectral response each other, but we did not make a correction of the spectral response. Therefore, there is considerable ambiguity in peak position of broad bands. In fact, we noticed that the peak position of a broad band shifted by 30 nm around 350 nm when changing a grating to the other. The cBN crystals, which were coated with gold to be electrically conductive, were cooled to ~110K by a liquid nitrogen-cooled cold stage for the CL measurements.

3. Results and discussion

3.1 Surface morphology

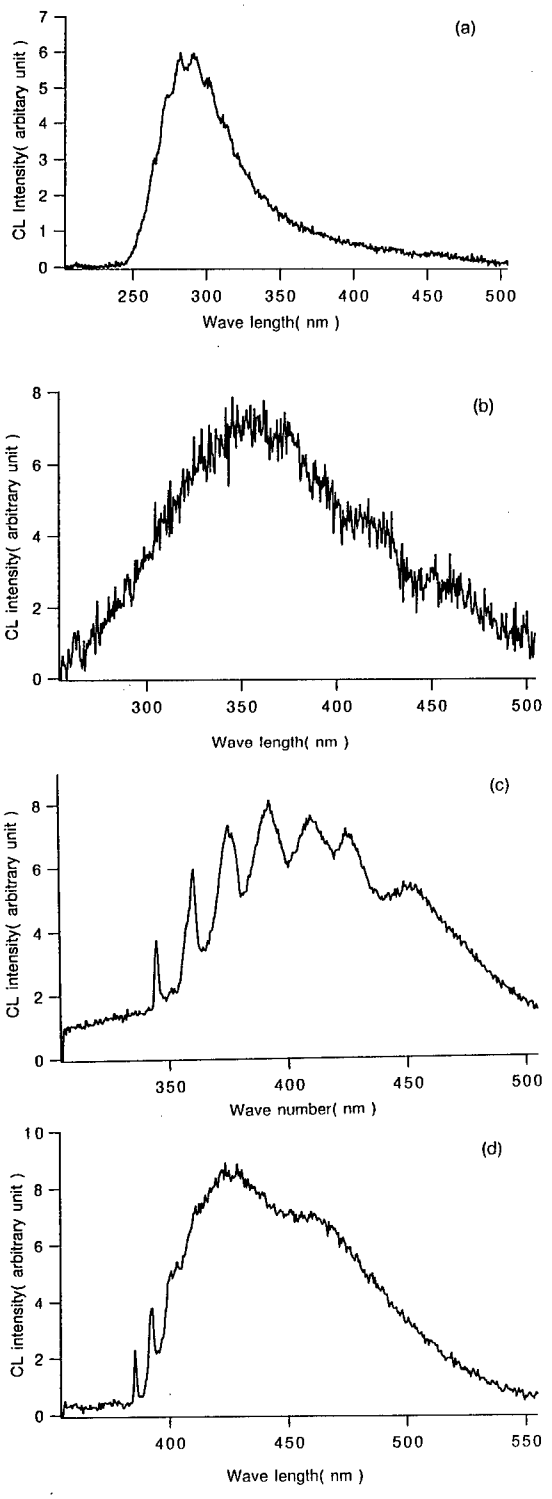

Fig.2 Cathodoluminescence spectra from (a) {111}B, (b) {111}B, (c) {100} and (d) {111}N.

Four {111} surfaces of cBN octahedron have different arrangements of surface atoms from the others, i.e. the four surfaces are terminated by boron atoms, whereas the others are by nitrogen atoms. The former and the latter surfaces are named {111}B and {111}N in this article, respectively. The two types of surfaces showed different morphology as described below. Following an earlier report(7), {111} surfaces that have edges perpendicular to striations on adjacent {100} surfaces were judged to be {111}B, and the others were {111}N.

{111}B surfaces were so flat that a scanning microscope(SEM) could not detect patterns on it, but an optical microscope(Nomarski type microscope) detected triangle growth hillocks on some of crystals, as shown in Fig.1(a).

On the other hand, {111}N surfaces were covered with vicinal surfaces and looked to be convex, as shown in Fig.1(b). The slope of the vicinal surfaces was so steep that it was difficult to focus whole surface with the optical microscope and that the slope was detected even by SEM. The vicinal surface may be of a growth hillock formed by the spiral growth mechanism, although the slope is so smooth that steps of spiral pattern were not detected. As shown in Fig.1(c), clear striations along a [110] direction were seen on {100}. The distinct striation gives rise to undulated surface, and the surface may not be a flat {100} in an atomic scale.

3.2 Cathodoluminescence spectra

Four kinds of luminescence centers were observed in a given crystal. Fig.2(a) shows a spectrum of a broad band with a peak around 300 nm. Detailed observation of the spectrum gives an indication of several shoulders between 250 and 300 nm. Shipilo et al(5) reported a similar spectrum in which several peaks are seen . They named the band the T- center. The band shown in Fig.2(a) must be the T- center, although peaks are not seen. If we take the spectrum with higher resolution or at lower temperature, sharp peaks would appear at the positions of shoulder. This center is observable even at room temperature, but intensity increases with decreasing temperature. The center was seen in both pre- and post-annealed crystals.

Fig.2(b) shows a broad band with a peak around 350 nm, which has not been undocumented till now. As noted above, the peak position was around 350 nm when the 300 nm blased grating was used. On the other hand, it was around 380 nm when the 500 nm

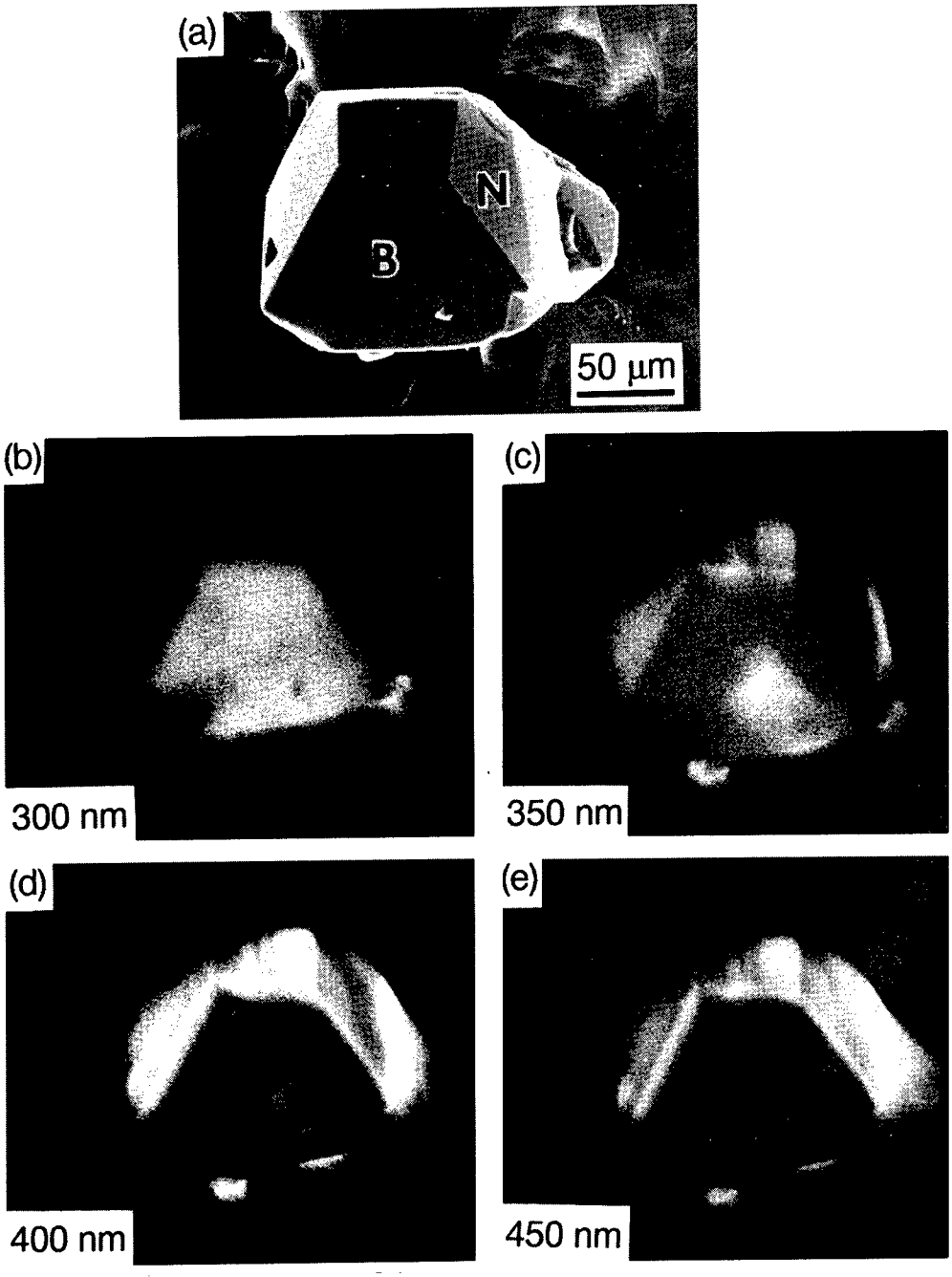

Fig.3 SEM and cathodoluminescence(CL) images of a cBN crystal; (a) SEM, CL at (b) 300 nm, (c) 350 nm, (d) 400 nm and (e) 450 nm. Letters, B and N, in the SEM image indicate {111}B and {111}N surfaces, respectively.

blased grating was used. In the luminescence centers of cBN reported so far, a broad band seen around 350 nm is only a band named PCL(4). This band, however, is seen in Be-doped crystals that exhibit blue color. The crystals investigated in this study are amber or brown color and are not Be-doped crystals. Thus, the band shown in Fig.2(b) is not PCL definitely.

Fig.2(c) shows a band with a zero phonon peak at 347 nm and several phonon assisted bands at the lower energy side. This band has been found in a variety of cBN crystals, and named UCL(4), although its defect structure has not been identified. This band was seen in the annealed crystals, but not in the pre-annealed crystals.

Fig.2(d) shows a band with a sharp peak at 388 nm. A broad peak is accompanied around 460 nm in this band, but intensity ratio between the 388 nm peak and the 460nm broad peak was not always constant, indicating that the broad band is of another optical center. The two peaks at 388 nm and 394 nm seen in the spectrum look to be the same as those described by Shipilo et al, who have named the band the O-center. This band was detected in as-grown crystals, but it intensity increased with annealing.

3.3 Cathodoluminescence image

Fig.3 shows CL luminescence images at various wavelength in addition to a SEM image of a representative crystal. A {111}B surface is bright at 300 nm as shown in Fig.3(b), indicating that the T center(Fig.2(a)) is seen only in {111}B.

A central part of {111}B is bright even at 350 nm (Fig.3(c)). The broad band shown in Fig.2(b) was seen in this part. This band was also limited to {111}B surface, although it was seen less frequently than the T center. Although both the T center and the broad band are seen in {111}B surfaces, their distribution is different definitely. Therefore, the bands are not of the same optical center.

{111}N and {100} surfaces are bright at 400 nm as shown in Fig.3(d). Both the regions are bright even at 450 nm(Fig.3(e)), but CL intensity ratio of {111}N to {100} is larger at 450 nm than at 400 nm, as shown in Fig.3(d) and (e), indicating that a band present in {111}N is different from that in {100}. In fact, the UCL center was seen from {100} and the O-center was from {111}N.

Intensity of the luminescence was not uniform even in each surface. Striations are clearly seen in the CL images of {100}, which reflect surface morphology. However,

inhomogeneities of the CL images in {111}B and {111}N did not show clear correlation with surface morphology.

Shipilo et al(5) described that the T- and O- centers are seen in crystals grown with doping Si, suggesting that the centers are Si-related. Based on this suggestion, the presence of the centers in {111} surfaces leads to a conclusion that silicon impurity is easily incorporated in {111}. This feature is the same as that of diamond, since it is well known for diamond that impurities such as nitrogen, boron and nickel are contained in {111} with the highest concentrations.

However, apart from diamond, the cBN crystals exhibit {111}B and {111}N terminated by boron and nitrogen, respectively, and two different Si centers are seen corresponding to the two types of {111}. This indicates that different Si related defect structure is formed even at the same growth condition, if surface structure is different.

Shipilo et al(5) also showed that another center, the G- center, are seen in Si-doped crystals in addition to the T- and O- centers, but we could not detected the G- center. The G-center is said to be seen in boron rich cBN crystals, whereas the O-center in nitrogen rich cBN. Thus, these two centers can not be detected in crystals grown in a condition. The crystals investigated in this study may be grown from a catalyst which produces nitrogen rich cBN crystals.

The O- and UCL centers increased in intensity with annealing. Change to paler color with annealing suggests that some impurities diffuse to form other types of optical centers with annealing. There is a report that complexes of impurities are formed with annealing in diamonds(8), suggesting that defect structures of the O- and UCL centers are some complexes of impurities.

4. Conclusion

Four kinds of optical centers were detected on one cBN crystal by cathodoluminescence spectroscopy. Two of them, named the T- and O- centers, have been suggested to be silicon related. Another is called the UCL center, but its structure has not been known. The other is an undocumented broad band. Each band clearly depended on growth surfaces. The O- and UCL centers increased intensity with annealing at 1600 °C under high pressure.

Acknowledgments

We would like to thank Mr. E.Iizuka of Showa Denko KK for providing cBN crystals used in this study and Dr. Mishima of NIRIM for showing his unpublished review paper on cBN.

References

1. N.D.Tkachev, V.B.Shipilo and A.M.Zaitzev(1985) Sov.Phys.Semicond. 19, 491)
2. A.M.Zaitzev, A.A.Melnikov and V.F.Stelmakh, Sov. Phys. Semicon. 21, 671 (1987)
3. V.B.Shipilo, E.M.Shishonok, A.M.Zaitzev, A.A.Melnikov and A.I.Olekhnovich, Phys.Stat.Solid, (a) 108, 431 (1988)
4. K.Era and O.Mishima, Mat. Res.Soc.Symp. Proc. 162, 555 (1990)
5. V.B.Shipilo, A.I.Lukomski and L.M.Gameza, J. Appl. Spectroscopy of USSR, 55, 567 (1991),
6. N.J.Pipkin, J. Mater. Sci 15 (1980)
7. M.Kagamida, H.Kanda, M.Akaishi, A.Nukui, T.Ohsawa and S.Yamaoka, J.Crystal Growth, 94, 261 (1989)
8. V.A.Nadolinny and A.P.Yelisseyev, Diamond and Related Materials, 3 (1993) 17

Materials Science Forum Vols. 258-263 (1997) pp. 1275-1280

N-VACANCY DEFECTS IN c-BN AND w-BN

R. Mota[1], P. Piquini[1], V. Torres[2] and A. Fazzio[3]
[1]Departamento de Física, Universidade Federal de Santa Maria, 97119-900, Santa Maria, RS, Brazil
[2]Departamento de Física, Universidade de Aveiro, 3810, Aveiro, Portugal
[3]Instituto de Física, Universidade de São Paulo, CxP 66318, 05315-970, São Paulo, SP, Brazil

Keywords:electronic structure, N-vacancy, BN

Abstract. Using the ab initio Hartree-Fock method in the molecular-cluster approach the neutral and doubly-positively charged N-vacancy in cubic boron nitride (c-$V_{[N]}$, c-$V_{[N]}^{+2}$) and in neutral wurtzite boron nitride (w-$V_{[N]}$) are studied. For all cases, after a total energy minimization, a C_{3v} local symmetry configuration is found. A charge trapped in the nitrogen vacancy is obtained resembling a F-center-type defect, like in alkali-halides. The possible role played by this F-center-type defect in the interpretation of EPR signals is discussed.

Introduction.

The group III nitrides exhibits several crystal structures. In particular, bulk boron nitride has been detected in different allotropic forms such as hexagonal (h-BN), zinc blende (c-BN), wurtzite (w-BN) and more recently in tubes (t-BN) [1]. For their electronic similarities with carbon, the h-BN and c-BN present properties close to that of graphite and diamond, respectively. The c-BN is the lightest of the III-V semiconductors, with a large band-gap (≈6.4 eV), which has several similarities to diamond, such as crystal structure, wide energy bands, extreme hardness, high thermal conductivity, high melting temperature etc. But while diamond is readily doped only p-type, the c-BN can be doped both p and n-type when suited impurities are added [2]. In this sense, c-BN is a potential candidate for high-temperature devices and is also an effective material for ultrahard materials applications. Thus, developments in producing high quality c-BN are worthwile from both basic science and technological viewpoints.

In any class of materials, defects play a role in determining the mechanical, thermal, optical and electronic properties. The c-BN and w-BN forms have a tendency to be nitrogen deficient during their growing process, forming vacancies and other native defects like antisite, C, H and O impurities [3].

In this paper we present theoretical results for N-vacancy in relaxed c-BN and w-BN crystal lattices. Particularly, our main interest in the present work is to investigate how this defect is related to the F-center-type defect, which is clearly observed in h-BN with an electron trapped in a nitrogen vacancy.

Theoretical Procedure.

We have studied the defects using a molecular-cluster model. The "pure crystal" has been simulated with 71-atoms $(N_{19}B_{16}H_{36})^{3+}$ in T_d-symmetry for the c-BN and a cluster with 64-atoms $(N_{16}B_{14}H_{34})^{2+}$ in C_{3v}-symmetry for the w-BN. The net charge 3+ (2+) at the cluster is necessary to get a neutral charge condition in c-BN (w-BN). The hydrogen atoms are introduced to saturate the dangling bonds at the cluster surface, as usual [4].

To study the electronic and structural properties we have used the all-electron Hartree-Fock-LCAO method. The atomic basis adopted here is the split-valence 3-21G basis set [5], which consists of 6s3p (3s) primitive Gaussian function contracted in the 3s2p (2s) basis function on each B and N (H) atoms. The calculations are performed using the program GAMESS [6].

N-vacancy and F-center Formation.

We show schematically in Fig. 1 the electronic energy levels in the gap region, using a defect molecule model for the defects in c-BN. In the left-hand side is shown the pure system with $a_1^2 t_2^6$ configuration. Our procedure to estimate the energy levels in the gap has been to compare the pure cluster with the defect clusters. Fortunately, in all the studied defects the densities of states at the top of valence band practically do not change. It means that the top of the valence band, used as a reference for the calculated electronic levels, is fairly well defined.

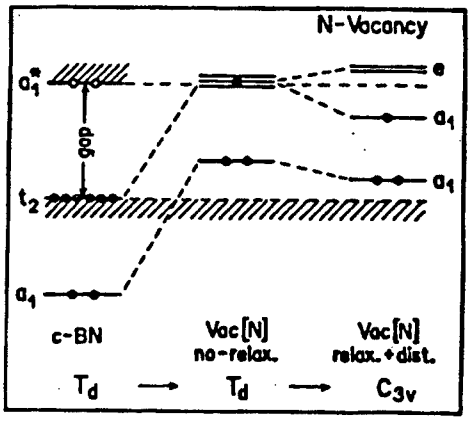

Fig. 1.Schematic representation of the electronic energy levels in the gap region for the "pure" c-BN in a T_d symmetry (left side), non-relaxed c-$V_{[N]}$ in a T_d symmetry (center) and relaxed + distorted c-$V_{[N]}$ in a C_{3v} symmetry (right side). The full circles represent the electrons.

In a previous paper [7] we have studied the electronic and structural properties of the boron-antisite, oxygen-impurity and N-vacancy neutral defects in c-BN. In this paper our main concern is to understand the electronic and structural properties of the N-vacancy in c-BN and w-BN. Particularly for these native defects, we intend to discuss the possible formation of a negative charge trapped in a nitrogen vacancy (F-center-type defect). In the case of c-$V_{[N]}$, the calculated breathing mode relaxation (A_1-mode) of the nearest-neighbor boron atoms gives an outward displacement of 0.31 Å for these atoms. As we expected, the t_2 orbital with one-electron provides a Jahn-Teller (JT) distortion. A small C_{3v}-mode distortion is observed with one boron atom (B_1) following a <111> direction and the other boron atoms (B_2, B_3, B_4) getting closer. On the other hand, in the w-$V_{[N]}$, where the N-site is in C_{3v} local symmetry, a JT distortion is not expected. We have performed an A_1-mode relaxation for the first neighbor B-atoms and an outward displacement around 0.27 Å is observed. As we shown in Fig. 1, the removal of the N atom in the c-BN, before lattice relaxation, results in two orbitals, an a_1 fully occupied in the gap region and a t_2 singly occupied resonant in the conduction band, in agreement

with Gubanov et al. and Castineira et al. [8]. After the total energy minimization, a C_{3v} configuration is obtained, with the t_2 orbital splitting in an a_1 plus an e orbitals, with a final configuration $1a_1^2 2a_1^1 e^0$. For our description in this paper, we will label the $1a_1^2$ as the "HOMO-1" orbital and $2a_1^1$ as the "HOMO" orbital. Besides the structural difference between c-BN and w-BN, our calculations have shown that the energy levels in the gap region for the case of w-$V_{[N]}$ are very similar to that in c-$V_{[N]}$.

In Fig. 2 we plot the total charge distributions for the pure c-BN and c-$V_{[N]}$ (a and b, respectively) and the wavefunctions for c-$V_{[N]}^{+2}$ in the plane that contains B_2-B_3-B_4 centers (Fig. 2c) and the wavefunction in the plane B_1-$V_{[N]}$-B_3 (Fig. 2d). From our calculations, we can observe that for the c-$V_{[N]}$, in the neutral charge state, the HOMO orbital has the charge located over the B_1-atom. On the other hand, the HOMO-1 orbital presents a charge distribution shared among the three equivalent (B_2, B_3 and B_4) boron atoms near the vacancy with a very high charge density concentrated in the vacancy region.

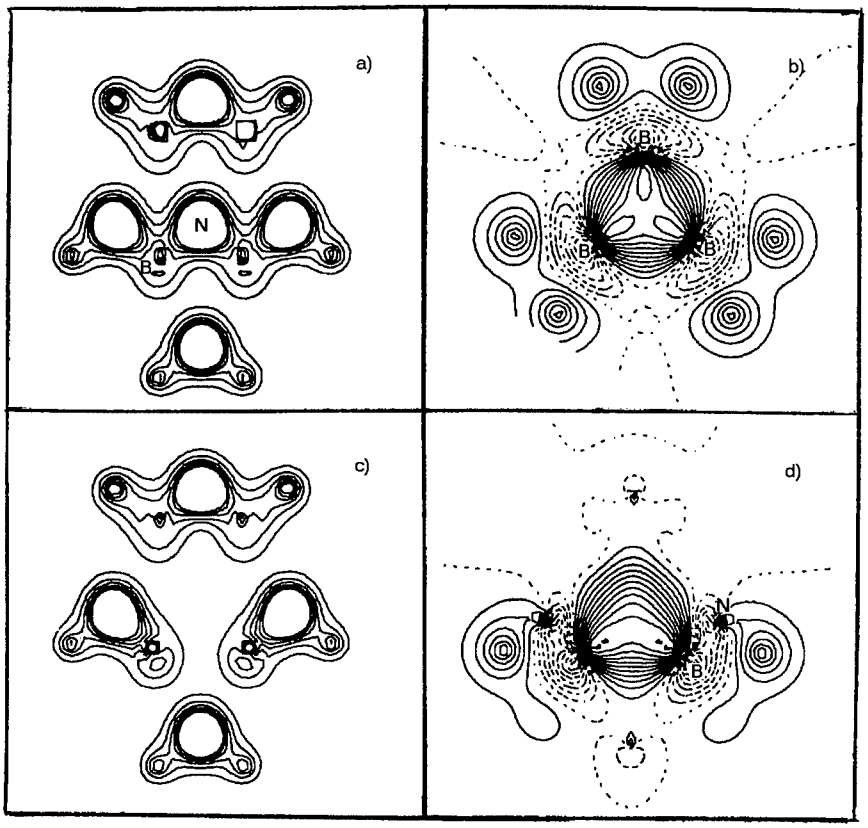

Fig. 2. Total charge distributions for the a) "pure" c-BN and b) c-$V_{[N]}$ at the (110) plane. The wavefunctions for the homo orbital in the c-$V_{[N]}^{+2}$ system at a plane containing c) the three equivalent boron atoms near the vacancy and d) two equivalent boron atoms and the vacancy region.

Similarly, in Fig. 3 we show the total charge distribution for "pure" w-BN and w-$V_{[N]}$ (Fig. 3a and 3b, respectively) together with the wavefunctions for the HOMO and

HOMO-1 orbitals in planes that contain two boron atoms and the vacancy region(Fig. 3c and 3e, respectively) and the three equivalent boron atoms (Fig. 3d and 3f, respectively)

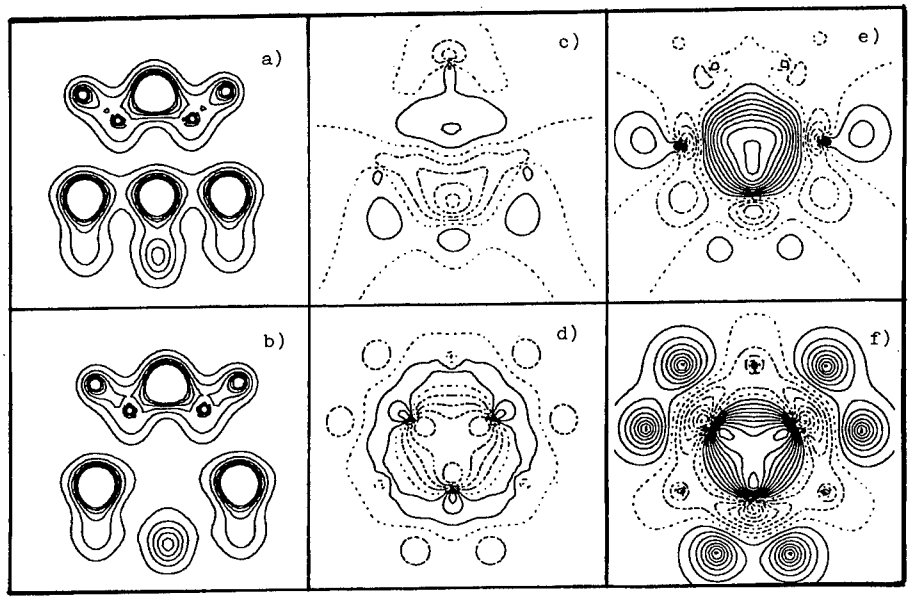

Fig.3. Total charge distributions for a) the "pure" w-BN and b) w-$V_{[N]}$ at the (110) plane. Wavefunctions for the HOMO (c and d) and HOMO-1 (e and f) orbitals at planes containing two borons atoms and the vacancy region (c and e) and the three equivalent boron atoms near the vacancy (d and f).

We can see that these systems (c-BN and w-BN) show a high electronic density concentrated in the vacancy region yielding a F-center-type defect with trapped electrons in the central region. In general, we can say that the paramagnetic defects are present in all BN structures and they can affect important electronic and structural properties [9]. It has been assumed [10] that they are predominantly resulting from a nitrogen vacancy with a negative charge trapped therein, such as F-centers in alkali halides [11]. BN in different allotropic forms has been analyzed by electron paragnetic resonance (EPR) and by nuclear magnetic resonance (NMR) [10].

In accordance with Fanciulli and Moustakas [12], it is experimentally observed that there is an increase in the spin density when the structure changes from cubic to hexagonal. Also, they observed that for the c-BN the EPR line is inhomogeneously broaded, differently to the observed signal for h-BN. In fact, for c-BN, the line shape is gaussian and its width is an order of magnitude larger than that of single unresolved components as estimated from h-BN [10].

Our charge density results for c-BN and w-BN indicate clearly that the corresponding HOMO charge densities are much smaller than for HOMO-1 in both neutral cases. Then, the weak EPR signal observed in the neutral charge state should be a direct consequence of this kind of charge distribution. However, as a prediction, we can predict that, as a consequence of the HOMO-1 orbital, a stronger EPR signal should be

detected in $V_{[N]}^{+2}$ or any complex $V_{[N]}$+X, where X is an acceptor impurity. As far as we know, there is no experimental data on this.
For h-BN, carbon incorporation changes the EPR signal and increases the concentration of spin significantly [12]. This result is consistent with the notion that carbon doping stabilizes the electron in a nitrogen vacancy. Similarly to h-BN case, a mechanism including a C-incorporation could lead to same effect as suggested by us through ionization. It means that the C-incorporation could result in an impurity level in the gap region which would accept electrons. This mechanism, leading to an EPR signal dominantly coming from HOMO-1 orbital, should presents similar characteristics to those suggested to be observed through double ionization.

Acknowledgments.
This work has been supported by Brazilian agencies CNPq/JNICT, FAPESP and FAPERGS

References.
[1] R.H. Wentorf, Jr., J. Chem. Phys. **36**, 1990 (1962); A.Meller, *Gmelin Handbuch der Anorganische Chemie*, Boron Compound, 3nd Supplement **3** (Springer-Verlag, Berlin, 1988) p. 1-91; see also *Properties of Group III Nitrides*, edited by J.H. Edgar (INSPEC, London, 1994).
[2] O. Mishima, J. Takanaka, S. Yamaoka, and O. Fukunaga, Science **238**, 181 (1987).
[3] L.J. Terminello, A. Chaiken, D.A. Lajuano-Smith, G.L. Dalt and T. Sato, J. Vac. Sci. Technol. **A12**, 2462 (1994).
[4] L.M. Scolfaro and A. Fazzio, Phys. Rev. **B36**, 7542 (1987).
[5] J.S. Binkley, J.A. Pople, and W.J. Hehre, J. Am. Chem. Soc. **102**, 939 (1980).
[6] M.W. Schmidt at al., J. Comput. Chem. **14**, 1347 (1993).
[7] P.Piquini, R. Mota, T.M. Schmidt, and A. Fazzio, to be published in Phys. Rev. B.
[8] V.A. Gubanov, L.A. Hemstreet, C.Y. Fong, and B.M. Klein, Appl. Phys. Lett. **69**, 227 (1996); J.L.P. Castimeira, J.R. Leite, L.M.R. Scolfaro, R. Enderlein, J.L.A. Alves, and H.W. Leite Alves, to be published in Mater. Sci. Eng.
[9] F. Zhang and G. Chen, Mat. Res. Soc. Symp. Proc. **242** (Materials Research Society, Pittsburgh), 613 (1992).
[10] M. Fanciulli and M. Corti, Phys. Rev. B **52**, 11872 (1995).
[11] M.P. Surh, H. Chacham, and S.G. Louie, Phys. Rev. B **51**, 7464 (1995).
[12] M. Fanciulli and T. D. Moustakas, Mat. Res. Soc. Symp. Proc. **242** (Materials Research Society, Pittsburgh), 605 (1992); Physica B **185**, 228 (1993).

Materials Science Forum Vols. 258-263 (1997) pp. 1281-1286

MULTIPHONON-ASSISTED TUNNEL IONISATION OF DEEP IMPURITIES IN HIGH-FREQUENCY ELECTRIC FIELD

I.N.Yassievich, V.I.Perel
Ioffe Physico-Technical Institute
Polytechnicheskaya 26, 194 021 St.Peterburg, Russia

Key words: deep impurities, tunnel ionisation, multiphonon transition, ac electric field.

Abstract. A theory of multiphonon-assisted tunnelling ionisation in alternating electric field is presented. It has been shown that the probability of tunnelling increases with increasing frequency of the electric field. The high-frequency effect manifests itself better at low temperature.

Introduction.

Ionisation by multiphonon-assisted tunnelling was extensively studied in semiconductors subjected to static electric fields [1-6]. Recently ionisation of semiconductor deep impurity centers has been observed in a field of far-infrared radiation, where photon energies are by a factor of several tens smaller than the binding energy of impurities [7-9]. It was shown that the results can be described by the application of the theory of multiphonon-assisted tunnel ionisation in dc electric field equal to the amplitude F of wave field. In these experiments, the emission rate was independent of the radiation frequency.

However, new experiments performed at lower temperature have demonstrated a frequency dependence. This work presents the consideration of the multiphonon-assisted tunnel ionisation in high-frequency electric field.

Probability of thermoactivated tunnel ionisation in semiclassical approximation.

Let's consider the process of thermoactivated tunnel ionisation in ac electric field. Thermal emission of carriers from deep impurity bound states into the continuum is usually accomplished by thermal activation of the vibration system. The system of local vibrations plus electron is characterised by two configuration potentials: the potential $U_1(x)$ which is adiabatic potential corresponding to the electron bound on the defect and the potential $U_2(x)$ which is potential energy of vibrations in the absence of electron on the defect (x - configuration co-ordinate of vibrations, see Fig.1.) the energy distance between minima of potentials $U_1(x)$ and $U_2(x)$ is a thermal binding energy ε_T.

Thermoactivated tunnel ionisation is thermal excitation to the energy level of E_1 with the following transition between two states: state 1 in which the system has an energy E_1 in adiabatic potential $U_1(x)$ and an electron is bound on the defect and state 2 in which local vibrations have energy E_2 in potential $U_2(x)$ and the electron on the defect is absent.

In the presence of an electric field this transition can be splitted in two stages: a) the transition from the state 1 to the state in which local vibration have energy E_2 in the potential $U_2(x)$ and electron has an energy on the defect equal to $-\varepsilon$ and b) the transition of electron under the action of electric field from the state on the defect with binding energy of ε into the free state. The transition a) occurs without help of electric field and the transition b) without action of vibrations. The transition a) is tunnelling of the defect vibration system between configuration potentials $U_1(x)$

and $U_{2\varepsilon}(x) \equiv U_2(x) - \varepsilon$ with the conservation of energy of the system, so that $E_1 - \varepsilon_T = E_2 - \varepsilon$ (see Fig.1).

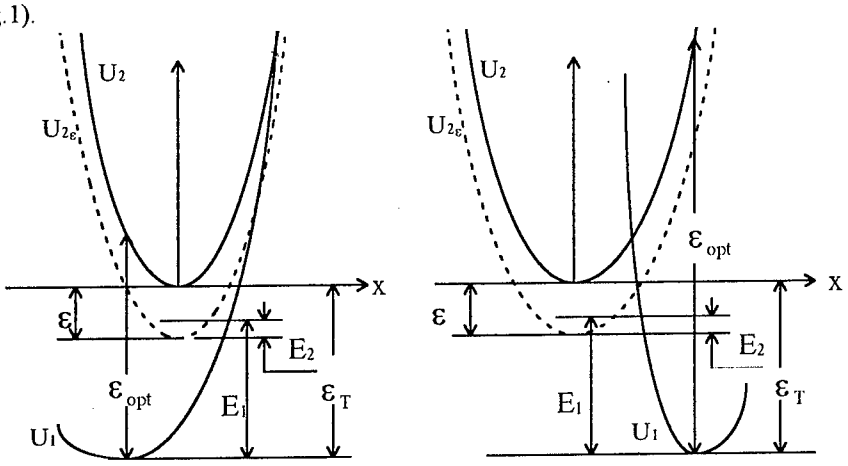

Fig.1 Two cases of adiabatic potential configurations corresponding to weak (a) and strong (b) interaction between electron and local vibrations. It is shown the thermal activation energy ε_T, the optical ionization energy ε_{opt}, the activation level of vibration system E_1, and electron energy $-\varepsilon$ for multiphonon tunnel process.

In semiclassical approximation, neglecting pre-exponential factors, the probability of such a transition is given by [10]:

$$P_{a)} \propto \exp -2(S_2 - S_1); \qquad S_i(E_i) = \frac{\sqrt{2M}}{\hbar} \int_{a_i}^{x_c} dx \sqrt{U_i(x) - E_i}, \tag{1}$$

where i = 1, 2, M is a mass corresponding to the given type of vibration, a_i is the turning point in potential $U_i(x)$ at the vibration energy E_i, and x_c is the meeting point of potentials $U_1(x)$ and $U_{2\varepsilon}(x)$. We assume that the position of adiabatic potentials corresponds to Fig.1a or Fig.1b.

The probability of electron tunnel transition b) under the action of alternating electric field F has been theoretically considered by Keldysh [11] (see also [10]).

$$P_{b)} \propto \exp(-2S_e(\varepsilon)) \tag{2}$$

where

$$S_e(\varepsilon) = -\frac{\varepsilon}{\hbar}\int_0^{\tau_e}\frac{1}{\gamma^2}\mathrm{sh}^2(\Omega\tau)d\tau + \frac{\varepsilon\tau_e}{\hbar}, \tag{3}$$

$$\gamma \equiv \sqrt{2m^*\varepsilon}\Omega / eF; \qquad \mathrm{sh}(\Omega\tau_e) = \gamma \tag{4}$$

Here m^* and e are the effective mass and the charge, respectively, and $\tau_e = \hbar\partial S_e / \partial\varepsilon$ has a meaning of electron tunnelling time. Equations (2-4) can be applied if $\varepsilon >> \hbar\Omega$.

The ionisation probability can be presented in the form:

$$e(F) \propto \iint P_{a)}P_{b)}\exp(-E_1 / k_BT)d\varepsilon dE_1 \tag{5}$$

where T is the temperature and k_B is the Boltzmann constant.

Integral (5) can be calculated by using saddle point method. In the case of relatively weak fields, saddle energy $\varepsilon << \varepsilon_T$. In this case exponent index can be expanded in a power series of ε. Taking into account that $E_1 - \varepsilon_T = E_2 - \varepsilon$, we obtain:

$$S_2 - S_1 \cong (S_2 - S_1)_{|_{\varepsilon=0}} - \varepsilon\frac{\tau_2}{\hbar}; \qquad \tau_2 = \hbar\left|\frac{\partial S_2}{\partial\varepsilon_2}\right|_{\varepsilon=0} \tag{6}$$

and the saddle point condition gives

$$\tau_2 = \tau_e; \qquad \tau_2 = \frac{\hbar}{2k_BT} \pm \tau_1 \tag{7}$$

where $\tau_1 = \hbar|\partial S_1 / \partial\varepsilon_1|_{\varepsilon=0}$. The upper and the lower signs are related to configuration shown in Fig. 1a and Fig. 1b, correspondingly. The first equation in (7) means that the electron tunnelling time coincides with the defect tunnelling time of the vibration system under the potential $U_2(x)$ and the second equation determines the temperature dependence of the tunnelling time τ_2, because τ_1 is practically independent of the temperature. Equations (4) and (7) allow to find the value of the optimal electron tunnelling energy ε:

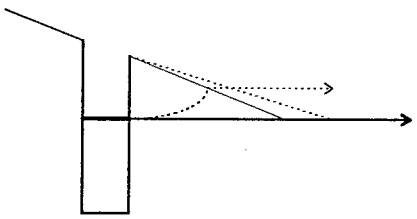

Fig.2 Schematic picture of electron tunneling under (—) dc and (····) ac electric field.

$$\varepsilon = e^2F^2\sinh^2(\Omega\tau_2) / 2m^*\Omega^2. \tag{8}$$

Finally we obtain for the ionisation probability:

$$e(F) = e(0)\exp\left(\frac{F^2}{F_c^2}\right); \qquad F_c^{*2} = \frac{3m^*\hbar}{e^2\tau_2^{*3}} \tag{9}$$

and

$$\tau_2^{*3} = \frac{3}{4\Omega^3}\left[\sinh(2\Omega\tau_2) - 2\Omega\tau_2\right] \tag{10}$$

At $\Omega\tau_2 << 1$ it follows from Eq. (10) $\tau_2^* = \tau_2$ and Eq. (9) transforms in result for dc field [5]. With increase of frequency τ_2^* increases exponentially which enhances tunnelling. The enhancement takes place due to absorption of field by the tunnelling electron (see Fig.2). One can see from Eqs. (8)-(9) that the frequency effect appears when $\Omega\tau_2 \geq 1$. According to Eqs.(7) the tunnelling time τ_2 is equal to the electron tunnelling time τ_e. Thus, the opposite condition $\Omega\tau_2 < 1$ means that the electric field does not change during the time of electron tunnelling τ_e. Naturally, in this limit the ionisation rate is independent of the electric field frequency. The time τ_2 increases with the temperature decrease and, therefore, the high frequency effect is better observed at low temperature.

Ionisation at low temperature.

With the decrease of the temperature, we arrive at the case, when thermal activation becomes practically impossible and ionisation can occur only from the bottom of the potential $U_1(x)$. For this case, the positions of adiabatic potentials $U_1(x)$ and $U_{2c}(x)$ are presented in Fig.3. With the rise of electric field , the potential $U_{2\varepsilon}(x)$ transforms from position 1 to the position 2.

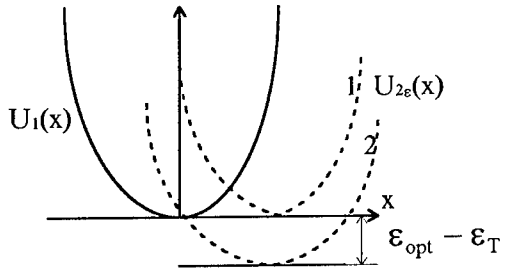

Fig.3 Adiabatic potentials corresponding to ionization at low temperature. Potential $U_{2\varepsilon}(x)$ should be situated between curves 1 and 2.

In position 2 (see Fig.3), the tunnelling of vibration system is absent and the ionisation takes place due to direct electron tunnelling from the ground state. In this case the ionisation rate $e(F) \propto P_b$ is determined by Eqs.(2) and (4) in which $\varepsilon = \varepsilon_{opt}$, ε_{opt} being the optical ionisation energy (see Fig.1). In relatively weak electric field ($\gamma > 1$), we get that the ionisation probability is given by

$$e(F) \propto \exp\left\{-\frac{\varepsilon_{opt}}{\hbar\Omega}\left[\ln\frac{8m\varepsilon_T\Omega^2}{e^2F^2} - 1\right]\right\}. \qquad (11)$$

In the opposite limit of high electric field $\gamma << 1$, the frequency dependence of ionisation probability is absent and

$$e(F) \propto \exp\left\{-\frac{4}{3}\frac{\varepsilon_{opt}^{3/2}\sqrt{2m}}{\hbar eF}\right\} \qquad (12)$$

In the position 1 (see Fig.3), the ionisation is accompanied by the tunnelling of vibration system. Here, the electron tunnelling takes place under lower barrier ($\varepsilon = \varepsilon_T$, see Fig.2). In the case of weak electron phonon interaction the difference between ε_{opt} and ε_T can be neglected.

In consideration presented above, we have not taken into account the discreteness of local vibration spectrum. The discreteness may induce the oscillation of ionisation rate, as function of electric field. The best condition for the observation of these oscillations should take place at low temperature and

for defects with strong electron-local vibration interaction (for example for DX-centers in III-V semiconductors).

Conclusion

In conclusion, we have shown that the ionisation rate increases with the increase of electric field frequency. High-frequency effect manifests itself better at low temperature.

Financial support by a grant of Russian Foundation of Fundamental Investigation is gratefully acknowledged.

References

1 A.F.Tasch, Jr. and C.T.Sah, Phys.Rev.**B1**, 800 (1970).
2 J.W.Walker and C.T.Sah, Phys.Rev. **B8**, 5597 (1973).
3 K.Irmscher, H.Klose and K.Maass, Phys.Status Solidi (a) **75**, K25 (1983).
4 S.Makram-Ebeid and M.Lannoo, Phys.Rev.**B25**, 6406 (1982).
5 V.Karpus and V.I.Perel, Zh.Eksp. Teor. Fiz. **91**, 2319 (1986) [Sov.Phys.JETP, **64**, 1376, (1986)].
6 V.N.Abakumov, V.I.Perel and I.N.Yassievich "Nonradiative Recombination in Semiconductors" ed. V.M.Agranovich and A.A.Maradudin Modern Problems in Condensed Matter Sciences Vol.**33** (North-Holland, Amsterdam 1991).
7 S.D.Ganichev, W.Prettl and P.G.Haggard Phys.Rev.Letters **71**, 3882, 1993.
8 S.D.Ganichev, I.N.Yassievich, W.Prettl, J.Dinner, B.K.Meyer and K.W.Benz Phys.Rev.Letters **75**, 1590, 1995.
9 S.D.Ganichev, I.N.Yassievich, W.Prettl, Semicond.Sci.Technol. **11**,679,1996.
10 L.D.Landau and E.M.Lifshitz Quantum Mechanics, Oxford, Pergamon 1977.
11 L.V.Keldysh Sov.Phys.Jetp, **20**, 1304, 1965.

Materials Science Forum Vols. 258-263 (1997) pp. 1287-1292

LONG-RANGE LATTICE RELAXATION FOR DONOR CENTERS IN SUPERCELL METHOD

S. Bednarek and J. Adamowski
Faculty of Physics and Nuclear Techniques, Technical University (AGH), 30-059 Kraków, Poland

Keywords: donor centers, lattice relaxation, supercell approximation.

Abstract. An application of the supercell approximation to point defects in semiconductors leads to the problems connected with a description of a lattice deformation around the defect. In the present paper, these problems are discussed in the framework of the phonon representation for the displacements of lattice ions with LA and LO phonons taken into account. The displacements of ions around the D^0 and D^- donor centers and their contribution to the total energy of the donor-relaxed lattice system have been calculated as a function of the size of the supercell for GaAs, GaN, GaP, AlAs, CdS, CdTe, ZnSe, ZnTe, CuBr, and CuCl. It is shown that the correct treatment of the lattice relaxation resulting from the long-range polar interaction with LO phonons requires the application of the supercell, which consists of several thousands of atoms. The induced long-range lattice relaxation is important even for the strongly localized donor states. It is argued that small supercells do not allow us to compare the energies of donor centers with different charge or electron localization.

1. Introduction

In *ab initio* calculations for point defects, a supercell approximation is usually applied. In this approximation, the point defect with its nearest neighborhood, which consists of the host-lattice ions, is periodically repeated in space, which allows us to introduce the periodic boundary conditions. The results of calculations performed within the supercell method are applicable to single (isolated) defects if the size of the supercell is sufficiently large in order to neglect the interaction with defects in the neighboring supercells. Therefore, the supercell method is suitable to a description of defect states, the electronic wave functions of which are strongly localized, i.e., spread over only on the nearest-neighbor ion distance, and the accompanying lattice deformation is short-range, i.e. only a few ions close to the defect are shifted from equilibrium positions [1-7].

It appears however that the donor impurities in semiconductors are surrounded by the lattice deformation having a long-range component [8-9]. The corresponding lattice relaxation energy depends on a charge state of the donor and a degree of the electron wave function localization. The contributions of this deformation to the donor binding energy are considerably different for different donor states. In the present paper, we consider the neutral (D^0) and negatively charged (D^-) donor centers of strong electron localization. We discuss the problem of distribution, range, and energy of the lattice deformation around the donor centers as well as their influence on the quality of calculations performed within the supercell approximation.

2. Theory

Shallow-level donor centers of weak and strong electron localization can be described with the help of the method elaborated by us [8-10] for isolated defects. In the present paper, we extend this method to a system of many defect centers in a crystal. The electrons are described in the one-band approximation and the crystal-lattice deformation – in the phonon representation. We will adopt a supercell approximation to our approach. For this purpose, we consider the

system consisting of many impurity centers, which is described by the Hamiltonian

$$H = \sum_{\vec{k}\sigma} E^c_{\vec{k}} b^\dagger_{\vec{k}\sigma} b_{\vec{k}\sigma} + \sum_{\vec{k}\vec{k}'\sigma j} V^{ed}_{\vec{k}\vec{k}'} e^{i(\vec{k}-\vec{k}')\cdot\vec{R}_j} b^\dagger_{\vec{k}\sigma} b_{\vec{k}\sigma} + \sum_{\vec{k}\vec{k}'\vec{q}\sigma\sigma'} V^{ee}_{\vec{q}} b^\dagger_{\vec{k}+\vec{q}\sigma} b^\dagger_{\vec{k}'-\vec{q}} b_{\vec{k}'\sigma'} b_{\vec{k}\sigma} + \sum_{\vec{q}s} \hbar\omega_{\vec{q}s} a^\dagger_{\vec{q}s} a_{\vec{q}s} + \sum_{\vec{q}s\sigma} (F_{\vec{q}s} a_{\vec{q}s} b^\dagger_{\vec{k}+\vec{q}\sigma} b_{\vec{k}\sigma} + H.c.) , \quad (1)$$

where $b^\dagger_{\vec{k}\sigma}$ and $b_{\vec{k}\sigma}$ are the operators of creation and annihilation of the one-electron Bloch state with energy $E^c_{\vec{k}}$, wave vector $\vec{k}$, and spin σ, $a^\dagger_{\vec{q}s}$ and $a_{\vec{q}s}$ are the creation and annihilation operators of one-phonon state with energy $\hbar\omega_{\vec{q}s}$, wave vector $\vec{q}$, and branch index s. We take into account the phonon branches s = LA, LO. $V^{ed}_{\vec{k}\vec{k}'}$ corresponds to the electron-donor center interaction and includes the long-range Coulomb potential screened by the static dielectric constant and short-range potential, which results from the exchange of atomic cores and donor-LA phonon interaction. $V^{ee}_{\vec{q}}$ is the Fourier transform of the electron-electron interaction potential, i.e., Coulomb potential screened by the high-frequency dielectric constant. The amplitudes of the electron-phonon interaction $F_{\vec{q}s}$ are taken on in the Fröhlich form for the LO phonons and – in the deformation-potential form for the LA phonons. The vectors $\vec{R}_j$ determine the positions of impurity centers at the substitutional sites, which can be arbitrarily distributed over the crystal. Hamiltonian (1) is obtained from the starting one [8] using the Platzman transformation, which eliminates the coupling of the phonon field with the impurity centers. The results of calculations with this Hamiltonian yield the relative lattice deformation around the impurity centers determined with respect to that with all the impurity centers being ionized [8, 9].

We consider the following two charge states of the donor impurity: neutral state D^0 and negatively charged state D^-, both with the strong electron localization. We assume that all the impurity centers in the crystal are in the same state D^α ($\alpha = 0, -$) and solve the eigenproblem for the ground state of Hamiltonian (1) by the variational method. We propose the trial state vector as the product $|\Psi^\alpha\rangle = |\psi^\alpha\rangle\,|\chi^\alpha\rangle$ of the electron state vector $|\psi^\alpha\rangle$ by the phonon state vector, which is taken on in the form

$$|\chi^\alpha\rangle = \exp\left(\sum_{\vec{q}s} g^\alpha_{\vec{q}s} a^\dagger_{\vec{q}s} - H.c.\right) |0\rangle_{ph} , \quad (2)$$

where $g^\alpha_{\vec{q}s}$ are the phonon amplitudes and $|0\rangle_{ph}$ is the phonon vacuum state. The electron states have been proposed in the following forms:

$$\left|\psi^0\right\rangle = \prod_j \sum_{\vec{k}} \varphi^0_{\vec{k}} e^{i\vec{k}\cdot\vec{R}_j} b^\dagger_{\vec{k}} |0\rangle_{el} , \quad (3)$$

for the neutral (D^0) donor center, and

$$\left|\psi^-\right\rangle = \prod_j \sum_{\vec{k}\vec{k}'} \varphi^-_{\vec{k}} \varphi^-_{\vec{k}'} e^{i(\vec{k}+\vec{k}')\cdot\vec{R}_j} b^\dagger_{\vec{k}\uparrow} b^\dagger_{\vec{k}'\downarrow} |0\rangle_{el} , \quad (4)$$

for the D^- center, where $|0\rangle_{el}$ denotes the electron vacuum state and the spin indices are omitted in Eq. (3). We assume that the ground state of the D^- center corresponds to the spin-singlet state. In Eqs. (3) and (4), the coefficients $\varphi^\alpha_{\vec{k}}$ are taken on in the form of Fourier transforms of exponential functions, i.e., $\varphi^\alpha_{\vec{k}} = C(k^2 + \lambda^2)^{-2}$, where C is the normalization constant and λ is the variational parameter, which determines a degree of localization of the electron. Ansatz (3) is a good approximation for the strongly localized states, for which the overlap of wave functions of the electrons bound to different centers is negligibly small.

The expectation values of Hamiltonian (1) have been calculated for the states $|\Psi^0\rangle$ and $|\Psi^-\rangle$ and minimized with respect to the phonon amplitudes $g^\alpha_{\vec{q}s}$, which leads to

$$g^\alpha_{\vec{q}s} = -Z^\alpha f^*_{\vec{q}s} \varrho^\alpha_{\vec{q}} \sum_j e^{i\vec{q}\cdot\vec{R}_j} \quad , \tag{5}$$

where Z^α is the number of electrons bound to the donor center, i.e., $Z^0 = 1$ and $Z^- = 2$, $f_{\vec{q}s} = F_{\vec{q}s}/\hbar\omega_{\vec{q}s}$, and

$$\varrho^\alpha_{\vec{q}} = \sum_{\vec{k}} \varphi^{\alpha *}_{\vec{k}} \varphi^\alpha_{\vec{k}+q} \, . \tag{6}$$

The lattice relaxation energy is calculated as the expectation value of the Hamiltonian of noninteracting phonons H_{ph}, i.e., the fourth term in Eq. (1),

$$E^\alpha = \langle \Psi^\alpha | \, H_{ph} \, | \Psi^\alpha \rangle = \sum_{\vec{q}s} \hbar\omega_{\vec{q}s} \left| g^\alpha_{\vec{q}s} \right|^2 = (Z^\alpha)^2 \sum_{\vec{q}s} \hbar\omega_{\vec{q}s} \left| f^*_{\vec{q}s} \varrho^\alpha_{\vec{q}} \sum_j e^{i\vec{q}\cdot\vec{R}_j} \right|^2 \, . \tag{7}$$

So far, the distribution of the substitutional impurity centers in the host-crystal lattice was arbitrary. Now, we assume that the impurity centers are periodically distributed over the lattice sites. Therefore, we construct a new lattice, which is composed of the supercells. Let us consider the host-crystal lattice of zinc-blende structure. We denote by N the number of elementary cells, $\vec{R}$ – direct-lattice vectors, $\vec{G}$ – reciprocal-lattice vectors, and B – first Brillouin zone of the host-crystal lattice; while N', $\vec{R}'$, $\vec{G}'$, and B' – the corresponding quantities for the periodic structure composed of the supercells. The supercells are constructed in such a manner that the impurity centers are located at the coordinate origin and at the sites determined by $\vec{R}' = n\vec{R}$, where n is a positive integer. Then, the supercell has the volume, which is n^3 times larger than the volume of the elementary cell, and consists of $2n^3$ ions (2 ions in the cell). The number of supercells $N' = N/n^3$. The new reciprocal lattice vectors are related to the old ones as follows: $\vec{G}' = (l/n)\vec{G}$, where $l = 1, \ldots, n$. Let us notice that a part of the new reciprocal-lattice vectors belongs to the first Brillouin zone of the host crystal lattice.

For the periodic distribution of impurity centers, we can perform the summations over j and $\vec{q}$ in Eq. (7), which yields the energy of the lattice relaxation resulting from the presence of N' impurity centers. We introduce the lattice relaxation energy per one impurity center (one supercell), i.e., $E^\alpha_n = E^\alpha/n^3$, which is calculated to be

$$E^\alpha_n = N'(Z^\alpha)^2 \sum_{\vec{G}' \in B,s} \hbar\omega_{\vec{G}'s} \left| f^*_{\vec{G}'s} \varrho^\alpha_{\vec{G}'} \right|^2 \, . \tag{8}$$

This energy is dependent on the size of supercell, determined by n. We note that in the right-hand side of Eq. (8) we sum over only the new reciprocal lattice vectors, which belong to the first Brillouin zone of the host crystal.

3. Results

Formula (8) can be used in a discussion of a dependence of the lattice relaxation energy per one impurity center on the supercell size applied in calculations. For this purpose, we exploit an example of strongly localized D^0 and D^- donor states in GaAs, using the parameters determined in Ref. [10]. Fig. 1 (a) displays the energetic contributions of LA and LO phonons to the lattice relaxation calculated per one donor center as functions of supercell size. For small supercells (small n), the calculations include only a small fraction of the energy of the lattice deformation, which accompanies the isolated impurity. The displacements of ions located outside the supercell are neglected, and simultaneously the symmetric distribution of impurity centers does not allow for a relaxation of a part of ions inside the supercell. The lattice relaxation energy per one donor center increases with the increasing size of the supercell and

tends to an asymptotic value. If the lattice deformation is caused by LA phonons, then, due to the short range of the deformation-potential interaction, the asymptotic value is reached for the supercells of the moderate size, i.e., at $n = 6$, which corresponds to 432 ions in the supercell.

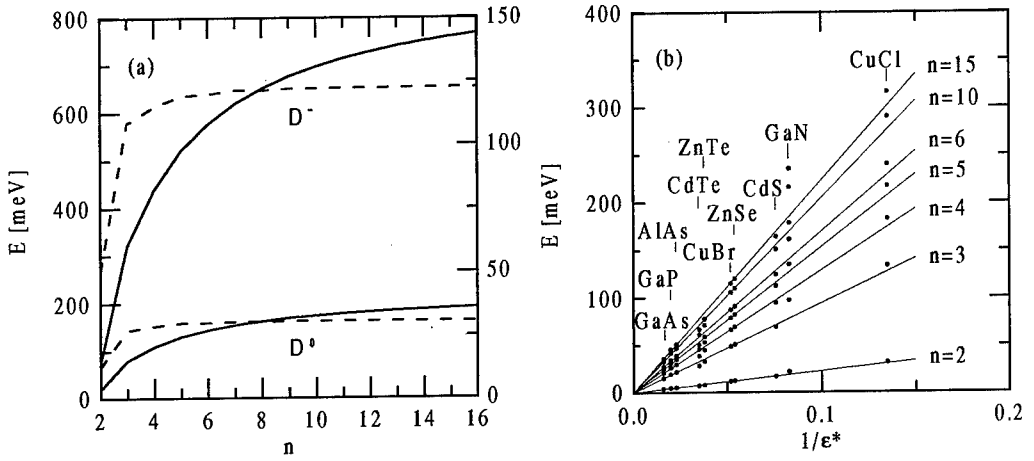

Figure 1: (a) Energy of lattice relaxation induced by LA and LO phonons associated with D^0 and D^- strongly localized donor states as a function of parameter n determining the size of supercell. Solid curves and right scale correspond to the LO phonons, dashed curves and left scale – LA phonons. (b) Energy of lattice relaxation for the strongly localized D^0 donor center resulting from electron-LO phonon coupling as a function of the inverse of the effective dielectric constant ε^* and supercell size. Dots correspond to the results of calculations for the chosen zinc-blende crystals, and straight lines – results of calculations with the values of lattice constant and parameter of electron localization taken to be the same as for GaAs.

The polar interaction via the exchange of LO phonons is long-range; therefore, the incorporation of the lattice relaxation resulting from this interaction requires the supercells of considerably larger size. This is visible in Fig. 1 (a), in which the curve corresponding the D^- center is still growing even at $n = 16$, i.e., for 8192 ions in the supercell.

The error of the estimates of the lattice relaxation energy, which results from the application of finite supercells, should be compared with the difference between the corresponding donor energy levels. The energy levels of the D^0 and D^- donor centers in GaAs have been calculated in Refs. [8, 9] in agreement with experiment. They differ between themselves by about 50 meV. The comparable accuracy for the lattice relaxation energy is reached with the use of supercells consisting of 1000 – 2000 atoms.

In the *ab initio* calculations [1-7], the energies of donor states in GaAs were calculated by the supercell method with the use of supercells, which contained from 18 to 64 atoms. These numbers of atoms are definitely too small in order to include the full relaxation of the crystal lattice. This affects the interpretation of the results of Refs. [1-7]. It is not possible to compare the energies of the defect states with different localization and/or charge. In particular, the application of small supercells does not allow us to determine the relative positions of energy levels of the D^0 donor center with respect to those of the D^- center. Nevertheless, the comparison of energy levels can be justified for the states of similar localization and the same charge, e.g., the ground-state energies of D^- centers in substitutional and interstitial positions [1-7]. For these centers, only the shifts of the nearest-neighbor ions considerably differ between themselves, but the long-range lattice deformation should be similar. Among the papers known to us, only in Ref. [11], the large enough cluster of atoms (1800 atoms) was applied to the

calculation of metastable donor states in CdF_2. However, the approach [11] is not an *ab initio* method, since it applies the empirical potentials of ions.

If we consider the polar crystals with the strong electron-LO phonon coupling, we obtain a considerable increase of the long-range lattice deformation in comparison to that for GaAs. In order to show this effect we concentrate our attention on the lattice deformation, which is associated with LO phonons. Substituting the electron-LO phonon interaction amplitude into Eq. (8), we get for the D^0 donor center

$$E_n^0 = \frac{2\pi e^2 N'}{\Omega \varepsilon^*} \sum_{\vec{G}' \in B} \frac{\left(\varrho^0_{\vec{G}'}\right)^2}{\vec{G}'^2} . \tag{9}$$

The expression in right-hand side of Eq. (9) consists of the three parameters: effective dielectric constant $\varepsilon^* = (\varepsilon_0 - \varepsilon_\infty)/\varepsilon_0\varepsilon_\infty$, where ε_0 (ε_∞) is the static (high-frequency) dielectric constant, lattice constant a, which is used in calculations of the reciprocal lattice vectors $\vec{G}'$, and electron localization parameter λ, which is included in the electron probability density $\varrho^0_{\vec{G}'}$ and is obtained from the calculations of donor energy levels. The polar properties of the material are determined by the effective dielectric constant ε^*. The relative differences between the lattice constants of zinc-blende crystals do not exceed 20%. For the strongly localized donor states, the localization parameter takes on similar values (λ = 0.3 - 0.7 of the reciprocal hydrogen Bohr radius). Therefore, the energy of the LO-phonon induced lattice relaxation is mainly determined by the effective dielectric constant and is inversely proportional to ε^*.

A bunch of straight lines in Fig. 1 (b) shows the dependence of the energy of the lattice relaxation associated with LO phonons on the size of supercell and the effective dielectric constant. The values of the lattice constant and electron localization parameter have been taken to be the same as those for the D^0 donor state in GaAs. The dots correspond to the lattice relaxation energy calculated for several zinc-blende semiconductors. The deviations of the positions of the dots from the straight lines result from taking into account the values of a and λ, appropriate for the considered semiconductors. In Fig. 1(b), we have also included the results for GaN, in spite of the fact that this material usually crystallizes in the wurtzite structure. However, GaN forms crystals of the zinc-blende structure as well. Defects in GaN have recently been studied by the supercell method [12, 13]. Fig. 1 (b) can be helpful if we want to determine how large supercell has to be used in order to include the lattice deformation associated with the donor center with the required accuracy. Fig. 1 (b) displays the lattice relaxation energy around the one-electron D^0 center calculated with respect to that of the ionized (positively charged) donor center. For the two-electron D^- donor center, the corresponding energy is four times larger [cf. Eq. (8)]. For CuCl, which is the most strongly polar among the considered materials, the difference between the lattice relaxation energy calculated with the supercell with n = 10 (2000 ions) and n = 15 (6750 ions) is estimated to be 26 meV for the D^0 center, and about 100 meV for the D^- center. Such corrections to the relaxation energy cannot be neglected in many applications. Therefore, the results of calculations, performed within the supercell approximation for the polar materials, should be treated with a large caution. This remark is valid not only for the donor centers but also for all these point defects, whose electronic states are formed from the conduction-band states.

4. Conclusions

In semiconducting compounds, the long-range component of the lattice deformation, which is associated with both the strongly and weakly localized impurity states, makes it difficult to describe the point defects with the use of the supercell method. When using a typical supercell, which includes no more than a hundred of ions, we neglect a considerable energetic contribution to the lattice relaxation, which originates from the remote ions located outside the supercell. The lattice deformation caused by the electron-LA phonon interaction possesses the moderate

range. In order to describe this deformation correctly, the supercell consisting of a few hundreds of ions is sufficiently large. However, the correct description of the lattice relaxation resulting from the interaction with LO phonons requires the application of the supercell, which consists of several thousands of ions. Such large supercells are especially important in the polar crystals. The range of lattice deformation and its energetic contribution should be taken into account when planning large-scale *ab initio* calculations with the help of the supercell method and when interpreting their results.

In summary, the present paper shows that the long-range phonon-induced lattice relaxation is important even for the strongly localized impurity centers. We have determined the size of the supercell required for performing the reliable *ab initio* calculations for the point defects.

Acknowledgments
This work has been partially supported by the Polish Scientific State Committee (KBN).

References

[1] D.J. Chadi and K.J. Chang, Phys. Rev. B **39**, 10063 (1989).

[2] S.B. Zhang and D.J. Chadi, Phys. Rev. B **42**, 7174 (1990).

[3] D.J. Chadi, Phys. Rev. B **46**, 6777 (1992).

[4] J. Dąbrowski and M. Scheffler, Materials Sci. Forum **83-87**, 735 (1992).

[5] E. Yamaguchi, K. Shiraishi, and T. Ohno, J. Phys. Soc. Japan **60**, 3093 (1991).

[6] T.M. Schmidt, A. Fazzio, and M.J. Caldas, Phys. Rev. B **53**, 1315 (1996).

[7] T.M. Schmidt and M.J. Caldas, in "Proc. 23rd Int. Conf. on the Physics of Semiconductors", ed. M. Scheffler and R. Zimmermann (Singapore: World Scientific, 1996), pp. 2745-2748.

[8] S. Bednarek and J. Adamowski, in "Proc. 7th Int. Conf. on Shallow-Level Centers in Semiconductors", ed. C.A.J. Ammerlaan and B. Pajot (Singapore: World Scientific, 1997), pp. 55-66.

[9] S. Bednarek and J. Adamowski, in "Proc. 23rd Int. Conf. on the Physics of Semiconductors", ed. M. Scheffler and R. Zimmermann (Singapore: World Scientific, 1996), pp. 2781-2784.

[10] S. Bednarek and J. Adamowski, Phys. Rev. B **55**, 2195 (1997).

[11] Y. Cai and K.S. Song, J. Phys.: Condens. Matter **7**, 2275 (1995).

[12] T. Mattila, A.P. Seitsonen, and R.M. Nieminen, Phys. Rev. B **54**, 1474 (1996).

[13] P. Bogusławski and J. Bernholc, in "Proc. 23rd Int. Conf. on the Physics of Semiconductors", ed. M. Scheffler and R. Zimmermann (Singapore: World Scientific, 1996), pp. 2889-2892.

Still available:

Defects in Semiconductors: ICDS-18
Eds. M. Suezawa and H. Katayama-Yoshida
ISBN 0-87849-716-1: 2268 pp, 4-vol. set (1996), CHF 600.00 / US$ 500.00
Proc. of the 18th Intl. Conference on Defects in Semiconductors, Sendai, Japan, 1995. The study of defects in semiconductors has never been independent of the progress in semiconductor technology. With rapid development in semiconductor device technology, novel types of defects as well as very peculiar behavior of defects in semiconductors have been found one after another. New subjects in the basic study of defects have often been arisen from experiences in the practical field. Great progress has also been achieved in device production technology on the basis of the knowledge clarified in the basic field.

The present publication presents a very comprehensive array of subjects, ranging from basic aspects of defect properties to practically important phenomena related to device production engineering. Among them, hydrogen-related problems, defects and impurities in GaN and related widegap semiconductors and grown defects in Czochralski-grown silicon may be regarded as highlights.

Contents Sections:

Materials-Related Defects and Dopants / Defects and Impurities in Low-Dimensional Structures / Special Defects / New Experimental Techniques / Defect-Related Phenomena / Technologically Important Problems.

Defects in Semiconductors: ICDS-17. Eds. H. Heinrich & W. Jantsch
ISBN 0-87849-671-8: 1722 pp, 3-vol. set (1994), CHF 520.00 / US$ 433.00
Proc. of the 17th Intl. Conference, Gmunden, Austria, 1993

Defects in Semiconductors: ICDS-16. Eds. G. Davies, G.G. DeLeo & M. Stavola
ISBN 0-87849-628-9: 1634 pp, 3-vol. set (1992), CHF 520.00 / US$ 433.00
Proc. of the 16th Intl. Conference, Lehigh University, USA, 1991

Defects in Semiconductors: ICDS-15. Ed. G. Ferenczi
ISBN 0-87849-584-3: 1506 pp, 3-vol. set (1989), CHF 520.00 / US$ 433.00
Proc. of the 15th Intl. Conference, Budapest, Hungary, 1988

Defects in Semiconductors: ICDS-14. Eds. H.J. von Bardeleben
ISBN 0-87849-551-7: 1722 pp, 3-vol. set (1986), CHF 480.00 / US$ 400.00
Proc. of the 15th Intl. Conference, Paris, France, 1986

The well-known ICDS conferences cover a broad range of topics in the fundamental science of imperfections in semiconductor materials, including the creation and/or origin, structure, electronic, optical, thermodynamical and chemical properties of defects.

Trans Tech Publications Ltd
Brandrain 6 • CH-8707 Uetikon-Zuerich • Switzerland
Fax +41 (1) 922 10 33 • e-mail: ttp@ttp.ch
http://www.ttp.ch

Your Direct Access

World Wide Web

Please visit us on the World Wide Web at

http://www.ttp.ch

where detailed information on all published titles is provided as well as:

- Online Shopping!
- Site Search!
- Full Tables of Contents!
- New & Forthcoming Titles!
- Periodicals & Book Series!
- Preview Service!
- Download Area!

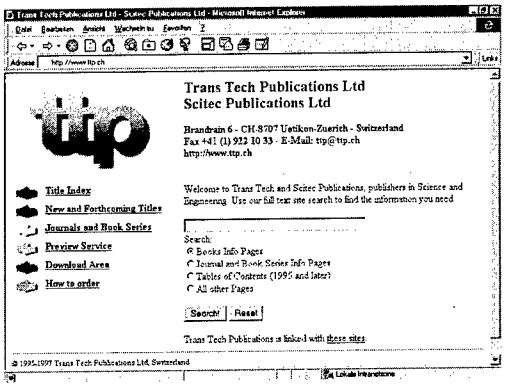

TTP Preview Service

Trans Tech Publications' preview service offers automatic delivery by e-mail of information on new books and periodical issues, including tables of contents - several weeks before the actual release of the respective publication.

Included are the following periodicals and book series:

- Advanced Manufacturing Forum
- Defect and Diffusion Forum
- Environmental Research Forum
- GeoResearch Forum
- Key Engineering Materials
- Materials Science Forum
- Molten Salt Forum
- Production and Logistics Forum
- Solid State Phenomena

This service is free of charge. For details please send an e-mail message containing the line
help
to **preview@ttp.ch**
or register online at http://www.ttp.ch

For regular e-mail please use the address **ttp@ttp.ch**

Trans Tech Publications Ltd
Brandrain 6 • CH-8707 Uetikon-Zuerich • Switzerland
Fax +41 (1) 922 10 33 • e-mail: ttp@ttp.ch
http://www.ttp.ch

Materials Science Forum

ISSN 0255-5476

As of January 1992 combined with Crystal Properties and Preparation

Editors, Editorial and Advisory Board

see front inside cover

Scope

Materials Science Forum specializes in the rapid publication of international conference proceedings in every area of Materials Science, Solid State Physics and Chemistry. This permits such proceedings to be conveniently referenced, abstracted and read. It also guarantees that the proceedings are available in major libraries within two to three months of the close of the conference.

Materials Science Forum also publishes, on a regular basis, collections of research and review papers on topics of current interest. Abstracted in all of the major abstract media, and available in practically all of the major libraries which service materials research communities, *Materials Science Forum* offers both very rapid publication (within two months of acceptance of the manuscript) and high visibility.

Internet

The table of contents of each volume is available on the World Wide Web at http://www.ttp.ch/perdcs/msf.htm.

Preview Service

Trans Tech Publications' Preview Service offers automatic delivery of tables of contents via e-mail - several weeks before the actual release of the respective publication. This service is free of charge. For more information, please visit our home page or send an e-mail to preview@ttp.ch containing simply the word *help* as the message body.

Subscription Information

Materials Science Forum is published in 30 volumes per year. In 1997, volumes 233-262 are scheduled to be published. The subscription rate is CHF 99.50 per volume (CHF 2985.00 per year).

Standing orders

Standing Orders are available for the following topical areas of interest: Pt. A: Electronic and Electro-optic Materials; Pt. B: Metal Physics; Pt. C: Ceramic Materials and Glasses; Pt. D: Ionic Materials, Oxides; Pt. E: Corrosion and Oxidation; Pt. F: Surfaces, Interfaces and Thin Films; Pt. G: Crystal Growth and Crystal Structures.

Standing orders for one or more of these sections may be placed: the topics are not meant to be exclusive, i.e. a given volume can be assigned to two or more of these sections. Should a title be assigned to more than one section, the subscriber will receive the respective title only once. The price per volume is CHF 99.50.

Trans Tech Publications Ltd

Brandrain 6 • CH-8707 Uetikon-Zuerich • Switzerland

Fax +41 (1) 922 10 33 • e-mail: ttp@ttp.ch

http://www.ttp.ch